Yusheng Xue
Yuping Zheng
Antonio GÓMEZ-EXPÓSITO   *Editors*

Proceedings of the 7th PURPLE MOUNTAIN FORUM on Smart Grid Protection and Control (PMF2022)

Springer

Proceedings of the 7th PURPLE MOUNTAIN FORUM on Smart Grid Protection and Control (PMF2022)

Yusheng Xue · Yuping Zheng ·
Antonio Gómez-Expósito
Editors

Proceedings of the 7th PURPLE MOUNTAIN FORUM on Smart Grid Protection and Control (PMF2022)

Editors
Yusheng Xue
NARI Group Co., Ltd.
Nanjing, Jiangsu, China

Yuping Zheng
NARI Group Co., Ltd.
Nanjing, Jiangsu, China

Antonio Gómez-Expósito
Department of Electrical Engineering
University of Sevilla
Seville, Spain

The excellent papers of the conference will be recommended to «Journal of Modern Power Systems and Clean Energy», «Automation of Electric Power Systems» for publication.

Contents

x　　　Contents

Design and Implementation of Twin Operation and Maintenance System for Power Grid Dispatching and Control System

Lacheng Pang[1], Xiaosong Zhu[2(✉)], Li Zhao[2], Shuibao Han[3], Zhanhua Lin[2], and Wenzong Liu[2]

[1] NARI Nanjing Control Systems Co., Ltd, Nanjing 211106, China
[2] Beijing Kedong Electric Power Control System Co., Ltd, Beijing 100192, China
chris.zhu@163.com
[3] Central China Branch of State Grid Corporation of China, Wuhan 430077, China

Abstract. Lack of real verified environment and difficult remote maintenance are two main challenges for power grid dispatching and control system, in this paper, we approached these challenges by constructing a digital twin operation and maintenance system based on virtualization technology. It migrates all application nodes of the control system to virtual hosts by P2V technology, sets embedded monitoring probes and does regular synchronization between the control system and the twin system, adopts the virtualized snapshot and clone technology to provide a multi-copy and multi-branch test environment for the twin operation and maintenance system, hundreds of virtual images are grouped to realize the centralized management of multiple twin operation and maintenance systems on the same platform. The system migration, synchronization, version management and centralized management of multiple twin systems are then completed on an experimental system. The experimental results demonstrate that the proposed twin platform can provide a real verification and practical environment for remote operation and maintenance.

Keywords: Digital twin · Virtualization · P2V · Snapshot · Embedded probes synchronization · Remote operation and maintenance

1 Status of Operation and Maintenance for Power Grid Dispatching and Control System

The power grid dispatching and control system is the core support system of smart grid. Since 2009, the power grid dispatching and control system D5000 has been widely used in 34 provincial and above dispatching control centers and hundreds of ground dispatching control centers [1–5]. As more and more power grid dispatching and control systems are put into operation, there are many more different versions and branches due to various demands. Therefore it is really nearly impossible to simulate the real online system, and perform centralized operation and maintenance for multiple systems.

There are two ways to simulate the dispatching and control systems. One is to manually build an independent test verification environment for a specific system manually, and synchronize data according to test needs. However, building a simulation test system typically requires longer leadtime and significant amount of hardware resources. The other alternative is to build a typical environment and simulate operation data to provide a general verification platform for functions and performance testing [6–9]. However, one typical environment cannot simulate the online system of different dispatching control centers. While the independent test environment can not keep evolving with the online system, some modules and even the entire system need to be rebuilt, when it is deployed to operation.

Given the recent development of Digital Twin [10–14], it provides a new perspective for building operation and maintenance systems. In addition to building twin models for power equipment [15], could we establish a twin environment for the smart grid dispatching and control system? Build a highly consistent twin operation and maintenance system, determine the embedded probes for physical system, synchronize changes during the whole life cycle of the physical system. In turn, the twin system provides a virtual consistent environment for practicing [16, 17], major changes verification,, and specific scenario reviews for the physical system.

This paper is concentrated on how to design and build a twin operation and maintenance system based on a virtualized platform. First it introduces the status and opportunities of system maintenance. In Sect. 2 it proposes two design schemes for 1:1 and 1:N twinning operation and maintenance systems to meet the needs of the dispatching control center and the remote support center. Follow up in Sect. 3, it answers three implementation questions, how to build a prototype twin system, how to maintain the consistency of the twin system, and how to provide multi-version management for the software environment. Section 4 shows the prototype of the 1: N twin operation and maintenance system. Finally, Sect. 5 concludes the apper with an outlines of future work.

2   Twin Operation and Maintenance System Design

2.1   1:1 Twin Operation and Maintenance System Design

1:1 twin operation and maintenance system is designed to fulfill the needs to build a real experimental verification environment for one real dispatching and control system. Figure 1 shows the architecture of 1:1 twin operation and maintenance system, which is composed with two parts: the twin operation and maintenance system platform and the software environment synchronization system.

The twin operation and maintenance system platform adopts open source software or domestic virtualization software to build the underlying virtualization management platform. The nodes of real dispatching and control system then migrated from physical to virtual through a migration module on the proxy server, which can find all the public nodes in the environment and migrate the whole node including operating system, applications and relevant data. After migration, the virtual machine is saved on the virtualization platform as a qemu2 image. In addition, the twin operation and maintenance
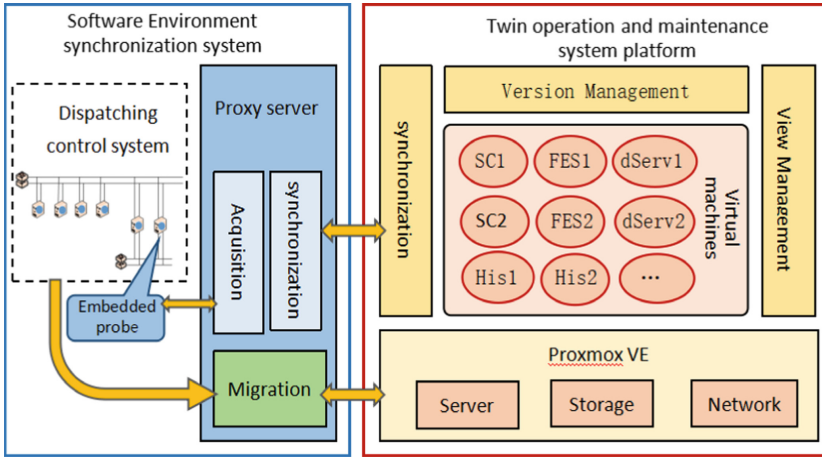
Fig. 1. Architecture diagram of twin operation and maintenance system.

system platform includes three core modules: synchronization module, version management module and view management module. The synchronization module receives the synchronous files from the software environment synchronization system and updates to the target host image by automatic matching. The version management module provides synchronous backup management and version management for virtual nodes based on snapshot. The view management module can orchestrate the virtual machines according to the application requirements, which is much convenient for user to do bulk operation on multiple virtual machines with relevant properties.

The software environment synchronization system includes several agent modules on application nodes and one acquisition module with one synchronization module on the proxy server. The acquisition module communicates with agent modules on the application nodes for probe monitor and change capture. The synchronization module regularly synchronizes the changed software environment to the twin operation and maintenance system platform in the form of files.

2.2 1:N Remote Twin Operation and Maintenance System Design

The twin operation and maintenance system platform is also designed to provide 1:N centralized remote maintenance management for multiple dispatching and control systems in the operation and maintenance center.

The remote operation and maintenance center connects the dispatching control center area III through the integrated data network. As shown in Fig. 2, there are two interacting modes: mode 1, the remote twin operation and maintenance system directly interacts with the embedded probes of the control system across the area I/III and integrated data network; mode 2, if there is a local twin operation and maintenance system, the remote twin operation and maintenance system interacts with the local twin system.

In the initial construction stage, there are many servers need to be converted. Whether it is converted from a real system by P2V (Physical to virtual) or migrated from the local
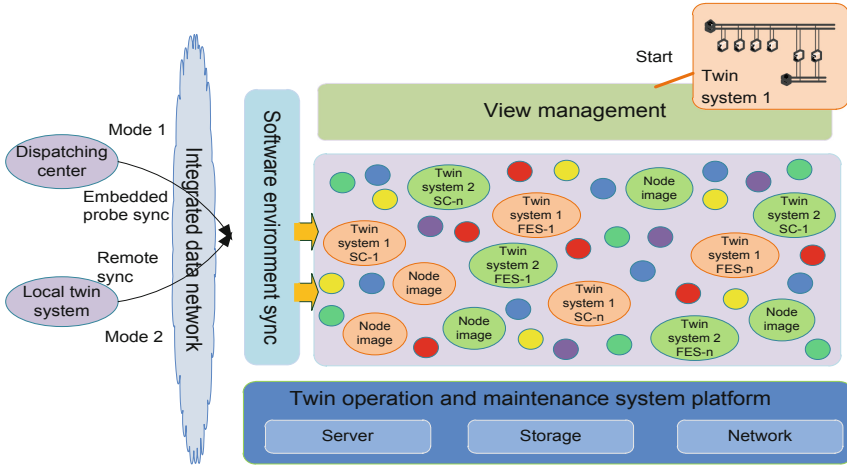
Fig. 2. Architecture diagram of remote twin operation and maintenance system.

twin system by V2V (Virtual to virtual), it is recommended to do export in the local proxy server first and do import in remote operation and maintenance after all the data is ready. If the real control system doesn't support migration, there's another way to build the virtualized environment by template installation and script-based configuration.

For the deployment of remote synchronization system, the synchronization module needs to be deployed on the proxy server in both area I and area III for mode 1. While for mode 2, a remote synchronization agent is deployed on the local twin system, and when the local twin system is synchronized, the synchronization information will also be sent to the remote twin operation and maintenance platform.

Actually not all the twin systems keep running on the twin operation and maintenance system platform. Most of them are usually saved in the platform in the state of static images. The virtual images belonging to the same control system are classified into a group, and isolated via VLAN or SDN. When the specific operation and maintenance environment needs to be started, the entire group can be startup in bulk, and the twin virtual environment is independent of each other.

3   Twin Operation and Maintenance System Implementation

3.1   Integrated Migration

To consistent with the online system in greatest extent, the P2V technology was tried for the first time in the dispatching and control system host nodes migration. The physical nodes in the running system were migrated from physical to virtual one by one. The operation system, applications and related data are exported from the hard disk as a whole image and imported into the virtual environment through the proxy server automatically [18, 19].

VMware Converter is a well-known P2V tool that converts physical machines into VMware virtual machines [20]. The twin operation and maintenance system platform

is designed on the domestic virtual platform or open source software. For example, the open source virtualization management platform Proxmox VE is used in the experimental environment, while the open source hard disk cloning tool Clonezilla is integrated to achieve the overall export and import of the hard disk or partition. At the same time, we collaborated with two domestic operating system partners in P2V development and testing. KylinSec export the hard disk into qcow2 image through qemu-img, while Beijing Linx Software do P2V through remote disk mapping and qemu-img convert. Now the image can be imported into virt-manager quickly, and the function will be integrated into the Linx cloud platform soon. The following table shows the P2V migration efficiency of three virtualized platforms (Table 1).

Table 1. Virtualization Platform P2V Comparison.

Platform	Proxmox VE	KylinSec cloud	Virt-manager (Beijing Linx)
Physical machine	OS: Rocky4.2 Disk: 600 G used: 61 G SW: SCADA	OS: Kylin 3.2 Disk: 465 G used: 21 G SW: DM 7	OS: Rocky 4.2 Disk: 500 G used: 21 G SW: MYSQL
Image size	5.7 G	9.2G	6.6 G
Export time	22 m	19 m	18 m
Import time	27 m	6 m	1 m

The system also provides a template-based migration for dispatching control centers who do not support P2V migration. First it needs to build templates for different application servers, such as scada server and db server etc., then clone the virtual nodes from the different templates, and customize the configuration parameters for auto-configure.

3.2 Embedded Probes Synchronization

To ensure the long-term consistency of the twin operation and maintenance system and the online system, some key positions of the application node are detected by agent [21]. The embedded probes include the system software versions, environment variables, system logs, and D5000 executable files, dynamic libraries, configuration files, model data, etc., and self-defined directories and files are also supported.

Figure 3 shows the entire process of embedded probes synchronization. The agent on application node collects the version information of key positions regularly and sends them to the proxy server for version comparison. When a version change is found, proxy server sends a synchronization request to the twin operation and maintenance platform. After confirmation, the proxy server asks for the changes from the application node and pushes them to the twin system by means of change files, installation logs and database table synchronization etc. The twin operation and maintenance platform finds the specific virtual node to synchronize and the embedded probes information table will be updated afterwards synchronization. The twin system platform also supports manually triggered system synchronization.
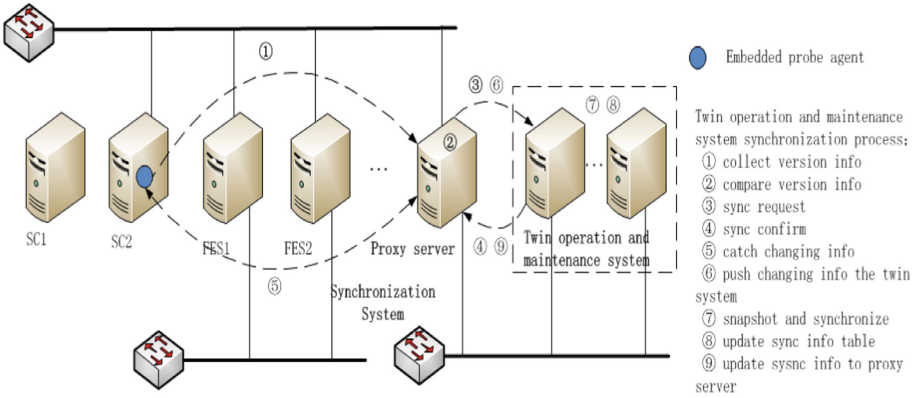
Fig. 3. Monitoring point synchronization process diagram.

3.3   Version Management

Regular backup is important for long-running systems, but it always takes a long time and occupies a large amount of disk. While snapshot provides a new way to preserves the state and data of a running virtual machine at a specific point in time, especially incremental snapshots, which can be done within a few seconds [22]. The essence of snapshot is to save a copy of the metadata (inode table) instead of data blocks. Therefore, the snapshot is really small in creating and will increase automatically with the change of the system.

Due to the low cost of snapshots, the twin operation and maintenance platform makes a snapshot before some important synchronization. It prevents the update failure from affecting the system; on the other hand it keeps different versions of the system, and people can enter the system in different periods through version management. The system also customizes the group-based batch snapshot, so people can generate several test environments at the same time and do testing for different versions or in different scenarios on the same platform.
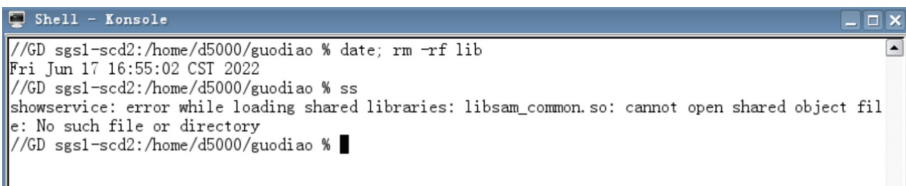
Fig. 4. Mis-operation on scd2.

As shown in Fig. 4, a maintenance person deleted the lib directory in the virtual machine scd2 during program upgrade by mistake, but since the snapshot version1 was made for scd2 before the operation, the system can be restored by rolling back to the snapshot version1.
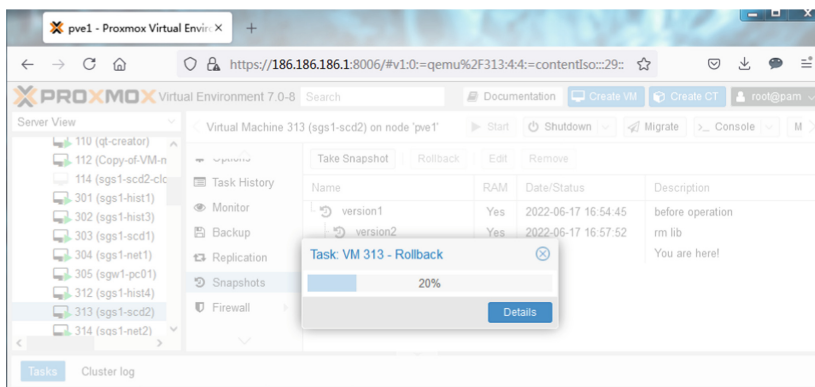
Fig. 5. Snapshot rollback for scd2.

On the other hand, the version management also provides the clone function, which can make a real copy for a host or a twin system. This is super convenient for engineers to create a testing environment in minutes.

4   Testing Result

The twin operation and maintenance system platform built in the laboratory is based on the Proxmox VE. Table 2 lists the hardware configuration of the test environment.

Table 2. Hardware environment of Proxmox.

Machine	3Pve2	Pve3	Pve4	Pve5
CPU	24*Xeon E52620v3@2.4 GHz			
Memory	224 G	192 G	128 G	64 G
Disk	300 G + 4T	300 G + 2T	300 G + 2T	300 G + 2T

Clonezilla, an open source hard disk clone tool, is used to do off-line P2V migration for SCADA nodes and database nodes from the test environment. It took about 2 h to migrate 3 nodes. Other nodes are installed through templates. It took about half day for template customization, and roughly 20 min for virtual node installation through template. It is more efficient to build systems in P2V than reinstallation, and the most important thing is the software environment created by P2V is highly consistent with the online system. Figure 6 shows all the virtual nodes of the twin system, which includes 1 database node, 2 SCADA nodes, 2 FES nodes, 2 file service nodes and a HMI workstation.

Customized the Proxmox pool management function provides a way to manage different twin systems on one platform. There are three twin systems containing more than 50 virtual nodes that are configured on the platform, and the entire twin operation and maintenance system (guodiao) includes an operation system and D5000 environment
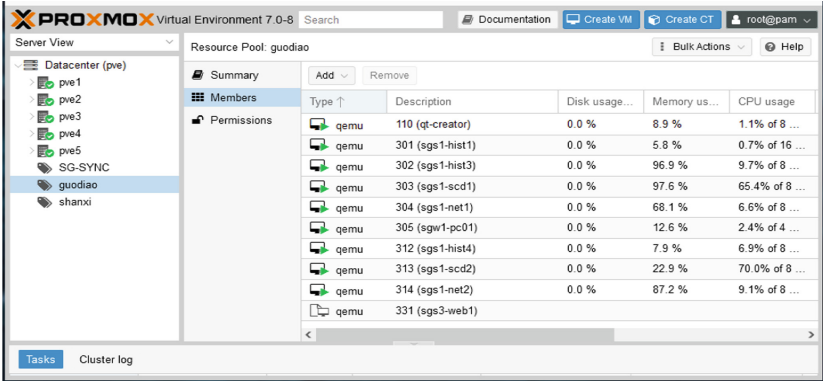
Fig. 6. Twin operation and maintenance systems group management.

of 8 nodes can be started in ten minutes. Figure 7 shows the HMI homepage of the system login from the PC virtual terminal.
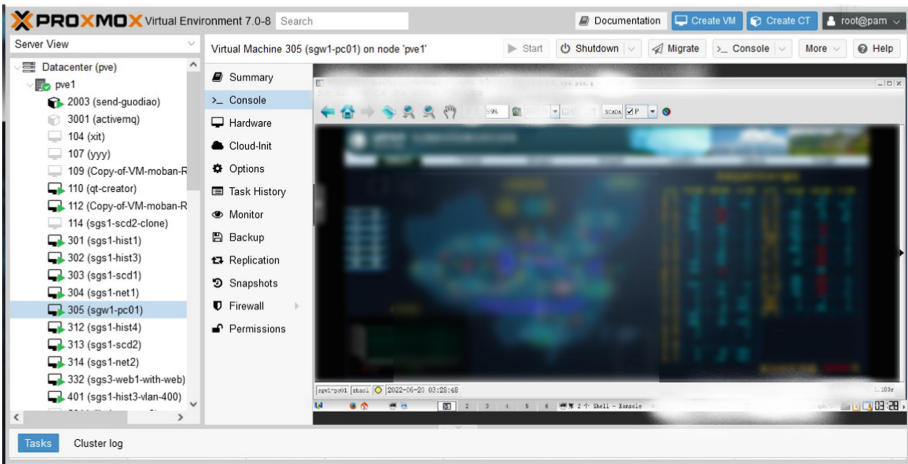
Fig. 7. HMI from PC virtual terminal.

5   Concluding Remarks

A method for constructing a twin operation and maintenance system is proposed in this paper. It supports both P2V and template based migration for twin system creation, enables embedded probes synchronization between the control system and the twin system regularly, provides centralized management of multiple twin systems on the same platform, and offers node-based and group-based version management. The twin operation and maintenance system platform can not only work as a realistic software testing

system for local maintenance, but also provide a verified environment for remote support centers. Now more than 50 engineers around the country can do practical operation and maintenance exercises on the twin platform. Given more research on the fault monitoring of the control system, it will provide a fault scenario simulation function for the control system in the future.

References

1. Shu, Y., Chen, G., Jingbo, H., et al.: Building a new electric power system based on new energy sources. Strat. Study CAE **23**(6), 61–69 (2021)
2. Xin, Y., Shi, J., Zhou, J., et al.: Technology development trends of smart grid dispatching and control system. Autom. Electr. Power Syst. **39**(01), 2–8 (2015)
3. Xin, Y., Tao, H., Shang, X., et al.: Smart grid dispatching and control system - support platform, 1st edn. China Electric Power Press, Beijing (2017)
4. Feng, S., Yao, J., Yang, S., et al.: Oveall design of integrated analysis centre for physically-distributed and logically integrated dispatch system Electr. Power Autom. Equipm. **35**(12), 138–144 (2015)
5. Yang, Q., Li, L., Li, Y., et al.: Test and verification technology for smart grid dispatching and control systems. Autom. Elect. Power Syst. **39**(1), 194–199 (2015)
6. Zhou, Y., Xie, S., Duan, X., et al.: Automatic simulation and test system for the power grid dispatching. Electr. Power. **08**, 62–64 (2006)
7. Liu, D., Yan, H., Ding, Z., et al.: Research on integration testing technology for main station in SCADA system. Power Syst. Technol. **29**(2), 62–67 (2005)
8. Lu, J., Wang, S., Ling, Q., et al.: Test and analysis system of automatic dispatching Distribut. Utilizat. **25**(6), 32–35 (2008)
9. Tian, F., Huang, Y., Shi, D.: Developing trend of power system simulation and analysis technology. Proceed. CSEE **34**(13), 2151–2163 (2014)
10. Gartner Research Top 10 Strategic Technology Trends for 2019: Digital Twins https://www.gartner.com/en/documents/3904569/, last updated 2019/3/13
11. Tao, F., Zhang, H., Qi, Q., et al.: Ten questions towards digital twin: analysis and thinking. Comput. Integr. Manuf. Syst. **26**(01), 5–21 (2020)
12. Uhlemann, T.H.J., Schock, C., Lehmann, C., et al.: The digital twin: demonstrating the potential of real time data acquisition in production systems. Procedia Manufact. **9**, 113–120 (2017)
13. Grieves, M., Vickers, J.: Digital twin: Mitigating unpredictable, undesirable emergent behavior in complex systems, 1st edn. Springer International Publishing, Switzerland (2017)
14. Qinglin, Q., Fei, T., Tianliang, H., et al.: Enabling technologies and tools for digital twin. J. Manufact. Syst. **58**(Part B), 3–21 (2021)
15. He, X., Ai, Q., Zhu, T., et al.: Opportunities and challenges of the digital twin in power system applications. Power Syst. Technol. **44**(06), 2009–2019 (2020)
16. Liu, G., Zhu, L., Weijie, Y., et al.: Application of digital twin virtual simulation experiment platform in practice teaching China Modern Educational Equipment **367**(8), 52–58 (2021)
17. Ye, Y., Yiqun, K., Hu, Y., et al.: Construction and application of engineering training model based on digital twin. Experim, Technol. Manage. **39**(4), 236–241 (2022)

18. Zheng, Z., Gu, J., Wu, Jinlong, et al.: Application of cloud computing in electric power system data recovery. Power Syst. Technol. **36**(9), 43–50 (2012)
19. Ma, K., Song, L., Xu, Tong: Application of business migration and virtualization technology in operation and maintenance of TV broadcasting system. Radio TV Broadcast Eng. **46**(11), 59–63 (2019)
20. Ionel, G.: Optimized P2V conversion using VMware converter standalone. Journal of Computer Science and Control Systems **8**(2), 24–28 (2015)
21. Shen, G., Liu, M., Gao, B., et al.: Research of key technologies of centralized operation and maintenance for power grid dispatching technical support system Electric Power Inf. Communic. Technol. **11**(11), 1–5 (2013)
22. Xiong, A., Wei, T., Yi, J.: Linux file system with snapshot function. J. Comput. Appli. **30**(suppl.1), 179–181 (2020)

Compressed Sensing Algorithm for Short Data Window in Distribution Network

Yuhan Cao[1]([✉]), Tonghua Wu[2], Wei Chen[1], Xiang Zeng[1], and Bing Luo[1]

[1] Huazhong University of Science and Technology, Wuhan, China
`m202071507@hust.edu.com`
[2] State Key Laboratory of Smart Grid Protection and Control, Nari Group Corporation,
Nanjing 211106, Jiangsu, China

Abstract. To effectively cope with the problems of surging data volume, high data acquisition cost, and congested communication transmission in distribution networks containing distributed new energy sources, this paper proposes a short data window data acquisition and intercommunication scheme based on compressed sensing theory and builds a corresponding model with the distribution network longitudinal differential protection data intercommunication process as a specific research scenario. The paper analyzes the shortcomings of the Gaussian random matrix, a universal observation matrix commonly used in traditional compressive sensing, in the distribution network, and constructs a deterministic matrix for the current signal characteristics of the distribution network to solve the problem of data reconstruction in the application of compressive sensing in the field of the power system. The problem of unstable recovery is solved. In addition, a sparse base satisfying the constrained isotropy condition is selected from the commonly used sparse bases for the constructed deterministic observation matrix, and a tracking algorithm with unbiased estimation is combined to design a targeted data compression reconstruction algorithm that can apply the compressive sensing theory to the distribution network longitudinal differential protection information intercommunication scenario in a more suitable way. This algorithm has a significant improvement in reconstruction accuracy, and the reconstruction time is short and adaptable to the real-time current signal of the distribution network.

Keywords: Compressed Sensing · Reconstruction · Observation matrix

1 Introduction

1.1 Compressed Sensing

Compressed sensing can complete sampling and compression of signals with sparse characteristics at a low sampling rate, realizing the projection of the original high-dimensional signal directly to the low-dimensional observed signal, and then the reconstruction algorithm accurately recovers the original signal, greatly reducing the pressure of sampling,

transmission, and storage. The reconstruction algorithm is the key to the practical application of compressed sensing theory, and how to improve the performance of the reconstruction algorithm (reconstruction effect, reconstruction speed, anti-interference ability, etc.) has been a hot topic of research [1–3].

In the traditional sense, signal processing usually goes through two processes: sampling and compression: firstly, the analog signal is digitized at a rate of not less than twice the signal bandwidth following the Nyquist sampling criterion, and the sampled digital signal contains all the information of the original analog signal; then the Fourier Transform (FT) or Wavelet Transform (WT) is applied to the signal. Transform (FT) or Wavelet Transform (WT) to adjust the transform domain of the sampled signal, and then only the key information of the recovered signal is retained in the new transform domain to achieve the purpose of compression [4–8]. The compressed perception theory combines the sampling process and the compression process to achieve a direct projection of the original high-dimensional signal to the low-dimensional observed signal, and then the reconstruction algorithm accurately recovers the original signal. The compressed signal can be stored or transmitted more conveniently and can be recovered close to the original signal by the inverse operation of the transformation in the compression process [9, 10]. A comparison of the traditional data sampling and compression framework and the data sampling and compression framework based on compression-awareness theory is shown in Fig. 1 and Fig. 2.
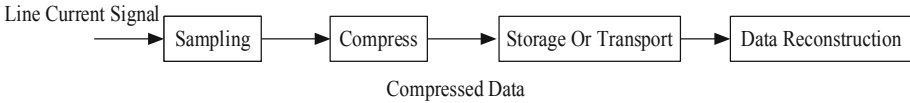
Fig. 1. Traditional data sampling compression framework.

Fig. 2. Data sampling compression framework based on compressed sensing.

The basic principle of compressed perception theory: let the original signal x can be considered as a high-dimensional data sequence, and let the original signal x be sparse under the sparse basis φ, then x can be expressed as:

$$x = \varphi s \tag{1}$$

$$y = \phi x \tag{2}$$

$$y = As \tag{3}$$

where φ is a sparse basis matrix of order $n \times n$ and ϕ is an observation matrix of order $m \times n$; n is the dimensionality of the signal x and m is the dimensionality of the signal x

after compression. The theoretical process of compressed perception is shown in Fig. 3 below.

The original signal is passed through the observation matrix to complete the projection of the data from high to low dimensions, which is the compression process of the signal, and the compressed data is transmitted afterward. Because the high-dimensional original signal does not contain information in all dimensions in the sparse transform domain, there are many non-zero values, so although it is an underdetermined equation solving problem, the compressed signal can be recovered to the original signal by the optimization-seeking algorithm or convex relaxation algorithm [11–15]. One issue that needs to be noted here is that the greedy algorithm-based optimization algorithm is close to unbiased estimation when the signal-to-noise ratio is high, but the convex relaxation algorithm must be a biased estimation algorithm, so the reconstruction algorithm in this paper uses a greedy class of algorithms [16].

1.2   Purpose of the Paper

The purpose of this paper is to propose a data compression recovery algorithm applied to the distribution network line longitudinal differential protection data intercommunication scenario, which is different from the existing research content that directly applies the pervasive compression-aware theory to the collection and compression recovery process of electrical quantity data in power systems. Instead, by analyzing the mechanism of the universal random observation matrix, i.e., the Gaussian random matrix for most signals, and then combining it with the characteristics of the specific real-time current signal of the distribution network, a deterministic observation matrix containing the Unitary matrix is proposed, which is characterized by the closing two ends of the matrix consisting of the Unitary matrix, and the number of columns of the Unitary matrix is determined by the sparse observation matrix.
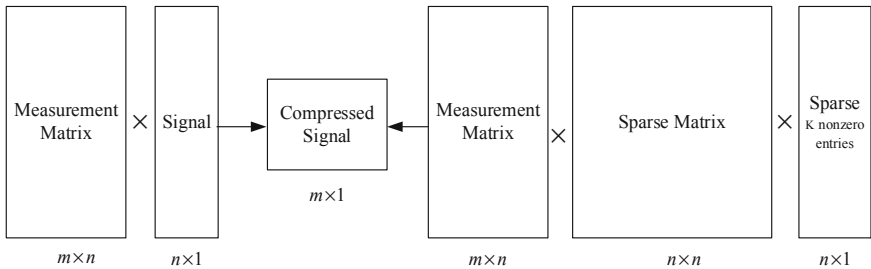
Fig. 3. The theoretical process of compressed perception.

Another point worth noting is that the real-time current signal sampled by the short data window is compressed and reconstructed, that is, sampled at a sampling frequency of $f = 4000$ Hz, and the 80-point sampling value of a period of 0.02 s is compressed to 16 points for data interconnection between longitudinal differential protection and data recovery and reconstruction. The fence effect can be solved by period extension and interpolation of missing data, but the goal of this paper is to compress the time domain

sampled values as accurately as possible for transmission and reconstruction recovery, so the construction of the unitary matrix and the selection of sparse bases in the compressed sensing theory is to take advantage of the fence effect of electrical quantities in power systems. In the selection of the sparse basis, according to the constructed observation matrix, the discrete Fourier transform basis or the discrete cosine basis is chosen to compare the sparsity s of both, and it is found that the difference in the value of the sparsity s is not significant after the analysis of the simulation results, at which time it is considered that the discrete Fourier transform basis contains complex numbers, which will bring a certain degree of reconstruction algorithm to the next Finally, in the selection of reconstruction algorithm, due to the large signal-to-noise ratio of the real-time current signal of the distribution network, the greedy class algorithm is used, which can minimize the error and achieve the effect of close to unbiased estimation by using the least-squares method and orthogonal projection principle to find the best. At the end of this paper, the simulation platform of longitudinal differential protection of the distribution network with new energy is built to test the performance of the algorithm and determine whether the protection is operating.

2 Observation Matrix Combined with Electrical Characteristics

2.1 Selection of Observation Matrix

According to Nyquist's sampling theorem: "The sampling frequency shall be greater than twice the highest frequency in the signal." This means that with equally spaced sampling, the frequency domain will be extended with a period of $1/\tau$, , and a low sampling frequency will cause period aliasing. In distribution network longitudinal differential protection devices, real-time current signals are usually sampled equally spaced (80 points of data are collected in 0.02 s of a cycle) obeying Nyquist's sampling law. If one wants to reduce the sampling frequency and reduce the amount of data that the protection device needs to transmit interchangeably, while still retaining as much information as possible contained in the real-time current signal, then unequal spacing sampling is required, which is the key step of compressive sensing theory, random subsampling. This is described mathematically as the selection of the observation matrix.

The observation matrix is an M × N matrix (M > N) for sampling and compression of sparse signals. The observation matrix in compressive sensing directly determines the information obtained after sampling and compression, which in turn affects the uniqueness of reconstruction and reconstruction accuracy. Therefore, the selection of a suitable observation matrix is a necessary foundation for the application of a compressive sensing framework. For the conditions that need to be satisfied by the observation matrix in compressed sensing, Candes and Tao et al. proposed the finite isometric property (RIP)[17], which is described as follows:

If $\delta_k \in (0, 1)$, any signal with k sparsity, its parameters satisfy Eqs. (1–3) in the compressive sensing framework, then it means that the corresponding sensing matrix A satisfies the k-order finite isometric property.

$$1 - \delta_k \|\theta\|_2^2 \le \|A\theta\|_2^2 \le 1 + \delta_k \|\theta\|_2^2 \tag{4}$$

where $\theta \in \sum_k \{\theta : \|\theta\|_0 \le k\}$, δ_k is the finite isometric constant of the sensing matrix A.

However, the RIP coefficients of the observation matrix are difficult to be found computationally, therefore, literature proves that the equivalence condition of RIP is that the observation matrix Φ is uncorrelated with the sparse basis ψ. It is shown that most of the uniformly distributed random matrices are not mutually representable with almost all of the sparse transformation matrices, satisfying the RIP property, and can be used for the observation of signals. There are three types of commonly used observation matrices: first, the elements in the matrix obey some random distribution, such as Gaussian random matrix, and Bernoulli random matrix; second, some rows in the orthogonal matrix are randomly selected to form the matrix, such as partial Fourier matrix, partial Hadamard matrix, etc.; third, the matrix applied to a specific signal, such as the circular matrix, Toplitz matrix proposed in the literature.

In particular, it should be noted that for analog signals, the sampling process is the measurement process and the sampled value is the measured value. Most of the signal observation processes obtained in compressive sensing are non-adaptive, which means that the selection of the observation vector does not depend on the specified signal. The real-time current signal on the feeder in the distribution network has its characteristics, so the observation matrix should be designed to be adaptive to the signal characteristics for the observation of the new road signal in the distribution network.

2.2 Adaptive Observation Matrix for Distribution Network

The current research applying compressive sensing theory to the field of power system data compression usually directly applies a Gaussian random matrix as the observation matrix, which usually causes two problems because of the characteristics of the original sampling data of the distribution network line current: first, the sampling value of the distribution network line current does not contain white noise with random distribution, and second, the use of a circumferential 0.02 s as the sampling observation window will lead to The fence effect occurs after converting the real-time sampled data for the time domain signal to the frequency domain.

To better understand the impact of the two features on the observation matrix, it is important to first understand the reasons for the previous large-scale use of the Gaussian random observation matrix in the communication field, and then to conduct a targeted analysis in conjunction with the characteristics of the distribution network itself.

(1) In the communication field, the Gaussian random matrix is usually used as the observation matrix, but this is because the original signal to be compressed in the communication field contains effective information signals and white noise, and when the Gaussian random matrix is used as the observation matrix for subsampling, the frequency domain is not extended with a fixed period, but a small part of the spectrum is moved haphazardly, and the frequency leakage is uniformly distributed throughout the frequency domain, where a large part of the effective information A large portion of the valid information can be detected by setting a threshold, and the remaining valid information can be recovered by a special tracking algorithm that analyzes the interference values and then restores the original signal. The detailed process is illustrated in the following figure.

Understanding the compression-aware process from a random subsampling perspective is shown in the figure above. For most signals, they usually contain white noise, which itself is uniformly distributed in the frequency domain, so it can be separated out during the tracking process.

This is simple to understand. Let's start with the observation model for compressed perception

$$y = Ax + n \qquad (5)$$

where y is the observed signal, A is the observation matrix, x is the original signal, and n is the white noise.

Knowing the observed signal y and the observation matrix A, we try to recover the original signal x with several observations much smaller than the sampling theorem. To solve this underdetermined problem, we need to assume that x itself (or in the transform domain) has a simple structure, for example, if x is a vector we assume that it is sparse to get; if x is a matrix we assume that it is low-rank. This result is generally satisfied in practice. Thus the optimization problem becomes

$$min\|x\|_{sig} s.t. \|y - Ax\| \leq \delta \qquad (6)$$

where x_{sig} is the constraint that x has a simple structure.

In this case, the observed signal is noisy, and since the purpose of our optimization is to find the solution of the one that satisfies the condition of being the simplest, compressed perception can achieve the effect of denoising.

In the distribution network, the current data collected in real-time whether steady state or transient data, line current sampling values converted to the frequency domain does not have a uniform distribution of white noise. This means that the observation model of the power system

$$y = Ax \qquad (7)$$

where y is the observed signal, A is the observation matrix, and x is the original signal, which does not contain white noise or bounded observation noise. Then the use of Gaussian random matrix as the observation matrix to eliminate the effect of white noise is not necessary, can be constructed by the specific circumstances of the observed signal in the frequency domain to adapt to the observation matrix of real-time current sampling data.

(2) The data is interchanged between protection devices at an interval of 0.02 s, and the use of a perimeter of 0.02 s as a sampling observation window will lead to a fence effect when the real-time sampling data for the time-domain signal is converted to the frequency domain.

2.3   Construct Deterministic Observation Matrix

Taking the sampling frequency $f = 4000$ Hz and 80 points per cycle as an example, the following figure shows the time domain waveform of current for normal operation, fault operation and the waveform after Fourier transform and Discrete Cosine Transform(DCT).

(a) Line current in normal operation   (b) Single-phase grounding fault line current
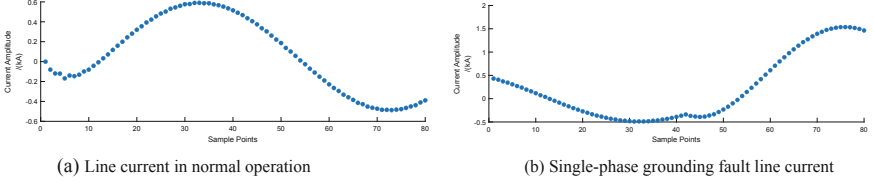
Fig. 4. Time domain current waveform of a cycle in distribution network.

(b) Line current in normal operation   (b) Single-phase grounding fault line current
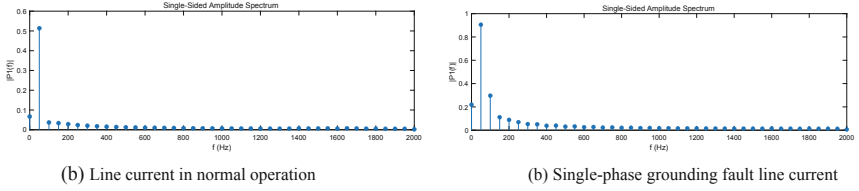
Fig. 5. Frequency domain current waveform transformed by FFT.

(c) Line current in normal operation   (b) Single-phase grounding fault line current
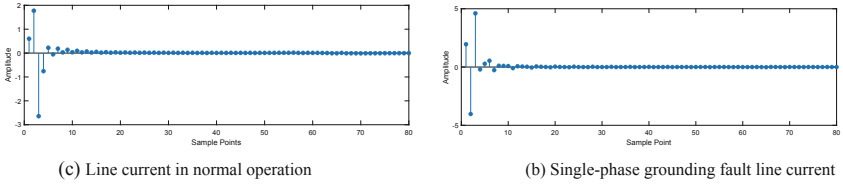
Fig. 6. Current waveform transformed by DCT.

Observing the above Fig. 4, Fig. 5 and Fig. 6, it is found that the current time-domain waveform shows fence effect after sparse basis discrete transform for normal operation, in-zone fault or out-of-zone fault, so the observation matrix can be constructed to target the effective information transmission. The observation matrix is constructed as shown in the following figure.

$$\boldsymbol{\Phi} = \left[\boldsymbol{B_t}, \, 0 \ldots 0, \, \boldsymbol{B_t^H} \right] \tag{8}$$

where $\boldsymbol{B_t} = [\boldsymbol{b_1}, \ldots, \boldsymbol{b_t}]$, $\boldsymbol{B_t}$ is the $m \times t$ order unitary $\boldsymbol{B_t}$ matrix, satisfying $\boldsymbol{B_t^H B_t} = \boldsymbol{B_t B_t^H} = \boldsymbol{E}$, noted as $\boldsymbol{B_t} \in \boldsymbol{U^{t \times t}}$, $\vec{\boldsymbol{b_i}}$ is $m \times 1$ dimensional column vector $i \in [1, t]$, t denotes the number of data points containing valid information under the sparse transform base.

3 Selection of the Sparse Basis

The sparse representation of current sampling values is the basis for applying compressed sensing theory to compress real-time sampling data, and it is necessary to select a suitable sparse transform base for the sparse representation of current signals. The sparsity of the current sampling value can be considered as the number of non-zero elements in the current sampling value itself, or the sampling value after sparse transformation. If

the number of non-zero elements is small, the signal is considered sparse. Obviously, under normal operating conditions or common fault conditions in power systems, there are only a finite number of values after transforming the current sampled values to the frequency domain, i.e., the current sampled values have good sparsity in the frequency domain.

Given that the compressed sensing theory requires that the observation matrix and the sparse basis cannot be sparsely represented to each other (otherwise, they cannot be solved), almost all the sparse basis matrices cannot represent the random observation vector. It is worth noting that the observation matrix containing the unitary matrix constructed in the previous section for the characteristics of the real-time current data of the distribution network is deterministic, so the selection of the sparse basis should be extra cautious. Considering that the distribution network current data is sparse in the frequency domain, the sparse basis matrix of the current sampling values usually uses a unit Fourier matrix, cosine matrix, or wavelet transform, etc. The selection of the sparse basis has a small range.

When choosing the sparse basis of variation, wavelet transform faces the problem of determining the wavelet basis, and the sparse result may change due to the change of wavelet basis, so this paper mainly compares the effect of Fourier transform basis and discrete cosine basis of variation on the sparse representation of current sampling value.

Since the observation matrix $\boldsymbol{\Phi}$ contains the unitary matrix $\boldsymbol{B_t}$ which is used to store the valid information in the current signal after the sparse transformation, the t in the unitary matrix $\boldsymbol{B_t}$ is determined according to the number of non-zero sampling points after the sparse transformation. If the number of non-zeros in the current signal after sparse transformation is more, the larger t is; if the number of non-zeros in the current signal after sparse transformation is less, the smaller t is.

As shown in the above Fig. 4, 5 and 6, under the discrete cosine transform base, the Unitary matrix t should be at least greater than 7; under the discrete Fourier transform base, the Unitary matrix t should be at least greater than 7. The calculation of the Unitary matrix t is determined by the number of points containing information after the conversion of the time domain waveform to the discrete sparse basis transform domain and considering the frequency leakage problem, the value of t is usually left with a certain safety margin. Under FFT sparse transformation basis in Fig. 5, the number of points containing effective information in frequency domain signals is $t = 2$ under normal conditions and $T = 7$ under fault conditions. The number of sampling points t containing valid information under the DCT sparse transform base of Fig. 6 is $t = 5$ for normal operation and $t = 7$ for fault operation, respectively; therefore, the following conclusions can be drawn.

It can be seen that the difference between discrete cosine transform base and Fourier transform base for sparse representation of real-time current sampling signal is not large, and it is reasonable to use discrete cosine transform base or Fourier transform base as the sparse base of real-time current signal for compressed data.

It is worth noting that when the FFT is used for the sparse transform, since the unit Fourier matrix is a complex matrix, the calculation containing complex numbers will bring difficulties to the design process of the reconstruction algorithm, so in the case that the difference between the FFT transform and the DCT transform on the observation

matrix is not large, it is recommended that the DCT is preferred as the sparse transform matrix.

In addition, in the compressed sensing theory, if there are only M non-zero values after transforming the current sampling value to the sparse domain, or the modulus of some non-zero values is much larger than other non-zero values, the sparsity of the current sampling value is M. Let the number of current sampling values in a certain window be j, and the number of signals after compressing the observation matrix is i, there is $M < i \ll j$. A segment of current sampling values of length j can be represented by the sparse basis $\boldsymbol{\Psi}^T = [\boldsymbol{\Psi}_1, \boldsymbol{\Psi}_2, \ldots, \boldsymbol{\Psi}_M]$ for sparse representation, i.e., $\boldsymbol{x} = \boldsymbol{\Psi K}$.

4 Reconstruction Recovery Algorithm

4.1 Mathematical Optimization Model

After the protection of the original data is compressed by the observation transformation, it still needs to be reconstructed to be restored to the protection of the original data. The reconstruction process is essentially an optimization problem, i.e., solving the original data after sparse representation with the compressed measurement value y as a known quantity. And the dimension of the measurement value y is greater than the sparse value K, the reconstruction process is the process of solving the $\boldsymbol{y} = \boldsymbol{\phi\Psi K} = \boldsymbol{AK}$ underdetermined equation, where $\boldsymbol{A}$ is the compressed sensing matrix, and the optimization model is as in Eq.

$$\{ \begin{matrix} \hat{\theta} = \arg min \|\theta\|_0 \\ s.t. y = A\theta \end{matrix} \tag{9}$$

The optimization model shown is a nonconvex combinatorial optimization model, and solving θ is an NP-hard problem, and the value theta cannot be obtained using analytical or numerical means. Solving this type of NP-hard problem usually uses greedy algorithms and other means to transform the nonconvex optimization model into a convex optimization model.

4.2 Recovery and Reconstruction Algorithm

The idea of the greedy algorithm is to reduce the error theta valuable in the iterative update of local optimization, and when the error is less than the specified range, the original signal can be considered to be restored. The following solution steps are designed based on this idea.

Input.

(1) The sensing matrix $A_{M \times N}$
(2) observation vector $Y_{N \times 1}$
(3) The sparsity K of the signal

Output.

(1) Signal sparsity indicates the sparse estimate $\hat{\theta}$
(2) $N \times 1$ dimensional residuals $r_K = y - A_k \times \hat{\theta}$

In the following flow: t represents the number of iterations, η_t denotes the set of indexes (column ordinal numbers) of t iterations, γ_t denotes the index (column ordinal number) found in the tenth iteration, a_j denotes the jth column of matrix A, A_t denotes the set of columns of matrix A selected by index η_t (matrix of size $M \times t$).
   Steps.

(1) Initialize $r_0 = y$, $\eta_0 = \varnothing$, $t = 1$;
(2) Find the index γ_t such that

$$\gamma_t = \arg \max_{j=1,2,\dots,N} |r_{t-1}, a_j| \tag{10}$$

(3) Let $\eta_t = \eta_{t-1} \cup (\gamma_t)$, $A_t = A_{t-1} \cup a_{\gamma_t}$;
(4) Find the least squares solution for $y = A_t \theta_t$
   $$\widehat{\theta_t} = \arg \min_{\theta_t} \|y - A_t \theta_t\| = (A_t^T A_t)^{-1} A_t y;$$
(5) Updating the residuals.

$$r_t = y - A_t \hat{\theta}_t = y - A_t (A_t^T A_t)^{-1} A_t y \tag{11}$$

(6) $t = t + 1$, returning to step (2) if $t \leq K$, otherwise stopping the iteration to step (7).
(7) The reconstructed $\hat{\theta}$ has a non-zero term at η_t, whose value is the value obtained from the last iteration $\hat{\theta}$.

5 Simulation Analysis

5.1 Simulation Platform

This paper uses MATLAB to simulate and verify the differential protection algorithm based on compression sensing, and the simulation model is shown in Fig. 7. Distribution network has distributed power supply with new energy, bus voltage is 11 kV. The sampling frequency is set to $f = 4000$ Hz, and the number of per cycle waveform sampling points is 80 points. Figure 7 model in the normal operating conditions of line 1, the midpoint F in the region of the phase A grounding fault simulation data, select one of the per cycle current sampling values, a total of 80 sampling values in the reconstruction window.
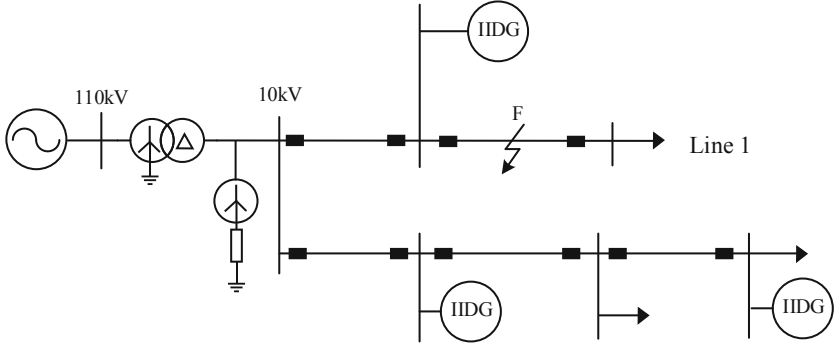
Fig. 7. Distributed distribution network topology with new energy.

5.2   Experimental Results and Analysis of Compressed Reconstruction Algorithm

The compressive reconstruction algorithm tested in this paper consists of three parts, firstly, the deterministic observation matrix constructed in Sect. 2 for the electrical quantity characteristics of the distribution network, secondly, the sparse basis matrix obtained from the discrete cosine transform composition, and finally, the data recovery reconstruction algorithm proposed by orthogonal matching tracking based on the orthogonal projection principle.

The experimental results consist of two parts, one is the data compression and reconstruction for the normal operation of the distribution network, and the reconstruction error is calculated, and the other is the data compression and reconstruction for the case of phase A ground fault occurred in the distribution network line, and the reconstruction error is calculated.

The error of the reconstruction result is expressed by the mean squared difference signal-to-noise ratio, MSE mean squared error, a statistical parameter that is the mean value of the sum of squares of the corresponding points of the original data and the compressed reconstructed data, calculated as follows:

$$\text{MSE} = \frac{1}{n} \sum_{i=1}^{m} w_i \left(y - \widehat{y}_i \right)^2 \tag{12}$$

In Eq. (12), where y_i is the original signal data, $\widehat{y}_i$ is the compressed reconstructed data, and $w_i > 0$. From here, it can be seen that as the MSE gets closer to 0, the better the compressed reconstructed performance of the model is.

The threshold coefficient in the reconstruction algorithm is 0.6, the error limit $\tau = 10^{-8}$, and the maximum number of iterations $t_{max} = 16$. After several simulations, it is found that the upper limit of iterations is not reached, which is due to the fact that multiple compressed sensing vectors are selected at the same time in each iteration to significantly reduce the number of cycles. Therefore, the upper limit of 16 iterations can basically satisfy the error limit $\tau = 10^{-8}$.

The sparsity k is taken as 5, because k indicates the number of points that contain valid information in the new transform domain of the sparsely transformed signal. The You matrix in the observation matrix is an $n \times t$ dimensional matrix, and both the left

and right ends of the observation matrix contain You matrices, so the maximum value of sparsity k is 16. Of course, when the sparsity k is greater than 16, data compression reconstruction can also be performed, but there may be cases of low reconstruction accuracy, considering that the performance limit of the algorithm is not the focus of this paper, so we will not go into too much detail here.
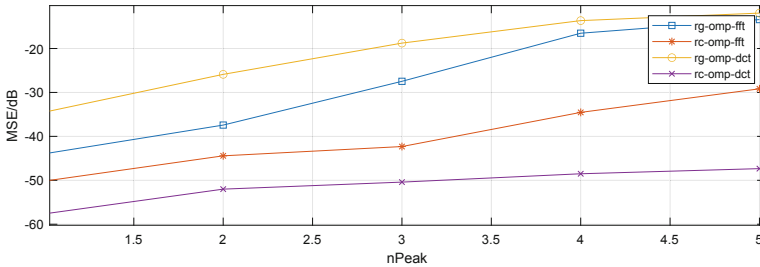
Fig. 8. Algorithm reconstruction error.

As can be seen from Figs. 4, 5 and 6, the current in normal operating conditions contains only the fundamental waveform, so at this time npeak = 1, when a single-phase ground fault occurs, taking into account the spectral leakage problem, according to the value of the sampling points on the sparse transform domain, the effective information is considered to leak to five points, at this time npeak = 5.

In Fig. 8 rc denotes the observation matrix as the deterministic matrix designed in this paper, rg denotes the Gaussian random observation matrix, omp is the reconstruction algorithm, fft and dct represent different sparse basis matrices.

Analysis of Fig. 8 shows that the error of the compressed reconstruction algorithm after adapting the electrical quantity characteristics of the distribution network is below -50 dB both under normal operating conditions and in the presence of ground faults, with superior performance compared to the results under the Gaussian observation matrix or when the fft transform base is used. It can even be considered non-existent.

6   Conclusion

Compressed sensing theory should consider the characteristics of the electrical quantities of the power system itself when applied to the data in the field of power system, and the algorithm directly applied to the communication field in the distribution network not only has poor performance of the algorithm for data compression and unstable recovery results, but also does not play the essence of the subsampling process in the compression-aware theory. The observation, sparsification, and reconstruction recovery algorithm of compressed sensing data based on the electrical quantity characteristics of the distribution network mentioned in this paper has a very high reconstruction accuracy and simple algorithm implementation, which provides a good research basis for the intercommunication of information between longitudinal differential protection in the future in the 5G communication environment.

References

1. Yi, Z., Yan, L., Wu, D.: Current status and development trend of power quality monitoring system. Power Syst. Prot. Control **43**, 138–147 (2015)
2. Huang, N., Hua, P., Xu, J., et al.: Power quality signal; data compression; normalized distance;one-class support vector machine. Trans. China Electrotech. Soc. **A2**, 181–188 (2015)
3. Ribeiro, M.V., Park, S.H., Romano, J.M.T., et al.: A novel MDL-based compression method for power quality applications. IEEE Trans. Power Del. **22**, 27–36 (2007)
4. Dash, P.K., Panigrahi, B.K., Sahoo, D.K., et al.: Power quality disturbance data compression, detection, and classification using integrated spline wavelet and S-transform. IEEE Trans. Power Del. **18**, 595–600 (2003)
5. Robinson, J., Kecman, V.: Combining support vector machine learning with the discrete cosine transform in image compression. IEEE Trans. Neural Networks **14**, 950–958 (2003)
6. Zheng, W., Wu, W.: A power quality event data compression based on combined wavelet packets. Adv. Technol. Electr. Eng. Energy **39**, 8–11 (2010)
7. Donoho, D.L.: Compressed sensing. IEEE Trans. Inf. Theory **52**, 1280–1306 (2006)
8. Tropp, J., Gilbert, A.: Signal recovery from random measurements via orthogonal matching pursuit. Trans. Inf. Theory **53**, 4655–4666 (2007)
9. Do, T.T., Lu, G., Nguyen, N., et al.: Sparsity adaptive matching pursuit algorithm for practical compressed sensing. IEEE Trans. Ind. Electron. **57**, 107–121 (2010)
10. Needell, D.: Topics in Compressed Sensing. University of California, California (2009)
11. Chen, L., Zhang, D., Wang, Z.: Research on power signal compression and reconstruction based on compressed sensing. Electr. Meas. Instrument. **54**, 95–100 (2015)
12. Liu, Y., Tang, W., Liu, B.: Data sparse analysis and improved reconstruction algorithm of power quality disturbance based on compressed sensing. Trans. China Electrotech. Soc. **33**, 3461–3470 (2018)
13. Liu, G., Wu, H., Shen, Y.: Novel reconstruction method of power quality data based on regularized adaptive matching pursuit algorithm. Chin. J. Sci. Inst. **36**, 1838–1844 (2015)
14. Stuti, S., Mishra, S., Singh, B.: Power quality event classification under noisy conditions using EMD-based de-noising techniques. IEEE Trans. Ind. Inf. **10**, 1044–1054 (2013)
15. Liu, Q., Shen, Y., Lei, W.: A hybrid FCW-EMD and KF-BA-SVM based model for short-term load forecasting. CSEE J. Power Energy Syst. **4**, 226–237 (2018)
16. Amaldi, E., Kann, V.: On the approximability of minimizing nonzero variables or unsatisfied relations in linear systems. Theor. Comput. Sci. **209**, 237–260 (1998)
17. Cands, E., Romberg, J., Tao, T.: Stable signal recovery from incomplete and inaccurate measurements. Commun. Pure Appl. Math. **59**(8), 1207–1223 (2006)

A Comparison Study of Mixed-Integer Formulations for Hydro-Thermal SCUC Problem

Li Chang[1]($\boxtimes$), Yanguang Chen[2], Jianjun Gao[2], Wen Wang[1], and Zhendong Zang[1]

[1] NARI Group Corporation (State Grid Electric Power Research Institute), Nanjing 211106, China
`2017212301@live.sufe.edu.cn`
[2] Cardinal Operations (Beijing) Co., Ltd., Beijing 100010, China

Abstract. This paper studies the mixed-integer linear programming (MILP) Reformulation of the hydro-thermal SCUC problem. On recognizing that the efficiency of the MILP solution scheme strongly depends on the model formulations, we propose several equivalent reformulation techniques for both the objective function and the constraints. For the objective function, we propose the convex hull-based reformulation and the dual representation-based reformulation. These formulations may either reduce the decision variable or tighten the problem. As for the constraints, we propose a tight reformulation for the vibration area constraints. We show that using the continuous relaxation of some binary decision variables in the start-stop constraint also returns the binary solution. We also rewrite the ramping constraints and propose a heuristic cut for the minimum ON and OFF time constraints. Based on the parameters from practical application, we provide computational results by comparing the above reformulations with the original formulation. The experiment results demonstrate that the proposed reformulations may substantially improve the efficiency of the MILP solver.

Keywords: Hydro-thermal SCUC · Reformulation · Piece-wise linear function · SOS · Compact model

1 Introduction

The security-constrained unit commitment (SCUC) model plays an essential role in the weekly and day-ahead planning in power systems. As a special case of this type of model, the hydro-thermal SCUC problem aims to find the optimal use of the available bulk generation resources for both thermal generating units and the hydroelectric units during the scheduling period (see, e.g., [1–5]). In the real world's applications, although there are different power generation modes including thermal power units, hydropower units, wind power units, and nuclear power units, the thermal power and hydropower units are the mainstream power generation modes in the current power industry. The large-scaled hydro-thermal SCUC is notorious hard to solve. This is due to the different characteristics of the different type of power generations [6–9, 25]. The inconsistency of the modeling methods of different power generation models can lead to non-compact

modeling formulation, which often leads to the low efficiency for the solution scheme. Therefore, it is necessary to study the efficiency of various formulations (see e.g., [26–28] for related research).

The mixed-integer linear programming (MILP) has become the most popular method to solve the hydro-thermal SCUC scheduling problem [6] largely due to the recent development in the MILP solution techniques. The seminar work [28] shows that different formulations of the MILP problems may lead to significant difference in the performance while solving the classical unit commitment (UC) problem. From a computational point of view, a reformulation with tighter continuous relaxation bound has a positive impact on the performance of a mixed-integer programming solver [10, 11]. That motivates efforts to obtain tighter reformulations of unit commitment problems in the sense of tighter continuous relaxation bound, for example see [12–14]. For the problem of similar structures, tighter reformulations are also extensively investigated in the literature [15–17]. However, tighter reformulations always require additional constraints. Even worse, the size of the reformulations may be larger than the original model. To overcome this drawback, under some restrictive assumptions, [18] creates a tighter reformulation of the same size as the original problem, based on the "inherent piecewise nature" discussed in [19]. Reference [17] proposes an alternative tighter reformulation of the original size based on the lifting-and-convexification technique. The two tighter reformulations of the original size can help improve the performance of mixed-integer programming solver for unit commitment problems and are still not feasible when the size of unit commitment problems grows large. Also, researchers often use SOS constraints to formulate the constraints of some hydropower-related vibration regions [20]. If these constraints bring in a large number of binary variables without compaction, the excessive scale of the model will also result in the model being difficult to solve. As for the thermal unit-based UC problem, [27] and [28] study the various tight and compact formulations which are promising in computational results.

Motivated by the previous research, in this paper, we propose different reformulations of the classic Hydro-thermal SCUC model, and test the efficiency of these reformulations in large scaled problems with randomly generated demands. We propose several equivalent reformulation techniques for both objective function and the constraints. For the objective function, we propose the convex hull based the reformulation and the dual representation based the reformulation. These formulations may either reduce the decision variable or tighten the problem. As for the constraints, we propose a tight reformulation for the vibration area constraints. We show that the using the continuous relaxation of some binary decision variables in start-stop constraint also returns the binary solution. We also rewrite the ramping constraints and propose a heuristic cut for the minimum ON and OFF time constraints. We then evaluate these reformulations in computational experiments. Note that, the objective function, the vibration-area constraints of hydropower units, the reconstruction of the ramping constraints and the proposed heuristic cut are new in the literature. Based on the modeling we described, we propose a novel modeling reconstruction method and analyze the impact of the reformulation of each type of constraints above, and finally prove that the combination of these reformulations may accelerate the solution process through a series of numerical experiments.

This paper is organized as follows. In Sect. 2, we present the classical mathematical model for the hydro-thermal SCUC problem. In Sect. 3, we propose various reformulations for the objective functions and constraints. We then conduct the numerical experiments in Sect. 4. Finally, some concluding remarks are given in Sect. 5.

2 Classical Hydro-Thermal SCUC Model Formulation

The SCUC problem aims to determine a scheduling of the generating units to meet the forecasted demand, which is considered as a mathematical programming problem, and due to the shutdown/ startup action, the binary variable is unavoidably brought into the problem, which makes this problem to be the mixed-integer linear programming problem (MILP). In this section, we provide the standard MILP formulation of the Hydro-thermal SCUC problem. For convenience of illustration, we adopt a simplified version of the formulation of the standard hydro-thermal SCUC formulation studied in [21, 22]. More complicated hydro-thermal SCUC model can be found in [23–25]. Note that, although our formulation is a simplified version, it includes all the essential constraints commonly used in the hydro-thermal SCUC problem. The basic parameters and the decision variables are as follows.

2.1 Notations

- Input Parameters (Table 1):

Table 1. The definition of the parameters.

Parameter	Definition
$\mathcal{G}$	Index set of the thermal power generator
$\mathcal{G}^h$	Index set of the hydropower generator
$\mathcal{T}$	Total number of periods;
$\mathcal{L}$	Number of lines
$C_{i,t,m}$	Pricing of the unit $i \in \mathcal{G}$ in the $m - th$ output interval at time $t \in \mathcal{T}$
T_i^{On}	Minimum-ON duration for generator $i \in \mathcal{G}$
T_i^{off}	Minimum-OFF duration for generator $i \in \mathcal{G}$
D_t	Total demand at time $t \in \mathcal{T}$
NS_i	Maximum number of startup action for generator $i \in \mathcal{G}$
ND_i	Maximum number of shutdown action for generator $i \in \mathcal{G}$
$SU_{i,t}$	Unit startup cost for generator $i \in \mathcal{G}$ and time $t \in \mathcal{T}$
$SD_{i,t}$	Unit shutdown cost for generator $i \in \mathcal{G}$ and time $t \in \mathcal{T}$
P_i^U and P_i^L	Maximum and minimum generation for unit $i \in \mathcal{G}$

(*continued*)

Table 1. (*continued*)

Parameter	Definition
RD_i and RU_i	Ramp-down and ramp-up rate for unit $i \in \mathcal{G}$
$R_i^{\max}$ and $R_i^{\min}$	Maximum and minimum reserve for unit $i \in \mathcal{G}$
R_t	Total reserve requirement of all generators
P_l	Power generation of l-th line in the power flow constraints, $l \in \mathcal{L}$
$Q_{j,\max}$ and $Q_{j,\min}$	Maximum and minimum of water discharge for unit $j \in \mathcal{G}^h$
$X_{j,\max}$ and $X_{j,\min}$	Maximum and minimum of water storage for unit $j \in \mathcal{G}^h$
$GSF_{i,l}$	Generation shift distribution factor by generators i to the grid line l
$\Im_{k,j}$	Time delay corresponding to water transporting from hydropower generator j to generator k, $j, k \in \mathcal{G}^h$
$J_j(t)$	Natural inflow for hydropower generator $j \in \mathcal{G}^h$ and time $t = 0, 1, \ldots, T$

- Decision Variables (Table 2):

Table 2. The definition of the variables.

Variable	Definition
$P_{i,t} \in \mathbb{R}$	Output power of thermal unit $i \in \mathcal{G}$ at time $t \in \mathcal{T}$
$P_{i,t,m} \in \mathbb{R}$	Allocated power of the unit $i \in \mathcal{G}$ in the $m-th$ output interval at time $t \in \mathcal{T}$
$I_{i,t} \in \{0, 1\}$	On/off status of i-th thermal unit, $i \in \mathcal{G}$ and $t \in \mathcal{T}$; If $I_{i,t} = 1$, the i-th generator is online; $I_{i,t} = 0$, otherwise;
$W_{i,t} \in \{0, 1\}$	Startup status of i-th thermal unit, $i \in \mathcal{G}$ and $t \in \mathcal{T}$
$Y_{i,t} \in \{0, 1\}$	Shutdown status of i-th thermal unit, $i \in \mathcal{G}$ and $t \in \mathcal{T}$
$R_{i,t}$	Amount of total reserve, $i \in \mathcal{G}$ and $t \in \mathcal{T}$
$X_j(t)$	Amount of water storage of hydropower generator $j \in \mathcal{G}^h$ at the time $t \in \mathcal{T}$
$Q_j(t)$	Amount of water discharge of hydropower generator $j \in \mathcal{G}^h$ at the time $t \in \mathcal{T}$
$\delta_{j,l,t}$	The binary variable represents whether the generation of hydropower generator $j \in \mathcal{G}^h$ at the time $t \in \mathcal{T}$ falls in the l-th interval

2.2 The Objective Function of the Hydro-Thermal SCUC Model

The objective function of our Hydro-thermal SCUC model is formulated as

$$\min \sum_{i \in G} \sum_{t=1}^{T} \left[F_{i,t}(P_{i,t}) + SU_{i,t}W_{i,t} + SD_{i,t}Y_{i,t} + f_{r,i}(R_{i,t}) \right] \tag{1}$$

where the cost function $F_{i,t}(\cdot)$ is a piece-wise linear function and the function $f_{r,i}(\cdot)$ is a linear function which characterize the costs of operations and penalty of energy reservation, respectively. Specifically, the objective function includes four terms, i.e., the first term is the cost of power generation, the second term is the start-up cost, the third term is the shutdown cost, and the last one is the cost related to reverse.

The function $F_{i,t}(\cdot)$ is the cost function for pricing of units. Suppose there are J intervals for the bid prices, i.e. ($\Delta_0 = 0, \Delta_1, \Delta_2, ..., \Delta_J$). The unit price is given as C_j for these intervals (see Fig. 1). To model this cost, we first introduce the pricing function, which is typically modeled by a piecewise linear function, e.g., the pricing function $f(P)$ has the following form,

$$f_i(P) = \begin{cases} C_{i,1} \ if \ \Delta_{i,0} \leq P \leq \Delta_{i,1} \\ C_{i,2} \ if \ \Delta_{i,1} \leq P \leq \Delta_{i,2} \\ \vdots \\ C_{i,J} \ if \ \Delta_{i,J-1} \leq P \leq \Delta_{i,J} \end{cases} \tag{2}$$
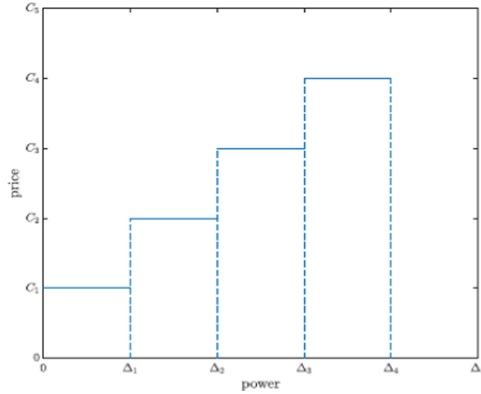
Fig. 1. The bid price

In this this pricing function, the unit price $C_j, j = 1, 2, ..., J$ is a strictly increasing sequence as follows,

$$C_{i,1} \leq C_{i,2} \leq C_{i,3} \leq \cdots \leq C_{i,J} \tag{3}$$

As the pricing function is a piece-wise linear function, the cost function $F_{i,t}(\cdot)$ can be expressed as follows,

$$F_{i,t}(P_{i,t}) = \sum_{m=1}^{J} C_{i,t,m} P_{i,t,m}, \ 0 \le P_{i,t,m} \le P_{i,m}^{\max} - P_{i,m}^{\min} \tag{4}$$

$$C_{i,t,1} \le C_{i,t,2} \le C_{i,t,3} \le \cdots \le C_{i,t,J} \tag{5}$$

$$P_{i,t} = \sum_{m=1}^{J} P_{i,t,m} \tag{6}$$

where the $C_{i,t,m} P_{i,t,m}$ represents the cost in interval $[\Delta_{i,t,m-1}, \Delta_{i,t,m}]$ in our Hydro-thermal model. In this formulation, one continuous decision variable is introduced for each interval. Thus, there are J variables for single plant in one time stage. Equality (4) represents that the cost equals to the price of each segment multiplied by the output value of each segment of units. Constraints (5) indicates that the price is a strictly increasing sequence. Equality (6) denotes $P_{i,t}$ as the summation of output of each segment of units.

2.3 The Basic Thermal Constraints of the Hydro-Thermal SCUC Model

There are three categories of constraints, namely, the unit commitment constraints for the thermal power generator, the security constraints, and the hydro-power constraints. As for the unit commitment constraint, we adopt the standard formulation which uses three types for binary variables to model the status of the generator, i.e.,

The basic start-stop constraints of thermal power units are as follows:

$$\sum_i P_{i,t} = D_t, \quad t \in \mathcal{T}, \tag{7}$$

$$I_{i,t} - I_{i,t-1} = W_{i,t} - Y_{i,t}, \quad t \ge 2, t \in \mathcal{T}, \forall i \in \mathcal{G}, \tag{8}$$

$$W_{i,t} + Y_{i,t} \le 1, \quad t \ge 2, \quad t \in \mathcal{T}, \quad \forall i \in \mathcal{G}, \tag{9}$$

$$\min\left\{T - t, T_i^{On} - 1\right\} \cdot W_{i,t} \le \sum_{k=t}^{t+\min\left\{T-t, T_i^{On}-1\right\}} I_{i,t}, \tag{10}$$

$$t \le T - 1, \quad t \in \mathcal{T} \ \forall \ i \in \mathcal{G},$$

$$\min\left\{T - t, T_i^{off} - 1\right\} \cdot Y_{i,t} + \sum_{k=t}^{t+\min\left\{T-t, T_i^{off}-1\right\}} I_{i,t} \le$$

$$\min\left(T - t, T_i^{off} - 1\right), \quad t \le T - 1, t \in \mathcal{T}, \forall i \in \mathcal{G}, \tag{11}$$

$$\sum_{t=1}^{T} W_{i,t} \le NS_i, \quad \forall i \in \mathcal{G}, \tag{12}$$

$$\sum_{t=1}^{T} Y_{i,t} \leq ND_i, \quad \forall i \in \mathcal{G}, \tag{13}$$

$$W_{i,t} \in \{0, 1\}, \quad Y_{i,t} \in \{0, 1\}, t \in \mathcal{T}, \quad \forall i \in \mathcal{G}. \tag{14}$$

$$I_{0,i} = I_{i,Init}, \quad \forall i \in \mathcal{G}, \quad I_{i,t} \in \{0, 1\}, \tag{15}$$

Constraint (7) represents that the total power generation should satisfy the total load (or power demand). Constraints (8) and (9) use three sets of decision variables to characterize generators' status and the on/off actions. Variable $I_{i,t}$ represents start-stop status of the unit i at time t; variable $W_{i,t} = 1$ represents that the unit i should be turned on at time t and $Y_{i,t} = 1$ means oppositely. Constraints (10) and (11) are the minimum ON time constraint and minimum OFF time constraints, respectively. Constraints (12) and (13) limit the total number of the start-up action and shut-down actions. Constraint (14) and (15) define the bound of the binary decision variables.

The basic ramping constraints are the second group of constraints. Ramping constraints generally limit the solution domain of the model, related to the upward ramping rate and the downward ramping rate, as well as the upper and lower generation limits of the units. These constraints are as follows.

$$P_{i,t} - P_{i,t-1} \leq RU_i I_{i,t-1} + P_i^L (I_{i,t} - I_{i,t-1}) + P_i^U (1 - I_{i,t}) \tag{16}$$

$$P_{i,t-1} - P_{i,t} \leq RD_i I_{i,t} - P_i^L (I_{i,t} - I_{i,t-1}) + P_i^U (1 - I_{i,t-1}), t \in \mathcal{T}, \forall i \in \mathcal{G}, \tag{17}$$

In the above formulation, when the unit is in normal operation, the range of lifting output of units is determined by RU_i and RD_i; when the unit is at the time of startup or shutdown, the range of lift output of units is determined by P_i^L or P_i^U.

We then turn to the security constraints of thermal power units, which are given in the following formulation,

$$I_{i,t} \times P_i^L \leq P_{i,t} \leq P_i^U \times I_{i,t}, \quad t = 1, \ldots, T, \forall i \in \mathcal{G}, \tag{18}$$

$$I_{i,t} \times R_i^{min} \leq R_{i,t} \leq R_i^{max} \times I_{i,t}, t = 1, \ldots, T, \forall i \in \mathcal{G}, \tag{19}$$

$$R_{i,t} + P_{i,t} \leq P_i^U, \quad t = 1, \ldots, T, \forall i \in \mathcal{G}, \tag{20}$$

$$\sum_i R_{i,t} \geq R_t, \quad t = 1, \ldots, T, \tag{21}$$

$$P_l + \sum_i GSF_{i,l} \cdot \Delta P_{i,t} \leq P_i^U, \quad t = 1, \ldots, T, l \in \mathcal{L}, \tag{22}$$

where the security constraints (18), (19) and (20) limit the upper and the lower bounds for the power and the reserve of the i-th generator, respectively. Constraint (21) provides

the lower bound of the total reserve at time t. . Constraint (22) imposes the bound for grid line of the transmit power.

The third class of constraints are for the Hydro-power Units. Roughly speaking, the hydro-power unit constraints are pure linear constraints which are simpler than the thermal generator. Such a simplification is from the fact that the startup/shutdown decisions can ignored without bringing large approximation error for hydro units. Even though, there are some difficulties arising from the water balancing constraints. As we need to record the water flow to limit the units water level, it results the following constraints,

$$X_j(t+1) = X_j(t) + J_j(t) - Q_j(t) + \sum_{k \in \mathfrak{Q}} \left[Q\big(t - \Im_{k,j}\big) \right],$$
$$t = 1, 2, \ldots, T, \forall j \in \mathcal{G}^h, \tag{23}$$

$$P_{HG,j}(t) = F_{HG,j}\big(Q_j(t), X_j(t)\big), \quad t = 1, 2, \ldots, T, \tag{24}$$

$$Q_{j,\min} \le Q_j(t) \le Q_{j,\max}, \quad t = 1, 2, \ldots, T, \tag{25}$$

$$X_{j,\min} \le X_j(t) \le X_{j,\max}, \quad t = 1, 2, \ldots, T, \tag{26}$$

$$X_j(1) = X_{j,1} \quad , \forall j \in \mathcal{G}^h, \tag{27}$$

where the constraints (23) represent water balancing equation, i.e., the amount of water stored at $t+1$ is equal to the amount of water stored at time t plus the natural inflow $J_j(t)$ and minus the discharge $Q_j(t)$ and plus the amount from other hydropower stations. Constraint (24) describes the fact that the power generated by hydropower generation is the function of amount of water stored and discharged. To simplify the discussion, we assume that the function $F_{HG,j}(Q, X)$ is linear function with respect to Q and X. . Constraints (25)–(27) impose the bounds of $X_j(t)$ and $Q_j(t)$ for $j \in \mathcal{G}^h$ and $t \in \mathcal{T}$.

The vibration-area constraints of hydro-power units represents the fact that the power generation of hydro-power units is not continuous, i.e., there are some areas of power generation $P_{HG,j}(t)$ which can not reach. Typically, the vibration-area constraint is formulated as,

$$P_{HG,j}(t) = \delta_{j,1,t}P_{j,\min} + \delta_{j,2,t}P_{j,1}^u + \cdots + \delta_{j,M+1,t}P_{j,M}^u + P_{j,1,t} + P_{j,2,t} + \cdots + P_{j,M,t} \tag{28}$$

$$\begin{cases} 0 \le P_{j,1,t} \le (P_{j,1}^d - P_{j,\min})\delta_{j,1,t} \\ 0 \le P_{j,2,t} \le (P_{j,2}^d - P_{j,1}^u)\delta_{j,2,t} \\ \vdots \\ 0 \le P_{j,M+1,t} \le (P_{j,\max} - P_{j,M}^u)\delta_{j,M+1,t} \end{cases} \tag{29}$$

$$\sum_{l=1}^{M+1} \delta_{j,l,t} \le 1 \tag{30}$$

where the constraint (28) means that the power generation of hydro-power units is determined by start and end points of vibration zones. Constraints (29–30) indicate that the power generation only belongs to a certain period of interval. Figure 2 plots the typical shape of the cost function, when the vibration zone is considered.
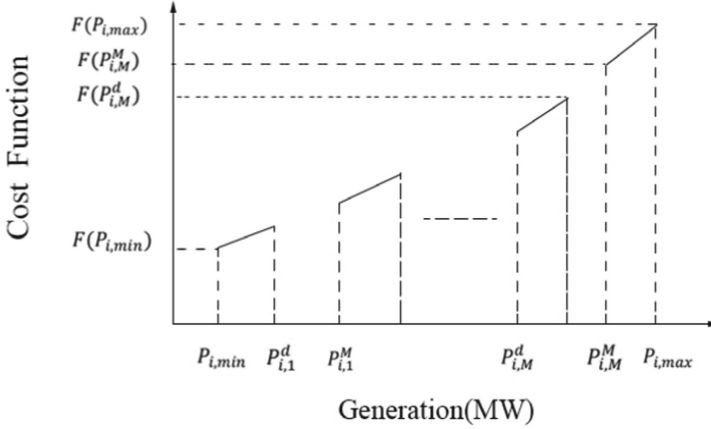
Fig. 2. Vibration zones of power generation of hydro-power units.

3   Compact Hydro-Thermal SCUC Model Formulation

In this section, we propose some novel equivalent formulations of the objective function and constraints, which may enhance the computational efficiency of the mixed-integer programming solver. Although the hydro-thermal SCUC problem considered in this paper ignores some constraints, these reformulations can be easily extended to the more sophisticated models. In the following parts, we mainly propose two groups of reformulations, one group is for the objective function and the other is for the constraints.

3.1   Alternative Formulations of the Objective Function

In the original standard MILP formulation, the objective function (e.g., Eq. (1)) is a piece-wise linear function. To model such a piece-wise linear function, we need to introduce a decision variable for each small interval. Such a formulation can be improved in the sense that the piece-wise linear objective can be represented with fewer variables. We propose two methods, the first one is based on the convex hull representation of the piece-wise linear function, which we called 'PWL' in the following part, and the second one is based on the Special-order-set, which is named the 'SOSR' method.

(I) In the 'PWL' method, we replace the decision variables $P_{i,t,m}$ in basic model by variables $P_{i,t}$. Indeed, we can eliminate the index m and decrease the number of decision variable. Based on the Eqs. (4–6), we can replace the function in the objective function by the following piecewise linear function,

$$F_{i,t}(P_{i,t}) = \begin{cases} C_{i,t,1}P_{i,t} \ P_{i,t} \in [P_{i,1}^{\min}, P_{i,1}^{\max}] \\ C_{i,t,1}P_{i,1}^{\max} + C_{i,t,2}(P_{i,t} - P_{i,2}^{\min}) \ P_{i,t} \in [P_{i,2}^{\min}, P_{i,2}^{\max}] \\ \vdots \\ \sum_{j=1}^{k-1} C_{i,t,j}P_{i,j}^{\max} + C_{i,t,k}(P_{i,t} - P_{i,k}^{\min}) \ P_{i,t} \in [P_{i,k}^{\min}, P_{i,k}^{\max}] \\ \vdots \end{cases} \tag{31}$$

To better illustrate this method, we adopt the following simplified formulation of the function (31). Clearly, function (32) is equivalent the function (31).

$$F(P) = \begin{cases} a_1 p + b_1 \ \Delta_0 \le p \le \Delta_1 \\ \vdots \\ a_j p + b_j \ \Delta_{j-1} \le p \le \Delta_j \\ \vdots \end{cases} \tag{32}$$

It is not hard to verify that function $F(p)$ is a convex function with respect to p when the conditions (3) or (5) hold. Then this piece-wise linear convex function, can be further represented as the maximum of a series of linear functions as follows,

$$F(p) = \max_{j=1,2,\cdots} \{a_j p + b_j\} \tag{33}$$

The above representation is also known as the convex hull of the piece-wise linear convex function. Using the formulation (33) we may rewrite the objective function $F_{i,t}(P_{i,t})$ in the following form,

$$\min\{\phi_{i,t}|\phi_{i,t} \ge a_j P_{i,t} + b_j, j = 1, 2, \ldots, m\} \tag{34}$$

Clearly, using the formulation (34) we may eliminate the index m in the original formulation, which may reduce the number of the decision variables.

(II) We then study the second formulation of the objective function. Comparing with the 'PWL' method, this method takes advantage of the dual formulation the piece-wise linear function. Due to the convexity of the objective function, any points in the convex set can be represented by the linear combination of the vertices of the convex set. We then introduce additional auxiliary variables $\lambda_{i,j,t}, j = 0, 1, 2, \ldots$. We then use Δ_j to denote each endpoint of the segment for the upper bound and lower of the power, i.e..,

$P_{i.k}^{\min}, P_{i,k}^{\max}$.Thus, the decision variable of the power generation can be expressed as,

$$s.t \begin{cases} P_{i,t} = \sum_{j=1}^{m} \Delta_j \lambda_{i,j,t} + \Delta_0 \lambda_{i,0,t} \\ \sum_{j=0}^{m} \lambda_{i,j,t} = \alpha_{i,t} \\ \lambda_{i,j,t} \geq 0, j = 1, 2, \ldots, m.t = 1, 2 \ldots \end{cases} \tag{35}$$

We then adopt the formulation of special-order-set to rewrite the cost function in the following form,

$$F_{i,t}(P_{i,t}) = \sum_{j=1}^{m} \lambda_{i,j,t}(a_j \Delta_j + b_j) + \lambda_{i,0,t}(a_1 \Delta_0 + b_1) \tag{36}$$

Different from the classic special order set techniques, this formulation doesn't consider new binary variables due to SCUC's special construction. Furthermore, due to the special structure of the SCUC problem, it can be easily verified that only two elements of the optimal solution $\lambda_{i,j,t}$ can be positive number while the other elements are zero for every thermal unit. This method can be denoted as "SOSR".

3.2 Reformulations of the Constraints

We then focus on the constraints. We propose the following methods to write the constraints of hydro-power units, the start-up constraints for thermal power units, the ramping constraints for the thermal unit, and the minimum ON time and OFF time constraints.

1) The reformulation of vibration-area constraints of hydro-power units

The constraints of the vibration-area, e.g., constraints (28–30) have the similar structure as the piecewise linear function. Thus, we may adopt the similar technique adopted for the objective function to rewrite such constraints. One advantage of this method is that it can reduce the number of decision variables. Note that to use this method, the power generation range of the hydro-power unit can be identified through the data preprocessing. In the following part, we call this reformulation as 'VCR'. Overall, the constraints (28–30) are reformulated as,

$$\sum_m \delta_{i,m,t} P_{i,m}^d \leq P_{i,t} \leq \sum_m \delta_{i,m,t} P_{i,m}^u \ (21) \tag{37.1}$$

$$\sum_{l=1}^{M+1} \delta_{i,l,t} + \delta_{i,l,0} = I_{i,t}, \delta_{i,l,t} \in \{0, 1\} \ (22) \tag{37.2}$$

The Constraints (28–30) can also be reformulated as SOS constraints (38.1–38.3). A Special-Ordered Set, or SOS constraint, is a highly specialized constraint that places restrictions on the values that variables in a given list can take. There are two types of SOS constraints. In an SOS constraint of type 1 (an SOS1 constraint), at most one

variable in the specified list is allowed to take a non-zero value. In an SOS constraint of type 2 (an SOS2 constraint), at most two variables in the specified, ordered list are allowed to take a non-zero value, and those non-zero variables must be contiguous in the list. By introducing a new continuous variable $\delta_{i,l,0}$ to form a new SOS1 constraint, the reformulation can be easily handled by the solver's internal algorithm. The method to reformulate is defined as 'VCRSOS' shown as below.

$$P_{HG,j}(t) = \delta_{j,1,t}P_{j,\min} + \delta_{j,2,t}P_{j,1}^{u} + \cdots + \delta_{j,M+1,t}P_{j,M}^{u} + P_{j,1,t} + P_{j,2,t} + \cdots + P_{j,M,t} \tag{38.1}$$

$$\begin{cases} 0 \leq P_{i,1,t} \leq \left(P_{i,1}^{d} - P_{i,\min}\right)\delta_{i,1,t} \\ 0 \leq P_{i,2,t} \leq \left(P_{i,2}^{d} - P_{i,1}^{u}\right)\delta_{i,2,t} \\ \vdots \\ 0 \leq P_{i,M+1,t} \leq \left(P_{i,\max}^{d} - P_{i,M}^{u}\right)\delta_{i,M+1,t} \end{cases} \tag{38.2}$$

$$\begin{aligned} \sum_{l=2}^{M+1} \delta_{i,l,t} + \delta_{i,l,0} &= 1 \\ \sum_{l=2}^{M+1} \delta_{i,l,t} + \delta_{i,l,0} &\in SOS \\ \delta_{i,l,t} &\in \mathbb{R} \end{aligned} \tag{38.3}$$

2) **The Reformulation of the Start-Stop Constraints of Thermal Power Units**

The constraints (8–9) define the basic logic for the ON and OFF decision of each thermal unit. Reference [28] has showed that these three sets of binary state variables combining with other thermal unit constraints provide the most the efficient way in modeling the unit commitment problem. We take one more step further by relaxing the binary decision variables $W_{i,t}$, $Y_{i,t}$ as the continuous variables in the unit interval. Our computational experiments show that, although we relax these variables as the continuous variable, these variables take the binary value automatically at the optimal solution. Clearly, such a transformation may reduce the number of binary variables significantly. By using this method, the constraints (8–9) become

$$\begin{cases} W_{i,t} - Y_{i,t} = I_{i,t} - I_{i,t-1} \\ W_{i,t} + Y_{i,t} \leq 1 \\ W_{i,t}, Y_{i,t} \in R^{+} \cup \{0\} \end{cases} \tag{39}$$

Note that in the above formulation the state variable I still only takes the binary value. In the following part, we refer the above formulation as 'SCR'.

3) **The Reformulation of the Ramping Constraints of Thermal Power Units**

The ramping constraints defined in (16–17) introduce some redundant binary decision variables. We are able to reformulate these constraints in a more concise and compact

form with fewer binary variables. More specifically, some binary variables in constraints (16–17) can be eliminated without damaging the logic of these constraints, i.e., it has,

$$P_{i,t} - P_{i,t-1} \leq RU_i I_{i,t-1} + (1 - I_{i,t-1})P_i^L$$
$$P_{i,t-1} - P_{i,t} \leq RD_i I_{i,t} + (1 - I_{i,t})P_i^L \tag{40}$$

In the following part, we refer the above reformulation of the ramping constraints as 'RCR' method.

1) **The Reformulation of the Minimum on Time and Minimum Off Time Constraints**

The constraints (10–11) model the logic of the minimum ON and OFF decision for the thermal units. Typically, the number of binary decision variables involved in these constraints are extreme large. We may reformulate constraints (10–11) in the following way, which may force the constraints to be more compact,

$$I_{i,t} - I_{i,t-1} \leq I_{i,\tau}, \tau \in [t + 1, \min(t + T_i^{on} - 1, T)] \tag{41}$$

$$I_{i,t-1} - I_{i,t} \leq 1 - I_{i,\tau}, \tau \in [t + 1, \min(t + T_i^{off} - 1, T)] \tag{42}$$

In practical implementation, the above formulation can be further strengthened by the minimum ON and OFF cut. More specifically, if there are special thermal units whose minimum and maximum time, T_i^{on} and T_i^{off}, are greater than T, then the unit status of the entire time period T can only be changed once. The logic means that the following inequality should hold,

$$\sum_{t=1}^{T} Y_{i,t} + \sum_{t=1}^{T} W_{i,t} \leq 1 \tag{43}$$

The above constraint provides a deep-cut on these binary variables. We then rewrite the above constraint (43) into two constraints, which takes advantage of the unit initial turn-on or turn-off status, i.e., it can be written as

$$\begin{cases} \sum_{t=1}^{T} W_{i,t} \leq 1, \sum_{t=1}^{T} Y_{i,t} = 0 \ if \ I_{i,1} = 0 \\ \sum_{t=1}^{T} Y_{i,t} \leq 1, \sum_{t=1}^{T} W_{i,t} = 0 \ if \ I_{i,1} = 1 \end{cases} \tag{44}$$

We refer this reformulation of the minimum on time constraints and minimum off time constraints is as the 'MTR' method.

4   Numerical Test

To discuss the issue of the actual efficiency of the proposed reformulations, we conduct some computational experiment experiments. This section aims to test efficiency of

reformulations and compare the proposed reformulation problem with original problem. The numerical tests are run on system equipped with Intel(R) Core (TM) i7-10510U CPU@2.30 GHz with memory 16 GB. We use Solver GUROBI 9.0. Default settings except that we set the time limit to 3,600 s. We use the python API of GUROBI 9.0 to change each constraint needed reconstructed after each reformulation. After the new dataset is input, we will solve the model and collect the optimal results.

Our experiment is mainly based on the dataset adjusted from a certain real grid in China which also contains hydropower-related data. The scale of the dataset is described as containing 3200 nodes, 292 thermal power units, 423 hydropower units and about 600 lines. Taking the generation period of the 5-stage of units as an example, there are at least 418464 continuous variables, at least 165312 binary variables, and at least 716,900 constraints in our hydro-thermal model, in which the demand is within the interval of [100000, 150000] with 96 stages one day. This dataset includes the parameters of basic properties of the generators, such as the switching cost, the minimum continuous switching time, the upper and lower limits of active power generator, the upper and lower limits of reactive power. It also includes grid topology, the backup data of the grid and the pricing data of power generation costs. The unit's number is 715 and the dimension of calculation is every 15 min and 24 h all day, which is a larger scale compared to the thermal problem. All these unit configs come from the real world.

To test the efficiency of various formulations of the objective functions and constraints, we randomly generate the testing cases by sampling the demand for 96 stages for one day. In this demand vector, each element represents the demand for one time stage which is draw from the interval of [100000, 150000] uniformly. We generate 20 tested cases and solve these problems by using various formulations.

To isolate the impact of different reformulations, we first exam three formulations of the objective function, namely, the original MILP objective function (given in Sect. 2.2), the convex hull based on piece-wise linear function (given in Sect. 3.1), and the SOS-based objective function (given in Sect. 3.2). In the following part, we call the above formulations of the objective function as the 'Original', 'PWL' and 'SOSR', respectively. Note that, in all these models, we only change the objective function, all the other constraints are identical to the original MILP formulation. Although these three reformulations are equivalent to each other, the number of decision variable introduced in the model and the number of the auxiliary constraints are different to each other. Table 3 reports the size of three reformulations. We can see that the all these three reformulations introduce similar number of binary decision variables. The SOSR has less constraints and the PWL has less number of continuous decision variables comparing with the original formulation.

We check the computational results for these reformulations. Table 4 shows the computation time and the objective function for 20 random generated instances. All these problems are solved by GUROBI 9.0. The columns 'time' represents the computational time (the unit is second) and the columns 'fval' means the best objective value returned by the solver under the limited computational time (e.g., the maximum computational time is 3600 s). In Table 4, we can see that the objective values of these formulations are identical to each other for all the tested cases, which verifies the equivalence of these

Table 3. The size of test problems

Formulation	Number of continuous variable	Number of binary variable	Number of constraints
Original	418464	165312	716990
SOSR	446496	165312	576830
PWL	334368	165312	716990

Table 4. Comparison results of different Reformulation for Objective Function.

Prob.	Original		PWL		SOSR	
	Time	Fval	Time	Fval	Time	Fval
1	2432.43	2.828E + 10	2736.32	2.828E + 10	2332.64	2.828E + 10
2	3600.41	2.834E + 10	3047.34	2.834E + 10	2789.46	2.834E + 10
3	2785.69	1.413E + 11	873.25	1.413E + 11	3600.47	1.413E + 11
4	3600.32	2.731E + 10	2123.78	2.731E + 10	3600.81	2.731E + 10
5	2697.45	1.327E + 11	3124.34	1.327E + 11	2647.68	1.327E + 11
6	2510.32	1.131E + 11	2800.75	1.131E + 11	2073.56	1.131E + 11
7	2677.34	5.656E + 10	2893.28	5.656E + 10	2635.48	5.656E + 10
8	2758.45	1.138E + 11	2545.48	1.138E + 11	2032.72	1.138E + 11
9	3600.39	2.652E + 10	3411.12	2.652E + 10	2571.69	2.652E + 10
10	2345.65	1.145E + 11	1123.45	1.145E + 11	1448.32	1.145E + 11
11	3343.35	8.484E + 10	3013.24	8.484E + 10	2767.08	8.484E + 10
12	3600.14	5.453E + 10	3600.35	5.453E + 10	3600.87	5.453E + 10
13	3431.42	8.679E + 10	2854.34	8.679E + 10	2765.12	8.679E + 10
14	2734.80	5.327E + 10	2167.34	5.327E + 10	2589.46	5.327E + 10
15	2629.38	2.836E + 10	3324.34	2.836E + 10	2789.82	2.836E + 10
16	3105.34	6.354E + 10	2967.64	6.354E + 10	3343.54	6.354E + 10
17	3435.35	4.539E + 10	2932.65	4.539E + 10	3600.23	4.539E + 10
18	2946.24	5.362E + 10	3033.24	5.362E + 10	2876.56	5.362E + 10
19	2629.18	2.453E + 11	2403.72	2.453E + 11	2804.34	2.453E + 11
20	2728.38	4.357E + 10	2545.78	4.357E + 10	3600.34	4.357E + 10

three formulations (Note that, for some cases, the solver is stopped by the maximum running time, however the GUROBI still returns the best feasible solution).

Table 5. Comparison stats of different reformulation for objective function.

Stats	Original	PWL	SOSR
Mean	2979.60	2676.09	2823.51
Std.	427.18	669.95	583.34
Min.	2345.65	873.25	1448.32
Medium	2772.07	2873.81	2778.27
Max.	3600.41	3600.35	3600.87

To better see the efficiency of these reformulations, we summarize some statistics of the computational time in Table 5. All of these statistics are computed from these 20 test instances. In Table 5, the row 'mean' and row'std' denote the mean value and the standard deviation value of the computational time of the 20 test instances, respectively. Similarly, the 'medium', 'min', and 'max' correspond to the medium value, minimum value and maximum value of the computational time. The reformulation of the objective function is the key factor for speeding up the solution process of Hydro-thermal SCUC problems. From Table 4 and Table 5, we can see that both reformulations provide a better result, i.e., the computational time of the two formulations is less than the original formulation. In detail, we can see that the reformulation 'PWL' provides significantly better mean and min computational time (i.e., the minimum computational time is 873s 1428s, and 2345s for the 'PWL', 'SOSR' and 'Original' methods). The reason that 'PWL' has a larger standard deviation is that it improves some cases dramatically, e.g., the reformulation 'PWL' provide some impressive improvement on case 3, which is almost **4.5 times** better than the original formulation.

Table 6 shows the definition of different notations of different formulations, facilitating readers to better understand. The reconstructed model is based on the original model which is defined as "Original" and the reformulated problem is defined as "Original + X" where X represents different formulation of constraints like "PWL", "SOSR", "VCR" or others.

Table 7 shows which of the two modeling methods we test in Sect. 3.3 is better, reformulating on the basis of the original modeling. Twenty cases above are tested. The average solution time for 20 cases is calculated shown as the Table 7 The average solution time of "VCR" is about 200 s less than the average solution time of "VCRSOS". Hence, we finally decide to adopt the first reformulation method VCR.

Table 8 and Table 9 respectively represent the average index of different reformulations of 20 cases especially the solving time indicating the improved solving efficiency. For the same case, the solution accuracy is with certain guarantee for the same optimal objective value. The difference is that the model in the PWL method has more constraints

Table 6. The definition of different notations of different formulations.

Formulation	Definition
Original	The original modeling
PWL	The objective function reformulation by piece-wise linear function
SOSR	The objective reformulation by special order set
VCR	The first reformulation of vibration-area constraints of hydro-power units
SCR	The reformulation of the start-stop constraints of thermal power units
RCR	The reformulation of the ramping constraints of thermal power units
MTR	The reformulation of the minimum on time constraint and minimum off time constraints
VCRSOS	The second reformulation of vibration-area constraints of hydro-power units(SOS)

Table 7. The definition of different notations of different formulations.

Formulation	Time	Fval	Number of continuous variables	Number of binary variables	Number of constraints
Original + VCR	2534.36	7.708E + 10	377856	165312	595076
Original + VCRSOS	2748.25	7.708E + 10	540288	84096	716990

but less continuous variables, while the model in the SOSR method has more continuous variables and fewer constraints. The number of continuous variables of "PLW" is 32% less than the one of "SOSR", while the number of constraints of "PLW" is 21% more than the one of "SOSR". The number of 0–1 variables is basically the same for both. We can observe that the solution efficiency of the final reformulation of the model increases about **65% to 80%** so that the solving time nearly decreases **by half** for some observed cases. As for the problem size, the number of constraints have relatively smaller impact, while the number of variables has a greater impact on the solution time. However, reducing either one of these factors and increasing the other factor does not necessarily reduce the solution time. However, when the number of constraints and the number of 0–1 variables and continuous variables are reduced, the solution time of the problem will decrease significantly.

Table 8. Average index of different reformulation for 20 cases(Based on PWL).

Formulation	Time	Fval	Number of continuous variables	Number of binary variables	Number of constraints
Original	2979.60	7.708E + 10	418464	165312	716990
PWL	2676.09	7.708E + 10	334368	165312	716990
PWL + VCR	2235.46	7.708E + 10	293760	165312	595076
PWL + VCR + SCR	2210.40	7.708E + 10	349824	109248	595076
PWL + VCR + SCR + RCR	1975.54	7.708E + 10	349824	109248	595076
PWL + VCR + SCR + RCR + MTR	1803.45	7.708E + 10	349824	109248	651140

Table 9. Average index of different Reformulation for 20 cases(Based on SOSR)

Formulation	Time	Fval	Number of continuous variables	Number of binary variables	Number of constraints
Original	2979.60	7.708E + 10	418464	165312	716990
SOSR	2823.51	7.708E + 10	446496	165312	576830
SOSR + VCR	2434.36	7.708E + 10	405888	165312	455006
SOSR + VCR + SCR	2339.42	7.708E + 10	461952	109248	455006
SOSR + VCR + SCR + RCR	2210.34	7.708E + 10	461952	109248	455006
SOSR + VCR + SCR + RCR + MTR	2103.04	7.708E + 10	461952	109248	511070

In different reformulation methods, it's obvious that the reformulation of vibration-area constraints of Hydro-power Units (VCR) and the reformulation of the minimum on time constraint and minimum off time constraints (MTR) play a key role in improving solving efficiency by decreasing half-time. See Fig. 3. Method x refers to the first column of Table 8 and Table 9. The "Fval", the number of continuous variables, binary variables and constraints keep the same with one arbitrary case.
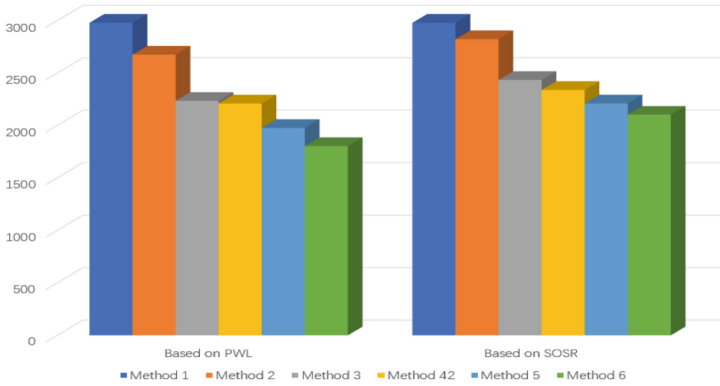
Fig. 3. Comparison results for both reformulations based on PWL and SOSR

5   Conclusion

In this paper, we propose various MILP reformulations for the hydro-thermal SCUC problem. For the objective function, we propose the convex-hull-based and duality-based reformulation, which may reduce the continuous decision variables. For the constraints, we propose the reformulation of vibration-area constraints, the start-stop constraints of thermal power units, the ramping constraints of thermal power units, and the minimum ON-time and minimum OFF-time constraints. Combining these novel reformulations may either reduce the size of the problem or make the model form compact for the solver. The preliminary computational results show that the proposed reformulations could help improve the performance of MILP solvers for SCUC problems significantly. As our standard model ignores some complicated constraints in hydro-thermal SCUC, it will be interesting to investigate which reformulations may improve the computational efficiency when these complicated constraints are involved.

References

1. Orero, S.O., Irving, M.R.: A genetic algorithm modelling framework and solution technique for short term optimal hydrothermal scheduling. IEEE Trans. Power Syst. **13**(2), 501–518 (1998)
2. Gil, E., Bustos, J., Rudnick, H.: Short-term hydrothermal generation scheduling model using a genetic algorithm. IEEE Trans. Power Syst. **18**(4), 1256–1264 (2003)
3. Piekutowski, M., Rose, I.A.: A Linear programming method for unit commitment incorporating generator configurations, reserve and plow constraints. IEEE Trans. Power Appar. Syst. **12**, 3510–3516 (1985)
4. Bansal, R.C.: Optimization methods for electric power systems: An overview. Int. J. Emerg. Electric Power Syst. **2**(1) (2005)

5. Fu, Y., Li, Z., Wu, L.: Modeling and solution of the large-scale security-constrained unit commitment. IEEE Trans. Power Syst. **28**(4), 3524–3533 (2013)
6. Fu, Y., Shahidehpour, M.: Fast SCUC for large-scale power systems. IEEE Trans. Power Syst. **22**(4), 2144–2151 (2007)
7. Su, C., Yuan, W., Cheng, C., et al.: Short-term generation scheduling of cascade hydropower plants with strong hydraulic coupling and head-dependent prohibited operating zones. J. Hydrol. **591**, 125556 (2020)
8. Kong, J., Skjelbred, H.I., Fosso, O.B.: An overview on formulations and optimization methods for the unit-based short-term hydro scheduling problem. Electric Power Systems Research **178**, 106027 (2020)
9. Cheng, C., Wang, J., Wu, X.: Hydro unit commitment with a head-sensitive reservoir and multiple vibration zones using MILP. IEEE Trans. Power Syst. **31**(6), 4842–4852 (2016)
10. Zheng, X., Sun, X., Li, D., et al.: Lagrangian decomposition and mixed-integer quadratic programming reformulations for probabilistically constrained quadratic programs. Eur. J. Oper. Res. **221**(1), 38–48 (2012)
11. Zheng, X., Sun, X., Li, D.: Improving the performance of MIQP solvers for quadratic programs with cardinality and minimum threshold constraints: a semidefinite program approach. Informs J. Comput. **26**(4), 690–703 (2014)
12. Frangioni, A., Gentile, C.: Perspective cuts for a class of convex 0–1 mixed integer programs. Math. Program. **106**(2), 225–236 (2006)
13. Frangioni, A., Gentile, C., Lacalandra, F.: Tighter approximated MILP formulations for unit commitment problems. IEEE Trans. Power Syst. **24**(1), 105–113 (2008)
14. Frangioni, A., Furini, F., Gentile, C.: Approximated perspective relaxations: a project and lift approach. Comput. Optim. Appl. **63**(3), 705–735 (2016)
15. Aktürk, M.S., Atamtürk, A., Gürel, S.: A strong conic quadratic reformulation for machine-job assignment with controllable processing times. Oper. Res. Lett. **37**(3), 187–191 (2009)
16. Günlük, O., Linderoth, J.: Perspective reformulations of mixed integer nonlinear programs with indicator variables. Math. Program. **124**(1), 183–205 (2010)
17. Wu, B., Sun, X., Li, D., et al.: Quadratic convex reformulations for semicontinuous quadratic programming. SIAM J. Optim. **27**(3), 1531–1553 (2017)
18. Frangioni, A., Gentile, C., Grande, E., et al.: Projected perspective reformulations with applications in design problems. Oper. Res. **59**(5), 1225–1232 (2011)
19. Tawarmalani, M., Sahinidis, N.V.: Semidefinite relaxations of fractional programs via novel convexification techniques. J. Global Optim. **20**(2), 133–154 (2001)
20. Zhao, Z., Cheng, C.T., Yan, L.: An efficient and accurate Mixed-integer linear programming model for long-term operations of large-scale hydropower systems. IET Renew. Power Gener. **15**(6), 1178–1190 (2021)
21. Diniz A L. Test cases for unit commitment and hydrothermal scheduling problems[C]//IEEE PES General Meeting. IEEE, 2010: 1–8
22. Amjady, N., Ansari, M.R.: Security-constrained unit commitment considering hydro units and ac network modeling by a new hybrid solution method composed of benders decomposition and outer approximation. Electric Power Compon. Syst. **40**(13), 1445–1469 (2012)
23. Norouzi, M.R., Ahmadi, A., Nezhad, A.E., et al.: Mixed integer programming of multi-objective security-constrained hydro/thermal unit commitment. Renew. Sustain. Energy Rev. **29**, 911–923 (2014)
24. Alvarez, A.M., Louveaux, Q., Wehenkel, L.: A machine learning-based approximation of strong branching. Informs J. Comput. **29**(1), 185–195 (2017)
25. Zhou, B., Geng, G., Jiang, Q.: Hydro-thermal-wind coordination in day-ahead unit commitment. IEEE Trans. Power Syst. **31**(6), 4626–4637 (2016)
26. Ostrowski, J., Anjos, M.F., Vannelli, A.: Tight mixed integer linear programming formulations for the unit commitment problem[J]. IEEE Trans. Power Syst. **27**(1), 39–46 (2011)

27. Morales-España, G., Latorre, J.M., Ramos, A.: Tight and compact MILP formulation for the thermal unit commitment problem. IEEE Trans. Power Syst. **28**(4), 4897–4908 (2013)
28. Carrión, M., Arroyo, J.M.: A computationally efficient mixed-integer linear formulation for the thermal unit commitment problem. IEEE Trans. Power Syst. **21**(3), 1371–1378 (2006)

Robust Optimal Dispatching Method for Electric Vehicles-Integrated Microgrid Under Uncertainties

Siyang Shao[1,2]([✉]), Xiang Ma[1,2], Wei Yuan[1,2], Kaiyu Zhang[3], Xiaofei Fu[3], and Chenhong Huang[3]

[1] NARI Group Corporation (State Grid Electric Power Research Institute), Nanjing 211106, China
shaosiyang@sgepri.sgcc.com.cn
[2] NARI Nanjing Control System Co., Ltd., Nanjing 211106, China
[3] State Grid Shanghai Municipal Electric Power Company, Shanghai 200122, China

Abstract. To address the uncertainties caused by renewable energy generation and load demand in microgrids, a novel robust optimal dispatching method is proposed with the consideration of "Vehicle to Grid". The model of disordered electric vehicles (EVs) charging and also the model of ordered EVs charging\discharing are firstly established. After that, the optimal dispatching model considering the uncertainties of renewable energy generation and load demand is proposed to minimize the operating cost of the microgrid. The column constraint generation algorithm is used to determine the worst-case scenario and then compute the optimal dispatching strategy. Case study is presented to demonstrate the effectiveness of the proposed method.

Keywords: Microgrid · Electric vehicles · Disordered charging · Ordered charging\discharging · Robust optimization · Column constraint generation

1 Introduction

To mitigate the impacts of large scale electric vehicles (EVs) integration into the power grids, the idea of "Vehicle to Grid" (V2G) is proposed in [1]. In V2G mode, EVs can serve as energy storage systems (ESSs) to discharge so as to provide power support to the power grid when necessary. Therefore, the ordered charging\discharging mechanism of EVs can improve the economical and environmental benefits of the microgrids [2, 3]. A bi-level optimization model is proposed in [4] for ordered charging\discharging of EVs. In [5], an improved model is proposed considering the time-of-use pricing mechanism in order to mitigate the negative impacts on the economical efficiency of microgrid

operation. However, the renewable energy generation and load demand in microgrids have shown the characteristics of intermittency and uncertainty, which will deteriorate the effectiveness of the dispatching strategy under the forecasting errors [6].

Stochastic optimization [7, 8] and robust optimization [9–12] are usually used in microgrid economical dispatching under uncertainties. Considering the uncertainty of renewable energy generation, a fuzzy chance-constrained programming model is proposed in [7] to maximize the operating benefit of the microgrid. On the basis of [7], the uncertainty of load is also included in [8] and the improved stochastic chance constrained programming model is proposed. However, to evaluate the probability distribution accurately, a large number of sampling is needed for stochastic optimization, which makes stochastic optimization methods computationally burdensome. Robust optimization is proposed to address the above-mentioned shortcoming of stochastic optimization and to reduce the risk of performance degradation of the microgrid under the worst-case scenarios. In [10], the uncertainty of the intermittent renewable energy is introduced and a novel multi-objectives robust dispatching model is proposed to accommodate the large scale integration of renewable energy. In [12], the Benders decomposition method is used to compute the multi-scenario robust dispatching strategy for microgrid operation.

In this paper, the idea of V2G is employed in the operation of grid-connected microgrid with the integration of EVs, ESSs, controllable distributed generation (CDG), and renewable energy generation (REG). Two models are established respectively to simulate the characteristics of disordered EV charging and ordered EV charging\discharging. After that, considering the uncertainties of renewable energy generation and load demand, a novel robust dispatching model is proposed to minimize the operating cost of the microgrid. The column constraint generation (CCG) algorithm is used to solve this robust dispatching model. Case study is presented to demonstrate the effectiveness of the proposed method.

2   Modelling of Microgrid

As is shown in Fig. 1, microgrids usually consist of controllable distributed generation, energy storage systems, renewable energy generation, conventional loads and electric vehicles. Besides, the central coordinator of the microgird generates the dispatching strategy by flexibly adjusting the active power exchange of all the above-mentioned components to meet the load demands.

2.1   Electric Vehicles

Only the private-owned electric vehicles are considered in this paper. So it can be assumed that these EVs have their regular travelling patterns. The capacities of the lithium battery of these EVs C_{EV} are equally 21.6 kWh, while the upper and lower limits of the state of charge (SOC) are 90% and 20% respectively. The demands of charging and discharging of EVs can be determined by Monte Carlo simulation [13].
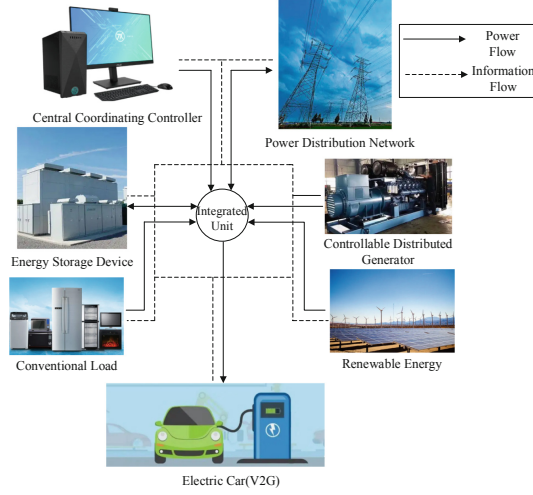
Fig. 1. Demonstration of the structure of the microgrid

The Temporal-Spacial Characteristic of EVs. The probabilistic density function of the travelling range S of EVs is given in (1):

$$f_s(x) = \frac{1}{x\sigma_s\sqrt{2\pi}}exp\left[-\frac{(\ln x - \mu_s)^2}{2\sigma_s^2}\right] \tag{1}$$

where $\mu_s = 8.92$ and $\sigma_s = 3.24$ as is proposed in [14].

Assuming that the instance of EV returning is also the instance that the EV charging starts, the probabilistic density function of the starting instance t_0 is given in (2):

$$f_t(x) = \begin{cases} \frac{1}{\sigma_t\sqrt{2\pi}}exp\left[-\frac{(\ln x - \mu_t)^2}{2\sigma_t^2}\right], \mu_t - 12 < x < 24 \\ \frac{1}{\sigma_t\sqrt{2\pi}}exp\left[-\frac{(\ln x - (\mu_t - 24))^2}{2\sigma_t^2}\right], 0 < x < \mu_t - 12 \end{cases} \tag{2}$$

where $\mu_t = 17.47$ and $\sigma_t = 3.41$.

Disordered EV Charging. In this case, the demand of EV charging is determined only by the owner's preference, without obeying any dispatching strategy. The duration of EV charging T_{ch} is given in (3):

$$T_{ch} = \frac{SW}{100P_{ch}\eta_{ch}} \tag{3}$$

where W is the power consumption every 100 km, P_{ch} is the active power of EV charging, and η_{ch} is the coefficient of charging efficiency.

Based on the starting instance t_0 and the duration of charging T_{ch}, the demand of EV charging can be generated by Monte Carlo simulation (Fig. 2).
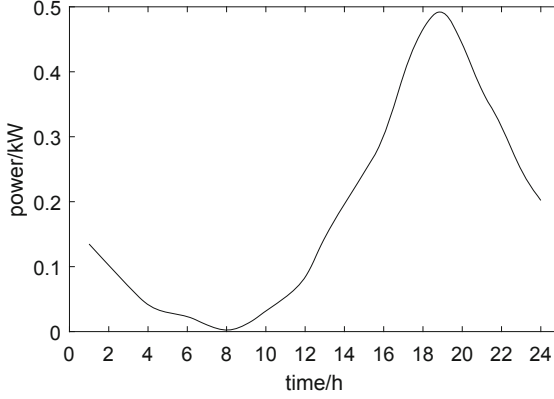
Fig. 2. Simulation of the load demand of disordered EV charging

Ordered EV Charging\Discharging. In V2G mode, EVs serve as a special kind of ESSs and can be used for peak shaving in power grids [15]. Then the maximum duration of EV discharging T_{dis}^{max} is given in (4):

$$T_{dis}^{max} = \frac{\Delta SOC \cdot C_{EV}}{P_{dis}} - \frac{SW}{100 P_{dis}} \tag{4}$$

where ΔSOC is the difference between the upper and lower limits of the SOC. P_{dis} is the active power of discharging. Considering the dispatching period as $T \in [0, 24]$, the practical duration of discharging T_{dis} is determined by (5):

$$T_{dis} = \begin{cases} 24 - t_0, t_0 + T_{dis}^{max} > 24 \\ T_{dis}^{max}, t_0 + T_{dis}^{max} \le 24 \end{cases} \tag{5}$$

Also, the duration of EV charging T_{ch} is defined in (6):

$$T_{ch} = \frac{P_{dis} T_{dis}^{max} - P_{dis} T_{dis}}{P_{ch} \eta_{ch}} \tag{6}$$

Based on the starting instance t_0, the practical duration of discharging T_{dis} and the duration of charging T_{ch}, the demand of ordered EV charging\discharging can be generated by Monte Carlo simulation as is shown in Fig. 3. It should be noted that, the positive value represents the state of charging while the negative value represents the state of discharging.

2.2 Controllable Distributed Generations

In this paper, the diesel generator is considered as the CDG, whose operating constraint is given in (7):

$$P_g^{min} \le P_g(t) \le P_g^{max} \tag{7}$$
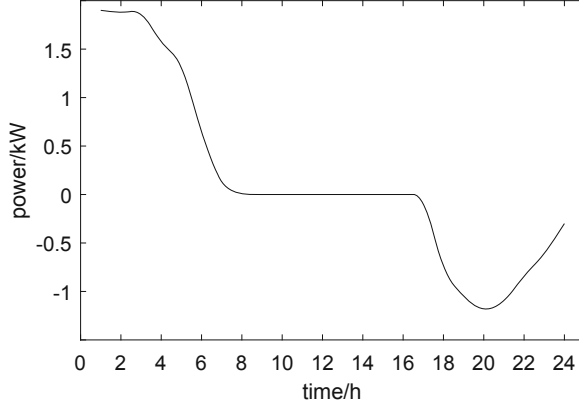
Fig. 3. Simulation of the load demand of ordered EV charging\discharging

where $P_g(t)$ is the active power generation of the diesel generator at t instance, while P_g^{max} and P_g^{min} represent the upper and lower limits of the active power generation.

The cost function for the operation and maintenance of the diesel generator is given in (8):

$$C_g(t) = \left(c_g^o + c_g^m \right) P_g(t) \tag{8}$$

where $C_g(t)$ is the total cost of the diesel generator at t instance, while c_g^o and c_g^m are the cost coefficients for operation and maintenance.

2.3 Energy Storage Systems

The operating constraints for ESS are given in (9–10):

$$0 \leq P_{ec}(t) \leq \zeta_e(t) P_{ec}^{max} \tag{9}$$

$$0 \leq P_{ed}(t) \leq [1 - \zeta_e(t)] P_{ed}^{max} \tag{10}$$

where $P_{ec}(t)$ and $P_{ed}(t)$ are the active power of charging and discharging of the ESSs at t instance, while P_{ec}^{max} and P_{ed}^{max} are the upper limits for charging and discharging. $\zeta_e(t)$ denotes the operating state of ES, with $\zeta_e(t) = 1$ representing charging state and $\zeta_e(t) = 0$ representing discharging state.

The remaining capacity of the ESS is also constrained by (11) and (12):

$$E_e^{min} \leq E_e(0) + \eta_{ec} \sum\nolimits_{t^*=1}^{T} \left[P_{ec}(t^*) \Delta t \right] - \frac{1}{\eta_{ed}} \sum\nolimits_{t^*=1}^{T} \left[P_{ed}(t^*) \Delta t \right] \leq E_e^{max} \tag{11}$$

$$\eta_{ec} \sum\nolimits_{t^*=1}^{T} \left[P_{ec}(t^*) \Delta t \right] = \frac{1}{\eta_{ed}} \sum\nolimits_{t^*=1}^{T} \left[P_{ed}(t^*) \Delta t \right] \tag{12}$$

As is in (11), the remaining capacity of the ESS needs to obey its upper and lower limits. $E_e(0)$ denotes the initial capacity of the ESS, η_{ec} and η_{ed} denote the efficiency

of charging and discharging respectively, while E_e^{max} and E_e^{min} denote the maximum and minimum remaining capacity. Based on (12), the charging capacity is equal to the discharging capacity so as to make the ESS to maintain the initial capacity $E_e(0)$ for the next dispatching period.

The operating cost of the ES is given in (13):

$$C_e(t) = c_e^o[P_{ec}(t) + P_{ed}(t)] \tag{13}$$

where $C_e(t)$ is the operating cost of the ESS at t instance and c_e^o is the cost coefficient.

2.4 Renewable Energy Generation and Loads

The photovoltaic (PV) generation is considered as the renewable energy generation in the microgrid. The uncertainties of PV and load can be modeled by (14):

$$U = \left\{ \begin{array}{c} u = [P_l(t), P_r(t)] \in \mathbb{R}^{T \times 2}, t = 1, \cdots, T \\ P_l^f(t) - \Delta_l(t) \leq P_l(t) \leq P_l^f(t) + \Delta_l(t) \\ P_r^f(t) - \Delta_r(t) \leq P_r(t) \leq P_r^f(t) + \Delta_r(t) \end{array} \right\} \tag{14}$$

where $P_l(t)$ and $P_r(t)$ are the load demand and the PV generation at t instance, $P_l^f(t)$ and $P_r^f(t)$ are the forecasting value at t instance, while $\Delta_l(t)$ and $\Delta_r(t)$ are the ranges of the forecasting errors.

According to [16], Eq. (14) can be linearized and then transformed into (15):

$$U = \left\{ \begin{array}{c} u = [P_l(t), P_r(t)] \in \mathbb{R}^{T \times 2}, t = 1, \cdots, T \\ P_l(t) = P_l^f(t) - \tau_l(t)\Delta_l(t) \\ P_r(t) = P_r^f(t) - \tau_r(t)\Delta_r(t) \\ 0 \leq \sum_{t=1}^{T} \tau_l(t) \leq \Gamma_l \\ 0 \leq \sum_{t=1}^{T} \tau_r(t) \leq \Gamma_r \end{array} \right\} \tag{15}$$

where $\tau_l(t)$ and $\tau_r(t)$ are the auxiliary variables, while Γ_l and Γ_r are the margin of uncertainty. Microgird operators can regulate the value of Γ_l and Γ_r according to their preference to risk and robustness.

2.5 The Interaction Between the Microgrid and the Distribution System

When there is power surplus or shortage in the microgrid, the microgrid needs to interact with the distribution system to meet the power balance as is given in (16):

$$P_g(t) + P_r(t) + P_{ed}(t) - P_{ec}(t) + P_{grid,b}(t) - P_{grid,s}(t) = P_l(t) + P_{evs}(t) \tag{16}$$

where $P_{grid,b}(t)$ and $P_{grid,s}(t)$ represent the purchasing and selling power at t instance. Apart from the constraint in (16), the following constraints also need to be met:

$$0 \leq P_{grid,b}(t) \leq \varphi_{grid}(t)P_{grid,b}^{max} \tag{17}$$

$$0 \leq P_{grid,s}(t) \leq \left[1 - \varphi_{grid}(t)\right] P_{grid,s}^{max} \tag{18}$$

where $P_{grid,b}^{max}$ and $P_{grid,s}^{max}$ are the maximum limits of purchasing and selling power. $\varphi_{grid}(t)$ denote the state of power exchange, with $\varphi_{grid}(t) = 1$ representing the state of purchasing and $\varphi_{grid}(t) = 0$ representing the state of selling.

The cost for power exchange with the distribution system is given in (19):

$$C_{grid}(t) = \omega(t)\left[P_{grid,b}(t) - P_{grid,s}(t)\right] \tag{19}$$

where $C_{grid}(t)$ is the cost for power exchange and $\omega(t)$ is the spot price for electricity at t instance.

3   Robust Dispatching Model of Microgrid with EVs

The objective for the proposed robust dispatching model is to minimize the operating cost for the microgrid. The objective function is given in (20):

$$\min C = \sum_{t=1}^{T}\left[C_g(t) + C_e(t) + C_{grid}(t)\right] \tag{20}$$

Meanwhile, the constraints that are defined in (7), (9–12), and (15–18) are considered in the proposed robust dispatching model.

For simplicity, the above-mentioned optimal dispatching model is rewritten in the form of matrix:

$$\min_{\boldsymbol{x}}\left\{\max_{\boldsymbol{u}\in U}\min_{\boldsymbol{y}\in\Omega(\boldsymbol{x},\boldsymbol{u})} q^T y\right\} \tag{21}$$

$$\boldsymbol{D}\boldsymbol{y} \geq \boldsymbol{d} \tag{22}$$

$$\boldsymbol{N}\boldsymbol{y} = \boldsymbol{n} \tag{23}$$

$$\boldsymbol{F}\boldsymbol{x} + \boldsymbol{G}\boldsymbol{y} \geq \boldsymbol{h} \tag{24}$$

$$\boldsymbol{R}\boldsymbol{y} = \boldsymbol{u} \tag{25}$$

where

$$\begin{cases} x = \left[\zeta_e(t), \varphi_{grid}(t)\right] \\ y = \left[P_g(t), P_l(t), P_r(t), P_{evs}(t), P_{ec}(t), P_{ed}(t), P_{grid,b}(t), P_{grid,s}(t)\right] \\ \qquad\qquad t = 1, \cdots, T \end{cases} \tag{26}$$

The proposed model is a bi-level optimization problem. The discrete variables $\boldsymbol{x}$, such as the operating state of ESS and the state of power exchange, are determined by the outer level problem. Meanwhile, the max-min problem in the inner level is computed to solve the continuous variables $\boldsymbol{u}$ and $\boldsymbol{y}$ and to search for the optimal dispatching strategy

to cope with the worst-case scenario under the uncertainties of PV generation and loads. The constraints in (7) and (11) are represented by (22). The equality constraints in (12) and (16) are represented by (23). The constraint in (15) is represented by (25). The other constraints are now represented by (24).

The column constraint generation algorithm [17] is used to compute the bi-level robust optimization model in (21)–(25). This optimization problem is decoupled into a main problem (MP) and a sub problem (SP). The main problem is given in (27)–(32):

$$\min_{x,\partial} \partial \tag{27}$$

$$\partial \geq \mathbf{q}^{\mathrm{T}} \mathbf{y}^{\nu}, \forall \nu \leq k \tag{28}$$

$$\mathbf{D}\mathbf{y}^{\nu} \geq \mathbf{d}, \forall \nu \leq k \tag{29}$$

$$\mathbf{N}\mathbf{y}^{\nu} = \mathbf{n}, \forall \nu \leq k \tag{30}$$

$$\mathbf{F}\mathbf{x} + \mathbf{G}\mathbf{y}^{\nu} \geq \mathbf{h}, \forall \nu \leq k \tag{31}$$

$$\mathbf{R}\mathbf{y}^{\nu} = \mathbf{u}^{\nu*}, \forall \nu \leq k \tag{32}$$

where k is the number of iterations. $\mathbf{y}^{\nu}$ represents the auxiliary variables after the νth iteration and $\mathbf{u}^{\nu*}$ represents the worst-case scenario solved by the sub problem after the νth iteration.

The sub problem is given in (33)–(37):

$$\max_{\mathbf{u} \in U} \min_{\mathbf{y} \in \Omega(\mathbf{x}^*, \mathbf{u})} q^T y \tag{33}$$

$$\mathbf{D}\mathbf{y} \geq \mathbf{d} \tag{34}$$

$$\mathbf{N}\mathbf{y} = \mathbf{n} \tag{35}$$

$$\mathbf{F}\mathbf{x}^* + \mathbf{G}\mathbf{y} \geq \mathbf{h} \tag{36}$$

$$\mathbf{R}\mathbf{y} = \mathbf{u} \tag{37}$$

where $\mathbf{x}^*$ represents the decision variable of the outer level. Based on the sub problem, the worst-case scenario $\mathbf{u}$ and the continuous variables $\mathbf{y}$ can be solved.

The strong duality theorem [19] is used to transform this bi-level sub problem into a single-level problem. Then the main problem and the sub problem are solved iteratively until the convergence is reached. The procedure is demonstrated in Fig. 4
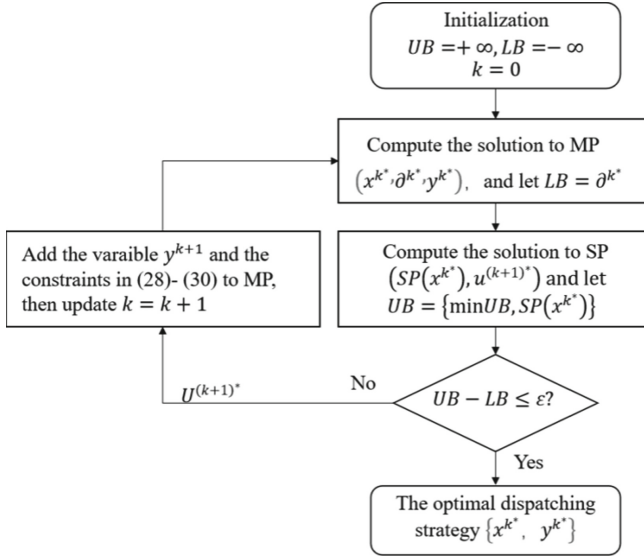
Fig. 4. Demonstration of the procedure of solving the robust optimal dispatching model by the CCG algorithm

4 Case Study

4.1 Description of Testing Microgrid

The grid-connected microgrid in Fig. 1 is used for case study. The overall period of dispatching is 24 h. The uncertainties of PV generation and load demands are considered. There are 150 EVs integrating to this community-wise microgrid. The margins of uncertainty are set as $\Gamma_l = 12$ and $\Gamma_r = 6$. The parameters of the diesel generator and the energy storage system are listed in Table 1 and Table 2 respectively. The rated capacity of the ESS is 1 MW·h while the initial available capacity is 500 kW·h.

Table 1. Parameters of the diesel generator

Component	P_g^{min}	P_g^{max}	c_g^o	c_g^m
Diesel Generator	40 kW	400 kW	0.52 Yuan/kW	0.15 Yuan/kW

According to historical data, the forecasting errors of PV generation and load demand are set as ±15%, as is shown in Fig. 5. The spot price for power exchange between the microgrid and the distribution system is shown in Fig. 6.

4.2 Comparative Results on Different EV Charging\Discharging Strategies

To compare the impacts of different EV charging\discharging strategies on the efficiency of microgrid operation, the following strategies are simulated:

Table 2. Parameters of the energy storage system

Component	P_{ec}^{max}	P_{ed}^{max}	E_e^{min}
ESS	250 kW	250 kW	300 kW·h
E_e^{max}	η_{ec}	η_{ed}	c_e^o
1000 kW·h	0.95	0.95	0.32 Yuan/kW
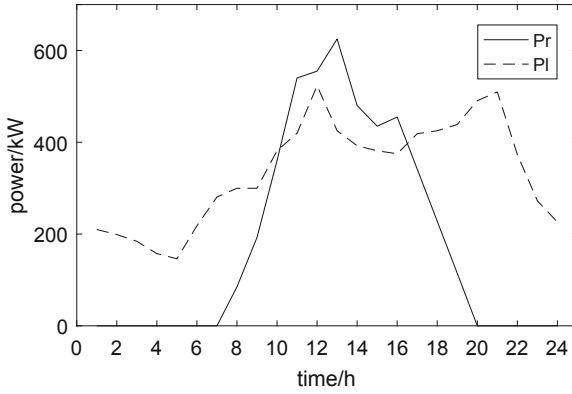
Fig. 5. The forecasting curves of PV generation and load demand
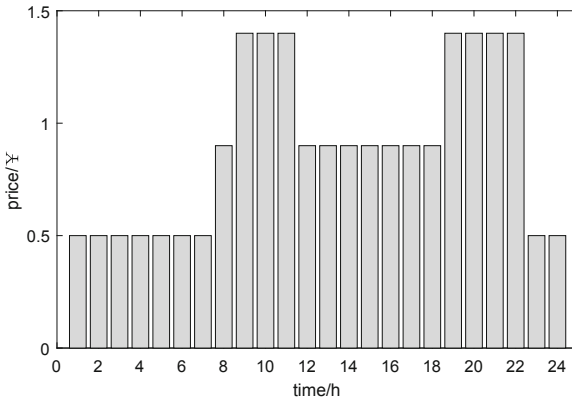
Fig. 6. The spot price of power exchange with the distribution network

Strategy 1: The disordered charging mode is adopted so the EVs only participate in the microgrid dispatching like conventional loads.

Strategy 2: The ordered charging\discharging mode is adopted so the EVs discharge during the peak-load period like the ESS.

The simulation results under these two strategies are shown in Fig. 7 and Fig. 8 respectively. It should be noted that the positive active power of ESS represents the

state of charging and vice versa. Also, the positive value of power exchange means the microgrid exports active power to the distribution network.
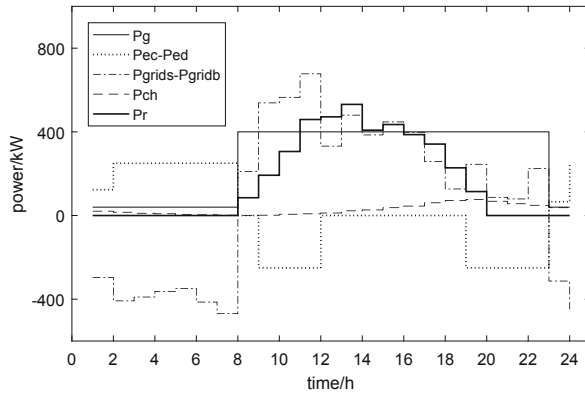
Fig. 7. Dispatching results under disordered charging strategy of EVs
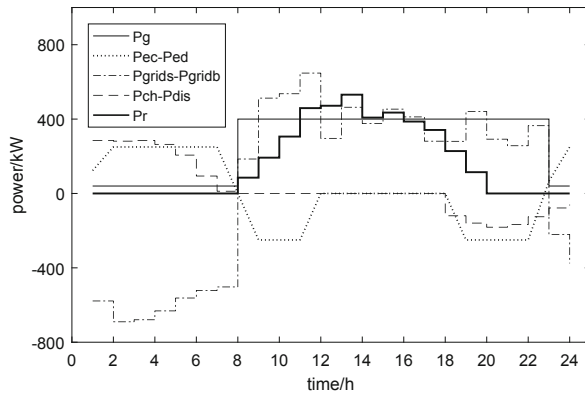
Fig. 8. Dispatching results under ordered charging\discharging strategy of EVs

The major difference between these two strategies is discussed as follows. Under the strategy of ordered EV charging\discharging (**Strategy 2**), the EVs discharge during the peak-load period from 18:00 to 24:00 and charge during the valley-load period from 0:00 to 7:00. But for the strategy of disordered EV charging (**Strategy 1**), the EVs charge during the peak-load period from 18:00 to 24:00, which inevitably increase the operating cost of the microgrid.

The comparison of the operating cost under different strategies is shown in Table 3. It can be seen that, under the ordered EV charging\discharging strategy, the EVs charge during the valley load-period and discharge like the ESS during the peak-load period. Therefore, the ordered EV charging\discharging strategy has the advantage of peak shaving and valley filling, which in turn reduces the cost of electricity purchasing from the distribution system when the spot price is relatively higher during the peak-load period. In comparison, the cost under the ordered EV charging\discharging strategy has reduced by about 20%, which significantly enhance the economical efficiency of the microgrid.

Table 3. Comparison of the economics of the two strategies

Strategy	1-disordered EV charging	2-ordered EV charging\discharging
Cost	1789.2 Yuan	Yuan

4.3 Sensitivity Analysis on Uncertainties of Renewable Energy and Loads

To study the influence of the uncertainties of PV generation and load demand on the economical efficiency of the microgrid, the sensitivity analysis is carried out by adjusting the margin of uncertainty. The following cases are considered:

Case 1: $\Gamma_l = 0$ and $\Gamma_r = 0$
Case 2: $\Gamma_l = 12$ and $\Gamma_r = 6$

In **Case 1**, the value of PV generation and load demand is equal to the forecasting result. In other words, the uncertainties are not considered. But in **Case 2**, the value of PV generation deviates from the forecasting results in 6 periods, and the value of load demand generation deviates from the forecasting results in 12 periods.

Under the above-mentioned cases, the operating costs of the microgrid are shown in Table 4. When the ordered EV charging\discharging mode (**Strategy 2**) is adopted, the cost of microgrid dispatching in day-ahead planning is 1454.4 Yuan under **Case 2** ($\Gamma_l = 12$ and $\Gamma_r = 6$), which is much higher than the cost of 363.5 Yuan under **Case 1** ($\Gamma_l = 0$ and $\Gamma_r = 0$). However, as the uncertainty is not taken into consideration, higher regulation cost is needed in real-time operation for **Case 1**. As a result, the total cost for **Case 1** is 1852.7 Yuan, while the total cost for **Case 2** is 1697.2 Yuan. The economical efficiency of **Case 2** is increased by 8.3%, which demonstrates that the uncertainties of renewable energy generation and load demand should be considered in day-ahead planning stage, which can address the impact of forecasting error on the microgrid and reduce the operating cost in real-time operation.

Table 4. Comparison of the simulation results under different setting of the margin of uncertainty (units: Yuan)

Strategy	Case 1: $\Gamma_l = 0$ and $\Gamma_r = 0$			Case 2: $\Gamma_l = 12$ and $\Gamma_r = 6$		
	Day-ahead planning	Real-time regulation	Total cost	Day-ahead planning	Real-time regulation	Total cost
1	734.2	1433.5	2167.7	1789.2	248.1	2037.3
2	363.5	1489.2	1852.7	1453.4	243.8	1697.2

5 Conclusion

In this paper, a novel robust optimal dispatching method is proposed. The model of disordered EV charging and also the model of ordered EV charging\discharing are firstly established. After that, the optimal dispatching model considering the uncertainties of renewable energy generation and load demand is proposed to minimize the operating cost of the microgrid. The column constraint generation algorithm is used to determine the worst-case scenario and then compute the optimal dispatching strategy. Numerical results show that:

1) Under the guidance of ordered EV charging and discharging strategy, EVs will discharge like energy storage systems during the peak-load period and then charge during the valley-load period. This makes the best of the time-of-use pricing mechanism and results in the peak shaving and the operating cost reduction of the microgrid.
2) By considering the uncertainties of renewable energy generations and load demands in day-ahead operation planning, the massive compensation that is caused by forecasting error during the operating stage can be avoided, which will enhance the robustness and economical effectiveness of microgrids.

References

1. Kempton, W., Tomic, J.: Vehicle-to-Grid power fundamentals: calculating capacity and net revenue. J. Power Sources **144**(1), 268–279 (2005)
2. Xiao, X., Chen, Z., Liu, N.: Integrated mode and key issues of renewable energy sources and electric vehicles' charging and discharging facilities in micro grid. Trans. China Electrotech. Soc. **28**(2), 1–14 (2013)
3. Zhang, W., Wu, B., Li, W., et al.: Discussion on development trend of battery electric vehicles in china and its energy supply mode. Power Syst. Technol. **33**(4), 1–5 (2009)
4. Yao, W., Zhao, J., Wen, F., et al.: A charging and discharging dispatching strategy for electric vehicles based on bi-level optimization. Autom. Electric Power Syst. **36**(11), 30–37 (2012)
5. Wang, J., Tang, J., Liu, S.: Orderly charging and discharging strategies for electric vehicles based on user responsiveness. Electron. Meas. Technol. **44**(01), 31–36 (2021)
6. Sang, B., Zhang, T., Liu, Y., et al.: Two-stage robust optimal scheduling of grid-connected microgrid under expected scenarios. Proc. CSEE **40**(19), 6161–6173 (2020)

7. Wang, J., Shi, J., Wen, F., et al.: Optimal operation of combined heat and power microgrid in CSP station considering demand response. Autom. Electric Power Syst. **43**(1), 1000–1026 (2019)
8. Yang, L., Ding, Z., et al.: Optimization of network loss scheduling strategy for CCHP microgrid. Electr. Meas. Instrument. **57**(7), 74–81 (2020)
9. An, Y., Zeng, B.: Exploring the modeling capacity of two-stage robust optimization: variants of robust unit commitment Mdoel. IEEE Trans. Power Syst. **30**(1), 109–122 (2014)
10. Xie, P., Peng, C., Yu, R.: Multi-objective robust optimized scheduling of power grid connected with large-scale intermittent power sources. Proc. CSEE **34**(19), 3063–3072 (2014)
11. Xiang, Y., Liu, J., Wei, Z., et al.: Robust model of microgrid energy optimization with uncertain renewable energy sources. Proc. CSEE **34**(19), 3063–3072 (2014)
12. Xu, Q., Deng, C., Zhao, W., et al.: A multi-scenario robust dispatch method for power grid integrated with wind farms. Power Syst. Technol. **38**(3), 653–661 (2014)
13. Chang, X., Song, Z., Wang, J.: Electric vehicle charging load prediction and system development based on monte carlo algorithm. High Voltage Apparat. **56**(08), 1–5 (2020)
14. Vyas, A., Santini, D.: Use of national surveys for estimating 'full' PHEV potential for oil use reduction (2008). http://www.transportation.anl.gov/pdfs/HV/525.pdf
15. Li, X., Tan, Y., Liu, X., et al.: A cost-benefit analysis of V2G electric vehicles supporting peak shaving in Shanghai. Electric Power Syst. Res. **179**, 106058 (2020)
16. Wei, W., Liu, F., Mei, S., et al.: Robust energy and reserve dispatch under variable renewable generation. IEEE Transa. Smart Grid **6**(1), 369–380 (2015)
17. Zeng, B., Zhao, L.: Solving two-stage robust optimization problems using a column-and-constraint generation method. Oper. Res. Lett. **41**(5), 457–461 (2013)
18. Boyd, S., Vandenberghe, L.: Convex Optimization. World Book Incorporation, Beijing (2013)
19. Gupt, A., Ahmed, S., Cheon, M.S., et al.: Solving mixed integer bilinear problems using MILP formulations. SIAM J. Optim. **23**(2), 721–744 (2013)

Marginal Unit Location Method Based on Dual Simplex Sensitivity Analysis

Yantao Zhang[1,2(✉)], Li Chang[1,2], Rongzhang Cao[1,2], Wen Wang[1,2], Zhendong Zang[1,2], and Shuomin Wu[1,2]

[1] NARI Group Corporation (State Grid Electric Power Research Institute), Nanjing 211106, Jiangsu, China
zhangyantao@sgepri.sgcc.com.cn

[2] State Key Laboratory of Smart Grid Protection and Control, Nanjing 211106, Jiangsu, China

Abstract. With the continuous settlement and trial operation in the domestic power spot market, the price volatility analysis scenarios of the LMP widely used by power spot pilot provinces have gradually increased, and the real-time nature has gradually increased. Since LMP is affected by many factors, and different factors are coupled with each other, it is impossible to quickly and accurately analyze the reasons for node price fluctuations and pricing units. Therefore, combined with the domestic spot market clearing and pricing two-stage optimization strategy and the mature dual simplex theory, a marginal unit location method based on dual simplex sensitivity analysis is proposed. The method supports different scenarios such as unit independent pricing, unit, and constraint slack variable joint pricing, etc. The rationality of the positioning method is verified by the PJM 5 node and practical example. The results show that the method is universal and has been applied to several spot pilots.

Keywords: Marginal unit · Locational marginal price · System marginal price · Network congestion · Sensitivity analysis

1 Introduction

Since 2019, the first batch of 8 pilot provinces in the domestic power spot market have carried out long-term continuous settlement trial operation, and the overall operation is in good condition. Except for Inner Mongolia and Fujian, other pilot provinces have adopted the locational marginal price (LMP). The theory of LMP originates from the concept of real-time electricity price proposed by F.C.Schweppe of MIT in 1980 [1], which represents variation in generation and transmission cost to the variation in load at the considered node [2–5]. LMP reflects the nodal price to deliver a supplementary increment of power to the other node with no breach of the system constraints [6]. Because of its space-time characteristics, it can effectively solve the congestion problem in complex power grids, such as ring main grids and power grids with many blocked lines [7, 8]. Recently, in order to solve the problem of congestion, the Inner Mongolia

power spot market has gradually transformed from the average electricity price model that is cleared by replacement of power generation rights to LMP model that is cleared by full power centralized bidding.

With the continuous trial operation of long-term uninterrupted settlement in the first batch of power spot pilot provinces, the fluctuation of LMP has become the focus of market participants. Therefore, analyzing the influencing factors of LMP and grasping the reasons for the fluctuation of LMP have become the key to the safe and stable operation of the power spot market. Literature [9–15] analyzes its impact on LMP from the aspects of data quality, Grid-connected new energy units, unit declared capacity and price, load forecast, line transmission capacity, and incoming water. Literature [16] classified and summarized the influencing factors of LMP, and analyzed and quantitatively verified the influencing factors of LMP from three levels: power supply side, grid side and load side. References [17, 18] analyzed the relationship between LMP and constraints such as the maximum and minimum output of units, slopes and landslides, and system reserve, and decomposed LMP into electricity price components related to unit operation constraints.

Although domestic and foreign scholars have conducted in-depth research on many influencing factors of LMP[9–18], due to too many influencing factors and the more complex constraints and clearing pricing methods involved in the actual operating system, market participation cannot quickly analyze the real-time fluctuations of LMP. Therefore, it is urgent to study the positioning method of the marginal units of the system, and to quickly grasp the trend of LMP by intuitively monitoring the changes of the marginal units of the system at different time, so as to effectively supervise the market participants with market power.

In this paper, combined with the two-stage optimization strategy of clearing and pricing in the current power spot market pilot provinces, and aiming at the application defects of the marginal unit identification method, a marginal unit location method based on dual simplex sensitivity analysis is proposed. This method can be applied to the rapid positioning of marginal units under different market models and different trading varieties. After the marginal units of the system are determined, visualization technology [19] is used to visually and quickly display the relationship between the marginal unit quotation and LMP, which provides a fast and effective auxiliary decision-making analysis method for LMP fluctuation and market power supervision in the power spot market.

2   Two-Step Optimization Strategy

The domestic power spot market pilots generally adopt a two-step optimization strategy of market clearing and pricing. The main reasons include the following three: 1) The algorithm relaxation penalty coefficients are different in the two steps of clearing and pricing; 2) The day-ahead market clearing model includes 0/1 variable, the shadow price cannot be calculated; 3) The LMPs of some pilot provinces adopt the pricing strategy of time decoupling.

The rules of the electricity spot market clearly stipulate that it is necessary to adhere to the safe, high-quality and economical operation of the power system to ensure continuous and reliable power supply. Therefore, in order to improve the robustness of the market

clearing algorithm to ensure that the global optimal solution can be found in extreme cases, the rationality of the boundary data is checked and the constraint slack variable is introduced to expand the feasible region to ensure the existence of the optimal solution. The constraint slack variable can also be understood as a virtual resource, which can be given a higher penalty price to make it tend to zero. In order to ensure that the clearing results meet the requirements of safe operation of the power grid, the power balance and network security constraints in the market clearing model select a high-order relaxation penalty coefficient to avoid virtual resources winning bids. However, once the virtual resource wins the bid, the penalty factor of the virtual resource is priced, which is seriously higher than the price of scarce electricity acceptable to the market. Therefore, after the market is cleared, the LMP is calculated by setting the virtual resource penalty coefficient acceptable to the market based on the winning result of the market clearing.

The power spot market includes the day-ahead market and the real-time market. The decision-making variables of the day-ahead market include the commitment status and output power of unit, and the real-time market decision variable only includes unit output. Since the commitment status of the unit is a 0/1 variable, the type of the day-ahead market clearing model is mixed integer linear programming model. Since the shadow prices of various constraints cannot be directly given, it is necessary to introduce the LMP calculation model to calculate the price after the market is cleared. Fixed the commitment status of units based on the results of the market clearing model, the LMP calculation model becomes a linear programming model that can calculate various constrained shadow prices.

The market clearing model takes the maximization of social welfare as the optimization objective, and comprehensively considers constraints such as unit operation, network security, and system operation. Most of the constraints are time-period decoupling constraints, and only the unit ramping up and down constraints are time-period coupling constraints, so that the LMP price components conduct each other between time periods. It increases the complexity of node price analysis and weakens the transparency of node price. Aiming at the above problems, a pricing method of time decoupling is proposed. Based on the winning bid results of market clearing, this method decouples the coupling of unit ramping up and down constraints to calculate LMP.

3   Spot Market Clearing Model

3.1   Objection Function

At present, the domestic spot pilot provinces generally adopt one-side clearing on the power generation side. Therefore, the optimization objective is to minimize the cost of power generation. After further introducing the slack variables of power balance and network security constraints, it can be expressed as:

$$
\min \sum_{i=1}^{N} \sum_{t=1}^{T} \left[C_{i,t}(P_{i,t}) + C_{i,t}^{U} \right] + \sum_{t=1}^{T} M_b \left[LB_t^+ + LB_t^- \right]
$$

$$
+ \sum_{l=1}^{NL} \sum_{t=1}^{T} M_l \left[SL_{l,t}^+ + SL_{l,t}^- \right] + \sum_{s=1}^{NS} \sum_{t=1}^{T} M_s \left[SL_{s,t}^+ + SL_{s,t}^- \right]
$$

(1)

where N and T are the numbers of units and time periods, respectively. $p_{i,t}$ is the power output of unit i at time t. $C_{i,t}(P_{i,t})$ is the operating cost of unit i at time t. $C_{i,t}^U$ is the start-up cost of unit i at time t. $SL_{l,t}^+$ and $SL_{l,t}^-$ are the positive and negative slack variables of network security constraints in branch l at time t. $SL_{s,t}^+$ and $SL_{s,t}^-$ are the positive and negative relaxation variables of network security constraints of section s at time t. M_l and M_s are the relaxation coefficients of branch l and section s, respectively. LB_t^+ and LB_t^- are the positive and negative slack variables of power balance constraint at time t. M_b are the relaxation coefficients of power balance constraint at time t.

3.2 Constraints

Constraints mainly include system operation constraints, unit operation constraints and network security constraints.

1) System operation constraints

System operation constraints include power balance constraint. It can be expressed as:

$$\sum_{i=1}^{N} P_{i,t} = D_t + LB_t^+ - LB_t^- \tag{2}$$

where D_t is the predicted system load at time t.

2) Unit operation constraints

The unit operation constraints include maximum and minimum power output constraints, ramping up and down constraints, minimum down-time and up-time constraints, etc., and their expressions are as follows:

$$\begin{aligned}
\alpha_{i,t} P_{i,t}^{\min} &\leq P_{i,t} \leq \alpha_{i,t} P_{i,t}^{\max} \\
y_{i,t} - z_{i,t} &= \alpha_{i,t} - \alpha_{i,t-1} \\
y_{i,t} + z_{i,t} &\leq 1 \\
\sum_{k=t-T_U}^{t-1} \alpha_{i,k} &\geq z_{i,t} T_i^u \\
\sum_{k=t-T_D}^{t-1} (1 - \alpha_{i,k}) &\geq y_{i,t} T_i^d \\
P_{i,t} - P_{i,t-1} &\leq \Delta P_i^U (1 - y_{i,t}) + P_{i,t}^{\min} y_{i,t} \\
P_{i,t-1} - P_{i,t} &\leq \Delta P_i^D (1 - z_{i,t}) + P_{i,t}^{\min} z_{i,t}
\end{aligned} \tag{3}$$

where $P_{i,t}^{\max}$ and $P_{i,t}^{\min}$ are the maximum and minimum power limits of unit i *at time t*, respectively. $\alpha_{i,t}$ is the commitment status of unit i at time t. ΔP_i^U and ΔP_i^d are maximum ramp up and down capacity of unit i, respectively. T_i^u and T_i^d are the minimum up-time and down-time of unit i. $y_{i,t}$ represents that the unit i changes from the offline status to the online status at time t. $z_{i,t}$ represents that the unit i changes from the online status to the offline status at time t.

The unit operating cost is expressed as follows:

$$P_{i,t} = \sum_{m=1}^{M} P_{i,t,m}$$
$$P_{i,m}^{\min} \leq P_{i,t,m} \leq P_{i,m}^{\max}$$
$$C_{i,t}(P_{i,t}) = \sum_{m=1}^{M} C_{i,t,m} P_{i,t,m} \qquad (4)$$
$$C_{i,t}^{U} = y_{i,t} C_{i}^{U}$$

where $P_{i,t,m}$ is the clearing power of unit i in the quotation interval m at time t. $C_{i,t,m}$ is the price of the unit i in the segmented quotation interval m at time t. $P_{i,m}^{\min}$ and $P_{i,m}^{\max}$ are the power of the left and right endpoints of the quotation interval m of unit i. C_{i}^{U} is the start-up cost of unit i.

3) Network security constraints

The network security constraints are expressed as follows:

$$-P_{l}^{\max} \leq \sum_{i=1}^{N} G_{l-i} P_{i,t} - \sum_{k=1}^{K} G_{l-k} D_{k,t} - SL_{l,t}^{+} + SL_{l,t}^{-} \leq P_{l}^{\max}$$
$$\qquad (5)$$
$$-P_{s}^{\max} \leq \sum_{i=1}^{N} G_{s-i} P_{i,t} - \sum_{k=1}^{K} G_{s-k} D_{k,t} - SL_{s,t}^{+} + SL_{s,t}^{-} \leq P_{s}^{\max}$$

where $P_{l}^{\max}$ and $P_{s}^{\max}$ are the capacity of transmission line l and section s, respectively. G_{l-i} is the generation shift factor (GSF) of unit i with respect to line l. G_{l-k} is the GSF of node k with respect to line l. $D_{k,t}$ is the predicted bus load at node k and time t. G_{s-i} is the GSF of unit i with respect to section s. G_{s-k} is the GSF of node k with respect to section s.

4 LMP Calculation Model

The LMP calculation model fixes the operating state of the unit, adjusts the slack variable penalty price in the optimization objective, and decouples the unit ramping up and down constraints. In order to avoid the large adjustment of the unit output due to the different penalty coefficients in the LMP calculation, the upper and lower limits of the unit output are reset to a small bandwidth based on the market bid results.

4.1 Objection Function

The optimization objective of the LMP calculation model is same as that of the spot market clearing model. Since the unit commitment status of the unit is fixed, there is no need to consider the start-up cost.

$$\min \sum_{i=1}^{N} \sum_{t=1}^{T} \left[C_{i,t}(P_{i,t}^{lmp}) + C_{i,t}^{U} \right] + \sum_{t=1}^{T} M_b \left[LB_t^+ + LB_t^- \right]$$

$$+ \sum_{l=1}^{NL} \sum_{t=1}^{T} M_l \left[SL_l^+ + SL_l^- \right] + \sum_{s=1}^{NS} \sum_{t=1}^{T} M_s \left[SL_{s,t}^+ + SL_{s,t}^- \right] \tag{6}$$

where $P_{i,t}^{lmp}$ is the output of unit i at time t; M_b, M_l and M_s are set as the market acceptable penalty price for the calculation of the scarcity pricing.

The LMP calculation model can also use the slack variable results of the spot market clearing model to correct the system load and transmission section limits, so that the power balance constraints and network security constraints are strictly established, and only the power generation cost is retained in the optimization objective. This price calculation method is not introduced in this paper.

4.2 Constraints

System operation, generation costs and grid security constraints are the same as in the market clearing model and will not be repeated here. Since the commitment status of the unit is fixed, there is no need to consider constraints such as the minimum start and stop time. However, it is necessary to correct the maximum and minimum output constraints of the unit, as well as unit ramping up and down constraints.

1) Maximum and minimum output constraints of the unit

$$P_{i,t}^{lmp} \leq \min \left(P_{i,t}^{\max}, P_{i,t} + \delta \right)$$
$$P_{i,t}^{lmp} \geq \max \left(P_{i,t}^{\min}, P_{i,t} - \delta \right) \tag{7}$$

where δ is the upper and lower adjustment range of the unit output power.

2) Unit ramping up and down constraints

$$P_{i,t}^{lmp} - P_{i,t-1} \leq \Delta P_i^u$$
$$P_{i,t-1} - P_{i,t}^{lmp} \leq \Delta P_i^d \tag{8}$$

In the formula, the time period decoupling of the unit output is realized by constructing the ramping up and down constraints of the unit output $P_{i,t}^{lmp}$ of the node price calculation model and the unit output of the market clearing model $P_{i,t-1}$. This constraint can be kept the same as the market clearing model for the spot pilot provinces with time-coupled pricing, but then the marginal units in each time period are not only composed of units in the current time period, but also include units whose output is adjusted in other related time periods. In order to clearly illustrate the principle of marginal unit positioning, this paper adopts the method of time decoupling to introduce.

5 Marginal Unit Positioning Method

5.1 Marginal Unit Identification Method

At present, the commonly used marginal unit location method is the marginal unit identification method, and its basic principle is the basic definition of LMP. Since there is no blockage in the node, if the load of a node increases by 1 MW, it will be provided by a unit in the node, so the node price is equal to the output price of the unit, and this unit can be called the marginal unit of the node. Therefore, it is only necessary to search for all units whose bid price is equal to the node price to obtain all possible marginal unit sets, and then filter out the units with limited constraints to obtain the marginal unit set.

From the basic principle of the marginal unit identification method, the premise of the establishment of this method is that the decision variable in the node electricity price calculation model only includes the unit output and does not include the slack variable. Therefore, when the network security constraints in the LMP calculation model are strictly established, the conclusion that the number of marginal units is equal to the number of blocking sections plus 1 can be obtained. When the LMP calculation model contains slack variables and the slack variables are not zero, the above conclusion no longer holds. At this time, the marginal unit identification method cannot accurately locate, so this paper proposes a marginal unit location method based on dual simplex sensitivity analysis.

5.2 Dual Simplex Sensitivity Analysis Method

In order to facilitate the derivation of the conclusion, the nodal price calculation model is abstracted and written in the standard form of linear programming:

$$\begin{aligned} \min Z_1 &= CX \\ AX &= b \\ X &\geq 0 \end{aligned} \tag{9}$$

where A is the constraint condition coefficient matrix (composed of constraint condition coefficients such as system operation, unit operation, network security, etc.). b is the constant term on the right side of the constraints (such as the system load in the power balance constraints, the network security constraints, etc.). C is the price coefficient (including unit declared price, relaxation constraint penalty coefficient, etc.). X represents decision variables (including unit output, slack variables, etc.). The above model is called problem P1, and the model type is linear programming model.

Construct problem P2 based on problem P1, see (10) for details:

$$\begin{aligned} \min Z_2 &= CX \\ AX &= b+d \\ X &\geq 0 \end{aligned} \tag{10}$$

where d can be regarded as the disturbance vector of the constant b on the right side of the constraint condition, for example, the system load disturbance on the right side of the power balance constraint is 1MW.

Next, write the dual problems of problem P1 and problem P2, which are called dual problems DP1 and DP2 respectively. See (11) for details.

$$
\begin{array}{cc}
DP1 & DP2 \\
\max W_1 = Yb & \max W_2 = Y(b+d) \\
YA = C & YA = C \\
Y \geq 0 & Y \geq 0
\end{array}
\tag{11}
$$

It can be seen from Eq. (11) that the dual problems DP1 and DP2 have the same feasible domain. If y^* is assumed to be the optimal solution to the dual problem DP1, it is also a feasible solution to the dual problem DP2. According to the weak duality theorem, the objective value of any feasible solution of the dual problem DP2 is less than the optimal value of the original problem P2. The specific expression is shown in (12):

$$
\min Z_2 \geq y^*(b+d) = y^*b + y^*d = \min Z_1 + y^*d
\tag{12}
$$

Assuming that only the j-th element d_j in the disturbance vector d is greater than zero (which can also be understood as the system load disturbance d_j at time j), and other elements are all zero, then Eq. (12) can be further simplified as Eq. (13):

$$
(\min Z_2 - \min Z_1)\big/_{d_j} \geq y^*d\big/_{d_j} = y_j^*
\tag{13}
$$

In formula (13), if $d_j=1$, it can be understood that after the electricity load on the right side of power balance constraint in problem P1 increases by 1MW and becomes problem P2, the change in power generation cost is greater than or equal to the shadow price y^* of the power balance constraint at time j. Therefore, it cannot be guaranteed that the optimal value change after the system load disturbance on the right side of the power balance constraint is equal to the shadow price of the power balance constraint (that is the energy price, which can also be called the reference nodal price). Therefore, the winning unit with output force change obtained by the system load disturbance cannot be determined as a marginal unit.

Although the power balance constraint shadow price is defined as the change in power generation cost caused by the small disturbance of the system load on the right side, the scope of the small disturbance is not clearly defined. Therefore, the first problem is to clarify the disturbance range of the system load on the right side, and ensure that the Eq. (13) is established when the disturbance is within this range. That is to say, to ensure that the optimal basis of the problems P1 and P2 are the same, the optimality criterion should satisfy the formula (14):

$$
\begin{array}{c}
B^{-1}b \geq 0 \\
C_N - C_B B^{-1}N \leq 0
\end{array}
\tag{14}
$$

where B is the optimal basis matrix of the problem P1; N is the non-optimal basis matrix; C_N is the price coefficient of the non-optimal basis variable; C_B is the price coefficient of the optimal basic variable; B^{-1} is the optimal basis Inverse matrix.

It can be seen from Eq. (14) that after the constant term perturbation d on the right side of problem P1 becomes problem P2, to ensure that the optimal basis remains unchanged, it only needs to satisfy Eq. (15):

$$B^{-1}(b+d) \geq 0 \qquad (15)$$

Since b is a constant term, the optimal basis inverse matrix B^{-1} has been calculated in the nodal price calculation model, so the maximum disturbance amount ϑ of the disturbance vector d can be calculated by formula (15), only the disturbance amount If d is within ϑ, the optimal basis can be guaranteed to remain unchanged, that is, the Eq. (13) is established. At this time, the cost change obtained by the small disturbance of the system load on the right side of the power balance constraint is the shadow price of the power balance constraint after normalization.

Since the disturbance amount d is disturbed within ϑ to obtain the problem P2 with the same optimal basis as the problem P1, the optimal solution of the problem P2 is $B^{-1}(b+d)$, see Eq. (16):

$$B^{-1}(b+d)=B^{-1}b + B^{-1}d \qquad (16)$$

In formula (16), since $B^{-1}b$ is the optimal solution of problem P1, the variation of problem P2 relative to the solution of problem P1 is $B^{-1}d$, so the non-zero elements in $B^{-1}d$ are marginal units. If the decision variables are not all units, for example, there are slack variables in power balance constraints and network security constraints. Then the non-zero elements may be composed of units and slack variables. In this case, the marginal unit identification method cannot be used to locate.

6   Case Analysis

In order to verify the validity of the results in this paper and clearly explain the rationality of the results, this paper uses the PJM 5-node and practical example to build calculation scenarios for testing. Through the comparative analysis of the marginal unit identification method and the sensitivity analysis method, the effectiveness and universality of the sensitivity analysis method are illustrated.

6.1   Basic Parameters of Standard Case

The PJM 5-node system is shown in Fig. 1, G1 ~ G5 are generator sets, L_A, L_B, and L_C are bus loads, and node A is set as the reference node. The marginal unit identification method and the sensitivity analysis method are respectively used to locate the marginal units to verify the validity of the results in this paper.

The branch parameters, unit parameters, and sensitivity data information of the calculation case are shown in Table 1, 2, and 3.
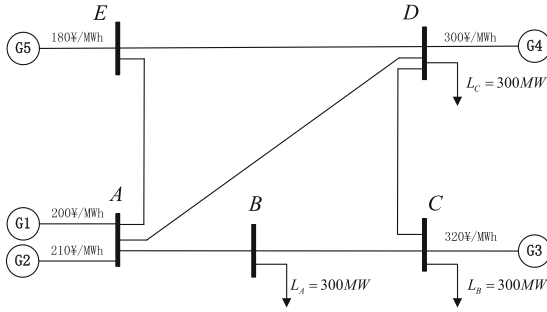
Fig. 1. PJM 5-node system

Table 1. Branch parameters and limit information

Branch	R/%	X/%	J0.5B/(10^−3)	Limit/MW
A-B	0.281	2.81	3.56	120 (Scenario 2)
A-D	0.304	3.04	3.29	—
A-E	0.064	0.64	15.63	—
B-C	0.108	1.08	9.26	—
C-D	0.297	2.97	3.37	—
D-E	0.297	2.97	3.37	250 (Scenario 1)

Table 2. Unit parameter information

Unit	Upper limit/MW	Lower limit/MW	Quotation/(RMB/MWh)
G1	110	0	200
G2	100	0	210
G3	520	0	320
G4	200	0	300
G5	600	0	180

6.2 Standard Scenario 1 Comparative Analysis

Standard case scenario 1 sets the branch D-E transmission limit to 250 MW. In the clearing results, the constraints are not relaxed. The blocking price of branch D-E is − 244.2 RMB/MWh, and the shadow price of the power balance constraint (that is, the

Table 3. Sensitivity data information

Branch	Node A	Node B	Node C	Node D	Node E
A-B	0	−0.6698	−0.5429	−0.1939	−0.0344
A-D	0	−0.1792	−0.2481	−0.4376	−0.0776
A-E	0	−0.1509	−0.2090	−0.3685	−0.8880
B-C	0	0.3302	−0.5429	−0.1939	−0.0344
C-D	0	0.3302	0.4570	−0.1939	−0.0344
D-E	0	−0.1509	−0.2089	−0.3684	0.1120

reference node price) is 210 RMB/MWh. The winning bid results of each unit are shown in Table 4:

Table 4. Unit winning bid results

Unit	Output/MW	Node	Nodal price/(RMB =/MWh)	Quotation/(RMB/MWh)
G1	110	Node A	210	200
G2	93.14	Node A	210	210
G3	0	Node C	261.04	320
G4	96.86	Node D	300	300
G5	600	Node E	182.66	180

1) Marginal Unit Identification Method

As shown in Table 4, according to the principle of the marginal unit identification method, it can be known that the electricity price of the nodes G2 and G4 is equal to the unit quotation and the unit constraints are not limited, so these two units form a marginal unit set. In order to verify whether G2 and G4 are marginal units, the load disturbance of reference node A can be selected by 1MW, and the output disturbance of the two marginal units can be calculated to verify whether the cost change is equal to the node price. The verification method is as follows [18]:

$$\Delta P_2 + \Delta P_4 = 1$$
$$0 \times \Delta P_2 - 0.3684 \Delta P_4 = 0 \tag{17}$$

where ΔP_2 and ΔP are the output changes of units G2 and G4, respectively. After calculation, $\Delta P_4 = 0$, $\Delta P_2 = 1$, , and the cost changes are:

$$\text{nodal price of node A} = 210 = 1 \times 210 \tag{18}$$

It can be seen from Eq. (18) that the cost change caused by the output change of G2 unit is equal to the price of node A, so G2 is a marginal unit.

2) Sensitivity Analysis Method

Since the price of the reference node is the shadow price of the power balance constraint, the price of reference node A is used as a case to verify for the sake of convenience. Since the market clearing model is unconstrained and relaxed, so the market clearing model is the same as the node price calculation model. For details as follows:

$$\begin{cases} \max 200x_1 + 210x_2 + 320x_3 + 300x_4 + 180x_5 \\ x_1 + x_2 + x_3 + x_4 + x_5 = 900 \\ x_1 + y_1 = 110 \\ x_2 + y_2 = 100 \\ x_3 + y_3 = 520 \\ x_4 + y_4 = 200 \\ x_5 + y_5 = 600 \\ -0.20896x_3 - 0.36850x_4 - 0.36849x_5 + y_6 = 31.381233 \end{cases} \quad (19)$$

The first line is the optimization objective, the second line is the power balance constraint, the 3rd to 7th lines are the output upper limit constraint, and the last line is the branch A-B transmission limit constraint. Among them, x_i, $i = 1, \cdots 5$ represent the output of units G1 ~ G5, and $y_j, j = 1, \cdots 6$ are non-negative variables introduced by the upper limit constraint of unit output from inequality to equality. After the node price calculation is completed, $x_b = (x_1, x_2, x_4, x_5, y_2, y_3, y_4)$ is the optimal basis vector. The optimal basis inverse matrix B^{-1} is shown in Table 5:

Table 5. Scenario 1 optimal base inverse matrix

900 resource restriction	110 resource limitation	100 resource restriction	520 resource limitation	200 resource restriction	600 resource restriction	31.48 resource constraints
0	1	0	0	0	0	0
1	−1	0	0	0	−1.304	2.714
0	0	0	0	0	0.304	2.714
0	0	0	0	0	1	0
−1	1	1	0	0	1.304	−2.714
0	0	0	1	0	0	0
0	0	0	0	1	−0.304	2.714

It is easy to know from formula (19) that $b = (900, 110, 100, 520, 200, 600, 31.48)$ is the right constant vector, $B^{-1}b = x_B = (110, 93.14, 96.86, 600, 6.86, 620, 103.14)$ is the optimal solution. Since the decision variable y_2 is the output upper limit constraint residual quantity of the unit G2, the sum of y_2 and x_2 is equal to the maximum technical output of the unit G2, and other units are similar.

Next, use Eq. (15) to analyze the sensitivity of the power balance constraint, and analyze the disturbance range of the constant on the right side. Solving the equation

system is easy to obtain the load disturbance range on the right side of the power balance constraint [900, 907]. When the load disturbance is less than 7MW, the optimal basis can be guaranteed to remain unchanged. Suppose the load disturbance is 1MW, that is, set d $= (1, 0, 0, 0, 0, 0, 0)$, then $B^{-1}d = (0, 1, 0, 0, -1, 0, 0)$. Currently, comparing with the elements of the optimal basis vector, it is easy to know that the disturbance of unit G2 is 1 MW, so G2 is a marginal unit, and its quotation of 210 RMB/MWh is the power balance constraint shadow price, that is, the reference node price.

6.3 Standard Scenario 2 Comparative Analysis

In the standard case scenario 2, the transmission limit of branch A-B is set to 120 MW. In the clearing result, the network security constraints of branch A-B are relaxed. The blocking price of branch A-B is -600 RMB/MW (relaxation penalty coefficient), and the shadow price of power balance constraint is 159.37 RMB/MWh. The blocking and clearing results of each unit are shown in Table 6:

Table 6. Unit winning bid results

Unit	Output /MW	Node	Nodal price/(RMB/MWh)	Quotation/(RMB/MWh)
G1	0	Node A	159.37	200
G2	0	Node B	561.26	210
G3	520	Node D	485.12	320
G4	0	Node D	27572	300
G5	380	Node E	180.00	180

1) Marginal Unit Identification Method

As shown in Table 6, according to the principle of the marginal unit identification method, the price of the node G5 of the unit is equal to the price of the unit, so it is a marginal unit. Since there is only one marginal unit, the price of the reference node should be equal to the quoted price of unit G5 of 180 RMB/MW, which is different from the price of the reference node of 159.37 RMB/MW. Therefore, the marginal unit identification method cannot accurately locate the marginal unit at this time.

2) Sensitivity Analysis Method

In the market clearing model, the safety constraint slack of branches A-B is used, so the market clearing model is different from the node price calculation model. The node price calculation model adopts the market acceptable penalty price of 600. The specific

model is:

$$\max 200x_1 + 210x_2 + 320x_3 + 300x_4 + 180x_5 + 600*x_{A-B}^{plus}$$

$$\begin{cases} x_1 + x_2 + x_3 + x_4 + x_5 = 900 \\ x_1 + y_1 = 110 \\ x_2 + y_2 = 100 \\ x_3 + y_3 = 520 \\ x_4 + y_4 = 200 \\ x_5 + y_5 = 600 \\ -0.54290x_3 - 0.19392x_4 - 0.03438x_5 + y_6 - x_{A-B}^{plus} = -301.9901967 \end{cases} \quad (20)$$

where x_{A-B}^{plus} is the network constraint relaxation variable of branch A-B. After the node price calculation is completed, the optimal basis vector is $x_b = \left(x_3, x_5, y_1, y_2, y_4, y_5, x_{A-B}^{plus}\right)$, and the optimal basis inverse matrix B^{-1} as shown in Table 7:

Table 7. Scenario 2 Optimal Base Inverse Matrix

900 resource restriction	110 resource limitation	100 resource restriction	520 resource limitation	200 resource restriction	600 resource restriction	−301.99 Resource constraints
0	0	0	one	0	0	0
1	0	0	−1	0	0	0
0	1	0	0	0	0	0
0	0	1	0	0	0	0
0	0	0	0	1	0	0
−1	0	0	1	0	1	0
−0.035	0	0	−0.509	0	0	1

It can be seen from formula (20) that b = (900, 110, 100, 520, 200, 600, 301.99) is the right constant vector, $B^{-1}b = x_B$ = (520, 380, 110, 100, 200, 220, 6.615) is the optimal solution. It can be seen that the output upper limit constraints of units G1, G2, G4, and G5 all have surplus, and the sum of the output and the winning bid is the maximum output. The network security constraint slack x_{A-B}^{plus}=6.615 MW of Branch A-B.

Next, use Eq. (15) to analyze the sensitivity of the power balance constraint, and analyze the disturbance range of the constant term on the right side. The load disturbance range on the right side of the power balance constraint is easily obtained by solving the system of equations [900, 1092]. Therefore, when the load disturbance is less than 192 MW, the optimal basis can be guaranteed to remain unchanged. Suppose the load disturbance on the right side is 1 MW, that is, set d = (1, 0, 0, 0, 0, 0, 0), then $B^{-1}d$=(0, 1, 0, 0, 0, −1 , −0.03438). Comparing with the elements of the optimal basis vector, it is easy to know that the disturbance amount of unit G5 is 1 MW, so G5 is

a marginal unit. In addition, the disturbance amount of the slack variable of branch A-B is $x_{A-B}^{plus} = -0.03438MW$, , and the penalty price coefficient in the optimization objective is 600 yuan/MWh. Therefore, the electricity price of the reference node is jointly determined by the physical unit G5 and the safety slack (virtual unit) of the branch A-B. The specific calculation formula is:

$$180 \times 1 + 0.03438 \times 600 = 159.37 \tag{21}$$

It can be seen from Eq. (21) that the sensitivity analysis method can accurately locate the scenario where marginal units and branch network security constraint slack variables (virtual units) are jointly priced, and it is more universal.

6.4 Practice Scenario Analysis

Considering the data confidentiality of the pilot provinces of the power spot market, only the application effect of the actual calculation example is given here. The energy price at a certain time in a pilot province is 21 RMB/MWh. Currently, there are 5 out-of-limit sections, and the marginal unit identification method finds 4 marginal units. The energy price cannot be obtained from the marginal unit set. The reason for the inability to accurately locate at this time is that the energy price is not purely priced by the unit. To solve this problem, the pilot provinces usually used sensitivity analysis method to locate marginal units and marginal sections.

Looking at the spot system positioning results, the energy price is jointly determined by a marginal unit and a marginal section. The price of the marginal unit is 289 RMB/MWh, the additional 1MW is 289 RMB, so the optimization target is increased by 289 RMB. The sensitivity of the marginal unit to the positive over-limit marginal section is −0.268, so the additional 1 MW of the unit can reduce the over-limit section by 0.268 MW. Since the cross-section over-limit penalty coefficient is 1000, the optimization objective decreases by 268 RMB due to the reduction of the over-limit limit. The increase in the unit cost minus the decrease in the slack cost of the section is the target change of 21 RMB, which is equal to the energy price.

7 Conclusion

Aiming at the problem that the marginal unit identification method cannot adapt to the LMP calculation model with constrained slack variables, this paper deduces the calculation method and discriminant principle for accurate positioning of marginal units based on the mature dual simplex algorithm theory and sensitivity analysis method. Because the method uses the optimal basis inverse matrix in the linear programming solution for calculation, the scene characteristics of the LMP calculation model of the electricity spot market are shielded. Therefore, this method is suitable for the marginal positioning problem of linear programming models in all industries, and has good universality. At the same time, the method can quickly and accurately locate the marginal units and marginal slack variables. The conventional provincial power grid 12-period marginal unit positioning calculation time only takes 2 s, which provides a fast and effective auxiliary analysis method for the rolling operation of the real-time market cycle.

References

1. Schweppe, F.C., Tabors, R.D., Kirt Ley, J.L., et al.: Home static utility control. IEEE Trans. Power Apparat. Syst. **99**(3), 1151–1163 (1980)
2. Li, Z., Daneshi, H.: Some observations on market clearing price and locational marginal price. In: 2005 IEEE Power Engineering Society General Meeting, pp. 2042–2049. IEEE (2005)
3. Pan, J., Kai, X.: Optimization principle of locational marginal pricing. Autom. Electric Power Syst. **30**(22), 38–42 (2006)
4. Fu, Y., Li, Z.: Different models and properties on lmp calculations. In: 2006 IEEE Power Engineering Society General Meeting. IEEE (2006)
5. Boyle, G.: Locational marginal price. https://www.pjm.com/, 01 June 2004
6. Bohn, R., Caramanis, M., Schweppe, F.: Optimal pricing in electrical networks over space and time. Rand J. Econ. **15**(3), 360–376 (1984)
7. Sun, K., Lan, Z., Lin, Z., et al.: Transmission congestion management mechanism of typical international power markets and possible guidance for China's power market. Power Syst. Prot. Control **48**(12), 170–177 (2020)
8. Zhang, J., Zhang, G., Yuan, S., et al.: Research on real-time operation congestion management based on node marginal price. Electr. Appl. **37**(21), 78–86 (2018)
9. Jia, L., Kim, J., Thomas, R.J., et al.: Impact of data quality on real-time locational marginal price. IEEE Trans. Power Syst. **29**(2), 627–636 (2014)
10. Sensfu, F., Ragwitz, M., Genoese, M.: The merit-order effect: a detailed analysis of the price effect of renewable electricity generation on spot market prices in Germany. Energy Policy **36**(8), 3086–3094 (2008)
11. Zhou, B., Zhao, W., Xuan, P., et al.: Research on the key influencing factors of power spot market locational marginal price. Guangdong Electric Power **33**(2), 86–92 (2020)
12. Dhayalini, K., Deepu, M.S., Sathiyamoorth, S., et al.: Analysing the economics of wind power based on locational marginal prices using restructured power systems. In: 2013 International Conference on Circuits, Power and Computing Technologies. IEEE (2013)
13. Dhabai, P.B., Tiwari, N.: Computation of locational marginal pricing in the presence of uncertainty of solar generation. In: 5th IEEE International Conference on Recent Advances and Innovations in Engineering- ICRAIE 2020. IEEE (2020)
14. Choi, D.H., Xie, L.: Impact analysis of locational marginal price subject to power system topology errors. In: IEEE SmartGridComm 2013 Symposium - Architectures and Models for the Smart Grid. IEEE (2013)
15. Li, Z., Zeng, Y., Zhou, C., et al.: Analysis of effect factors of nodal price based on electric spot market clearing simulation. Electr. Technol. **21**(5), 41–47 (2020)
16. Zhao, S., Wang, S., Yang, X., et al.: Study on the Influence of "source-grid-load" factors on the locational marginal price of power spot market. (5), 41–47 (2020)
17. Thatte, A.A., Choi, D.H., Xie, L.: Analysis of locational marginal prices n look-ahead economic dispatch. In: 2014 Power Systems Computation Conference. IEEE (2015)
18. Shi, X., Zheng, Y., Xue, B., et al.: Effect analysis of unit operation constraints on locational marginal price of unit nodes. Power Syst. Technol. **43**(8), 2658–2664 (2019)
19. Qin, H., Wang, Q., Chen, X.: The analysis and visualization of locational marginal pricing. Power Syst. Technol. **20**(6), 12–15 (2007)

The Analysis of AC Faults in AC/DC Hybrid Distribution System with SOP

Peng Jin[1], Tonghua Wu[1], Hai Wu[1], Guo Hu[1(✉)], and Qian Shen[2]

[1] NARI Group Co., Ltd., State Key Laboratory of Smart Grid Protection and Operation Control, Nanjing 211000, China
huguo@sgepri.sgcc.com.cn

[2] School of Automation, Nanjing University of Science and Technology, Nanjing 210094, China

Abstract. AC/DC hybrid distribution system becomes increasingly necessary for integration of distributed renewable energy resources (DER) and management of carbon emissions. However, the fault characteristics of AC/DC hybrid power distribution network are vastly different from traditional AC distribution system for their varied structures. Considering the strong capability in controlling power flow and fault current of soft open point (SOP), this paper establishes the model of AC fault sequence network of hybrid distribution system with SOP, in which positive and negative separation control strategy is adopted by the converter. The model includes traditional AC equivalent network, DC equivalent network, back-to-back converter and its control system, based on which the AC fault characteristics in AC/DC hybrid distribution system are analyzed. Through utilizing PSCAD/EMTDC, different simulation scenarios are carried out to verify the effectiveness of AC fault modeling and analysis method of AC/DC hybrid power distribution system with SOP, thus providing a theoretical basis for AC side protection scheme of AC/DC hybrid system.

Keywords: AC/DC hybrid distribution system · AC fault · Positive and negative separation control · Sequence network · Fault characteristic analysis

1 Introduction

With the rapid development of power electronics, flexible DC transmission and distribution technology has gradually become a research hotspot at home and abroad [1, 2]. Among them, the research on flexible HVDC transmission system is relatively sufficient, and some practical projects have been put into operation [3, 4], while the research on DC distribution network is still in the stage of exploration and development. Some countries such as the United States, Japan and China have proposed their respective development directions and typical architectures [5–7]. Compared with the traditional AC distribution network, the flexible DC distribution network has the advantages of low loss, high power supply capacity, high reliability. Besides, it can realize power flow control among DERs and DC loads [8–10]. Based on the existing mature theory of AC distribution network, AC/DC hybrid distribution system can make full use of the advantages of the

DC distribution network, so it has gradually become the development trend of the future distribution system [11, 12].

The SOP, which is also termed as flexible AC/DC hybrid device or back-to-back converter, is usually used between two distribution lines instead of the tie switch. The introduction of SOP not only improves the capability in controlling of power flow and fault current, but also brings many new challenges such as the effective analysis of fault characteristics and reliable operation of traditional relay protection [13]. According to the fault location, the faults in AC/DC hybrid power distribution system mainly include DC faults and AC faults. Among them, the research on the DC faults mainly focus on the response mechanism of the flexible AC/DC device and its protection and control strategy. For example, literature [14] divides and analyzes the DC fault characteristics of a single converter station in a multi-terminal AC/DC system. Reference [15] designs a DC protection scheme based on a communication system and DC circuit breaker, which can effectively identify the faults inside and outside the area. Reference [16] uses a single-pole ground fault as an example to verify the proposed LC injection effectiveness of offline fault location methods. For AC faults (including AC grid-side fault and AC valve-side fault) in the AC/DC hybrid distribution system, the output characteristics of the SOP mainly depend on the control strategy adopted by the internal converter, which means that traditional AC fault equivalent analysis model is no longer applicable to the AC/DC hybrid system [17]. Therefore, it is necessary to study AC faults considering the control strategy of SOP, which can be used as the theoretical basis for formulating the AC side protection scheme of the AC/DC hybrid distribution system.

At present, the commonly used control methods of SOP include master-slave control [1], droop control [18] and margin control [19], among which the master-slave control method is an relatively easier way to realize the stable operation of the hybrid distribution network compared with other methods [20]. Therefore, this paper conducts specific research based on this control method, that is one converter adopts DC voltage and reactive power control (referred to as VQ control), and the other converter uses active and reactive power control (referred to as PQ control). When a symmetrical type AC fault occurs, the AC side voltage keeps three-phase symmetry, while when an asymmetric type AC fault occurs, the symmetry of the AC side voltage will be broken and it will contain a large number of negative sequence components. The converter adopting conventional control method will output negative sequence current, which will not only aggravate the asymmetry of the grid and affect the fault recovery of the power grid, but also bring double frequency harmonic component to the DC bus voltage and affect the safe and stable operation of the system [12]. Therefore, in order to suppress the negative-sequence current component under asymmetric conditions, it is necessary to introduce positive and negative sequence separation control.

Therefore, this paper studies the AC side fault characteristics of flexible AC/DC hybrid power distribution system with SOP. Firstly, the AC fault characteristics are analyzed for both of the constant power end and constant voltage end according to the positive and negative sequence separation control strategy adopted by the converters. Secondly, the AC fault complex sequence network of the AC/DC hybrid distribution system with SOP is established, and the theoretical analysis of the fault characteristics is carried out. Finally, the simulation model of a typical AC/DC hybrid distribution system

is built in PSCAD/EMTDC, and the rationality of the AC fault analysis in this paper is verified through simulation examples.

2 Output Characteristics Analysis of SOP

Figure 1 shows the structure of a typical AC/DC hybrid distribution system with SOP. HV_1 and HV_2 are 110 kV high-voltage AC busbars, MV_1 and MV_2 are 10 kV medium-voltage AC busbars, T_1 and T_2 are 110 kV/10 kV transformer, C is the capacitor on DC side for voltage stabilization, f_1 and f_2 are the faults on the AC valve side, and f_3 and f_4 are the faults on the AC grid side, T_3 and T_4 are the optional coupled transformer, which usually uses connection mode of Δ/Y so as to block the circulation of the zero-sequence component between the AC and DC systems [21].
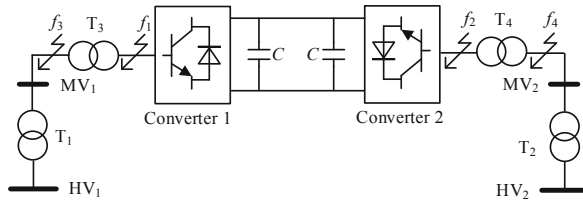
Fig. 1. Structure of typical AC/DC hybrid distribution system with SOP

2.1 Analysis of Positive and Negative Sequence Separation Control Method

In order to achieve a faster dynamic response, the converters at the constant power end and the constant voltage end both introduce a current inner control loop, in which the PI regulator controls the I_d and I_q of the actual current to track the reference current I_{dref} and I_{qref} respectively under the d-q synchronous rotating coordinate system. Then, the reference voltage signals V_α and V_β are obtained from dq-$\alpha\beta$ transverter block. At last, the drive signals of the switching devices are generated through Space Vector Modulation (SVM).

When the positive and negative sequence separation control method is considered, in order to suppress the negative sequence current generated by the converter during asymmetric AC fault without affecting the overall control effect, the negative sequence current reference values $I_{dref(2)}$ and $I_{qref(2)}$ is set to 0, and the positive sequence current reference values $I_{dref(1)}$ and $I_{qref(1)}$ are still determined by the output of the PQ or VQ outer loop controller. Figure 2 shows the double-loop control block diagram considering voltage feedforward and current coupling. U_d and U_q are the AC valve side voltage components under the d-q axis, and the subscripts 1 and 2 represent the positive sequence and negative sequence components of each variable respectively. L_s is the filter inductance, and the power frequency angular frequency $\omega_n = 314$ rad/s.
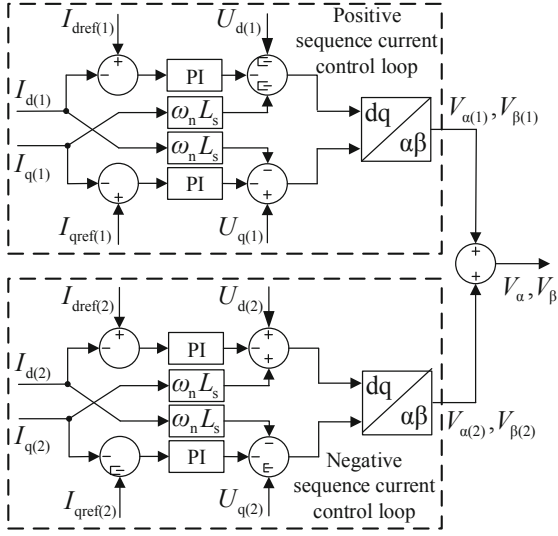
Fig. 2. Diagram of positive and negative double control loop

2.2   Analysis of AC Fault on the Constant Power Side

When an AC fault occurs at the constant power end, the d-axis component $U_{d(1)\_1}$ of the positive sequence voltage and the active power P_1 of the converter will drop instantaneously. In order to ensure that P_1 tracks its given value P_{ref}, the active power outer-loop controller responds quickly, thus leading to an increase in its output $I_{dref(1)\_1}$. With the control of the current inner-loop controller, the positive sequence current d-axis component $I_{d(1)\_1}$ will also rise up. Due to the limited overcurrent capability of the converter, a current limiter is introduced. If $U_{d(1)\_1}$ drops and the corresponding target current exceeds the limit range, $I_{dref(1)\_1}$ will remain at the limit value to ensure that the current will not exceed the maximum allowable value.

In addition, to fully utilize the power transfer capability of SOP, Q_{ref_1} is usually set to 0. Before the AC fault, the reactive power Q_1 of the converter is maintained near zero under the reactive power controller, and the drop of $U_{d(1)\_1}$ during the fault will not cause the change of Q_1. Therefore, the control effect of the positive sequence current q-axis component $I_{q(1)\_1}$ remains unchanged regardless of whether the AC side the fault occurs on.

2.3   Analysis of AC Fault on the Constant Voltage Side

When an AC fault occurs at the constant voltage side, the voltage $U_{d(1)\_2}$ and the active power P_2 also drops instantaneously. Due to the power support of the converter on the other side, P_1 can remain unchanged from that before the fault, so part of the power reduced by the converter on this side is absorbed by the DC-side capacitor, which causes the DC-side voltage E_{dc} to fluctuate or even unstable. In order to make E_{dc} track its given value E as much as possible, the voltage outer loop controller causes its output $I_{dref(1)\_2}$

to fluctuate. Also due to the current limiter, no matter how $U_{d(1)\_2}$ drops, $I_{d(1)\_2}$ is always maintained within the limiting range. Similar to the reactive power control of the converter at the constant power side, since Q_{ref_2} is generally set to 0, the characteristics of this control loop remain unchanged regardless of whether the AC side the fault occurs on.

In conclusion, with the positive and negative sequence separation control method introduced, when an AC side fault occurs, it can be equivalent to a positive sequence current source, and its current is affected by the positive sequence voltage on the valve side, and limited by the amplitude.

3   AC Fault Analysis of AC/DC Hybrid System with SOP

Combined with the traditional fault sequence network analysis of AC distribution network given in the literature [22], the equivalent model of SOP and different types of AC faults in AC/DC hybrid distribution system are theoretically analyzed, including three-phase short fault, two-phase short fault, two-phase grounding fault and single-phase grounding fault.

3.1   Characteristic Analysis of Three-Phase Short Fault
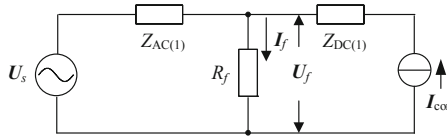
Fig. 3. Positive sequence network of three-phase short fault

Taking the direction from AC side to DC side as the positive direction of the current, the positive sequence network of a three-phase short fault is shown in Fig. 3. Since the fault is a symmetrical fault, no other sequence networks need to be involved. U_s is the fault virtual voltage source, R_f is the transition resistance, I_{con} is the equivalent positive sequence current source of the converter, and $Z_{AC(1)}$ is the positive sequence impedance of the AC side, $Z_{DC(1)}$ is the positive sequence impedance of the DC side. It can be seen from Fig. 3 that when a three-phase short fault occurs, the fault current and voltage can be expressed as

$$I_f = \frac{U_s + Z_{AC(1)}I_{con}}{Z_{AC(1)} + R_f}$$

$$U_f = I_f R_f \tag{1}$$

Compared with the same fault in the traditional AC distribution network, the change of the fault current is closely related to the magnitude of R_f, which means the smaller the R_f is, the greater the drop of the AC positive sequence voltage, and the greater the amplitude of I_{con}, and the larger the coefficient $k_1 = Z_{AC(1)}/(Z_{AC(1)} + R_f)$, the more obvious the fault current change is.

3.2 Characteristic Analysis of Two-Phase Short Fault
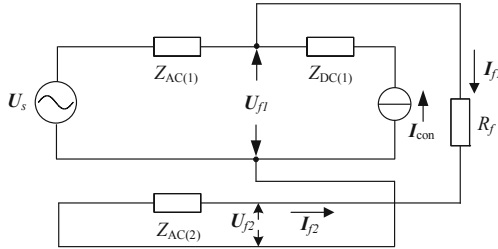
Fig. 4. Compound sequence network of tow-phase short fault

Figure 4 shows the compound sequence network of two-phase short fault, where $Z_{AC(2)}$ is the negative sequence impedance of the AC side at the fault point. It can be seen from the figure that under the condition that the positive and negative sequence impedances are regarded as equal, the fault sequence current and voltage of two-phase short fault can be expressed as

$$I_{f1} = \frac{U_f + Z_{AC(1)}I_{con}}{2Z_{AC(1)} + R_f}$$
$$I_{f1} = -I_{f2} \qquad (2)$$
$$I_{f0} = 0$$
$$U_{f1} = U_{f2} = I_{f1}Z_{AC(1)}$$

Similar to Sect. 3.1, compared with the same fault in the traditional AC distribution network, the change of the fault current is also related to the magnitude of R_f and I_{con}, which will not be repeated here.

3.3 Characteristic Analysis of Two-Phase Grounding Fault
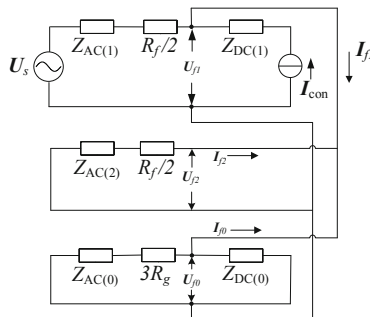
Fig. 5. Compound sequence network of two phase grounding fault

Figure 5 shows the compound sequence network of two-phase grounding fault, where $Z_{AC(0)}$ is the zero-sequence impedance of the AC side, $Z_{DC(0)}$ is the zero-sequence impedance of the DC side, and R_f is short transition resistance, R_g is the ground transition resistance. It can be seen from the figure that under the condition that the positive and negative sequence impedances are regarded as equal, the fault sequence current and voltage of two-phase grounding fault can be expressed as

$$
\begin{aligned}
I_{f1} &= \frac{U_f + Z_{AC(1)}I_{con}}{Z_{AC(1)} + R_f/2 + (Z_{AC(1)} + R_f/2)//Z_{\Sigma(0)}} \\
I_{f2} &= -I_{f1}\frac{Z_{\Sigma(0)}}{Z_{AC(1)} + R_f/2 + Z_{\Sigma(0)}} \\
I_{f0} &= -I_{f1}\frac{Z_{AC(1)} + R_f/2}{Z_{AC(1)} + R_f/2 + Z_{\Sigma(0)}} \\
U_{f1} &= U_{f2} = U_{f0} = I_{f1}\frac{(Z_{AC(1)} + R_f/2)Z_{\Sigma(0)}}{Z_{AC(1)} + R_f/2 + Z_{\Sigma(0)}}
\end{aligned}
\tag{3}
$$

The Zero-sequence equivalent impedance $Z_{\Sigma(0)}$ can be expressed as

$$
Z_{\sum(0)} = (3R_g + Z_{AC(0)})//Z_{DC(0)}
\tag{4}
$$

Compared with the same fault in the traditional AC distribution network, the change of the fault current is closely related to the configuration of coupled transformer and the grounding impedance of the DC side. When the fault is located on the AC grid side, $Z_{DC(0)}$ can be regarded as infinite and $Z_{AC(0)}$ is zero as the connection mode of the coupled transformer, which means the fault current distribution is exactly the same as that of the traditional AC distribution network. While, when the fault point is on the AC valve side, $Z_{AC(0)}$ is regarded as infinite, and $Z_{DC(0)}$ is closely related to the grounding method of the neutral point of the DC side. The greater the grounding impedance and the greater the $Z_{DC(0)}$, the more obvious the fault current change will be.

3.4 Characteristic Analysis of Single-Phase Grounding Fault
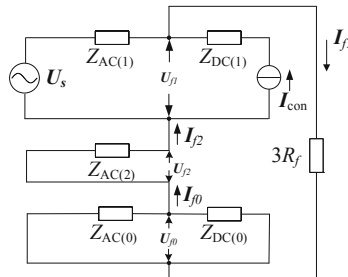
Fig. 6. Compound sequence network of single-phase grounding fault

Figure 6 shows the compound sequence network of single-phase grounding fault. It can be seen from the figure that under the condition that the positive and negative sequence

impedances are regarded as equal, the fault sequence current and voltage can be expressed as

$$I_{f1} = \frac{U_s + Z_{AC(1)}I_{con}}{2Z_{AC(1)} + 3R_f + Z_{\Sigma(0)}}$$

$$I_{f1} = I_{f2} = I_{f0}$$

$$U_{f1} = U_s - Z_{AC(1)}(I_{f1} + I_{con}) \qquad (5)$$

$$U_{f2} = -I_{f1}Z_{AC(1)}$$

$$U_{f0} = -I_{f1}Z_{\Sigma(0)}$$

The Zero-sequence equivalent impedance $Z_{\Sigma(0)}$ can be expressed as

$$Z_{\Sigma(0)} = Z_{AC(0)}//Z_{DC(0)} \qquad (6)$$

Similar to Sect. 3.3, compared with the same fault in the traditional AC distribution network, the change of the fault current is also related to the connection of the coupled transformer and the grounding method of the DC side, which will not be repeated here.

4   Simulation

In order to verify the rationality of the theoretical AC fault characteristic analysis of AC/DC hybrid distribution system with SOP above, the PSCAD/EMTDC simulation software is used to build a system model as shown in Fig. 1. Among them, inverter 1 adopts PQ control, inverter 2 adopts VQ control, and the neutral point of the main transformer adopts an ungrounded mode. The settings of the simulation parameters are shown in Table 1.

Table 1. Setting of simulation parameters.

Simulation parameters	Settings
AC side rated voltage/kV	10
DC side rated voltage/kV	20
DC side voltage regulator capacitor C/μF	500
AC side inductance/H	0.01
Rated active power of converter at constant power end/MW	5
Current limit/kA	±1.0

4.1   Simulation of Three-Phase Short Fault

At 0.3 s, a three-phase short fault f_1 occurs on the AC grid side of the constant power terminal, and the transition resistance R_f is 10 Ω. The simulation waveforms are shown

in Fig. 7. It can be seen that $U_{d(1)\_1}$ drops after the fault occurs, and after the dynamic response of the control loop is stabilized, the current $I_{d(1)\_1}$ of the converter 1 rises from the original 0.56 kA to 0.74 kA. P_1 and Q_1 can be maintained approximately equal to those before the fault due to the power controller, and E_{dc} is maintained the rated value by the opposite side converter voltage controller. When the fault occurs in the traditional AC distribution network under the same conditions, the fault phase current is 1.42 kA, while the fault phase current in the AC/DC hybrid distribution network with SOP is 1.24 kA, which is 12.7% lower than the former.
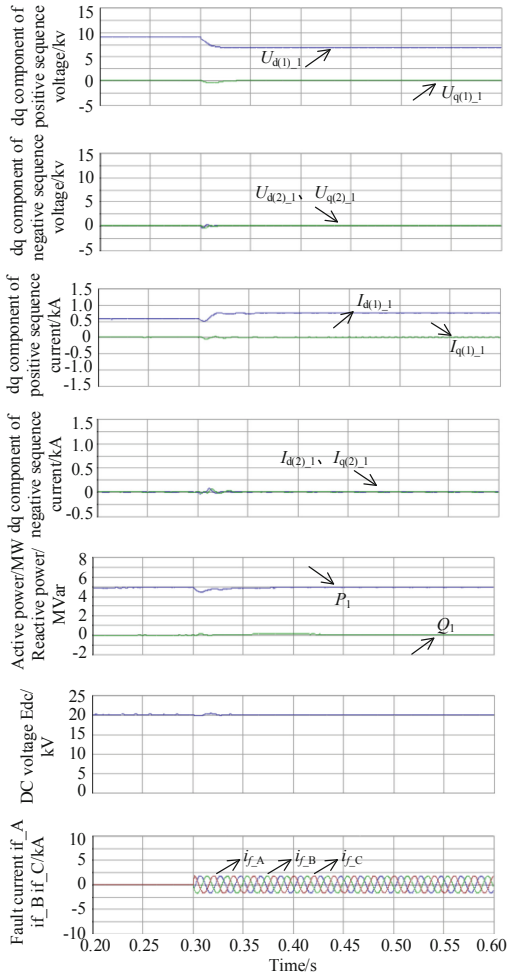
Fig. 7. Simulation waveforms of three-phase short fault in the constant power terminal ($R_f = 10$ Ω)

In the scenario before, since the drop of $U_{d(1)\_1}$ does not make $I_{d(1)\_1}$ reach the current limit value, the active power output of the inverter 1 remains unchanged. If R_f
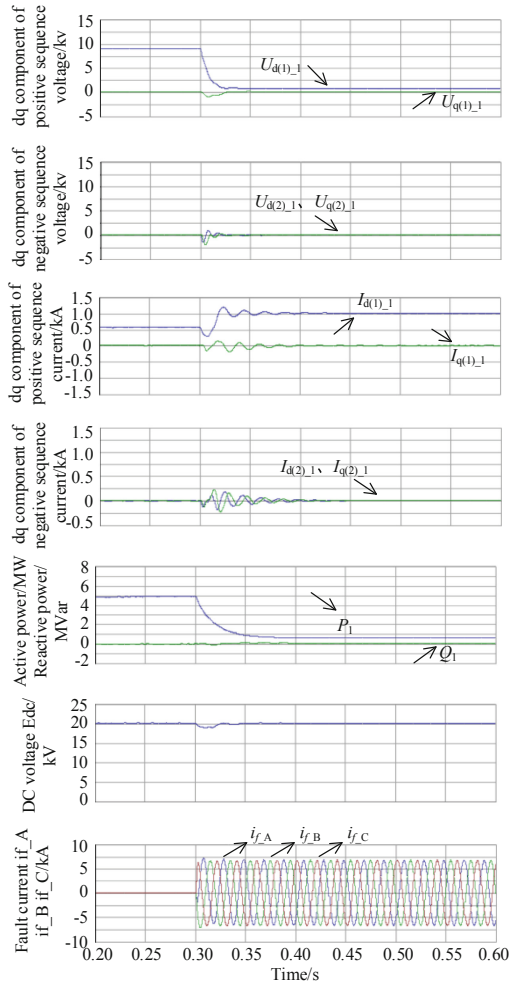
Fig. 8. Simulation waveforms of three-phase short fault in the constant power terminal ($R_f = 0.5$ Ω)

is further reduced, $U_{d(1)\_1}$ will decrease more, and the inverter 1 needs to provide a larger current to maintain the active power. At this time, the required $I_{d(1)\_1}$ may exceed the current limit width. To simulate this scenario, R_f is set to 0.5 Ω, other simulation conditions remain unchanged, and the simulation waveforms are shown in Fig. 8. It can be seen that as the falling degree of $U_{d(1)\_1}$ increases, $I_{d(1)\_1}$ is further raised until it is limited to 1.0 kA, but it is still less than the actual required amount, so the converter 1 cannot keep P_1 the same as before the fault. The simulation also shows that P_1 decreases from 5 MW before the fault to 0.6 MW. Q_1 and E_{dc} are not affected by the fault due to their respective controllers, and are stable at about 0MVar and 20 kV respectively. When the fault occurs in the traditional AC distribution network under the same conditions,

the fault phase current is 5.30 kA, while the fault phase current in the AC/DC hybrid distribution network with SOP is 4.73 kA, which is 10.8% lower than the former.
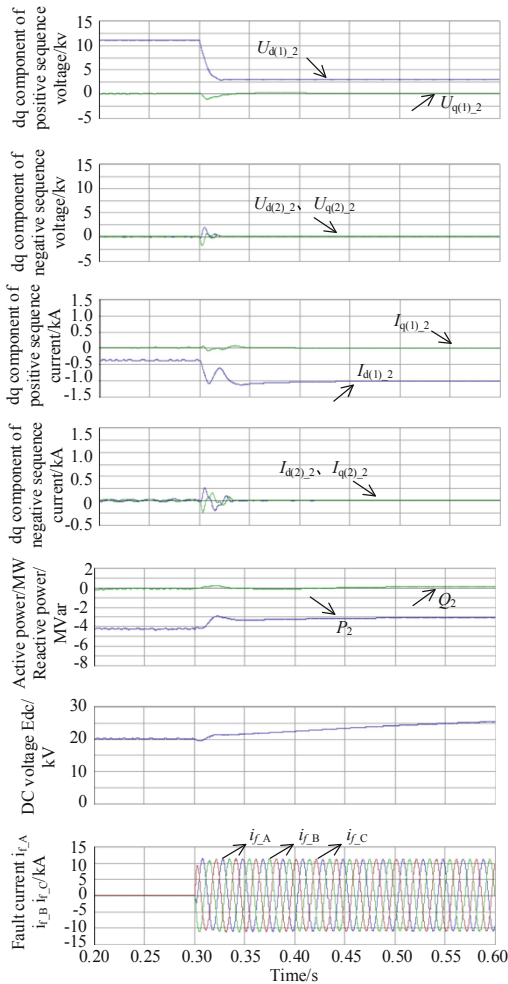
Fig. 9. Simulation waveforms of three-phase short fault in the constant voltage terminal

Then, the location of the fault is changed to f_2, which is on the AC grid side of the constant voltage terminal, and other simulation conditions are consistent with those in Fig. 8. The simulation waveforms are shown in Fig. 9, from which it can be seen that $U_{d(1)\_2}$ drops after the fault occurs, and the current $I_{d(1)\_2}$ of the converter 2 drops from the original -0.38 kA until it is limited to -1.0 kA, but it is still larger than the actual value required amount. Therefore, the ability to accept the active power P_2 of the converter 2 decreases, and the residual active power on the DC side increases, thus resulting in the continuous rise of E_{dc} and the imbalance of the DC control loop. Besides, the control of Q_2 is not affected by the fault and is maintained at about 0MVar. Under this

simulation condition, the fault phase current is 7.78 kA, which is 5.9% higher than the fault current 7.32 kA under the same conditions in the traditional distribution network. To be clarified, the active power flow direction is that the constant power terminal flows to the constant voltage terminal, and the equivalent positive sequence current sources of the constant power terminal and the constant voltage terminal are in opposite directions, which leads to an increasing trend of the fault current in this simulation, while the fault current shows a weakening trend in Fig. 7, 8.

If the three-phase short fault is f_3 or f_4, which is located on the AC valve side, the impact of the positive sequence current source on the fault characteristics of the system is similar to that of the fault point located on the AC grid side, and will not be repeated here.

4.2   Simulation of Two-Phase Short Fault

At 0.3 s, a two-phase short fault f_1 occurs on the AC grid side of the constant power terminal, and the transition resistance R_f is 2 Ω. The waveforms of the simulation are shown in Fig. 10. After the fault occurs, the negative sequence voltage appears on the AC valve side. While due to the control strategy adopted by the converter, the negative sequence component of the current is well suppressed. Similar to Fig. 7, the drop of $U_{d(1)\_1}$ after the fault causes $I_{d(1)\_1}$ to rise from 0.56 kA to 0.77 kA, and the amplitude is smaller than the current limit value, so the converter 1 can maintain the same as before the fault. Q_1 and E_{dc} is maintained due to their respective controllers, and as the influence of the negative sequence current suppression, the double frequency fluctuation of E_{dc} is significantly weakened. If R_f is further reduced, so that $I_{d(1)\_1}$ reaches the current limit value, similar to Fig. 8, the converter's ability to transmit active power will decrease, while other control objects remain unaffected by the fault. The waveform is not drawn out.

When the fault f_2 is at the constant voltage end, and the decrease of $U_{d(1)\_2}$ is small, $I_{d(1)\_2}$ is still within the limit, and all control objects can be kept stable. When $U_{d(1)\_2}$ has a relatively large decrease, as $I_{d(1)\_2}$ reaches to the limit value, the active power exchange capacity of the converter decreases, and the remaining active power on the DC side makes E_{dc} rise continuously until it becomes unstable, and Q_2 is maintained by its controller. The specific waveform is no longer drawn.

If the two-phase short fault is f_3 or f_4, which is located on the AC valve side, the impact of the positive sequence current source equivalent on the fault characteristics of the system is similar to that of the fault located on the AC grid side, and will not be repeated here.

If the fault type is two-phase short grounding fault, the influence of the equivalent positive sequence current source of SOP on the positive sequence and negative sequence fault characteristics of the system is similar to that of two-phase short fault, so it will not be repeated here.

From the analysis in Sect. 4.1 and 4.2, it can be seen that after the SOP is introduced, the distribution network becomes dual-power supply system, which also changes the fault current distribution. Therefore, the existing three-stage overcurrent protection will lose its selectivity, which may lead to mal-operation or refused operation of protection
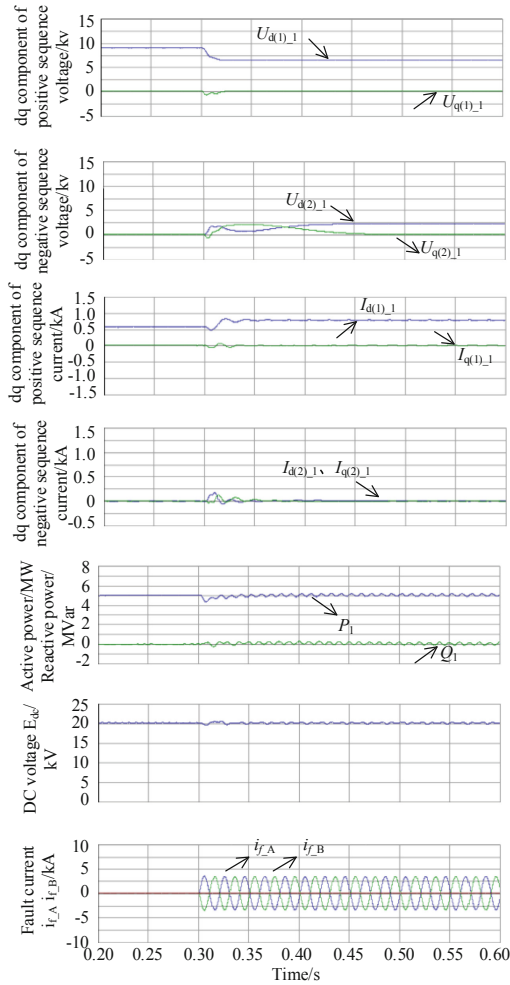
Fig. 10. Simulation waveforms of two -phase short fault in the constant power terminal

relay downstream of the fault. At the same time, if the SOP is not disconnected from the grid in time, it may cause islanding effect and non-synchronized closing shock.

For the directional elements in directional overcurrent protection and longitudinal directional protection, due to the negative sequence current suppression and low voltage ride-through control strategy of the SOP, the fault current characteristics during faults are quite different from that of the synchronous machine. As a result, the traditional 90° wiring directional component and positive-sequence voltage polarized directional component cannot calculate the fault current direction correctly.

For differential protection, due to the fault current provided by the constant power stage and constant voltage terminal during the fault, the SOP can be treated as the weak-infeed side, and by adding measures such as "low-voltage differential current start-up component", it can prevent the starting element on the side of the SOP from not starting.

4.3   Simulation of Single-Phase Grounding Fault

Figure 11 shows the simulation waveforms of the single-phase grounding fault f_3 and f_4 on the AC grid side at the constant power terminal at 0.3 s, and the transition resistance is 0.1 Ω. After the fault occurs, the voltage of the faulty phase decreases to approximately 0, and the voltage of the non-faulty phase rises to about twice the original value. The positive and negative sequence voltages remain unchanged. Therefore, the output characteristics of the converter are basically stable, thus the equivalent positive sequence current source I_{con} is equal to that before the fault and the power and voltage loops have no dynamic adjustment process. Due to the grounding method of the AC grid side of the main transformer and the coupling transformer, the $Z_{\Sigma(0)}$ mainly depends on the zero-sequence distributed capacitive reactance to the ground, and its magnitude is much larger than other sequence impedances. Therefore, the fault current change caused by I_{con} is extremely small. Compared with the same fault in the traditional AC grid, the fault characteristics have not changed substantially. The same is true when the fault point is at the constant voltage side. The positive and negative sequence voltages on the AC side of the converter at the constant voltage side are basically equal to those before the fault, and the SOP has no dynamic adjustment process.
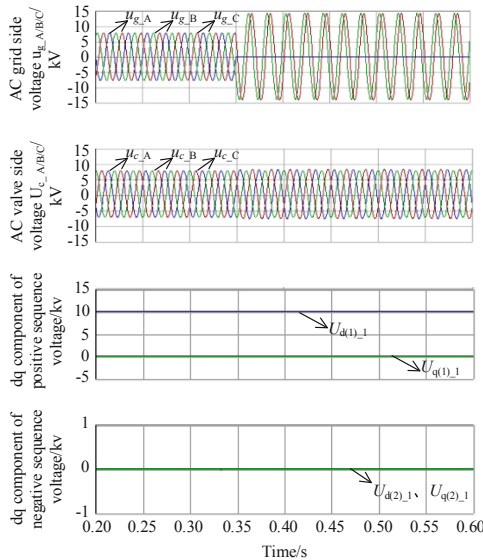
Fig. 11. Simulation waveform of single-phase grounding fault on AC grid side of constant power terminal

Figure 12 shows the simulation waveforms of the single-phase grounding fault f_1 on the AC valve side at the constant power terminal at 0.3 s under the condition that the midpoint of the DC side capacitor is directly grounded, and the transition resistance is 0.1 Ω. After the fault occurred, in addition to the drop of the positive sequence voltage on the valve side of the converter, a negative sequence voltage also appeared.

The positive sequence current of the converter increased from 0.56 kA to 0.69 kA, the negative sequence current was effectively suppressed, and the fault current is 2.95 kA. The fundamental frequency vibration occurs in the positive and negative voltages of the DC side, but the voltage between the electrodes is basically unaffected. Reference [12] conducted a detailed theoretical analysis of this DC characteristic phenomenon.
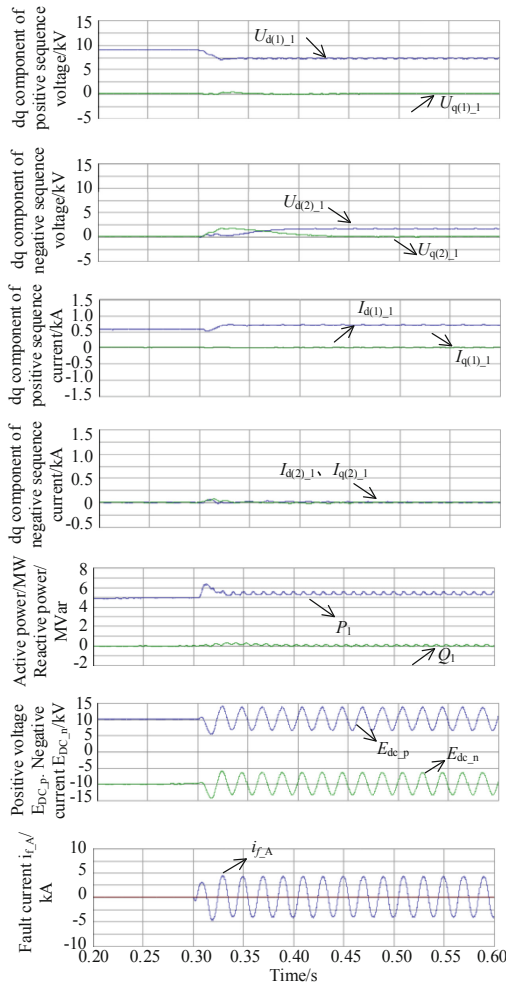
Fig. 12. Simulation waveform of grounding short-circuit fault on AC valve side of constant power side

When a single-phase grounding fault occurs on the AC valve side, $Z_{DC(0)}$ is closely related to the grounding method of the DC side. The midpoint grounding resistance of the DC capacitor is 100 Ω, and other conditions remain unchanged from the previous simulation example. The simulation results show that the fault characteristics of other quantities are similar to those in Fig. 12, except that the fundamental frequency vibration

amplitude of the DC positive and negative voltages is close to zero. The fault current is 2.79 kA. Compared with Fig. 12, the change of fault current is slightly reduced but not obvious, which is mainly because that the neutral point is directly grounded on the valve side of the connected transformer, so $Z_{AC(0)} << Z_{DC(0)}$, that is, $Z_{\Sigma(0)} \approx Z_{AC(0)}$, resulting in $Z_{DC(0)}$ has little effect on the fault current.

From the analysis in this section, it can be seen that for the directional element in the directional zero-sequence overcurrent protection, when the DC side of SOP is not grounded, the zero-sequence equivalent impedance of the SOP is infinite, thus the zero-sequence directional element is not affected in most cases.

5 Conclusion

(1) When the drop of positive sequence voltage on the valve side is small during fault, the positive sequence current of the converter will be within the limiting value, and the output power and DC voltage of the SOP remain controllable. When the positive sequence current reaches the limit and the fault is located at the constant power end, the active power output of the converter will decrease, and the DC voltage will remain stable. If the fault point is located at the constant voltage end, the active power of the local converter will be reduced, and the active power remaining may cause the DC voltage to be unstable. Under the condition that the negative sequence component is effectively suppressed, the SOP in the fault negative sequence network is equivalent to an open circuit state, and the double-frequency fluctuation of the DC voltage can be well suppressed.

(2) When a short fault occurs, the equivalent positive sequence current source of the SOP can enhance or weaken the fault current, which depends on the power flow direction and the transition resistance.

(3) When a grounding fault occurs and the fault is on the AC grid side, the zero-sequence impedance of the DC side tends to be infinite, and the equivalent current of the converter need to be added to the positive sequence network. When the fault is on the AC valve side, the zero-sequence impedance of the DC side is closely related to the grounding method of the midpoint of the DC capacitor. What's more, the fundamental frequency vibration voltage amplitude of each pole is inversely proportional to the grounding impedance of the midpoint, and the voltage between poles remains relatively stable.

Based on the research results of this paper, we' will continue to analyze the fault characteristics of other fault types, such as single-phase disconnection fault, disconnection with grounding fault, DC fault, etc.

References

1. Baran, M.E., Mahajan, N.R.: DC distribution for industrial systems: opportunities and challenges. IEEE Trans. Power Electron. **39**(6), 1596–1601 (2003)
2. Flourentzou, N., Agelidis, V.G., Demetriades, G.D.: VSC-based HVDC power transmission systems: an overview. IEEE Trans. Power Electron. **24**(3), 592–602 (2009)
3. Steffen, R., Steffen, B.: Modulation losses and semiconductor requirements of modular multilevel converters. IEEE Trans. Ind. Electron. **57**(8), 2633–2642 (2010)
4. Hagiwara, M., Maeda, R., Akagi, H.: Control and analysis of the modular multilevel cascade converter based on double-star chopper-cells (MMCC-DSCC). IEEE Trans. Power Electron. **26**(6), 1649–1658 (2011)
5. Boroyevich, D., Cvetković, I., Dong, D., et al.: Future electronic power distribution systems a contemplative view. In: International Conference on Optimization of Electrical and Electronic Equipment, Basov, Russia, pp. 1369–1380. IEEE (2010)
6. Kakigano, H., Miura, Y., Ise, T.: Low-voltage bipolar-type DC microgrid for super high quality distribution. IEEE Trans. Power Electron. **25**(12), 3066–3075 (2010)
7. Jiang, D., Zheng, H.: Research status and developing prospect of DC distribution network. Autom. Elect. Power Syst. **36**(8), 98–104 (2012)
8. Song, Q., Zhao, B., Liu, W., et al.: An overview of research on smart DC distribution power network. Proc. CSEE **33**(25), 9–19 (2013)
9. Cui, F., Guo, J., Jing, P., et al.: A review of DC power distribution technology. Power Syst. Technol. **38**(3), 556–564 (2014)
10. Zhang, Z., Lin, P., Wang, X., et al.: Review on relay protection of AC/DC hybrid distribution grids. Power Syst. Prot. Control **47**(5), 179–187 (2019)
11. Zheng, S., Zhao, J., Tan, K., et al.: Research on protection and control of AC/DC distribution network considering DC flexible device. Power Syst. Prot. Control **46**(19), 132–136 (2018)
12. Qi, X., Pei, W., Li, L., et al.: Fault characteristic analysis of dual active bridge converter based multi-voltage-level AC/DC hybrid distribution network. Proc. CSEE **39**(6), 1582–1591 (2019)
13. Peng, K., Zhang, C., Xu, B., et al.: Key issues of fault analysis on distribution system with high-density distributed generations. Autom. Electr. Power Syst. **41**(24), 184–192 (2017)
14. Yang, J., Fletcher, J.E., O'Reilly, J.: Short-circuit and ground fault analyses and location in VSC-based DC network cables. IEEE Trans. Ind. Electron. **59**(10), 3827–3837 (2012)
15. Dai, Z., Ge, H., Chen, B., et al.: Line protection schemes for flexible medium voltage DC distribution networks. Autom. Elect. Power Syst. **41**(17), 78–86 (2017)
16. Jia, K., Li, L., Xuan, Z., et al.: Study on fault location method and simulation for VSC-DC distribution network based on disturbance injection. Power Syst. Prot. Control **47**(04), 99–106 (2019)
17. Liu, S., Mei, H., Liu, B., et al.: The analysis of the AC faults in flexible DC system based on the separation of positive and negative sequence. Proc. CSU-EPSA **32**(02), 68–76 (2020)
18. Karlsson, P., Svensson, J.: DC bus voltage control for a distributed power system. IEEE Trans. Power Electron. **18**(6), 1405–1412 (2003)
19. Tang, G., Xu, Z., Liu, S., et al.: A novel DC voltage control strategy for VSC-MTDC systems. Autom. Electr. Power Syst. **37**(15), 125–132 (2013)
20. Ji, Y., Yuan, Z., Zhao, J., et al.: A suitable voltage control strategy for DC distribution power network. Proc. CSEE **36**(02), 335–341 (2016)
21. Wu, J., Wu, D., Zhu, J., et al.: Grounding method design of multi-terminal flexible DC distribution. Proc. CSEE **37**(9), 2551–2560 (2017)
22. Xu, B., Li, T., Xue, Y.: Relay Protection and Automation of Distribution Network, p. 65. Electric Power Press, Beijing (2017)

Low Carbon Economic Operation of Integrated Energy Systems Considering Power-to-Gas Thermal Recovery and Demand Response

Xiaoyue Zhang[(✉)], Jin Wang, Ting Liu, Shuhao Zhao, Bing Gao, and Huajian Wu

Changsha University of Science and Technology, Changsha 410114, China
1550961814@qq.com

Abstract. It is of great significance to explore the low-carbon operation and efficient energy utilization of integrated energy systems under the goal of dual-carbon. In order to solve the abandoned wind problem caused by the " thermal determining electricity" mode of combined heat and power units. Firstly, in the aspect of low carbon technology, the strong exothermic characteristics of the power to gas methanation process are explored and a residual thermal recovery model of power to gas is established. Secondly, based on the user's perceived inertia of thermal comfort and the delay of thermal network transmission, the thermal load demand response model of load side is established. In addition, an optimal operation model of the integrated energy system considering the thermal recovery characteristics of power to gas and thermal demand response is established. Finally, comparing the simulation results for three operation modes, the effectiveness of the proposed model with the minimized system operation cost, is verified to improve wind power consumption and to promote low-carbon economic operation of the total system.

Keywords: Thermal recovery · Carbon trading · Thermal demand response · Integrated energy systems · Low carbon operation

1 Introduction

The massive combustion of traditional fossil energy sources has caused serious environmental pollution problems, while the large-scale grid connection of wind power has brought huge challenge of wind abandonment. Integrated energy systems (IES) take advantage of the complementarity of different resources to achieve efficient use of energy and synergistic optimization, and then increase the utilization of energy [1]. Demand response (DR) can guide customers to adjust their energy consumption according to price changes or incentives to reduce the load demand during peak periods [2–4]. Therefore, it is important to deeply explore the dispatchable potential of thermal loads to improve the low carbon economic operation of the system.

Combined heat and power (CHP) units are the core component units of IES and often operate with thermoelectric coupling during the thermal season, resulting in limited regulation capacity of CHP units. It limits wind power resource consumption and adds the

pressure of system carbon emissions at the same time [5–7]. The human body perceives temperature changes with a certain lagging and ambiguity, and the thermal load can be regarded as a flexible load to further decouple the thermometric constraint [8]. In the literature [9], a thermal demand response model was developed considering the thermal inertia and transmission delay of thermal loads, and the simulation showed that this method can alleviate thermo-electric conflict in CHP systems and promote the consumption of wind power. The technology of power to gas (P2G) can be used to convert the surplus wind power at night into natural gas, thus enhancing the utilization of wind power [10]. And it has been studied in domestic and overseas, which mainly focused on the role of peak-shaving and consumption of wind power [11–13]. The literature [14] divided the P2G technology into two categories: electric to hydrogen and electric to methane, and finely modeled the two stages on the basis of the operational characteristics of P2G. The literature [15] aggregated CHP units, wind power, P2G, and carbon capture as a virtual power plant, and the simulation showed that its carbon recycling approach effectively dissipated abandoned wind and improves carbon utilization. The literature [16] analyzed the co-operating characteristics of carbon capture units and P2G, and constructed an optimized operation model of electricity-gas IES in a low-carbon scenario. The above studies focused on the role of P2G in low-carbon operation alone, and few papers have investigated the thermal recovery characteristics of P2G. However, a large amount of thermal is released during the P2G methanation reaction, and considering the thermal recovery characteristics of power-to-gas conversion provides a new method for "thermal-electro coupling". It is important to make research on how to utilize P2G residual thermal recovery and thermal demand response for decoupling CHP units to improve energy utilization efficiency.

In summary, based on the existing research, the paper establishes a low carbon economic operation model considering the thermal recovery characteristics of P2G and the thermal load demand response. Firstly, the paper describes the thermal recovery mechanism of P2G elaborately. Secondly, the thermal demand response model is introduced to further explore the low carbon potential of the load side of the system. Finally, the simulation results verify that the proposed model can effectively consume more wind power and reduce carbon emissions, with the lowest total system operation cost.

2 The Structural Framework of IES and the Main Units Modeling

The structure of the IES studied in this paper is shown below. The wind power units, the carbon capture unit, the CHP unit and the electric storage unit share the electric load, the carbon capture unit, the CHP unit and the thermal storage unit share the thermal load, and the P2G can convert the electricity into natural gas to supply the gas turbine, while recovering the thermal energy generated by the reaction for thermal energy supply (Fig. 1).

(1) The mathematical model of carbon capture unit

A part of the CO_2 produced during the operation of thermal power units in IES is captured by the carbon capture system and used to provide carbon materials for P2G, and the remaining part is released to the atmosphere. There is energy consumption during the
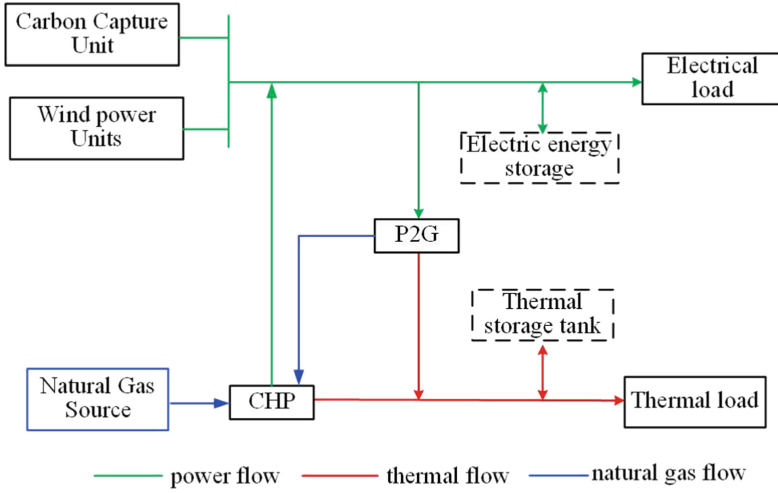
Fig. 1. Structure framework diagram of IES.

capture process of carbon capture system, and the total energy consumption of carbon capture $P_{CCS,t}^{cap}$ is composed of two parts: operational energy consumption $P_{CCS,t}^{o}$ and fixed energy consumption $P_{CCS,t}^{b}$. Therefore, the net output power of carbon capture is the difference between the output power of thermal power unit and the total energy consumption of capture.

$$
\begin{cases}
P_{CCS,t}^{net} = P_{G,t} - P_{CCS,t}^{cap} \\
P_{CCS,t}^{cap} = P_{CCS,t}^{b} + P_{CCS,t}^{o} \\
P_{CCS,t}^{o} = \lambda_{GE} Q_{CCS,t}^{CO_2} \\
Q_{CCS,t}^{CO_2} = e_{ccs} \eta_{ccs} \sum_{t=1}^{T} P_{G,t}
\end{cases}
\tag{1}
$$

where, λ_{GE} is the energy consumption per unit of CO_2 captured, $Q_{CCS,t}^{CO_2}$ is the amount of CO_2 captured in the time period, e_{ccs} is the carbon emission intensity of the carbon capture system, η_{ccs} is the carbon capture rate of the carbon capture system in the time period, and $P_{G,t}$ is the active output of the conventional thermal power unit in the time period t.

(2) CHP unit

The mathematical model expression for the CHP unit is shown below [17]:

$$
\begin{cases}
P_{CHP,t} = P_{CHP,e,t} + P_{CHP,h,t} \\
P_{CHP,e,t} = V_{CHP,t} H_g \eta_{CHP,e} \\
P_{CHP,h,t} = V_{CHP,t} H_g \eta_{CHP,h}
\end{cases}
\tag{2}
$$

where, $P_{CHP,t}$, $P_{CHP,e,t}$, $P_{CHP,h,t}$ are the total output of CHP, the electric output and the thermal output respectively, and $\eta_{CHP,e}$, $\eta_{CHP,h}$ are the electric and thermal conversion efficiency of CHP, respectively. The thermal value of natural gas is 9.98 KWh/m^3.

(3) Energy storage unit

IES energy storage devices include electric energy storage and thermal storage tanks. Electric energy storage can be used to reduce peaks and fill valleys and promote wind power consumption by "low storage and high discharge", and the thermal storage tank can be used to relieve the contradiction between thermal energy and power supply and demand by shifting the thermal load period. The mathematical model is expressed as follows [9].

$$\begin{cases} E_{ES,t} = (1 - \mu_{ES})E_{ES,t-1} + (P_{ESC,t}\eta_{ESC} - P_{ESD,t}/\eta_{ESD})\Delta t \\ H_{HS,t} = (1 - \mu_{HS})H_{HS,t-1} + (H_{TSC,t}\eta_{TSC} - H_{TSD,t}/\eta_{TSD})\Delta t \end{cases} \tag{3}$$

where, $E_{ES,t}$, μ_{ES}, $P_{ESC,t}$, $P_{ESD,t}$, η_{ESC} and η_{ESD} are the capacity, rate of loss, charging power, discharging power, charging efficiency and discharging efficiency of the electric energy storage respectively in the time period t, $H_{HS,t}$, μ_{HS}, $H_{TSC,t}$, $H_{TSD,t}$ η_{TSC} and η_{TSD} are the capacity, rate of loss, thermal storage power, thermal discharge power, thermal storage efficiency and thermal discharge efficiency of the thermal storage tank respectively in the time period t.

3 Model for P2G Thermal Recovery and Thermal Demand Response

3.1 Analysis of P2G Thermal Recovery

The P2G operation process mainly consists of two stages: electrolysis of water to produce hydrogen and methanation, which is the use of surplus renewable energy to produce H_2 and O_2 by electrolysis, and methanation, which is the process of using the H2 generated in the first stage to react with CO_2 to produce methane [18]. The process of methanation in P2G will release a lot of thermal energy, which can theoretically be recycled and injected into the thermal network to further improve energy utilization efficiency. The chemical equation is shown as follows:

$$\begin{cases} 2H_2O \rightarrow 2H_2 + O_2 \\ 4H_2 + CO_2 \rightarrow CH_4 + 2H_2O, \Delta H = -165.01\,kJ/mol \end{cases} \tag{4}$$
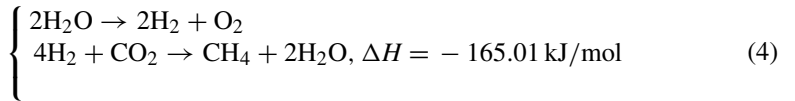
The above equation indicates that 165 kJ of thermal energy is released for each mole of methane generated, and the mathematical formula considering the P2G thermal characteristics per unit time can be expressed as follows:

$$\begin{cases} v_{CH_4} = \dfrac{\rho_{H_2}(P_{P2G}/v_{H_2}) \cdot (Q_{CH_4}/\rho_{CH_4})M_{CH_4}}{4M_{H_2} \times 1000 \times 3600} \\ H_{P2G,CH_4} = \dfrac{\rho_{H_2}(P_{P2G}/v_{H_2})}{4M_{H_2}} \dfrac{\Delta H}{3600}\eta_{P2G}^{CH_4/heat} \end{cases} \tag{5}$$

where, v_{CH_4}, H_{P2G,CH_4} are the yield of methane and the thermal release of methanation process respectively, and P_{P2G} is the power output of P2G. All of their units are MWh. Q_{CH_4} is the thermal value of CH_4. ρ_{H_2}, ρ_{CH_4} are the density of H_2 and CH_4 respectively, M_{H_2}, M_{CH_4} are the molar mass of H_2 and CH_4 respectively, v_{H_2} is the rate of hydrogen production by electrolysis, $\eta_{P2G}^{CH_4/heat}$ is the ratio of thermal release of P2G methanation process to thermal supply, which is taken as 0.8. The energy supply model considering the reaction thermal of P2G is shown as follows:

$$\begin{cases} P_{P2G,g,t} = P_{P2G,t} \cdot \eta_{P2G,e} \\ P_{P2G,h,t} = P_{P2G,t} \cdot \eta_{P2G,h} \end{cases} \tag{6}$$

where, $P_{P2G,g,t}$, $P_{P2G,h,t}$, $P_{P2G,t}$ are the gas power, thermal power and electrical power output of P2G respectively in the time period t. $\eta_{P2G,e}$, $\eta_{P2G,h}$ are the operating efficiency and thermal recovery efficiency of P2G respectively.

3.2 Thermal Demand Response Model

The thermal load has a certain degree of adjustability, and when the indoor temperature is maintained within a small error interval, the user does not perceive the temperature change significantly. In this paper, the mathematical relationship between indoor temperature variation and thermal power and ambient temperature is described using a one-order thermal model of the building as follows:

$$\begin{cases} T_{in,t+1} = T_{in,t}e^{-\Delta t/\tau} + \left(RQ_t^{load} + T_{out,t}\right)\left(1 - e^{-\Delta t/\tau}\right) \\ \tau = RC_{air} \end{cases} \tag{7}$$

where, $T_{in,t}$, $T_{out,t}$ are the indoor temperature and outdoor temperature in time period t. R is the equivalent resistance, C_{air} is the specific thermal capacity of the indoor temperature, Q_t^{load} is the thermal power delivered to the building by the thermal source in time period t, and Δt is the dispatch time of the unit.

Due to the ambiguity of the user's perception of temperature, the following constraints exist for the indoor temperature range:

$$T_{\min} \leq T_{in,t} \leq T_{\max} \tag{8}$$

where, $T_{\min}$, $T_{\max}$ are the minimum and maximum indoor comfort temperature respectively.

4 Low Carbon Economic Operation Modeling of Integrated Energy Systems

The carbon trading mechanism refers to the mechanism of trading carbon allowances in the carbon trading market to restrain the carbon emissions of enterprises. Enterprises make their production arrangements according to the distributed carbon quotas, and if the actual carbon emissions are more than the distributed carbon quotas, they will need to purchase the carbon quotas from the carbon trading market. On the contrary, they can

sell the remaining carbon quotas to make profits [19]. At present, carbon quotas in the electrical industry are mainly allocated without compensation, and this paper adopts the baseline method for quota distribution.

$$E_{\text{IES},p} = E_{\text{G},p} + E_{\text{CHP},p} = \sum_{t=1}^{T} \left[(\delta_e (1 - \eta_{\text{CCS}}) P_{\text{G},t}) + \delta_h P_{\text{CHP}} \right] \tag{9}$$

where, $E_{\text{G},p}$, $E_{\text{CHP},p}$ are the carbon emission of carbon capture unit and CHP unit respectively, and δ_h, $\delta_{CHP,h}$ are the carbon emission factor of thermal power unit and CHP unit respectively. It is taken as 1.08 t/MWh and 0.392 t/MWh respectively [20].

$$E_{\text{IES},a} = E_{\text{G},a} + E_{\text{CHP},a} = \sum_{t=1}^{T} \left[\beta_e (P_{\text{G},t} + P_{\text{CHP}}) \right] \tag{10}$$

where, $E_{\text{G},a}$, $E_{\text{CHP},a}$ is the carbon emission allowance of carbon capture unit and CHP unit respectively, and β_e is the carbon emission allowance of unit power output, which is 0.728 t/MWh.

4.1 Objective Functions

This paper establishes a low carbon economy model with the objective of minimizing the total operating cost of IES. The objective function mainly includes the operating cost of each unit, the cost of carbon trading, the cost of operation for P2G, the cost of carbon sequestration and the cost of abandoned wind. It is shown as follows:

$$\min F = f_{\text{G}} + f_{\text{P2G}} + f_{\text{CHP}} + f_{\text{CO}_2} + f_{\text{qf}} + f_{fc} \tag{11}$$

$$\begin{cases} f_{\text{G}} = \sum_{t=1}^{24} \left(a_1 P_{\text{G},t}^2 + b_1 P_{\text{G},t} + c_1 \right) \\ f_{\text{CHP}} = k_{\text{CH}_4} \left(\sum_{t=1}^{T} 1000 P_{\text{CHP,e},t} / H_{\text{gas}} - V_{\text{CH}_4} \right) \\ f_{\text{P2G}} = k_{\text{P2G}} \sum_{t=1}^{T} P_{\text{P2G},t} \\ f_{\text{qf}} = k_{\text{qf}} \sum_{t=1}^{T} \left(P_{\text{w},t} - P_{\text{ws},t} \right) \\ f_{fc} = k_{CO_2} (Q_{\text{CCS},t}^{\text{CO}_2} - Q_{\text{P2G},t}^{\text{CO}_2}) \\ f_{\text{CO}_2} = k_{CO_2} (E_{\text{IES},p} - E_{\text{IES},a}) \end{cases} \tag{12}$$

where, F is the operating cost of IES, f_G, f_{CHP} are the operating cost of conventional unit and CHP unit respectively, f_{P2G} is the operating cost of P2G, f_{qf} is the cost of wind abandonment, f_{fc} is the cost of carbon sequestration, f_{CO_2} is the cost of carbon trading. a_1, b_1, c_1 are the fuel cost coefficient of conventional units, k_{CH_4} is the unit price of natural gas, k_{P2G} is the operating cost coefficient of P2G, k_{qf} is the cost coefficient of wind abandonment per MW, k_{CO_2} is the cost of CO_2 sequestration per ton, $P_{w,t}$ is the wind power output forecast, and $P_{ws,t}$ is the actual wind power output.

4.2 Constraints

(1) Constraint of power balance

$$P_{P2G,h,t} + H_{CHP,t} + H_{TSD,t} - H_{TSC,t} = \rho H_{L,t} \tag{13}$$

$$P_{CCS,t}^{net} + P_{ws,t} + P_{CHP,e,t} + P_{ESD,t} = P_{L,t} + P_{P2G,t} + P_{ESC,t} \tag{14}$$

where, $P_{L,t}$, $H_{L,t}$ are electrical load and thermal load in time period t. ρ is the thermal load regulation factor.

(2) Constraints of conventional unit

$$\begin{cases} P_{G,min} \leq P_{G,t} \leq P_{G,max} \\ R_{G,down} \leq |P_{G,t} - P_{G,t-1}| \leq R_{G,up} \end{cases} \tag{15}$$

where, $P_{G,min}$, $P_{G,max}$ are the minimum and maximum output of conventional unit, and $R_{G,up}$, $R_{G,down}$ are the upward and downward climbing output of conventional unit respectively.

(3) Constraints of CHP unit

$$\begin{cases} R_{CHP,down} \leq P_{CHP,e,t} - P_{CHP,e,t-1} \leq R_{CHP,up} \\ \max(\chi_1 H_{CHP,t} + \chi_2, P_{CHP,e,min} - \gamma H_{CHP,t}) \leq P_{CHP,e,t} \leq P_{CHP,e,max} - \gamma H_{CHP,t} \end{cases} \tag{16}$$

where, $R_{CHP,up}$, $R_{CHP,down}$ are the upward and downward climbing output of the CHP unit respectively, and χ_1, χ_2 are the elasticity coefficients of the electricity and thermal respectively.

(4) Constraint of wind power output

$$0 \leq P_{ws,t} \leq P_{w,t} \tag{17}$$

(5) Constraint of P2G

$$0 \leq P_{P2G,t} \leq P_{P2G,\,max} \tag{18}$$

where, $P_{P2G,\,max}$ is the maximum value of output of the P2G.

(6) Constraints of carbon capture equipment

$$\begin{cases} 0 \leq P_{CCS,t}^o \leq P_{CCS,max}^o \\ P_{CCS,max}^o = \lambda_{GE} e_{ccs} P_{G,t} \\ \left| P_{CCS,t+1}^{cap} - P_{CCS,t}^{cap} \right| \leq \Delta P_{CCS}^{cap} \\ 0 \leq Q_{P2G}^{CO_2} \leq Q_{CCS,t}^{CO_2} \end{cases} \tag{19}$$

where, $P_{\text{CCS,max}}^{\text{o}}$ is the maximum output value of carbon capture equipment operating energy consumption, and $\Delta P_{\text{CCS}}^{\text{cap}}$ is the climbing constraint of carbon capture equipment capture energy consumption.

(7) Constraint of electrical energy storage

$$
\begin{cases}
E_{\text{ES,min}} \leq E_{\text{ES},t} \leq E_{\text{ES,max}} \\
0 \leq P_{\text{ESC},t} \leq \tau_{\text{ESC},t} P_{\text{ESC,max}} \\
0 \leq P_{\text{ESD},t} \leq \tau_{\text{ESD},t} P_{\text{ESD,max}} \\
0 \leq \tau_{\text{ESC},t} + \tau_{\text{ESD},t} \leq 1 \\
E_{\text{ES},0} = E_{\text{ES},24}
\end{cases}
\tag{20}
$$

where, $E_{\text{ES,min}}$, $E_{\text{ES,max}}$ are the maximum and minimum values of the capacity of the electric energy storage respectively. $\tau_{\text{ESC},t}$, $\tau_{\text{ESD},t}$ are binary variables that represent the charge and discharge of the electric energy storage at time t, with charge being 1 and discharge being 0. $E_{\text{ES},0}$, $E_{\text{ES},24}$ are the initial and final values of the electric energy storage during the day respectively. The thermal storage constraint is similar to the electrical energy storage constraint which will not be repeated here.

5 Analysis of Case

5.1 Setting of Simulation Parameters

In this paper, the solution is based on MATLAB by calling CPLEX in the YALMIP environment. To verify the feasibility of the method proposed in this paper, an integrated energy system in a region is used as an arithmetic scenario for analysis. The parameters related to each unit of the system are referred to the literature [15] and literature [17]. The carbon trading price is set as 50 yuan/t. The abandoned wind cost factor is set as 300 yuan/MW, and the cost of operation of P2G is set as 130 yuan/MW. The predicted output curves of wind power and loads are shown in Fig. 2.

5.2 Setting of Simulation Modes

In order to analyze the effectiveness of considering the thermal recovery characteristics of P2G and the thermal demand response on the optimized operation of IES, three different operation modes are established for comparative analysis.

Mode 1: Without considering the thermal recovery characteristics of P2G and the thermal demand response.
Mode 2: Considering the thermal recovery characteristics of P2G but without considering the thermal demand response.
Mode 3: Considering the thermal recovery characteristics of P2G and the thermal demand response.
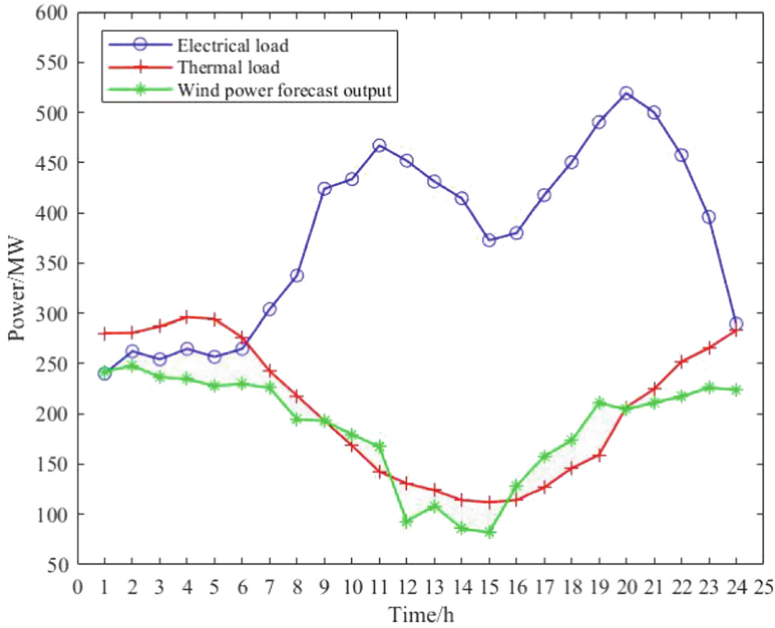
Fig. 2. A figure of electricity, thermal load and wind power forecast output.

5.3 Analysis of Simulation Results

(1) Analysis of thermal power and consumption of wind power under three operation modes

Figures 3 and 4 show the thermal power curve and the electrical power curve under mode 2 respectively. And Figs. 5 and 6 show the CHP thermal output curve and wind power consumption curve under the three operation modes respectively. From Figs. 3, 4, 5 and 6, it is shown that the thermal output of the CHP unit and the wind power dissipation of the system are the lowest under mode 3. Under mode 1, the thermal storage unit and CHP take on the task of thermal energy supply. However, the thermal load is high at the time of 0–7, and the adjustment capacity of the thermal storage device is limited, so the electric output of CHP units is at a high level to meet the demand for thermal energy supply, which seriously squeezes space for wind power connection and causes a large amount of wind abandonment. Mode 2 considers the thermal recovery from P2G, which reduces the wind abandonment rate about 7.76% compared to mode 1. This is because the P2G is in a fully-generated state at the time of wind abandonment. And the surplus wind power is consumed while the residual thermal recovery is used to cooperate with the thermal supply, which decouples the "thermal to electric" constraint of CHP. As a result, the wind power network can be increased. Compared to mode 2, mode 3 is reduced by 2.18% in wind abandonment rate, because considering thermal demand response can reduce the thermal demand during the high output period of wind power, and the thermal output of CHP is reduced, which further improves the capacity

of wind power consumption. It effectively proves that considering P2G residual thermal recovery and thermal demand response can effectively improve the problem of wind abandonment.
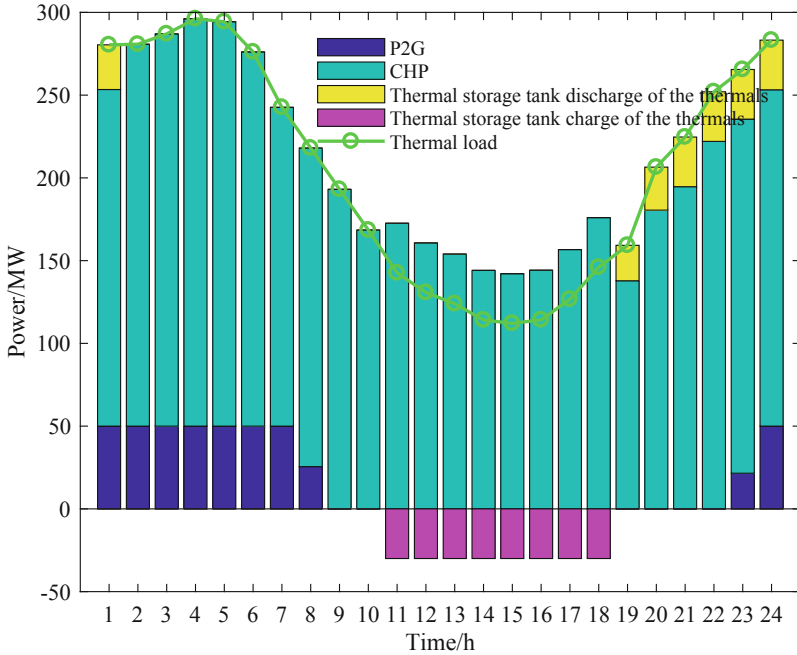
Fig. 3. Thermal power curve under mode 2

(2) Comparison of optimization results under 3 operation modes

Analysis of Table 1 and Figs. 4, 5 and 6 shows that the total operating cost of mode 2 is lower than that of mode 1 by 183,500 RMB, the abandoned wind power reduces by 349.58 MWh, and the carbon emission reduces by 502.97 t. Because of considering the exothermic characteristics of P2G under mode 2, which can undertake part of the thermal task of CHP unit. The electric output of CHP during night time is reduced accordingly, which increases the utilization rate of wind power. At the same time, the carbon emissions of conventional units are reduced. The operating cost of mode 3 is the smallest among the three operating modes, and the amount of abandoned wind is reduced about 98.02 MWh compared with mode 2. This is because after considering the thermal demand response, the thermal load is reduced during 23–6 pm, and the CHP thermal output is reduced by 6%, which could further promote the consumption of wind power. Mode 1 benefits the most from the carbon trading market, because the CHP emission factor is smaller than the carbon allowance and the CHP output of mode 1 is the largest, but it will lead to heavy wind abandonment cost. The simulation results show that mode
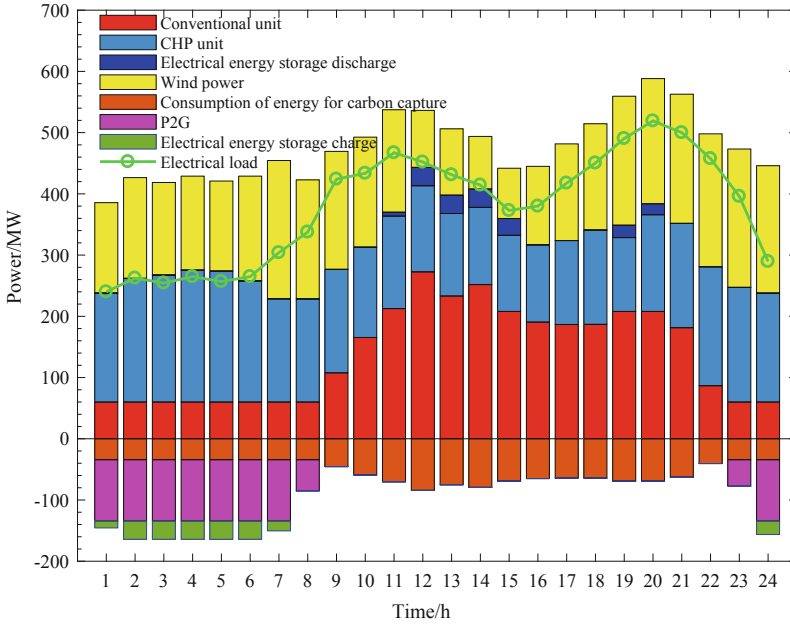
Fig. 4. Electrical power curve under mode 2
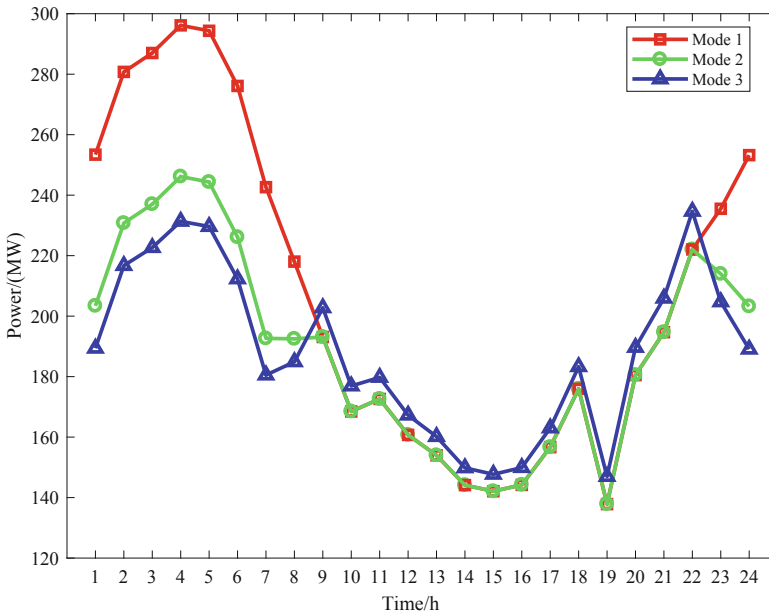
Fig. 5. Thermal power curve under mode 2
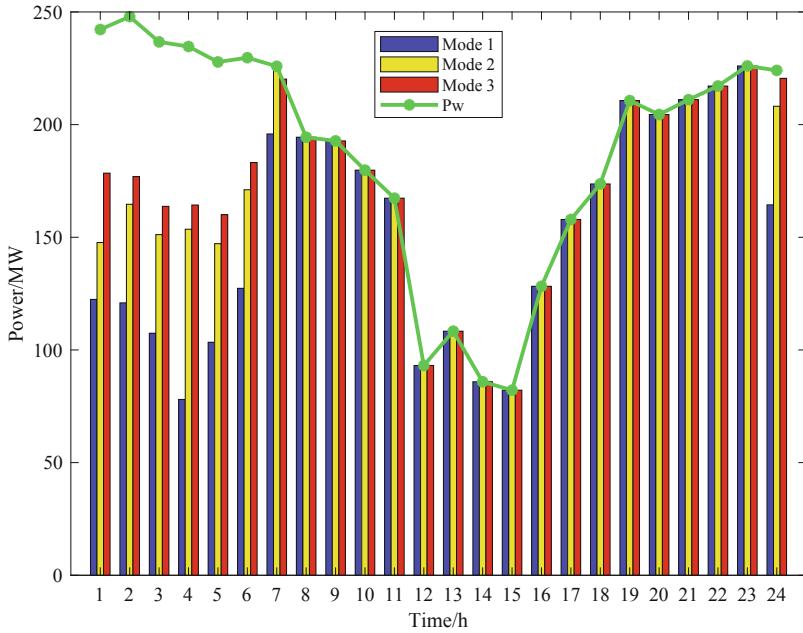
Fig. 6. Thermal power curve under mode 2

Table 1. Comparison of IES optimized operation results under 3 operation modes.

Operation modes	Total operating cost (million yuan)	Carbon trading cost (million yuan)	Winds abandonment (MWh)	Carbon emissions (t)
Mode 1	179.73	−17.10	849.17	5785.40
Mode 2	161.38	−16.56	499.59	5282.43
Mode 3	155.23	−16.11	401.57	5255.19

3 has the smallest amount of wind abandonment and carbon emission, which verifies that considering the thermal recovery characteristics of P2G and thermal demand response can promote the wind power consumption and reduce the carbon emission of the system.

6   Conclusion

In this paper, in order to address the wind abandonment problem caused by CHP thermo-electric coupling, an optimal operation model of IES considering the thermal recovery characteristics of P2G and thermal demand response is proposed, and consider the cost of operation of each unit, the cost of carbon trading, the cost of P2G operation and the cost of wind abandonment as the objective function. The following conclusions are obtained from the simulation results:

P2G can be utilized to convert the surplus wind power to natural gas at night, and make full use of the thermal energy released by methanation which can reduce the thermal energy output of CHP units, improve the flexibility of CHP unit regulation, and provide more space for wind power to connect to the electricity grid. Taking into account the thermal demand response on the load side, which can further explore the emission reduction potential on the user side, and consider the ambiguity of the user's perception of temperature, which can reduce the thermal output of the system to some extent. Considering the thermal recovery of P2G and thermal demand response at the same time can effectively reduce the carbon emission of the system, promote the consumption of wind power, and achieve low carbon economic operation of IES.

References

1. Yu, X., Xu, X., Chen, S., et al.: A brief description of integrated energy systems and energy internet. Trans. China Electrotech. Soc. **31**(01) (2016)
2. Fan, S., Yihan, G., Guangyu, H., Zuyi, L.: Discussion on demand response mechanism for new power systems. Autom. Electr. Power Syst. **46**(07), 1–12 (2022)
3. Aghaei, J., Alizadeh, M.I.: Demand response in smart electricity grids equipped with renewable energy sources: a review. Renew. Sustain. Energy Rev. **18**, 64–72 (2013)
4. Wang, C., et al.: Key technologies and prospects of demand-side resource utilization for power systems dominated by renewable energy. Autom. Electr. Power Syst. **45**(16), 37–48 (2021)
5. Benalcazar, P., Kaszyński, P., Kamiński, J.: Assessing the effects of uncertain energy and carbon prices on the operational patterns and economic results of CHP systems. Energies **14**(24) (2021)
6. Jena, S., Kar, S.K.: Defining indispensability of storage for raised renewable penetration in conventional and thermoelectric coupled microgrid: modeling, analysis and validation. Int. J. Energy Res. **44**(7) (2020)
7. Yang, L., Liang, X., Wang, X., et al.: Combined thermal and power economic dispatch considering peak power trading to improve the secondary consumption capacity of wind power. Power Syst. Technol. **44**(05), 1872–1880 (2020)
8. Wang, Y., et al.: Economic and efficient multi-objective operation optimization of integrated energy system considering electro-thermal demand response. Energy **205** (2020). Prepublish
9. Fang, S., Zhou, R., Xu, F., et al.: Optimal operation of integrated energy system for campus microgrid considering integrated demand response of electric and thermal multiple loads. Proc. CSU-EPSA **32**(01), 50–57 (2020)
10. Straka, P.: A comprehensive study of Power-to-Gas technology: technical implementations overview, economic assessments, methanation plant as auxiliary operation of lignite-fired power station. J. Clean. Prod. **311** (2021)
11. Ma, Y., Zhang, F., Ding, L.: Optimal capacity configuration of power-to-gas, gas tank and natural gas generation unit with participation of curtailed wind power in frequency regulation of power grid. Autom. Electr. Power Syst. **44**(07), 79–86 (2020)
12. Ban, M., Yu, J., Shahidehpour, M., et al.: Integration of power-to-hydrogen in day-ahead security constrained unit commitment with high wind penetration. J. Mod. Power Syst. Clean Energy **5**(3), 337–349 (2017)

13. Zhang, D., Susanna, Y., Wang, X., He, J., Dong, H.: Economic dispatch of integrated electricity-heat-gas energy system considering generalized energy storage and concentrating solar power plant. Autom. Electr. Power Syst. **45**(19), 33–42 (2021)
14. Yu, J., Shi, Q.Y., Yang, Z.F., Dai, W., Wang, X.B.: Day-ahead scheduling method of power-to-gas system considering operating characteristics of water electrolysis and methanation. Autom. Electr. Power Syst. **43**(18),18–25 (2019)
15. Zhou, R., Deng, Z., Xu, J., et al.: Carbon cycle of carbon capture gas-fired cogeneration units and their virtual power plant optimization. Electr. Power **53**(09), 166–171 (2020)
16. Yongli, W.Y., et al. Economic and efficient multi-objective operation optimization of integrated energy system considering electro-thermal demand response. Energy **205** (2020). Prepublish
17. Sun, H., Liu, Y., Peng, C., Meng, J.: Optimization scheduling of virtual power plant with carbon capture and waste incineration considering power-to-gas coordination. Power Syst. Technol. **45**(09), 3534–3545 (2021)
18. Zhang, K., Guo, X., Han, S., Sun, L.: Capacity planning of electric-to-gas conversion units based on electric-to-gas reaction thermal application and cooperative game. Power Syst. Technol. **45**(07), 2801–2811 (2021)
19. Wei, Z., Zhang, S., Sun, G., Xu, X., Chen, S., Chen, S.: Low carbon economic operation of electricity-gas interconnection integrated energy system based on carbon trading mechanism. Autom. Electr. Power Syst. **40**(15), 9–16 (2016)
20. Zhang, X., Liu, X., Zhong, J.: Integrated energy system planning considering reward and penalty ladder type carbon trading and electricity- thermal transfer load uncertainty. Proc. CSEE **40**(19), 6132–6142 (2020)

Multi-objective Optimization Planning for Integrated Electricity and Gas System Considering Dynamics of Gas System

Wang Chunyi[1], Liu Lei[2], Yang Xiaoting[2], Zhang Lele[2], Huang Qingqiang[2], Chen Miao[2], and Zhao Qi[3(✉)]

[1] State Grid Shandong Electric Power Co. Ltd., Jinan 250001, China
[2] State Grid Rizhao Power Supply Co. Ltd., Rizhao 276827, China
[3] School of Electrical Engineering, Shandong University, Jinan 250061, China
`upc_zq@163.com`

Abstract. The integrated electricity and gas systems (IEGS) has become the focus of research in recent years because of its high energy efficiency. To achieve a compromise between the economic and environmental benefits, a multi-objective optimization planning method for IEGS is proposed in this paper to minimize the life cycle cost and total carbon dioxide (CO_2) emissions. Different from power system, the gas flow at the two terminals of a gas pipeline is usually different because of its slow dynamics. The dynamic model of gas system that can describe the line-pack storage of gas is built in form of differential equations based on the law of fluid mechanics. The differential equations are then discretized with the Wendroff scheme to reduce the computational complexity. The discretized dynamic model is considered in the multi-objective planning method as constraints to achieve better economic and environmental benefits by making full use of the line-pack storage gas. To obtain a compromise solution of the two objectives, the multi-objective optimization problem is transmitted into a single-objective one to maximize the comprehensive satisfaction with the fuzzy function. Simulation results demonstrates the effectiveness of the proposed planning method.

Keywords: Integrated electricity and gas systems · Dynamics of gas system · Multi-objective planning

1 Introduction

The survival and development of human beings are inseparable from energy, and the sustainable development of human society requires the sustainable supply of energy. As the energy crisis and environmental pollution problem arises in recent years because of the abuse of traditional fossil energy, people seek to solve these problems with the renewable energy generation. The intermittent characteristics of renewable sources, however, limits their widely equipment in modern power systems. To improve the penetration of renewable energy sources and improve the energy efficiency, the integrated energy

system (IES) is proposed to balance the requirement and generation of power via energy conversion [1, 2]. The IES breaks the separate planning and independent operation of each energy system to coordinate and optimize them in the planning, construction and operation stages [3].

There are complex coupling relationships among various energy systems in IES. Reasonable and precise modeling of each energy system and accurate characterization of the coupling relationship in IES are the basis and key of planning. Literature [4] introduces the concept of energy hub and constructs a nonlinear model of integrated energy system including energy center and power-to-gas devices. Literature [5] adopts the steady-state model of gas system and performs piecewise linearization for it to construct a planning model for the collaborative expansion of power-to-gas equipment with the goal of minimizing the total investment and operating costs. However, most of the existing researches of planning method for IEGS are based on the steady-state model of gas system, ignoring the dynamic process and line-pack storage of it. Theoretically, the fully consideration of the line-pack storage gas in the planning stage of IEGS will achieve better economic benefits. To address this issue, the dynamic model of gas system is built in this paper to precisely describe the gas flow in pipes, and an optimization problem is further formed based on the dynamic model to account for the influence of line-pack storage of gas.

As the global warming is drawing more and more attention in these years, the renewable energy generation is seen as one of the main ways to achieve low-carbon development. However, the intermittent of renewable energy generation limits its widely deployment in power systems. The IEGS can play an important role in absorbing the excess renewable energy generation by transforming it into gas via the power to gas (P2G) units. The P2G process generates hydrogen firstly with the electrolyzed water reaction. The hydrogen is then transmitted into methane together with CO_2 and injected into the gas system. When the generated methane is consumed, no extra CO_2 is emitted considering the absorbed CO_2 in the P2G process. In this situation, the equipment of P2G units can achieve better environmental protection property.

There are some researches have both considered the economic benefits and environmental protection property of IES in the planning stage. Based on the multi-objective mixed integer linear programming method, an expansion planning model of integrated electricity and gas systems with high penetration rate of renewable energy is proposed, which reduces the emissions of greenhouse gases [6]. Literature [7] takes the lowest life cycle cost and the lowest annual CO_2 emissions as the optimization objectives, and conducts a multi-objective optimal configuration study on the capacity of the key equipment in the micro-energy grid. A multi-objective optimal dispatching model for an integrated electricity and gas systems with P2G is proposed, which considers the three objectives of the lowest system operating cost, the lowest environmental pollution cost and the lowest wind curtailment cost [8]. To achieve better environmental protection property by transmitting the excess wind generation to gas with the P2G units, while keep the economic benefits at the same time, a multi-objective planning method for IEGS is proposed in this paper to decide the location and capacity of CHP and P2G units.

In the multi-objective optimization problem, each sub-objective may be contradictory to each other, and a game relationship is formed between the performance of different

objectives. It is impossible to make multiple sub-objectives achieve the optimum at the same time, and only coordination and compromise can be made among them, so that the performance of each sub-objective is as optimal as possible. At present, the commonly used multi-objective optimization methods include weighted summation method, ε-constraint method, multi-objective intelligent optimization algorithm and so on [9]. Among them, the weighted summation method and the ε-constraint method convert the multi-objective optimization problem into a single-objective optimization problem, and then solve it with the help of mathematical programming tools. However, when the dimensions of different optimization objectives are different, simply using coefficients for weighting has a certain degree of subjectivity, which will result in inaccurate results. Therefore, the fuzzy membership function is used in this paper to fuzzify and normalize each single objective. The membership degree of each objective is weighted and summed to construct a comprehensive satisfaction objective function, so that the multi-objective problem can be transformed into a single-objective problem for solving.

The main contributions of this paper are threefold:

1) The dynamic model of gas system is built based on the laws of fluid mechanics to precisely describe the gas flow in pipes, with which the line-pack storage of gas is counted.
2) A multi-objective optimization planning model for IEGS is built to achieve the balance between the economic benefits and environmental protection property. The optimization model is subjected to the built dynamic model of gas system to account for the line-pack storage gas to achieve better economic benefits.
3) The multi-objective planning model is transmitted into a single-objective one with the fuzzy weighting method to be solved efficiently.

The rest of this paper is organized as follows. Section 2 presents the model of IEGS, in which the dynamic model of gas is built and discretized. Section 3 shows the proposed multi-objective optimization planning model for IEGS. Simulation results is shown in Sect. 4 to demonstrate the effectiveness of the proposed method. Finally, Sect. 5 concludes the paper.

2 Model of Integrated Electricity and Gas System

The IEGS consists of the distribution system, the gas system and the coupling components. The distribution system is modeled with the DistFlow model as a quasi-steady system at each time instant. The dynamic model of gas system is built in the form of differential equations based on the law of fluid mechanics to describe the slow dynamic process of gas system. These differential equations are then dissected with the Wendroff difference method to be solved efficiently. The distribution system and gas system are coupled with each other via gas turbine and P2G units, which can achieve the energy conversion according to the operation states.

2.1 Distribution System Model

Compared to gas system, the dynamic process of distribution system is much faster because of the difference of transmission medium. In this case, the distribution system

can be modeled as a quasi-steady state on each time section. To facilitate the optimization solution, the DistFlow model in (1) based on the second-order cone relaxation is used to describe the power flow of the distribution system [10].

$$
\begin{cases}
P_{i,t} + \sum_{ji \in \Omega(i)} (P_{ji,t} - r_{ji}I_{ji,t}^2) = \sum_{ik \in \Psi(i)} P_{ik,t} \\
Q_{i,t} + \sum_{ji \in \Omega(i)} (Q_{ji,t} - x_{ji}I_{ji,t}^2) = \sum_{ik \in \Psi(i)} Q_{ik,t} \\
U_{i,t}^2 = U_{j,t}^2 - 2(r_{ji}P_{ji,t} + x_{ji}Q_{ji,t}) + (r_{ji}^2 + x_{ji}^2)I_{ji,t}^2 \\
\left\| \begin{matrix} 2P_{ji,t} \\ 2Q_{ji,t} \\ I_{ji,t}^2 - U_{j,t}^2 \end{matrix} \right\|_2 \leq I_{ji,t}^2 + U_{j,t}^2
\end{cases}
\tag{1}
$$

where $\Omega(i)$ is the branch set of node i as the end node. $\Psi(i)$ is the branch set of node i as the head node in the DN. $P_{i,t}$ and $Q_{i,t}$ are the active and reactive power of the node i at time step t, respectively. $P_{ji,t}$ and $Q_{ji,t}$ are the active and reactive power at branch ji, respectively. $U_{i,t}$ is the bus voltage amplitude. $I_{ji,t}$ is the branch current amplitude. r_{ji} and x_{ji} are the branch resistance and reactance, respectively.

2.2   Gas System Model

Different from the electrical energy transmitted at the speed of light, gas is transmitted via fluid, which has a slow transmission speed and long transient process. When the gas load changes, the gas system will go through a slow dynamic process from the start of response to the steady state. Therefore, the dynamics of gas system must be considered to characterize the actual state of it.

The energy flow of gas along pipelines is driven by pressure, which is related to the composition, temperature, density and other factors of the gas. Three equations are used to describe the dynamic transmission process of gas, i.e., the momentum equation, the material-balance equation and the equation of state [11]. These three equations are expressed as,

$$
\frac{\partial(\rho\omega)}{\partial t} + \frac{\partial(\rho\omega^2)}{\partial x} + \frac{\partial\rho}{\partial x} + g(\rho - \rho_a)\sin\alpha + \frac{\lambda}{d}\frac{\omega^2}{2}\rho = 0
\tag{2}
$$

$$
\frac{\partial\rho}{\partial t} + \frac{\partial(\rho\omega)}{\partial x} = 0
\tag{3}
$$

$$
p = c^2\rho
\tag{4}
$$

where x is the spatial distance and t is the time. ρ and ρ_α represent the gas density at the horizontal plane and at the angle of α with the horizontal plane in kg/m^3, respectively. p is the gas pressure in Pa. ω is gas velocity in m/s; g is gravitational acceleration in m/s^2. d is the diameter of pipeline in m. λ is the friction coefficient of the pipeline. c is the speed of sound, and the unit is m/s.

Equation (2) is also known as the Navier-Stokes equation, the terms in which are as follows: the first term represents the acceleration effect of gas flow; the second term

represents the convective effect of gas; the third term represents the hydrostatic effect of gas; The fourth term represents the effect of the horizontal height of the pipeline on the momentum; the fifth term represents the second-order deviatoric stress tensor component. It's usually assumed that the gas pipelines are in the same horizontal position, that is, $\alpha = 0$. Besides, ignoring the convective effect that only exists when the gas velocity is close to the speed of sound. The formula (2) can be simplified as:

$$\frac{\partial(\rho\omega)}{\partial t} + \frac{\partial\rho}{\partial x} + \frac{\lambda}{d}\frac{\omega^2}{2}\rho = 0 \tag{5}$$

To linearize the model, the average gas velocity $\overline{\omega}$ of gas is used to approximate a factor of the quadratic term for gas velocity in the third term of Eq. (5). Defining the mass flow rate $M = \rho\omega A$ and bringing it into Eq. (3) and Eq. (5). A set of simplified partial differential equations describing the dynamic characteristics of the gas network are obtained as,

$$\frac{\partial\rho}{\partial t} + \frac{\partial M}{A\partial x} = 0 \tag{6}$$

$$\frac{\partial M}{A\partial t} + \frac{\partial p}{\partial x} + \frac{\lambda\overline{\omega}}{2dA}M = 0 \tag{7}$$

where M is the mass flow rate in kg/s, A is the cross-sectional area of the pipeline in m^2.

The partial differential Eqs. (6) and (7) are discretized in time and space by the Wendroff difference method to obtain linear algebraic equations. The specific difference format of Wendroff difference method is shown in Eq. (8).

$$\begin{cases} \frac{\partial X}{\partial t} = \frac{1}{2}(\frac{X_{i+1,t+1}-X_{i+1,t}}{\Delta t} + \frac{X_{i,t+1}-X_{i,t}}{\Delta t}) \\ \frac{\partial X}{\partial x} = \frac{1}{2}(\frac{X_{i+1,t+1}-X_{i,t+1}}{\Delta x} + \frac{X_{i+1,t}-X_{i,t}}{\Delta x}) \end{cases} \tag{8}$$

where Δt represents the time step; Δx represents the space step.

By applying (8), Eq. (6) and (7) can be transformed to (9) and (10).

$$\rho_{j,t+1} + \rho_{i,t+1} - \rho_{j,t} - \rho_{i,t} + \frac{\Delta t}{L_{ij}A_{ij}}[M_{j,t+1} - M_{i,t+1} + M_{j,t} - M_{i,t}] = 0 \tag{9}$$

$$\frac{1}{A_{ij}}(M_{j,t+1} + M_{i,t+1} - M_{j,t} - M_{i,t}) + \frac{\Delta t}{L_{ij}}[p_{j,t+1} - p_{i,t+1} + p_{j,t} - p_{i,t}]$$
$$+ \frac{\lambda\overline{\omega}_{ij}\Delta t}{4d_{ij}A_{ij}}(M_{j,t+1} + M_{i,t+1} + M_{j,t} + M_{i,t}) = 0 \tag{10}$$

where $M_{i,t}$ and $M_{j,t}$ are the mass flow rates of gas at the head and end of pipeline ij at time step t, respectively. $\rho_{i,t}$ and $\rho_{j,t}$ are the gas densities at the head and end of pipeline ij at time step t, respectively. $p_{i,t}$ and $p_{j,t}$ are the gas pressures at the head and end of pipeline ij at time t, respectively. L_{ij}, A_{ij} and d_{ij} are the length, cross-sectional area and diameter of the gas pipeline ij, respectively. $\overline{\omega}_{ij}$ is the average gas velocity of gas in pipeline ij.

Therefore, the momentum equation and the material balance equation describing the dynamic process of gas flow in pipeline have been simplified to dynamic gas flow differential model based on the Wendroff difference format.

2.3 Modeling of Coupling Equipment

The gas turbines and P2G units are considered in this paper to achieve the bidirectional conversion of energy. The relationship between the power generation and gas consumption of gas turbine is shown as,

$$P_{n,t}^{gt} = \eta_{in} M_{i,t}^{gt} \tag{11}$$

where the subscript i and n link the gas mass flow rate consumption of node i in the gas system with the active power generation of node n in the power system. η_{in} represents the conversion efficiency of the GT, and the unit is MW · s/kg. $P_{n,t}^{gt}$ is the active power generated by the gas turbine at node n of the power system at time step t. $M_{i,t}^{gt}$ is the mass flow rate of gas consumed by the gas turbine at node i of the gas system at time t.

The relationship between the gas produced by the P2G unit and the power consumed is as follows,

$$M_{i,t}^{p2g} = \eta_{is} P_{s,t}^{p2g} \tag{12}$$

where the subscript i and s link the gas mass flow rate generation of node i in the gas system with the active power consumption of node s in the power system. η_{is} represents the conversion efficiency of the P2G, and the unit is kg/(s · MW). $P_{s,t}^{p2g}$ is the active power consumed by the power-to-gas unit at the node s of the power system at time t. $M_{i,t}^{p2g}$ is the mass flow rate of gas generated by the power-to-gas unit at node i of the gas system at time t.

3 Multi-objective Optimization Planning Method of IEGS

3.1 Objective Function

The planning model proposed in this paper both considering the economy benefits and environmental protection. The objective of economic benefits aims to minimize the life cycle cost of IEGS, while the second one aims to minimize the total carbon dioxide emissions [12].

Objective Function 1: Life Cycle Cost. The life cycle cost of IEGS includes equipment investment cost, system operation cost, equipment maintenance cost and total residual value of equipment during the planning cycle.

The present value coefficient is introduced, and the costs incurred in each year are converted into the present value at the beginning of the planning period. The formula for calculating the present value coefficient is shown in (13). The formula for calculating the life cycle cost is shown in (14).

$$R^j = (1 + r)^{-j} \tag{13}$$

$$F_g = C_{inv} + \sum_{j=1}^{n} R^j (C_{ope}^j + C_{mai}^j) - R^n F_{rv} \tag{14}$$

where j represents the number of years from the beginning of the planning cycle to the cost occurred; r is the discount rate. n is the total number of years in the planning cycle. C_{inv} is the equipment investment cost. R^j is the present value coefficient of the jth year in the planning cycle. R^n is the present value coefficient at the end of the planning period. C_{ope}^j and C_{mai}^j are the system operation cost and equipment maintenance cost of the jth year in the planning period, respectively. F_{rv} is the residual value of the equipment at the end of the planning period.

The equation for calculating the equipment investment cost is shown as,

$$C_{inv} = sum(c_{GT} * \boldsymbol{Q}^{gt}) + sum(c_{P2G} * \boldsymbol{Q}^{p2g}) \tag{15}$$

where c_{GT} and c_{P2G} are the unit capacity investment cost of the gas turbine and the power-to-gas unit, respectively. $\boldsymbol{Q}^{gt}$ and $\boldsymbol{Q}^{p2g}$ represent the capacity matrices of configured gas turbines and power-to-gas units on each coupling node in the integrated electricity and gas systems, respectively.

The system operating cost in the jth year is calculated with,

$$C_{ope}^j = \sum_{t=1}^{8760} (c_{grid}(t)P_{grid}(t)\Delta t + c_{gas}M_{gas}(t)\Delta t) \tag{16}$$

where $c_{grid}(t)$ is the electricity price at time t. c_{gas} is the price of gas. $P_{grid}(t)$ is the power purchased from the upper power grid. $M_{gas}(t)$ is the mass flow rate of gas purchased from the gas source.

The equipment maintenance cost in the jth year can be obtained by,

$$C_{mai}^j = \sum_{t=1}^{8760} \left(c_{gt}^{mai} P^{gt}(t)\Delta t + c_{p2g}^{mai} P^{p2g}(t)\Delta t \right) \tag{17}$$

where c_{gt}^{mai} and c_{p2g}^{mai} are the unit output power maintenance cost of the gas turbine and the P2G unit, respectively. $P^{gt}(t)$ and $P^{p2g}(t)$ are the active power generated by the gas turbine and the active power consumed by the P2G unit at time t, respectively.

The depreciation and residual value of each configured equipment is also considered in the life circle cost of IEGS. The depreciation cost $C_{Dep,j}$ of the mth equipment in each year of its life is calculated as,

$$\begin{cases} C_{dep,m} = C_{inv,m}(1 - \delta_m)/T_m \\ C_{inv,m} = c_{inv,m} \times Q_m \end{cases} \tag{18}$$

where δ_m is the net residual value rate of the mth equipment. T_m is the life of the mth equipment; $(1 - \delta_m)/T_m$ is the depreciation rate of the mth equipment in each year of its life cycle. $C_{inv,m}$ is the investment cost of the mth equipment. $c_{inv,m}$ is the unit capacity investment cost of the mth equipment. Q_m is the configuration capacity of the mth equipment.

The total residual value of each equipment at the end of the planning period is obtained with,

$$F_{rv} = \sum_{m=1}^{M_x} (C_{inv,m} - \sum_{t=1}^{Y_m} C_{dep,m}) \tag{19}$$

where M_x is the total number of equipment owned at the end of the planning period. Y_m is the total number of operation years of the mth equipment from configuration to the end of the planning cycle.

Objective Function 2: Total CO$_2$ Emissions During the Planning Period. The carbon dioxide emissions of the integrated electricity and gas systems mainly come from the purchase of power and gas. The calculation formula of total CO$_2$ emissions is as follows:

$$F_c = n * (\sum_{t=1}^{8760} (\alpha_e P_{grid}(t)\Delta t + \alpha_{gas} P_{gas}(t)\Delta t)) \tag{20}$$

where $P_{gas}(t)$ is the gas power purchase from gas source at time t; α_e is the carbon dioxide emission coefficient of power purchase. α_{gas} is the carbon dioxide emission coefficient of gas power purchase.

3.2   Constraints

Distribution Network Constraints. The distribution network constraints, including node voltage constraint, branch capacity constraint and the power purchase constraint, are shown as,

$$\begin{cases} P_{grid}(t) \geq 0 \\ U_{i,\min} \leq U_{i,t} \leq U_{i,\max} \\ P_{ji,\min} \leq P_{ji,t} \leq P_{ji,\max} \\ Q_{ji,\min} \leq Q_{ji,t} \leq Q_{ji,\max} \end{cases} \tag{21}$$

where $U_{i,\min}$ and $U_{i,\max}$ are the lower limit and upper limit of the node i voltage, respectively. $P_{ji,\min}$ and $P_{ji,\max}$ are the lower limit and upper limit of branch active power, respectively. $Q_{ji,\min}$ and $Q_{ji,\max}$ are the lower limit and upper limit of the branch reactive power, respectively.

Gas Network Constraints.   Gas network constraints include the gas flow balance equation at each node, the gas pressure continuity equation, the gas state equation, the pressure limit at the node, the flow limit at the head and end of the pipeline and the gas purchase limit.

The above constraints are shown as,

$$
\begin{cases}
M_{i,t}^{gas} + M_{i,t}^{p2g} - M_{i,t}^{L} - M_{i,t}^{gt} + \sum_{ki \in \Omega(i)} M_{ki,t}^{E} - \sum_{ij \in \Psi(i)} M_{ij,t}^{F} = 0 \\
p_{i,t} = p_{ki,t}^{E} = p_{ij,t}^{F} \\
p_{i,t} = c^2 \rho_{i,t} \\
p_{i\,\min} \leq p_{i,t} \leq p_{i\,\max} \\
M_{ij\,\min}^{F} \leq M_{ij,t}^{F} \leq M_{ij\,\max}^{F} \\
M_{ij\,\min}^{E} \leq M_{ij,t}^{E} \leq M_{ij\,\max}^{E} \\
M_{i,t}^{gas} \geq 0
\end{cases}
\tag{22}
$$

where $M_{i,t}^{gas}$ is the output gas flow of gas source. $M_{i,t}^{gt}$ is the gas consumption flow of the gas turbine connected at node i of the gas system at time step t. $M_{i,t}^{p2g}$ is the output gas flow of the power-to-gas unit at node i of the gas system at time step t. $M_{i,t}^{L}$ is the gas load flow of node i at time step t. $M_{ki,t}^{E}$ and $p_{ki,t}^{E}$ are the gas flow and gas pressure at the end of the pipeline with node i as the end node at time t, respectively. $M_{ij,t}^{F}$ and $p_{ij,t}^{F}$ are the gas flow and gas pressure at the head of the pipeline with node i as the head node at time t, respectively. $\Omega(i)$ is the pipeline set with node i as the end node in the gas network. $\Psi(i)$ is the pipeline set with node i as the head node in the gas network. $p_{i,t}$ and $\rho_{i,t}$ are the gas pressure and gas density at node i at time t, respectively. c is the speed of sound. $p_{i\,\min}$ and $p_{i\,\max}$ are the lower limit and upper limit of the gas pressure at node i, respectively. $M_{ij\,\min}^{F}$ and $M_{ij\,\max}^{F}$ are the lower limit and upper limit of the gas flow at the head of pipeline, respectively. $M_{ij\,\min}^{E}$ and $M_{ij\,\max}^{E}$ are the lower limit and upper limit of the gas flow at the end of pipeline, respectively.

Wind Farm Output Power Constraints. The absorbed power of the wind farm at each time step is less than its predicted power. The wind farm output power constraint is,

$$
0 \leq P_{wfc}(t) \leq P_{wf}^{\max}(t)
\tag{23}
$$

where $P_{wfc}(t)$ is the absorbed power of the wind farm at time step t. $P_{wf}^{\max}(t)$ is the maximum predicted power of the wind farm at time step t.

Coupling Equipment Constraints. Capacity configuration constraints of gas turbines and P2G units on each candidate node are as shown as,

$$
\begin{cases}
0.05 * x_{gt}(k) \leq Q_k^{gt} \leq Q_{\max}^{gt} * x_{gt}(k) \\
1 * x_{p2g}(k) \leq Q_k^{p2g} \leq Q_{\max}^{p2g} * x_{p2g}(k)
\end{cases}
\tag{24}
$$

where Q_k^{gt} and Q_k^{p2g} represent the gas turbine capacity and power-to-gas unit capacity configured on the kth candidate node, respectively. $k = 1, 2, \cdots, K$, K represents the total number of candidate configuration nodes for gas turbines and power-to-gas units. $Q_{\max}^{gt}$ and $Q_{\max}^{p2g}$ represent the upper limit for the capacity configuration of gas turbines and power-to-gas units on each candidate node, respectively. $x_{gt}(k)$ and $x_{p2g}(k)$ are 0–1 integer variables of whether a gas turbine and a power-to-gas unit are configured at the kth candidate position, respectively.

Output power constraints for gas turbines and power-to-gas units are shown as,

$$\begin{cases} 0 \leq P_{n,t}^{gt} \leq Q_n^{gt} \\ 0 \leq P_{s,t}^{p2g} \leq Q_s^{p2g} \end{cases} \tag{25}$$

where $P_{n,t}^{gt}$ is the active power generated by the gas turbine at node n of the distribution network at time t; Q_n^{gt} is the configuration capacity of the gas turbine at node n of the distribution network. $P_{s,t}^{p2g}$ is the active power consumed by the power-to-gas unit at node s of the distribution network at time step t. Q_s^{p2g} is the configuration capacity of the power-to-gas unit at node s of the distribution network.

4 Weighted Fuzzification Processing of Multiple Objects

In multi-objective optimization problem, the sub-objectives may be contradictory to each other and a game relationship is formed between the performance of different objectives. It is impossible to make multiple sub-objectives achieve the optimum at the same time. We can only coordinate and compromise among multiple objectives, so that the performance of each sub-objective can be optimized as much as possible. To coordinate the two contradictory objectives in the planning model, the fuzzy membership function is used to fuzzify and normalize the multi-objective and then the membership degrees of each objective are weighted and summed. In this case, the multi-objective planning problem can be transformed into a single-objective one [13].

Since it is hoped that the life cycle cost and the total amount of carbon dioxide emissions are both as small as possible, the "lower semi-trapezoid" membership functions of the two objectives are respectively established, as shown in Fig. 1 and Fig. 2. The greater the membership of the objective, the higher the satisfaction with the objective [14].
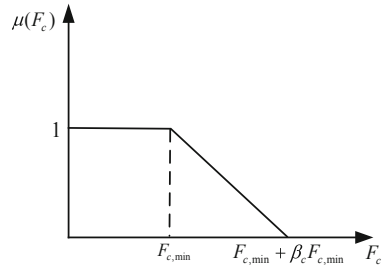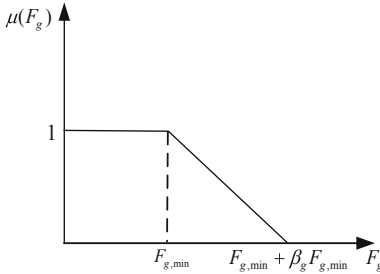
Fig. 1. Membership function of objective 1   **Fig. 2.** Membership function of objective 2

The membership function formula corresponding to objective 1 is shown as,

$$\mu(F_g) = \begin{cases} 1 & F_g \leq F_{g,\min} \\ \frac{F_{g,\min}+\beta_g F_{g,\min}-F_g}{\beta_g F_{g,\min}} & F_{g,\min} < F_g \leq F_{g,\min} + \beta_g F_{g,\min} \\ 0 & F_g > F_{g,\min} + \beta_g F_{g,\min} \end{cases} \tag{26}$$

The membership function formula corresponding to objective 2 is shown as,

$$\mu(F_c) = \begin{cases} 1 & F_c \leq F_{c,\min} \\ \frac{F_{c,\min}+\beta_c F_{c,\min}-F_c}{\beta_c F_{c,\min}} & F_{c,\min} < F_c \leq F_{c,\min} + \beta_c F_{c,\min} \\ 0 & F_c > F_{c,\min} + \beta_c F_{c,\min} \end{cases} \quad (27)$$

where $\mu(F_g)$ and $\mu(F_c)$ are the satisfaction functions of the life cycle cost objective and the total carbon dioxide emissions objective in the planning period, respectively; $F_{g,\min}$ and $F_{c,\min}$ are the optimal solutions of the two single-objective planning models, respectively. $F_{g,\min}$ and $F_{c,\min}$ represent the theoretical minimum value of the life cycle cost and the total carbon dioxide emissions in the planning period; β_g and β_c are resiliency satisfaction of objective 1 and objective 2, respectively; $\beta_g F_{g,\min}$ and $\beta_c F_{c,\min}$ represent the increase allowed by the planner in the life cycle cost and carbon dioxide emissions during the planning period, respectively.

The overall satisfaction objective function is constructed by the weighted sum of the satisfaction of objective 1 and objective 2, to realize the transformation from multi-objective to single-objective. The established multi-objective weighted fuzzy planning model is as follows,

$$\begin{cases} \max \mu = \max\left(a_1 \mu_{F_g} + a_2 \mu_{F_c}\right) \\ a_1 + a_2 = 1 \\ F_g + \mu_{F_g}\beta_g F_{g,\min} \leq F_{g,\min} + \beta_g F_{g,\min} \\ F_c + \mu_{F_c}\beta_c F_{c,\min} \leq F_{c,\min} + \beta_c F_{c,\min} \\ 0 \leq \mu_{F_g} \leq 1 \\ 0 \leq \mu_{F_c} \leq 1 \\ \boldsymbol{H}(\boldsymbol{x}) = \boldsymbol{0} \\ \boldsymbol{G}(\boldsymbol{x}) \leq \boldsymbol{0} \end{cases} \quad (28)$$

where μ is the overall satisfaction. μ_{F_g} and μ_{F_c} are the satisfaction with the minimum life cycle cost objective and the satisfaction with the minimum total carbon dioxide emissions objective in the planning period, respectively. a_1 and a_2 are the weight coefficients of the two objectives. $\boldsymbol{H}(\boldsymbol{x})$ represents all equality constraints in the planning model. $\boldsymbol{G}(\boldsymbol{x})$ represents all inequality constraints in the planning model.

5   Case Study

An integrated electricity and gas systems coupled by an IEEE 33-node distribution system and a 7-node gas system is used for simulation. The structure of the integrated electricity and gas systems is shown in Fig. 3. Wind farms WF1 and WF2 are connected to node 8 and node 27 of the distribution network, with capacities of 4 MW and 5 MW, respectively. Typical daily electricity load, gas load and wind farm predicted output power curves in summer, winter and transition season are shown in Fig. 4, Fig. 5 and Fig. 6, respectively. The time-of-use price of purchase electricity by the distribution network from the upper-level grid is shown in Fig. 7. The parameter values involved in the planning model are shown in Table 1 and Table 2. Planning period n is 8 years. The transformed single-objective planning is problem is solved with the CPLEX solver equipped in MATLAB.

Fig. 3. Structure diagram of integrated electricity and gas systems.

Fig. 4. Electricity loads in typical day.

Fig. 5. Gas loads in typical day.

Fig. 6. Predicted output of wind power generation.

Fig. 7. Time-of-use price curve of power system.

Table 1. Equipment parameters.

Equipment type	Parameter	Numerical value
Gas turbine	Lifetime	25 years
	Investment cost per unit capacity	7×10^6 yuan/MW
	Unit output power maintenance cost	0.05 yuan/KW
	Gas-to-power conversion efficiency	1.8 MWs/kg
	Equipment net residual value rate	6%
Power to gas	Lifetime	25 years
	Investment cost per unit capacity	8×10^6 yuan/MW
	Unit output power maintenance cost	0.05 yuan/KW
	Power-to-Gas conversion efficiency	$0.11 \, kg/(s \cdot MW)$
	Equipment net residual value rate	6%

Table 2. Other parameters.

Parameter	Numerical value
Planning cycle	8 years
Discount rate	8%
Gas price	0.4 yuan/kg
CO_2 emissions coefficient of purchase electricity	968 g/KWh
CO_2 emissions coefficient of purchase gas	220 g/KWh
Weight factor for objective 1	0.5
Weight factor for objective 2	0.5
Resiliency satisfaction for objective 1	0.5
Resiliency satisfaction for objective 2	0.5

5.1   Methods Setting

This section sets up the following four optimization planning methods for comparative analysis:

Method 1: The steady state model of the gas system is considered with the objective of minimizing the life cycle cost.
Method 2: Considering the dynamic model of gas system with the objective of minimizing the life cycle cost.

Method 3: Considering the dynamic model of gas system with the objective of minimizing the total amount of carbon dioxide emissions in the planning period.

Method 4: Considering the dynamic model of gas system as well as minimizing the life cycle cost objective and the minimum total carbon dioxide emissions objective, i.e., the proposed method.

5.2 Simulation Results and Analysis

Table 3 and 4 show the planning results and life circle cost of method 1 and method 2, respectively. As shown in Table 3, when the dynamic model of gas network is considered in method 2, the capacity of GT configured is larger and the life cycle cost is lower. This is because the gas stored in the pipeline can be used when considering the dynamic model of the gas system, which reduces the gas purchase cost and can make the configuration capacity of GT higher to convert the gas into power.

Table 3. Comparison of equipment configuration results in methods 1–2

Coupling nodes	Grid nodes	4	26	6	9	13	29
	Gas network nodes	2	3	4	5	6	7
Method 1	GT/MW	0.2466	0	0	0	0	0
	P2G/MW	—					
Method 2	GT/MW	1.0801	0	0	0	0	0
	P2G/MW	—					

Table 4. Comparison of planning cost in methods 1–2

Cost/(10 million yuan)	Method 1	Method 2
Total investment cost of equipment	0.1599	0.7001
Annual operating cost	3.1863	2.4029
Annual maintenance cost	0.0035	0.0149
Total operating and maintenance cost for the planning period	18.330	13.894
Total residual value of equipment	0.0652	0.2856
Life cycle cost	18.425	14.308

Table 5 shows the comparison of the equipment configuration results of methods 2–4. Table 6 shows comparison of the life circle cost and CO_2 emission of them. It can be seen from Table 5 and 6 that P2G units are not configured in method 2 due to its high investment cost. However, its environmental protection property is poor since the excess wind power are abandoned, which cause more CO_2 emission in thermal power generator. As a contrast, to optimize the environmental protection property, the

configuration capacity of the gas turbine and the P2G unit is high in method 3. It's life circle cost, however, is unacceptable compared to the other two methods.

Table 7 shows the sub-objective satisfaction and comprehensive satisfaction value of method 4. It can be seen from Table 6 that method 4 comprehensively considering the minimum life cycle cost objective and the minimum total carbon dioxide emissions objective, can effectively achieve a compromise between the economy benefits and environmental protection property. It can be seen from Table 6 that the method 4 improves the environmental protection property compared with the method 2 and improves the economic benefits compared with the method 3.

Table 5. Comparison of equipment configuration results of methods 2–4

Coupling nodes	Grid nodes	4	26	6	9	13	29
	Gas network nodes	2	3	4	5	6	7
Method 2	GT/MW	1.0801	0	0	0	0	0
	P2G/MW	–					
Method 3	GT/MW	10	10	10	10	10	10
	P2G/MW	10	10	10	10	10	10
Method 4	GT/MW	4.6134	0	0	0	0	0
	P2G/MW	0	1.02	0	0	0	0

Table 6. Comparison of planning cost and total CO_2 emissions of methods 2–4

Examples	Planning objectives	Life cycle cost /(10 million yuan)	Total CO_2 emissions /kg
Method 2	Minimum life cycle cost	14.308	6.3602×10^7
Method 3	Minimal total CO_2 emissions	61.818	4.7701×10^7
Method 4	The highest overall satisfaction	15.218	5.4593×10^7

Table 7. Satisfaction of each sub-objective and comprehensive satisfaction value

Classification	Value
Life cycle cost objective satisfaction μ_{F_g}	0.7919
Satisfaction with total carbon dioxide emissions objective μ_{F_c}	0.8729
Comprehensive satisfaction μ	0.7110

6 Conclusion

In this paper, a multi-objective optimization planning method for IEGS considering the dynamic characteristics of gas system is proposed to achieve a compromise between economic benefits and environmental protection property. The dynamic model of gas system that describes the gas flow in pipes precisely is firstly built in the form of differential equations based on the law of fluid mechanics. By considering this dynamic model in planning stage, line-pack storage gas in pipelines is accounted to achieve better economic and environmental benefits. The P2G units are considered in the planning method for its advantages in improving the wind power absorption to achieve better environmental protection property. The multi-objective of minimum life cycle cost and total CO_2 emissions objectives are transformed into a single one to maximize the comprehensive satisfaction with the fuzzy membership function. An IEGS consists of an IEEE 33-node distribution network and a 7-node gas network is used for simulation calculation. Simulation results demonstrates the effectiveness of the proposed method. In our future work, the multi-objective planning method for integrated gas-heat-power system considering the dynamics of gas and heat system will be studied.

References

1. Cheng, H., Hu, X., Wang, L., et al.: Review on research of regional integrated energy system planning. Autom. Electr. Power Syst. **43**(7), 2–13 (2019)
2. Jingwei, Y., Ning, Z., Yi, W., et al.: Multi-energy system towards renewable energy accommodation: review and prospect. Autom. Electr. Power Syst. **42**(4), 11–24 (2018)
3. Dan, W., Liu, L., Jia, H., et al.: Review of key problems related to integrated energy distribution systems. CSEE J. Power Energy Syst. **4**(002), 130–145 (2018)
4. Zhang, X., Shahidehpour, M., Alabdulwahab, A., et al.: Optimal expansion planning of energy hub with multiple energy infrastructures. IEEE Trans. Smart Grid **6**(5), 2302–2311 (2015)
5. Wang, D., Qiu, J., Meng, K., et al.: Coordinated expansion co-planning of integrated gas and power systems. J. Mod. Power Syst. Clean Energy **5**(3), 314–325 (2017)
6. Hby, A., As, A., Jmg, B.: A multi-objective mixed integer linear programming model for integrated electricity-gas network expansion planning considering the impact of photovoltaic generation. Energy **222**, 119933 (2021)
7. Liu, W., Wang, D., Xiaodan, Y.U., et al.: Multi-objective planning of micro energy network considering P2G-based storage system and renewable energy integration. Autom. Electr. Power Syst. **42**(16), 11–20 (2018)
8. Zeng, H., Liu, T., He, C., et al.: Multi-objective optimization for integrated-gas and electricity energy system considering power-to-gas. Electr. Meas. Instrum. **8**, 16 (2019)
9. Wang, Y., Huang, F., Tao, S., et al.: Multi-objective planning of regional integrated energy system aiming at exergy efficiency and economy. Appl. Energy **306**, 118120 (2022)
10. Xin, M.A., Guo, R., Wang, L., et al.: Day-ahead scheduling model for AC/DC active distribution network based on second-order cone programming. Autom. Elect. Power Syst. **42**(22), 144–150 (2018)
11. Chen, X., Wang, C., Wu, Q., et al.: Optimal operation of integrated energy system considering dynamic heat-gas characteristics and uncertain wind power. Energy **198**, 117270 (2020)
12. Dong, S., Wang, C., Liang, J., et al.: Multi-objective optimal day-ahead dispatch of integrated energy system considering power-to-gas operation cost. Autom. Electr. Power Syst. **42**(11), 8–15 (2018)

13. Ding, X., Sun, W., Harrison, G.P., et al.: Multi-objective optimization for an integrated renewable, power-to-gas and solid oxide fuel cell/gas turbine hybrid system in microgrid. Energy **213**, 118804 (2020)
14. Olson, D.L., Wu, D.: Simulation of fuzzy multiattribute models for grey relationships. Eur. J. Oper. Res. **175**(1), 111–120 (2006)

Correlation Analysis Method of Load Change Between Different Intelligent Cables

Ran Hu[1], Bing Li[1], Siyong Huang[2], Jinyang Wang[2], Zhenyu Lin[2], Xianghao Li[2], Zhidong Wang[2], and Ling Yang[2(✉)]

[1] Shenzhen Power Supply Bureau Co., Ltd., Shenzhen 518000, China
huran@sz.csg.cn
[2] College of Electric Power, South China University of Technology, Guangzhou 510006, China
epyangl@scut.edu.cn

Abstract. Power cables are widely used in modern power systems. When the correlation between cables in the same area is obtained, it will be beneficial for operators to grasp the operation status of multiple cables more quickly. In this paper, a method that can be used to quantify the correlation of power cables by simulation is proposed. Using this method, it is very convenient to calculate the correlation coefficient between different cables, and quantify the correlation between cables through the simulation results. The correctness and feasibility of the cable correlation calculation method proposed in this paper are verified by an example.

Keywords: Cable · Correlation · Simulation

1 The Introduction

The medium voltage power cable is one of the important equipment for transmitting electric energy in the power system. Taking core cities such as Shenzhen as an example, medium-voltage cables account for 92% and the original value of their assets accounts for 70% of the distribution network assets. Moreover, 40% of the cables have been in operation for more than 20 years. On the abnormal operation of cables, it is necessary to transfer the load to the adjacent cables. Therefore, analyzing the load correlation between adjacent cables will help to better grasp the load changes of each relevant cable during the fault process. And then providing theoretical support for reliable scheduling. In addition, the staff can judge the operation state of other cables if they know the correlation between cables. And they can deal with the abnormal operation of the cable in time. Moreover, they can understand which cables can currently carry more load according to the correlation when performing load transfer.

Current research on cables has few analytical relevance between the various cables. Through the correlation analysis of cables, if a cable is overloaded, other cables with strong correlation may also be overloaded. Moreover, when the load of the cables needs

to be transferred, most cases rely on the experience of the staff without enough theoretical support. Therefore, this paper proposes a simple correlation calculation method to quantify the correlation coefficient by simulation. It can provide theoretical support for the use of correlation coefficient.

2   Theoretical Analysis

Taking the single-phase simplified circuit between a single power supply and a load as an example, this paper analyzes the changes of load and line transmission power. The specific circuit and simplified form are shown in Fig. 1.
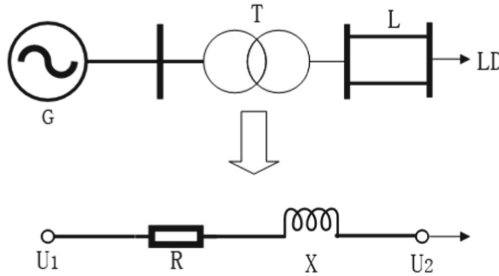
Fig. 1. Simple circuit of a single power supply and its simplified diagram

In the circuit:

$$R = R_T + \frac{R_L}{2} \tag{1}$$

$$X = X_T + \frac{X_L}{2} \tag{2}$$

R and X are the equivalent resistance and reactance of the circuit. R_T and X_T are the equivalent resistance and reactance of the transformer. And R_L and X_L are the equivalent resistance and reactance of the transmission line.

From the equivalent circuit, the formula can be obtained as follows:

$$\dot{U}_1 - \dot{U}_2' = (R + X) \times \dot{I} \tag{3}$$

The node voltage can be derived as follows by substituting power for current:

$$\begin{aligned} \dot{U}_2' &= \dot{U}_1 - (R + X) \times \dot{I} \\ &= \dot{U}_1 - \frac{P_1 R + Q_1 X}{U_1} - j\frac{P_1 X - Q_1 R}{U_1} \end{aligned} \tag{4}$$

Similarly, the node power can be obtained as follows:

$$P_2 + jQ_2 = P_1 + jQ_1 - \dot{I}^2 \times (R + jX)$$

$$= P_1 + jQ_1 - \frac{P_1^2 + Q_1^2}{U_1^2}(R + Q) \tag{5}$$

According to the formula, the increase of the generator terminal voltage will increase the voltage and power of the node connected to it.

However, in the practical system, each node will carry a local load, as follows (Fig. 2):
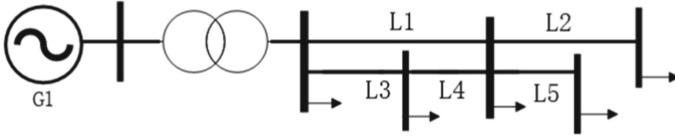
Fig. 2. The actual complex circuit

The connection between the nodes is more complicated. It will have a greater impact on the power distribution of the system. In addition, the load changes frequently, and the degree of variation is large [2]. So that if the above analysis is applied to the practical system, it will be difficult to obtain the expression.

In order to explore the correlation between cables in the practical system, this paper adopts the method of model simulation and data analysis. In detail, This paper establishes a model in MATLAB and simulates the power change of each cable. The correlation between cables is analyzed from the power change curve [3].

3   The Detailed Implementation

The specific steps of the method used in this paper are as follows:

(1) Determine the specific parameters of each electrical component in the system.
(2) Use Matlab to build the model of the system.
(3) Select the specific analysis area and determine the target cable for the analysis.
(4) Adjust the generators in the analysis area to obtain the power variation curve of the target cable.
(5) Analyze the target cables in pairs.
(6) Normalize the power data of the cables being compared and calculate the correlation coefficient.
(7) Get the correlation coefficients of all target cables with each other.

The flow chart is as follows (Fig. 3):
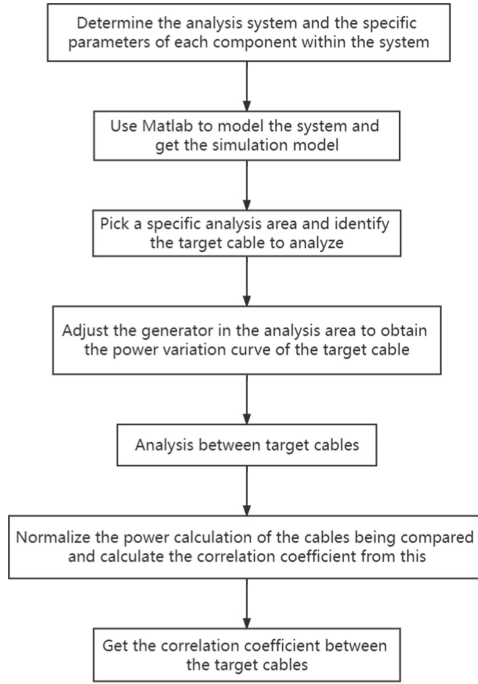
Fig. 3. The flow chart

The specific method for calculating the correlation coefficient in step (6) is as follows:

Step1: Current cable a and cable B are the analysis targets. The power variation arrays of cables A and B are obtained by the above method as follows:

$$S_A = [A_1, A_2, A_3, \cdots, A_n] \tag{6}$$

$$S_B = [B_1, B_2, B_3, \cdots, B_n] \tag{7}$$

The correlation coefficient is mainly reflected by the change trend between the two groups of variables, but the power between the two cables may have a large numerical difference. So that normalization is carried out first [1].

First, calculate the mean and variance of the two groups of power arrays. The specific calculation method is as follows:

$$\mu_A = \frac{\sum_{i=1}^{n} A_i}{n} \tag{8}$$

$$\mu_B = \frac{\sum_{i=1}^{n} B_i}{n} \tag{9}$$

$$\sigma_A = \frac{\sum\limits_{i=1}^{n}(A_i - \mu_A)^2}{n} \qquad (10)$$

$$\sigma_B = \frac{\sum\limits_{i=1}^{n}(B_i - \mu_B)^2}{n} \qquad (11)$$

Then calculate the normalized array. The calculation formula is as follows:

$$[a_1, a_2, a_3, \cdots, a_n] \qquad (12)$$

$$[b_1, b_2, b_3, \cdots, b_n] \qquad (13)$$

$$a_i = \frac{A_i - \mu_A}{\sigma_A}(i = 1, 2, \cdots, n) \qquad (14)$$

$$b_i = \frac{B_i - \mu_B}{\sigma_B}(i = 1, 2, \cdots, n) \qquad (15)$$

Step2: Calculate the correlation coefficient for normalized data. Defining the following series:

$$D = \left[d_1, d_2, d_3, \cdots, d_{n-1}\right] \qquad (16)$$

This array is calculated as follows:

$$d_i = \frac{a_{i+1} - a_i}{b_{i+1} - b_i}(i = 1, 2, \cdots, n - 1) \qquad (17)$$

Each element of the array is the ratio of the variation between the power of cable A and the power of cable B.

Defining the correlation coefficient θ. The calculation formula is as follows:

$$\theta = |\mu_d - 1| \qquad (18)$$

$$\mu_d = \frac{\sum\limits_{i=1}^{n-1} d_i}{n - 1} \qquad (19)$$

Therefore, it can determine that if the ratio of the change value of the power between cable A and cable B is closer to 1, it means that the change trend between them is more similar. So that the value of θ is smaller.

4 Case Study

In this paper, the common 39-node system is used for modeling and simulation verification. The system includes 10 generators, 39 nodes, and many devices such as transmission lines, loads, transformers. Specific steps are as follows:

Step1: Determine the parameters of each component of the system

The specific parameters to be confirmed are as follows:

(1) Type and load of each node. It is necessary to determine whether each node is a type *PQ* node or a type *PU* node, or a balanced node, and the active power and reactive power required by the load carried by each node.
(2) Impedance and admittance of transmission lines.
(3) Rated parameters of generators.
(4) Rated parameters of excitation system.

The specific IEEE39 node system is as shown in the Fig. 4. The symbol G represents the generator, and the symbol Bus represents each node. It have 39 nodes. The connection
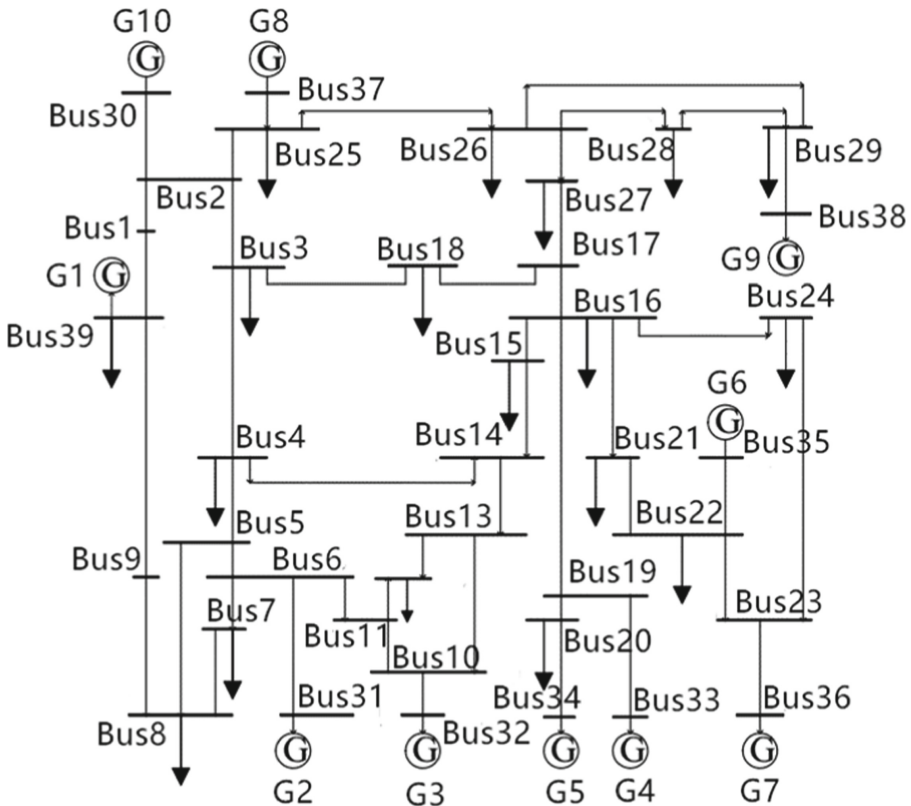
Fig. 4. The specific IEEE39 node system

between the nodes is the power cable. And the arrow represents the load carried by the node [4].

Step2: Build a matlab model for simulation

After establishing the IEEE39 node system and determining the parameters, the model can be built in Matlab, as follows [5] (Fig. 5):
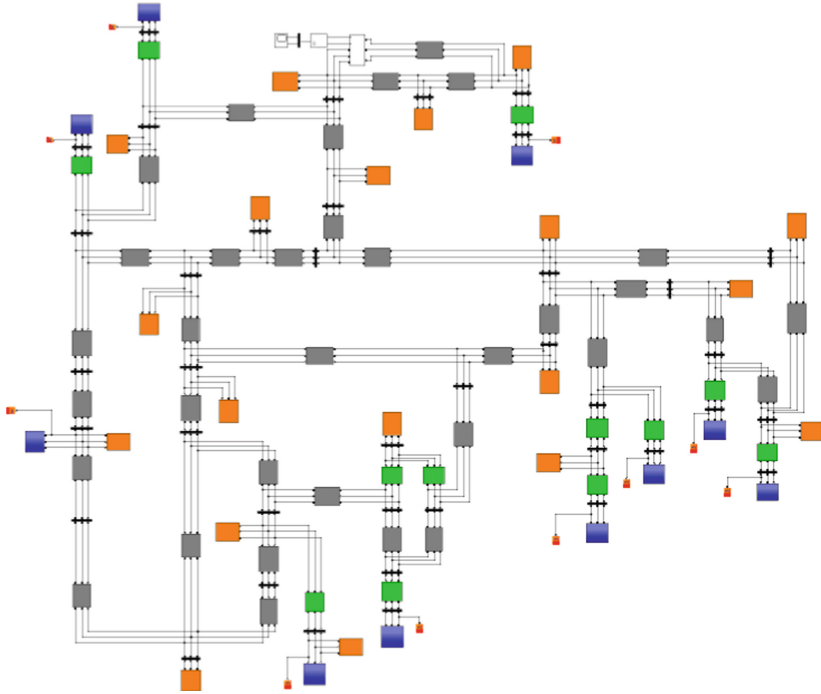
Fig. 5. The simulation model

If each transmission line in the system is observed and analyzed, it will be very complicated due to the large number of transmission lines and variables. Moreover, the correlation is low between cables with long distance.

Therefore, in order to carry out a simple analysis, this paper decides to conduct a separate adjustment analysis on the generator G9. Considering that if too few cables are analyzed, the analysis may not be universal. So that this paper selects 5 cables that are close to the G9 generator for analysis. The 5 cables are: "Line29to26", "Line29to28", "Line28to26", "Line26to27", "Line26to25". They represent: power cables between nodes 29 and 26, power cables between nodes 29 and 28, power cables between nodes 28 and 26, power cables between nodes 26 and 27, power cables between nodes 26 and 25. The details as follows (Fig. 6):
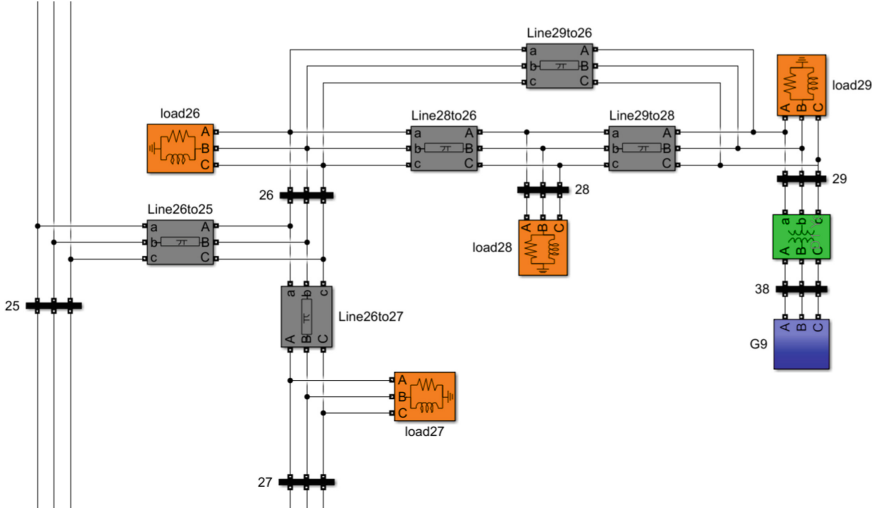
Fig. 6. The model of the target area to be observed

In order to observe the correlation between the five cables, this paper changes the rated voltage of the generator G9 excitation system to observe the variation of the power transmission of each cable under different conditions.

Step3: Change the rated voltage of the generator G9 excitation system for simulation analysis

The per unit voltage of the excitation system of the generator G9 is:

$$U_{G9} = 0.83 \tag{20}$$

So we change its value and observe how the active power and reactive power transmitted by each cable will change under different values.

(1) Increase the value of U_{G9}

Let U_{G9} be the following values respectively:

$$0.83 \times (1 + 0.1) = 0.913 \tag{21}$$

$$0.83 \times (1 + 0.2) = 0.996 \tag{22}$$

$$0.83 \times (1 + 0.3) = 1.079 \tag{23}$$

The value of U_{G9} is increased by 10% each time then the simulation is carried out. And the power change curve transmitted by the five cables is obtained as follows:

The analysis of the results: It can be clearly seen from the Fig. 7 that for the cables "Line29to28", "Line29to26" and "Line28to26", the active power transmitted by them
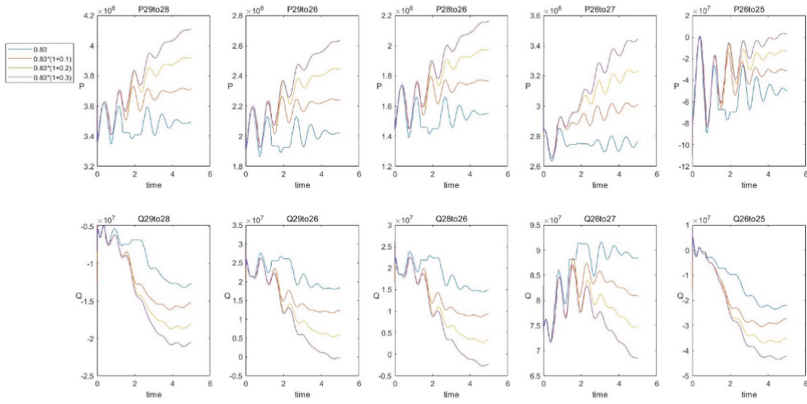
Fig. 7. The variation curve of active power and reactive power

is not exactly the same in value. But the trends of the power they transmit are basically similar. Moreover, with the increase of the value of U_{G9}, the active power transmitted by the three cables all show an increasing trend of change and the trend of variation is still close. Therefore, we can consider these three cables to be highly correlated.

As for the cable "Line26to27", the trend of variation of the power transmitted by them also similar with the aforementioned three cables. And the transmitted active power also increases with the increase of the value of U_{G9}. However, for the cable "Line26to25", the change trend of its transmission power is significantly different from the remaining four cables, so it is not highly correlated with the remaining four cables.

When we observe the active power transmitted by these five cables, we can find that they all have obvious oscillation characteristics in the first 2 s, and gradually become stable after 2 s. If we observe the change curve of the reactive power transmitted, we can see that the cables "Line29to26" and "Line28to26" have strong similarity in value and the trend of variation, so it can be considered that with the highest degree of correlation among the five cables are: "Line29to26" and "Line28to26".

(2) Decrease the value of U_{G9}

Let U_{G9} be the following values, respectively:

$$0.83 \times (1 - 0.1) = 0.747 \tag{24}$$

$$0.83 \times (1 - 0.2) = 0.664 \tag{25}$$

$$0.83 \times (1 - 0.3) = 0.581 \tag{26}$$

The value of U_{G9} is increased by 10% each time then the simulation is carried out. And the power change curve transmitted by the five cables is obtained as follows (Fig. 8):

The analysis of the results: Similarly, observing the change curve of the active power transmitted by the five cables firstly. It can be seen that the active power transmitted by
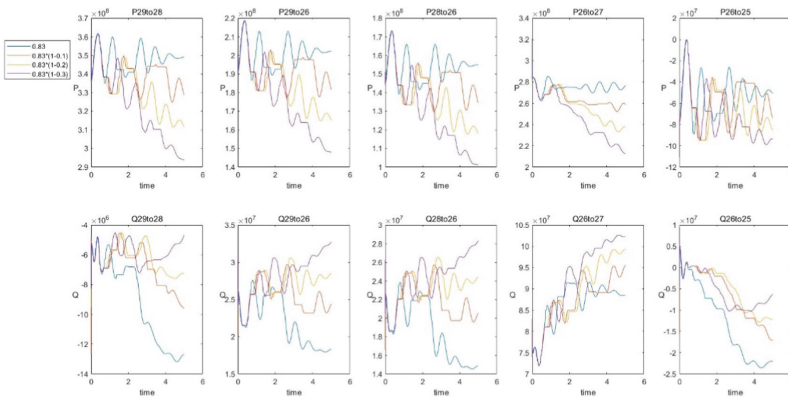
Fig. 8. The variation curve of active power and reactive power

the cables "Line29to28", "Line29to26" and "Line28to26", has a highly similar trend of variation over time. For cables "Line26to27" and "Line26to25", their transmission power trends are not very similar to the rest of the cables. The five cables basically meet the characteristics that the transmitted active power decreases as the value of U_{G9} decreases. Observing the change curve of the reactive power transmitted by the five cables, it can also be found that the cables "Line29to26" and "Line28to26" have a strong correlation in value and trend, so it can be considered that these two cables have the highest similarity.

To sum up, the cables with the highest correlation are "Line29to26" and "Line28to26". And the ones with lower correlation with the other cables are "Line26to27" and "Line26to25".

Step4: Use the correlation analysis method to analyze the correlation coefficient of each cable

The above method of correlation analysis is applied to the data obtained by the simulation. Then the correlation coefficients between the five cables are calculated when considering active power and reactive power. The final results are as follows (Table 1):

Table 1. The correlation coefficient between each cable

	Line29to28	Line29to26	Line28to26	Line26to27	Line26to25
Line29to28	0	0.378	0.154	2.323	12.162
Line29to26	0.378	0	0.038	2.420	11.513
Line28to26	0.154	0.038	0	2.453	11.335
Line26to27	2.3237	2.420	2.453	0	27.240
Line26to25	12.162	11.513	11.335	27.240	0

As can be seen from the results, the correlation coefficient of each cable with itself is 0. The two cables with the strongest correlation are "Line29to26" and "Line28to26".

The two cables with the largest correlation coefficient, that is, the weakest correlation, are "Line26to25" and "Line26to27".

After the correlation between cables is obtained, the operation status of other cables can be quickly judged by the operation status of a certain cable. For example, if the operating state of the cable "Line29to26" is abnormal, it can be quickly determined by the correlation coefficient that "Line28to26" is also in an abnormal operating state with a high probability. Therefore, these two cables can be prioritized for further detection and processing, rather than all the remaining cables being detected and processed out of order.

5 Conclusion

In this paper, a calculation method is proposed, which can be used to calculate the correlation between different cables in the same area. The method can be used to calculate the correlation coefficient between each pair of cables quickly and conveniently. It will be beneficial for operators to grasp the operation status of multiple cables more quickly. The correctness and feasibility of the cable correlation calculation method proposed in this paper are verified by an example.

References

1. Wang, J., Xiong, X., Hu, J., et al.: Safety strategy of power transmission channel coordinated with transfer capability support for power system emergency. Int. J. Electr. Power Energy Syst. **110**, 232–245 (2019)
2. Fan, J., Mao, A., Liu, Y., et al.: Analysis of the short-time overload capability of the transmission section based on the load and ambient temperature curve. Power Syst. Prot. Control **46**(1), 116–121 (2018)
3. Hu, Z., et al.: Fast image recognition of transmission tower based on big data. Prot. Control Mod. Power Syst. **3**(3), 149–158 (2018). https://doi.org/10.1186/s41601-018-0088-y
4. Wu, Y., Li, X., Tang, X., et al.: Dynamic optimization of under-frequency load shedding strategy based on load shedding contribution factor. Smart Power **47**(1), 105–109 (2019)
5. Li, Q., Zhou, W., Tian, Z., et al.: Optimization method of circuit current redistribution in a trench with multiple cable conduits to limit maximum temperature. Elect. Meas. Instrum. **55**(3), 129–136 (2018)

Security and Stability Checking Method of Dispatching Plan Considering Uncertainty of New Energy

Zhou Haifeng[1,2(✉)], Sha Licheng[3], Pan Qi[1,2], Xu Wei[1,2], Li Yinghao[3], Xia Xiaoqin[1,2], and Liu Jiacheng[1,2]

[1] NARI Group Corporation (State Grid Electric Power Research Institute), Nanjing 211106, China
zhouhaifeng@sgepri.sgcc.com.cn

[2] State Key Laboratory of Smart Grid Protection and Control, Nanjing 211106, China

[3] State Grid Beijing Electric Power Company, Beijing 100032, China

Abstract. The uncertainty of new energy power forecasting makes it difficult to implement the dispatching plan. Therefore, a security and stability checking method of the dispatching plan considering the uncertainty of new energy is proposed. The security and stability margin minimization calculation model considering the uncertainty constraints of new energy is established. A high-risk planning situation set that may lead to the abnormal implementation of the planning is generated based on the conservative principle. Based on the high-risk planning situation set, the security and stability of the assessment fault set are evaluated by quantitative analysis method. The security and stability check results and the implementation of the dispatching plan are obtained considering the uncertainty of the new energy power forecasting. The effectiveness of the proposed method is verified by an example of actual power grid.

Keywords: New energy · Uncertainty · Dispatching plans · Security check

1 Introduction

In order to meet the rapid growth of energy demand and the efficient utilization of clean energy, China has made breakthroughs in new energy power generation technology and achieved large-scale application in the past ten years [1]. However, the output of new energy sources such as wind power and photovoltaics show random and uncertain characteristics, which are different from conventional power sources. Large-scale new energy integration brings huge challenges to the power grid dispatching operation and planning [2-4].

Subject to uncertain factors such as climate and weather, the existing new energy power prediction technologies usually cannot provide accurate output power of new energy stations. Certain errors exist in the prediction results. Therefore, the new energy power prediction gives the prediction error band under a certain confidence probability

[5-7]. The security and stability check function of existing dispatch plans in the dispatching control centers at all levels usually does not consider the uncertainty of the new energy power forecasting. They still use the new energy forecasting power curve with the highest occurrence probability for deterministic security and stability check [8-9]. In this way, the conclusion of the security and stability check of the dispatch plan is quite different from the actual situation of power grid, which cannot effectively guide the actual power grid dispatching operation. Therefore, taking the uncertainty of new energy power prediction into account in the security and stability check of the dispatch plan is an urgent problem to be solved during the dispatch plan making process.

For the security and stability check method of the dispatch plan considering the uncertainty of new energy, the existing researches mainly include the probabilistic power flow method [10-12], the scenario analysis method [13-16] and the confidence interval method [16-18]. The probabilistic power flow method describes the uncertain variables through the probability model. This method uses the probability analysis method to obtain the probabilistic distribution results of the power flow output, which is mainly used in the static security check of the dispatch plan. The scenario analysis method generates a series of operating scenarios by sampling and combining uncertain variables, and uses multiple possible deterministic operating scenarios to characterize the uncertain variables. However, too many scenario combinations lead to lower computational efficiency. Although the amount of computation can be reduced through scenario clustering and reduction techniques, it also brings the risk of scenario leakage. The confidence interval method determines the upper and lower boundaries of uncertain variables based on a certain confidence level. This method generates large and small operation situation of power system for security check, which greatly reduces the operation situation that require security check. However, this method has the problem that the calculation results are too conservative.

Considering the shortcomings of the existing methods, a security and stability check method of the dispatching plan considering the uncertainty of new energy is proposed. The probability distribution of the prediction error of new energy power is obtained based on the statistical analysis of historical data. The security and stability margin minimization model considering the uncertainty constraints of the new energy power prediction is established. A high-risk planning situation set that may lead to the abnormal implementation of the dispatching plan is generated. Based on the high-risk planning situation set, the security and stability of the assessment fault set are evaluated by quantitative analysis method. The security and stability check and evaluation results of the dispatching plan considering the uncertainty of new energy are obtained.

2   Fundamental Principle

The security and stability check of the dispatching plan is used to determine whether there are high-risk periods that do not meet the security and stability requirements of power grid and the distribution of high-risk periods. Therefore, the key to the security and stability check of the dispatching plan considering the uncertainty of new energy lies in how to efficiently and accurately identify the high-risk planning situation that may lead to the abnormal implementation of the dispatching plan, and realize the rapid

check of the high-risk planning situation set and the evaluation of the implementation of the dispatching plan.

2.1 Identification of High-Risk Planning Situation

The confidence interval of new energy power prediction and its influence factors on the security and stability of the power grid can be obtained. Therefore, a large number of to-be-checked planning situation can be generated to describe the uncertainty of the new energy power forecast through power flow adjustment. Among them, most of the planning situation to be checked are not high-risk planning situation that make it difficult to implement the scheduling schedule. Instead, they are prone to the waste of a large number of computing resources and the annihilation of key information. Therefore, how to identify the high-risk planning situation that may lead to the abnormal implementation of the dispatching plan from a large number of planning situation to be checked is the key to the security and stability check of the dispatching plan considering the uncertainty of new energy.

The security and stability characteristics of the power grid are closely related to the operating state of the power grid. Therefore, the switching state of the power grid equipment and the power injection of the nodes determine the operating state of the power grid. Based on the deterministic planning data and the new energy forecast data with the highest occurrence probability, the deterministic reference planning situation required for the traditional security and stability check can be generated. The difference between the plan to be checked considering the uncertainty of new energy and the deterministic reference plan is that the predicted power of new energy stations is different. If the difference between the planning situation to be checked and the reference planning situation is not large, the security and stability assessment results of the plan to be checked can be quickly estimated according to the security and stability check results of the reference plan, the change degree of the operation situation of the two power grids and the relevant security and stability quantitative indicators [19]. The estimation formula is as follows:

$$\eta_l' = \eta_l - \alpha \sum (\lambda_{l,i} \Delta P_i) \tag{1}$$

where, η_l' is the safety and stability margin of the planning situation to be checked, η_l is the safety and stability margin of the reference planning situation, $\lambda_{l,i}$ is the influence factor of the active power change of the new energy station on the safety and stability margin, ΔP_i is the per-unit value of the change in the active power output of the new energy station, α is a parameter that considers the complexity and nonlinearity of the safety and stability problem, and is used to improve the reliability of the safety and stability margin estimation under complicated operating conditions.

The difference between the planning situation to be checked considering the uncertainty of new energy and the deterministic reference planning situation is that the predicted power of new energy stations is different. Therefore, a security and stability margin minimization model considering the constraints of the new energy power prediction error can be constructed based on the security and stability quantitative index of the reference

planning situation. According to the conservatism principle, the plan to be checked corresponding to the minimum value of the security and stability margin can be found within the confidence interval of the new energy power prediction. It can be used as a high-risk planning situation that may lead to the abnormal implementation of the dispatching plan.

2.2   Check of High-Risk Planning Situation

The security and stability check of the dispatching plan needs to check the planning situation of multiple periods in the future. Therefore, even if only one high-risk planning situation is considered for each period, the calculation amount is still very considerable. In this way, it is particularly important to improve the computational efficiency of the security and stability check of the dispatch plan considering the uncertainty of new energy sources. In addition, the security and stability issues of power system is complex and nonlinear. There may be a certain deviation between the estimated value of security and stability margin based on the minimum model of security and stability margin and the actual value during the identification process of high-risk planning situation, and even subversive qualitative conclusions in critical cases. Therefore, for the high-risk period when the estimated value of the security and stability margin is far from the critical value, the estimation result obtained in the identification process of the high-risk planning situation can be directly used as the result of the security and stability check, so as to improve the calculation efficiency of the security and stability check of the dispatch plan. First of all, for the high-risk period of critical safety, the method of literature [20] is used to integrate and generate high-risk planning situation data based on the new energy active power plan and other deterministic plan data. Then, the cluster computing capacity of the parallel computing platform is used to form a scheduling queue. Finally, the method of literature [21] is used to conduct multi-situation grouping parallel security check. The security and stability check results of critical safety high-risk period are obtained, so as to improve the reliability and accuracy of the security and stability check conclusion.

2.3   Evaluation of the Feasibility of Dispatching Plan

In order to measure the distribution of the risk period of the dispatch plan, after the security and stability check of all high-risk planning situation is completed, the risk index of the dispatch plan can be obtained according to whether the plan can be implemented in each period. The calculation formula is as follows:

$$R = \frac{\sum_{i=1}^{N} r_i}{N} \tag{2}$$

where, R is the risk degree of the index for evaluating the high-risk period of the dispatching plan, r_i is the scalar of whether the scheduling of period i can be implemented, which can be implemented as 1, can not be implemented as 0, and N is the total number of periods.

3 Margin Minimization Model

Based on the security and stability quantitative analysis method, the security and stability quantitative indicators such as the overload margin of each assessment fault in the reference planning situation, the overload safety weak branch, and the sensitivity of the active power of the new energy station to the active power of the overload safety weak branch can be obtained. The new energy power prediction error range in the actual system is generally not large. The overload safety weak branch and active power sensitivity of the to-be-checked planning situation and the reference planning situation are basically the same. Therefore, the security and stability margin minimization model considering the confidence interval constraints of new energy power prediction can be constructed based on the security and stability quantitative index of reference planning.

3.1 Objective Function

The objective function of the security and stability margin minimization model set in this paper is as follows:

$$\min\left(\eta_{k.l} - \frac{\alpha}{P_{lmt.l}} \sum_{i=1}^{N} \left(\lambda_{k.l.i}\left(P_i' - P_i\right)\right)\right) \tag{3}$$

where: $\eta_{k.l}$ is the overload safety margin of the overload safety weak branch l of the assessment fault k under the evaluation of the reference plan, α is the parameter reflecting the influence of the change of the active power of the new energy station on the overload safety margin, $P_{lmt.l}$ is the active power limit of the overload safety weak branch l, N is the number of new energy stations, $\lambda_{k.l.i}$ is the sensitivity of the active power of the new energy station i to the active power of the overload safety weak branch l under the reference planning situation, P_i' is the active power of new energy station i under the planning situation to be checked, and P_i is the active power of new energy station i under the reference planning situation.

3.2 Constraints

The constraints of the safety and stability margin minimization model set in this paper include:

1) Spatial inequality constraint

$$P_{i.\min} \le P_i' \le P_{i.\max} \tag{4}$$

where, $P_{i.\max}$ and $P_{i.\min}$ are the maximum and minimum values of the active power output of the ith new energy station, respectively.

2) Confidence interval inequality constraint

$$P_{i.\min}' \le P_i' \le P_{i.\max}' \tag{5}$$

where, $P_{i.\max}'$ and $P_{i.\min}'$ are the upper and lower limits of the confidence interval for the active power output of the ith new energy station, respectively.

3) Power balance equation constraint

$$\sum_{u=1}^{U} \left(P'_u - P_u\right) + \sum_{d=1}^{D} \left(P'_d - P_d\right) = 0 \tag{6}$$

where, U is the number of new energy stations with increased output, D is the number of new energy stations with reduced output, P'_u is the active power of the uth new energy station with increased output under the planning situation to be checked, P'_d is the active power of the dth new energy station with reduced output under the planning situation to be checked, P_u is the active power of the uth new energy station with increased output under the reference planning situation, P_d is the active power of the dth new energy station with reduced output under the reference planning situation.

3.3 Solution Method

The new energy stations with low active power sensitivity have little influence on the overload safety of the equipment under fault assessment. The uncertainty of some new energy stations with low active power sensitivity can be ignored. The new energy stations with similar active power sensitivity can be merged to effectively reduce the dimension of uncertainty variables. In this way, the solving efficiency of the security and stability margin minimization model can be improved. According to formula (7), the active power sensitivity of the new energy station is per unit, and the per-unit value of the active sensitivity of each new energy station can be obtained.

$$\lambda'_{k.l.i} = \frac{\lambda_{k.l.i}}{\max(|\lambda_{k.l.i}|, k \in N)} \tag{7}$$

where, $\lambda'_{k.l.i}$ is the per-unit value of the sensitivity of the active power of the new energy station i to the active power of the overload safety weak branch l in the reference planning situation.

Based on the active power sensitivity of new energy power stations after per unit, the new energy power stations whose absolute value of active power sensitivity is less than the specified threshold value are excluded. The associated new energy power station set G of each assessment fault can be obtained. Sort the associated new energy power station sets from large to small according to the active power sensitivity, and combine the new energy power stations that satisfy formula (8) to obtain the aggregated associated equivalent new energy power station set G'.

$$\left|\lambda'_{k.l.i} - \lambda'_{k.l.j}\right| < \varepsilon, \ i, j \in G' \tag{8}$$

where, $\lambda'_{k.l.i}$ and $\lambda'_{k.l.j}$ are the per-unit values of the sensitivity of the active power of the new energy station i and the new energy station j to the active power of the overload safety weak branch l of the assessment fault k under the reference planning situation, and ε is the active sensitivity grading interval greater than 0.

For the active power sensitivity of the equivalent new energy station, the average value of the active power sensitivity of the associated new energy station can be taken. For

the confidence interval of the equivalent new energy station, the power prediction error confidence interval of the equivalent new energy station can be obtained by analyzing the massive historical data of the power grid and counting the distribution relationship of the prediction error. The predicted power of the new energy station and the error confidence interval can be superimposed to obtain the predicted power confidence interval of the new energy station. The security and stability margin minimization model is established. The overload safety margin of all overload safety weak branches of each assessment fault and active power output of the corresponding equivalent new energy station can be obtained. Active power output of the equivalent new energy station is decomposed into the corresponding new energy station according to the adjustable space of the new energy station.

If the safety and stability margin minimization model is established for all the overload safety weak branches of the assessment fault set, the calculation amount will be very large. The calculation task of the security and stability margin minimization model of all overload safety weak branches in the assessment fault set can be distributed to the calculation cluster, so as to further improve the calculation efficiency. The grouping parallel method is used to calculate the overload safety margin of all overload safety weak branches in the assessment fault set and their corresponding active power output of new energy stations. The active power output of the new energy station corresponding to the minimum overload safety margin is selected as the new energy active power plan corresponding to the high-risk planning situation.

4   Design of Security Check Process

The security and stability check steps of the dispatching plan considering the uncertainty of new energy are as follows:

(1)   Based on the new energy power forecast data with the highest probability of occurrence, conventional unit power generation plan, load forecast, tie line plan, and shutdown and rehabilitation plan, a deterministic reference plan is generated;

(2)   Based on the reference planning situation, the security and stability quantitative assessment is carried out on the assessment fault set, and the security and stability quantitative assessment results under the reference planning situation are obtained;

(3)   Build a security and stability margin minimization model that takes into account the uncertainty constraints of new energy power prediction, and solve the new energy active power plan corresponding to the minimum security and stability margin;

(4)   Based on the new energy active power plan data, combined with the conventional unit generation plan, load forecast, tie line plan, and shutdown and rehabilitation plan, a high-risk plan to be checked is generated;

(5)   Based on the high-risk planning situation set, the security and stability of the assessment fault set are quantitatively evaluated, and the security and stability check and evaluation results of the dispatching plan considering the uncertainty of new energy are obtained (Fig. 1).
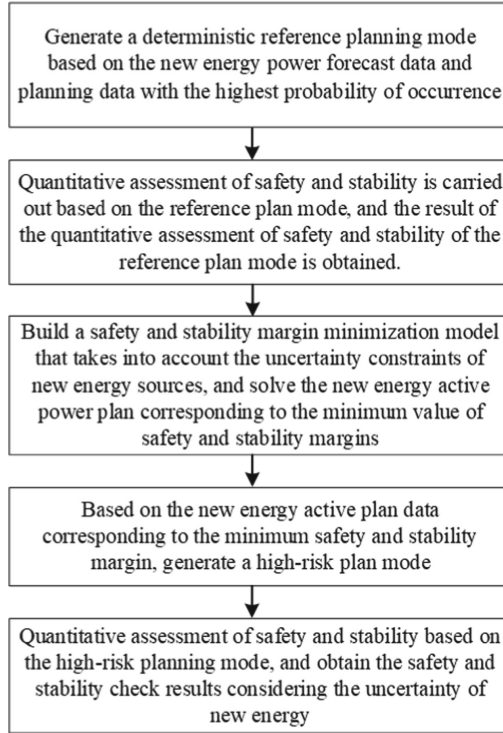
Fig. 1. Schematic diagram of security check process

5 Example

The security and stability checking method of dispatching plan proposed in this paper has been applied to the security and stability checking system of day ahead plan of a regional power grid with large-scale new energy. Taking a day-ahead plan data in March 2022 as an example, the local network diagram of the power grid is shown in Fig. 2.

5.1 Dispatching Plan Check

A 96-point day-ahead reference plan is generated based on the integration of new energy active power forecast, conventional unit generation plan, load forecast, tie line plan, and decommissioning and recommissioning plan. There are 331 contingencies in the assessment fault set for the day-ahead security check, and there are 735 branches in the equipment overload monitoring element set. The equipment overload safety assessment is carried out for the assessed fault based on the 96-point day-ahead reference plan. The fault with the minimum equipment overload safety margin is double-line N-2 fault from N4 to N6. The equipment with weak equipment overload safety at some planned times under the contingency is shown in Table 1.

Assuming that the binning interval ε of the active power sensitivity per unit value of new energy stations is 0.01. Based on the active power sensitivity of reference planning
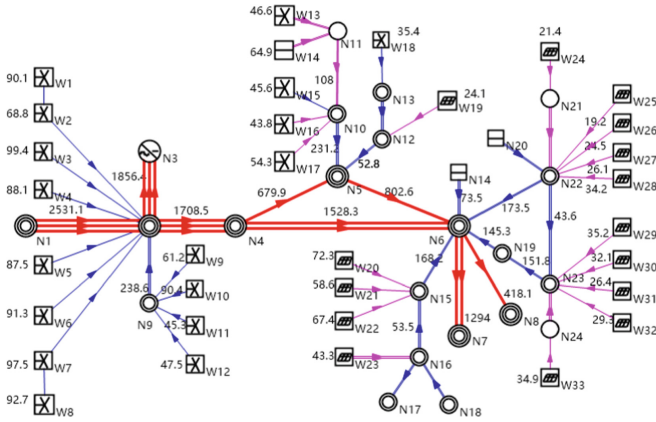
Fig. 2. Schematic diagram of the local network of a regional power grid

Table 1. Equipment overload safety weak equipment

Section time	Monitoring element	Margin
10:30	N4-N5	10.35
	N5-N6	3.41
13:30	N4-N5	32.12
	N5-N6	24.34
22:30	N4-N5	45.08
	N5-N6	34.17

situation and historical data, the station aggregation and probability statistics of the new energy station can be obtained, and the aggregation results of equivalent new energy stations are shown in Table 2.

Table 2. Active sensitivity calculation results

Group number	Equivalent new energy station	Average sensitivity	Confidence interval
1	W1 ~ W8	0.585	0.481
2	W9 ~ W12	0.521	0.428
3	W13 ~ W19	−0.158	0.832
4	W20 ~ W23	−0.083	−0.084
5	W24 ~ W33	−0.038	−0.042

According to formula (3) and formula (6), the margin minimization model of equipment with weak overload safety is established. The minimum estimated margin of equipment with weak overload safety under double-line N-2 fault from N4 to N6 and its corresponding new energy active power plan can be obtained, as shown in Table 3 and Table 4.

Table 3. Overload safety margin estimation results

Section time	Monitoring element	Minimum margin
10:30	N4-N5	10.33
	N5-N6	3.39
13:30	N4-N5	32.10
	N5-N6	24.32
22:30	N4-N5	45.06
	N5-N6	34.15

Table 4. The minimum margin at 10:15 corresponds to the new energy active power plan

Group number	New energy station	Active plan value
1	W1 ~ W8	751.17
2	W9 ~ W12	256.62
3	W13 ~ W19	330.44
4	W20 ~ W23	229.52
5	W24 ~ W33	269.04

For the planned period when the minimum margin is far from the critical value (such as 13:30 and 22:30 in Table 3), the estimation result is directly used as its security and stability check result. For the planned period where the minimum estimated value of margin is close to the critical value (such as 10:30 in Table 3), the high-risk planning situation is generated based on the new energy active plan shown in Table 4 and integrated with the conventional unit generation plan, load forecast, tie line plan and decommissioning and recommissioning plan. The parallel computing cluster is used to perform security check on the critical state planning situation. The calculation results are shown in Table 5.

5.2 Risk Leakage Analysis

For the planned time of 10:30, the scenario method is used to check the security and stability. The equivalent aggregation and confidence interval of new energy stations are

Table 5. Check results of high-risk planning situation

Section time	Monitoring element	Margin	Calculation method
10:30	N4-N5	10.42	Detailed calculation
	N5-N6	3.45	
13:30	N4-N5	32.10	Quick estimate
	N5-N6	24.32	
22:30	N4-N5	45.06	Quick estimate
	N5-N6	34.15	

consistent with the method in this paper. Multi-dimensional discretization sampling is carried out for equivalent new energy stations, and 13284 scenarios can be obtained. Further, the safety assessment results of equipment overload under different numbers of clusters can be obtained as shown in the Table 6.

Table 6. Scenario check result

Number of clusters	Monitoring element	Margin
15	N4-N5	10.45
	N5-N6	3.41
10	N4-N5	11.32
	N5-N6	3.54
5	N4-N5	13.23
	N5-N6	5.04

It can be seen that when the number of clusters changes greatly, the deviation of the equipment overload safety margin obtained by the scenario method is larger. When there is less clustering data, the scenario method may have risk leakage. However, the method proposed in this paper does not have this problem.

5.3   Computational Performance Analysis

A total of 40 servers are configured in the parallel computing cluster, each server has 4 CPUs, 16 cores. The main frequency is 2.27 GHz, the operating system is Rocky4.2, and the calculation program is written in Fortran and C++ languages.

The parallel computing capacity of situation is 4, and the parallel computing capacity of tasks is 640. The maximum time for establishing the overload margin minimization model of a single situation and a single fault is about 0.2 s. The maximum time for overload safety assessment of a single situation and single fault equipment is about

0.8 s. The proportion of high-risk planning situation of critical safety is 10%. Aiming at 96-point planned times and 331 contingencies in the day-ahead plan, the minimum model calculation of equipment overload margin can be completed through 24 iterations. The detailed equipment overload evaluation calculation can be completed through 3 iterations. Considering the time-consuming of parallel platform information interaction, the method proposed in this paper takes about 10 min.

Under the same computing resources, the scenario method is used to check the security and stability of the same plan data. Assuming that the average number of scenario clustering data under a single fault is no more than 20, the maximum time for overload safety assessment of a single fault equipment is about 0.8s. The detailed equipment overload assessment calculation can be completed through 480 iterations for 96-point planned times and 331 contingencies in the day-ahead plan. Further, the scenario method takes about 30 min considering the time-consuming of scenario clustering and parallel platform information interaction. It can be seen that, the method proposed in this paper has great advantages in computing performance and can meet the requirements of online applications.

6   Conclusion

This paper proposes a security and stability check method of dispatching plan considering uncertainty of new energy. The conclusions are as follows:

(1) The security and stability margin minimization calculation model considering the uncertainty constraints of new energy is established. The security and stability check results and the implementation of the dispatching plan are obtained considering the uncertainty of new energy. This method greatly reduces operation situation that require security check and effectively reduces the risk leakage;

(2) The dimension of uncertain variables is effectively reduced through aggregation of new energy stations. The security and stability margin minimization model and security and stability evaluation are carried out by using large-scale cluster parallel computing platform. Above all, the performance requirements of security and stability check of dispatching plan can be meet.

References

1. Guoping, C., Yu, D., Zhifeng, L.: Analysis and reflection on high-quality development of new energy with chinese characteristics in energy transition. Proceedings of the CSEE **40**(17), 5493–5505 (2020)
2. Yusheng, X., Xing, L., Feng, X., et al.: A review on impacts of wind power uncertainties on power systems. Proceedings of the CSEE **34**(29), 5029–5040 (2014)

3. Zhigang, L., Wenchuan, W., Mohammad, S., et al.: Adaptive robust tie-line scheduling considering wind power uncertainty for interconnected power systems. IEEE Trans. Power Syst. **31**(4), 2701–2713 (2015)

4. Mohannad, A., Payman, D., Shiyuan, W., et al.: Power grid optimal topology control considering correlations of system uncertainties. IEEE Trans. Ind. Appl. **55**(6), 5594–5604 (2019)

5. Weisheng, W., Zheng, W., Cun, D., et al.: Status and error analysis of short-term forecasting technology of wind power in China. Automation of Electric Power Systems **45**(1), 17–27 (2021)

6. Zuoxia, X., Boyang, Q., Yang, L., et al.: Comparative study of reformed neural network based short-term wind power forecasting models. IET Renew. Power Gener. **16**(5), 885–899 (2022)

7. Rosemary, T., Jethro, B.: A review of very short-term wind and solar power forecasting. Renew. Sustain. Energy Rev. **153**(10), 43–58 (2022)

8. Xiaoyuan, X., Han, W., Zheng, Y., et al.: Overview of power system uncertainty and its solutions under energy transition. Automation of Electric Power Syst. **45**(16), 2–13 (2021)

9. Yi, L., Zhi, C., Guofang, Z., et al.: Implementation scheme of security check in provincial power grid suitable for operation of electricity spot market. Automation of Electric Power Syst. **45**(16), 216–223 (2021)

10. Junxiao, C., Ji, L., Renjie, Y., Ting, G.: Static security verification method of active distribution network based on probabilistic load flow. ZheJiang Electric Power **39**(07), 36–41 (2020)

11. Chi, Z., Hongbo, L., Zewei, F.: Security verification method of distribution network considering the uncertainties of distributed generations. Proceedings of the CSU-EPSA **28**(S1), 51–55 (2016)

12. Dawei, W., Kedi, Z., Qixin, C., et al.: A data-driven probabilistic power flow method based on convolutional neural networks. Int. Trans. Electrical Energy Syst. **30**(7), 1–20 (2020)

13. Bin, B., Mingliang, H., Jiang, L., et al.: Scenario reduction method of new energy including wind power and photovoltaic. Power System Protection and Control **49**(15), 141–149 (2021)

14. Jingxian, Y., et al.: An uncertain hydro/PV/load typical scenarios generation method based on deep embedding for clustering. Proceedings of the CSEE **40**(22), 7296–7305 (2020)

15. Xiaocong, Z., Wenda, Z., Ruoying, Y., et al.: Assessment of renewable energy accommodation capability based on typical scenario construction. In: 2019 IEEE 9th Annual International Conference on CYBER Technology in Automation, Control, and Intelligent Systems (CYBER). pp 459–462. IEEE, Suzhou, China (2019)

16. Shuqiang, Z., Tianran, J., Zhiwei, L., et al.: Wind power scenario generation for multiple wind farms considering temporal and spatial correlations. Power System Technol. **43**(11), 3997–4004 (2019)

17. Shouxiang, W., Qun, X., Gaolei, Z., et al.: Modeling of wind speed uncertainty and interval power flow analysis for wind farms. Automation of Electric Power Syst. **33**(21), 82–86 (2009)

18. Tao, D., Rui, B., Fangxing, L., et al.: Interval power flow analysis using linear relaxation and optimality-based bounds tightening (OBBT) methods. IEEE Trans. Power Syst. **30**(1), 177–188 (2014)

19. Taishan, X., Yanling, D., Yanhong, B., et al.: A classification rolling contingency screening method for on-line transient security and stability assessment. Automation of Electric Power Syst. **42**(13), 182–188 (2018)

20. Haifeng, Z., Wei, X., Yanhong, B., et al.: Power flow data generation of security check for dispatching plans based on similar day selection. Power System Protection and Control **43**(18), 87–93 (2015)

21. Shengming, W., Taishan, X., Jian, G., et al.: Multi-scheme concurrent security check of dispatching schedule. Southern Power System Technol. **11**(05), 56–62 (2017)

Identification of Redundant Security Constraints in Robust SCUC Problems

Qia Ding[1], Zizhuo Wang[2], Meng Zheng[2(✉)], Yantao Zhang[1], and Chunling Lu[1]

[1] NARI Group Corporation (State Grid Electric Power Research Institute), Nanjing 211106, China

[2] Cardinal Operations (Beijing) Co., Ltd., Beijing 100010, China

streamzheng@163.com

Abstract. Security-constrained unit commitment (SCUC) is a fundamental problem in power systems and electricity markets. However, SCUC could be hard to solve due to the highly complicated security constraints which often result in numerical difficulties. In this paper, we develop an efficient method to identify the redundant security constraints as a preprocessing procedure. Different from the conventional redundancy detection methods which treat problem parameters as fixed, our proposed method considers the uncertainty of the GSDF parameters leveraging the theory of robust optimization. In principle, our detection procedure aims to locate the security constraints which remain redundant even if the parameters might be inaccurate and thus reinforces the robustness compared to the conventional methods. To enhance efficiency, we further show that under mild conditions a simple greedy method is sufficient to identify redundancy even in the presence of uncertainty. Numerical results on the IEEE 118-node test system verify the validity and robustness of our method.

Keywords: Security-constrained unit commitment · Redundant constraints · Constraint reduction method · Robust optimization · Mixed-integer linear programming

1 Introduction

The unit commitment (UC) problem is one of the essential daily tasks an independent system operator (ISO) or regional transmission organization (RTO) must accomplish to clear a daily electric power market [1]. In practice, we also need to incorporate security constraints into the UC model to ensure the robustness of the decisions. Therefore, the resulting Security Constrained Unit Commitment (SCUC) problem is significant in power system optimal dispatching [2]. The objective of SCUC is to minimize the system operating cost while satisfying unit and system constraints, such as power balance, system spinning and operating reserve requirements, minimum on/off time limits, ramping up/down limits, limits on state and control variables including real and reactive power generation, controlled voltages, settings of tap-changing and phase-shifting transformers, and so on. Typically, SCUC is a nonlinear large-scale mixed-integer optimization

problem with massive binary variables and constraints, and various techniques have been successfully applied to solve this problem. Among the successful attempts, one major line of research approximates SCUC using mixed-integer linear programming (MILP). It adopts mathematical programming techniques such as Lagrangian relaxation (LR) [3, 4], Benders' decomposition (BD) [5, 6], and branch and cut (BC) [7, 8]. Besides the above mathematical programming techniques, another line focuses on meta-heuristics [9, 10], which efficiently generate high-quality approximate solutions. For a comprehensive survey on the heuristics designed for SCUC, we refer the readers to [11]. Although efficient methods have been developed, in practice, SCUC remains challenging as the number of security constraints becomes large, and the numerical conditioning worsens [12]. As a result, SCUC problems are generally much more complicated than the UC or generation scheduling problems which do not consider the security constraints.

In addition to the large size of the problem, there are various uncertain factors when managing the operational security of the power systems. Two distinct approaches have been studied to address the impact of uncertainties arising from the power system operations: the scenario-based approach [13] and the interval-based approach [14, 15]. Recently, a new robust approach has received significant attention. In the robust optimization approach, one seeks commitment and dispatch, which are immunized against all possible uncertain situations. For example, [16] proposed a two-stage adaptive robust SCUC model. The first stage determines the robust UC solution concerning all possible net injections, and the second handles the worst-case dispatch. The authors of [17] applied a robust UC model to the wind and pumped-storage coordination problem. The model in [18] and [19] are designed to minimize a combination of commitment cost, the weighted expected generation cost, and the worst-case violation cost.

While most of the robust optimization based SCUC models in the literature focus on the uncertainty arising from the dispatch cost or generator actions, this paper instead focuses on the uncertainty of the security constraints and considers the uncertainty of the parameter Generator Shift Distribution Factor (GSDF). The GSDF, also known as the K-factor, is a measure of sensitivity for the power flow in a particular line concerning any change in the current injected at the generator buses of the system [20]. To the best of our knowledge, we are the first to consider the robust constraint-reduction method for the SCUC problem where the GSDF lies in a ball uncertainty set. The main contribution of this paper is to provide a fast approach to the reduction procedure.

As discussed earlier, the SCUC problem is often computationally challenging due to its large size and incorporating robustness may further add to the challenge. To address this difficulty, we note that most security constraints are inactive or redundant in operation and do not affect the feasible domain. If these inactive or redundant security constraints can be identified and eliminated, it is possible to simplify the problems significantly. Here we briefly review the four kinds of constraint-reduction methods that are commonly used in the literature.

The first method is based on the contingency filtering technique. In this method, a severity index is defined according to an empirical formula and is proposed to depict the severity of the influence of the contingency state on the system [21]. The less important contingency state is removed by ranking the severity index to reduce the scale of the problem. However, the experience-based sorting methods may be inaccurate and remove

active fault state constraints. The second method finds all the active constraints through a simple iterative process. The main idea is to extract an easy-solved subproblem from the original problem. The violated constraints are added step by step according to the results and solved iteratively until all the constraints are satisfied [22]. The iterative method is generally used to consider the contingency state of the SCUC problem. Note the iteration steps may be huge when the scale of the SCUC is large. The third method explores the relation between the power flow security constraints in the SCUC problem. The method based on the power flow relation is efficient in time but is restricted to certain types of power flow. For example, [23] can only reduce parallel branches' security constraints instead of non-parallel branch units. The fourth method builds an auxiliary optimization problem that is easy to solve based on the original problem [24, 25]. In this method, actual redundant constraints are identified but the scale of the auxiliary optimization problem could also be huge, and the computational complexity may be similar to the original SCUC model.

In this paper, we develop an efficient method to identify the redundant security constraints as a preprocessing procedure. Different from the conventional redundancy detection methods where parameters are fixed, our proposed method considers the inaccuracy of the GSDF parameters and builds a robust optimization model. Our experiments on the IEEE118 node test system justify the effect of our approach. Compared to the conventional constraint-reduction methods, our method guarantees the security of the SCUC problem in the presence of parameter uncertainty. It can help the operator make safe and economic unit operation decisions quickly.

The rest of this paper is organized as follows. Section 2 provides the mathematical model of SCUC and extends it to consider the uncertainty of the GSDF parameter. Section 3 presents the fast SCUC solution procedure. Numerical testing results are given and analyzed in Sect. 4. We conclude the paper in Sect. 5.

2 SCUC Model with Uncertainty

We first briefly review the MILP formulation of the SCUC problem. We consider an operator who makes power generation decisions in a T-period time horizon. There are N units indexed by i, M load buses indexed by j, L transmission lines indexed by l, T periods indexed by t. In the SCUC problem, the operator aims to minimize the total power system operation costs, which are defined as the sum of (i) energy production cost, (ii) startup cost, and (iii) shutdown cost over the entire scheduling horizon. The objective function can be written as follows:

$$\min \sum_{i=1}^{N} \sum_{t=1}^{T} \sum_{k=1}^{K} c_{i,k} P_{i,k,t} + \sum_{i=1}^{N} \sum_{t=1}^{T} (SU_i u_{i,t} + SD_i v_{i,t}), \tag{1}$$

where $c_{i,k}$ is the incremental cost of segment k of unit i [\$/MWh].

The main decision variables of the operators include positive and continuous variables and binary variables:

- $P_{i,k,t}$: power generation of segment k of unit i at period t [MW],

- $r_{i,t}$: spinning reserve provided by unit i at period t [MW],
- $u_{i,t}$: startup status of unit i at period t, which takes value of 1 if the unit starts up at period t and 0 otherwise,
- $v_{i,t}$: shutdown status of unit i at period t, which takes value of 1 if the unit shuts down at period t and 0 otherwise,
- $y_{i,t}$: commitment status of unit i at period t, which is equal to 1 if the unit is online and 0 offline.

In addition, we have the following parameters in this problem:

- SU_i: start-up cost of unit i [$],
- SD_i: shut-down cost of unit i [$],
- $D_{j,t}$: net load demand of bus j at period t [MW],
- D_t: system load demand at period t [MW],
- $T_i^{i,\text{min}u}$: min-up time for unit i [h],
- $T_i^{i,\text{min}d}$: min-down time for unit i [h],
- Ru_i: ramp-up rate for unit i [MW/h],
- Rd_i: ramp-down rate for unit i [MW/h],
- $\overline{Ru_i}$: startup ramp rate for unit i [MW/h],
- $\overline{Rd_i}$: shutdown ramp rate for unit i [MW/h],
- $P_i^{\min}$: minimum capacity of unit i [MW],
- $P_i^{\max}$: maximum capacity of unit i [MW],
- R_t: spinning reserve requirement at period t [MW],
- $F_l^{\max}$: transmission line limit of line l [MW],
- A^U: $L \times N$ matrix relating unit generations to power flows on transmission lines
- $a_{l,i}$: (l, i)-th component of A^U, denoting the Generator Shift Distribution Factor (GSDF) of unit i toward branch l,
- B^D: $L \times M$ matrix relating bus loads to power flows on transmission lines,
- $b_{l,j}$: (l, j)-th component of B^D.

In the SCUC problem, there are many constraints to be considered, including:

1) *Power System Requirements:* the constraints guarantee the balance between generation and load and the provision of spinning reserve:

$$\sum_{i=1}^{N} P_{i,t} = \sum_{j=1}^{M} D_{j,t} = D_t, \quad \forall t,$$
$$\sum_{i=1}^{N} r_{i,t} \geq R_t, \qquad \forall t. \tag{2}$$

2) *Minimum Up* and *Downtime:* the minimum number of periods that the unit must be online and offline are ensured with:

$$\left(y_{i,t} - y_{i,t-1}\right)T_i^{T,\text{min}u} + \sum_{a=t-T_i^{T,\text{min}u}}^{t-1} y_{i,a} \geq 0, \qquad \forall i, \forall t,$$
$$\left(y_{i,t-1} - y_{i,t}\right)T_i^{T,\text{min}d} + \sum_{a=t-T_i^{T,\text{min}d}}^{t-1} \left(1 - y_{i,a}\right) \geq 0, \quad \forall i, \forall t. \tag{3}$$

3) *Logical Constraint:* the constraints ensure that $u_{i,t}$ and $v_{i,t}$ take the appropriate values when the unit i starts up or shuts down.

$$
\begin{aligned}
u_{i,t} + v_{i,t} &\le 1, & \forall i, \forall t, \\
y_{i,t} - y_{i,t-1} &= u_{i,t} - v_{i,t}, & \forall i, \forall t, \\
u_{i,t}, v_{i,t}, y_{i,t} &\in \{0,1\}, & \forall i, \forall t.
\end{aligned}
\tag{4}
$$

4) *Generation Limits:* the generation limits over the power output are set as follows:

$$
P_i^{\min} y_{i,t} \le P_{i,t} \le P_i^{\max} y_{i,t}, \ \forall i, \forall t.
\tag{5}
$$

5) *Ramping Limits:* the constraints ensure that the unit operates within the ramp rate:

$$
\begin{aligned}
P_{i,t} - P_{i,t-1} &\le Ru_i y_{i,t-1} + \overline{Ru_i} u_{i,t}, & \forall i, \forall t, \\
P_{i,t-1} - P_{i,t} &\le Rd_i y_{i,t-1} + \overline{Rd_i} v_{i,t}, & \forall i, \forall t.
\end{aligned}
\tag{6}
$$

6) *Transmission line limits* (security *constraints*):

$$
-F_l^{\max} \le \sum_{i=1}^{N} a_{l,i} P_{i,t} - \sum_{j=1}^{M} b_{l,j} D_{j,t} \le F_l^{\max}, \ \forall l, \forall t.
\tag{7}
$$

For brevity, we denote $\widetilde{\mathbf{a}} = [\mathbf{a}; -\mathbf{a}]$, $\widetilde{\mathbf{b}} = [\mathbf{b}; -\mathbf{b}]$ and $\widetilde{\mathbf{F}}_l^{\max} = \left[\mathbf{F}^{\max}; -\mathbf{F}^{\max}\right]$ to be the augmented power transfer distribution factor matrix and the augmented transmission line limit vector, respectively. Then the security constraints can be expressed compactly by

$$
\sum_{i=1}^{N} \tilde{a}_{l,i} P_{i,t} - \sum_{j=1}^{M} \tilde{b}_{l,j} D_{j,t} \le \overline{F}_l^{\max}, \ \forall l.
\tag{8}
$$

In the above formulation, the Generator Shift Distribution Factor (GSDF) defines the branch power flow change caused by the generator output power shift. If the active power of node i has a change of ΔP_i, then the transition of the active power of the branch l is given by

$$
\Delta P_l^i = a_{l,i} \times \Delta P_i.
\tag{9}
$$

Given the generator output power transfer distribution factor ΔP_i, the conducting matrix Y_i and node-branch correlation vector M_l, we can compute $X_i = Y_i^{-1}$ and get GSDF by

$$
a_{l,i} = \frac{1}{x_l} M_l^{\mathrm{T}} X_i.
\tag{10}
$$

It should be noted that the matrix X_l is related to the selection of balance nodes, and different nodes will lead to different GSDF coefficients. Also, the node voltage equation of the power system is a set of nonlinear equations with respect to the node voltage. In practice, it is generally solved by iterative methods, such as the G-S method, Newton

Raphson algorithm, and the PQ decomposition, which could yield uncertainty in the solution [26]. Hence, the GSDF in the SCUC model could be inaccurate.

To account for the inaccuracy of the GSDF in the SCUC model, a solution is to incorporate robustness. In the robust approach, $a_{l,i}$ can be modeled as a deterministic vector that lies in a ball centered at a nominal steering vector a_0, such a way to capture robustness has been widely used in the literature, see, e.g., [27, 28]. The goal then is to design a robust optimization model that yields the best possible performance for all possible values of $a_{l,i}$ in the uncertainty set. For branch l, let $a_{i,t} = \overline{a}_{i,t} + x_{i,t}$ where $x \in \mathcal{B}^n(0, \delta) := \{\mathbf{x} : \sum_{i=1}^{N} x_{i,t}^2 \leq \delta\}$ and $\overline{a}_{i,t} \geq 0$. The security constraints are re-written as

$$\sum_{i=1}^{N} (x_{i,t} + \overline{a}_{i,t}) P_{i,t} - \sum_{j=1}^{M} \tilde{b}_{l,j} D_{j,t} \leq \tilde{F}_l^{\max}, \ \forall l, \forall x \in \mathcal{B}^n(0, \delta), \tag{11}$$

where $\mathcal{B}^n(0, \delta) := \{\mathbf{x} : \sum_{i=1}^{N} x_{i,t}^2 \leq \delta\}$.

The SCUC model given in this section is a nonlinear problem that can be solved by a commercial solver. However, due to the consideration of uncertain parameters, the scale of the SCUC problem could be huge. In the following section, we introduce fast and efficient constraint reduction methods to reduce the scale of the SCUC problem and speed up the solution procedure.

3 Identifying Redundant Constraints with Uncertainty

In this section, we develop an efficient method to identify the redundant security constraints in the context of robust optimization. One major motivation of redundancy detection originates from the observation that over 85% of the security constraints are redundant and only a small part of transmission lines provides useful information for transmission planning, thus affecting the total operating cost [24]. This section gives a sufficient condition to identify redundant security constraints with uncertain parameters.

Firstly, the definitions of redundant constraints and active constraints are given. Redundant constraints are defined as: for an optimization problem, if the feasible domain of the optimization problem does not change after removing a constraint, the removed constraint is redundant. In contrast, if the feasible domain of the optimization problem changes after a constraint is removed from its constraint set, the removed constraint is an active constraint. Note that the definition of redundant constraint is not related to the objective function but only depends on the feasible domain.

According to the definition, whether a constraint is redundant depends on whether it limits the feasible domain of the optimization problem to which it belongs. Taking Fig. 1 as an example, constraints 4, 5, 6, 7, and 8 are redundant constraints, and 1, 2, and 3 are active constraints.

In practice, the computational complexity of identifying one security constraint is similar to the original SCUC model. To address this problem, [24] proposed identifying a large subset of the redundant security constraints, which is realized by relaxing the feasible domain of the original model.

In Fig. 2, we can find that if a security constraint is redundant on the relaxed feasible domain, it must be redundant on the original feasible domain; however, if the security
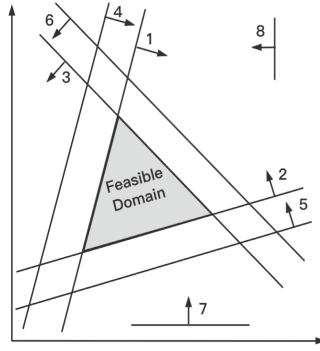
Fig. 1. Illustration of redundant and active constraints
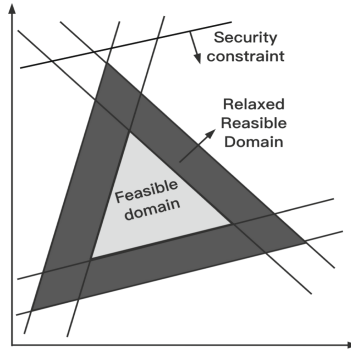
Fig. 2. Security constraints and original feasible domain and relaxed feasible domain

constraint is active on the original feasible domain, we cannot determine whether it is redundant on the relaxed feasible domain. According to [24], we relax the original feasible domain by (i) neglecting the feasible domain of integer variables and considering the integer numbers to be continuous, leading to a security-constrained economic dispatch problem; (ii) keeping only power balance constraint and generation output limits; (iii) relaxing the generation output limits by $0 \leq P_{i,t} \leq P_i^{\max}$.

Using this relaxation, Proposition 1 can quickly identify redundant security constraints with uncertainties. For the security constraint k at time t, we consider

$$
Z_{k,t}^+ = \max_{\mathbf{P}} \max_{\mathbf{x} \in \mathcal{B}^n(0,\delta)} \quad \sum_{i=1}^{N} \left(x_{k,i} + \bar{a}_{k,i} \right) P_{k,t} - \sum_{j=1}^{M} b_{k,j} D_{j,t}
$$

$$
\text{subject to} \quad \sum_{i=1}^{N} P_{i,t} = D_t, \\
0 \leq P_{i,t} \leq P_i^{\max}, \forall i \in \mathcal{I}.
$$

(12)

Proposition 1. If $\overline{Z}_{k,t}^+ \leq \overline{F}_k^{\max}$, then the k-th security constraint at a time t is redundant.

The above detection problem, due to its nonlinear nature, is generally complex, but as we will show later, under some assumptions of the problem structure, we can solve

the problem quite efficiently using a greedy algorithm. To this end, we first compute the optimal $x_i^*(P)$ given any P. By simple calculation, we have $x_i^*(P) = \frac{\sqrt{\delta P_i}}{\sqrt{\sum_{i=1}^N P_i^2}}$. Then we simplify the objective function by plugging in the solution $x_i^*(P)$ and analyze the resulting formulation. Without loss of generality, we assume $\delta = 1$ and drop the period index t from now on and we arrive at the following nonlinear optimization problem:

$$\max_P \quad \sum_{i=1}^N \overline{a}_i P_i + \sqrt{\sum_{i=1}^N P_i^2}$$

$$\text{subject to} \quad \sum_{i=1}^N P_i = D$$

$$0 \leq P_i \leq P_i^{\max}$$

$$(13)$$

Notice that the above problem is nonconvex in nature and is intractable due to the $\mathcal{NP}$-hardness [29]. To address the issue, we first propose the following greedy algorithm as an approximation (Fig. 3).

Algorithm 1. Greedy algorithm for redundancy detection

input $\{\overline{a}_i\}_{i=1,\ldots,N}, D, P_i^{\max}$

sort $\{\overline{a}_i\}$ in descending order $\sigma(N)$ such that $\overline{a}_{\sigma_1} \geq \cdots \geq \overline{a}_{\sigma_N}$

initialize $R=D, Z_1=0, Z_2=0, P_i^*=0, \forall i$

for $i=1,\ldots,N$

    if $R \geq P_{\sigma(i)}^{\max}$
        $Z_1 \leftarrow Z_1 + \overline{a}_{\sigma(i)} P_{\sigma(i)}$
        $Z_2 \leftarrow Z_2 + (P_{\sigma(i)}^{\max})^2$
        $P_i^* \leftarrow P_{\sigma(i)}^{\max}$
        $R \leftarrow R - P_{\sigma(i)}^{\max}$
    else
        $Z_1 \leftarrow Z_1 + \overline{a}_{\sigma(i)} R$
        $Z_2 \leftarrow Z_2 + R^2$
        $P_i^* \leftarrow R$
        break
    end

end for

output $Z=Z_1+\sqrt{Z_2}, P^*$

Fig. 3. Pseudocode of the greedy algorithm

Remark 1. Though the above algorithm is proposed for Z^+ for brevity, we can easily generalize it to Z^-, the lower transmission limit, by sorting $\{a_i\}$ in ascending order.

As is presented in Algorithm 1, our greedy algorithm ignores the nonlinear part $\sqrt{\sum_{i=1}^N P_i^2}$ and models the section redundancy detection as if a continuous knapsack

whose capacity is the load parameter D and at each step, we greedily choose the unit $\sigma(i)$ and fill the knapsack using the quantity $a_{\sigma(i)} P^{\max}_{\sigma(i)}$ till its capacity runs out.

As our numerical experiments will suggest, this method works well for practical redundancy detection if $P^{\max}_i$ is small. To justify this, we prove, in a special case where $P^{\max}_i = P^{\max}$, that the greedy algorithm is optimal. Recall that we need to solve the following problem characterized by $(D, \{\bar{a}_i\}, P^{\max})$.

$$\max_P \quad f(P) + g(P) := \sum_{i=1}^N \bar{a}_i P_i + \sqrt{\sum_{i=1}^N P_i^2} \tag{14}$$

$$\text{subject to} \qquad P \in \mathcal{K}_N^D$$

where $f(P) := \sum_{i=1}^N \bar{a}_i P_i$, $g(P) := \sqrt{\sum_{i=1}^N P_i^2}$ and $\mathcal{K}_N^D := \left\{P : \sum_{i=1}^N P_i = D, 0 \leq P_i \leq P^{\max}\right\}$ encapsulates the feasible domain. Also, recall that the solution generated by Algorithm 1 is denoted by P^*. Our proof is rather simple and works by showing that the two auxiliary problems $\max_{P \in \mathcal{K}_N^D}\{g(P)\}$ and $\max_{P \in \mathcal{K}_N^D}\{f(P)\}$ share the same structure of optimality. Such structures are summarized by the following two lemmas.

Lemma 1. Given D and $P^{\max}$ and the permutation $\sigma(N) = \{\sigma(1), \ldots, \sigma(N)\}$ that sorts $\bar{a}_i$ in the descending order $(\bar{a}_{\sigma(1)} \geq \bar{a}_{\sigma(1)} \geq \cdots \geq \bar{a}_{\sigma(N)})$,

$$\begin{aligned}\overline{P}^N_{\sigma(i)} &= P^{\max}, & 0 \leq i < d \\ \overline{P}^N_{\sigma(i)} &= D - d \cdot P^{\max}, & i = d \\ \overline{P}^N_{\sigma(i)} &= 0, & d < i \leq N\end{aligned} \tag{15}$$

is optimal for the problem $\max_{P \in \mathcal{K}_N^D}\{g(P)\}$, where $d = \lfloor \frac{D}{P^{\max}} \rfloor$. More specially, we have

$$\max_{P \in \mathcal{K}}\{g\left(\overline{P}^N\right)\} = \sqrt{d(P^{\max})^2 + (D - d \cdot P^{\max})^2}. \tag{16}$$

Proof. Since we assume that the detection problem is feasible, it follows that $N P^{\max} \geq D$. Thus $d \leq N$ and $\{\overline{P}^N_{\sigma(i)}\}$ are feasible since $0 \leq \overline{P}^N_{\sigma(i)} \leq P^{\max}$ and

$$\sum_{i=1}^N \overline{P}^N_i = \sum_{i=1}^N \overline{P}^N_{\sigma(i)} = P^{\max}d + D - P^{\max}d = D \tag{17}$$

Also, we can simply exclude the case where $P^{\max} > D$ since in this case $\mathcal{K}_N^D$ degenerated into a simplex and the optimal solution is an arbitrary vertex. Hence, we focus on the case $D/N \leq P^{\max} \leq D$ and prove by induction. For convenience, given $P \in \mathcal{K}_k^D$, we define $h^k(P) := \sum_{i=1}^k P_i^2$.

Induction Hypothesis

$$H(k) := [\text{Lemma 1 holds for } N = k]. \tag{18}$$

Base Case

For $k = 1$ or 2, we can easily verify the result.

Inductive Step

Assume that $H(k)$ holds for $k = m - 1$, then for $H(m)$, we sucessively deduce that

$$
\begin{aligned}
\max_{P \in \mathcal{K}_m^D} \{h^m(P)\} &= \max_{P \in \mathcal{K}_m^D} \left\{ \max_{P' \in \mathcal{K}_{m-1}^{D-P_m}} h^{m-1}(P') + P_m^2 \right\} \\
&= \sqrt{\lfloor \tfrac{D-P_m}{P^{\max}} \rfloor (P^{\max})^2 + \left(D - P_m - \lfloor \tfrac{D-P_m}{P^{\max}} \rfloor \cdot P^{\max} \right)^2} + P_m^2,
\end{aligned}
\tag{19}
$$

where the second equality is by $H(m-1)$ and it can be verified that the maximum of the above expression is obtained by at most three points:

$$
P_m \in \left\{ P^{\max}, D - P^{\max} \lfloor \tfrac{D}{P^{\max}} \rfloor, 0 \right\},
\tag{20}
$$

where $D - P^{\max} \lfloor \tfrac{D}{P^{\max}} \rfloor$ is always a feasible optimal solution. Last taking $P_m = \overline{P}_m = D - P^{\max} \lfloor \tfrac{D}{P^{\max}} \rfloor$ and applying $H(m-1)$, we know that $\overline{P}^{m-1}$ contains exactly $\lfloor \tfrac{D}{P^{\max}} \rfloor$ entries of $P^{\max}$ and the rest are all zeros. Concatenate $\overline{P}^{m-1}$ and $\overline{P}_m$ and leveraging the symmetry between $\{P_i\}$, it immediately follows that $H(m)$ holds. By the principle of mathematical induction, this completes the proof.

∎

In addition, we also have the following lemma.

Lemma 2. $P^* \in \text{argmax}_{P \in \mathcal{K}_N^D} \{f(P)\}$.

Proof. The result follows immediately from the optimality of the greedy algorithm in the continuous knapsack problem.

∎

With the above lemmas, for the case where $P_i^{\max} = P^{\max}$, $\forall i$, we have the following theorem which guarantees the optimality of the greedy approach.

Theorem 1 (Optimality under equal maximum power). Given a redundancy detection problem whose involved generators have a uniform maximum power parameter, then Algorithm 1 is optimal.

Our theoretical result justifies the use of greedy algorithm when the generators are similar in their configurations. In the next section, we conduct numerical experiments to further validate the efficiency of our proposed robust detection method.

4   Numerical Results

To verify the robust constraint reduction method proposed in Sect. 3, we test our results through experiments on the modified IEEE118-bus system consisting of 186 branches

(7 parallel branches) and 54 units. The detailed parameters of the original IEEE118-bus systems can be found in [30]. The total number of periods is set to be 24. The corresponding SCUC problem-solving software is developed using Matlab with Gurobi 9.10. The simulation environment is a computer with Intel Xeon CPU and 128 GB memory.

Considering the uncertainty of the parameter, we make some modifications to the original dataset while preserving the topology of the original network. Specifically, we increase the number of generators (unit) to 270 and modify the unit power range by tightening them and removing the branches whose power range is too extensive. Note that in practice, we can always do the conversion by virtually splitting a unit into several smaller ones such that the power ranges of the units are almost identical. In addition, let the minimum power of each generator be 0 for ease of exposition (Fig. 4).
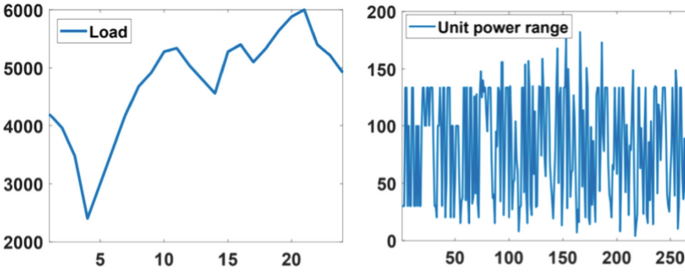
Fig. 4. Left: a load of the modified IEEE 118 instance; Right: the unit power range (upper) for each of the 270 generators, values deviating too far are truncated to the mean.

Based on the above setting, the model ends up with $2TL = 2 \times 24 \times 186 = 8928$ security constraints, each taking the form of

$$P_i^{\min} \leq \sum_{i \in \mathcal{N}} \bar{a}_i P_i + D \leq P_i^{\max}, \tag{21}$$

where D corresponds to the constant from the load parameters and $\bar{a}_i$ denotes the original modeling data.

To characterize the uncertainty within the GSDF data, we check redundancy based on the perturbed coefficients for each security constraint $\{\hat{a}_i\}$. More specifically, given the accuracy parameter $\delta \geq 0$, denote $\hat{a} = \bar{a} + \epsilon$, where ϵ is taken uniformly from the ball $\mathcal{B}_\delta$. Next, we define the way to evaluate the efficiency of detecting redundant constraints. We use a method that is frequently used in the machine learning context. Assume that a model contains N redundant constraints and a constraint-reduction method can identify $T + F$ of them, where T is the number of truly redundant constraints and F is the number of active constraints, then we define two important estimators as $Precision = \frac{T}{T+F}$ and $Recall = \frac{T}{N}$. In the numerical experiment, we choose $\delta \in \{0.0, 10^1, 10^2, 10^3\}$ to be various degrees of inaccuracy. For robust approaches, we set the radius of the uncertainty ball to be 100.0.

It can be seen from Table 1 that the robust constraint-reduction method obtains less *precision* but higher *recall* as the accuracy of the model becomes worse. In the SCUC

Table 1. Robustness of the methods.

Uncertainty parameter δ	Conventional constraint reduction method (pre-solve)		Robust constraint reduction method	
	Precision (#)	Recall (#)	Precision (#)	Recall (#)
0	0.85 (7588)	1.00	0.78 (6963)	1.00
10^1	0.85 (7588)	1.00	0.55 (4910)	1.00
10^2	0.84 (7500)	0.89	0.52 (4642)	1.00
10^3	0.85 (7580)	0.59	0.50 (4464)	1.00
10^4	0.81 (7230)	0.34	0.47 (4196)	1.00

scenarios, security, in other words, *recall*, is much more critical. Thus, our proposed approach is a more robust method when facing inaccurate GSDF data. For the sake of completeness, we also present the solution time and objective value before and after reduction as follows.

Table 2. SCUC with and without constraints reduction.

Solution statistics	Before constraints reduction	After constraints reduction
Objective	1.3995E+06	1.3995E+06
Solution time (s)	27.75	25.92

Table 2 illustrates that the solution time reduces after constraints reduction and the objective stays the same. We note that although our approach generally detects fewer redundant constraints due to the stricter criterion, such a cost should be justified by the robustness it offers when the security constraints must be enforced.

5 Conclusions

This paper builds a robust optimization model for the SCUC problem considering the uncertainty of the Generator Shift Distribution Factor (GSDF). A corresponding constraint-reduction method is proposed to simplify the SCUC problem by developing a sufficient condition to relax the original feasible domain. Then it is equivalent to a knapsack-type problem that a greedy algorithm can efficiently solve. The numerical results on the IEEE118 node test system show that using this model to calculate the SCUC problem under the uncertain GSDF gives better robustness and stability against uncertain parameters. Hence, it can help the operator quickly make safe and economic unit operation decisions.

The SCUC model used in this paper is based on the DC power flow equation and does not consider constraints such as voltage amplitude. In future work, we will study the more accurate SCUC problem described by the AC power flow equation and find

more effective constraint-reduction methods for obtaining feasible solutions to SCUC problems.

References

1. Sen, S., Kothari, D.P.: Optimal thermal generating unit commitment: a review. Int. J. Electr. Power Energy Syst. **20**(7), 443–451 (1998)
2. Shahidehpour, M., Yamin, H., Li, Z.: Market Operations in Electric Power Systems: Forecasting, Scheduling, and Risk Management. Wiley, New York (2003)
3. Wang, S.J., Shahidehpour, S.M., Kirschen, D.S., et al.: Short-term generation scheduling with transmission and environmental constraints using an augmented Lagrangian relaxation. IEEE Trans. Power Syst. **10**(3), 1294–1301 (1995)
4. Al-Agtash, S.: Hydrothermal scheduling by augmented Lagrangian: considering transmission constraints and pumped-storage units. IEEE Trans. Power Syst. **16**(4), 750–756 (2001)
5. Fu, Y., Shahidehpour, M.: Fast SCUC for large-scale power systems. IEEE Trans. Power Syst. **22**(4), 2144–2151 (2007)
6. Martínez-Crespo, J., Usaola, J., Fernández, J.L.: Security-constrained optimal generation scheduling in large-scale power systems. IEEE Trans. Power Syst. **21**(1), 321–332 (2006)
7. Hobbs, B.F., Rothkopf, M.H., O'Neill, R.P., Chao, H.P.: The Next Generation of Electric Power Unit Commitment Models. Springer, New York (2006). https://doi.org/10.1007/b108628
8. Guan, X., Zhai, Q., Papalexopoulos, A.: Optimization-based methods for unit commitment: Lagrangian relaxation versus general mixed-integer programming. In: 2003 IEEE Power Engineering Society General Meeting (IEEE Cat. No. 03CH37491), vol. 2, pp. 1095–1100. IEEE (2003)
9. Gaing, Z.L.: Particle swarm optimization to solve the economic dispatch considering the generator constraints. IEEE Trans. Power Syst. **18**(3), 1187–1195 (2003)
10. Trivedi, A., Srinivasan, D., Pal, K., et al.: Enhanced multiobjective evolutionary algorithm based on decomposition for solving the unit commitment problem. IEEE Trans. Ind. Inf. **11**(6), 1346–1357 (2015)
11. Yang, N., Dong, Z., Wu, L., et al.: A comprehensive review of security-constrained unit commitment. J. Mod. Power Syst. Clean Energy **10**(3), 562–576 (2021)
12. Lv, J., Ding, T., Bie, Z., et al.: A novel linearization variant of reliability costs in the optimal scheduling model. IEEE Trans. Power Syst. **32**(5), 4140–4142 (2017)
13. Wu, L., Shahidehpour, M., Li, T.: Stochastic security-constrained unit commitment. IEEE Trans. Power Syst. **22**(2), 800–811 (2007)
14. Wang, Y., Xia, Q., Kang, C.: Unit commitment with volatile node injections by using interval optimization. IEEE Trans. Power Syst. **26**(3), 1705–1713 (2011)
15. Wu, L., Shahidehpour, M., Li, Z.: Comparison of scenario-based and interval optimization approaches to stochastic SCUC. IEEE Trans. Power Syst. **27**(2), 913–921 (2011)
16. Bertsimas, D., Litvinov, E., Sun, X.A., et al.: Adaptive robust optimization for the security-constrained unit commitment problem. IEEE Trans. Power Syst. **28**(1), 52–63 (2012)
17. Jiang, R., Wang, J., Guan, Y.: Robust unit commitment with wind power and pumped storage hydro. IEEE Trans. Power Syst. **27**(2), 800–810 (2011)

18. Chen, Y., Wang, X., Guan, Y.: Applying robust optimization to MISO look-ahead unit commitment. In: Proceedings of FERC Technical Conference Increasing Real-Time and Day-Ahead Market Efficiency Through Improved Software, pp. 1–6 (2013)
19. Zhao, C., Guan, Y.: Unified stochastic and robust unit commitment. IEEE Trans. Power Syst. **28**(3), 3353–3361 (2013)
20. Kumar, A., Ghose, T.: sensitivity factor analysis of hybrid AC–DC distribution system and overload alleviation using modified generator shift distribution factor. In: Reddy, M.J.B., Mohanta, D.K., Kumar, D., Ghosh, D. (eds.) Advances in Smart Grid Automation and Industry 4.0. LNEE, vol. 693, pp. 777–785. Springer, Singapore (2021). https://doi.org/10.1007/978-981-15-7675-1_78
21. Capitanescu, F., Wehenkel, L.: A new iterative approach to the corrective security-constrained optimal power flow problem. IEEE Trans. Power Syst. **23**(4), 1533–1541 (2008)
22. Xavier, A.S., Qiu, F., Wang, F., et al.: Transmission constraint filtering in large-scale security-constrained unit commitment. IEEE Trans. Power Syst. **34**(3), 2457–2460 (2019)
23. Molzahn, D.K.: Identifying redundant flow limits on parallel lines. IEEE Trans. Power Syst. **33**(3), 3210–3212 (2018)
24. Zhai, Q., Guan, X., Cheng, J., et al.: Fast identification of inactive security constraints in SCUC problems. IEEE Trans. Power Syst. **25**(4), 1946–1954 (2010)
25. Ding, T., Qu, M., Bai, J., et al.: Fast identifying redundant security constraints in SCUC in the presence of uncertainties. IET Gener. Transm. Distrib. **14**(13), 2441–2449 (2020)
26. Cain, M.B., O'neill, R.P., Castillo, A.: History of optimal power flow and formulations. Federal Energy Regul. Comm. **1**, 1–36 (2012)
27. Duan, C., Jiang, L., Fang, W., et al.: Data-driven affinely adjustable distributionally robust unit commitment. IEEE Trans. Power Syst. **33**(2), 1385–1398 (2017)
28. Martínez, J.M.: Local minimizers of quadratic functions on Euclidean balls and spheres. SIAM J. Optim. **4**(1), 159–176 (1994)
29. Ge, D., Jiang, X., Ye, Y.: A note on the complexity of L_p minimization. Math. Program. **129**(2), 285–299 (2011)
30. Fu, Y., Shahidehpour, M., Li, Z.: Security-constrained unit commitment with AC constraints. IEEE Trans. Power Syst. **20**(2), 1001–1013 (2005)

Architecture Design of Embedded EMS Based on Control Optimization Configuration and Automatic Differentiation Technology

Shufeng Dong[(✉)], Zhenchong Wu, Xinyi Zheng, Chengsi Xu, Mingyang Ge, Kunjie Tang, and Kaicheng Lu

College of Electrical Engineering, Zhejiang University, Hangzhou 310027, China
dongshufeng@zju.edu.cn

Abstract. Under the construction layout of the new power systems, changes such as a large number of new energy sources put forward higher requirements for the management and control of the energy system. This paper proposes an embedded energy management system (EMS) architecture to achieve more lightweight, efficient, dedicated, and development-friendly intelligent management of energy systems. The control optimization configuration technology based on activity on edge (AOE) network makes the development of control strategy without programming, and can be completed only through simple file configuration, avoiding the problems of embedded device software solidification and difficulty in secondary development. And the optimization problem modeling and calculation engine are decoupled by automatic differentiation technology, so that the core code can be reused, so as to reduce the complexity of EMS program and improve the speed of power grid analysis and control. Finally, in order to explain the usage method in detail, it analyzes the example of energy storage-assisted AGC frequency regulation, through which the effectiveness and practicability of the embedded EMS are verified.

Keywords: Embedded · Energy management system · Control optimization configuration · Automatic differentiation technology · AOE network

1 Introduction

As the control center of the regional energy system, the energy management system (EMS) is responsible for monitoring, analyzing and decision-making control of various equipment within its jurisdiction [1], so as to achieve stable, economical and low-carbon optimal operation of the energy system. However, under the carbon peaking and carbon neutrality goals, the new power system construction brought about by the increase in the installed proportion of wind and solar energy and other renewable energy sources, the prominent importance of energy storage devices, and carbon emission restrictions, and other new changes, the optimal control ability of the energy management system put forward higher requirements. In addition to the urgent need to enhance functions,

traditional EMS has performance problems such as: heavy structure that requires multi-level hardware support such as servers, controllers, and IoT gateways, low versatility that needs to be developed one by one for different application scenarios, and low processing efficiency caused by the increased computing load after the introduction of distributed energy resources. These issues also limit the low-carbon development of modern energy systems.

Aiming at the above problems, this paper proposes an embedded EMS solution. By integrating multi-level hardware functions such as data acquisition, analysis and calculation, and real-time control, a lightweight, efficient and dedicated integrated energy management system is realized. Thus the EMS is plug-and-play, which facilitates efficient monitoring and comprehensive coordinated control of a large number of scattered new energy, energy storage and other equipment.

Faced with the problems of software solidification and difficulty in secondary development of embedded devices, this paper uses control optimization configuration technology in embedded EMS, so that the development of control strategies does not need to write programs, and only needs to configure related files in a "building block" style [2]. This solves the contradiction between the lack of programming foundation and the lack of on-site experience of the on-site debugging personnel, and greatly improves the efficiency of industrial control [3]. The control optimization configuration technology gives users a general platform for self-defining control strategies without involving the modification of the embedded EMS internal code. This improves the optimal control ability of EMS to deal with complex and multiple controlled equipment, and conforms to the higher requirements of energy management system in the context of energy transformation. Faced with the limited storage unit and computing resources of embedded devices, this paper adopts automatic differentiation algorithm [4, 5]. It overcomes the large rounding and truncation errors caused by the numerical differentiation method of finite difference approximation, and the exponential growth problem of the symbolic expression of symbolic differentiation with the increase of function complexity. This greatly improves the speed, efficiency and reliability of the optimization problem calculation.

2   Architecture Design of Embedded EMS

2.1   Embedded EMS Architecture

Embedded EMS refers to an energy management system whose hardware consists of a single embedded device, with highly integrated and tailorable software and hardware, friendly interaction. It is designed with micro kernel structure and modular structure. It realizes the decoupling of control problem modeling and calculation based on control configuration technology, supports the configuration of control model in the form of the most intuitive mathematical formula. It supports a variety of communication protocols and tailorable protocol stack, with the advantages of low cost, small size, high performance and fast deployment. It has both specificity and flexibility, and can complete a variety of advanced application functions of energy management, such as data acquisition and monitoring, scheduling control, etc. The system architecture diagram of embedded EMS is shown in Fig. 1, which is divided into hardware layer, operating system layer

and application layer from bottom to top. The operating system layer includes operating system kernel, hardware driver framework, startup program, system components, hardware abstraction layer and system interface. The operating system provides a system call interface for functional applications through the system interface. The hardware device access interface is provided through the hardware abstraction layer. System components communicate with the application layer through a message bus. The application layer includes basic applications, business applications and corresponding containers. Data exchange between applications through a message bus.
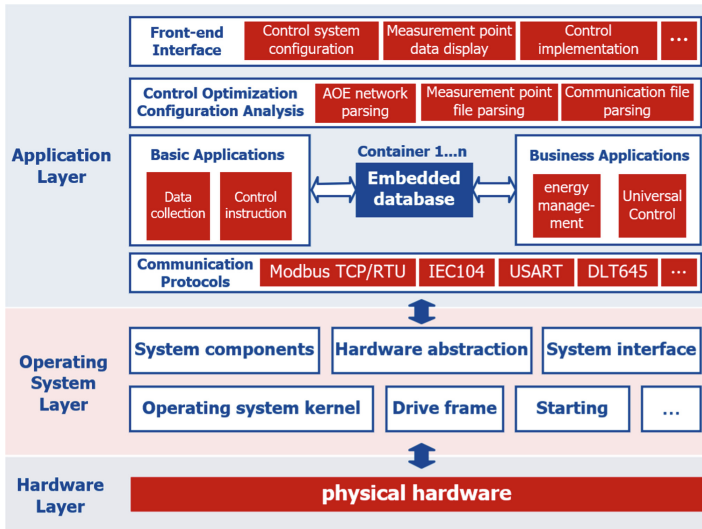
Fig. 1. The embedded EMS's architecture.

Specifically, the application of basic functions includes basic functions such as data collection, status monitoring, and control instruction issuance of the controlled device. Business applications include energy management applications such as topology analysis, abnormal judgment and alarm, scheduling plan arrangement, report file generation, and general control strategy development and application based on control optimization configuration technology. The real-time data and historical data generated by the application are stored in the embedded database of EMS. Embedded databases eliminate the overhead associated with additional client-server configuration, require less memory, are faster, perform better. It also allows data to be managed through structured query languages rather than raw text files.

2.2 Control Flow of Embedded EMS

The main process of optimizing control development using embedded EMS is as follows.

(1) Establish a mathematical model of the control object and determine the data point variables to be collected;

(2) Design an event-driven control strategy according to the control objective, and convert it into an AOE network structure. The AOE network will be introduced in more detail in the next section;

(3) Design the AOE network configuration file in a standardized format, define the basic information, variables, events and actions of the control network, and support the realization of non-customized control strategies;

(4) Import the control configuration file in the front-end operation interface of the embedded EMS, and run the control.

2.3 Advantages of Embedded EMS

The existing EMS has many pain points. The embedded EMS adopts new design ideas, which has many advantages, such as portability, efficiency, low code, easy expansion and so on.

(1) For a long time, EMS has been composed of servers, data gateways, controllers and other multi-layer devices. For small and medium-sized users, their cost budget and management scale are limited. Such equipment architecture is cumbersome and complex, which has brought many problems. The compatibility between different devices is difficult to be guaranteed, and users need to select products in a targeted and planned way. A large number of equipment often involve many manufacturers and suppliers, and the price space is occupied layer by layer. Users often pay higher prices or sacrifice part of their performance, and even passively buy auxiliary services. The communication interaction between layered devices inevitably brings the security risk of data leakage.

Embedded EMS only uses a single hardware device to solve the above problems. The software and hardware of Embedded EMS are highly integrated, plug and play, convenient and flexible. It can also be easily deployed in existing equipment spaces such as control cabinets and switchgear cabinets, providing a safer, more autonomous, more controllable and more diverse energy management solution.

(2) Traditional EMS solutions are mainly customized and developed for the large power grid side or a specific distributed energy system. Therefore, at the beginning of design and development, there is a clear plan for the scene and the energy equipment to be managed. EMS only needs to ensure the communication and management requirements with the dispatched and managed energy equipment in the current scene, and its expansibility and versatility are limited.

Embedded EMS supports a variety of communication protocols, and the protocol stack can be tailored, and is designed with micro kernel structure and modular structure, which makes it have good expansibility and versatility in the actual use. For different application scenarios, only module calls and parameter configuration are required for embedded EMS.

(3) EMS was usually developed as a large-scale system in the past, and the control strategy and logic were described and implemented in code language, which took a long time to develop. In the subsequent operation and maintenance process, special programming technical background personnel are required for maintenance and

debugging. If EMS needs to be developed for a large number of small and medium-sized users one by one, the labor cost is incalculable, and the development time is difficult to adapt to such a rapidly changing energy market.

Embedded EMS realizes the control function by configuring the AOE network after transforming the control strategy into a visual AOE network. This method not only simplifies the design of control strategy, but also realizes low code friendly interaction with users and developers. The system development and configuration of embedded EMS are as simple as "building blocks".

3   Control Optimal Configuration Based on AOE

The purpose of the control optimization configuration research is to realize the decoupling of modeling and calculation of optimization control problems. Users only need to write the optimization model in the most intuitive mathematical formula form, and can complete the development of optimization algorithm without calculating the Jacobian matrix and Hessian matrix. Control optimization configuration is the key technology to realize embedded EMS by decoupling problem modeling from computing engine, improving program reusability, reducing complexity and realizing more efficient and reliable computing. Control optimization configuration includes general modeling of control strategy and optimization solution technology based on automatic differentiation. This section first introduces the concept and design method of control optimization configuration.

3.1   Internal Correlation Between Control Strategy and AOE

AOE network is a directed acyclic graph with nodes representing events and edges representing activities. Events refer to the state of the whole or part of the system described by AOE. When the actual state of the system conforms to the definition of node events, it is said that node events are triggered; Activity refers to the action of the system during the transition between different states. When the system actually acts according to the instructions defined by the edge, it is said that the edge or action is executed. AOE network is often used to describe and analyze the planning and implementation process of a project in the engineering field.

The typical AOE network model is shown in Fig. 2, which contains 5 nodes and 5 directed edges connecting. Each node represents an event. Each edge performs the set action, and the direction of the edge specifies the execution order of AOE.

Control strategy is an implementation scheme constructed to make a system or equipment achieve the set objectives. For the execution process of control strategy, the process can be divided into a series of events and a set of transition relations between adjacent events with connection relationship under a certain order constraint according to the physical order of time and space or the logical order of design.

This way of expressing control strategy by a set composed of the change relationship between events and adjacent events is called "event driven" paradigm. The existence of control strategy is always to make the controlled object achieve the set goal. In the process from the initial state to the goal, the strategy is the response of the control
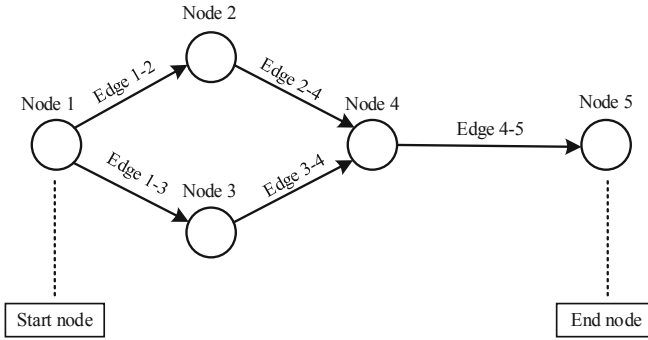
Fig. 2. The composition of AOE network.

device when the controlled object is in different states. When an event is triggered, the controlled object is in a certain state, and the change of adjacent events corresponds to the change of the controlled object from the current state to the next state, that is, the control strategy is actually a collection of multiple events and event change relations, and takes the event transfer as the driving force to drive the sequential execution of the whole strategy [6, 7]. The "event driven" essence of control strategy is the internal factor that can be described by AOE. Specifically, the nodes of AOE represent events, and the directed edges connected between adjacent nodes represent the transition relationship between adjacent events, so any control strategy can be modeled in the form of AOE.

3.2 Design Method of Control Optimal Configuration

Configuration refers to the flexible and diverse combination of existing units in the way of visual display to realize the generation of strategy. According to the scene and application requirements, engineers can select from the basic unit components of the configuration system and combine multiple components to complete the development of control strategy and realize the control of target objects.

In AOE control optimization configuration, the nodes and directed edges of AOE are the basic component units of configuration. Corresponding to the event driven paradigm of the control strategy in Sect. 3.1, the node of AOE represents the event and the edge represents the action. When the event represented by a node is triggered, the action represented by its outgoing edge will be executed according to the rules of the node type. Nodes and edges are standardized into various types as shown in Table 1 and Table 2 according to the action mode. When in use, component units and types are selected according to demand.

In the division of event types, considering that one or more transition relationships can be caused by an event, in the actual control, for several directed edges representing the transition relationship derived from this node, select all or one to execute according to some logic. The control flow unit that executes all or one branch in this order can be regarded as an atomic operation, and the other control flows can be constructed through the combination of this atomic unit, Therefore, it is reasonable and feasible for node event types to be normalized into two types: condition and branch judgment. In the

Table 1. Node event type of AOE network.

Event type	Name	Content
Condition	Condition Node	If the expression of the node is true within the set time, the node event is triggered, and all actions triggered by the node (i.e. all branches sent by the node) are executed in parallel
Switch	Branch logic judgment node	When the expression of the node is true, edge 1 acts, otherwise edge 2 acts
Switch2	Branch action judgment node	If all actions pointing to this node are executed successfully, edge 1 acts; otherwise, edge 2 acts

Table 2. Directed edge action type of AOE network.

Action type	Name	Content
None	No action	Do nothing
SetPoints	Set points	Assign values to actual measuring points or define calculation points
Solve	Solving equations	Solve linear or nonlinear equations
MILP	Mixed integer linear programming	Solving mixed integer linear programming problems
NLP	Nonlinear programming	Solving nonlinear programming problems

division of directed edge action types, based on the type of mathematical method, it divides almost all common engineering application methods, including empty action, point setting, solving equations and solving optimization problems, which will provide strong support for the development of control strategy.

In the above control optimization configuration, the trigger conditions of design control AOE are simple repetition, event driven and time driven. The format of optimization control action setting is as follows:

Objective function: min(Objective function expression)
Constraint condition : Constraint expression ≥ 0 (1)
Variable definition : Variable name : [Minimum value/Maximum value]

The event trigger type, action selection mode and action type in the proposed control optimization configuration can fully describe the control process, have strong universality, and can model various control strategies required by EMS.

4 Optimization Solution Technology Based on Automatic Differentiation

There are a lot of optimization problems in the operation control of power system and Microgrid, such as optimal power flow, reactive power optimization, energy storage power distribution and so on [8]. The existing commercial and open source nonlinear programming solvers need users to calculate Jacobian matrix and Hessian matrix, resulting in complex application. In addition, the derivative is calculated according to the differential expression entered by the user. When the differential expression is complex, the calculation efficiency will be reduced [9]. This paper integrates automatic differential algorithm in the embedded EMS as the basis of control optimization configuration, realizes the decoupling of optimization problem modeling and calculation engine, and improves the efficiency and reliability of the optimization calculation.

4.1 Automatic Differential Principle

In mathematics and computational algebra, automatic differentiation is a numerical method used to calculate the derivative of a dependent variable to an independent variable. In addition, it is also a computer program, which is different from our "analytical method" of manually calculating differentiation. Automatic differentiation does not have the problem of losing accuracy as numerical differentiation, nor is it prone to the problem of expression expansion as symbolic differentiation. It is fast and can maintain high accuracy.

When calculating the derivative of complex function expression, the chain rule can make the execution logic of computer program more clear. Symbolic differentiation uses the four operations of derivation and the derivation rule of compound function to calculate the functional expression of derivative, and then takes the value of independent variable to calculate the derivative. However, the function expression of the derivative after the calculation is not simplified, and the volume is huge, which brings a burden to the computer storage and calculation.

If the original function can be divided into multi-layer composite functions, and the derivatives of each layer of composite functions can be calculated directly in the middle of the calculation, the computational complexity of each step will be greatly reduced and the storage space required will not be large [10]. Automatic differentiation is based on this principle, which includes forward mode and reverse mode.

For the function $y = f(x)$, it can be expressed as:

$$\begin{cases} y = f_n(w_n) \\ w_n = f_{n-1}(w_{n-1}) \\ \cdots\cdots \\ w_i = f_{i-1}(w_{i-1}) \, (i = 1, 2 \cdots n) \\ \cdots\cdots \\ w_1 = f_0(w_0) \\ w_0 = x \end{cases} \tag{2}$$

In the forward mode, $\frac{dw_i}{dx}$ is calculated from the following formula. Deduce it step by step, until $\frac{dy}{dx}$ is obtained.

$$\frac{dw_i}{dx} = \frac{dw_i}{dw_{i-1}} \frac{dw_{i-1}}{dx} \tag{3}$$

When calculating $\frac{dw_i}{dx}$, $\frac{dw_{i-1}}{dx}$ has been calculated. Only $\frac{dw_i}{dw_{i-1}}$ needs to be calculated. After the disassembly of composite functions, the calculation of $\frac{dw_i}{dw_{i-1}}$ has become very simple.

The calculation method of the reverse mode is opposite to the above method. In the reverse mode, $\frac{dy}{dw_i}$ is calculated from the following formula. Deduce it step by step, until $\frac{dy}{dw_0}$ $(\frac{dy}{dx})$, is obtained.

$$\frac{dy}{dw_i} = \frac{dy}{dw_{i+1}} \frac{dw_{i+1}}{dw_i} \tag{4}$$

When calculating $\frac{dy}{dw_i}$, $\frac{dy}{dw_{i+1}}$ has been calculated. Only $\frac{dw_{i+1}}{dw_i}$ needs to be calculated. After the disassembly of composite functions, the calculation of $\frac{dw_{i+1}}{dw_i}$ has become very simple.

The functions with multiple independent variables can also use the forward mode or the reverse mode to calculate the partial derivatives of each order [11]. The calculation amount of the reverse mode is less than that of the forward mode, so the reverse mode is adopted to improve the calculation speed.

4.2   Examples of Automatic Differentiation

When analyzing the economic distribution of load, if the goal is to minimize the fuel consumption of the system, the consumption micro increase rate of the computer group is required, which is the differential of the fuel consumption characteristics of the unit. Taking the calculation of consumption micro increment rate as an example, the following shows how the automatic differentiation technology is applied to the calculation of the derivative of practical problems.

Assume that the fuel consumption characteristic of a thermal power unit is:

$$F = 4.0 + 0.30P + 0.00070P^2 \text{(t/h)} \tag{5}$$

where F is the fuel consumption and P is the power generation of the thermal power unit. It is assumed that the generating power of the thermal power plant at this time is $P = 200MW$. The incremental rate of consumption is the first derivative of fuel consumption to power generation. According to the principle of automatic differentiation, the fuel

consumption function can be expressed as:

$$\begin{cases} y = w_1 + w_2 + w_4 \\ w_4 = 0.00070w_3 \\ w_3 = P^2 \\ w_2 = 0.30P \\ w_1 = 4.0 \end{cases} \tag{6}$$

The steps to calculate the consumption micro increase rate using the forward mode are as follows.

$$\begin{cases} \dfrac{\partial w_1}{\partial P} = 0 \\[2mm] \dfrac{\partial w_2}{\partial P} = 0.30 \\[2mm] \dfrac{\partial w_3}{\partial P} = 2 \times 200 = 400 \\[2mm] \dfrac{\partial w_4}{\partial P} = \dfrac{\partial w_4}{\partial w_3} \dfrac{\partial w_3}{\partial P} = 0.00070 \times 400 = 0.28 \\[2mm] \dfrac{\partial y}{\partial P} = \dfrac{\partial w_1}{\partial P} + \dfrac{\partial w_2}{\partial P} + \dfrac{\partial w_4}{\partial P} = 0.58 \end{cases} \tag{7}$$

The steps to calculate the consumption micro increase rate using the reverse mode are as follows.

$$\begin{cases} \dfrac{\partial y}{\partial w_4} = 1 \\[2mm] \dfrac{\partial y}{\partial w_3} = \dfrac{\partial y}{\partial w_4} \dfrac{\partial w_4}{\partial w_3} = 0.00070 \\[2mm] \dfrac{\partial y}{\partial w_2} = 1 \\[2mm] \dfrac{\partial y}{\partial w_1} = 1 \\[2mm] \dfrac{\partial y}{\partial P} = \dfrac{\partial y}{\partial w_3} \dfrac{\partial w_3}{\partial P} + \dfrac{\partial y}{\partial w_2} \dfrac{\partial w_2}{\partial P} + \dfrac{\partial y}{\partial w_1} \dfrac{\partial w_1}{\partial P} = 0.00070 \times 400 + 1 \times 0.30 + 0 = 0.58 \end{cases} \tag{8}$$

It can be seen from the calculation results that the micro increase rate of consumption calculated by the two modes is the same, which is the same as the result of the traditional calculation method. In the computer, the derivative calculation based on automatic differentiation needs to store the calculation results of each step, but there is no need to store a large number of mathematical expressions. The calculation results of each step are accurate, and there is no accumulation of errors. In the numerical calculation of practical problems, automatic differentiation technology is fast and accurate.

4.3   Optimization Model Solution Based on Automatic Differentiation

Automatic differentiation is mainly used to solve nonlinear programming problems. Nonlinear programming problems need to calculate Jacobian matrix and Hessian matrix of multivariate functions. Jacobian matrix is a matrix composed of first-order partial derivatives, and Hessian matrix is a matrix composed of second-order partial derivatives. Automatic differentiation can quickly calculate the partial derivatives of each order, so as to speed up the solution of nonlinear programming problems.

The optimization model is directly expressed by mathematical expression. As long as the optimization model is input, the Jacobian matrix and Hessian matrix can be calculated by automatic differentiation. Based on the optimization library "*ipopt*", the nonlinear optimization problem can be solved. This method does not need programming to realize the programming language description of the pattern and calculate the corresponding derivative matrix.

Based on the above methods, the optimization problem solving computing platform *EasySolve* (http://sgool.zju.edu.cn:53040/) is developed to directly input the mathematical expression of the optimization model, including optimization objectives, constraints and optimization variables. The computing platform realizes the automatic parsing of strings, and returns the optimization results of each optimization variable to the user after solving. Based on the computing platform, the decoupling between model solving and problem modeling is realized.

The simple and quick solution of optimization problem is the basis of realizing control optimization configuration. Adding the action of solving optimization problems to the control optimization configuration can complete more complex control strategies and meet the requirements of power system and microgrid operation control [12].

5   Case Analysis

Battery energy storage system has the advantages of fast response, strong short-term throughput power and easy to change the regulation direction. It has a broad application prospect in the field of AGC frequency regulation. Energy storage frequency regulation control will be an important function of the microgrid EMS.

This paper realizes the embedded energy storage power distribution optimization control function based on control optimization configuration and automatic differentiation technology, and verifies the effectiveness and practicability of the proposed embedded EMS architecture. After receiving the remote regulation command of the energy storage battery issued by the main control system, the embedded EMS obtains each energy storage output command through optimization according to the constraints such as the state of charge (SOC) and the charge and discharge total mileage of the energy storage, and controls the energy storage output, so as to achieve the purpose of energy storage assisting AGC frequency modulation [13, 14].

5.1   Optimal Model Configuration of Energy Storage Power Distribution

The objective function is established by minimizing the sum of SOC equalization degree and power change penalty. Since it is difficult to solve the quadratic equation introduced

into variance optimization, the absolute value of the deviation between SOC and average value and the absolute value of the deviation between power and average value are used as the objective function.

$$\min_{P} \omega_1 \sum_{i=1}^{8} (|SoC_i - SoC_{mean}||SoC_i^0 - SoC_{mean}|) + \omega_2 \sum_{i=1}^{8} (e^{|SoC_i^0 - SoC_{mean}|} |P_i - P_{mean}|)$$

$$(9)$$

where ω_1 is the influence weight of the SOC balance; ω_2 is the power variation penalty weight; SoC_{mean} is the average SOC; SOC_i^0 is the current SOC value of the battery; P_i is the current power value of the battery; P_{mean} is the current average power of the battery; SoC_i is the SOC value of the second battery at the next time under the power operation optimized by the power allocation strategy.

The optimized constraints include the upper and lower limits of battery charge and discharge power and SOC.

$$\begin{cases} \sum_{k=1}^{n} (u_k - v_k) = P_D \\ u_i^{\min} \leq u_i \leq u_i^{\max}, \ v_i^{\min} \leq v_i \leq v_i^{\max} \qquad (i = 1, 2 \cdots n) \\ SoC_{\min} \leq SoC_i(t) + (u_i - v_i) \dfrac{dt}{Q_R} \leq SoC_{\max} \end{cases}$$

$$(10)$$

where u_i is the discharge power; v_i is the charging power; P_D is the actual discharge or charging power of the battery storage; dt is the charge and discharge time; Q_R is the battery capacity.

According to the established energy storage power distribution model, the control strategy based on control optimization configuration technology is designed, and the process is shown in the figure below (Fig. 3).

The above control strategy is represented by AOE topology, as shown in Fig. 2. There are four actions in this process. Action 1 is intermediate quantity calculation, which starts after the communication event node is triggered, calculates the SOH (state of health) of the energy storage battery, and then calculates the current actual capacity of the battery; Action 2 is to optimize and solve the established model, and optimize the problem model through low code; Action 3: the optimization solution is successful and the optimization strategy is issued; Action 4 is to issue the default strategy if the optimization solution fails (Fig. 4).

There are 82 measuring points in this calculation case, including eight energy storage start and stop commands, total charge and discharge mileage, SOC, output power, working state, output power command, rated mileage, rated capacity, maximum charging power, maximum discharge power, as well as remote control commands and remote adjustment commands received by the system.

5.2   Optimization Results of Energy Storage Power Distribution

Based on the proposed control optimization configuration and automatic differentiation technology, the optimization model is directly configured into the embedded device in

Start

Receive frequency regulation mode signal

Generator 1 regulating frequency

Generator 2 regulating frequency

2 generators regulating frequency independently

obtain P_Σ

Same as the frequency regulation control strategy of the generator 1

The batteries are divided into 2 independent groups and numbered respectively. Each group has the same frequency regulation control strategy as the generator 1

Obtain the battery historical charging and discharging mileage M_{his} and battery SOC

$S_{oc} < S_{ocmax}$
$(S_{oc} > S_{ocmin})$

Set the battery that reaches the limit to standby

Output

Calculate the actual capacity of the available battery
$E_{act} = (1 - 0.2 M_{his} / M_\Sigma) E_r$

Receive new P_Σ

Calculate the offset reference power of the available battery
$E_{cdev} = (S_{ocref} - S_{oc}) E_{act}$
$(E_{ddev} = (S_{oc} - S_{ocref}) E_{act})$

Number the batteries from large to small according to the offset reference value. The positive battery number is 1 to m, and the negative number is $m + 1$ to the total number of available batteries

Receive new P_Σ

After a certain time interval

After a certain time interval

$\sum_{i=1}^{m} P_{cmax,i} > P_\Sigma$
$(\sum_{i=1}^{m} P_{dmax,i} > P_\Sigma)$

Under the condition that the first m batteries meet the maximum charging (discharging) power, distribute P_Σ in proportion according to $E_{cdev}(E_{ddev})$, otherwise the output is $P_{cmax}(P_{dmax})$; Other batteries are available for standby

Output

The output of the first m batteries is $P_{cmax}(P_{dmax})$. Under the condition that the remaining available batteries meet the maximum charging (discharging) power, the remaining command P_Σ' is distributed proportionally according to $E_{cdev}(E_{ddev})$, otherwise the output is $P_{cmax}(P_{dmax})$.

Output

Fig. 3. Control strategy flow chart.

the form of mathematical formula. Run and solve the energy storage power allocation optimization model in the embedded device raspberry pie, and the simulation results are shown in Fig. 5, Fig. 6, Fig. 7 and Fig. 8.

It can be seen from Fig. 5 and Fig. 6 that the actual total output power of the energy storage battery is basically consistent with the change of the command power, the power distribution of each energy storage battery is relatively balanced, and the power change trend is similar. Figure 7 shows that the energy storage SOC reaches equilibrium after about 5 h under the action of configuration control. From Fig. 8, it can be seen that the SOC standard deviation decreases from 37 to about 3.09. Therefore, the control goal of
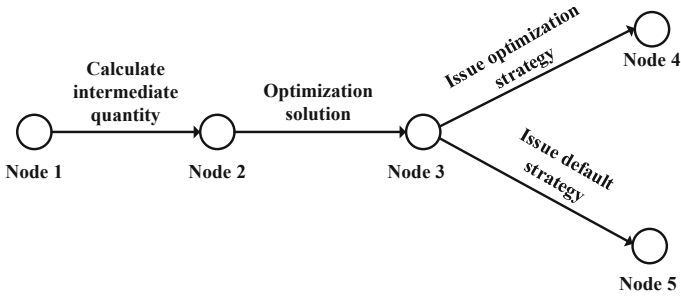
Fig. 4. The AOE topology of control strategy.
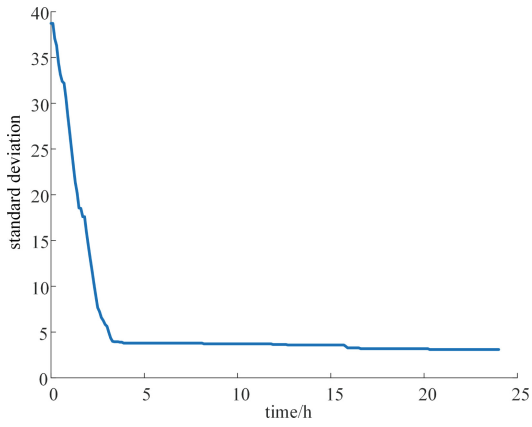
Fig. 5. The command power and actual output power of all energy storage battery packs.
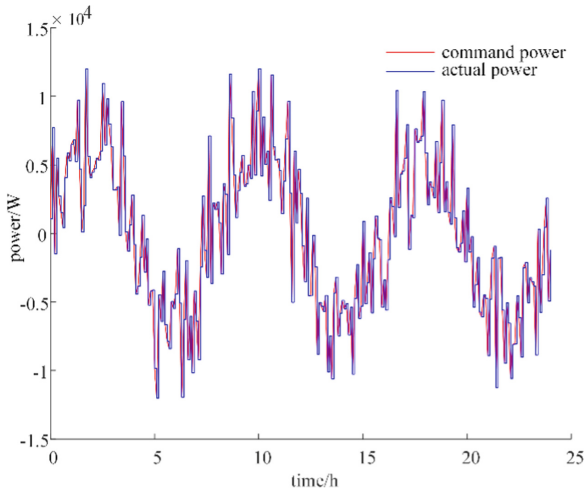
Fig. 6. The actual output power of each energy storage battery pack.
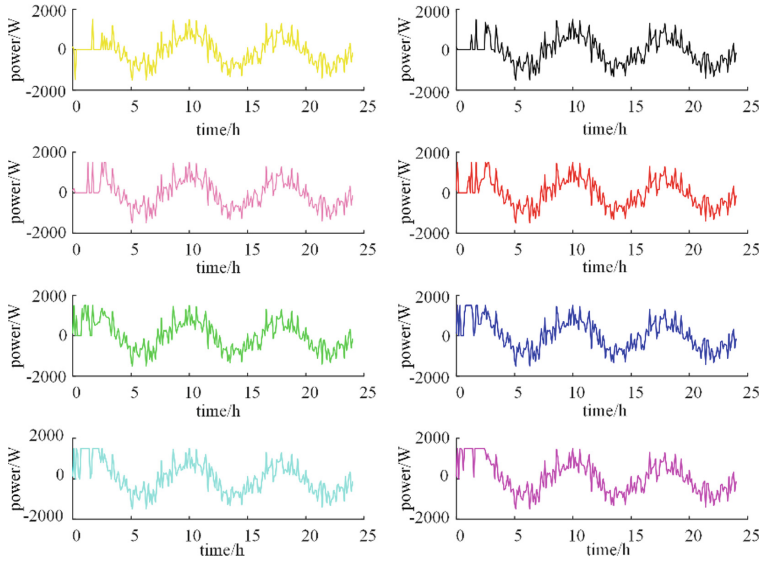
Fig. 7. The SoC change of each energy storage pack.
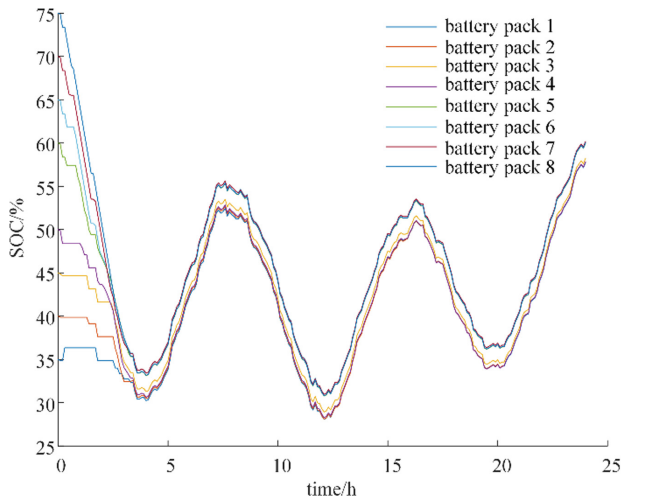
Fig. 8. The curve of SoC standard deviation.

power distribution of energy storage is realized and the control effect is good. The above case analysis verifies the effectiveness and practicability of the proposed embedded EMS based on control optimization configuration.

6 Conclusions

This paper presents an embedded energy management system architecture. Based on the control optimization configuration technology, it is possible to realize the custom development of control strategy without writing code and only through simple file configuration. Based on automatic differentiation technology, it can realize fast processing and calculation under limited hardware resources.

The embedded architecture eliminates the heavy structure and high cost of traditional multi-level hardware equipment, making the energy management system more efficient and dedicated. The decoupling of problem modeling and solution engine, on the one hand, realizes the code reuse of the solution engine, reduces the amount and complexity of program writing, and further improves the operation efficiency. On the other hand, it makes users focus on the problem modeling itself, and realizes the strategy development approach with lower threshold in the way of configuration.

With the transformation of the energy system and the rapid development of intelligence, a more lightweight, efficient, dedicated, and user-friendly embedded energy management system will ensure the stable and economic operation of the regional energy system under the massive access of new energy. It will help the construction of our new power system construction and the progress of the carbon peaking and carbon neutrality goals.

References

1. Bose, A.: Smart transmission grid applications and their supporting infrastructure. IEEE Trans. Smart Grid **1**(1), 11–19 (2010)
2. Lai, Y.: Research on Embedded Control Strategy Configuration and Monitoring Configuration Technology. University of Electronic Science and Technology of China (2006)
3. Yilin, S., Xinchu, C.: Research on modular configuration technology of control strategy. Electr. Eng. **2016**(01), 62–65 (2016)
4. Griewank, A., Walther, A.: Evaluating Derivatives: Principles and Techniques of Algorithmic Differentiation. Society for industrial and applied mathematics, USA (2008)
5. Zhang, C., Cheng, Q., Cao, J.: Automatic differential system for C language and its application. Computer Appl. Res. **26**(1), 155–158 (2009)
6. Wang, B., Zhang, R., Feng, G., Manandhar, U., Guo, G.: Event-triggered deadbeat predictive control for DC microgrid. Acta Automatica Sinica **48**(x), 1–11 (2021)
7. Heemels, W.P.M.H., Johansson, K.H., Tabuada, P.: An introduction to event-triggered and self-triggered control. In: Proceedings of the 51st IEEE Conference on Decision and Control, pp. 3270–3285. IEEE, Maui, Hawaii, USA (2012)
8. Wood, A.J., Wollenberg, B.F., Sheble, G.B.: Power Generation, operation, and Control, 3rd edn. Wiley, Hoboken, New Jersey, USA (2014)
9. Geng, G., Jiang, Q.: An automatic differentiation based interior-point method for optimal power flow. Automation of Electric Power Systems **32**(23), 41–45 (2008)
10. Raju, A.P., Amarnath, J., Subbarayudu, D., Reddy, M.R.: First order derivative computation of jacobian matrices in load flow algorithms using automatic differentiation. In: 2011 - 14th International Symposium on Electrets, pp. 81–82 (2011). https://doi.org/10.1109/ISE.2011.6084992

11. Enciu, P., Gerbaud, L., Wurtz, F.: Automatic differentiation applied for optimization of dynamical systems. IEEE Trans. Magn. **46**(8), 2943–2946 (2010). https://doi.org/10.1109/TMAG.2010.2044770

12. Zhang, B., Sun, H., Wu, W.: New GENERATION of EMS with 3-dimensional coordination. Automation of Electric Power Systems **370**(13), 1–6+22 (2007)

13. Dong, S., Tang, K., Liu, L., Zhao, H., Xu, C., Lin, L.: The teaching method of energy storage control experiment based on Simulink and low-code controller. Energy Storage Science and Technology. https://doi.org/10.19799/j.cnki.2095-4239.2021.0723

14. Li, X., Ma, R., Wang, L., Wang, S., Hui, D.:Energy management strategy for hybrid energy storage systems with echelon-use power battery. In: 2020 IEEE International Conference on Applied Superconductivity and Electromagnetic Devices (ASEMD), pp. 1-2 (2020). https://doi.org/10.1109/ASEMD49065.2020.9276135.

Prediction of Day-Ahead Electricity Price Based on N-BEATSx Model Optimized by SSA Considering Coupling Between Features

Feihong Xu[1(✉)], Xianliang Teng[1,2], Jixiang Lu[1,3], Tao Zheng[1,2], and Yulong Jin[1,2]

[1] NARI Group Corporation (State Grid Electric Power Research Institute), Nanjing 211106, China
994192843@qq.com
[2] NARI-TECH Nanjing Control System Ltd, Nanjing 211106, China
[3] State Key Laboratory of Smart Grid Protection and Control, Nanjing 211106, China

Abstract. With the continuous advancement of Chinese electricity market reform, the continuous improvement of the market mechanism and the integration of a large number of new energy sources have brought great challenges to the market's clear electricity price forecast. The new energy output, load data, and tie-line power schedule are fused to obtain an improved input feature variable, which can better reflect the electricity price trend. Then, the maximum information coefficient method (MIC) was used to analyze the correlation between each characteristic variable and electricity price, and an interpretable time series prediction model (N-BEATSx) based on neural network base expansion analysis of fusion characteristic variables was adopted. It is interpretable and can solve nonlinear forecasting problems of time series with the trend, seasonality, and significant random fluctuations. For the selection of hyperparameters in the N-BEATSx prediction model, the sparrow search algorithm (SSA) is used for optimization, the optimal grid structure hyperparameters are obtained with the minimum loss function of the validation set as the objective function. To verify the validity of the proposed model, the Shanxi Province market electricity price data is taken as an example to analyze and compare with other forecasting models, the results show that the proposed model can predict the electricity price of the day before clearing well.

Keywords: Electricity market · Electricity price prediction · Feature coupling · SSA · N-BEATSx model

1 Introduction

In the context of building an electricity market in China, provinces and cities have gradually opened up the electricity sales side and introduced a competition mechanism to reflect the orientation of market-oriented electricity prices based on the behavior of various market players. Therefore, an accurate market electricity price forecast will help

the strategic research of various market entities, so that they can make corresponding decisions according to the electricity price at different times, to obtain corresponding benefits and achieve the purpose of improving efficiency, reducing costs, and promoting the sustainable and healthy development of the power industry [1].

In recent years, the research methods used to solve electricity price prediction are mainly divided into two categories. One is traditional machine learning based on statistics, which learns relevant features from time series data and then makes predictions. The network structure is simple and often relies on feature engineering, but the accuracy rate is high, and related methods include random forest (RF), extreme learning machine (ELM), support vector machine (SVM), extreme gradient boosting (XGB), etc. [2–5]. With the improvement of computer computing power, algorithms based on neural network models have begun to emerge. This is because of its nonlinear modeling ability and excellent parallel ability, making it a model that has been studied more in the field of forecasting, such as multi-layer perception neural network (MLP), feedforward neural network (FFNN), wavelet neural network (WNN) [6–8], etc. The second type of method, deep learning (DL), was born from the condition. At present, it has achieved remarkable results in image recognition and language translation. In recent years, it has been gradually applied in power market load forecasting [9–11] and electricity price Predict [12–14]. Because of its larger model and the ability to deal with large-scale data cross-learning, it can better solve complex prediction problems. To solve the problem that the long-term sequence gradient disappears or explodes in the neural network, some scholars have proposed a long short-term memory network (LSTM) [15], which has better performance than a traditional machine-learning model in many time series problems. The Recurrent Gate Unit Network (GRU) [16] reduces a gating unit based on LSTM, thereby reducing the calculation speed, but it is prone to overfitting and has poor stability. In addition to the LSTM-based architecture mentioned above, an algorithm (N-BEATSx) [17] with a deep stack consisting of fully connected layers connected by forward and backward residual links was proposed in 2019. In the M4 competition, it has demonstrated its advanced performance and is also very computationally efficient. Then the N-BEATSx algorithm [18] improved by scholars adds a stack to the original basis to highlight the influence of characteristic factors, which has a better prediction effect in comparison, but there are 5 key points in the model structure. The hyperparameters, including the learning rate *lr*, the decay rate *decay_lr*, the training batch *b,* and the polynomial degree *P* in the interpretable model and the harmonic parameter *h.* The training batch, learning rate, and decay speed affect the convergence speed of the model, and the polynomial degree and harmonic parameters affect the model's fitting effect on the trend and seasonality, thus affecting the prediction accuracy. Hyperparameters are usually selected by manual experience and retrograde, with poor generality and high uncertainty.

Our main contributions in this paper compared with existing research are summarized as follows.

1) Considering many uncertainties of electricity price forecast, the N-BEATSx model is adopted. Using its double residual mechanism can effectively mine deep data. For the hyperparameters in the model, the sparrow search algorithm is used for optimization, which can avoid the error of human subjective experience, and has better convergence

and global search ability than other optimization algorithms. This combined model has not yet been used in electricity price forecasting algorithms.

2) In terms of input variables, compared with most kinds of literature, temperature, date, load, and new energy output are considered [12–14, 19–21]. This paper studies the relationship between the coupling and electricity price including the characteristics of load, new energy output, and tie-line power schedule, and proposes a new characteristic variable, which can reflect the bidding space of thermal power units and can more effectively reflect the changing trend of market electricity prices.

Several sets of comparative experiments verify that the prediction method proposed in this paper has good reliability and high prediction accuracy.

2 Analysis of the Influencing Factors of Electricity Price

2.1 Maximum Information Coefficient

The maximum information coefficient (MIC) is an excellent calculation method of data correlation, which is used to measure the degree of correlation between two data. It has universality, fairness, and symmetry [21], and has high robustness. Compared with traditional correlation algorithms, it can better reflect the degree of association between attributes [22].

Assuming that there is a binary data set D containing some correlation, divide the binary data into x columns and y rows, and then calculate the probability of each unit in the divided grid G to get the data set on the grid the probability distribution, in this way, the maximum mutual information of the two variables is obtained. After transforming the division directions of the x and y axes, the above method is also used to obtain maximum mutual information, and the two maximum mutual information are normalized and compared. The larger one is the MIC value of the binary data set. The calculation formula for:

$$I^*[D(x, y)] = max(D|G) \tag{1}$$

$$M(D)_{x,y} = \frac{I^*[D(x, y)]}{lgmin\{x, y\}} \tag{2}$$

$$F(D)_{MIC} = \max_{xy \leq B(n)} \{M(D)_{x,y}\} \tag{3}$$

where n is the total number of points in the data set D; $B(n)$ is the correlation constraint of grid division G, generally taken $n^{0.6}$; $M(D)$ is the feature matrix of the data set D, I and I^* are the mutual information and maximum information respectively; F is the MIC value of the data set D, the value range is [0,1], the closer the value is to 1, the stronger the correlation between the two attributes.

2.2   Electricity Price Correlation Analysis

(1)   Electricity load demand

Electricity cannot be stored as easily as other commodities, and its production requires precise timing conditions. Therefore, all supply and demand factors will have a direct impact on the price of electricity in the spot market. In addition to the production cost, when the electricity load demand decreases, the electricity price will decrease, the lower the electricity demand, the more sufficient the competition on the power generation side, and the lower the market electricity price. Therefore, the demand for electricity load has a great influence on the price of electricity, which is one of the main factors that constitute the fluctuation of electricity price.

(2)   Tie-line power schedule

With the continuous improvement of the construction of the power market, most of the power will enter the market for trading, and from the perspective of the Chinese resource endowment, there will be a lot of power transmission from west to east and north to south, so consider the area and accept it. Or the power delivered is also an important factor in predicting the market electricity price.

(3)   New energy output factors

Considering the market policy of giving priority to new energy power generation and the expansion of the scale of new energy units, the amount of new energy power generation is very unstable. If there is more new energy power generation, the thermal power unit will output less, and if there is less new energy power generation, the thermal power unit There will be more output, so the output fluctuation of new energy will always affect the changes in market electricity prices.
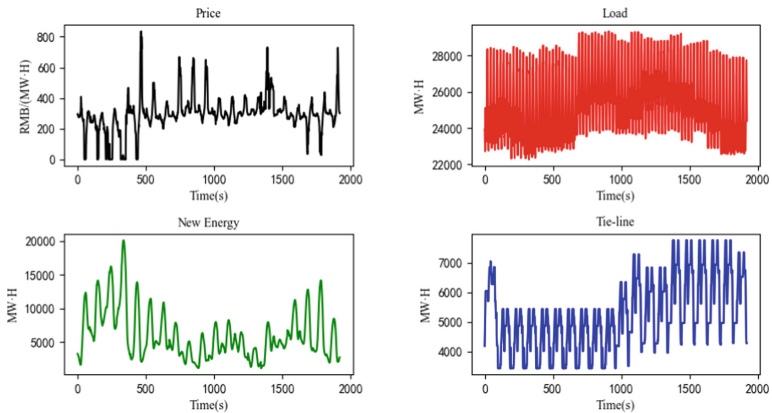
Fig. 1. Load, new energy output, tie-line power schedule, and electricity price curve

Figure 1 shows the correlation curve between electricity price and load, new energy output, and tie-line power schedule in Shanxi Province. To intuitively feel the mapping relationship between electricity price and various influencing factors, it is necessary to use the maximum information coefficient (MIC) method. The specific principle is

briefly described in Sect. 2.1. Compared with the classical Pearson method, this method can mine more nonlinear relationships between features and has higher robustness. This paper selects the data of electricity price, load, tie line plan, and new energy output from June 1st to July 31st, 2021 in China's Shanxi power market. The sampling interval of each type of data is 15 min, and a total of 61 days are collected, through the calculation and analysis of the data sets, the MIC algorithm is used to obtain the correlation between electricity price and load, electricity price and tie-line power schedule, electricity price and new energy output. The analysis results are shown in Table 1, it can be found that the load, new energy output, and electricity price have a high correlation, while the tie-line power schedule has a general correlation with electricity price.

Table 1. Correlation between electricity price and features factors

	Price-Sysload	Price-Tieline	Price-New energy
MIC	0.5207	0.4089	0.5449

With the continuous improvement and construction of the power market, the competitive relationship in the transaction has also been more fully reflected, so to reflect the supply and demand relationship in the power market. This paper explores the coupling relationship between characteristic variables and proposes a new external variable, the bidding space, which is obtained by dividing the output of new energy by the difference between the load and the tie-line power schedule. Received external calls will be sent out, so the difference obtained by subtracting the tie-line power schedule from the load is the net load, which is to be purchased through the electricity market. As the penetration rate of new energy continues to increase, considering the market policy that new energy gives priority to power generation, the output of new energy always affects the operation of thermal power units. Therefore, dividing the output of new energy by the net load can obtain the market supply and demand relationship. Therefore, this article will use the term bidding space to define, that is, the larger the bidding space, the lower the electricity price, and the smaller the bidding space, the higher the electricity price. The specific calculation formula is:

$$bidspace = \frac{newenergy}{space} = \frac{newenergy}{(sysload - tieline)} \tag{4}$$

In the formula: *newenergy* is the output data of new energy, *sysload* is the load demand, and *tieline* is the tie-line plan. According to the MIC correlation coefficient, it is found that its correlation with electricity price reaches 0.5428, which is stronger than that of tie-line power schedule and load. Therefore, this new characteristic variable can theoretically improve the accuracy of electricity price prediction. Will be verified with actual data.

In addition to the relevant influencing factors of electricity price, the time series of electricity price itself can also reflect the trend of electricity price fluctuations. Therefore, to explore the periodic strength of electricity price, the current electricity price sequence

is used as a reference to analyze the relationship between the electricity price sequence in the past time and the current electricity price sequence. To mine the regular information between electricity price series.

Figure 2 shows the correlation between the electricity price series of China's Shanxi electricity market on June 7, 2021, and the electricity price series of previous days, where d-1 represents the electricity price series 1 day ago, and d-2 represents the electricity price series 2 days ago, until the electricity price series 6 days ago. As can be seen from Fig. 1, the color blocks in the upper left corner and the lower right corner are darker, and the correlation coefficient of MIC is higher, while the color of other color blocks is lighter, and the correlation coefficient of MIC is lower, because the electricity price data of these 7 days Two of them are weekends, and the behavior pattern of users' electricity consumption is different from that of working days, which also reflects the obvious periodicity of electricity price data. And it can be seen that for the forecast day, the electricity prices of the two days before the forecast date have a high correlation. Therefore, in the subsequent forecast model, the electricity prices of the past two days will be used to predict the electricity price of the current day.
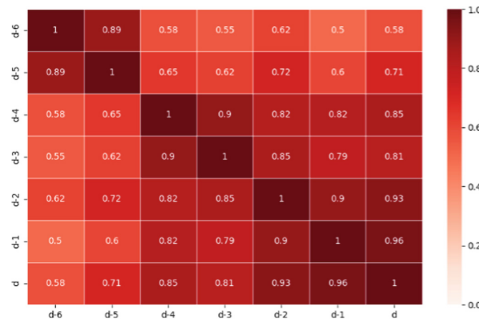
Fig.2. Heatmap between historical electricity price and current electricity price based on MIC

3 Related Theories and Methods

3.1 N-BEATSx Model

Interpretable Time Series Forecasting Based on Neural Network Base Extension Analysis of Fused Feature Variables (N-BEATSx) is a deep learning architecture based on forward and backward residual links, which is suitable for a wide range and deep expressive time series forecasting model, and this pure deep learning model can explain the time series very well through its architecture.

The N-BEATSx network model is an improved algorithm based on neural basis expansion analysis for interpretable times series forecasting (N-BEATS). Compared with the N-BEATS model, which only receives the target variable corresponding to the backtracking period, that is, by establishing an interpretable model of the trend function (Eq. 13) and the seasonal function (Eq. 14), the N-BEATSx model A new layer of feature
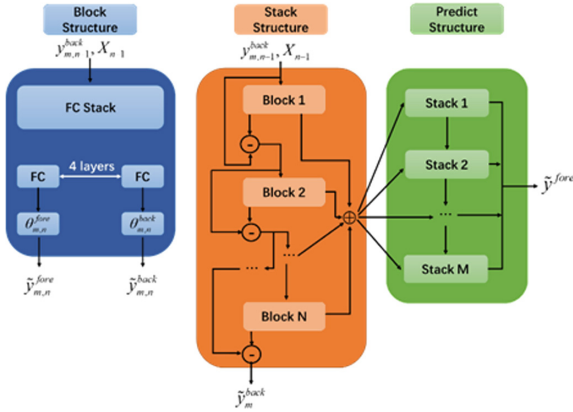
Fig. 3. N-BEATSx model structure diagram

structure (Eq. 15) is added to the interpretability model, which is used to enhance the learning of correlation in the series through the input of feature variables. For example, it can learn long-term seasonal effects from date variables. The network structure is shown in Fig. 3, and the working method is as follows:

(1) Block structure

$$f_{m,n} = Fcnn_{m,n}(y_{m,n-1}^{back}, X_{n-1}) \tag{5}$$

$$\theta_{m,n}^{back} = Linear^{back}(f_{m,n}) \tag{6}$$

$$\theta_{m,n}^{fore} = Linear^{back}(f_{m,n}) \tag{7}$$

$$\tilde{y}_{m,n}^{back} = K_{m,n}^{back}\theta_{m,n}^{back} \tag{8}$$

$$\tilde{y}_{m,n}^{fore} = K_{m,n}^{fore}\theta_{m,n}^{fore} \tag{9}$$

(2) Stack structure

$$y_{m,n+1}^{back} = y_{m,n}^{back} - \tilde{y}_{m,n}^{back} \tag{10}$$

$$\tilde{y}_m^{fore} = \sum_{n=1}^{N} \tilde{y}_{m,n}^{fore} \tag{11}$$

(3) Prediction structure

$$\tilde{y}^{fore} = \sum_{n=1}^{N} \tilde{y}_m^{fore} \tag{12}$$

(4)   Interpretable structure

$$\tilde{y}_{m,n}^{trend} = \sum_{i=0}^{P} t^i \theta_{m,n,i}^{trend} \tag{13}$$

$$\tilde{y}_{m,n}^{sea} = \sum_{i=0}^{H/2-1} cos(2\pi i \frac{t}{h})\theta_{m,n,i}^{sea} + sin(2\pi i \frac{t}{h})\theta_{m,n,i+H/2}^{sea} \tag{14}$$

$$\tilde{y}_{m,n}^{ex} = \sum_{i=0}^{Nx} X_i \theta_{m,n,i}^{ex} \tag{15}$$

In the formula: *Fcnn* is the fully connected neural network, $(y_{m,n-1}^{back}, X_{n-1})$ is the input data, $f_{m,n}$ is the number of hidden layers, $\left(\theta_{m,n}^{back}, \theta_{m,n}^{fore}\right)$ are the learning coeffi-cients of backward prediction and forward prediction, respectively, $\left(K_{m,n}^{back}, K_{m,n}^{fore}\right)$ are the backward and forward basis vectors of the block, and $\left(\tilde{y}_{m,n}^{back}, \tilde{y}_{m,n}^{fore}\right)$ is the backward and forward prediction components in the block transformed by the basis vector respec-tively, $y_{m,n+1}^{back}$ are the residuals of the previous prediction, which will be learned as the input variables of the next level, $\tilde{y}_m^{fore}$ are the prediction components output by a stack, $\tilde{y}^{fore}$ are the final output of the entire model, time vector $t^T = [0, 1, 2, ..., H]/H, H$ is the step size of the time series, P is the maximum polynomial degree which is the coefficient of the trend model, h is a hyperparameter, plays the role of suppressing harmonics, N_X is the number of characteristic variables, and $X = [X_1, X_2, ..., X_{Nx}]$ is the characteristic vector.

3.2   SSA Intelligent Optimization Model

Sparrow Search Algorithm (SSA) is a new type of swarm intelligence optimization algorithm, which was proposed in 2020, mainly inspired by the foraging behavior and anti-predation behavior of sparrows. In the process of foraging for sparrows, it is divided into a producer and a scrounger. The finder is responsible for finding food in the pop-ulation and provides foraging areas and directions for the entire sparrow population, while the joiner uses the finder. to get food. To obtain food, sparrows can usually forage using two behavioral strategies, finder, and joiner. Individuals in a population moni-tor the behavior of other individuals in the population, and attackers in the population compete for food resources with their high-intake peers to increase their predation rate. In addition, sparrow populations engage in anti-predation behavior when they become aware of the danger.

The sparrow collection looks like this:

$$X = \begin{bmatrix} X_{11} & X_{12} & ... & X_{1d} \\ X_{21} & X_{22} & ... & X_{2d} \\ ... & ... & ... & ... \\ X_{n1} & X_{n2} & ... & X_{nd} \end{bmatrix} \tag{16}$$

where n is the scale of the sparrow and d is the dimension of the variable.

The fitness values of sparrows are as follows:

$$Fit(X) = \begin{bmatrix} f([X_{11}\ X_{12}\ ...\ X_{1d}\ ]) \\ f([X_{21}\ X_{22}\ ...\ X_{2d}\ ]) \\ ...\ ...\ ... \\ f([X_{n1}\ X_{n2}\ ...\ X_{nd}\ ]) \end{bmatrix} \qquad (17)$$

Among them, each row represents the fitness value of each individual.

During each iteration, the scrounger position update formula is:

$$X_{i,j}^{t+1} = \begin{cases} X_{i,j}^t \cdot \exp(-\frac{i}{\alpha \cdot iter_{max2}}), & ifR_2 < ST \\ X_{i,j}^t + Q \cdot L, & ifR_2 \geq ST \end{cases} \qquad (18)$$

Among them, t represents the current iteration number, $j = 1, 2, 3, ..., d$, $iter_{max}$ is a constant representing the maximum number of iterations. $X_{i,j}$ represents the position of the i-th sparrow in the j-th dimension. $\alpha \in (0, 1]$ is a random number. $R_2 (R_2 \in [0, 1])$ and $ST (ST \in [0.5, 1])$ represent the warning value and the safety value, respectively. Q is a random number that obeys normal distribution. L is represented as a $1 \times d$ matrix where each element in the matrix is all one.

At the time of $R_2 < ST$, this meant that there were no predators around the foraging environment at this time, and the finder could execute a wide range of search operations. If $R_2 \geq ST$ this means that some sparrows in the population have detected a predator and alerted the rest of the population, all of which need to fly quickly to other safe places to forage.

The location update for joiners is described as follows:

$$X_{i,j}^{t+1} = \begin{cases} Q \cdot \exp(\frac{X_{worse} - X_{i,j}^t}{i^2}), & if i > n/2 \\ X_P^{t+1} + \left| X_{i,j} - X_P^{t+1} \right| \cdot A^T (AA^T)^{-1} \cdot L, & otherwise \end{cases} \qquad (19)$$

Among them, X_P is the optimal position currently occupied by the finder, and X_{worse} represents the current global worst position. A represents a $1 \times d$ matrix, in which each element is randomly assigned to 1 or -1. At that time of $i > n/2$, this indicates that the i-th joiner with a lower fitness value did not get food and was in a very hungry state. At this time, he needs to fly to another place to forage for more energy.

The vigilante's location update is described as follows:

$$X_{i,j}^{t+1} = \begin{cases} X_{best}^t + \beta \left| X_{i,j}^t - X_{best}^t \right|, & if f_i > f_g \\ X_{i,j}^t + K \cdot \left(\frac{\left| X_{i,j}^t - X_{worse}^t \right|}{(f_i - f_w) + \varepsilon} \right), & if f_i = f_g \end{cases} \qquad (20)$$

Among them, X_{best} is the current global optimal position. β as a step size control parameter, it is a random number that obeys a normal distribution with a mean of zero and a variance of one. $K \in [-1, 1]$ is a random number, and f_i is the fitness value of the current sparrow individual, f_g and f_w are the current global best and worst fitness values. ε is constant to avoid zeros in the denominator.

4   SSA-N-BEATSx Prediction Model

4.1   Data Preprocessing

Due to the influence of unstable factors such as equipment failure and human interference during the data collection process, there are usually abnormal data in the collected data. Abnormal electricity price data will affect the accurate prediction of electricity prices. Therefore, outlier processing is performed on the collected data, and the steps are as follows.

Step 1: Use the box plot to discriminate the data, as shown in Fig. 4, it can be seen that there are a small number of abnormal values in the electricity price and new energy forecast, which will be cleaned through step 2.
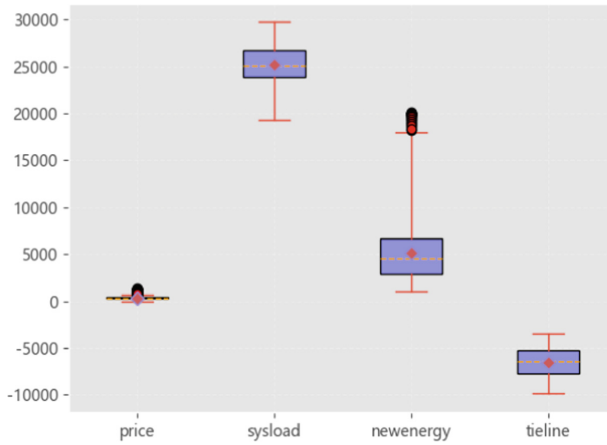
Fig. 4. Unusual data detected by boxplots

Step 2: Removing the above outliers will result in partial missing of time series data. To ensure the prediction effect, it is necessary to fill in the missing data. Missing values can be imputed using Lagrange interpolation [23].

Since the characteristics of the neural network activation function make it sensitive to data in [0, 1], it is necessary to normalize the input.

$$y = \frac{x - x_{\min}}{x_{\max} - x_{\min}}$$ (21)

In the formula: y is the normalized data, x is the input data, x_{min} is the minimum value of the input data, x_{max} is the maximum value of the input data.

4.2   SSA-N-BEATSx Prediction Model

After the data is processed, the SSA-N-BEATSx network model is constructed to predict the electricity price data of the next day through the electricity price data and eigenvectors

of the past two days. N-BEATSx takes Mean Absolute Error (MAE) as the loss function, Adam is used as the optimizer, considering the uncertainty of the learning rate lr、decay speed $decay\_lr$、train bitch b、the polynomial degree P and harmonic parameter h in the interpretable model, so combined with artificial Based on the range value given by experience, the Sparrow Smart Optimization Algorithm (SSA) is used to find the optimal solution of the parameters through iteration, to bring it into the model to calculate the final predicted value.

The flowchart of the SSA-N-BEATSx model is shown in Fig. 5:
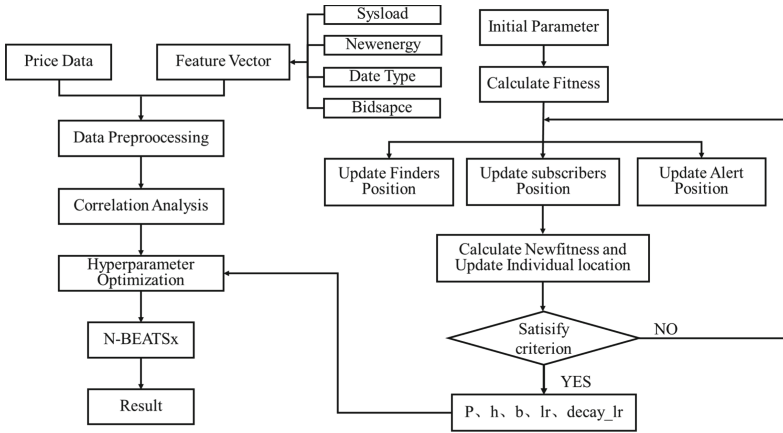
Fig. 5. SSA-N-BEATSx model flowchart

4.3 Model Comparison Design

(1) Input variable comparison

To study the influence of the proposed feature variables on the prediction accuracy of the model, multiple sets of different input parameters were selected to construct a variety of prediction models, and the model output was 96 electricity price series on the predicted day.

Model 1: This model fully considers the model of various input variables, and adds relevant characteristic variables, such as load, new energy output, and data type, because the temperature characteristics have been considered in the calculation of load forecast and new energy output forecast. Therefore, the temperature factor is not added here.

Model 2: Based on Model 1, this model especially considers the coupling between feature relationships, and introduces the feature quantity of bidding space. The specific meaning and correlation have been described above, and theoretically its prediction effect is the best.

(2) Algorithm structure comparison

To verify that the proposed model has better predictability than traditional neural networks, the following comparison models are proposed.

Model A: VMD-LSTM model + input variables in model 2

Model B: N-BEATSx model (only considers temporality in the original sequence)

Model C: N-BEATSx model + Input Variables in Model 2

Model D: SSA-N-BEATSx model + input variables in model 2

The experiment of setting model A is because Variational Mode Decomposition (VMD) is a common time series decomposition method, which can decompose a series with large fluctuation into multiple high-frequency components and low-frequency components with certain time characteristics. Components, which can be used as a comparison with the interpretable model that comes with the N-BEATSx model. The experiment of setting model B is to test the pure N-BEATSx model, which has little dependence on feature engineering and can use its performance to mine strong relationships in the original sequence.

5 Case Analysis

5.1 Parameter Setting

The SSA parameter settings include the number of sparrows participating in the search n is 10, the learning rate *lr*, the learning decay speed *decay_lr*, the polynomial degree *P*, the harmonic parameter *h*, and the training batch *b* are five parameters optimized and initialized to form a 10×5 search matrix, using MAPE as the fitness function, and select 100 for the maximum number of iterations *iter* is considered in many experiments, the convergence is reached at about 50 iterations. The specific optimization results are shown in Table 2 and Fig. 6.

Table 2. Optimization results of SSSA-N-BEATSx parameters

Iterative update times	lr	decay_lr	P	h	b	Fitness
1	0.001	0.5861	3.2126	1.8955	32	0.0305
2	0.0006	0.6451	2.8359	1.417	106	0.0281
3	0.0075	0.7614	2.5708	1	179	0.0270
4	0.0082	0.7988	2.2893	1	125	0.0248
5	**0.0083**	**0.7628**	**2.4332**	**1**	**128**	**0.0229**

5.2   Evaluation Indicators

The evaluation indicators used root mean square error (RMSE), mean absolute error (MAE), mean absolute percentage error (MAPE), and symmetric mean absolute percentage error (SMAPE), the formula is as follows.

$$RMSE = \sqrt{\frac{1}{n}\sum_{i}^{n}(\tilde{y}_i - y_i)^2} \tag{22}$$

$$MAE = \frac{1}{n}\sum_{i}^{n}|\tilde{y}_i - y_i| \tag{23}$$

$$MAPE = \frac{100\%}{n}\sum_{i=1}^{n}\left|\frac{\tilde{y}_i - y_i}{y_i}\right| \tag{24}$$

In the formula, $\tilde{y}_i$ is the predicted value of electricity price, y_i is the actual value of electricity price.
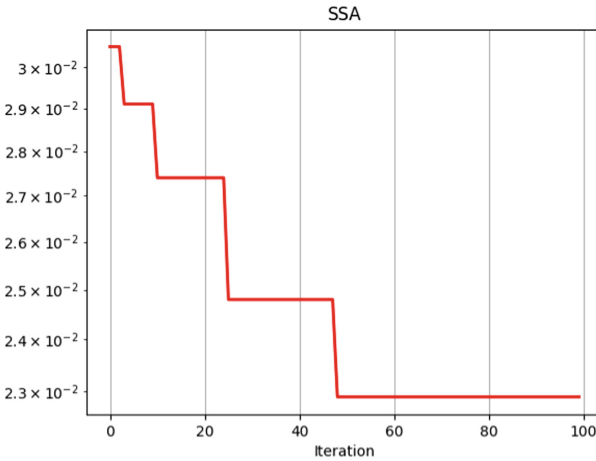
Fig. 6. Fitness optimization curve of SSSA-N-BEATSx parameters

5.3   Prediction Example

In this paper, the Keras library in deep learning is used to build the SSA-N-BEATSx model. The experimental data set to select the electricity price, load, new energy output, and tie-line power schedule of the Shanxi electricity market from June 1 to July 31, 2021, as Data set to predict the electricity price of the Shanxi electricity market at the next 96 min on August 1, 2021. The following first compares the prediction effect of electricity price under different input characteristics through experiments.

As can be seen from Table 3, whether it is the N-BEATSx model or the LSTM model, the error of Model 2 is the smallest, and the MAPE is reduced by 21.6% and 15.5%,

respectively, which reflects the power transfer between areas in this paper. Increasing the importance of the characteristic variable of bidding space can better reflect the characteristics of electricity prices and improve the prediction accuracy compared with the traditional simple single characteristic variable.

Then, the prediction effects of electricity prices under different algorithm structures are compared through experiments, as shown in Table 4 and Fig. 7.

Table 3. Model prediction error under different input

Model	Algorithm	MAE	MAPE	RMSE
1	N-BEATSx	16.024	4.062%	20.829
2	**N-BEATSx**	**12.719**	**3.184%**	**17.569**
1	LSTM	32.438	8.898%	39.493
2	LSTM	26.665	7.523%	32.702

Table 4. Model prediction error under different alogrithms

Model	Algorithm	MAE	MAPE	RMSE
A	VMD-LSTM	26.432	6.932%	34.909
B	N-BEATSx	21.347	5.383%	25.792
C	N-BEAYSx (excluded features)	12.319	3.184%	17.569
D	**SSA-N-BEAYSx**	**8.542**	**2.229%**	**11.728**
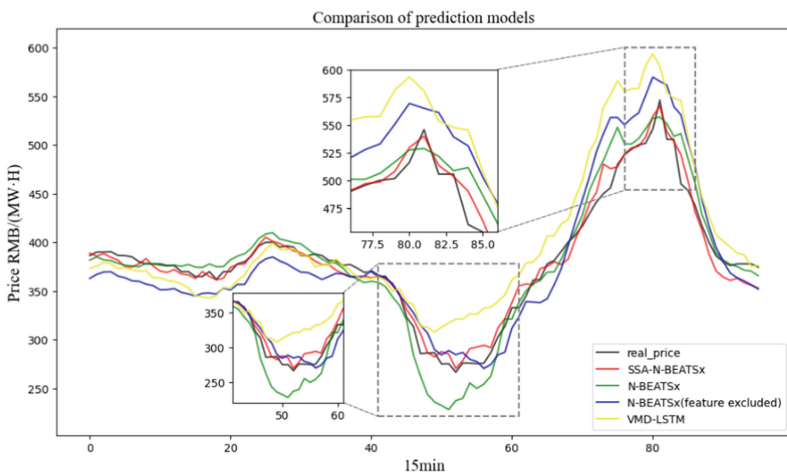
Fig.7. Price prediction curve under different algorithms

Observing Table 4, comparing model A and model B, it can be found that using the pure deep learning N-BEATSx model without considering additional feature variables, the prediction effect is still better than the model based on the traditional deep learning LSTM algorithm, MAE, MAPE and RMSE decreased by 19.2%, 22.3%, and 26.1%, respectively. It can be seen that the N-BEATSx model is better than the traditional LSTM deep learning algorithm in data mining, and its explanatory structural design also makes the algorithm better than VMD-LSTM for better predictions. Because through the algorithm of time series decomposition, whether it is STL, EMD, or VMD, sequence decomposition residues will appear, which will bring certain errors to the prediction model. Comparing Model C and Model D, it can be found that the model optimized by the Sparrow Algorithm (SSA) has higher prediction accuracy than the model without optimization, MAE, MAPE, and RMSE decreased by 30.6%, 27.3%, and 30.0%, respectively, it can be seen that the selection of hyperparameters plays a crucial role in the prediction of the model. This is because the selection of P and h parameters affects the fitting of the model trend and seasonality. If the value is too high or too low, the unit structure inside the model will lose its original meaning. Looking at Fig. 7, you can see that the model proposed in this paper has a good prediction effect on the entire 96-point time series, especially in the peak and valley period, compared with other algorithms, it has a higher degree of the fitting. Overall better predictive performance.

6 Conclusion

This paper proposes a characteristic variable that considers the load, new energy output, and tie-line power schedule, and the coupling relationship between the characteristics, which represents the degree of influence on the electricity price, and constructs the SSA-N-BEATSx model to compare with other traditional deep learning algorithms. The data of the Shanxi power market are verified, and the main conclusions are as follows.

(1) This new characteristic variable, which refers to the tie-line power schedule and characteristic coupling relationship, has the same strong correlation with the electricity price series itself and with the historical load and new energy output, compared with only considering the load and time. These characteristics of new energy output can better reflect the supply and demand relationship in the market, reflect the fluctuation of the electricity price that has been cleared recently, and have been verified through the comparison model, which better improves the accuracy of electricity price forecasting, and has a certain universality.

(2) As a newly proposed deep learning algorithm, the N-BEATSx model is rarely used in electricity price forecasting, but as a pure deep learning model, its interpretable structure proves that it is better than the general time series decomposition based on statistical principles. The prediction model has a better effect, such as variational mode decomposition (VMD), and the calculation speed is faster, which can be widely used in time series prediction in the future.

(3) The Sparrow Algorithm (SSA) is used to iteratively optimize the network hyperparameters, which solves the shortcomings of poor model versatility and high uncertainty caused by manual experience selection.

References

1. Zou, Y., Teng, X., Wang, Y., et al.: Electricity price forecast based on stacked autoencoder in spot market environment. In: Proceedings of the 2019 Academic Annual Meeting of the Electricity Market Professional Committee of the Chinese Society for Electrical Engineering and the National Electricity Trading Institutions Alliance Forum, pp. 308–315 (2019)
2. Wei, Q., Chen, S., Huang, W., et al.: Forecasting method of clearing price in spot market by random forest regression. Proceedings of the CSEE **41**(04), 1360–1367+1542 (2021)
3. Shen, Z.: Research on Electricity Price Forecast Based on Extreme Learning Machine and MapReduce. Donghua University (2019)
4. Chen, J., Tao, C., Ma, G., et al.: Forecasting method of spot market clearing price based on data mining and support vector machine. Power System and Clean Energy **36**(10), 14–19+27 (2020)
5. Wang, D., Luo, H., Grunder, O., et al.: Multi-step ahead electricity price forecasting using a hybrid model based on two-layer decomposition technique and bp neural network optimized by firefly algorithm. Appl. Energy **190**, 390–407 (2017)
6. Dudek, G.: Multilayer perceptron for GEFCom2014 probabilistic electricity price forecasting. Int. J. Forecast. **32**(3), 1057–1060 (2016)
7. Peesapati, R., Kumar, N.: Electricity price forecasting and classification through wavelet–dynamic weighted PSO–FFNN approach. IEEE Syst. J. **12**(4), 3075–3084 (2017)
8. Pindoriya, N.M., Singh, S.N., Singh, S.K.: An adaptive wavelet neural network-based energy price forecasting in electricity markets. IEEE Trans. Power Syst. **23**(3), 1423–1432 (2008)
9. Lu, J., Zhang, Q., Yang, Z., et al.: Short-term load forecasting method based on CNN-LSTM hybrid network model. Automation of Electric Power Systems, pp. 1–7 (2019)
10. Shen, Y., Zhang, J., Liu, J.: Short-term load forecasting of power system based on similar day method and PSO-DBN. In: 2018 2nd IEEE Conference on Energy Internet and Energy System Integration (EI2), pp. 1–6 (2018)
11. Feng, R., Zhao, L., Yang, Y., et al.: LSTM short-term load forecasting model considering electricity price and attention mechanism. Science and Technology Bulletin **36**(11), 57–62, 68 (2020)
12. Yin, H., Ding, W., Chen, S., et al.: Day-ahead electricity price forecasting of electricity market with high proportion of new energy based on LSTM-CSO model. Power System Technol. **46**(02), 472–480 (2022)
13. Han, S., Hu, F., Chen, Z., et al.: Day-ahead market marginal price forecasting based on GCN-LSTM. Proceedings of the CSEE **42**(09), 3276–3286 (2022)
14. Wu, W., Liao, W., Miao, J., et al.: Using gated recurrent unit network to forecast short-term load considering impact of electricity price. Energy Procedia **158**, 3369–3374 (2019)
15. Hochreiter, S., Schmidhuber, J.: Long short-term memory. Neural Comput. **9**(8), 1735–1780 (1997)
16. Cho, K., Van Merriënboer, B., Gulcehre, C., et al.: Learning phrase representations using RNN encoder-decoder for statistical machine translation. In: Proceedings of the 2014 Conference on Empirical Methods in Natural Language Processing (EMNLP), pp. 1724–1734 (2014)
17. Oreshkin, B.N., Carpoy, D., Chapados, N., et al.: N-BEATS: neural basis expansion analysis for interpretable time series forecasting. In: 8th International Conference on Learning Representations, ICLR (2020)

18. Olivares, K.G., Marciasz, G., et al.: Neural Basis Expansion Analysis with Exogenous Variables: Forecasting Electricity Prices with NBEATSx. ArXiv preprint arXiv: 2104.05522 (2021)
19. Zhao, Y., Wang, X., Jiang, C., et al.: A novel short-term electricity price forecasting method based on correlation analysis with the maximal information coefficient and modified multi-hierarchy gated LSTM. Proceedings of the CSEE **41**(01), 135–146+404 (2021)
20. Xuefeng, J.I.A., Cunbin, L.I.: Real-time electricity price forecasting of electricity market using DeepESN considering short-term load impact. Smart Power **49**(01), 64–70 (2021)
21. Justin, B.K., Gurinder, S.A.: Equitability mutual information and the maximal information coefficient. PNAS **111**(9), 3354–3359 (2014)
22. Wang, Z., Song, H., Li, S., et al.: Process monitoring based on logarithmic transformation and maximal information coefficient-PCA. Science Technology and Engineering **17**(16), 259–265 (2017)
23. Zhou, J., Zhang, J.: Interpolation model and statistical data test and application. Statistics and Decision (5): 78–80 (2016)

Adaptability Analysis of Asynchronous Interconnected LCC-HVDC with Additional Frequency Control Strategy

Yifei Jin[1], Lin Ye[1(✉)], Yongning Zhao[1], Wei Chen[2], Yuqi Han[2], and Yunche Su[2]

[1] College of Information and Electrical, China Agricultural University, Beijing 100091, China
yelin@cau.edu.cn
[2] State Grid Sichuan Economic Research Institute, Chengdu 610000, China

Abstract. Two AC systems that are asynchronously interconnected will have the problem of lack of mutual support ability due to blocking the sharing of frequency modulation resources. In order to improve the frequency response characteristics of the asynchronous interconnected system, an additional frequency control strategy (AFC) with line commutated converter based HVDC (LCC-HVDC) participation is proposed. The strategy improves the transient characteristics of the system frequency response by adding frequency-var additional control. And the strategy also improves the voltage stability of the grid frequency regulation process by adding voltage-var additional control and adjusting the switching mode of the AC filter in LCC-HVDC. Finally, an equivalent model is built in PSCAD/EMTDC. The adaptability of LCC-HVDC to the proposed additional frequency control strategy is analyzed by a case study.

Keywords: LCC-HVDC · Additional Frequency Control · Frequency Response Characteristics · Frequency Response Indicators · Adaptability Analysis

1 Introduction

In recent years, high-voltage direct current (DC) transmission technology in China has been developed and applied at a high speed. One of its technologies, the voltage source converter based high voltage direct current transmission (VSC-HVDC) technology has the advantages of strong controllability, high sensitivity, decoupled active and reactive power output, etc. Not limited by the short-circuit capacity of the alternating current (AC) grid, VSC-HVDC has a wide range of prospects in different regions, such as AC grid asynchronous interconnection, new energy grid connection, island operation, and other fields [1]. Dozens of VSC-HVDC projects have been put into operation in China and abroad, mainly utilized in offshore wind power grid connection, long-distance DC transmission, AC grid asynchronous interconnection, and other practical scenarios [2].

Asynchronous interconnection of power systems can effectively improve the safety and stability of interconnected regional grids. There is no AC channel, avoiding the transmission of tidal currents via AC lines when DC blocking occurs, then, the problem

of inter-regional power angle instability is effectively suppressed. By isolating the two interconnected regional grids through DC lines, the frequency phases can be different between the regions, and faults on one side of the system will not be transmitted to the other side to avoid the expansion of accidents. In addition, the DC control response time is short, and the control purpose can be achieved quickly after the fault is cleared, which can make the system recover to a stable state quickly [3].

Related studies have conducted extensive research around the access of new energy generation to the asynchronous interconnected grid and the participation of new energy in flexible DC transmission systems. Reference [4] analyzes the fault characteristics on the AC side of the flexible DC feeder, and the results shows that the zero-sequence current protection can still correctly identify the ground fault when wind power is connected to the flexible direct system. In reference [5], the transient characteristics of asynchronous interconnection to islanding are studied, and the increase of unit start-up and unit rotation standby in the islanding can reduce the frequency fluctuation during the fault recovery.

Among them, the research on new energy participating in asynchronous interconnection frequency regulation mainly includes fault ride-through control strategy [6], droop control strategy [7], virtual inertia control strategy [8], and so on. Reference [9] studies the problem of a doubly-fed induction generator (DFIG) participating in power grid frequency regulation via VSC-HVDC grid connection. It is proposed that the greater the inertia of the DC capacitor, the greater the DFIG reserve capacity, and the better the frequency regulation effect of the two synergies. Reference [10] proposes that photovoltaic power generation is connected to the flexible interconnection area, and the virtual inertia time constant when the frequency of the receiving end power grid is artificially coupled affects the stability of the system frequency.

Existing research focuses on the frequency regulation in the process of asynchronous interconnection fault recovery and the frequency regulation of new energy grid connections, without considering the coordination effect of additional frequency control strategies.

To solve the problem of lack of mutual support capability, an additional frequency control strategy with line commutated converter based HVDC (LCC-HVDC) participation is proposed in this paper. Firstly, the DC transmission system structure and control mode are introduced, and an additional frequency control strategy for asynchronous interconnection is proposed, which can further improve the frequency transient characteristics of the system and voltage stability during frequency regulation. Finally, the adaptability of LCC-HVDC to the proposed additional frequency control strategy is analyzed by building an equivalent model simulation in PSCAD/EMTDC.

The rest of this paper is structured as follows. The structure and control mode of HVDC transmission system is described in Sect. 2. An asynchronous interconnection additional frequency control strategy is presented in Sect. 3. Case study is presented in Sect. 4. The conclusions are drawn in Sect. 5.

2   Structure and Control Mode of HVDC Transmission System

2.1   LCC-HVDC Transmission System Model

The general DC transmission system, also known as the LCC-HVDC system, which adopts a converter valve based on thyristor commutation control, and the basic converter unit is a 12-pulse converter containing two converter valves. The schematic diagram of the steady-state operation of the bipolar DC system is shown in Fig. 1.
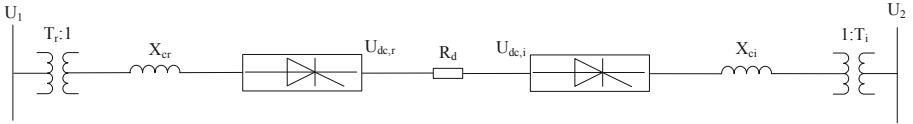
Fig. 1. Schematic diagram of steady-state operation of bipolar DC system.

The steady-state operation equation of the bipolar LCC-HVDC transmission system is as follows:

$$\begin{cases} U_{dc,r} = U_{dc,or}\cos\alpha - R_{cr}I_{dc} \\ U_{dc,or}\cos\alpha = RI_{dc} + U_{dc,oi}\cos\beta \\ U_{dc,i} = U_{dc,oi}\cos\beta - R_{ci}I_{dc} \\ R = R_{cr} + R_{dc} + R_{ci} \end{cases} \tag{1}$$

Where $U_{dc,or}$ is the ideal no-load DC voltage of the rectifier, $U_{dc,oi}$ is the ideal no-load DC voltage for the inverter, X_{cr} and X_{ci} are the equivalent reactance of rectifier side and inverter side converter transformers, $R_{cr} = 3X_{cr}/\pi$, $R_{ci} = 3X_{ci}/\pi$, $U_{dc,r}$ and $U_{dc,i}$ are the DC voltages on the rectifier side and the inverter side respectively, R_{dc} is the DC transmission line resistance, α is the trigger angle of the rectifier, β is the trigger angle of the inverter, I_{dc} is the Current in the DC Transmission Line.

Common control methods for DC transmission systems are as follows:

(1) Constant DC current control

Keep the DC current I_{dc} constant at the set value by controlling the trigger angle α or β.

(2) Constant DC voltage control

Keep the DC voltage constant at the set value by controlling the trigger angle α or β. This process is generally completed through the voltage regulation link on the inverter side.

(3) Fixed rectifier side minimum trigger angle control

If the trigger angle on the rectifier side is too small, the forward voltage on the thyristor will be too low, which is not conducive to the stability of the commutation process.

(4) Fixed inverter side maximum trigger angle control

By controlling the maximum trigger angle of the inverter side, the inverter side trigger angle caused by the overshoot of the controller in special cases is avoided, thereby avoiding the problem of commutation failure.

(5) Low Voltage Current Limit Control

The low voltage current limit control can limit the DC current when the DC voltage is reduced to avoid commutation failure and help the system to return to normal.

When the LCC-HVDC rectifier station is connected with the VSC-HVDC inverter station, the coordinated control without delay can be realized through the transmission of the control signal.

2.2 VSC-HVDC System Model

For the VSC-HVDC or VSC-MTDC power transmission system, the converter station has a greater impact on the frequency change. The main parts of the converter station are VSC converters, converter transformers, converter reactors, and filters [11]. The one-line diagram of the VSC system is shown in Fig. 2.
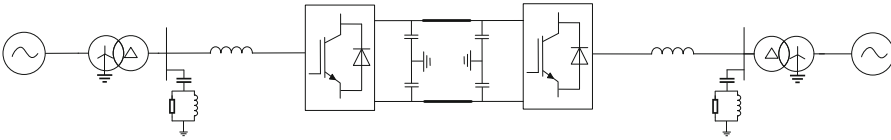
Fig. 2. One-line diagram of the VSC system.

The steady-state operation equation of the VSC converter is.

$$\begin{cases} P_v = U_v U_c Y_c \sin \sigma \\ Q_v = U_v U_c Y_c \cos \sigma + U_v^2 Y_c \\ P_c = P_v = U_{v,dc} I_{v,dc} \\ Q_c = Q_v \\ U_c = \frac{\mu M}{\sqrt{2}} U_{v,dc} \end{cases} \tag{2}$$

where P_c and Q_c are the active and reactive power absorbed by VSC converter respectively, $X_{v,c}$ is the commutation reactance of VSC converter, $Y_c = 1/\sqrt{R_c^2 + X_{v,c}^2} \approx 1/X_{v,c}$, $\sigma = \theta_t - \theta_c$, θ_t and θ_c are the voltage phase angles of the AC side busbar and the VSC valve side busbar respectively, P_v and Q_v are the active power and reactive power injected into the VSC converter for the AC bus respectively, U_c is the AC voltage on the limiting valve side of the VSC converter, μ is DC voltage utilization, M is VSC converter modulation ratio.

The common control methods of the VSC-HVDC system are divided into active power control and reactive power control. The active power control method includes:

(1) Constant DC voltage control.

$$U_{dc} = U_{dc}^{ref} \tag{3}$$

(2) Constant active power control.

$$U_{dc} I_{dc} = P_{dc}^{ref} \tag{4}$$

Where U_{dc}^{ref} is the DC voltage reference, P_{dc}^{ref} is the active power reference value.

The reactive power control method includes:

(1) Constant AC voltage control.

$$U = U^{ref} \tag{5}$$

(2) Constant reactive power control.

$$Q_c = Q_c^{ref} \tag{6}$$

Where U^{ref} is the AC Voltage Reference value, Q_c^{ref} is the reactive power reference value.

3 Asynchronssous Interconnection Additional Frequency Control Strategy

When a fault occurs in the asynchronous interconnected AC system, the DC modulation caused by the fault will affect the frequency and voltage stability of the AC system. This paper proposes an additional frequency control strategy with LCC-HVDC participation as shown in Fig. 3, including the frequency-var additional control, voltage-var additional control and frequency controller additional control.
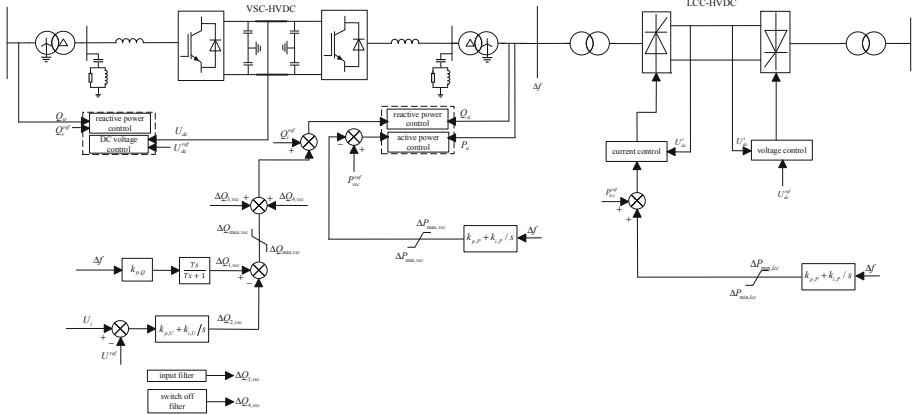
Fig. 3. Additional frequency control strategy diagram.

In Fig. 3, $\Delta P_{\max,lcc}$ is the maximum limit for LCC-HVDC active power regulation, $\Delta P_{\min,lcc}$ is the minimum limit for LCC-HVDC active power regulation, $\Delta P_{\max,vsc}$ is the maximum limit for VSC-HVDC active power regulation, $\Delta P_{\min,vsc}$ is the minimum limit for VSC-HVDC active power regulation, $k_{p,P}$ and $k_{i,P}$ are PI parameters of the additional frequency controller.

3.1 Frequency-Var Additional Control

When the active power of the AC system is unbalanced, the stability of the frequency of the AC system can be improved by adjusting the active load. Therefore, the frequency-var additional control is added to the constant reactive power control link of the VSC-HVDC inverter station. Then adjust the reactive power emitted by the VSC-HVDC inverter station so that the voltage change causes the voltage-sensitive active load to change, thereby suppressing frequency fluctuations. The frequency-var additional control structure diagram is shown in Fig. 4.

$$\Delta f \longrightarrow \boxed{k_{p,Q}} \longrightarrow \boxed{\frac{Ts}{Ts+1}} \quad \Delta Q_{1,vsc} \longrightarrow$$
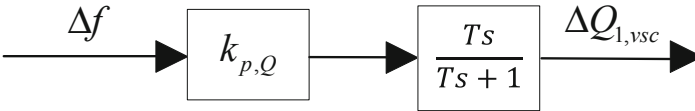
Fig. 4. Frequency-var additional control structure diagram.

In Fig. 4, $\Delta f = f - f^{ref}$, $k_{p,Q}$ is the frequency-reactive additional controller gain time constant, T is the time constant of the DC blocking link, which is used to generate the frequency differential signal, $\Delta Q_{1,vsc}$ is the reactive power regulation of VSC-HVDC.

When the system frequency drops, the LCC-HVDC rectifier station reduces the active power absorbed from the system, injects reactive power into it and then raises the bus voltage.

3.2 Voltage-Var Additional Control

In the process of frequency regulation of the asynchronous interconnection system, when the voltage fluctuates, the VSC-HVDC inverter station will automatically compensate the reactive power according to the voltage deviation and control the voltage near the reference value. When the reactive power regulation capacity of the VSC-HVDC inverter station reaches the maximum value, the LCC-HVDC rectifier station needs to switch the AC filter. At this time, the VSC-HVDC quickly replenishes the reactive power and restores the original state to suppress the voltage mutation caused by switching the filter. The voltage-var additional control structure diagram is shown in Fig. 5.

$$U_i \longrightarrow \otimes \longrightarrow \boxed{k_{p,U} + k_{i,U}/s} \quad \Delta Q_{2,vsc} \longrightarrow$$
$$\underset{+}{} \quad \underset{-}{}$$
$$U^{ref}$$
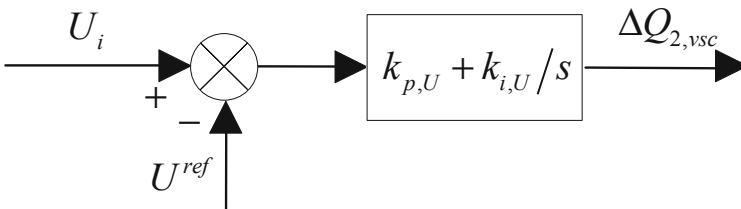
Fig. 5. Voltage-var additional control structure diagram.

In Fig. 5, U_i is the amplitude of the AC voltage on the inverter side, $k_{p,U}$ and $k_{i,U}$ are PI parameters of the voltage-var additional controller, $\Delta Q_{2,vsc}$ is the reactive power regulation of VSC-HVDC.

3.3 Frequency Controller Additional Control

The VSC-HVDC transmission system can usually coordinate and control the power transmission of new energy with independent active power and reactive power, and the wind power photovoltaic penetration rate of the grid on the rectifier side is high, which reduces the inertia of the AC system and increases the system's resistance to frequency fluctuations. Risk. Therefore, by changing the active power command value and reactive power command value of the system, the generator speed of the AC system can be changed, thereby affecting the frequency stability of the system.

The control process of the additional control of the frequency controller is divided into two parts:

The first stage is when the active power unbalances occur in the system, the LCC-HVDC rectifier station and the VSC-HVDC inverter station are put into the additional control link of the frequency controller at the same time to achieve the purpose of quickly suppressing the system frequency fluctuation.

The second stage is to start and stop the additional frequency control link of the VSC-HVDC inverter station according to the active power adjustment after entering the frequency recovery stage. If the active power regulation capacity of LCC-HVDC is still surplus, the VSC-HVDC inverter station exits the additional frequency control link.

4   Case Study

The case study section studies the adaptability of Longquan-Zhengping LCC-HVDC to additional frequency control. Based on the PSCAD/EMTDC simulation software, the electromagnetic transient simulation model of the HVDC asynchronous interconnection transmission system is established. And the adaptability of LCC-HVDC to additional frequency control strategy in asynchronous interconnection transmission system is analyzed.

4.1   System Setting

The simulation example of LCC-HVDC adopts a quasi-steady model, which equals the generated power and load demand respectively. The LCC-HVDC rectifier station adopts the constant power control mode and calculates the DC reference value according to the reference value of the active power and the actual value of the DC voltage, to obtain the trigger angle command of the rectifier station. The LCC-HVDC inverter station adopts a constant voltage control method to maintain a constant voltage value of the DC line.

The VSC-HVDC simulation example adopts a single-converter multi-DC wiring scheme based on a half-bridge modular multilevel converter (MMC), which consists of a back-to-back converter unit. The rated transmission power of the unit is 1000 MW, and the rated voltage of the DC side is $\pm$ 300 kV. The converter transformer adopts

a single-phase double-winding structure with a rated capacity of 300 MV• A. Among them, MMC modeling adopts a behavioral model, which can synthesize the operating characteristics of the blocking state and the non-blocking state, and has a high simulation accuracy while reducing the complexity of the modeling.

The control system model of VSC-HVDC can be divided into the dual-unit layer, single-unit layer, and converter layer according to the function. The dual-unit layer contains control functions such as inter-unit coordinated control, AC voltage control, and additional control. The single-unit layer includes functions such as DC voltage control, active power control, reactive power control, and blocking and unlocking control. The converter layer includes functions such as phase-locked loop control, fault ride-through control, and current decoupling control.

The parameter settings of the system are shown in Table 1. The parameter settings of the Fig. 4 and the Fig. 5 refer to the paper [12].

In Table 1, $U_{\min}^f$ is the lower limit of the dead zone of the constant voltage control of the AC filter.

Table 1. Parameter settings.

Parameter	Value	Parameter	Value
$k_{p,P}$	300	$\Delta P_{\max,vsc}$	200 MW
$k_{i,P}$	500	$\Delta P_{\min,vsc}$	−200 MW
$k_{p,Q}$	400	$\Delta Q_{\max,vsc}$	300 MVar
$k_{p,U}$	10	$\Delta Q_{\min,vsc}$	−300 MVar
$k_{i,U}$	50	U^{ref}	1.007 p.u
T	8 s	$U_{\min}^f$	1.005 p.u
$\Delta P_{\max,lcc}$	300 MW	$\Delta P_{\min,lcc}$	−300 MW

Compare and analyze the control effects of the following two control methods:

(1) asynchronous interconnection system without additional frequency controller (without control).
(2) asynchronous interconnection system with an additional frequency controller shown in Fig. 3 (Additional Frequency Control).

In the actual operation of the power grid, the frequency fluctuation of the asynchronous interconnection transmission system is mainly divided into two cases. One is the loss of power generation of the system, such as when a trip accident occurs, the power generation is less than the load, and the system frequency decreases; the other is the system load loss. When the generated power is greater than the load, the system frequency increases. During the simulation and verification in this paper, two disturbance situations, the system load drop and the load increase are respectively set to analyze the the adaptability of LCC-HVDC to the proposed additional frequency control strategy.

4.2   Frequency Response Characteristic Indicators

In order to evaluate the frequency response characteristics of the asynchronous interconnection system, the following three frequency analysis indicators are used to analyze the frequency response characteristics of the system [13]. The better the frequency response characteristics of LCC-HVDC, the stronger its adaptability to the proposed additional frequency control strategy.

a. Rate of change of frequency (RoCoF), marked as r_{ocof}. It is defined as the rate of frequency change when the system performs inertia response before a frequency modulation action after a system failure. This indicator reflects the inertia response characteristics of the system, The larger r_{ocof} is, the worse the inertia response characteristics.

b. Frequency Nadir (FN), marked as f_{nadir}. It is defined as the system frequency point with the largest deviation from the normal frequency before a frequency modulation action makes the system frequency return to normal. This indicator reflects the frequency transient response characteristics of the system. The greater the deviation of f_{nadir} from the normal frequency, the worse the transient characteristics of the frequency response of the system. Therefore, When f_{nadir} is lower than the system load shedding frequency threshold, it means that the spare capacity of the system for primary frequency regulation is insufficient.

c. Settling Frequency (SF), marked as f_{sf}. It is defined as the system frequency after one frequency modulation action is over. Since the primary frequency modulation is a differential frequency modulation, there is a deviation between f_{sf} and the normal frequency. The greater the deviation, the worse the steady-state characteristic of the system frequency response.

4.3   Results and Discussion

The frequency stability of the asynchronous interconnected LCC-HVDC system is simulated and analyzed below to verify the rationality of the proposed additional frequency control strategy and its parameter settings. And the adaptability of LCC-HVDC to additional frequency control strategy in asynchronous interconnection transmission system is analyzed.

(1) The system reduces the load by 150 MW.

The simulation graph of the system reducing the 150 MW load is shown in Fig. 6.

It can be seen from Fig. 6, after the system loses the load, the system frequency first increases rapidly, and then through the joint adjustment of the additional frequency control and the unit speed regulation, the stable operation is quickly restored, and finally stabilized at 60.26 Hz.

The active power absorbed by LCC-HVDC is reduced to suppress the rise of the system frequency. The results of the frequency response index are shown in Table 2.

It can be seen from Table 2 that the RoCoF and settling frequency of the system after the additional frequency control strategy is adopted are significantly reduced compared with those without control, indicating that the strategy can ensure the stability of the system frequency when the system reduces the load.

(2) The system increases the load by 150 MW.
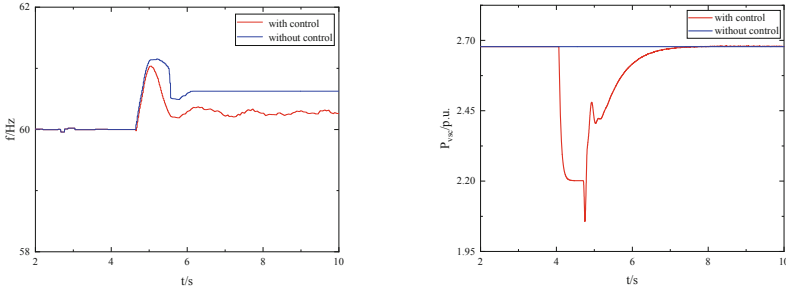
Fig. 6. Simulation waveform of the system reducing 150 MW load. The left picture is the system frequency, while the right one is the active power absorbed by LCC-HVDC.

Table 2. Frequency response indicators of case 1.

Control method	r_{ocof}/(Hz• s^{-1})	f_{nadir}/Hz	f_{sf}/Hz
With AFC	2.6410	61.0354	60.2660
Without AFC	2.8974	61.1456	60.6254
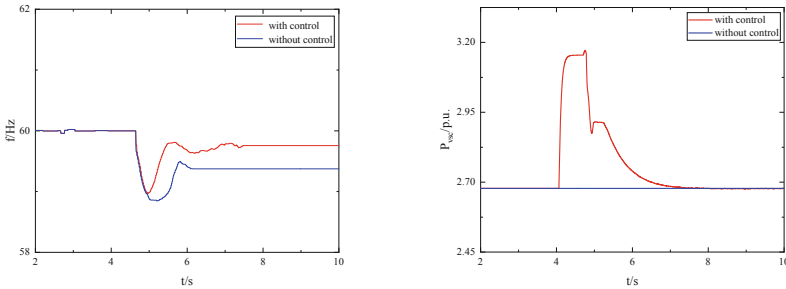
Fig. 7. Simulation waveform of the system increasing 150 MW load The left picture is the system frequency, while the right one is the active power absorbed by LCC-HVDC.

The simulation graph of the system increasing 150 MW load is shown in Fig. 7.

In Fig. 7, after the system increases the load, the system frequency first drops rapidly, and then the additional frequency control starts and participates in frequency adjustment, and the system frequency gradually recovers to 59.78 Hz.

The active power absorbed by LCC-HVDC increases and the downward trend of the system frequency is suppressed. The results of the frequency response index are shown in Table 3.

In Table 3, compared with the no-control method, the frequency stability of the system after using the additional frequency control strategy is stronger, and the frequency

Table 3. Frequency response indicators of case 2.

Control method	r_{ocof}/(Hz· s^{-1})	f_{nadir}/Hz	f_{sf}/Hz
With AFC	1.9859	59.0567	59.7841
Without AFC	2.3325	58.8428	59.3662

response characteristics of the system are significantly improved. The LCC-HVDC has good adaptability to the proposed DC control strategy.

Comparing the simulation results in Tables 2 and 3, it can be found that the additional frequency control strategy proposed in this paper can effectively suppress the frequency fluctuation and alleviate the frequency stability issues caused by the asynchronous interconnection whether the asynchronous interconnection grid with LCC-HVDC participated increases or decreases the load.

5   Conclusion

Based on analyzing the feasibility of additional frequency control between LCC-HVDC and VSC-HVDC, this paper proposes an additional frequency control strategy suitable for LCC-HVDC asynchronous interconnection operation mutual support and builds an equivalent frequency control strategy in PSCAD/EMTDC. The model simulation analyzes the adaptability of LCC-HVDC to the DC frequency control strategy. The results show that the LCC-HVDC has good adaptability to the proposed additional control strategy, which can effectively suppress the frequency fluctuation of the asynchronous interconnected grid and reduce the instability effect caused by the system frequency regulation process.

The parameters of the additional frequency control strategy proposed in this paper are obtained through simulation analysis, focusing more on the principle verification of the control strategy, and further in-depth research will be carried out according to the actual project engineering.

References

1. Castro, L.M., Acha, E.: On the dynamic modeling of marine VSC-HVDC power grids including offshore wind farms. IEEE Trans. Sustain. Energy **11**(4), 2889–2900 (2020)
2. Sihang, W., Xiangyu, Z., Wenxuan, J., et al.: A modular multilevel converter with integrated energy dissipation equipment for offshore wind VSC-HVDC system. IEEE Trans. Sustain. Energy **13**(1), 353–362 (2022)

3. Yi, C., Dichen, L., Jun, W., et al.: Emergency generator tripping control method for sending end of asynchronous interconnection system. Elec. Power Autom. Equipment **38**(8), 131–137 (2018)
4. Liming, Z., Ke, J., Tianshu, B., et al.: AC-side fault analysis of a VSC-HVDC transmission system connected to offshore wind farms and the impact on protection. Power Syst. Prot. Control **49**(20), 20–32 (2021)
5. Qichao, C., Hui, L., Wenchuan, W., et al.: Stability control strategy for conversion from grid-tied to island operation of asynchronous interconnected power grids based on VSC-HVDC. Elec. Power Autom. Equipment **40**(4), 32–39 (2020)
6. Xiangwu, Y., Desheng, W., Xiaoxue, W., et al.: Research on the wind power-storage joint control based on fault ride-through and frequency regulation of wind turbine. Proc. CSEE **41**(17), 5911–5922 (2021)
7. Yuanyuan, T., Qingfen, L., Dichen, L., et al.: Droop control strategy for wind power decentralized integration based on VSC-HVDC systems. Autom. Elec. Power Syst. **40**(3), 103–109 (2016)
8. Huibiao, Y., Qi, J., Li, X., et al.: Virtual inertia control strategies for double-stage photovoltaic power generation. Autom. Elec. Power Syst. **43**(10), 87–94 (2019)
9. Shenglu, L., Tingting, S., Jiejie, H., et al.: Dynamic power flow algorithm with coordinated regulation of power system frequency with DFIG and VSC-HVDC. Power Syst. Technol. **43**(12), 4433–4439 (2019)
10. Yongan, D., Liyan, D., Yan, X.: Frequency regulation for PV generation connected to an interconnection area by VSC-HVDC. Power Syst. Protect. Control **49**(6), 1–9 (2020)
11. Mochamad, R.F., Preece, R.: Assessing the impact of VSC-HVDC on the interdependence of power system dynamic performance in uncertain mixed AC/DC systems. IEEE Trans. Power Syst. **35**(1), 63–74 (2020)
12. Jia, L., Yongjun, X., Wei, Y., et al.: Reactive power coordinated control for improving transient characteristics of DC side of LCC-HVDC using parallel VSC-HVDC. Power Syst. Technol. **46**(1), 101–110 (2022)
13. Lingkang, Z., Dahu, L., Wei, Y., et al.: Dual-loop supplementary frequency control for BTB-VSC-HVDC. Elec. Power Autom. Equipment **38**(12), 113–120 (2018)

Coordinated Frequency Regulation Method for Offshore Wind Farm Connected Through an HVDC Link Based on Droop Control

Qiang Li[1,2], Huachun Han[1,2(✉)], and Weijia Tang[1,2]

[1] Jiangsu Electric Power Test and Research Institute Company, Nanjing 211103, China
598543427@qq.com
[2] State Grid Jiangsu Electric Power Company Electric Power Research Institute, Nanjing 211103, China

Abstract. In order to suppress the disturbance of the frequency of the onshore AC power grid due to the grid connection of offshore wind farm, this paper proposes a coordinated control method of frequency support of offshore wind farm connected through an HVDC link based on droop control, and establishes a simulation system of measurement-feedback-adjustment of nearest level approximation modulation (MFR-NLM) of onshore converter station and offshore converter station. Firstly, the simulation model of offshore wind farm connected through an HVDC link system is established, and the model uses modular multilevel converter (MMC) and NLM modulation. Secondly, the mathematical function expression of the DC voltage setting signal and the measured value of the voltage, the frequency setting signal and the measured value of the frequency are constructed based on the droop control method. Finally, the improved recent level modulation method of the additional DC voltage controller and frequency controller are designed to realize a new type of measurement-feedback-regulation control of onshore converter stations and offshore converter stations. The simulation results show that the proposed method can convert the AC frequency signal and the DC voltage signal to each other, so that the offshore wind farm can change the power output according to the frequency deviation, and realize the frequency support of the onshore AC power grid.

Keywords: Offshore Wind Farm · HVDC · Droop Control · Frequency Support

1 Introduction

As clean energy, wind power has developed rapidly in recent years. Compared with onshore wind power, offshore wind power has more abundant wind resources [1]. Long-distance offshore wind farms usually use permanent magnet synchronous generators for power generation, which are integrated into the onshore grid through an HVDC link [2]. Due to the uncertainty of wind power [3], wind farms cannot adjust their output power according to dispatching instructions in real time, so the grid connection of offshore

wind power will affect the frequency of the onshore AC power grid, so the output power of offshore wind farm must be controlled [4, 5]. In addition, when the frequency of the onshore power grid changes due to load changes or faults, the offshore wind farm can participate in the frequency support. That is, with or without communication method [6], two-terminal [7] or multi-terminal [8–10] HVDC lines are controlled [11]. In order for offshore wind farms to recognize the frequency deviation of the onshore grid and make a response, the control methods of the onshore converter station [12] and the offshore converter station need to be modified [13].

In order to provide frequency support for the onshore AC power grid, reference [14] proposed a mathematical model for the offshore wind farm connected through VSC-HVDC link to identify the onshore frequency deviation and respond to the frequency support by using the droop control principle, but did not study how to determine the droop coefficient. Reference [15] proposed the calculation method of the droop coefficient, designed the DC voltage controller of the converter and the offshore wind farm controller, and realized the frequency support of the offshore wind farm connected through an HVDC link system to the power grid, but did not study the offshore wind farm frequency control of the field bus. Reference [16] proposed a method for offshore wind farm voltage source converter (WFVSC) to control the frequency of offshore wind farms, and established a model of power flow distribution for each converter station of multi-terminal HVDC transmission. The frequency support of the multi-terminal HVDC system to the AC power grid is improved, but the additional capacitor equipment will increase the construction investment. Reference [17] proposed a ratio-based multi-terminal VSC-HVDC frequency support method, which does not depend on the parameters and structure of the AC circuit, but has a large time delay and cannot respond within tens of milliseconds. Reference [18] directly estimates the frequency deviation of the onshore AC power grid according to the terminal DC voltage of the offshore converter station, and controls the offshore wind farm to quickly respond to the power, and realizes the real-time frequency support for the onshore power grid. However, the accuracy of this method is not enough, and the frequency support limited ability. Reference [19] proposed a method to update the droop coefficient when the VSC-HVDC system fails, which improved the stability of the VSC-HVDC system, but did not study the power response. Reference [20] proposed an automatic frequency control (AFC) strategy for offshore wind farms to support the grid frequency, but the response of this method has a delay of several hundred milliseconds, which cannot meet the requirements of fast response.

Aiming at the above problems, this paper proposes a droop control-based coordinated frequency modulation control method for offshore wind farm connected VSC-HVDC link. The onshore converter adopts DC voltage control, simulates the frequency-power droop curve of the synchronous generator, measures the frequency deviation of the onshore power grid, and converts it into a variable DC voltage setting signal and adds it to the modulation process of the NLM signal. The result is a change in output power. Offshore converters use frequency control and power control. Since the wind farm simulation model in this paper adopts a permanent magnet synchronous generator, the offshore converter uses the frequency-power droop characteristics of the synchronous generator

to control the output power of the offshore wind farm according to the changing frequency setting value. Compared with the virtual synchronous generator control method, the control process of the droop control is relatively simple, and no power oscillation occurs.

2   Design of Converter Control Mode

The key to offshore wind farm connected through an HVDC link is to control the modulation signals of the onshore and offshore converters. The onshore converter converts the frequency deviation signal of the onshore AC grid into the DC voltage change of the HVDC system, and the offshore converter converts the DC voltage change information of the HVDC system into the frequency deviation signal of the offshore wind farm. When the offshore wind farm recognizes the signal, it adjusts its own power output based on the change of the signal. The offshore wind farm connected through an HVDC link is shown in Fig. 1.
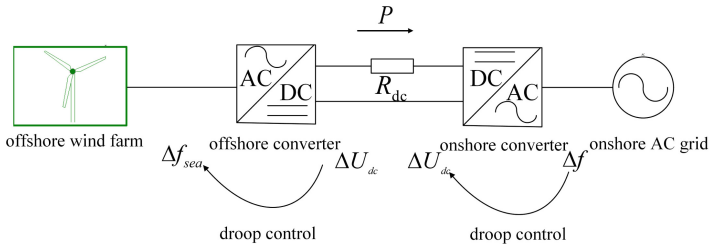
Fig. 1. Offshore wind farm-HVDC system diagram

2.1   Control of Onshore Converter

The onshore converter is responsible for inverting the direct current of the HVDC system, and sending the inverted electric energy into the alternating current grid. The received nearest voltage level (NLM) signal of the onshore converter can control the conduction time and conduction angle of the IGBT. Before generating the NLM signal, the NLM signal generator will first receive the modulation signal, and the modulation signal is the key to simulate the synchronous generator to realize the droop control of the onshore converter. The modulation signal includes V_{on}^{set}, which represents the set voltage at the end of the HVDC transmission line, that is, the set voltage of the onshore converter. In a general VSC-HVDC system, the converter connected to the transmission end grid also has a set voltage, which is equal to the reference voltage at the end of the HVDC system and is a fixed value. However, in the onshore converter mentioned in this paper, in order to transmit the onshore frequency deviation information, it is necessary to add droop control and make the setting voltage a quantity that can be changed in real time according to the onshore frequency deviation.

The formula of the droop curve can be obtained as shown in (1):

$$f = f_{ref} + K(P - P_{ref}) \tag{1}$$

The droop control curve is shown in Fig. 2.
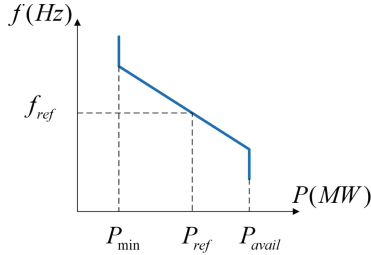
Fig. 2. Frequency-power droop diagram

In the formula, f is the actual frequency of the AC power grid, f_{ref} is the reference frequency of the AC power grid and takes 50 Hz, K is the droop coefficient, and P is the active power of the HVDC transmission line flowing to the converter station. P_{ref} is reference output power for onshore converters. Equation (1) shows that the onshore converter should change its transmission power according to the frequency change of the onshore power grid. Here, the onshore converter does not directly change its own transmission power, but transmits the grid frequency deviation signal to the offshore wind farm side, and the offshore wind farm will change the output power according to this signal. In this way, it is ultimately manifested as a change in the transmission power of the onshore converter.

In order to transmit the frequency deviation signal of the onshore power grid, the DC setting voltage of the onshore converter should be made a variable quantity. On the basis of the reference voltage, two changing components can be added. One component is proportional to difference between the actual frequency of the power grid and the reference voltage. In this paper, the change of the setting voltage will eventually cause the change of the transmission power of the HVDC system. It can be considered that the setting voltage of the onshore converter is a function of the transmission power of the HVDC system, so the transmission power can be regarded as another one component, the expression for the DC set voltage is shown in (2).

$$V_{on}^{set} = V_{on}^{ref} + K_f(f - f_{ref}) - K_p P \tag{2}$$

In the formula, V_{on}^{ref} is the reference voltage of the onshore converter. The control block diagram of V_{on}^{set} is shown in Fig. 3.

The amount of change of V_{on}^{set} is proportional to the amount of change in the frequency of the AC grid, that is, $\Delta V_{on}^{set} = K \Delta f$. The function of transmitting the frequency deviation information of the AC power grid to the HVDC system is realized by V_{on}^{set}. In this expression, V_{on}^{set} and V_{on}^{ref} are per unit values. The values of K_f and K_p are specified
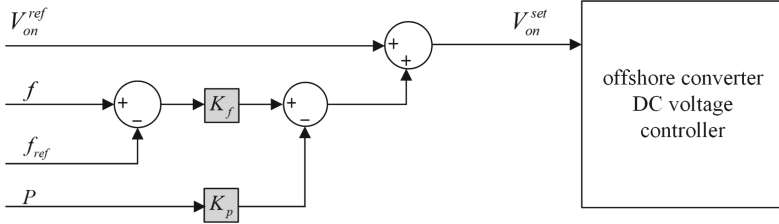
Fig. 3. Onshore converter droop control

as formulas (3) and (4).

$$K_f = \frac{0.02 + K_p P}{\Delta f_{max}} \tag{3}$$

$$K_p = \frac{R_{dc}}{V_{on}^{ref}} \tag{4}$$

In the above formula, in order to simplify the control process, let Δf_{max} be a fixed value, because the frequency deviation of the power grid is usually within $\pm 0.2 Hz$, and the value of Δf_{max} can be 0.2. The resistance per unit length of the DC transmission line is 0.0181, and the offshore wind farm distance is more than 50 km [15], so the value of R_{dc} is 0.905 Ω, and the value of V_{on}^{ref} is 1 (the nominal DC voltage of the HVDC system is 100 kV).

After applying the modulation method designed in this paper to the onshore converter, the onshore converter will measure the frequency deviation of the AC side and respond, that is, according to the value of V_{on}^{set} changed by the droop control, thereby changing the DC voltage of the HVDC system.

2.2 Control of Offshore Converter

The AC side of the offshore converter is connected to the offshore wind farm, and the DC side is connected to the HVDC system. In 1.1, the set voltage at the end of the HVDC system has changed, which leads to a change in the actual voltage at the same end. The role of the offshore converter here is to convert the voltage change information of the HVDC system into an offshore wind farm changes in AC frequency.

In the control process of the onshore converter, it has been set that the DC voltage variation of the HVDC system is proportional to the frequency variation of the onshore AC system. Therefore, in order to make the frequency variation of the offshore wind farm reflect the frequency deviation of the onshore AC power grid, the frequency variation of the offshore wind farm is also proportional to the variation of the DC voltage of the HVDC system. Comparing the above formula, the expression that can be constructed in formula (5).

$$f_{sea}^{set} = f_{sea}^{ref} + K_V (V_{off}^{set} - V_{off}^{ref}) \tag{5}$$

Where f_{sea}^{ref} is the reference value of the offshore wind farm frequency, f_{sea}^{set} is the set value of the offshore wind farm frequency, V_{off}^{ref} is the reference voltage of the offshore converter, and V_{off}^{set} is the set voltage of the offshore converter. The control block diagram of the offshore converter station is shown in Fig. 4.
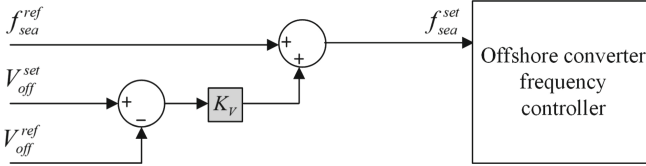
Fig. 4. Offshore converter droop control

Due to the existence of the resistance of the DC transmission line, the voltage drop will occur on the transmission line, and the active power loss will be generated. According to this, the calculation formula of V_{off}^{ref} and V_{off}^{set} can be calculated according to the values of V_{on}^{ref} and V_{on}^{set}. That is, in formula (5), we have

$$V_{off}^{set} = V_{on}^{set} + \frac{P}{V_{on}^{set}} R_{dc} \tag{6}$$

$$V_{off}^{ref} = V_{on}^{ref} + \frac{P}{V_{on}^{ref}} R_{dc} \tag{7}$$

The frequency support of the offshore wind farm connected with HVDC link system requires a response within tens of milliseconds. The method proposed in this paper does not rely on communication equipment. Both the offshore converter station and the onshore converter station adopt the local control method, which can meet the requirements of rapid response. The offshore converter station performs feedback adjustment by measuring the voltage change on the DC side of the converter, and transmits the DC voltage change signal converted from the frequency deviation signal of the onshore grid to the offshore wind farm. So far, the frequency deviation signal of the onshore AC power grid has been successfully transmitted to the offshore wind farm side through the HVDC system.

3   Design of Control Mode for Offshore Wind Turbine

In Sect. 1, this paper adopts the droop control method for the onshore and offshore converters, and realizes the function of transmitting the frequency deviation signal of the onshore AC grid to the offshore wind farm, that is, the offshore wind farm can identify the frequency deviation of the onshore grid. It can be considered that the originally independent offshore wind farm and the onshore AC grid have a certain coupling relationship through the droop control method, and this coupling relationship is based on the signal transmission without communication mode. The onshore power grid requires

a frequency support response within tens of milliseconds, and this communication-free control method can meet the frequency support time requirements.

The offshore wind farm mentioned in this paper uses permanent magnet synchronous generators, which can perform droop control when the wind speed and the power output are stable. In addition, permanent magnet synchronous generator uses full power converters, so its output power can be precisely adjusted and equivalent [4]. At this time, the frequency-power of the offshore wind farm satisfies the formula (8).

$$f_{sea} = f_{sea}^{ref} + K_{fsea}(P_{out} - P_{ref}) \qquad (8)$$

In the formula, f_{sea} is the actual frequency of the offshore wind farm, f_{sea}^{ref} takes the value of 50 Hz, K_{fsea} is the power coefficient, P_{out} is the active power actually emitted by the offshore wind farm, and P_{ref} is the active power output when the actual frequency of the offshore wind farm is equal to the reference frequency.

The value of K_{fsea} can be obtained according to the simulation test, it is equal to the slope of the frequency-power droop characteristic curve of the offshore wind farm. The offshore wind farm can be directly connected to the load, and part of the load can be suddenly cut off at a certain time, so that the frequency of the offshore wind farm will increase. At this time, another set of measured values of frequency f_{sea}^m and power P_{out}^m is obtained. We have.

$$K_{fsea} = \frac{f_{sea}^m - f_{sea}^{ref}}{P_{out}^m - P_{ref}} \qquad (9)$$

When the frequency of the onshore AC grid changes, according to the frequency-power droop curve of the synchronous generator, in order to bring the grid frequency back to the reference value of 50 Hz, the output power of the offshore wind farm must be changed. In this paper, the frequency setting value f_{sea}^{set} of the offshore wind farm is used as an intermediate variable, which is set by the offshore converter. According to formula (8), as long as the output power P_{out} of the offshore wind farm is adjusted so that the actual frequency f_{sea} of the offshore wind farm reaches f_{sea}^{set}, then P_{out} at this time is the target power output for frequency support of the offshore wind farm connected through an HVDC link collaborative control system.

In order to find the output power P_{out} of an offshore wind farm, both Under-frequency and overfrequency conditions need to be considered.

(1) Under the condition of underfrequency, according to the frequency-power droop characteristic curve, the offshore wind farm should increase the output, therefore, the offshore wind farm should have enough power margin when it is in operation. The power output of the offshore wind farm in operation shall not exceed 90% of the maximum power of the wind turbine at the current wind speed. Under the condition of underfrequency, in order to increase the power output, we can make

$$P_{out}' = 1 + K_{over}(f_{sea}^{set} - f_{sea}^{ref}) \qquad (10)$$

$$K_{over} = \frac{0.4 f_{sea}^{ref}}{V_{off}^{ref}} \qquad (11)$$

In the formula, P'_{out} is the underfrequency power gain coefficient, and K_{over} is the underfrequency correction coefficient.

(2) Under the condition of overfrequency, the power output response of PMSM can be divided into inertia response and governor response. The inertial response of the power is proportional to the rate of change of the offshore wind farm frequency, and the governor response will take into account the DC side voltage variation of the offshore converter. Under overfrequency conditions, in order to reduce the power output, it is possible to make:

$$P''_{out} = -K_{in}\frac{df_{sea}}{dt} + \frac{f_{sea}^{ref}(V_{off}^{set} - V_{off}^{ref})}{K_{gov}V_{off}^{set}} \tag{12}$$

$$K_{in} = \frac{2Hf_{sea}^{ref}}{V_{off}^{ref}} \tag{13}$$

In the formula, P''_{out} is the output power of offshore wind farm under the condition of overfrequency. K_{in} is the inertia coefficient. K_{gov} is the governor coefficient, takes the value of 0.01. And H is the inertia constant, takes the value of 4.

Combining Eq. (10) and (12), the offshore wind farm output is obtained as

$$P_{out} = 0.9P_{set} \times P'_{out} + P''_{out} \tag{14}$$

The method used in this paper controls the power output of the offshore wind farm, so that the offshore wind farm can participate in the frequency support of the onshore AC grid, whether it is due to the frequency deviation caused by the onshore AC grid itself, or due to the uncertainty of offshore wind farm. The resulting frequency deviation can be supported by this method to support the frequency of the onshore AC grid.

4   Analysis of Simulation Results

4.1   Simulation Model Parameter Settings

The installed capacity of the offshore wind farm model used in this paper is 250 MW, the wind turbine is a permanent magnet synchronous generator, the wind speed is 12 m/s, the wind speed is constant, and the power output of the wind turbine can reach the maximum. The onshore AC power grid has an installed capacity of 1000 MW and a load of 800 MW. The total resistance value of the HVDC transmission line is 0.905 Ω. Other detailed system parameters are shown in Table 1, as suggested by [4]. The recovery problems of wind turbines after frequency modulation and the influence of AGC and inertia of onshore units is not considered in the simulation.

4.2   Model Simulation Under Underfrequency Conditions

In the 10th s of the simulation, the onshore AC grid increases the load of 100MW, and the onshore AC grid enters the underfrequency operation state.

Table 1. Parameter table of offshore wind farm connected through an HVDC link system

Items	Value
Offshore Wind Farm Reference Frequency	50 Hz
Offshore wind farm bus voltage	50 kV
Resistance per unit length of HVDC transmission lines	0.0181 Ω/km
Total length of HVDC transmission lines	50 km
DC nominal voltage of HVDC transmission line	100 kV

(a) Onshore AC grid frequency

(b) DC setting-voltage

(c) DC Voltage

(d) Offshore wind farm setting-frequency

(e) Offshore wind farm frequency

(f) Offshore wind farm power output
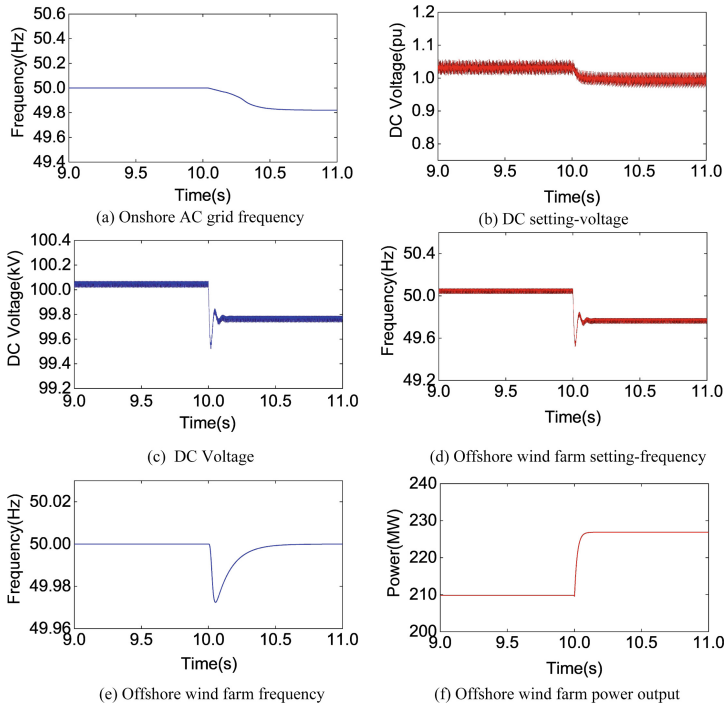
Fig. 5. Simulation results under underfrequency conditions

Figures 5 and 6 are simulation results under underfrequency operation. At the 10.00 s, the onshore power grid is put into 100MW load, and the 10.00 s-10.50 s is the transient response stage. After 10.50 s, the offshore wind farm connected an HVDC link system reaches a steady state again. At this time, the frequency of the onshore power grid is 49.82 Hz. The base value of DC setting-voltage is 100 kV, which is the same as the nominal voltage of the DC link.

Figures 5(a) and (b) show that before the 10.00th second, the frequency of the onshore grid is 50 Hz, and the per-unit value of the DC voltage of the HVDC system is 1.02. After 10.00 s, the onshore converter responded quickly, and the per-unit value of the DC voltage dropped to 0.99. The onshore converter met the demand for rapid response and converted the frequency deviation signal into a voltage change signal. Figure 5(c) and (d) show that before the 10.00th second, the voltage of the HVDC system is 100.03 kV, and the frequency of the offshore wind farm is set to 50.02 Hz. After the 10.00th second, the DC voltage drops rapidly and fluctuates, and finally The second steady-state value of 99.77 kV is reached, and the offshore wind farm setting frequency changes synchronously, reaching the second steady-state value of 49.78 Hz. The onshore converter successfully reduced the voltage of the HVDC system, and the offshore converter successfully converted the DC voltage change signal into a frequency change signal. Figure 5(e) and (f) show that after the 10.00s, the busbar frequency of the offshore wind farm decreased to 49.970 Hz, the offshore wind farm recognized the frequency deviation of the busbar, and the output power increased from 210 MW to 227 MW, an increase of 8.09%, in line with the 10% margin, the offshore wind farm frequency then increases to the second steady-state value of 49.997 Hz. At this time, the offshore wind farm has identified the frequency deviation of the onshore power grid, and has responded by generating additional power to support the frequency of the onshore power grid.
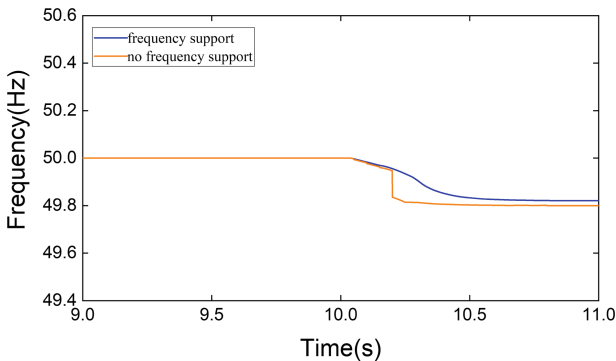
Fig. 6. Frequency comparison with frequency support and no frequency support under under-frequency conditions

Figure 6 compares the frequency deviation with and without frequency support. In the case of no frequency support, a sudden load of 100 MW on the grid will reduce the frequency to 49.80 Hz. After the support, the lowest value of the frequency was raised to 49.82 Hz, an increase of 0.02 Hz. The increase shows that, comparing the method of no frequency support, the method of frequency support proposed in this article has a significant frequency support effect. The coordinated frequency regulation method of the offshore wind farm connected through an HVDC link system designed in this paper plays a frequency support role under the underfrequency condition.

4.3   Model Simulation Under Overfrequency Conditions

This simulation adopts the method of abruptly removing the 100 MW load, which causes the frequency of the onshore grid to increase. In the 10th s of the simulation, the load of the onshore AC grid is reduced by 100 MW, and the onshore AC grid enters the state of overfrequency operation.

Figures 7 and 8 are simulation results under overfrequency operating conditions. At the 10.00 s, the onshore power grid removes 100 MW of load. After 10.50 s, the offshore wind farm connected through an HVDC link system reaches a steady state again, and the onshore grid voltage at the second steady state is 50.006 Hz.

(a) Onshore AC grid frequency

(b) DC Setting-voltage

(c) DC Voltage

(d) Offshore wind farm setting frequency

(e) Offshore wind farm frequency

(f) Offshore wind farm power output
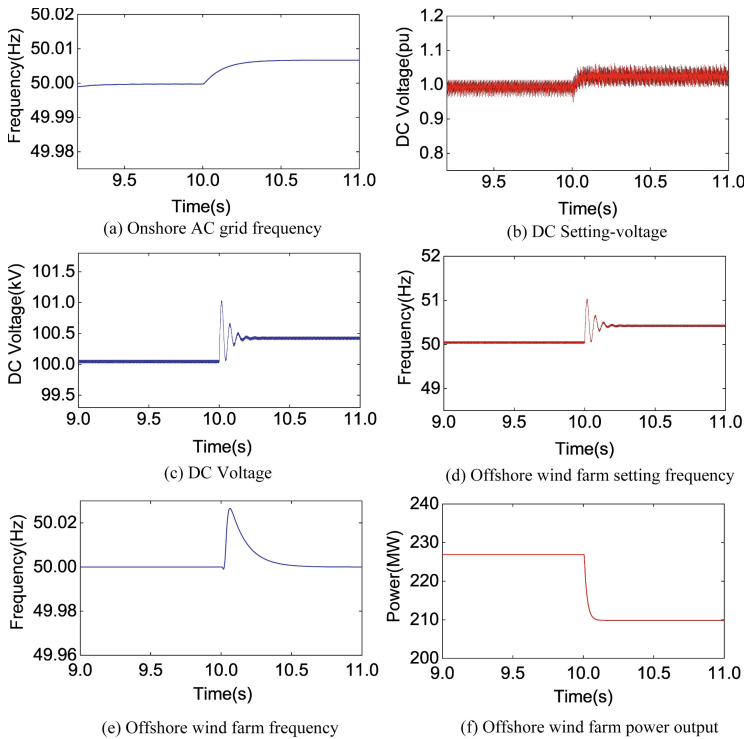
Fig. 7. Simulation results under overfrequency conditions

Figures 7(a) and (b) show that before the load is put into operation at the 10.00th second, the frequency of the onshore grid is 50 Hz, and the per-unit value of the DC voltage of the HVDC system is 1. After the load was cut off at 10.00 s, the onshore converter responded quickly, the DC voltage per unit value rose to 1.04, and the onshore converter successfully converted the frequency deviation signal into a voltage change signal. Figures 7(c) and (d) show that before the 10.00th second, the voltage of the HVDC system is 100.01 kV, and the frequency of the offshore wind farm is set to 50.1 Hz. After the 10.00th second, the DC voltage rises rapidly and fluctuates, and finally The second steady state value of 100.4 kV is reached, and the offshore wind farm

setting frequency is increased to the second steady state value of 50.4 Hz. The onshore converter successfully increased the voltage of the HVDC system, and the offshore converter successfully converted the DC voltage change signal into a frequency change signal. Figure 7(e) and (f) show that after the 10.00s, the frequency of the offshore wind farm busbar rises to the highest point of 50.025 Hz, the offshore wind farm recognizes the frequency deviation of the busbar, and the output power drops from 226 MW to 212 MW. The frequency of the offshore wind farm decreased to the second steady state value of 50.002 Hz. The offshore wind farm quickly recognized the frequency deviation of the onshore grid and responded immediately by reducing the output power to support the frequency of the onshore grid.
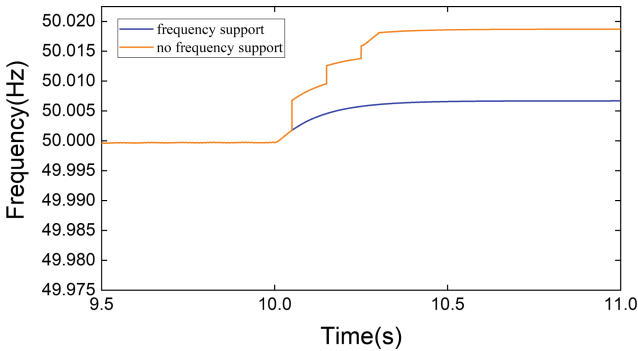
Fig. 8. Frequency comparison between frequency support and no frequency support under over-frequency conditions

Figure 8 compares the frequency deviation with and without frequency support. In the case of no frequency support, the power grid suddenly cuts off 100 MW of load, which will increase the frequency to 50.018 Hz. After the frequency is supported, the highest value of the frequency is reduced to 50.004 Hz, a decrease of 0.014 Hz. The decrease shows that, comparing the method of no frequency support, the method of frequency support proposed in this article has a significant frequency support effect. The coordinated frequency modulation method of the offshore wind farm connected through an HVDC link system designed in this paper plays a frequency support role under the overfrequency condition.

5   Conclusion

This paper proposes a droop control-based coordinated frequency modulation method for offshore wind farm connected through an HVDC link systems, which realizes the conversion of AC frequency deviation signal to DC voltage change information without communication, so that offshore wind farms can identify frequency deviation of onshore grid. And the output power of the offshore wind farm itself is changed to achieve the purpose of frequency support for the onshore AC power grid. The simulation results show that after adopting the droop control method for the onshore and offshore converters, the

voltage of the HVDC system and the frequency of the sending-end offshore wind farm can be controlled nearby, so that the offshore wind farm can change the power output. Under the overfrequency condition, the coordinated frequency control method proposed in this paper can reduce the frequency deviation of the onshore power grid by at most 0.014 Hz; under the underfrequency condition, the frequency deviation of the onshore power grid can be reduced by at most 0.020 Hz, realizing the realization of offshore wind farm and HVDC system coordinated control frequency support.

References

1. Liu, H., Chen, Z.: Contribution of VSC-HVDC to frequency regulation of power systems with offshore wind generation. IEEE Trans. Energy Convers. **30**(3), 918–926 (2015)
2. Miao, Z., Fan, L., Osborn, D., Yuvarajan, S.: Wind farms with HVDC delivery in inertial response and primary frequency control. IEEE Trans. Energy Convers. **25**(4), 1171–1178 (2010)
3. de Prada, M., Igualada, L., Corchero, C., Gomis-Bellmunt, O., Sumper, A.: Hybrid AC-DC offshore wind power plant topology: optimal design. IEEE Trans. Power Syst. **30**(4), 1868–1876 (2015)
4. Chen, H., Zheng, X.: Research on Frequency Support Of Offshore Wind Power VSC-MTDC grid connected system. Acta Energiae Solaris Sinica (2022)
5. Silva, B., Moreira, C.L., Seca, L., Phulpin, Y., Pecas Lopes, J.A.: Provision of inertial and primary frequency control services using offshore multiterminal HVDC networks. IEEE Trans. Sustain. Energy **3**(4), 800–808 (2012)
6. Martínez Sanz, I., Chaudhuri, B., Strbac, G.: Inertial response from offshore wind farms connected through DC grids. IEEE Trans. Power Syst. **30**(3), 1518–1527 (2015)
7. Chen, D., Fan, X., Zhao, J., et al.: Integrated control strategy of VSC inverter supplying power to the isolated grid. Elec. Power Eng. Technol. (2020)
8. Wang, G., Lu, S., Zhang, X., et al.: An improved control strategy for wind farm with VSC-HVDC under unbalanced voltage. Elec. Power Eng. Technol. (2020)
9. Jiang, Y., Zhang, J.: Multi-stage planning of offshore wind farm considering wind power accommodation level and load increase. Elec. Power Autom. Equipment (2022)
10. Liu, Z., Xia, C., Du, Z.: Control strategy on optimal redistribution of unbalanced power for offshore wind farms integrated VSC-MTDC. Proc. CSEE (2020)
11. Bianchi, F.D., Domnguez-Garca, J.L.: Coordinated frequency control using MT-HVDC grids with wind power plants. IEEE Trans. Sustain. Energy **7**(1), 213–220 (2016)
12. Yao, G., Yang, H., Zhou, L., et al.: Development status and key technologies of large-capacity offshore wind turbines. Autom. Elec. Power Syst. (2017)
13. Deng, F., Chen, Z.: Operation and control of a DC-grid offshore wind farm under DC transmission system faults. IEEE Trans. Power Delivery **28**(3), 1356–1363 (2013)
14. Phulpin, Y.: Communication-free inertia and frequency control for wind generators connected by an HVDC-link. IEEE Trans. Power Syst. **27**(2), 1136–1137 (2012)
15. Kou, P., Liang, D.L., Wu, Z.H., et al.: Frequency support from a DC-grid offshore wind farm connected through an HVDC-link: a communication-free approach. IEEE Trans. Energy Convers. **33**(3), 1297–1310 (2018)

16. Wang, W.Y., Li, Y., Cao, Y.J., et al.: Adaptive droop control of VSC-MTDC system for frequency support and power sharing. IEEE Trans. Power Syst. **33**(2), 1264–1274 (2018)
17. Kirakosyan, A., El-Saadany, E.F., El Moursi, M., et al.: An improved frequency support algorithm for MT-HVDC systems. IEEE Trans. Power Delivery (2021)
18. Sborio-Romano, O., Bidadfar, A., Sakamuri, J.N., et al.: Communication-less frequency support from offshore wind farms connected to HVDC via diode rectifiers. IEEE Trans. Sustain. Energy **12**(1), 441–450 (2021)
19. Yogarathinam, A., Chaudhuri, N.R.: Stability-constrained adaptive droop for power sharing in AC-MTDC grids. IEEE Trans. Power Syst. **34**(3), 1955–1965 (2019)
20. Bidadfar, A., Sborio-Romano, O., Sakamuri, J.N., et al.: On feasibility of autonomous frequency-support provision from offshore HVDC Grids. IEEE Trans. Power Delivery **35**(6), 2711–2721 (2020)

Research on Orderly Charging Strategy of Electric Vehicles in Charging-Swapping-Storage Integrated Station Based on Demand Transfer

Jiarui Wang[1], Dexin Li[1], Rongqing Yi[2], Chang Liu[1], Qixiang Wang[3(✉)], and Jingweijia Tan[3]

[1] State Grid Jilin Electric Power Research Institute, Changchun, Jilin Province 130021, China
[2] State Grid Jilin Electric Power Company Limited, Changchun, Jilin Province 130000, China
[3] Jilin University, Changchun, Jilin Province 130012, China
`wangyxw23@163.com`

Abstract. With the rapid growth of the scale of electric vehicles, the corresponding energy management mode is also adjusting its structure and optimizing its strategy to alleviate customers' charging anxiety while tapping into the potential of electric vehicles. Charging-Swapping-Storage integrated station is a new type of centralized energy supply equipment that integrates charging station, swapping station and energy storage station as required by the times. Aiming at the problem of orderly charging of electric vehicles in the integrated station of electric vehicles, the structure of the integrated station is firstly constructed. Then the mathematical models of charging station, swapping station and cascade energy storage station in the integrated station are established respectively. In the next step, based on the charging behavior characteristics of fast charging vehicles and electric buses, combined with the mechanism of time-sharing electricity price, user satisfaction in the process of charging and swapping services as the constraint, and maximizing the daily benefit of charging and swapping at integrated station as the goal, an orderly charging and discharging scheduling strategy based on demand transfer is proposed. The simulation results verify that the proposed orderly charging and discharging scheduling model of the integrated station can meet the demand of electric vehicle charging load. Moreover, it has the advantages of reducing operation and electricity purchase costs, curbing load fluctuation, and improving customer satisfaction.

Keywords: Electric vehicle · Charging-swapping-storage integrated station · Orderly charging strategy · Coordinated planning · Customer satisfaction

1 Introduction

Charging-Swapping-Storage Integrated Station(CSSIS)[1] is a new type of electric vehicle (EV) charging facility that can give full play to the dispatchable potential of charging

station and swapping station, effectively reduce load power fluctuation [2], and meet the diverse charging and swapping needs of users. Although the EVs centralized charging and swapping facility has problems such as strict requirements for power distribution facilities, the high power fast charging, charging and discharging integrated facilities planning brings the service level improvement is still very attractive to operators and electric vehicle users. The disorderly and random charging of EVs bring great challenges to the operation and management of power grid [3]. Therefore, how to respond to the power grid side of the fluctuating electricity price mechanism, effective charging and swapping management of different types of EVs has great research value.

There are plenty of studies on the separate optimization of charging stations or swapping stations. Paper [4] proposes two EV aggregator scheduling strategies: fixed contract and flexible contract (charging and discharging as one dispatching unit at a time) in order to maximize profits and minimize load fluctuation. An example for the battery swapping station, an orderly charging model of the battery swapping station is established in paper [5]. Their objective is to minimize the sum of square deviations of load curves and to consider the requirements of customer satisfaction. Because of its comprehensive service ability, integrated station has attracted more attention recently. The research about it focuses on the analysis and modeling [6], optimization of operation and cost [7] - [11], selection of address and volume [11], etc. Literature [6] provides a mathematical model of the CSSIS for EVs. Based on the model, an orderly charging strategy is provided. In terms of operation optimization, the efforts of works are multifaceted. Literature [7] uses travel chain to predict load of EV, its optimization goal is also to minimize costs of integrated station. In work [8], the authors introduce measures of carbon emission reduction for the operation process analysis of the integrated station. They construct AND carbon net increase model AND carbon trading mechanism aiming to reduce the annual environmental emissions and comprehensive cost. Paper [9] proposes a sliding window charging optimization strategy suitable for CSSIS and microgrid, chance constrained programming is taken into account. Paper [10] explores the optimal charging operation framework based on the mixed queueing network model proposed by their group. Work [11] proposes a CSE optimization model considering the power flow constraints and uncertainties of EV and battery charging. As for selection of address and volume, paper [12] uses Voronoi diagram to divide the service scope, and constructs a multi-objective location model to determine the location, combined with queuing theory and voltage power constraints to determine the station equipment capacity. Literature [13] proposes an improved queuing model M/M/K/K. The author analyzes the expected profit of long - term operation of multi - service power station. Their research subjects are not a strict CSSIS, but their conclusions coincide with ours. That is with number of vehicles swapping service increases, the integrated service station can get more profit. For present optimization works, majorities from the perspective of orderly scheduling on the grid side, while we consider a demand transfer model based on user response under incentive mode.

This paper mainly studies the joint scheduling problem of charging and swapping in the CSSIS. Firstly, we establish the integrated operation and planning model according to the structure and operation characteristics of CSSIS. Combining with the charging and swapping demand of users in one day, we build a charging and swapping scheduling

model of CSSIS based on demand transfer. Finally, an example is given to verify the effectiveness of the scheduling model.

2   CCSIS Model

2.1   Structure of CSSIS

The integrated station is an PEV (Plug EV) centralized rapid energy supply and storage facility, its composition is shown in Fig. 1, which mainly consists of battery charging station (BCS), battery swapping station (BSS), energy storage station (ESS) and in-station dispatching mechanism [6]. BCS generally consists of fast charging piles, which can achieve PEV high-power fast charging in a short period of time. Decommissioned batteries are deployed in the cascade system to form the ESS storage station. Compared with traditional new energy storage systems, ESS can maximize the residual value of spent batteries and reduce the economic and environmental pressure of spent batteries for EVs. The dispatching mechanism is the dispatching center within the integrated station, which allows real-time monitoring of the tide and information flow of the power station. It supervises and coordinates in-station status and off-station scheduling plan.
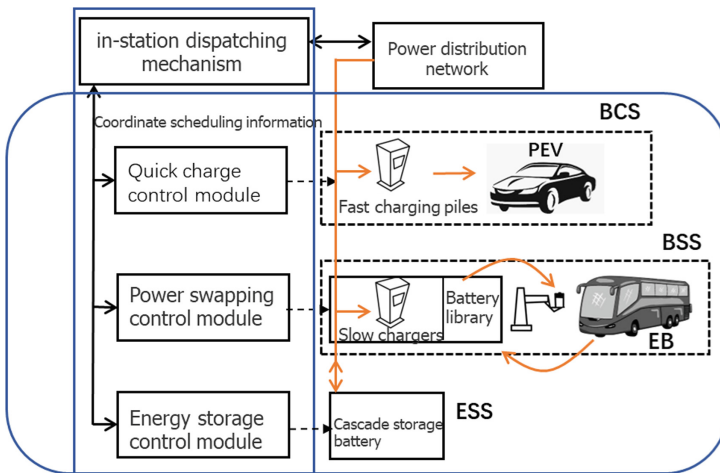
Fig. 1. The black arrows represent the information flow and the orange arrows represent the energy flow. In addition, EV here includes PEV for charging and Electric bus (EB) for swapping electricity.

2.2   BCS Model

Charging station is PEV centralized charging facilities that provide fast electrical energy services to fast charging users. In order to ensure the service quality and battery life of

PEV fast charging, this paper assumes that BCS does not participate in discharge. The charging power $P_{BCS}(t)$ is:

$$P_{BCS}(t) = N_C(t) \cdot P_{c\,max} \tag{1}$$

$$O \leq N_C(t) \leq N_{BCS} \tag{2}$$

In the expression, $P_{BCS}(t)$ is the power consumption of the BCS at time period t, and $N_C(t)$ is the number of fast charging users in the BCS at time period t. P_{cmax} is the maximum output power of the fast charging pile, N_{BCS} is the total number of fast charging piles in BCS.

According to the results of the National Household Travel Survey [14] conducted by the US Department of Transportation in 2011, the driving characteristics, network access time and other key parameters of PEV users are obtained. PEV network access time is in normal distribution, $\mu = 16.0$, $\sigma = 4.0$. Monte Carlo method is used in this paper to generate the raw data. Generally, when PEV users do not reach or approach the limit driving behavior (vehicle SOC is close to or less than or equal to the lower limit of SOC), they will choose home decentralized charging [8]. As the vehicle SOC has almost reached its lowest value, PEV mainly seeks fast charging service. Therefore, the PEV energy demand Soc is set as 0.8.

2.3 BSS Model

The power battery (PB) is charged from the electric bus by a split-box DC charger. Participation of EB power battery in discharge in BSS will greatly shorten battery life, so it is considered that EB does not participate in discharge. Its charging power $P_{BSS}(t)$ is:

$$P_{BSS}(t) = N_S(t) \cdot P_{s\,max} \tag{3}$$

$$O \leq N_S(t) \leq N_{BSS} \tag{4}$$

where $P_{BSS}(t)$ is the power of the BSS at time period t, and $N_S(t)$ is the number of swapped batteries in the slow charging mode at time period t. P_{smax} is the maximum output power of the slow chargers, N_{BSS} refers to the total number of chargers in BSS.

EB is characterized by long operating hours and strict travel (departure/arrival/stop) times and route planning. Due to EB's "on-time " operation characteristics, its daily electricity demand is basically under control. The main operation period of the bus is from 06: 00 to 23: 00, and the battery swapping process is carried out during the bus operation. The buses on the line start towards each other between the first and last stations, and the energy swapping behavior between 07:00–22:00 can be regarded as uniform distribution [15]. After business hours, EB energy is usually at a low level, and the fast swapping station provide a mode to swap energy to better meet the PEV's dispatch needs. This paper assumes that the residual load of the EB is 15%, the PB with 95% energy needs to be replaced for EB, and the demand is Soc 0.8.

2.4 ESS Model

Decommissioned batteries with different loss levels form the cascade energy storage structure in ESS station. These batteries come from batteries that have reached the end of their life and have reduced capacity and discharge efficiency. Due to the reduced performance, there is some loss of function during use. They also fail to reach the upper and lower limits of energy storage during charging and discharging. ESS output planning strategy: To regulate its own charging and discharging power according to the time-share electricity purchase price and changes in ECS and ESS power of the integrated station. The charge-discharge model of ESS is as follows:

$$-P_{ED\,\max} \leq P_{ESS}(t) \leq P_{EC\,\max}\forall t \tag{5}$$

$$E_{ESS}(t) = E_{ESS}(t-1) + P_{ESS}(t)\Delta t \tag{6}$$

$$E_{e\,\min} \leq E_{ESS}(t) \leq E_{e\,\max} \tag{7}$$

$$E_{ESS}(t) = E_{ESS}(t+T_k) \tag{8}$$

P$_{ECmax}$ and P$_{EDmax}$ respectively represent the upper and lower limits of the charging and discharging power of the ESS. E$_{emin}$ and E$_{emax}$ represent the upper and lower limits of the ESS. The addition of Tk to Eq. 8 indicates that energy storage recovers to the initial level after completing a scheduling cycle.

To sum up, the integrated station model is established as follows:

$$P_{CSE}(t) = P_{BCS}(t) + P_{BSS}(t) + P_{ESS}(t) \tag{9}$$

$$E_{CSE}(t) = E_{BCS}(t) + E_{BSS}(t) \tag{10}$$

P$_{CSE}$(t) is the charging power of the CSSIS during the time period t; E$_{CSE}$(t) is the total energy of the CSSIS at end of time period t. In addition, the normal operation of CSSIS needs to meet periodic constraints.

3 Charge and Discharge Scheduling of Integrated Station Based on Demand Transfer

3.1 Scheduling Strategy

In the daily operation of the integrated station, the power of BCS, BSS and ESS are dispatched separately, and the day is divided into 96 time periods (every 15 min as a time period) to build a daily optimal dispatch model. The operation of BCS follows a first-come, first-served queuing model, and BSS's charging scheduling for swapping batteries coordinates BCS operation on the basis of meeting the fixed daily bus swapping load and accepting the demand for BCS transfers within each time unit. ESS further plays the role of coordinating the load and eliminating peaks and valleys.

The essence of the demand transfer strategy is to give full play to the energy storage and orderly charging capabilities of BSS and ESS in integrated station on the one hand, and relieve the charging pressure of BCS on the other hand. The premise that this scheduling can be realized is demand-side response based on certain incentives. Specifically, this article uses a discount to attract customers to convert the original charging into a swapping service. The scheduling strategy is shown in Fig. 2.
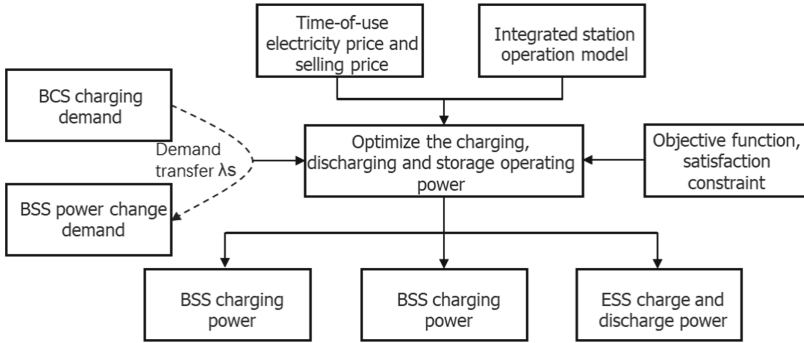
Fig. 2. Scheduling flow

Demand Transfer in BCS. Demand transfer model: Converting Some of the demand at BCS during the current time period into demand at BSS. This will relieve the charging pressure at BCS and reduce the overall load power of BCS and the waiting time for users. at the same time, the dispatching potential of the battery orderly charging can be fully utilized through the BSS, and the power reserve obtained at a lower price can be exchanged for a higher economic benefit. Since the cost of BSS is higher than that of BCS, a scheduling discount Θ is introduced into the strategy to make the price of battery swapping close to the price of charging, so as to improve the response ability of users to the demand transfer strategy. By optimizing the charging and discharging behavior of the integrated station throughout the day, we explore the possibility of scheduling space to improve the mutual benefits of the integrated station and the customer. The scheduling model of BCS is as follows:

$$E_{BCS,ac}(t) = E_{BCS,ac}(t) + \eta_C P_{BCS}(t-1)\Delta t \tag{11}$$

$$E_{Cneed}(t) = ceil(\lambda_s N_c(t)) E_{PEV} \Delta SOC_{PEV} \tag{12}$$

$$E_{BCS,ac}(Tk) = \sum_{t=1}^{Tk} E_{Cneed}(t) \tag{13}$$

In the expression, $E_{BCS,ac}$ is the accumulated acquired energy of the BCS, E_{Cneed} is the energy demand of the BSS at each time period, η_C represents the charging efficiency of the BCS, and λ_s represents the demand transfer rate. ΔSOC_{PEV} Represents the

percentage of energy demand of PEV. Formula 13 represents the total energy obtained in one day of the BCS to meet the charging demand after the demand transfer.

Demand Transfer in BSS. The charging behavior of PBs in BSS includes disorderly charging and orderly charging. In this paper assumed that disorderly charging refer to swapping and charge PBs immediately once EBs arrive at BSS without considering other information. In contrast, orderly charging behavior has scheduling potential. During the charging process of BSS, we make the assumption that each of the two types of batteries (PBs, PEV Batteries) in the BSS is a lithium battery of the same type and size. In the BSS, the batteries is prepared for PBs as well as PEV batteries in advance. The chargers has suitable interfaces for their charging. The BSS receives part of the demand from the BCS, and charges the electricity at the current swapping price, giving a certain discount.

$$E_{Sneed}(t) = (1 + R_{BSS})N_S(t) \cdot E_{PB}\Delta SOC_{PB} + floor(\lambda_s N_c(t))E_{PEV}\Delta SOC_{PEV} \forall t \quad (14)$$

$$E_{BSS}(t) = E_{BSS}(t-1) + \eta_s \Delta t P_{BSS}(t-1) - E_{Sneed}(t-1) \quad \forall t \quad (15)$$

$$E_{BSS}(t) \geq E_{Sneed}(t) \quad (16)$$

In the formula 14, E_{Sneed} represents the battery swapping demand of the BSS during each time period, N_S represents the number of vehicles reaching the BSS in each time period, SOC_{PB} and SOC_{PEV} respectively represent the SOC ratio of EBs and PEVs, η_S is the charging efficiency of motors in the BSS, E_{PB} represents the upper limit of energy of PB, R_{BSS} stands for the battery swapping margin of the BSS. The BSS needs to coordinate the demand of the BCS and arrange the charging power of the BSS under the premise of meeting the margin of battery swapping demand in each time period.

3.2 Optimization Objective

Objective Function. Optimization objective: maximize the daily operating income of integrated station. To be specific, the integrated station is planned collaboratively with the goal of maximizing the daily operating profit function F. The objective function is as follows:

$$F = max(C_{BCS} + C_{BSS} - D_{CSE}) \quad (17)$$

$$C_{BCS} = \sum_{t=1}^{Tk} P_{BCS}(t)\Delta t \cdot \gamma_c(t) \quad (18)$$

$$C_{BSS} = \sum_{t=1}^{Tk} E_{Sneed}(t) \cdot \gamma_s(t) \quad (19)$$

$$C_{BSS} = \sum_{t=1}^{Tk} \gamma_s(t)((1 + R_{BSS})N_S(t) \cdot E_{PB}\Delta SOC_{PB} + \theta floor(\lambda_s N_c(t))E_{PEV}\Delta SOC_{PEV})$$

$$(20)$$

In these formulas, C_{BCS} refers to the total fee charged by the BCS after charging service, C_{BSS} refers to the total fee charged by the BSS and D_{CSE} refers to the total cost of daily electricity purchase of integrated station. Among them, γ_C, γ_S and γ_{CSE} respectively represent the time-sharing electricity selling price of BCS, BSS and electricity purchasing price of integrated station. θ represents the discount parameter involved in dispatching.

The Constraint. 1. Substation Power Constraint: The total load power of the charging and swapping station cannot exceed the interactive power range of the connecting line, and the constraint is:

$$P_{g,min} \leq P_{CSE} \leq P_{g,max} \tag{21}$$

2. Power balance constraint: To limit the power fluctuation of the integrated station within a certain range throughout the day. The power variance of integrated station satisfies $\sigma < \sigma_0$.

$$\sigma = \frac{1}{T} \sum_{i=1}^{Tk} \left[P_{CSE}(t) - \frac{1}{Tk} \sum_{i=1}^{Tk} P_{CSE}(t) \right]^2 \tag{22}$$

3. User satisfaction constraint: In this paper, user satisfaction refers to the satisfaction based on the charging speed of PEV owners. Specifically, it is the ratio of the total energy demand of the actual BCS to the residence time of all vehicles. Proportional to the total energy obtained per unit time:

$$Q = \frac{\sum_{t=1}^{Tk} N_C(t) \cdot E_{PEV} \Delta SOC_{PV}}{P_{c\max} \cdot (\sum_{t=1}^{Tk} N_{c,ac}(t)\Delta t + t_s \sum_{t=1}^{Tk} floor(\lambda_s N_c(t)))} \tag{23}$$

$$N_{C,ac}(t) = N_{C,ac}(t-1) - N_L(t-1) + ceil(\lambda_s N_c(t)) \tag{24}$$

Q is the user's charging satisfaction, $N_{C,ac}$ are the accumulated vehicles staying in the BCS, N_L is the number of vehicles leaving in each time period. The integrated station is required to achieve certain satisfaction constraints during operation. $Q >= Q_0$.

4. CSSIS run constraint: The instance needs to satisfy the CSSIS operation model constraints of Eqs. 1 through 8.

4   Simulation Verification

4.1   Solution of Model

The decision variables in the above model are the charging power of BCS, BSS, the charging and discharging power of ESS at each time period, and the overall demand transfer rate λ_S. Solved in Matlab 2020 using solver cplex12.10 and yalmip toolbox. Combining with the actual situation and the demand transfer scheduling strategy proposed in this paper, the joint scheduling mode of BSS and BCS can be obtained, and the demand response potential and schedulable potential of BSS are further calculated.

Table 1. Parameter settings.

Parameter	Value	Parameter	Value
N_{BCS}	25	η_C	0.8
N_{BSS}	50	η_S	0.8
P_{cmax}	100	SOC_{PB}	0.8
P_{smax}	40	SOC_{PEV}	0.8
P_{EDmax}	500	E_{PB}	300
P_{ECmax}	500	E_{PEV}	50
ηe	0.8	$P_{g,min}$	5000
E_{emin}	6000	$P_{g,max}$	1000
E_{emax}	1000	σ_0	750
Θ	0.75	Q_0	1.2

In this paper, the number of EVs in a region is used as an example for calculation and analysis. CSSIS service area provides charging and swapping services for 540 PEVs and 60 EBs, and there are 60 sets of backup PBs, 5 sets of swapping motors and split-box chargers which are available for slow charging of up to 50 batteries simultaneously. BCS is equipped with 25 fast charging piles. The ESS capacity is 6kW·h, the initial state of charge (SOC) is 50%, and the discount rate θ is set to 0.75. For other system parameters, see Table 1 above. These data can be changed to replace the variables in the paper without affecting the optimization solution of the problem. (For example, the discount rate θ, different discount rates correspond to different response rates).

4.2   Results Analysis

In order to effectively compare the optimization results obtained by different charging modes of EB and PEV in CSSIS and verify the effectiveness of the proposed method, a qualitative and quantitative comparison of the CSSIS charging and discharging power under the two charging modes will be performed in this section: Orderly scheduling based on demand transfer and disorderly charging with the manner of instant service.

Figure 3 illustrates the demand transfer process over time. The blue line represents the actual new growth charging demand that arrives at BCS over time, while the red line represents the demand reach at each time period after the demand transfer strategy. Green indicates the actual charging demand of BCS in each time period under the first-come-first-served mode after scheduling. The black lines represent the number of PEVs which leave the BCS after satisfying their charging requirements within each time period. The meaning of this graph is that after the demand transfer strategy, the actual new growth demand of BCS (blue) becomes the new demand (red). In this case, the demand transfer rate $\lambda_S = 0.25$, gives the maximum daily operating economy for the given dispatch discount rate θ.

Figure 4 reflects the demand of disorderly charging, following the instant service mode. The power consumption reaches its maximum at the peak of the network. Here we
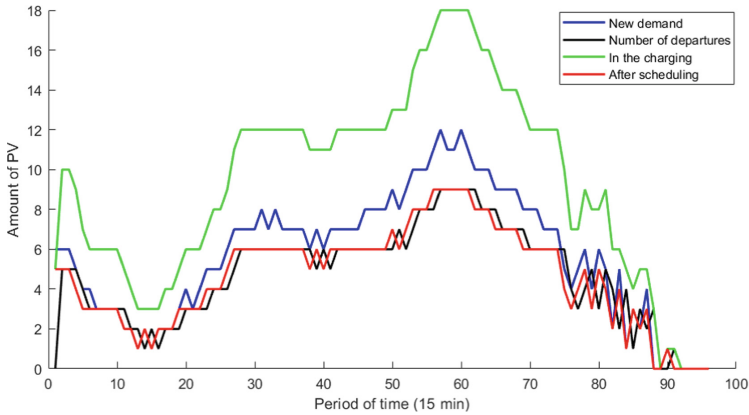
Fig. 3. Demand scheduling

do not show the power curve of ESS, just think that ESS only plays a role in balancing the load of power grid and CSSIS.
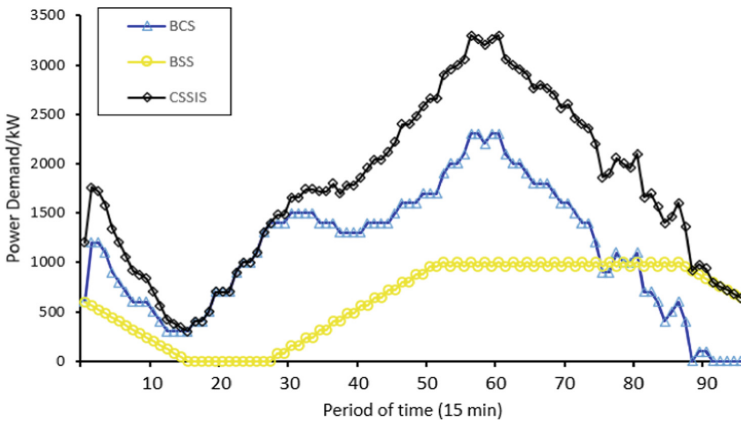
Fig. 4. Disorderly charge

Power demand curves based on demand transfer of CSSIS in each time period are shown in Fig. 5. As can be seen from Fig. 5, during the time period from 0 o 'clock to 7 o 'clock (0–28), when the load is light and the electricity price enters the valley phase, the CSSIS purchases electricity from outside network with a upper power, and stores energy for the backup battery bank in ESS and BSS on the basis of satisfying the charge and swapping of BSS and BCS. From 10 to 15 o 'clock, 18 to 21 o 'clock (40 to 60, 72 to 84), the load is heavy. This stage meets the charging demand of the BCS and performs the minimum charging based on the margin constraint of the BSS reserve energy after accepting the demand transfer. ESS remains in a continuous process of discharge. From 22 to 24 o 'clock (88 to 96), CSSIS achieves a constraint on the balance between start

and end charging in a cycle by increasing the charging power. During the rest of the flat price time periods, CSSIS charges and stores energy with medium power.
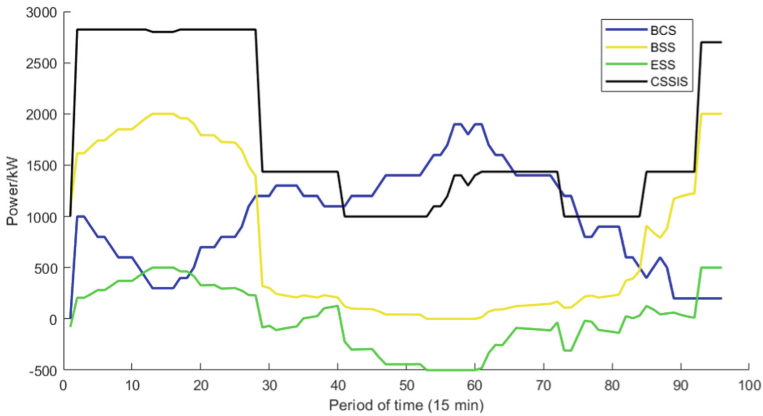
Fig. 5. Orderly scheduling

As shown in the Figs. 4 and 5, compared with disorderly charging, the maximum power demand of orderly charging is 2800kW /h, which is smaller than the maximum value of disorderly charging of 3300kW /h. This indicates that orderly charging can reduce the charge demand power during peak period, which is of great significance for alleviating the peak-valley difference of power grid. Table 2 shows comparison of two scheduling strategy:

Table 2. Optimization scheduling strategy comparison.

	Profits	Variance	Improvement of satisfaction
Disorderly charge	18203	845	0
Orderly scheduling	22901	750	33.2%

Through quantitative analysis of BSS, CSSIS, standard deviation of load fluctuation, comprehensive daily cost and customer satisfaction during unorderly charging and orderly charging, it is obvious that orderly charging can effectively alleviate the peak-to-valley difference of the power grid, reduce comprehensive daily operating cost, and play a role in improving customer satisfaction with charging and swapping.

The energy change curve of CSSIS orderly charging is shown in Fig. 6. Both BSS and ESS return to the initial value at the end of a cycle. In BCS, the accumulated demand energy and the accumulated acquired energy converge at the end of the cycle, which means that BCS has met the electricity charging demand of the day**.**
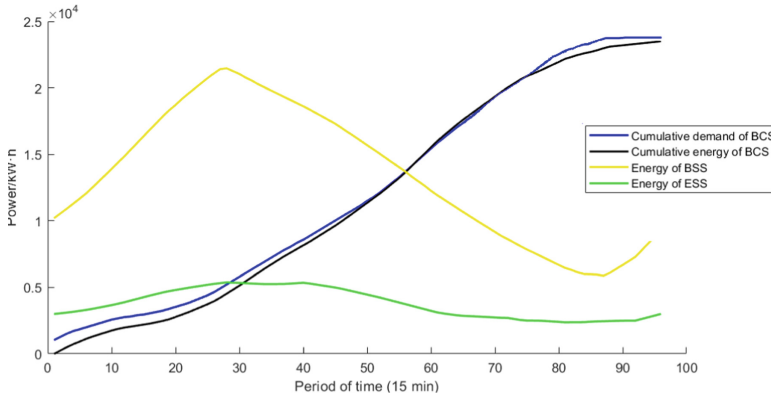
Fig. 6. Energy curves of CSSIS

5 Conclusion

The Charging-Swapping-Storage integrated station has the advantages of smoothing EV load fluctuation, eliminating peaks and valleys to achieve an environmentally friendly and sustainable economic operation mode. This paper sets up the model of integrated station. Combined with the behavior characteristics of electric vehicles, establishing the demand transfer scheduling strategy model of orderly charging, and analying the customer satisfaction index. Finally, combined with the fluctuation of time-sharing electricity price, constructing the optimization function to maximize the benefits of one-day integrated station, and solving it with the help of Cplex solver to achieve collaborative scheduling. The results show that CSSIS has great potential to participate in optimal dispatching of power grid. In the future, we will explore more flexible incentive strategies based on demand transfer in more complex scenarios.

References

1. Hongtao, Y., Gang, W., He, Z., et al.: Robust optimal scheduling of active distribution network considering with the charging-swapping-storage integrated station. Proc. CSEE **40**(8), 2453–2468 (2020)
2. Hongtao, Y., Gang, W., He, Z., et al.: Model predictive control based optimal operation of distribution network with charging-swapping-storage integrated station. Autom. Elec. Power Syst. **44**(5), 187–197 (2020)
3. Lingling, M., Yang Jun, F., Cong, et al.: Review on impact of electric car charging and discharging on power grid. Power Syst. Protect. and Control **41**(3), 140–148 (2013)
4. Hui, H., Yifan, W., et al.: Dispatching strategy of EV aggregator under price and incentive demand response. Power Syst. Technol. **46**(04), 1259–1269 (2022). https://doi.org/10.13335/j.1000-3673.pst.2021.0719

5. Minli, H., Aiqing, Y.: Study on coordinated charging strategy for battery swapping station based on improved cuckoo search algorithm. Proc. CSEE **38**(04), 10751083+1284 (2018). https://doi.org/10.13334/j.02588013.pcsee.170070
6. Jue, H., Gang, W., Hongtao, Y., et al.: Modeling of EV charging-swapping-storage integrated station. Elec. Power Construct. **41**(06), 44–51 (2020)
7. Ting, Y., Xing, D., Kun, H., et al.: Optimal dispatching strategy and application of EV charge-exchange-storage integrated power plant. Power Demand Side Manage. **23**(04), 67–72 (2021)
8. Chenke, H., Jizhong, Z., Lan, L.Y., et al.: Coordinated planning of EV charging-swapping-storage integrated station and active distribution network considering carbon reduction. Trans. China Electrotech. Soc. **37**(01), 92111 (2022). 10.19595/ j.cnki.1000-6753.tces.211255
9. Fang, L.I.U., Xiu, Y.A.N.G., et al.: Economic operation of microgrid containing charging-swapping-storage integrated station under uncertain factors of wind farm and photovoltaic generation. Power Syst. Technol. **39**(03), 669–676 (2015). https://doi.org/10.13335/j.1000-3673.pst.2015.03.013
10. Sun, B., Tan, X., Tsang, D.H.K.: Optimal charging operation of battery swapping and charging stations with QoS guarantee. IEEE Trans. Smart Grid **9**(5), 4689–4701 (2017)
11. Wang, Y., Yang, Y., Zhang, N., et al.: An integrated optimization model of charging station/battery-swap station/energy storage system considering uncertainty. In: 2017 IEEE International Conference on Energy Internet (ICEI), pp. 77–82. IEEE (2017)
12. Menglong, Z., Gang, W., Lan, Z., Hongtao, Y., ChenKe, H., Yu, M.: Planning of electric vehicle charging, changing and storage integrated station in AC and DC distribution network Autom. Elec. Power Syst. **45**(18), 52–60 (2021)
13. Esmailirad, S., Ghiasian, A., Rabiee, A.: An extended M/M/K/K queueing model to analyze the profit of a multiservice EV charging station. IEEE Trans. Veh. Technol. **70**(4), 3007–3016 (2021)
14. García-Villalobos, J., Zamora, I., Eguia, P., et al.: Modelling social patterns of plug-in EVs drivers for dynamic simulations. In: 2014 IEEE International EV Conference, Florence, Italy, pp. 1–7, 17–19 December 2014
15. Bin, Q., Dongyuan, S., Pingping, X., Lin, Z.: Electric bus changing station -- optimization planning of battery charging station. Autom. Elec. Power Syst. **38**(02), 64–69+84 (2014)

Research on the Influence Mechanism of Carbon Trading on the Behavioral Decision-Making of Power Market Entities in Jiangsu Province

Xiujia Yan[1], Chen Wu[2(✉)], and Guiyuan Xue[2]

[1] State Grid Jiangsu Electric Power Co., Ltd., Nanjing 210024, China
[2] State Grid Jiangsu Electric Power Co., Ltd. Economic Research Institute, Nanjing 210008, China
cwusgcc@gmail.com

Abstract. In 2020, China put forward the strategic goal of "carbon peaking and carbon neutrality", which will strongly promote the adjustment of industrial structure and the transformation of energy structure. The power industry is the key to building a clean, low-carbon, safe and efficient energy system. The carbon emission trading market is one of the most effective political tools to control carbon emission. The power industry, as an energy-intensive industry, is an important control object in the carbon market. The essence of the integrated development of the carbon market and the power market is to promote the development of the power industry in a cleaner, more efficient low-carbon direction. However, the impacts of carbon market transactions on the power market entities still need to be explored. Therefore, based on the development status of Jiangsu power market, this paper studies the impacts of carbon trading on the behavioral decision-making of Jiangsu power market entities through game theory, constructing an optimal profit model for each market entity under carbon trading. It also puts forward relevant suggestions for the integrated development of carbon market and power market.

Keywords: Carbon trading · Power market · Behavioral decision-making · Optimal profit model

1 Introduction

China's rapid economic development has led to increasing fossil energy consumption. To address climate change and achieve sustainable development, China announced that carbon dioxide emissions of China strive to peak by 2030 and work towards carbon neutrality by 2060 [1]. To achieve the above carbon peaking and carbon neutrality targets, industrial restructuring and energy structure transformation are imperative. Currently, the most typical market-incentivized carbon emission reduction tool is the carbon trading mechanism.

On July 16, 2021, the China national carbon market officially went online for trading. In the initial phase of trading, 2,225 key emitting power generation companies were

included in the trading [2, 3]. The power sector is currently the largest single carbon emitting sector in China, accounting for about 51% of total emissions from all sectors. According to the National Bureau of Statistics, thermal power generation will still account for 70.6% of total power generation in 2021, making the power sector the largest emitter of CO_2 in China. The inclusion of the power sector in the carbon emissions trading system reflects the key policy objective of controlling carbon emission from power generation enterprises with the guidance of the carbon market, but it also brings common challenges to the power market and the carbon market [4–6].

In May 2021, Jiangsu Department of Ecology and Environment issued the "Provincial Department of Ecology and Environment 2021 Work Plan on Carbon Peaking and Carbon Neutrality". The work plan points out that we should strengthen the top-level design of carbon peak work, promote carbon peak work in key areas, establish a carbon emission reduction testing and assessment system, and strengthen the organizational guarantee of carbon peak work [7, 8]. Jiangsu Province will continue to strengthen the target constraint and peak leading and make efforts in six aspects including building a green low-carbon development system, promoting low-carbon development in key areas, and carrying out pilot projects in low-carbon cities. These policies and plans also provide support and motivation for Jiangsu Province to actively participate in national carbon trading.

This paper studies the influence of carbon trading on the behavioral decision-making of power market entities in Jiangsu through game theory, constructing the optimal profit model of each market entity under carbon trading. The rest of this paper is organized as follows. First, a trading framework of Jiangsu power market under carbon trading is designed in Sect. 2. Then, an optimal profit model for each entity is established in Sect. 3. Section 4 verifies the effectiveness of the presented model based on the trading framework of Jiangsu power market. Finally, Sect. 5 draws the conclusions of this work.

2 Trading Framework of Jiangsu Power Market Under Carbon Trading

2.1 Carbon Market Trading Rules

- **(1) Trading models**

European Union's carbon trading market takes the form of a primary carbon market and a secondary carbon market, in which the primary market is the issuance market, used for the allocation of carbon quotas by the government to trading entities. The secondary market is the circulation market, which is used for the trading of the surplus or deficient parts of the trading subjects' allotment, and the secondary market is carried out based on the primary market. Unlike European Union's two-level carbon trading market, there is only one carbon market in China at present. The shape of China's future carbon trading market is still being explored.

- **(2) Carbon trading management modes of power generation enterprises**

There are three main types of carbon trading management modes for power generation enterprises.

① **Self-management:** power generation enterprises carry out carbon trading-related work on their own.

② **Centralized management:** power generation groups with multiple power generation enterprises set up or specify a management organization at the group company level to centrally manage the carbon trading-related work of their power generation enterprises. This model takes into full consideration the existing distribution and management institutions, multiple power supply types and specialized service resources. By adopting the centralized management mode, power generation groups with multiple power generation enterprises can give full play to the scale advantages of group companies, control market risks, reduce compliance costs and maximize group interests.

③ **Entrusted management:** power generation enterprises entrust external professional institutions to carry out part or all the carbon trading-related work.

2.2   Jiangsu Power Market Trading Rules

- **(1) Trading subjects**

The main trading entities of Jiangsu power market include various power generation enterprises, power users (wholesale market users, retail market users), power grid enterprises, power dispatching agencies and energy storage enterprises.

- **(2) Trading modes**

In terms of trading methods, the trading in Jiangsu's power market is mainly divided into medium and long-term power market trading and power spot market trading. The "Jiangsu Electricity Spot Trading Rules" stipulates that electricity spot market trading was divided into day-ahead market trading, real-time market trading and auxiliary service market trading, and that the medium- and long-term market should realize multiple trading methods to complement each other, provide multi-frequency trading, and realize the effective connection with the electricity spot market. The medium- and long-term market should be complemented by multiple trading methods, provide multi-frequency trading, and achieve effective connection with the electricity spot market.

2.3   Trading Framework of Jiangsu Power Market Under Carbon Trading

The carbon trading market aims to reduce CO_2 emissions and promote the achievement of carbon-neutrality target through the control and trading of carbon emissions from high-energy-consuming industries. For the power market, thermal power generators with high energy consumption are the main trading subjects. After the state issues carbon quotas, thermal power generators complete compliance requirements by trading carbon quotas on the carbon emission trading platform. During the trading process, the fluctuation of carbon price will affect the buying and selling of carbon allowances, thus creating cost perturbation for thermal power generators. In this context, each power

market entity has its own optimization game objective. Thermal power generators need to fulfill their carbon quota compliance requirements on the one hand, meet the needs of power consumers on the other. The power grid companies need to meet the demand of power consumers based on the balance of power generation. The final sales price of electricity will also cause fluctuations in the demand of electricity consumers. Therefore, to ensure their own interests are maximized, each entity in the power market needs to find the optimal strategy.

3 Optimal Profit Model for Each Entity in the Power Market Under Carbon Trading

3.1 Model Assumptions

In the power market trading, the main entities include power generators, transmission, and distribution providers (power companies) and power consumers. This study assumes that thermal power generators are the power generators included in the carbon trading market; renewable energy generators no longer receive government subsidies. Under the carbon trading market, each entity is influenced by the carbon price and carbon quota, and the entities all make decisions with the goal of maximizing their own interests. Based on this, this study constructs the profit function of each entity in the power market under the carbon trading market.

- **(1) Thermal power generators**

    The profit of thermal power plant operators is mainly affected by several factors, including generation revenue, generation cost, carbon emission reduction cost, and carbon allowance trading cost. In this study, only thermal power plant operators that are included in the carbon trading market are considered, and they are divided into thermal power plant operators that need to buy carbon quotas and thermal power plant operators that need to sell carbon quotas. Assume that there are N_{in} thermal power producers who need to buy carbon allowances, their profit function R_{in} can be expressed by (1). There are N_{out} thermal power producers who need to sell carbon allowances, and their profit function R_{out} can be represented by (2).

$$R_{in} = P_f y_i - C_f(y_i) - C_{ec}(\beta_{in}) - P_c(\theta y_i - \beta_{in} - \alpha), i = 1, 2, \cdots, N_{in} \quad (1)$$

$$R_{out} = P_f y_j - C_f(y_j) - C_{ec}(\beta_{out}) - P_c[\alpha - (\theta y_i - \beta_{out})], j = 1, 2, \cdots, N_{out} \quad (2)$$

where $R_{in}(R_{out})$ refers to the profit function of thermal power producers who need to buy (sell) carbon allowances, Pf P_f denotes the market transaction price of electricity for thermal power generators, y denotes the electricity generation capacity, C_f denotes the cost function of the thermal power producer, β denotes the amount of carbon emission reduction [9], Cec C_{ec} denotes the carbon abatement cost function, θ is the carbon emission factor per unit of electricity generation, P_c denotes the carbon price, α α denotes the carbon allowance. If the total carbon emissions of thermal power generators

$(\theta y_i - \beta_{in})$ is greater than the carbon allowance α, then the power producer needs to buy carbon allowances. Conversely, a thermal power producer can sell carbon allowances.

It is assumed that both the cost function and carbon abatement cost function of thermal power generators are quadratic functions. The cost function of thermal power producer is constructed as:

$$C_f(y_i) = \frac{1}{2}a_{fc}y_i^2 + b_{fc}y_i + c_{fc}, i = 1, 2, \cdots, N_f \tag{3}$$

where C_f is the production cost function of thermal power plant merchants; a_{fc}, b_{fc}, and c_{fc} are the generation cost coefficients of thermal power plant merchants, N$_f$ N_f is the number of thermal power plant merchants in the market.

To simplify the calculation, this study assumes the same abatement cost function for thermal power producers [10].

$$C_{ec}(\beta_i) = \frac{1}{2}a_e\beta_i^2 + b_e\beta_i + c_e, i = 1, 2, \cdots, N_f \tag{4}$$

where C_{ec} is the carbon abatement cost function for thermal power generators. a_e, b_e, and c_e are the carbon abatement cost coefficients of thermal power producer.

- **(2) Renewable energy generators**

Since renewable energy generators are not included in the carbon emissions trading market, their profits are mainly influenced by generation revenues and generation costs. Assuming that there are N_r renewable energy generators in the power system, their profit function R_r can be represented as:

$$R_r = P_r z - C_r(z) \tag{5}$$

where P_r denotes the market transaction price of electricity for renewable energy generators, z is the renewable energy feed-in tariff, C$_r$(z) $C_r(z)$ denotes the cost of electricity generation of the renewable energy generator.

To simplify the calculation, this study assumes that the cost of generation is the same for each renewable energy generator, and the generation cost function is expressed as:

$$C_r(z_j) = \frac{1}{2}a_r z_j^2 + b_r z_j + c_r, j = 1, 2, \cdots, N_r \tag{6}$$

where a_r, b_r, and c_r are the generation cost coefficients of renewable energy generators.

- **(3) Powercompanies**

Power companies are transmission and distribution operators in the power market, and their revenue sources are mainly state access revenues from transmission and distribution. Therefore, its profit function can be expressed as:

$$R_g = P_g X - C_g(X) \tag{7}$$

where R_g denotes the profit function of the grid enterprise, P_g is the average transmission and distribution price, X is the total transmission and distribution volume of the power company, which is equal to the electricity purchased by customers, $C_g(X)$ denotes the cost function of the power company. It should be noted the cost of power grid enterprise consists of fixed cost and variable cost. To simplify the calculation, the variable cost only considers the influence of line loss. Therefore, the cost is expressed as a function of electricity transmission and distribution, which is calculated by the system power flow.

- **(4) Power consumers**

The consumer surplus can be used to represent the consumer's profit in power market transactions. To correctly calculate consumer surplus, the consumer's demand curve needs to be determined first. To simplify the calculation, this paper assumes that the inverse demand function of the final consumer is a linear function, expressed as:

$$P = a - bX \tag{8}$$

where P denotes the consumer's purchase price of electricity, a denotes the intercept of the demand function, and b denotes the slope of the demand function ($b > 0$). Integrating the consumer demand function gives the consumer surplus U, as shown in (9).

$$U = \int_0^X P(X)dx - PX = aX - \frac{1}{2}bX^2 - PX \tag{9}$$

3.2 Objective Function and Constraints of the Model

- **(1) Objective function**

In this paper, we consider that under the condition of non-cooperative game, each market player makes decision to maximize its own interests to achieve market equilibrium, and the corresponding objective function is shown in (10).

$$W = \max R_f + \max R_r + R_g + \max U$$
$$= \max \sum_{i=1}^{N_f} \left[P_f y_i - C_f(y_i) - C_{ec}(\beta_i) - P_c(\theta y_i - \beta_i - \alpha) \right] + \max \sum_{j=1}^{N_r} [P_r z_i - C_r(z_i)]$$
$$+ \max \left[P_g X - C_g(X) \right] + \max \int_0^X P(X)dx - P \tag{10}$$

where W represents the total social welfare function under non-cooperative game conditions, which consists of the profit functions of thermal power generators, renewable energy generators, and power companies, as well as consumer surplus. N_f and N_r N_r are the number of thermal power generators and renewable energy generators, respectively. Here, the carbon emission reduction marginal cost P_c is considered known quantity. The decision variables include thermal power generation output y_i and new energy generation power generation z_i. The thermal power generation carbon emission reduction β_i,

carbon allowance α, and the total amount of power transmission and distribution X are calculated according to above decision variables.

- **(2) Constraints**

According to the operation of the power market and the behavior characteristics of each entity, the constraints mainly include the cost of each market entity about default, market equilibrium constraints and policy constraints.

① **Cost constraint**

Generation cost function constraint: assuming that the generation cost function for both fossil and renewable energy sources is an increasing function with respect to generation capacity.

$$C'_f(Y) \geq 0, C''_f(Y) \geq 0 \tag{11}$$

$$C'_r(Z) \geq 0, C''_r(Z) \geq 0 \tag{12}$$

Emission reduction cost function constraint: assume that the emission reduction cost function is also an increasing function with respect to the amount of emission reduction.

$$C'_{ec}(\beta) \geq 0, C''_{ec}(\beta) \geq 0 \tag{13}$$

② **Market equilibrium constraint**

Electricity equilibrium constraint: Assume that the market reaches equilibrium when the total electricity produced by thermal and renewable generators is fully purchased by consumers.

$$X = Y + Z \tag{14}$$

$$Y = \sum_{i}^{N_f} y_i \tag{15}$$

$$Z = \sum_{j}^{N_r} z_j \tag{16}$$

where Y denotes the total generation capacity of the N_f thermal power producers in the market; Z represents the total generation capacity of the N_r renewable power producers in the market.

Carbon market price constraint: Under the condition of market equilibrium, the marginal abatement cost of the power industry is equal to the carbon price.

$$C'_{ec} = P_c \tag{17}$$

The amount of power generators: in the carbon trading market, thermal power generators are the thermal power generators that make carbon quota purchases and sales; the

number of power generators in the whole market is the sum of thermal power generators and renewable power generators.

$$N_f = N_{in} + N_{out} \tag{18}$$

$$N = N_f + N_r \tag{19}$$

③ **Policy constraints**

Percentage of renewable energy generation: The government requires that a certain percentage of electricity delivered by the grid must include renewable energy generation, with a range constraint as:

$$\gamma \geq \frac{z}{x} \tag{20}$$

where γ is the ratio of renewable energy generation to total electricity generation, the minimum limit of this ratio is set by the state.

Power price: Renewable and thermal generators receive equal power prices, both equal to the difference between the price paid by the customer for electricity and the transmission and distribution costs, as shown in (21).

$$P_f = P_r = P - P_g \tag{21}$$

4   Case Study

(1)   Data assumptions and parameter settings.

In this paper, we refer to the generation cost coefficients in [11–13] and make appropriate adjustments to some parameters with the actual situation to determine the corresponding parameters as Table 1. Among them, the average transmission and distribution price is referred to the transmission and distribution price table of Jiangsu power grid. Meanwhile, according to the prediction of State Grid Jiangsu Electric Power Co., the electricity consumption of the whole society is set as 637.4 billion kWh with an average annual growth rate of 4.5%.

(2)   Decision analysis of thermal power generators in Jiangsu Province.

It can be seen from Fig. 1(a) that with the increase of social electricity demand, both thermal power generation and renewable power generation increase continuously, but the gap between the two power generating forms gradually decreases, and the growth rate of renewable power generation is faster. From Fig. 1(b), it also can be seen that with the increase of carbon price, the proportion of thermal power generation to total power generation gradually decreases and the proportion of renewable power generation gradually increases and gradually stabilizes. Due to the carbon emission reduction requirements, thermal power generators need to trade quotas in the carbon trading market, and the increase of carbon price indirectly increases the carbon emission reduction cost of thermal power generators, which in turn affects their power generation. Renewable energy

Table 1. Values of model parameters.

Parameters	Values	Units
a_{fc}	$4.56 * 10^{-14}$	CNY/kWh^2
b_{fc}	0.26	CNY/kWh
c_{fc}	0	CNY
a_r	$8.53 * 10^{-13}$	CNY/kWh^2
b_r	0.55	CNY/kWh
c_r	0	CNY
a_e	$4 * 10^{-7}$	$CNY/t^2\ CO_2$
b_e	0	$CNY/t\ CO_2$
c_e	0	CNY
b	$2 * 10^{-14}$	CNY/kWh^2
a	0.7	CNY/kWh
P_g	0.21	CNY/kWh
θ	$7.8 * 10^{-4}$	tCO_2/kWh

generators, on the other hand, do not have the pressure to reduce carbon emissions and are more inclined to increase their power generation under the same price conditions. This further indicates that the carbon trading market can promote the consumption of renewable energy power.
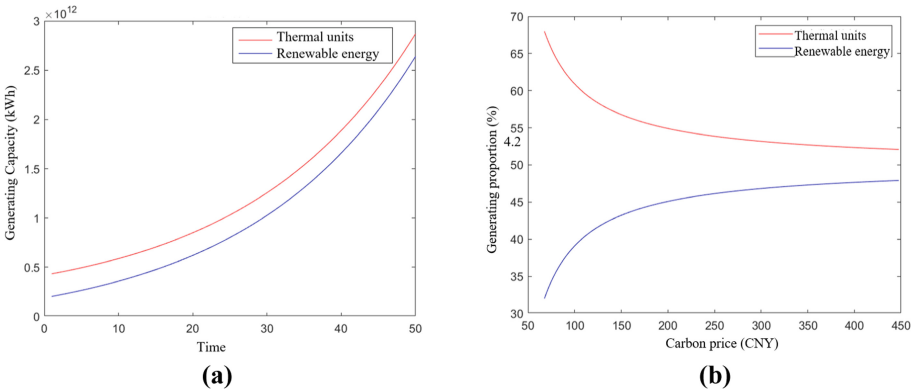
Fig. 1. Changes in generating capacity and proportion under the carbon trading market.

From the perspective of thermal power generators, this study divides thermal power generators participating in carbon trading into those who need to buy carbon quotas and those who need to sell carbon quotas. The impact of carbon price and carbon quotas on their optimal profits is shown in Fig. 2(a) and Fig. 2(b), assume that they differ only
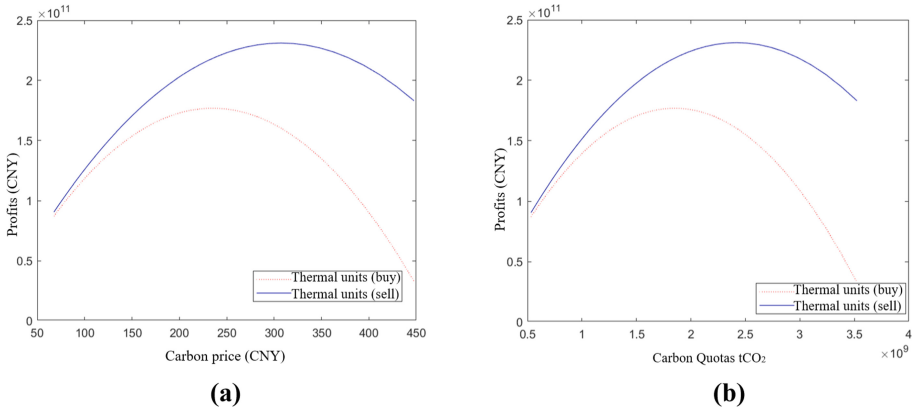
Fig. 2. Impacts of carbon price and carbon quotas on thermal power producers' profits.

in terms of emission reduction technology. In particular, the overall profit of generators who need to buy carbon quotas is lower than that of generators who need to sell carbon quotas, since buyers need to bear the cost of buying carbon quotas, while sellers can reap the additional profit of selling carbon quotas.

As far as the buyer of carbon quotas is concerned, on the one hand, as the carbon price rises, its profit grows slowly and then gradually declines. Buyer thermal power generators have been required to buy carbon quotas in the carbon trading market due to their backward emission reduction technology, and when the carbon price rises to about CNY 200–250, the cost of buying carbon quotas is too high, making their profits gradually decline. On the other hand, since carbon quotas are affected by power generation and power demand, an increase in carbon quotas means an increase in social demand for power, and thermal power producers need to supply more electricity, thus emitting more CO_2. The buyer of thermal power generation needs to pay for the excess CO_2 emissions, which in turn makes it less profitable.

The seller power producer, on the other hand, has advanced emission reduction technology and has excess carbon quotas to sell in the carbon trading market. Therefore, their profits will gradually increase as the carbon quota increases and the carbon price rises. However, when the carbon quota exceeds a certain amount, its power generation is larger and the carbon abatement technology cannot be profitable for it, thus the profit gradually decreases.

Therefore, in the context of the carbon market, thermal power producers will control their power generation according to their own interests and buy or sell carbon quotas at the right carbon price. With the development of carbon trading market, thermal power producers will gradually tend to reduce some of their carbon emissions by improving and upgrading their own technology and introducing advanced equipment to maximize their benefits.

(3) Decision-making analysis of power companies in Jiangsu Province.

As shown in Fig. 3(a) and Fig. 3(b), both carbon price and carbon quota have a negative impact on the profit of power companies. At present, the revenue source of power companies is mainly the state access revenue from transmission and distribution, and the transmission and distribution price are not much affected by the feed-in tariff and sales tariff. Therefore, for power companies, the more electricity they need to transmit and distribute, the higher the profit. However, in the carbon trading market, the increase in carbon price will increase the cost of thermal power generators, who will raise the feed-in tariff to ensure their own profit, which will eventually be transmitted to the customer side. Higher power prices will cause power consumers to reduce their demand for electricity, thus reducing the transmission and distribution capacity of power companies. Therefore, the increase of carbon price and carbon quota will indirectly reduce the profit of power companies.
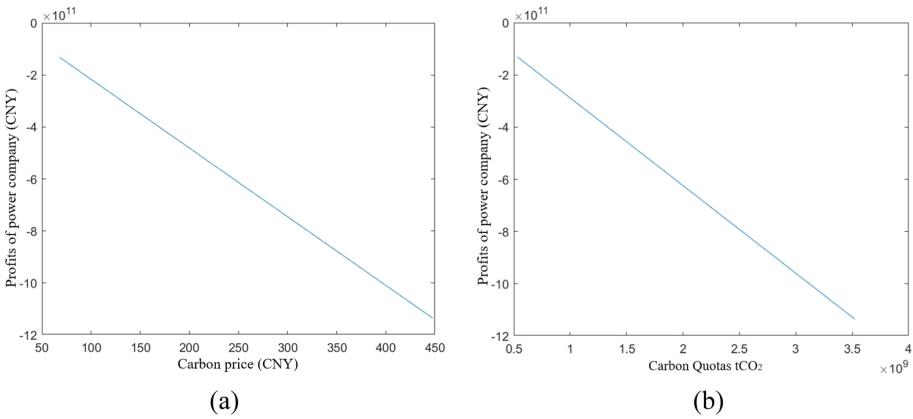
Fig. 3. Impact of carbon price and carbon quotas on the profit of power company.

Although power companies are not directly involved in the carbon trading market, the carbon trading market has a large impact on them. Therefore, to ensure a smooth supply of electricity and maximize their own interests, power companies need to pay attention to the dynamics of the carbon trading market and keep abreast of the impact of changes in power prices and carbon quotas on the power generation industry.

(4) Decision analysis of power consumers in Jiangsu Province.

The power consumers targeted in this study are residential power consumers whose profits are mainly consumer surplus. As shown in Fig. 4, with higher carbon prices, the profits of power consumers will decrease. With higher carbon prices, electricity prices will be greatly influenced by carbon prices. Thermal power producers will transfer the cost of carbon prices to feed-in tariffs, and power companies will attach the cost to the sales prices. With the increase in power prices, to maximize their own benefits, power consumers will reduce their demand for electricity.
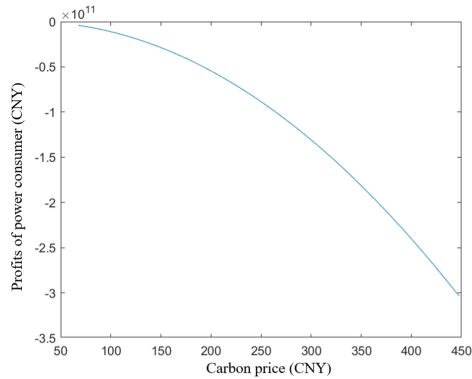
Fig. 4. Impact of carbon price and carbon quotas on the profits of power consumer.

5   Conclusions

Based on the trading rules of the carbon market and the development status of the power market in Jiangsu, this paper establishes a multi-agent objective function for thermal power generators, renewable energy generators, power grid companies and power users. It is found that the increase of carbon price has a significant impact on thermal power producers and renewable energy power generation, and the increase of carbon price and carbon quota will affect the optimal profit of each subject, thereby affecting their decision-making.

In the market environment, carbon price and power price are mutually influenced, and the carbon cost will affect the competitiveness of enterprises in the power market. Therefore, it is necessary to further improve the market mechanism and establish a transmission mechanism for carbon prices and power prices to ensure that prices are at a reasonable level.

References

1. He, K.: Low carbon transformation of energy and economy aiming for the peaking of carbon emission and carbon neutrality. J. Environ. Econ. **6**(1), 1–9 (2021)
2. Shi, D., Li, P.: Industrial carbon emission structure simulation and policy impact under the target of "double carbon. Reform **12**, 1–15 (2021)
3. Feng, Y., Zhou, Y.: Construction of carbon market and electricity market under dual carbon target. Finan. Minds **6**(4), 102–123 (2021)
4. Lin, B., Jia, Z.: What will china's carbon emission trading market affect with only electricity sector involvement? A CGE based Study. Energy Econ. **78**, 301–311 (2019)
5. Feng, T., Li, R., Zhang, H.: Induction mechanism and optimization of tradable green certificates and carbon emission trading acting on electricity market in China. Resour. Conserv. Recycl. **169**, 105487 (2021)
6. Ji, B., Chang, L., Chen, Z., et al.: Blockchain technology based design and application of market mechanism for power carbon emission allowance trading. Autom. Electric Power Syst. **45**(12), 1–10 (2021)

7. Xu, G., Luan, H.: Spatial difference and influencing factors of carbon dioxide emission efficiency in Jiangsu: analysis based on improved three stage SBM-DEA model. Ecol. Econ. **34**(07), 33–38 (2018)
8. Wang, L., Chen, H., Chen, S.: Dynamic evolution and empirical analysis of coordinated and coupling development of energy-economy-environment-society at urban level—a case study of Jiangsu Province. Transa. Beijing Inst. Technol. **24**(01), 1–23 (2021)
9. Wang, Y., Wu, J., Wang, H., et al.: Analysis of interactions between carbon emission trading market and medium- and long-term electricity market. Proc. CSU-EPSA **32**(10), 44–54 (2020)
10. Zhang, L., Li, Y., Jia, Z.: Impact of carbon allowance allocation on power industry in china's carbon trading market: computable general equilibrium based analysis. Appl. Energy **229**, 814–827 (2018)
11. Ma, Z., Ye, W., Cai, S.: A study on the coordinated development of china's carbon market and electricity market based on SICGE model. Macroeconomics **5**, 145–153 (2019)
12. Chen, R.: Evolutionary Game and Chaos Control of Power Market Based on Heterogeneous Behavioral Decision-makings. Changsha University of Science & Technology (2010)
13. Zuo, Y.: Research on Market Behavioral Decisions of Power Producers under RPS. North China Electric Power University (2018)

A Fast Calculation Method of SCUC Based on Deep Learning

Lizhang Cong[1(✉)], Jianxue Wang[1], Hongrui Yin[1], Qian Yang[1], Zhengting Jiang[1], and Xuxia Li[2]

[1] School of Electrical Engineering, Xi'an Jiaotong University, Xi'an 710049, China
xjtuclz@163.com

[2] Economic and Technological Research Institute State Grid Shanxi Electric Power Company, Taiyuan 030021, China

Abstract. Under the background of the rapid change of power system and the wide application of artificial intelligence technology, it is of great significance to research how to combine artificial intelligence technology and Security Constrained Unit Commitment (SCUC) problem. This paper proposes a fast calculation method of SCUC based on deep learning (DL-SCUC). The proposed method uses off-line training convolution neural network (CNN) to extract features and learn rules of the time sequence information of unit startup and shutdown. In the on-line calculation, the integer variable reduction strategy is used, and the unit startup and shutdown scheme is arranged based on the trained CNN, which greatly reduces the difficulty of subsequent calculation of SCUC. The proposed method combines artificial intelligence with optimization methods, which not only improves the calculation speed but also ensures the feasibility of the solution. Case studies based on the modified XJTU-ROTS2017 testing system show that DL-SCUC can effectively improve the calculation speed of SCUC problem and has high accuracy.

Keywords: SCUC · Deep learning · Fast calculation method

1 Introduction

Smart grid has always been the inevitable trend of power system development. Considering the rapid development of power system, the Security Constrained Unit Commitment (SCUC) problems which are treated as the foundation of dispatching electric power will be facing a lot of challenges. At the same time, with the wide application of artificial intelligence technology in power system, the relationship between artificial intelligence technology and SCUC problem will be closer and more attention will be paid to it [1].

Under the background of the rapid change of energy, SCUC problem is facing endless theoretical challenges, and its solution is a typical NP hard problem with relatively low efficiency. It is of theoretical significance to research the accelerated solution algorithm of SCUC. [2] proposes a fully parallel stochastic optimization SCUC method to efficiently

and quickly solve the SCUC problem of large-scale power systems with wind power. [3] proposes a linearized SCUC model that combines economic dispatching and clustering unit commitment, sacrificing part of the accuracy to obtain a higher calculation speed. [4] researches how to accelerate the solution of large-scale UC through variable reduction. The idea is to relax the time-series coupling constraints to obtain a single time segment subproblem. Finally, the UC integer variables are fixed with a relaxation solution to achieve the purpose of variable reduction.

In recent years, artificial intelligence is booming and has been widely used in power system. Deep learning technology has achieved good results in solving practical problems of power system, such as transmission line fault judgment [5], transmission line icing recognition [6] and defect text classification of power equipment [7]. As the basis of power distribution and dispatching, security-constrained unit commitment (SCUC) will face a lot of challenges directly. The traditional physical model driven unit commitment decision-making method may not be able to meet the actual needs of the rapid development of power system. Some scholars focus on how to apply artificial intelligence to SCUC. [8] proposes a data-driven SCUC calculation method, which directly learns the relationship between inputs and decision results through long short-term memory networks and massive historical decision-making data training. Literature [9] and [10] adopt similar ideas and use data-driven methods to construct a SCUC expert system, which effectively reduces the computational complexity. The above literature shows that it is feasible to use artificial intelligence to solve SCUC problems.

However, in practical application, the complex network structure and the huge number of units have posed a great challenge to the training of the neural network. The accuracy and security of artificial intelligence methods cannot be guaranteed. For this reason, this paper proposes a fast calculation method of SCUC based on deep learning (DL-SCUC). The main contributions of this paper are as follows:

- Through a convolution neural network (CNN) and a full connect neural network, this paper extracts data features and obtains the startup and shutdown scheme of the unit. This method can greatly reduce integer variables and the difficulty of subsequent calculation.
- In this paper, the solution of linearized SCUC is used as the input of CNN to ensure the accuracy of the model and reduce the difficulty of neural network training.
- The proposed method combinates artificial intelligence and mathematical optimization, and designs a correction mechanism to ensure the feasibility of the solution.

The remaining of this paper is organized as follows: Sect. 2 establishes the basic SCUC model. Section 3 elaborates the model framework and the training methods of depth learning Sect. 4 analyzes the application effect of the proposed algorithm in XJTU-ROTS2017 testing system [11]. Finally, Sect. 5 is the conclusion of this paper.

2 Basic Model

In this section, we plan to establish a short-term SCUC model considering coal-fired generator, hydropower, renewable energy and energy storage system.

2.1 Objective Function

The objective function of the model is to minimize the economic operation cost of the power system:

$$\min \quad \sum_{i \in \Omega_{TG}} \sum_{t=1}^{T} (F_{i,t}^{TG} + SU_i^{TG} u_{i,t}^{TG} + SD_i^{TG} d_{i,t}^{TG}) + \beta^{NE} \sum_{i \in \Omega_{NEG}} \sum_{t=1}^{NT} (\overline{P}_{i,t}^{NE,R} - P_{i,t}^{NE})$$

$$(1)$$

where Ω_{TG}/Ω_{NEG} is the set of coal-fired units/renewable energy units; $F_{i,t}^{TG}/SU_i^{TG}/SD_i^{TG}$ is the fuel cost/startup cost/shutdown cost of coal-fired units; $u_{i,t}^{TG}/d_{i,t}^{TG}$ is the indication variable of whether the coal-fired units starts/shuts down; $\overline{P}_{i,t}^{NE,R}/P_{i,t}^{NE}$ is the predicted output/actual output of renewable energy; β^{NE} is the unit cost of abandoned resources of renewable energy; T is the number of hours included in the running simulation timescale, which in this paper is 24 h.

2.2 Constraints

Since this paper mainly focuses on the reduction of integer variables in coal-fired units, Other constraints, such as operation constraints of hydropower units and renewable energy units, energy storage operation constraints, system power balance constraints, etc., are not described in this paper. Please refer to [12, 13] for details. The constraints about coal-fired units are as follows:

$$x_{i,t}^{TG} - x_{i,t-1}^{TG} = u_{i,t}^{TG} - d_{i,t}^{TG}, \quad \forall i \in \Omega_{TG}, t = 1, \cdots, T \tag{2}$$

$$P_{i,t}^{TG} = \sum_{m=1}^{NM} P_{i,t,m}^{TG}, \quad \forall i \in \Omega_{TG}, t = 1, \cdots, T \tag{3}$$

$$x_{i,t}^{TG} \underline{P}_{i,m}^{TG} \leq P_{i,t,m}^{TG} \leq x_{i,t}^{TG} \overline{P}_{i,m}^{TG}, \quad \forall i \in \Omega_{TG}, t = 1, \cdots, T, m = 1, \cdots, NM \tag{4}$$

$$-RD_i^{TG} - d_{i,t}^{TG} \left(\underline{P}_i^{TG} - RD_i^{TG} \right) \leq P_{i,t}^{TG} - P_{i,t-1}^{TG} \leq RU_i^{TG} + u_{i,t}^{TG} \left(\underline{P}_i^{TG} - RU_i^{TG} \right)$$
$$, \quad \forall i \in \Omega_{TG}, t = 1, \cdots, T \tag{5}$$

$$\sum_{j=t}^{t+T_i^{TG,on}-1} x_{i,j}^{TG} \geq u_{i,t}^{TG} T_i^{TG,on}, \quad \forall i \in \Omega_{TG}, t = 1, \cdots, T \tag{6}$$

$$\sum_{j=t}^{t+T_i^{TG,off}-1} \left(1-x_{i,j}^{TG}\right) \geq d_{i,t}^{TG} T_i^{TG,off}, \quad \forall i \in \Omega_{TG}, t = 1, \cdots, T \qquad (7)$$

where $x_{i,t}^{TG}$ is the indication variable of the coal-fired unit state, which is 1 if the unit is online and 0 otherwise. $\underline{P}_{i,m}^{TG}$, $\overline{P}_{i,m}^{TG}$ is the lower and upper bounds of the m-th output interval of thermal power unit i after piecewise linearization RU_i^{TG}/RD_i^{TG} is maximum ascent rate and maximum descent rate of coal-fired unit i. $T_i^{TG,on}/T_i^{TG,off}$ is the minimum startup/shutdown time of coal-fired unit i.

Equation (3) denotes coal-fired unit operation constraint. In this way, $u_{i,t}^{TG}$ and $d_{i,t}^{TG}$ are limited. Equation (4) is the state logic constraint of coal-fired unit. Equation (5) is the climbing constraint of coal-fired unit. This form restricts the unit to climb to $\underline{P}_{i,1}^{TG}$ first when it changes from off state to on state; When changing from power on state to power off state, the power can only be reduced to $\underline{P}_{i,1}^{TG}$ before power off. Equation (6) and Eq. (7) are constraints about the minimum startup and shutdown time of coal-fired units. When $u_{i,t}^{TG} = 1$, the unit i changes from the off state to the on state at time t, and then at least from time t to time $t + T_i^{TG,on} - 1$, the unit shall maintain the on state, that is, as shown in Eq. (6), all $x_{i,t}^{TG} = 1$ within this period shall be limited; When $d_{i,t}^{TG} = 1$, in the same way, it can be analyzed that Eq. (7) limits all $x_{i,t}^{TG} = 0$ in this period; When $u_{i,t}^{TG} = 0$ or $d_{i,t}^{TG} = 0$, the constraint corresponding to the variable has no effect.

Due to the existence of integer variables such as $x_{i,t}^{TG}, u_{i,t}^{TG}$ and $d_{i,t}^{TG}$, SCUC problem is a mixed-integer linear programming problem, which is difficult to solve directly because of the NP hard characteristic. Therefore, the following chapters mainly focus on these integer variables to research methods to improve the calculation speed of SCUC.

3 Calculation Method of SCUC Based on Deep Learning

In this section, we propose an accelerated SCUC calculation method based on deep learning, named DL-SCUC. The DL-SCUC method is divided into three modules: linear relaxation module, deep learning module and correction module, which is shown in Fig. 1. The linear relaxation module calculates a linear problem and obtains the relaxation solution of integer variables as the input of deep learning module. The deep learning module analyzes the data provided by linear relaxation module through a CNN network to obtain the state of each unit. The correction module is used to ensure the feasibility of the solution, and provide detailed scheduling scheme according to the results obtained from the deep learning module.
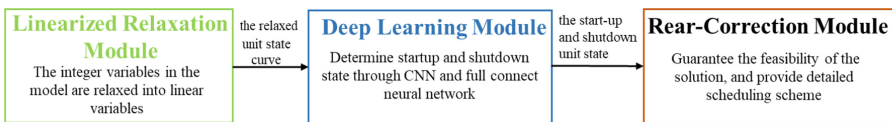
Fig. 1. The flowchart of DL-SCUC

Here, we assume that the unit only be startup or shutdown at most in one day. This is based on the fact that coal-fired units take a long time to startup or shutdown and consume serious fuel, so they will not startup or shutdown many times in one day. This coincides with the principle of minimizing the number of decision variables and reducing the scale of the problem in the optimization model.

3.1 Linearized Relaxation Module

In order to obtain the approximate solution quickly, we apply linear relaxation to the original SCUC problem. Compared with the basic model, the model needs to add the following constraints:

$$\begin{cases} 0 \leq x_{i,t}^{TG} \leq 1 \\ 0 \leq u_{i,t}^{TG} \leq 1, \forall i \in \Omega_{TG}, t = 1, \cdots, T \\ 0 \leq d_{i,t}^{TG} \leq 1 \end{cases} \tag{8}$$

The optimal solution of the linear problem provides a lower bound for the original problem. Because of its linear characteristic, the solution after linear relaxation is often infeasible for the original problem. The $x_{i,t}^{TG}$ obtained from the model is often a decimal between 0 and 1. However, considering that the model has the same constraints as the original problem except Eq. (8), the solution provided by the linear problem also reflects the state of the unit to a certain extent. It can provide boundary conditions for effectively solving mixed integer problems. So, we take the relaxed unit state curve $\{x_{i,1}^{TG}, x_{i,2}^{TG}, \ldots x_{i,T}^{TG}\}$ as the input of deep learning module. If historical data is directly used as training data, we may need to consider historical load curve, renewable energy output curve, unit parameters, grid information, etc., which will greatly increase the difficulty of training. And using the proposed method, the input data of each unit has only t dimension, which can effectively reduce the dimension of input parameters.

3.2 Deep Learning Module

The function of the deep learning module is to determine the state of each unit according to the relaxed unit state curve obtained by the linear relaxation module.

Since we assume that the unit can only be startup or shutdown once a day at most, the unit has only four states: keep on, keep off, have startup operation and have shutdown operation. If the unit keeps on or keeps off, $x_{i,t}^{TG}$ shall be kept in the state of 1 or 0 throughout the day; If the unit has startup operation, it means that $x_{i,t}^{TG}$ can change from 0 to 1. Similarly, if the unit has shutdown operation, it means that $x_{i,t}^{TG}$ can change from 1 to 0. By this way, the original problem becomes a classic classification problem in the field of artificial intelligence.

CNN is often used to deal with classification problems. Its unique convolution layer and pooling layer design enable it to effectively extract features and learn rules from a large number of samples [14]. The CNN module design is shown in the Fig. 2. The convolutional neural network is designed as lenet5 structure. Two convolution layers and two pooling layers are constructed. After convolution and pooling, full connection operation is carried out to output the probability corresponding to each unit state.
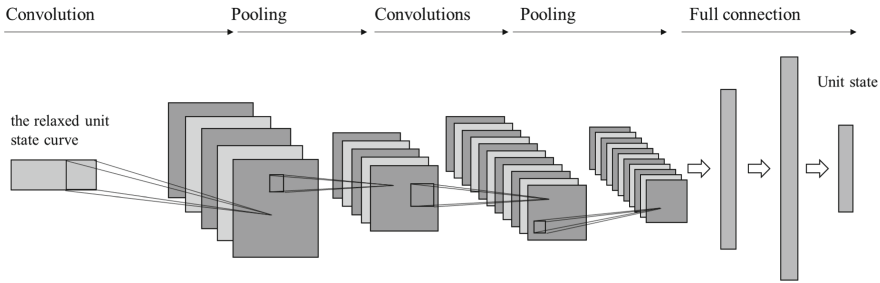
Fig. 2. CNN model for identifying unit state

After CNN, the model also needs a fully connected neural network to consider the state influence of each unit, so as to obtain the modified results. The fully connected neural network is mainly used to consider the interaction between units. This is mainly used to handle some units in intermediate state. For example, if the relaxed unit state curve of a unit is {0.5, 0.5, …, 0.5}, We may not be sure what the state of the unit is through CNN. In this case, we need to consider the relationship between the units through the full connect neural network. Determine the state of the unit through the states of other units.
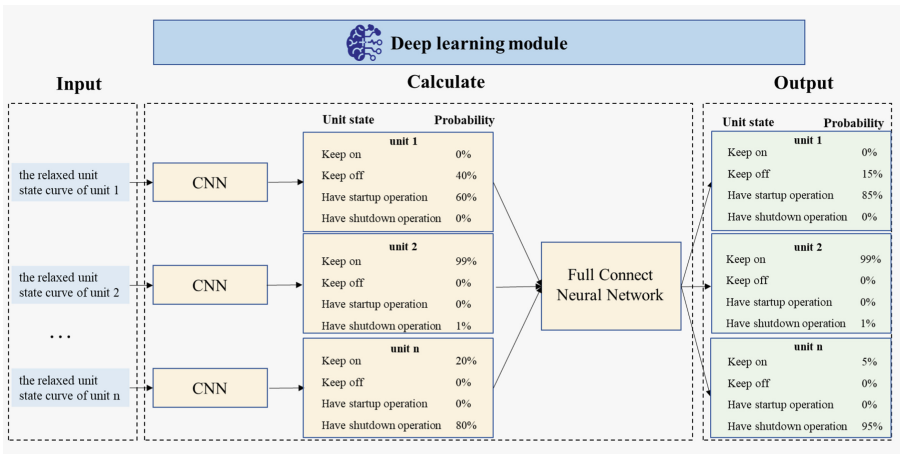
Fig. 3. The framework of deep learning module

The overall framework of the deep learning module is shown in the Fig. 3. Firstly, the state probability of each unit is obtained by analyzing the relaxed unit state curve of each unit using CNN. Then, through a full connect neural network, considering the interaction between the units, the original startup and shutdown scheme is modified, and the final startup and shutdown scheme of each unit is obtained.

3.3 Correction Module

This module correction module is used to ensure the feasibility of the solution, and provide detailed scheduling scheme. In order to ensure the feasibility of the solution, the iterative correction mechanism is designed in the correction module. The specific process is shown in Fig. 4. Once there is no solution to the model, we will relax the unit in keeping on or keeping off state and try to allow them to have shutdown operation or startup operation. By means of iteration, the limitation on the unit state is gradually released until there is a feasible solution. Theoretically, if we release all restrictions about the unit states, the solution calculated by the post correction module must be consistent with the result obtained by directly solving SCUC model.
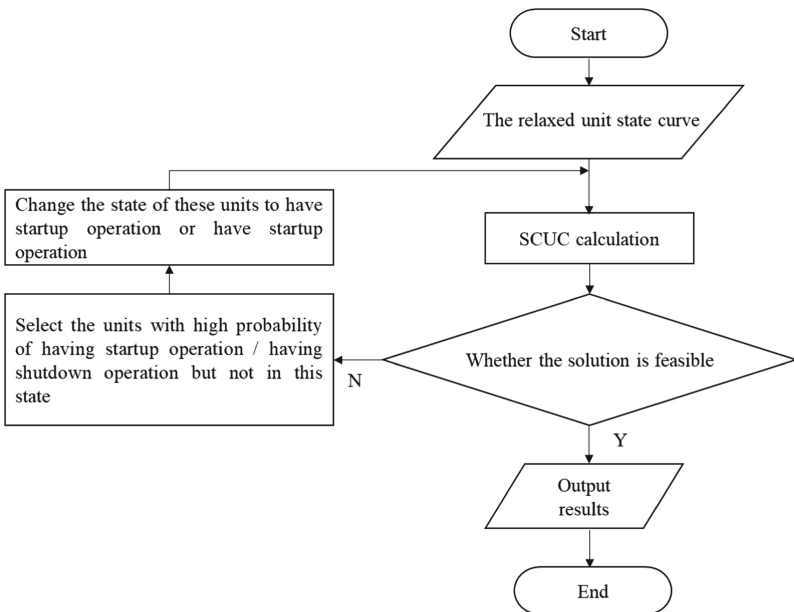
Fig. 4. Flowchart of correction module

The SCUC model mentioned here needs to add constraints about reducing coal-fired unit variables.

If the unit keeps on, it needs to meet Eq. (9):

$$u_{i,t}^{TG} = d_{i,t}^{TG} = 0, x_{i,t}^{TG} = 1 : \forall i \in \Omega_{TG}, t = 1, \cdots, T \tag{9}$$

If the unit keeps off, it needs to meet Eq. (9):

$$u_{i,t}^{TG} = d_{i,t}^{TG} = 0, x_{i,t}^{TG} = 0 : \forall i \in \Omega_{TG}, t = 1, \cdots, T \tag{10}$$

If the unit has startup operation, we can be deduced that:

$$\sum_{t=1}^{T} u_{i,t}^{TG} \leq 1, d_{i,t}^{TG} = 0 : \forall i \in \Omega_{TG}, t = 1, \cdots, T \tag{11}$$

Similarly, if the unit has shutdown operation, we can be deduced that:

$$\sum_{t=1}^{T} d_{i,t}^{TG} \leq 1, u_{i,t}^{TG} = 0 : \forall i \in \Omega_{TG}, t = 1, \cdots, T \tag{12}$$

In this paper, the detailed scheduling information is not directly given through artificial intelligence, but given through the traditional optimization method, which can ensure that the solution results must meet the constraints described in Sect. 2, and also reduces the training difficulty of the model.

It is worth noting that the proposed method is still effective when the system parameters vary. For example, when some units are overhauled, only the boundary conditions of the linearized relaxation module and the correction module need to be modified to ensure that the unit is in the keeping off state. When some lines are overhauled, for the linearized relaxation module and the correction module, similarly, we only need to modify the boundary conditions before calculating. For the deep learning module, if the results given by the current neural network are still accurate, there is no need to make corrections. If the current neural network performance is not ideal, we need to regenerate the samples according to the new grid structure and conduct off-line training again.

4 Case Studies

The DL-SCUC algorithm proposed in this paper will be tested in XJTU-ROTS2017 testing system and an actual system to verify the effectiveness of the model. Through the bootstrap technology of time series [15], we generate a large number of typical scene results based on historical data for model training. The model sets the convolution kernel size to (1, 5) and uses the crossentropyloss function as the loss function.

4.1 XJTU-ROTS2017 Testing System

In this section, XJTU-ROTS2017 testing system [11] is used to verify the effectiveness of the proposed algorithm. The testing system includes renewable energy, coal power, hydropower and energy storage system, which is a 44-bus system.

The recognition accuracy of the unit startup and shutdown of the convolutional neural network on the test set is 99.38%. In this paper, 365 scenarios in a certain level year are calculated, and the results are shown in the following tables:

Table 1. Calculation results of XJTU-ROTS2017 testing system

Algorithm	Average error (%)	Maximum error (%)	Total elapsed time (s)
SCUC	–	–	249.72
DL-SCUC	0.04	0.84	89.36

Table 2. Main indicators results of XJTU-ROTS2017 testing system

Index	SCUC	DL-SCUC
Operation costs (billion yuan)	9.37	9.37
Total RE curtailment rate (%)	0.12	0.12
Availability Hours of Wind	2537.82	2537.59
Availability Hours of Solar	1575.76	1575.72
Availability Hours of Thermal	4191.27	4191.37
Availability Hours of Hydro	2292.00	2292.00

As we can see in Table 1 and Table 2, the average error of DL-SCUC is only 0.04%, which is very close to the solution result of SCUC. In addition, DL-SCUC also reduces the total calculation time of 365 scenarios from 249.72s to 89.36s. Compared with the traditional optimization algorithm, the proposed method can guarantee high calculation accuracy and improve the calculation speed.

Figure 5 and Fig. 6 shows the calculation results of the proposed DL-SCUC and the SCUC under the typical scenario of four seasons. The left side is the calculation result of the traditional SCUC model, and the right side is the calculation result of the proposed DL-SCUC. The scenarios selected are March 15th, June 15th, September 15th and December 15th, which represent the four seasons of the system. In Fig. 5, dark color means the unit is online and light color means the unit is offline. It can be seen that the results about SCUC and DL-SCUC are basically the same. The error of the DL-SCUC is completely within the acceptable range.

(a) Spring by SCUC

(b) Spring by DL-SCUC

(c) Summer by SCUC

(d) Summer by DL-SCUC

(e) Autumn by SCUC

(f) Autumn by DL-SCUC

(g) Winter by SCUC

(h) Winter by DL-SCUC
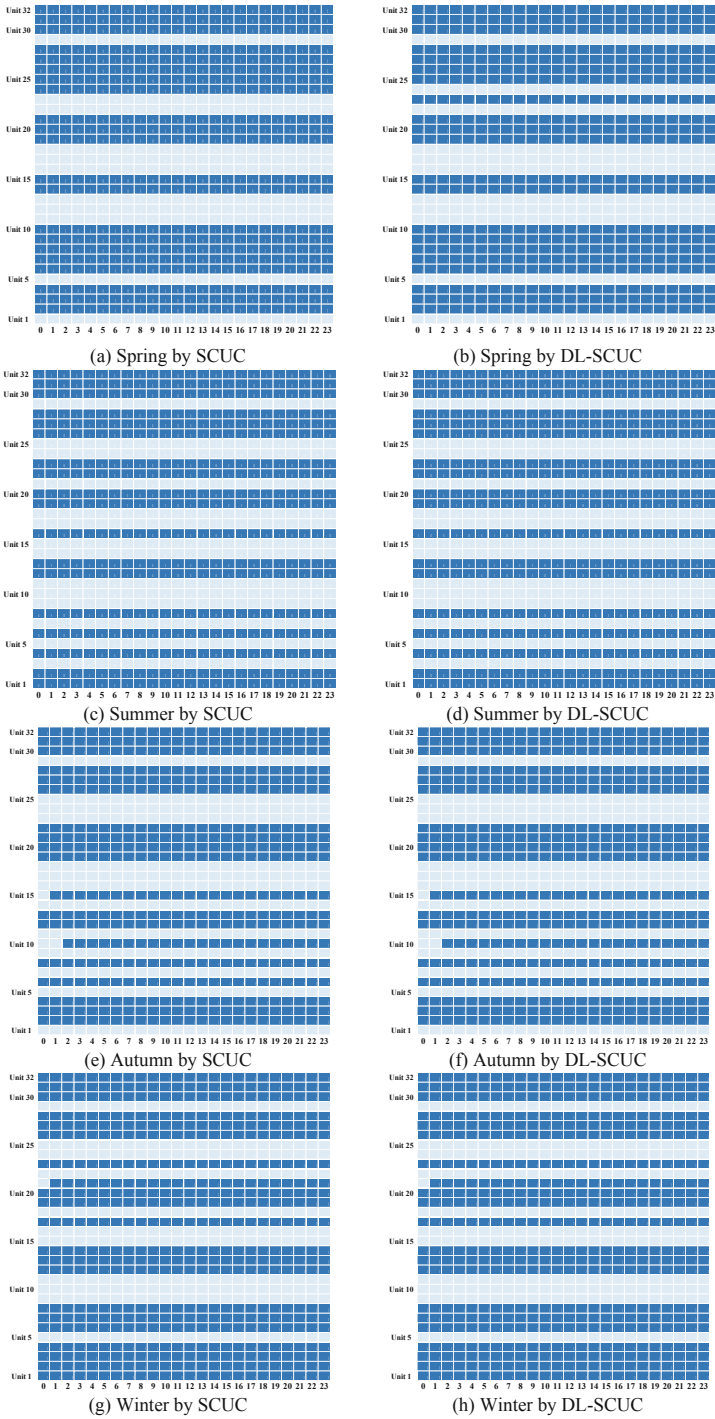
Fig. 5. Unit states in typical days
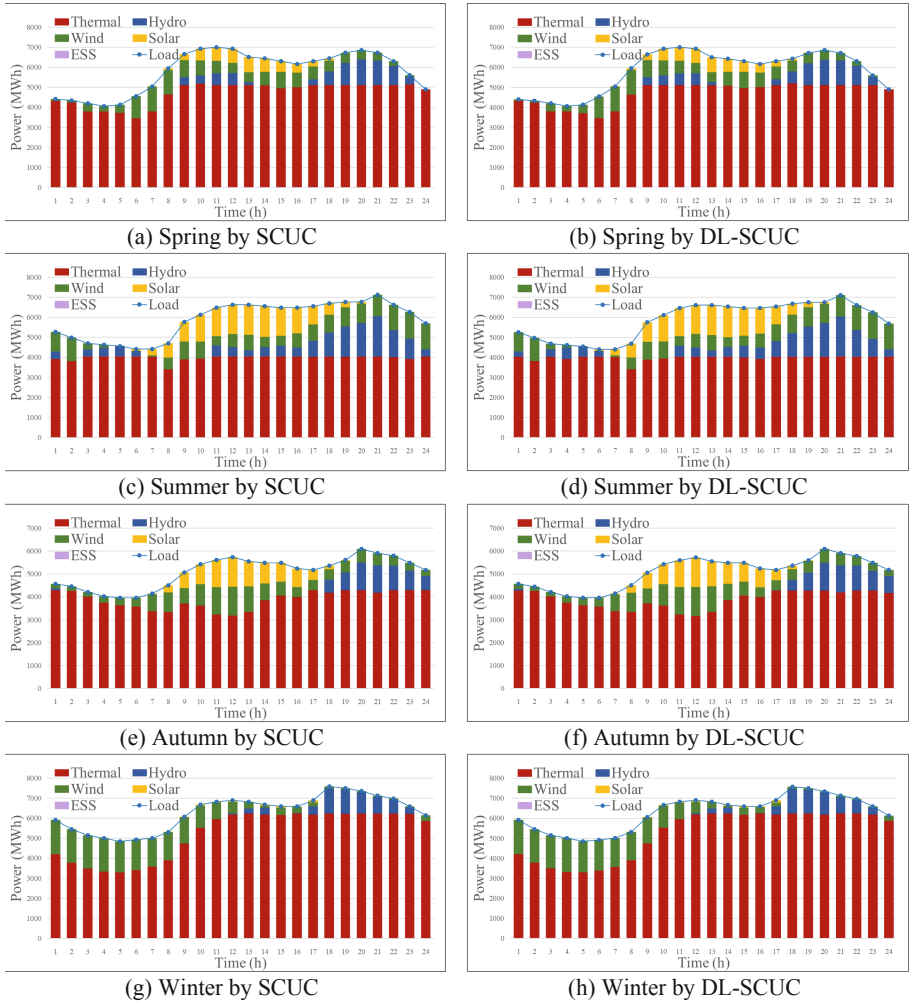
Fig. 6. Electricity balance information in typical days

4.2 Actual System

This paper also tests a provincial actual system in a certain level year. In the actual system, the installed capacity of wind power reached 28338 MW, the installed capacity of photovoltaic reached 34605 MW. The installed capacity of renewable units accounted for more than 50%. The number of thermal power units has reached 173 and the number of buses has reached 860, which is a great challenge for SCUC calculation. After the comparative calculation of 365 scenes throughout one year, the results are shown in Table 3 and Table 4:

Table 3. Calculation results of an actual system

Algorithm	Average error (%)	Maximum error (%)	Total elapsed time (s)
SCUC	–	–	16431.60
DL-SCUC	0.12	0.95	4453.89

Table 4. Main indicators results of an actual system

Index	SCUC	DL-SCUC
Operation costs (billion yuan)	60.42	60.53
Total RE curtailment rate (%)	4.08	4.23
Availability Hours of Wind	1835.12	1831.78
Availability Hours of Solar	1261.50	1252.63
Availability Hours of Thermal	3526.45	3532.87
Availability Hours of Hydro	4790.57	4790.57

It can be seen from the table that the proposed method still performs well in complex systems and has high calculation accuracy.

5   Conclusion

This paper proposes a fast calculation method of SCUC based on deep learning named DL-SCUC. The DL-SCUC adopts the combination of artificial intelligence and optimization methods. On the one hand, the artificial intelligence method is used to accelerate the solution process, on the other hand, the optimization method is used to ensure that the results are reasonable. Through this framework, we can reduce most integer variables, which simplifies the complexity of the problem. The effectiveness and superiority of the model are verified by XJTU-ROTS2017 testing system. The case studies shows that the solution of the proposed model is close to the optimization method, and the calculation speed is significantly improved.

References

1. Ju, P., Zhou, X., Chen, W., et al.: "Smart Grid Plus" research overview. Electric Power Autom. Equip. **38**(05), 2–11 (2018). (in Chinese)
2. Wang, C., Fu, Y.: Fully parallel stochastic security-constrained unit commitment. IEEE Trans. Power Syst. **31**, 3561–3571 (2016)
3. Du, E., Ning, Z., Kang, C., et al.: A high-efficiency network-constrained clustered unit commitment model for power system planning studies. IEEE Trans. Power Syst. **34**(4), 2498–2508 (2018)

4. Yin, H., Yang, Q., Chen, X., et al.: A Parallel two-stage sequential operation simulation framework based on MTUC and STUC[C]. In: 2021 6th Asia Conference on Power and Electrical Engineering (ACPEE) (2021)
5. Wei, D., Gong, Q., Lai, W., et al.: Research on internal and external fault diagnosis and fault-selection of transmission line based on convolutional neural network. Proc. CSEE **36**(S1), 21–28 (2016). (in Chinese)
6. Lin, G., Wang, B., Peng, H., et al.: Identification of icing thickness of transmission line based on strongly generalized convolutional neural network. Proc. CSEE **38**(11), 3393–3401 (2018). (in Chinese)
7. Liu, Z., Wang, H., Cao, J., et al.: A classification model of power equipment defect texts based on convolutional neural network. Power Syst. Technol. **42**(02), 644–651 (2018). (in Chinese)
8. Yang, N., Ye, D., Lin, J., et al.: Research on data-driven intelligent security-constrained unit commitment dispatching method with self-learning ability. Proc. CSEE **39**(10), 2934–2946 (2019). (in Chinese)
9. Yang, N., Yang, C., Wu, L., et al.: Intelligent data-driven decision-making method for dynamic multi-sequence: an E-Seq2Seq based SCUC expert system. IEEE Trans. Industr. Inf. **18**(5), 3126–3137 (2021)
10. Tong, W., Zhang, Y.-J.A., Wang, S.: Deep learning to optimize: security-constrained unit commitment with uncertain wind power generation and BESSs. IEEE Trans. Sustain. Energy **13**(1), 231–240 (2022). https://doi.org/10.1109/TSTE.2021.3107848
11. Wang, J., Wei, J., Zhu, Y., et al.: The reliability and operational test system of a power grid with large-scale renewable integration. CSEE J. Power Energy Syst. **6**(3), 704–711 (2020)
12. Lotfjou, A., Shahidehpour, M., Fu, Y., et al.: Security-constrained unit commitment with AC/DC transmission systems. IEEE Trans. Power Syst. **25**(1), 531–542 (2010)
13. Padhy, N.P.: Unit commitment-a bibliographical survey. IEEE Trans. Power Syst. **19**(2), 1996–1205 (2004)
14. Zhou, F., Jin, L., Dong, J.: Review of convolutional neural network. Chin. J. Comput. **40**(06), 1229–1251 (2017). (in Chinese)
15. Yun, L.: The Bootstrap Estimation in Time Series. Michigan Technological University, Michigan (2015)

A Time-Series Decomposition Algorithm for Long-Term Security-Constrained Unit Commitment Considering Energy Storage System

Ziqiang Wang[1]([envelope]), Lizhang Cong[2], Qian Ma[1], Yang Xiao[2], Chunxiao Liu[1], and Jianxve Wang[2]

[1] China Southern Power Grid Power Dispatching Control Center, Guangzhou 510000, China
wangziqiang@csg.cn
[2] School of Electrical Engineering, Xi'an Jiaotong University, Xi'an 710049, China

Abstract. With the increase of load and the penetration of renewable energy in the new power system, the change of power structure and the enhancement of randomness put forward higher requirements for power system scheduling. In order to make full use of renewable energy and provide power system scheduling quickly and accurately, this paper proposes a time-series decomposition algorithm of long-term security-constrained unit commitment (SCUC) including energy storage system (ESS). According to the operating characteristics of ESS, the SCUC model with ESS is established. Then, in order to make full use of the parallel computing power of the computer and improve the calculation speed, this paper presents an algorithm to decouple the long-term SCUC model into several short-term SCUC problems that can be solved in parallel according to the time series. The analytical target cascading (ATC) algorithm is used to coordinate each subproblem and correct the coupling relationship between adjacent subproblems. The proposed method is tested on modified XJTU-ROTS2017 testing system. Case studies show that the algorithm can effectively improve the calculation speed and accuracy of long-term SCUC problem.

Keywords: SCUC · Time-series decomposition · Energy storage system · ATC

1 Introduction

The large-scale installation of renewable energy represented by wind power and photovoltaic makes the power output more random, intermittent and fluctuating, which poses new challenges to the traditional scheduling strategy [1, 2]. How to quickly and accurately formulate the power generation plan in new power system with high proportion of renewable energy has attracted more and more scholars' attention. At present, China's installed capacity structure is dominated by large coal-fired thermal power units, which have many startup steps and long startup and shutdown time. It is necessary to formulate the unit startup and shutdown sequence according to the long time scale, so as to

improve the unit average load rate and the overall economy and energy saving of the system. Besides, in order to cope with the long-term volatility and make full use of renewable energy, it is imperative to research long-term SCUC problem [3].

With the increase of time scale, the complexity of SCUC model increases exponentially. Therefore, it is very difficult to study a practical solution algorithm to control the optimization time within a reasonable range. [4] proposed a load segmentation technology, which combines the daily load curve according to the similarity principle, thus greatly reducing the number of optimization periods and reducing the problem scale; [5] proposed a two-stage heuristic greedy algorithm and proved its superiority by comparing it with the traditional MILP solver; [6] proposed a time-series decomposition strategy to reduce the computational time cost of SCUC, and introduced the concept of coupling interval to deal with the time-series coupling constraints, which inspire this paper. It can be seen from the relevant research and analysis that the long-term SCUC algorithm needs to be further explored, and it will be of certain significance to study the long-time scale optimal scheduling method.

In the existing studies, the energy storage system (ESS) and other power sources of the system are often involved in the optimal dispatching. In combination with different factors such as economy, environmental protection and safety, research is carried out around improving the overall economy of system operation and coping with the fluctuation of wind and solar output. There are differences in optimization objectives and solution algorithms. For example, [7] aims at minimizing the total operating cost of thermal power, and optimizes the output of pumped storage units and thermal power units. [8] established a robust unit commitment model with the objective of minimizing the system operation cost and the penalty cost of wind power output boundary deviation. [9] aims at minimizing the total power generation cost of the system, and introduces a double-layer inverse robust optimization algorithm to optimize the working conditions of pumped storage units. [10] considers three objectives: total fuel consumption, pollutant gas emissions and power purchase cost, fully considers network security constraints and operation scheduling constraints, and constructs a multi-objective security constrained dynamic optimization model for power system with multiple wind farms and pumped storage power stations.

On the basis of previous studies, combined with the actual needs of power system, this paper proposes a time-series decomposition algorithm for long-term security-constrained unit commitment considering ESS. In this paper, the charging and discharging characteristics of ESS are fully considered, and a long-term unit commitment model with ESS is constructed. Considering the difficulty of solving long-term SCUC and the actual needs of short-term and long-term coordination of large-scale coal-fired unit operation plan, this paper decomposes the long-term SCUC into several short-term SCUC problems that are easy to solve. Based on ATC algorithm, this paper proposes a coordination framework considering renewable energy units and ESS, and finally realizes the connection of power generation plan. The validity of the proposed model is verified by a modified XJTU-ROTS2017 testing system [11].

The remaining of this paper is organized as follows: Sect. 2 establishes the SCUC model with ESS. In Sect. 3, a time-series decomposition algorithm method is proposed. Section 4 analyzes the application effect of the proposed algorithm in XJTU-ROTS2017 testing system. Finally, Sect. 5 is the conclusion of this paper.

2 Basic Model

In this section, a SCUC model considering ESS is established as the basic model of subsequent sections.

2.1 Objective Function

The objective function of the model is to minimize the economic operation cost of the power system, which includes the operating cost of thermal units and the abandoned resource cost of renewable energy.

$$
\min \sum_{i \in \Omega_{TG}} \sum_{k=1}^{ND} (F_{i,k}^{TG} + SU_i^{TG} u_{i,k}^{TG} + SD_i^{TG} d_{i,k}^{TG}) + \beta^{NE} \sum_{i \in \Omega_{NEG}} \sum_{k=1}^{ND} \sum_{t=1}^{ND^T} (\sum \overline{P}_{i,k,t}^{NE,R} - E_{i,k}^{NE}) \tag{1}
$$

where ND/ND^T is the number of days/hours per day included in the operating simulation timescale; Ω_{TG}/Ω_{NEG} is the set of thermal units/renewable energy units; $F_{i,k}^{TG}/SU_i^{TG}/SD_i^{TG}$ is the fuel cost/startup cost/shutdown cost of thermal unit i; $u_{i,k}^{TG}/d_{i,k}^{TG}$ is the indication variable of whether the thermal unit is startup/shutdown; $\overline{P}_{i,k,t}^{NE,R}/E_{i,k}^{NE}$ is the predicted output/actual generating capacity of renewable energy units; β^{NE} is the cost of curtailment resources of renewable energy units.

2.2 ESS Constraints

ESS is different from other power supply characteristics. ESS has both of generator characteristic and load characteristics. In this paper, ESS constraints include charge and discharge power constraints, energy constraints, periodically regulated electric quantity constraints and logic constraints of charge and discharge state of ESS, which are shown in Eq. (2) to (5).

Charge and Discharge Power Constraints

$$
\begin{cases}
0 \leq P_{i,t}^{ESS,c} \leq x_{i,t}^{ESS,c} \overline{P}_i^{ESS,c} \\
0 \leq P_{i,t}^{ESS,d} \leq x_{i,t}^{ESS,d} \overline{P}_i^{ESS,d}
\end{cases}, \quad \forall i \in \Omega_{ESS}, t = 1, \cdots, T \tag{2}
$$

where, Ω_{ESS} is the set of ESS; $\overline{P}_i^{ESS,c}/\overline{P}_i^{ESS,d}$—Maximum charge/discharge power of ESS I; $x_{i,t}^{ESS,c}/x_{i,t}^{ESS,d}$ is Charge/discharge state variable; $P_{i,t}^{ESS,c}/P_{i,t}^{ESS,d}$ is charge/discharge power of ESS i.

Energy Constraints

$$
\begin{cases}
\underline{E}_i^{ESS} \leq E_{i,t}^{ESS} \leq \overline{E}_i^{ESS} \\
E_{i,t+1}^{ESS} - E_{i,t}^{ESS} = \left(P_{i,t}^{ESS,c} \eta_i^{ESS,c} - \dfrac{P_{i,t}^{ESS,d}}{\eta_i^{ESS,d}} \right) \Delta t
\end{cases}, \quad \forall i \in \Omega_{ESS}, t = 1, \cdots, T \tag{3}
$$

where, $E_{i,t}^{ESS}$ is electric quantity of stored energy I at time t; $\overline{E}_i^{ESS}/\underline{E}_i^{ESS}$ is maximum/minimum energy allowed for ESS i; $\eta_i^{ESS,c}/\eta_i^{ESS,d}$ is charge/discharge efficiency of ESS i.

Periodically Regulated Electric Quantity Constraints
The charging and discharging process of ESS will generally be completed within a certain period. Typical forms include daily regulation and weekly regulation, that is, the ESS quantity at the beginning of the regulation period is as the same as the end. Constraints are shown in Eq. (4).

$$E_{i,t}^{ESS}\Big|_{t=kT_{adj}^{ESS}} = E_{0,i}^{ESS}, \quad \forall i \in \Omega_{ESS}, \forall k \in \mathbb{N} \tag{4}$$

where T_{adj}^{ESS} is regulation period of ESS; $E_{0,i}^{ESS}$ is initial ESS quantity.

Logic Constraints of Charge and Discharge State Constraints
In order to limit the charging and discharging of ESS at the same time, it is necessary to add a mutual exclusion Eq. (5).

$$x_{i,t}^{EES,c} + x_{i,t}^{ESS,d} \leq 1, \quad \forall i \in \Omega_{ESS}, t = 1, \cdots, T \tag{5}$$

2.3 Renewable Energy Constraints

$$0 \leq P_{i,t}^{NE} \leq \overline{P}_{i,t}^{NE}, \quad \forall i \in \Omega_{NE}, t = 1, \cdots, T \tag{6}$$

$$P_{i,t}^{NE,curt} = \overline{P}_{i,t}^{NE} - P_{i,t}^{NE}, \quad \forall i \in \Omega_{NE}, t = 1, \cdots, T \tag{7}$$

Renewable energy is a clean resource and should be preferentially consumed. Generally, the power of abandoned resources should be added to the objective function in the form of penalty term.

Other constraints include the operating constraints of various types of generators, power balance and load reserve constraints of the power system, network security constraints, etc. For the sake of simplicity, it will not be repeated here. For details, please refer to literature [12, 13].

3 Time-Series Decomposition Algorithm

In order to making full use of the parallel computing power of the computer, we decouple the long-term SCUC problem into short-term SCUC problems according to time sequence. Solving these short-term SCUC problems in parallel can reduce the complexity of the model and improve the computing speed. However, the results solved in parallel may not be feasible due to the solutions cannot guarantee the constraints between coupling time intervals (such as ramp constraints, charge and discharge of ESS and so on). In order to ensure the feasibility and accuracy of the solution, this paper uses ATC algorithm to coordinate the sub problems.

3.1 Time-Series Decomposition

Without losing generality, here, a complete SCUC problem is decomposed into three sub intervals in time sequence, which are respectively s_-, s, s_- +. Referring to [6], The time-series decomposition process is shown in Fig. 1. In order to deal with the constraints with time coupling relationship between different intervals, The initial time of each sub interval (except the first sub interval) is taken as the coupling time, which means that each coupling time will be calculated twice by the adjacent sub interval. This method can greatly reduce the difficulty of modeling, and simplifies the coupling constraints.

Original problem interval

Time-Series Decomposition

Sub intervals
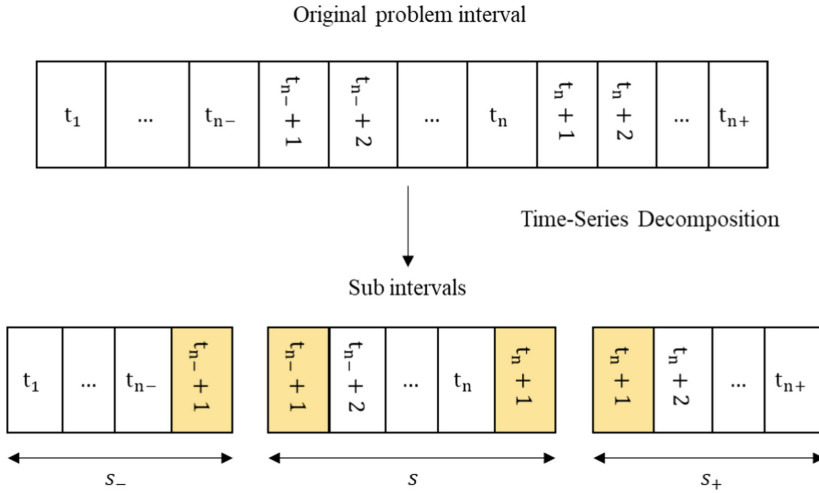
Fig. 1. Time-series decomposition process

3.2 ATC Algorithm

In this section, this paper mainly describes how to use the ATC algorithm to coordinate the coupling variables. ATC algorithm turns the model into a two-layer structure. The upper model is mainly used to coordinate coupling variables, and the lower model is used to deal with short-term SCUC problems in parallel which constraints are described in Sect. 2. Through iterative solution, the target and response variables (exclusive variables in ATC algorithm) are continuously updated to gradually reduce the difference of coupling variables in each sub interval, and finally a feasible solution is obtained. The overall algorithm framework is shown in the Fig. 2.

Upper Level Problem

The upper model mainly coordinates the coupling variables of each sub interval according to the feedback of the lower model (called response variable in ATC algorithm), and gives the recommended value (called target variable in ATC algorithm) to guide the lower model. The objective function is shown in Eq. (8).

$$\min \quad \lambda^\dagger (\chi - \gamma^k) + \rho(\chi - \gamma^k)^2 \tag{8}$$
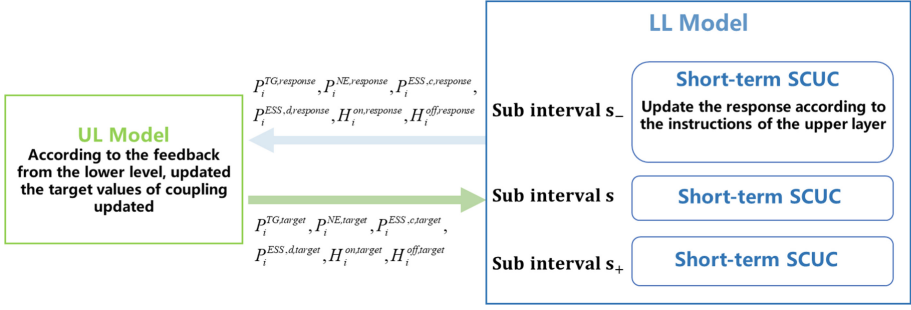
Fig. 2. ATC algorithm structure

where, χ is the target variable in the ATC algorithm framework and the decision variable in the upper model $\chi = \{P_i^{TG,\,target},\ P_i^{NE,\,target},\ P_i^{ESS,\,c,\,target},\ P_i^{ESS,\,d,\,target},\ H_i^{on,\,target},\ H_i^{off,\,target}\}$; γ is the response variable in the ATC algorithm framework and is a known quantity in the upper model. $\gamma = \{P_i^{TG,\,response},\ P_i^{NE,\,response},\ P_i^{ESS,\,c,\,response},\ P_i^{ESS,\,d,\,response},\ H_i^{on,\,response},\ H_i^{off,\,response}\}$; λ, ρ is penalty factors, which are updated as follows:

$$\lambda^k = \lambda^{k-1} + 2\rho(\chi^k - \gamma^k) \tag{9}$$

$$\rho^k = \rho^{k-1} \times \rho^0 \tag{10}$$

ESS constrains at coupling time:

$$P_{i,t_0,(s_-,s)}^{ESS,c,target} - P_{i,t_0,(s,s_-)}^{ESS,c,target} = 0, \quad t_0 = n_- + 1 \tag{11}$$

$$P_{i,t_0,(s_-,s)}^{ESS,d,target} - P_{i,t_0,(s,s_-)}^{ESS,d,target} = 0, \quad t_0 = n_- + 1 \tag{12}$$

$$P_{i,t_0,(s_+,s)}^{ESS,c,target} - P_{i,t_0,(s,s_+)}^{ESS,c,target} = 0, \quad t_0 = n + 1 \tag{13}$$

$$P_{i,t_0,(s_+,s)}^{ESS,d,target} - P_{i,t_0,(s,s_+)}^{ESS,d,target} = 0, \quad t_0 = n + 1 \tag{14}$$

where Eqs. (11) and (12) are related to the charge and discharge coupling constraints between s_- and s intervals. Where Eqs. (13) and (14) are related to the charge and discharge coupling constraints between s and s_+ intervals. Where (s_-, s) represents the variables related to interval s in interval s_-, similarly, (s, s_-) represents the variables related to interval s_- in interval s; t_0 is the coupling time; Superscript *target* means they are target variables.

In addition, it is also necessary to consider the coupling constraint of periodically regulated electric quantity. In order to simplify the complexity of the model, it is suggested to set the duration of the sub interval as the ESS regulation period, or allow it to be divided with no remainder by the ESS regulation period.

Renewable energy unit constraints at coupling time:

$$P_{i,t_0,(s_-,s)}^{NE,target} - P_{i,t_0,(s,s_-)}^{NE,target} = 0, \quad t_0 = n_- + 1 \tag{15}$$

$$P_{i,t_0,(s_+,s)}^{NE,target} - P_{i,t_0,(s,s_+)}^{NE,target} = 0, \quad t_0 = n + 1 \tag{16}$$

Thermal power unit constraints at coupling time:

$$P_{i,t_0,(s_-,s)}^{TG,target} - P_{i,t_0,(s,s_-)}^{TG,target} = 0, \quad t_0 = n_- + 1 \tag{17}$$

$$P_{i,t_0,(s_+,s)}^{TG,target} - P_{i,t_0,(s,s_+)}^{TG,target} = 0, \quad t_0 = n + 1 \tag{18}$$

$$H_{i,t_0,(s_-,s)}^{on,target} - H_{i,t_0,(s,s_-)}^{on,target} = 0, \quad t_0 = n_- + 1 \tag{19}$$

$$H_{i,s_-,t_0,(s_+,s)}^{off,target} - H_{i,t_0,(s,s_+)}^{off,target} = 0, \quad t_0 = n_- + 1 \tag{20}$$

$$H_{i,t_0,(s_-,s)}^{on,target} - H_{i,t_0,(s,s_-)}^{on,target} = 0, \quad t_0 = n + 1 \tag{21}$$

$$H_{i,t_0,(s_+,s)}^{off,target} - H_{i,t_0,(s,s_+)}^{off,target} = 0, \quad t_0 = n + 1 \tag{22}$$

where $H_{i,t_0,(s_-,s)}^{on,target}/H_{i,t_0,(s_-,s)}^{off,target}$ is minimum startup/shutdown time that interval s_- wants interval s to maintain, $H_{i,t_0,(s,s_-)}^{on,target}/H_{i,t_0,(s,s_-)}^{off,target}$ is minimum startup/shutdown time that the s_- interval wants the s interval to maintain in the initial period. The detailed calculation process of the above coupling variables related to the minimum startup and shutdown time can be seen in [6].

System power balance constraint at coupling time:

$$\sum_{i\in\Omega_{TG}} P_{i,t_0,(s_-,s)}^{TG,target} + \sum_{i\in\Omega_{NE}} P_{i,t_0,(s_-,s)}^{NE,target} - \sum_{i\in\Omega_{ESS}} P_{i,t_0,(s_-,s)}^{ESS,c,s_-,target} + \sum_{i\in\Omega_{ESS}} P_{i,t_0,(s_-,s)}^{ESS,d} = \sum_{i\in\Omega_D} P_{i,t_0}^D$$
$$, \quad t_0 = n_- + 1 \tag{23}$$

$$\sum_{i\in\Omega_{TG}} P_{i,t_0,(s,s_+)}^{TG,target} + \sum_{i\in\Omega_{NE}} P_{i,t_0,(s,s_+)}^{NE,target} - \sum_{i\in\Omega_{ESS}} P_{i,t_0,(s,s_+)}^{ESS,c,s_-,target} + \sum_{i\in\Omega_{ESS}} P_{i,t_0,(s,s_+)}^{ESS,d} = \sum_{i\in\Omega_D} P_{i,t_0}^D$$
$$, \quad t_0 = n + 1 \tag{24}$$

Lower Level Problem

The lower level model is mainly used to solve the short-term SCUC problem of each sub interval. The constraints of ATC lower level model are basically as same as those of classical SCUC, and no additional processing is required. The objective function (as

shown in Eq. (25)) needs to be slightly modified, the penalty function is added to relax the coupling constraints.

$$
\begin{aligned}
\min \quad & \sum_{i \in \Omega_{TG}} \sum_{k=1}^{ND} (F_{i,k}^{TG} + SU_i^{TG} u_{i,k}^{TG} + SD_i^{TG} d_{i,k}^{TG}) + \beta^{NE} \sum_{i \in \Omega_{NEG}} \sum_{k=1}^{ND} (\sum_{t=1}^{ND^T} \overline{P}_{i,k,t}^{NE,R} - E_{i,k}^{NE}) \\
& - \lambda_{s,s_-}^k (\chi_{s,s_-}^{k-1} - \gamma_{s,s_-}) + \rho(\chi_{s,s_-}^{k-1} - \gamma_{s,s_-})^2 \\
& + \lambda_{s,s_+}^k (\chi_{s,s_+}^{k-1} - \gamma_{s,s_+}) + \rho(\chi_{s,s_+}^{k-1} - \gamma_{s,s_+})^2
\end{aligned} \tag{25}
$$

where χ is the target variable in the ATC algorithm framework and is a known quantity in the lower model $\chi = \{P_i^{TG, target}, P_i^{NE, target}, P_i^{ESS, c, target}, P_i^{ESS, d, target}, H_i^{on, target}, H_i^{off, target}\}$; γ is the response variable in the ATC algorithm framework and is the decision variable in the lower model. $\gamma = \{P_i^{TG, response}, P_i^{NE, response}, P_i^{ESS, c, response}, P_i^{ESS, d, response}, H_i^{on, response}, H_i^{off, response}\}$.

Calculation Process

The algorithm for solving the long-term SCUC problem through ATC is as follows:

Step 1: decompose the long-term time interval into several sub intervals.

Step 2: ignore the ATC penalty term, solve the short-term SCUC problem of each sub interval in parallel as the initial solution.

Step 3: solve the upper model to get the initial solution of χ^0.

Step 4: initialize the parameters λ^0 and ρ^0.

Step 5: judge whether the convergence conditions Eq. (26) are met. If not, set the overlap generation times $k = k + 1$, if satisfied, exit the iteration process.

$$
|\chi^k - \gamma^k| > \varepsilon \tag{26}
$$

Step 6: solve the ATC lower level problem in parallel, and get the solution of γ^k.

Step 7: solve the ATC upper level problem to get the solution of χ^k.

Step 8: update the parameters, and return to step 5.

4 Case Studies

4.1 Introduction of Modified XJTU-ROTS2017 Testing System

XJTU-ROTS2017 testing system is a power system including thermal power, wind power and photovoltaic power [11]. The system contains 44 buses and 32 thermal units. After the modified, the installed capacity of renewable energy is 7000 MW, that of thermal power is 10400 MW, and the installed capacity of renewable energy accounts for more than 40%. In order to cope with the drastic fluctuation of renewable energy, ESS with about 15% of the installed capacity of renewable energy is installed in region A where renewable energy is enriched.

In this paper, the calculation time scale is set as one month, and the regulation period of ESS is one day. The computer processor is an Intel (R) Core (TM) i7-9700 @ 3.60 GHz.

4.2   Comparison of Solution Accuracy

The overall calculation results are shown in Table 1. It can be seen that it is very difficult to directly calculate the long-term SCUC problem. The algorithm proposed not only ensures accuracy, but also improves the speed of calculation. The overall solution speed is increased by 15 times. It has certain advantages in solving complex SCUC problems. As can be seen from Fig. 3, the convergence speed of the algorithm is fast. There is no oscillation during the iteration.

Table 1.   Results of long-term SCUC and proposed method

Algorithm	Operation cost (billion yuan)	Iteration	Elapsed time (s)	Redundancy ratio (%)
Long-term SCUC	7.8649	–	1834	–
Proposed method	7.9015	19	121	0.4654

(a)   (b)
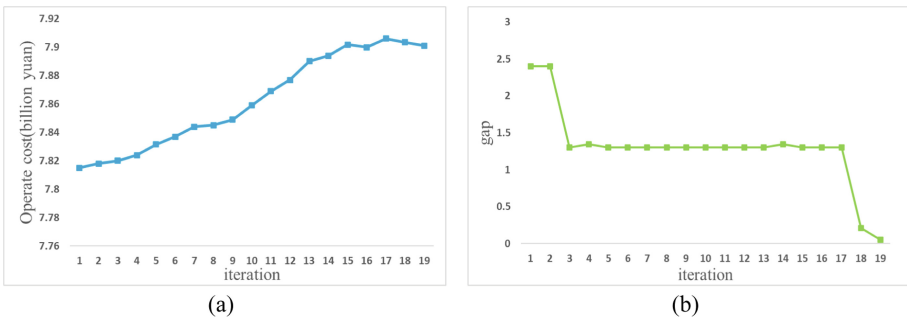
Fig. 3.   (a) Relationship between gap and operation cost and (b) Relationship between gap and iteration

4.3   Energy Storage Operation Results

In this typical month, the average charging and discharging times of stored energy system are 42 times, and the discharging availability hours are 54. Typical day and typical week operation information is shown in Fig. 4 and Fig. 5.

The stored energy is discharged at peak time and charged at valley time, which plays an important role of peak load shifting, and relieves the peak shaving pressure of traditional units.
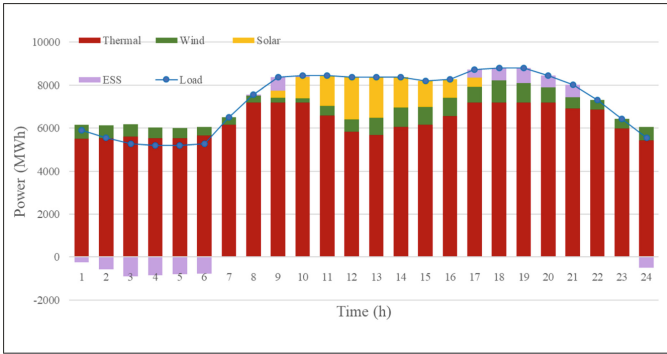
Fig. 4. Electricity balance information of typical day
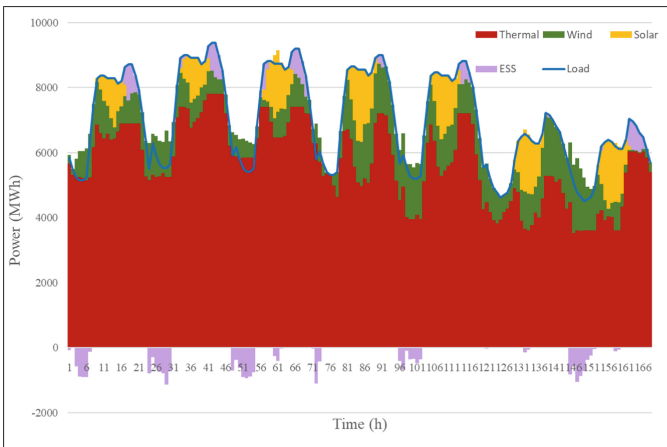
Fig. 5. Electricity balance information of typical week

5 Conclusion

For the power system with high proportion of renewable energy, this paper proposes a long-term SCUC time-series decomposition algorithm considering ESS. Firstly, the SCUC model with ESS is established by considering the power characteristics and load characteristics of energy storage. Then, we simplify the original problem by the method of time-series decomposition. Finally, we use ATC algorithm to coordinate the coupling variables of energy storage, renewable energy and thermal power units between each sub interval. The results show that the proposed model can make full use of the thread resources of the computer, obviously improve the calculation speed under the premise of losing a certain accuracy, and has advantages in the SCUC problem with a long-time scale. In addition, this paper also analyzes the operation characteristics of ESS, and quantitatively demonstrates the role of ESS in the new power system.

References

1. Bagheri, A., Zhao, C., Qiu, F., et al.: Resilient transmission hardening planning in a high renewable penetration era. IEEE Trans. Power Syst. **34**(2), 873–882 (2019)
2. Yuan, X.: Overview of problems in large-scale wind integrations. J. Mod. Power Syst. Clean Energy **1**(1), 22–25 (2013)
3. Aoki, K., Itoh, M., Satoh, T., et al.: Optimal long-term unit commitment in large scale systems including fuel constrained thermal and pumped-storage hydro. IEEE Trans. Power Syst. **4**(3), 1065–1073 (1989)
4. Li, X.: Research on optimization method of monthly power generation and purchase plan in power system. Chongqing University (2013). (in Chinese)
5. Franz, A., Zimmermann, J.: A two-stage heuristic approach for solving the long-term unit commitment problem with hydro-thermal coordination in large-scale electricity systems. In: South Kuta: 2016 IEEE International Conference on Industrial Engineering and Engineering Management (IEEM), pp. 70–74. IEEE (2016)
6. Safdarian, F., Mohammadi, A., Kargarian, A.: Temporal decomposition for security-constrained unit commitment. IEEE Trans. Power Syst. **35**(3), 1834–1845 (2019)
7. He, Y., Guo, S., Zhou, J., et al.: The quantitative techno-economic comparisons and multi-objective capacity optimization of wind-photovoltaic hybrid power system considering different energy storage technologies. Energy Convers. Manage. **229**, 113779 (2021)
8. Zhao, N., You, F.: Can renewable generation, energy storage and energy efficient technologies enable carbon neutral energy transition. Appl. Energy **279**, 115889 (2020)
9. Gomes, J.G., Telhada, J., Xu, H., et al.: Optimal operation scheduling of a pump hydro storage system coupled with a wind farm. IET Renew. Power Gener. **15**(1), 173–192 (2021)
10. Xiao, Y., Fan, X., Wang, X., et al.: Review on electricity market towards high proportion of renewable energy. Proc. CSEE **38**(3), 663–674 (2018). (in Chinese)
11. Wang, J., Wei, J., Zhu, Y., et al.: The reliability and operational test system of a power grid with large-scale renewable integration. CSEE J. Power Energy Syst. **6**(3), 704–711 (2020)
12. Padhy, N.P.: Unit commitment-a bibliographical survey. IEEE Trans. Power Syst. **19**(2), 1996–1205 (2004)
13. Lotfjou, A., Shahidehpour, M., Fu, Y., et al.: Security-constrained unit commitment with AC/DC transmission systems. IEEE Trans. Power Syst. **25**(1), 531–542 (2010)

Online Transient Stability Control Strategy Matching Method Based on Time-Varying Index of Power Grid

Zhongqing Sun[✉], Fusuo Liu, Feng Xue, Zhaowei Li, and Wei Li

NARI Group Corporation (State Grid Electric Power Research Institute), 19th Chengxin Avenue, Jiangning District, Nanjing, China
sunzhongqing@sgepri.sgcc.com.cn

Abstract. The strong uncertainty environment in which renewable energy is the main power grid has the possibility of sudden changes in power supply or topology, and there is a risk of mismatch of transient control strategies. Therefore, a fast evaluation method for online transient control strategy in strong uncertainty environment is proposed. First, based on the Extended Equal Area Criterion (EEAC), after the grid operation scenario changes rapidly, the difference in stability margin between different processing methods for grid time-varying factors is calculated to define the grid time-varying degree; Then, the key parameter matching index is established in combination with the key network characteristics of the power grid, which is matched with the examples in the historical database established offline, and the control measures are obtained according to the principle of conservatism; Finally, check and verify in the current grid mode, and send to the device for executing after the verification is passed. The simulation of the actual power grid online data shows that the proposed method can basically solve the situation that the online strategy is not suitable due to the rapid change of power flow or topology change in the power grid in a short time.

Keywords: Strong uncertainty · Rapid change of scenarios · EEAC · Time-varying · Historical scenario matching

1 Introduction

With the rapid development of UHVDC, new energy and power market, the operation mode of power system becomes more and more changeable, which means the uncertainty increases significantly. The intraday fluctuation of the power transmission section of the power grid is beyond million kilowatts, and the power change on the minute-level time scale can reach about 1% of the installed capacity (about 1000 MW). It is difficult to ignore the impact on the transient time scale, especially after the power grid failure [1–3].

Such severe uncertainty makes the traditional operation control strategy based on the pre-determined operation mode unable to meet the requirements of the grid operation control. At present, for the uncertainty of the grid operation scenarios, the reference

[4] proposed a two-layer optimal power flow model for static voltage stability margin (SVSM) interval calculation, and obtained the SVSM interval considering the output fluctuation of renewable energy stations; Reference [5] developed a transient evaluation method for AC-DC hybrid power grids based on the generation of sampling blind number sample space and considering the uncertain transient stability evaluation index. Different models and indicators are proposed in the above methods, which play a role in assisting the accurate judgment of the security and stability of the grid under the uncertainty of the operation scenarios. All of them need to be combined with the time-domain simulation of the grid to determine the transient security and stability of the grid.

In the off-line strategy formulation or the online security and stability analysis with a period of 5 to 15 min, the time-domain simulation method can be considered to analyze the security and stability characteristics of the power grid [6]. Reference [7] proposed to study the probability of wind power fluctuations in the short term based on historical data of wind power, and to conduct online safety assessment calculations. Reference [8] considers the power angle, voltage, frequency margin and mode information of a single predicted fault, and combines information such as power flow changes and component switching to filter out the subset of faults that need to be further simulated in the current power grid, which improves the speed of online evaluation.

However, when the grid scenario changes suddenly, the time-domain simulation search strategy method that takes a long time cannot be applied, which may cause a mismatch period of grid stability strategy. Therefore, it is necessary to consider at least a seconds-level evaluation method.

Using machine learning technology to evaluate transient stability is to establish the mapping relationship between some key parameters of the system, such as generator power angle, active power, etc., and transient stability margin [9], so as to avoid or partially avoid model driving and mechanism analysis. It can meet the evaluation speed requirements of seconds or even milliseconds. Related technologies include grid search and particle swarm algorithm [10], decision tree [11, 12], light gradient boosting machine [13], support vector machine [14, 15] and other data-driven statistical analysis. However, the generalization ability of machine learning methods based on local information is extremely limited in strong nonlinear and time-varying power systems, and it is difficult to meet the robustness requirements of practical engineering applications [16].

The power system is a strongly nonlinear non-Hamiltonian system, and all parameters contain time variables, so it is impossible to judge the stability of the power system by analytical methods. The time-varying law of the power grid is described by analyzing three EEAC calculation methods that account for time-varying factors in different degrees: Static EEAC (SEEAC) [17], Dynamic EEAC (DEEAC) [18], and Integrated EEAC (IEEAC) [19].

Therefore, a stability strategy matching method based on the time-varying index and network characteristics of the power grid is proposed. In the historical database constructed by online and offline cases, the time-varying index is first matched, and then the network characteristic index is matched, and the method closest to the historical database and the calculation result of its stability strategy are selected as the control measures for the current power grid mode. After the verification is passed, the device is issued to replace the on-duty strategy table.

2 Influence of Rapid Change of Power Grid Operation Mode on Stability

In engineering, the strategy table is usually formulated based on offline simulation, and the real-time query method [20]. Therefore, when formulating the strategy table, it is necessary to scan the expected fault set to determine the most serious boundary conditions, and obtain the scenario of the system with the worst stability characteristic. On this basis, the conservative control strategy is calculated. In order to ensure the reliability of the security and stability control device, the parameters that can be easily detected by the device, such as the section power representing local characteristics, are generally set as the query method of the strategy table by the operating experience.

Due to the large-scale grid connection of renewable energy generators, the non-negligible power fluctuations of renewable energy will bring very difficult challenges to the formulation of power grid security and stability control strategies. At the same time, when the grid topology changes suddenly, it will also cause the risk of mismatch in the strategies formulated by the online system. If a serious fault occurs, the stability of the system will be destroyed, and the safe and stable operation of the power grid cannot be guaranteed.

Therefore, it is necessary to adjust the on-duty strategy table of the system affected by the sudden change of the power grid mode online to ensure the safe and stable operation of the power grid. However, if the complete online calculation process of grid state estimation, scenario data generation, and security strategy search starts again at this time, the grid will have a blank period of security control strategies of at least in minute-level. If a fault occurs within this period, the security and stability of the grid will not be guaranteed.

Therefore, in order to ensure the safety and stability of the power grid in the event of a sudden change in the power grid, the traditional strategy search of simulation analysis will not be applicable. To reduce the influence of strong uncertainty on emergency control strategy of power grid, a rapid evaluation method of the strategy needs to be proposed.

3 Time-Varying Index

3.1 The Contradiction Between Simulation Accuracy and Speed

If the system does not contain any non-Hamiltonian factors, the map system must be a steady Hamiltonian system. The generator mechanical power P_m and electromagnetic power P_e at any time section are only single-valued formulas of the power angle δ. If non-Hamiltonian factors are introduced into the system, the time variable t will be included in the functions of mechanical power and electromagnetic power of each generator. Obviously, the formulas of P_m and P_e with respect to t in the map system cannot be clearly obtained at this time, and the analysis can only be carried out by relying on numerical integration. The contradiction between accuracy and speed in numerical integration cannot be solved, but when the transient time-varying degree of the power grid is low, the integration with a large step can more accurately reflect the security and stability characteristics of the power grid.

Therefore, taking the time-varying degree of the one operating case as an indicator, matching the current grid scenario in the historical database. On the premise that the time-varying index is the closest, matching the power grid parameters can effectively improve the accuracy and robustness of the matching.

3.2 Quantitative Assessment of Transient Stability

The traditional EAC method is only suitable for the stability analysis of the Hamiltonian system with one generator, and cannot be included in any controller or complex model, nor can it be used for multi-generator systems. EEAC maps the multi-generator rotor angular trajectory with the mechanical power and electromagnetic power in the multi-generator space to a series of single generator spaces. Form the trajectory in the OMIB system, so as to strictly define the stability margin of the time-varying OMIB system. SEEAC, DEEAC and IEEAC are the three stages in the development of the EEAC algorithm and the three complementary steps in the EEAC algorithm framework [21].

SEEAC assumes the power grid as a multi-generator system of ideal two-group dynamics with classical models, at this time, the system can be degenerated into a classical One Machine as Infinite Bus (OMIB). This means that whether the A curve in the fault or the A curve after the fault can be calculated according to the initial working conditions. It is only one single-step Taylor series expansion will be used to obtain the rotor angle and acceleration of the mapped system at the time of fault clearing. Therefore, the analytical solution of the stability margin can be obtained with only a very small computing time. SEEAC completely ignores the time-varying nature of images.

The calculation process of DEEAC is equivalent to relaxing the ideal two-group dynamics process in SEEAC. The method of segment-by-segment correction is used to divide the power grid into multiple classical OMIB systems during the fault and after the fault is cleared. Therefore, DEEAC can partially reflect time-varying factors. Since DEEAC uses only 4 times of Taylor series expansions, the computing time does not increase much.

IEEAC strictly considers all dynamic equations in the multi-generators space of the power grid, and performs complete integration at each step size, and maps them to the single-machine phase step by step to form a time-varying OMIB system. Therefore, its computing time is greatly increased compared with the other two methods. According to the actual simulation experience, the simulation time of IEEAC is increased by about 2 orders of magnitude.

The three-stage EEAC can calculate the acceleration area and deceleration area in the OMIB map system according to their respective assumptions and calculation steps, so as to obtain the first-swing stability margin of the power grid:

$$\eta = A_{dec}(\delta_\tau) - A_{inc}(\delta_\tau) \tag{1}$$

where, η is the stability margin of the power grid, $A_{dec}(\delta_\tau)$ is the deceleration area with the fault clear angle δ_τ, $A_{inc}(\delta_\tau)$ is the acceleration area with the fault clear angle δ_τ.

3.3 Time-Varying Index Calculation

The time-varying in the transient process is mainly reflected in the fluctuation of the load with the grid voltage and frequency, the change of the transient potential of the generator,

the influence of the grid controller and the grid damping, and the non-coherence of the system.

The stronger the above-mentioned time-varying factors, the stronger the difference in accuracy of the stability margins calculated by using SEEAC and DEEAC with single or multiple Taylor expansions.

The time-varying of the map system is the source of error in SEEAC and DEEAC. Since DEEAC takes into account some time-varying factors, the time-varying can be reflected by the difference of the stability margin of the two algorithms. The specific calculation method is as follows:

$$\sigma(\tau) = \frac{\left| \eta^{DE}(\tau) - \eta^{SE}(\tau) \right|}{\max\left\{ \left| \eta^{SE}(\tau) \right|, \left| \eta^{DE}(\tau) \right| \right\}} \tag{2}$$

where, $\sigma(\tau)$ represents the time-varying index, $\eta^{DE}(\tau)$ represents the stability margin obtained by DEEAC when the fault clearing time is τ, and $\eta^{SE}(\tau)$ represents the stability margin obtained by SEEAC.

4 Selection of Characteristic Parameters of Power Grid

In the matching process, only relying on the time-varying index of the power grid will lead to the situation that the degree of time-varying power grid is the same or close, but the grid structure, power output, and load are all far from each other. Therefore, after completing the time-varying index matching, it is necessary to further match the power grid network characteristic index, so as to complete the matching of the power grid control measures and improve the matching accuracy.

Among them, the synchronous and asynchronous power supply can be judged by its participation factor greater than the set threshold value, and the load, topology, etc. can be judged by the parameter sensitivity greater than the set threshold value.

4.1 Participation Factor of Transient Power Angle Stability of Synchronous Power Supply

According to the energy distribution of each generator in different groups, the EEAC method gives the generator participation factor of transient power angle stability, and clarifies the influence degree of each generator on a certain power angle stability mode. The participation factor of synchronous power supply can be calculated as follow:

$$\lambda_n = \frac{E_{kn}}{E_{kmax}} \tag{3}$$

where, λ_n is the participation factor, E_{kn} is the acceleration kinetic energy of the generator at the dynamic saddle point (DSP), E_{kmax} is the maximum acceleration kinetic energy of all generators at the DSP.

4.2 Participation Factor for Transient Power Angle Stability of Asynchronous Power Supply

In the transient process after the failure, the power of asynchronous power source will change, which will affect the power angle difference between the synchronized generators and the transient stability of the system, and it does not participate in the swing of the synchronized generators. The key factor that affects the stability is the relative distance between the asynchronous power supply and the synchronous fleet. The closer the asynchronous power supply is to the leading group, the more power its output will deteriorate the security and stability of the power grid. On the contrary, the closer the asynchronous power source is to the legging group, the better its output will be to the safety and stability of the power grid. The participation factor of asynchronous power supply can be calculated as follow:

$$\lambda_i = \frac{\sum_{j=1}^{N} \left(a_j / x_{i,j}\right)}{N} ij \tag{4}$$

where, λ_i is the participation factor of asynchronous power supply, a_j is the participation factor of synchronous power supply, $x_{i,j}$ is the Equivalent reactance between the busbar of asynchronous power supply i and the busbar of synchronous generator j, N is the number of generator in leading or legging group.

4.3 Sensitivity of Load and Topology to Transient Power Angle Stability Margin

For power grid parameters such as load and topology, the perturbation method is used to calculate its sensitivity to the transient power angle stability margin of the power grid.

$$\lambda_k = \frac{\Delta \eta}{\Delta C} \tag{5}$$

where, λ_k is the sensitivity of load and topology to the power angle stability margin, $\Delta \eta$ is the variation of stability margin, ΔC is the variation of the load or the change of topology.

5 Rapid Evaluation of Online Transient Control Strategies

This paper considers the use of indicators representing network characteristics and transient characteristics, and matching with the historical scenarios, so as to achieve rapid adjustment of the strategy. The specific strategy matching method flow is shown in Fig. 1.
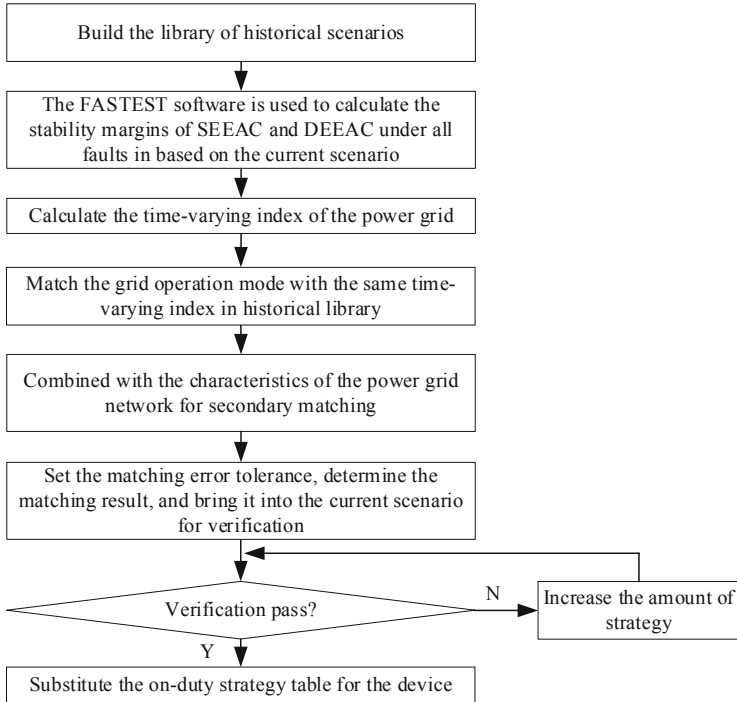
Fig. 1. The flow chart of strategy rapid evaluation

5.1 Build the Library of Historical Scenarios

In the process of daily operation and offline simulation, a large amount of historical data will be generated. The online system will also generate a set of data every 5 min based on the state estimation of the dispatching system. The large amount of historical data basically covers possible scenarios of the power grid. Collect and summarize all historical data to form a historical library.

The data in the historical database needs to be processed as follows:

The power grid characteristic index is extracted to form the power grid characteristic index library $A^k \left\{ P^k_{sec\,tion}, G^k_{gen}, L^k_{load}, T^k_{topo} \right\}$. Where, $P^k_{sec\,tion}$ represents the section power of historical data k, G^k_{gen} represents the generator startup mode of historical data k, L^k_{load} represents the load situation t of historical data k, and T^k_{topo} represents the topological structure of historical data k.

Extract the stable characteristic index to form the stable characteristic index library $S^k \left\{ \eta^{kSE}, \sigma^k \right\}$. Where, η^{kSE} represents the margin result of historical data k calculated by SEEAC, and σ^k represents the time-varying index result of historical data k calculated by SEEAC and DEEAC.

5.2   Set Match Error Indicators

According to the actual power grid conditions and dispatching experience, set various matching error indicators $\lambda\{\lambda_{\sec tion}, \lambda_{gen}, \lambda_{load}, \lambda_{topo}, \lambda_\eta, \lambda_\sigma\}$, where $\lambda_{\sec tion}$ represents the error indicator of section power, λ_{gen} represents the error indicator of the generators startup mode, λ_{load} represents the error indicator of the load condition, λ_{topo} represents the error indicators of the topology structure, λ_η represents the stability margin error indicators calculated by SEEAC, and λ_σ represents the error index of the time-varying power grid.

5.3   Matching in Historical Database Based on Current Grid Scenario

The matching method of each index is shown in formulas (6)–(11).

$$P^0_{\sec tion} - \lambda_{\sec tion} \le P^k_{\sec tion} \le P^0_{\sec tion} + \lambda_{\sec tion} \tag{6}$$

$$G^0_{gen} - \lambda_{gen} \le G^k_{gen} \le G^0_{gen} + \lambda_{gen} \tag{7}$$

$$L^0_{load} - \lambda_{load} \le L^k_{load} \le L^0_{load} + \lambda_{load} \tag{8}$$

$$T^0_{topo} - \lambda_{topo} \le T^k_{topo} \le T^0_{topo} + \lambda_{topo} \tag{9}$$

$$\eta^{0SE} - \lambda_\eta \le \eta^{kSE} \le \eta^{0SE} + \lambda_\eta \tag{10}$$

$$\sigma^0 - \lambda_\sigma \le \sigma^k \le \sigma^0 + \lambda_\sigma \tag{11}$$

After the matching is completed, some relevant historical data and its corresponding stability strategy table will be get. According to the principle of conservatism, the strategy with the most conservative values in the table will be selected as the stability strategy of the current grid mode.

5.4   Verification

(1) After the stability strategy is matched, check the strategy based on the current grid mode data, and simulate whether the grid can maintain safe and stable operation after faults;

(2) If the power grid can ensure safe and stable operation, the strategy will be sent to the device, and the corresponding value in the current strategy table will be replaced;

(3) If the power grid cannot guarantee safe and stable operation, further increase the amount of control measures, and return to step (1) to re-check and verify;

6 Case Analysis

Taking the actual system in the HB power grid as an example, the total capacity of unit S is 2560 MW (8 * 320 MW), and the stations B and C are wind power grid integration bus, and the maximum capacity is 2000 MW. Station A is a photovoltaic grid integration bus with a maximum transmission capacity of 1050 MW. In this case, the FASTEST is used for the simulation.

According to the online data and base case for daily operation in this region, construct a sample database based on 1000 cases, calculate the time-varying index σ, and the emergency control strategy table of the power grid under each case. In this system, when three-phase-to-ground N-2 fault happens on the line A-D, the generators in bus S will lose synchronous to the main grid power. For different working conditions, the strategy of tripping different numbers of generators in bus S is adopted to ensure the power angle stability. The construction of this region is shown in Fig. 2.
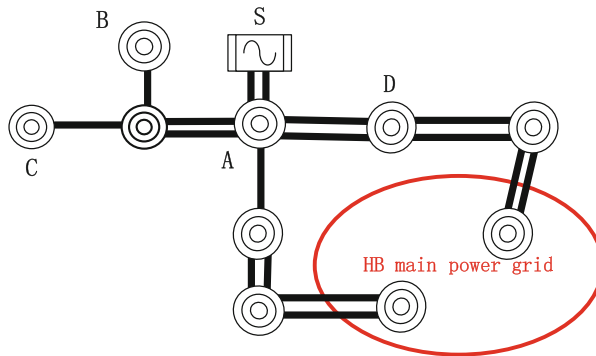
Fig. 2. The construction of target region

Selecting one scenario in the basic library to calculate and analyze the participation factors of the synchronous power supply, asynchronous power supply and load. During the grid parameter matching, the output of generator S, the total wind power of C and B, and the total solar power of the A station are the key factors, and the remaining parameters have little influence on the safety and stability characteristics of the power grid. The specific results are shown in Table 1.

Table 1. Participation factors.

Network feature	Participation factor
Generator S	1
Wind power of B and C	0.464
Solar power of A	0.688
Load	0.013

Eight examples are randomly generated, and the online transient control strategy evaluation method is used to match their transient control strategies. Table 2 shows the boundary conditions, time-varying index, and matching results with the historical database of the 8 calculation examples.

Table 2. Matching results for different cases (MW).

Scenarios		Output of generator S		Wind power	Solar power	Time-varying index	Strategy
		Output	Operating number				
1	Current case	2144	7	340	458	0.038	/
	Matching result	2098	7	450	415	0.037	Tripping 1 generator
2	Current case	2360	8	486	755	0.304	/
	Matching result	2422	8	399	713	0.304	Tripping 1 generator
3	Current case	2409	8	576	685	0.117	/
	Matching result	2368	8	624	623	0.118	Tripping 1 generator
4	Current case	2468	8	854	558	0.269	/
	Matching result	2459	8	812	620	0.264	Tripping 2 generator
5	Current case	2483	8	664	384	0.284	/
	Matching result	2477	8	687	352	0.289	Tripping 3 generator
6	Current case	2560	8	872	423	0.444	/
	Matching result	2560	8	855	451	0.443	Tripping 4 generator
7	Current case	2560	8	532	420	0.39	/
	Matching result	2560	8	488	445	0.411	Tripping 3 generator
8	Current case	2560	8	342	610	0.367	/
	Matching result	2560	8	388	565	0.359	Tripping 3 generator

After the results are matched, the control strategy is checked and verified in each operation scenario, which can meet the requirements of safe and stable operation of the power grid.

7 Conclusion

Aiming at the problem that there is a minute-level mismatch risk of online strategies after the sudden change of the power grid, this paper proposes a rapid evaluation method for transient control strategies, and the specific conclusions are as follows:

1) The artificial intelligence algorithm has no mechanism support and cannot guarantee the robustness of the strategy. The strategy search method cannot meet the time requirements, and the power grid may have a minute-level strategy blank period, resulting in operational risks;
2) The SEEAC and DEEAC algorithms that completely ignore and partially reflect the time-varying factors of the power grid are used to describe the time-varying degree of the power grid, thereby improving the accuracy and robustness of the strategy matching process;
3) Through the participation factors of various parameters of the power grid during the transient period, the key parameters that can describe the transient stability of the region is obtained;
4) The time-varying index and the key parameters of power grid are used as matching elements to form the framework of the rapid evaluation method, and the effect of mode matching is verified in the actual power grid, which can meet the requirement of safe and stable operation of the power grid.

References

1. Xue, Y., Lei, X., Xue, F., et al.: A review on impacts of wind power uncertainties on power systems. In: Proceedings of the CSEE, vol. 34, no. 29, pp. 5029–5040 (2014)
2. Bao, Y., Zhang, J., Jiang, Y., et al.: Online assessment method of available transfer capacity considering uncertainties of renewable energy output. Electr. Power Autom. Equip. **40**(04), 71–76 (2020)
3. Gomez-quiles, C., Gil, H.A.: Price and resource-related uncertainty in the estimation of the revenue of a wind farm. IEEE Trans. Power Syst. **26**(4), 2074–2083 (2011)
4. Chen, G., Liu, W., Yang, Y., et al.: Calculation of Static voltage stability margin interval for AC/DC hybrid power system considering the uncertainty of renewable energy[J/OL]. Power Syst. Technol., 1–11 (2022)
5. Liu, Y.: Study on safety and stability assessment of AC/DC hybrid power grid considering the uncertainty of loads and new energy generator outputs. Southeast University (2019). https://doi.org/10.27014/d.cnki.gdnau.2019.003551

6. Bao, Y., Zhang, J., Xu, T., et al.: Online transient stability risk assessment method considering the uncertainty of wind power output. South. Power Syst. Technol. **15**(11), 42–48 (2021). https://doi.org/10.13648/j.cnki.issn1674-0629.2021.11.005

7. Lü, Y., Lu, G., Xie, C., et al.: Online probabilistic security assessment considering centralized integration of large scale wind power. Power Syst. Technol. **42**(04), 1140–1148 (2018). https://doi.org/10.13335/j.1000-3673.pst.2017.2897

8. Xu, T., Du, Y., Bao, Y., et al.: A classification rolling contingency screening method for on-line transient security and stability assessment. Autom. Electr. Power Syst. **42**(13), 182–188 (2018)

9. Wang, T., Liu, J., Zhu, S., et al.: Transient stability assessment and emergency control strategy based on random forest in power system. Power Syst. Technol. **44**(12), 4694–4701 (2020)

10. Pannell, Z., Ramachandran, B., Snider, D.: Machine learning approach to solving the transient stability assessment problem. In: Proceedings of IEEE Texas Power and Energy Conference, College Station, TX, USA, February 2018, pp. 1–6 (2018)

11. Baltas, N.G., Mazidi, P., Ma, J., Fernandez, F., Rodriguez, P.: A comparative analysis of decision trees support vector machines and artificial neural networks for on-line transient stability assessment. In: Proceedings of International Conference on Smart Energy Systems and Technologies, Seville, Spain, September 2018, pp. 1–6 (2018)

12. Sun, K., Likhate, S., Vittal, V., et al.: An online dynamic security assessment scheme using phasor measurements and decision trees. IEEE Trans. Power Syst. **22**(4), 1935–1943 (2007)

13. Zhou, T., Yang, J., Zhou, Q., et al.: Power system transient stability assessment method based on modified LightGBM. Power Syst. Technol. **43**(06), 1931–1940 (2019). https://doi.org/10.13335/j.1000-3673.pst.2019.0085

14. Hu, W., et al.: Real-time transient stability assessment in power system based on improved SVM. J. Mod. Power Syst. Clean Energy **7**(1), 26–37 (2018). https://doi.org/10.1007/s40565-018-0453-x

15. Moulin, L.S., Alves, D., El-Sharkawi, M.A., et al.: Support vector machines for transient stability analysis of large-scale power systems. IEEE Trans. Power Syst. **19**(2), 818–825 (2004)

16. Xue, Y., Huang, T., Chen, G., et al.: Review on case filtering in transient stability analysis. Autom. Electr. Power Syst. **43**(06), 1–14 (2019)

17. Xue, Y.S., van Citsem, T., Pavella, M.: A simple direct method for fast transient stability assessment of large power system. IEEE Trans. Power Syst. **3**(2), 400–412 (1988)

18. Xue, Y.S., Pavella, M.: Critical-cluster identification in transient stability studies. IEEE Proc. C Gener. Transm. Distrib. **140**(6), 481–489 (1993)

19. Xue, Y.: A theoretical proof of DEEAC. Autom. Electr. Power Syst. **17**(7), 7–19 (1993)

20. Xu, T., Ding, M., Peng, H., et al.: A parallel algorithm for determining an online emergency control strategy of transient security and stability for AC-DC power systems. Autom. Electr. Power Syst. **39**(10), 174–180 (2015)

21. Xue, Y.: Quantitative Study of General Motion Stability and an Example on Power System Stability. Phoenix Science Press, Nanjing (1999)

A Distribution Grid Accessible Distributed PV Capacity Measurement Method Based on Local Consumption

Tingting Lin[✉] and Guilian Wu

Economic and Technology Institute, State Grid Fujian Electric Power Co., Ltd., Fuzhou 350000, China
2454673596@qq.com

Abstract. A distribution grid accessible distributed PV capacity measurement method proposed by paper is based on the premise of ensuring the safe and stable operation of the grid and avoiding back-feeding to the 220 kV grid and above, following the principle of "local consumption". Local consumption means reverse flow caused by distributed PV can be delivery under 220 kV grid, but reverse flow cannot cause overload. The proposed method calculates the accessible capacity of substations, lines, and distributions from high voltage to low voltage in a hierarchical manner. Considering many factors affecting the accessible distributed PV capacity, the calculation not only considers the bearing capacity constraint of the power grid, but also considers voltage deviation, short-circuit current and other constraint checks. Finally, taking a 220 kV substation as an example, the calculation method is measured and analyzed in detail to evaluate the accessible capacity of substation, lines and distribution at each level in calculating area. The method is simple, feasible, and calculation results can be used to guide PV development orderly and guide power grid construction and transformation timely in area of insufficient accessible capacity.

Keywords: Stratified zoning consumption · Access capacity · Rooftop distributed PV · Bearing capacity

1 Introduction

Under the background of county PV development [1, 2], the process of "passive to active" in the distribution network will be accelerated, and the distribution network will face challenges in efficient consumption and safe carrying [3–8]. It is an important mean to ensure efficient consumption and safe carrying by guiding the orderly development and access of PV.

At present, some researches have been achieved in distribution grid accessible distributed PV capacity measurement method [9–16]. Under the premise of considering voltage deviation, voltage fluctuation and network power flow constraints, and taking into account that the short-circuit capacity does not exceed the limit, the literature [9,

10] established an optimization model with the goal of maximizing the distributed PV access capacity, and obtained the distributed power source. The impact of access on the short-circuit capacity of the system is limited, and the voltage deviation and voltage fluctuation constraints are the main influencing factors that restrict the maximum access capacity of distributed power generation, but the article lacks consideration of the impact of energy storage devices and electric vehicles on the access capacity of PV. Reference [11] proposed a calculation model of the maximum access capacity of distributed power generation considering the constraints of voltage level and branch capacity, and proposed an improved pattern search method to solve the above mathematical model. References [12, 13] analyzed the method for calculating the access capacity of distributed power generation based on the proximity and correlation between distributed power and load. Reference [14] proposes a maximum accessible capacity of distributed PV power sources considering grid flexibility and static safety and stability constraints, and calculates distributed PV access capacity for three-segment single radiation, single contact, and double contact respectively, it is concluded that in areas with the main purpose of maximizing access to distributed PV, such as "PV poverty alleviation", it is recommended to retain radial wiring. Reference [15] comprehensively considers thermal power units, distributed power sources, and reactive power compensation devices, and proposes a calculation model for the maximum access capacity of distributed power sources for transmission and distribution coordination. Reference [16] proposed to take into account the medium-low voltage synergy to increase the PV capacity of the low-voltage distribution network, and to reduce the total voltage deviation from the transformer tap and active distribution network voltage regulation to increase the access capacity.

Existing methods for distribution grid accessible distributed PV capacity are widely using genetic algorithms and multi-objective optimization algorithms for optimization, so as to ensure that the power quality in a reasonable range while PV access capacity is the largest. However, the existing methods lack the consideration of upper-level on lower-level distribution network, and its calculation is time-consuming and complicated. This paper proposes a method to quickly calculate accessible capacity meeting the principle of local consumption. Finally, taking the power grid of a southern province as an example, which verifies the scientificity and feasibility of the calculation method proposed in this paper.

2 A Distribution Grid Accessible Distributed PV Capacity Measurement Method

2.1 Preparation for Calculation

Select the area to be measured and collect the basic information, historical load characteristics, power output characteristics, network topology in the regional power grid. Mainly include the following:

1) Basic equipment information: rated capacity of all 220 kV substations, all 110 kV substations, all 35 kV substations, all 10 kV lines and all distributions and DG connected to grid.

2) Operational data: including historical load characteristics, power output characteristics of equipment at each level in the area to be measured, distributed PV and other power sources that have been approved for access during the measurement period.

3) Network topology information: the wiring diagram of the primary grid in the area to be measured, including the 110/35 kV substation contact method, the 10 kV line wiring method, etc.

2.2 Calculation Method

The calculation method of the distributed PV capacity of the regional grid is shown in Fig. 1. First of all, preparing for the calculation information and calculating the initial accessible capacity of all devices in regional grid. Then, calculating the adjusted accessible capacity follow calculating order of 220 kV, 110 kV, 35 kV, 10 kV, 0.38 kV. Taking high-voltage equipment as a unit, the accessible capacity of its medium and low-voltage
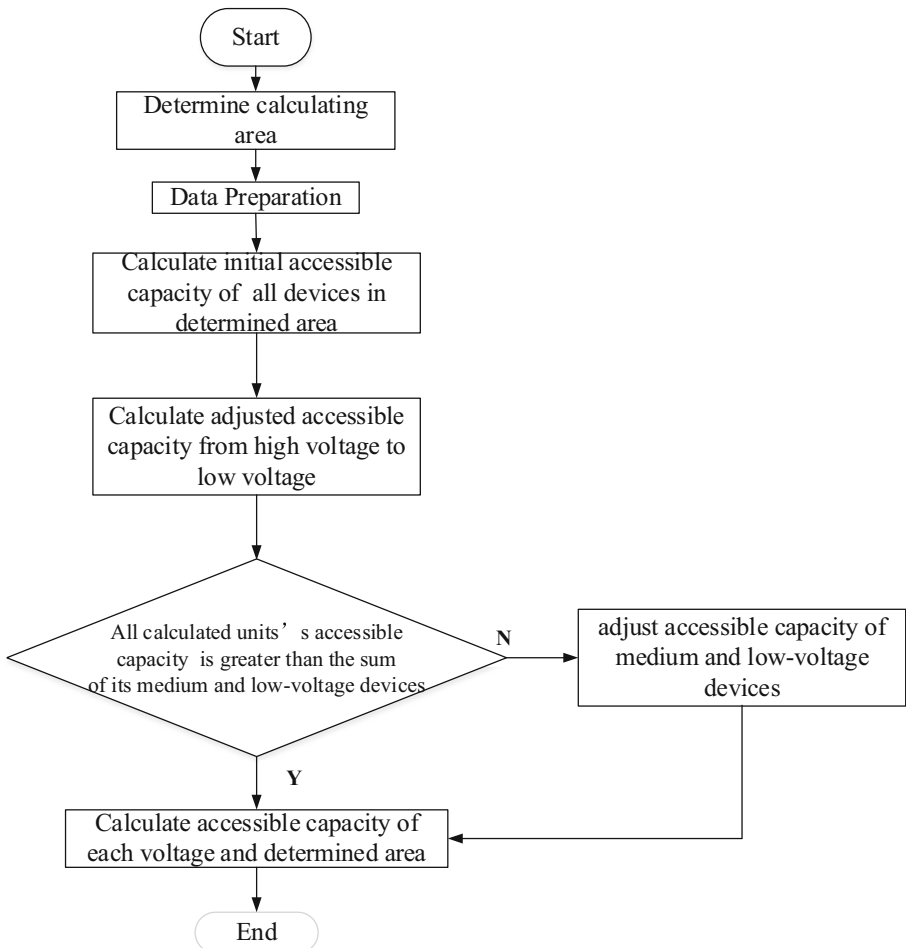
Fig. 1. Calculation method diagram of grid accessible distributed PV capacity

side devices need to adjust to satisfy that the sum of its medium and low-voltage side devices is not greater than its own high side accessible capacity, and meets the constraints of voltage deviation and short-circuit current. After all 220 kV equipment and its related equipment have been calculated, reduce calculation voltage grade taking 110 kV devices as calculating unit. After all 110 kV equipment and its related equipment have been calculated, reduce calculation voltage grade following order of 35 kV, 10 kV and 0.38 kV. Devices need to be calculated including 220 kV substation, 110 kV substation, 35 kV substation, 10 kV lines and distribution.

2.3   Calculation of Accessible Capacity of 220 kV Substation

Accessible capacity of 220 kV substation is to meet the requirement of no reverse power transmission to 220 kV and above power grid, which can be calculated as follow:

$$S_{ms-220} = S_{\min} + P_{110} + P_{35} \tag{1}$$

In formula (1), $S_{ms\text{-}220}$ is accessible capacity of 220 kV substation, $S_{\min}$ is minimum load value of 220 kV substation from 11am to 2pm within the last year, P_{110} is the output of 110 kV conventional power supply when $S_{\min}$ appears. P_{35} is the output of 35 kV conventional power supply when $S_{\min}$ appears.

2.4   Initial Accessible Capacity of 110–0.38 kV Equipment

Initial accessible capacity of 110 kV substations, 35 kV substations, 10 kV lines and distribution is to meet the requirement of reverse load flow without overloading, which means reverse road rate should be less than 80%, which can be calculated as formula (2).

$$S_{ms} = \begin{cases} S_{\mathrm{m}} + 80\% \times S_e & S_{\mathrm{m}} > -S_e \times 80\% \\ 0 & S_{\mathrm{m}} \le -S_e \times 80\% \end{cases} \tag{2}$$

In formula (2), S_{ms} is initial accessible capacity of device. S_{m} is minimum load of devices from 11am to 2pm within the last year. S_{e} is rated capacity of devices.

2.5   Accessible Capacity of 110–0.38 kV Equipment Considering Constrains

Considering upper and lower grid constraints and also power quality constrains, accessible capacity correction of device j, $S_{ms}^{j'}$ can be calculated as formula (3):

$$S_{ms}^{j'} = \begin{cases} S_{ms}^{j} & (\sum S_{ms-M} + \sum S_{ms-L}) \le S_{ms-H} \\ k_j \times S_{ms}^{j} & (\sum S_{ms-M} + \sum S_{ms-L}) > S_{ms-H} \end{cases} \tag{3}$$

In formula (3), S_{ms-H} is the accessible capacity of high-voltage devices selected in the calculation unit; $\sum S_{ms-M}$ is the sum of the medium-voltage side of the selected unit without considering constraints; $\sum S_{ms-L}$ is the sum of the low-voltage side of the selected unit without considering constraints; S_{ms}^{j} is initial accessible capacity of device

j, it needed to multiply by a factor k_j to satisfy that the sum of medium-voltage and low-voltage sides is not greater than its high side accessible capacity; $S_{ms}^{j'}$ is accessible capacity of device j considering constrains,; k_j is conversion factor, the value is between 0 and 1, which is determined by the load level and distributed power connected to devices.

2.6 Calculation Accessible Capacity of Regional Grid

Accessible capacity of regional grid is the minimum value between 220 kV, 110 kV, 35 kV, 10 kV, 0.38 kV, which can calculate by formula (5).

$$A_{ms} = \min(\sum S_{ms-220}, \sum S_{ms-110}, \sum S_{ms-35}, \sum S_{ms-10}, \sum S_{ms-0.38}) \quad (4)$$

In formula (4), S_{ms-220} is the sum of all 220 kV substations accessible capacity consider upper and lower constrains; S_{ms-110} is the sum of all 110 kV substations accessible capacity consider upper and lower constrains; S_{ms-35} is the sum of all 35 kV substations accessible capacity consider upper and lower constrains; S_{ms-10} is the sum of all 10 kV lines accessible capacity consider upper and lower constrains; $S_{ms-0.38}$ is the sum of all distribution accessible capacity consider upper and lower constrains.

3 Example Analysis

Taking a 220 kV substation in a southern province as an example, the regional accessible capacity is the minimum value between 220 kV, 110 kV, 35 kV, 10 kV, 0.38 kV. The electrical wiring of the 220 kV Huayang Substation is shown in Fig. 2. The medium-voltage devices of Huayang substation includes 3 110 kV substations, which named 110 kV shunchang substation, 110 kV xintun substation and 110 kV jinxi substation. The low-level devices of Huayang substation includes 6 10 kV lines.
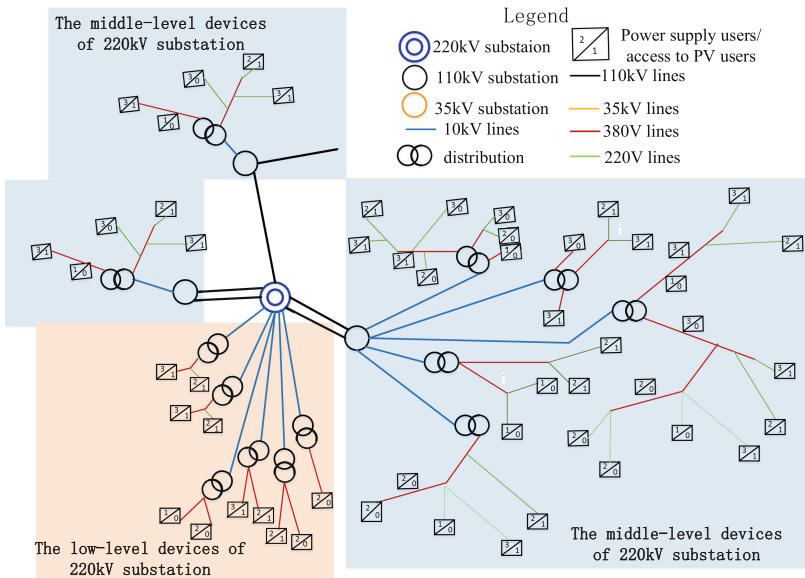
Fig. 2. Wiring diagram of 220 kV Huayang substation

3.1   Initial Accessible Capacity of All Voltage Devices

The minimum load value of 220 kV substation from 11am to 2pm within the last year is 4.2 MW, the power other than distributed power connected to 220 kV substation is 49.3 at the same time. Therefore, the maximum accessible capacity of 220 kV Huayang Substation is 53.5 MW.

The minimum load value and rated capacity of medium-voltage devices and low-level of 220 kV substation is listed in Table 1. According to formula (3), the maximum accessible capacity can be calculated.

Table 1. Initial accessible capacity of medium-voltage and low-voltage of 220 kV substation.

Voltage level	Substation	Rated capacity (MVA)	Minimum load value (MW)	maximum accessible capacity (MW)
110 kV	Shunchang	63	1.1	51.5
110 kV	Xintun	113	−10.5	79.9
110 kV	Jinxi	110	0	88
10 kV	LINE 1	8.7	0.18	7.14
10 kV	LINE 2	7.7	0.06	6.22
10 kV	LINE 3	5.9	0.01	4.73
10 kV	LINE 4	8.7	0.02	6.98
10 kV	LINE 5	7.7	0.12	6.28
10 kV	LINE 6	5.9	0.04	4.76
Totally	–	–	–	255.51

3.2   Accessible Capacity Considering Constrains

Taking 220 kV Huayang substation as high unit, its medium-voltage side devices are Shunchang, Xintun and Jinxi 110 kV substation respectively, its low-voltage side devices are line 1 to line 6 respectively. The sum of medium-voltage and low-voltage of 220 kV substation is 255.51 MW, which is more than 220 kV substation. According to formula (3), 110 kV substation and 10 kV lines needed to multiply by factor to satisfy that the sum of medium-voltage and low-voltage of 220 kV substation is less than 220 kV substation, the adjusted accessible capacity is listed in Table 2.

As all 220 kV substation and its related medium-voltage and low-voltage devices accessible capacity is calculated finished, then deduced calculating voltage, taking 110 kV devices as unit. Firstly calculating all its related medium and low-voltage devices' initial accessible capacity, then adjusted its capacity to satisfy formula (3). As all devices' accessible capacity in Fig. 2 is calculated, calculating the sum of each voltage devices respectively, the regional accessible capacity in Fig. 2 can be calculated as formula (4). Table 3 gives the sum of each voltage, and its regional accessible capacity.

Table 2. Adjusted accessible capacity of medium-voltage and low-voltage of 220 kV substation.

Voltage level	Substation	Initial accessible capacity (MW)	Factor k_j	Adjusted accessible capacity (MW)
110 kV	Shunchang	51.5	0.21	10.82
110 kV	Xintun	79.9	0.15	11.99
110 kV	Jinxi	88	0.18	15.84
10 kV	LINE 1	7.14	0.5	3.57
10 kV	LINE 2	6.22	0.4	2.49
10 kV	LINE 3	4.73	0.25	1.18
10 kV	LINE 4	6.98	1.42	2.96
10 kV	LINE 5	6.28	0.4	2.51
10 kV	LINE 6	4.76	0.45	2.14
Totally	–	255.51	–	53.5

Table 3. Regional accessible capacity in Fig. 2.

Voltage level	The sum of the voltage devices (MW)
220 kV	53.5
110 kV	38.65
10 kV	46.57
0.38 kV	60.12
Regional accessible capacity	38.65

In Table 3, the regional accessible capacity in Fig. 2 is 38.65 MW, which is not only the sum of the accessible capacity of 110 kV devices, but also the minimum value of whole voltage. So, the total planned PV development scale should be less than 38.65 MW to ensure grid safety, and accessed capacity of each devices under 220 kV voltage should be limited in Table 3 under current grid. The calculating should be dynamic update to guide PV development orderly and priority access to area of sufficient capacity.

4   Conclusion

Under the background of county PV development, in order to ensure PV development orderly and grid connection safety, grid companies need to timely disclose the regional accessible distributed PV capacity. The method proposed in paper is based on the premise of avoiding back-feeding to the 220 kV grid and above, which due to distributed power supply connected to grid. Firstly calculating initial accessible capacity of all devices,

which calculation is meet the requirement of reverse load flow without overloading. Then calculating adjusted accessible capacity from high voltage to low voltage, which taking high-voltage equipment as a unit, adjusted its medium-voltage devices and low-voltage devices to satisfy that the sum of medium and low-voltage devices is not greater than its own high side accessible capacity, and meets the constraints of voltage deviation and short-circuit current.

The method proposed in this paper not only considers the influence of constraints such as voltage deviation and short-circuit current, but also considers the load situation and the actual operation of the grid. The calculation will be obtained quickly to avoid the problems of long calculation time and large amount of calculation due to the lack of reasonable initial values in genetic algorithm and multi-objective optimization algorithm.

Finally, taking the 220 kV substation as an example, the calculation method proposed in this paper is calculated and analyzed layer by layer. The initial and adjusted accessible capacity are analyzed respectively, also the regional accessible capacity is calculated. The method is simple and feasible, and provides an efficient and feasible solution for distributed PV capacity accessible to the distribution network in the whole range.

References

1. National Energy Administration: Notice of the National Energy Administration on the announcement of the entire county (city, district) rooftop distributed PV development pilot list, 08 September 2021. http://zfxxgk.nea.gov.cn/2021-09/08/c_1310186582.htm

2. National Energy Administration: Notice of the Comprehensive Department of the National Energy Administration on the submission of the entire county (city, district) rooftop distributed PV development pilot program, 24 June 2021. http://gdsolar.org/dongtaiinfo_1879.html

3. Xie, H.: The closing year of the "Thirteenth Five-Year Plan"! A Summary of the High Quality Reform and Development of State Grid, 05 January 2021. http://www.xinhuanet.com/energy/2021-01/05/c_1126947972.htm

4. Li, Q., Ye, X., Hu, J., et al.: Outlook and critical issues of large-scale development on distributed energy resources. Distrib. Energy **5**(2), 5–6 (2020)

5. Xiang Chi, X., Ouyang, W.F., et al.: Influence of distributed residential PV systems on voltage quality of rural power distribution area and its accommodation measure. Smart Grid **4**(10), 1044 (2016)

6. Cai, Y., Tang, W., Xu, O., et al.: Review of voltage control research in LV distribution network with high proportion of residential PVs. Power Syst. Technol. **42**(1), 220–221 (2018)

7. Ding, M., Wang, W., Wang, X., et al.: A review on the effect of large-scale PV generation on power systems. In: Proceedings of the CSEE, vol. 34, no. 1, pp. 3–5 (2014)

8. Chen, W., Ai, X., Wu, T., et al.: Influence of grid-connected PV system on power network. Electr. Power Autom. Equip. **33**(2), 28–30 (2013)

9. Weng, Y., Cheng, R., Ma, W., et al.: Maximum integration capacity of distributed PV power considering voltage fluctuation. Smart Power **46**(11), 30–31 (2018)

10. Zou, H., Han, X., Liao, Q., et al.: Penetration capacity calculation for distributed generation considering voltage quality and short circuit capacity constrains. Power Syst. Technol. **40**(8), 2277–2279 (2016)

11. Wang, C., Zhang, N., Zhao, J., et al.: Maximum capacity calculation of distributed generators considering fluctuation characteristics. In: Proceedings of the CSU-EPSA, vol. 28, no. 8, pp. 38–39 (2016)

12. Liu, J., Huang, W.: Analysis on grid-connectible capacity of distributed PV generation in case of PV generation distribution close to load distribution. Power Syst. Technol. **39**(2), 300–305 (2015)
13. Zhou, L., Zhang, D., Li, C., et al.: Access capacity analysis considering correlation of distributed PV power and load. Autom. Electr. Power Syst. **41**(4), 56–60 (2017)
14. Ye, B., Zhu, Z., Ma, J., et al.: Research on permitted penetration capacity of distributed PV generation based on flexible network structure. Electr. Meas. Instrum. **56**(11), 5–6 (2019)
15. Wu, M., Xu, B., Ji, Y., et al.: Transmission-distribution-network-coordinated calculation method of maximum integration capacity of distributed generations. Power Syst. Technol. **43**(11), 3383–3384 (2019)
16. Zhao, D., Ren, Y., Cheng, X.: Analysis of distributed PV acceptance capacity in low voltage distribution network. Mod. Electr. Power **38**(4), 3383–3384 (2021)
17. Technical Guideline for Evaluating Power Grid Bearing Capability of Distributed Resources Connected to Network: DL/T 2041–2019. China Electric Power Press, Beijing (2019)
18. Xu, J., Yu, J., Li, C., et al.: Analysis on maximum allowable access capacity of distributed power source based on voltage stability. Hunan Electr. Power **41**(3), 22–24 (2021)
19. Wuhan University: A grid accessible distributed generation capacity measurement method considering short-circuit capacity constraints: 201410058582.9, 02 July 2014
20. Design Code for Connecting to Distribution Network for distributed Generation: Q/GDW11147-2013. China Electric Power Press, Beijing (2014)

Analysis of Low Carbon Operation of High Penetration Renewable Energy System Considering Energy Storage Configuration

Yuehan Wang[✉], Haiyang Wan, and Wenxia Liu

North China Electric Power University, Beijing 102206, China
wyh17778194396@163.com

Abstract. To address the source-load power balance problem of high penetration renewable energy systems in the context of "carbon neutrality", the impact of system low-carbon transition on operation economy and reliability is analyzed in this paper, taking into account the output characteristics and power supply costs of thermal power, wind power and energy storage. Considering the flexibility resources such as energy storages and electric energy replacement loads, the paper proposes a low-carbon operation strategy for high penetration renewable energy system to reduce the comprehensive economic cost of energy storage configuration, unit operation and carbon capture. Finally, the case study demonstrates the effectiveness of proposed strategy in guaranteeing the economic and reliable operation of the system.

Keywords: Carbon neutrality · High penetration renewable energy system · Source-load balance · Wind power · Energy storage configuration

1 Introduction

In recent years, climate change and environmental pollution problems have come to the fore, and countries around the world have put forward carbon emission reduction policies. With the promotion of China's "dual carbon" goals, a large number of renewable energy sources such as wind power have been integrated into the power system. By the end of 2021, the installed capacity of wind turbines in China has reached 330 million kilowatts, accounting for 13.87% of the entire system, effectively alleviating the energy crisis and environmental degradation. However, the uncertainty of renewable energy output leads to increased fluctuation of source load, which increases the peak shaving pressure of the system. How to guarantee the economic and reliable operation of high proportion renewable energy system is an urgent problem to be solved.

Traditional studies usually adopt the regulation of source-side unit output and grid-side topology transformation to smooth source-load fluctuations. Reference [1] proposed an optimization method for thermal unit peaking shaving strategy to promote renewable energy accommodation by improving the flexibility of thermal units. Considering the influence of grid topology on wind power accommodation rate, network reconfiguration

was used in [2, 3] to achieve cooperative source-network dispatch. The above studies only consider conventional power sources. However, in a high penetration renewable energy system, conventional power sources can hardly provide sufficient inertia support and have insufficient ability to cope with source-load fluctuations.

Energy storage (ES) devices and electrical energy replacement loads can smooth fluctuations through the transfer of electrical energy in the space-time dimension, and have a good peak-shaving and valley-filling effect [4–6]. It provides an effective means for low-carbon economic operation of the high penetration renewable energy system and ensuring real-time system power balance. A multi-objective low-carbon economic scheduling method was proposed in [7] considering energy storages and renewable energy access. Aiming at the problem of curtailment of wind and solar power in high-proportion renewable energy systems, a collaborative optimization method considering network reconfiguration and economic scheduling of mobile energy storages was proposed in [8]. The above studies are based on energy storage devices with fixed parameters to balance the system power. Since the energy storage cost is relatively expensive, utilizing a large amount of energy storages will increase the system cost and reduce the utilization efficiency of resources. In terms of electrical energy replacement loads, reference [9] proposed an incentive-based demand response strategy to achieve efficient consumption of renewable energy by regulating the power consumption of controllable loads. Reference [10] analyzed the effect of flexible loads and energy storages on improving wind power utilization by various price-based demand response programs. The above studies have achieved some results in using energy storage and electrical energy replacement loads to promote renewable energy accommodation, but they have not fully considered the economic influences such as energy storage configuration and thermal power carbon capture. It is difficult for a single flexibility measure to meet the demand for efficient consumption of high penetration of renewable energy and low carbon operation of the system. In addition, among the studies considering renewable energy and energy storages, there are few research on optimal scheduling taking into account low-carbon objective.

To address the above shortcomings, this paper proposes a low-carbon operation strategy for high penetration renewable energy system with the objective of reducing the comprehensive economic costs of energy storage allocation, unit operation and carbon capture. The system power balance is met by coordinating thermal units, energy storage systems and flexible loads to guarantee the economy and reliability of system operation. Finally, the effectiveness of the proposed strategy is verified by the simulation results.

2 Cost Types of High Penetration Renewable Energy System Considering Energy Storage Configuration

In this paper, we consider that the high proportion renewable energy system contains thermal power units, wind turbines and flexible loads. In order to promote the efficient accommodation of renewable energy, a certain capacity of energy storage devices can be configured with wind turbines. In addition, thermal power units are retrofitted with carbon capture equipment to reduce carbon emissions. In the low carbon operation of a high penetration renewable energy system, the system cost mainly includes thermal power unit cost, wind turbine cost, energy storage cost and load scheduling cost.

2.1 Cost of Thermal Power Units

The cost of thermal power units contains the cost of coal consumption, the cost of operation and maintenance and the cost of carbon capture. The calculation methods of three types of costs are shown in Eqs. (1)–(3).

$$f^{\text{G,CoPG}} = \frac{\Delta t}{60} C^{\text{Coal}} \sum_{t \in \Omega_T} \sum_{j \in \Omega_G} \left(a_j^{\text{G}} (P_{j,t}^{\text{G}})^2 + b_j^{\text{G}} P_{j,t}^{\text{G}} + c_j^{\text{G}} u_{j,t}^{\text{G}} \right) \tag{1}$$

$$f^{\text{G,CoOM}} = 0.5 f^{\text{G,CoPG}} \tag{2}$$

$$f^{\text{G,CoCC}} = \frac{\Delta t}{60} C^{\text{CoCC}} \sum_{t \in \Omega_T} \sum_{j \in \Omega_G} d^{\text{G}} P_{j,t}^{\text{G}} \tag{3}$$

where $f^{\text{G,CoPG}}$ is the total coal consumption cost of thermal power units. Δt is the time step and its value is 15 min. C^{Coal} is the unit price of coal. Ω_T is the set of time. Ω_G is the set of thermal power units. a_j^{G}, b_j^{G} and c_j^{G} are the coal consumption coefficients for the j-th thermal power unit. $P_{j,t}^{\text{G}}$ is the output of the j-th thermal power unit at time t. $u_{j,t}^{\text{G}}$ is the operating state of the j-th thermal power unit at time t. If the unit is working, then $u_{j,t}^{\text{G}} = 1$, otherwise $u_{j,t}^{\text{G}} = 0$. $f^{\text{G,CoOM}}$ is the total operation and maintenance cost of thermal power units. f^{CoCC} is the total carbon capture cost. C^{CoCC} is the parameter of the carbon capture cost. d^{G} is the carbon emission parameter of thermal power unit.

2.2 Cost of Wind Turbines

The cost of wind turbines contains the cost of operation and maintenance and the cost of abandoned wind power. The two types of costs are calculated as shown in Eqs. (4)–(5), respectively.

$$f^{\text{WT,CoOM}} = \frac{\Delta t}{60} C^{\text{WT,CoOM}} \sum_{t \in \Omega_T} \sum_{j \in \Omega_{WT}} P_{j,t}^{\text{WT}} \tag{4}$$

$$f^{\text{WT,CoWC}} = \frac{\Delta t}{60} C^{\text{WT,CoWT}} \sum_{t \in \Omega_T} \sum_{j \in \Omega_{WT}} (P_{j,t}^{\text{WT,max}} - P_{j,t}^{\text{WT}}) \tag{5}$$

where $f^{\text{WT,CoOM}}$ is the total operation and maintenance cost of wind turbines. $C^{\text{WT,CoOM}}$ is the unit operation and maintenance cost of wind turbines. Ω_{WT} is the set of wind turbines. $P_{j,t}^{\text{WT}}$ is the output of the j-th wind turbine at time t. $f^{\text{WT,CoWC}}$ is the total cost of abandoned wind power. $C^{\text{WT,CoWT}}$ is the parameter of the abandoned wind power cost. $P_{j,t}^{\text{WT,max}}$ is the maximum output of the j-th wind turbine at time t.

2.3 Cost of Energy Storages

The cost of energy storages contains investment power cost, investment energy cost and operation and maintenance cost. The three types of costs are calculated as shown in Eqs.

(6)–(8), respectively [11].

$$f^{\text{ES,CoESP}} = \frac{C^{\text{CoESP}} \sum\limits_{j \in \Omega_{ES}} P_j^{\text{ES,max}}}{T^{\text{day}}} \cdot \frac{r(r+1)^{T^{\text{year}}}}{(r+1)^{T^{\text{year}}} - 1} \tag{6}$$

$$f^{\text{ES,CoESC}} = \frac{C^{\text{CoESC}} \sum\limits_{j \in \Omega_{ES}} E_j^{\text{ES,max}}}{T^{\text{day}}} \cdot \frac{r(r+1)^{T^{\text{year}}}}{(r+1)^{T^{\text{year}}} - 1} \tag{7}$$

$$f^{\text{ES,CoOM}} = \frac{\Delta t}{60} C^{\text{ES,CoOM}} \sum\limits_{j \in \Omega_{ES}} (P_{j,t}^{\text{ES,ch}} + P_{j,t}^{\text{ES,dch}}) \tag{8}$$

where $f^{\text{ES,CoESP}}$ is the investment power cost of energy storages. C^{CoESP} is the unit power cost of energy storages. Ω_{ES} is the set of energy storages. $P_j^{\text{ES,max}}$ is the maximum charge power and discharge power of the j-th energy storage. $f^{\text{ES,CoESC}}$ is the investment energy cost of energy storages. C^{CoESC} is the unit energy cost of energy storages. $E_j^{\text{ES,max}}$ is the maximum capacity of the j-th energy storage. r is the depreciation rate. T^{year} is the full life cycle years of energy storage. T^{day} is the number of working days of energy storage in a year. $f^{\text{ES,CoOM}}$ is the operation and maintenance cost of energy storages. C^{CoOM} is the unit energy operation and maintenance cost of energy storages.

2.4 Cost of Load Scheduling

It is assumed that the load types in the system can be classified as shiftable loads, interruptible loads and non-interruptible loads. The first two types of loads can participate in the process of peak shaving and valley filling through demand-side response in the system economic scheduling. The cost of load scheduling includes subsidized cost and load shedding cost of shiftable loads and load shedding cost of interruptible load. In addition, the third type of load will cause greater economic losses after being shed due to its higher importance. The three types of costs are calculated as shown in Eqs. (9)–(12), respectively.

$$f^{\text{CoSL}} = \frac{\Delta t}{60} \sum\limits_{t \in \Omega_T} \sum\limits_{j \in \Omega_N} ((C^{\text{CoSL}}(1 - \sum\limits_{t \in \Omega_T} y_{j,t}^{\text{SL}}) - C^{\text{SCoSL}} u_{j,t}^{\text{SL}})(P_{j,t}^{\text{SL,max}} - P_{j,t}^{\text{SL}})) \tag{9}$$

$$y_{j,t}^{\text{SL}} = u_{j,t}^{\text{SL}}(1 - u_{j,t-1}^{\text{SL}}) \tag{10}$$

$$f^{\text{CoIL}} = \frac{\Delta t}{60} C^{\text{CoIL}} \sum\limits_{t \in \Omega_T} \sum\limits_{j \in \Omega_N} (P_{j,t}^{\text{IL,max}} - P_{j,t}^{\text{IL}}) \tag{11}$$

$$f^{\text{CoNIL}} = \frac{\Delta t}{60} C^{\text{CoNIL}} \sum\limits_{t \in \Omega_T} \sum\limits_{j \in \Omega_N} (P_{j,t}^{\text{NIL,max}} - P_{j,t}^{\text{NIL}}) \tag{12}$$

where f^{CoSL}, f^{CoIL} and f^{CoNIL} are the scheduling costs of shiftable loads, interruptible loads and non-interruptible loads, respectively. C^{SCoSL} is the unit subsidized cost of

shiftable loads. C^{CoSL}, C^{CoIL} and C^{CoNIL} are the unit load shedding cost of shiftable loads, interruptible loads and non-interruptible loads, respectively. Ω_N is the set of buses. $P_{j,t}^{\mathrm{SL}}$, $P_{j,t}^{\mathrm{IL}}$ and $P_{j,t}^{\mathrm{NIL}}$ are the power of the shiftable loads, interruptible loads and non-interruptible loads at j-th bus at time t. $u_{j,t}^{\mathrm{SL}}$ is the operating state of the shiftable loads connected to node j at time t. If the loads are operating, then $u_{j,t}^{\mathrm{SL}} = 1$, otherwise $u_{j,t}^{\mathrm{SL}} = 0$. $y_{j,t}^{\mathrm{SL}}$ is the sign that the shiftable loads start to operate. If the loads start to operate, then $y_{j,t}^{\mathrm{SL}} = 1$, otherwise $y_{j,t}^{\mathrm{SL}} = 0$. $P_{j,t}^{\mathrm{SL,max}}$, $P_{j,t}^{\mathrm{IL,max}}$ and $P_{j,t}^{\mathrm{NIL,max}}$ are the maximum power of the shiftable loads, interruptible loads and non-interruptible loads at j-th bus at time t.

Equation (9) represents that when shiftable loads are shed, the scheduling cost should be equal to its load shedding cost. When the shiftable loads are operating properly, the scheduling cost should be equal to the subsidized cost of its load transfer.

2.5　Benefits of Carbon Reduction

The electricity of traditional thermal power units can be reduced through the grid connection of wind power, thereby realizing the benefits of emission reduction of greenhouse gases and pollutants (mainly including CO2, carbon dust and suspended particulate matter, etc.) [12].

$$f^{\mathrm{BoCR}} = \frac{\Delta t}{60} C^{\mathrm{BoCR}} \sum_{t \in \Omega_T} \sum_{j \in \Omega_{WT}} d^{\mathrm{G}} P_{j,t}^{\mathrm{WT}} \tag{13}$$

where, f^{BoCR} is the benefits of carbon reduction. C^{BoCR} is the environmental cost per unit load output.

3　Optimal Configuration Model of Energy Storage for Low Carbon Economic Operation

Energy storage can smooth the fluctuation of wind turbine output and play the role in peak-shaving and valley-filling, which is conducive to improving the overall system economy. Since energy storage devices are more expensive, the selection of energy storage with appropriate power and capacity is a prerequisite for system economy and source-load balance. Based on this, this section takes the minimum cost of each type in the above section as the objective function. A mixed integer linear programming model is established with the output of the generators, the maximum charge/discharge power and capacity of the energy storage to be selected, the charge/discharge power of the energy storage, and the load power as the decision variables.

3.1　Objective Function

The objective function consists of the four component costs described in Sect. 2. The objective function can be expressed as:

$$\begin{aligned}
\min \quad & f^{\mathrm{G,CoPG}} + f^{\mathrm{G,CoOM}} + f^{\mathrm{CoCC}} + f^{\mathrm{WT,CoOM}} + f^{\mathrm{WT,CoWC}} + f^{\mathrm{ES,CoESP}} \\
& + f^{\mathrm{ES,CoESC}} + f^{\mathrm{ES,CoOM}} + f^{\mathrm{CoSL}} + f^{\mathrm{CoIL}} + f^{\mathrm{CoNIL}} - f^{\mathrm{BoCR}}
\end{aligned} \tag{14}$$

3.2 Constraints

The thermal unit operating constraints include unit output constraint, climbing constraint, minimum start-up and shutdown duration constraint and standby capacity constraint. The thermal unit operating constraints are shown in Eqs. (15)–(18).

$$u_{j,t}^G P_j^{G,\min} \le P_{j,t}^G \le u_{j,t}^G P_j^{G,\max} \tag{15}$$

$$-R_j^{G,D} u_{j,t}^G \le P_{j,t+1}^G - P_{j,t}^G \le R_j^{G,U} u_{j,t}^G \tag{16}$$

$$\begin{cases} \displaystyle\sum_{t}^{t+T_j^{G,U,\min}-1} u_{j,t}^G = T_j^{G,U,\min} \ \ if \ u_{j,t}^G(1 - u_{j,t-1}^G) = 1 \\[4mm] \displaystyle\sum_{t}^{t+T_j^{G,D,\min}-1} u_{j,t}^G = T_j^{G,D,\min} \ \ if \ u_{j,t-1}^G(1 - u_{j,t}^G) = 1 \end{cases} \tag{17}$$

$$\sum_{j\in\Omega_G} (P_j^{G,\max} - P_{j,t}^G) \ge R^C \sum_{j\in\Omega_N} (P_{j,t}^{SL} + P_{j,t}^{IL} + P_{j,t}^{NIL}) \tag{18}$$

where $P_j^{G,\min}$ and $P_j^{G,\max}$ are the maximum and minimum output of the j-th thermal power unit, respectively. $R_j^{G,U}$ and $R_j^{G,D}$ are the upward and downward climbing power per unit time of the j-th thermal power unit, respectively. $T_j^{G,U,\min}$ and $T_j^{G,D,\min}$ are the minimum start-up and shutdown duration of the j-th thermal power unit, respectively. R^C is the factor of standby capacity.

The wind turbine operating constraints include the unit output constraint, as shown in Eq. (19).

$$0 \le P_{j,t}^{WT} \le P_{j,t}^{WT,\max} \tag{19}$$

The rated capacity of the energy storage should normally meet its discharge at the maximum discharge power for at least two hours, so the rated capacity of the energy storage device being configured and the maximum charge/discharge power should satisfy Eq. (20) [13]. The operating constraints of energy storage devices include maximum charge/discharge power constraints, charge/discharge state constraints and capacity constraints.

$$E_j^{ES,\max} \ge T_j^{ES,\min} P_j^{ES,\max} \tag{20}$$

$$0 \le P_{j,t}^{ES,ch} \le \delta_{j,t}^{ES,ch} P_j^{ES,\max} \tag{21}$$

$$0 \le P_{j,t}^{ES,dch} \le \delta_{j,t}^{ES,dch} P_j^{ES,\max} \tag{22}$$

$$\delta_{j,t}^{ES,ch} + \delta_{j,t}^{ES,dch} \le 1 \tag{23}$$

$$E_{j,t+1}^{\text{ES}} = E_{j,t}^{\text{ES}} + (P_{j,t}^{\text{ES,ch}} \eta_j^{\text{ES,ch}} - \frac{P_{j,t}^{\text{ES,dch}}}{\eta_j^{\text{ES,dch}}}) \Delta t \qquad (24)$$

$$E_j^{\text{ES,max}} O_j^{\text{ES,min}} \leq E_{j,t}^{\text{ES}} \leq E_j^{\text{ES,max}} O_j^{\text{ES,max}} \qquad (25)$$

where $T_j^{\text{ES,min}}$ is the duration of the j-th energy storage discharged at maximum power. $\delta_{j,t}^{\text{ES,ch}}$ and $\delta_{j,t}^{\text{ES,dch}}$ are the charging and discharging states of the j-th energy storage at time t. If it is in charging state, then $\delta_{j,t}^{\text{ES,ch}} = 1$, $\delta_{j,t}^{\text{ES,dch}} = 0$. If it is in discharging state, then $\delta_{j,t}^{\text{ES,ch}} = 0$, $\delta_{j,t}^{\text{ES,dch}} = 1$. $P_{j,t}^{\text{ES,ch}}$ and $P_{j,t}^{\text{ES,dch}}$ are the charge/discharge power of the j-th energy storage at time t. $\eta_j^{\text{ES,ch}}$ and $\eta_j^{\text{ES,dch}}$ are the charge/discharge efficiency of the j-th energy storage. $O_j^{\text{ES,min}}$ and $O_j^{\text{ES,max}}$ are the minimum and maximum SOC of the j-th energy storage.

The shiftable load scheduling constraints are shown in Eqs. (25)–(26).

$$\sum_{t}^{t+T_j^{\text{SL}}-1} u_{j,t}^{\text{SL}} = T_j^{\text{SL}} \ if \ \sum_{t \in \Omega_T} y_{j,t}^{\text{SL}} = 1 \qquad (26)$$

$$P_{j,t}^{\text{SL}} = u_{j,t}^{\text{SL}} P_{j,t}^{\text{SL,max}} \qquad (27)$$

where T_j^{SL} is the continuous operating time of the shiftable load connected to bus j. Equation (25) represents that when the shiftable loads are operating at time t, the loads need to be in operating state for the next $T_j^{\text{SL}} - 1$ periods. Equation (26) indicates that the power of the shiftable loads can only be $P_{j,t}^{\text{SL,max}}$ or 0.

The system operation constraints include bus active power balance constraints, load flow constraints and line capacity constraints as shown in Eqs. (25)–(26).

$$\sum_{k \in \Omega_{out}(j)} P_{jk,t} - \sum_{i \in \Omega_{in}(j)} P_{ij,t} = P_{j,t}^{\text{G}} + P_{j,t}^{\text{WT}} - (P_{j,t}^{\text{SL}} + P_{j,t}^{\text{IL}} + P_{j,t}^{\text{NIL}}) \qquad (28)$$

$$(w_{ij,t} - 1)M \leq P_{ij,t} - \frac{\theta_i - \theta_j}{x_{ij}} \leq (1 - w_{ij,t})M \qquad (29)$$

$$-w_{ij,t} P_{ij}^{\max} \leq P_{ij,t} \leq w_{ij,t} P_{ij}^{\max} \qquad (30)$$

where $w_{ij,t}$ is the switch state of line ij at time t. If it is in closed state, then $w_{ij,t} = 1$, otherwise $w_{ij,t} = 0$. M is a large constant. x_{ij} the reactance of line ij. $P_{ij}^{\max}$ is the maximum value of the load flow on line ij. $P_{jk,t}$ is the load flow on line ij at time t. $\Omega_{out(j)}$ and $\Omega_{in(j)}$ are the sets of child buses and parent buses of bus j.

4 Case Study

The mixed-integer linear programming problem (MILP) constructed in this paper can be solved using the well-established commercial solver GUROBI, which is specifically modeled in MATLAB R2021a.

4.1 System Structure and Parameters

The simulation time step set in this paper is 15 min and the unit cost of carbon capture is 60 RMB/t. The maximum capacity of energy storage that can be configured is 300 MWh. The schematic structure of the improved 3-machine 6-node system is shown in Fig. 1. The 3rd node with the wind turbine connected can be configured with energy storage. The prediction curves of wind power output and load power on a typical day are shown in Fig. 2. The rated power of three types of loads at each node are shown in Table 1.
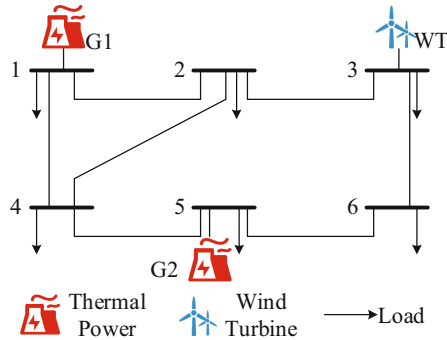
Fig. 1. The schematic structure of the improved 3-machine 6-node system.
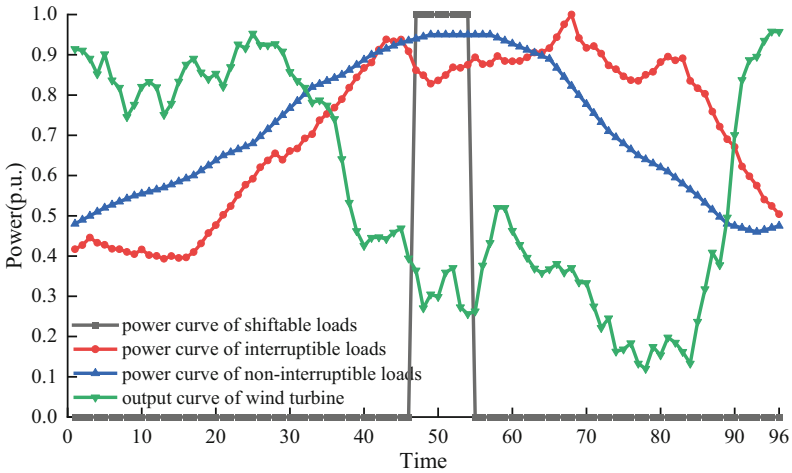
Fig. 2. The prediction curves of wind power output and load power on a typical day.

Table 1. Rated power of three types of loads at each node

	Shiftable load (MW)	Interruptible load (MW)	Non-interruptible load (MW)
Node 1	0	40	160
Node 2	300	0	0
Node 3	0	90	60
Node 4	0	210	140
Node 5	0	80	20
Node 6	0	180	120

4.2 Simulation Results

The optimal location for energy storage configuration is node 3. The optimal capacity of energy storage is 275 MWh and the maximum charge power and discharge power is 77 MW. The total cost of the system is 2.73 million RMB, and the value and proportion of each type of cost are shown in Table 2. The economic scheduling results of the units and loads are shown in Fig. 3. The actual total carbon emissions of the system with and without the cost of carbon capture Eq. (3) and the benefits of carbon reduction Eq. (13) are 7426 t and 9335 t, while the emission reductions of greenhouse gases and pollutants of the system are 7453 t and 7286 t. The results show that the proposed method can reduce the total carbon emissions of the system.

Table 2. The value and proportion of each type of cost.

Type of cost	Value (thousand RMB)	Proportion
$f^{G,CoPG}$	1204.14	44.08%
$f^{G,CoOM}$	602.07	22.04%
f^{CoCC}	445.56	16.31%
$f^{WT,CoOM}$	424.56	15.54%
$f^{WT,CoWC}$	34.07	1.25%
$f^{ES,CoESP}$	65.19	2.39%
$f^{ES,CoESC}$	232.81	8.52%
$f^{ES,CoOM}$	17.46	0.64%
f^{CoSL}	600.00	21.96%
f^{CoIL}	0.52	0.02%
f^{CoNIL}	0.00	0.00%
f^{BoCR}	894.41	32.74%
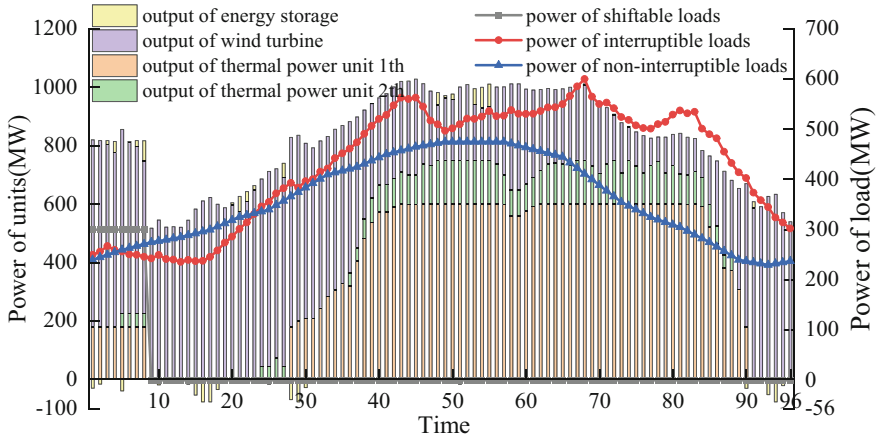
Fig. 3. The economic scheduling results of the units and loads.

4.3 Analysis of the Impact of Wind Power Output and Load Power Uncertainty

There are large uncertainties in the magnitude of both wind power output and load power. To measure the degree of influence of the two types of uncertainties on the optimization results of energy storage configuration, seven typical scenarios are designed with the fluctuation intervals of wind power output and load power as $[0.8P_{j,t}^{\mathrm{WT,max}}, 1.2P_{j,t}^{\mathrm{WT,max}}]$ and $[0.8P_{j,t}^{\mathrm{SL,max}}, 1.2P_{j,t}^{\mathrm{SL,max}}]$, respectively. The simulation results are shown in Table 3.

Table 3. Sensitivity analysis of uncertainty factors.

Scenario	Wind power	Load power	Total cost (thousand RMB)	Location of ES	Capacity of ES (MWh)	Maximum output of ES (MW)
1	$0.8\,P_{j,t}^{\mathrm{WT,max}}$	$P_{j,t}^{\mathrm{SL,max}}$	4766.13	3	300	43
2	$0.8\,P_{j,t}^{\mathrm{WT,max}}$	$1.2\,P_{j,t}^{\mathrm{SL,max}}$	22396.85	3	300	29
3	$P_{j,t}^{\mathrm{WT,max}}$	$0.8\,P_{j,t}^{\mathrm{SL,max}}$	1765.78	3	0	0
4	$P_{j,t}^{\mathrm{WT,max}}$	$P_{j,t}^{\mathrm{SL,max}}$	2731.96	3	275	77
5	$P_{j,t}^{\mathrm{WT,max}}$	$1.2\,P_{j,t}^{\mathrm{SL,max}}$	17729.20	3	300	34
6	$1.2\,P_{j,t}^{\mathrm{WT,max}}$	$0.8\,P_{j,t}^{\mathrm{SL,max}}$	1793.62	3	104	52
7	$1.2\,P_{j,t}^{\mathrm{WT,max}}$	$P_{j,t}^{\mathrm{SL,max}}$	2463.06	3	102	40

From the solution results of each scenario in the table above, the following three conclusions can be observed:

(1) When the wind power is normal (scenarios 3, 4, and 5), the configuration capacity of energy storage increases with the increase of the load. This is because when the load is too large, the total output of the power supply cannot meet the supply of all loads. At this time, the system will configure energy storage to reduce the total economic loss of system load reduction.
(2) When the load power is normal (scenarios 1, 4, and 7), the capacity of the energy storage configuration decreases with the increase of the wind turbine output. This is because when the output of the wind turbine is too large, on the premise that the normal power supply of all loads can be satisfied, the cost of configuring energy storage is higher than the cost of abandoning wind, and the system will reduce the configuration capacity of energy storage to improve the system economy.
(3) The amount of the load power has a greater impact on the results of total operating cost of the system and energy storage configuration. On the one hand, as shown in Scenarios 2 and 5, when the load power is 1.2 times of the original, the system will lead to a large amount of load shedding due to insufficient source-side output, and the total system operating cost will be greatly increased. On the other hand, as shown in Scenario 3, when the load power is 0.8 times of the original, the system will choose not to be equipped with energy storage at this time due to the sufficient source-side power and the high cost of energy storage configuration.

5   Conclusion

In this paper, a low-carbon operation strategy for high penetration renewable energy system is established based on the analysis of the impact of system low-carbon transition on operation economy and reliability. To address the source-load power balance problem, the optimal configuration model of energy storage for low carbon economic operation is proposed. The following conclusions can be made according to the case study: Energy storages and electrical energy replacement loads can smooth the fluctuations of high penetration renewable energy system and bring significant environmental benefits. However, the uncertainties of wind power output and load power will have a greater impact on the overall operating cost of the system. When making a low-carbon and economical operation strategy, it is necessary to consider the optimal configuration of energy storage. The robust operation strategy for high penetration renewable energy system will be the future research work.

References

1. Li, L., Liu, X.: Control strategy optimization for thermal power unit adapted to deep peak shaving for large-scale new energy source integration. Electr. Power **53**(1), 155–161 (2020)
2. Jiang, N.: Research on wind power consumption methods by source-grid-load coordination in CHP system. Harbin Institute of Technology (2021)

3. Zhang, B., Liu, C., Lin, Z., et al.: Distribution network reconfiguration with high penetration of renewable energy considering demand response and soft open point. Autom. Electr. Power Syst. **45**(8), 86–94 (2021)
4. Zhao, H., Wu, Q., Hu, S., et al.: Review of energy storage system for wind power integration support. Appl. Energy **137**(1), 545–553 (2015)
5. Yang, Y., Bremner, S., Menictas, C., et al.: Battery energy storage system size determination in renewable energy systems: a review. Renew. Sustain. Energy Rev. **91**(8), 109–125 (2018)
6. Yao, L., Yang, B., Cui, H., Zhuang, J., Ye, J., Xue, J.: Challenges and progresses of energy storage technology and its application in power systems. J. Mod. Power Syst. Clean Energy **4**(4), 519–528 (2016). https://doi.org/10.1007/s40565-016-0248-x
7. Lu Q., Li M., Wei W.: Low-carbon economic dispatch of power system with energy storage and wind power based on parametric programming. Electr. Power Autom. Equip., 1–10 (2022)
8. Sun, W., Liu, W., Zhang, J.: Collaborative optimization for dynamic reconfiguration of distribution network and mobile energy storage in background of high proportion of renewable energy. Autom. Electr. Power Syst. **45**(19), 80–90 (2021)
9. Jiang, Y., Ren, Z., Li, Q., et al.: An accommodation strategy for renewable energy in distribution network considering coordinated dispatching of multi-flexible resources. Trans. China Electrotech. Soc. **37**(7), 1820–1835 (2022)
10. Hossein, E., Amin, Y., Sajjad, G.: Demand response programs in power systems with energy storage system-coordinated wind energy sources: a security-constrained problem. J. Clean. Prod. **335**, 130342 (2022)
11. Ma, L., Xie, L., Ye, L., et al.: Cooperative operation strategy of dual energy storage under multiple objectives and multiple operation conditions. Autom. Electr. Power Syst. **45**(20), 38–48 (2021)
12. Liu, W., Niu, S., Shi, D., et al.: Optimal allocation of ADS battery energy storage considering operation strategy and investment subject benefit. Power Syst. Technol. **39**(10), 2697–2704 (2015)
13. Yang, L., Cao, Y., Wei, W., et al.: Configuration method of energy storage for wind farms considering wind power uncertainty and wind curtailment constraint. Autom. Electr. Power Syst. **44**(16), 45–52 (2020)

Research on Early Warning Method of Power System Operation Risk Based on Chaos Algorithm

Shang Dai[1(✉)], Tao Zhu[1], Bo Lun Wang[1], Yu Yang Wang[1], and Xiao Xiang Lu[2]

[1] State Grid Jiangsu Electric Power Co., Ltd., Nanjing 210000, People's Republic of China
sunchong@sgepri.sgcc.com.cn
[2] NARI-TECH Nanjing Control Systems Ltd., Nanjing 211106, People's Republic of China

Abstract. In view of the current situation that the existing power grid operation risk assessment cannot be directly applied to the distribution network operation risk early warning, a power system operation risk early warning method based on chaos algorithm is proposed, the power system operation risk categories and incentives are analyzed, and the power system operation risk evaluation index is constructed based on chaos algorithm, which simplifies the power system operation risk early warning steps. Finally, it is confirmed by experiments, The power system operation risk early warning method based on chaos algorithm has high practicability and accuracy, and fully meets the research requirements.

Keywords: Chaos algorithm · Power system · Risk early warning

1 Introduction

The safe operation of distribution network is an important part of the safe operation of the whole power grid, and it is the key link to improve the operation level of power supply system. Statistics show that about 80% of power outages are caused by distribution system failures. Therefore, it has become an urgent problem to accurately warn the potential risks in the operation of distribution network, find out the weak links and improve them, so as to improve the security of power supply [1]. The operation of distribution network will be affected by its own conditions and meteorological conditions. Early warning of distribution network operation risk is to accurately evaluate the potential loss of power grid (i.e. load outage loss) under the influence of complex factors by using scientific risk analysis and evaluation methods [2]. At present, the operation risk analysis of power components, network and system as a whole has been widely used in the fields of power system reliability, safe operation analysis and power grid planning. However, there are still some difficulties if it is directly applied to the operation risk early warning of distribution network: the risk indicators are mainly used to evaluate the operation status of distribution network, and the future risk early warning is not considered enough; Second, the abnormal operation mode of the power grid is not considered enough, and the index system is not comprehensive enough [3]. Third, the risk index cannot be used to compare the hazards of risk events under different working conditions of the power grid.

In order to solve the above problems, this paper introduces the chaos algorithm theory, analyzes the scenario factors that affect the operation risk of distribution network, and defines the set of distribution network operation scenarios and future scenarios, namely, time scenarios, space scenarios, natural scenarios, distribution network operation scenarios and their combinations [4]. Then a series of risk indicators are used to express the distribution network operation scenario risk, including unavailability scenario risk, power loss scenario risk, load loss scenario risk, overload scenario risk and voltage out of limit scenario risk. The example analysis shows that this method can scientifically warn the potential risks in the operation of distribution network.

2   Early Warning of Power System Operation Risk

2.1   Power System Operation Risks and Incentives

The primary task of power grid security risk management is to accurately define the risk management related processes, identify and analyze the risks through technical means and certain standards, rate the risks, and establish corresponding control measures [5]. The purpose of power system risk assessment is to assess the potential impact of disturbance events on the system. The traditional operation risk assessment method represents the size of system risk by multiplying the probability of disturbance events and the severity of the possible consequences of the disturbance [6]. The traditional operation risk assessment indicators include expected load loss indicators, current/voltage out of limit indicators, system status indicators, etc., while the distribution network plays an important role in distributing electric energy in the power network. Therefore, the operation risk of the power system is normalized to the load loss risk of the power system, and the factors causing the operation risk of the power system are analyzed according to the common protection modes of the distribution network and the main factors causing the protection action, as shown in Table 1:

Table 1. Power system operation risks and incentives

Risk	Cause
Load risk caused by overcurrent	Fault and overload of system and equipment
Controllable load loss risk	Overload

Taking the overhead transmission line as an example, the transmission line is mainly composed of foundation, tower, ground wire, insulator, hardware grounding device and other components, and its scoring standards are shown in the Table 2. The chaotic algorithm theory is applied to define the risk scenarios of the factors affecting the operation risk of distribution network, and a complete set of power system operation scenarios is established [7]. Then, a set of comprehensive risk indicators is established to express the risk of distribution network operation scenarios by using the power grid risk assessment theory; Finally, an example shows that this method can show the risk changes under

various scenarios that may be faced in the operation of distribution network, so as to scientifically warn the operation risk [8]. If all components are in normal status, the line status is defined as normal, and its status score is obtained by multiplying the deducted score of each component by the weight accumulation. If some components in the line are in abnormal status (attention, abnormal or serious), the status of the line depends on the status of the component with the most serious deterioration, and its status score is the status score of the component with the most serious deterioration.

Table 2. Line unit evaluation criteria based on Chaotic Algorithm

Line unit	Normal state		Attention state		Abnormal state	Critical state
	Total points deducted	Individual deduction	Total points deducted	Individual deduction	Individual deduction	Individual deduction
Basics	<15	≤10	<15	13–25	30–33	40
Tower	–	≤10	–	13–25	30–33	40
Ground wire	<17	≤10	<17	13–25	30–33	40
Insulation	<15	≤10	<15	13–25	30–33	40
Fittings	<25	≤10	<25	13–25	30–33	40
Grounding	–	≤10	–	13–25	30–33	40
Subsidiary	<25	≤10	<25	13–25	30–33	40
Environment	–	≤10	–	13–25	30–33	40

Scientifically and accurately define the power grid security risk, and clarify the tasks and objectives of the above links: power grid security risk early warning management refers to a scientific management method to realize the safe and stable operation of the power grid by identifying and analyzing the potential risks that may lead to power grid accidents, and taking scientific and effective measures to control or resolve them. Power grid security risk identification refers to the process of systematic and scientific analysis, induction and identification of potential or inherent factors affecting power grid security according to certain standards and in combination with the operation characteristics of Guangxi power grid, and objective evaluation of the possible consequences of accidents [9]. On the basis of power grid risk identification, power grid security risk assessment is to integrate the probability of various risk factors, the magnitude of load loss, the number and importance of power plants and stations (possible voltage loss) and the risk index value of other factors into a single index value to represent the possibility and loss degree of the risk, and compare it with the risk standard to determine the level of the risk, so as to determine the corresponding risk control measures; Power grid security risk control is to select the optimal control scheme to reduce or avoid risks based on scientific risk identification and evaluation according to the objectives and purposes of safety production. It is the core part of the risk early warning management standard [10]. Clear division of responsibilities can guarantee the technical support of each discipline;

The process management can ensure the close cooperation of all disciplines in risk control, make the risk control work orderly, and achieve the purpose of risk control. The figure shows the operation method for power grid security risk assessment of the dispatching center (Fig. 1).
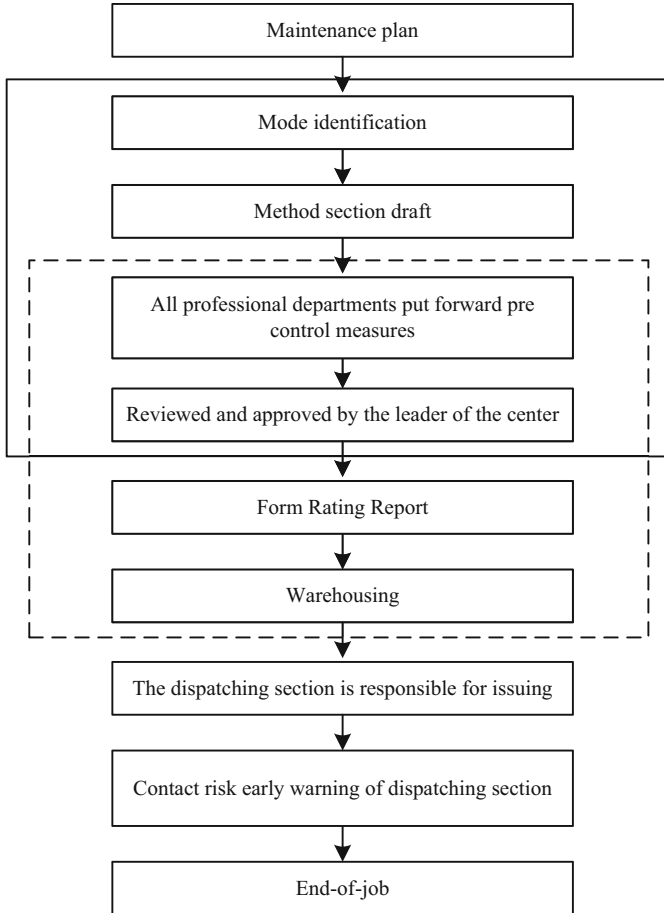
Fig. 1. Operation model for power grid security risk assessment of dispatching center

Risk refers to the variation range and amplitude of potential loss. For power grid, it is the combination of fault probability and impact. Power scholar Vita et al. Gave the basic definition of power system risk assessment, that is, comprehensively measure the possibility and severity of uncertain factors faced by the power system, and its mathematical expression is

$$R_{ijk}(X_p) = \sum_i P_r(E_i) S_{ev}(E_i, X_p) \tag{1}$$

where: X is the system operation mode; E is the i-th fault; P_r is the probability of fault E4; $S_{ev}(E_i, X_p)$ is the loss severity of the system after the i-th fault under X_1 operation mode, and RA (x) is the operation risk index of the system under X operation mode. The operation risk early warning of distribution network based on chaos algorithm is to analyze the process and evaluate the results of the possible scenarios of adverse events in the future, and give the future situation of the adverse events. Each scenario is a specific condition, and under each specific condition, the corresponding results will be obtained through the interaction of various factors within the system [11]. All these possible scenarios related to adverse events are combined to form the future scenario of the distribution system, that is, the operation risk of the distribution network. The early warning method of the operation risk of the distribution network based on the chaotic algorithm is shown in the Fig. 2.
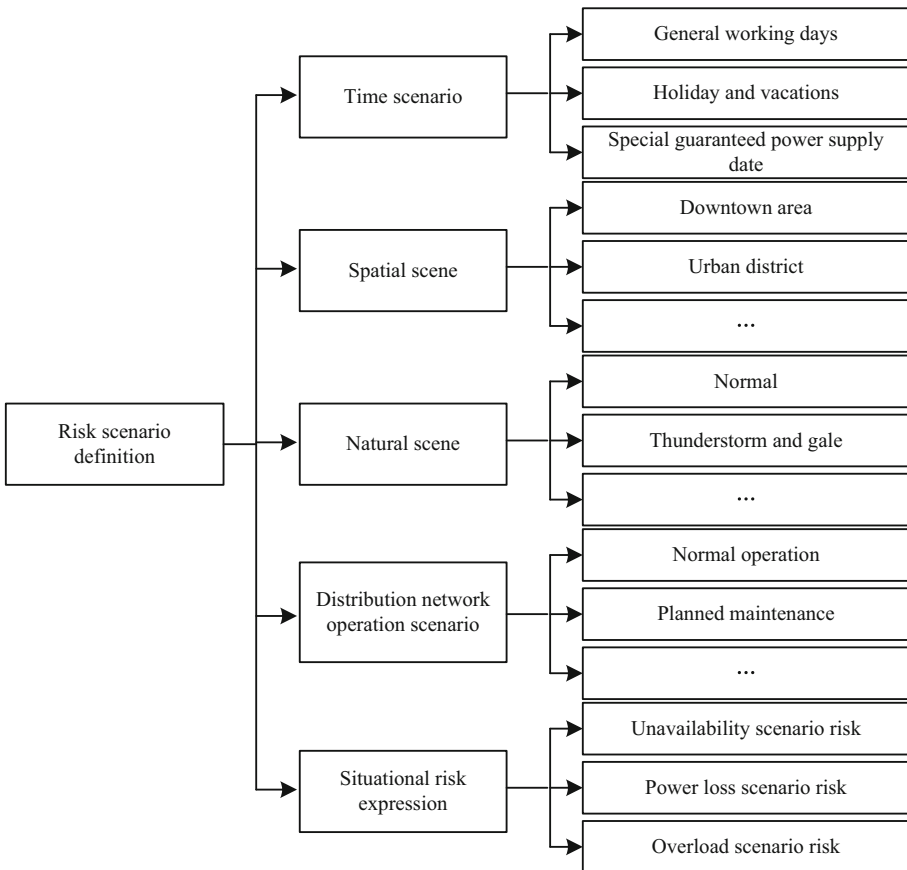
Fig. 2. Distribution network operation risk early warning framework based on Chaos Algorithm

This method is divided into two parts: chaos algorithm definition and risk expression. The definition of chaos algorithm is to determine the possible scenario set of distribution

network in the future, which is a process of rehearsing the future scenario [12]. Scenario risk expression is to extract the indicators that can be used to describe the risk, and obtain the results after comprehensive evaluation of these indicators in the future scenarios, and use the results as the results of risk analysis.

2.2   Evaluation Index System of Power System Operation Health

The power system operation health evaluation index system can be used for comprehensive evaluation of power grid security, and the basic ideas are the same. It generally includes seven links: clarifying the evaluation purpose and object, establishing the index system, determining the index weight, building the evaluation model, analyzing the evaluation results and making decisions [13]. The establishment of the index system is the key and basic link of the comprehensive evaluation process, and it should follow certain principles. This paper follows the principles of adaptability, representativeness, systematization and operability when analyzing and selecting the main influencing factors of power system operation health. Herfindahl H_{s_i} index is a representative index to measure market concentration. It uses the sum of the squares of the market size of each market competitor to measure the ten calculation formula

$$I_{HHI} = H_N - H_i \sum_{H_i=1}^{H_N} \left(100H_{s_i}\right)^2 \tag{2}$$

where, H_N is the market share of the N-th supplier in the evaluation period, and H_i is the number of suppliers in the market in the evaluation period. TOP4 index refers to the market share of the four largest suppliers in the market, reflecting the market concentration. Calculation formula:

$$RD = \frac{\sum_{T_i=1}^{4} TZ_i}{I_{HHI}} \tag{3}$$

RIS index of chaotic algorithm refers to the total supply capacity and market share of all suppliers except one supplier in a certain period of time. T index is the critical point to measure whether an independent market supplier has market power. The market power of each power generation enterprise can be identified through RIS index. In this paper, the representative Z_i is used to represent the market power of the largest power generation enterprise in the market to be evaluated.

$$RSI_1 = \frac{\sum_{n_k=1}^{n} P_{R_k} - P_{R_1}}{RD} - \frac{\sum_{R_k=1, R_k=R_1}^{n} P_{n_k}}{RD} \tag{4}$$

where P_{R_k} refers to the remaining supply capacity of supplier, P_{n_k} refers to the available supply capacity of supplier r within the evaluation cycle; RD represents the total capacity demand in the market during this time period. Based on the analysis of the influencing factors of power system operation health in the previous section, 36 indicators are preliminarily determined as alternative indicators, as shown in the Table 3 below.

Table 3. Initial establishment of power system operation health evaluation index

Target layer	System layer	State layer	Index layer	Number
Operation health of power market	Supply side	Market structure	HHI	A
			Top-4	B
			RSI	C
			Lerner Index	D
		Market benefit	Proportion of producer surplus	E
			Linkage index of on grid electricity price and power generation cost	F
	Demand side	Demand side market response	User satisfaction	G
			Enthusiasm of users to participate in demand response	H
	Market coordinated operation	Market transactions	Proportion of market trading electricity	I
			Declared supply-demand ratio	J
			Turnover rate	K
			Declared capacity retention ratio	L

There are many factors that affect the operation health of power system, but not all indicators should be used as indicators for the evaluation of the operation health of power system. Therefore, it is necessary to screen the original indicator base, and screen the indicators according to the principles of importance or discrete state [14]. At present, the main indicator screening methods include expert survey method, minimum mean square error method, minimum maximum deviation method, etc. in this paper, the expert survey method is used to screen the indicator system, Six groups of power related experts were invited to conduct a questionnaire survey on the indicator system of power system operation health and the qualitative indicators of power system operation status in the subsequent case analysis [15]. For the preliminarily determined evaluation index system, a semi closed questionnaire survey is conducted by Delphi method, and the results of each round are sent to experts as a reference. This step is repeated until consistent results are obtained. The selected evaluation index system consists of 23 indexes, as shown in the Table 4.

Table 4. Power system operation health evaluation index system

Target layer	System layer	State layer	Index layer	Number
Operation health of power market	Supply side	Market structure	HHI	W1
			Top-4	W2
			RSI	W3
			Lerner Index	W4
		Market benefit	Proportion of producer surplus	W5
			Linkage index of on grid electricity price and power generation cost	W6
	Demand side	Demand side market response	User satisfaction	W7
			Enthusiasm of users to participate in demand response	W8
	Market coordinated operation	Market transactions	Proportion of market trading electricity	W9
			Declared supply-demand ratio	W10
		Market construction	Market transaction setting indicators	W11
			Market supervision level, information disclosure degree	W12
	Market security	Power system security	Power system reliability	W13
		Power economic security	Transaction price stability, high bid winning rate	W14
	Sustainable development	Energy security	Dye diversity index	W15
		Environmental sustainability	Proportion of clean energy power generation	W16

The risk assessment of chaos algorithm is based on the importance of load loss and load size. Risk s can be used to determine the possibility of loss accident Φ and the severity r of this loss

$$S = RSI_1 - \Phi r \tag{5}$$

In the optimization algorithm based on chaotic particle swarm optimization, the individual is called particle and the group is called particle swarm optimization, which is equivalent to the simulation of seagull's predatory behavior. When a flock of seagulls prey randomly, even if the specific location of the food cannot be determined, they can find the nearest area to the food, search the area, and then quickly find the food. The basic optimal formula of particles in the optimization algorithm based on chaotic particle swarm optimization is:

$$\begin{aligned} Y_i^{m+1} = {} & pY_i^m + z_{1i} \times r_1 \times \left(q_i^m - X_i^m\right) + X_i^{m+1} - X_i^m \\ & + z_{2i} \times r_2 \times \left(U^m - X_i^m\right) \end{aligned} \tag{6}$$

In the formula: p is the factor of inertia; r_1 and r_2 are (1, 1.5) interval random values with uniform distribution obeying property; z_{1i} and z_{2i} are the optimized factor; m is the number of operations; X_i^m is the space region of the particle I when the operation is m times; Y_i^m is the velocity of particle I activity at m times of operation; q_i^m represents the extreme value of the individual obtained by the number of operations of the particle from its original position to its current position; U^m represents the global extreme value obtained by the number of operations of particle I from its original position to its current position [16]. Therefore, the calculation method of urban power failure can be given, that is, the risk of power failure is equal to the probability of load power failure caused by emergencies and the result of loss caused by load power failure. If the distribution network has I loads, the active power of the load is p, and when the distribution network fails, the probability set of load loss is $\{\varphi_1, \varphi_2, \varphi_3 \cdots \cdots \varphi_i\}$, loss load set is $\{P_1, P_2, P_3, ..., P_i\}$, Then when the distribution network operation fault occurs, the outage risk s can be defined as:

$$S = Y_i^{m+1} \sum_{n=1}^{i} \varphi_n P_n \tag{7}$$

where P_n is the active power of the lost load, which is determined by the operation state of the distribution network, φ_n is the probability of load loss, which is determined by the operation fault state of the distribution network. Equipment importance evaluation and ranking is a further analysis and evaluation for equipment level based on equipment failure probability evaluation. Risk is defined as the combination of "the possibility of causing system impact and the severity of such impact" in the operation of power system [17]. The operation risk level of the power system is measured by the operation risk index, and its calculation is shown in the formula.

$$\text{Risk}(X_i) = S \sum \text{Prob}(X_i)\text{Sev}(X_i) \tag{8}$$

where, (X_i) represents the operational risk value, and X represents the ith risk event; t_h is the probability of occurrence of event h; I_h^2 refers to the impact of event x on the

system. During the operation of rectifier grid, the current exceeding the rated value and time shall be corresponding one by one. The power conservation rules of the grid are as follows:

$$I_j^2 \times t_j = \sum_{h=1}^{m} I_h^2 \times (t_h - t_{h-1}) \tag{9}$$

According to the formula, the t_j:

$$t_j = \sum_{h=1}^{m} I_h^2 \times (t_h - t_{h-1})/I_j^2 \tag{10}$$

When t_j is the set rated current value is reached, the system will send an early warning signal; When t_j is the set rated current value is exceeded, the system will send a serious warning signal; When t_j is less than the set rated current value, no signal will be sent. Risk assessment can grasp the operation risk of power grid as a whole, but it cannot quantify the impact of different equipment on the operation risk of the system from the equipment level [18]. The evaluation of equipment importance can analyze the composition of power grid operation risk from the source, provide key decision-making information for local control of power grid risk, and greatly ensure the safe operation of power grid and reduce the cost of risk control. When the operation scenario of the distribution network is "normal operation", the 2 km section of several lines fails, and the loads B and C can be powered by the interconnection line. The outage time is the time when QS1 is switched on and qs3 is switched on, which is 1 h. When the 3 km section of the main line fails, the load point a can restore power supply by switching off Q1 for 1 h. Load point B cannot supply power until the line is repaired. The time is 4 h. Load point C is powered by the tie line. Open Q2 and close QS. When 1 km section of the trunk line fails for 1 h, load points a and B only need to open QS2 and restore power supply by the main power supply. The time is 1 h, while load point C needs to be repaired by this section of the line. The time is 4 h (Tables 5 and 6).

The results of deterministic risk assessment and probabilistic risk assessment are classified into general, alarm and emergency levels according to the risk classification standard library. The specific values of the boundaries of different risk levels can be modified and maintained according to the user's experience and the results of simulation analysis to meet the needs of users [19]. For situations with high alarm and emergency risk levels, analyze the causes of high risk levels, provide risk assessment results by classification, visually display various specific risk information causing high risk levels, and automatically identify and locate various risk sources on the geographic map. Issue push warning information for high-risk indicators, high-risk areas and equipment of the power grid. After the alarm is detected, it can quickly generate alarm information and inform the operation and system maintenance personnel according to the user-defined alarm mode.

2.3 Realization of Power System Operation Risk Early Warning

Risk early warning refers to the prediction and alarm of possible risks in the future according to the changes of internal conditions and external environment. With the

Table 5. Ring network wiring fault and consequence analysis

Element		Load points A and D			Load points B and E			Load points C and F		
		λ/ (times $\cdot a^{-1}$)	r/h	M/(h·a^{-1})	λ/ (times $\cdot a^{-1}$)	r/h	M/(h·a^{-1})	λ/ (times $\cdot a^{-1}$)	r/h	M/(h·a^{-1})
Power supply trunk line	2 km section	0.75	1.00	3.00	0.25	1.00	0.25	0.50	4.00	1.00
	2 km section	0.25	4.00	0.25	0.50	1.00	2.00	0.25	1.00	0.50
	1 km section	0.5	1.00	0.50	0.50	4.00	0.50	0.25	1.00	1.00
Branch line	3 km section	0.5	4.00	2.00	–	–	–	–	–	–
	2 km section	–	–	–	0.50	4.00	2.00	–	–	–
	1 km section	–	–	–	–	–	–	0.50	4.00	0.50
Total		2.00	2.89	5.76	1.76	2.72	4.76	1.50	2.00	3.00

Table 6. Radial wiring fault and consequence analysis

Element		Load points A and D			Load points B and E			Load points C and F		
		λ/ (times $\cdot a^{-1}$)	r/h	M/(h·a^{-1})	λ/ (times $\cdot a^{-1}$)	r/h	M/(h·a^{-1})	λ/ (times $\cdot a^{-1}$)	r/h	M/(h·a^{-1})
Power supply trunk line	2 km section	0.75	1.00	3.00	0.25	4.00	0.25	0.50	4.00	1.00
	2 km section	0.25	4.00	0.25	0.50	1.00	2.00	0.25	4.00	2.00
	1 km section	0.5	1.00	0.50	0.50	4.00	2.00	0.25	4.00	1.00
Branch line	3 km section	0.5	4.00	2.00	–	–	–	–	–	–
	2 km section	–	–	–	0.50	4.00	2.00	–	–	–
	1 km section	–	–	–	–	–	–	0.50	4.00	2.00
Total		2.00	2.89	5.76	1.76	3.58	6.26	1.50	4.00	6.00

reform and development of the power system, the environment of the power system is becoming more and more complex [20]. The development of the power system affects the direct interests of the market players and the healthy and orderly development of the whole society. Therefore, it is necessary to establish a risk assessment system for power system operation health, predict the risk, and then perceive the risk in advance and take corresponding measures. Especially in the power industry, the risk early warning system has played an important role in ensuring the business activities of power generation enterprises and power users. Under the new power reform, the development of the power system is still immature. It is necessary to have a risk early warning system for the operation health of the power system to assist government departments, power system entities, power trading centers and regulatory agencies to predict possible risks in the future and send early warning signals in time, Allowing market participants and regulators to make decisions and control them in time can minimize the losses caused by risks. According to the risk information collected by the multi-source information integration platform, the redundant data is screened and the relevant data are combined to identify and generate the corresponding possible risk scenarios, so as to determine the corresponding risk scenario model as the object of power system operation risk analysis and assessment (Fig. 3).

Risk scenario	Risk source	Information system
Grid fault scenario	Status information of power grid dry equipment	Production management system
Grid operation mode scenario	External natural environment information of power grid equipment	Meteorological early warning system
Grid load movement scene	Grid topology	Traffic management system
	Power grid maintenance information	Dispatching management system
	Load flow information	Load forecasting system

Fig. 3. Information flow of risk identification based on Chaotic Algorithm

According to the occurrence probability grade of power grid fault scenario and the consequence severity grade of power grid fault scenario (deterministic risk assessment), the rating rules of probabilistic risk assessment are formulated through fuzzy processing. With reference to the dispatching decision-making scheme of the dispatching operator, a measure knowledge base is developed according to its pre control measures for risk scenarios such as single power supply (Fig. 4).
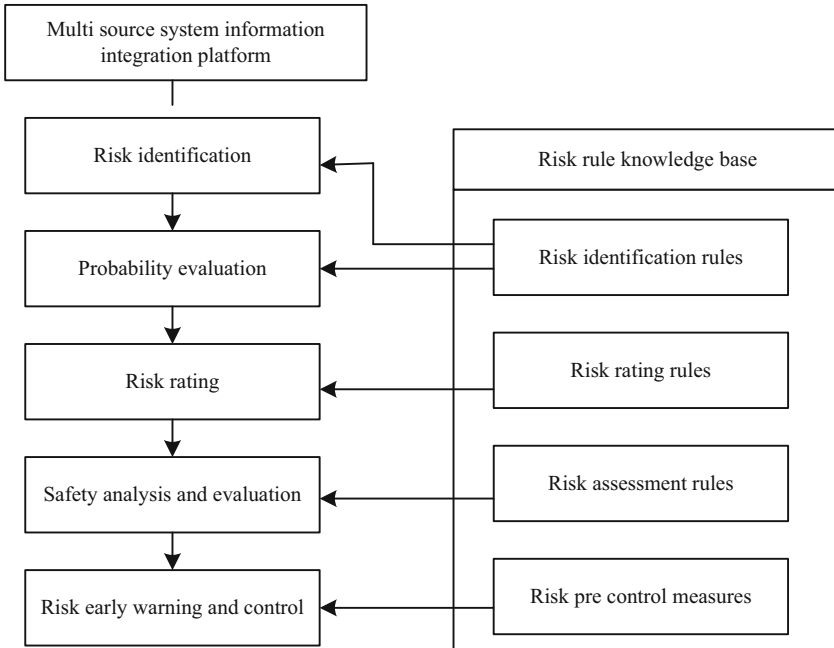
Fig. 4. Application of risk rule knowledge base

The main function of the risk analysis module is to carry out risk assessment. The early warning system designed in this paper is oriented to the power grid system. Based on the current operating state and the historical load data, it carries out static stability analysis for the specific operating state during planned maintenance and equipment maintenance. The function of the risk control module is to carry out maintenance in advance for the

equipment plants and stations that are at risk weak points during equipment maintenance, and strengthen patrol inspection for the weak points during equipment maintenance. Figure 5 shows the software design flow chart of the risk control module.

Times	This paper designs the optimal route selection method selection time (s)	The traditional optimal route selection method is time-consuming (s)
1	0.265	1.468
2	0.321	2.164
3	0.265	2.464
4	0.136	3.489
5	0.326	2.487
6	0.154	3.159
7	0.356	2.196
8	0.246	1.414
9	0.136	0.946
10	0.214	3.164

After the analysis of the risk analysis module, when the affected load is to be put into standby operation in other plants and stations and other lines, it is necessary to retrieve the standby lines and the operation and maintenance units of the plants and stations. Before equipment maintenance, patrol and maintain these standby lines and their plants and stations to prevent power failure after the load is put into operation. The failure probability during equipment operation is not only closely related to the health status of the equipment itself, but also significantly affected by the external operating environment. The premise of effectively ensuring the accuracy of power grid probability risk assessment is to comprehensively consider the failure probability assessment of internal and external causes of equipment outage, implement the uncertain factors such as equipment status and meteorological disasters faced by power grid operation into the basic events of system failure such as equipment outage, and realize the modeling of uncertain factors. The equipment condition evaluation, defect management and meteorological early warning system widely carried out by power enterprises provide a strong basis for comprehensive equipment outage probability evaluation and rating based on equipment health and considering the external natural environment.
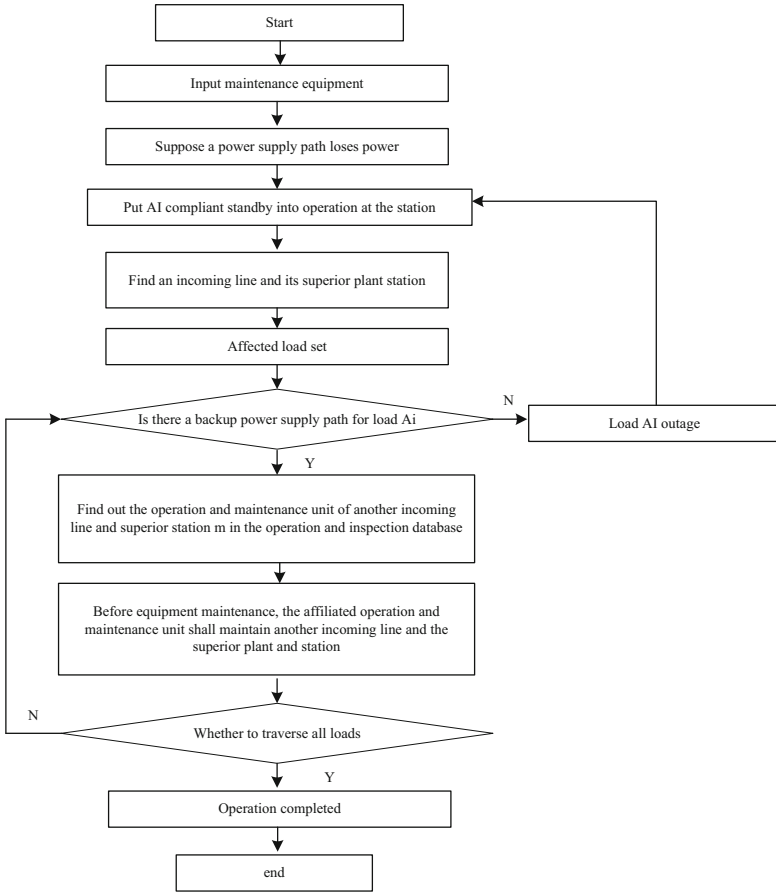
Fig. 5. Design flow chart of risk control module

3 Analysis of Experimental Results

The data transmission and transmission of the power grid real-time operation risk management and control system is mainly reflected in the power grid energy management module, which includes the master station, the production management system and the dispatching operation execution and distribution system. The master station releases the latest power grid operation data information to the master system every 5 min to provide its necessary power grid operation load and other basic parameters. The production management system, as the source of storing and managing preset data, provides preset data information. The dispatching operation execution and distribution system sends dispatching operation instructions regularly by the dispatcher for analysis and decision-making of the risk management and control system. Based on this analysis, the simulation environment parameters shown in Table 7 are set.

After the simulation environment parameters are set, the rating index of the simulation analysis is determined. Considering that the risk early warning of power operation

Table 7. Simulation environment parameters

Parameter name	Numerical value	Parameter name	Numerical value
CPU	12 core 2.2 GHz	Edition	5.2
Ram capacity	8 GB	Operating system	Windows 10
Memory	16G	Operating frequency	3.5 GHz

data leakage needs to have the characteristics of real-time and high precision, the early warning accuracy, recall rate and the harmonic mean value of recall rate and risk early warning accuracy are set as the three evaluation indicators of this simulation analysis. The results of evaluation index parameters are explained in Table 8.

Table 8. Result interpretation of evaluation index parameters

	There is no actual risk of leakage	Actual risk of leakage
Early warning: no leakage risk	PN	QN
Early warning: there is a risk of leakage	QM	PM

Traditional information clustering and fusion processing methods are introduced respectively, and compared with the risk early warning methods in this paper for simulation analysis. Simulation analysis is carried out in 2000 groups of test groups of different sizes. The results are as follows: the comparison results of the accuracy of risk early warning methods are shown in the Fig. 6:
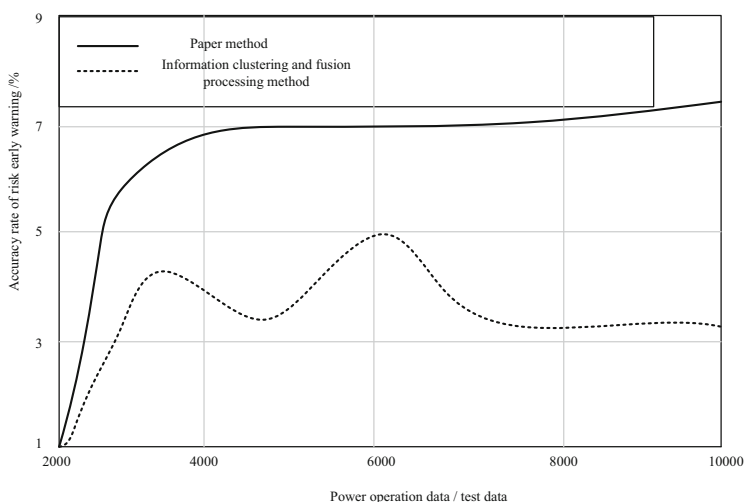
Fig. 6. Comparison results of early warning accuracy

The theoretical values, measured values and early warning relative errors of the three voltages and currents are further compared and analyzed. The results are shown in Table 9.

Table 9. Comparison and analysis of early warning errors of two methods

Frequency	Voltage					
	Traditional method			Paper method		
	Theoretical value p.u.	Measured value p.u.	Error p.u.	Theoretical value p.u.	Measured value p.u.	Error p.u.
2	1.2732	1.2611	0.0121	1.2732	1.2719	0.0013
4	0.4142	0.4061	0.0081	0.4135	0.4132	0.0003
6	0.1821	0.1181	0.0640	0.1816	0.1756	0.0060
Frequency	Electric current					
	Traditional method			Paper method		
	Theoretical value p.u.	Measured value p.u.	Error p.u.	Theoretical value p.u.	Measured value p.u.	Error p.u.
2	1.5877	0.6527	0.9350	1.5881	1.5809	0.0072
4	1.8955	1.3473	0.5482	1.8955	1.8945	0.0010
6	1.6458	1.3715	0.2743	1.6461	1.6456	0.0005

It can be seen from the table that the comparison and analysis of the traditional method and the method in this paper for early warning of harmonics generated by voltage and current can be found that the measurement error of this method is small, so the higher the accuracy of early warning. To sum up, the design of this paper and the police is reasonable.

4   Conclusions

Combining the theory of chaos algorithm and power grid risk assessment, a distribution network operation risk early warning method based on chaos algorithm is established. Firstly, the risk scenarios of the factors affecting the distribution network operation risk are defined, and then a reasonable risk index is established to express the scenario risk. This method can scientifically warn the operation risk of distribution network under the influence of a variety of complex factors, and can play a useful guiding role in the construction and operation of distribution network. With the advance of smart grid research and construction, distributed energy and Microgrid operation will become increasingly common in distribution networks. On the basis of this method, the above factors are taken into account in order to scientifically warn the operation risk of distribution network under the background of the rapid promotion of smart grid.

References

1. Lian, J., Fang, S., Zhou, Y.: Model predictive control of the fuel cell cathode system based on state quantity estimation. Comput. Simul. **37**(07), 119–122 (2020)
2. Balaska, N., Ahmida, Z., Belmeguenai, A., Boumerdassi, S.: Image encryption using a combination of Grain-128a algorithm and Zaslavsky chaotic map. IET Image Proc. **14**(6), 1120–1131 (2020)
3. Meng, L., Yin, S., Zhao, C., Li, H., Sun, Y.: An improved image encryption algorithm based on chaotic mapping and discrete wavelet transform domain. Int. J. Netw. Secur. **22**(1), 155–160 (2020)
4. Yang, F.: A fractional-order CNN hyperchaotic system for image encryption algorithm. Phys. Scr. **96**(3), 035209 (2021). (17pp)
5. Sharma, E., Deo, R.C., Prasad, R., Parisi, A.V.: A hybrid air quality early-warning framework: an hourly forecasting model with online sequential extreme learning machines and empirical mode decomposition algorithms. Sci. Total Environ. **709**, 135934.1-135934.23 (2020)
6. Zhu, Y., Li, G., Tang, S., Jiang, W., Zheng, Z.: Parameter identification method of hydraulic automatic gauge control system based on chaotic wolf pack optimization algorithm. AIP Adv. **11**(5), 055302 (2021)
7. Mohammed, R., Jawad, L.M.: Secure image encryption scheme using chaotic maps and RC4 algorithm. Solid State Technol. **63**(3), 3449–3465 (2020)
8. Ouertani, M.W., Manita, G., Korbaa, O.: Chaotic lightning search algorithm. Soft Comput. **25**(3), 2039–2055 (2020). https://doi.org/10.1007/s00500-020-05273-0
9. Zhao, R., et al.: Selfish herd optimization algorithm based on chaotic strategy for adaptive IIR system identification problem. Soft Comput. **24**(10), 7637–7684 (2019). https://doi.org/10.1007/s00500-019-04390-9
10. Zhang, C., Ding, S.: A stochastic configuration network based on chaotic sparrow search algorithm. Knowl. Based Syst. **220**(10), 106924 (2021)
11. Chen, Y., Ran, Y., Wang, Z., Li, X., Yang, X., Zhang, G.: An extended MULTIMOORA method based on OWGA operator and Choquet integral for risk prioritization identification of failure modes. Eng. Appl. Artif. Intell. **91**, 103605.1-103605.12 (2020)
12. Khalilzadeh, M., Shakeri, H., Zohrehvandi, S.: Risk identification and assessment with the fuzzy DEMATEL-ANP method in oil and gas projects under uncertainty. Procedia Comput. Sci. **181**(3), 277–284 (2021)
13. Singh, V.P., Ujjwal, R.L.: Threat identification and risk assessments for named data networking architecture using SecRam. Int. J. Knowl. Based Intell. Eng. Syst. **25**(1), 33–47 (2021)
14. Lo, H.-W., Shiue, W., Liou, J.J.H., Tzeng, G.-H.: A hybrid MCDM-based FMEA model for identification of critical failure modes in manufacturing. Soft Comput. **24**(20), 15733–15745 (2020). https://doi.org/10.1007/s00500-020-04903-x
15. Le, V.D., Ngoc, T.T., Le, C.Q.: Analyze the sub-synchronous resonance risk of thermal power plants and take an effective solution to suppress: a case study for Vietnamese power system. J. Electr. Syst. **16**(4), 448–477 (2020)
16. Wu, J., Wu, Z., Mao, X., Wu, F., Tang, H., Chen, L.: Risk early warning method for distribution system with sources-networks - loads-vehicles based on fuzzy C-mean clustering. Electr. Power Syst. Res. **180**, 1060591–10605913 (2020)
17. Suo, C., Sun, H., Zhang, W., Zhou, N., Chen, W.: Adaptive safety early warning device for non-contact measurement of HVDC electric field. Electronics **9**(2), 329 (2020)
18. Li, X., Liu, J., Bai, M., Li, J., Yu, D.: An LSTM based method for stage performance degradation early warning with consideration of time-series information. Energy **226**(10), 120398 (2021)

19. Findlay, M., Peaslee, D., Stetter, J.R., Waller, S., Smallridge, A.: Distributed sensors for wildfire early warnings. J. Electrochem. Soc. **169**(2), 020553 (2022). (13pp)
20. Kandanaarachchi, S., Anantharama, N., Munoz, M.A.: Early detection of vegetation ignition due to powerline faults. IEEE Trans. Power Deliv. **36**(3), 1324–1334 (2021)

Reactive Power Optimization Control Method for Wind Farms to Actively Participate in Grid Voltage Regulation

Lin Yang[1,2(✉)], Jingbo Liu[2,3], Jie Su[1], Linlin Wu[2,3], and Yan Li[2,3]

[1] Department of Automation, North China Electric Power University, Baoding 071003, China
ylemail1998@163.com

[2] State Grid Jibei Electric Power Co., Ltd., Research Institute, Beijing 100045, China

[3] Grid-Connected Operation Technology for Wind-Solar-Storage Hybrid System State Grid Corporation Key Laboratory, Beijing 100045, China

Abstract. The traditional method of wind farms following the voltage command of the main station can easily lead to frequent fluctuations of the reactive power source in the station and insufficient reactive power margin in the station, thereby reducing the safety margin of the voltage of the wind farm. To this end, a reactive power coordination and optimal control method for wind farms participating in actively voltage regulation of power grids is proposed. First, based on the wind farm power prediction data and voltage sensitivity, the voltage fluctuation trajectory of the grid connection point is predicted; by coordinating the reactive power output of the fan and SVG, the adjustment frequency of reactive power equipment is effectively reduced. Secondly, the detailed operation scenarios are divided according to the voltage drop amplitude. By adjusting the control mode of SVG, the voltage fluctuation can be quickly suppressed when the voltage fluctuates slightly, and the maximum reactive power regulation capability can be released when the voltage fluctuates greatly, effectively restraining the further deterioration of the voltage. It realizes the actively voltage regulation function under the condition of voltage fluctuation, and ensures the normal operation of the active power of the unit. Finally, the wind farm simulation test model is built based on the RT-LAB platform, which verifies the effect of the proposed method in reducing the frequency of reactive power regulation, improving the reactive power margin and voltage support capability compared with the traditional AVC control strategy. It provides a new solution for realizing actively voltage regulation of wind farms.

Keywords: Actively voltage regulation of wind farms · Voltage fluctuation trajectory prediction · Reactive power coordination optimization · Voltage support capability · Magnitude of voltage drop

1 Introduction

The wind power gathering area is generally located at the end of the power grid, and the interaction between the weak grid structure and the random fluctuations of wind

resources results in severe voltage fluctuations at the grid connection point of the wind farm. Wind farms are equipped with a Automatic Voltage Control (AVC) system to perform periodic (usually tens of seconds to tens of seconds) reactive power regulation for wind turbines and Static Var Generator (SVG), which can realize the stable operation of the grid-connected point voltage of the wind farm.

In the normal adjustment period of AVC, once a transient fault occurs at the grid connection point of the wind farm (usually tens of milliseconds to hundreds of milliseconds), the wind farm will further deteriorate the fault voltage due to the lack of transient reactive power support capability, which will lead to off-grid accident of wind turbines. The dispersion of wind turbines, the difference in reactive power regulation characteristics between wind turbines and SVG, and the complexity of the grid structure of wind farms make the coordinated control of reactive power and voltage in wind farms facing great challenges.

Reference [1] evaluates the overall control capability of the wind farm by analyzing the operating constraints and characteristics of the Doubly Fed Induction Generator (DFIG), and proposes a wind farm voltage control strategy and control task allocation method. Reference [2] proposes a control strategy in which DFIG works in the maximum power point tracking mode under normal circumstances, and then uses SVG to regulate the voltage first, and then DFIG supplements the voltage regulation. Reference [3] proposes a reactive power control strategy of DFIG and Static Var Compensator (SVC) for transient voltage stability of wind farms. Before the transient fault ends, part of the SVC is actively cut off to reduce the risk of transient overvoltage after the grid fault. Reference [4] proposes a coordinated control strategy for reactive power equipment based on wind farm power prediction. Through power prediction, capacitor and inductor groups are switched in advance. References [5, 6] analyze the reactive power range of DFIG, and describe the methods and strategies for DFIG to control voltage and reactive power. References [7, 8] analyzed the coordinated control of reactive power and voltage at different time scales of new energy stations.

References [1–8] are mainly aimed at the reactive power and voltage control strategies under normal operating conditions of wind farms, or the response strategies of individual equipment during transient faults. The research on the coordinated control of reactive power equipment and the actively support ability of wind farms involves less.

In order to improve the reactive power margin of wind farms and enhance the actively voltage support capability, this paper proposes a reactive power coordination optimization strategy suitable for large-scale wind farms to participate in actively voltage regulation of power grids. Based on the traditional AVC, wind power prediction is introduced, and based on the power prediction data, the voltage fluctuation trajectory curve of the grid connection point of the wind farm is calculated and drawn. Combined with the reactive power regulation capability of each equipment in the wind farm, coordinate the distribution of reactive power of each equipment. Secondly, different operating scenarios are divided according to the depth of voltage drop, so as to realize the refinement of reactive power and voltage control, and improve the actively support capability of wind farms. By actively participating in the voltage regulation control of the wind farm, the reactive power regulation capability of the wind farm can be fully utilized, and the economy and stability of the system operation can be improved.

2 Introduction the Characteristics of Reactive Power and Voltage Regulation in Wind Farms

2.1 The Grid Structure of the Wind Farm

The wind farm consists of two parts: the wind turbine collection system and the station collection system. The wind farm is composed of multiple wind turbines, reactive power compensation devices and other equipment. According to the installed capacity, it is generally designed as a structure of single boost transformer and multiple boost transformers. The grid structure of a typical wind farm system is shown in Fig. 1.
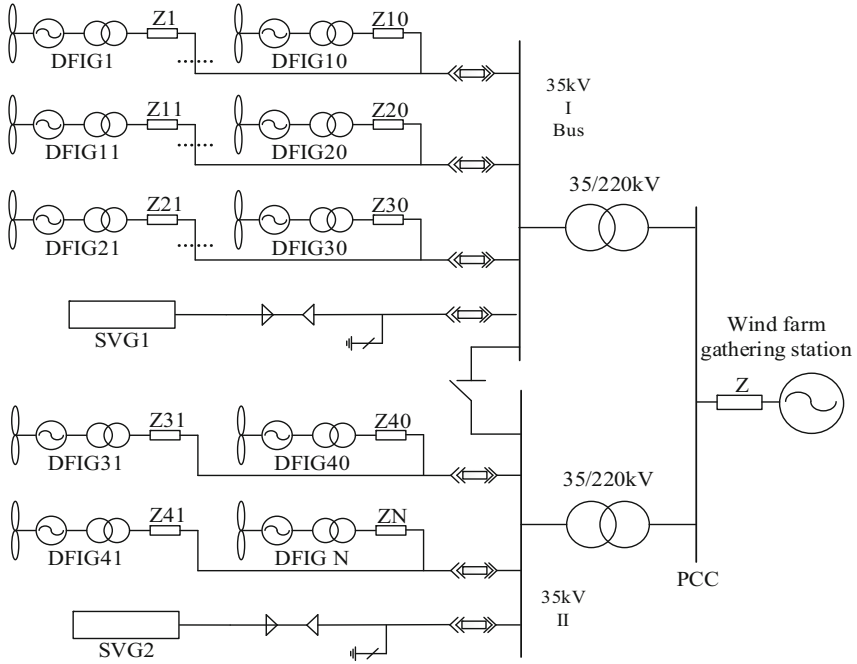
Fig. 1. Wind farm system architecture with multiple busbars.

2.2 Reactive Power Regulation Characteristics of Wind Turbines

Adjustment range of reactive power on the stator side of DFIG [5, 6]:

$$\begin{cases} Q_{smax} = -\dfrac{3U_s^2}{2\omega X_s} + \sqrt{\dfrac{9U_s^2 X_m^2 I_{rmax}^2}{X_s^2} - P_s^2} \\ Q_{smin} = -\dfrac{3U_s^2}{2\omega X_s} - \sqrt{\dfrac{9U_s^2 X_m^2 I_{rmax}^2}{X_s^2} - P_s^2} \end{cases} \tag{1}$$

In the formula: Q_{smin}, Q_{smax} are the minimum and maximum value of the reactive output on the stator side, respectively; I_{rmax} is the maximum allowable current of the

rotor-side converter; U_s is the voltage on the stator side; X_s is the reactance on the stator side; P_s is the output active power; X_m stands for mutual inductance; ω stands for synchronous rotational angular velocity.

Ignoring the winding loss of the fan and the switching loss of the converter, it can be known from the power relationship between the DFIG stator and the rotor that the grid-side converter injected power is $P_g = P_r = sP_s$, and s is the DFIG slip. Then the adjustment range of the reactive power of the grid-side converter:

$$\begin{cases} Q_{gmax} = \sqrt{P_{gmax}^2 - (sP_s)^2} \\ Q_{gmin} = -\sqrt{P_{gmax}^2 - (sP_s)^2} \end{cases} \tag{2}$$

From formula (1) (2), the reactive power adjustment range of DFIG can be obtained as:
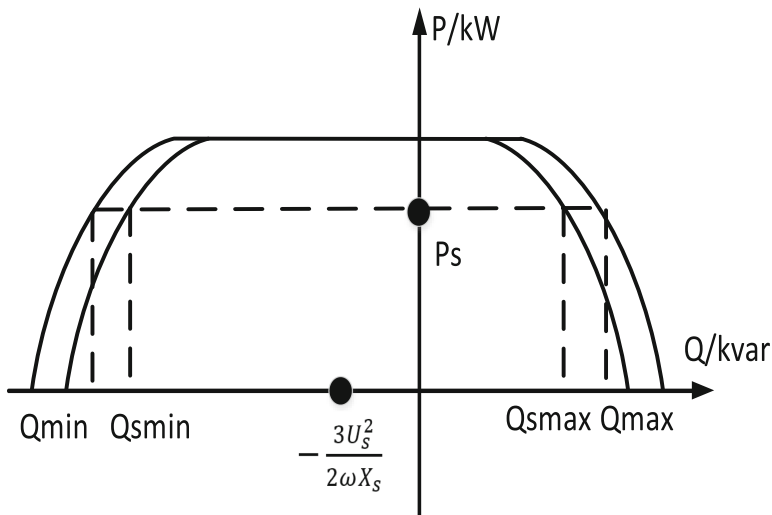
Fig. 2. Reactive power adjustment range of DFIG

It can be seen from Fig. 2 and Formula 2 that the reactive power adjustment range of DFIG is affected by active power. The greater the active power, the smaller the reactive power adjustment range.

2.3 Reactive Power Adjustment Characteristics of Reactive Power Compensation Device

The working principle of SVG is to connect the self-commutated bridge circuit to the power grid through the reactor, and use the on-off of the three-phase bridge arm to adjust the amplitude and phase of the output voltage on the AC side, so as to achieve the purpose

of controlling the output reactive power.

$$\begin{cases} L\frac{di_d}{dt} = -Ri_d + \omega Li_q - u_d + e_d \\ L\frac{di_q}{dt} = -Ri_q - \omega Li_d - u_q + e_q \end{cases} \quad (3)$$

In the formula: i_d and i_q are the active and reactive components of the compensation current, respectively; u_d is the output voltage of the SVG; e_d, e_q are the grid voltage.

According to the adjustment characteristics of different reactive power equipment, they are arranged as follows:

Table 1. Reactive device regulation characteristics table

Device classification	Device unit	Compensation characteristics	Compensation position	Response time
Static device	OLTC/SCB	Discrete step adjustment	Concentrate	Seconds, slow
Dynamic device	SVG/SVC	Continuous smooth dynamic adjustment	Concentrate	Millisecond, fast
Wind Turbine	DFIG/PMSG	Continuous smooth adjustment but limited compensation for single machine	Dispersion	Within 1 s, relatively fast

It can be seen from Table 1 that SVG not only has a fast response time, but also has a continuous and smooth dynamic adjustment capability. By making full use of this adjustment feature of SVG, voltage fluctuations can be suppressed in a timely and effective manner.

2.4 Automatic Voltage Control System

At present, the wind farm realizes the voltage tracking control of the grid connection point through the reactive power voltage control system. When it is detected that the actual voltage exceeds the target voltage control dead zone, the AVC recalculates the reactive power adjustment command and adjust the reactive power output of the wind turbine or reactive power compensation device to realize the voltage tracking control of the grid connection point.The voltage at the grid-connected point of the wind farm can basically be controlled stably, but the voltage fluctuation during the AVC regulation period cannot be effectively suppressed. The structure diagram of the reactive power and voltage control system is shown in Fig. 3.
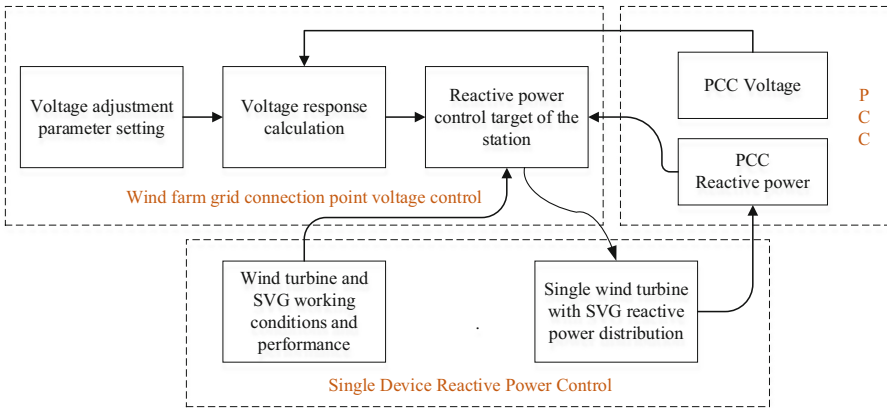
Fig. 3. Automatic voltage control

3   The Principle of Actively Voltage Regulation of Wind Farms

3.1   Analysis of Actively Adjustment Target

The voltage at the grid connection point of the wind farm is greatly affected by the active power fluctuation. When actively participating in the grid voltage control, the wind power needs to be considered. According to the characteristics of rapid changes in wind speed, the wind power is monitored in real time [7].

Voltage Sensitivity Analysis
Assuming that the system has N nodes, except for the balance node 1, all are PQ nodes. The relationship between the voltage Vi and the current Ii of the PQ node obtained through the impedance matrix is as follows [8]:

$$
\begin{bmatrix} V_1 \\ V_2 \\ \vdots \\ V_N \end{bmatrix} = \begin{bmatrix} 1 & 0 & 0 & \cdots & 0 \\ Z_{21} & Z_{22} & Z_{23} & \cdots & Z_{2N} \\ Z_{31} & Z_{32} & Z_{33} & \cdots & Z_{3N} \\ \vdots & \vdots & \vdots & \ddots & \vdots \\ Z_{N1} & Z_{N2} & Z_{N3} & \cdots & Z_{NN} \end{bmatrix} \begin{bmatrix} V_1 \\ I_2 \\ \vdots \\ I_N \end{bmatrix}
\tag{4}
$$

In order to analyze the sensitivity coefficient of the voltage change of the node j relative to the power injection of the node i, let the current of the nodes other than the node i be zero, then the voltage V_j of the node j is determined by the current I_i and Z_{j1} at the node i. Among them, the voltage V_j is divided into the imaginary part and the real part, and I_i is represented by the known active power P and reactive power Q, and the sorting can be obtained:

$$
V_j^{re} + jV_j^{im} = Z_{j1}V_1 + Z_{ji}\frac{P_i - jQ_i}{V_i^{re} - jV_i^{im}}
\tag{5}
$$

From the formula 5, the partial derivatives of the voltage V with respect to P_i and Q_i can be obtained, and then the sensitivity of the voltage of node j to the active power and reactive power at node i can be obtained.

$$V_j \frac{\partial V_j}{\partial P_i} = V_j^{re} \left(\frac{\partial V_j^{re}}{\partial P_i} \right) + V_j^{im} \left(\frac{\partial V_j^{im}}{\partial P_i} \right) \tag{6}$$

$$V_j \frac{\partial V_j}{\partial Q_i} = V_j^{re} \left(\frac{\partial V_j^{re}}{\partial Q_i} \right) + V_j^{im} \left(\frac{\partial V_j^{im}}{\partial Q_i} \right) \tag{7}$$

From Eq. 6 and Eq. 7, it can be known that when the active power and reactive power change, the voltage at the grid connection point will also change. The active-voltage prediction can be achieved by Eq. 6.

Voltage Prediction

Based on ultra-short-term wind power prediction, the resolution of power prediction data can reach the minute level by means of interpolation fitting [9], so that the power prediction data can be consistent with the time dimension of the voltage regulation cycle. Based on the power prediction curve of the wind farm, combined with the sensitivity coefficient of the active power affecting the voltage, the voltage change is predicted.

The voltage at the grid connection point of the wind farm is easily affected by power fluctuations on the farm side. The voltage deviation ΔV caused by the power changes ΔP and ΔQ is:

$$\Delta V = \frac{\partial V_{pcc}}{\partial P} \Delta P + \frac{\partial V_{Pcc}}{\partial Q} \Delta Q \tag{8}$$

In the formula: the variable $\partial V_{pcc}/\partial P$ represents the active-voltage sensitivity coefficient of the grid connection point, and the variable $\partial V_{pcc}/\partial Q$ represents the reactive power-voltage sensitivity coefficient of the grid connection point.

According to the prediction result of active power in a period of time in the future, the next voltage variation interval can be obtained, as shown in Fig. 4.

As can be seen from Fig. 4, when the active power changes, the predicted voltage will also change accordingly. Taking 1min as an adjustment period, by comparing the active power difference between this period and the previous period, combined with the voltage sensitivity coefficient, the fluctuation of the voltage in this period is obtained.

Actively Voltage Regulation Commands

Considering the reactive power margin of the fan, according to the flow chart shown in Fig. 5, the reactive power adjustment instructions for allocating the reactive power equipment are calculated. When the voltage of the grid-connected point is within the controllable range, the reactive power of the wind turbine is used to realize the stable control of the voltage of the grid-connected point; when the voltage of the grid-connected point exceeds the set range, the reactive power adjustment instructions of the wind turbine and SVG are determined according to the subdivision scene.

The voltage change is predicted through the prediction algorithm, so that the wind farm generates additional capacitive reactive power before the voltage drops at the grid
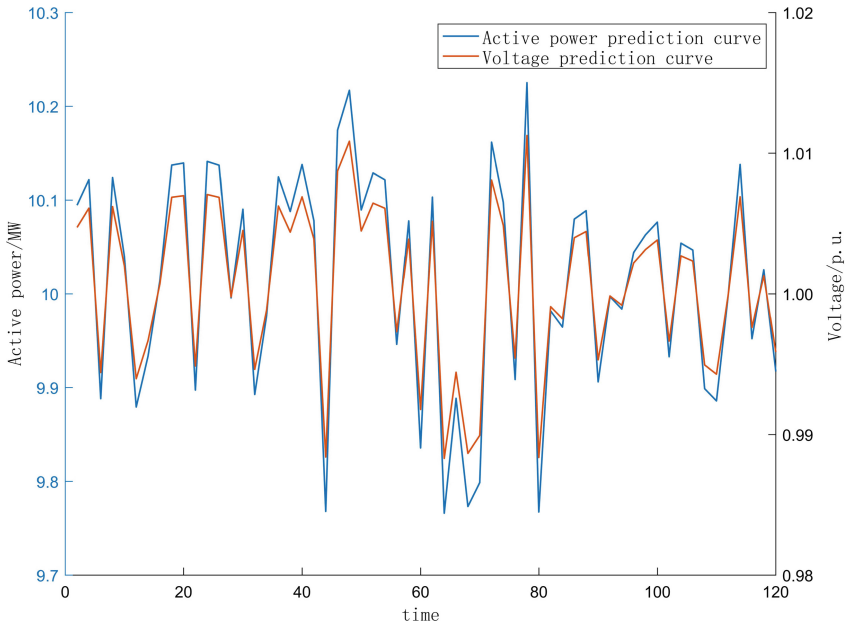
Fig. 4. Voltage prediction example

connection point, so as to raise the grid connection point voltage to near the target value. The inductive reactive power is added before the voltage rises at the grid connection point to reduce the voltage of the grid connection point to the target value, it can effectively reduce the adjustment frequency of reactive power equipment in the wind farm, and finally achieve the purpose of actively participating in the grid voltage regulation. The time is segmented according to the active power prediction result, and the voltage change is considered to be zero in the same time period. On the basis of the prediction result in Fig. 4, the average value of the predicted voltage fluctuation in the next control cycle is taken as a reference, and the voltage command value is obtained as shown in Fig. 6.

It can be seen from the results that the command value of actively voltage regulation is opposite to the change trend of the voltage prediction curve. When the predicted voltage increases, the command value decreases, which reduces the reactive power output of the system and achieves the purpose of balancing the voltage.

3.2   Analysis of Reactive Power Margin

The reactive power margin of wind farm mainly includes two parts: wind turbine and SVG. According to the power prediction results, combined with formulas (1) and (2), the reactive power adjustment capability of the wind turbine in the next 4 h can be obtained, thereby calculating the reactive power margin of the wind turbine. The working mode of SVG is mainly constant reactive power mode, and on this basis, its reactive power margin is calculated in real time. According to the voltage regulation command in Fig. 6, the reactive power variation range and output curve of the system can be obtained as shown in Fig. 7.
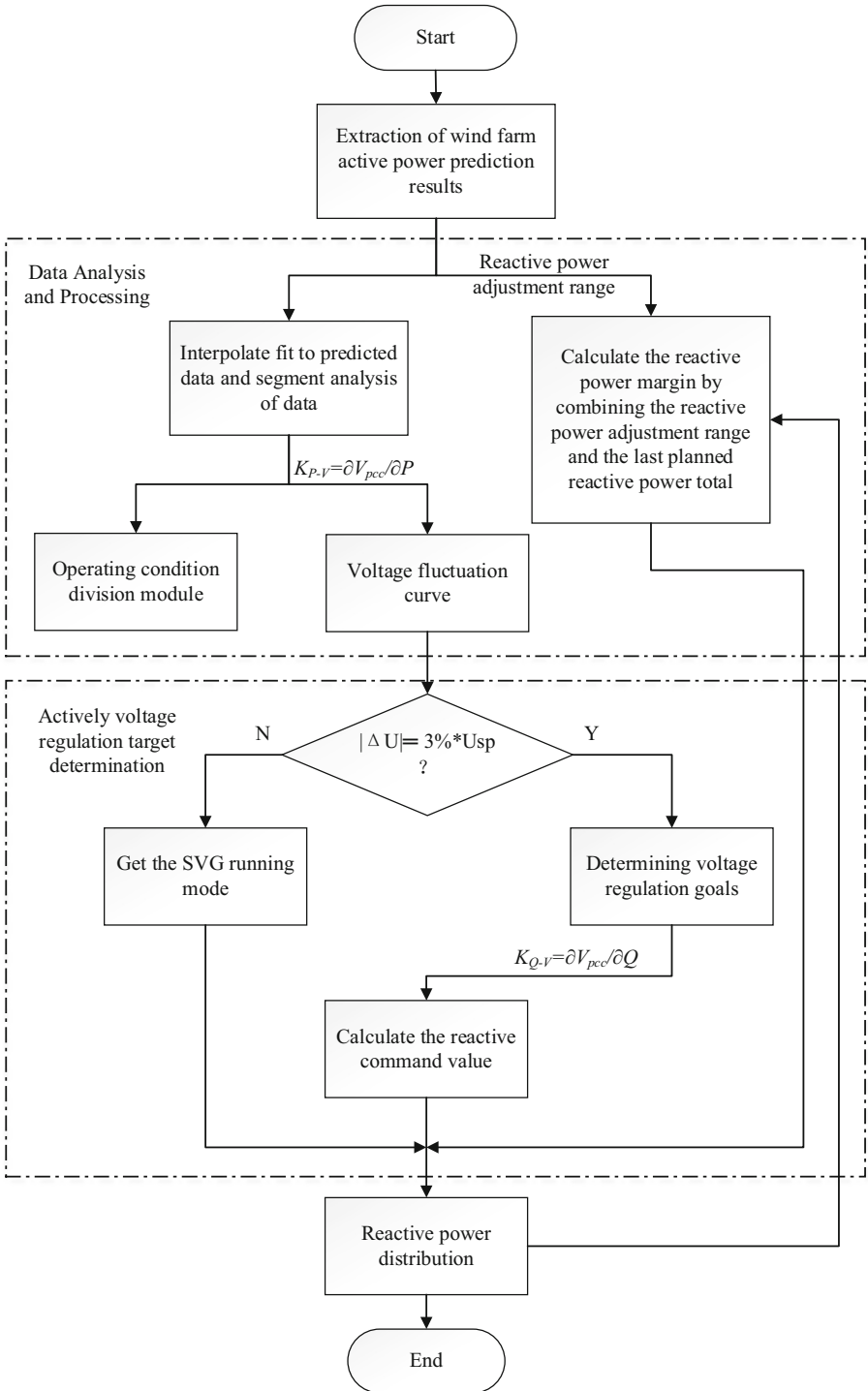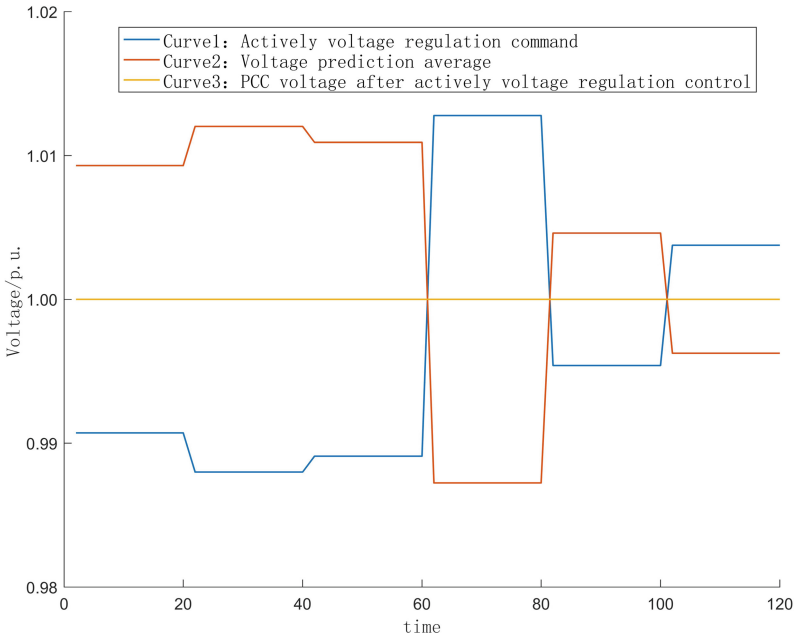
Fig. 5. Actively voltage regulation flowchart

Fig. 6. Actively voltage regulation command value
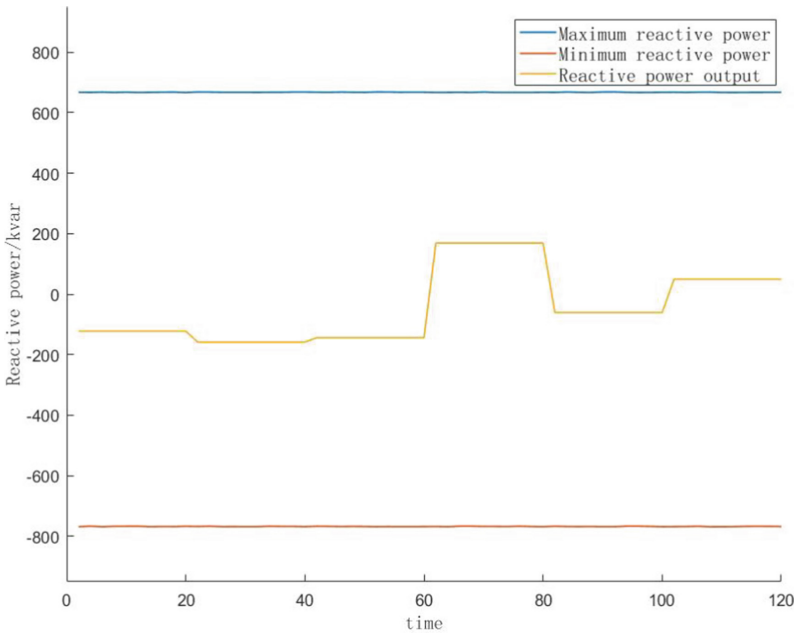

Fig. 7. Reactive power change curve

The reactive power margin in different time periods can be obtained from Fig. 7. Among them, the blue curve represents the maximum value of the reactive power regulation of the wind turbine; the red curve represents the minimum value of the wind turbine's reactive power regulation; the yellow curve represents the reactive output value of the current state of the wind turbine.

3.3 Reactive Power Coordination Optimization

In order to fully ensure the dynamic reactive power margin of SVG, in reactive power allocation, wind turbine deployment should be given priority, and SVG adjustment should be used as a supplement to suppress disturbances.

In a cycle of 15 min, coordinate reactive power allocation between wind turbines and SVG. When the reactive power is allocated, the working mode of the SVG is the fixed reactive power mode, and the reactive power allocation between the wind turbine and the SVG is determined by the actively adjustment target. The reactive power distribution method adopted by the wind turbine is proportional distribution of reactive power margin. The specific distribution principles are as follows:

$$Q_{i\_ref} = \left(\frac{Q_{i\_max}}{Q_{all\_max}} \right) * Q_{all\_ref} \qquad (9)$$

In the formula: Q_{i_max} is the upper limit of the maximum reactive power output of a single fan, and Q_{all_max} is the maximum reactive power upper limit of all wind turbines.
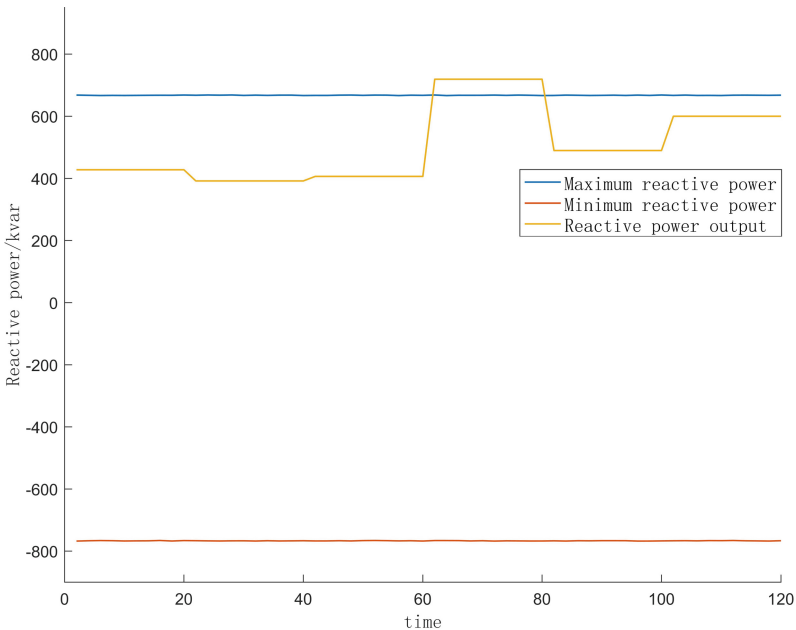

Fig. 8. Insufficient reactive power margin of wind turbines

As shown in Fig. 8, the reactive power margin of the wind turbine is insufficient to support the system voltage regulation. At this time, the wind turbine should maximize the reactive power output. After the wind turbine is adjusted, SVG is responsible for supplementing the rest of the reactive power. When the reactive power required for the voltage regulation of the power plant can be borne by the wind turbine, the reactive power output in the SVG constant reactive power mode is appropriately reduced.

4 Reactive Power Coordinated Optimal Control Strategy for Actively Voltage Regulation of Wind Farms

According to the degree of deviation between the grid-connected point voltage and the target voltage, the ramp amplitude and ramp rate of active power, wind farms can be divided into different operating scenarios [10, 11]. Coordinate the reactive power control of the new energy station in each scenario, optimize the operation status of the equipment in the station, and achieve the effect of improving the voltage support capacity of the station.

Based on the voltage regulation characteristics of SVG and wind turbines, the coordinated control method of providing voltage support together under different voltage sag and power ramp events is analyzed. First of all, formulate a reasonable operating scene division method. According to the voltage drop degree, ramp amplitude and ramp rate in each scenario, the classification criteria for different operating scenarios are determined. Secondly, research and analyze the different control modes of SVG and wind turbines. Finally, the control modes of DFIG and SVG are coordinated according to the degree of voltage drop in each scenario [12–14].

4.1 Differentiation of Operating Conditions

According to the different operating conditions, a differentiated reactive power optimization control method is adopted to improve the actively support capability of the wind farm in all aspects.

According to the degree of voltage drop/rise of the wind farm system, the grid voltage change can be divided into different operation scenarios. The operating conditions are mainly divided into two categories: steady state mode and fault transient mode [15–19]. The detailed classification criteria are shown in Table 2.

As can be seen from Table 2, when the system voltage is in the range of [0.95 p.u., 1.05 p.u.], the system voltage is controlled by the AVC. When the voltage exceeds this range, the system adopts the fault transient mode to improve the grid voltage stability.

As shown in Fig. 9, for the steady state mode, two operating scenarios are divided. The difference of the system's actively support mode is reflected in the operation mode of SVG. When the voltage fluctuation is ±3%, the SVG adopts the constant reactive power mode, and does not need to suppress the voltage fluctuation in real time. When the voltage fluctuation is 3%–5%, in order to avoid the large voltage fluctuation causing the system voltage to exceed the normal range, the voltage fluctuation of the system should be stabilized in time, and the SVG adopts the constant voltage mode. At the same time, in the division of scenarios 1 and 2, the influence of power ramping on the voltage

Table 2. Operating condition division standard table

Voltage range	Control modes of DFIG and SVG
0.97 p.u.–1.03 p.u	AVC control mode (SVG constant reactive power mode)
1.03 p.u.–1.05 p.u	AVC control mode (SVG constant voltage mode)
0.95 p.u.–0.97 p.u	
1.05 p.u.–1.10 p.u	SVG switches to fault transient mode
0.90 p.u.–0.95 p.u	
1.10 p.u.–1.30 p.u	Both DFIG and SVG switch to fault transient mode
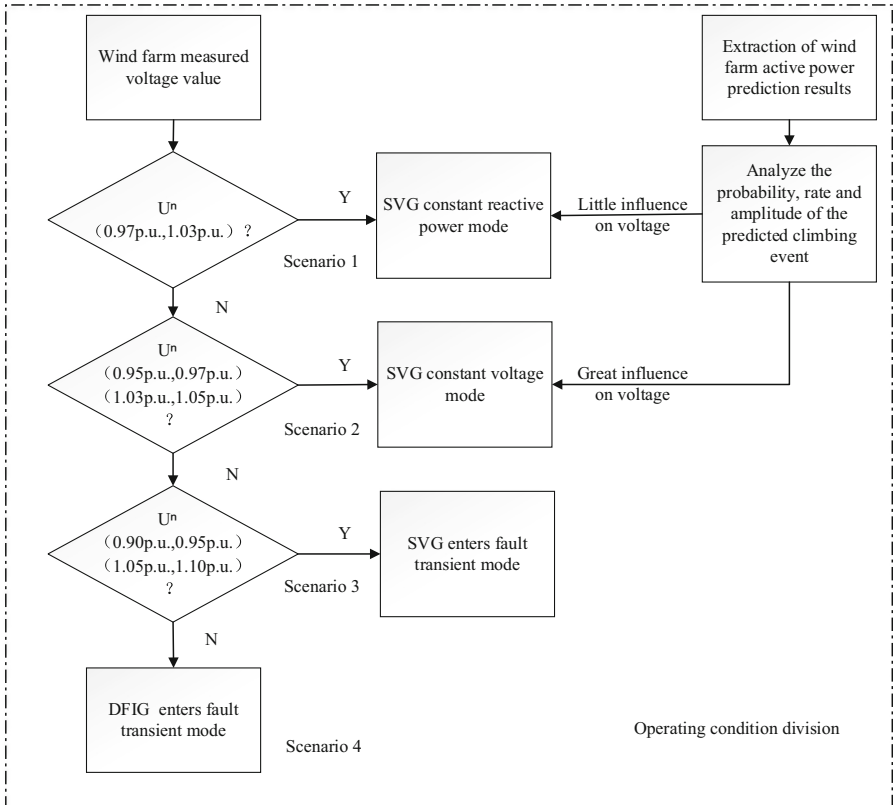
Fig. 9. Flow chart of operating condition distinction

of the grid-connected point is referred to. When the change of active power causes the voltage of the grid-connected point to rapidly exceed the dead zone range of the voltage control, SVG will use the constant voltage mode to It is guaranteed to suppress frequent fluctuations of grid voltage during power ramping.

When the system voltage exceeds 5%, the control mode of the SVG is converted to the fault transient mode to provide support for the system voltage in time. When the voltage exceeds 10%, the voltage support capacity of the SVG is insufficient. At this time, the wind turbine is also put into the fault transient mode to improve the voltage support capacity [20–22].

4.2   Reactive Power Optimization Control Method for wind Farms to Actively Participate in Grid Voltage Regulation

Based on the above analysis, when the system voltage is in the range of [0.95 p.u., 1.05 p.u.], the reactive power optimization control method for the wind farm to actively participate in the grid voltage regulation is as follows:

(1) Perform periodic (15 min) power prediction for the wind farm, and use the classification algorithm to perform segmentation processing to calculate the current and future reactive power margin and voltage fluctuation range of the system.
(2) According to the voltage fluctuation range, reactive power margin and required reactive power obtained in step 1, calculate the actively voltage regulation command value in the regulation period.
(3) After the command value is determined, a reasonable coordination and distribution of reactive power is carried out to the wind turbine.
(4) After wind turbine reactive power distribution is completed, if the voltage range is between [1.03 p.u., 1.05 p.u.] and [0.95 p.u., 0.97 p.u.], SVG will switch from constant reactive power mode to constant voltage mode operation.
(5) After the voltage adjustment of the adjustment period is completed, when the next period starts, return to step 1.

When the voltage fluctuation exceeds ±5%, the control mode of the SVG is switched to the fault transient mode. When the voltage fluctuation exceeds ±10%, the control mode of the wind turbine will also be switched to the fault transient mode.

5   Example Analysis

5.1   Example Description

In order to verify the voltage support capability and stability of the reactive power optimization control method for wind farms to actively participate in grid voltage regulation under different operating conditions, a wind farm simulation model was established based on RT-LAB, as shown in Fig. 10. Among them, wind farm 1 is modeled according to the grid structure shown in Fig. 1, and wind farm 2, as a power fluctuation simulation system, is modeled in a single-machine equivalent manner.

Wind farm 1 has a total of 50 DFIGs with a rated power of 2 MW and an SVG with a rated capacity of 30 Mvar. The power factor of the wind turbines is ±0.95, and the reactive power adjustment range is ±37.5 Mvar. Wind farm 1 is equipped with an AVC control system, and its adjustment period is set to 20 s. The rated power of wind farm 2
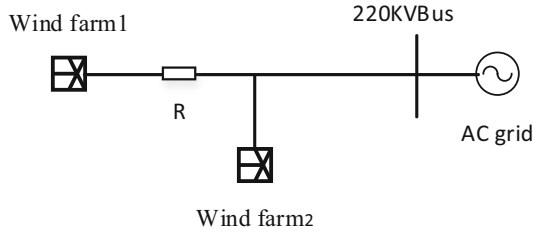
Fig. 10. Wind farm wiring diagram

is 200 MW, and the adjustment period of its reactive AVC control system is set to 15 s. The length of the line between wind farm 1 and wind farm 2 is 9.55 km.

Taking wind farm 1 as an example, the simulation parameter settings of each wind turbine are shown in Table 3.

Table 3. DFIG simulation parameter setting table

Parameter type	Parameter values	Parameter type	Parameter values
Power rating	2 MW	Capacitance	0 F
DFIG voltage	690 V	Frequency	50 Hz
Resistance	0.001 Ω	Proportional	0.2
Inductance	0.001 H	Integral	1.5

5.2 Simulation Calculation and Analysis

In order to verify the effect of the proposed control strategy, simulations are carried out for different operating scenarios that may be involved in the wind farm in Fig. 9.

Scenario 1: Voltage is operating in normal range.

By changing the active power of the fan, the active power and voltage fluctuations caused by wind changes are simulated.

The red curve in Fig. 12 represents the voltage change curve of the traditional AVC when the system voltage fluctuates; the green curve represents the voltage change curve of the control strategy proposed in this paper when the system voltage fluctuates. As can be seen from Fig. 11 and Fig. 12, when the fan output changes, the traditional AVC control is limited by the period control, and the system voltage cannot be adjusted in time after the system voltage fluctuates. The control strategy of changing the voltage command in advance based on the power prediction result can change the reactive power output value of the system before the voltage change, so as to ensure that the voltage in the next adjustment cycle does not fluctuate greatly.

Scenario 2: working condition with small voltage fluctuation amplitude.

Set up short-circuit faults of different degrees on the grid side to simulate the scene of voltage fluctuation. At 15 s, a simulated fault is put into operation, and the voltage
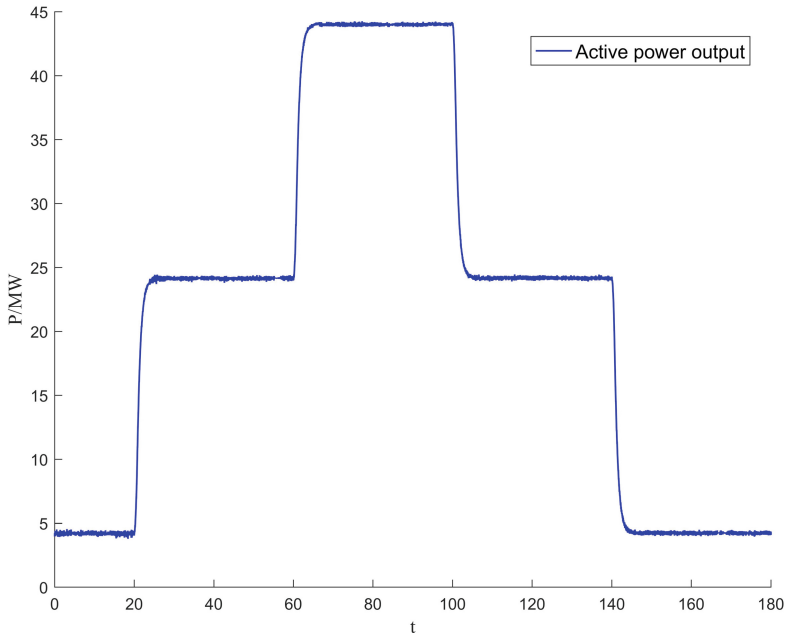
Fig. 11. Active power output change curve of wind farm
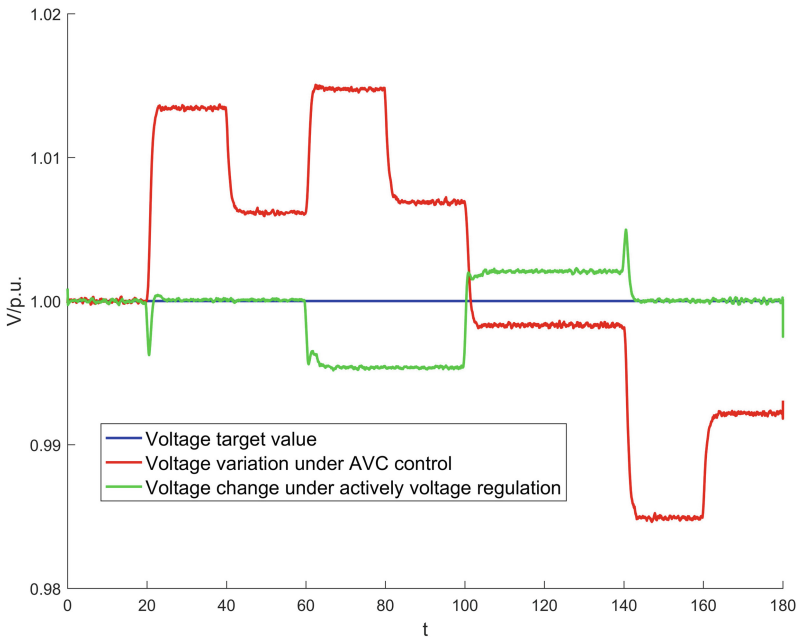
Fig. 12. The voltage variation curve of station 1 under scenario 1

drops to 0.95 p.u.; at 100 s, the fault disappears and the voltage is raised to 1.05 p.u. The simulation waveforms are shown in Fig. 13 and Fig. 14.

In the traditional AVC control strategy, SVG still runs in constant reactive power mode. When the control strategy proposed in this paper is adopted, the SVG will enter the constant voltage control mode during the fault period, and the reactive power output of the wind turbine is still controlled by the AVC. The voltage change at the PCC point and the SVG reactive power output are shown in Fig. 13 and Fig. 14, respectively.
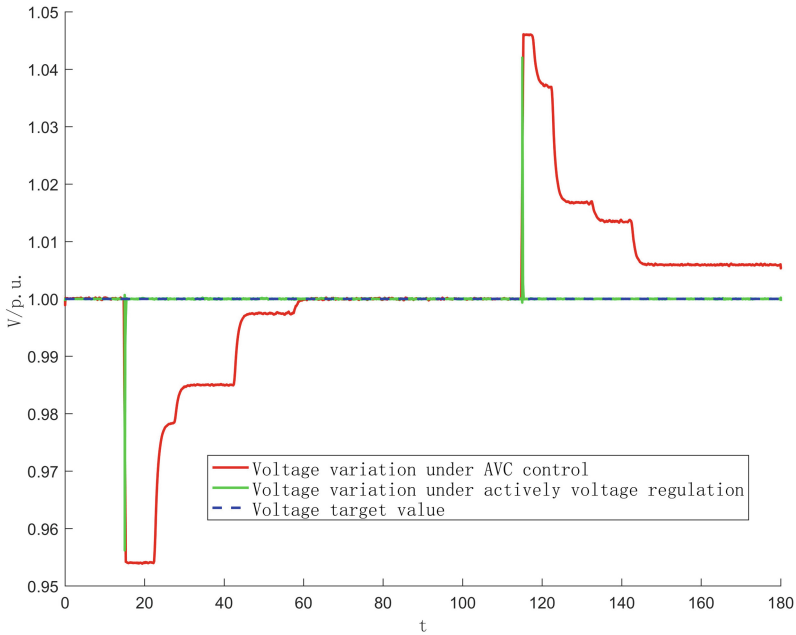
Fig. 13. Voltage change curve of station 1 under scenario 2

As can be seen from Fig. 13, when the voltage drops to 0.95 p.u., the SVG control mode switches from constant reactive power to constant voltage mode, which can quickly adjust the voltage to near the target value. Reduces the likelihood of voltage dropping below 0.95 p.u. during a control cycle. It can be seen from Fig. 14 that at the moment of the fault, the SVG enters the voltage control mode to maintain the system voltage stability. Compared with the traditional control strategy, when the voltage fluctuation range is expanded, the control strategy proposed in this paper can quickly realize the stable control of the voltage.

Scenario 3: The condition of a large voltage drop.
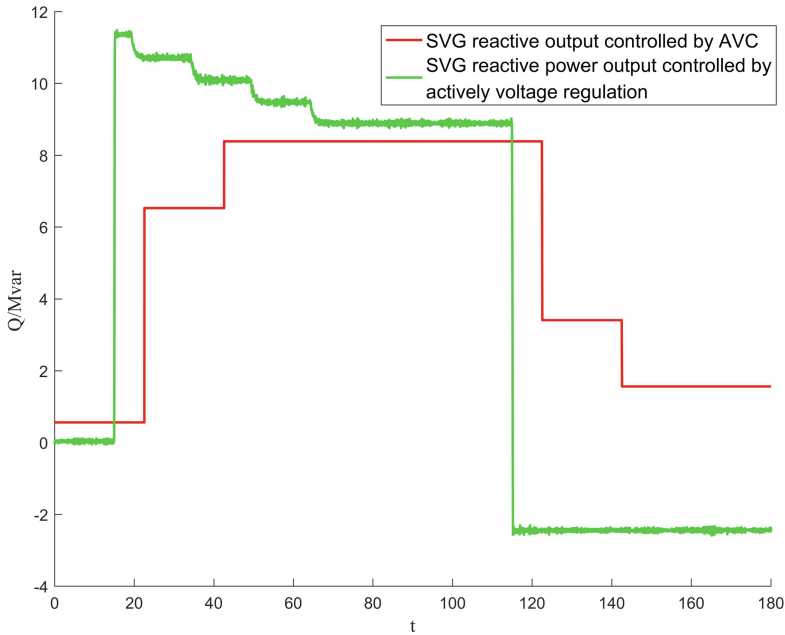
Fig. 14. SVG reactive power variation curve in scenario 2

Set up short-circuit faults of different degrees on the grid side to simulate the scene of a sharp drop in voltage. At 15 s, a simulated fault was put in and the voltage dropped to 0.90p.u.

It can be seen from Fig. 15 and Fig. 16 that the voltage drop of the grid is relatively large. When it exceeds the set limit range, the SVG operation mode switches to the transient fault state, and the voltage is raised in time (the voltage is raised from the minimum 0.9 pu to 0.935 pu), When the AVC is in the next adjustment cycle, a reactive power command is issued to the wind turbine, and the voltage is further raised. The wind turbine and SVG reach full capacitive reactive power, and the voltage is maintained between 0.96 p.u. and 0.97 p.u.

When the voltage fluctuation is within the allowable range, the traditional AVC is controlled according to the period, and the suppression ability of the voltage fluctuation is weak. In this paper, the operating conditions are divided in more detail. When the voltage fluctuation is small, the reactive power is adjusted periodically based on the result of the power prediction, which effectively suppresses the voltage fluctuation in the period and provides a reliable voltage support. At the same time, the traditional AVC only provides limited active support for the voltage of the system when a high-low breakdown fault occurs. The active participation of the wind farm in the voltage regulation of the power grid can raise/lower the voltage in time to maintain voltage stability when the voltage sag/raise is small. At the same time, considering that when the voltage drop/rise is large, the voltage support capacity of SVG is limited, and DFIG is used to improve the voltage support capacity.
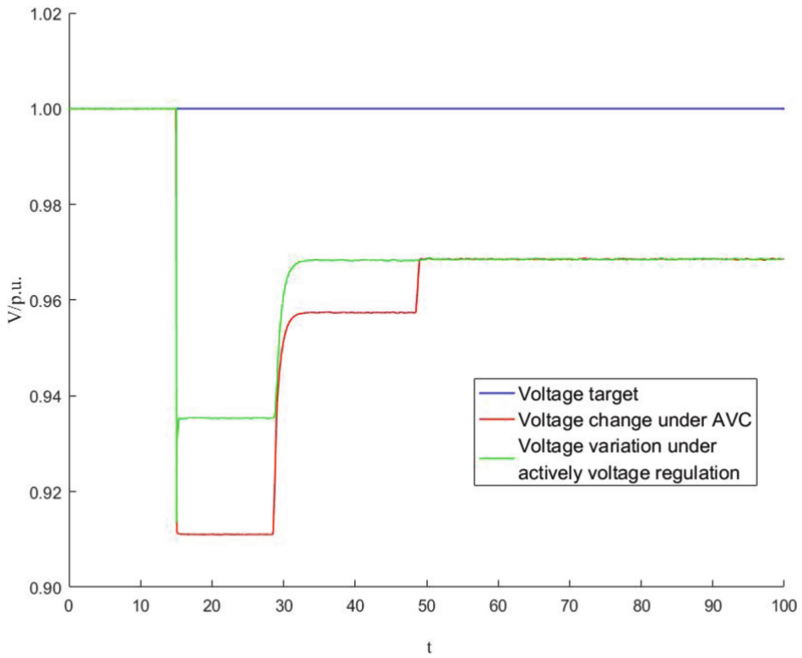
Fig. 15. The voltage variation curve of station 1 in scenario 3
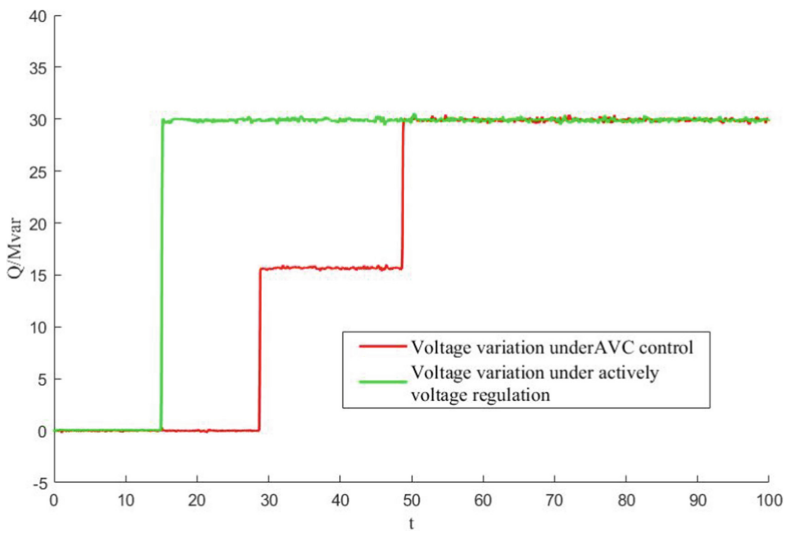
Fig. 16. SVG reactive power variation curve in scenario 3

6 Conclusion

Aiming at the problem of insufficient voltage support capacity at the grid-connected point of wind farms, this paper proposes a reactive power optimization control strategy that utilizes wind farms to participate in active voltage regulation of the power grid. A detailed simulation model is constructed through the RT-LAB simulation platform, and the proposed control strategy is simulated. The simulation results show that the proposed control strategy has significant effects in reducing the frequency of reactive power regulation, improving the reactive power margin and actively voltage support compared with the traditional AVC control strategy.

In the follow-up research, the coordinated control of wind turbines and SVG under transient faults can be considered, and the actively voltage regulation strategy in different scenarios can be improved.

References

1. Wang, Y., Li, P.: Study on reactive power and voltage coordinated control strategy for power system with large-scale wind power integration. Adv. Technol. Electr. Eng. Energy **38**(03), 47–55 (2019)
2. Yang, L., Liao, J., Guo, C., et al.: Voltage control strategy of DFIG coordinating with SVG under power-limited operation. Electric Power Constr. **41**(10), 125–132 (2020)
3. Liu, H., Fan, Y., Zhong, X.: Reactive power control strategy considering transient voltage stability of wind farms. Power Capac. React. Power Compensat. **38**(03), 167–172 (2017)
4. Ren, C., Cheng, L., Fan, G., et al.: Study on coordination control optimization of reactive power equipment of wind farm considering wind power prediction and voltage distribution. Power Capac. React. Power Compens. **41**(02), 175–180+186 (2020)
5. Wang, S., Li, G., Zhou, M.: The reactive power adjusting mechanism & control strategy of doubly fed induction generator. Proc. CSEE **34**(6), 2714–2720 (2014)
6. Cui, Y., Xu, M., Tang, Y., et al.: Reactive control strategy of DFIG wind farm based on reactive sensitivity of collection system. Power Syst. Technol. **39**(09), 2418–2423 (2015)
7. Wang, X., Liu, W., Xia, P., et al.: Reactive power optimization control method for PV station participating in active voltage regulation of power grid. Electr. Power Autom. Equip. **40**(07), 76–83 (2020)
8. Zhang, Z., Wang, C., Dong, X.: Coordinated voltage control strategy of wind farms based on hierarchical model predictive control. Autom. Electric Power Syst. **42**(8), 92–100 (2018)
9. Zhao, L., Chen, Z., Ding, L., et al.: A weighted ensemble classification method for time series data based on regularized extreme learning machine. Comput. Eng. Sci. **44**(03), 545–553 (2022)
10. Bao, Z., Ji, L., Chang, X., et al.: Active voltage support control strategy for a renewable generation farm during unbalanced voltage sags. Power Syst. Prot. Control **49**(16), 161–169 (2021)
11. Qiao, Y., Han, L., Li, M.: Interval estimation of forecasting error based on wind power ramp features and cloud model. Autom. Electric Power Syst., 1–17 (2023)
12. Zhao, J., Hu, X., Lv, X., et al.: Research on coordination control strategy of DFIG wind farm with crowbar circuit. Adv. Technol. Electr. Eng. Energy **35**(10), 17–22 (2016)
13. Zhao, H., Wu, Q., Guo, Q., et al.: Coordinated voltage control of a wind farm based on model predicted control. IEEE Trans. Sustain. Energy **16**(4), 440–1451 (2016)

14. Yang, X., Liu, G., Li, A., et al.: A predictive power control strategy for DFIGs based on a wind energy converter system. Energies **10**(8), 1098 (2017)
15. Lu, Y., Lin, S., Liu, M., et al.: Computation of static voltage stability margin for power system considering fluctuation interval of wind farm output. Autom. Electric Power Syst. **42**(8), 92–100 (2018)
16. Xia, P., Liu, W., Zhu, D., et al.: Multi-time scale optimal control method of reactive power and voltage based on model predictive control. Electric Power Autom. Equip. **39**(3), 64–70 (2019)
17. Yu, Z., Tang, Y., Dai, J., et al.: Voltage/var control strategy of PV plant based on adaptive adjustment of active power. Power Syst. Technol. **44**(05), 1900–1907 (2020)
18. Wang, Y., Liao, Y., Song, Y., et al.: Distributed optimal control strategy of reactive power and voltage in wind farm. High Volt. Eng., 1–10 (2016)
19. Li, D., Wang, J., Zhang, J., et al.: Research on reactive power and voltage control strategy of photovoltaic grid-connected inverter based on self-adapted model prediction control method. Renew. Energy Res. **39**(08), 1087–1093 (2021)
20. Liu, J., Cui, Z., Wu, Y., et al.: Technical performance test and improvement measure study for dynamic reactive compensation devices applied in large-scale wind power system. Electric Power **12**(5), 25–31 (2016)
21. Zhao, H., Wu, Q., Wang, J., et al.: Combined active and reactive power control of wind farms based on model predictive control. IEEE Trans. Energy Convers. **32**(3), 1177–1187 (2017)
22. Morshed, M.J., Sardoueinasab, Z., Fekih, A.: A coordinated control for voltage and transient stability of multi-machine power grids relying on wind energy. Int. J. Electr. Power Energy Syst. **109**, 95–109 (2019)

Black-Start Scheme for the Interdependent Power and Natural Gas Transmission Systems

Lingyu Guo[1], Yang Du[1], Zhongguang Yang[1], Boyuan Cao[1], Xingang Yang[1], Xianghong Xiong[1], Jun Kan[2(✉)], and Zhaoqi Huang[2]

[1] Electric Power Research Institute of State Grid Shanghai Municipal Electric Power Company, Shanghai 200437, China
[2] Beijing Jiaotong University, Beijing 100044, China
kanjun@bjtu.edu.cn

Abstract. With the development of gas fired generators in the power transmission system and widespread of electricity-driven compressors in the gas transmission system, the two systems are closely interconnected. During generator start-up stage after blackout, restart of generators and restoration of electricity-driven compressors are interdependent. In this paper, a novel generator start-up strategy decision-making method considering interdependencies between power and natural gas systems is proposed. First, the generator start-up and critical loads restoration problem is formulated as an integer linear program. Then, the gas dynamics simulation tool is adopted to simulate the gas transmission system restoration process to obtain the time of gas supply restoration for gas fired generators. Furthermore, combining with generator start-up sequence and the simulation results, generator start-up strategy is developed. Finally, the effectiveness of the proposed method is validated by numerical simulation on a coupled system which is composed by IEEE-39 system and Belgium-20 gas system.

Keywords: Black-start scheme · Power transmission system · Gas transmission system · Interdependencies · Natural gas dynamics

1 Introduction

At present, power transmission system and gas transmission system are becoming more and more interconnected. On the one hand, under the background of China new power system construction and the "3060 double carbon" goal, as regulating power sources with high power generation efficiency, strong flexibility and low CO_2 emission intensity, the proportion of gas-fired generators continues to increase. On the other hand, for the consideration of environmental protection and cost control, electricity-driven gas compressors are widely used in natural gas system [1]. The high interdependencies between power and gas transmission networks may increase the potential risk of cascading failures or blackout, and bring new challenges for system restoration [2]. An example is the blackout that affected much of Texas on February 15, 2021. Due to the

outage of compressors and other electricity-driven equipment caused by power supply interruption, the pressure of pipelines and supply of natural gas were influenced, which limited the generation of gas-fired generators, resulting in further power outage [3]. After blackout, it is of great necessity and importance to adopt the efficient restoration plan to restart all generators and restore the system. This paper is concerned with generator optimal start-up sequence after blackout to restore the system quickly and reduce economic losses [4].

Continuous efforts have been devoted to the research of power system restoration [5, 6]. For the analysis of coordinated restoration for power and gas system, most of works focus on repair crew dispatch [7] and power-gas integrated system service restoration [8–11]. As for interdependent power and gas transmission systems, in [12], Monte Carlo Simulation and Markov State Transition were used to calculate the system restoration potential for different natural disasters, showing that interdependent power and gas system have stronger restoration potential, but without providing specific restoration strategy. A framework is proposed for restoration optimization of coupled power and gas systems in [13], resilience is enhanced by the coordinated restoration of critical components in power and gas systems. But generator start up characteristics and natural gas dynamics are not considered. To the best of our knowledge, the optimal generator start-up sequence for interdependent power and gas systems is seldom reported.

In this paper, the concept of generator start-up considering interdependencies between power and gas transmission systems is introduced. It is challenging to develop a generator start-up strategy considering interdependencies of two systems. Firstly, Restart of gas fired generators is affected by both cranking power and gas supply. The restoration of gas supply for gas fired generators is dependent on power supply restoration of electricity-driven compressors. Meanwhile, power supply restoration is dependent on restart of generators. Secondly, compared with power transmission system, gas transmission system has larger time constant, and gas dynamics are described by partial differential equations, which are difficult to compute.

A novel generator start-up method considering interdependencies between power and gas systems is proposed in this paper, which is aimed to restore the black-start capability (BSC) quickly after blackout. First of all, the generator start-up and critical loads restoration problem is formulated as an integer linear program, where electricity-driven compressors are considered as critical loads. Then, gas dynamics simulation tool is adopted to simulate the gas transmission system restoration process to obtain the time of gas supply restoration for gas fired generators. Furthermore, combining with generator start-up sequence model and simulation result, generator start-up strategy is developed. Finally, the effectiveness of the proposed method is validated by numerical simulation on a coupled system which is composed by IEEE-39 system and Belgium-20 gas system.

Compared with the state-of-the-art, the contributions of this paper include:

1) It is aimed at optimizing generator start-up sequence considering interdependencies between power and gas transmission systems to restore the BSC quickly after blackout.
2) An integer linear program is proposed to formulate the generator start-up and critical loads restoration problem.

3) A simulation based method is proposed to obtain the gas supply restoration time for gas fired generators.

2 Solution Framework

In this section, the solution framework of generator start-up problem for interdependent power and gas transmission system is introduced.

Figure 1 shows the solution framework. Generator start-up sequence and critical loads restoration (GSUS-CLR) optimization model is constructed to obtain the critical loads restoration time, which is the input of gas dynamics simulation module. Combining generator start-up sequence determined by GSUS optimization model and gas supply restoration time for gas fired generators determined by gas dynamics simulation, generator start-up strategy can be developed.
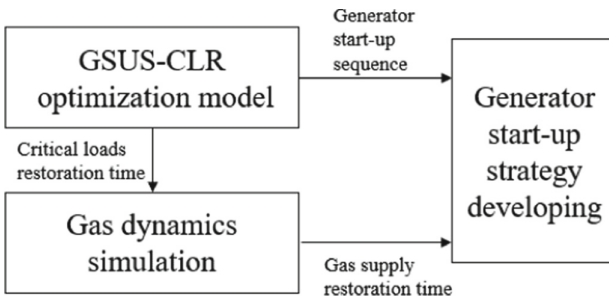
Fig. 1. Solution framework.

The reminder of this paper is organized as follows. Section 3 formulates the generator start-up and critical loads restoration problem as an integer linear program. Section 4 proposes a simulation based method to obtain the gas supply restoration time for gas fired generators. Section 5 introduces the procedure to develop generator start-up strategy. Case studies are presented is Sect. 6. Section 7 concludes the study.

3 GSUS-CLR Optimization Model

In this section, generator start-up and critical loads restoration problem is formulated as an integer linear program.

3.1 Notations

For sets, let S_{NBS} denote the set of non-black-start (NBS) generator, S_{BS} denote the set of black-start (BS) generator, S_{F} denote the set of gas fired generator, S_T denote the set of restoration time, S_{G} denote the set of generator in the system, S_{B} denote the set of bus in the system, S_{L} denote the set of transmission line in the system, $S_{\mathrm{B\text{-}BS}}$ denote the set of bus that is connected to black-start generator in the system, $S_{\mathrm{B}}/S_{\mathrm{B\text{-}BS}}$ denote the

set of bus besides the bus that is connected to black-start generator, $S_{1-b,i}$ denote the set of line that are connected to bus i, S_{LD} denote the set of critical load in the system.

For parameters, let C_i denote the capacity of the generator, P_i^{crk} denote the cranking power to restart the generator, K_i denote the ramping rate of the generator, P_i^{max} denote the maximum power output of generator, t_i^{crk} denote the cranking time of generator, t_i^{CH} denote the maximum start-up time of the generator, t_i^{CL} denote the minimum start-up time of the generator.

For decision variables, let $u_{g,i}^t$ denote the start-up status of generator, $u_{f,i}^t$ denote the gas supply status of gas fired generator, $u_{b,i}^t$ denote the energizing status of the bus, $u_{g,i}^{tb-}$ denote the energizing status of bus connected to generator, $u_{l,ij}^t$ denote the energizing status of the line, $u_{ld,ij}^t$ denote the pick-up status of critical load, $u_{ld,i}^{tb-}$ denote the energizing status of bus connected to critical load.

3.2 Objective Function

The overall system BSC is defined as the total on-line generation capability to help expedite system restoration [14]. Therefore, objective function is maximizing the black start capability of the system [15] and restoring the critical loads quickly, which is mathematically expressed as:

$$\max \left\{ \sum_{i \in S_{NBS}} \sum_{t \in S_T} \left(C_i - P_i^{crk}\right) u_{g,i}^t + \sum_{i \in S_{LD}} \sum_{t \in S_T} u_{ld,i}^t \right\} \tag{1}$$

3.3 Constraints

Generation Capability Curve
Generation capability curve of a generator is shown in Fig. 1.

In order to linearize the nonlinear generation capability curve, this paper adopts the method proposed in reference [15]. This method only introduces generator start-up status $u_{g,i}^t$ as the decision variables for linearization, which improves the computation efficiency.

The linearized generation capability function is as follows:

$$\begin{aligned}
P_{g,i}^t = K_i \bigg\{ & t - \sum_{j \in S_t} \left(1 - u_{g,i}^{j-\text{ceil}(t_i^c)}\right) \\
& - u_{g,i}^{t-\text{ceil}(t_i^c)} \left(1 - \text{res}(t_i^c)\right) - \sum_{j \in S_t} u_{g,i}^{j-\text{ceil}(t_i^c + C_i/K_i)} \\
& + u_{g,i}^{t-\text{ceil}(t_i^c + C_i/K_i)} \left(1 - \text{res}(t_i^c + C_i/K_i)\right) \bigg\} \\
& - u_{g,i}^t P_i^{crk}, t \in S_T, i \in S_G
\end{aligned} \tag{2}$$
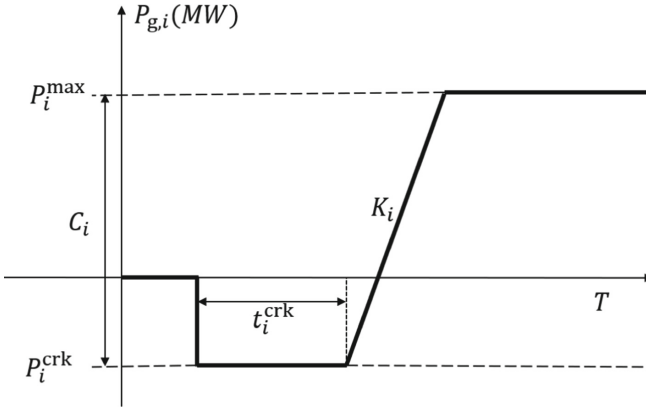
Fig. 2. Generation capability curve.

where, the introduced ceil and res functions are defined as follows:

$$\text{ceil}(x) = \begin{cases} x & x \in Z \\ \text{the least integer larger than } x & x \notin Z \end{cases} \quad (3)$$

$$\text{res}(x) = \text{ceil}(x) - x \quad (4)$$

Generator Start-Up Constraints

$$t_i^{\text{CL}} \leq \sum_{i \in S_T} \left(1 - u_{\text{g},i}^t\right) + 1 \leq t_i^{\text{CH}}, \quad i \in S_{\text{G}} \quad (5)$$

$$\sum_{i \in S_{\text{G}}} P_{\text{g},i}^t \geq 0, \quad t \in S_T \quad (6)$$

$$u_{\text{g},i}^{t+1} \leq u_{\text{b-g},i}^t, \quad t \in S_{T-1}, i \in S_{\text{NBS}} \quad (7)$$

$$u_{\text{g},i}^t \leq u_{\text{g},i}^{t+1}, \quad t \in S_{T-1}, i \in S_{\text{NBS}} \quad (8)$$

$$u_{\text{g},i}^t = 0, \quad t \in S_T, i \in S_{\text{F}} \quad (9)$$

Constraints (5) is the start-up time constraints of the generator, which means start-up time should be within critical minimum and maximum intervals for all generators [4]. Constraint (6) is the power constraint of the system, which means there should be adequate black-start resources to meet the cranking power requirement for NBS generators for each time step. Constraints (7) indicates that the generator is cranked only after the bus that the generator is connected to is energized. Constraints (8) represents once a generator is started, it will not be tripped. Constraints (9) indicates gas fired generators are not available to be restarted because of lacking of gas supply.

Transmission Path Constraints
By searching over the status of each bus and line at each time step, the optimal

transmission paths to crank NBS generators and pick up critical loads can be found.

$$0 \leq u_{1,ij}^{t+1} \leq u_{b,i}^t + u_{b,j}^t, t \in S_{T-1}, ij \in S_L \tag{10}$$

$$0 \leq u_{b,i}^t \leq \sum_{ij \in S_{1-b,i}} u_{1,ij}^t, t \in S_T, i \in S_B/S_{B\text{-}BS} \tag{11}$$

$$0 \leq u_{1,ij}^t \leq u_{1,ij}^{t+1}, t \in S_{T-1}, ij \in S_L \tag{12}$$

$$0 \leq u_{b,i}^t \leq u_{b,i}^{t+1}, t \in S_{T-1}, i \in S_B \tag{13}$$

$$u_{b,i}^{t=1} = 1, i \in S_{B\text{-}BS} \tag{14}$$

$$u_{b,i}^{t=1} = 0, i \in S_B/S_{B\text{-}BS} \tag{15}$$

$$u_{1,ij}^{t=1} = 0, ij \in S_L \tag{16}$$

Constraint (10) indicates that if a line is energized at time $t + 1$, then at least one of its connected buses is energized at time t. Constraint (11) means that if a bus is energized at time t, then at least one of its connected lines is energized at time t. Constraints (12) and (13) respectively indicate that the transmission line and bus will not be de-energized. Once energized. Constraints (14)–(16) represent the initial state of lines and buses.

Coordination of Cranking NBS Generators and Picking Up Critical Loads
During the power system restoration, on the one hand, NBS generators need to be cranked to restore the generation capability, on the other hand, the power supply of electricity-driven compressors should be restored as soon as possible to ensure the successful start-up of the gas-fired units. Therefore, picking up of critical loads is integrated into the real power constraint for generator start-ups. By determining the status of the critical load at each time step, pickup of critical loads and cranking of NBSUs are coordinated.

$$\sum_{i \in S_G} P_{g,i}^t - \sum_{j \in S_{LD}} u_{ld,j}^t P_{ld,j}^t \geq 0, \quad t \in S_T \tag{17}$$

$$u_{ld,i}^{t+1} \leq u_{b\text{-}ld,i}^t, \quad t \in S_{T-1}, i \in S_{LD} \tag{18}$$

$$u_{ld,i}^t \leq u_{ld,i}^{t+1}, t \in S_{T-1}, i \in S_{LD} \tag{19}$$

Constraint (17) is the system power constraint, that is, sufficient generation should be available to pick up critical loads. Constraint (18) indicates that the bus connected with critical load should be energized before the load is picked up. Constraint (19) indicates once the load is picked up, it will not be curtailed. In this paper, the substations where the electricity-driven compressors obtain power supply are considered as the critical loads.

Generator start-up sequence considering critical loads restoration (GSUS-CLR) model is summarized as follows:

Max (1)
s.t. (2)–(19)

GSUS-CLR is an integer linear program, commercial optimizer can be used to solve it.

4 Gas Dynamics Simulations

In this section, a simulation based method is proposed to obtain the time of gas supply restoration by using a simulation tool.

4.1 Fluid Dynamics for the Gas Flow

The natural gas flow driven by the pressure along the pipelines in correspondence to its ingredients, temperature, density, pressure, etc. The gas states such as velocity, temperature, density, pressure, etc. can be linked by the one-dimensional fluid dynamics along the pipe. Generally, this process can be described using 3 partial differential equations (PDEs) which are the energy equation, the momentum equation and the material-balance equation and 1 algebra equation which is the equation of state [16]. Considering the complexity of mathematical model for gas flow dynamics, this paper adopted the commercial simulation tool to simulate the gas dynamics during the system restoration.

4.2 PipelineStudio

PipelineStudio is a complete pipeline engineering tool that delivers rapid and accurate offline pipeline management design, planning and hydraulic analysis for natural gas and liquid pipelines through advanced simulation techniques. Engineers and planners are able to use reliable and accurate information to make decisions, leading to improvements in pipeline design, performance, and throughput [17].

This paper uses PipelineStudio to simulate the gas dynamics after power supply restoration for electricity-driven compressors. The input of PipelineStudio includes gas transmission system data and the time step that electricity-driven compressors power supply restored. And corresponding output is the dynamic response of gas transmission system. By doing this, gas supply restoration time of gas fired generators can be obtained.

5 Procedure to Determine Generator Start-Up Strategy

In this section, the method to update the generator start-up strategy is proposed and the procedure to the procedure to determine generator start-up strategy for interdependent power and gas transmission systems is introduced.

5.1 Method to Update the Generator Start-Up Strategy

The method to update generator start-up strategy includes: 1) run generator start-up sequence considering all generators (GSUS-ALL) model to obtain all generators start-up sequence; 2) update gas fired units start-up sequence.

GSUS-ALL Optimization Model
Compared with GSUS-CLR model, all the generators in the system are considered and critical loads restoration are not considered in GSUS-ALL optimization model. Consequently, GSUS-ALL optimization model can be formulated as follows:

$$\max \quad \left\{ \sum_{i \in S_{\text{NBS}}} \sum_{t \in S_T} \left(C_i - P_i^{\text{crk}} \right) u_{\text{g},i}^t \right\} \tag{20}$$

s.t. (2)–(8), (10)–(16)

GSUS-ALL is also a integer linear program, which can be easily solved by commercial solvers such as Mosek.

Update of Start-Up Time for Gas Fired Generators
Start-up of gas fired units is affected by both cranking power provided by power transmission system and gas provided by gas transmission system. Start-up time for gas fired units is the time when provide of both cranking power and gas satisfied. Cranking time for gas fired generators is given by running GSUS-ALL, and gas supply restoration time is determined by PipelineStudio simulation. For cranking time and gas supply restoration time, the later one is chosen as start-up time for gas fired generators.

5.2 Procedure to Determine Generator Start-Up Strategy for Interdependent System

Figure 2 shows the procedure determine generator start-up strategy for interdependent power and gas transmission system, which contains 5 steps: 1) obtain system data; 2) run GSUS-CLR to obtain critical loads restoration time; 3) run PipelineStudio to obtain gas supply restoration time; 4) run GSUS-ALL to obtain generator start-up sequence without considering gas supply restoration time for gas fired generators; 5) update gas fired units start-up sequence with gas supply restoration time.

As system restoration progresses, it is inevitable that the system condition will change, which may make developed strategy infeasible. When this situation arises, the proposed optimization model can be modified by adding initial status constraints of main components based on current system condition. By doing so, the strategy can be updated based on current system condition to make sure strategy is feasible.

6 Simulation Results

In this section, the proposed generator start-up strategy determination method is tested. The GSUS-CLR model and GSUS-ALL have been programmed using Conex of Julia
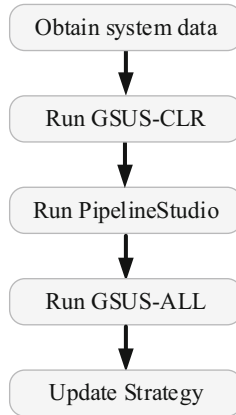
Fig. 3. Procedure to determine generator start-up strategy for interdependent power and gas transmission system.

and Mosek has been chosen to solve the model. PipelineStudio 4.2.1.0 has been used to simulate the gas dynamics.

6.1 System Information

Test case is discussed using the interdependent system composed by IEEE 39 bus system [18] and Belgium 20 node gas system [19]. The topology of test case is shown in Fig. 3. Generator and transmission line parameters can be found in [18], and pipe parameters can be found in [19]. For power transmission system, G10 is set as black-start generator, G1, G3, and G4 are gas fired generators, loads at bus 25 and bus 29 are set as critical loads. For gas transmission system, CP1 and CP2 are electricity-driven compressors. Gas nodes 20, 10 and 12 supply natural gas to gas-fired generators respectively. Power loads 25 and 29 supply power to electricity-driven compressors CP1 and CP2 respectively.

Assume after blackout, the system has to black-start. And gas systems is influenced due to outage of electricity-driven compressors, which makes gas supply for gas fired generator infeasible because of low gas pressure level. The entire restoration horizon is divided into 40 time-steps, and per time step is 10 min. That is, per unit value of time is 10 min. And G10 is assumed to be restarted at $t = 0$.

6.2 Restoration Strategy

The restoration actions sequence of the system is shown in Fig. 4. The bold lines show the optimal transmission lines to crank the generators, and different colors indicate the time for different restoration actions. Table 1 shows the generator start-up sequence. By $t = 16$ p.u., all generators are cranked and restarted. Gas fired generators G1, G3 and G4 are restarted relatively later compared with other generators. This is because of large time constant of gas transmission system, which usually takes hours to restore the pressure of gas supply node.
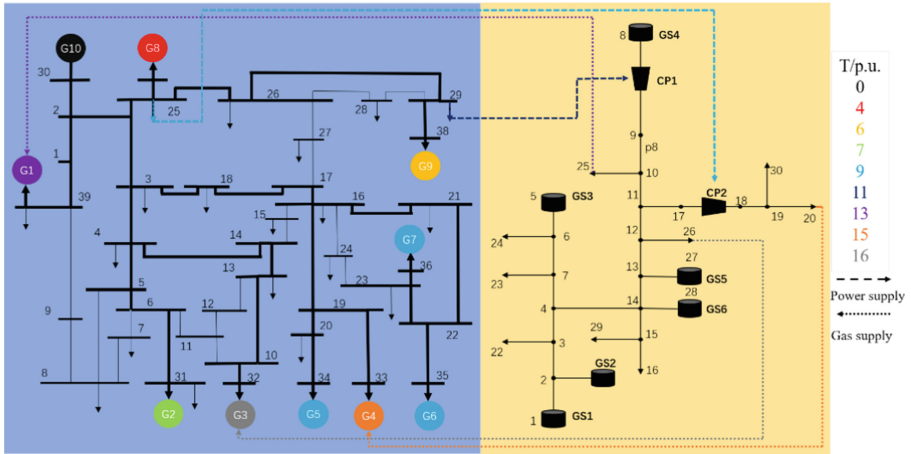
Fig. 4. Interdependent system topology with restoration actions.

Table 1. Generator start-up sequence.

Gen.	G1	G2	G3	G4	G5	G6	G7	G8	G9	G10
T_{start} (p.u.)	13	7	16	15	9	9	9	4	6	0

Restoration time of electricity-driven compressors is shown in Table 2. All electricity-driven compressors are restored by $t = 11$ p.u.. The restoration of compressors leads to restoration of gas pressure, which result in restoration of gas supply of gas fired generators. Thus, restoration of electricity-driven compressors and cranking of NBS generators should be coordinated to make sure that all generators are restarted successfully.

Table 2. Power supply restoration time of electricity-driven compressors.

Electricity-driven compressor	*CP1*	*CP2*
T_{start} (p.u.)	11	9

The energized time of buses and lines are shown in Table 3 and Table 4.

The comparison of system generation capability curve is shown in Fig. 5. Clearly, if interdependencies between two systems are not considered, NBS generators can be restarted earlier and system generation capability can be restored faster. However, gas supply for gas fired generators may not be available because of the outage of electricity-driven compressors, and then the gas-fired generators cannot be restarted successfully. By considering interdependencies between power and gas transmission systems, gas pressure restoration dynamics is simulated, and gas supply for gas fired generators is restored, making the generator start-up procedure feasible.

Table 3. Energized time of all lines.

Line	T_{start} (p.u.)	Line	T_{start} (p.u.)	Line	T_{start} (p.u.)	Line	T_{start} (p.u.)	Line	T_{start} (p.u.)
1	2	*11*	6	*21*	5	*31*	4	*41*	8
2	3	*12*	6	*22*	6	*32*	4	*42*	8
3	2	*13*	6	*23*	6	*33*	4	*43*	3
4	2	*14*	5	*24*	6	*34*	41	*44*	1
5	3	*15*	4	*25*	4	*35*	35	*45*	5
6	3	*16*	15	*26*	20	*36*	6	*46*	7
7	4	*17*	6	*27*	7	*37*	6		
8	4	*18*	5	*28*	20	*38*	7		
9	5	*19*	5	*29*	7	*39*	7		
10	5	*20*	15	*30*	3	*40*	8		

Table 4. Energized time of all buses.

Line	T_{start} (p.u.)	Line	T_{start} (p.u.)	Line	T_{start} (p.u.)	Line	T_{start} (p.u.)
1	2	*11*	6	*21*	6	*31*	6
2	1	*12*	6	*22*	7	*32*	7
3	2	*13*	5	*23*	7	*33*	7
4	3	*14*	4	*24*	6	*34*	8
5	4	*15*	5	*25*	2	*35*	8
6	5	*16*	5	*26*	3	*36*	8
7	25	*17*	4	*27*	4	*37*	3
8	5	*18*	3	*28*	4	*38*	5
9	4	*19*	6	*29*	4	*39*	3
10	6	*20*	7	*30*	0		

6.3 Gas Dynamics

With inputting restoration time of electricity-driven compressors into PipelineStudio, gas supply restoration time for gas fired generators can be obtained by running PipelineStudio. Figure 4 shows the gas pressure curves generated by PipelineStudio. Natural gas nodes 20, 25 and 26, which correspond to $X_{reg}20$, $X_{reg}25$, $X_{reg}26$ respectively, provide gas to gas-fired generators. The pressure curves of natural gas nodes 20, 25 and 26 are shown in Fig. 4. It is assumed that the gas-fired generators can be started when the gas pressure reaches 6 MPa. The gas supply restoration time for gas nodes 20, 25 and 26 is shown in Table 5. Clearly, it can be seen that natural gas nodes 20, 25 and 26 take more than 100 min to restore the gas supply. Compared with restoration actions that generally take around 10 min in power system, gas supply restorations in gas system
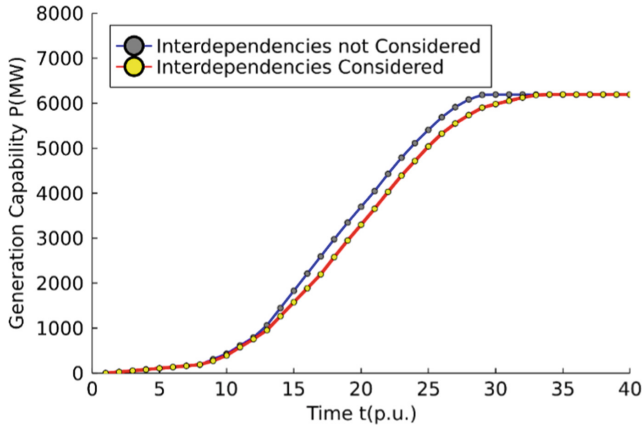
Fig. 5. Comparison of system generation capability curve

take more time because of larger time constant. Therefore, it is necessary to consider the gas dynamics for gas transmission system, which makes the strategy more feasible (Fig. 6).
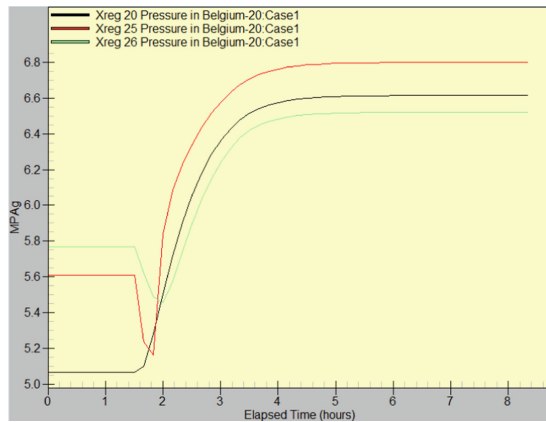
Fig. 6. Pressure curves of the gas supply nodes of the gas fired generators.

Table 5. Gas supply restoration time for gas nodes

Gas nodes	*20*	*25*	*26*
T (p.u.)	15	13	16

7 Conclusions

This paper proposed a new method to determine generator start-up strategy for inter-dependent power and gas transmission systems. Due to close interconnection between power and gas transmission systems, the restart of gas fired generators is influenced by gas transmission systems. It is important to restore the power supply of electricity-driven compressors as soon as possible during generator start-up stage, so that gas supply of gas fired generators would retore timely. Meanwhile, gas dynamics play an important role in gas supply restoration because of large time constant of gas system. The proposed method takes into account of interdependencies between two systems and gas dynamics, and case studies indicate that proposed method is effective.

References

1. Hou, Y., Ding, Y., Bao, M., et al.: Analysis of Texas blackout from the perspective of electricity-gas coupling and its enlightenment to the development of China's new power system[J/OL]. In: Proceedings of the CSEE. https://doi.org/10.13334/j.0258-8013.pcsee.212202. (in Chinese)
2. Bao, Z., Zhang, Q., Wu, L., et al.: Cascading failure propagation simulation in integrated electricity and natural gas systems. J. Mod. Power Syst. Clean Energy **8**, 961–970 (2020)
3. An, X., Sun, H., Zhang, X., et al.: Analysis and lessons of Texas power outage events on February 15, 2021. In: Proceedings of the CSEE, vol. 41, no. 10, pp. 3407–3415+3666 (2021). (in Chinese)
4. Sun, W., Liu, C.-C., Zhang, L.: Optimal generator start-up strategy for bulk power system restoration. IEEE Trans. Power Syst. **26**(3), 1357–1366 (2011)
5. Liu, Y.: Power System Restoration Theory and Technology, 1st edn. Science Press, Beijing (2014)
6. Liu, Y., Fan, R., Terzija, V.: Power system restoration: a literature review from 2006 to 2016. J. Mod. Power Syst. Clean Energy **4**(03), 332–341 (2016)
7. Lin, Y., Chen, B., Wang, J., et al.: A combined repair crew dispatch problem for resilient electric and natural gas system considering reconfiguration and DG islanding. IEEE Trans. Power Syst. **34**(4), 2755–2767 (2019)
8. Li, G., Yan, K., Zhang, R., et al.: Resilience-oriented distributed load restoration method for integrated power distribution and natural gas systems. IEEE Trans. Sustain. Energy **13**(1), 341–352 (2021)
9. Li, J., Xu, Y., Wang, Y., et al.: Resilience-motivated distribution system restoration considering electricity-water-gas interdependency. IEEE Trans. Smart Grid **12**(6), 4799–4812 (2021)
10. Li, X., Du, X., Jiang, T., et al.: Coordinating multi-energy to improve urban integrated energy system resilience against extreme weather events. Appl. Energy **309**, 18455 (2022)
11. Yun, J., Yan, Z., Zhou, Y., et al.: Multi-time collaborative restoration for integrated electrical-gas distribution system based on rolling optimization. CSEE J. Power Energy Syst., 1–13 (2020)
12. Qi, S., Wang, X., Shao, C., et al.: Resilience analysis of integrated electricity and natural gas energy system under extreme events. Power Syst. Technol. **3**(1), 41–51 (2019). (in Chinese)

13. Sang, M., Ding, Y., Bao, M., et al.: Resilience-based restoration strategy optimization for interdependent gas and power networks. Appl. Energy **302**, 117560 (2021)
14. Liu, C.-C., Liou, K.-L., Chu-Ron, F., et al.: Generation capability dispatch for bulk power system restoration: a knowledge based approach. IEEE Trans. Power Syst. **8**(1), 316–325 (1993)
15. Jiang, Y., Chen, S., Liu, C.-C., et al.: Blackstart capability planning for power system restoration. Int. J. Electr. Power Energy Syst. **86**, 127–137 (2017)
16. Yan, M.Q.: Engineering Analysis of Gas Transportation & Distribution, 1st edn. Petroleum Industry Publishing, Beijing (2007)
17. https://www.emerson.com/en-us/catalog/emerson-pipelinestudio
18. Sun, W., Liu, C.-C.: Optimal transmission path search in power system restoration. In: 2013 IREP Symposium Bulk Power System Dynamics and Control - IX Optimization, Security and Control of the Emerging Power Grid, Rethymnon, Greece (2013)
19. De Wolf, D., Smeers, Y.: The gas transmission problem solved by an extension of the simplex algorithm. Manag. Sci. **46**(11), 1454–1465 (2000)

Analysis Method of Fragmented Storage and Dynamic Loading of Distribution Network Topology Data

Sheng-zhi Yang[(✉)], Wei Cheng, Shi-jin Liu, Feng You, Feng Lin, Sen Peng, Shen-liang Wang, Sheng-sheng Li, and Cheng-long Xu

Nanjing NARI Information and Communication Technology Co., Ltd., Nanjing 211106, China
`yangshengzhi2@sgepri.sgcc.com.cn`

Abstract. Due to the huge amount of data in the distribution network, the topology analysis method directly based on database query has low performance problems. To meet the performance requirements of various business applications for topology analysis, current mainstream method is an in-memory analysis method based on full data caching. This method loads all topology data into memory building a memory-based topology network, and then topology analysis starts. Although this traditional method indeed solve performance problems, it also brings series of problem such as slow service startup (it takes a long time to load full data into memory), untimely cache update, and data inconsistency. This paper proposes a distribution network topology data storage scheme and a corresponding data dynamic loading-analysis method. Main features of the improved method are: Adopting slice-storage strategy, using single feeder as a data slice to store connection information of all conductive equipments outside the station; Using single station as a data slice to store all conductive equipments' connection information in the station room; Each data fragment stores "inter-chip connection device object" information to realize splicing of each data fragment. Based on storage scheme above, a dynamic loading method of topology data is proposed. This method can improve the speed of reading distribution network topology data so that topology analysis service does not need to load entire distribution network topology data into memory in advance. It also carries out dynamic loading of data on demand, reducing server's requirement for memory resources and service start-up time, while effectively circumventing the technical difficulties of real-time update of memory topology network.

Keywords: Power grid topology analysis · Sharded storage · Dynamic loading · Topology modeling

1 Introduction

At present, the distribution network topology data model is usually constructed based on the CIM topology model in the IEC 61970 standard or the SG-CIM topology model

formulated by the State Grid Corporation [1–5]. The traditional topological data storage method generally adopts database for structured storage, that is, terminal tables and the connection node tables are constructed in the database to describe the connection relationship between conductive devices [6]. This method usually takes a single device and a single terminal/connection node as storage unit, i.e., each device and each terminal/connection node corresponds to one record in the database [7]. However, the number of distribution network equipments in a provincial power company can reach tens of millions, which means corresponding terminals/connection nodes could only be larger [8]. Too many records in equipment terminal tables and connection node tables results in very low data query efficiency. In addition to the above storage model based on terminal tables and connection node tables, current production management system (PMS 2.0) of State Grid Corporation of China adopts the power grid GIS model to store power grid topology information. The advantage of this model is that it realizes the integrated management of GIS graphics and topology information of grid network and improve convenience of linkage maintenance of equipment graphics and topology information on the GIS platform [9, 10]. This storage solution, however, still faces the obstacle of too many data records and excessive resource usage, resulting in slow startup of the topology analysis service and low analysis efficiency.

On the premise of using the above storage method, in order to meet the performance requirements of business applications for topology analysis, the topology analysis service have to pre-load all topology data into the server memory to complete the construction of the topology network [11]. This greatly increases the consumption of server memory resources, and pre-loading topology data will make the service startup time incredibly long, reaching hours. Such service cannot be deployed in containers (such as Docker deployment), which is in line with the current system cloud deployment trend resulting in extremely inconvenience to system operation and maintenance. In addition, due to high update frequency of the distribution network, the topology data is usually updated daily. Therefore, real-time update of the memory topology network must be considered, which greatly increases the complexity of data processing and easily causes data inconsistency, thereby affects the performance and accuracy of topology analysis.

At present, some scholars and engineers at home and abroad are exploring the use of graph database to store power grid topology information to solve the problem of topology analysis efficiency of large-scale power grid data [12]. Graph database (GDB) is a technology for parallel analysis and processing of massive data on the Internet that has emerged in recent years. Its original concept comes from graph theory [13, 14]. Since the power system network topology can be expressed intuitively with graphs and can be easily accessed in parallel, the application of graph database to power system analysis can improve the computational efficiency of massive data processing in power systems [15]. Reference studies the power grid topology analysis based on graph database and verifies the advantages of the graph database relative to the relational database [16]. There is a problem in separation of equipment model and ledger information. Therefore, the author believes that the topology relationship of power grid equipment is the core information of power grid management and is inseparable from key information such as equipment resources, assets, graphics, etc., ensuring the consistency of these data is a key factor in designing data storage scheme for power grid equipment. Therefore, if

the equipment resources, assets, and graphics information are stored in the relational database while the topology information is stored in the graph database, it will have difficulty in ensuring transaction consistency during daily data entry and maintenance, meanwhile it is very easy to cause inconsistency between topology data and other data, which directly affects the subsequent data application [17]. Upon analysis above, in order to make the research results convenient for engineering application, this paper does not use graph database to store the grid topology information.

This paper focus on technical defects of current data loading mode with a condition of application of current topology data network and actual business requirements. In this case, a discovery shown up for distribution network data storage and real time data loading basing sharding strategy.

2   Main Thoughts

In order to solve problems above, this paper proposes a distribution network topology data storage method and dynamic data loading method based on sharding strategy. This method can greatly improve the loading efficiency of topology data compared with traditional methods. Through the on-demand dynamic loading strategy, the topology analysis service does not need to load entire distribution network topology data into memory in advance, which can effectively reduce the server hardware resource requirements and service start-up time. It also effectively circumvent the technical difficulties of the traditional method of real-time update of memory topology network, thus greatly improving the accuracy of topology analysis results.

In order to better illustrate the technical solution, the definitions or explanations of related technical terms are now given as follows:

Terminals and connection nodes: In the CIM/SG-CIM standard, the topology information model of power equipment is represented by the terminal-connection node model. Each conducting equipment (Conducting Equipment) contains several electrical points, called terminals (Terminal) [18]. The Connectivity Node is the resistance-free fusion point of the terminals of the conductive devices and the terminals are fused together through the connection nodes to express the topological connection between the devices [19, 20]. The relationship between conductive devices, terminals, and connection nodes can be simply summarized as: a conductive device contains one or more terminals; a connection node is fused with one or more terminals. As shown in Fig. 1, conductive device A contains two terminals: terminal A-1 and terminal A-2. Conductive device B contains two terminals: terminal B-1 and terminal B-2. Conductive device C contains two terminals: terminal C-1 and terminal C-2. Terminal A-2 and terminal B-1 are fused together through connection node a, and terminal B-2 and terminal C-1 are fused together through connection node b.

3   Topological Data Storage Model

The distribution network usually uses feeder as the daily management and operation unit. In applications such as distribution network operation and maintenance, fault handling, etc., distribution network topology analysis is divided into local topology analysis and
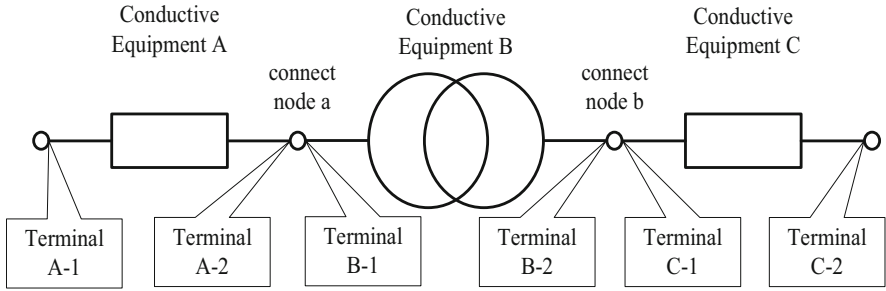
Fig. 1. Schematic diagram of terminals and connection nodes of conductive equipment.

global topology analysis. The data scope of local topology analysis is limited to one feeder or one station building; the data scope of global topology analysis is the entire distribution network in a certain area, thus topology tracking across feeders and stations is required. It can be seen that the smallest data loading scope for distribution network topology analysis is usually feeder and station. In view of the above characteristics, this paper adopts the sharding storage strategy, and divides the distribution network topology data into a series of data fragments based on feeder and station, and stores data fragments as units. Specifically, a single feeder is used as a data slice to store the connection information of all conductive devices within the feeder; a station is used as a data slice to store the connection information of all conductive devices in the station. The storage format of the above data fragments adopts the Json document format. The main advantage of this data sharding storage strategy is that a single feeder or a single station building is used as a data fragment for overall storage, which can easily realize the overall loading of feeder/station topology data, greatly improving the speed of topology data loading.

According to the above ideas, this paper designs two collections based on MongoDB database, namely: feeder topology collection and station topology collection. These two sets are similar to two tables in a relational database, and the details are as follows:

3.1 Feeder Topology Collection

The feeder topology collection stores the topology information of all feeders. The topology information of each feeder is stored as a Json document (Document) as a data fragment. The main fields of the document include "feeder ID", "equipment object array", "connection relationship array" and so on. in:

"Feeder ID" is the unique identifier of the feeder in the power grid production management system.

The "equipment object array" contains all out-of-station conductive device objects in the feeder, and each out-of-station conductive device object could also be describes as a JSONObject. In this paper, the above conductive device objects are classified into two categories: "ordinary device object" and "inter-slice connection device object". "Ordinary device object" refers to a device that is not connected to other data fragments and its attributes include device type, device ID, voltage level and other attributes commonly used in topology analysis; "Inter-slice connection device object" includes two types of

off-site liaison switches and internal and external connection lines. Among them, the off-site tie switch is a topological connection device between two feeders (as shown in Fig. 2). The switch is stored in the two connected feeder topology data slices at the same time, whose attributes include device type, device ID, etc. It has properties commonly used in topology analysis such as voltage level and the opposite side feederID, which records the ID of the other connected feeder. The connection line inside and outside the station is the connection device between the outlet connector in the station and the cable connector outside the station. It belongs to the topological connection device between the station and the feeder (as shown in Fig. 3). Its attributes used in topology analysis such as device type, device ID, and voltage level are widely used attributes. It also has the attribute "connected station ID", through which the connected station building is recorded.
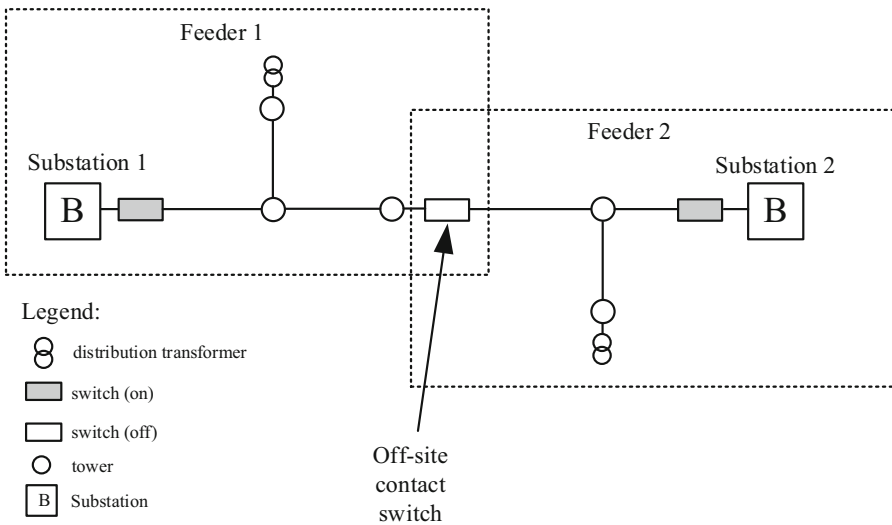
Fig. 2. Inter-segment connection equipment-off-site contact switch diagram.

The "connection relationship array" contains the connection relationship information between all out-of-station conductive devices in the feeder. Each connection relationship object can also be expressed within a JSONObject. Its properties include terminal ID, terminal sequence number, conductive device type, conductive device ID, and connection node ID properties. The terminal ID is the unique identification of the device terminal; the terminal sequence number refers to the sequence number of the terminal in the conductive device, which expresses the location information of the terminal in the conductive device to which it belongs; the conductive device type refers to the type code of the conductive device to which the terminal belongs; the conductive device ID refers to the unique identification of the conductive device to which the terminal belongs; connection node ID refers to the unique identification of the connection node to which the terminal is connected.

3.2 Station Topology Collection

The station topology collection stores the topology information of the equipment in the station of all power distribution station buildings. The topology information of each station is stored as a JSON document (Document) as a data slice. The main fields of the document include "station ID", "equipment object array" and "connection relationship array", etc. in:

"Station building ID" is the unique identification of the station building in the power grid production management system.

The "equipment object array" contains all the conductive device objects in the station building, and each conductive device object info in the station is also a JSONObject. In this paper, the above conductive device objects are divided into two categories: "ordinary device object" and "inter-slice connection device object". "Ordinary device object" refers to a device that is not connected to other data fragments, and its attributes include device type, device ID, voltage level and other attributes commonly used in topology analysis. "Inter-slice connection device object" refers to the outgoing connector in the station (as shown in Fig. 3). The outgoing line connector in the station is connected with the connecting line inside and outside the station. Its attributes include equipment type, equipment ID, voltage level and other attributes commonly used in topology analysis, and it has the "connected feeder ID" attribute, which records the connected feeder ID through this attribute.

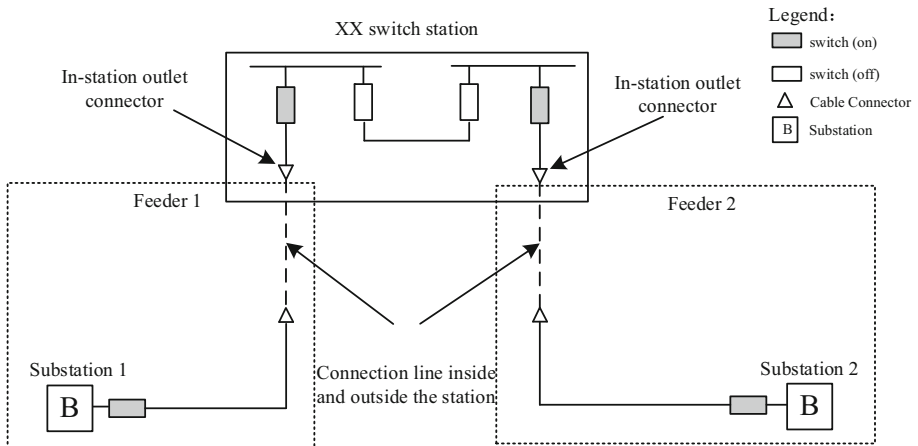**Fig. 3.** Inter-segment connection equipment - schematic diagram of outgoing connectors in the station.

The "connection relationship array" contains the connection relationship information between all conductive devices in the station building. Each connection relationship object is also a JSONObject. Its properties include terminal ID, terminal sequence number, conductive device type, conductive device ID, and connection node ID properties. The terminal ID is the unique identification of the device terminal; the terminal sequence number refers to the sequence number of the terminal in the conductive device, which

refers to the location information of the terminal in the conductive device to which it belongs; the conductive device type refers to the type code of the conductive device to which the terminal belongs; the conductive device ID refers to the unique identification of the conductive device to which the terminal belongs; connection node ID refers to the unique identification of the connection node to which the terminal is connected.

Compared with the traditional storage model based on terminal/connection node table, the above model has main advantages apparently: when performing topology data loading analysis, the traditional method needs to read a large number of records of devices and terminals/connection nodes with low loading speed while new method uses a single feeder or a single station building as a data slice for overall storage, which can realize the overall loading of feeder/station building topology data, which greatly improve the speed of topology data loading.

4 Dynamic Loading Method of Topology Data

Different types of topology analysis require different data range. Based on the above topology data model, which realizes each data fragment through the information of "inter-slice connection device object" stored in each data fragment, the splicing can form a complete distribution system topology network to progress topology analysis across feeders and stations. This method is applied before topology analysis to provide required topology data. By applying this method, the topology analysis service does not need to load entire distribution system topology data into the memory in advance. Instead, it loads the data fragments according to the needs of analysis, so as to realize the on-demand data loading, which greatly reduces the memory resources occupied in server. It also reduces the service startup time and facilitates the operation and maintenance of the service. At the same time, the technical problem of real-time updating of the topology network in memory is prevented. Main points of the method are as follows:

4.1 Initial Data Fragment Loading

Determine the initial data fragment according to the starting device of this topology analysis and load the data, which is used by the topology analysis service to build a topology network in memory. It would be accurate to be specifically divided into the following two situations:

Case 1: If the originating device is an off-site device, according to the feeder ID of originating device, the data fragment corresponding to the feeder to which it belongs is queried from the feeder topology data slicing;
Case 2: If the originating device is an in-station device, according to the station ID of originating device, the data fragment corresponding to the station to which it belongs is queried from the station topology data slicing.

If the data range required for this topology analysis is limited to the initial data fragment, no subsequent steps are required; if a larger data range is required, further steps should be taken.

4.2   Inter-shard Connection Device Object Query

Query all inter-shard connection device objects in initial data fragment. It would be accurate to be specifically divided into the following two situations:

Case 1: The type of initial data fragmentation is feeder, then query all off-site tie switches and two device objects of off-site and off-site connection lines in its device object array;

Case 2: The type of the initial data fragmentation is the station, then query all in-station outgoing connector objects in its device object array.

4.3   Directly Connected Data Fragment Loading

By using acquired connection device objects from shards, it would be utterly needed to determine the IDs of all connected data fragments and load the data for the topology analysis service to build a topology network in memory. It would be accurate to be specifically divided into the following three situations:

Case 1: The type of the connected device object between the shards is an off-site tie switch, then the ID of the connected feeder data fragment is determined according to its "opposite feeder ID" attribute, and then the corresponding data fragments of feeder is queried from the feeder topology set according to feeder ID;

Case 2: The type of the connected device object between shards is the connection line inside and outside the station, then the ID of the connected station building data fragment is determined according to its "connected station ID" attribute, and then the corresponding data fragments of station is queried from the station topology set according to station ID;

Case 3: The type of the connected device object between shards is the outgoing line connector in the station, then the ID of the connected feeder data fragment is determined according to its "connected feeder ID" attribute, and then the corresponding data fragments of station is queried from the station topology set according to feeder ID.

Those operations complete the loading of data fragments directly connected to the initial data fragment. If topology analysis needs to further expand the data range, step 4.4 is required to complete the loading of data fragments indirectly connected to the initial data fragment.

4.4   Indirectly Connected Data Fragment Loading

By using each connected data fragment acquired in step 4.3, it would be demanded to query the inter-shard connection device objects contained in order to find the ID of the connected data fragment according to the connection information of the inter-shard connection device, and complete the data loading. The connected data fragments can be loaded through circulation and iteration methods in the achievement to above ideas, until the loaded data range meets the requirements of this topology analysis.

4.5   In-Memory Topology Network Construction

After the completion of topology data loading, the topology network needs to be built in memory for topology analysis. Main step of the construction is to convert the topological connection information of the device into a topological analysis graph model.

The paper defines a graph model for topology analysis, which specifically includes a vertex model and an edge model.

The main attributes of the vertex include: "Vertex ID", "Vertex Device Type", "Vertex Device ID", "Terminal Connectivity". "Vertex ID" is the unique identifier of the vertex; "Vertex Device Type" represents the device type code of the device corresponding to the vertex; "Vertex Device ID" represents the unique identifier of the device corresponding to the vertex; "Terminal connection status" refers to the device corresponding to the vertex the interconnected state of all terminals. As an abstract representation of the electrical connectivity within devices, this property corresponds to the on and off states of switch-like devices, and can be used for topology tracking considering switch states. This property is an enumeration type, and each enumeration value represents a terminal connection state, for example: use the value "200" to indicate the state "the total number of device terminals is 2, and the No. 1 terminal and No. 2 terminal are not connected", in this case, the value can represent the "min" state of an ordinary two-terminal switch. For another example, the value "301" is used to indicate the state "the total number of equipment terminals is 3, in which the No. 1 terminal is not connected to the No. 2 terminal, the No. 1 terminal is connected to the No. 3 terminal, and the No. 2 terminal is not connected to the No. 3 terminal". This state value can represent the "left closed" state of a three-terminal bidirectional isolating switch. For another example, use the value "401" to indicate the state "The total number of equipment terminals is 4, of which the No. 1 terminal is not connected to the No. 2 terminal, the No. 1 terminal is not connected to the No. 3 terminal, the No. 1 terminal is not connected to the No. 4 terminal, and the No. 2 terminal is not connected. The terminal is connected to the No. 3 terminal, the No. 2 terminal is connected to the No. 4 terminal, and the No. 3 terminal is connected to the No. 4 terminal." This state value can represent the "BC" state of a four-terminal T-switch.

The main attributes of the edge include: "Edge ID", "Edge Device Type", "Edge Device ID", "Start Vertex ID", "Start Terminal", "End Vertex ID", "End Terminal". The "Edge ID" is the unique identifier of the edge; the edge is mainly divided into two types in the paper, the first type of edge is an abstract concept, which represents the connection relationship of the device, and the attributes of "Edge Device Type" and "Edge Device ID" are both Empty, the other type of edge represents line-type devices, such as lines, wires, cables, etc. Its "Edge Device Type" refers to the code of the corresponding device type, and "Edge Device ID" refers to the unique identifier of the corresponding device; "Start Vertex ID" Refers to the vertex ID connected to the head end of the edge; "Start Terminal" refers to the terminal number of the device connected to the head end of the edge, which is used to describe more precisely which terminal of the device the head end of the edge is connected to; The vertex ID of the end connection; "End Terminal" refers to the terminal number of the end connection of the edge, which is used to describe more precisely which terminal of the device the edge end is connected to.

In the paper, the dynamic topology tracking of the power grid is realized through the three attributes of the "Start Terminal", "End Terminal" and the "Terminal Connectivity" of the vertex. The base principle is: during the topology tracking process, it would generally started to trace from assumed that the end vertex (denoted as A) of a certain edge (denoted as E), to the end vertex (denoted as B). B represents a switch device, and the "End Terminal" of E is T, indicating that the connection position of E and B is at terminal T. Then, through the "Terminal Connectivity" (corresponding to the actual switch state) attribute of B, the connection relationship between other terminals of B and terminal T is obtained. To get the terminal connected to T, it would be needed to find the edge connected to B at the terminal according to the "start terminal" or "end terminal" attribute of the edge, and perform the next trace procedure; for the terminal that is not connected to T, it would stop tracking at the terminal.

The steps of constructing a memory topology network based on the graph model are as follows:

1) Vertex construction

The discovery first maps all conductive devices to vertices in the graph, creates corresponding vertices for each device, and assigns the device type and device ID to the "vertex device type" and "vertex device ID" attributes of the vertex respectively.

For switch devices, establish a mapping relationship between "switch state" and "terminal connection status", and convert the device's "switch state" information into the "terminal connection state" attribute of the vertex according to this relationship.

2) Establish the mapping relationship between the connection node and the device terminal, device body and vertex

At present, the topological connection information model of power grid equipment usually follows the CIM/SG-CIM standard, that is, the electrical connection relationship between devices is expressed by the connection relationship between device terminals and connection nodes. Thereby, the mapping relationship between the connection node and the device terminal and the device body can be established.

At the same time, there is a one-to-one correspondence between the device body and the vertices constructed in step (1). Therefore, through the above mapping relationship, the device terminal, device body, and vertex information connected to the connection node can be quickly searched, which provides support for the construction of the next edge.

3) Edge construction

The discovery constructs the edge of the graph structure according to the connection relationship between devices, and specifically constructs the corresponding edge according to the connection node. The basic method is: for each connected node, find the set of connected devices, denoted as S. If S contains a busbar (or running rod), then construct an undirected edge connected to the busbar (or running rod) for the rest of the equipment in S, and assign the "start vertex" of the edge according to the mapping

relationship in step (2). Attribute values such as ID, "Starting Terminal", "Ending Vertex ID", "Ending Terminal"; To the edge, and according to the mapping relationship in step (2), assign the edge's "start vertex ID", "start terminal", "end vertex ID", "end terminal" and other attribute values.

4) Compression of graph data

In order to reduce resource occupation and improve analysis efficiency, the discovery performs merging processing on specific vertices and edges to reduce the amount of graph data. Specifically, the vertices that meet the following requirement are processed: the vertex device type is a line type device (such as wire, cable, line) and the vertex is associated with two edges (volume equal to 2). The processing method is shown in Fig. 4: the vertex to be processed is V, the two edges associated with V are E1, E2, and V, E1, and E2 are merged into a new edge, which is recorded as E3. The "edge device type" and "edge device ID" attributes of E3 are taken from the "vertex device type" and "vertex device ID" of V; the first and last vertex information of E3 are respectively taken from the other side vertex information of E1 and E2. After completing the formation of the new edge E3, delete V, E1, E2.
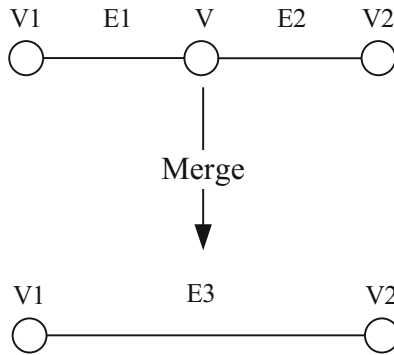
Fig. 4. Schematic diagram of vertex and edge merging processing.

To sum up, the main work of the topology network construction is to construct the vertex set and the edge set of the graph model according to the conductive device information. The detailed steps are as follows (as shown in Fig. 5):

1) Start traversing all conductive devices;
2) According to the information of the current conductive device, construct a graph vertex and add it to the set of graph vertices;
3) Query the topological connection information of the current conductive equipment, and update the mapping relationship table between connection nodes, terminals and equipment, hereinafter referred to as the connection node mapping table;
4) Repeat steps (2) to (3) till all conductive devices have been traversed;
5) Start traversing the connection node mapping table;

6) Obtain the list of conductive devices associated with the current connection nodes;

7) If conductive equipments contain busbars (or running rods), connect the rest of the equipment with busbars (or running rods), construct edges, and add a set of incoming edges;

8) If conductive equipments do not contain busbars (or running rods), connect these equipments in pairs to build an edge, and add a set of incoming edges;

9) Repeat steps (6) to (8) till all connected nodes have been traversed;

10) Merge vertices of line type devices and its associated two edges to complete the compression of the graph data;

11) Construct a graph structure using the set of nodes and edges generated above.
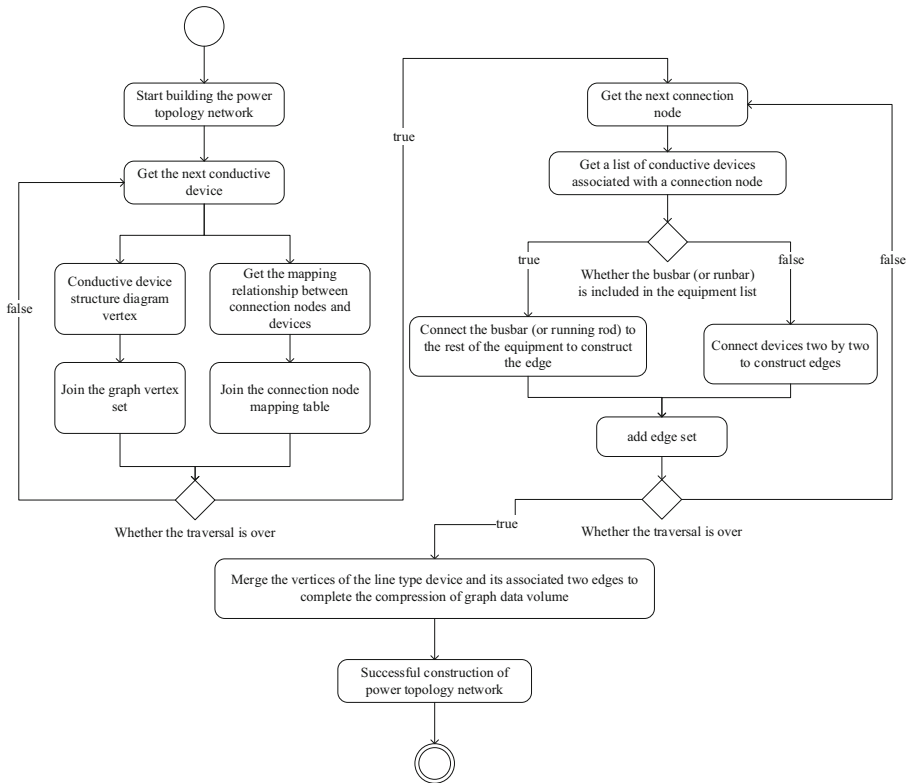

Fig. 5. Topological network construction process.

5 System Implementation and Experimental Analysis

The research results of this paper take the goal of being engineering and practical as consideration. On the premise of meeting the scale application of primary equipment in provincial power companies, it is planned to develop a lightweight integrated graph

analysis platform prototype system for power grid topology analysis and data retrieval. Its goal is to have the advantages of high running performance, small hardware resource occupation, and easy deployment, operation and maintenance.

5.1 System Scenario Data Loading

Take two typical topology analysis scenarios in distribution network application as examples:

1) Loading of complete topology data for a single feeder

For topology analysis scenarios within a single feeder, the complete topology data of the feeder needs to be loaded. The complete topology data includes all the conductive devices outside the station and the conductive devices in the station within the feeder. The specific process is as follows (as shown in Fig. 6):
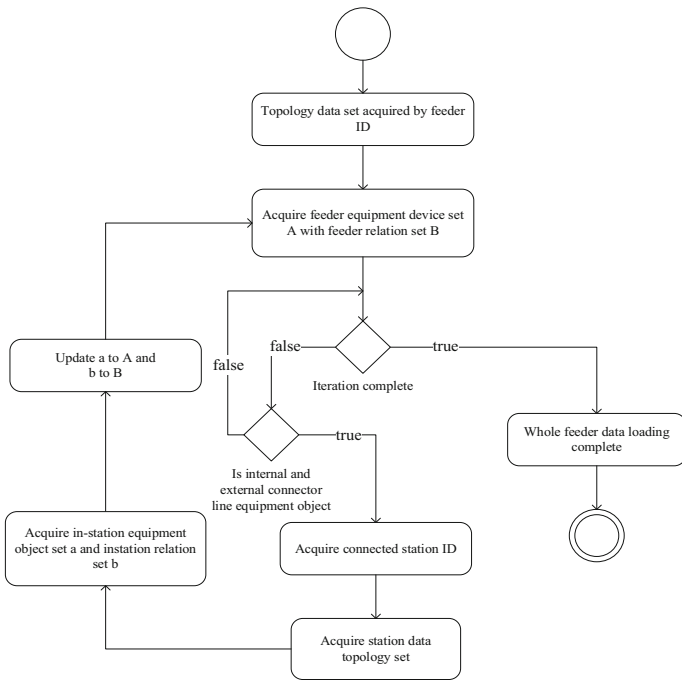

Fig. 6. Single feeder topology data loading process.

(1–1) Enter the feeder ID to be loaded;

(1–2) According to the input feeder ID, query the feeder topology collection in the database to obtain the device object array (referred as A) and the connection relation array corresponding to the feeder, in order to build a topology network for topology analysis service;

(1–3) Start traversing the device object array A;

(1–4) If the current equipment object type is an internal and external connection line object, obtain its "connected station ID" attribute, and query the station building topology set in the database according to this attribute to obtain the equipment object of the corresponding data block of the station building Arrays and connection relation arrays, which are used by the topology analysis service to build a topology network in memory;

(1–5) Repeat steps (1–1) to (1–4) till all device objects in the device object array A have been traversed;

(1–6) The process is complete.

2) Loading of contact feeder topology data

For the cross-feeder topology analysis scenario, in addition to complete topology data of the current feeder, it is also necessary to load the complete topology data of the feeder that is connected to the current feeder. The specific process is as follows:

(2–1) Enter the ID of the current feeder;

(2–2) According to the input current feeder ID, query the feeder topology set in the database to obtain the device object array of the data shard corresponding to the current feeder, denoted as B;

(2–3) Start traversing the device object array B;

(2–4) If the current equipment object type is an off-site tie switch object, obtain its "opposite feeder ID" attribute, and query the feeder topology set in the database according to this attribute to obtain the equipment object corresponding to the data block of the opposite feeder array and connection relation array, which are used by the topology analysis service to build a topology network in memory;

(2–5) Repeat step (2–1) to (2–4) till all device objects in the device object array B have been traversed;

(2–6) The process is complete.

5.2 Experiment and Result Analysis

In order to verify the specific advantages of the analysis mode based on fragmented storage and dynamic loading of topology data proposed in this paper, the research team developed a power grid GIS one-picture display system, and conducted related experiments based on power grid topology data of a provincial power company of the State Grid. The total number of equipment with grid topology (including low-voltage equipment) is more than 200 million. The research results in this paper are compared with the load topology data based on relational database Oracle 11 g query and the load analysis method based on fully cached topology data. In order to obtain accurate experimental results, these three topology data loading modes use the same topology search algorithm and the same topology data loading algorithm, the same amount of device data and are deployed on the same hardware server (operation system: CenterOS 7.7; memory: 1T; main frequency: 2.2 GHz). Main indicators as startup time, service memory usage, topology analysis time, and containerized deployment Equal pros and cons would be thoroughly investigated and compared.

Table 1 shows the resource occupied by different topology data loading modes under the situation of using same number of devices. It can be seen from the table that with the increase of devices, the shard dynamic loading mode and the relational database loading mode occupy less memory resources, and the service startup time is shorter, while the full topology data loading mode service startup time and memory usage size with further increase of devices. Currently mainstream containerized deployment has harsh requirements on the server's memory.

Table 1. Resource consumption of multi-mode startup.

The number of devices/10 million	Data loading mode	Service startup time/S	Service startup occupies memory/G
0.0326	A	0.89	0.1
	B	10	0.58
	C	0.83	0.1
0.132	A	0.88	0.1
	B	63.2	2.01
	C	0.84	0.1
0.587	A	0.86	0.1
	B	890.6	8.3
	C	0.79	0.1
1.235	A	0.73	0.1
	B	1278.7	12.8
	C	0.76	0.1
5.648	A	0.87	0.1
	B	5163.8	64
	C	0.88	0.1

Note: A - Relational data loading mode; B - Fully cached data loading mode; C - Shard dynamic loading mode.

Table 2 shows the situation of unconditional topology search in multiple modes. It can be seen that with the increase of the number of search devices, the total search time gradually increases. The shard dynamic loading mode used in this paper occupies less memory for topology search than the other two loading modes. When the number of participating topology searches reaches the scale of 10,000, the average device search time in the shard dynamic loading mode shows a steady increase.

To sum up, compared with the traditional topology data loading mode, the research results in this paper have the advantages of small memory footprint, fast service startup, high search efficiency, and unlimited containerized deployment when dynamically loading topology data and analyzing and searching for more than million-level data would take the advantage.

Table 2. Multimodal topology search data.

The number of devices/10 million	Data loading mode	Search time/s	Service search occupies memory/G	Average search time per device/10^{-5}s
0.0326	A	13.63	0.8	0.418
	B	0.386	0.763	0.118
	C	0.392	0.3	0.120
0.132	A	54.32	1.5	4.115
	B	1.55	0.9	0.117
	C	1.59	0.3	0.120
0.587	A	396.25	6	6.750
	B	9.91	3.6	0.169
	C	9.96	2	0.170
1.235	A	689.73	12	5.580
	B	21.93	6.5	0.178
	C	22.04	5	0.178
5.648	A	3456.41	20	6.120
	B	138.89	16	0.246
	C	138.93	8	0.246

Note: A - Relational data loading mode; B- Full cache data loading mode; C - Shard dynamic loading mode;

6   Conclusion

In comparison of other control group, the method proposed in this paper has the following technical effects:

(1)   Using a single feeder or a single station building as a data block for overall storage can easily realize the overall loading of feeder/station topology data, which greatly improves the speed of topology data reading.

(2)   By applying the topology data dynamic loading method proposed by the present discovery, the topology analysis service does not need to load the entire distribution network topology data into the memory in advance, but dynamically loads the data in blocks according to the needs of the topology analysis, which greatly reduces the occupation to the memory meeting resource requirements easier, and reduce the service startup time, which is convenient for service operation and maintenance. At the same time, the technical problem of real-time updating of the memory topology network is prevented.

References

1. Shuyong, C., Shufang, S., Lanxin, L., et al.: A review of smart grid technology. Power Grid Technol. **33**(8), 1–7 (2009)
2. Bin, W., Guangyu, H., Shufeng, D., et al.: Self-generation of full graphics and 3D visualization based on CIM. Automat. Electr. Power Syst. **34**(4), 55–58 (2010)
3. Shuming, S., Feng, L.: An automatic generation technology of plant and station wiring diagram based on CIM. Automat. Electr. Power Syst. **32**(21), 4 (2008)
4. Jianmin, Z., Jian, L.: Automatic generation of distribution one-line diagram based on CIM/SVG and object-oriented. Automat. Electr. Power Syst. **32**(22), 61–65 (2008)
5. Meng, L., Lijun, Q., Qing, G., Cuijuan, H.: Power grid topology analysis based on CIM model. Electr. Power Sci. Eng. **27**(09), 18–22 (2011)
6. Ying, Z., Yan, H.: GIS power grid topology and its implementation in ORACLE database. Zhejiang Electr. Power **29**(12), 48–50 (2010)
7. Tianhua. L.: GIS-based substation equipment management and power grid topology analysis. Harbin Engineering University (2009)
8. Zhan, C., Crane, A.D., Bullock, A.J.: Power transmission and distribution systems:
9. Guangyi, L., et al.: "one map of power grid" spatiotemporal information management system. Electr. Power Inf. Commun. Technol. **18**(01), 7–17 (2020)
10. Yang, L., Lisheng, L., Yong, S., et al.: A method and system for verifying topological data of distribution network: cn112597634a (2021)
11. Zhou Yuncheng, X., Zailin, T.P.: Research on the storage and maintenance method of distribution network GIS data model based on CIM. Power Syst. Protect. Control **40**(15), 104–109 (2012)
12. Hua, H., Jiangpeng, D., Yi, W., et al.: Construction of power grid CIM/E model and network topology based on graph database. Automat. Electr. Power Syst. **43**(22), 8 (2019)
13. TinkerPop Documentation [EB/oL] (2 April 2019). http://tinkerpop.apache.org/docs/current/reference/#intro
14. Ziyu, L.I.N.: Principles and Applications of Big Data Technology. People 's Posts & Telecomm-unications Publishing House, Beijing (2015)
15. Guangyi, L., Kewen, L., Di, S., et al.: Graph computation and its applications in smart grid. In: IEEE International Congress on Big Data (Big Data Congress), June 25–30, pp. 507–510. Hon01ulu, USA (2017)
16. Aihua, Z., Hongbin, Q., Kunlun, G., et al.: Research on power grid topology analysis technology based on graph database. Power Inf. Commun. Technol. **16**(8), 5 (2018)
17. Houming, J., Hao, S., Zhen, K.: A fast power network topology analysis method based on graph database. Comput. Syst. Appl. **21**(12), 173–176 (2012)
18. Yan, G., Ming, D., Rui, B., Yin, D., Wei, Y.: Graphical modeling and analysis of power grid topology based on CIM. J. Hefei Univ. Technol. (Natural Science Edition) **33**(05), 657–660 (2010)
19. Juan, W., Yanghong, T., Kejun, L.: Research and application of dynamic topology analysis method of distribution network based on node branch link matrix. Comput. Appl. Res. **34**(05), 1463–1467 (2017)
20. Ziming, Y., Yan, X.: Power system topology optimization combining deep reinforcement learning and domain knowledge. Power Syst. Automat. **46**(1), 9 (2022)

Optimal Dispatch of Integrated Energy System with Low-Carbon Complementation of Source Side and Load Side

Zhongqi Jiang[1(✉)], Xiwei Zheng[2], and Qiang Chen[1]

[1] Anhui Province Key Laboratory of Renewable Energy Utilization and Energy Saving, Hefei University of Technology, Hefei, China
hfutjiangzhongqi@163.com

[2] Anhui Electric POWER Transmission and Transformation Co, Hefei, China

Abstract. Under the background of carbon peaking and carbon neutrality, the energy industry is faced with the severe conflict between the pressure of carbon emissions reduction and the cost of energy supply. An optimal dispatching method of integrated energy system with low-carbon complementation of source side and load side under a ladder-type carbon trading mechanism is proposed in this paper. Firstly, the model of carbon capture in source side and the model of auxiliary devices and integrated demand response in load side are introduced. Then, the ladder-type carbon trading mechanism is introduced, and an optimal dispatching model aiming at the minimum total operating cost of the integrated energy system is established. Through the case study, it is verified that under different carbon trading mechanisms, the optimal dispatching model can effectively weaken the peak-valley contradiction of the electric and heating load and reduce carbon emissions, and the model under ladder-type carbon trading mechanism can achieve full wind power consumption, which has better low-carbon economic characteristics.

Keywords: Integrated energy system · Low-carbon economy dispatching · Carbon capture · Integrated DEMAND response · Carbon trading mechanism

1 Introduction

Global warming has become one of the major problems facing human society. Developing low-carbon economy is of great significance to sustainable development. Thermal power generation is the main source of carbon emissions at present, accounting for more than 1/3 of the total carbon emissions [1]. Therefore, in the context of carbon peaking and carbon neutrality, it is increasingly important to develop renewable energy power generation and gas-fired power generation to replace coal-fired power generation.

The reduction of power plant carbon emissions from the source side can be solved from two aspects. First, from the perspective of technology, carbon capture equipment and renewable energy generation can be introduced. Secondly, from the perspective of policy, carbon trading mechanism should be established to guide the increasing output

of cleaning units [2]. As the proportion of clean energy power generation increases, its strong uncertainty also increases the peak-valley difference of equivalent load of the system, which aggravates the peak load adjustment pressure of the power grid and also increases the reserve capacity of thermal power units, making it impossible to reduce the start-up of high-carbon units and seriously restricting the consumption of renewable energy. Therefore, a comprehensive consideration of the uncertainty of renewable energy and the characteristics of carbon capture power plants makes the coordinated operation of the above two become a new idea of low-carbon economic dispatch [3, 4].

With the rise of the idea of Energy Internet, the coupling of power grid with other energy forms such as heat network and the construction of Integrated Energy System (IES) has become a hot research topic. As an important part of IES, Combined Heat and Power (CHP) plant effectively improve energy efficiency [5], but are still limited by the traditional operation of " determining electricity by heat ". Generally, there are two solutions: One is Thermal Energy Storage (TES), and the other is Demand-Side Management (DSM) [6]. The effects of TES and DSM do not overlap, but are complementary [7, 8].

Current studies mainly focus on the scheduling of carbon capture or electricity load demand response in a single energy system. There are still the following research gaps in this field: 1) Most of the current literatures use carbon trading mechanism with fixed carbon price, which fails to fully tap the guiding value of carbon trading market, resulting in low weight of carbon emission reduction in optimization objectives; 2) Few literatures have carried out detailed verification of the source side and load side coordination of carbon capture thermal power plants and integrated demand response, and explored their low-carbon performance under different carbon trading mechanisms.

Therefore, this paper proposes an optimal dispatch method of integrated energy system with low carbon complementary source side and load side under the ladder-type carbon trading mechanism. Firstly, the model of carbon capture in source side and the model of auxiliary devices and integrated demand response in load side are analyzed. Then, an optimization dispatch model under the ladder-type carbon trading mechanism was established with the objective function of minimizing the total operating cost of the integrated energy system within the scheduling cycle. Commercial optimization software CPLEX was used to solve the problem. Through example analysis, it is verified that under different carbon trading mechanisms, the model can optimize the electric and heating load curve, weaken the peak-valley contradiction of the electric and heating load, achieve full wind power consumption and reduce carbon emissions. The combination of ladder-type carbon trading mechanism, carbon capture and integrated demand response can better meet the requirements of economy and low carbon.

2 Low-Carbon Complementary Model of Source Side and Load Side

2.1 Structural of the System with Low-Carbon Complementation of Source Side and Load Side

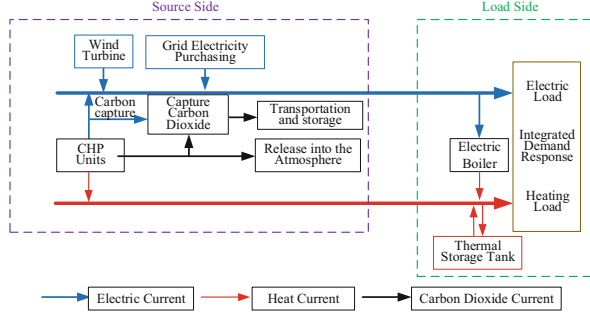The renewable energy generation in the system only considers wind power, and the system structure is shown in Fig. 1.

Fig. 1. Structural diagram of an integrated energy system

2.2 Model of the Carbon Capture in Source Side

Carbon Capture model of CHP Units. In the process of gas power generation, CHP units can use waste heat recovery device for external heating, which improves the economic performance and efficiency of the whole syste [9]:

$$\begin{cases} P_{\text{CHP}i,t}^{\text{e}} = P_{gi,t}\eta_{\text{GT}}^{\text{e}} \\ P_{CHPi,t}^{\text{h}} = P_{gi,t}\eta_{\text{GT}}^{\text{h}} \end{cases} \tag{1}$$

where i is the serial number of CHP unit, is the serial number of the period, $P_{gi,t}$ is the natural gas power the CHP unit consumed; $P_{\text{CHP}i,t}^{\text{e}}$、$P_{\text{CHP}i,t}^{\text{h}}$ respectively are the electrical power and heating power of CHP unit; $\eta_{\text{GT}}^{\text{e}}$、$\eta_{\text{GT}}^{\text{h}}$ represent the gas-electric and gas-heat conversion efficiency of the CHP unit, respectively.

The carbon capture model is as follows:

$$E_{\text{CHP}i,t}^{\text{CO}_2,\text{total}} = e_g P_{gi,t}\Delta t \tag{2}$$

$$E_{\text{CHP}i,t}^{\text{CO}_2,cap} = \eta_{\text{CHP}i,t} E_{\text{CHP}i,t}^{\text{CO}_2,\text{total}} \tag{3}$$

$$P_{\text{CHP}i,t}^{\text{R}} = \lambda_{\text{CHP}}^{cap} E_{\text{CHP}i,t}^{\text{CO}_2,cap} / \Delta t \tag{4}$$

$$P_{\text{CHP}i,t}^{\text{CO}_2,cap} = P_{\text{CHP}i,t}^{\text{R}} + P_{\text{CHP}}^{\text{B}} \tag{5}$$

$$P_{\text{CHP}i,t}^{\text{e,J}} = \begin{cases} P_{\text{CHP}i,t}^{\text{e}}, & \text{Unit } i \text{ is not equipped with carbon capture} \\ P_{\text{CHP}i,t}^{\text{e}} - P_{\text{CHP}i,t}^{\text{CO}_2,cap}, & \text{Unit } i \text{ is equipped with carbon capture} \end{cases} \tag{6}$$

where $E_{\text{CHP}i,t}^{\text{CO}_2,\text{total}}$ is the total carbon emission of the CHP unit during the period t; e_g is the parameter of carbon emission intensity per unit of natural gas; Δt is the duration of a unit time range and the value is 1 h; $E_{\text{CHP}i,t}^{\text{CO}_2,cap}$ is the carbon emission captured by the CHP unit installed with carbon capture device; $\eta_{\text{CHP}i,t}$ is the carbon capture rate of the CHP unit installed with carbon capture device; $P_{\text{CHP}i,t}^{\text{R}}$ is the operating energy

consumption of CHP unit caused by carbon capture; λ_{CHP}^{cap} is the energy consumption of capturing per unit of CO_2; $P_{CHPi,t}^{CO_2,cap}$ is the total energy consumption of CHP unit caused by carbon capture; P_{CHP}^{B} is the fixed energy consumption of carbon capture; $P_{CHPi,t}^{e,J}$ is the net output of CHP unit.

2.3 Model of Auxiliary Device and Integrated Demand Response in Load Side

Combining the integrated demand response with auxiliary device on load side can fully develop advantage of multi-energy coupling characteristic in IES, exploit the regulation ability of the heating load, smooth the electric load curve, and weaken the opposite peak-valley characteristics of electric and heating load.

Model of Thermal Storage Tank. The model of thermal storage tank was referred to Ref [10].

Model of Electric Boiler. The electric boiler works in the high wind power generation period, uses the wind power to produce heat power and reduces the electric-heat coupling output undertaken by CHP units meanwhile, which further expands the space for wind power to supply electric load. The model of electric boiler was referred to Ref [10].

Electricity Demand Response. Electric load consists of fixed load and flexible load in this study. The electric flexible load is divided into two types: time-shifting load and interruptible load

$$P_t^{DR} = P_t^L + P_t^{TSL} - P_t^{IL} \tag{7}$$

where P_t^{DR} is the electric load power after demand response; P_t^L is the electric load power before demand response; P_t^{TSL} is the time-shifting electric load power, positive when moving into this period, negative when moving out; P_t^{IL} is the interruptible electric load power in period t.

The characteristic of time-shifting load is that the total amount of electricity consumption remains unchanged and the time of electricity consumption can be flexibly changed, which can be described by the following formula:

$$P_{t,min}^{TSL} \leq \left| P_t^{TSL} \right| \leq P_{t,max}^{TSL} \tag{8}$$

$$\sum_{t=1}^{T} P_t^{TSL} = 0 \tag{9}$$

where $P_{t,max}^{TSL}$ and $P_{t,min}^{TSL}$ are the maximum and minimum values of the time-shifting load power during period t.

Interruptible load is a part of the load that the user can interrupt to relieve the power supply pressure during periods of power shortage or high electricity price. It can be described as:

$$0 \leq P_t^{IL} \leq P_{t,max}^{IL} \tag{10}$$

where $P_{t,max}^{IL}$ is the maximum interruptible load power in period t.

Thermal Demand Response. Heating load consists of fixed load and time-shifting load in this study.

$$H_t^{DR} = H_t^L + H_t^{TSL} \tag{11}$$

where H_t^{DR} is the heating load power after demand response; H_t^L is the heating load power before demand response; H_t^{TSL} is the time-shifting heating load power, positive when moving into this period, negative when moving out.

Time-shifting heating load meets the following constraints:

$$0 \le \left| H_t^{TSL} \right| \le H_{t,max}^{TSL} \tag{12}$$

$$\sum_{t=1}^{T} H_t^{TSL} = 0 \tag{13}$$

where $H_{t,max}^{TSL}$ is the maximum interruptible heating load power in period t.

3   Ladder-Type Carbon Trading Mechanism

The regulatory authorities issue free carbon emission quota to IES. When the carbon emission generated by IES is lower than the quota, the remaining quota can be sold in the carbon trading market; otherwise, the excess quota needs to be purchased. The unit carbon trading price of traditional carbon trading mechanism is fixed, and its ability to restrain carbon emissions is limited. Compared with the traditional carbon trading mechanism, the ladder-type carbon trading mechanism has a stricter constraint effect on carbon emissions.

In the ladder type carbon trading mechanism proposed in this paper, the part of carbon emissions beyond carbon quota is divided into multiple carbon emissions interval, carbon trading price of each interval is incremental. It means that the more carbon emissions exceed the carbon quota, the price of carbon trading increases accordingly.

The actual carbon emissions E_{CO_2}, carbon quota E_c and carbon trading cost C_{CT} are calculated as follows:

The carbon emission source is CHP units and grid electricity purchasing. The carbon emission is captured and sequestered by carbon capture device. The actual carbon emission of IES (including N_g units) within a dispatching cycle is calculated according to Eq. (14):

$$E_{CO_2} = \sum_{t=1}^{T} \sum_{i=1}^{N_g} (E_{CHP i,t}^{CO_2,total} - E_{CHP i,t}^{CO_2,cap}) + e_b \sum_{t=1}^{T} P_t^b \Delta t \tag{14}$$

$$E_c = \delta_h \sum_{t=1}^{T} \sum_{i=1}^{N_g} \left(\varphi P_{CHP i,t}^e + P_{CHP i,t}^h \right) \Delta t + \delta_e \sum_{t=1}^{T} P_t^b \Delta t \tag{15}$$

$$C_{CT} = \begin{cases} c_0(E_{CO_2} - E_c), & 0 \le E_{CO_2} \le E_c \\ c(E_{CO_2} - E_c), & E_c < E_{CO_2} \le E_c + v \\ cv + c(1 + \alpha)(E_{CO_2} - E_c - v), & E_c + v < E_{CO_2} \le E_c + 2v \\ c(2 + \alpha)v + c(1 + 2\alpha)(E_{CO_2} - E_c - 2v), & E_{CO_2} > E_c + 2v \end{cases} \tag{16}$$

where e_b is the parameter of carbon emission intensity per unit electricity purchased from the grid; E_c is the carbon emission quota within a dispatching cycle [1]; δ_h is the carbon emission quota coefficient of CHP units; δ_e is the carbon emission quota coefficient of grid electricity purchasing; φ is the conversion coefficient of electric power to heating power of CHP unit [2]; C_{CT} is the carbon trading cost of a dispatching cycle; c_0 is the price of selling excess carbon emission allowances; c is the carbon trading base price; α is the ladder growth rate of carbon trading price; v is the upper limit of every interval of carbon emissions.

4 Optimal Dispatch Model of Integrated Energy System

4.1 Model of Stochastic Wind Power

The research shows that wind speed follows Weibull distribution. According to the wind speed probability density function (PDF) and the relationship between wind power output and wind speed, the wind power output PDF can be deduced as [10]:

$$f_o(P_t^W) = \begin{cases} (khv_{in}/\gamma P_*)\left[((1 + hP_t^W/P_*)v_{in})/\gamma\right]^{k-1} \times \exp\left\{-\left[((1 + hP_t^W/P_*)v_{in})/\gamma\right]^k\right\} \\ P_t^W \in [0, P_*] \\ 0, \qquad otherwise \end{cases} \tag{17}$$

$$h = (v_*/v_{in}) - 1 \tag{18}$$

where P_t^W is the output power of wind power generation, which is an uncertain quantity; k is the shape coefficient, which describes the shape of wind speed PDF; P_* is the rated output power of the wind turbine; v_{in} is the cut-in wind speed; v_* is rated wind speed; γ is the scale coefficient, reflecting the average wind speed of a certain period.

4.2 Objective Function

The total operating cost of IES consists of the following parts:

$$\min F = \min(C_b + C_g + C_{CT} + C_{TY} + C_W + C_{IL}) \tag{19}$$

where F is the total cost of the dispatching model; C_b is the cost of purchasing power from the grid; C_g is the cost of generating power and heat and providing reserve capacity for CHP units; C_{CT} the carbon trading cost; C_{TY} is the cost of CO_2 transportation and storage; C_W is the wind abandoning penalty cost and C_{IL} is the compensation cost of interruptible power load.

$$C_b = \sum_{t=1}^{T} c_t^b P_t^b \Delta t \tag{20}$$

where c_t^{b} is the price of grid electricity in period t; P_t^{b} is the electricity purchased from the grid in period t.

$$C_{\mathrm{g}} = \sum_{t=1}^{T} \sum_{i=1}^{N_{\mathrm{g}}} (\frac{P_{gi,t}\Delta t}{Q_{\mathrm{gas}}}\lambda_t^{\mathrm{g}} + C_i^{\mathrm{open}} S_{i,t} + r_{gi}R_{\mathrm{CHP}i,t}\Delta t) \tag{21}$$

where Q_{gas} is low calorific value of natural gas; λ_t^{g} is natural gas price; C_i^{open} is the startup cost of the CHP unit; $S_{i,t}$ is the startup variable of the CHP unit in period t, where 1 represents startup and 0 represents shutdown; r_{gi} is the reserve cost of the CHP unit; $R_{\mathrm{CHP}i,t}$ is the reserve capacity of the CHP unit during the period t.

$$C_{\mathrm{TY}} = \sigma_{\mathrm{ty}}(\sum_{t=1}^{T} \sum_{i=1}^{N_{\mathrm{g}}} E_{\mathrm{CHP}i,t}^{\mathrm{CO_2,cap}}) \tag{22}$$

where σ_{ty} is the price of transportation and storage of per unit carbon dioxide.

$$C_{\mathrm{W}} = \sum_{t=1}^{T} K_{\mathrm{W}} P_{\mathrm{wq},t}\Delta t \tag{23}$$

$$P_{\mathrm{wq},t} = E(P_t^{\mathrm{W}}) - P_{\mathrm{w},t} \tag{24}$$

where K_{W} is the penalty cost per unit of wind abandoning volume; $P_{\mathrm{wq},t}$ is the wind abandoning power; $E(P_t^{\mathrm{W}})$ is the expected wind power output; $P_{\mathrm{w},t}$ is the actual consumption of wind power.

$$C_{\mathrm{IL}} = \sum_{t=1}^{T} K_{\mathrm{IL}} P_t^{\mathrm{IL}}\Delta t \tag{25}$$

where K_{IL} is the compensation coefficient of interrupted electrical load.

4.3   Operational Constraints

a.   Power balance constraints:

$$\sum_{i=1}^{N_{\mathrm{g}}} P_{\mathrm{CHP}i,t}^{\mathrm{e,J}} + P_{\mathrm{w},t} + P_t^{\mathrm{b}} = P_t^{\mathrm{DR}} + P_{\mathrm{eb},t} \tag{26}$$

$$\sum_{i=1}^{N_{\mathrm{g}}} P_{\mathrm{CHP}i,t}^{\mathrm{h}} + H_{\mathrm{DC},t}^{\mathrm{HSS}} - H_{\mathrm{CH},t}^{\mathrm{HSS}} + H_{\mathrm{eb},t} = H_t^{\mathrm{DR}} \tag{27}$$

where $P_{\mathrm{eb},t}$ is the power consumed by the electric boiler.

b. CHP units constraints:

CHP units operation constraints are shown in Ref [12].
Carbon capture constraints are shown in (2)–(6).

c. Thermal storage tank constraints are shown in Ref [10].
d. Electric boiler constraints are shown in Ref [10].
e. Wind power output constraint:

$$0 \leq P_{w,t} \leq E(P_t^W) \tag{28}$$

f. Reserve capacity constraint: Due to the inclusion of wind power random variable, the reserve capacity is an uncertain constraint condition, and Chance Constrained Programming (CCP) is used to deal with the uncertain problem.

$$P_{rob} \left\{ \sum_{i=1}^{N_g} R_{CHPi,t} \geq E\left(P_t^W\right) - P_t^W \right\} \geq \alpha \tag{29}$$

where α is the artificially set confidence, which can balance economy and reliability; P_t^W is the wind power output during period t, which is an uncertain quantity. The method how to transform this chance constraint into a deterministic constraint refers to Ref [11].

g. Integrated demand response constraints are shown in (7)–(13).

5 Model Solving

5.1 Probabilistic Serialization Processing of Wind Power

After the PDF of wind power output is discretized by using Sequence operation theory (SOT), opportunity constraint can be transformed into deterministic constraint. The probability sequence can be expressed as:

$$\sum_{i=0}^{N_a} a(i) = 1, a(i) \geq 0 \tag{30}$$

The length of probability sequence is:

$$N_{a,t} = \left[\frac{P_{max,t}^W}{q} \right] \tag{31}$$

where q is the discretization step size; $P_{max,t}^W$ is the maximum possible wind power. The probabilistic sequence obtained by discretization has a total of $N_{a,t}+1$ states, of which the output of the $u_{a,t}$ state is $u_{a,t}q$, and the corresponding probability is $a(u_{a,t})$.

According to the PDF of wind power output $f_o(P_t^W)$, the corresponding probability sequence $a(u_{a,t})$ can be obtained:

$$a(u_{a,t}) = \begin{cases} \int_0^{q/2} f_o(P_t^W) dP_t^W, & u_{a,t} = 0 \\ \int_{u_{a,t}q-q/2}^{u_{a,t}q+q/2} f_o(P_t^W) dP_t^W, & 0 < u_{a,t} < N_{a,t} \\ \int_{u_{a,t}q-q/2}^{u_{a,t}q} f_o(P_t^W) dP_t^W, & u_{a,t} = N_{a,t} \end{cases} \tag{32}$$

Wind power output expectation $E(P_t^W)$ can be obtained from the probability sequence:

$$E(P_t^W) \sum_{u_{a,t}=0}^{N_{a,t}} u_{a,t}q \cdot a(u_{a,t}) \tag{33}$$

5.2 Handling of Chance Constraints

To deal with chance constraint (29), a 0–1 variable $\omega_{u_{a,t}}$ is introduced as:

$$\omega_{u_{a,t}} = \begin{cases} 1, & \sum_{i=1}^{N_g} R_{\mathrm{CHP}i,t} \geq E(P_t^W) - u_{a,t}q \\ 0, & \text{otherwise} \end{cases}, \forall t, u_{a,t} = 0, 1, ..., N_{a,t} \tag{34}$$

Formula (34) represents: in any period, when the total reserve capacity is not less than the difference between the power which wind power supplies to load and its expected value, the decision variable is 1, otherwise 0. Thus, opportunity constraint is transformed into certainty constraint.

In combination with the wind power output probability sequence, (29) can be transformed into (35):

$$\sum_{u_{a,t}=0}^{N_{a,t}} \omega_{u_{a,t}} a(u_{a,t}) \geq \alpha \tag{35}$$

Since the expression in (34) is incompatible with the solution format of mixed integer linear programming, (36) is used to replace (34):

$$\left(\sum_{i=1}^{N_g} R_{\mathrm{CHP}i,t} - E(P_t^W) + u_{a,t}q \right) \Big/ \tau \leq \omega_{u_{a,t}} \leq 1 + \left(\sum_{i=1}^{N_g} R_{\mathrm{CHP}i,t} - E(P_t^W) + u_{a,t}q \right) \Big/ \tau \tag{36}$$

where τ is an extremely large positive number.

(35) and (36) can replace (29) to convert the chance constraint of reserve capacity into deterministic constraint, so as to solve mixed integer linear programming with CPLEX programming.

6   Case Study

To verify the effectiveness of the proposed scheduling model, a case study of IES in north China was conducted.

6.1   Parameters Settings

The wind turbine parameters are referenced [10]. There are two CHP units in total, and only carbon capture equipment is added to CHP unit 1, while no modification is made to CHP unit 2. The maximum power of incoming load is set at 10% of the load power demand in each period, and the maximum power of outgoing load is set at 20% of the load power demand in each period. The maximum interruptible load is set at 15% of the load power demand in each period. The maximum power transferred to the heating load is set at 10% of the heating load demand in each period, and the maximum power removed from the heating load is set at 20% of the heating load demand in each period. Other system parameters and carbon trading ladder price are shown in Table A1, and CHP units parameters are shown in Table A2. The electricity purchase price of IES from the superior power grid is shown in Table A3.

In a dispatching cycle, the expected output of wind power, electric load demand and heating load demand are shown in Fig. 2.
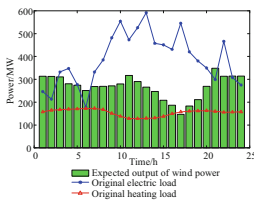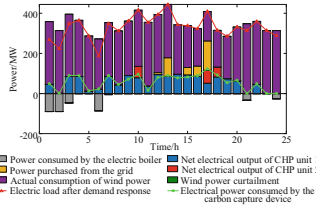

Fig. 2.   Basic data of IES

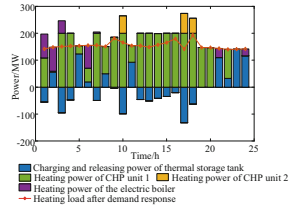**Fig. 3.**   IES electric power supply optimization result

Fig. 4.   IES heating power supply optimization result

6.2   IES Optimal Dispatch Results

Figure 3 shows the IES power system optimal operation strategy within a scheduling period. It can be seen that in order to ensure power supply during the peak period of electricity price (period 9–12, period 18–21), IES increases the output of CHP units and reduces the purchasing power from grid and carbon capture power, so that most of the power generated by CHP unit 1 is supplied to the load side, and it is avoided to purchase power from the grid during the peak period of electricity price, so as to improve the economic benefit of IES. The carbon capture power during period 13–17 is relatively high, because the electricity load demand is larger and wind power output is insufficient, which leads to higher output of CHP units and more carbon emissions. Because at this time, the grid electricity price is in the flat period, IES can make up the power supply to the load side by purchasing power from the grid. As a result, the IES can improve the carbon capture power to avoid to produce too much carbon transaction costs, and the net electrical output of CHP unit 1 is reduced slightly. In the periods when the electric load

demand and electricity price are both low and the heat load is high (period 1–4, period 22–24), IES increases the carbon capture power and reduces the net electrical output of CHP units, which provides more consumption space for wind power while reduces the carbon emission and ensures the low-carbon characteristic of IES. In addition, the wind curtailment power is always 0 during the dispatching cycle, indicating that the wind power is 100% absorbed by IES.

Figure 4 shows the optimal operation strategy of IES heating system, the releasing power of the thermal storage tank is positive and the charging power is negative. It can be seen that, in the period when the electricity price and load are both high (period 10, period 17–18), the IES thermal load demand is shared by the two CHP units. This is because in order to guarantee the electric power supply in these periods, the electric thermal coupling output of CHP units is high. When the wind power is abundant (period 1–6, period 21–24), the electric boiler starts to supply part of the heat load and reduce the heating production pressure of CHP units. The thermal storage tank storages heat in the daytime when the output of CHP units is high and the demand of heat load is small while it releases heat at night, reducing the electric thermal coupling output of CHP units at night together with the electric boiler, and increasing the consumption of wind power.

## 6.3 Analysis of the Complementation of Source-Load Low-Carbon Performance Under Different Carbon Trading Mechanism

This section sets up eight cases, traditional carbon trading price is set to 300 ¥/t. The case settings are shown in Table 1, √ means considering and × said don't consider. Figure 5 and Fig. 6 shows the comparison of different cases under the two carbon trading mechanisms, and each group of data has been normalized. Figure 7 shows the wind power curtailment and carbon emissions in 8 cases, and Fig. 8 s the comparison of related costs in 8 cases.

**Table 1.** Different settings of eight cases

Case	1	2	3	4	5	6	7	8
Traditional carbon trading mechanism	√	√	√	√	×	×	×	×
ladder-type carbon trading mechanism	×	×	×	×	√	√	√	√
carbon capture	×	√	×	√	×	√	×	√
integrated energy system	×	×	√	√	×	×	√	√

According to Fig. 5 and Fig. 6, it can be seen that the advantage of carbon capture lies in the significant reduction of carbon emissions, while the disadvantage lies in the high operating pressure of CHP units and the high cost of electricity purchase in peak periods. This is because part of the electric power produced by CHP units is used for capture, and the net output of the CHP unit is reduced, thus increasing the consumption space of wind power. Although part of the electric power for carbon capture will make it necessary to increase the electricity purchased from the grid and the electricity generation from CHP units during the peak load period.

The advantage of integrated demand response lies in optimizing load curve and reducing electricity purchase cost, while the disadvantage lies in weak carbon emission reduction effect and high carbon transaction cost. This is because the demand response is based on the essence of reformulating the load curve according to the cost of producing electric and heating power and the situation of electric thermal coupling output of CHP units in each period. Due to the low electric power supply cost in the peak period of wind power, the system will move the time-shifting electric load into these periods to absorb wind power as much as possible, and transfers part of heat load which is originally high in these periods to the daytime properly to weaken the peak-valley contradiction of the electric and heating load. In this way, IES can decrease the heating production pressure of CHP units at night. Thus the electric thermal coupling output of CHP units decreases, which gives rise to further expansion of wind power consumption space. During the periods of high electricity price, part of the load is moved out or interrupted, which greatly reduces the electricity purchase cost and the total cost, proving the economy of the integrated demand response. Integrated demand response reduces carbon emissions by increasing the ratio of wind power utilization, reducing the energy supply of CHP units and power purchased from the grid. However, due to the limited amount of wind power and load adjustment, it is impossible to achieve a drastic cut in the energy supply of CHP units, so the effect of reducing carbon emissions is not as direct and significant as carbon capture.
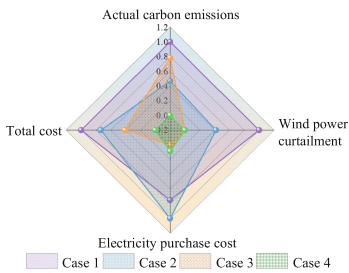

**Fig. 5.** Comparison of cases under traditional carbon trading mechanism
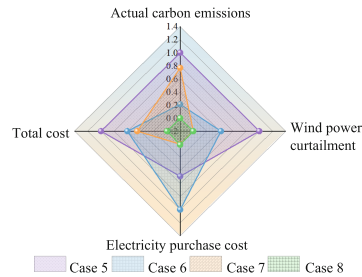
Fig. 6. Comparison of cases under ladder-type carbon trading mechanism

The effect of combining the two is significantly better. It indicates that under two different carbon trading mechanisms, carbon capture and integrated demand response have similar complementary properties, and the combination of the two can achieve more significant effects of carbon reduction and wind power consumption.

Figure 7 and Fig. 8 prove that the ladder-type carbon trading mechanism can effectively reduce carbon emissions, but it has almost no impact on the amount of wind power consumption. This is because the ladder-type carbon trading mechanism strictly limits carbon emissions through the high price of the second and third intervals, so that it does not exceed the range of the first interval except the peak period of electricity and heat consumption. Wind power usage is in essence directly related to the load demand, while the ladder-type carbon trading mechanism does not affect the load demand in each period, so it has no influence on the total wind power curtailment.
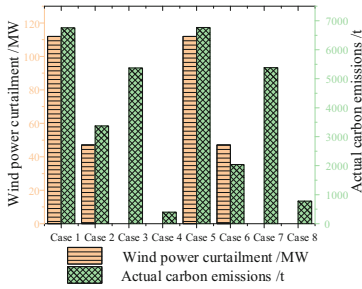
Fig. 7. Comparison of wind power curtailment and carbon emissions in different cases
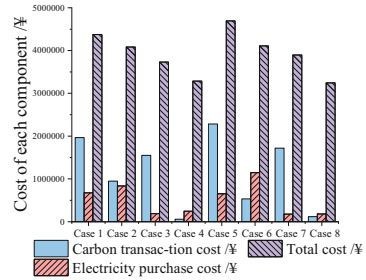
Fig. 8. Comparison of cost of each component in different cases

7 Conclusion

This paper proposes an optimal dispatching method of integrated energy system considering the low-carbon complementarity of source side and load side under ladder-type carbon trading mechanism. It realizes flexible scheduling of the system and enhances the low-carbon economy of the system through the coordination of ladder-type carbon trading mechanism, source-side carbon capture and load-side comprehensive demand response. The following conclusions are obtained through case analysis:

The dispatching model proposed in this paper combines source side carbon capture with load side integrated demand response and verifies that the two have similar complementary properties under different carbon trading mechanisms, and explores the advantages and disadvantages of both. The combination of the two can weaken the peak-valley contradiction of the electric and heating load through peak shaving and valley filling, make the actual carbon emissions decrease when the output of CHP units increases, so that IES has a good low-carbon economy on the basis of ensuring the reliability of energy supply. Moreover, the cost, wind power consumption and carbon emissions of this model are optimal under the ladder-type carbon trading mechanism.

Appendices

Table A1. Parameters of the system

CHP units	$P_{\text{CHP}i,\max}^{\text{e}}$ /MW	$P_{\text{CHP}i,\min}^{\text{e}}$ /MW	$r_{\text{CHP}i}^{\text{u}}$ /MW	$r_{\text{CHP}i}^{\text{u}}$ /MW	C_i^{open} /¥	r_{gi} /¥
1	300	50	150	150	100	40
2	200	50	150	150	160	50

Table A2. Parameters of gas CHP unit

Time frame	Concrete time	Electricity price（¥/kWh）
Peak period	8:00-12:00，18:00-22:00	1.206
Flat period	6:00-8:00，12:00-18:00	0.825
Valley period	1:00-6:00，22:00-1:00	0.4425

Table A3. Time-of-use price

Time frame	Concrete time	Electricity price(¥/kWh)
Peak period	8:00–12:00, 18:00–22:00	1.206
Flat period	6:00–8:00, 12:00–18:00	0.825
Valley period	1:00–6:00, 22:00–1:00	0.4425

References

1. Chen, J., Hu, Z., Chen, J., Chen, Y., Gao, M., Lin, M.: Optimal dispatch of integrated energy system considering lad-der-type carbon trading and flexible double response of supply and demand. High Voltage Eng. **47**(09), 3094–3310 (2021)
2. Zhang, X., Liu, X., Zhong, J.: Integrated energy system planning considering a reward and punishment ladder-type carbon trading and electric-thermal transfer load uncertainty. Proc. CSEE **40**(19), 6132–6142 (2020)
3. Rúa, J., Mai, B., Nord, L.O., et al.: Does CCS reduce power generation flexibility? A dynamic study of combined cycles with post-combustion CO_2 capture. Int. J. Greenhouse Gas Control **95**, 102984 (2020)
4. Huo, D., Gu, C.H., Ma, K., Wei, W., Xiang, Y., Le Blond, S.:Chance-constrained optimization for multi-energy hub systems in a Smart city. IEEE Trans. Ind. Electron **66**(2), 1402–1412 (2019)
5. Ma, Y, Wang, H., Hong, F., et al.: Modeling and optimization of combined heat and power with power-to-gas and car-bon capture system in integrated energy system. Energy **5,** 121392 (2021)
6. Sweetnam, T., Spataru, C., Barrett, M, et al.: Domestic demand-side response on district heating networks. Build. Res. Inf. **2018**, 1–14 (2008)
7. Romanchenko, D., Nyholm, E., Odenberger, M., et al.: Impacts of demand response from buildings and centralized thermal energy storage on district heating systems. Sustain. Cities Soc. **64**, 102510 (2020)
8. Capone, M., Guelpa, E., Mancò, G., et al.: Integration of storage and thermal demand response to unlock flexibility in district multi-energy systems-ScienceDirect. Energy **237,** 121601 (2021)
9. Wei, Z., Huang, Y., Gao, H., Shui, Y.: Joint economic scheduling of power-to-gas and thermo-electric decoupling CHP in regional energy inter-net. Power Syst. Technol. **42**(11), 3512–3520 (2018)
10. Li, Y., Wang, C., Li, G., et al.: Improving operational flexibility of integrated energy system with uncertain renewable generations considering thermal inertia of buildings. Energy Conv. Manag. **207**(March), 11252 (2020)

11. Jin, P., Ai, X., Xu, J.: An economic operation model for isolated microgrid based on sequence operation theory. Proc. CSEE **32**(25), 8 (2012)
12. Cui, Y., Deng, G., Zhao, Y., Zhong, W., Tang, Y., Liu, X.: Economic dispatch of power system with wind power considering the complementarity of low-carbon characteristics of source side and load side. Proc. CSEE **41**(14), 4799–4815 (2021)

Trading Mechanism of Virtual Power Plants Participating in the Electricity Spot Market

Tao Yu[1], Yaxuan Han[2(✉)], Wei Wang[1], Yupeng Huang[1], Heping Jia[2], and Dunnan Liu[2]

[1] State Grid Shanghai Municipal Electric Power Company, No. 1122 Yuanshen Road, Pudong New Area, Shanghai, China
[2] North China Electric Power University, No. 2, Beinong Road, Beijing, Changping District, China
hanyaxuan0123@163.com

Abstract. The comprehensive development of the spot market has become the focus of electricity market construction in China in the next stage. The development and operation of virtual power plants in the future will be mainly realized in the context of the electricity spot market. And exploring the mechanism for virtual power plants to participate in the electricity spot market is of great significance for tapping the potential of distributed resources and encouraging virtual power plants to aggregate multiple entities to participate in the electricity market. To this end, this paper first proposes a multi-objective aggregation optimization model considering the uncertainty of new energy output, and then proposes a trading mode and framework system for virtual power plants to participate in the electricity spot market according to the current rules. Finally, based on the above analysis, a multi-objective decision-making model for virtual power plants to participate in spot market transactions is established, and the effectiveness of the model is proved. Through the systematic analysis, the development of virtual power plants in the future are discussed.

Keywords: Virtual power plant · Electricity spot market · Trading mechanism · Multi-objective optimization · Decision model

1 Introduction

With the further advancement of the power system reform and the gradual increase in the proportion of renewable energy, it is urgent for demand-side resources to participate in the operation and regulation of the power grid, coordinate with the power generation side, and reduce the randomness and volatility of both sides [1]. From the perspective of the market, with the gradual establishment of the competitive electricity market, the types of demand-side entities are diversified, and the new market entities such as distributed generations, energy storage facilities, and electric vehicles are becoming increasingly active, and new market mechanisms and business models need to be established to support the development of these entities [2–4]. The gradual integration of new technologies and the

energy field represented by information technology and control technology has provided a technical guarantee for demand-side resources to participate in the electricity market [5–7].

At present, virtual power plants (VPPs) mainly participate in demand response and peak regulation auxiliary services [8, 9]. With the advancement of the reform of electricity marketization, as a key link connecting medium and long-term transactions and real-time operation, the comprehensive development of the spot market has become the core and focus of the next stage of China's electricity market construction [10, 11]. Development and operation of VPPs in the future will be mainly realized in the context of the electricity spot market. However, the market mechanism that was originally designed for traditional generators and loads was not well adapted to VPPs [12].

Due to the characteristics of resources aggregated, VPPs have more complex characteristics, and there are obvious differences between VPPs and traditional plants [13, 14]. In terms of utility function, VPPs can provide peak shaving and valley filling services, capacity resources, frequency regulation backup and other services that have been market-oriented, which blurs the market positioning of VPPs [15, 16]. In terms of physical constraints, charging and discharging restrictions of energy storage batteries and behavioral laws of electric vehicles make VPPs have unique energy limitations and particular modeling methods [17, 18]. In terms of cost characteristics, VPPs have greater uncertainty after aggregating resources with uncertainty, and there is no fixed value for discharge costs, which is depended on the price of the charging period and the opportunity cost of other periods with inability to discharge [16, 19, 20]. The complex costing will challenge the decision-making of market members and the regulation of organizers. Therefore, VPPs have special characteristics in many terms.

In order to promote the participation of VPPs in the electricity spot market, organizers need to clarify the adaptability and inadequacy of the existing market mechanism, study the participation methods suitable for VPPs, and clarify the elements of the mechanism that need to be adjusted.

VPPs will support the large-scale new energy connecting to the power grid, alleviate the fluctuation, and improve the utilization rate of new energy [13]. Different from the traditional power generation side and demand side resources, VPPs have a variety of advantages such as real-time and flexibility, and their mechanisms for participating in market transactions should also have their particularities [21]. Under the background of the electricity marketization, it is of great significance to connect the power auxiliary service market, demand response and electricity spot market. And the mechanism of electricity spot market for VPPs should be explored to tap the potential of distributed resources and encourage VPPs to aggregate multiple entities to participate in the electricity market [22].

To this end, this paper first proposes two indicators of the minimum reliability expectation value and confidence capacity, analyzes the uncertainty of new energy output. On the basis of summarizing the internal resource output characteristics and output cost of VPPs, an internal aggregation optimization model with uncertainty and lowest cost as the goal is established. Then the trading mode and framework system for VPPs to participate in the electricity spot market according to the current spot market rules is proposed. Above all, a two-stage decision-making model for VPPs to participate in spot market

transactions is established. The effectiveness of the model is validated with an example. Through the systematic sorting out of the trading mechanism of VPP participation in the electricity market, the development direction of future mechanism design is discussed.

2   Uncertainty Analysis of New Energy Output

The reliability of wind and PV power plants can be evaluated from three aspects: the probability of power outages, the time of blackouts, and the amount of power outages, and they can be described by the minimum expected value of reliability, δ_{wind} and δ_{solar}.

$$\delta = \frac{1}{N^Y} \sum_{Y=1}^{N^Y} \frac{1}{T} \sum_{o=1}^{N^o} \delta(Z_{Y,o}) D(Z_{Y,o}) \tag{1}$$

where $\delta(Z_{Y,o})$ is the least reliability expected function, $Z_{Y,o}$ is the system state at the o time point in the Yth simulation, and $D(Z_{Y,o})$ is the duration of the system in that state. N^o is the number of system states and N^Y is the number of simulation calculations.

The wind and PV power station are equivalent to conventional power plants of the same type, and the auxiliary function method is used to calculate the confidence capacity C_{wind} and C_{solar} . The minimum expected value for reliability δ affected by capacity credit C and system load L.

The capacity credit of PV and wind turbines under different loads is calculated by formula (1) and the sequential Monte Carlo method, and the δ_{wind}-C_{wind} and δ_{solar}-C_{solar} curves are plotted, as shown in Fig. 1 and Fig. 2.

According to the calculation method of conventional unit reliability index [23], the δ_{usual}-C_{usual} curve of conventional unit is plotted. The flowchart is shown in Fig. 1, where N is the number of samples.

First, the minimum expected value of reliability corresponding to the capacity of the wind power station is found on the δ_{wind}-C_{wind} curve, and then the corresponding capacity is found on the δ_{usual}-C_{usual} curve of the value, which is the capacity credit of the wind power station. The PV power station can be obtained in the same way.

$$\delta_{usual}(C_{usualo}, L_o) = \delta_{wind}(C_{windo}, L_o) \tag{2}$$

C_{usualo} , C_{windo} is the installed capacity of conventional units and wind turbines, and the L_o is the system load.

The total reliability δ_{all} of all aggregated wind and PV power plants is calculated as shown in Eq. (3).

$$\delta_{all} = \delta_{all}\left(\sum_{i=1}^{n} C_i\right) \tag{3}$$

n is the number of all wind farms and photovoltaic power plants, C_i is the capacity credit of the ith wind power station or PV power station.
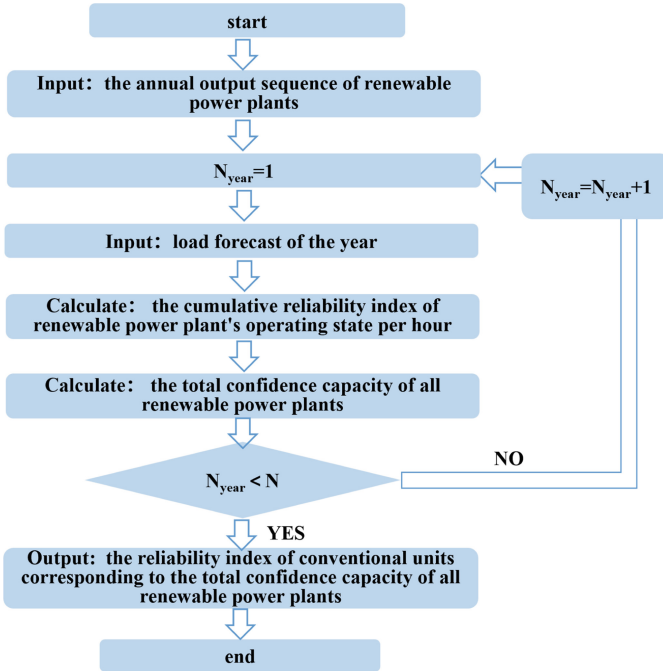
Fig. 1. Reliability metric calculation process.
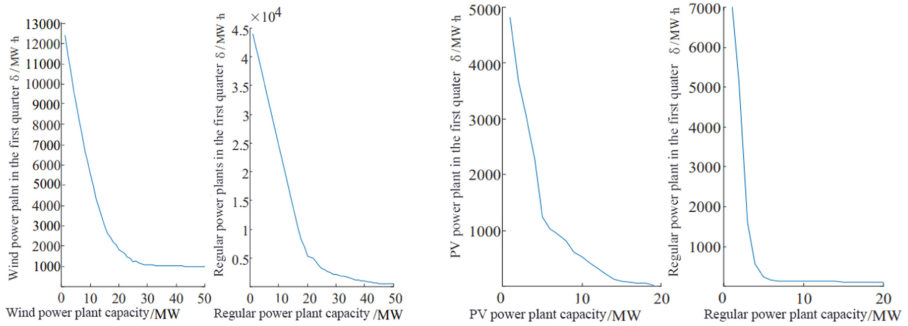
Fig. 2. Capacity credit diagram of wind power and PV power plants in first quarter.

3 Model of VPPs Participating in the Electricity Spot Market

3.1 Trading Mode

The role of VPPs is similar to that of traditional power plants, and when optimized with the goal of maximizing the overall revenue, the main mode of VPP participating in the electricity market is a hybrid model of bilateral mode and joint venture mode [24, 25]. In the model, there exists a power trading center and at the same time allows both virtual power plants and users to conduct bilateral transactions independently. Under this more

flexible model, electricity buyers and sellers in the market have full autonomy in decision-making and can decide on their own how to participate in electricity transactions. At the same time, the VPPs have multiple profit channels under this mode, which can greatly improve the revenue. VPPs can participate in the competition of multiple trading markets at the same time, including the day-ahead market (DA) real-time market (RT). And the VPPs will reasonably select different markets to participate in the competition according to its own output. VPPs participating in the DA market needs to predict the power generation one day in advance and reasonably arrange power generation plan according to the forecast output. Because the forecast has a certain degree of error, so it needs a RT market to ensure the RT balance of power supply [26].

The DA market and RT market both have short trading cycle, in which the VPPs usually serve as the price receiver, that is, their bidding strategy will not cause price fluctuations in both markets. In the spot market, virtual power plants are divided into two categories according to whether they participate in RT market bidding, which also determines whether virtual power plants need to submit RT market bidding curves. When the VPP participates in the RT market bidding, the VPP operator will generate the bidding curve of price and electricity according to its own optimized decision model to the trading market, indicating the willingness of the VPP to buy and sell electricity in the market. And before formulating its own decision model the VPP operator needs to consider the impact of its uncertainty factors, including output volatility, spot electricity price uncertainty, load demand uncertainty. When not participating in the RT market bidding, the VPPs can only rely on the DA market transaction to ensure the balance of electricity. But at present, there are more uncertainties and strong real-time in the electricity market, which will make the VPPs in a very passive situation.

3.2 Framework

This paper aims at the structure of multi-VPPs composed of multiple regional VPPs, and studies the multi-VPP trading strategy based on game theory. When two or more VPPs are connected and managed through a centralized control center, the structure formed is a multi-VPP structure [27]. The control mode of multiple VPPs in this paper is a combination of decentralized control and completely decentralized control, which means the power generation units within multiple VPPs are not fully autonomous, and multiple VPPs are not completely independent of each other. They are in a state of mutual competition but interrelated, and each VPP combines its own output and other VPP information to develop its own strategy to participate in market competition, as shown in Fig. 3.

3.3 Bidding Model

The factors that affect the trend of the market price expectation curve in different scenarios include the daily market price expectation curve and the behavior of competitors in different scenarios, based on which VPPs adjust their profit model and achieve the goal of maximizing the profitability of participation in the spot market, as shown in the
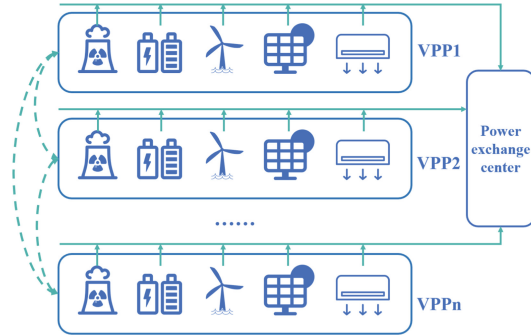
Fig. 3. Multi-VPP trading structure.

function (4), which is constructed based on the goal of maximizing the profit in the DA energy market combined with the DA frequency modulation (FM) market.

$$\sum_{h \in H} q_h \cdot \left\{ \max\left[\sum_{t \in T} p_{t,h}^1 \sum_{i \in I} \left(D_{i,t,h}^+ + D_{i,t,h}^- \right) + \sum_{t \in T} p_{t,h}^2 \sum_{i \in I} \left(R_{i,t,h}^+ + R_{i,t,h}^- \right) + \sum_{t \in T} p_{t,h}^3 \left(\sum_{i \in I} D_{i,t,h} - \sum_{k \in K} l_{k,t,h} \right) \right] \right\}$$
(4)

Parameters of various entities aggregated by VPPs constitute a collection *I*, and aggregated loads constitute a collection *K*. Among them, it is an expected scenario *h* in the typical scene set *H*. In this scenario, the clearance price of the FM capacity of the service market, the clearance price of the FM mileage of the service market, and the system marginal clearance price of the energy market in the DA market at time *t* are *P1 t,h, P2 t,h, P3 t,h*. Under the above conditions, *D + i,t,h* and *D- i,t,h* on behalf of the DA independent system operators in the FM market accepted the capacity of the up/down FM of unit *i*. *R + i,t,h* and *R- i,t,h* on behalf of the DA independent system operators in the service market accepted up/down FM mileage of unit *i*. $D_{i,t,h}$ on behalf of the DA independent system operators on the market to accept the reported capacity of unit *i*. $l_{k,t,h}$ represents the declaration curve of the load *k* accepted by the independent system operators in the DA market.

Calculate the probability-weighted average of all classical scenarios and the price of the market clearance before the day, establish the second stage optimization model, and combine the two-layer model with external optimization to calculate the total revenue of VPPs under different profit modes.

The dispatching agency and the power trading center are the followers in the game, and the joint market clearance is carried out according to the power demand and the quotation of each subject, and the function is established with the goal of minimizing the total purchase cost.

$$\sum_{h \in H} q_h^{\max} \cdot \min \left\{ \begin{array}{l} \sum_{u \in U} S_{u,t,h} \cdot D_{u,t,h} + \sum_{u \in U} \left[S_{u,t,h}^{D,AS} (D_{u,t,h}^+ + D_{u,t,h}^-) + S_{u,t,h}^{R,AS} (R_{u,t,h}^+ + R_{u,t,h}^-) \right] + \\ \sum_{t \in T} \sum_{i \in I} \left(S_{i,t,h}^{dis} \cdot D_{i,t,r} - S_{i,t,h}^{ch} \cdot l_{i,t,r} \right) + \sum_{i \in I} \left[S_{i,t,h}^{D,AS} (D_{i,t,h}^+ + D_{i,t,h}^-) + S_{i,t,h}^{R,AS} (R_{i,t,h}^+ + R_{i,t,h}^-) \right] \end{array} \right\}$$
(5)

U is a collection of regular units. $S_{u,t,h}$, $SD,AS\ u,t,h$, $SR,AS\ u,t,h$ are the quotation of the FM capacity and mileage of the unit u at time t under the scenario h in the electric energy market and the auxiliary service market. $Sdis\ i,t,h$ and $Sch\ i,t,h$ are respectively the charging and discharging quotation mileage of the entity i at time t under the scenario h in the electric energy market. $SD,AS\ i,t,h$ and $SR,AS\ i,t,h$ are respectively the quotation of the FM capacity and mileage in the auxiliary service market. $D_{u,t,h}$ is the up/down frequency regulation capacity of the conventional unit accepted by the independent system operator in the DA energy market. $D+\ u,t,h$ and $D-\ u,t,h$ are the unit up/down frequency regulation mileage accepted by the independent system operator in the DA FM market. $R+\ u,t,h$ and $R-\ u,t,h$ are the unit up/down frequency regulation mileage accepted by the independent system operator in the current service market.

The relevant constraints for Eq. (4) include grid power transmission constraints, VPP up-and-down mileage constraints, and VPP capacity up-and-down capacity constraints, as shown in Eqs. (6)–(8).

$$\left| D_{I,t,h}^{out} - D_{I,t,h}^{in} \right| \le D_{\max}^{em} \tag{6}$$

At time i, the difference between the electricity sold and purchased by the VPP in the DA energy market should be less than the maximum bidding power in the market.

$$\begin{cases} D_{i,t,h}^{+} \le R_{i,t,h}^{+} \le \alpha_i D_{i,t,h}^{+} \\ D_{i,t,h}^{-} \le R_{i,t,h}^{-} \le \alpha_i D_{i,t,h}^{-} \end{cases} \tag{7}$$

In the scenario h of DA service market, the FM mileage $R^{+}_{i,t,h}$ and $R^{-}_{i,t,h}$ of the unit i at time t should be greater than its FM power $D^{+}_{i,t,h}$ and $D^{-}_{i,t,h}$, which should be less than the FM electricity reported. α_i is an FM mileage multiplier, which is used to calculate the actual moving mileage of the unit for every up/down 1MW of FM capacity. It is calculated by comparing the total mileage of all FM resources in the previous period with the total capacity.

$$\begin{cases} 0 \le D_{i,t,h}^{out} + D_{i,t,h}^{+} \le P_{i,\max}^{dis} \\ 0 \le D_{i,t,h}^{in} + D_{i,t,h}^{-} \le P_{i,\max}^{ch} \end{cases} \tag{8}$$

The sum of the FM capacity and the purchased/sold capacity reported by the unit in the service market is less than the maximum charging and discharging power $Pch\ i,max$ and $Pdis\ i,max$ of the VPP in the DA market.

Equation (5) needs to meet the power balance constraint of the electric energy market, and the power constraint of the conventional unit is shown in Eq. (9)–(10).

$$\sum_{i \in I} \left(D_{u,t,h} - l_{i,t,r} \right) = L_t - \sum_{u \in U} S_{u,t,h} \tag{9}$$

L_t is the size of the system load at the moment t.

$$P_{u,t,h}^{-} - P_{g,\min} \le P_{u,t,h} \le P_{g,\max} - P_{u,t,h}^{+} \tag{10}$$

The output of the unit u at time t is constrained. $P_{g,min}$ and $P_{g,max}$ are the maximum and minimum output of the unit.

Based on the above functions, the profit model optimization system and method of the spot market of VPP are constructed, which belongs to the nonlinear and mixed integer optimization problem, and the system is established based on Matlab to solve the profit model with the largest output total return. The logic of the model is shown in Fig. 4.
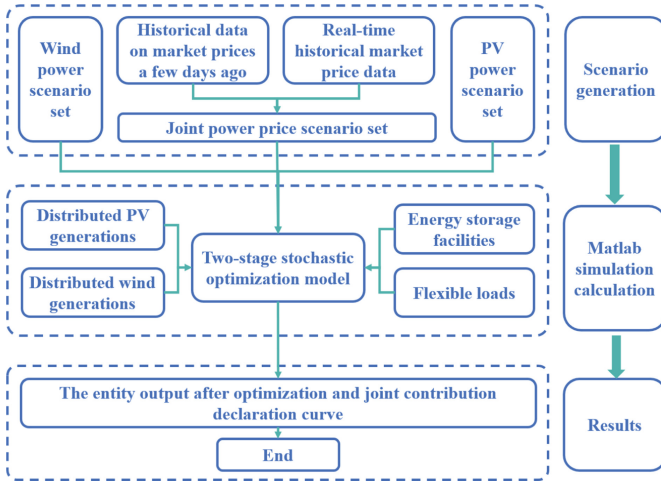

Fig. 4. A two-stage model of VPPs participating in the spot market.

4   Numerical Example

In this paper, a VPP composed of wind units, PV units, energy storage facilities and flexible loads is selected as an example for verification. Distributed wind turbines are rated at 8 MW and 10 MW in maximum output. Distributed PV units are rated at 5 MW and 7 MW in maximum output. The maximum storage capacity of energy storage batteries is l0 MWh, the minimum storage capacity is l MWh, and the initial capacity is 5 MWh. The maximum charging power is 1.5 MW/h, and the maximum discharge power is 2 MWh.

The results of the internal resource optimization are shown in the Fig. 5.

Figure 5 shows the wind-solar-storage hybrid power generation. The charging and discharging time of energy storage reflects the peak and valley of load power consumption to a certain extent. The period from 1:00 am to 7:00 am has high wind power generation, and the excess power generation flows to the energy storage facilities. 10:00 am, 18:00 pm to 20:00 pm, and 24:00 pm are the load peaks, and the energy storage facilities discharge to make up for the shortage of new energy generation in the VPP. By coordinating the charging and discharging of energy storage facilities, the VPP reduces the abandonment of wind and solar energy.

Figure 6 show the adjustment effect of the VPP on the load. By adjusting the flexible load to shift the peak and fill the valley, the originally large peak-to-valley difference is reduced, which is beneficial to the safety and stability of the power system.
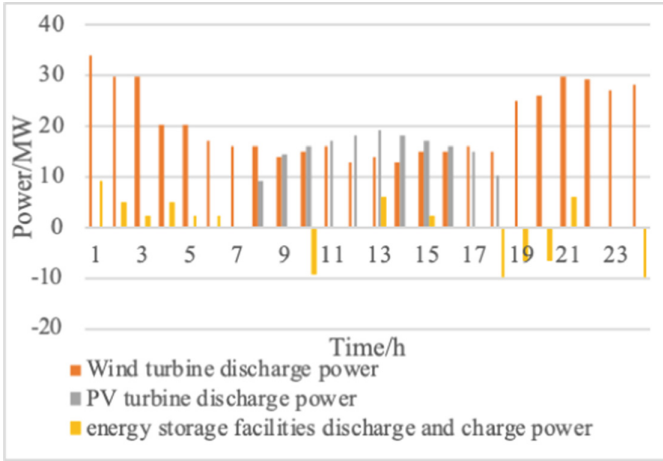
Fig. 5. Charging and discharging power of each entity after internal optimization of VPP.
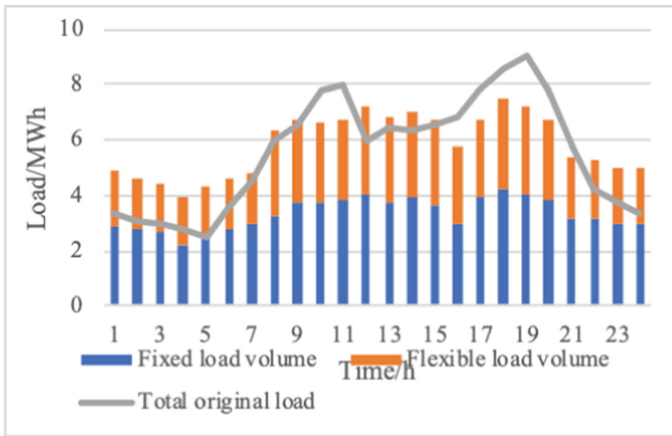
Fig. 6. Internal optimized load of VPP.

The models under ten electricity price scenarios are calculated to obtain the two-stage decision-making results of VPPs participating in spot market transactions.

Based on the internal balance adjustment of the virtual power plant, the virtual power plant externally participates in the spot market as a power plant to obtain benefits. For the analysis of the previous decision-making, it can be seen from Fig. 7 that the daily declaration output curve of the VPP can be divided into three stages: the first stage is from 0 am to 8 am, because the system only has wind power output at night, so the amount of declaration is low. The second stage is from 9 am to 15 pm. This stage is gradually increased with distributed PV power generation, and the system's joint declaration volume gradually increases. The third stage is from 16 pm to 23 pm. As the

Fig. 7. VPP joint declaration output curve.

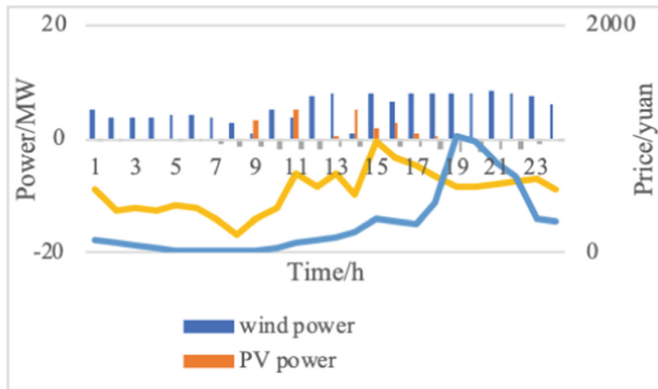peak of electricity consumption is approaching, the DA market price rises, and the joint declaration volume of the system reaches the highest value.

5   Conclusion

The VPP aggregates the diverse and scattered small and micro entities into a whole, and is dispatched by the VPP operator in a unified manner, which makes good use of the complementarity of the output of the small and micro entities and improves the overall economic benefits. This paper explores a two-stage decision-making model for VPPs that include distributed power generation, energy storage batteries, and flexible compliance to participate in electricity spot market. The research shows that the model can effectively support VPP operators to optimize the reporting strategy under spot market conditions, make decisions scientific and effective, and improve the profits. In the next stage, the consideration is how VPP operators can make joint strategic quotations in multiple markets such as the medium and long-term market, the spot market and the auxiliary service market to improve profits.

References

1. Hong, L., Junkai, L., Shida, Z., Shaoyun, G., Baijie, Y., Chengshan, W.: Distributionally robust co-optimization of the demand-side resources and soft open points allocation for the high penetration of renewable energy. IET Renew. Power Gener. **16**(4), 713–725 (2021)
2. Yongliang, L., Zhenhua, Y., Xuwei, X., Junwei, M., Dongge, Z., Shaoyong, G.: Research on the Mechanism of Aggregate and Distributed Generation Participating in the Power Market. IOP Conf. Ser. Earth Environ. Sci. **1011**(1), (2022)
3. Visser, L.R., et al.: An operational bidding framework for aggregated electric vehicles on the electricity spot market. Appl. Energy **308,** 118280 (2022)

4. Rui, S., Jeremiah, R., Sergio, C., Sarah, K, Noah, K.: Evaluating emerging long-duration energy storage technologies. Renew. Sustain. Energy Rev.**159** (2022)
5. Hamed, B., Rahmat-Allah, H., Soghra, N.: Monte-Carlo-based data injection attack on electricity markets with network parametric and topology uncertainties. Int. J. Electr. Power Energy Syst.**138** (2022)
6. Chen, S., Bai, Y., Zhang, Y., Liu, X., Zhang, J., Gao, T., *et al.*: A framework of decentralized electricity market based on the collaborative mechanism of blockchain and edge computing. In: 2019 International Conference on Service Operations and Logistics, and Informatics (SOLI), pp. 219–223. IEEE, Zhengzhou (2019)
7. Zhiyong, S., Weiping, L, Yanghua, Z., Yanshan, H.: Research on intelligent power automation technology based on edge computing of power Internet of Things. In: E3S Web of Conferences, vol. 204 (2020)
8. Zhang, H., Gong, C., Ju, W., Pan, G., Wang. W.: Optimization dispatch modeling for demand response considering supply and demand balance and security constraints. In: 2021 Power System and Green Energy Conference (PSGEC), pp. 166–170 IEEE, Shanghai (2021)
9. Ya, L., Deliang, Z., Xuanyuan. W.: A peak regulation ancillary service optimal dispatch method of virtual power plant based on reinforcement learning. In: 2019 IEEE Innovative Smart Grid Technologies - Asia (ISGT Asia), pp. 4356–4361. IEEE, Chengdu (2019)
10. Han, B., Cai, Z., Chen, Z., Pan, A., Liu, J.: Analysis of peak regulation auxiliary service market under the deepening stage of the spot market construction. In: 6th Asia Conference on Power and Electrical Engineering (ACPEE), pp. 651–657. IEEE, Chongqing (2021)
11. Mu, C., *et al.*: The coordination mechanism of forward market and spot market under the cost-based electricity market model for Yunnan. In: 6th Asia Conference on Power and Electrical Engineering (ACPEE) pp. 634–639. IEEE, Chongqing (2021)
12. Cui, Y., et al.: the mechanism of virtual power plant participating in the peak regulation auxiliary service market. In: 3rd Asia Energy and Electrical Engineering Symposium (AEEES), pp. 1010–1015. IEEE, Chengdu (2021)
13. Han, Y., Wang, W., Yu, T., Huang, Y., Liu, D., Jia, H.: Analysis of economic operation model for virtual power plants considering the uncertainties of renewable energy power generation. In: IEEE Sustainable Power and Energy Conference (iSPEC), pp. 1980–1985. IEEE, Nanjing (2021)
14. Kailing, C., Wen, G., Haiqun. W.: Optimal operation method of virtual power plant considering power deviation rate. In: IEEE/IAS Industrial and Commercial Power System Asia (I&CPS Asia), pp. 1381–1386. IEEE, Chengdu (2021)
15. Mao, T., Sun, L., Xie, P., Wu, W., Han, S., Guo, X.: A calculation method for levied peak electricity price dealing with virtual power plant peak shaving subsidy. In: 4th International Conference on Energy, Electrical and Power Engineering (CEEPE), pp. 1053–1057. IEEE, Chongqing (2021)
16. Wen, C., Jing, Q., Junhua, Z., Qingmian, C., Yang, D.Z.: Bargaining game-based profit allocation of virtual power plant in frequency regulation market considering battery cycle life. IEEE Trans. Smart Grid **12**(4), (2021)
17. Ye, L., Zhao, L., Dong, S., Chen, S.: Dispatch in electric vehicles embedded virtual power plants considering safety constraints. In: 3rd International Conference on Circuits, Systems and Devices (ICCSD), pp. 143–147. IEEE, Shenzhen (2019)
18. Mahdi, R., Jahanbani, A.F., Oluwaseyi, O., Jahanbani, A.A.: Two-stage interval scheduling of virtual power plant in day-ahead and real-time markets considering compressed air energy storage wind turbine. J. Energy Storage **45** (2022)
19. Michelle, M.H., Jairo José, E.O.: Bidding strategy for VPP and economic feasibility study of the optimal sizing of storage systems to face the uncertainty of solar generation modelled with IGDT. Energies **15**(3), (2022)

20. Yang, F., Zhang, Z., Yong, W., Wei, J., Lu, Z., Yun, B.:Optimal day-ahead dispatch of virtual power plant with aggregated multi-type electric vehicles via a stackelberg game approach. In: 6th Asia Conference on Power and Electrical Engineering (ACPEE), pp. 645–650. IEEE, Chongqing (2021)

21. Zhang, Z., Yong, W., Yang, F., Wei, J., Zhu, M.: Real-time active power dispatch for virtual power plant via a multi-agent leader-follower game approach. In: 3rd Student Conference on Electrical Machines and Systems (SCEMS), pp. 875–880. IEEE, Ji'nan (2020)

22. Yang, L., Zhigao, J., Bowei, G.: Assessing China's provincial electricity spot market pilot operations: Lessons from Guangdong province. Energy Policy **164** (2022)

23. Yan, Y., Ding, Y., Guo, C., Wang, R., Cheng, L., Sun, Y.: Operating reliability analysis of peaking generating units considering start-up failures and degradation. In: 2nd International Symposium on Stochastic Models in Reliability Engineering, Life Science and Operations Management (SMRLO), pp. 168–171. IEEE, Beer Sheva, Israel (2016)

24. Wang, Y., Kong, B., Zhou, L., Yang, M., Jiang, Y., Bai, X.: Multi-objective matching method of bilateral transactions in medium and long-term power markets. In: 8th International Conference on Advanced Power System Automation and Protection (APAP), pp. 1357–1361. IEEE, Xi'an (2019)

25. He, H., et al.: Joint operation mechanism of distributed photovoltaic power generation market and carbon market based on cross-chain trading technology. IEEE Access **8** (2020)

26. Mahdi, R., Jahanbani, A.F., Oluwaseyi, O., Jahanbani, A.A.: Two-stage interval scheduling of virtual power plant in day-ahead and real-time markets considering compressed air energy storage wind turbine . J. Energy Storage **45** (2022)

27. Wang, Y., Ai, X., Tan, Z., Yan, L., Liu, S.: Interactive dispatch modes and bidding strategy of multiple virtual power plants based on demand response and game theory. IEEE Trans. Smart Grid **7**(1), (2016)

A Reliability Prediction Method Based on the Barrel Theory for Engineering Applications for Key Components of Relay Protection

Zheng Xu[(✉)], Hualiang Zhou, Yu Xia, Yunhua Gan, and Zhiyang Zou

NARI Group Corporation, Nanjing 211106, China
`Xuzheng0221@163.com`

Abstract. Reliability prediction of relay protection devices is an important technical means to improve the inherent reliability performance of relay protection devices. The current reliability prediction mainly adopts the GJB/Z 299C standard and the U.S. military standard MIL-HDBK-217, both of which consider each stress in a series model and do not consider the role of individual stresses on the overall failure rate, resulting in less accurate predicted values for the basic failure rate of components. Therefore, in this paper, a barrel theory analysis method is used to propose the calculation method of partial stress failure rate focusing on the failure mode of aluminum electrolytic capacitors on power supply boards, and a common coefficient to evaluate the interaction between each stress is given. The prediction results are also compared with the traditional reliability prediction standards, and it is found that the failure rate of aluminum electrolytic capacitors is greatly improved, and the life of relay protection devices is shortened to 12 years under normal environment and 6 years under the worst environment, which is consistent with the statement in the "Regulations for the Operation and Management of Microcomputer Relay Protection Devices" that the service life of re-lay protection devices should not be less than 12 years.

Keywords: Relay protection devices · Barrel theory · Reliability prediction · Stress characteristics · Operating failure rate · Acceleration factor

1 Introduction

The relay protection device is the first defense line for the safe and stable operation of the grid. When a fault occurs in the grid equipment, the protection device is required to remove the faulty equipment correctly and quickly to avoid affecting the normal work of other parts. In recent years, large-scale power outages around the world have been directly or indirectly related to the incorrect running of protection devices to some extent. This is because electromagnetic and thermal stresses, which are strongly associated with the stable operation of relay protection devices, play a vital role in their reliable running [1, 2]. The environmental stresses in substations have special characteristics: firstly, the

distribution of industrial frequency electromagnetic fields due to their energy transfer and distribution functions and the intricate distribution of high frequency electromagnetic fields due to faults and switching operations; secondly, the variety of equipment in the station can cause uneven distribution of thermal fields due to more heat loss and heat dissipation. Therefore, an accurate and reasonable assessment of the reliability of relay protection devices, to provide a basis for their regular maintenance and decommissioning and replacement, has also become a current research direction of great interest.

The failure rate of protection devices not only increases over time, but also increases maintenance costs and accident risks. Previously, the safe and stable operation of secondary equipment was achieved through repair and maintenance methods, but this practice not only affects the reliability of protection devices by introducing human factors, but also causes the problem of insufficient field operation and maintenance personnel. In addition, the current age of the maintenance and repair cycle of relay protection equipment is an empirical engineering value that lacks systematic, scientific, and accurate predictions. Therefore, in order to avoid economic losses caused by blind replacement of equipment and safety hazards associated with continued operation, scientific and reasonable reliability prediction and life estimation of protection devices are of great significance to improve the safety, reliability and economy of power systems [3].

2 Reliability Prediction Method

2.1 Reliability Prediction Methods in Relay Protection Devices

Reliability prediction for relay protection devices refers to the work performed to estimate the reliability of a relay protection device under given operating conditions. Specific metrics measured in terms of product failure rate (λ), mean time between failures (MTBF), reliability (R), and other metrics [4, 5]. Usually, the higher reliability of relay protection equipment, the longer its service life, the greater the MTBF, the higher the reliability, and the lower corresponding product failure rate. The role of reliability prediction is to estimate the reliability parameters of relay protection equipment in different operating environments based on the reliability data or empirical data of similar products or the units that make up the product, as the product itself does not or has fewer corresponding data.

As shown in Fig. 1, the "bathtub curve" divides the product life cycle into three phases: 1. Infant mortality period, early failures; 2. Period of useful life, approximately constant failure rate; 3. Wear out period, wear failures [6]. Cause using constant failure rate is still the most relevant approach for estimating the predicted reliability of a system, reliability prediction methods are mainly for products where the failure occurs in the period of useful life [7].

2.2 Comparison of Various Reliability Prediction Methods

Reliability prediction is based on the reliability prediction manuals, also known as the reliability prediction standard, which provides basic data and prediction methods. Common reliability standards include IEC/TR 62380 of the International Electrotechnical
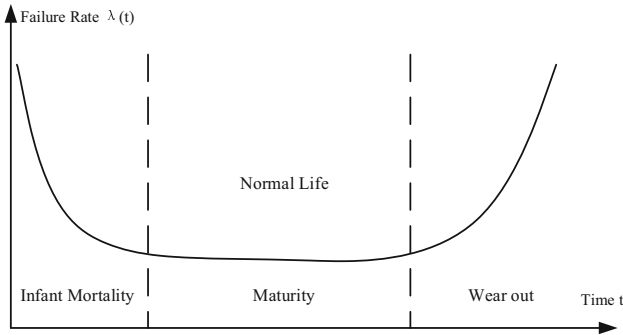
Fig. 1. Bathtub curve

Commission, SR-332 of Bell Labs, MIL-HDBK-217 of the U.S. military standard, and GJB/Z 299C of the national standard. Other well-known standards for enterprise reliability prediction include Siemens SN29500, FIDES-Guide, a FIDES Group company, and Quanterion Solutions 217Plus [8, 9].

In these standards, GJB/Z 299C is benchmarked against MIL-HDBK-217 and formulated with reference to it. The two standards are comprehensive in terms of component categories and provide 2 expected methods of component counting method and component stress analysis method, but their disadvantage is that both have not been updated for many years, and the predicted standard value of component failure rate is lower than the actual situation. And Bell Labs SR-332, Siemens SN29500, FIDES Group Inc. FIDES and Quanterion Solutions 217Plus standards are all corporate standards, all with their own predicted models and corresponding applicable scenarios. With the development of their own enterprises and the times, corporate standards are representative and up-to-date.

At the same time, reliability prediction methods can be divided into three categories, the most commonly used is the method based on basic empirical model, like the U.S. military standard and Bell Labs standard, the advantage of this method is that it can actually respond to failure rate and defect density, and can be used as a good indicator of field reliability, but its disadvantage is that this kind of model is difficult to keep updated continuously, it is difficult to obtain high-quality field data, and it is difficult to distinguish quality and environment such relevant variables. The other two are the failure physics-based approach and the test data-based approach, respectively.

Since the circuit composition and hardware platform architecture in protection devices are known, it is more accurate to use the stress model analysis method to predict reliability in relay protection devices. However, even for the same standard and the same method, there are still differences in the stress analysis method models used for reliability estimation of the same components. The reason for this is the difference in the source of components. In the GJB/Z 299C manual, when using the stress analysis method to calculate the working failure rate of domestic capacitors, the temperature is considered, but the effect of electrical stress is not considered, as in Eq. 1 below. While in the analysis of foreign imported capacitors using the GB/Z 299C standard, it is only when calculating the working failure rate that both the temperature coefficient π_T and

the electrical stress coefficient π_S are considered, as in Eq. 2 below.

$$\lambda_P = \lambda_b \pi_E \pi_Q \pi_{CV} \pi_{SR} \pi_K \pi_{ch} \tag{1}$$

$$\lambda_P = \lambda_b \pi_E \pi_Q \pi_T \pi_S \pi_{ch} \tag{2}$$

This indicates that the accuracy of the model of the stress analysis method will be more fully considered as the performance of the component being expected evolves, reducing the uncertainties and making the failure rate more accurate as well. As shown in Fig. 2 below.
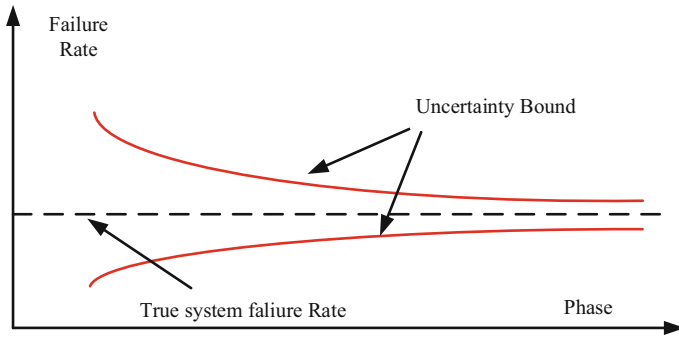

Fig. 2. Component failure rate trend

Therefore, with the widespread use of domestic devices in relay protection devices, it will also continue to promote the improvement of the manufacturing process of domestic devices. Also with the progress of material physics, the original use of the 299C standard for relay protection devices is not expected to meet the requirements, and the majority of researchers are looking for a method that is applicable to the reliability expectation within relay protection devices.

Since the power supply board is the most failure-prone board in relay protection devices, the replacement rate of the power supply board reaches about 40% as can be seen in the replacement statistics of the failed boards in a provincial company for three years from 2017–1019 [10]; and the failure rate of electrolytic capacitors accounts for 60% of the total number of failed devices in the power supply boards [11]. Based on this, this paper adopts the barrel theory, mainly considers the failure causes of power supply boards and electrolytic capacitors in protection devices, and proposes an engineering-oriented reliability prediction method.

3   New Reliability Prediction of Relay Protection Devices Based on Barrel Theory

3.1   Advantages of Reliability Prediction Based on the Barrel Theory

The barrel theory, also known as the short board theory, proposed by Laurence J. Peter, the core content of which is: a barrel holds the amount of water, and does not depend on

the highest piece of wood on the wall of the barrel, but precisely on the shortest piece of the wall [12]. In the relay protection device, the power board is prefer to failure, and the electrolytic capacitor in the power board is the key component that affects the reliability of the power board, and its life is shorter compared to other components, so the life of the electrolytic capacitor determines the life of the whole board and protection device. The lifetime of aluminum electrolytic capacitors is mainly influenced by temperature and electrical stress. With the current technology level, the life time can be predicted by determining the basic failure rate and the corresponding acceleration factor.

3.2   Reliability Prediction New Method of Aluminum Electrolytic Capacitors

Traditional reliability prediction methods are usually presented in series. If any one of the N components fails, the system will fail, and the operating failure rate model is represented as formula 3 follows.

$$\lambda_{system} = \sum_{i=1}^{n} N_i \lambda_{pi} \pi_i \tag{3}$$

The operating failure rate of each specific component consists of two parts, the basic failure rate and the stress acceleration factor, as shown in the following Eq. 4. Usually, the basic failure rate is obtained through the reliability standard, or the data is obtained by testing under standard conditions; while the acceleration factor is analyzed by the stress model, so as to obtain the corresponding factor.

$$\lambda_p = \lambda_b \pi_e \pi_q \pi_s \tag{4}$$

A better approach, according to the Reliability Information Analysis Center (RIAC) in the United States, is to combine additive and multiplicative models to predict the failure rate of each type of failure mechanism separately [13]. Each of these failure rate terms is then accelerated by the stress or component characteristics applicable to the object of study. This model takes the following form:

$$\lambda_p = \lambda_0 \pi_0 + \lambda_e \pi_e + \lambda_c \pi_c + \lambda_i \pi_i + \lambda_{sj} \pi_{sj} \tag{5}$$

This method has universal applicability, however, in the power system, the power secondary equipment has unique environmental stress: the equipment operates in high temperature and high humidity environment for a long time, is affected by overvoltage and overcurrent after switch-blade operation, and the complex electromagnetic environment and electromagnetic interference in the substation, all of which urgently need to be improved on the original reliability prediction method [14].

Based on this, this paper proposes a method for reliability prediction of aluminum electrolytic capacitors in relay protection devices, which takes into account both specific failure modes and stress profiles based on the traditional failure rate model, the effects of electrical stress and temperature stress already considered in the traditional failure rate model, and the effects induced by electromagnetic interference. The model approach can be continuously updated based on the collection of field failure rates and failure mode percentage information. Based on the aluminum electrolytic capacitor failure mode analysis and stress profile analysis, the specific model is as follows.

$$\lambda_p = \lambda_0 \pi_0 + \lambda_e \pi_e + \lambda_T \pi_T + \lambda_Q \pi_Q + \lambda_i \pi_i \tag{6}$$

where π_0 is the operating failure acceleration factor; π_e is the environmental acceleration factor; π_c is the temperature stress acceleration factor; λ_i is the electromagnetic induced stress failure rate, and π_Q is the quality factor accelerated failure factor.

The specific reliability prediction method is divided into two parts, one is the estimation of the stress model acceleration factor, the specific model needs to be analyzed in relation to the actual stresses endured and the criteria, and the second is the calculation of the partial stress failure rate in the test environment, once the π factor is defined for each component of the modeling and once the failure rate is assigned in the cause of failure, the basic failure rate can be determined. Considering that the prediction method in this paper targets failure in the period of useful life. The basic failure rate is as formula 7 follows:

$$\lambda_b = \frac{P_{FC}\lambda_{obs}}{\pi_0} \tag{7}$$

where λ_{obs} is the failure rate observed in the test, P_{FC} is the weighting factor under the corresponding failure rate and failure mode, π_0 is the acceleration factor under the test conditions, and λ_b is the fundamental failure rate to be found.

The advantages of this method are: 1. The mode of fixing the basic failure rate of fixed components in the traditional method is improved to make up for the unreliable data brought about by factors such as environment, layout and quality, and greatly improve the accuracy of the basic failure rate in reliability estimation. 2. The location of the test data collection and test site is not fixed, it can be the test chamber or the data statistics in the field, and the data obtained is applicable to the corresponding conditions.

4 Reliability Prediction Steps of Relay Protection Devices Based on Barrel Theory

4.1 Failure Mode Analysis of Electrolytic Capacitors

The electrolytic capacitor is the component with the highest failure rate in the power supply board of relay protection devices. This is due to design defects, dielectric wear, voltage, current, temperature, mechanical stress and other intrinsic or extrinsic factors may cause the capacitor to fail. Aluminum electrolytic capacitors may fail due to open circuit, breakdown, liquid leakage, degradation of electrical parameters and other phenomena during operation by the above factors. Specific failure modes are shown in the following Table 1.

4.2 Electrolytic Capacitor Stress Profile Analysis

The detailed methodology is accomplished by assessing whether each stress is a major, minor factor in the damage pattern. A 3:1 ratio weighting between the primary and secondary factors was then used to estimate the percentage of failure attributable to these stresses.

Operating temperature, overcurrent and overvoltage are the primary stresses that accelerate the operating failure mode; the stresses that accelerate the environmental

Table 1. Electrolytic capacitor failure mode.

Failure mode	Failure phenomenon	Cause of failure
Open circuit	Aluminum foil disconnected from the lead wire	Abnormal external stress on lead wire, poor contact between lead wire and aluminum foil
Short circuit	No insulating effect of oxide film and electrolyte	Over-voltage, overcurrent and high temperature effects; metal particle adhesion, burrs in aluminum foil and leads
Electrical capacity decrease	The cathode and anode aluminum foil front-to-back area decreases and the electrolyte dries out	Over-voltage, over-current and high temperature effects; insufficient electrolyte capacity
Electrolyte leakage	Internal temperature rise	Overvoltage, ripple current and temperature rise from charging and discharging, internal temperature rise leading to increased ESR

causes of failure are vibration, corrosive stress, aging stress and humidity. Each of the five failure modes is listed at the top of the table indicated, and each accelerated stress is listed on the left side of the table. Each combination is identified by a space, a "P" (primary) or an "S" (secondary). The relative percentages of relevant failures caused by accelerated stress are listed on the right. In the literature [15] and [16], the failure modes and failure rate categories of electrolytic capacitors were analyzed in detail to obtain the percentage of various failure modes of aluminum electrolytic capacitors. Then the composition and degree percentage of the failure category corresponding to each failure mode is analyzed by the analysis table of electrolytic capacitor failure modes and failure modes. The analysis table of electrolytic capacitor failure modes is follows (Table 2).

4.3   Partial Stress Failure Rate and Acceleration Factor Under Normal Stress Conditions

Work Failure Rate λ_0 and Acceleration Factor π_0. Since most of the failures of the components in the protection devices in operation come from the thermal stresses of the components during normal operation and the thermal stresses due to electromagnetism, which bring about a temperature increase. Therefore, with reference to the FIDES standard, the Arrhenius model with the ratio of electrical stress coefficients is used for calculation, as formula 8 shown below.

$$\pi_0 = \gamma_0 \times \left(\frac{1}{S_{reference}} \times S \right)^3 \cdot e^{11604 \times Ea \times \left[\frac{1}{293} - \frac{1}{T_{ambient}+273} \right]} \tag{8}$$

where the electrical stress ratio is 0.55 (Operating voltage over rated voltage), Other parameters are as Table 3 follows:

Table 2. Electrolytic capacitor failure mode.

Failure category	Accelerated stress	Failure mode					
		Open circuit	Short circuit	Capacity decrease	Leakage	Weighted	Total %
		19%	69%	2%	10%	3:1	
Work failure	High temperature	P		S	P	8.48	52.68
	Overcurrent	S	P	P		22.10	
	Overvoltage	S	P	P		22.10	
Environmental failure	Vibration	S				1.81	21.52
	Corrosion stress		S			6.57	
	Aging		S			6.57	
	Humidity		S			6.57	
Ambient temperature	Temperature cycling		S	S	S	7.71	7.71
Quality Failure	Product Quality	S	S	S	S	9.52	9.52
Induced failure	Induced overload	S	S	S		8.57	8.57

Table 3. Other parameters in work failure acceleration factor.

$\lambda_0 \left(\text{Unit} : 10^{-6} \right)$	γ_0	$S_{reference}$	Ea
0.4	0.85	0.5	0.4

It can be obtained that the work failure rate acceleration factor $\pi_0 = 2.34$ under normal ambient temperature 40 °C; the work failure rate acceleration factor $\pi_0 = 5.70$ under the worst ambient temperature 60 °C. Also, since the work failure failure ratio in the stress profile analysis is 52.68%, the work failure rate $\lambda_0 = 0.09 \times 10^{-6}$ is obtained by bringing into the formula 8.

Environmental Failure Rate λ_e and Acceleration Factor π_e. Using the national military standard environmental category definition of environmental type, according to the definition of environmental category, in the normal environment, the relay protection device is considered to be located in the environmental category of "general ground fixed", said in ordinary buildings or better ventilation on the fixed rack, by the vibration, shock impact is very small environmental conditions, the corresponding environmental coefficient to take 1.5. Under the worst conditions, the relay protection device is considered to be located in the environmental category of "bad ground fixed", which means

that only the rudimentary weather protection facilities of the ground environment or underground pits, the environmental conditions are relatively harsh.

Finally, the corresponding environmental stress coefficients in the 299C inlet part stress method are used to express, and the corresponding environmental coefficients are respectively taken as 1.5 and 2.5. Substituting the environmental fault percentage data into the formula 8, $\lambda_e = 0.0574 \times 10^{-6}$.

Ambient Temperature Failure Rate λ_T and Acceleration Factor π_T. The acceleration coefficient of ambient temperature failure rate is compared with the acceleration coefficient of electromagnetic thermal stress in the operating state, which only takes into account the effect of ambient temperature on the components, so the acceleration coefficient can be calculated using the Arrhenius model, where the formula 9 follows where k is the Boltzmann constant, $k = 8.62 \times 10^{-5} (eV/K)$.

$$\pi_T = e^{\frac{E_a}{k}[\frac{1}{T_0} - \frac{1}{T_1}]} = e^{\frac{E_a}{k}[\frac{1}{273+40} - \frac{1}{273+T_1}]} \tag{9}$$

Substitute the ambient temperature to get: under normal environment (40 °C), $\pi_T = 1$; under the worst environment (60 °C): $\pi_T = 2.4361$. Substitute the ambient temperature fault percentage data into the formula to get, $\lambda_e = 0.0308 \times 10^{-6}$.

Quality Grade Failure Rate λ_Q and Acceleration Factor π_Q. The quality grade of components is inseparable from the specifications implemented in their production process. The stringency of the quality control required by the specifications determines the quality grade of the components. According to literature [17], the quality grade of electrolytic capacitor material in relay protection devices is chosen as R grade, which corresponds to an acceleration factor $\pi_Q = 0.1$ in 299C. Substituting the quality level fault percentage data into the formula yields, $\lambda_Q = 0.3808 \times 10^{-6}$.

Induced Failure Rate λ_i and Acceleration Factor π_i. The induced factor failure rate model refers to the induced failure rate model in the FIDES standard, and the induced factors considered are mechanically induced, electrically induced and thermally induced, and the specific model can be expressed as the following Eq. 10 [18].

$$\pi_i = (\pi_{placement} \times \pi_{application} \times \pi_{ruggedising})^{0.511 \times \ln(C_{sensitivity})} \tag{10}$$

where $\pi_{placement}$ indicates the effect of the location of the item in the device or system. Aluminum electrolytic capacitors belong to the analog power interface function, $\pi_{placement} = 2.5$; $\pi_{application}$ indicates the influence of application environment on electrolytic capacitors, and the weight of each induced stress environment is indicated by the application coefficient P_{mark}, which is divided into three levels. The corresponding application coefficients P_{mark} increase in steps of 1, 3.2, and 10. The specific application environments are listed in the following Table 4.

Using the proportional weighting formula 11, the acceleration factor $\pi_{application} = 3.0$ in the protection cell; the acceleration factor $\pi_{application} = 3.07$ in the outdoor area.

$$\pi_{application} = \frac{1}{66} \cdot \sum_{k=Criteria} Pmarks_k \cdot Pos_k \tag{11}$$

Table 4. Application environment assessment table.

Application Environment	Grade (application factor P_{mark})	Weights
User type	Level 1/General public/$P_{mark} = 3.2$	20
User qualification level	Level 1/Qualified/$P_{mark} = 3.2$	10
System mobility	Level 0/Moderate contingencies/$P_{mark} = 1$	4
Product manipulation	Level 1/Manipulation without displacement or disassembly/$P_{mark} = 3.2$	15
Type of electrical network	Level 1/Slightly disturbed network /$P_{mark} = 3.2$	4
Exposure to human activity	Level 1/Possible activity in the product zone/$P_{mark} = 3.2$	8
Exposure to machine disturbance	Level 1/Indirect exposure /$P_{mark} = 3.2$	3
Exposure to the weather	Level 0/Relay protection cell $P_{mark} = 1$; Level 1/Outdoor areas $P_{mark} = 3.2$	2

$\pi_{ruggedising}$ indicates the effect of overstress in the product development process, and the default value is 1.7. Since the effect of electromagnetic stress on the aluminum electrolytic capacitor is not a major factor, it is not considered as a major factor in the consideration. $C_{sensitivity}$ indicates the sensitivity coefficient of overstress in the model, and the $C_{sensitivity} =$ of the aluminum 6.4. Substituting into Eq. 11, the induced coefficient $\pi_i = 11.1854$ in the relay protection cell; the induced coefficient $\pi_i = 11.4328$ in the outdoor area. Substituting the induced factor failure percentage data into the formula 8, $\lambda_i = 0.003065 \times 10^{-6}$.

Finally, bringing back to Eq. 6, the failure rate of aluminum electrolytic capacitor λ_p under normal stress conditions can be obtained: $\lambda_p = 0.4 \times 10^{-6}$.

4.4 Prediction of Work Failure Rate Under Specific Environmental Stress

Considering the worst case of relay protection device operation, it is assumed that the internal temperature rise and ambient temperature of the device is the worst 60 °C, and the ambient condition is the worst condition. Under this stress condition, the partial stress acceleration coefficient is calculated, and the operating failure rate of aluminum electrolytic capacitor under severe environmental stress $\lambda_p = 0.804 \times 10^{-6}$ is obtained.

5 Relay Protection Device Failure Rate Results and Analysis

5.1 Results Comparison of 299C and Barrel Theory Prediction Reliability

The reliability of relay protection devices is predicted by different methods and the results are compared. The basic failure rate of individual components on each board in the relay protection device is referred to GJB/Z 299C standard.

Using this new method, data on the failure rate of electrolytic capacitors in power supply boards can be obtained. As shown in the following Table 5, the failure rate of the aluminum electrolytic capacitors can reach 50%, which is almost 2–4 times of other failure components.

Table 5. Failure rate of electrolytic capacitors on the power supply board

Component name	Quantity	Running failure rate (Unit: 10^{-6})
…	…	…
PCB board	1	0.11232
Aluminum electrolytic capacitors	20	0.5175
Photocouplers	30	0.277425
…	…	…

Table 6. Application environment assessment table.

Predicted method	λ_p under normal conditions (Unit: 10^{-6})	λ_p under adverse conditions (Unit: 10^{-6})	Notes
299C	2.13626	5.27933	CPU board
299C	0.52760	0.93954	I/O board
299C	0.21617	0.46159	AC board
299C	0.70846	1.20916	Operation board
299C	2.14493	5.27933	Power supply board
Barrel principle	4.33005	9.34118	Power supply board
299C	0.72974	1.71021	LCD board
299C	0.18308	0.76079	Back board

Comparing the results with the reliability prediction results obtained using the "barrel theory" method. Normal and adverse environmental pressures are shown in Table 6 (Unit: 10^{-6}). As can be seen from the Table 6, the reliability of the power supply board accounts for a major part of the overall reliability of the protection device. The failure rate of the power supply board and the CPU board is relatively high and can reach several times that of the other boards ().

The overall failure rate of the device can be estimated by using Eq. 12 [18] (Table 7).

$$\text{MTBF} = \frac{1}{\sum_{i=1}^{n} \lambda_{\text{p\_board(i)}}} \tag{12}$$

Table 7. Overall failure rate of the device under different environmental stresses.

Standard	Normal environmental stress	Adverse environmental stress
Total Failure Rate (299C)	5.80379×10^{-6}	15.85359×10^{-6}
MTBF (299C)	19.6691 (years)	7.2006(years)
Total Failure Rate (barrel theory)	8.83137×10^{-6}	19.70181×10^{-6}
MTBF (barrel theory)	12.9261(years)	5.7941(years)

5.2   Results Analysis of 299C and Barrel Theory Prediction Reliability

Analysis of Reliability Prediction Results of Relay Protection Devices. From the expected results, the expected life of the protection device based on the "barrel theory" is much lower than the expected life based on 299C reliability. The main reasons are: 1. 299C expected manual has not been updated since 2006, and some emerging electronic components in the manual cannot find the corresponding basis, such as stable performance, high-frequency filtering performance of tantalum capacitors in the 299C manual cannot find the corresponding basis. As a result, the basic failure rate of some components is estimated more conservatively. 2. The observed failure rate data calculated as the normal standard environmental stress is obtained from the observed data in Quanterion Solutions' 217Plus standard, which may vary due to the different environ-mental stresses during the observed test, resulting in a high failure rate when observed.

The main reasons for the shortening of the service life of the protection devices in terms of their expected reliability process are: 1. Based on the traditional multiplicative form of the operate failure rate model, various stress correlations in the internal are not taken into account, resulting in less accurate modeling of stresses. 2. In the traditional stress model analysis method, the internal stress acceleration coefficients, except for the temperature stress, are based on the trial statistics, which makes the stress model not accurate enough.

Meanwhile, the failure rate of the electrolytic capacitors in the two methods is account for a great portion in the supply board, which means the electrolytic capacitors have played a significant role and thus have huge influence in the supply board.

Analysis of Strengths and Weaknesses of Barrel Theory Prediction Reliability Method. The advantages of the reliability prediction method based on the "barrel theory" are: 1. The ability to obtain the probability of occurrence of the corresponding failure modes through specific test data and to collate the failure causes corresponding to each failure mode through the failure analysis process, thus achieving a proportional division of the overall failure rate under a specific environmental stress and making the calculation more accurate. 2. The new method has some reliability growth. As the process level of electronic components improves, the ratio of failure rate and failure modes observed under standard stress will change, and the traditional estimation method that loses data support becomes no longer accurate and applicable, but the idea of this method and the model under standard stress can still be re-established for the new period of reliability prediction.

However, this new method still has shortcomings: 1. The new method is only applicable to failures that occur between the "Period of useful life", because the probability of failure tends to stabilize during this period. 2. This method considers electromagnetic interference at high frequencies, but due to the episodic nature of electromagnetic interference in relay protection devices, it is categorized in this case in the category of induced interference failure. With the progress of electronic products process, the case of failure modes caused by other energy storage components failure causes in relay protection devices will take up a larger proportion, and further research is needed for the model in terms of electromagnetic immunity of components.

6   Conclusion

As the first line of defense to protect the safe and stable operation of the power grid, the failure rate and maintenance cost of relay protection devices will rise year by year as the time of commissioning grows. Therefore, the scientific and reasonable reliability prediction of protection devices is of great significance to improve the safety, reliability and economy of power system.

This paper adopts the barrel theory analysis method, focuses on the failure mode of aluminum electrolytic capacitors on power supply boards, proposes a calculation method for the basic failure rate of partial stresses in protection devices, which can be updated by combining specific environmental stresses and test data, and gives an acceleration factor for evaluating each partial stress. The prediction results are also compared with the traditional reliability standard prediction method, which all found that the failure rate of the electrolytic capacitors accounts for a significant portion of the overall failure rate of power supply boards and even has great influence on the life of the relay protection devices.

References

1. Zheng, H.: The interference in the substation and the measures to improve the safe operation of relay protection. Guangdong Sci. Technol. **22**, 160–162 (2008)
2. Kong. H.: Analysis of common accidents and prevention of relay protection in power system. Value Eng. **39**(18), 72–73 (2020)
3. Wang, Y.: Research on reliability test of secondary equipment of power system. Southeast University, pp. 2–3 (2016)
4. He, J.: Reliability of relay protection. Power Syst. Automat. 5–17 (1983)
5. Zhang, X., Wu, Z., Chen, X., Huang, X.: Reliability assessment of substation secondary equipment based on environmental stress analysis. Zhejiang Electr. Power **28**(03), 16–19 (2009)
6. Xia, B.: Analysis of the life of relay protection devices and discussion of the life impact mechanism. Technol. Innov. Appl. **14**, 180 (2017)

 7. FIDES guide: Reliability methodology for electronic systems (2009)
 8. Yuan, J., Ma, J., Wang, S., Zhou, L., Zhou, H.: Smart energy meter reliability prediction technology. Power Autom. Equip. **33**(07), 161–166 (2013)
 9. Huang, Y., Lu, T., Dang, S., Chen, L.: Reliability prediction of smart meter metering unit based on GJB/Z 299C. J. Harbin Univ. Technol. **26**(06), 104–111 (2021)
10. Zhou, Z., Li, X., Cui, L., Ni, S., Wang, S.: Relay protection device power board failure response measures. Henan Sci. Technol. **40**(18), 38–41 (2021)
11. Du, Y.: Analysis of the impact of aluminum electrolytic capacitor failure on the health of DC/DC converters. Capital Normal University, pp. 1–2 (2012)
12. Zang, C.: Research and application of a comprehensive evaluation method based on the barrel principle. Chengdu University of Technology (2012)
13. RIAC-HDBK-217Plus, Handbook of217plus Reliability Prediction models (2015)
14. Nie, G., Zheng, L., Yu, D., Lei, T., Li, X.: A review of manual-based reliability prediction correction methods. Electr. Prod. Reliab. Environ. Test. **38**(S2), 97–100 (2020)
15. Tian, H., Xu, D.:.Failure analysis of aluminum electrolytic capacitors. In: 2020 China House-hold Appliance Technology Conference, pp. 1900–1905. Suzhou Samsung electronics Co, Suzhou (2020)
16. Zhang, H.: Failure analysis of electrolytic capacitor winding process and implementation of its control system, Guizhou University, pp. 7–9 (2021)
17. GJB 2649: Failure rate sampling plans and procedures for military electronic component parts (1996)
18. Radu, M.: Reliability and fault tolerance analysis of FPGA platforms. In: Applications and Technology (LISAT) Conference 2014. pp. 1–4, IEEE Long Island Systems, USA (2021)

A Real-Time Dispatch Algorithm for PEV Aggregators for V2G Regulation Under the Performance-Based Compensation Scheme

Dapeng Chen[1,2](✉) , Qing Liu[1], Yu Ding[3], and Haiwang Zhong[2]

[1] China Electric Power Planning and Engineering Institute, Beijing 100035, China
dpchen@eppei.com
[2] Department of Electrical Engineering, Tsinghua University, Beijing 100084, China
[3] China Minmetals Corporation, Beijing 100010, China

Abstract. In this paper, a real-time dispatch algorithm is proposed to maximize the total profit that an aggregator can win in the frequency regulation market where a performance-based compensation scheme is engaged. Under this scheme, the PEV aggregator's performance of following the regulation signals will affect the compensation it receives for the frequency regulation service. With the proposed algorithm, the aggregator optimally allocates the regulation power and baseline charging power to PEVs to respond to the regulation signals for maximum profit. Comprehensive simulation studies, which are based on the codes and data of PJM power market, have been carried out to verify the proposed algorithm. Compared with the droop-based approach, the simulation results show that the proposed algorithm can improve the total profit of the aggregator in both cases of dynamic and traditional regulation signals.

Keywords: Aggregator · Frequency regulation · Vehicle-to-grid (V2G) · Plug-in electric vehicle (PEV)

1 Introduction

The number of plug-in electric vehicles (PEVs) increases rapidly, which will bring significant impact on the power system's planning and operation [1–4]. For power systems, PEV is not only a kind of load, but also an important ancillary service provider. By providing various ancillary services such as voltage regulation [5], smoothing of renewable energy sources [6], spinning reserve [7], frequency regulation [8, 9] and so on, PEVs can not only benefit the power systems, but also make profit for their owners.

Frequency regulation is an essential ancillary service and will play an increasingly important role with the development of intermittent and stochastic renewable energy generation. Due to the fast-response characteristic of the PEV battery systems, PEVs can provide higher quality regulation service compared with the traditional providers (the generators). Participating in frequency regulation, PEVs can get profit when they are plugged into the power grid to satisfy their charging demands.

Since an individual PEV can hardly affect the frequency, an aggregator is expected to combine and dispatch a large group of PEVs to participate in frequency regulation [10]. The primary function of PEVs is to satisfy their owners' transportation usage. Hence, the V2G regulation strategies should take both the charging demands and regulation instruction signals into account. In the regulation markets, the compensation for the service providers mainly includes two parts: one is related to the reserved regulation capacity and the other is related to the real-time responses of the providers.

Consequently, the PEV aggregators' strategies in the regulation market consist of two steps. Firstly, the aggregators decide the bidding strategies to optimize the regulation capacity at each period [11–14]. Secondly, in real time, after receiving the regulation signals, the aggregators control the charging/discharging power of each PEV to coordinate the charging demands and regulation instructions [15–20].

Before 2011, in most regulation markets, the second part of the compensation is merely based on the energy injected to or discharged from PEVs. In some markets, the opportunity cost (the lost profit in the energy market because of providing regulation service) is also included in the compensation. Under this compensation scheme the real-time dispatch strategies of PEV aggregators are relatively simple. Generally, besides responding to the regulation signals, the objective of the real-time dispatch strategy is to satisfy the PEVs' charging demands [15–19]. In [20], the aggregator's profit is taken into account when allocating the regulation power to PEVs. In 2011, the FERC (U.S.A.) issued the Order No. 755 [21] in which a new performance-based compensation scheme is presented. The ISOs are required to introduce the new scheme into the regulation markets [22–25]. Under this scheme, the compensation for regulation service consists of two parts, i.e., capacity and mileage payment. The latter compensates for the providers' actual amount of up/down operation during the services. Based on the PJM's RegD-type regulation signal data and price data from March 1, 2016 to February 28, 2017 [26], it can be calculated that the mileage payment amounts for about 21% of the total regulation profit.

The key improvement of the new scheme is that the payment of capacity and/or mileage are/is dependent on the providers' performance of following the regulation signals. Under the new scheme, the aggregators' strategy in the regulation market becomes more complex, especially for the second step strategies, because the real-time response of the aggregator will influence its regulation performance. In [27], a robust optimization framework is used to optimal the PEV aggregators' regulation strategy under the new compensation scheme. The schedule of the regulation capacity is analyzed in [27] while the real-time dispatch strategy after receiving the regulation signal is not investigated.

In this work a real-time dispatch algorithm for PEV aggregators to provide regulation service under the performance-based compensation scheme is proposed. Beside the regulation profit, the aggregator should consider the charging/discharging profit and the charging demands of PEVs. Furthermore, the performance of the aggregator has a tight relationship with the real-time responses to the regulation signals. Consequently, under the new compensation scheme, PEV aggregators need a new real-time dispatch algorithm for profit maximization when providing regulation service.

2 Charging/Discharging Profit and Compensation for PEV Owners

On workdays, many PEVs will stay at the parking lots in the daytime (8:00 a.m.–5:00 p.m.). The managers of such parking lots can act as aggregators to use these PEVs to provide regulation service. It is assumed that once a PEV is plugged into the power grid, it will provide the aggregator with the information of its initial SOC and its desired SOC at leaving. Generally, PEVs can be categorized into two types: TYPE 1 whose desired SOCs are greater than or equal to the initial ones, and the others are TYPE 2. Beside the capacity and mileage profit, an aggregator participating in the regulation market will also earn from the energy sold when discharging PEVs and pay for the energy consumed when charging PEVs. Moreover, in this paper the aggregator will pay PEV owners for compensation if it fails to satisfy their charging demands. Consequently, to consider the total profit of the aggregator, the charging and discharging profit and the compensation for PEV owners should be analyzed.

2.1 Charging Profit

The charging profit is based on the desired SOC, initial SOC and final SOC. Specifically, PEVs of TYPE 2 should not be charged for energy consumed because their desired SOCs are smaller than the initial ones. As for PEVs of TYPE 1, between the final SOC and the desired SOC, the charging profit is based on the smaller one. That is to say, even though the final SOCs are larger than their desired ones, the aggregator will not get extra payment for their additionally charged power. The charging profit the aggregator can get from the ith PEV can be expressed as

$$r_i^{\text{ch}} = \max[(\min(D_i^{\text{SOC}}, F_i^{\text{SOC}}) - I_i^{\text{SOC}})B_{\text{c}}p^{\text{sell}}, 0] \tag{1}$$

where D_i^{SOC} and F_i^{SOC} are the desired and final SOC (p.u.) at the departure time of the ith PEV, respectively; I_i^{SOC} is the initial SOC (p.u.) of the ith PEV when arriving; B_{c} is the battery capacity; p^{sell} is the price of energy charged to the PEV owners.

In real-time dispatch, F_i^{SOC} is unknown in advance. At instant t, it is assumed that the ith PEV is charged with its maximum charging power before it leaves and its final SOC in this case is the estimated F_i^{SOC} which will be detailed in Sect. 3. At instant t, the charging profit of the ith PEV is

$$r_i^{\text{ch}}(t) = P_i^{\text{ch}}(t)(\alpha_i \beta_i p^{\text{sell}} - p^{\text{buy}}(t))\Delta t/3600 \tag{2}$$

where $P_i^{\text{ch}}(t)$ is the charging power of the ith PEV (at the power grid side); $p^{\text{buy}}(t)$ is the price the aggregator paid to the power grid; α_i denotes an indicator function, which is equal to 1 if the estimated F_i^{SOC} is smaller than D_i^{SOC} and is equal to 0 otherwise; similarly, β_i is equal to 1 if the D_i^{SOC} is larger than I_i^{SOC} and is equal to 0 otherwise.

The degradation cost of batteries are assumed to be zero when the PEVs are charged for regulation service.

2.2 Discharging Profit

The degradation cost due to discharging can be calculated by multiplying the cost per kilowatt by the number of kW discharged by a PEV [20, 28]. The discharging profit of the ith PEV at instant t can be expressed as

$$r_i^{\mathrm{dc}}(t) = P_i^{\mathrm{dc}}(t)(p^{\mathrm{e}}(t) - c)\Delta t / 3600 \tag{3}$$

$$c = c_{\mathrm{d}} + c_{\mathrm{el}}/\eta^{\mathrm{dc}} \tag{4}$$

where $P_i^{\mathrm{dc}}(t)$ is the discharging power of the ith PEV (at the power grid side); $p^{\mathrm{e}}(t)$ is the energy price at instant t; c is the total cost per kWh of the ith PEV for bidirectional frequency regulation; c_{d} represents the cost of battery degradation per kWh; c_{el} is the cost of the purchased power per kWh; η^{dc} is the discharging efficiency.

The second term on the right-hand side of Eq. (4) represents the unit loss of energy discharged.

2.3 Compensation for PEV Owners for Energy Deficiency

The aggregator has to compensate the PEV owners for the charging demands that are not satisfied. The compensation paid to the ith PEV is expressed as

$$C_i^{\mathrm{com}} = \max[p_i^{\mathrm{com}} B_{\mathrm{c}}(D_i^{\mathrm{SOC}} - F_i^{\mathrm{SOC}}), 0] \tag{5}$$

where p_i^{com} is the compensation price for the ith PEV owner, which can be specified by PEV owners in contract.

For the ith PEV, when charging it with its maximum charging power, the time it takes to suffice its charging demand is expressed as

$$T_i(t) = (D_i^{\mathrm{SOC}} - R_i^{\mathrm{SOC}}(t))B_{\mathrm{c}}/(P^{\mathrm{max}}\eta^{\mathrm{ch}}) \tag{6}$$

where P^{max} is the maximum charging power of PEVs and η^{ch} is the charging efficiency; $R_i^{\mathrm{SOC}}(t)$ represents the real-time SOC of the ith PEV at instant t.

Suppose t_i^{rem} represents the remaining time of the ith PEV before it leaves. If $T_i > t_i^{\mathrm{rem}}$, the aggregator has to pay the PEV owner for compensation, in which case $\alpha_i = 1$.

3 The Real-Time Dispatching Algorithm

3.1 Dispatch Priority

The aggregator dispatches PEVs for V2G regulation considering their charging demands. PEVs with relatively large charging demands are prioritized for regulation-down service. The electric energy deficient ratio (EEDR) is defined to describe the charging demand of a PEV. The EEDR can be positive or negative:

$$\mathrm{EEDR}_i(t) = D_i^{\mathrm{SOC}} - R_i^{\mathrm{SOC}}(t) \tag{7}$$

At instant t, a positive EEDR means that the PEV has a charging demand, while a negative one indicates that the PEV has the potential to be discharged.

The weighting factors w based on the EEDRs are introduced to indicate the priorities of different PEVs in real-time dispatch:

$$w_i(t) = \frac{\text{EEDR}_i(t) - \text{EEDR}^{\min}(t)}{\text{EEDR}^{\max}(t) - \text{EEDR}^{\min}(t)} \tag{8}$$

where $\text{EEDR}^{\max}(t)$ and $\text{EEDR}^{\min}(t)$ represent the maximum and minimum EEDR among all PEVs at instant t.

The weighting factor is in the range of [0, 1]. In the proposed algorithm, PEVs with larger weighting factors will be allocated with more charging power. Limited to the total baseline charging power, PEVs with relatively small weighting factors may not be charged even though their baseline charging power is set before the operating hour. The weighting factors change with EEDRs in real time. The more energy a PEV is needed, the more charging power it will be allocated. Therefore, to decide the compensation for PEV owners for energy deficiency, we define the estimated F_i^{SOC} as the final SOC when the ith PEV is charged with its maximum charging power in the remaining time.

3.2   The Objective Function

An objective function is established based on the compensation scheme in PJM power market [22, 29]. In the PJM power market, the mileage is calculated as the sum of the absolute differences between the two consequent regulation signals. The overall performance score is expressed as a weighted average of the performance score components:

$$A = k_1 S^{\text{pre}} + k_2 S^{\text{cor}} + k_3 S^{\text{delay}} \tag{9}$$

where k_1, k_2 and k_3 are unit-less scalars ranging from 0 to 1 and $k_1 + k_2 + k_3 = 1$; S^{pre}, S^{cor} and S^{delay} represent the scores of precision, correlation and delay, respectively.

To alleviate the notation, the time dependence with t can be removed from the variables since this algorithm is based on real-time decision and is solved at each instant.

Let binary variables x_i^{ch} and x_i^{dc} represent the charging/discharging states of the ith PEV. If $x_i^{\text{ch}} = 1$, the ith PEV will be charged; if $x_i^{\text{dc}} = 1$, the ith PEV will be discharged. P_i^{ch} and P_i^{dc} represent the power delivered to or from a PEV.

The objective function is

$$\max_{x_i^{\text{ch}}, x_i^{\text{dc}}, P_i^{\text{ch}}, P_i^{\text{dc}}} R_{\text{period}}^{\text{cap}} + R_{\text{period}}^{\text{mil}} + \sum_{i=1}^{N} (R_i^{\text{ch}} + R_i^{\text{dc}} - C_i^{\text{com}}) \tag{10}$$

subject to:

$$R_{\text{period}}^{\text{cap}} = C_{\text{period}}^{\text{cap}} \cdot p_{\text{period}}^{\text{cap}} \cdot A_{\text{period}} \tag{11}$$

$$R_{\text{period}}^{\text{mil}} = M_{\text{period}}^{\text{mil}} \cdot p_{\text{period}}^{\text{mil}} \cdot A_{\text{period}} \tag{12}$$

$$R_i^{\text{ch}} = (\alpha_i \beta_i p^{\text{sell}} - (p^{\text{buy}} - w_i^1/\varphi_1))P_i^{\text{ch}}\Delta t/3600 \ \forall i \tag{13}$$

$$R_i^{\text{dc}} = (p_0^{\text{e}} - (c + w_i^2/\varphi_2))P_i^{\text{dc}}\Delta t/3600 \ \forall i \tag{14}$$

$$C_i^{\text{com}} = \alpha_i p_i^{\text{com}}(\text{EEDR}_i \cdot B_{\text{c}} - P^{\max}\eta^{\text{ch}}t_i^{\text{rem}} - (P_i^{\text{ch}}\eta^{\text{ch}} - P_i^{\text{dc}}/\eta^{\text{dc}})\Delta t/3600) \tag{15}$$

$$R_i^{\text{SOC}} + (P_i^{\text{ch}}\eta^{\text{ch}} - P_i^{\text{dc}}/\eta^{\text{dc}})\Delta t/(3600 \cdot B_{\text{c}}) \leq \text{SOC}_i^{\max} \ \forall i \tag{16}$$

$$R_i^{\text{SOC}} + (P_i^{\text{ch}}\eta^{\text{ch}} - P_i^{\text{dc}}/\eta^{\text{dc}})\Delta t/(3600 \cdot B_{\text{c}}) \geq \text{SOC}_i^{\min} \ \forall i \tag{17}$$

$$\alpha_i = \begin{cases} 1 & \text{EEDR}_i \cdot B_c > P^{\max}t^{\text{rem}}\eta^{\text{ch}} \\ 0 & \text{else} \end{cases} \ \forall i \tag{18}$$

$$\beta_i = \begin{cases} 1 & D_i^{\text{SOC}} > I_i^{\text{SOC}} \\ 0 & \text{else} \end{cases} \ \forall i \tag{19}$$

$$w_i^1 = \begin{cases} 0 & S^{\text{act}} > 0 \\ w_i & \text{else} \end{cases} \ \forall i \tag{20}$$

$$w_i^2 = \begin{cases} w_i & S^{\text{act}} > 0 \\ 0 & \text{else} \end{cases} \ \forall i \tag{21}$$

$$p_0^{e} = \begin{cases} p^{e} & S^{\text{act}} > 0 \\ 0 & \text{else} \end{cases} \tag{21}$$

$$S^{\text{act}} = S \cdot C^{\text{cap}} - \sum_{i=1}^{N} P_i^{\text{base}} \tag{22}$$

$$0 \leq P_i^{\text{ch}} \leq x_i^{\text{ch}}P^{\max} \ \forall i \tag{23}$$

$$0 \leq P_i^{\text{dc}} \leq x_i^{\text{dc}}P^{\max} \ \forall i \tag{24}$$

$$x_i^{\text{ch}} + x_i^{\text{dc}} \leq 1 \ \forall i \tag{25}$$

$$\sum_{i=1}^{N} (P_i^{\text{ch}} - P_i^{\text{dc}}) \leq M^{\text{power}} \tag{26}$$

$$R = \sum_{i=1}^{N} (P_i^{\text{dc}} - P_i^{\text{ch}}) \tag{27}$$

where $R_{\text{period}}^{\text{cap}}$ and $R_{\text{period}}^{\text{mil}}$ represent the capacity and mileage profit for a certain period, respectively; R_i^{ch} and R_i^{dc} represent the charging and discharging profit, respectively; φ_1

and φ_2 are constant values larger than 1; $SOC_i^{\min}$ and $SOC_i^{\max}$ are the minimum and maximum SOC (p.u.) of the ith PEV; S^{act} represents the actual charging/discharging power that the aggregator should provide; S is the regulation signal (p.u.) for regulation up/down and C^{cap} is the contracted capacity for regulation up/down; P_i^{base} represents the baseline charging power of the ith PEV; M^{power} is the maximum instantaneous power restricted by the distribution system; R represents the aggregator's response to the regulation signal.

Generally, A is averaged over a certain period (e.g., 5 min). Hence, $R_{\mathrm{period}}^{\mathrm{cap}}$ and $R_{\mathrm{period}}^{\mathrm{mil}}$ are included and they are calculated with formula (3) and (4). However, because the objective function is calculated every Δt after receiving a regulation signal, the estimated values of $M_{\mathrm{period}}^{\mathrm{mil}}$ and A_{period} for this period are adopted to calculate $R_{\mathrm{period}}^{\mathrm{mil}}$ and $R_{\mathrm{period}}^{\mathrm{cap}}$ (the contracted capacity is given). Assume T is the number of regulation signals received during a certain period. The mileage at the current instant t can be calculated based on the regulation signal received. The mileage of the succeeding instants is regarded as the mean of the mileage before instant t:

$$M_{t+1}^{\mathrm{mil}} = \cdots = M_T^{\mathrm{mil}} = (M_1^{\mathrm{mil}} + \cdots + M_{t-1}^{\mathrm{mil}})/(t-1) \tag{28}$$

where M_t^{mil} represents the mileage at instant t of this period.

As for A, it is closely related to the aggregator's every single response (including the precision, responding rate, etc.). The responses before the instant t are known and the responses of the succeeding instants are assumed to be equal to that of the current instant. When the charging power is needed, PEVs with larger weighting factors are considered to make larger charging profit. The battery cost of PEVs with smaller weighting factors is considered to be smaller if the discharging power is required.

The main purpose of the weighting factor is to guide the aggregator to satisfying the charging demands of PEVs when it responds to the regulation signals. Without the weighting factor, a number of PEVs are probably still with high EEDRs in the last few hours before they leave, and the aggregator may choose to charge them and its performance of following the regulation signals will be degraded. Therefore, the dispatch flexibility of the aggregator can be enhanced by using the weighting factor. φ_1 and φ_2 are set to reduce the weighting factors' influence on the objective function.

3.3 Detailed Procedure of the Proposed Algorithm

The flow chart of the real-time dispatch algorithm is shown in Fig. 1. Firstly, the aggregator will decide β_i of each PEV according to D_i^{SOC} and I_i^{SOC} from Steps 1 to 5. Before receiving the regulation signal at each instant t, the aggregator examines whether the charging demand of a PEV can be sufficed during the remaining time according to Eq. (6) and Step 6. Accordingly, the indicator α_i is decided. Steps 1 to 10 are essential to calculate the charging profit of the aggregator and the compensation it pays to the PEV owners.

From Steps 11 to 13, the aggregator collects the data of the PEVs, such as the real-time SOCs and charging/discharging power. The EEDR of each PEV is calculated according to $R_i^{\mathrm{SOC}}(t)$ and D_i^{SOC} then the weighting factors are decided.

From Steps 14 to 17, after receiving a regulation signal, S^{act} is calculated according to Eq. (22) and then problem (10)-(27) is solved to dispatch PEVs optimally.

After the dispatch at instant t, Steps 1 to 13 are repeated to calculate the parameters for the next regulation signal. For example, $R_i^{\mathrm{SOC}}(t+1)$ is calculated as

$$R_i^{\mathrm{SOC}}(t+1) = R_i^{\mathrm{SOC}}(t) + \frac{\Delta t (P_i^{\mathrm{ch}}(t)\eta^{\mathrm{ch}} - P_i^{\mathrm{dc}}(t)/\eta^{\mathrm{dc}})}{3600 \cdot B_{\mathrm{c}}} \tag{29}$$

In the proposed algorithm, only Steps 15 to 17 are executed after receiving a regulation signal, which guarantees the computational efficiency.
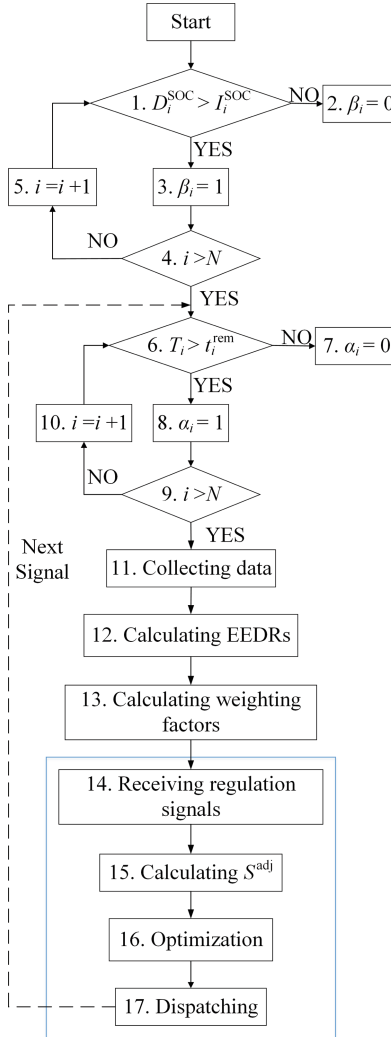
Fig. 1. The flow chart of the real-time dispatch algorithm.

4 Case Study

4.1 Parameter Setting

To simplify the analysis, we assume an ideal AGC system with no communication delay. As for the accuracy performance, we assume the delay effect is ignored due to the fast response of PEVs and concentrate only on the precision score [30]. In this paper, for each Δt set of calculations the performance score will be averaged over a five minute period.

The parameters adopted in the case studies are listed in Table 1. It is assumed that a parking lot as an aggregator is formed by 800 PEVs whose plug-in duration is from 8:00 a.m. to 5:00 p.m.. All PEVs can be dispatched by the aggregator for regulation service. To calculate cd, the relevant parameters in [20] are used, except that the total cost of the battery is set at \$ 260/kWh [31]. For convenience, a unique compensation price p^{com} is adopted for all PEV owners. The total baseline charging power is equal to 717.89 kW each hour. As the initial SOCs and desired SOCs may vary with PEVs, normally distributed scenarios within the up- and down-limits are used to describe the SOC levels of PEVs, as shown in Table 2.

Table 1. Parameters adopted in the case studies.

Parameters	TYPE 1	TYPE 2
Number of PEVs	560	240
Battery capacity (kWh)	32	
Charging/discharging efficiency	0.9/0.9	
Maximum V2G power (kW)	10	
Maximum/minimum SOC (p.u.)	0.98/0.1	
Compensation price for PEV owners (\$/kWh)	1	
Price of energy charged to PEV owners (\$/kWh)	0.05	
Total baseline charging power (kW)	717.89	
φ_1/φ_2	10,000/10,000	

Real power market data from PJM is used in the case studies [26]. The energy price, regulation market capacity clearing price and regulation market performance clearing price are hourly prices. The aggregator pays for the energy consumed at the hourly locational marginal price (LMP).

Table 2. Simulation scenarios of the EVs with normally distributed battery SOCs.

Parameters	TYPE 1	TYPE 2
Initial SOC (p.u.)	SOC $\sim$ N(0.35, 0.01) SOC $\in$ [0.2, 0.5]	SOC $\sim$ N(0.7, 0.01) SOC $\in$ [0.6, 0.8]
Desired SOC (p.u.)	SOC $\sim$ N(0.74, 0.01) SOC $\in$ [0.5, 0.98]	SOC $\sim$ N(0.5, 0.01) SOC $\in$ [0.4, 0.6]

Two cases for two types of regulation signals, dynamic and traditional regulation signals are examined. For convenience, they are labeled as Case 1 and Case 2, respectively. Remarkable difference can be found in the energy content between the dynamic and traditional regulation signal.

It is assumed that the regulation signals are sent to the aggregator every 10 s, which is adequate for measuring energy delivered to the PEVs. Nevertheless, the proposed algorithm can be solved quickly enough for cases that the regulation services are required more frequently.

4.2 Results Analysis

The proposed algorithm is simulated in MATLAB (R2013b) using CPLEX (Version 12.6) and the computer configuration is: Intel(R) i7–6700 (3.4GHz), memory of 8 GB. The average computing time of this algorithm is 0.2954 s, which can be reduced by using more powerful computers.

The droop-based control approach for V2G regulation in [17] is used for comparison. Based on this approach, the aggregator dispatches PEVs according to their SOCs, charging/discharging power and charging demands after receiving a certain regulation signal. It is assumed that all the regulation capacity of the aggregator is accepted by the ISO and the capacity of regulation up is equal to that of regulation down.

Figure 2 shows the total profit of 9-h operation with the proposed algorithm and the droop-based approach respectively. Compared with the droop-based approach, the proposed algorithm can increase the aggregator's total profit by 1.41% in Case 1 and 1.24% in Case 2, respectively. Apparently, the proposed algorithm is more effective than the droop-based approach in enhancing the aggregator's profit in both cases.

The final EEDRs are shown in Fig. 3 and Fig. 4. It can be seen that the proposed algorithm performs better than the droop-based approach in satisfying the charging demands of the PEV owners in Case 1. This is not obvious in Case 2 because the final EEDRs of PEVs are smaller than zero, which means all charging demands are sufficed.
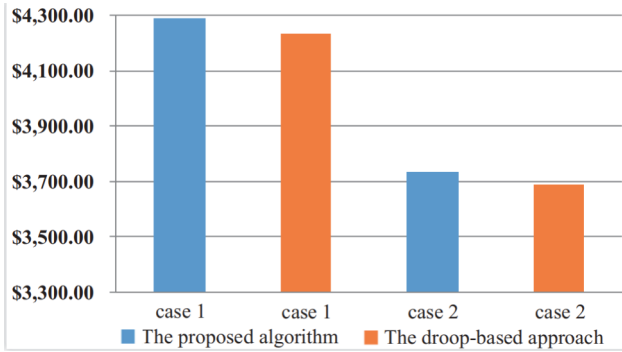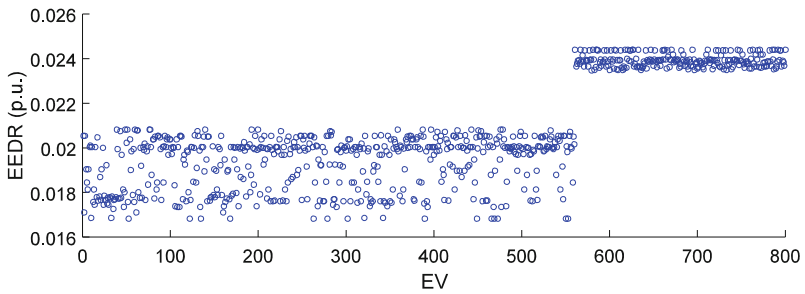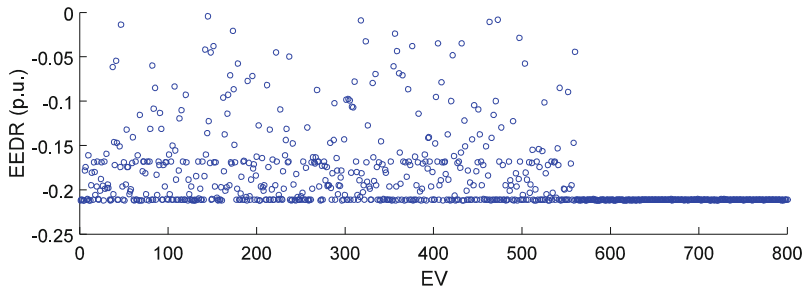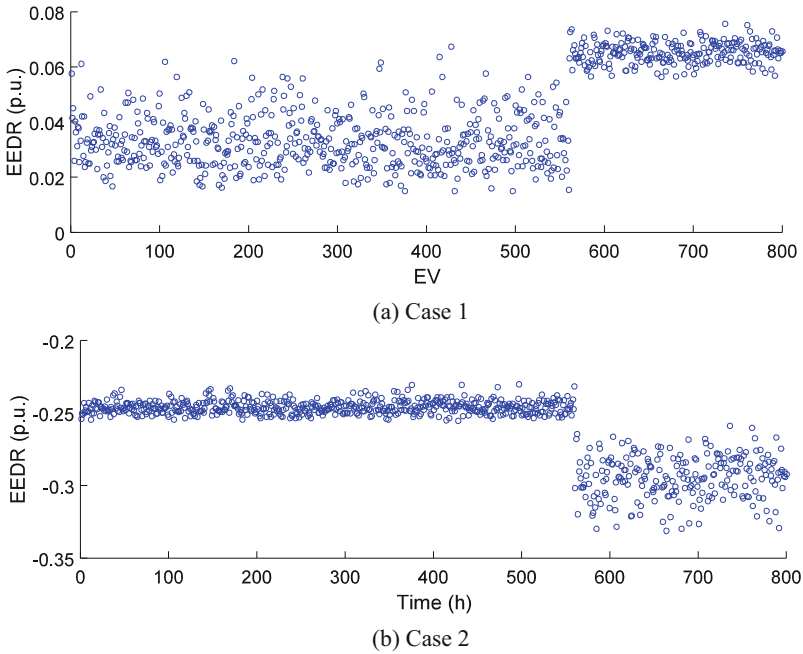
**Fig. 2.** Total profit of the aggregator for one day.

(a) Case 1

(b) Case 2

Fig. 3. The final EEDRs of PEVs calculating with the proposed algorithm.

(a) Case 1

(b) Case 2

Fig. 4. The final EEDRs of PEVs calculating with the droop-based approach.

The summations of the absolute differences between the regulation signals and their responses are shown in Fig. 5 and Fig. 6 (Positive values represent that the responses of the aggregator are larger than the regulation signals, while the negative ones correspond to the opposite). Based on the droop-based approach, PEVs follow the regulation signals more closely, thus the capacity and mileage profit is higher. However, the total profit of the aggregator is lower than that of the proposed algorithm as shown in Fig. 2. As shown in Fig. 5, in Case 1, the aggregator's responses are almost the same as the regulation signals except in the last two hours when the capacity and mileage prices are low and the aggregator has to satisfy the charging demands of PEVs. Therefore, the differences become lager. During the last hour, satisfying the charging demands of PEVs incurs the degradation of the aggregator's performance of following the signals. Compared with Case 1, the aggregator performs worse in Case 2 because continuous charging/discharging power is needed in this case. If the compensation of energy deficiency for PEV owners is zero and the capacity and mileage profit cannot cover the energy cost, the aggregator will stop charging the PEVs. Similarly, if the capacity and mileage profit and energy price are not high enough, the aggregator will not discharge PEVs. Consequently, the aggregator's performance is more likely to degrade in Case 2.
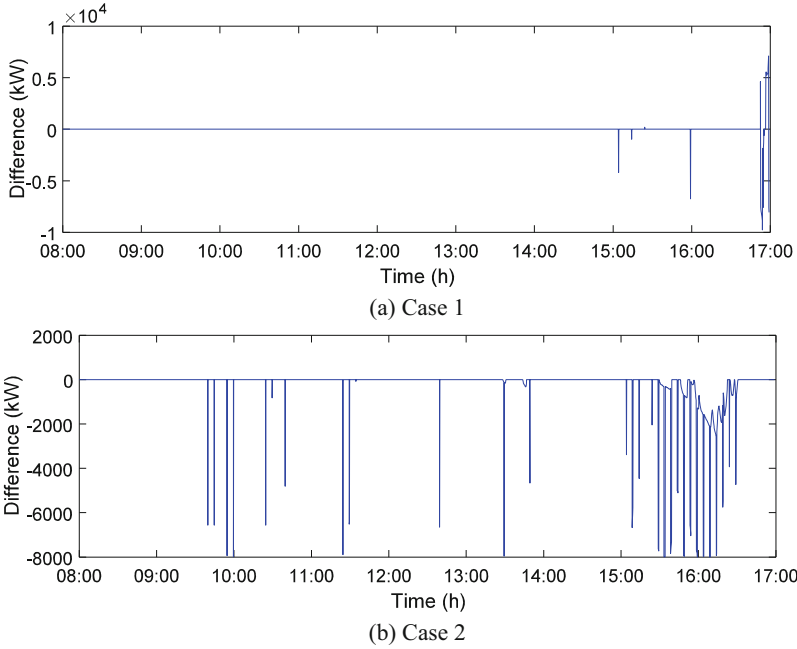
Fig. 5. The difference between the regulation signal and its response calculating with the proposed algorithm.
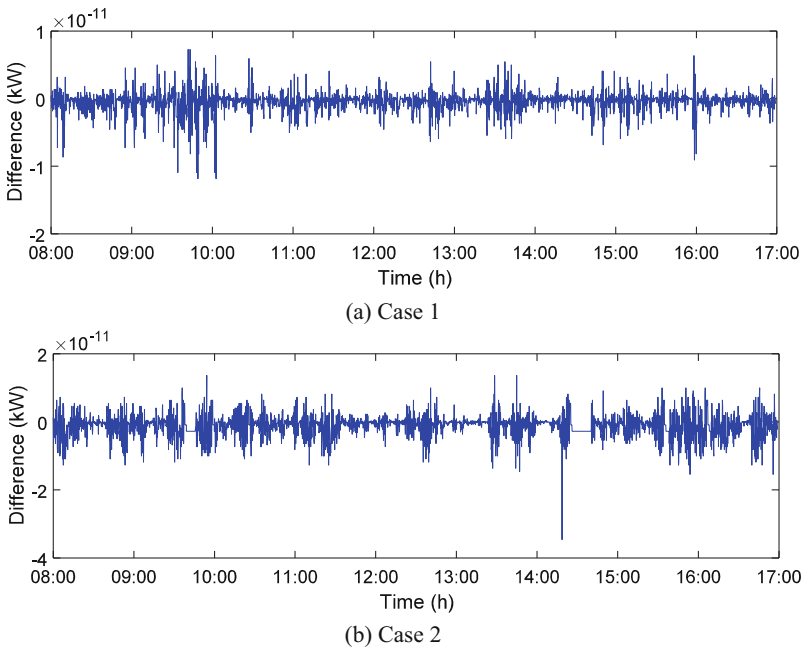
Fig. 6. The difference between the regulation signal and its response calculating with the droop-based approach.

5   Conclusion

Due to the fact that the charging/discharging power and SOCs of PEVs change in real time, PEV aggregators ought to dispatch PEVs optimally to respond to the unpredictable regulation signals, especially in a regulation market with the performance-based compensation scheme. In this paper, a real-time dispatch algorithm for aggregators to provide regulation service under the new compensation scheme is proposed. This algorithm maximizes the profit of the aggregator, considering the capacity and mileage profit, charging/discharging profit, battery cost, the charging demands and the compensation for PEV owners. With the data of PJM market, the proposed algorithm is extensively simulated in MATLAB using CPLEX. The proposed algorithm is compared with the droop-based approach for V2G regulation, and the former can improve the total profit of the aggregator by 1.41% and 1.24% in the case of dynamic and traditional regulation signals, respectively.

References

1. Global EV Outlook: Understanding the Electric Vehicle Landscape to 2020, International Energy Agency, Report, 2013. http://www.iea.org/publications/globalevoutlook 2013.pdf
2. Habib, S., Kamran, M., Rashid, U.: Impact analysis of vehicle-to-grid technology and charging strategies of electric vehicles on distribution networks–a review. J. Power Sources **277**, 205–214 (2015)
3. Luo, Z., Hu, Z., Song, Y., Xu, Z., Lu, H.: Optimal coordination of plug-in electric vehicles in power grids with cost-benefit analysis–Part I: Enabling techniques. IEEE Trans. Power Syst. **28**(4), 3546–3555 (2013)
4. Luo, Z., Hu, Z., Song, Y., Xu, Z., Lu, H.: Optimal coordination of plug-in electric vehicles in power grids with cost-benefit analysis–Part II: A case study in china. IEEE Trans. Power Syst. **28**(4), 3556–3565 (2013)
5. Yong, J.Y., Ramachandaramurthy, V.K., Tan, K.M., Mithulananthan, N.: Bi-directional electric vehicle fast charging station with novel reactive power compensation for voltage regulation. Int. J. Electr. Power Energy Syst. **64**, 300–310 (2015)
6. Luo, X., Xia, S., Chan, K.W.: A decentralized charging control strategy for plug-in electric vehicles to mitigate wind farm intermittency and enhance frequency regulation. J. Power Sources **248**, 604–614 (2014)
7. Dallinger, D., Krampe, D., Wietschel, M.: Vehicle-to-grid regulation reserves based on a dynamic simulation of mobility behavior. IEEE Trans. Smart Grid **2**(2), 302–313 (2011)
8. Jian, L., Zheng, Y., Xiao, X., Chan, C.: Optimal scheduling for vehicle-to-grid operation with stochastic connection of plug-in electric vehicles to smart grid. Appl. Energy **146**, 150–161 (2015)
9. Han, S., Han, S., Sezaki, K.: Development of an optimal vehicle-to-grid aggregator for frequency regulation. IEEE Trans. Smart Grid **1**(1), 65–72 (2010)
10. Sarker, M.R., Dvorkin, Y., Ortega-Vazquez, M.A.: Optimal participation of an electric vehicle aggregator in day-ahead energy and reserve markets. IEEE Trans. Power Syst. **31**(5), 1–10 (2015)

11. Tan, J., Wang, L.: A game-theoretic framework for vehicle-to-grid frequency regulation considering smart charging mechanism. IEEE Trans. Smart Grid (2016)
12. Lam, A.Y., Leung, K.-C., Li, V.O.: Capacity estimation for vehicle-to-grid frequency regulation services with smart charging mechanism. IEEE Trans. Smart Grid **7**(1), 156–166 (2016)
13. Sortomme, E., El-, M.A.: Optimal scheduling of vehicle-to-grid energy and ancillary services. IEEE Trans. Smart Grid **3**(1), 351–359 (2012)
14. Vagropoulos, S.I., Bakirtzis, A.G.: Optimal bidding strategy for electric vehicle aggregators in electricity markets. IEEE Trans. Power Syst. **28**(4), 4031–4041 (2013)
15. Sortomme, E., El-, M.A.: Optimal charging strategies for unidirectional vehicle-to-grid. IEEE Trans. Smart Grid **2**(1), 131–138 (2011)
16. Liu, H., Hu, Z., Song, Y., Lin, J.: Decentralized vehicle-to-grid control for primary frequency regulation considering charging demands. IEEE Trans. Power Syst. **28**(3), 3480–3489 (2013)
17. Liu, H., Hu, Z., Song, Y., Wang, J., Xie, X.: Vehicle-to-grid control for supplementary frequency regulation considering charging demands. IEEE Trans. Power Syst. **30**(6), 3110–3119 (2015)
18. Karfopoulos, E.L., Panourgias, K.A., Hatziargyriou, N.D.: Distributed coordination of electric vehicles providing v2g regulation services. IEEE Trans. Power Syst. **31**(4), 2834–2846 (2016)
19. Vagropoulos, S.I., Kyriazidis, D.K., Bakirtzis, A.G.: Real-time charging management framework for electric vehicle aggregators in a market environment. IEEE Trans. Smart Grid **7**(2), 948–957 (2016)
20. Escudero-Garzás, J.J., García-Armada, A., Seco-Granados, G. : Fair design of plug-in electric vehicles aggregator for v2g regulation. IEEE Trans. Vehic. Technol. 61(8), 3406–3419 (2012)
21. Federal Energy Regulatory Commission, Order No. 755: Frequency Regulation Compensation in the Organized Wholesale Power Markets (2011). http://www.ferc.gov
22. PJM Manual 12: Balancing Operations (August 2016). http://www.pjm.com/~/media/documents/manuals/m12.ashx
23. NYISO Manual 14: Accounting and Billing Manual (December 2014). http://www.nyiso.com/public/webdocs/marketsoperations/documents/ManualsandGuides/Manuals/Administrative/acctbillmnl.pdf
24. CAISO Business Requirements Specification: Pay For Performance Regulation, Document Version: 1.4. http://www.caiso.com/Documents/BusinessRequirementsSpecification-Pay-Performance.pdf
25. MISO Market Settlements Calculation Guide, MS-OP-029-r23. https://www.misoenergy.org/Library/Repository/Tariff%20Documents/BPM%20005%20-%20Market%20Settlements.zip
26. PJM power market data. http://www.pjm.com
27. Yao, E., Wong, V.W., Schober, R.: Robust frequency regulation capacity scheduling algorithm for electric vehicles. IEEE Trans. Smart Grid **8**(2), 984–997 (2017)
28. White, C.D., Zhang, K.M.: Using vehicle-to-grid technology for frequency regulation and peak-load reduction. J. Power Sources **196**(8), 3972–3980 (2011)
29. PJM Manual 28: Operating Agreement Accounting, Nov. 2016. http://www.pjm.com/~/media/documents/manuals/m28.ashx
30. Ko, K., Han, S., Sung, D.K.: Performance-based settlement of frequency regulation for electric vehicle aggregators IEEE Trans. Smart Grid (2016)
31. Dinger, A.: Batteries for electric cars: Challenges, opportunities, and the outlook to 2020. Boston Consulting Group (2010)

Bayesian Network Modeling for New Power System Carbon Emission with Natural Disaster Chain and Carbon Change Estimation

Jianmin Zhang[1(✉)], Yukuan Wang[1], Kang Chang[2], Feng Xue[2], and Yusheng Xue[2]

[1] School of Automation, Hangzhou Dianzi University, Hangzhou 310018, China
zhangjmhzcn@hdu.edu.cn

[2] NARI Technology Development Limited Company, Nanjing 211111, China

Abstract. The renewable and low carbon resources, like hydropower, photovoltaic, wind power, as well as the transmission and distribution network on the earth are vulnerable to the natural disaster chain which will seriously affect the carbon decreasing performance of evolving the new type of power system, thus it is urgent to reveal the relationship between natural disaster chain and the performance of carbon emission decreasing from the new type power system. To this end, a concept of carbon changes in power systems is put forward in this paper on the base of the analysis of the impact of natural disasters on the power system, and a Bayesian network of "natural disaster-power system-carbon change" is provided to describe the influence of natural disaster chain on carbon emission trajectory of the power system. Combined with the characteristics of the natural disaster chain, a multi-Bayesian network carbon change estimation method considering the interaction of multiple disasters is proposed. And the feasibility of the proposed method is verified by a disaster chain case of "rainstorm - landslide – flood".

Keywords: Natural disaster · disaster chain · New power system · Bayesian network · carbon change

1 Introduction

In 2020, the Chinese government made the commitment to "carbon peaking by 2030" and "carbon neutrality by 2060" at the 75th Session of the United Nations General Assembly. In 2021, the Chinese government put forward a work plan and a series of carbon-related reform measures. As the main source of carbon emission, the electric power system will bear the brunt, its supply and demand factors will change, and the direction of future development and reform will also be deeply affected [1]. On one hand, as the main source of carbon emissions, the power system needs to be transformed into a new type of electric power system, that is, on the power side, solar, wind, hydro and other clean energy power generation will replace fossil energy power generation; and on the energy consumption side, the energy from coal, gas, and oil will be replaced by electric energy. At the same time, low-carbon flow power scheduling and operation are

introduced. On the other hand, low-carbon power systems also mean greater exposure to climate and environmental impacts, and their vulnerability to extreme natural disasters will seriously threaten the carbon reduction ability of the new power system. Therefore, it is necessary and urgent to reveal the correlation between the natural disaster chain, the new power system and carbon emission.

China is a country with a vast area and a complex geographical environment. There are great differences in climatic environment and geographical conditions in different regions, so there are a variety of natural disasters and their causes are complex. Different types of disasters are often interrelated, that is, the concept of "multiple disasters" [2]. Some literature also put forward three classifications of "multiple disasters": disaster chain, disaster group, and disaster experience [2, 3]. Among them, the disaster chain that attracts the most attention is defined as a series of phenomena caused by the occurrence of a disaster, which has the characteristics of temporality, inducibility, and expansibility. Studies on disaster chains have been accumulated for years, and some typical cases have been given [2, 3].

As a large-scale distributed complex system with real-time and integrity, power system is vulnerable to extreme natural disasters. In 2009, cold air in the southern Brazilian states of Santa Catarina and Paraná caused hurricanes, heavy rainfall, and intense thunderstorms, resulting in power outages throughout Paraguay. Brazil's 18 states, about 44% of the land, were affected by the accident [4]. The successive disasters of earthquake and tsunami in Japan in 2011 even led to the reactor explosion and leakage accident of nuclear power plant, which triggered a global crisis [5]. On the basis of thinking about small probability and large risk events of power systems, some domestic scholars have pointed out the importance of power systems actively responding to extreme composite disaster risks, and proposed the estimation of power system failure rate for disaster chain and disaster group [6]. It is not hard to imagine that under these extreme disasters, the overall running state of the power system has undergone drastic changes, and the carbon emission has even undergone unexpected changes, which is undoubtedly an unstable factor that cannot be ignored for the macro carbon reduction plan such as "carbon neutrality 2060".

At present, the research on the interaction mechanism and process of "natural disaster-new power system-carbon emission" is rare, due to its large system with great uncertainties. A Bayesian network is an effective tool for reasoning and modeling complex uncertain systems [7]. In view of these characteristics, this paper firstly models and analyzes each part separately, and then introduces a Bayesian network to construct the "natural disaster-new power system-carbon emission" association model system from the perspective of carbon, forming a network that can be estimated by inference. The paper is arranged as follows: The second section proposes the concept of carbon change of power system based on natural disasters, power systems, and carbon emission; the third section proposes the estimation method of carbon change of disaster chain based on Bayesian networks; the fourth section verifies the availability of the proposed method with the case of "rainstorm-landslide-flood".

2 Basic Concepts, Basic Models, and Basic Research Ideas

2.1 Natural Disaster Theory and Modeling of Carbon Change Pathway

The formation of natural disasters is a very complicated process of the atmosphere-earth system. The long-term analysis and research on the formation process of disasters have deepened the understanding of disaster mechanisms and gradually formed the basic theoretical framework of disaster theory. The theory of the regional disaster system advocates those disasters (D_S) are the products of the surface variation of the earth, resulting from the comprehensive effects of disaster-causing factors (H), disaster-inducing environment (E) and disaster-bearing body(S) [8], it can be expressed as following.

$$D_S = E \cap H \cap S \tag{1}$$

After introducing the consideration of carbon emission and carbon sink, the generation and action path of disasters can be expressed in Fig. 1 in combination with the regional disaster system theory. Two correlation models are proposed in the figure, namely the natural disaster model and the carbon disaster model. In the disaster model, the carrier is described as a natural system, human engineering, and human society. The human engineering of this paper is mainly a power system. In the figure, the disaster loss is described as social damage, engineering damage, and natural damage, among which the dotted line corresponds to the human society, human engineering, and natural system in the disaster-bearing body, and its influence is very complex. A carbon disaster is a disaster caused by a natural disaster, which is manifested as the increase of carbon emission and the decrease of carbon sink, which is summarized as the carbon change proposed in this paper.
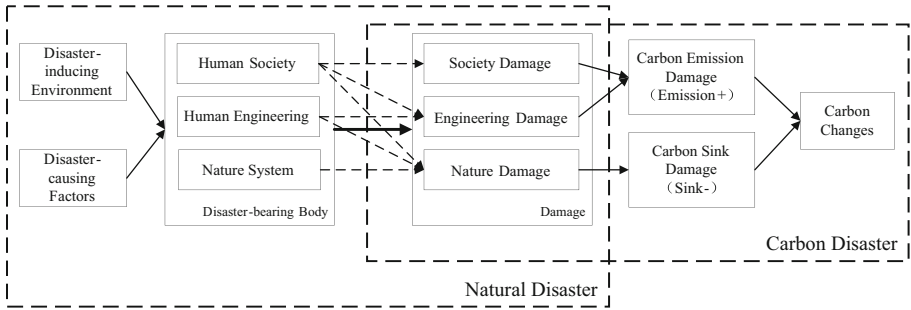
Fig. 1. Occurrence of disasters and their effect pathway on carbon change

In this paper, with the help of the knowledge meta-model [9], the disaster chain is modeled as follows:

$$C_{DE} = (\mathbf{N}, \mathbf{R}) \tag{2}$$

In formula (2), C_{DE} is the final carbon change; $\mathbf{N}$ is the set of event nodes, and is expressed as follows:

$$\mathbf{N} = \{\mathbf{D}_i\}; i \in [1, n] \tag{3}$$

where $\mathbf{D}_i$ is the *ith* disaster object and *n* is the total number of disaster objects. In order to introduce Bayesian network modeling, the disaster object is regarded as a set of disaster elements in this paper, which is expressed as follows:

$$\mathbf{D}_i = \{E_{ij}\}; \text{j} \in [1,l] \tag{4}$$

where E_{ij} is the *jth* disaster element for disaster object *i*, and *l* is the size of disaster elements.

In formula (2), $\mathbf{R}$ is the set of induced time sequence relations, which is represented by formula (5) below.

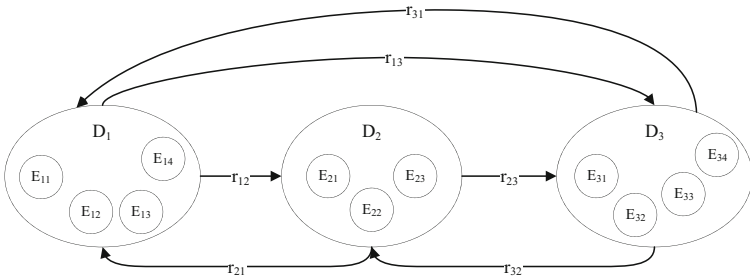$$\mathbf{R} = \{r_{ij}\}; i \in [1, n]; j \in [1, n] \tag{5}$$

Fig. 2. Schematic diagram of disaster chain modeling

Meanwhile, based on the above modeling, a schematic diagram of disaster chain is given as shown in Fig. 2.

2.2 Power System

The power system can be divided into a primary system composed of power generation and transmission and distribution equipment and a secondary system composed of automatic control equipment. As the main body of the modern power supply system and the main carrier of electricity load, the primary system has a wide range of equipment distribution, and tight coupling, and is vulnerable to the influence of the movement process of the atmosphere-earth system and natural disasters. In particular solar, wind, hydro, and other clean energy power generation as the main power generation, and the power grid connected to such power sources are more sensitive to weather, geology, environment, and other factors, and more vulnerable to natural disasters. Typhoons, lightning, rainstorm, mountain fire, ice disaster, and other natural disasters will cause multiple equipment failures in the power system, resulting in power flow transfer and automatic device maloperation and failure to operate, and even large-scale power failure [10]. This paper focuses on the primary power system and discusses the emission increasement caused by natural disasters on primary equipment. The influence mechanism of the disaster on secondary equipment and the resulting emission increasement need to be further studied.

For the power system under the impact of natural disasters, this paper extracts the primary equipment directly affected by the disaster as the power system object in the model, and regards it as the set of primary equipment state elements for the need of Bayesian network modeling, as shown in formula (6) below.

$$\mathbf{F} = \{E_j\}; j \in [1, m] \tag{6}$$

where E_j is the state of *jth* primary equipment in a power system.

Equipment state elements can include equipment operation state, equipment construction damage, equipment functional damage, and other variables that represent the disaster damage to power primary equipment, and their specific forms are actually similar to the disaster diagram.

2.3   Carbon Changes

Carbon change is the combination of "carbon emission increasement" and "carbon sink reduction". In this paper, it is pointed out that the impacts of natural disasters bring about additional carbon emissions. As direct measurement of carbon emissions is difficult, conversion methods such as emission factor method, mass balance method and actual measurement method are commonly used for estimation [11]. For the primary power system, carbon change mainly comes from the following two sources:

(1) Physical carbon change, that is, the carbon estimation of resources required by the system to repair physical damage. From the perspective of carbon change, it is difficult to draw a conclusion directly from the physical damage degree. The physical damage repair of power primary equipment belongs to an engineering project, which requires comprehensive resource allocation in terms of manpower, materials, and management. Part of the carbon assessment of the project has been proposed [12, 13]. The carbon estimation and engineering carbon estimation processes of engineering cases are presented respectively in those papers, but the estimation of physical change still requires complex and detailed data, which is usually difficult to obtain.

(2) Functional carbon change, it refers to the additional carbon emissions generated by replacing the functions of other redundant devices in the system with those of damaged equipment functions. For the primary power system, this point is obvious. Once the low-carbon electric energy of new energy cannot be delivered to the user side due to natural disasters, the thermal power output has to be increased and the low-carbon electric energy is replaced by high-carbon electric energy to meet the demand. The above example can be expressed simply in formula 7:

$$L_C = (E_T - E_N) \times \Delta P \times t \tag{7}$$

E_T represents the thermal power emission factor per unit power, E_N represents the renewable energy emission factor substituted, ΔP represents the total amount of power substituted in the primary system, and t represents the total time used for substitution.

3   Estimation of the Losses of Disaster Chain Based on the Bayesian Network

3.1   Expansion of the Emergency Chain

Emergency is a complex system under the action of natural and social environment, it is a unity of structure and behavior, and can have a destructive effect on the natural and social environment. Using the knowledge of systems engineering theory, the composition of emergencies can be combined. There are three categories of elements: input, state, and output. Formulated as follows [14]:

$$E = (I, S, O) \tag{8}$$

where I represents the input factor set, S represents the state factor set, and O represents the output factor set. The three sets can be expressed by the formula as follows [14]:

$$I = \{i_r | 1 \leq r \leq l\} \tag{9}$$

$$S = \{s_j | 1 \leq j \leq m\} \tag{10}$$

$$O = \{o_k | 1 \leq k \leq n\} \tag{11}$$

Natural disaster is a kind of emergency, and it can also be modeled by the above emergency model. In this study, compared with natural disaster itself, this paper pays more attention to the whole of "natural disaster-new power system-carbon emissions", and the final result will be carbon emission oriented rather than disaster oriented. Based on this model framework, this paper proposes a natural disaster-new power system-carbon emission model, as shown in Fig. 3.
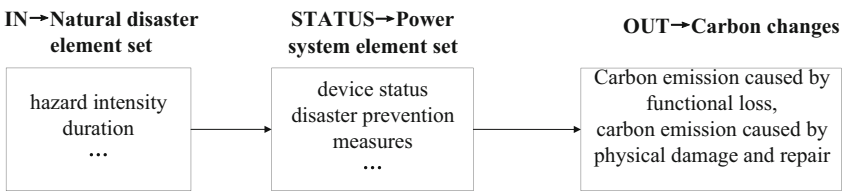

Fig. 3. "Natural disaster-power system-carbon change" system model

The system model shown in Fig. 3 can only describe a "single disaster-new power system-carbon emission" system, so it is necessary to introduce disaster chain model in series to form a multi-disaster system, as shown in Fig. 4.
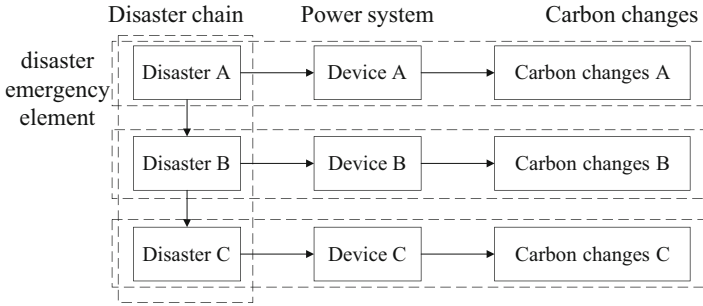
Disaster chain   Power system   Carbon changes

Fig. 4. Disaster emergencies in disaster chain series

3.2 Bayesian Network Inference and Estimation

As a kind of emergencies, disasters are uncertain, so it is suitable to use Bayesian networks for representing and reasoning uncertain problems as modeling tools [7]. The Bayesian network of a single disaster emergency element is composed of a triple $G = (N, E, P)$, where N is the node set, E is the directed edge set between two nodes with causality, and P is the probability set of all nodes in the network. The Bayesian network composed of this triple can be shown in Fig. 5. Then the joint probability distribution of all factors in the network composed of a single emergency is as follows [7, 8]:

$$p(i_1, i_2, \ldots, i_l, s_1, s_2, \ldots, s_m, o_1, o_2, \ldots, o_n) = \prod_{r=1}^{l} p(i_r) \prod_{j=1}^{m} p(s_j | i_1, i_2, \ldots, i_m) \cdot$$

$$\prod_{j=1}^{m} p(s_j | s_1, s_2, \ldots, s_m) \prod_{k=1}^{n} p(o_k | s_1, s_2, \ldots, s_n) \tag{12}$$
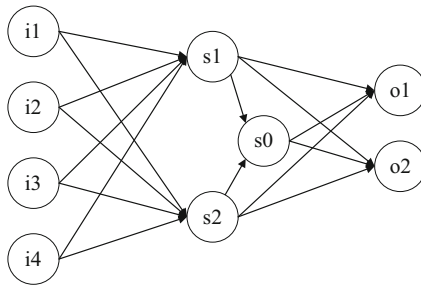

Fig. 5. Bayesian network

In the Fig. 5, the probability contained in the probability set is assigned to each node of the network. In the network, the probability of a single node can be obtained by Bayesian formula. Taking a node as an example, its probability can be calculated as follows:

$$p(s_1) = \sum p(i_1, i_2, i_3, i_4)p(s_1|i_1, i_2, i_3, i_4) \tag{13}$$

Equation (13) can also be used to derive the probability distribution of other nodes, that is, the probability distribution of each node can be obtained through the prior probability distribution of the forward node connected to the directed edge and its own posterior probability distribution. The probability distribution of output o_1 and o_2 can be obtained through the derivation of the whole Bayesian network layer by layer and node by node.

Due to the characteristics of temporality and inducibility, it can be considered that with the gradual advancement of each link in the disaster chain, each node in each link is closely related to the node in the previous link, and at the same time, it is not interrelated as much as possible through the selection of nodes, showing the following probability distribution:

$$p(i_{A1}, i_{A2}, \ldots, i_{Ah}) = \prod_{r=1}^{h} p(i_{Ar}) \tag{14}$$

$$p(i_{B1}, i_{B2}, \ldots, i_{Bm}) = \prod_{j=1}^{m} (\sum p(i_{Bj}|i_{A1}, i_{A2}, \ldots, i_{Ah})p(i_{A1}, i_{A2}, \ldots, i_{Ah})) \tag{15}$$

$$p(i_{C1}, i_{C2}, \ldots, i_{Cn}) = \prod_{k=1}^{n} (\sum p(i_{Ck}|i_{B1}, i_{B2}, \ldots, i_{Bm})p(i_{B1}, i_{B2}, \ldots, i_{Bm})) \tag{16}$$

For a Bayesian network, there are usually some observable nodes. At this time, the values of these nodes in the network is determined, which can be used as evidence variable to reversely deduce the value and probability of updating other nodes, which is equivalent to using the value of evidence variable as a priori knowledge to update the network. Taking S_1 in Fig. 5 as an example, if S_1 is taken as the evidence variable, i_1:

$$p(i_1) = \frac{p(s_1)}{p(s_1|i_1)} \tag{17}$$

Thus, the probability distribution of disaster chain Bayesian networks for multiple disaster emergency elements can be derived respectively, and the disaster chain relationship is in series to form a disaster chain Bayesian network for carbon change as shown in Fig. 6. Although the network structure is more complex, the end node of the network is still a carbon change node. This means that the results of network inference estimation are still carbon change oriented.

Through the disaster chain Bayesian network for carbon change described in this section, the key elements are extracted as nodes in the modeling, and various possible values of each node are fully considered. The priori probability and posterior probability
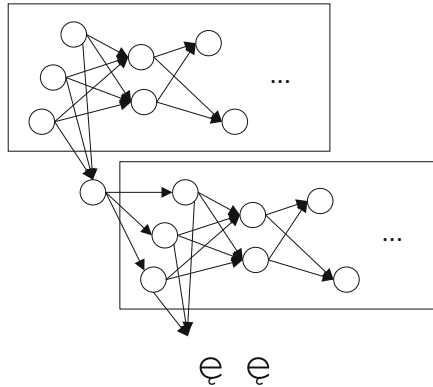
Fig. 6. Disaster chain bayesian network

of each node are refined, so that the whole network can be updated with a given evidence variable. The value probability of each power system node and carbon change node in the complex network can be calculated, and the estimation of power system disaster situation and carbon change are given.

4   Case Study

4.1   Case Introduction

Assuming that there is a new power system topology as shown in Fig. 7, thermal power, hydropower and photovoltaic power generation systems provide power to the user load and have no energy exchange with the external grid; it is considered that the system has a degree of robustness under the impact of extreme natural disasters, and the whole system can still operate in fault state when some power generation nodes and transmission and transformation facilities fail. Assuming that all equipment in the power system is fully fault-free before each disaster occurs in the disaster chain.
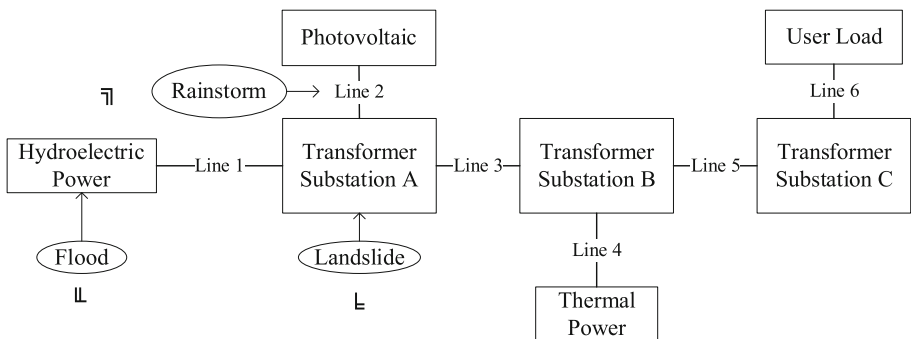
Fig. 7. Power system topology diagram of demonstration case

The "rainstorm-landslide-flood" disaster chain is applied to the primary power system, and primary equipment with specific impact of disasters can be out of action due to the impact. The simulation is implemented by MATLAB toolbox Bayes Net Toolbox for MATLAB [15].

4.2 Case Analysis and Calculation

Referring to disaster historical data and professional literature [16–18], the elements of natural disasters, power systems and carbon changes are extracted, and the Bayesian network node table of the disaster chain is obtained as Table 1. Among them, the initial state of equipment S_{ai}, S_{bi}, S_{ci}, disaster switch nodes i_{bc}, i_{cc}, disaster-inducing environment i_{br}, i_{cr}, direct disaster-causing factor i_{cex} and the initial disaster-related reference variables i_{a1}, i_{a2}, i_{a3}, i_{a4} of disaster chain can be used as evidence variables.

Table 1. Bayesian network node table

Sub-network	Natural disaster	Electrical system	Carbon change
Rainstorm	Maximum wind scale i_{a1}	Initial state of equipment s_{ai}	A Function loss o_{a1}
	Rainfall accumulation i_{a2}	Equipment status s_{a0}	A Physical loss o_{a2}
	Rainstorm intensity i_{a3}	Construction damage s_{a1}	
	Duration i_{a4}	line damage s_{a2}	
Landslide	Whether happened i_{bc}	Initial state of equipment s_{bi}	B Function loss o_{b1}
	Mountain crack depth i_{br}	Equipment status i_{b0}	B Physical loss o_{b2}
	Volume of soil and rock i_{b1}	Construction damage i_{b1}	
	Slip height i_{b2}	Transmission and transformation equipment damage i_{b2} i_{b2} i_{b2} i_{b2} i_{b2} i_{b2}	
Flood	Whether happened i_{cc}	Initial state of equipment s_{ci}	C Function loss o_{c1}
	River cross-sectional area i_{cr}	Equipment status s_{c0}	C Physical loss o_{c2}
	Upstream flow i_{cex}	Construction damage s_{c1}	
	Peak stage i_{c1}	Transmission and transformation equipment damage s_{c2}	
	Duration i_{c2}	Initial state of equipment s_{c3}	

The Bayesian network based on this table is shown in Fig. 7. In the figure, the values of disaster switch nodes i_{br} and i_{cr} are "yes" or "no", according to the input variables of the previous disaster sub-network. If the values are determined as "yes", that is, the corresponding sub-network is effective. It needs to continue downward reasoning, and if the values are "no", then the derivation and summary of the carbon change estimation of each sub-network are completed. According to the specific disaster-causing mechanism of the disaster chain, the external input variables are also introduced according to the actual needs in the derivation of each sub-network, such as the upstream flow in the "flood" sub-network. In the case, this paper believes that the disaster-causing mechanism of the disaster is that in the disaster chain, a large amount of soil and rock silt rivers are caused by landslide disasters, and the cross-sectional area of rivers is reduced. At this time, if the upstream inflow reaches the disaster-causing threshold, the flood will be triggered.

The damage of primary system equipment needs to be oriented to the calculation of carbon change. Since it is still difficult to estimate the specific physical change, the power system nodes should mainly characterize the functional changes of equipment (such as power generation and transmission capacity) rather than specific physical damage. In order to overcome the difficulties caused by incomplete and inaccurate data, this paper abstracts the values of power system nodes and physical loss nodes, and replaces specific physical quantities with discrete expert evaluation indexes. Taking into account the node value and probability too much will bring difficulties to the realization of the network, this paper takes binary processing for all nodes in the network.
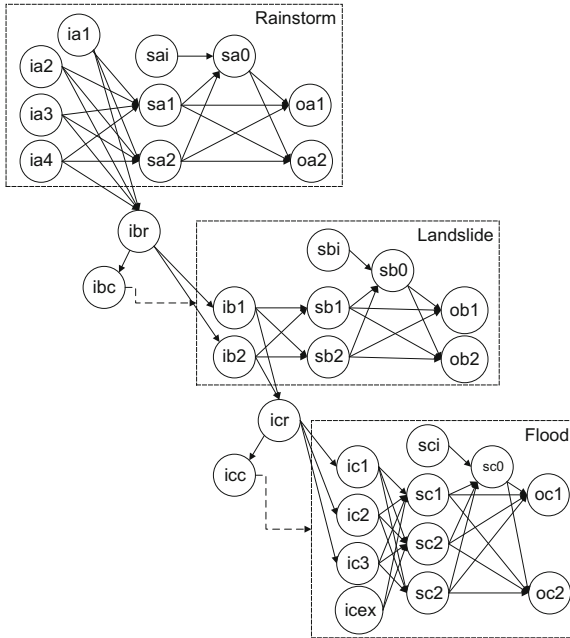
The Bayesian network of the case established in MATLAB toolbox is shown in Fig. 8. For the convenience of simulation calculation, the disaster switch points i_{br} and i_{cr} as evidence variables are not set in the network. The conditional probability and evidence variables of each node are set to Bayesian network, and the posterior probability of each node of the network is updated as Table 2. In Table 2, in order to distinguish the specific sources of nodes, we mark nodes with similar names from three subnets with A, B and C. State values of some variables seem continuous, but they may not. Take A Function loss o_{a1} as example, it has two state values (0, 360) and [1781, 3116]. If Line 2 is heavily damaged and in shutdown, all the power supply from Photovoltaic can't reach User Load, then A Function loss is in [1781, 3116]. If Line 2 keeps working, the lost of power supply is little, A Function loss o_{a1} reaches (0, 360).

For the calculation of priori probability, an example is given in Appendix to show the obtainment of priori probability in Bayesian network. In the example, s_{a1} is calculated using given condition probability and basic priori probability by Bayesian formula:

$$p(s_{a1} = 0) = \sum_{i_{a1}, i_{a2}, i_{a3}, i_{a4}} p(s_{a1} = 0 | i_{a1}, i_{a2}, i_{a3}, i_{a4}) p(i_{a1}, i_{a2}, i_{a3}, i_{a4}) \qquad (18)$$

$$p(s_{a1} = 1) = \sum_{i_{a1}, i_{a2}, i_{a3}, i_{a4}} p(s_{a1} = 1 | i_{a1}, i_{a2}, i_{a3}, i_{a4}) p(i_{a1}, i_{a2}, i_{a3}, i_{a4}) \qquad (19)$$

The given condition probability and basic priori probability refer to papers putting forward theory and formulas about probabilities distribution in disaster, power system and carbon emission research fields. The condition probability is showed in Appendix

Fig. 8. Bayesian network of the case

Table 1, and complete calculation process of (18) and (19) is showed as (a-1) and (a-2) in Appendix.
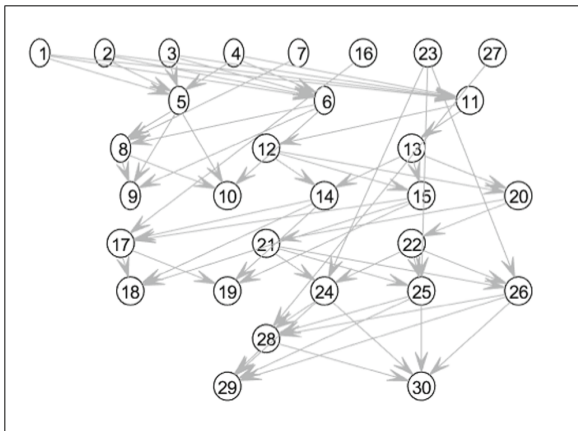
Fig. 9. Implementation of the Bayesian network in MATLAB

Table 2. Variable value and priori probability

Node type	Variable name	State values	Priori probability
Evidence variable	Whether happened i_{ac}	No, yes	(1.000, 0.000)
	Maximum wind scale i_{a1}	(-, grade 7), [8 grade, -)	(0.000, 1.000)
	Rainfall accumulation i_{a2} ai2(mm)	(50, 100), [100, 250)	(0.000, 1.000)
	Rainstorm intensity i_{a3} (mm/min)	Cloudburst, catastrophic cloudburst	(0.000, 1.000)
	Duration i_{a4} (h)	(-,3), [3,-)	(0.000, 1.000)
	A equipment initial state s_{ai}	Good, general	(0.000, 1.000)
	B equipment initial state s_{bi}	Good, general	(1.000, 0.000)
	Upstream flow i_{cex} (m³/s)	(-, 500), [500,-)	(0.000, 1.000)
	C equipment initial state s_{ci}	Good, general	(1.000, 0.000)
	B Whether happened i_{bc}	No, yes	(0.000, 1.000)
	C Whether happened i_{cc}	No, yes	(0.000, 1.000)
Target variable	Device status s_{a0}	Working, Shutdown	(0.368, 0.632)
	A Civil damage s_{a1}	Non-damage or mild damage, severe damage	(0.880, 0.120)
	A Line damage s_{a2}	Non-damage or mild damage, severe damage	(0.360, 0.640)
	A Function loss o_{a1} (tCO₂)	(0, 360), [1781, 3116)	(0.277, 0.723)
	A Physical loss o_{a2} (tCO₂)	A small amount, a large number	(0.509, 0.491)
	Mountain Crack depth i_{br} (m)	(-, 83.4), [83.4, -)	(0.312, 0.688)
	Volume of soil and rock i_{b1} (m³)	(-, 4000000), [4000000, -)	(0.288, 0.712)
	Slip height i_{b2} (m)	(-, 200), [200, -)	(0.525, 0475)
	B equipment status s_{b0}	Working shutdown	(0.683, 0.317)
	B construction damage s_{b1}	Non-damage or mild damage, severe damage	(0.439, 0.561)

(*continued*)

Table 2. (*continued*)

Node type	Variable name	State values	Priori probability
	Transmission and transformation B equipment damage s_{b2}	Non-damage or mild damage, severe damage	(0.550 0.450)
	B Function loss o_{b1} (tCO2)	(0, 1480], [18554, 31806)	(0.528, 0.472)
	B Physical loss o_{b2} (tCO2)	A small amount, a large number	(0.595, 0.405)
	River blockage degree i_{cr}	(10%, 30%), [30%,50%)	(0.571, 0.429)
	Peak stage i_{c1} (m)	(-, 110), [110, -)	(0.445, 0.555)
	Duration i_{c2} (h)	(-, 3), [3, -)	(0.314, 0.686)
	C equipment status s_{c0}	Working, shutdown	(0.239, 0.761)
	C construction damage s_{c1}	Non-damage or mild damage, severe damage	(0.567, 0.433)
	C Transmission and transformation C equipment damage s_{c2}	Non-damage or mild damage, severe damage	(0.490, 0.510)
	C Generators damage s_{c3}	Non-damage or mild damage, severe damage	(0.485, 0.515)
	C Function loss o_{c1} (tCO^2)	(0, 6600], [22054, 33081)	(0.289, 0.711)
	C Physical loss o_{c2} (tCO^2)	A small amount, a large number	(0.520, 0.480)

4.3   Results Analysis

In this part, the reasoning results of multiple Bayesian networks processed by basic calculation are summarized in tabular form, and the maximum probability is used as the estimated value of each group of probabilities, and the reasons and practical significance are analyzed.

Firstly, the power loss of primary system equipment shutdown under the impact of disaster chain can be estimated as Table 3. It can be seen from Fig. 7 that the shutdown of impacted equipment will cause the power of photovoltaic power station and hydropower station to be unable to reach the user side, resulting in power loss. It can be seen from the whole disaster chain duration that the power loss accident will almost certainly occur, and it is estimated that at least one photovoltaic power loss accident and one hydropower

power loss accident will occur. The estimation results reveal the potential threat of the disaster chain and the potential operation risk of the power system in the disaster chain, which plays a certain warning role for the disaster prevention and mitigation of the power primary system.

Table 3. Power loss accident estimation for next disaster chain

No serious power loss	Loss of photovoltaic power	Loss of hydropower power	Loss of photovoltaic and hydropower power
4.40%	11.51%	10.19%	73.90%

The general estimation results of functional carbon change from Bayesian network inference are summarized in Table 4. Once the low carbon power of photovoltaic power station and hydropower station cannot reach the user side, it is necessary to improve the proportion of high carbon power (thermal power) in the energy structure to meet the load. Through some simple assumptions, the carbon emission difference before and after can be estimated by the emission factor method, namely the functional carbon change. According to the inference results of Bayesian network output, the probability distribution of function carbon change under disaster chain can be calculated, and the function change of primary system is estimated to be 18 000–40000 $t\ CO_2$.

Table 4. Functional carbon change estimation of next disaster chain

Functional loss/tCO_2	<18000	18000–40000	40000–67000
Probability	15.91%	49.83%	34.26%

From the Bayesian network inference results, this paper can obtain the approximate estimation results of physical carbon change, summarized in Table 5. Due to the difficulty in estimating the physical loss of primary power system, this part divides the case of physical loss into four levels: no significant loss, line-level, single-station-level and multi-station-level. According to the inference result of Bayesian network output, the probability distribution of physical carbon change under disaster chain can be calculated, and the physical carbon change of primary power system is estimated as single station level.

Table 5. Physical loss estimation of the next system in disaster chain

Physical loss	No significant loss	Line-level	Single-station-level	Multi-station-level level
Probability	16.04%	15.44%	48.47%	20.05%

5   Conclusion

In this paper, the three concepts in names as natural disaster, new power system and carbon changes are connected in series. A concept of "carbon changes" in power system is put forward on the base of the analysis of the impact of natural disasters on power system, and a Bayesian network of "natural disaster-power system-carbon change" is provided to describe the influence of natural disaster chain on carbon emission trajectory of power system. Combined with the characteristics of the natural disaster chain, a multi-Bayesian network carbon change estimation method considering the interaction of multiple disasters is proposed. And the feasibility of the proposed method is verified by a disaster chain case of "rainstorm - landslide - flood".

It should be pointed out that it is difficult to determine the accurate values of each node of the Bayesian network proposed in this paper, so abstracted and discrete binarized values are used instead. In the future, in-depth research on the accurate datafication of these nodes should be conducted, so as to improve the accuracy of Bayesian network inference model.

In addition, this paper also introduces the carbon emission data of power system projects as the basis of disaster carbon emission calculation. This kind of data also has great comprehensiveness and specificity. At present, there are difficulties to obtain the carbon emission equivalent of various primary equipment, which makes the physical carbon emission estimation proposed in this paper difficult to be in datafication and can only give an approximate scale rating, which is also one of the problems to be solve.

Appendix

Table 6. Condition probability of example

Variable name	Prepositive variable	Prepositive variable value	Probability of 0	Probability of 1
sa1	ia1, ia2, ia3, ia4	0, 0, 0, 0	0.85	0.15
		1, 0, 0, 0	0.8	0.2
		0, 1, 0, 0	0.23	0.77
		0, 0, 1, 0	0.242	0.758
		0, 0, 0, 1	0.24	0.76
		1, 1, 0, 0	0.12	0.88
		1, 0, 1, 0	0.92	0.08
		1, 0, 0, 1	0.12	0.88
		0, 1, 1, 0	0.32	0.68
		0, 1, 0, 1	0.12	0.88
		0, 0, 1, 1	0.55	0.45
		1, 1, 1, 0	0.88	0.12
		1, 1, 0, 1	0.42	0.58
		1, 0, 1, 1	0.32	0.68
		0, 1, 1, 1	0.13	0.87
		1, 1, 1, 1	0.88	0.12

$$p(s_{a1}=0) = \sum_{i_{a1},i_{a2},i_{a3},i_{a4}} p(s_{a1}=0|i_{a1},i_{a2},i_{a3},i_{a4})p(i_{a1},i_{a2},i_{a3},i_{a4})$$

$= p(s_{a1}=0|i_{a1}=0,i_{a2}=0,i_{a3}=0,i_{a4}=0)p(i_{a1}=0,i_{a2}=0,i_{a3}=0,i_{a4}=0) + p(s_{a1}=0|i_{a1}=1,i_{a2}=0,i_{a3}=0,i_{a4}=0)p(i_{a1}=1,i_{a2}=0,i_{a3}=0,i_{a4}=0)$

$+p(s_{a1}=0|i_{a1}=0,i_{a2}=1,i_{a3}=0,i_{a4}=0)p(i_{a1}=0,i_{a2}=1,i_{a3}=0,i_{a4}=0) + p(s_{a1}=0|i_{a1}=0,i_{a2}=0,i_{a3}=1,i_{a4}=0)p(i_{a1}=0,i_{a2}=0,i_{a3}=1,i_{a4}=0)$

$+p(s_{a1}=0|i_{a1}=0,i_{a2}=0,i_{a3}=0,i_{a4}=1)p(i_{a1}=0,i_{a2}=0,i_{a3}=0,i_{a4}=1) + p(s_{a1}=0|i_{a1}=1,i_{a2}=1,i_{a3}=0,i_{a4}=0)p(i_{a1}=1,i_{a2}=1,i_{a3}=0,i_{a4}=0)$

$+p(s_{a1}=0|i_{a1}=1,i_{a2}=0,i_{a3}=1,i_{a4}=0)p(i_{a1}=1,i_{a2}=0,i_{a3}=1,i_{a4}=0) + p(s_{a1}=0|i_{a1}=1,i_{a2}=0,i_{a3}=0,i_{a4}=1)p(i_{a1}=1,i_{a2}=0,i_{a3}=0,i_{a4}=1)$

$+p(s_{a1}=0|i_{a1}=0,i_{a2}=1,i_{a3}=1,i_{a4}=0)p(i_{a1}=0,i_{a2}=1,i_{a3}=1,i_{a4}=0) + p(s_{a1}=0|i_{a1}=0,i_{a2}=1,i_{a3}=0,i_{a4}=1)p(i_{a1}=0,i_{a2}=1,i_{a3}=0,i_{a4}=1)$

$+p(s_{a1}=0|i_{a1}=0,i_{a2}=0,i_{a3}=1,i_{a4}=1)p(i_{a1}=0,i_{a2}=0,i_{a3}=1,i_{a4}=1) + p(s_{a1}=0|i_{a1}=1,i_{a2}=1,i_{a3}=1,i_{a4}=0)p(i_{a1}=1,i_{a2}=1,i_{a3}=1,i_{a4}=0)$

$+p(s_{a1}=0|i_{a1}=1,i_{a2}=1,i_{a3}=0,i_{a4}=1)p(i_{a1}=1,i_{a2}=1,i_{a3}=0,i_{a4}=1) + p(s_{a1}=0|i_{a1}=1,i_{a2}=0,i_{a3}=1,i_{a4}=1)p(i_{a1}=1,i_{a2}=0,i_{a3}=1,i_{a4}=1)$

$+p(s_{a1}=0|i_{a1}=0,i_{a2}=1,i_{a3}=1,i_{a4}=1)p(i_{a1}=0,i_{a2}=1,i_{a3}=1,i_{a4}=1) + p(s_{a1}=0|i_{a1}=1,i_{a2}=1,i_{a3}=1,i_{a4}=1)p(i_{a1}=1,i_{a2}=1,i_{a3}=1,i_{a4}=1)$

$= 0.85 \times 0 + 0.8 \times 0 + 0.23 \times 0 + 0.242 \times 0 + 0.24 \times 0 + 0.12 \times 0 + 0.92 \times 0 + 0.12 \times 0 + 0.32 \times 0 + 0.12 \times 0 + 0.55 \times 0 + 0.88 \times 0 + 0.42 \times 0 + 0.32 \times 0 + 0.13 \times 0 + 0.88 \times 1$

$= 0.88$

(a-1)

$$p(s_{a1}=1) = \sum_{i_{a1},i_{a2},i_{a3},i_{a4}} p(s_{a1}=1|i_{a1},i_{a2},i_{a3},i_{a4})p(i_{a1},i_{a2},i_{a3},i_{a4})$$

$= p(s_{a1}=1|i_{a1}=0,i_{a2}=0,i_{a3}=0,i_{a4}=0)p(i_{a1}=0,i_{a2}=0,i_{a3}=0,i_{a4}=0) + p(s_{a1}=1|i_{a1}=1,i_{a2}=0,i_{a3}=0,i_{a4}=0)p(i_{a1}=1,i_{a2}=0,i_{a3}=0,i_{a4}=0)$

$+p(s_{a1}=1|i_{a1}=0,i_{a2}=1,i_{a3}=0,i_{a4}=0)p(i_{a1}=0,i_{a2}=1,i_{a3}=0,i_{a4}=0) + p(s_{a1}=1|i_{a1}=0,i_{a2}=0,i_{a3}=1,i_{a4}=0)p(i_{a1}=0,i_{a2}=0,i_{a3}=1,i_{a4}=0)$

$+p(s_{a1}=1|i_{a1}=0,i_{a2}=0,i_{a3}=0,i_{a4}=1)p(i_{a1}=0,i_{a2}=0,i_{a3}=0,i_{a4}=1) + p(s_{a1}=1|i_{a1}=1,i_{a2}=1,i_{a3}=0,i_{a4}=0)p(i_{a1}=1,i_{a2}=1,i_{a3}=0,i_{a4}=0)$

$+p(s_{a1}=1|i_{a1}=1,i_{a2}=0,i_{a3}=1,i_{a4}=0)p(i_{a1}=1,i_{a2}=0,i_{a3}=1,i_{a4}=0) + p(s_{a1}=1|i_{a1}=1,i_{a2}=0,i_{a3}=0,i_{a4}=1)p(i_{a1}=1,i_{a2}=0,i_{a3}=0,i_{a4}=1)$

$+p(s_{a1}=1|i_{a1}=0,i_{a2}=1,i_{a3}=1,i_{a4}=0)p(i_{a1}=0,i_{a2}=1,i_{a3}=1,i_{a4}=0) + p(s_{a1}=1|i_{a1}=0,i_{a2}=1,i_{a3}=0,i_{a4}=1)p(i_{a1}=0,i_{a2}=1,i_{a3}=0,i_{a4}=1)$

$+p(s_{a1}=1|i_{a1}=0,i_{a2}=0,i_{a3}=1,i_{a4}=1)p(i_{a1}=0,i_{a2}=0,i_{a3}=1,i_{a4}=1) + p(s_{a1}=1|i_{a1}=1,i_{a2}=1,i_{a3}=1,i_{a4}=0)p(i_{a1}=1,i_{a2}=1,i_{a3}=1,i_{a4}=0)$

$+p(s_{a1}=1|i_{a1}=1,i_{a2}=1,i_{a3}=0,i_{a4}=1)p(i_{a1}=1,i_{a2}=1,i_{a3}=0,i_{a4}=1) + p(s_{a1}=1|i_{a1}=1,i_{a2}=0,i_{a3}=1,i_{a4}=1)p(i_{a1}=1,i_{a2}=0,i_{a3}=1,i_{a4}=1)$

$+p(s_{a1}=1|i_{a1}=0,i_{a2}=1,i_{a3}=1,i_{a4}=1)p(i_{a1}=0,i_{a2}=1,i_{a3}=1,i_{a4}=1) + p(s_{a1}=1|i_{a1}=1,i_{a2}=1,i_{a3}=1,i_{a4}=1)p(i_{a1}=1,i_{a2}=1,i_{a3}=1,i_{a4}=1)$

$= 0.15 \times 0 + 0.2 \times 0 + 0.77 \times 0 + 0.758 \times 0 + 0.76 \times 0 + 0.88 \times 0 + 0.08 \times 0 + 0.88 \times 0 + 0.68 \times 0 + 0.88 \times 0 + 0.45 \times 0 + 0.12 \times 0 + 0.58 \times 0 + 0.68 \times 0 + 0.87 \times 0 + 0.12 \times 1$

$= 0.12$

(a-2)

References

1. Tan, X., Liu, J., et al.: Power supply and demand situation in the 14th five year plan under the goal of "dual carbon." Electric Power **54**(05), 1–6 (2021)

2. Shi, P., Lu, L., et al.: Disaster system: disaster group, disaster chain and disaster experience. J. Nat. Disasters **23**(06), 1–12 (2014)
3. Han, J., Wu, S., et al.: Geohazard chain. Earth Sci. Front. (06), 11–23 (2007)
4. Lin, W., Sun, H., et al.: Analysis and enlightenment of "11.10" blackout in Brazil. Autom. Electric Power Syst. **34**(07), 1–5 (2010)
5. Xue, Y., Xiao, S.: Comprehensive defense of small probability events with high risk: reflections on power outage and nuclear leakage caused by successive natural disasters in Japan. Autom. Electric Power Syst. **35**(08), 1–11 (2011)
6. Xue, Y., Wu, Y., et al.: Stability analysis of power system under complex natural disasters. Autom. Electric Power Syst. **40**(04), 10–18 (2016)
7. Qiu, J., Liu, L., et al.: Modeling method and application of emergency chain based on Bayesian network. J. Syst. Eng. **27**(06), 739–750 (2012)
8. Shi, P.: Second time on the theory and practice of disaster research. J. Nat. Disasters (04), 8–19 (1996)
9. Wang, Y.: Knowledge and representation of model management. J. Syst. Eng. **26**(06), 850–856 (2011)
10. Xue, Y., Wu, Y., et al.: Expansion of power failure prevention framework to natural disaster warning. Autom. Electric Power Syst. **37**(16), 18–26 (2013)
11. IPCC/UNEP/OECD/IEA: Revised 1996 IPCC guidelines for national greenhouse gas inventories. Intergovernmental Panel on Climate Change, United Nations Environment Program, Organization for Economic Co-Operation and Development, International Energy Agency, Paris (1997)
12. Ji, S., Gao, C., et al.: Carbon emission accounting of wind farm based on life cycle. Acta Ecol. Sin. **36**(04), 915–923 (2016)
13. Kwan, C.C., Leung, T.M., et al.: A review on life cycle assessment, life cycle energy assessment and life cycle carbon emissions assessment on buildings. Appl. Energy **143**, 395–413 (2015)
14. Qiu, J., Shi, H., et al.: Event-based qualitative knowledge representation model. Syst. Eng. **27**(10), 1–8 (2009)
15. How to use the Bayes Net Toolbox [OL] (2007). http://bayesnet.github.io/bnt/docs/usage.html
16. Huang, R.: Large landslide and its mechanism in China since the 20th century. Chin. J. Rock Mech. Eng. (03), 433–454 (2007)
17. Rui, Y., He, B., et al.: The 2015.6.18 flash flood disaster and its prevention in Suining county, Hunan province. China Flood Drought Manag. **25**(05), 60–63 (2015)
18. Wang, L., Huang, H., et al.: Spatiotemporal dynamic analysis of 7.20 flood disaster in Henan province. J. Catastrophology 1–10 (2022)

Dynamic Loading and Rendering Method for Large-Scale Power Grid Spatial Data

Wei Cheng[✉], Shenliang Wang, Feng You, Feng Lin, Shijin Liu, Sen Peng,
Chenglong Xu, Shengsheng Li, and Yu Pang

Nanjing NARI Information and Communication Technology Co., Ltd., Nanjing 211106, China
chengwei5@sgepri.sgcc.com.cn

Abstract. The scale of power grid equipment is huge, and the large amount of power grid spatial data is very likely to cause data display performance degradation. Therefore, the smooth display of power grid spatial data under large data volume has become a key technical problem to be solved in the construction of grid GIS applications. For the grid spatial data and its application characteristics, a large-scale grid spatial data dynamic loading and rendering method is proposed. The method uses MongoDB database to store grid spatial data; controls front-end data loading through grid resource data display rules and line data hierarchical compression to reduce network transmission and front-end drawing pressure; dynamically schedules data according to viewport range and establishes request cache and data cache on the client side to improve device rendering efficiency; uses HTML5 technology for data multi-threaded parsing of data and real-time drawing of device symbols. It has been proven that this method can significantly improve the fluency, interactivity and flexibility of existing grid GIS applications in Web graphics display in large data volume scenarios, and greatly improve the user experience.

Keywords: Power grid GIS · Vector · Spatial data · HTML5

1 Introduction

Graphic display of power grid equipment is the basic function of power grid GIS application. The business applications of grid power generation, transmission, substation, distribution, and electricity consumption all need to be integrated with geospatial information to improve grid resource management and visual analysis capabilities [1–11]. The data volume of low-power grid equipment in most provinces in the country has reached tens of millions or even hundreds of millions. Therefore, realizing the efficient display of large-scale power grid spatial data on the Web side has become an urgent problem to be solved in related applications.

At present, the Web graphics display based on massive spatial data mainly has the following implementation schemes:

(1) Real-time dynamic grid rendering. This solution is currently the mainstream method for displaying large-scale power grid spatial data on the web. The main idea is that the client sends a graphics rendering request to the server according to the current viewport range, and the server queries data from the database in real time according to the request range and renders it as a picture and returns it to the client for display. This method does not require high rendering capabilities on the client side, and its main disadvantages are: 1) The server side undertakes the tasks of data retrieval and graphics rendering at the same time, and the load is large; 2) Since the Web side obtains static pictures, it is difficult to realize the human-computer interaction functions such as the flickering of graphic elements and the dynamic highlighting of mouse clicks [12]; 3) The client cannot dynamically change the color and style of graphic elements, which makes it difficult to meet the important requirements of many power applications, such as switch setting, device live coloring, and simulated power failure analysis.

(2) Raster tile rendering. According to a specific two-dimensional space hierarchical grid segmentation scheme, the method pre-generates a grid tile set with a certain spatial range and number of layers on the server side, that is, a grid tile pyramid. When browsing the map, the client obtains all the corresponding tiles from the server according to the viewport range, and finally splices into a complete map. Because it is pre-formed, this method reduces the pressure of real-time drawing on the server, but there are still shortcomings 2) and 3) of the first solution.

(3) Vector tile rendering [13–15]. In recent years, with the rapid development of HTML5 technology, the ability of browser vector drawing has been greatly improved. From this, the vector tiling technique was developed, which splits vector data into a series of descriptive files in a pyramid-building manner, organized in formats such as GeoJson or MVT [13]. The client requests the corresponding vector tile data for drawing according to the window range. This method overcomes the shortcomings of grid rendering, and has the advantages of interactivity, controllable style, and small size. However, this method will divide and store spatial objects in multiple tiles, which is extremely unfavorable for front-end editing-type function development, and some highly interactive business functions are also difficult to implement. Therefore, this method is still only suitable for background images. Show.

In order to solve the insufficiency of the existing grid GIS application in the web-side graphic display technology, this paper makes full use of the high-performance vector drawing capabilities and many new features of HTML5, and implements a web-oriented large-scale grid spatial data vector display method, which can significantly Improve the fluency, interactivity and flexibility of graphic display of existing Web GIS applications in the power industry, and improve user experience.

2 Design

2.1 Overall Design

In this paper, MongoDB database is used for the storage of grid spatial data. Through data display rules and line (including overhead line and cable) draw thinning, the amount

of data loaded for graphics browsing is reasonably controlled to reduce network transmission and front-end drawing pressure; during graphics browsing, data is dynamically scheduled according to the viewport range, and the number of requests is reduced by establishing request cache in the front-end to establish data cache to enhance rendering speed; finally, HTML5 technology is used for multi-threaded data parsing on the Web side and real-time symbolic rendering. The general idea is shown in Fig. 1.
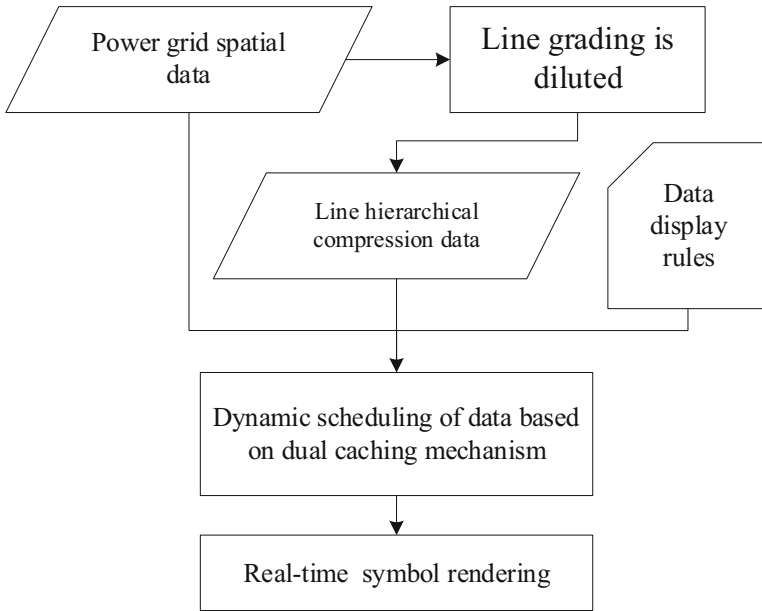
Fig. 1. Overall design of the method.

2.2 Grid Spatial Data Storage

GIS applications have very high requirements on the performance of spatial data services, including real-time response, high concurrency, and high throughput. Based on sufficient technical research, this paper uses MongoDB database to store power grid spatial data. MongoDB has the following characteristics in storing grid spatial data:

(1) Rich indexing and data query interface support, both attribute indexing and spatial indexing: In addition to supporting attribute indexing similar to that of relational databases, the caching system also specifically supports spatial data storage and spatial indexing, providing range queries by rectangle, polygon, point, circle and other geometric elements.
(2) Supports automatic data sharding and natively supports massive data storage: Provides automatic data sharding (Auto-Sharding) storage technology. A horizontally scalable database cluster that dynamically adds or removes nodes. With this technology, more data volumes can be easily supported.

(3) Cache progressive loading: MongoDB is not a pure memory library and supports persistent storage of data. Therefore, when the cache service starts, it is not necessary to load all the data from the relational database to the memory at one time, and it can gradually load the data after starting through its own persistent storage. This solves the problem that the traditional cache service takes too long to start.

2.3   Data Display Rule Making

Due to the large amount of grid resource data, certain data display rules must be designed to control the number of devices displayed on each screen. According to the characteristics of power grid GIS applications, on a small-scale map (such as 1:20000000), only the power station and line information of a high voltage level (above 500 kV) needs to be displayed; on a large-scale map (such as 1:1000), it is necessary to display the station inside the power station. Primary equipment, tower and column equipment. Based on the above requirements, this paper designs a hierarchical display rule for power grid resource data. The rule first determines the minimum display scale and the maximum display scale of the map, and divides the scale range into several continuous intervals, each interval is called a display level, such as L0, L1, L2…Ln. Each level contains four properties: level ID, minimum scale, maximum scale, visible devices. The level ID is the unique identification of the display level; the minimum scale and the maximum scale specify the scale range corresponding to the level; the visible device refers to the device type and its voltage level displayed under the display level.

When the client is browsing graphics, it will determine the display level according to the current map scale, and then obtain the device type and voltage level to be displayed according to the display level, and finally obtain the corresponding device data from the server for rendering.

2.4   Line Data Compression

Transmission lines are important information displayed by grid GIS applications. Line types include overhead lines and cable lines. The amount of line data depends on the number of nodes, and in the grid data model, the nodes of overhead lines correspond to the towers one by one. The huge number of towers leads to a very large amount of line data loaded when displaying large scale (such as nationwide, province-wide or city-wide) grid lines, which imposes a serious burden on data transmission and front-end rendering. Therefore, data compression is necessary to ensure smooth graphics viewing.

In this paper, a line data hierarchical compression method is designed. The main idea is to conduct hierarchical line thinning according to the scale range, and the thinning algorithm uses the Douglas-Pook algorithm [16]. In this method, a number of compression levels are established, and each compression level contains five attributes: level ID, minimum scale, maximum scale, voltage level, and dilution threshold. The minimum scale and maximum scale specify the scale range of the level; the voltage level defines the range of voltage levels for dilution (since the large range of lines is mainly for high-voltage trunk lines, lines with higher voltage levels need to be compressed); the dilution threshold refers to the Douglas threshold used for the level, and the larger the threshold, the stronger the dilution. The higher the threshold, the stronger the thinning. The thinned

line data can be cached in the memory of the query service or stored in the database MongoDB.

3   Realization

3.1   Dynamic Loading of Data

In this paper, data loading is done using on-demand loading and local caching strategies.

The basic principle of on-demand loading is that although the total amount of data is large, the amount of data displayed per screen is always limited, so only a smaller amount of data can be loaded according to display needs. This includes two aspects: determining the spatial scope of data retrieval based on the current viewport range; and determining the type of equipment and voltage level to be retrieved based on the current map scale, combined with the data display rules. Through the filtering of the above two layers of conditions, the amount of data loading can be greatly reduced.

To improve the display efficiency, this paper establishes a request cache and a data cache on the client side. The request cache stores the data query requests sent by the client each time, and the content is the space range and display level of the request. Its role is to quickly determine whether a new data request is included by existing requests, if it is included, the client does not need to send, which will reduce repeated requests. The data cache stores the device information returned by each query, including spatial location information and attribute information, and is used to cache all the acquired device data. In this paper, the data cache is used as a direct data source for client-side device drawing, i.e., the client will quickly retrieve the device objects in the current viewport range from the request cache for graphical drawing.

Since the use of both caches involves finding existing requests or device data by spatial extent, the R-tree structure is used for the storage structure of the cache. Therefore, the R-tree [17] structure is used for the storage structure of the cache. R-tree is a spatial index data structure widely used today. The R-tree enables fast retrieval of spatial objects in a specified spatial range. It is a highly balanced tree, consisting of intermediate nodes and leaf nodes. Each node corresponds to a region, the intermediate node stores the region range of all its child nodes, and the regions of all its children nodes fall within its region range; the leaf node's stores the outer rectangle of all spatial objects within its region range. According to this data structure of the R-tree, when it is necessary to query the objects in the specified spatial range, it is only necessary to iterate through the spatial objects contained in a few leaf nodes and determine whether the conditions are satisfied. This approach makes it unnecessary to iterate through all the objects and significantly improves efficiency.

The main process of dynamic loading of data is as follows:

(1)   Client-side cache container creation

The client creates two R-tree structures as request cache and data cache, denoted as *RTreeRequest*, *RTreeData*. Each data request is stored as an entry in *RTreeRequest*, denoted as *(I, L)*. I is the minimum outer rectangle of the entry, which is the spatial rectangle range of the data request, and L is the display level ID corresponding to the

data request. Each device is stored as an entry in *RTreeData*, denoted as *(R, Data)*. R is the minimum outer rectangle of the spatial graph of the device, and Data is the spatial information and attribute information of the device.

(2) The client determines the display level and space range

The client gets the current map scale and matches the corresponding display level in the data display rules according to the scale, which is recorded as *LC*. The client gets the geospatial range (a rectangular range) of the current screen display and extends the range appropriately, such as the length and width of the range are extended by 20% to form the data query spatial range, which is recorded as *IC*. The reason for this expansion is that the client will cache the requested space range, so that when the map panning is performed, the new screen space range does not need to be requested again if it does not exceed the actual space range of the last data request. This reduces the number of data requests and reduces the pressure on the server.

(3) The client sends a data query request

If there is a request entry *(In, Ln)* whose query range In contains *IC* and display level *Ln* is equal to *IC,* then there is no need to send the request and the process is terminated; if there is no request entry that meets the above conditions, then send a data query request to the server with request parameters including spatial rectangle range *IC*, display level *LC* and current scale *SC*. If there is no request entry that meets the above conditions, a data query request is sent to the server with parameters including the spatial rectangular range *IC*, display level *LC* and the current scale *SC*.

(4) The server side executes the query and returns the result

The server side determines the query conditions based on the request parameters. The spatial range condition is *IC*. The attribute condition is device type and voltage level filter condition, which is determined by display level *LC* combined with display rules.

For non-line equipment, the server queries data from MongoDB according to the above spatial conditions and attribute conditions and returns it to the client in *GeoJson* format. For line equipment, the query data source is firstly determined by data compression rules according to the scale *SC* and voltage level conditions of this request. If the original data is queried, the processing is the same as that for non-line devices; if the compressed data is queried, the compression level is calculated, and the compressed data of the corresponding level is queried from the server memory cache or MongoDB and returned to the client.

(5) Client-side device data parsing and caching

After the client gets the query results from the server, it needs to parse the *GeoJson* string into memory objects and save them in the local data cache *RTreeData*. When the amount of returned data is large, the data parsing process is time-consuming and the state of the page is unresponsive, resulting in lagging graphics browsing. In order

to improve the smoothness of graphics browsing, this paper adopts the multi-threaded solution provided by HTML5 for data parsing and duplicate data rejection. The specific method is: the client opens a Web Worker background thread in advance, and the main thread of the page gets the query *GeoJson* string, then passes the string and the set of loaded device IDs to the background thread, which performs data parsing to generate memory objects and rejects the loaded devices according to the set of loaded device IDs to form the set of newly loaded device objects and passes them to the main thread. The main thread obtains the set of newly loaded device objects and inserts them all into the local device data cache *RTreeData*.

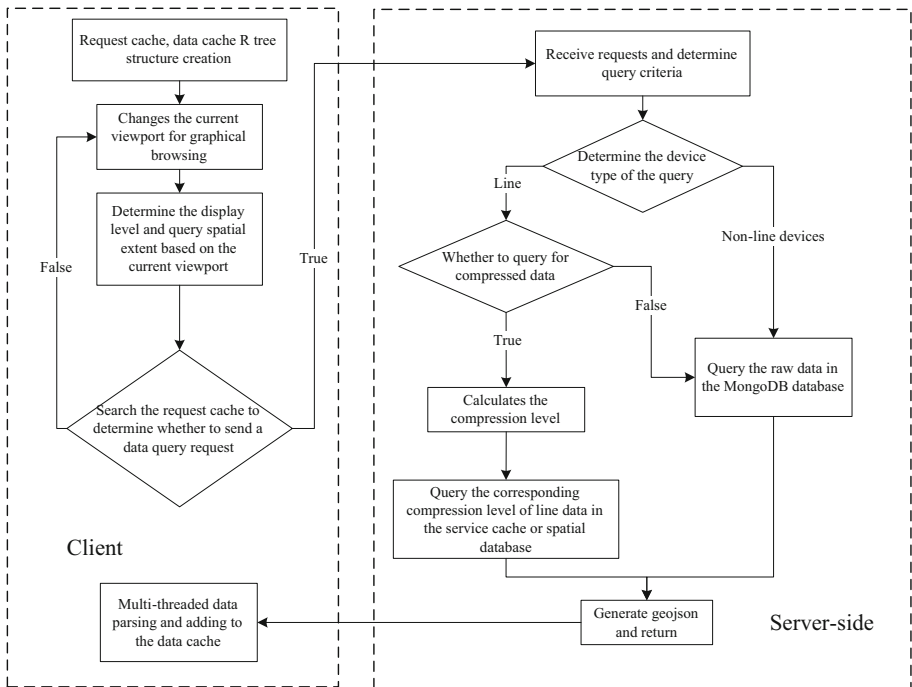The detailed process of data loading is shown in Fig. 2.

Fig. 2. Data dynamic loading process.

3.2 Real-Time Rendering of Data

Power grid GIS applications have many important requirements, such as device highlighting, analog switch setting, analog live coloring, and analog power failure analysis, all of which need to change the color, symbol, and style of the device in real time on the client side. At present, the conventional server-side rendering method is difficult to meet the above requirements, and this paper adopts the client-side real-time rendering strategy. The biggest advantage is that the color and style of the device graphics can be dynamically changed, and the above functions can be easily realized.

When the user browses the map and the viewport of the map changes, the client will start rendering the data in real time. The process is mainly divided into two steps: the first step is to quickly extract the device objects within the geographic range of the current viewport from the local data cache based on the R-tree search method to form a set of device objects to be rendered. In the second step, for each device in the set, the symbol information of the device is obtained, and the symbol is drawn.

In this paper, the Canvas element provided by HTML5 is used as the canvas for map drawing, and the basic geographic and power grid equipment symbols are drawn in real time on the canvas (Canvas) through JavaScript script.

The graphic symbols of power grid equipment are mainly divided into two categories: line symbols and point symbols. Linear symbols refer to symbols of equipment such as cables, overhead lines, and connecting lines in stations, which are represented by solid lines or dotted lines, which are relatively simple to draw. Dot symbols include most of the grid equipment (up to several hundred) symbols such as transformers, current transformers, circuit breakers, etc. Each point symbol is composed of several basic primitives (polyline, polygon, circle, ellipse, ellipse arc, Bezier curve, text, etc.). This paper creates a new Canvas element for each point symbol, uses the graphics drawing interface provided by Canvas to complete the drawing of all the basic primitives of the symbol, and then draws it to the Canvas of the map, so as to realize the real-time drawing of device symbols. Compared with the conventional way of displaying equipment symbols using static pictures (such as PNG and SVG), this real-time drawing method can dynamically change the color of symbols, which well meets the dynamic coloring requirements required by power grid operation analysis applications.

The implementation process of the client to implement device symbolic rendering is shown in Fig. 3, which mainly includes the following steps:

(1) Start graphic browsing, pan or zoom the map, and change the current viewport range;
(2) Search the device objects in the current window range from the data cache, form a set of devices to be rendered, and traverse the set of devices to be rendered;
(3) Determine whether the traversal ends, if so, end, if not, turn to step (4);
(4) Obtain the next device, obtain the symbol corresponding to the device, and determine the type of the device symbol. If it is a linear symbol, directly draw a solid or dashed line on the canvas of the map, and turn to step (3); if it is a point First, create a new canvas (Canvas) element, and draw the basic primitives of the symbol on this element; then convert the canvas (Canvas) element into an image (Image) element; finally, use the *drawImage* method provided by HTML5 to draw the image on the map. on the canvas, and go to step (3).
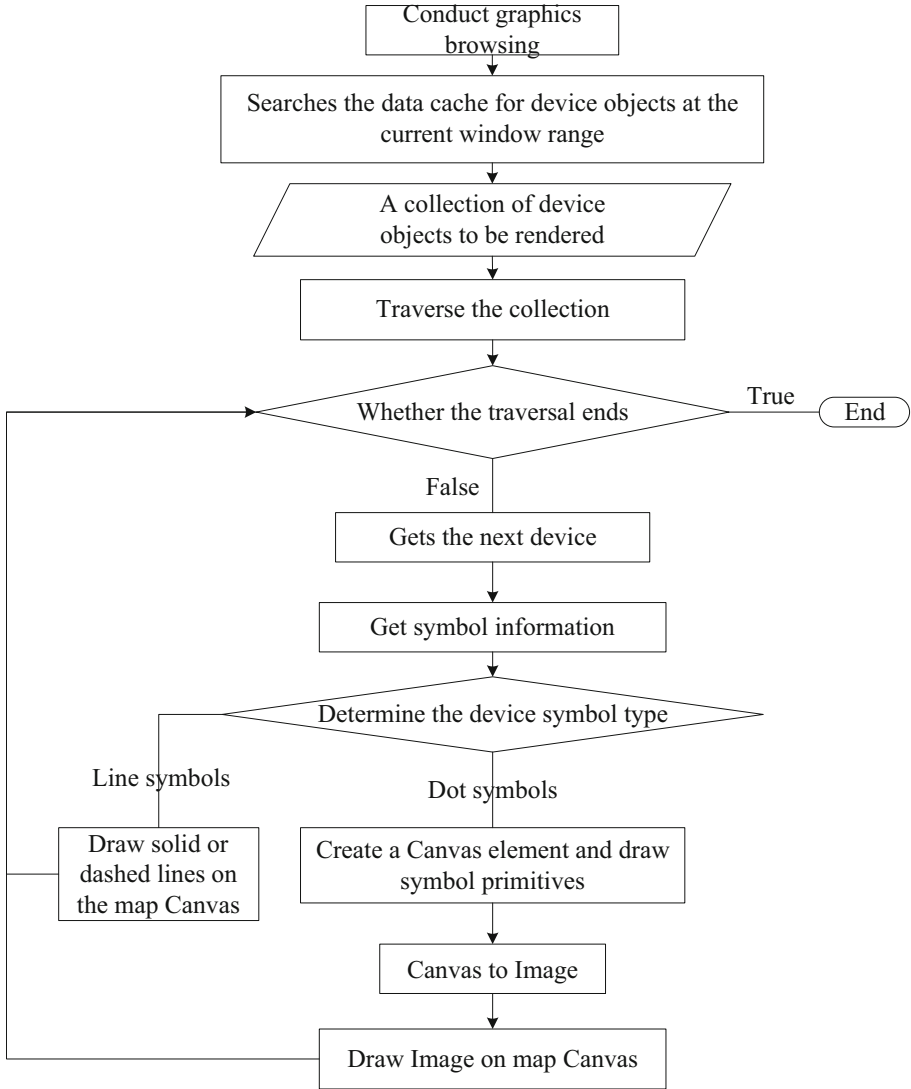
Fig. 3. Data real-time rendering process.

4 Testing and Verification

4.1 Test Data and Program Implementation

Based on the method in this paper, the research team developed a power grid GIS one map display system. Based on the power grid resource data of a certain province, the power grid resource GIS display test is carried out. The provincial power grid equipment (including low-voltage equipment) has a total of more than 200 million, of which the

data volume of lines (including overhead line segments and cable line segments) is more than 20 million.

The power grid resource spatial database tested adopts MongoDB 4.0, the query service is implemented in Java, and the Web terminal is implemented in JavaScript and HTML5.

4.2   Graphic Rendering Effect

Figure 4 shows the overall display effect of the line in a large geographical range; Fig. 5 shows the partial display effect of the line; Fig. 6 shows the rendering effect of the wiring diagram in the station after the map is enlarged.
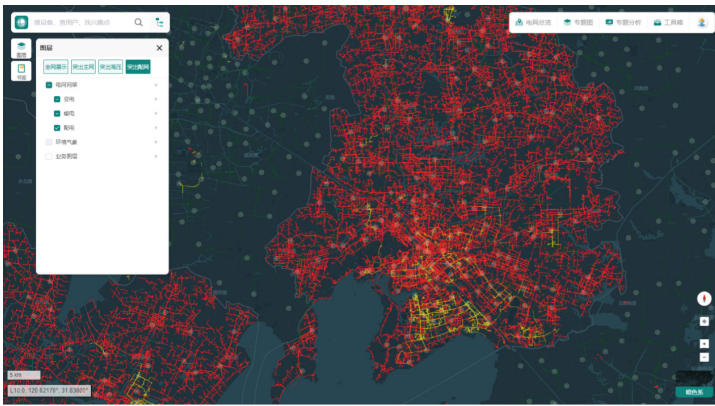

Fig. 4. Rendering effect of large-scale power grid resource map - overall display of lines

Fig. 5. Rendering effect of large-scale power grid resource map - partial display of lines
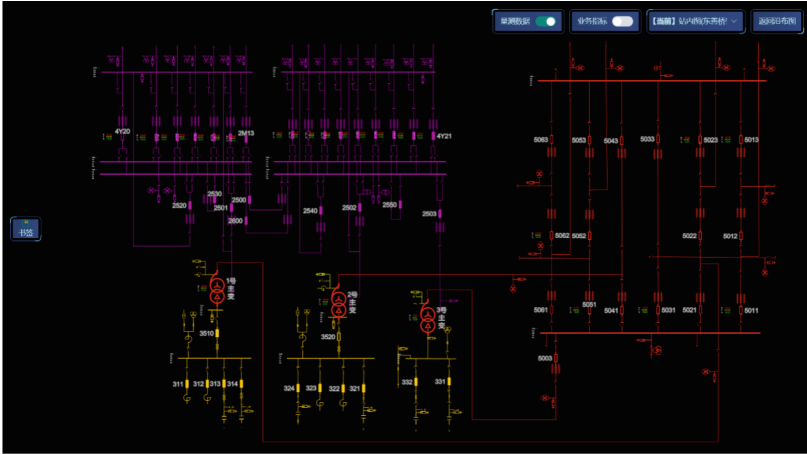
Fig. 6. Rendering effect of power grid resource map - wiring diagram in the station

4.3 Caching and Data Compression Effects

Perform 5 independent random browsing tests on the client side, and each browsing includes map zooming out, zooming in, and panning operations. The test records the number of client viewport changes and the number of actual line query requests during the browsing process. From the test results, since some repeated requests are avoided by using the request cache, the number of data requests is significantly less than the number of viewport changes. It can be seen that the request cache has a significant effect on reducing the pressure of server-side data query and client-side data parsing. In addition, to verify the effect of line data compression, the line query request returns both the original data and the compressed data, and the total amount of data of both lines is counted. From the comparison of results, through line compression, the amount of data transmission is greatly reduced, thereby reducing the pressure on client rendering. The specific test results are shown in Table 1.

Table 1. Client random roaming test results.

Test number	Viewport changes	Number of requests	The total amount of data received on the line	
			Uncompressed	Compression
Test 1	120	15	8.5	0.8
Test 2	52	8	3.1	0.3
Test 3	82	9	15.8	1.2
Test 4	20	6	14.3	1.1
Test 5	36	10	21.4	1.6

4.4 Comparative Analysis

At present, State Grid Corporation of China's power grid GIS applications are mainly concentrated in production management, distribution network repair and other business systems. The web-side grid graphic display method in the above system is as follows: every time the map viewport changes, the client sends a graphic request to the server, and the server immediately queries the data from the database and renders it as a picture for display to the client. The display component adopts Flex. Compared with the above schemes, this method mainly has the following two advantages:

(1) The method in this paper uses client-side real-time rendering, which is more interactive than server-side rendering, and can instantly change the color and style displayed by the device. Therefore, the method in this paper is easier to implement common functions such as device highlighting, device click query, analog switch setting, and charged coloring. In addition, the graphics rendering is completed by the client, the amount of data transmitted over the network is small, and the server pressure is light.

(2) In the above system, a service rendering request is performed every time the viewport changes, and the method in this paper reduces repeated requests due to the use of request caching, avoids sending data requests every time the viewport changes, and reduces the pressure on the server.

5 Conclusion

In this paper, we propose a Web-oriented dynamic loading and vectorization display method for massive spatial data of power grid resources for power grid spatial data and application characteristics. It has been verified by actual measurement: 1) This method can support the high-performance display of massive power grid spatial data on the web side; 2) Due to the vectorized rendering on the web side, it is very suitable for the setting of analog switches, dynamic charging and coloring of equipment required for power grid operation analysis applications. Dynamic annotation data refresh requirements, while facilitating the realization of object flickering, mouse movement/click dynamic highlighting and other effects, can provide a better user experience. The research results of this paper have been applied to many large-scale power grid GIS application systems.

References

1. Shi, X.H.: Grid GIS and Its Applications. China Electric Power Press, Beijing (2010)
2. Zhang, D., Wu, H., She, Y.: Research on the maintenance mechanism and key technologies of grid resource data based on unified grid resource model. Electr. Appl. **S2**, 423–427 (2015)
3. Tang, K., Zhong, Y., Wu, H., He, P., Xu, L., Qi, W.: Design and application of basic data quality management tools for power grid GIS. Power Inf. Commun. Technol. **02**, 98–101 (2016)
4. Yi, Y.Q., Xi, J.F., Lei, W.G.: Research on multi-source multi-temporal multi-resolution spatial data quality control technology system for power grid GIS. South. Energy Constr. **S1**, 122–125 (2016)

5. Wang, H., Liu, K.: Construction and application of low voltage distribution network GIS combined with electric power camping and distribution integrated information platform. Power Informatiz. **8**(1), 71–74 (2010)
6. Liu, T.: Analysis of construction and application benefits of GIS geographic information service platform for power grid. Digit. Technol. Appl. **10**, 235–236 (2012)
7. Lin, F., Guo, B., Qian, W.: Grid geo-graphic application architecture for public grid GIS platform. Power Syst. Autom. **35**(24), 63–67 (2011)
8. Chen, J., Wan, G., Sun, G., Liu, W., Yao, S.: Development and application of GIS platform power grid planning auxiliary decision system. J. Power Syst. Autom. **22**(06), 99–103 (2010)
9. Huang, W., Yan, B., Tan, M., et al.: Research on optimal design of wind power collection system for offshore wind farms considering the influence of obstacles Area. Mod. Electr. Power **35**(1), 6–13 (2018)
10. Dufilie, A., Grinstein, G.: Feathered tiles with uniform payload size for progressive transmission of vector data. In: Pfoser, D., Li, K.-J. (eds.) W2GIS 2013. LNCS, vol. 8470, pp. 19–35. Springer, Heidelberg (2014). https://doi.org/10.1007/978-3-642-55334-9_2
11. Maiellaro, N., Varasano, A.: One page multimedia interactive map. ISPRS Int. J. Geo Inf. **6**, 34 (2017)
12. Gaffuri, J.: Toward web mapping with vector data. In: Xiao, N., Kwan, M.-P., Goodchild, M.F., Shekhar, S. (eds.) GIScience 2012. LNCS, vol. 7478, pp. 87–101. Springer, Heidelberg (2012). https://doi.org/10.1007/978-3-642-33024-7_7
13. Mapbox Co.: Mapbox Vector Tile Specification [EB/OL], 19 January 2016. https://www.mapbox.com/vector-tiles
14. Zhu, X., Zhou, Z., Li, J., Zhao, Y., Peng, Y.: Research on network vector map tile technology. Mapp. Bull. **11**, 106–109+117 (2016)
15. Sun, C.-L., Huo, L., Gao, Z.-H.: Research on vector data organization method based on vector tiles. Mapp. Spat. Geogr. Inf. (04),122–124 (2016)
16. Cromley, R.G., Campbell, G.M.: Integrating quantitative and qualitative aspects of digital line simplification. Cartogr. J. **29**(1), 25–30 (1992)
17. Guttman, A.: R-trees: a dynamic index structure for spatial searching. In: Proceedings of the ACM SIGMOD International Conference on Management of Data, Boston, pp. 47–54 (1984)

Low-Carbon Economy
of Electricity-Heat-Gas-Hydrogen Integrated
Energy System Considering P2G Research
on Dual Objective Scheduling

Hui Wang[1,2]($\boxtimes$), Xu Liao[1,2], Shuaishuai Lv[1,2], Yuliang Zhang[1,2],
and Chengdong Yang[1,2]

[1] Changchun Institute of Technology, Changchun 130012, China
254425251@qq.com
[2] National and Local Joint Engineering Research Center for Measurement, Control and Safe
Operation of Intelligent Distribution Networks, Changchun 130012, China

Abstract. Based on the strict control of carbon emission rights and carbon emission quotas in various countries, this paper proposes a dispatching strategy for the conversion of abandoned wind power into natural gas, and realizes the transfer and consumption of electric energy. In addition, P2G and carbon capture storage and utilization are added to the traditional electricity-heat-gas-hydrogen integrated energy system, which accelerates the process of further realizing "carbon neutrality". Secondly, the economic goal is to consider the tiered carbon trading and wind curtailment costs as the total operating cost; the real carbon emission of the system after carbon capture is taken as the low-carbon goal. By constructing different discrete preference weights between the two goals, the CPLEX solver is used to obtain the complete the Pareto frontier. Finally, the optimal compromise solution and the day-ahead optimal scheduling reference value are obtained according to the fuzzy membership function. Comparing the participation analysis considering P2G, it proves the superiority of the proposed strategy.

Keywords: Electricity-heat-gas-hydrogen integrated energy system · P2G · Stepped carbon trading · Pareto frontier · Fuzzy membership function

1 Introduction

With the continuous development of information technology, the energy crisis and the environmental crisis are constantly pouring in [1]. In the face of the new trend of low-carbon energy in the world, our country is based on the goal of low-carbon development, and gradually enters the road of technological update and innovative development [2]. However, in my country's power industry, fossil fuels are mainly used as the main body, and its carbon emissions account for a considerable proportion. Therefore, there is still a long way to go to achieve the "double carbon" goal.

The integrated energy system IES (Integrated Energy System) contains a variety of energy sources that are coordinated with each other. Therefore, in this paper, the electric-heat-gas-hydrogen model is added to the original IES, and the P2G is refined, which can meet different loads under suitable output conditions, making the system more economical and stable.

Due to the uncertainties of most clean energy, the problem that must be dealt with in different periods is how to absorb the energy of abandoned wind and make the huge power system operate in a low-carbon economy [3]. However, as a key technology to solve the problem of wind curtailment, P2G equipment converts electric energy into natural gas, and transports it to the natural gas network in large-scale storage or normal temperature pipelines to generate profits for users to use [4]. In fact, P2G includes two working processes, that is, the electrolysis of water to produce hydrogen and the reaction of hydrogen and carbon dioxide through a methane reactor to produce methane. In the second reaction, a strong exothermic process will be generated in this reactor, and the industry can consider heat recovery and utilization of this process, and cooperate with CHP (Combined Heat and Power) to supply heat, which can improve energy efficiency. And in the original two reaction processes, the efficiency of electric methane production was 55%, while the electric hydrogen production efficiency was 80%. Therefore, it is extremely important to refine the process of electric hydrogen production [5].

References [6, 7] proposed a two-layer optimal dispatch model for a power-natural gas integrated energy system that considers the rational utilization of abandoned wind from power-to-gas conversion and the optimal operation of natural gas systems, but ignores the factors generated by carbon capture. Therefore, this paper adds a carbon capture storage (CCUS) device to the electric thermal hydrogen IES. Regarding CCUS technology, it is the only solution that can significantly reduce fossil fuel carbon emissions in power generation and industrial production. At the same time, the IEA believes that to achieve the goal of carbon neutrality and carbon peaking, CCUS technology captures 15%-30% of carbon dioxide. CCUS technology is the core technology and key technology for large-scale emission reduction of fossil energy in the future, and it is also the underpinning technology for our country to achieve carbon neutrality in the future [8]. References [9, 10] proposed a stepped carbon trading mechanism to restrict carbon emissions, but in the process of model calculation, only positive carbon trading was considered, and the negative carbon trading was not reflected in the literature.

Therefore, this paper considers the stepped carbon trading mechanism on the traditional P2G model. After adding the CCUS device, the total carbon emission of the system is the lowest as the first carbon emission target. In this process, the fuzzy membership function is used to obtain the maximum carbon emission The optimal compromise solution is used to compare the carbon emissions under different conditions of adding P2G and not adding P2G, so as to illustrate the progress of this scheduling strategy [11]. In addition, the two-stage operation benefit analysis of P2G, including CHP with adjustable thermoelectric ratio, also involves the impact of the hydrogen fuel cell (Hydrogen Fuel Cell) operation strategy used in electric hydrogen production on the economic operation of IES, constructing The second goal of low-carbon economic operation with the smallest total operating cost of IES is established, and a dual-objective model of carbon emission and operating cost is constructed. The CPLEX solver is used to solve the

problem. In two different scenarios, the optimal economic operation is obtained through analysis. Strategy.

2 Structure Diagram of Electricity-Heat-Gas-Hydrogen Integrated Energy System with P2G

Under the IES system, which is composed of a combination of various energy sources, each energy structure can adapt to each other to meet the load consumption. Under the original stepped carbon trading mechanism, this paper not only refines the application characteristics of P2G to absorb photovoltaic and wind power, but also considers the different constraints under the negative carbon trading mechanism, and also adds the thermoelectric ratio of CHP equipment. The characteristics of the adjustment, and the gas boiler GB (gas boiler). Its graph is shown in Fig. 1.
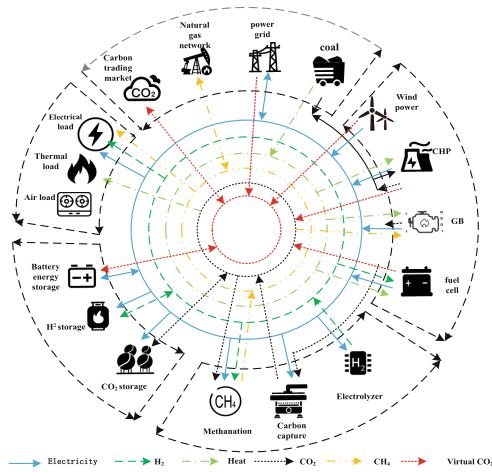

Fig. 1. Structure diagram of electricity-heat-gas-hydrogen integrated energy system

3 Modeling of Carbon Allowances and Stepped Carbon Trading (Linearized Model)

3.1 Actual Carbon Emissions

The process of hydrogen from natural gas produced by the methane reactor MR (Methane Reactor) can absorb a part of CO2, and the carbon recovered in this process will reduce the actual emission of carbon, so it should be considered. The actual carbon emission

model is as follows:

$$
\begin{cases}
E^T = E_{buy,o} + E_{to,o} - E_{MR,o} \\
E_{buy,o} = \sum_{t=1}^{T} (m_1 + n_1 P_{buy,o}(t) + q_1 P_{buy,o}^2(t)) \\
E_{to,o} = \sum_{t=1}^{T} (m_2 + n_2 P_{to,o}(t) + q_2 P_{to,o}^2(t)) \\
P_{to,o}(t) = P_{CHP,d}(t) + P_{CHP,e}(t) + P_{GB,e}(t) \\
E_{MR,o} = \sum_{t=1}^{T} \lambda P_{MR,t}(t) \\
E_{P2G,o} = \sum_{t=1}^{T} \delta P_{P2G,t}(t)
\end{cases}
\tag{1}
$$

In the formula: E^T, $E_{buy,o}$ are the actual carbon emissions of IES and superior power purchases respectively, $E_{to,o}$ is the actual total carbon emissions of MR, GB, and CHP; $P_{buy,o}(t)$ is the power purchased during t, $E_{MR,o}$ is the amount of CO_2 recovered by MR, $E_{MR,t}$ is the power absorbed by the methane reactor during t period, $P_{CHP,e}(t)$, $P_{CHP,d}(t)$, $P_{GB,e}(t)$, $P_{to,o}(t)$ is the cogeneration power, cogeneration gas, gas boiler, and total output power in the t period; m_1, n_1, q_1, m_2, n_2 and q_2 are the parameters of thermal power units and methanated carbon emissions, respectively; $P_{P2G,t}(t)$ is The power absorbed by the electric-to-gas process per unit time is the parameter of the MR equipment to absorb CO_2. It is the parameter of CO_2 absorption in the process of P2G equipment electricity to gas conversion; $P_{CHP,o}(t)$ is the natural gas power output by P2G in t period.

3.2 Initial Quota of Carbon Emission Rights

Regarding the initial quota of carbon emission, the government has clear regulations, which generally adopts the method of free distribution, and the carbon emission of IES mainly includes the upper-level thermal power unit, GB, and gas load. The initial quota model is

$$
\begin{cases}
E_{IES} = E_{buy} + E_{GB} + E_{CHP} \\
E_{buy} = \chi_e \sum_{t=1}^{T} P_{buy}(t) \\
E_{CHP} = \chi_g \sum_{t=1}^{T} (P_{CHP,d}(t) + P_{CHP,e}(t)) \\
E_{GB} = \chi_g \sum_{t=1}^{T} P_{GB}(t)
\end{cases}
\tag{2}
$$

In the formula: E_{IES}, E_{buy}, E_{CHP}, and E_{GB} are the carbon emission allowances of IES, superior power purchase, CHP, and GB, respectively; χ_e and χ_g are the carbon emission quotas for the unit electricity consumption of coal-fired units and the unit natural gas consumption of natural gas-fired units, respectively; $P_{buy}(t)$ is the electricity purchased by the superior in the t period; $P_{GB}(t)$ is the thermal energy output in the t period, and T is the dispatch period.

To sum up the above, the carbon trading volume that IES participates in is

$$E_{IES,t} = E_{CO_2} - E_{IES} \qquad (3)$$

3.3 Ladder Carbon Trading

$$S_{CO2}^T = \begin{cases} -\mu\gamma - \mu(1+\sigma)\gamma + \mu(1+\sigma)^2(T_i + 2\gamma) & T_i \leq -2\gamma \\ -\mu\gamma + \mu(1+\sigma)(\gamma + T_i) & -2\gamma \leq T_i \leq -\gamma \\ \mu T_i & -\gamma \leq T_i \leq \gamma \\ \mu\gamma + \mu(1+\sigma)(T_i - \gamma) & \gamma \leq T_i \leq 2\gamma \\ \mu\gamma + \mu(1+\sigma)\gamma + \mu(1+\sigma)^2(T_i - 2\gamma) & T_i \geq 2\gamma \end{cases} \qquad (4)$$

In the formula: S_{CO2}^T is the stepwise carbon transaction cost parameter; μ is the unit price of carbon transaction; γ is the length of the carbon emission interval; σ is the carbon emission price growth rate; T_i is the time ladder.

4 Low-Carbon Economy Dual-Objective Model and System Modeling Constraints

4.1 Objective Function

1) Operating cost target

In the original IES, this paper comprehensively considers the coordination of multiple energy sources, and aims to minimize the total operating cost S^T with the main network purchase and sale cost, natural gas network cost, thermal power cost, penalty cost of wind abandonment and carbon transaction cost as follows:

$$\begin{cases} S^T = S_{DW}^T + S_{RE}^T + S_{GW}^T + S_{DG}^T + S_{CO_2}^T \\ S_{DG}^T = \lambda_{DG} \sum\limits_{t=1}^{T} P_{DG}(t) \\ S_{DW}^T = \sum\limits_{t=1}^{T} (E_{Dbuy,o}(t) \cdot P_{Dbuy,o}(t) - E_{Dsell,o}(t) \cdot P_{Dsell,o}(t)) \\ S_{GW}^T = \sum\limits_{t=1}^{T} (G_{Gbuy,o}(t) \cdot P_{Gbuy,o}(t) - G_{Gsell,o}(t) \cdot P_{Gsell,o}(t)) \\ S_{RE}^T = \sum\limits_{t=1}^{T} (\mu \cdot (E_{RE,o}(t))^2 + v \cdot E_{RE,o}(t) + o) \cdot P_{Rbuy,o} \end{cases} \qquad (5)$$

In the formula: S_{DW}^T, S_{GW}^T, S_{RE}^T, are the purchase and sale cost of the power grid, the purchase and sale cost of the gas grid, and the heat and power cost, respectively, S_{DG}^T is the cost of wind abandonment; λ_{DG} is the unit wind abandonment penalty cost coefficient; $P_{DG}(t)$ is the wind abandonment power in the t period. $E_{Dbuy,o}(t)$ is the amount of electricity purchased per unit time, and $E_{Dsell,o}(t)$ is the amount of electricity sold per unit time; $G_{Gbuy,o}(t)$ is the amount of gas purchased per unit time, $G_{Gsell,o}(t)$ is the amount of gas purchased per unit time; $E_{RE,o}(t)$ is the amount of heat

supplied by the thermal power boiler, $P_{Dbuy,o}(t)$, $P_{Dsell,o}(t)$, $P_{Gbuy,o}(t)$, $P_{Gsell,o}(t)$, $P_{Rbuy,o}(t)$ are the power purchased by the grid in a unit time, and the amount of electricity sold by the grid. Electric power, gas power grid purchase power, gas grid power sales power, thermal power purchase power. μ, v, o are the coefficients of each order of thermoelectric cost. represents the stepped carbon transaction cost (see Eq. (4)). The model constructed in this paper is suitable for both positive carbon transaction costs and negative carbon transaction costs.

2) Actual carbon emission target

As shown in Sect. 3.1, the original actual carbon emission target.

3) Fuzzy membership function to obtain the optimal compromise solution

In order to facilitate the fuzzification of the dual objective function in this paper, the carbon emissions and operating costs are normalized, as shown in Eq. 6:

$$\begin{cases} s_{CO_2} = E_O^T/E^T \\ s_{RUN} = S_O^T/S^T \end{cases} \tag{6}$$

In the formula: s_{CO2} and s_{RUN} represent the carbon emission ratio and operating cost ratio, respectively, and E_O^T and S_O^T represent the carbon emissions before optimization and the total operating cost, respectively.

According to the optimized dual-objective requirements, the trapezoidal function among the six membership functions selected here is shown in Fig. 2, and the following model functions can be obtained:

$$\varphi(s) = \begin{cases} 1, & s \le s^{\min} \\ (s^{\max} - s)/(s^{\max} - s^{\min}), & s^{\min} < s < s^{\max} \\ 0, & s \ge s^{\max} \end{cases} \tag{7}$$

In the formula: s_{CO2} and s_{RUN} are respectively brought into the function $\varphi(s)$, and $\varphi(s_{CO2})$ and $\varphi(s_{RUN})$ are obtained and respectively represent the membership values of s_{CO2} and s_{RUN}; and $s_{CO2}^{\max}$ and $s_{CO2}^{\min}$ after they are brought in represent the set maximum and minimum values of s_{CO2} respectively; and The obtained $s_{CO2}^{\max}$ and $s_{CO2}^{\min}$ represent the set maximum and minimum values of s_{RUN}, respectively.
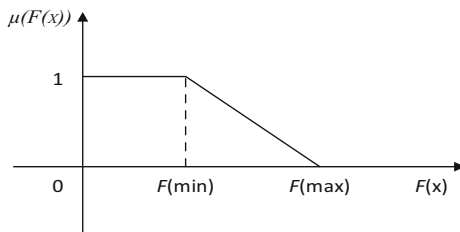

Fig. 2. Fuzzy membership trapezoidal function diagram

Fuzzy Membership Optimization:

The 100 data values of the two targets are imported one by one and different data values are obtained, and finally the data is solved by the function maximum and minimum rule [12]. Transforming the bi-objective satisfaction of f_i into a satisfaction maximization problem under all constraints, the following model is obtained:

$$
\begin{cases}
\mu = \max\{f_i\} \\
f_i = \min\big(\varphi(s_{CO_2}), \varphi(s_{RUN})\big)
\end{cases}
\tag{8}
$$

In the formula: f_i represents the optimal solution of the single operation cost and carbon emission of the fuzzy membership value, and the membership value corresponding to the f_i corresponding to the final μ value is brought into the atomic formula, and the optimal solution can be obtained. Running costs and carbon emissions.

4.2 System Model Constraints

4.2.1 Hydrogen Balance Constraints of Electric Heating Gas

1) Electric power balance constraints

Considering the uncertainty of wind turbines, based on reducing the frequency fluctuations caused by the main grid connection. The sale of electricity to the upper power grid is not considered here.

$$
\begin{cases}
P_{buy,d}(t) = P_{Load,d}(t) + P_{EL,d}(t) + P_{ES,d}(t) - P_{DG,d}(t) - \\
P_{CHP,d}(t) + P_{HFC,d}(t) \\
0 \le P_{buy,d}(t) \le P^M_{buy,d}(t)
\end{cases}
\tag{9}
$$

2) Thermal power balance constraints

$$
P_{Load,r}(t) + P^r_{ES}(t) = P_{HFC,r}(t) + P_{CHP,r}(t) + P_{GT,r}(t)
\tag{10}
$$

In the formula: $P_{Load,r}(t)$ is the heat load in the t period; $P^r_{ES}(t)$ is the power input to the thermal storage in the t period.

3) Natural gas balance constraints

$$
\begin{cases}
P_{buy,g}(t) = P_{Load,g}(t) + P_{ES,g}(t) + P_{CHP,g}(t) - \\
P_{GT,g}(t) - P_{MS,g}(t) \\
0 \le P_{buy,g}(t) \le P^M_{buy,g}(t)
\end{cases}
\tag{11}
$$

4) Hydrogen balance constraints

$$
P^{H_2}_{EL}(t) = P^{H_2}_{MS}(t) + P^{H_2}_{HFC}(t) + P^{H_2}_{ES}(t)
\tag{12}
$$

In the formula: $P^{H_2}_{ES}(t)$ is the input power of hydrogen storage in t period.

4.2.2 Modeling of Key Equipment

1) Combined heat and power CHP

Based on the original electrical-thermal model, the constraints are relatively simple. Therefore, this paper restricts the consideration of P2G in the electrical-thermal gas-hydrogen modeling.

$$
\begin{cases}
P_{CHP,d}(t) = \eta^d P_{CHP,o}(t) \\
P_{CHP,r}(t) = \eta^r P_{CHP,o}(t) \\
P_{CHP,o}^{\min}(t) \le P_{CHP,o}(t) \le P_{CHP,o}^{\max}(t) \\
\Delta P_{CHP,o}^{\min}(t) \le P_{CHP,o}(t+1) - P_{CHP,o}(t) \le \Delta P_{CHP,o}^{\max}(t) \\
\tau_{CHP}^{\min} \le P_{CHP,r}(t)/P_{CHP,d}(t) \le \tau_{CHP}^{\max}
\end{cases}
\tag{13}
$$

In the formula: $P_{CHP,o}(t)$ is the natural gas power input to CHP in t period; $P_{CHP,d}(t)$ and $P_{CHP,r}(t)$ are the electricity and heat energy output by CHP in t period, respectively; η^d and η^r are the conversion efficiency of CHP into electricity and heat energy respectively. $P_{CHP,o}^{\min}(t)$ and $P_{CHP,o}^{\max}(t)$ are the natural gas input into CHP, respectively The upper and lower limits of power; $\Delta P_{CHP,o}^{\min}(t)$ and $\Delta P_{CHP,o}^{\max}(t)$ are the upper and lower limits of CHP climbing, respectively $\tau_{CHP}^{\min}$ and $\tau_{CHP}^{\max}$ are the upper and lower limits of the thermoelectric ratio of CHP, respectively.

2) Energy storage (electric heating gas hydrogen)

$$
\begin{cases}
0 \le P_{ES,m}^{sto}(t) = H_{ES,m}^{sto}(t)P_{ES,m}^{\max}(t) \\
0 \le P_{ES,m}^{fre}(t) = H_{ES,m}^{fre}(t)P_{ES,m}^{\max}(t) \\
P_{ES,m}(t) = P_{ES,m}^{sto}(t)\eta_{ES,m}^{sto} - P_{ES,m}^{fre}(t)/\eta_{ES,m}^{fre} \\
T_m(t) = T_m(t-1) + P_{ES,m}(t)/P_{ES,m}^{rat} \\
T_m(1) = T_m(t) \\
H_{ES,m}^{sto}(t) + H_{ES,m}^{fre}(t) = 1 \\
T_m^{\min} \le T_m(t) \le T_m^{\max}
\end{cases}
\tag{14}
$$

In the formula: $P_{ES,m}^{sto}(t)$ and $P_{ES,m}^{fre}(t)$ are the charging and discharging power of the mth energy storage device in the period t respectively; $P_{ES,m}^{\max}(t)$ is the single charge and discharge maximum power of the mth energy storage device; $H_{ES,m}^{sto}(t)$ and $H_{ES,m}^{fre}(t)$ are binary variables, respectively The charging and discharging state parameters of m types of energy storage devices in the t period, $H_{ES,m}^{sto}(t) = 1$, $H_{ES,m}^{fre}(t) = 0$ indicates that they are in the charging state, $H_{ES,m}^{sto}(t) = 0$, $H_{ES,m}^{fre}(t) = 1$ indicates that they are in the discharging state; $P_{ES,m}(t)$ is the final state of the mth energy storage device in the t period. $\eta_{ES,m}^{sto}$ and $\eta_{ES,m}^{fre}$ are the charging and discharging efficiencies of the mth energy storage device, respectively; $T_m(t)$ is the capacity of the mth energy storage device in the t period; $P_{ES,m}^{rat}(t)$ is the rated capacity of the mth energy storage device; $T_m^{\min}$ and $T_m^{\max}$ are respectively are the upper and lower limits of the capacity of the mth energy storage device.

3) P2G technology conversion model

In this paper, CCUS is introduced into the traditional P2G model to capture the amount of carbon dioxide, while P2G is mainly used as one of the main technologies

to solve the problem of wind abandonment, and it also converts the methane for transportation or storage [13]. The P2G operation network process is shown in Fig. 3.
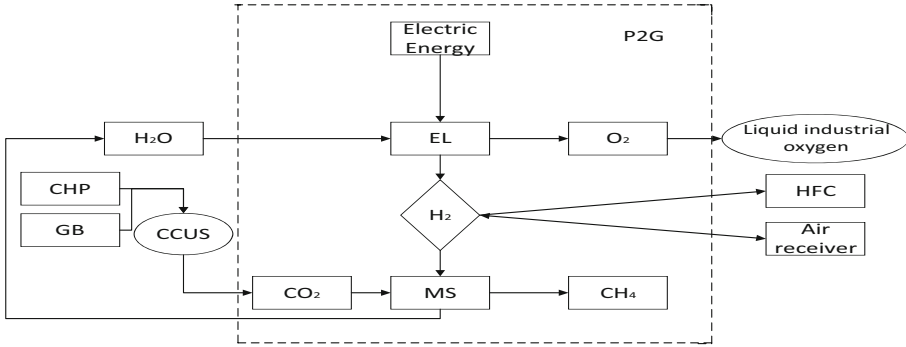

Fig. 3. P2G system conversion structure diagram

EL is actually a water electrolysis device, which converts the original electrical energy into hydrogen energy. Of course, the generated oxygen can also be stored as industrial oxygen. At the same time, a part of the hydrogen is input to the MR and reacts with carbon dioxide to produce methane, and a part is stored, and a considerable part is Hydrogen energy is converted into heat and electricity through HFC [14]. The model of the above energy conversion is as follows.

1) EL equipment

$$
\begin{cases}
P_{EL}^{H_2}(t) = \eta_{EL}^{H_2} P_{EL}^d(t) \\
P_{EL,d}^{\min}(t) \le P_{EL}^d(t) \le P_{EL,d}^{\max}(t) \\
\Delta P_{EL,d}^{\min}(t) \le P_{EL}^d(t+1) - P_{EL}^d(t) \le \Delta P_{EL,d}^{\max}(t)
\end{cases}
\tag{15}
$$

In the formula: $P_{EL}^d(t)$ is the electric energy input to EL in t period; $P_{EL}^{H_2}(t)$ is the hydrogen energy output by EL in T period; $\eta_{EL}^{H_2}(t)$ is the energy conversion efficiency of EL; $P_{EL,d}^{\max}(t)$ and $P_{EL,d}^{\min}(t)$ are the upper and lower limits of electric energy input to EL, respectively; $\Delta P_{EL,d}^{\max}(t)$ and $\Delta P_{EL,d}^{\min}(t)$ are the upper and lower limits of EL climbing.

2) MR equipment

$$
\begin{cases}
P_{MR}(t) = \eta_{MR} P_{MR}^{H_2}(t) \\
P_{MR,H_2}^{\min}(t) \le P_{MR}^{H_2}(t) \le P_{MR,H_2}^{\max}(t) \\
\Delta P_{MR,H_2}^{\min}(t) \le P_{MR}^{H_2}(t+1) - P_{MR}^{H_2}(t) \le \Delta P_{MR,H_2}^{\max}(t)
\end{cases}
\tag{16}
$$

In the formula: $P_{MRS}^{H_2}(t)$ is the hydrogen energy input to the MR in the t period; $P_{MR}(t)$ is the natural gas power output by the MR in the t period; η_{MR} is the

energy conversion efficiency of the MR; $P^{max}_{MR,H_2}(t)$ and $P^{min}_{MR,H_2}(t)$ are the upper and lower limits of the hydrogen energy input to the MR, respectively; $\Delta P^{max}_{MR,H_2}(t)$ and $\Delta P^{min}_{MR,H_2}(t)$ are the upper and lower limits of MR climbing.

3) HFC equipment

In the energy conversion model HFC with adjustable thermoelectric ratio, the sum of its thermoelectric conversion efficiencies can be regarded as a constant variable and adjusted by a regulator [15]. Its conversion model is:

$$
\begin{cases}
P^d_{HFC}(t) = \eta^d_{HFC} P^{H_2}_{HFC}(t) \\
P^r_{HFC}(t) = \eta^r_{HFC} P^{H_2}_{HFC}(t) \\
P^{min}_{HFC,H_2}(t) \leq P_{HFC,H_2}(t) \leq P^{max}_{HFC,H_2}(t) \\
\Delta P^{min}_{HFC,H_2}(t) \leq P_{HFC,H_2}(t+1) - P_{HFC,H_2}(t) \leq \Delta P^{max}_{HFC,H_2}(t) \\
\tau^{min}_{HFC} \leq P^r_{HFC}(t)/P^d_{HFC}(t) \leq \tau^{max}_{HFC}
\end{cases}
\tag{17}
$$

In the formula: $P^{H_2}_{HFC}(t)$ is the hydrogen energy input to the HFC in the t period; $P^d_{HFC}(t)$ and $P^r_{HFC}(t)$ are the electric and thermal energy output by the HFC in the t period, respectively; η^d_{HFC} and η^r_{HFC} are the conversion efficiencies of the HFC into electricity and heat, respectively; $P^{max}_{HFC,H_2}(t)$ and $P^{min}_{HFC,H_2}(t)$ are the hydrogen input into the HFC, respectively The upper and lower limits of energy; $\Delta P^{max}_{HFC,H_2}(t)$ and $\Delta P^{min}_{HFC,H_2}(t)$ are the upper and lower limits of HFC climbing respectively; τ^{max}_{HFC} and τ^{max}_{HFC} are the upper and lower limits of HFC's thermoelectricity, respectively.

5   Case Analysis

In order to verify the effectiveness of this optimization strategy, the following two examples are set up for verification, and the optimal scheduling is carried out with a cycle of 24 h a day. Introducing the Pareto frontier graph of P2G and without P2G, the optimal economic point A before optimization (11,555.56, 4574.94), the optimal economic point A′ (9876.56, 4000.00) after optimization; the optimal carbon emission point B before optimization (11,782.47, 4552.55), the optimal carbon emission point B′ after optimization (10,069.96, 3877.05). Before and after the introduction of P2G, the cost of the lowest cost point and the lowest carbon emission point was reduced from 11,555.56 to 9876.56. Carbon emissions are reduced from 4552.55 to 3877.05, which can optimize both economical operating costs and carbon emissions. As shown in Fig. 4 below.

(1) Risk preference selects the optimal compromise membership value after optimization

Aiming at the difficult problem of economic low-carbon dual-objective decision-making, an optimal compromise solution selection method based on fuzzy membership function is introduced, which can take into account the optimal balance of
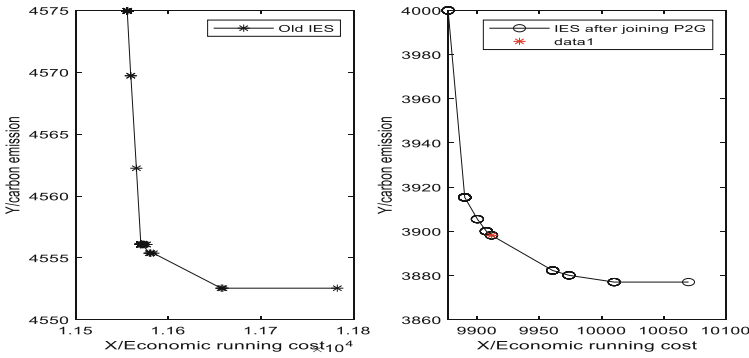
Fig. 4. Comparison of optimal fuzzy membership degrees

economic and low-carbon dual benefits. The comparison shows that the position of the optimal compromise point is selected at the position of data1 in the figure. The membership value of the optimal compromise solution is 0.37, at this time. $E_O^T = 9912$, $S_O^T = 3898$. The benefit comparison table before and after the ladder-type carbon trading mechanism is shown in Table 1.

Table 1. Comparison of benefits before and after the step-by-step carbon trading mechanism considering P2G

Parameter	Parameter value		
	Scenario 1	Scenario 2	optimization
Carbon emissions/kg	4555.37	3877.05	14.9%
Carbon trading cost/yuan	227.50	163.80	11.6%
Abandoned wind and light output/kW.h	134.21	44.74	66.7%
total cost/yuan	11,583.80	10,010.15	13.6%

(2) Optimal daily output balance diagram of electric heating gas and hydrogen
   Considering the P2G state, after the IES economic operating cost and carbon emissions are dual-objective optimal scheduling calculations, and using the commercial solver Cplex in the MATLAB simulation software to solve, the optimal output balance diagram of electric heating gas and hydrogen can be obtained as follows: shown in Fig. 5.
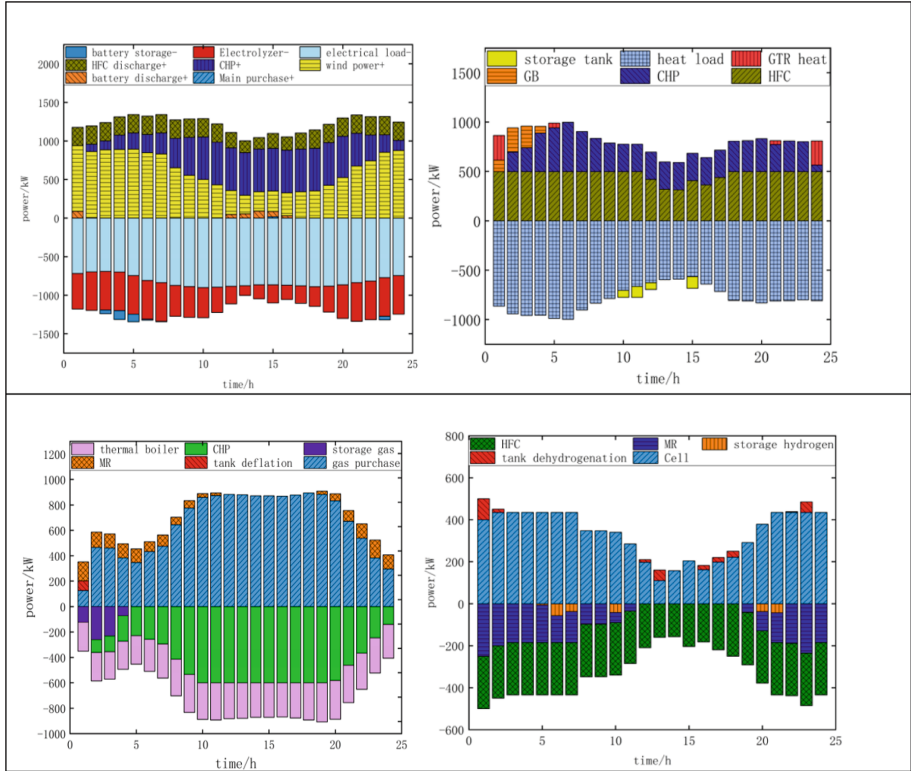
Fig. 5. Optimal output balance diagram of electric heating gas and hydrogen

6   Conclusion

This paper is supported by the Jilin Provincial Department of Science and Technology (20210402057GH).

In the original IES, while considering CCUS, this paper conducts a detailed comparative analysis of the two stages of P2G, and constructs a dual-objective optimal dispatch model by considering the cost of stepped carbon trading, the cost of wind curtailment, and the carbon emission target. And through research and analysis:

1) Considering the two stages of P2G's electric hydrogen production and conversion to methane, it promotes wind power consumption, further promotes the efficient utilization of hydrogen energy, and reduces the problem of system energy loss. In addition, in the P2G equipment, the heat recovery and utilization of the strong exothermic process of methanation is carried out, and the heat supply is coordinated with CHP, which can improve the energy utilization rate.

2) The introduction of CO2 storage can realize full-scale carbon capture when thermal power units with peak load are in operation. At night, the abandonment of wind and light is serious, that is, when thermal power units are not in operation, carbon storage devices are used to release carbon for methanation and power consumption,

which is conducive to the utilization of electricity. This peak-filling method enables the stable operation of the power system.

3) When considering HFC to achieve short-term and high-efficiency storage of hydrogen energy, introducing methane to achieve stable storage after electricity production of hydrogen to methane or using existing natural gas pipelines for safe and cheap transportation is conducive to long-term storage and even seasonal energy storage.

References

1. Cao, Y., Chen, S., Hu, X., Ming, T., Dilidar, A.: The value realization of electric power big data under the construction of energy internet. China Sci. Technol. Inf. (06), 142–143 (2022)
2. Du, J.: Energy internet: a new pivot for low-carbon transformation (part 1). Shanxi Daily, 23 February 2022. https://doi.org/10.28713/n.cnki.nshxr.2022.000930.
3. Gong, X., Wang, J., Wang, L., Zhang, H., Qian, J., Deng, M.: Low-carbon economic operation of electric-gas interconnection integrated energy system with electricity-to-gas interconnection. J. Electric Power Sci. Technol. **35**(02), 76–83 (2020). https://doi.org/10.19781/j.issn.1673-9140.2020.02.010
4. Ma, S.: Research on wind power consumption in electric-gas integrated energy system considering P2G technology. Sci. Technol. Innov. (09), 43–48 (2022)
5. Qiu, B., Song, S., Wang, K., Yang, Z.: Optimal operation of regional integrated energy system considering demand response and stepped carbon trading mechanism. J. Electric Power Syst. Autom. 1–16 (2022). https://doi.org/10.19635/j.cnki.csu-epsa.000869
6. Zhang, R., Jiang, T., Li, G., Chen, H., Li, X., Ning, R.: Two-layer optimal dispatching of a power-gas integrated energy system considering power-to-gas absorption of wind power. Chin. J. Electr. Eng. **38**(19), 5668–5678+5924 (2018)
7. Cui, Y., Yan, S., Zhong, W., Wang, Z., Zhang, P., Zhao, Y.: Optimal dispatching of thermoelectric power in a regional integrated energy system with electricity-to-gas conversion. Power Grid Technol. **44**(11), 4254–4264 (2020). https://doi.org/10.13335/j.1000-3673.pst.2019.2468
8. Luo, P., Yan, W., Wang, Y., Li, J., Lv, Q.: Robust optimal scheduling of electric-gas-heat integrated energy system considering CCUS. High Voltage Technol. 1–14 (2022). https://doi.org/10.13336/j.1003-6520.hve.20210257
9. Wang, L., Lin, J., Dong, H., Zeng, M., Wang, Y.: Optimal scheduling of integrated energy systems considering stepped carbon trading. J. Syst. Simul. 1–12 (2022). https://doi.org/10.16182/j.issn1004731x.joss.22-0189
10. Qin, T., Liu, H., Wang, J., et al.: Low-carbon economic dispatch of electricity-heat-gas integrated energy system based on carbon trading. Autom. Electric Power Syst. **42**(14), 8–13, 22 (2018)
11. Qian, K., et al.: Multi-objective optimal scheduling of charging stations based on fuzzy membership degree. Electric Power Constr. **41**(02), 118–124 (2020)
12. Liu, D., Su, H.: The application of applied mathematics and fuzzy mathematics in geotechnical engineering - comment on "engineering mathematics." Chin. J. Geotech. Eng. **41**(10), 1977 (2019)
13. Wu, H., Li, W., Ding, X.: Analysis and suggestions on my country's carbon capture, utilization and storage policy under the "dual carbon" target. Electric Power Constr. **43**(04), 28–37 (2022)

14. Yin, Z., Zhao, Y., Yang, J., Li, S., Gao, H., Liu, J.: Collaborative optimization of electrical energy system with P2G devices based on scenario analysis. Electric Power Constr. **42**(03), 1–9 (2021)
15. Shi, J., Xu, J., Zeng, B., Zhang, J.: Two-layer optimal operation of regional integrated energy system based on adjustable thermoelectric ratio mode. Power Grid Technol. **40**(10), 2959–2966 (2016). https://doi.org/10.13335/j.1000-3673.pst.2016.10.006

Research on Congestion Management Based on Distribution Locational Marginal Price

Zhiwei Wang[1], Rui Liu[1(✉)], Xiuli Wang[2], Wenzhuo Wang[1], Xin Liu[1], and Yifei Wang[2]

[1] Northwest Branch of State Grid Corporation of China, Xi'an 710048, China
`liurui_EE@163.com`
[2] School of Electrical Engineering, Xi'an Jiaotong University, Xi'an 710049, China

Abstract. The distribution locational marginal price is an important congestion management method for the distribution network with a high proportion of distributed new energy. The refined formulation of the distribution locational marginal price is conducive to the allocate the electric energy economically and enhance the enthusiasm of both the generation side and the consumption side to participate in congestion management. Based on the linear optimal power flow model, a method for calculating the distribution locational marginal price by iteratively updating the loss factor is proposed. The price is divided into four parts: energy, loss, voltage and congestion. For a typical distribution network example, the proposed method is used to calculate the electricity price and different components of each node. The results show that the value and composition of the electricity price can reflect the actual operation of the system and solve the congestion.

Keywords: Distribution locational marginal price · Linearized power flow model · Distribution network congestion management · Loss factor

1 Introduction

With the rapid increase of the proportion of distributed new energy and flexible loads, the distribution network has changed from the power and price-accepting network to a new network with flexibilities. At present, while the unified electricity market is cleared, only the power and node voltage constraints of the transmission system are checked. The topology structure and safe operation requirements of the medium and low voltage distribution network should be taken into consideration, too [1].

In the future distribution network, the probability of congestion will greatly increase. In southern Germany, the power generation capacity of distributed power sources has far exceeded the load capacity of the system, and the overload of cables and transformers will seriously affect the system security [2]. Therefore, how to improve the ability of Distribution System Operator (DSO) to manage congestion will become the key to promoting the development of active distribution networks in the future.

In order to solve the problem of distribution network congestion, DSO can adopt direct control methods, such as distribution network reconfiguration, load reduction,

and power output adjustment methods [3–5]. Another method is indirect control, which uses market-based methods to alleviate the system congestion problem, including Local Energy Trading [6], Local Flexibility Market (LFM) [7], Locational Marginal Price (LMP) [8] etc., by providing a trading platform to motivate electricity generation and consumption customers to participate in the congestion management of the distribution network. This kind of market is cleared after the wholesale market which provides the clearing price without the consideration of distribution network topology constraints. The price of nodes in distribution network differs due to line transmission losses, voltage exceeding and congestion caused by the load, which helps to increase or decrease the corresponding load and contributes to alleviating the congestion situation.

When a node increases the unit power load, the marginal cost it needs to increase is defined as Distribution Locational Marginal Price (DLMP). The calculation of DLMP needs to construct an optimal power flow model. Compared with the transmission network, the R/X value of the distribution network is larger, so the DC power flow is not applicable. Although the AC power flow model or the second-order cone power flow model has higher calculation accuracy, it cannot distinguish the influence of different factors in the system on the electricity price [9, 10]. The linear power flow model can obtain different components of the marginal electricity price of the distribution network node while ensuring the accuracy.

Reference [11] divides the node electricity price into three parts: energy, loss and congestion. It is concluded that whether the system loss is considered will affect the final price result. Reference [8] establishes three methods for expressing line power flow, and the conclusion shows that the method based on marginal loss is more feasible. Reference [12] proposed a DLMP calculation method considering reactive power price and voltage constraints. However, it does not take into account the line power flow constraints. Reference [13] proposes a linear node marginal price calculation model that takes into account system losses. But the line power flow constraints in this paper only consider the active power constraint, where the reactive power is ignored. Reference [14] uses the method of inscribed regular polygon to linearize the line transmission power constraint, and linearizes the influence of the line power flow constraint on DLMP.

Based on the shortage of existing research on congestion management, this paper uses the linear power flow model based on literature [12] to calculate the DLMP. Aiming to minimize the total cost of purchasing electricity, and considering the constraints of line transmission capacity and node voltage amplitude, a calculation method through iteratively updating line loss factors is proposed, which ensures the accuracy of the results and simplifies the computational complexity. The accuracy and effectiveness of the congestion management method proposed in this paper are verified by comparing with the results of the AC power flow model.

2   Optimal Power Flow Model of Distribution Network

2.1   Objective Function

$$\min \sum_{i \in \mathcal{G}} C_i^P P_i^G + C_i^Q Q_i^G \tag{1}$$

2.2 System Constraints

1) **System Power Balance Constraints**

$$
\begin{cases}
\sum_{i \in \mathcal{N}} \left(P_i^G - P_i^D \right) - \sum_{k \in \mathcal{L}} P_k^{Loss} = 0, \left(\lambda_{all}^P \right) \\
\sum_{i \in \mathcal{N}} \left(Q_i^G - Q_i^D \right) - \sum_{k \in \mathcal{L}} Q_k^{Loss} = 0, \left(\lambda_{all}^Q \right)
\end{cases}
\tag{2}
$$

where: P_i^D, Q_i^D are the active and reactive power of the load at node i respectively; P_k^{Loss}, Q_k^{Loss} are the active and reactive power loss on line k respectively; $\mathcal{N}$, $\mathcal{L}$ are the set corresponding to all nodes and all lines in the system.

2) **Node Power Balance Constraints**

$$
\begin{cases}
P_i^G - P_i^D + \sum_{j \in \mathcal{A}(i)} F_{ji}^P - \sum_{j \in \mathcal{C}(i)} \left(F_{ij}^P + P_{ij}^{Loss} \right) = 0, \left(\lambda_i^P \right) \\
Q_i^G - Q_i^D + \sum_{j \in \mathcal{A}(i)} F_{ji}^Q - \sum_{j \in \mathcal{C}(i)} \left(F_{ij}^Q + Q_{ij}^{Loss} \right) = 0, \left(\lambda_i^Q \right)
\end{cases}
\tag{3}
$$

where: $\mathcal{A}(i)$, $\mathcal{C}(i)$ are the set of parent nodes and child nodes of node i respectively; F_{ij}^P, F_{ij}^Q are the active and reactive power transmitted by the line between nodes i and j respectively.

3) **Node Voltage Constraints**

$$
\begin{cases}
V_i - V_i^{max} \le 0, \left(\mu_i^+ \right) \\
-V_i + V_i^{min} \le 0, \left(\mu_i^- \right)
\end{cases}
\tag{4}
$$

4) **Line Transmission Capacity Constraints**

$$
\sqrt{\left(F_k^P \right)^2 + \left(F_k^Q \right)^2} \le S_k^{max}
\tag{5}
$$

where: F_k^P, F_k^Q are the active and reactive power flow flowing on line k respectively; S_k^{max} is the maximum transmission capacity of line k.

The regular polygon constraint equation is used for approximation [15].

$$
\mathbf{r^P} F_k^P + \mathbf{r^Q} F_k^Q \le \mathbf{r^S} S_k^{max}, \left(\boldsymbol{\rho_k} \right)
\tag{6}
$$

5) **Power Constraints**

$$
\begin{cases}
P_i^{G,min} \le P_i^G \le P_i^{G,max}, \left(\alpha_g^{P,-}, \alpha_g^{P,+} \right) \\
Q_i^{G,min} \le Q_i^G \le Q_i^{G,max}, \left(\alpha_g^{Q,-}, \alpha_g^{Q,+} \right)
\end{cases}
\tag{7}
$$

2.3 Lagrange Function

Synthesizing the above system safe operation constraints, the Lagrange equation is constructed as Eq. (8).

$$L = \sum_{i \in G} C_i^P P_i^G + C_i^Q Q_i^G$$

$$+ \lambda_{all}^P \left(\sum_{i \in \mathcal{N}} \left(P_i^G - P_i^D \right) - \sum_{k \in \mathcal{L}} P_k^{Loss} \right) + \lambda_{all}^Q \left(\sum_{i \in \mathcal{N}} \left(Q_i^G - Q_i^D \right) - \sum_{k \in \mathcal{L}} Q_k^{Loss} \right)$$

$$+ \sum_{i \in \mathcal{N}} \lambda_i^P \left(P_i^G - P_i^D + \sum_{j \in \mathcal{A}(i)} F_{ji}^P - \sum_{j \in \mathcal{C}(i)} \left(F_{ij}^P + P_{ij}^{Loss} \right) \right)$$

$$+ \sum_{i \in \mathcal{N}} \lambda_i^Q \left(Q_i^G - Q_i^D + \sum_{j \in \mathcal{A}(i)} F_{ji}^Q - \sum_{j \in \mathcal{C}(i)} \left(F_{ij}^Q + Q_{ij}^{Loss} \right) \right)$$

$$+ \sum_{i \in \mathcal{N}} \mu_i^+ \left(V_i - V_i^{max} \right) + \sum_{i \in \mathcal{N}} \mu_i^- \left(-V_i + V_i^{min} \right) + \sum_{k \in \mathcal{L}} \rho_k \left(\mathbf{r^P} F_k^P + \mathbf{r^Q} F_k^Q - \mathbf{r^S} S_k^{max} \right)$$

$$+ \sum_{g \in \mathcal{G}} \alpha_g^{P,+} \left(P_g^G - P_g^{G,max} \right) + \sum_{g \in \mathcal{G}} \alpha_g^{P,-} \left(-P_g^G + P_g^{G,min} \right)$$

$$+ \sum_{g \in \mathcal{G}} \alpha_g^{Q,+} \left(Q_g^G - Q_g^{G,max} \right) + \sum_{g \in \mathcal{G}} \alpha_g^{Q,-} \left(-Q_g^G + Q_g^{G,min} \right)$$

$$(8)$$

3 Calculation Method of DLMP Based on Linear Power Flow Model

3.1 Calculation Model of DLMP

According to the Lagrange equation, the active and reactive power of the load are respectively derived. DLMP are obtained as shown in Eqs. (9)–(12).

$$\Omega_i^P = \Omega_{energy}^P + \Omega_{loss}^P + \Omega_{voltage}^P + \Omega_{congestion}^P \tag{9}$$

$$\begin{cases}
\Omega_{energy}^{P} = -\lambda_{all}^{P} - \lambda_{i}^{P} \\[2mm]
\Omega_{loss}^{P} = -\lambda_{all}^{P} \sum_{k \in \mathcal{L}} \dfrac{\partial P_{k}^{Loss}}{\partial P_{i}^{D}} - \lambda_{all}^{Q} \sum_{k \in \mathcal{L}} \dfrac{\partial Q_{k}^{Loss}}{\partial P_{i}^{D}} \\[4mm]
\quad - \sum_{n \in \mathcal{N}} \lambda_{n}^{P} \sum_{j \in \mathcal{C}(n)} \dfrac{\partial P_{nj}^{Loss}}{\partial P_{i}^{D}} - \sum_{n \in \mathcal{N}} \lambda_{n}^{Q} \sum_{j \in \mathcal{C}(n)} \dfrac{\partial Q_{nj}^{Loss}}{\partial P_{i}^{D}} \\[4mm]
\Omega_{voltage}^{P} = \sum_{n \in \mathcal{N}} \left(\mu_{n}^{+} - \mu_{n}^{-} \right) \dfrac{\partial V_{n}}{\partial P_{i}^{D}} \\[4mm]
\Omega_{congestion}^{P} = \sum_{n \in \mathcal{N}} \lambda_{n}^{P} \dfrac{\partial \left(\sum_{j \in \mathcal{A}(n)} F_{jn}^{P} - \sum_{j \in \mathcal{C}(n)} F_{nj}^{P} \right)}{\partial P_{i}^{D}} \\[6mm]
\quad + \sum_{n \in \mathcal{N}} \lambda_{n}^{Q} \dfrac{\partial \left(\sum_{j \in \mathcal{A}(n)} F_{jn}^{Q} - \sum_{j \in \mathcal{C}(n)} F_{nj}^{Q} \right)}{\partial P_{i}^{D}} + \sum_{k \in \mathcal{L}} \rho_{k} \dfrac{\partial \left(\mathbf{r}^{P} F_{k}^{P} + \mathbf{r}^{Q} F_{k}^{Q} \right)}{\partial P_{i}^{D}}
\end{cases} \tag{10}$$

$$\Omega_{i}^{Q} = \Omega_{energy}^{Q} + \Omega_{loss}^{Q} + \Omega_{voltage}^{Q} + \Omega_{congestion}^{Q} \tag{11}$$

$$\begin{cases}
\Omega_{energy}^{Q} = -\lambda_{all}^{Q} - \lambda_{i}^{Q} \\[2mm]
\Omega_{loss}^{Q} = -\lambda_{all}^{P} \sum_{k \in \mathcal{L}} \dfrac{\partial P_{k}^{Loss}}{\partial Q_{i}^{D}} - \lambda_{all}^{Q} \sum_{k \in \mathcal{L}} \dfrac{\partial Q_{k}^{Loss}}{\partial Q_{i}^{D}} \\[4mm]
\quad - \sum_{n \in \mathcal{N}} \lambda_{n}^{P} \sum_{j \in \mathcal{C}(n)} \dfrac{\partial P_{nj}^{Loss}}{\partial Q_{i}^{D}} - \sum_{n \in \mathcal{N}} \lambda_{n}^{Q} \sum_{j \in \mathcal{C}(n)} \dfrac{\partial Q_{nj}^{Loss}}{\partial Q_{i}^{D}} \\[4mm]
\Omega_{voltage}^{Q} = \sum_{n \in \mathcal{N}} \left(\mu_{n}^{+} - \mu_{n}^{-} \right) \dfrac{\partial V_{n}}{\partial Q_{i}^{D}} \\[4mm]
\Omega_{congestion}^{Q} = \sum_{n \in \mathcal{N}} \lambda_{n}^{P} \dfrac{\partial \left(\sum_{j \in \mathcal{A}(n)} F_{jn}^{P} - \sum_{j \in \mathcal{C}(n)} F_{nj}^{P} \right)}{\partial Q_{i}^{D}} \\[6mm]
\quad + \sum_{n \in \mathcal{N}} \lambda_{n}^{Q} \dfrac{\partial \left(\sum_{j \in \mathcal{A}(n)} F_{jn}^{Q} - \sum_{j \in \mathcal{C}(n)} F_{nj}^{Q} \right)}{\partial Q_{i}^{D}} + \sum_{k \in \mathcal{L}} \rho_{k} \dfrac{\partial \left(\mathbf{r}^{P} F_{k}^{P} + \mathbf{r}^{Q} F_{k}^{Q} \right)}{\partial Q_{i}^{D}}
\end{cases} \tag{12}$$

DLMP is divided into four components: energy, loss, voltage and congestion. Therefore, it is necessary to construct the linear model of the active and reactive power flowing through each line, line losses and voltage with respect to the active and reactive power of the node power.

3.2 Linear Model of Line Power Flow with Respect to Node Power

The distribution network is radial, and the line power flow can be expressed as the sum of the load of each node and the loss of each line downstream of the line.

$$\begin{bmatrix} \mathbf{F^P} \\ \mathbf{F^Q} \end{bmatrix} = \begin{bmatrix} \mathbf{A} & \mathbf{0} \\ \mathbf{0} & \mathbf{A} \end{bmatrix} \begin{bmatrix} \mathbf{P^D} - \mathbf{P^G} \\ \mathbf{Q^D} - \mathbf{Q^G} \end{bmatrix} + \begin{bmatrix} \mathbf{T} & \mathbf{0} \\ \mathbf{0} & \mathbf{T} \end{bmatrix} \begin{bmatrix} \mathbf{P^{Loss}} \\ \mathbf{Q^{Loss}} \end{bmatrix} \tag{13}$$

$$A(k, j) = \begin{cases} 1, \ j \in \mathcal{B}(k) \\ 0, \ j \notin \mathcal{B}(k) \end{cases} \tag{14}$$

$$T(k, l) = \begin{cases} 1, \ l \in \mathcal{L}(k) \\ 0, \ l \notin \mathcal{L}(k) \end{cases} \tag{15}$$

where: $\mathcal{B}(k)$, $\mathcal{L}(k)$ are the set of downstream nodes and lines of line k respectively.

3.3 Calculation of Loss Factor

The active and reactive losses of the line can be expressed as:

$$\begin{cases} P_k^{Loss} = \dfrac{\left(F_k^P\right)^2 + \left(F_k^Q\right)^2}{V_j^2} R_k \\ Q_k^{Loss} = \dfrac{\left(F_k^P\right)^2 + \left(F_k^Q\right)^2}{V_j^2} X_k \end{cases}, j \in \mathcal{T}(k) \tag{16}$$

where: $\mathcal{T}(k)$ is the end node of line k.

Loss Factor (LF) is defined as the sensitivity of line loss to node power. The derivatives of the line power flow and line loss with respect to the node power are obtained through calculating the partial derivatives of Eqs. (13) and (16) with respect to the node load power respectively. Eq. (17) is obtained by synthesizing the derivation results of the those.

$$\begin{cases} V_j^2 \dfrac{\partial P_k^{Loss}}{\partial P_n^D} - 2R_k \left(F_k^P \left(A(k, n) + \sum_{l \in \mathcal{B}(k)} \dfrac{\partial P_l^{Loss}}{\partial P_n^D} \right) + F_k^Q \sum_{l \in \mathcal{B}(k)} \dfrac{\partial Q_l^{Loss}}{\partial P_n^D} \right) = 0 \\ V_j^2 \dfrac{\partial P_k^{Loss}}{\partial Q_n^D} - 2R_k \left(F_k^P \sum_{l \in \mathcal{B}(k)} \dfrac{\partial P_l^{Loss}}{\partial Q_n^D} + F_k^Q \left(A(k, n) + \sum_{l \in \mathcal{B}(k)} \dfrac{\partial Q_l^{Loss}}{\partial Q_n^D} \right) \right) = 0 \\ V_j^2 \dfrac{\partial Q_k^{Loss}}{\partial P_n^D} - 2X_k \left(F_k^P \left(A(k, n) + \sum_{l \in \mathcal{B}(k)} \dfrac{\partial P_l^{Loss}}{\partial P_n^D} \right) + F_k^Q \sum_{l \in \mathcal{B}(k)} \dfrac{\partial Q_l^{Loss}}{\partial P_n^D} \right) = 0 \\ V_j^2 \dfrac{\partial Q_k^{Loss}}{\partial Q_n^D} - 2X_k \left(F_k^P \sum_{l \in \mathcal{B}(k)} \dfrac{\partial P_l^{Loss}}{\partial Q_n^D} + F_k^Q \left(A(k, n) + \sum_{l \in \mathcal{B}(k)} \dfrac{\partial Q_l^{Loss}}{\partial Q_n^D} \right) \right) = 0 \end{cases} \tag{17}$$

By solving the first and third equations in Eq. (17), the sensitivity of the line active power loss and reactive power loss to the node active power can be obtained; by solving the second and fourth equations, the sensitivity of line active power loss and reactive power loss to node reactive power can be obtained.

3.4 Linear Model of Line Loss with Respect to Node Power

Perform Taylor expansion of the line loss at a certain operating point, ignoring the quadratic and higher-order terms.

$$
\begin{cases}
P_k^{Loss}\left(\mathbf{P^G},\mathbf{P^D}\right) \approx P_k^{Loss}\left(\widehat{\mathbf{P}}^{\mathbf{G}},\widehat{\mathbf{P}}^{\mathbf{D}}\right) + \sum_{i\in\mathcal{N}} \frac{\partial P_k^{Loss}}{\partial P_i^D}\left(P_i^D - \widehat{P}_i^{D}\right) + \sum_{i\in\mathcal{N}} \frac{\partial P_k^{Loss}}{\partial Q_i^D}\left(Q_i^D - \widehat{Q}_i^{D}\right) \\
Q_k^{Loss}\left(\mathbf{P^G},\mathbf{P^D}\right) \approx Q_k^{Loss}\left(\widehat{\mathbf{P}}^{\mathbf{G}},\widehat{\mathbf{P}}^{\mathbf{D}}\right) + \sum_{i\in\mathcal{N}} \frac{\partial Q_k^{Loss}}{\partial P_i^D}\left(P_i^D - \widehat{P}_i^{D}\right) + \sum_{i\in\mathcal{N}} \frac{\partial Q_k^{Loss}}{\partial Q_i^D}\left(Q_i^D - \widehat{Q}_i^{D}\right)
\end{cases}
\tag{18}
$$

Define the loss coefficient matrix as below.

$$
\left[\mathbf{J^{PP}}\right]_{kn} = \frac{\partial P_k^{Loss}}{\partial P_n^D} \quad \left[\mathbf{J^{PQ}}\right]_{kn} = \frac{\partial P_k^{Loss}}{\partial Q_n^D} \quad \left[\mathbf{J^{QP}}\right]_{kn} = \frac{\partial Q_k^{Loss}}{\partial P_n^D} \quad \left[\mathbf{J^{QQ}}\right]_{kn} = \frac{\partial Q_k^{Loss}}{\partial Q_n^D}
\tag{19}
$$

The linear expression of the line loss with respect to the node power is obtained.

$$
\begin{bmatrix} \mathbf{P^{Loss}} \\ \mathbf{Q^{Loss}} \end{bmatrix} = \begin{bmatrix} \mathbf{J^{PP}} & \mathbf{J^{PQ}} \\ \mathbf{J^{QP}} & \mathbf{J^{QQ}} \end{bmatrix} \begin{bmatrix} \mathbf{P^D} - \mathbf{P^G} \\ \mathbf{Q^D} - \mathbf{Q^G} \end{bmatrix} + \begin{bmatrix} \boldsymbol{\kappa}^{\mathbf{PLoss}} \\ \boldsymbol{\kappa}^{\mathbf{QLoss}} \end{bmatrix}
\tag{20}
$$

where: $\boldsymbol{\kappa}^{\mathbf{PLoss}}$, $\boldsymbol{\kappa}^{\mathbf{QLoss}}$ are constant vectors which can be calculated as follows.

$$
\begin{cases}
\boldsymbol{\kappa}^{\mathbf{PLoss}} = \widehat{\mathbf{P}}^{Loss} - \mathbf{J^{PP}}\left(\widehat{\mathbf{P}}^{\mathbf{D}} - \widehat{\mathbf{P}}^{\mathbf{G}}\right) - \mathbf{J^{PQ}}\left(\widehat{\mathbf{Q}}^{\mathbf{D}} - \widehat{\mathbf{Q}}^{\mathbf{G}}\right) \\
\boldsymbol{\kappa}^{\mathbf{QLoss}} = \widehat{\mathbf{Q}}^{Loss} - \mathbf{J^{QP}}\left(\widehat{\mathbf{P}}^{\mathbf{D}} - \widehat{\mathbf{P}}^{\mathbf{G}}\right) - \mathbf{J^{QQ}}\left(\widehat{\mathbf{Q}}^{\mathbf{D}} - \widehat{\mathbf{Q}}^{\mathbf{G}}\right)
\end{cases}
\tag{21}
$$

where: $\widehat{\mathbf{P}}^{\mathbf{D}}, \widehat{\mathbf{Q}}^{\mathbf{D}}, \widehat{\mathbf{P}}^{\mathbf{G}}, \widehat{\mathbf{Q}}^{\mathbf{G}}$ are the reference values of the active and reactive power of the node load and generation respectively.

3.5 Linear Model of Node Voltage with Respect to Node Power

The linear expression of line power flow and node power can be obtained by substituting Eq. (20) into Eq. (13).

$$
\begin{bmatrix} \mathbf{F^P} + \mathbf{P^{Loss}} \\ \mathbf{F^Q} + \mathbf{Q^{Loss}} \end{bmatrix} = \begin{bmatrix} \mathbf{A} + \tilde{\mathbf{T}}\mathbf{J^{PP}} & \tilde{\mathbf{T}}\mathbf{J^{PQ}} \\ \tilde{\mathbf{T}}\mathbf{J^{QP}} & \mathbf{A} + \tilde{\mathbf{T}}\mathbf{J^{QQ}} \end{bmatrix} \begin{bmatrix} \mathbf{P^D} - \mathbf{P^G} \\ \mathbf{Q^D} - \mathbf{Q^G} \end{bmatrix} + \begin{bmatrix} \boldsymbol{\Psi}_\kappa^{\mathbf{PLoss}} \\ \boldsymbol{\Psi}_\kappa^{\mathbf{QLoss}} \end{bmatrix}
\tag{22}
$$

where: $\tilde{\mathbf{T}} = \mathbf{T} + \mathbf{I}$.

The linear relationship between node voltage and node power can be obtained by referring the method in [12].

$$
\begin{bmatrix} \mathbf{V} \\ \delta \end{bmatrix} = \begin{bmatrix} \mathbf{F_1} & \mathbf{F_2} \\ \mathbf{F_3} & \mathbf{F_4} \end{bmatrix} \begin{bmatrix} \mathbf{P^D} - \mathbf{P^G} \\ \mathbf{Q^D} - \mathbf{Q^G} \end{bmatrix} + \begin{bmatrix} \boldsymbol{\eta}^{\mathbf{V}} \\ \boldsymbol{\eta}^{\delta} \end{bmatrix}
\tag{23}
$$

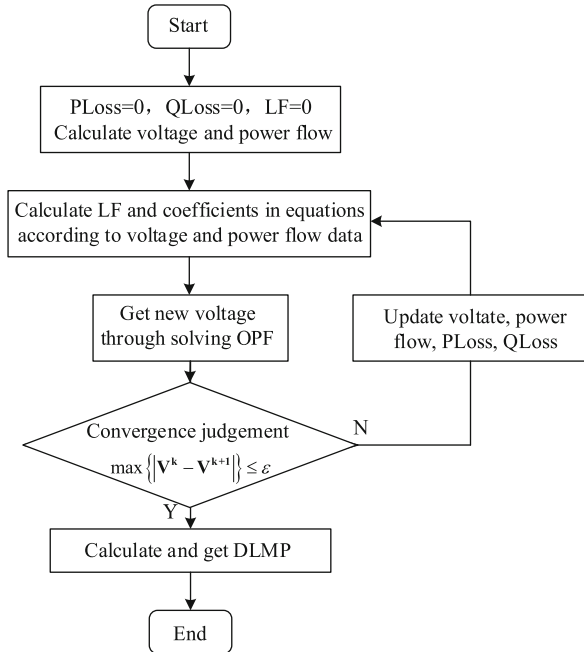So far, the approximate linear expressions are obtained.

Fig. 1. Schematic diagram of DLMP calculation process

3.6 DLMP Calculation Process

In this paper, an iterative calculation method is proposed. The schematic diagram of the calculation process is shown in Fig. 1.

4 Case Study

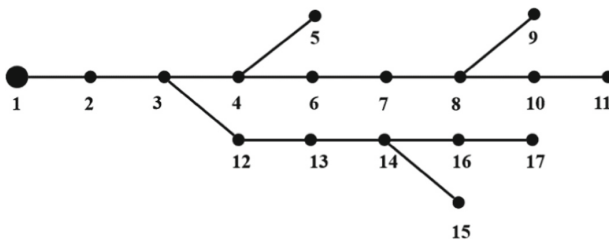In this paper, the typical 17-node distribution network in the reference [16] is used (Fig. 2).

Fig. 2. Node system structure diagram

4.1   Analysis of Calculation Results of DLMP

This study sets up the following two scenarios to calculate and analyze DLMP. Three identical distributed power sources are placed at nodes 9, 11, and 17. The price of active power and reactive power of balance node are set as 50€/MW and 5€/MVar. In scenario 1, the power flow constraint of line 3–12 is set as 4MW. Two scenarios are set for studying the model built in this paper and parameters are shown in Table 1.

Table 1. Parameters for different scenarios

Scenario	Active output range/MW	Reactive output range/MVar	Active power price/€/MW	Reactive power price/€/MVar	Voltage range/p.u
1	[0, 1.3]	[−0.65, 0.65]	55	5.5	[0.8, 1.2]
2	[0, 5]	[−2.5, 2.5]	25	2.5	[0.95, 1.05]

According to the model without considering the line loss (S-OPF), the linear power flow model (L-OPF) constructed in this study, and the MatPower AC power flow model (ACOPF), the optimal power flow is calculated, and the DLMP results are compared.

In scenario 1, lines 3–12 is congested. Comparing the DLMP values under different models, as shown in Fig. 3, due to the congestion of line 3–12, the active power price of node 12 and its downstream nodes increases as a whole, and the corresponding load decreases, thus the congestion is solved. The composition of DLMP of each node under the L-OPF model is shown in Fig. 4. It can be seen that the marginal price of active and reactive power nodes is composed of three parts: energy, loss and congestion. Due to the power flow of lines 3–12 reaches the capacity limit, DLMP of node 12 and its downstream nodes are added the congestion part.

The results show that line congestion has significant impact on DLMP, and only affects the price of congested line and its downstream nodes. Therefore, the location of line congestion can be inferred according to the part corresponding to the congestion in DLMP.

In scenario 2, the voltage of node 11 reaches the upper limit. The composition of DLMP under different models is shown in Fig. 5, which consists of three parts: energy, loss and voltage. It can be seen from the figure that on the basis of energy price, both the voltage and the loss parts act to reduce the DLMP. The reason is that node 11 is located at the end of the line and is equipped with a distributed power source with a large output, which leads to the voltage rise. Nodes 8-10 are most affected, and the DLMP is significantly lower than that of other nodes. Other nodes are less affected, but the electricity price still has dropped to varying degrees.

The results show that the line voltage over-limit has obvious impact on DLMP and affects the nodes of whole system. All nodes can be guided by the price to adjust the power and participate in the voltage management of the distribution network.
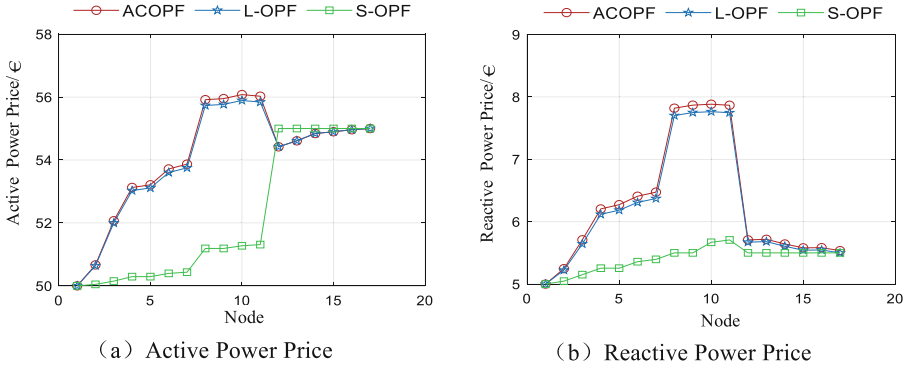
（a）Active Power Price （b）Reactive Power Price

Fig. 3. The Price of Each Node in Scenario 1

（a）The Component of Active Power Price （b）The Component of Reactive Power Price
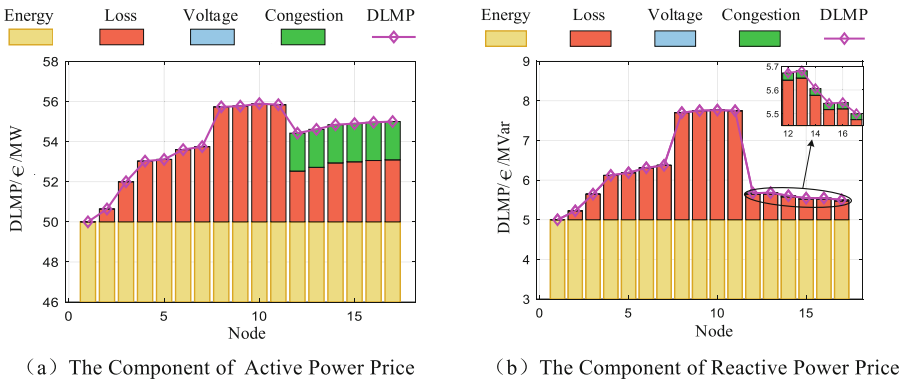
Fig. 4. The Composition of DLMP of Each Node in Scenario 1

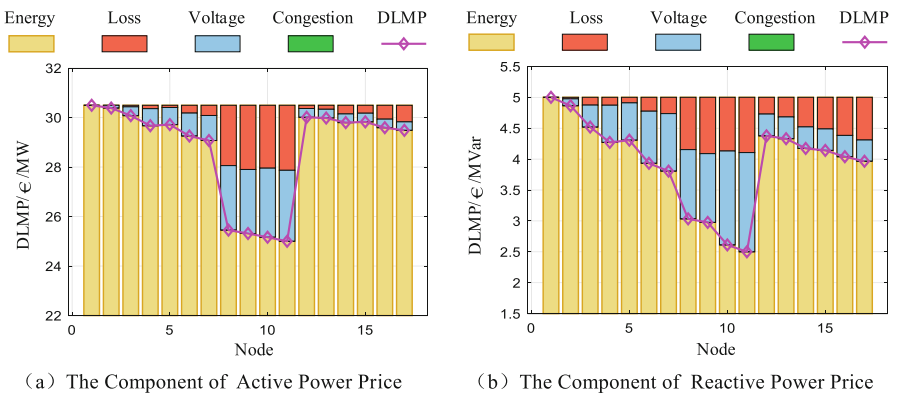（a）The Component of Active Power Price （b）The Component of Reactive Power Price

Fig. 5. The Price of Each Node in Scenario 2

5   Conclusion

According to the operation characteristics of the distribution network, this paper studies the congestion management method based on DLMP, and proposes a method to solve the DLMP by iteratively calculating the loss factor. The main conclusions are as follows:

1) DLMP can successfully solve the congestion problem in the distribution network. The linear power flow model decouples the active and reactive power, and the power price is divided into four independent parts: energy, loss, congestion and voltage. The case study results show that different components can reflect the operating status of the system;
2) The comparison results of the calculation examples show that the DLMP calculated by this method is basically consistent with the results of the AC power flow model. At the same time, the requirements for initial data are low, the calculation process is simple, and it is feasible in practical applications.

DLMP is used in distribution network congestion management with high effectiveness and low construction cost. In the future distribution network, coordination and complementation of multiple energy sources and flexible loads will become a trend. The further research of corresponding DLMP calculation method and market clearing model is required.

References

1. Ciavarella, R .: Congestion Management in distribution grid networks through active power control of flexible distributed energy resources. In: IEEE Milan PowerTech, pp. 1–6. IEEE, Milan (2019)
2. Fan, M.: Application scenarios and functions of intelligent distribution network in Europe. Distribut. Utilization **2**, 32–40 (2015)
3. Huang, S.: Review of congestion management methods for distribution networks with high penetration of distributed energy resources. In: IEEE PES Innovative Smart Grid Technologies, Europe, pp. 1–6. IEEE, Istanbul, Turkey (2014)
4. Shariatkhah, M.H.: Using feeder reconfiguration for congestion management of smart distribution network with high DG penetration. In: CIRED 2012 Workshop: Integration of Renewables into the Distribution Grid, pp. 1–4. IET, Lisbon (2012)
5. Dolan, M.J.: Reducing distributed generator curtailment through active power flow management. IEEE Trans. Smart Grid **5**(1), 149–157 (2014)
6. Khorasany, M.: Market framework for local energy trading: a review of potential designs and market clearing approaches. IET Gener. Transm. Distrib. **12**(22), 5899–5908 (2018)
7. Bouloumpasis, I.: Congestion management using local flexibility markets: recent development and challenges. In: 2019 IEEE PES Innovative Smart Grid Technologies Europe, pp. 1–5. IEEE, Bucharest, Romania (2019)
8. Papavasiliou, A.: Analysis of distribution locational marginal prices. IEEE Trans. Smart Grid **9**(5), 4872–4882 (2018)
9. Lu, Y.: Decentralized dynamic optimal power flow in distribution networks with distributed generation and energy storage devices. Power Syst. Technol. **43**(02), 434–444 (2019)
10. Gao, H.: Optimal power flow research in active distribution network and its application examples. Proceedings CSEE **37**(06), 1634–1645 (2017)

11. Yong, F.: Different models and properties on LMP calculations. In: 2006 IEEE Power Engineering Society General Meeting, p. 11. IEEE, Montreal, QC, Canada (2006)
12. Yuan, H.: Novel linearized power flow and linearized OPF models for active distribution networks with application in distribution LMP. IEEE Trans. Smart Grid **9**(1), 438–448 (2016)
13. Yu, Y.: A Linear LMP model for active and reactive power with power loss. In: 2019 IEEE Sustainable Power and Energy Conference, pp. 1699–1704, IEEE, Beijing, China (2019)
14. Mieth, R.: Distribution electricity pricing under uncertainty. IEEE Trans. Power Syst. **35**(3), 2325–2338 (2019)
15. Hamed, S., Marti, J.R., et al.: Linear current flow equations with application to distribution systems reconfiguration. IEEE Trans. Power Syst. **30**(4), 2073–2080 (2015)
16. Houssem, R.: Comprehensive review of radial distribution test systems. Res. Effici. Technol. **3**, 1–12 (2019)

Research on Real-Time LVRT and Off-Grid Discrimination Technology for the PV Power Station

Wei Chen[(✉)], Xindong Li, Daojun Zha, Yichuan Bai, Xiaofan Hou, and Dan Wu

NARI Group Corporation (State Grid Electric Power Research Institute), Nanjing 211106, China
chenwei12@sgepri.sgcc.com.cn

Abstract. As PV grid-connected capacity has been increasing, a serious challenge to grid security and stability is brought. When the power grid fails, the capacity of off-grid units in a PV power station cannot be directly monitored, which makes it difficult to achieve real-time and accurate control of the generator tripping and load-shedding strategies of system protection. In this paper, a real-time low voltage ride through (LVRT) and off-grid discrimination technology for the PV power station is presented based on the reactive power-supported LVRT control strategy from the perspective of engineering application. Through this technology, the capacities of PV units in three different operating states: Normal operation, LVRT, and off-grid can be calculated in time, which provides a quantitative reference for accurate generator tripping and load-shedding control strategy to improve the security and stability of the grid containing a high percentage of new energy access. Finally, the feasibility and accuracy of the discrimination technology are verified by simulation.

Keywords: Low voltage ride through (LVRT) · Voltage dip · PV off-grid · Real-time discrimination

1 Introduction

In recent years, with the rapid development of PV power generation technology, the PV power generation connection scale is getting larger and larger, and a large number of power electronic devices connect to the grid. This has changed the grid pattern, and its vulnerability also easily leads to the problem of large-scale off-grid in the case of a fault occurs, which brings challenges to the security and stability of the power system [1–3]. In 2016, SA Power Networks experienced six consecutive voltage dips, and most of its wind turbines experienced continuous LVRT failure, which eventually led to large-scale new energy off-grid [4]. In the "Three-North" region of China, due to the large-scale centralized development of new energy and the weak grid frame, voltage stability issue of the system caused by faults at the feed end is prominent. At present, several large-scale new energy off-grid accidents have occurred [5–7].

In reference [8], the reasons leading to wind turbine off-grid are analyzed, measures for retrofitting wind turbines and improving the wind farm collector system and protection configuration from the angle of engineering application are proposed, and the solutions that can reasonably avoid large-scale off-grid accidents are raised combined with the characteristics of large wind power bases. In reference [9], the off-grid time sequence of wind power and PV is studied, and the impact of new energy off-grid on the important AC cross-section of the AC system it is connected to is qualitatively and quantitatively analyzed. In reference [10], the fault process of large-scale new energy off-grid in the UHVDC feeder grid is analyzed. Then, in view of the shortcomings of the existing measures to cope with new energy off-grid, a frequency emergency control technology scheme and its implementation method that uses information such as DC phase commutation failure as a trigger condition are proposed according to the characteristics of the fault process.

So far, there has been little research on real-time LVRT and off-grid discrimination technology for PV power generation at home and abroad. As there are a large number of PV power station units, accurate monitoring of each unit depends on a high-speed communication network in the station, which requires a huge construction volume and high construction cost. Therefore, on the premise of satisfying stability control requirements, we need to carry out research on simplified and centralized real-time off-grid discrimination technology for the PV power station based on the in-place message. In this paper, a real-time LVRT and off-grid discrimination technology is proposed based on the LVRT control strategy for PV power stations. By monitoring the electrical quantity at grid-connected points, the unit capacity of the PV power station in different operating states when a failure occurs is calculated, which provides a reference for generator tripping and load shedding control, thus improving the safety and stability of the power system.

2 PV Power Generation System and Its Control Model

A simplified schematic diagram of the PV power generation system is shown in Fig. 1. Grid Connection Diagram of PV Power Generation System.
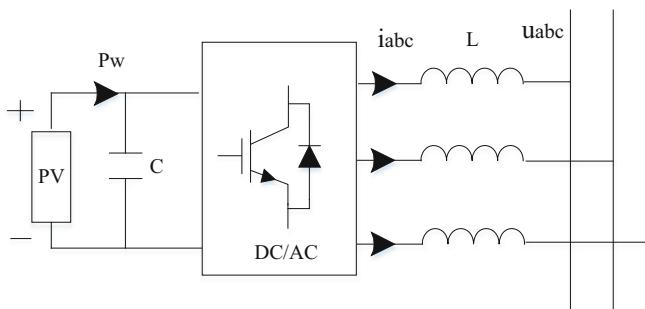

Fig. 1. Grid Connection Diagram of PV Power Generation System.

The PV inverter transmits the electric energy converted from solar energy absorbed by the PV unit into the grid, and the active power at its two ends should be kept in balance. The following expression can be obtained:

$$u_{dc}C\frac{du_{dc}}{dt} = P_W - \frac{3}{2}U_dI_d - U_rI_d \tag{1}$$

where

u_{dc}—bus voltage of PV DC link;
P_W—the maximum power output from the PV unit;
C—DC link voltage stabilizing capacitance;
U_r—Equivalent voltage loss of inverter;
U_d and I_d—Voltage and current at the grid-connected point in dq coordinates.
The control strategy of PV grid-connected inverter is shown in Fig. 2 [11–13]:
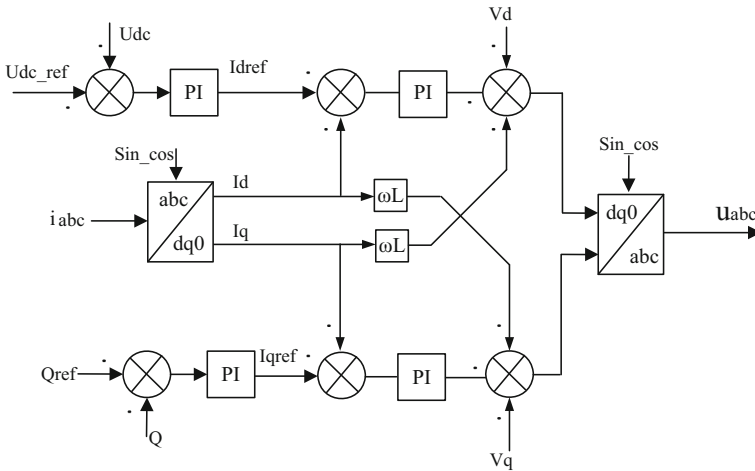
Fig. 2. Control Strategy of PV Grid-Connected Inverter.

The control strategy in the figure adopts a double closed-loop control structure, whose outer loop is the voltage loop and the inner loop is the grid-connected current loop. Through abc/dq0 transformation, the grid-connected current is decoupled into two components: the active component and the reactive component. The v_d and v_q control equations are as below:

$$v_d = -\left(K_{ip}+K_{iI}/s\right)\left(i_d^* - i_d\right) + \omega L i_q + e_d \tag{2}$$

$$v_q = -\left(K_{ip}+K_{iI}/s\right)\left(i_q^* - i_q\right) + \omega L i_d + e_q \tag{3}$$

where

v_d and v_q—reference value of inverter output voltage;
K_{ip} and K_{iI}—PI regulator capacity ratio and integration gain;
i_d^* and i_q^*—current reference values;
e_d and e_q—disturbance of grid voltage.

3 LVRT Control Scheme Based on Reactive Power Supported

In the national standard *GB/T19964-2012 Technical Requirements for Connecting Photovoltaic Power Station to Power System*, as shown in Fig. 3, the following requirements are set forth for large PV power stations [14]:
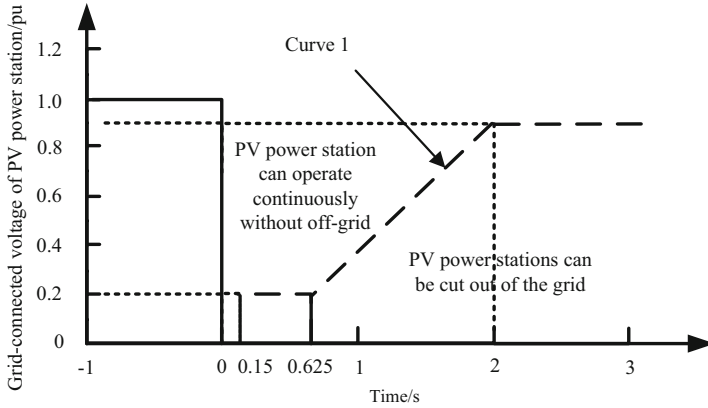

Fig. 3. LVRT Capability Requirements for PV Power Station.

1) The PV power station should be able to run continuously without off-grid for 0.15s after the voltage at the grid-connected point of the PV power station drops to zero. It can be cut out of the grid when the voltage at the grid-connected point drops below curve 1.
2) PV power station recovers to the value before the fault with at least 30% of rated power per second after fault clearing.
3) The response time of dynamic reactive current is not more than 30ms and reactive current should satisfy:

$$\begin{cases} I_T \geq 1.5(0.9 - U_g)I_N & 0.2 \leq U_g \leq 0.9 \\ I_T \geq 1.05I_N & U_g < 0.2 \\ I_T = 0 & U_g > 0.9 \end{cases} \tag{4}$$

where

U_g—Per-unit value (pu) of voltage at the grid-connected point of PV station;

I_N—Rated grid-connected current of the inverter.

PV is generally connected to the grid with a unity power factor in normal operation, and reactive power is issued when a fault occurs. Its control strategy is divided into two parts: active control and reactive control.

The external regulation characteristics of the active part mainly depend on the outer voltage loop, and the control equation of the active current can be obtained:

$$i_d = k_{p1}(u_{dc}^* - u_{dc}) + k_{i1} \int (u_{dc}^* - u_{dc})dt \tag{5}$$

where

u_{dc}^*—DC link bus voltage limit;

u_{dc}—DC link bus voltage;

k_{p1} and k_{i1}—Outer loop PI controller capacity ratio and integration gain of the active control part.

From Eq. (4), it is known that the PV output reactive current should satisfy the following:

$$\begin{cases} I_q = 1.5(0.9U_N - U_d)I_N & 0.2 < U_d < 0.9 \\ I_q = 1.05I_N & U_d < 0.2 \end{cases} \tag{6}$$

where

U_N—Rated voltage at the grid-connected point;

U_d—Voltage at the grid-connected point in dq coordinates;

I_N—Rated current of the inverter.

Then the reactive current satisfies the equation as shown in (7).

$$\begin{cases} L\frac{di_q}{dt} = k_{p2}\left(i_q^* - i_q\right) + k_{i2} \int \left(i_q^* - i_q\right)dt - \omega L i_d \\ i_q^* = 1.5(0.9U_N - U_d)I_N & 0.2 < U_d < 0.9 \\ i_q^* = 1.05I_N & U_d < 0.2 \end{cases} \tag{7}$$

where

i_q^*—Set value of inverter reactive power;

k_{p2} and k_{i2}—PI controller capacity ratio and integration gain of the reactive power control part.

Due to the capacity limitation of the inverter itself, the active current should satisfy the inequation constraints:

$$i_d \leq \sqrt{i_{\text{lim }it}^2 - i_q^{*2}} \tag{8}$$

Then the control model of the PV station during LVRT is shown in the following equation:

$$\begin{cases} u_{dc}C\frac{du_{dc}}{dt} = P_W - \frac{3}{2}U_d I_d - U_r I_d \\ i_d = k_{p1}\left(u_{dc}^* - u_{dc}\right) + k_{i1} \int \left(u_{dc}^* - u_{dc}\right)dt \\ L\frac{di_q}{dt} = k_{p2}\left(i_q^* - i_q\right) + k_{i2} \int \left(i_q^* - i_q\right)dt - \omega L i_d \\ i_q^* = 1.5(0.9U_N - U_d)I_N & 0.2 < U_d < 0.9 \\ i_q^* = 1.05I_N & U_d < 0.2 \\ i_d \leq \sqrt{i_{\text{lim }it}^2 - i_q^{*2}} \end{cases} \tag{9}$$

It can be seen from the above formula that the simplified mathematical model of photovoltaic is also composed of several nonlinear differential equations. In order to solve its numerical solution, it needs to be discretized and appropriately deformed.

Discretize and mathematically deform Eq. (9) to obtain the iterative format of voltage output response during low-voltage crossing, as shown in the following equation.

$$
\begin{cases}
u_{dc}(k+1) = \frac{T_s}{C}\left[P_W(k) - \frac{3}{2}U_d(k)I_d(k) - U_rI_d(k)\right] \big/ u_{dc}(k) + u_{dc}(k) \\
i_{\{d}(k+1) = k_{p1}\left[u_{dc}^* - u_{dc}(k+1)\right] + k_{i1}\sum_{j}^{k+1}\left[u_{dc}^* - u_{dc}(j)\right] \\
i_q^* = 1.5(0.9U_N - U_d)I_N \quad 0.2 < U_d < 0.9 \\
i_q^* = 1.05I_N \qquad\qquad U_d < 0.2 \\
i_q(k+1) = \frac{T_s}{L}\left\{k_{p2}\left[i_q^*(k) - i_q(k)\right] + k_{i2}\sum_{j}^{k}\left[i_q^*(k) - i_q(j)\right] - \omega L i_d(k+1)\right\} + i_q(k) \\
i_d(k+1) \le \sqrt{i_{\lim it}^2 - i_q^*(k)^2} \qquad \text{k} = 1,2\cdots\text{n}
\end{cases}
$$

$$(10)$$

4   Real-Time LVRT and Off-Grid Discrimination Technology

Since all units are controlled by the LVRT scheme described above during the fault, according to Kirchhoff's Current Law, the active current $I_{d\Sigma}$ and reactive current $I_{q\Sigma}$ at the outlet detection point of the PV station can be expressed as:

$$
\begin{cases}
I_{d\Sigma} = I_{d1} + I_{d2} + \ldots + I_{dn} \\
I_{q\Sigma} = I_{q1} + I_{q2} + \ldots + I_{qn}
\end{cases}
$$

$$(11)$$

Let the PV station have m PV units with a single capacity of α MW. After the fault occurs, due to the influence of different transmission line impedances and other practical factors, the operating states of the units can be classified into normal operation, LVRT and off-grid. Where.

θ—Unit capacity ratio of units in normal operation;

η—Capacity ratio of LVRT units;

λ—Capacity ratio of off-grid units, that is,

$$\theta + \eta + \lambda = 1 \tag{12}$$

Considering that each unit has similar active and reactive power output characteristics under the same control strategy, then

$$\theta = \frac{i_{d\_mea} - i_{d\_lvrt}}{i_{d\Sigma\_cal}} \tag{13}$$

$$\eta = \frac{i_{q\_mea} - i_{q\_normal}}{i_{q\Sigma\_cal}} \tag{14}$$

where

i_{d_mea} and i_{q_mea}—Measured values of active and reactive currents of the grid-connected point;

i_{d_lvrt}—Active current output from the unit working in LVRT state;

i_{q_normal}—Reactive current output from the unit in normal operation;

$i_{d\Sigma\_cal}$—Sum of active currents output assuming all the units operate normally;

$i_{q\Sigma\_cal}$—Sum of reactive currents output assuming all the units working in LVRT state.

It is known that the power factor of units in normal operation $\cos\varphi$, then combining Eqs. (9) and (10), it can be obtained that,

$$
\begin{cases}
i_{d\_lvrt} = \sum_1^{m\cdot\eta} \left(\sqrt{i_{\lim it}^2 - i_q^{*2}} \right) \\
i_{d\Sigma\_cal} = \sum_1^{m} \left[k_{p1}\left(u_{dc}^* - u_{dc} \right) + k_{i1} \int \left(u_{dc}^* - u_{dc} \right) dt \right] \\
i_{q\_normal} = \sum_1^{m\cdot\theta} \left\{ \left[k_{p1}\left(u_{dc}^* - u_{dc} \right) + k_{i1} \int \left(u_{dc}^* - u_{dc} \right) dt \right] \tan\varphi \right\} \\
i_{q\Sigma\_cla} = \sum_1^{m} [1.5(0.9U_N - U_d)I_N]
\end{cases}
\tag{15}
$$

Substituting Eq. (14) into Eqs. (12) and (13), obtain

$$
\begin{cases}
\theta = \dfrac{i_{d\_mea} - \sum_1^{m\cdot\eta} \left(\sqrt{i_{\lim it}^2 - i_q^{*2}} \right)}{\sum_1^{m} \left[k_{p1}\left(u_{dc}^* - u_{dc} \right) + k_{i1} \int \left(u_{dc}^* - u_{dc} \right) dt \right]} \\
\eta = \dfrac{i_{q\_mea} - \sum_1^{m\cdot\theta} \left\{ \left[k_{p1}\left(u_{dc}^* - u_{dc} \right) + k_{i1} \int \left(u_{dc}^* - u_{dc} \right) dt \right] \tan\varphi \right\}}{\sum_1^{m} [1.5(0.9U_N - U_d)I_N]}
\end{cases}
\tag{16}
$$

where

$i_{\lim it} = 1.2I_N,$
$\begin{cases}
i_q^* = 1.5(0.9U_N - U_d)I_N & 0.2 < U_d < 0.9 \\
i_q^* = 1.05I_N & U_d < 0.2
\end{cases}.$

Correspondingly, the proportion of off-grid capacity of PV units during the fault is:

$$
\lambda = 1 - \theta - \eta
\tag{17}
$$

The normal operating unit capacity value of the PV station during the fault is the product of m, α and θ, the LVRT unit capacity value is the product of m, α and η, and the off-grid unit capacity value is the product of m, α and λ.

5 Simulation Verification

The simulation model for the 9 MW PV station built in PSCAD/EMTDC is shown in Fig. 4, and the specific parameters of the simulation model are shown in Table 1. A single-phase grounding fault is set at the midpoint of the 220 kV overhead line, and the current at the grid-connected point is monitored to simulate the fault's steady state.

Table 1. Parameters of 9 MW PV Station.

Item	Parameter	Item	Parameter
Unit Capacity	3 MW	220 kV line length	40 km
Box transformer wiring method	d-yn11-yn11	220 kV line resistance	0.019 Ω/km
Transformation ratio of Box Transformer	35 kV/0.27 kV/0.27 kV	220 kV line impedance	0.2463 Ω/km
Short circuit impedance of box transformer	6.50%	220 kV line capacitance	0.0148 μF/km
Main transformer wiring method	Yn-d11	Cable type of collector wire	YJV22-26/35 kV-3 × 50 mm^2
Transformation ratio of main transformer	220 kV/35 kV	Collector wire resistance	0.1669 Ω/km
Short circuit impedance of main transformer	10.50%	Collector wire reactance	0.0503 Ω/km
Temperature	25 ℃	Collector wire capacitance	0.0108 MΩ * km
Illumination intensity	1,000 W/m^2	Collector wire length	1 km
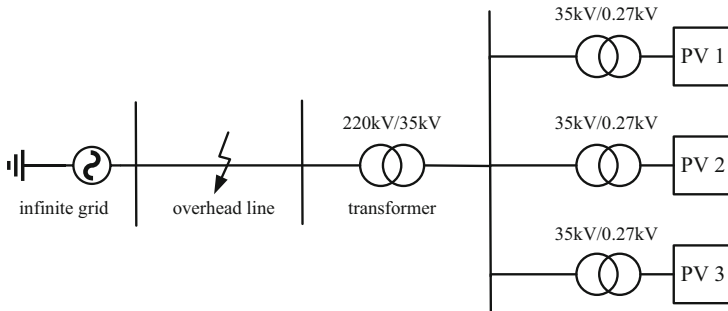
Fig. 4. Topological Structure of PV Power Station Simulation Model.

When the system runs to 0.3 s, a short-circuit ground fault occurs at phase A of the 220 kV overhead line. As shown in Fig. 5, the voltages at grid-connected points drop to 0pu and 0.5pu respectively. The three PV units are respectively in normal operation, LVRT, and off-grid states, which means $\theta_1 = \eta_1 = \lambda_1 = \theta_2 = \eta_2 = \lambda_2 = \frac{1}{3}$, the power factor of a normal operating unit is $\cos \varphi = 1$. The output currents of PV units are shown

in Fig. 6 and Fig. 7. Substituting the known quantities into Eqs. (16) and (17), obtain

$$\begin{cases} \theta_1 + \eta_1 + \lambda_1 = 1 \\ \theta_1 = \frac{0.084 - 3 \times \eta_1 \times 0.027}{0.180} \\ \eta_1 = \frac{0.054 - 3 \times \theta_1 \times 0.060 \times \tan \varphi}{0.156} \end{cases} \tag{18}$$

$$\begin{cases} \theta_2 + \eta_2 + \lambda_2 = 1 \\ \theta_2 = \frac{0.111 - 3 \times \eta_2 \times 0.056}{0.180} \\ \eta_2 = \frac{0.029 - 3 \times \theta_2 \times 0.060 \times \tan \varphi}{0.081} \end{cases} \tag{19}$$

After calculation, $\theta_1 = 0.333$, $\eta_1 = 0.346$, $\lambda_1 = 0.321$, $\theta_2 = 0.290$, $\eta_2 = 0.358$, and $\lambda_2 = 0.352$ are obtained. Ignoring the errors caused by the simulation environment, the actual values of the unit off-grid capacity ratio are basically consistent with the calculated values, which verifies the feasibility and accuracy of the above real-time LVRT and off-grid discrimination technology (Table 2).

Table 2. Actual and Calculated PV Power Station Output Currents (kA).

PV	I_{d_mea1}	I_{d_mea2}	I_{q_mea1}	I_{q_mea2}	$I_{d\Sigma\_cal1}$	$I_{d\Sigma\_cal2}$	$I_{q\Sigma\_cal1}$	$I_{q\Sigma\_cal2}$
1	0.060	0.060	0	0	0.060	0.060	0.052	0.027
2	0.024	0.051	0.054	0.029	0.060	0.060	0.052	0.027
3	0	0	0	0	0.060	0.060	0.052	0.027
Total	0.084	0.111	0.054	0.029	0.180	0.180	0.156	0.081
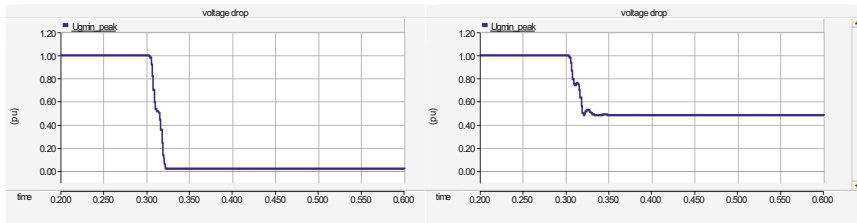
Fig. 5. Voltage Dip Curve.
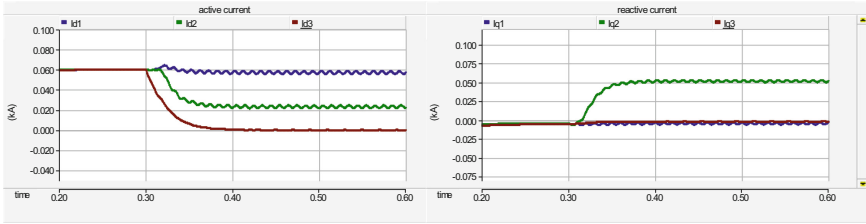
Fig. 6. Active and reactive Current Curve of PV Power Station when Voltage Drops to 0pu.
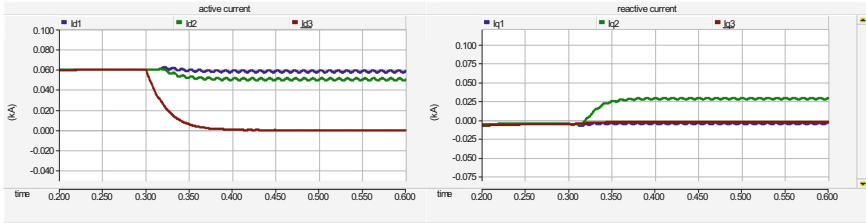
Fig. 7. Active and reactive Current Curve of PV Power Station when Voltage Drops to 0.5pu.

6   Conclusion

Based on the reactive power supported LVRT control scheme and considering the engineering practice, in this paper, a real-time LVRT and off-grid discrimination technology for PV power stations is proposed. Through theoretical analysis and simulation verification, the following conclusions are obtained: This real-time LVRT and off-grid discrimination technology delivers more accurate discrimination of the off-grid capacity of PV power stations during voltage dips, which provides technical support for the development of grid stability control measures such as generator tripping and load shedding and is conducive to the realization of such accurate grid stability control measures. During the discrimination process, it only needs to monitor the current at the grid-connected point of PV stations, which requires a lower calculation volume, provides the highly real-time capability, and low implementation cost. The simulation result proves the effectiveness of the proposed real-time off-grid discrimination technology.

References

1. Massing, J.R., Stefanello, M., Grundling, H.A., Pinheiro, H.: Adaptive current control for grid-connected converters with LCL filter. IEEE Trans. Indust. Electron. **59**(12), 4681–4693 (2012)

2. Yasser, A., Mohamed, I., Rahman, M.A.: Robust line-voltage sensorless control and synchronization of LCL-filtered distributed generation inverters for high power quality grid connection. IEEE Trans. Power Electron. **27**(1), 87–98 (2012)

3. Huang, B., Zhang, Y., Wang, C.: New energy development and issues in China during the 14th five-year plan. Electric Power **53**(1), 1–9 (2020)

4. Australian Energy Market Operator. Update report—black system event in South Australia on 28 September 2016 [R]. Australian Energy Market Operator Limited, Australian (2016)

5. Tu, J., et al.: Study on wind turbine generators tripping caused by HVDC contingencies of wind-thermal-bundled HVDC transmission systems. Power Syst. Technol. **39**(12), 3333–3338 (2015)

6. Wang, N., Ma, Y., Ding, K., Zhou, S., Zhou, Q.: Analysis on root reasons of WTGs nuisance tripping in Jiuquan wind power base. Automat. Electr. Power Syst. **36**(19), 42–46 (2012)

7. Sun, H., Zhang, Z., Lin, W., Tang, Y., Luo, X., Wang, A.: Analysis on serious wind turbine generators tripping accident in northwest China power grid in 2011 and its lessons. Power Syst. Technol. **36**(10), 76–80 (2012)

8. He, S., Dong, X.: Cause analysis on large-scale wind turbine tripping and its countermeasures. Power Syst. Protect. Control **40**(01), 131–137+144 (2012)

9. Wu, P., Chen, H., Zhao, B., Xu, S., Yi, J., Zhang, J.: Study on interaction and stability characteristics of bundled wind-PV-thermal power transmitted with AC/DC system. Power Syst. Technol. **40**(07), 1934–1942 (2016)

10. Huo, C., Li, Z., Ke, X., Qie, Z., Wang, C., Tu, J.: Emergency frequency control for large-scale disconnection of renewable energy in the UHVDC sending grid. Electr. Power Eng. Technol. **39**(04), 42–47+60 (2020)

11. Zhou, J., Liu, J., Chen, Y., Li, J.: Low voltage ride-through control of high power inverter for gird-connection of photovoltaic generation. Power Syst. Technol. **37**(07), 1799–1807 (2013)

12. Cao, D., Zhang, Y., Zhao, Y., Wang, Y., Xu, H., Wang, Y.: Research of control technique of zero voltage ride-through for grid-connected PV inverter. Acta Energ. Solar. Sin. **37**(02), 366–372 (2016)

13. Wei, Z., Wang, J., Ru, X., Song, F., Wang, T., Li, G.: Zero voltage ride-through control strategy of photovoltaic grid-connected inverter based on compensation for phase of feed-forward grid voltage. Automat. Electr. Power Syst. **40**(04), 78–84 (2016)

14. GB/T19964-2012. Technical requirements for connecting photovoltaic power station to power system (2012)

Deep Reinforcement Learning for Strategic Bidding in Incomplete Information Market

Qi Wu, Caixin Yan, and Zhifeng Qiu[✉]

Central South University, Changsha 410083, Hunan, China
zhifeng.qiu@csu.edu.cn

Abstract. In order to achieve carbon peaking and carbon neutrality, the electricity marketization reform is gradually advancing. Power generators use the dark bid auctions mechanism to bid, resulting in the market being in a state of incomplete information. Therefore, the accurate market equilibrium results and the analysis of the transaction behavior of power generators have a significant impact on the stable operation of the market. Based on the incomplete information market in which generators are not aware of other bidding strategies and cost functions, this paper establishes a bi-level model of generator quotation, and interacts with bidding and clearing information. Based on the deep reinforcement learning (DRL) technology in artificial intelligence, this paper proposes a generator decision-making method with online learning function, and finally finds the optimal bidding strategy of the generator that meets the load demand in a short time. In generally, this paper simulates the quotation behavior of generators under incomplete information, sets up multi-scenario experiments to compare and analyze the market equilibrium, so as to provide suggestions for market rules. Results show that the DRL algorithm based on Deep Deterministic Policy Gradient is suitable for solving market equilibrium problems in complex environments. The bi-level model can simulate the real market operation and competition condition, help power generators make correct bidding strategies and achieve Nash equilibrium results. This paper has reference value for finding the equilibrium of multiple interests in the design of market mechanism.

Keywords: Deep reinforcement learning · Incomplete information · Market equilibrium · Bi-level model

1 Introduction

At present, the power system reform is gradually breaking the original electricity market model integrating power generation, transmission and distribution. The design of the operation mechanism in the electricity market has become one of the core issues of market construction [1]. For the mechanism design problem in the electricity market, since the trading behavior of members affects the market to some extent [2], it is necessary to analyze their possible behaviors and the market equilibrium state. For the research on the problem of generator bidding and market equilibrium, the traditional solution to is to use a

game theory method [3–5], which can take into account the competition and cooperation between different subjects [6], but requires more assumptions and simplifications, limited to network elements of static games with complete information. When it does not match the actual situation, the obtained Nash equilibrium may have a certain deviation.

In order to simulate the real situation of many members competing for market share under incomplete market information and the rational bidding behavior of generators to maximize their own income, a growing number of researches use artificial intelligence methods such as reinforcement learning (RL) to solve the problem. In the existing research, reference [7] established the comprehensive income model to verify the influence of medium and long-term contracts on the bidding of generators. Reference [8] proposed an improved RL automaton algorithm, which models the generator quotation behavior and market clearing process as a repeated game problem, and helps generators to optimize the quotation in the case of incomplete information. As a new type of artificial intelligence algorithm, RL can repeatedly explore and solve problems by trial and error in a dynamic environment. It has low requirements for accurate mathematical models, complete information and parameter settings, and provides the possibility to solve complex system optimization decisions [9].

However, the RL algorithms in the above literature mostly use Q-learning and its deformation algorithms, which are restricted by the limited dimension of the Q value table and can only deal with low-dimensional and discrete situations [10]. Therefore, the model can only be simplified, and the continuous state space is transformed into a finite state space, which lacks the authenticity and integrity of the information. The deep reinforcement learning algorithm (DRL) has certain advantages in dealing with high-dimensional uncertain problems due to its combination of deep neural network (DNN) and RL. So, it can solve the decision-making problem of multi-party interactive games [11]. Reference [12] compares the difference in benefits obtained by Double Deep Q network (DDQN) and traditional Q-learning algorithms. Experiments show that DDQN can help generators make better decisions in the face of complex environments, which reflects the effectiveness and superiority of the algorithm. Reference [13] studies the behavior of market participants based on DRL and proposes a learning mechanism for market participants under the DRL framework. But DDQN is still essentially limited by the Q-value table and can only deal with discrete problems. To further apply DRL to continuous action space, the Deep Deterministic Policy Gradient (DDPG) algorithm is used to solve the Markov decision process (MDP) with continuous state space [14]. Also consider the physical non-convex properties of market participants [15] to design more favorable bidding strategies.

At present, there are few studies on the application of DDPG algorithm in solving market equilibrium problems. Reference [15] established a bi-level model of the bidding market, considering the non-convex operating characteristics of complex markets, but lacked the analysis of the clearing mechanism and the market equilibrium state. Reference [16] studies the bidding strategy of generators, but only stays at the level of mathematical modeling, ignoring the physical process of information interaction between generators and the market. In fact, the behavior of generators is closely related to the market. The revenue of power generators is closely related to the market price, and the bidding strategies varies under different market mechanisms [17]. The design of the

market mechanism needs to consider the behavior of power generators, and the bidding strategy of power generators also affects the market clearing. Since the research on the above problems, this paper establishes a bi-level model of generators quotation in the incomplete information market, and apply the DDPG algorithm to solve the market equilibrium to find the optimal strategy. Though the simulation of improved IEEE-3 and IEEE-30 model, different market mechanisms are simulated to help generators and managers make strategic decisions and set market rules from a macro perspective. The superiority of DDPG algorithm is verified by arithmetic examples.

2   Basic Model of Market Under Incomplete Information

The electricity market can be divided into complete information market and incomplete information market according to the degree of information disclosure. This paper assumes that the internal information of power generators is not public, all power generators do not know the relevant information of other competitors, and the market is in a state of incomplete information. In this section, starting from the market structure, the bidding model of generators, the load demand side and the market clearing model of the power trading center are established respectively, to establish a bi-level optimization model for generators to participate in bidding, and carry out research work.

2.1   Market Structure

The market mechanism is the main factor that affects the bidding of the main body and the equilibrium of the market. Combined with the current situation of electricity market construction, the market rules of this article are formulated:

1) The electricity market adopts the dark bidding auction mechanism [18]. Each generator independently conducts strategic bidding according to the existing information, and formulates its own bidding strategy to obtain the maximum profit. After obtaining the quotation information of power generators, the independent system operators (ISO) will clear the market based on the social welfare maximization and disclose the nodal price. After many times of information exchange between power generators and operating agencies, the entire market will reach a state of equilibrium, that is, the Nash equilibrium. In this equilibrium state, no entity can obtain more profits by changing its own bidding strategy, and the generators can obtain their own optimal bidding strategy and maximum profit.
2) The market clearing method is unified clearing according to the marginal price, that is, the last unit that meets the load demand is quoted as the marginal unit. The price is defined as the marginal price to determine the quantity and price of the remaining units.
3) The market transaction mode is the power bank mode, and the market members include power generators and users, as well as independent system operator. The following is a modeling analysis of the clearing process of generators, users and ISO.

2.2   Generators Bidding Model

In this paper, the supply function equilibrium (SFE) model is used to construct the bidding strategy of generators. In the SFE model, the power generators participating in the market competition make quotations according to their own marginal costs, which avoids the false bidding behavior. The nodal price and the bid-winning quantity are determined by the market, which reflects the influence of the market on the behavior of the main body, as well as the dual control of price and quantity, and ensures the fairness and stability of the market.

Power generators participate in market bidding in the form of quotation and volume [19]. The cost function is expressed as a quadratic function of its output power per unit time:

$$C_g(P_{Gi}) = a_{Gi}P_i^G + \frac{1}{2}b_{Gi}P_i^{G^2}, \forall i \in \Omega_m \tag{1}$$

$$C_g^m(P_{Gi}) = a_{Gi} + b_{Gi}P_i^G, \forall i \in \Omega_m \tag{2}$$

where $C_g(P_{Gi})$ is the cost function of the generator, $C_g^m(P_{Gi})$ is the marginal cost function of the generator, a_{Gi} and b_{Gi} are the linear and quadratic coefficients of the cost function, respectively, Ω_m is the set of generators, and P_i^G is the output power of the generator.

Generators bidding procedure based on marginal cost. The intercept or slope or a combination of the two can be used as the bidding strategy coefficient [15]. In this paper, the intercept is used as the strategy coefficient for bidding.

The optimization model of generators aiming at maximizing profit is:

$$\max_{\lambda_i} R_i = \lambda_i P_i^G - C_g(P_{Gi}), \forall i \in \Omega_m \tag{3}$$

$$a_{Gi}^{\min} \leq a_{Gi} \leq a_{Gi}^{\max} \tag{4}$$

where λ_i is the market clearing electricity price, R_i is the profit value of the generator, $a_{Gi}^{\min}$ and $a_{Gi}^{\max}$ is the upper and lower limit of the quotation of the generator set, respectively.

2.3   Load Demand Model

The load participates in the market in the form of quoted volume without quotation [19]. Corresponding to the generator bidding model, a linear demand model of the load is established:

$$C_d^k(P_{Dj}) = c_{Dj} + d_{Dj}P_j^D, \forall j \in \Omega_k \tag{5}$$

$$C_d(P_{Dj}) = \int C_d^k(P_{Dj})dP_j^D = c_{Dj}P_j^D + \frac{1}{2}d_{Dj}P_j^{D^2}, \forall j \in \Omega_k \tag{6}$$

where $C_d^k(P_{Dj})$ is the demand function of the load, $C_d(P_{Dj})$ is the integral of the load demand, used to represent the benefit of the load, c_{Dj} and d_{Dj} are the intercept and slope of the demand function, respectively, Ω_k is the load set, and P_j^D is the marked force in the load.

2.4   Market Clearing Model

After receiving the quotation information of each power generator, ISO form the total quotation curve and the total demand curve to match and clear the unified marginal price, and determine the winning amount of electricity and electricity price. Considering various constraints such as generator output limit, load output limit, power balance constraint, nodal power flow constraint, etc., the direct-current (DC) optimal power flow is used to establish a market clearing model for maximizing social welfare as follows:

$$\max_{a_{Gi}} \pi = \sum_{j=1, j \in \Omega_k}^{k} (c_{Dj} P_j^D + \frac{1}{2} d_{Dj} P_j^{D^2}) - \sum_{i=1, i \in \Omega_m}^{m} (a_{Gi} P_i^G + \frac{1}{2} b_{Gi} P_i^{G^2}) \qquad (7)$$

$$s.t. \begin{cases} P_i^{G\min} \leq P_i^G \leq P_i^{G\max}, \forall i \in \Omega_m \\ P_j^{D\min} \leq P_j^D \leq P_j^{D\max}, \forall j \in \Omega_k \\ \sum_{i=1, i \in \Omega_m}^{m} P_i^G - \sum_{j=1, j \in \Omega_k}^{k} P_j^D = 0 \\ PTDF(P_i^G - P_j^D) \leq L_{\max} \end{cases} \qquad (8)$$

where $P_i^{G\min}$ and $P_i^{G\max}$ are the minimum and maximum output values of the generator sets, respectively, $P_j^{D\min}$ and $P_j^{D\max}$ are the minimum and maximum output values of the load, respectively, Ω_m and Ω_k are the set of all generator sets and loads participating in the bidding, P_i^G and P_j^D are respectively Indicates the declared amount of electricity from the generator and the load. PTDF is the power transmission transfer distribution factor [20], which can effectively constrain the power flow of the model and $L_{\max}$ express the maximum capacity limit of the transmission line.

2.5   Bi-level Bidding Model of Generators

In the electricity market with incomplete information, generators participate in bidding based on their own data and submit the data to electricity operators. In order to maximize their own profits, the power generator adopts the optimal bidding strategy, which will affect the market clearing and further affect the nodal price and market equilibrium. The power operator integrates the quotation information of each generator and the market operation parameters for centralized and unified clearing. The result will affect the next quotation of generators and make them make timely strategic adjustments. Therefore, a bi-level model of generator bidding is established. The upper model is the bidding decision-making layer of generators, aiming at maximizing the profit of generators; the lower model is the market clearing layer, aiming at maximizing social welfare. The interaction between the bi-level model is carried out through bidding information and clearing information. The model diagram is shown in Fig. 1.
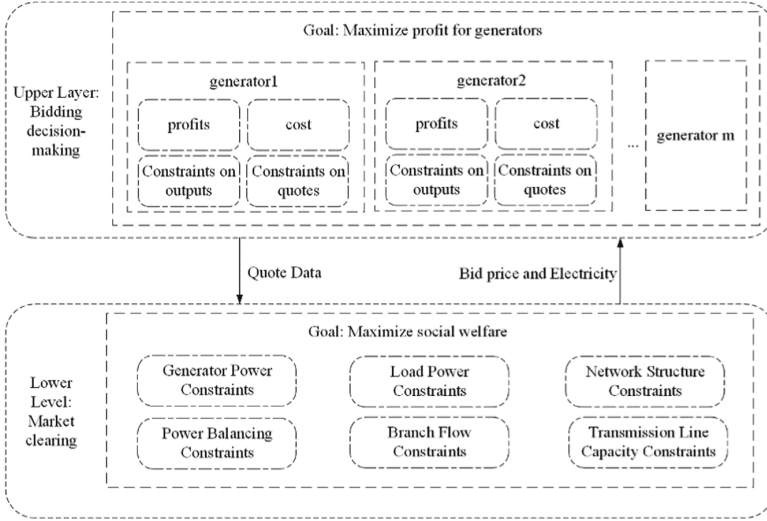
Fig. 1. Schematic diagram of the bi-level model diagram.

3 Deep Reinforcement Learning Solving Algorithms

3.1 MDP Model

Artificial intelligence is a technology that simulates human behavior through computer programs to perform specific tasks. Machine learning is an important branch. At present, common machine learning algorithms can be divided into: supervised learning, unsupervised learning and DRL [21]. As a basic modeling method of DRL, MDP can effectively solve the control and decision-making process in complex environmental systems. In this method, each agent can automatically perceive the current state s_{gt} within the time interval t, and take action a_{gt} according to a certain strategy p_{gt}, thereby changing the environmental state and obtaining a reward r_{gt}, the reward is accumulated over time as a payoff. The goal of each generator is to maximize its own returns:

$$R_g = \sum_{t=1}^{T} \gamma^{t-1} r_{gt} \tag{9}$$

where T is the total number of time intervals, and $\gamma \in [0, 1]$ is the discount factor, indicating the importance of future returns to the current decision.

Therefore, an MDP model of incomplete information electricity market is established, which is described by a quadruple $\{s_{gt}, a_{gt}, p_{gt}, r_{gt}\}$, where s_{gt} represents the state space, a_{gt} represents the action space, p_{gt} represents the policy, and r_{gt} represents the reward function, as follows:

1) State space: State is the basis of action selection and it is the expression of the environmental characteristics observed by the agent. In this model, the state space includes the electricity price of each node of the system and the total load demand.
2) Action space: The DDPG algorithm can handle continuous action space. In this model, the action space is the quotation curve given by the quotation coefficient.

3) Strategy: Conditional probability distribution about actions given by states. In this model, the strategy is the set of coefficients of the generator bidding strategy.
4) Reward function: The reward function serves as the feedback of the environment after the agent performs an action. In this model, since the market is a rational electricity market, generators only care about their own profit returns, so the profit of each generator is used as the reward function. As shown in formula (3).

3.2 DDPG Algorithm

Different from the requirements in the game theory method, the DDPG algorithm is more suitable for dealing with the market equilibrium under incomplete information, and transforming the optimization problem of finding the best strategy into the update problem of the search experience. The DDPG algorithm combines deep learning technology and actor-critic algorithm and is suitable for continuous action space. The actor is the action function, which is used to generate the action of the interaction between the agent and the environment. The critic is the judgment function, which is used to evaluate the pros and cons of the action performed by the agent. In the DDPG algorithm, the actor-critic network is approximated by a deep neural network DNN. It includes four neural networks, namely actor network, target actor network, critic network, and target critic network.

In the state s_t, the action $a_t = \pi\left(s_t | \theta_t^\pi\right)$ is executed through the policy function π, and get the next moment state s_{t+1} and the current state reward value R_t. Update the action-value function via the Bellman equation and compute the Q value:

$$Q^\pi(s_t, a_t) = \mathrm{E}\left[r_t(s_t, a_t) + \gamma Q^\pi(s_{t+1}, \pi(s_{t+1}))\right] \tag{10}$$

$$Y_i = R_i + \gamma Q^\pi(s_{t+1}, \pi(s_{t+1})) \tag{11}$$

Minimize the loss function using the gradient descent algorithm:

$$L = \frac{1}{N} \sum_i \left(Y_i - Q\left(s_t, a_t | \theta^Q\right)\right) \tag{12}$$

Store the amount (s_t, a_t, r_t, s_{t+1}) of state transitions in an experience pool. Each time randomly pick a state from the pool to transition and update four network parameters at the same time. The policy function is updated with a small batch of samples using the experience replay pool:

$$\nabla_{\theta^\pi} J \approx \frac{1}{N} \sum_i \left[\nabla_a Q\left(s, a | \theta^Q\right)\Big|_{s=s_i, a=\pi(s_i)} \nabla_{\theta^\pi} \pi\left(s | \theta^\pi\right)\Big|_{s=s_i}\right] \tag{13}$$

An exponential smoothing method is used to update the target network, where $\rho \ll 1$ ensures the stationarity of the algorithm training:

$$\theta^{Q'} \leftarrow \rho\theta^Q + (1 - \rho)\rho\theta^{Q'} \tag{14}$$

$$\theta^{\pi'} \leftarrow \rho\theta^\pi + (1 - \rho)\rho\theta^{\pi'} \tag{15}$$
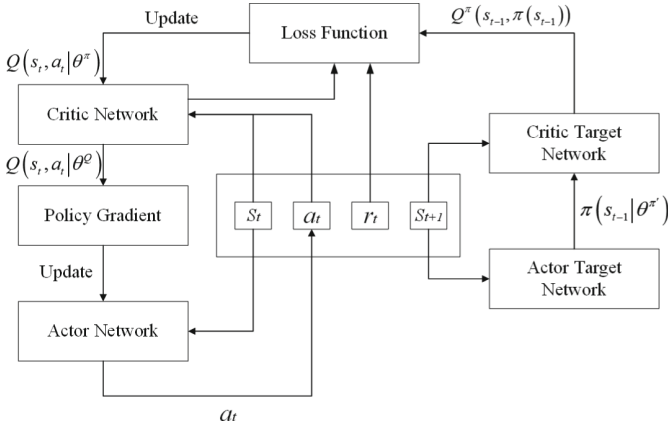
The DDPG algorithm framework is shown in Fig. 2.

Fig. 2. DDPG algorithm framework diagram.

3.3 A Bi-level Model Solution Based on DRL

This paper uses the DDPG method to solve the bi-level model. The lower-level clearing model is a linear programming problem, solved by convex optimization, providing a training environment for agent behavior. It outputs nodal price and profit as status and reward value, respectively. The upper-level bidding decision is a complex adaptive system problem. The DDPG algorithm will be used to train the generator to obtain the optimal bidding strategy. By constructing the influence of the transaction behavior of generators on the market, analyze the market equilibrium state and compare different results in multiple scenarios.

The structure diagram and flow chart of the market equilibrium analysis based on DRL are shown in Fig. 3 and Fig. 4, respectively.
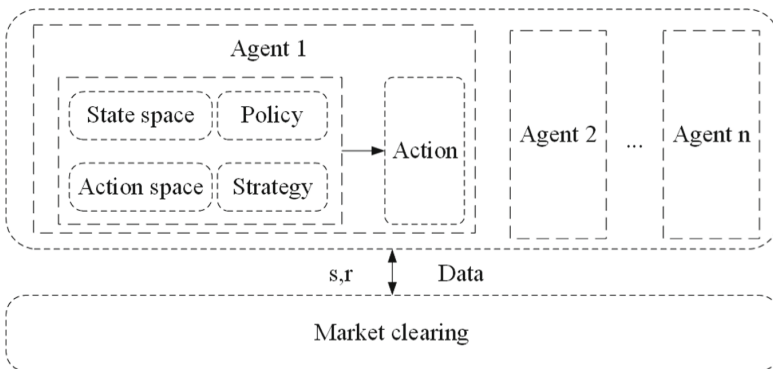
Fig. 3. DRL structure diagram of generator quotation decision.
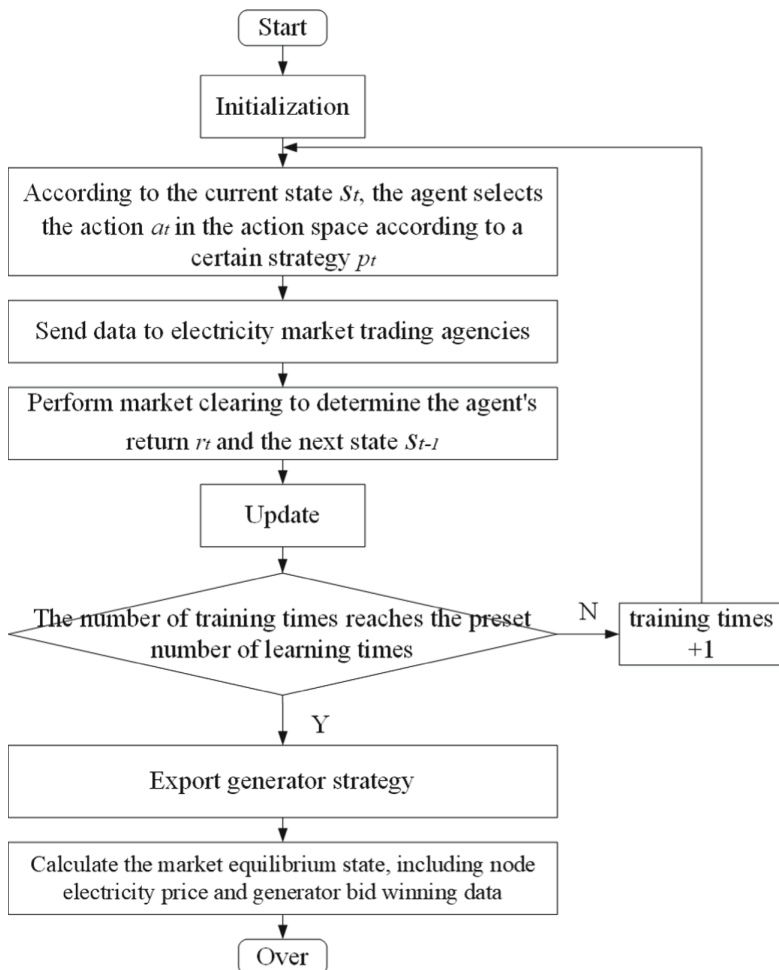
Fig. 4. DRL flow chart of generator quotation decision.

4 Case Analysis

4.1 IEEE-3 Model Test System

This section simulates the incomplete information market based on the improved IEEE-3 system for simulation verification. In addition, a comparative analysis is carried out for different situations of the transmission line capacity limit requirements of lines 1–2. The 3-node network topology is shown in Fig. 5. The following Table 1 [22] gives the basic parameter information. The impedance between the nodes in the network is the same, and the influence of the capacity of other transmission lines is not considered except for the upper limit of the transmission line 1–2.
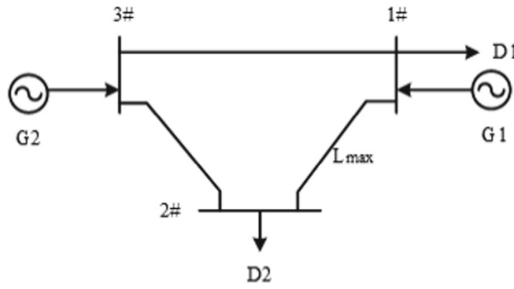
Fig. 5. 3-Node network topology diagram.

Set the experimental simulation parameters. Among them, the maximum number of experimental simulations $T = 10000$; the number of training initial sessions $T_{cap} = 500$; the number of training sessions $T_{tra} = 9000$; the update rate $\rho = 10^{-3}$; the discount factor $\gamma = 0$.

Table 1. 3-Node network basic parameter table.

Bus	Generators				Loads			
i	a_{Gi} (¥/MW)	b_{Gi} (¥/MW^2)	$P_i^{G\,min}$ (MW)	$P_i^{G\,max}$ (MW)	c_{Dj} (¥/MW)	d_{Dj} (¥/MW^2)	$P_j^{D\,min}$ (MW)	$P_j^{D\,max}$ (MW)
1#	15	0.01	0	500	40	−0.08	0	500
2#					40	−0.06	0	666.67
	—							
3#	18	0.008	0	500				
					—			

The Impact of Transmission Line Congestion on Market Equilibrium

Consider two situations for comparative analysis: i. Line 1–2 transmission capacity is limited, that is, $L_{max} = 25MW$; ii. Line 1–2 transmission capacity is unlimited, that is, $L_{max} = 1000MW$. The rest of the parameters remain unchanged. Set up comparative experiments for analysis.

i. When the line capacity is limited.
   When the transmission line capacity is limited, the individual bidding strategies and profit changes of generators are shown in Fig. 6(a) and Fig. 6(b), respectively. As the training progresses, it gradually converges to a stable solution. This result is the optimal strategy combination and maximum return.

ii. When the line capacity is unlimited.
   When the transmission line capacity is unlimited, the individual bidding strategies and profit changes of generators are shown in Fig. 7(a) and Fig. 7(b), respectively. As the training progresses, it gradually converges to a stable solution. This result is the optimal strategy combination and maximum return.

(a) Bidding strategy of generators

(b) Profits of generators
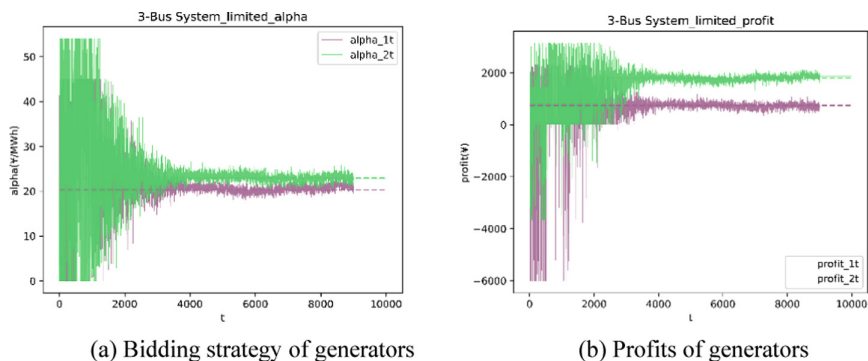
Fig. 6. Generator strategy and profit results in the case of limited line capacity.

(a) Bidding strategy of generators

(b) Profits of generators
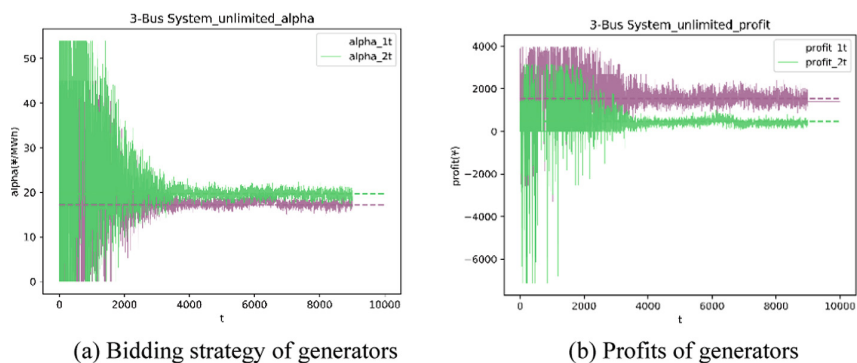
Fig. 7. Generator strategy and profit results in the case of unlimited line capacity.

Under the training of the DDPG algorithm, the strategy training process adopted by each agent and the change trend of the total reward under each sequence are shown in the figure above. In the early stage of the algorithm, the calculated value of the critic network on the state action value function is quite different from the actual value. In addition, the algorithm randomly explores the action space, resulting in poor actual effect of the agent in selecting actions. At this time, the strategy is inaccurate, resulting in large fluctuations in the training value. As the training progresses, after 4000 iterations, the critic network can accurately calculate the state action value, and the actor network can output the optimal action in the current state. At this point, the strategy values gradually converge and the total reward of the sequence gradually stabilizes. The optimal value is obtained at the end of the training and the market reaches equilibrium.

Comparing the impact of transmission line capacity restrictions on bidding strategies of generators under incomplete information, the relevant data are shown in Table 2.

Table 2. Equilibrium strategy combination and payoff in different blocking situations.

Situation	Generators	Policy (¥/MW)	Nodal Price (¥)	Profit (¥)	Amount (MW)	Cost (¥)	Income (¥)	Social Welfare (¥)
Limited $L_{max} = 25MW$	G1	20.29	21.53	730.68	123.67	1931.51	2662.19	3823.69
	G2	22.98	25.29	1776.91	289.49	5546.11	7323.01	
Unlimited $L_{max} = 1000MW$	G1	17.24	21.05	1580.34	381.18	6444.19	8024.53	5282.85
	G2	19.68	21.05	405.69	171.48	3204.17	3609.87	

Based on the above data, the relevant analysis is as follows:

1) Nodal Price Analysis:
   In an ideal power market, generators at any node in the system can freely supply power to the load, ensuring the maximum degree of freedom in the market. However, the actual power transmission system greatly limits this degree of freedom due to the constraints of transmission line capacity, and because of the further expansion of the scale of the generation and consumption markets, the degree of congestion may be further deepened. Usually, power generators will manipulate market power through nodal prices after realizing the status of the network nodes they are in. In generally, the generators in the load pocket have higher quotations, while the generators in the load delivery area have low quotations. However, due to network congestion, the power generators who quoted low prices in the delivery area could not send electricity into the area, so they could only call the high-priced units in the load pocket, resulting in an increase in the node electricity price in the load pocket area during this period.
   When the transmission line capacity is unlimited, the nodal price is the same for all generators. But when the capacity is limited, the nodal price is different for each other, and it is higher than when there is no constraint. This is because power generators use market power to raise electricity prices in a small range and increase their bidding strategies to obtain higher profits, resulting in the rise of node electricity prices. When the limit exists, the nodal price is a linear combination of the quotations of the two units and is no longer determined by a single unit. The nodal price serves as an effective signal reflecting the market supply and demand. The rise in electricity prices reflects the scarcity of electricity. In the case of severe congestion in the transmission system, the unified electricity market is divided into multiple markets, and the blocked part will lead to part of the market surplus. This surplus part cannot belong to independent system operators, otherwise they will be motivated to deliberately create transmission congestion; nor can it be returned

to market members, otherwise the incentive effect of marginal electricity prices on economic behavior will be weakened. Reasonable solution to transmission line congestion is a key issue in market mechanism design. The first is to adjust the network structure and parameters as much as possible to change the network flow and resolve congestion; when the operation optimization cannot be satisfied, the transmission plan of each market participant should be reasonably adjusted under the premise of fair competition and economic security to ensure the stable operation of the system.

2) Profit and Competitiveness Analysis:

The improvement of the bidding strategy does not necessarily increase the profit of power generators. As can be seen from Table 2, although the bidding strategy for both generators is higher in the presence of capacity constraints than in the absence of constraints, it leads to different degrees of increase and decrease in profits. Due to the existence of line 1–2 blockage, G1 has a certain cost advantage, but cannot provide enough power to D2, so that D2 can only turn to the higher cost G2 to purchase power, resulting in a subversive change in the amount of power bid by the two generators, which ultimately also leads to a change in generation revenue and profit.

3) Social Welfare Analysis:

As far as social welfare is concerned, the social welfare in the unlimited situation is higher than that in the limited situation, indicating that the strategic bids by the generators are made at the cost of reducing the social welfare. Therefore, when setting market rules, in order to prevent this phenomenon from happening, it is necessary to increase the capacity limit of the transmission line as much as possible. Even if the bid-winning power within the generator set will change, the user group will benefit in terms of node electricity price and social welfare. It can also reduce the influence of power generators using their own quotations to manipulate market power while ensuring the interests of multiple parties as much as possible.

Verification of DDPG Data Generalization Ability

In fact, the electricity load of residential users fluctuates in real time, which makes it impossible for the actual load to be the same as the load during algorithm training. Therefore, this section studies the data generalization ability of the generator decision-making model based on DDPG, using three sets of data with different loads, respectively high, medium and low levels, using the DDPG model trained in this paper to participate in generator quotations. And calculate the corresponding market equilibrium data under the unlimited transmission line.

The specific results are shown in Table 3.

Table 3. Balance strategy combination and income situation under different load data.

Level	Generators	Policy (¥/MW)	Nodal Price (¥)	Profit (¥)	Amount (MW)	Cost (¥)	Income (¥)	Social Welfare (¥)
High	G1	0	31.59	7048.65	500	8749.99	15798.65	26744.64
	G2	28.97	31.59	4034.09	328.41	6342.84	10376.93	
Medium	G1	17.24	21.05	1580.34	381.18	6444.19	8024.53	5282.85
	G2	19.68	21.05	405.69	171.48	3204.17	3609.87	
Low	G1	21.67	23.81	1427.68	180.65	2872.84	4300.52	722.58
	G2	53.98	23.81	0	0	0	0	

The above results can show that no matter what level of load is used for data training, the DDPG algorithm can accurately converge and find the optimal value, and the results are consistent with the actual situation. The bi-level model of generator bidding decision-making based on the DDPG algorithm is effective when faced with the generalized data that has never been trained. It can help generators choose appropriate quotations to achieve market equilibrium, which proves that the model has good data generalization ability.

4.2   IEEE-30 Model Test System

This section conducts a more general verification based on the improved IEEE-30 system, the principle is the same as above. The 30-node network topology is shown in Fig. 8, and the basic parameters of the generators and loads are shown in Table 4 and Table 5 [21]. The impedance between the nodes in the network is the same, and the influence of the capacity of other transmission lines is not considered except that the upper limit of the transmission line 6–8, 12–14, and 10–17 is 10, 8, and 10 MW, respectively.

Two sets of comparative experiments are also set up to consider the cases with and without the limitation of the transmission line capacity. The specific results are shown in Table 6.

From the data in Table 6, we can draw a conclusion similar to that of the 3-node system. The limitation of transmission capacity will lead to the increase of nodal price to varying degrees, and the reduction of social welfare, but the profit of power generators may not necessarily increase. In the case of the same transmission line capacity limit, there will also be a phenomenon that individual power generators use market power to cause unfair competition in the market. Therefore, it is necessary to increase the capacity limit of transmission lines as much as possible to alleviate the degree of congestion while ensuring the safe and stable operation of the market. In addition, in this example, regardless of whether the transmission line capacity is limited or not, the data at the market equilibrium solution shows that G5 has reached its maximum output limit, indicating that the maximum output value of the generator has a certain effect on the market equilibrium result. The upper and lower limits of generator output cannot be
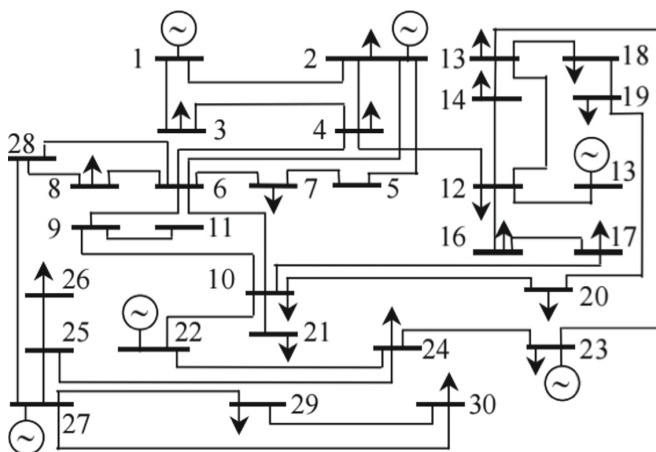
Fig. 8. 30-Node network topology diagram.

Table 4. 30-Node network basic parameter table of generators.

Name	Bus	Generators			
I	i	a_{Gi} (¥/MW)	b_{Gi} (¥/MW^2)	$P_i^{G\,\text{max}}$ (MW)	$P_i^{G\,\text{min}}$ (MW)
G1	1#	18	0.25	100	5
G2	2#	20	0.20	80	5
G3	13#	25	0.20	50	5
G4	22#	22	0.20	80	5
G5	23#	22	0.20	50	5
G6	27#	16	0.25	120	5

ignored when analyzing market equilibrium. Overall, winning bid and revenue of G6 are significantly larger than other power generators, because G6 has the lowest power generation cost and has an advantage in market competition. Compared with using the node price to manipulate the market power, it is more conducive to the success of the bidding by the power generator by reducing its own cost to make a real. When there are multiple power generators in a large-node system, market regulators need to be alert to the collusion among power generators to increase their own profits at the expense of social welfare. In this regard, relevant laws and regulations can be improved, and power generators can be guided to make real quotations and information disclosure, thereby form a good, stable and fair power market environment.

Table 5. 30-Node network basic parameter table of loads.

Name	Bus	Loads		Name	Bus	Loads	
I	i	c_{Dj} (¥/MW)	d_{Dj} (¥/MW^2)	i	i	c_{Dj} (¥/MW)	d_{Dj} (¥/MW^2)
D1	2	120	−5.0	D11	17	90	−3.5
D2	3	130	−5.5	D12	18	95	−3.5
D3	4	120	−4.5	D13	19	90	−3.5
D4	7	135	−5.0	D14	20	90	−3.5
D5	8	150	−5.0	D15	21	160	−6.0
D6	10	95	−3.0	D16	23	120	−5.0
D7	12	150	−5.5	D17	24	150	−6.0
D8	14	125	−4.0	D18	26	100	−4.5
D9	15	100	−4.5	D19	29	95	−3.5
D10	16	150	−5.0	D20	30	125	−4.5

Table 6. Equilibrium strategy combination and payoff in different blocking situations.

Type	Equilibrium Policy (¥/MW)					
	G1	G2	G3	G4	G5	G6
Limited	21.08	24.19	34.32	27.24	0	24.84
Unlimited	22.75	24.04	0	25.35	0	19.76
Type	Nodal Price (¥)					
	G1	G2	G3	G4	G5	G6
Limited	36.33	36.28	41.19	35.01	46.65	43.01
Unlimited	37.52	37.52	37.52	37.52	37.52	37.52
Type	Profit (¥)					
	G1	G2	G3	G4	G5	G6
Limited	653.13	618.66	437.98	353.98	982.73	1301.90
Unlimited	716.71	726.31	375.86	573.89	525.86	897.70
Type	Amount (MW)					
	P_1^G	P_2^G	P_3^G	P_4^G	P_5^G	P_6^G
Limited	61.01	60.45	34.34	38.81	50	72.65
Unlimited	59.07	67.38	50	60.84	50	71.03
Type	Social Welfare (¥)					
Limited	17705.66					
Unlimited	20322.23					

Through the comparison and analysis of the above-mentioned multi-scenario experiments, it can be shown that the bi-level model of generator bidding decision-making established in this paper can effectively solve the intelligent bidding behavior of generators. It has certain data generalization ability, and can simulate the impact of different market mechanisms on the bidding behavior strategy of power generators. It can be well-used in power systems of various scales, helping power generators and managers to make strategic decisions and market rules from a macro perspective.

5   Conclusion

In order to solve the equilibrium problem of the incomplete information market, based on the literature review and existing research, this paper proposes to use the DDPG algorithm to solve the bi-level optimization model of power generation bidding. Through the comparative analysis of multi-scenario experiments, the following conclusions are drawn:

1) The DDPG algorithm used in this paper can be applied to solve the market equilibrium problem in a complex environment. The method can simulate the real market operation and the competition of power generators, which is helpful for generators to make strategic bids and guide the design of market rules;
2) Even if multiple generators are in the incomplete information market, they can still achieve equilibrium through mutual competition, and at the equilibrium point, the profits of each generator are not affected by the bidding strategy;
3) The power market is the basis for generators bidding, and the behavior of generators also affects the market equilibrium. By modeling the process of information interaction between power generators and the market, studying the strategic quotation behavior of generators in the power market has important engineering value and practical significance for ensuring the benefits of market entities, maintaining the fair and stable market order, promoting the rational distribution of resources, and improving the market rules and mechanisms.

References

1. Jianxiao, W., Haiwang, Z., Qing, X., Yang, W., Xiaowen, L., Xinzhi, G.: Design of electricity market competition mechanism based on fair value distribution. Automat. Electr. Power Syst. **43**(2), 11 (2019)
2. Liu, D., Gao, Y., Wang, W., Dong, Z.: Research on bidding strategy of thermal power companies in electricity market based on multi-agent deep deterministic policy gradient. IEEE Access **99**, 1 (2021)
3. Tiannan, M., Ying, D., Quanfeng, G., Lilin, P., et al.: Multi-agent non-cooperative game competition model in power market based on Berge-NS equilibrium. Electr. Power Automat. Equip. **39**(6), 192–204 (2019)

4. Wenhui, Z., Hannan, Y., Wei, H.: Electricity market equilibrium model based on non-cooperative game of wind and fire network. Power Syst. Technol. **42**(1), 103–109 (2018)
5. Yi, T., Jing, L., Tingting, M., Ning, C., Xiaofeng, L., Bingtuan, G: A game theoretical approach based bidding strategy optimization for power producers in power markets with renewable electricity. Energies **10**(5), 627 (616 pp.). (2017)
6. Jun, L., Chao, W., Jinshen, C., Xiaoming, L., Yuewen, L.: A multi-market entity revenue model for urban energy internet based on game theory. Automat. Electr. Power Syst. **43**(14), 8 (2019)
7. Heng, F., Chunbo, H., Shuhai, F., Yifan, W.: Bidding model of generator considering the medium and long-term contract. In: Proceedings of the 2019 Academic Annual Meeting of the Electricity Market Professional Committee of the Chinese Society for Electrical Engineering and the National Electricity Trading Institutions Alliance Forum, China, pp. 336–342 (2019)
8. Qiangang, J., Sijie, C., Yiyan, L., Zheng, Y., Chengke, X.: Bidding strategy of generators based on learning automata in limited information environment. Automat. Electr. Power Syst. **45**(6), 133–139 (2021)
9. Qingkai, S., Xiaojun, W., Yi, W., Yizhi, Z., Zhao, L.: Comprehensive energy market transaction optimization decision based on multi-agent Nash-Q reinforcement learning. Automat. Electr. Power Syst. **45**(16), 124–133 (2021)
10. Yinghao, C., Hao, W., Jiansong, Z.: Navigation application of Q-learning neural network. In: International Conference on System Science and Engineering, pp. 1–4. IEEE (2020)
11. Yixiao, Y., Jiajun, Y., Ming, Y., Yuan, G.: Integrated scheduling of wind farm energy storage system forecasting and decision-making based on deep reinforcement learning. Automat. Electr. Power Syst. **45**(1), 9 (2021)
12. Pengpeng, Y., Beibei, W., Peng, X., Gaoqin, W., Yaxian, Z.: Three-stage bidding strategy of generators based on deep double-Q network under incomplete information. China Power **54**(11), 12 (2021)
13. Shi, B., Huang, L., Shi, R.: A deep reinforcement learning-based approach for pricing in the competing auction-based cloud market. Serv. Orient. Comput. Appl. 1–13 (2022)
14. Xu, H., Sun, H., Nikovski, D., Kitamura, S., Mori, K., Hashimoto, H.: Deep reinforcement learning for joint bidding and pricing of load serving entity. IEEE Trans. Smart Grid 1 (2019)
15. Ye, Y., Qiu, D., Sun, M., Papadaskalopoulos, D., Strbac, G.: Deep reinforcement learning for strategic bidding in electricity markets. IEEE Trans. Smart Grid **11**(2), 1343–1355 (2020)
16. Liang, Y., Guo, C., Ding, Z., Hua, H.: Agent-based modeling in electricity market using deep deterministic policy gradient algorithm. IEEE Trans. Power Syst. **99**, 1 (2020)
17. Chengpeng, T., Lizi, Z., Fang, L., Yunjian, L.: Research on the pricing mechanism of electricity spot market based on multi-agent reinforcement learning (Part I): Bi-level optimization model of generator quotation under different pricing mechanisms. Proc. CSEE **41**(02), 536–553 (2021)
18. Chang, X., Beibei, W., Shengnan, Z., Jian, T., et al.: Solving electricity market equilibrium based on bi-level particle swarm optimization. Power Syst. Technol. **42**(4), 7 (2018)
19. Yonghua, S., Minglei, B., Yi, D., Changzheng, S., Nan, S.: Review of Chinese electricity spot market key issues and its suggestions under the new round of Chinese power system reform. Proc. CSEE **40**(10), 15 (2020)
20. Zili, Y., Yuxing, C.: A power flow computation method for reduction grid based on power transfer distribution factor. Power Syst. Protect. Control **44**(17), 6 (2016)

21. Minrui, J., Dawei, X., Tianhua, C., Huijun, L., Xiaochun, X., Shuai, W.: Research and engineering practice on reactive power control based on deep reinforcement learning in local power grid. In: Proceedings of 2021 International Top-Level Forum on Engineering Science and Technology Development Strategy, pp. 487–505. Springer, Singapore (2022). https://doi.org/10.1007/978-981-16-7156-2_34

22. Jianlin, Y., Zheng, Y.: Branch-and-bound method for solving linear supply function equilibrium models considering transmission constraints. Proc. CSEE **13**, 7 (2010)

Reliability Analysis of Complex Stability Control System Based on GO Methodology

Yuan Sun[✉], Juan Wang, Yuting Song, and Guosen Lin

NARI Group Corporation (State Grid Electric Power Research Institute), Nanjing 210003, China
sunyuan7@sgepri.sgcc.com.cn

Abstract. The reliability of the security and stability control system has an important impact on the stable operation of the regional power grid. As the scale of the stability control system becomes larger and the function becomes more and more complex, it is necessary to analyze the reliability of the complex stability control system. In this paper, a new reliability analysis method, GO methodology, is introduced into the field of reliability analysis of stability control system. Firstly, establish the GO diagram of the stability control system, and then analyze its reliability based on hardware failure, software failure and communication channel failure from quantitative and qualitative perspectives. Finally, calculate the failure probability of the stability control system. In quantitative analysis, considering the influence of common signals, we revise the calculation results. The calculation results correspond to the results of qualitative analysis. Therefore, the results are used as the basis for the reliability analysis of the stability control system.

Keywords: Security and stability control system · Reliability · GO methodology · Quantitative analysis · Qualitative analysis

1 Introduction

The security and stability control system (hereinafter referred to as the stability control system) is the second line of defense of the power grid security defense. From the system level, it solves some complex problems encountered in the operation of the power grid and provides a guarantee for the stable operation of the power system. Over the years, several "Blackouts" have occurred worldwide [1–5], and the accident analysis shows that the failure of the stability control system is one of the main reasons. Different from the relay protection device, the stability control system can protect the main network system in a wide area and on a large scale through layered design and station-to-station interconnection [6]. If the stability control system fails to work normally, the consequences will be serious. Nowadays, under the "Double Carbon" goal, the high proportion of new energy access and the deep power-electronized power grid will inevitably bring new challenges to the stable operation of the power system [7]. Therefore, the research on the reliability of the stability control system is of great importance.

In recent years, with the rapid development of ultra-high voltage AC/DC power grid, the provincial stability control systems of each grid have been gradually improved.

Compared with the past, the stability control systems are larger in scale, more complex in layer design and control logic. Also, there is a great increase in the amount of control measures and the range of fortification. Currently, it is very necessary to analyze the reliability of large-scale complex stability control systems. At present, the research on the reliability of the stability control system at home and abroad has just started, and little research on its research method is available [8]. But, the reliability research of relay protection devices is relatively mature, and the commonly used methods include Markov state space method, Monte Carlo method, GO methodology based on success flow, etc. [9–15]. Some scholars have introduced Markov state space method and Monte Carlo method into reliability analysis of stability control system, and achieved certain results [16–18]. Domestic scholars' research on the reliability of the stability control system mainly focuses on the hardware reliability of the stability control device or the operation mode of the device, etc. There is a lack of relevant research on the probability of the large-scale stability control system's effective action under the existing strategies. This paper combines the GO methodology with the reliability research of stability control system, and proposes a general analysis method. The GO methodology is a success-oriented system probability analysis technology [19], which can intuitively reflect the control relationship between various levels in the stability control system, and is suitable for solving the reliability analysis problem of complex systems. Therefore, taking the provincial stability control system of sending-end DC power grid as an example, this paper employs it to calculate the probability of the system's effective action based on the software and hardware failure.

2 The Working Principle and Analysis Basis of the Stability Control System

2.1 System Structure and Action Process

Figure 1 is a structural diagram of stability control system of a provincial power grid. Take this as an example for analysis. The system is a typical four-layer structure. The first layer is the co-control master station, the decision-making layer of the entire system. With a redundant configuration mode of two stations at different places and two sets of devices at each station, it is to take generator-shedding measures after a DC fault occurs. Under normal operation, being the master site, the co-control master station 1participates in logical judgment and actually works, and the co-control master station 2 is standby. The standby site only participates in the logical judgment and does not actually work. When the two sets of devices of the co-control master station 1 fail at the same time, the co-control master station 2 switches to the master site, and the two sets of devices at each site are independent of each other. The second layer is the AC sub-station of converter station and the 750 kV AC sub-station, which is responsible for summarizing the capacity information of the units that can be switched in this area and sending it to the co-control master station, receiving and executing the generator-shedding command issued by the co-control master station, and also responsible for forwarding DC fault information to the co-control master station (this function is only available in the AC sub-station of converter station). The devices at each site at this
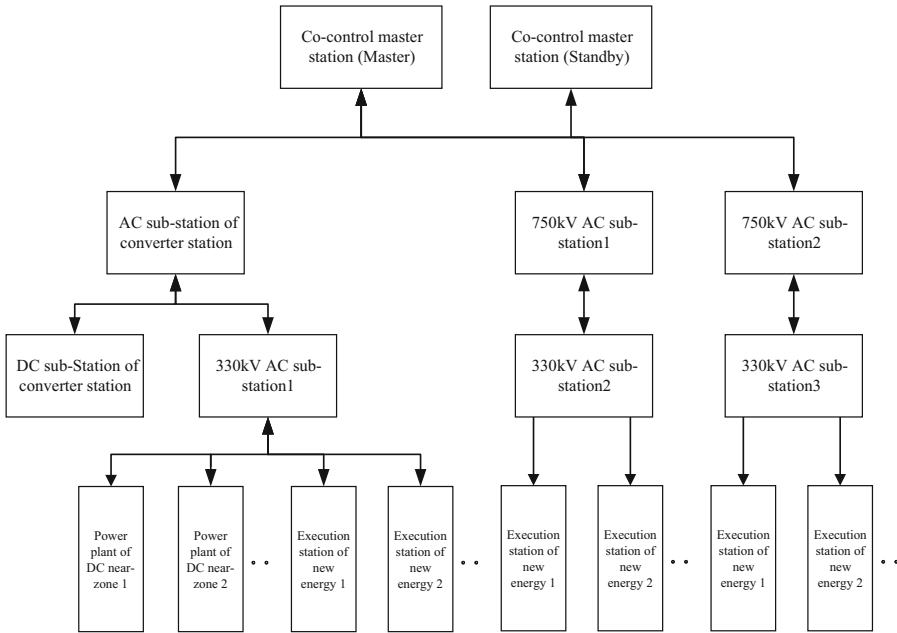
Fig. 1. Structure diagram of stability control system

level are dual redundant, and the dual devices are independent of each other. The third layer is the DC sub-station of converter station and 330 kV AC sub-station, which is responsible for summarizing the capacity information of the units that can be switched in this area and sending it to the 750 kV AC sub-station, receiving and executing the generator-shedding command issued by the 750 kV AC sub-station. It is responsible for judging the DC fault and sending it to the AC sub-station of converter station (this function is only available in the DC sub-station of converter station). The devices at each site at this level are dual redundant, and the dual devices are independent of each other. The fourth floor is the power plant of DC near-zone and the execution station of new energy, which is responsible for taking generator-shedding measures. The device of power plant is a double redundant configuration, and the dual devices are independent of each other, and the device of execution station of new energy is a single configuration. In the actual situation, according to the characteristics of each region, the number of execution stations in each region is different, and the configuration of the two execution stations in each region is unified in this paper.

The main function of the stability control system is to take generator-shedding measures to balance the excess power in the grid when a DC failure occurs. The process is shown in Fig. 2.

When the device of DC sub-station of converter station recognizes the DC fault, it calculates the loss of DC and sends it to the device of AC sub-station of converter station. The co-control master station device calculates the number of units to be switched according to the pre-designed strategy, and allocates it to the device of 750 kV AC sub-station and the AC sub-station of converter station. It is forwarded to the device of
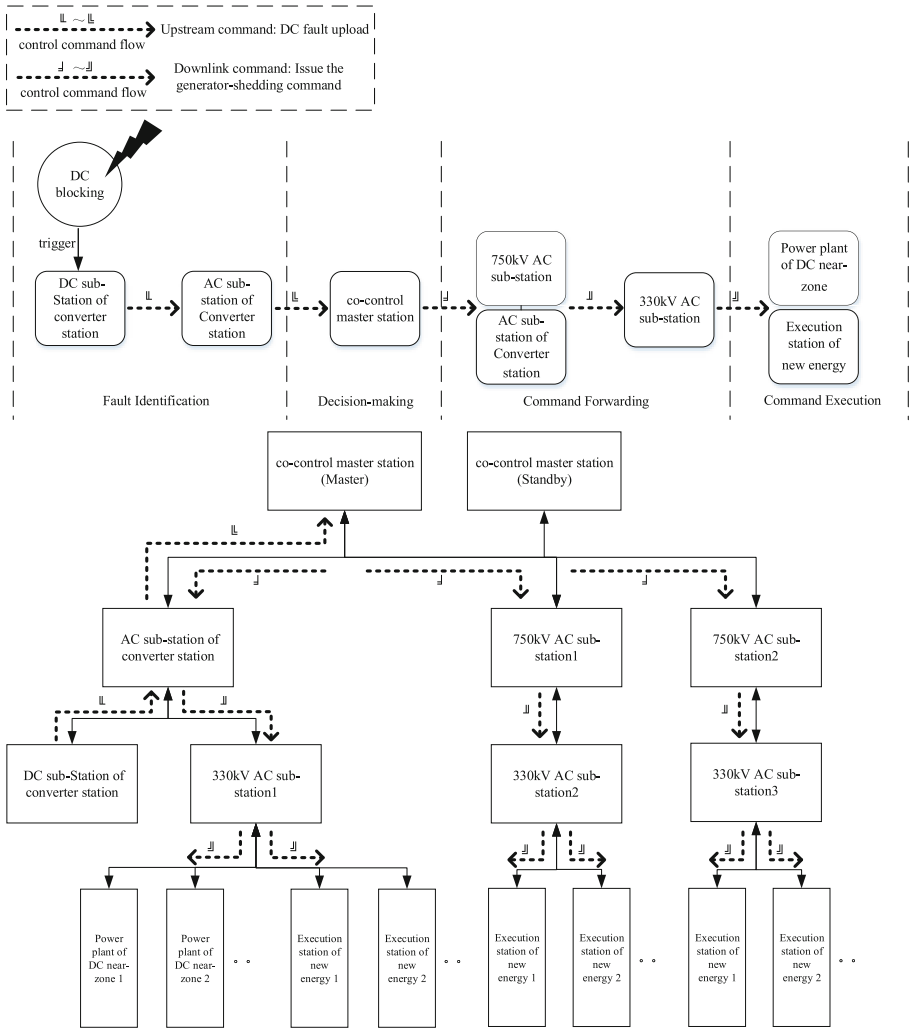
Fig. 2. Schematic diagram of the action process of the stability control system

corresponding 330 kV AC sub-station, and the device of 330 kV AC sub-station selects the execution station of local power plant and new energy after receiving the command.

2.2   Reliability Index of the Stability Control System

The reliability of the stability control system can generally be evaluated by the system's rejection rate and the system's misoperation rate. In the above model, the system's rejection means when a DC fault occurs, the two sets of devices in the system do not take corresponding measures. For example, two sets of devices at a site have hardware failures or software defects at the same time, causing both sets of devices to fail at the same time. System's misoperation can be understood as the stability control system not

taking measures according to the preset strategy. For example, when a DC fault occurs, the stability control system should cut off 200MW units according to the preset strategy, but the actual capacity of generator-shedding calculated by the stability control system is 300 MW due to software defects.

At present, the design principles of hardware of the stability control device is that when a module failure occurs, the device is locked. That is to say the set of devices fails. Therefore, the hardware failure is more likely to cause the stability control device's rejection; Generally, multiple anti-error criteria are set to reduce the probability of device's misoperation; at the same time, compared with hardware failure, the system software will undergo a strict multi-link testing process before the device leaves the factory, and the software reliability is generally not affected by the service life. Therefore, the probability of software defects is less than the probability of hardware failures.

From the perspective of the impact on the power grid, the stability control system's rejection is far more harmful than the stability control system's misoperation. Therefore, this paper starts with the failure of the stability control system and calculates the system's rejection rate as the basis for reliability analysis. The more common defects that can lead to device failure can be roughly divided into three categories, namely device hardware failure, device software failure and communication channel failure. This paper focuses on the application of the GO methodology in the reliability analysis of the stability control system. There are certain assumptions about the relevant data, see Table 1 [20].

Table 1. Data of the device hardware and software failure

Fault type	Failure rate/h^{-1}	Repair time/h
Device hardware failure	2.965×10^{-6}	24 h
Device software failure	3.75×10^{-6}	12 h
Communication channel failure	13.92×10^{-6}	24 h

3   Establishment of GO Map of the Stability Control System

Based on Fig. 2, the GO model of the stability control system is established, and the two-state unit (type 1 operator) is used to represent the co-control master station, substations at various levels, and various types of execution station devices; a single signal generator (type 5 operator) is used to represent DC failure that occurs and is identified by the device. For various types of execution station devices, if a certain station fails, the impact on the stability control system is only the loss of part of the controllable resources. If the remaining controllable resources are sufficient, it can be approximately considered that the failure of the station device has no effect on the stability control system. Therefore, an OR gate (type 2 operator) is used to represent the logical relationship of the two execution stations of near-zone power plant, and an M to K gate (type 11 operator) is used to represent the six execution stations of new energy. M is 6, K is 5 (Fig. 3).

The stability control system is a repairable system, and its steady-state availability (average working probability) can be calculated from the failure rate and repair rate. The
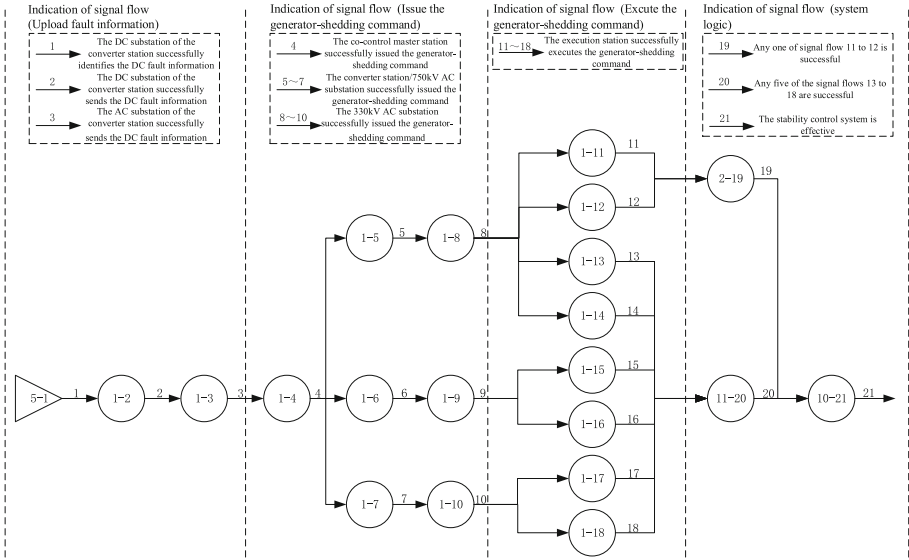
Fig. 3. GO diagram of the stability control system

calculation formula is as follows.

$$P_0 = \left(\frac{\mu_{hardware}}{\lambda_{hardware}+\mu_{hardware}}\right) \times \left(\frac{\mu_{software}}{\lambda_{software}+\mu_{software}}\right) \times \left(\frac{\mu_{channel}}{\lambda_{channel}+\mu_{channel}}\right) \quad (1)$$

Substitute the parameters in Table 1 into Eq. 1 and we can obtain $P_0 \approx 0.9995500$. For a site with a single set of configuration, such as each execution station of new energy, the average working probability of stable control is P_0; for a site with double sets of redundant configuration, such as each AC substation or power plant, if any of the two sets of devices at the site is available, the station stability control function is available, and the average working probability is $P_1 = 1 - (1 - P_0)^2 = 0.9999998$; a site with dual-station in different places and each station is configured with dual sets, such as the co-control master station, only when the four sets of devices in the dual-site fails at the same time, the function of the co-control master station will fail. The average working probability is $P_2 = 1 - (1 - P_0)^4 = 1 - (0.00045)^4 \approx 1$; in this order of magnitude, it can be approximately considered that the co-control master Steady control will not fail.

To sum up, the types, unit names and working probabilities of each operator of the stability control system are listed in Table 2 by number. In the table, No. 3 and No. 5 are listed as AC substations of the converter station. In order to avoid repeated calculation of the working probability of the AC substation of the converter station in the quantitative analysis, let the working probability of the AC substation of the No.5 converter station be 1 in the follow-up calculation. In addition, the case where the occurrence of a DC fault is not identified by the device is not considered.

Table 2. Data of operator of the stability control system

Numbering	Type	Unit name	Probability of work
1	5	DC fault identification	1
2	1	DC substation of converter station	0.9999998
3	1	AC substation of converter station	0.9999998
4	1	Co-control master station	1
5	1	AC substation of converter station	1
6, 7	1	750 kV AC substation	0.9999998
8, 9, 10	1	330 kV AC substation	0.9999998
11, 12	1	Execution station of power plant	0.9999998
13, 14, 15 16, 17, 18	1	Execution station of new energy	0.99955
19	2	OR gate	
20	11	M takes N gate	
21	10	AND gate	

4   Reliability Analysis of the Stability Control System

4.1   Quantitative Analysis with Common Signals

P_C (i) represents the success probability of operator i, and the physical meaning is the correct action of the station's stability control device. P_S(i) represents the success probability of the signal flow i, and the physical meaning is that the control command flow is successfully transmitted to the station's stability control device. The probability formula algorithm is adopted along the signal flow direction, and the system success probability is quantitatively calculated according to the operator probability calculation formula. The expression of the calculation result is as follows. In order to simplify the subsequent calculation process, we suppose:

$$
\begin{aligned}
a_1 &= P_C(1)P_C(2)P_C(3)P_C(4) \\
a_2 &= P_C(5)P_C(8) \\
a_3 &= P_C(6)P_C(9) \\
a_4 &= P_C(7)P_C(10)
\end{aligned}
\tag{2}
$$

1) Signal flow 19

$$
\begin{aligned}
P_S(19) &= P_S(11) + P_S(12) - P_S(11)P_S(12) \\
&= a_1 a_2 P_C(11) + a_1 a_2 P_C(12) \\
&\quad -a_1^2 a_2^2 P_C(11)P_C(12)
\end{aligned}
\tag{3}
$$

Since there are common signals a1 and a2 in the signal flow 11 and the signal flow 12, it is necessary to modify the formula (3). In the expansion of the probability product

of the signal flow, replace the high-order term with the first-order term and the corrected result is as follows [21]:

$$P_S(19) = a_1a_2P_C(11) + a_1a_2P_C(12) - a_1a_2P_C(11)P_C(12) \tag{4}$$

2) Signal flow 20

$$P_S(20) = \left[\prod_{j=1}^{6} P_S(13+j)\right] + \left\{\sum_{j_1=1}^{6}[1 - P_S(13+j_1)] \prod_{j=1,j\neq j_1}^{6} P_S(13+j)\right\} \tag{5}$$

Since signal flow 13 and signal flow 14 share common signals a1 and a3, signal flow 15 and signal flow 16 share common signals a1 and a4, and signal flow 17 and signal flow 18 share common signals a1 and a5, it is necessary to correct formula (5). After correction, the result after correction is:

$$P_S(20) = a_1a_2a_3a_4\left\{\left\{\sum_{j_1=1}^{6}[1 - P_C(13+j_1)] \prod_{j=1,j\neq j_1}^{6} P_C(13+j)\right\} + \prod_{j=1}^{6} P_C(13+j)\right\} \tag{6}$$

3) Signal flow 21

$$P_S(21) = P_S(19)P_S(20) \tag{7}$$

Since signal flow 19 and signal flow 20 have common signals a1 and a2, Eq. (7) needs to be revised, and the revised result is:

$$P_S(21) = a_1a_2a_3a_4[P_C(11) + P_C(12) - P_C(11)P_C(12)]$$
$$\left\{\left\{\sum_{j_1=1}^{6}[1 - P_C(13+j_1)] \prod_{j=1,j\neq j_1}^{6} P_C(13+j)\right\} + \prod_{j=1}^{6} P_C(13+j)\right\} \tag{8}$$

Substituting the parameters of Table 2 into formula (8), the probability of correct action of the stability control device can be obtained as:

$$P_S(21) \approx 0.9999955661 \tag{9}$$

Equation (9) shows that the stability control device of a certain site fails at the same time due to hardware failure, software failure or channel failure, and the probability that the stability control system eventually fails is about 0.0000044339.

4.2   Direct Qualitative Analysis Through State Probability

The principle of qualitative analysis of GO is as follows. Firstly, calculate the failure probability of each order cut set of all operators except logical operators in the GO graph, and then sum the failure probability of each order cut set to obtain the probability of system failure. As for the cut set, it is supposed that among all operators except the logical

Table 3. Minimum cut set of the stability control system

Numbering	Order of cut set	Operator number in the cut set	Failure probability of cut set/10^{-6}
1	1	1	0
2	1	2	0.2
3	1	3	0.2
4	1	4	0
5	1	5	0
6	1	6	0.2
7	1	7	0.2
8	1	8	0.2
9	1	9	0.2
10	1	10	0.2
11	2	11, 12	0.0000002
12	2	13, 14	0.2025
13	2	13, 15	0.2025
14	2	13, 16	0.2025
15	2	13, 17	0.2025
16	2	13, 18	0.2025
17	2	14, 15	0.2025
18	2	14, 16	0.2025
19	2	14, 17	0.2025
20	2	14, 18	0.2025
21	2	15, 16	0.2025
22	2	15, 17	0.2025
23	2	15, 18	0.2025
24	2	16, 17	0.2025
25	2	16, 18	0.2025
26	2	17, 18	0.2025

operator, the failure of the operator is a first-order cut of the system if a certain invalid operator causes the system to fail with the rest of the operators remaining unchanged. Except the first-order cut set, select two of the remaining operators. If the system fails, with these two operators failing at the same time and the state of the other operators remaining unchanged, then the two operators failing at the same time can be seen as a second-order cut set of the system. In this way, the cut sets of each order of the system can be obtained. Based on the above, the qualitative analysis of the stability control system is carried out, and the results are shown in Table 3.

Based on Table 3, the sum of the probability of occurrence of the minimum cut set of the stability control system is 0.0000044375. Since the minimum cut sets are not completely independent, the result of the qualitative analysis is an approximation of the probability of system failure. This result is basically consistent with the previous quantitative analysis results.

This paper demonstrates the availability and correctness of the GO methodology in the reliability analysis of the stability control system from both quantitative and qualitative perspectives. At the same time, the analysis process also shows that the GO methodology has intuitive and efficient advantages in modeling, calculation and analysis.

5 Conclusion

Based on the model of provincial stability control system, this paper introduces the GO methodology into the field of reliability analysis of large-scale stability control systems, and discusses the modeling and calculation methods of the GO methodology in the reliability analysis of complex stability control systems. This paper analyzes the action model of the stability control system of the provincial power grid under a single DC fault. In terms of the action model of the stability control system of the larger sub-center-level power grid under the multiple DC cascading faults, we can expand the application of GO method in modeling and calculation based on this paper. Compared with other methods, the GO methodology performs better in the reliability analysis of multi-scenario and large-scale stability control systems.

In this paper, the probability of software defects is an assumed value. In fact, different from the hardware platform, the software of each station in the stability control system is different, and the device software also includes various application modules, and there are various types of logical relationships among them. In the future research, the software reliability can be studied separately to improve the research of the stability control system's reliability.

References

1. Wang, W., Lin, W., He, G., et al.: Enlightenment of 2021 Texas blackout to the renewable energy development in China. Proc. CSEE **41**(12), 4033–4043 (2021)
2. Yi, J., Bu, G., Guo, Q., et al.: Analysis on blackout in Brazilian power grid on March 21 2018 and its enlightenment to power grid in China. Automat. Electr. Power Syst. **43**(2), 1–9 (2019)
3. Shao, Y., Tang, Y., Yi, J., et al.: Analysis and lessons of blackout in Turkey power grid on March 31, 2015. Automat. Electr. Power Syst. **40**(23), 9–14 (2016)
4. Lin, W., Tang, Y., Sun, H., et al.: Blackout in Brazil power grid on February 4 2011 and inspirations for stable operation of power grid. Automat. Electr. Power Syst. **35**(9), 1–5 (2011)

5. Lin, W., Guo, Q., Yi, J., et al.: Analysis on blackout in Argentine power grid on June 16, 2019 and its enlightenment to power grid in China. Proc. CSEE **40**(9), 2835–2841 (2020)
6. Zhao, L., Wang, M., Ni, M., Li, X.: Analvsis of hardware system's reliability of security and stability control device. Power Syst. Protect. Control **13**, 67–73 (2016)
7. Han, X., Li, T., Zhang, D., et al.: New issues and key technologies of new power system planning under double carbon goals. High Volt. Eng. **47**(9), 3036–3046 (2021)
8. Luo, J., Dong, X., Cui, X., et al.: Discussion on reliability of large scale security and stability control system. Power Syst. Protect. Control **46**(8), 65–72 (2018)
9. Xiong, X., Chen, X., Zheng, C., Yu, R.: Overview of research on state evaluation of relaying protection system. Power Syst. Protect. Control **05**, 51–58 (2014)
10. Zheng, F., Wu, J., Huang, Q., Du, A.: Five-state space model and assessment method for reliability of dual-redundant relay protection system. Automat. Electr. Power Syst. **20**, 26–31+39 (2016)
11. Zhang, Z., et al.: Reliability evaluation of protective relay system based on process layer network. Power Syst. Protect. Control **18**, 142–148 (2013)
12. Xu, Z., Li, X., Yang, L., Zhou, D., Zhao, Y.: Reliability assessment and analysis on digital substation system. Automat. Electr. Power Syst. **05**, 67–71 (2012)
13. Li, H., Lin, X., Yu, K., et al.: Based on continuous time Markov chain prediction model of action behavior of relay protection device. Proc. CSEE **38**(Supplement 1), 121–128 (2018)
14. Lin, S., Lin, X., Feng, D.: Reliability evaluation of relay protection for traction substation of urban rail transit. J. Southw. Jiaotong Univ. **53**(6), 1102–1109 (2018)
15. Ye, Y., Xie, M., Wang, J., et al.: Real time reliability analysis of relay protection system in intelligent substation based on Markov model and GO methodology. Power Syst. Protect. Control **47**(2), 47–55 (2019)
16. Peng, Y., Dong, X., Zhou, H., et al.: Reliability evaluation of power grid security and stability control system. Power Syst. Protect. Control **48**(13), 123–131 (2020)
17. Qie, Z., Li, W., Cui, X., et al.: Reliability analysis of repairable stability control system based on hierarchical Markov. Electr. Power **53**(3), 101–109 (2020)
18. Li, B., Dong, X., Yan, Y., et al.: Reliability assessment of large scale security and stability control system based on control efficacy reduction mode. Electr. Power **53**(5), 32–38 (2020)
19. Shen, Z., Huang, X.: GO Methodology Principle and Application: An Analysis Method of System Reliability. Tsinghua University Press, Beijing (2004). (in Chinese)
20. Zhu, J., Qiu, W., Sun, N., et al.: Reliability analysis of security and stability control system architecture based on sequential Monte Carlo method. Automat. Electr. Power Syst. **45**(15), 21–27 (2021)
21. Shen, Z., Gao, J.: Principle of GO Methodology and improved quantitative analysis method. J. Tsinghua Univ. (Sci. Technol.) **6**, 16–20 (1999). (in Chinese)

A ConvLSTM-Based Approach to Wind Turbine Gearbox Condition Prediction

Liu Jin[1]($\boxtimes$), Hao Wenbo[1], Ji You[1], Wang Lei[2], and Jing Fei[1]

[1] Electric Power Research Institute of State Grid Heilongjiang Electric Power Co., Ltd., Harbin, China
33852988@163.com
[2] State Grid Heilongjiang Electric Power Co., Ltd., Harbin Power Supply Company, Harbin 150000, China

Abstract. Diagnosis and prediction of the health status of wind turbines is of great importance to ensure the normal operation of wind power systems, and gearbox breakdowns are a common type of fault in wind turbines. This paper presents a data-driven prediction method for the main health parameters of wind turbine drive chains based on convolutional long short-term memory neural networks (ConvLSTM). Based on the wind farm operational data obtained in the field, the Spearman correlation coefficient method is used to pre-process the data, which reduces the data dimensionality of the training of sthe prediction model and improves the prediction accuracy. The ConvLSTM is used to perform a time-series processing of the dataset and a convolution operation on the time series weight parameters to achieve a secondary reconstruction of the dataset feature vectors. The reconstructed data is used to train convolutional neural networks for the prediction of the main health parameters during the wind turbine gearbox operation. The analysis of the algorithm shows that the proposed method has high prediction accuracy and the model training time is moderate.

Keywords: Wind turbine · Gear box · State prediction · Neural network · ConvLSTM

1 Introduction

The "dual carbon" goal of reducing carbon emissions has been formulated in China [1], and building a new power system with new energy as the main part is the crucial link to achieve "dual carbon". Wind power is the most important power source for new power systems and has become the third largest energy source in China [2]. The harsh operating environment of wind turbines can easily cause gearbox damage [3, 4]. Gearbox damage to a certain extent will cause wind turbine faults [5] and safety accidents [6, 7]. Therefore, predicting the future state is of great significance for timely fault removing, preventing accidents, and ensuring the safe operation of wind turbines [8–10], according to the current operating data and damage situation of the wind turbine gearbox.

Modern wind farms have a complete Supervisory Control and Data Acquisition (SCADA) system [11–13], which can collect various operational data of wind power equipment in a precise and comprehensive manner. In references [14, 15], SCADA data are used to analyze and predict the operating state of gearboxes. The references [16, 17] studied the pre-processing of SCADA data and the screening of relevant variables, and locate the fault source according to the change of variable characteristics. References [18, 19] combined the historical data of wind turbines, the current state of wind turbines and change trend of wind turbines to predict the situational risk of wind turbines.

At present, the typical prediction models based on data mainly include radial basis function, long short-term memory network, support vector machine and random forest algorithm [20–22]. However, when these methods process data of continuous time series, they are still processed according to a single time series, and do not consider the time correlation among continuous time series data, which affects the prediction accuracy. LSTM is a special kind of recurrent neural network which is suitable for long continuous time series tasks. Different LSTM and variant architectures have been proposed for different application purposes [25, 26]. Reference [27] proposed the Vanilla LSTM model, which has the advantages of no input gate, forgetting gate and output gate, and does not require input and output activation functions. However, Vanilla LSTM cannot capture the correlation among adjacent sequences. To overcome this limitation, many scholars have constructed hybrid LSTM and LSTM composite structures, such as FRS-CLSTM [28] and FC-LSTM [29]. But when processing one-dimensional tensor problems, there may be a problem of mismatching temporal and spatial correlations. Reference [30] proposed a convolutional long short-term memory (ConvLSTM) model for the multi-period continuous time prediction problem, which can effectively capture spatiotemporal features and perform multi-step spatiotemporal prediction.

In this paper, the ConvLSTM model is used to predict the operating state of the wind turbine gearbox. Multiple sets of operating parameters of wind turbines are extracted from the wind farm SCADA system to form the original dataset. The original dataset was pre-processed to decrease the dimension of feature vectors by using Spearman correlation coefficient method. The ConvLSTM network is used to perform the convolution operation on the weight parameters of the dimensionality decreasing time series data to realize the secondary reconstruction of the feature vector of the dataset. According to the operating experience, the gearbox oil temperature, low-speed bearing temperature, high-speed bearing temperature and main bearing temperature are taken as typical health parameters of the gearbox, and the reconstructed data is used for deep neural network training to establish multiple target prediction models. The algorithm example analysis shows that the prediction accuracy of the method in this paper is significantly improved which compares with traditional machine learning or classical neural network, and the model training time is moderate, which verifies the effectiveness of the method.

2   Fault Types Analysis of Wind Turbine Gearbox

The wind turbine drive chain is a transmission component that transmits the power obtained by the wind wheel to the entire shaft system of the generator, which includes the main shaft, gearbox, coupling and other mechanical parts. Gearbox is an important

part of the transmission chain, which is used to transmit the mechanical energy of the wind turbine and increase the rotation speed. It is the weak point of the wind turbine. Fault will cause a long-term shutdown of the turbine and large maintenance investment. The operating environment of the wind turbine is harsh, and the turbine is easily affected by sand, rain, snow, and freezing. In addition, the instability of wind speed and wind direction makes the wind turbine run in an alternating load state for a long time, which is easy to cause damage to the gearbox. When the damage reaches a certain level, various faults and even safety accidents may occur. Typical fault types of gearboxes are shown in Table 1.

Table 1. Gearbox typical faults and their characteristic performance

Fault type	Reason description	Measurement features
Gear damage	Hard objects or poor lubrication lead to abnormal tooth surface wear	Gearbox oil temperature is too high
Gearbox main bearing damage	Rolling element pitting, cracks, surface spalling	Gearbox main bearing temperature is too high
Gearbox front bearing damage	Rolling element pitting, cracks, surface spalling	Gearbox front bearing temperature is too high
Gearbox rear bearing damage	Rolling element pitting, cracks, surface spalling	Gearbox rear bearing temperature is too high
Gearbox oil pump overload	Gear oil is viscous due to low gear oil temperature	Gearbox oil temperature is too low
Gearbox oil overheat	Insufficient gearbox lubrication, damaged fans, poor rotation of components	Gearbox oil temperature is too high
Low gear oil level	Oil level switch damage, gear oil viscosity, oil leakage	Gearbox oil level is too low

The gearbox is in the engine room, and the health state of the gearbox is generally checked by manual regular inspection, vibration analysis and oil detection. It will cause problems such as slight hidden dangers and faults which seriously threatens the safe operation of wind turbines because they are not easy to detect and found in time. It can be seen from Table 1 that the typical fault of the gearbox can be directly reflected when some monitoring values exceed the normal range, so the health status of the fan gearbox can be reflected through the analysis of these quantities. At the same time, because the wind turbine system is a whole, so the monitoring quantity of the wind turbine will change to some extent during the progressive evolution of gearbox damage. If the future health parameters of the gearbox can be predicted according to the monitoring quantities of the wind turbine at the early stage of the gearbox damage evolution, it can be prevented in time before the gearbox damage causes serious consequences [23, 24]. In this paper, the gearbox oil temperature, gearbox main bearing temperature, front bearing temperature,

rear bearing temperature and gearbox oil level are used as the health parameters of the gearbox, and a health state prediction model based on deep learning is established.

3   Data Preprocessing

3.1   Wind Turbine Operation Data Collection

The wind turbine is equipped with a large number of sensors to monitor the operation of the wind turbine, and the sensing data of the entire wind farm is collected and stored through the SCADA system. The main functions of a wind farm SCADA system include:

(1)   Real-time monitoring function
       The SCADA system can monitor wind turbine active power, reactive power, voltage, current, temperature, wind speed, wind direction, yaw start state, motor operation and other signals in real time.
(2)   Alarm function
       When the main control system of the wind turbine unit detects a fault in a certain part of the unit, it will synchronously transmit it to the SCADA system, display the failure of the unit, list the content, type and time of the alarm point, and issue an alarm.
(3)   Fault diagnosis function
       The SCADA system can locate and diagnose the faults and alarms of wind turbines according to the alarm information, it also can provide auxiliary decision-making information and make statistics on the faults.
(4)   Database function
       The SCADA system can store the collected wind turbine operational data to the server database for data statistics, storage and report.

In this paper, the measurement data of 15 wind turbines are obtained from the SCADA system of a wind farm. Each wind turbine is equipped with 85 sensors, and 85 characteristic quantities can be obtained. The data collection time was from February 2016 to October 2018, the sampling period was 1 min, and the characteristic data totaled about 180,000 sets. Each set of data includes the measurement values of 85 sensors of 15 wind turbines in a time section. First, the abnormal data whose measured values are outside the normal range are screened, and the entire set of data at the corresponding sampling time is eliminated, and the remaining data can be retained as valid data sets. Then, the correlation analysis is performed on the filtered valid data, and the feature quantities with high correlation are decreased [31, 32].

3.2   A Subsection Sample

Feature correlation analysis plays an extremely important role in dimensionality decreasing of sample data, and it is one of the key technologies for sample data pre-processing in machine learning [16, 33].

Pearson coefficient method [34] is a common method for data correlation analysis, but this method requires sample data which is obtained in pairs from normal distribution and approximate to standard normal distribution, and the data should be equidistant within the logical range. However, wind turbine data does not fully meet these requirements. Therefore, this paper adopts the Spearman correlation coefficient method to analyze the correlation of wind turbine data. The Spearman correlation coefficient is used to estimate the correlation between two variables, and the variable correlation can be described by a monotonic function. If the value sets of the two variables do not have the same elements, when one of the variables can be expressed as a monotonic function of the other variable (both variables have the same change trend), the coefficient between the two variables can reach $+1$ or -1. The Spearman correlation analysis equation can be defined as:

$$\rho = \frac{\sum_i (a_i - \bar{a})\left(b_i - \bar{b}\right)}{\sqrt{\sum_i (a_i - \bar{a})^2 \sum_i \left(b_i - \bar{b}\right)^2}} \tag{1}$$

In addition to the four characteristic quantities of gearbox oil temperature, main bearing temperature, front bearing temperature, rear bearing temperature and gearbox oil level, correlation analysis is carried out on the collected data of other characteristic quantities, and the Spearman correlation coefficient greater than the threshold value is discarded. In this paper, when the threshold value is 0.95, the feature dimension of wind power monitoring data can be decreased from 85 to 28. The decreased feature quantities are listed in Table 2. Spearman heat map analysis was performed on the reduced feature quantity. The results are shown in Fig. 1. The chromaticity of each small square indicates the strength of the correlation between the two variables. The heavier the color is, the higher the correlation is between the two variables. The diagonal line is the self-correlation of the characteristic quantity, and the color is the heaviest. As can be seen from Fig. 1, the color of the cross-correlation block is lighter, which indicates that the cross-correlation of the characteristic quantity after decreasing is lower, and the decreasing effect is better.
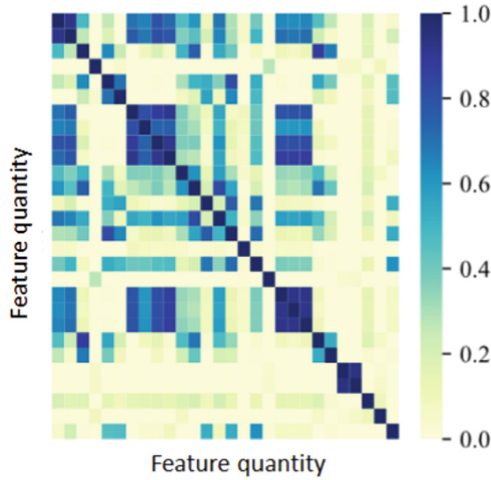
Fig. 1. Spearman parameter heatmap

3.3 Generation of Model Training Samples

The generation process of the model training samples is shown in Fig. 2. The interval set is 5 min between adjacent vectors in the reduced data, and 12-h vectors (v_1, v_13,… v_145) are continuously extracted, and each interval is 1 h to form a training set feature vector. The training set target vector dimension is 336. The target vector selects the target vector (T_2881…) which is after 10 days as the corresponding training set target vector.
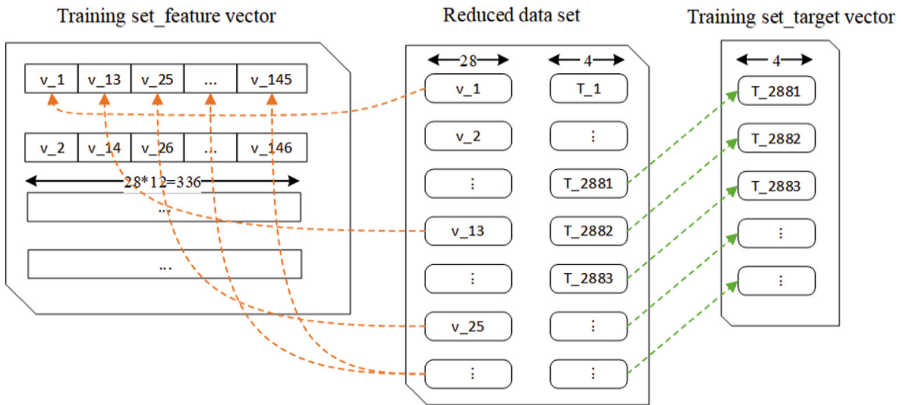
Fig. 2. Model training sample generation graph

Table 2. Gearbox typical faults and their characteristic performance

Variable	Feature name	Unit	Mean	Minimum	Maximum
cvet_wit	Cabin air inlet temperature	°C	30.5	−18.0	82.0
cvet_git	Generator air inlet temperature	°C	28.4	−40.0	69.2
cvet_grs	Generator speed	r/min	984.4	−40.8	1770.2
cvet_orp	Generator export active power	kW	−15.4	−700.9	699.3
cvet_cgc	Grid side current	A	373.5	0.0	1977.3
cvet_cgv	Grid side voltage	V	501.2	0.0	766.0
evmt_cbit	Cabin temperature	°C	20.0	−13.8	46.0
evmt_cbbit	Temperature inside the cabin cabinet	°C	28.4	0.0	44.1
evmt_tbbit	Tower footing temperature	°C	25.5	0.0	850.0
evmt_hubt	Hub temperature	°C	19.1	−40.0	43.0
gbox_oilit	Gearbox inlet oil temperature	°C	43.2	−7.7	70.9
gert_cu1t	Engine room generator coil temperature	°C	66.0	−3.3	136.4
gert_cci1t	Water cooling inlet temperature	°C	29.4	−7.1	79.5
gert_ccot	Water cooling outlet temperature	°C	46.1	−6.9	91.6
gert_slprt	Engine room generator slip ring temperature	°C	42.3	−9.6	104.4
hydr_oilp	Hydraulic station oil pressure detection	bar	150.5	0.0	167.6
hydr_oilt	Hydraulic station oil temperature	°C	15.8	−10.9	44.1
pith_r1p	Axis 1 pitch angle	°	24.5	−238.0	181.7
pith_r1bbt	Axis 1 backup power cabinet temperature	°C	28.4	−40.0	45.0
pith_r2bbt	Axis 2 backup power cabinet temperature	°C	27.8	−40.0	45.0
pith_r3bbt	Axis 3 backup power cabinet temperature	°C	27.6	−40.0	45.0
pith_r1gc	Pitch shaft motor current	A	2.6	0.0	21.7
wind_spd1	Cabin wind speed	m/s	6.1	0.0	33.2

(*continued*)

Table 2. (*continued*)

Variable	Feature name	Unit	Mean	Minimum	Maximum
wind_dir1	Cabin wind direction 1	°	176.2	0.0	359.3
wind_dir2	Cabin wind direction 2	°	171.4	0.0	359.0
yaw_yawp	Yaw position	°	−175.1	−880.2	634.9
yaw_dirp	Wind direction deviation	°	69.0	−179.2	358.6
stat_gfan1n	Number of generator fan starts	n	968.8	0.0	2141.0

4 Gearbox State Prediction Model Algorithm and Model Realization

4.1 ConvLSTM Model and Algorithm Description

The structure of the ConvLSTM model is shown in Fig. 3, and the model algorithm is shown in Eq. (2):

$$
\begin{cases}
i(t) = \sigma(W_{h(t-1)} * h_{t-1} + W_{xt} * x_t + b_i) \\
f(t) = \sigma((W_{hf} * h_{t-1} + W_{xf} * x_t + b_f) \\
c\prime(t) = \tanh(W_{hc\prime} * h_{t-1} + W_{xc\prime} * x_t + b_c) \\
c(t) = f(t) \cdot c(t-1) + i(t) \cdot c\prime(t) \\
o(t) = \sigma(W_o * h_{t-1} + W_{xo} * x_t + b_h) \\
h(t) = \tanh[c(t) \cdot o(t)])
\end{cases}
\tag{2}
$$

where $i(t)$ is the input gate, $f(t)$ is the forgetting gate, $o(t)$ is the output gate, $c(t)$ is the memory unit state, $h(t)$ is the memory unit output, Σ is the sigmoid activation function, and * is the convolution operation. In this model, a LeakyReLU activation function is added after the ConvLSTM exit $h(t)$, so that the output value $h(t)$ of ConvLSTM can be segmented and mapped as in Eq. (3) LeakyReLU serves to speed up the model training and avoid the gradient disappearance by the σ function.

$$
Y(t) = \begin{cases}
h(t) & h(t) > 0 \\
\alpha h(t) & h(t) \leq 0, \alpha \in (0, 1)
\end{cases}
\tag{3}
$$

where α is the default value usually set to 0.02.

For the error back-propagation of the ConvLSTM unit, we do it by stage-wise forward propagation of the gradients $\delta(h)$ and $\delta(c)$ of $h(t)$ and $c(t)$. The loss function $L(t)$ consists of $L(t-1)$ and $L(t)$. Among them, the gradient of $\delta(h)$ is composed of the output gradient error of the current layer at time t and the error of the previous time $t-1$, namely:

$$
\begin{aligned}
\delta(h)(t) &= \frac{\partial L}{\partial h(t)} \\
&= \frac{\partial l(t)}{\partial h(t)} + \left(\frac{\partial h(t-1)}{\partial h(t)}\right)^T \frac{\partial L(t-1)}{\partial h(t-1)}
\end{aligned}
\tag{4}
$$

The gradient of $\delta(c)$ is also composed of the output gradient error of the current layer at time t and the error of the previous layer at time t − 1, namely:

$$\delta(c)(t) = \frac{\partial L}{\partial c(t)}$$

$$= \left(\frac{\partial c(t-1)}{\partial c(t)}\right)^T \frac{\partial L(t-1)}{\partial c(t-1)} + \left(\frac{\partial h(t)}{\partial c(t)}\right)^T \frac{\partial L(t)}{\partial h(t)} \tag{5}$$

The gradient of the weight $W(h)$ is calculated as:

$$\frac{\partial L}{\partial Wf(t)} = \sum_1^t \left[\partial C(t) \odot C(t-1) \odot f(t) \odot (1-f(t))\right] h(t-1)^T \tag{6}$$
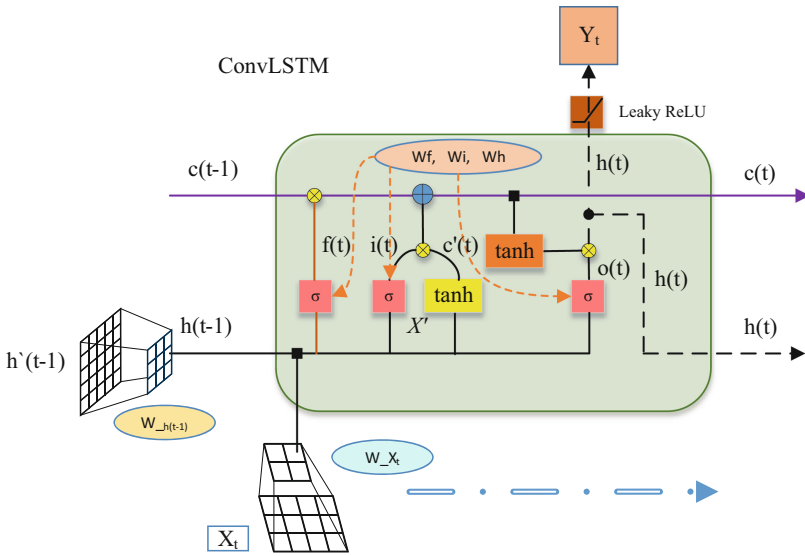
Fig. 3. ConvLSTM algorithm process

4.2   Implementation of State Prediction Network Model

To achieve the prediction goal, the prediction network shown in Fig. 5 is proposed in this paper. The prediction network consists of 3 layers of neural network, namely ConvLSTM layer, convolutional neural network layer (Conv_3D) and fully connected layer (FC). The ConvLSTM layer network is responsible for incorporating the temporal characteristics between feature vectors in training, the convolutional neural network is responsible for extracting the reinforcement vector features, and the fully connected layer is responsible for fitting the extracted features. Each batch of training is fed with k temporal data simultaneously, forming an m*1-dimensional tensor. After the ConvLSTM network,

ConvLSTM replaces the one-dimensional tensors with a spatial, temporal, and numerical three-dimensional tensors and integrates a convolution operation in the transformation of the input Xt to the state ht-1 and the state ht-1 to the state Ct-1. This operation can add time series to the vector features, which strengthens the temporal connection between the features and helps to improve the model fitting accuracy.

Figure 5 details the parameter setting of the model and the working process of the data flow. The data "D" is transformed through the Reshape layer and the data dimension change from [None, 336] to [None, 1, 12, 28, 1]. After the ConvLSTM layer, the data dimension change to [None, 11, 27, 20]. After the ConvLSTM layer, a batch regularization BN layer is used to speed up the training and convergence of the network and to control the gradient explosion to prevent gradient disappearance and overfitting. After the BN layer, it enters the Conv_1_1D convolution layer number of convolution kernel channels of 20, a step size of 1, a kernel is (2×2), and a convolution dimension of [None, 10, 26, 20]. The convolutional layer Conv_1_1D extracts the feature vector and extends the feature channels from 1 to 20 channels. Maxpooling and Dropout layers are added between Conv_1_1D and Conv_2_1D. Maxpooling layer can retain the main features while reducing the parameters and computation, preventing overfitting and improving the model generalization ability. The Dropout layer randomly abandons some neurons during training, and each batch of training nodes is randomly selected to avoid overfitting. After the data passes through the Conv_2_1D layer, the dimension becomes [None, 4, 12, 10]. After activation by the Leaky RuLU layer, the dimensionality becomes [None, 480] by the Flatten layer. The flattened data can be directly connected to the fully connected layer, through the Dense_1 to Dense_3 fully connected layers with dimensions [None, 2000], [None, 2000] and [None, 1] in that order. The fully connected layers have redundant parameters, which can fully map the "distributed features" extracted from the convolutional layer to the network space and enhance the representation capability of the model. It also prepares the output target for the dimension matching transformation. Finally, the data reaches the output layer. The model uses four single-target prediction models to form the entire prediction system, and the four single-target models correspond to the four state parameters of the gearbox for prediction. Target_1 represents "Cabinet Gearbox Oil Temperature", Target_2 represents "Gearbox Low Speed Bearing Temperature", Target_3 represents "Gearbox High Speed Bearing Temperature" and Target_4 represents "Gearbox Side Main Bearing Temperature".

Note: None is the number of single training batch vectors, and the batch set in this experiment is None = 1000.

In this paper, the coefficient of determination R2 is used as the evaluation index of the model. The closer the coefficient of determination is to 1, the higher the accuracy of the model is indicated, and the expression is:

$$R^2 = 1 - \frac{SSR}{SST} \tag{7}$$

where SST is the total sum of squares; SSR is the regression sum of squares.

4.3 Algorithm Flow

The flow of the gearbox state prediction method proposed in this paper is shown in Fig. 6, which mainly includes the following steps:

(1) Extract the wind turbines historical data from the SCADA system to form the initial data set.
(2) Preprocess the initial data set. Each input vector of the processed data set is a continuous 12 h wind turbine state volume, and the target prediction value is the wind turbine gearbox state after 10 days.
(3) Construct ConvLSTM prediction network model to fit training to the 4 prediction targets respectively. Determine the data forward transmission path, start to calculate the loss function loss value, update the weight and bias of each network layer, calculate the loss and reverse the transmission error, and update the weight.
(4) When the model is trained in certain batches, the loss function loss curve is smoothed, and the model with the highest evaluation index R^2 is selected and saved as the final prediction network model. Figure 4 is a flow chart of dataset acquisition.
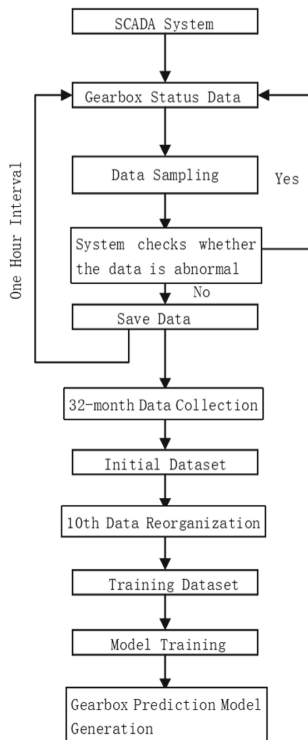
Fig. 4. Data collection flow chart

5   Experimental Results

5.1   Algorithm Flow

This paper involves models and their comparisons all done on the same computer. The computer configuration and simulation environment are as follows: Win64, Intel i7-11700K, DDR4-3200-32GB, RTX-3080Ti (10 GB), Python3.6, Keras 2.2.4. In addition to the models involved in the proposed method, single hidden layer feedforward neural network (SLF), support vector machine regression model (SVR), random forest (RF), convolutional neural network (CNN) and long-short memory neural network (LSTM) are chosed as control models.
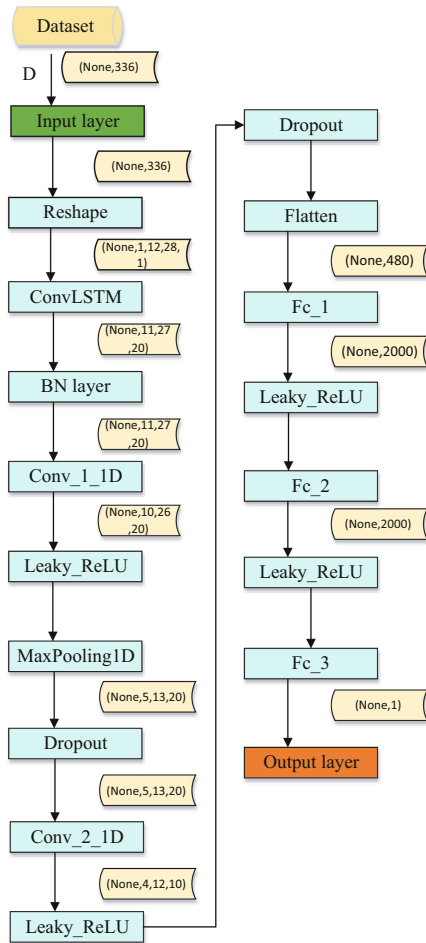
Fig. 5. Proposed model structure diagram

5.2 Model Prediction Accuracy

Table 3 shows the R2 scores of the performance of the models in the experiment. In the prediction score of "Cabinet Gearbox Oil Pressure", the R2 value of the SLF model is the lowest (0.69), the RF is the highest (0.82), and the ConvLSTM is (0.81). The ConvLSTM model score is only 1.2% lower than the highest value. In the prediction of "gearbox low speed bearing temperature", the SVR model has the lowest R2 value (0.74) and the ConvLSTM model has the highest score (0.85), which is 3.7% higher than the CNN model. In the prediction of "gearbox high-speed bearing temperature", the SLF model has the lowest R2 value (0.75) and the ConvLSTM model has the highest score (0.84), which is 2.4% higher than the CNN model score; in the prediction of "gearbox side main bearing temperature", the SLF model has the lowest R value (0.66), SVR is the highest (0.82), and ConvLSTM is (0.81). The ConvLSTM model scored 1.2% lower than the top value.
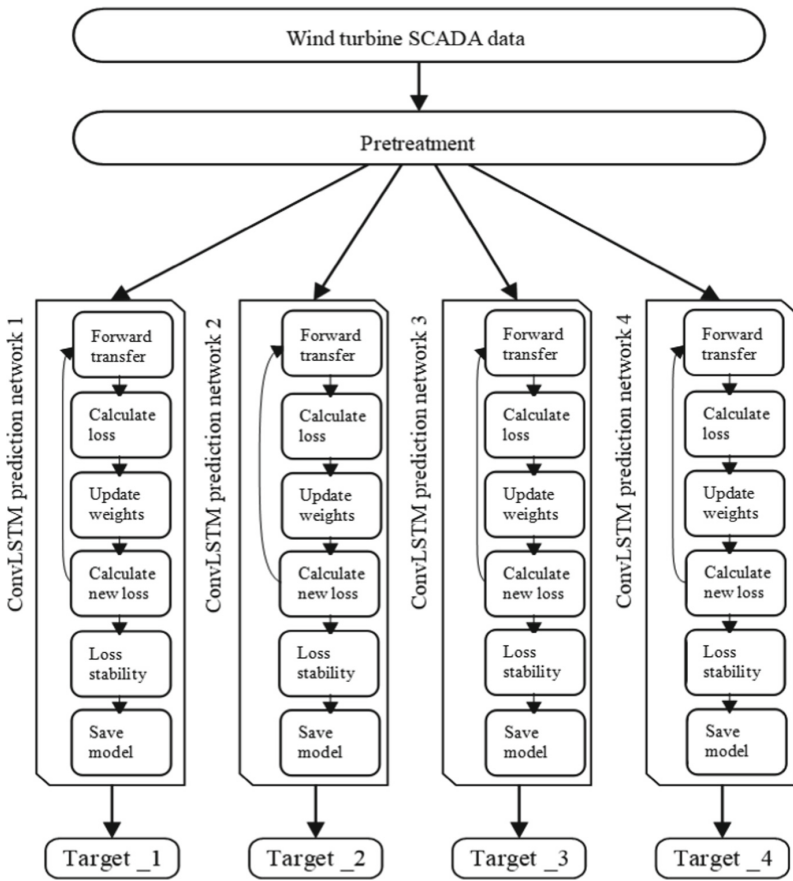
Fig. 6. Model algorithm flow chart

Among the total R^2 values of each model, the SLF model has the lowest value of 2.87, the SVR and RF have the same value of 3.10, the CNN model value has a value of 3.11, and the LSTM model value has a value of 3.07. The proposed ConvLSTM model has a value of 3.31 and obtains the highest score, exceeding the SLF model by 15.3% and the CNN model in second place by 6.4%. Although the proposed model does not have the highest score for every objective, it maintains a high score in every predicted objective calculation. The prediction synthesis is strong and can cope with different prediction data distributions.

Table 3. Comparison of the fitting performance of the models (R^2)

Model	Target_1	Target_2	Target_3	Target_4	Total
SLF	0.69	0.77	0.75	0.66	2.87
SVR	0.76	0.74	0.78	0.82	3.10
RF	0.82	0.77	0.79	0.72	3.10
CNN	0.72	0.83	0.82	0.74	3.11
LSTM	0.78	0.73	0.79	0.77	3.07
ConvLSTM	0.81	0.85	0.84	0.81	3.31

Table 4. Models training time

Model	Time consuming (min)
SLF	22.78
SVR	710.49
RF	1083.58
CNN	382.15
LSTM	239.66
ConvLSTM	760.54

5.3 Model Training Time

The training time of a model is also an important metric for model performance evaluation. The training time directly determines whether the model can be widely used. The training time statistics of each model are shown in Table 4. SLF has the simplest structure with only 3 layers and the shortest training time of 22.78 min. CNN and LSTM follow with 382.15 and 239.66 min, respectively.

Compared with the first three models, the models of SVR and RF are time-consuming. 710.49 min for the SVR model and 1083.58 min for the RF model. When the sample

size is small (less than 1000 samples) and the number of feature dimensions is less than 20, the accuracy of SVR and RF is higher and less time-consuming.

As the sample size (more than 28,000 samples for a single wind turbine) and the amount of data features increases, the training elapsed time for SVR and RF increases exponentially, but the accuracy does not improve significantly. The time complexity of SVR itself is proportional to the vector product of the sample size and the number of features. The time complexity of SVR is $O((s * k * \log s)^m)$, where s is the number of samples, k is the number of features, and m is the number of predicted targets. In the case of large amount of data, number of features and multiple targets, the training time of SVR is geometrically doubled. Random forest RF sets w search trees with similar complexity as SVR $O((s * k * \log s)^m)$. The computational work of SVR and RF is all done by CPU, which is lower than the deep neural network algorithm done by CPU and GPU. The model complexity of SVR and RF are exponentially related, and the training time consuming of complex models increases exponentially. SVR and RF are not optional algorithms when dealing with big data, high-latitude features, and multi-object prediction tasks.

The time complexity of the deep neural network model is $O(\sum_{i=1}^{D} (M_i^2 * K_i^2 * C_{i-1} * C_i))$. M is the complexity of the single network model, K is the convolution scale, and C is the number of convolution channels. The network depth of the ConvLSTM model exceeds that of the CNN and LSTM models, and the entire training time takes 760.54 min. The time complexity of the ConvLSTM model is a cumulative relationship in terms of the number of predicted targets. In large data volume, multi-feature variables and multi-objective tasks, the time complexity of the cumulative growth is lower than exponential and is more likely to be widely used.

6 Conclusion

In this article, a forecasting method which uses the ConvLSTM neural network for wind turbine gearbox health prediction was established and trained with the real data obtained from wind farm SCADA. The final prediction model can accurately predict the gearbox state parameters for the next 10 days using 12 h of sampled data. The experimental results show that the ConvLSTM model is 15.3% more accurate than the classic SLF model, 6.8% higher than the SVR and RF models, and 7.8% and 6.4% higher than the LSTM and CNN models, respectively. The ConvLSTM model is particularly suitable for wind turbine data prediction tasks with time-series characteristics and has the advantages of high accuracy, controllable time consumption and high efficiency.

References

1. Liu, J., Ma, L., Wang, Q., et al.: Offshore wind power supports China's energy transition. Strateg. Study CAE **23**(01), 149–159 (2021)
2. Li, H., Liu, D., Yao, D.: Analysis and reflection on the development of power system towards the goal of carbon emission peak and carbon neutrality. Proc. CSEE **41**(18), 6245–6259 (2021)
3. Liang, Y., Fang, R.: An online wind turbine condition assessment method based on SCADA and support vector regression. Automat. Electr. Power Syst. **37**(14), 7–12 (2013)

4. Li, Z., Liu, J.: Ultra-short-term wind speed prediction based on GA and LSSVM in wind farm. Electr. Eng. **13**, 56–59+66 (2021)
5. Li, D., Liu, Y., Zhao, Y., et al.: Fault diagnosis method of wind turbine planetary gearbox based on improved generative adversarial network. Process. CSEE **41**(21), 7496–7507 (2021)
6. Chen, H., Jing, S., Wang, X., et al.: Fault diagnosis of wind turbine gearbox based on wavelet neural network. J. Low Freq. Noise Vibrat. Active Control **37**(04), 977–986 (2019)
7. Wang, G., Zhao, H., Guo, S., et al.: Numeric optimal sensor configuration solutions for wind turbine gearbox based on structure analysis. IET Renew. Power Gener. **11**(12), 1597–1602 (2017)
8. Sequeira, C., Pacheco, A., Galego, P., et al.: Analysis of the efficiency of wind turbine gearboxes using the temperature variable. Renew. Energy **135**(05), 465–472 (2018)
9. Teng, W., Xian, D., Hao, C., et al.: Compound faults diagnosis and analysis for a wind turbine gearbox via a novel vibration model and empirical wavelet transform. Renew. Energy **136**, 393–402 (2019)
10. Wang, H., Wang, Y., Wang, S., et al.: High and low voltage ride through control strategy for DFIG wind power system based on variable dynamic voltage command value. High Volt. Eng. 1–11 (2021)
11. Dao, P.B., Staszewski, W.J., Barszcz, T., et al.: Condition monitoring and fault detection in wind turbines based on cointegration analysis of SCADA data. Renew. Energy S0960148117305931 (2018)
12. Huang, R., Tang, B., Yang, Y., et al.: Condition monitoring of wind turbine gearbox based on LSTM neural network fusing SCADA data. Acta Energ. Solar. Sinica **42**(01), 235–239 (2021)
13. Xu, S., Wu, W., Zhu, T., et al.: Convex relaxation based iterative solution method for stochastic dynamic economic dispatch with chance constrains. Automat. Electr. Power Syst. **44**(17), 43–51 (2020)
14. Sequeira, C., Pacheco, A., Galego, P., et al.: Analysis of the efficiency of wind turbine gearboxes using the temperature variable. Renew. Energy **135**, 465–472 (2018)
15. Chen, B., Zappalá, D., Crabtree, C.J., et al.: Survey of commercially available SCADA data analysis tools for wind turbine health monitoring. Durham University School of Engineering & Computing Sciences (2014)
16. Wang, Y., Ma, X., Qian, P.: Wind turbine fault detection and identification through PCA-based optimal variable selection. IEEE Trans. Sustain. Energy **9**(4), 1627–1635 (2019)
17. Yang, W., Tavner, P.J., Crabtree, C.J., et al.: Wind turbine condition monitoring: Technical and commercial challenges. Wind Energy **17**(5), 673–693 (2014)
18. Cao, M., Qiu, Y., Feng, Y., et al.: Study of wind turbine fault diagnosis based on unscented Kalman Filter and SCADA Data. Energies 9(10) (2016)
19. Ding, X., Han, N., Teng, W.: Fault identification of direct drive wind turbine based on deep learning. Renew. Energy Resour. **36**(10), 1535–1540 (2018)
20. Yang, Y., Liu, A.X., Hong, W., et al.: Fault early warning of wind turbine gearbox based on multi-input support vector regression and improved ant lion optimization. Wind Energy **24**(08), 812–832 (2021)
21. Zhang, Y., Liu, Y., Mu, Y.: Distributed model predictive control of wind-solar hybrid power generation system. Control Eng. China **28**(03), 501–509 (2021)
22. Liu, X., Wang, Y., Ji, Z.: Short-term wind power prediction method based on random forest. J. Syst. Simulat. 1–10 (2021)
23. Shang, Q., Sun, M.: Optimal dispatching of power grid based on wind power and heat storage heating system. Acta Energ. Solar. Sinica **42**(07), 65–70 (2021)
24. Li, W., Zang, C., Liu, D., et al.: Electric and heating combined system dispatch based on multi-objective and two-stage stochastic programming method. Inf. Control 1–12 (2021)

25. Trifa, A., Sbai, A.H., Chaari, W.L.: Enhancing assessment of personalized multi-agent system through ConvLSTM. Procedia Comput. Sci. **112**, 249–259 (2017)
26. Yao, W., Huang, P., Yao, J., et al.: A FRS-CLSTM wind speed prediction model based on deep learning. Acta Energ. Solar. Sinica **41**(09), 324–330 (2020)
27. Yang, Y., Dong, J., Sun, X., et al.: A CFCC-LSTM model for sea surface temperature prediction. IEEE Geosci. Remote Sens. Lett. **15**(2), 207–211 (2017)
28. Xingjian, S.H.I., Chen, Z., Wang, H., et al.: Convolutional LSTM network: A machine learning approach for precipitation nowcasting. Adv. Neural Inf. Process. Syst. 802–810 (2015)
29. Chen, H., Zhou, Y., Wang, C., et al.: Economic analysis of spinning reserve system based on improved CNN-LSTM short term wind power prediction. High Volt. Eng. 1–11 (2021)
30. Ding, X., Xu, J., Tang, H., et al.: Typical fault feature extraction method of wind turbine gearing chain. Renew. Energy Resour. **38**(03), 319–325 (2020)
31. Zheng, Y., Sun, C., Li, J., et al.: Association rule analysis on confidence of features for transformer faults. High Volt. Eng. **38**(01), 82–88 (2012)
32. Miao, J., Xie, D., Wang, X., et al.: Correlation analysis between oscillation mode and impact factor of doubly-fed induction generator. Proc. CSEE **39**(17), 5049–5060+5286 (2019)
33. Han, Y., Li, T.: Online prediction of short-term wind speed and power generation based on phase space reconstruction. Control Eng. China **26**(08), 1503–1508 (2019)
34. Almasi, M., Saniee Abadeh, M.: A new MapReduce associative classifier based on a new storage format for large-scale imbalanced data. Clust. Comput. **21**(4), 1821–1847 (2018). https://doi.org/10.1007/s10586-018-2812-9

Integrated Energy System Expansion Planning Considering Concentrating Solar Power Plants

Xingquan Ji[1], Kaixuan Wang[1], Yumin Zhang[1(✉)], Xingshang Bai[2], Yingye Zhu[1], and Xiaohu Liu[1]

[1] College of Electrical Engineering and Automation, Shandong University of Science and Technology, Qingdao 266590, China
ymzhang2019@sdust.edu.cn

[2] Daguan Reservoir Operation and Maintenance Center of Linqu, Shandong 262614, China

Abstract. The flexible and controllable output of concentrating solar power plants can improve the economy and reliability of system operation. To this end, a comprehensive energy system expansion planning method that takes into account concentrating solar power plants is proposed. Firstly, the model of concentrating solar power plant is established according to the energy conversion characteristics of concentrating solar power plants; then, the integrated energy system expansion planning model of concentrating solar power plant is proposed considering the costs of system investment, operation, wind abandonment and power shortage; finally, the IEEE14-NGS14 system is used to verify the effectiveness of the proposed model. The results show that the concentrating solar power plants can reduce the system costs, which is important for improving the wind power consumption and energy utilization of the integrated energy system.

Keywords: Concentrating solar power plants · Integrated energy system · Economics

1 Introduction

In recent years, China's economy has been developing rapidly, but the accompanying serious environmental pollution and energy crisis problems have to draw the attention of human beings. In order to achieve sustainable development, countries all over the world are actively engaged in energy transformation [1]. In this process, concentrating solar power (CSP) plants have received wide attention from domestic and foreign experts and scholars because of their high energy efficiency and cleanliness [2]. In [3], an intraday scheduling model is proposed, which combines CSP plants with thermal storage and biomass power plants that maximizes the environmental benefits brought by concentrating solar power plants. In [4], photovoltaic generation and CSP plant is combined to study the operation of photothermal power plants in power systems with high penetration of renewable energy. In [5], a strategy is proposed to replace the peaking of thermal power units with CSP plants. By comparing the economic parameters under different

strategies, the optimal installed ratio of different power is derived. In [6], a stochastic planning model with transmission lines, CSP plants, wind farms and gas turbines is proposed. The model investigates the short-term uncertainty of solar and wind energy. In [7], a scenario-based stochastic framework for optimal scheduling of CSP plants under market price uncertainty is proposed to obtain the optimal output curve. In [8], a day-ahead dispatching strategy that combines a concentrating solar power plant with some responsive residential and industrial loads is proposed to consider the uncertainty of electricity prices and concentrating solar power plant generation. In [9], a profit-sharing mechanism is proposed, which combines a concentrating solar power plant and a wind farm with the aim of maximizing the market day-ahead revenue.

Regarding the study of integrated energy system planning, the key technologies for integrated low-carbon energy system planning are summarized in [10], and the integrated carbon capture technologies and cross-region level integrated low-carbon energy system planning approaches are also discussed. In [11], an optimal capacity planning of integrated energy systems through the coordination and complementarity of multiple energy sources is performed to achieve the optimal utilization of resources under limited financial constraints. In [12], a multi-objective robust planning model for integrated energy systems is proposed with the minimum fuel cost, wind power abandonment and end-user-side peak-valley load variance as the objective functions. In [13], considering the impact of wind power uncertainty on integrated energy system planning, the variation of each cost of the system under different wind power penetration rates is investigated.

In summary, although the above-mentioned literature has studied the model of concentrating solar power plants and the stochastic nature of market operation, it has not been applied to the integrated energy system to study the impact of concentrating solar power plants on the integrated energy system planning, and for this reason, this paper proposes an integrated energy system expansion planning method that takes into account the concentrating solar power plants. Firstly, the model of concentrating solar power plant is established, and then the IES expansion optimization planning model is established with the objective of minimizing the sum of the costs of system investment, operation, wind abandonment and power shortage; finally, the IEEE14-NGS14 algorithm system is analyzed and verified, and the results show the effectiveness of the proposed model.

2   IES Structure

The basic structure of IES is shown in Fig. 1.

On the supply side, most of the electricity required by IES is provided by the grid and wind farms, while the natural gas network is mainly responsible for the natural gas energy required by IES. On the energy coupling side, power to gas (PTG) equipment converts electrical energy into natural gas energy to improve the system's capacity to consume new energy; combined heat and power (CHP) equipment consumes natural gas energy in the system and generates electrical and thermal energy to maximize energy utilization efficiency; gas boilers consume natural gas energy and generate thermal energy. On the energy demand side, the electric load provides electricity for customers, while the gas load and heat load mainly provide natural gas and heat energy for customers.

IES can also be regarded as an energy center where energy is produced, transmitted, stored and consumed, which can effectively improve the efficiency and flexibility of integrated energy system supply.
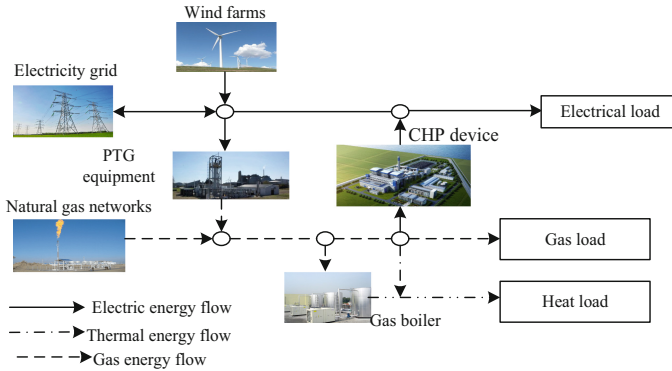
Fig. 1. IES basic structure

3   Concentrating Solar Power Plants Model

The main structure and energy flow of a concentrating solar power plant is shown in Fig. 2. The concentrating solar power plant is mainly composed of four parts: light field, heat storage system, heat transfer fluid and power generation system. The light field collects sunlight and converts it into heat energy to the heat transfer fluid; part of the heat energy in the heat transfer fluid is balanced with the heat storage system, and the other part is converted into electricity to the power generation system; the power generation system transmits the remaining electricity to the grid.
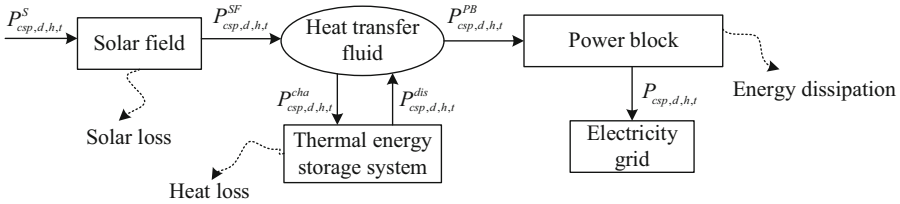
Fig. 2. Main structure and energy flow of CSPP

The power balance inside the concentrating solar power plant is shown in Eqs. (1)–Eq. (4).

$$P^{SF}_{csp,d,h,t} = \eta_{s-th} u_{csp,d,h,t} P^{S}_{csp,d,h,t} \tag{1}$$

$$P^{SF}_{csp,d,h,t} - P^{PB}_{csp,d,h,t} - P^{cha}_{csp,d,h,t} + P^{dis}_{csp,d,h,t} = 0 \tag{2}$$

$$P^{SC}_{csp,d,h,t} = (1 - u_{csp,d,h,t})\eta_{s-th}P^{S}_{csp,d,h,t} \tag{3}$$

$$P_{csp,d,h,t} = \eta_{th-p}P^{PB}_{csp,d,h,t} \tag{4}$$

where, $P^{SF}_{csp,d,h,t}$ is the original solar radiation, η_{s-th} is the solar thermal conversion efficiency, $u_{csp,d,h,t}$ is a random variable between 0 and 1, $P^{S}_{csp,d,h,t}$ is the thermal power after conversion. $P^{PB}_{csp,d,h,t}$ is the thermal power delivered by the heat transfer fluid to the power generation system at time t, $P^{cha}_{csp,d,h,t}$ and $P^{dis}_{csp,d,h,t}$ are the heat storage and heat release power of the heat storage system at time t. η_{th-p} is the solar thermal conversion efficiency, $P_{csp,d,h,t}$ is the electrical power output of the concentrating solar power plant at time t.

The energy equation related to the heat transfer fluid is:

$$E^{TESS}_{csp,d,h,t} = E^{TESS}_{csp,d,h,t-1}(1 - \gamma_{tess}) + \eta_{cha}P^{cha}_{csp,d,h,t} - P^{dis}_{csp,d,h,t}/\eta_{dis} \tag{5}$$

$$E^{TESS}_{\min} \le E^{TESS}_{csp,d,h,t} \le E^{TESS}_{\max} \tag{6}$$

$$0 \le P^{cha}_{csp,d,h,t} \le x^{storage}_{csp,d,h,t}P^{cha}_{\max} \tag{7}$$

$$0 \le P^{dis}_{csp,d,h,t} \le \left(1 - x^{storage}_{csp,d,h,t}\right)P^{dis}_{\max} \tag{8}$$

where, $E^{TESS}_{csp,d,h,t}$ is the thermal energy stored in thermal energy storage system(TESS) at time t, $E^{TESS}_{\min}$ is the minimum amount of heat storage to prevent the molten salt from solidifying, $E^{TESS}_{\max}$ is the maximum amount of heat storage to prevent the molten salt from overheating, $x^{storage}_{csp,d,h,t}$ is the heat storage and discharge state of the heat storage device, 1 indicates heat storage and 0 indicates heat discharge; $P^{cha}_{\max}$ and $P^{dis}_{\max}$ indicate the maximum heat storage and discharge power of the heat storage device, respectively, γ_{tess} is the heat dissipation coefficient, η_{cha} and η_{dis} indicate the heat storage and discharge efficiency, respectively.

4 Integrated Energy System Expansion Planning Model for Concentrating Solar Power Plants

4.1 Objective Function

The objective function of IES expansion planning for concentrating solar power plants is to minimize the total cost of the planning scheme, including investment cost, operation cost, power shortage cost, wind abandonment cost, light field operation and maintenance cost, heat storage system operation and maintenance cost, light abandonment cost, and the resulting environmental benefits, expressed as:

$$\min Z = \sum_{t=1}^{T} \lambda_t \left((1 - \gamma \frac{\lambda_T}{\lambda_t}) C_{inv}(t) + C_{op}(t) + C_{eens}(t) + C_w(t) \right)$$

$$+ \sum_{t=1}^{T} \lambda_t \left(C_{sc}(t) + C_{sf}(t) + C_{tes}(t) - C_{hy}(t) \right) \tag{9}$$

where, Z is the total planning cost; $C_{inv}(t)$ is the investment cost; $C_{op}(t)$ is the operation cost; $C_{eens}(t)$ is the power shortage cost; $C_w(t)$ is the wind abandonment cost; $C_{sc}(t)$ is the light abandonment cost; $C_{sf}(t)$ is the solar field operation and maintenance cost; $C_{tes}(t)$ is the heat storage system operation and maintenance cost; $C_{hy}(t)$ is the environmental benefit. λ_t is the present value coefficient in year t, γ is the capital recovery rate.

The investment cost is expressed as:

$$C_{inv}(t) = \sum_{i=1}^{N_i} \left(B_i P_i^{\max} \frac{1 - \varepsilon_i}{M_i} (T - T_i^c)(x_{i,t} - x_{i,t-1}) \right) + \sum_{l=1}^{N_l} \left(B_l P_l^{\max} \frac{1 - \varepsilon_l}{M_l} (T - T_l^c)(x_{l,t} - x_{l,t-1}) \right)$$

$$+ \sum_{f=1}^{N_f} \left(B_f P_f^{\max} \frac{1 - \varepsilon_f}{M_f} (T - T_f^c)(x_{f,t} - x_{f,t-1}) \right) + \sum_{c=1}^{N_c} \left(B_c P_c^{\max} \frac{1 - \varepsilon_c}{M_c} (T - T_c^c)(x_{c,t} - x_{c,t-1}) \right)$$

$$+ \sum_{p=1}^{N_p} \left(B_p P_p^{\max} \frac{1 - \varepsilon_p}{M_p} (T - T_p^c)(x_{p,t} - x_{p,t-1}) \right) \tag{10}$$

where, N_i, N_f, N_c, N_p and N_l denote the number of conventional units, gas boilers, CHP units, PTG units and transmission lines, respectively; B_i, B_l, B_f, B_c and B_p denote the investment cost per unit capacity of conventional units, gas boilers, CHP units, PTG units and transmission lines, respectively; $x_{i,t}$, $x_{l,t}$, $x_{f,t}$, $x_{c,t}$ and $x_{p,t}$ denote the operation status of conventional units, gas boilers, CHP units, PTG units and transmission lines, respectively; $P_i^{\max}$, $P_l^{\max}$, $P_f^{\max}$, $P_c^{\max}$ and $P_p^{\max}$ denote the capacity of the above equipment, respectively; T_i^c, T_l^c, T_f^c, T_c^c and T_p^c denote the minimum operation years of the above equipment respectively. Considering that the life cycle of the equipment is usually longer than its planning life, depreciation is applied, ε_i, ε_l, ε_f, ε_c and ε_p are the net residual value ratio of the above equipment, M_i, M_l, M_f, M_c and M_p are the service life of the above equipment, respectively.

The operating costs are expressed as:

$$C_{op}(t) = \sum_{d=1}^{d_0} \sum_{h=1}^{24} \left(\sum_i^{N_i} P_{i,d,h,t} O_i + \sum_f^{N_f} H_{f,d,h,t} O_f + \sum_c^{N_c} P_{c,d,h,t} O_c + \sum_p^{N_p} P_{p,d,h,t} O_p + \sum_{gs}^{N_{gs}} S_{gs,d,h,t} O_{gs} \right) \tag{11}$$

where, N_{gs} indicates the number of natural gas sources; d_0 is the number of typical days; O_i, O_f, O_c, O_p and O_{gs} indicates the unit operating cost of conventional units, gas boilers, CHP units, PTG units and natural gas sources, respectively; $P_{i,d,h,t}$, $H_{f,d,h,t}$, $P_{c,d,h,t}$, $P_{p,d,h,t}$ and $S_{gs,d,h,t}$ indicates the output value per hour per typical day per year of the above equipment, respectively.

The cost of insufficient electricity is expressed as:

$$C_{eens}(t) = C_{eens}^0 \cdot \sum_{b=1}^{N_b} \Delta L_b(t) \qquad (12)$$

where, C_{eens}^0 and ΔL_b are the cost per unit of electrical energy deficit and the amount of electrical energy deficit for energy center b, respectively.

The cost of wind abandonment is expressed as:

$$C_w(t) = C_w^0 \sum_{b=1}^{N_b} \Delta C_b(t) \qquad (13)$$

The present value coefficient is expressed as:

$$\lambda_t = 1/(1+\tau)^{t-1} \qquad (14)$$

where, C_w^0 is the cost per unit of abandoned wind; ΔC_b is the amount of abandoned wind at energy center b; τ is the capital discount rate.

The cost of light abandonment is expressed as:

$$C_{sc}(t) = C_{sc}^0 \sum_{csp=1}^{N_{csp}} \Delta C_{csp}(t) \qquad (15)$$

The optical field operation and maintenance costs are expressed as:

$$C_{sf}(t) = \sum_{d=1}^{d_0} \sum_{h=1}^{24} OM^{SF} P_{csp,d,h,t}^{SF} \eta_{th-p} \qquad (16)$$

where, C_{sc}^0 is the unit cost of light abandonment; ΔC_{csp} is the amount of light abandoned by the concentrating solar power plant; OM^{SF} is the unit operation and maintenance cost coefficient of the solar field.

The operation and maintenance costs of the thermal storage system are:

$$C_{tes}(t) = \sum_{d=1}^{d_0} \sum_{h=1}^{24} OM^{tes} (P_{csp,d,h,t}^{out}/\eta_{dis}) \eta_{th-p} \qquad (17)$$

When operating in grid-connected operation, concentrating solar power plants are able to reduce the emission of environmental pollutants and, as a result, generate certain environmental benefits, expressed as:

$$C_{hy}(t) = \sum_{d=1}^{d_0} \sum_{h=1}^{24} \rho^{csp} P_{csp,d,h,t} \qquad (18)$$

where, OM^{tes} is the unit operation and maintenance cost coefficient of thermal storage system; ρ^{csp} is the environmental benefit coefficient of grid-connected concentrating solar power plant.

4.2 Constraints

The constraints for integrated energy system expansion planning include: equipment commissioning status constraints, operational constraints, power system constraints, thermal system constraints, and natural gas system constraints.

Equipment Commissioning Status Constraints

When the device to be commissioned is put into the integrated energy system, the commissioning status changes from 0 to 1 and remains the same in subsequent years. If the year to be commissioned is less than the minimum commissioning year of the device, the device does not participate in commissioning.

Expressed as follows:

$$x_{a,t-1} \leq x_{a,t} \quad \forall a \in i^+, l^+, f^+, c^+, p^+, \forall t \tag{19}$$

$$x_{a,t} = 0 \quad \forall a \in i^+, l^+, f^+, c^+, p^+, \forall t < T_a^c \tag{20}$$

where, i^+, l^+, f^+, c^+ and p^+ indicates the candidate devices for conventional units, transmission lines, gas boilers, CHP and PTG respectively; $x_{a,t}$ is 0–1 variable indicating the commissioning status of different devices, where 1 indicates a commissioned device, 0 indicates a device to be commissioned, T_a^c indicates the minimum commissioning year in which each device can be put into operation.

Operational Constraints

The output constraints for conventional units are:

$$P_i^{\min} x_{i,t} \leq P_{i,d,h,t} \leq P_i^{\max} x_{i,t}, i \in \{U, i^+\} \tag{21}$$

The transmission line tide constraints are:

$$\left| P_{l,d,h,t}^s \right| \leq P_l^{\max} x_{l,t}, l \in \{L, l^+\} \tag{22}$$

$$\left| P_{l,d,h,t} - B_l\left(\theta_{m,d,h,t} - \theta_{n,d,h,t}\right) \right| \leq M\left(1 - x_{l,t}\right), \forall l \in \{L, l^+\} \tag{23}$$

where, U represents the existing conventional unit, L represents the existing transmission line, l^+ represents the candidate line, $P_{l,d,h,t}$ is the transmission power of the transmission line, B_l is the line conductance, θ is the phase angle of the nodes at both ends of the line, M is a large number and is taken 10^{15} here.

The operating constraints of the gas boiler are:

$$H_f^{\min} x_{f,t} \leq H_{f,d,h,t}^s \leq H_f^{\max} x_{f,t}, \forall f \in \{F, f^+\} \tag{24}$$

$$H_{f,d,h,t} = \eta_{heat}^{furnace} G_{f,d,h,t} \tag{25}$$

where, F represents the existing gas boiler, $H_{f,d,h,t}$ represents the heat production power of the gas boiler, $G_{f,d,h,t}$ represents the gas consumption power of the gas boiler, $\eta_{heat}^{furnace}$ represents the thermal efficiency of the gas boiler.

The operational constraints of the CHP device are:

$$P_c^{\min} x_{c,t} \leq P_{c,d,h,t}^s \leq P_c^{\max} x_{c,t}, \forall c \in c^+ \tag{26}$$

$$P_{c,d,h,t} = \eta_{ele}^{CHP} G_{c,d,h,t} \tag{27}$$

$$H_{c,d,h,t} = \eta_{heat}^{CHP} G_{c,d,h,t} \tag{28}$$

where, $P_{c,d,h,t}$ and $H_{c,d,h,t}$ respectively represent the electricity and heat generation power of the CHP unit, $P_c^{\min}$ and $P_c^{\max}$ are the minimum and maximum output power of CHP unit, $G_{c,d,h,t}$ is the gas consumption power of CHP unit, η_{ele}^{CHP} and η_{heat}^{CHP} are the electrical efficiency and thermal efficiency of CHP unit, respectively.

The operating constraints of the PTG unit are:

$$G_{p,d,h,t} = \eta_p P_{p,d,h,t} \tag{29}$$

$$P_p^{\min} x_{p,t} \leq P_{p,d,h,t}^s \leq P_p^{\max} x_{p,t}, \forall p \in p^+ \tag{30}$$

where, η_p is the efficiency of the PTG, $G_{p,d,h,t}$ is the gas production power of the PTG.

Power System Constraints

The power supply and demand balance constraint equation and the wind abandonment constraint equation are as follows:

$$\Delta P_{b,d,h,t} = L_b^e + \sum_{p \in b} P_{p,d,h,t} - \sum_{c \in b} P_{c,d,h,t} - \sum_{i \in b} P_{i,d,h,t} - \sum_{r(l) \in b} P_{l,d,h,t}$$
$$+ \sum_{k(l) \in b} P_{l,d,h,t} - \sum_{csp \in b} P_{csp,d,h,t} - \sum_{w \in b} P_{w,d,h,t} \tag{31}$$

$$P_{w,d,h,t} \leq \rho P_w^{\max} \tag{32}$$

$$\Delta C_{b,d,h,t} = \rho P_w^{\max} - P_{w,d,h,t} \tag{33}$$

where, $\Delta P_{b,d,h,t}$ represents the hourly power deficit of each energy center per year, L_b^e is the electrical load of energy center b. $p \in b$ denotes the PTG device p located at energy center b, and so on. $r(l)$ and $k(l)$ are the end and start nodes of the line, respectively. $P_w^{\max}$ represents the maximum value of the wind farm output, $P_{w,d,h,t}$ represents the actual wind farm output, $\Delta C_{b,d,h,t}$ represents the abandoned wind power, ρ represents the probability of the wind farm output reaching its maximum value, which is in accordance with certain seasonal fluctuations.

Thermal System Constraints

$$L_{ht}^b = \sum_{c \in b} H_{c,d,h,t} + \sum_{f \in b} H_{f,d,h,t} \tag{34}$$

where, L_b^{ht} is the heat load of the energy center b, $c \in b$ denotes the CHP unit c at the energy center b, $f \in b$ denotes the gas boiler f at energy center b.

Natural Gas System Constraints

The natural gas system needs to meet the natural gas supply and demand balance, the upper and lower limits of gas production from the source, and the upper and lower limits of natural gas flow constraints, expressed as follows.

$$\sum_{r(pp)\in b} G_{pp,d,h,t} - \sum_{k(pp)\in b} G_{pp,d,h,t} + \sum_{gs\in b} S_{gs,d,h,t} = L_b^g + \sum_{c\in b} G_{c,d,h,t} + \sum_{f\in b} G_{f,d,h,t} - \sum_{p\in b} G_{p,d,h,t}$$
(35)

$$G_{gs}^{\min} \leq G_{gs,d,h,t} \leq G_{gs}^{\max}$$
(36)

$$G_{pp}^{\min} \leq G_{pp,d,h,t} \leq G_{pp}^{\max}$$
(37)

where, L_b^g is the gas load of the energy center b, $G_{pp,d,h,t}$ represents the gas flow rate per hour per typical day of the year for gas pipeline pp; $r(pp)$ and $k(pp)$ denote the termination and start nodes of the gas pipeline, respectively, $G_{gs}^{\max}$ and $G_{gs}^{\min}$ denote the upper and lower limits of gas production from the gas source, respectively, $G_{pp}^{\max}$ and $G_{pp}^{\min}$ denote the upper and lower limits of gas flow rate.

The IES extended planning model for the above-mentioned concentrating solar power plant is a mixed integer linear programming model, and the optimal solution can be obtained by calling a commercial solver.

5   Case Studies

5.1   Test System

The IEEE14-NGS14 coupled electric-gas-thermal system is used as an example to effectively validate the integrated energy system expansion planning of the proposed meter and concentrating solar power plant, which is solved by calling the MIP solver using GAMS software. The example system is shown in Fig. 3. The power network contains 12 conventional units (7 existing, 5 candidates), 27 transmission lines (20 existing, 7 candidates), 1 concentrating solar power plant, 2 wind farms and 14 electric loads; the natural gas network contains 2 gas sources, 13 gas pipelines and 3 gas loads; the thermal network contains 12 gas boilers (7 existing, 5 candidates). The interconversion of energy sources is carried out through coupling devices CHP and PTG, and the system contains four candidate CHP units and four candidate PTG units. The conventional units, transmission lines, gas boilers, CHP and PTG parameters are described in the literature [13]. The system planning horizon is 10 years, the payback rate is 10%, the annual discount rate is 5%, and the annual growth rates of electricity, heat and gas loads are 2.5%, 2.5% and 5%, respectively. The unit cost of electricity deficiency is set at 420 USD/MWh, the unit cost of wind and light abandonment is 380 USD/MWh, the environmental benefit coefficient is 70 USD/MWh, the light field operation and maintenance cost coefficient of

the concentrating solar power plant is 8 USD/MWh, and the operation and maintenance cost coefficient of the thermal storage system is 4 USD/MWh.

To illustrate the effectiveness of the proposed integrated energy system expansion planning model for concentrating solar power plants, four typical operation scenarios are set as follows:

1) Scenario 1. Decoupled expansion optimization planning of the system without considering the concentrating solar power plant;
2) Scenario 2. Decoupled expansion optimization planning of the system, taking into account the input of the concentrating solar power plant;
3) Scenario 3. Decoupled expansion optimization planning of the system without considering the concentrating solar power plant;
4) Scenario 4. The system is optimized for coupled expansion, taking into account the input of the concentrating solar power plant.
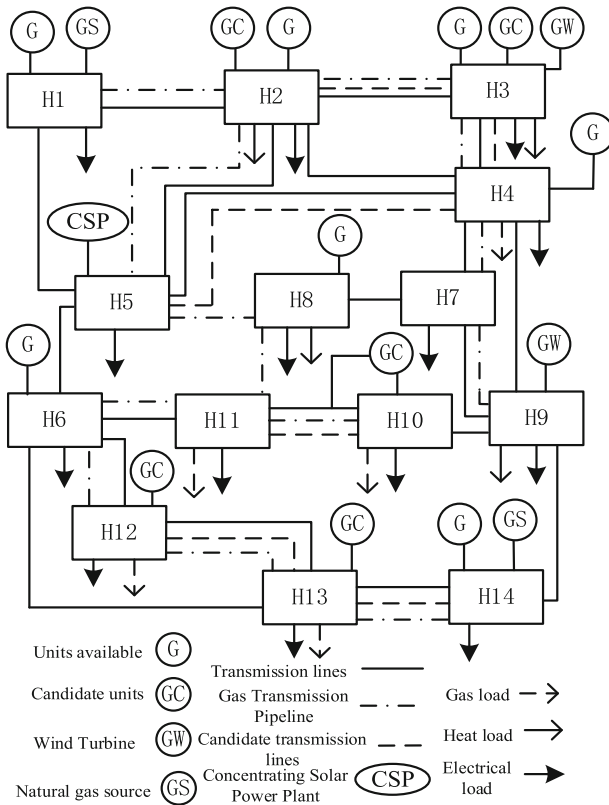
Fig. 3. IEEE14-NGS14 test system

5.2 Planning Results

Decoupling planning means not adding coupling devices, such as CHP devices and PTG devices, to the system and analyzing the changes of each cost in the system; coupling planning means adding coupling devices to the system. The specific planning results are shown in Tables 1 and 2.

As seen in Table 1, the inclusion of the concentrating solar power plant reduces the commissioning of transmission line L22 in Scenario 2. Regarding the comparative analysis of the decoupling and coupling scenarios, the system reduces the commissioning of gas boilers after adding the coupling device and prefers the commissioning of CHP and PTG devices with high energy conversion efficiency.

As shown in Table 2, after joining the concentrating solar power plant, the investment cost, operation cost, electric energy shortage cost, wind abandonment cost and total cost of the system are significantly reduced in both decoupling and coupling cases. This indicates that the concentrating solar power plant can convert light energy into electrical energy to generate electricity, thus reducing the operating cost of the system and improving the service life of the unit; at the same time, the PTG device can convert electrical energy into natural gas energy and improve the wind power consumption capacity of the system, making the wind abandonment cost of the coupled planning scheme generally lower than that of the decoupled planning scheme.

Table 1. Planning results in different scenarios

Categories	Scenario 1	Scenario 2	Scenario 3	Scenario 4
Conventional units	G10(6),G11(2)	G10(6),G11(2)	G9(3),G10(6) G12(4)	G9(3),G10(6), G11(2)
Transmission lines	L24(6),L22(7)	L24(6)	L24(6),L25(6)	L24(6),L26(4)
Gas boilers	F8(4),F9(4), F10(3),F12(6)	F8(4),F9(4), F10(3),F12(6)	F8(4),F9(4)	F8(4),F9(4)
CHP	–	–	C1(1),C2(1), C3(1)	C1(1),C2(1), C3(1)
PTG	–	–	P1(2),P3(2), P4(6)	P1(2),P3(2)

Note: G, L, F, C and P represent conventional units, transmission lines, gas boilers, CHP units and PTG units respectively, and the numbers in parentheses indicate the year of commissioning of the corresponding equipment.

Table 2. Costs for different scenarios

Cost/10^9 *USD*	Scenario 1	Scenario 2	Scenario 3	Scenario 4
Investment costs	0.283	0.256	0.910	0.792
Operating costs	22.484	22.144	20.422	20.162
Wind abandonment costs	0.0718	0.0648	0.00692	0.00604
Power shortage costs	0.706	0.556	0.325	0.203
Light field operation and maintenance costs	–	0.024	–	0.024
Thermal storage system operation and maintenance costs	–	0.0034	–	0.00335
Abandoned light costs	–	0.584	–	0.584
Environmental benefits	–	0.233	–	0.233
Total costs	23.545	23.398	21.664	21.542

The Impact of Concentrating Solar Power Plants on IES

The impact of concentrating solar power plants on IES is mainly reflected in the impact on conventional units, the amount of abandoned wind and the amount of power deficit.

1) Analysis of the output status of conventional units

The change curve of the output state of the conventional unit is shown in Fig. 4. It can be seen that the output of conventional units under different scenarios shows different changing trends. Under scenario 1, the output of conventional units increases year by year, and the rising trend is flat from the overall viewpoint; from the local viewpoint, the increase of units in the 2nd and 6th years is slightly larger because the conventional units G10 and G11 are put into operation in these two years respectively; after joining the concentrating solar power plant, the output of conventional units still shows a rising trend, but slightly decreases compared with scenario 1. This is because the concentrating solar power plant can use the initial heat storage capacity to generate electricity, thus making the output of conventional units decrease and reducing the operating cost of the system. Under scenario 3, the unit output increases significantly in years 2 and 6 because the conventional units need to generate more electricity to meet the system needs when the PTG units are put in place in years 2 and 6. The output of the conventional unit in scenario 4 is smaller than that in scenario 3 after the addition of concentrating solar power plant, which indicates that the addition of concentrating solar power plant can provide electrical energy to the system, thus extending the life of the unit and improving the economy of the integrated energy system. At the same time, the thermal storage device inside the concentrating solar power plant can transfer the thermal energy stored during the low load period to generate electricity during the peak load period, with good controllability and dispatchability.

2) Trend analysis of wind disposal volume

Figure 5 shows the annual variation of wind abandonment. From the figure, it can be seen that there is a significant reduction in wind abandonment after adding the concentrating solar power plant in the decoupling case. This indicates that the concentrating solar power plant can store heat when there is sufficient light, thus reducing power generation, allowing more wind power to go online, and improving the wind power consumption capacity of the system. In the coupled case, no wind abandonment occurs after the PTG is put into operation in the 2nd year. This indicates that the PTG device can convert the excess wind energy into natural gas energy and reduce the wind abandonment. Meanwhile, comparing the wind abandonment in year 1 of scenario 3 and scenario 4, it is found that the wind abandonment in scenario 4 is lower than that in scenario 3, which indicates the positive effect of the concentrating solar power plant on wind power consumption.
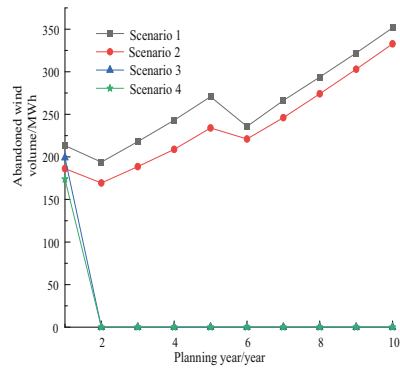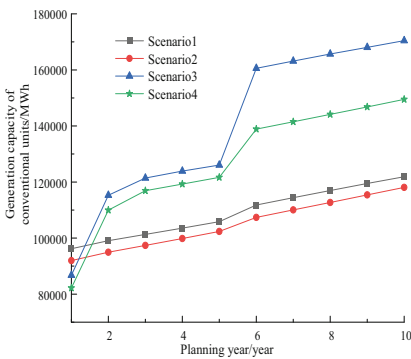
Fig. 4. Variation curve of output of conventional unit

Fig. 5. Trend of wind disposal volume

Trend of Electricity Shortage Changes

Figure 6 shows the annual trend of electrical energy deficit. It can be seen that the electrical energy deficit decreases significantly after the addition of the concentrating solar power plant. In scenario 2, the power deficit showed a decreasing trend in the 2nd and 6th years because one conventional unit G11 was put in the 2nd year and one conventional unit G10 and one transmission line L24 were put in the 6th year, so the power deficit decreased significantly in these two years. In scenario 4, the decrease of the electric energy deficit in the 2nd and 6th years is obvious because one conventional unit G11 is put in the 2nd year and one conventional unit G10 and one transmission line L24 are put in the 6th year, thus increasing the power supply capacity of the system. After the 6th year, no power deficit occurred, indicating the positive effect of the concentrating solar power plant on reducing the system load loss.
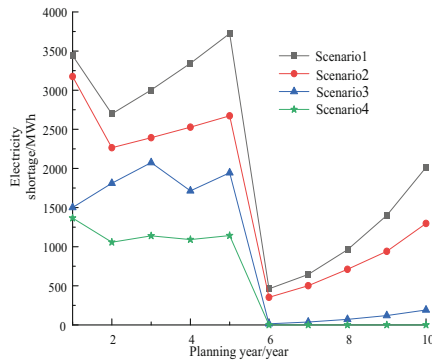
Fig. 6. Change trend of power shortage

6 Conclusion

Based on the flexible and dispatchable characteristics of concentrating solar power plant, this paper proposes a comprehensive energy system expansion planning method that takes into account the concentrating solar power plant, and uses the IEEE14-NGS14 electric-gas-thermal coupling system to effectively validate the method. The results show that after adding the concentrating solar power plant, the investment cost, operation cost, power shortage cost, wind abandonment cost and total cost of the system all show a decreasing trend. It indicates that the concentrating solar power plant can collect sunlight for power generation, reduce the operating cost of the unit and improve the economy of the integrated energy system; meanwhile, the heat transfer fluid in the concentrating solar power plant can exchange energy with the heat storage system, reduce the heat release when the light intensity is high and improve the wind power consumption capacity of the system.

At present, concentrating solar power plants only consider the one-way conversion of light energy - heat energy - electric energy, and need to rely on gas boilers and CHP units to maintain when the system is short of heat energy. If the electric auxiliary heating link can be added to the concentrating solar power plant, the two-way conversion of electric energy and thermal energy can be realized, which is of great value and significance to reduce the operating cost of the system and improve the service life of the unit.

References

1. Olujobi, O.J.: The legal sustainability of energy substitution in Nigeria's electric power sector: Renewable energy as alternative. Protect. Control Mod. Power Syst. **5**(1), 1–12 (2020). https://doi.org/10.1186/s41601-020-00179-3
2. Global Wind Energy Council. Global wind statistics 2019. Belgium (2019)
3. Khaloie, H., Mollahassani-Pour, M., Anvari-Moghaddam, A.: Optimal behavior of a hybrid power producer in day-ahead and intraday markets: a bi-objective CVaR-based approach. IEEE Trans. Sustain. Energy **12**(2), 931–943 (2020)
4. Du, E., Zhang, N., Hodge, B.M., et al.: Operation of a high renewable penetrated power system with CSP plants: A look-ahead stochastic unit commitment model. IEEE Trans. Power Syst. **34**(1), 140–151 (2018)

5. Li, X., Wang, X., Li, F., et al.: Wind-thermal-CSP bundling model with an adjustable heat storage strategy for CSP stations. IEEE Access **9**, 25984–25992 (2021)
6. Alraddadi, M., Conejo, A.J., Lima, R.M.: Expansion planning for renewable integration in power system of regions with very high solar irradiation. J. Mod. Power Syst. Clean Energy **9**(3), 485–494 (2020)
7. Yu, D., Ebadi, A.G., Jermsittiparsert, K., et al.: Risk-constrained stochastic optimization of a concentrating solar power plant. IEEE Trans. Sustain. Energy **11**(3), 1464–1472 (2019)
8. Zhao, Y., Lin, Z., Wen, F., et al.: Risk-constrained day-ahead scheduling for concentrating solar power plants with demand response using info-gap theory. IEEE Trans. Indust. Inf. **15**(10), 5475–5488 (2019)
9. Wu, Z., Zhou, M., Wang, J., et al.: Profit-sharing mechanism for aggregation of wind farms and concentrating solar power. IEEE Trans. Sustain. Energy **11**(4), 2606–2616 (2020)
10. Zhang, S., Wang, D.-Y., Cheng, H.-Z., et al.: Key technologies and challenges of low-carbon integrated energy system planning under double carbon target. Power Syst. Automat. **46**(08), 189–207 (2022)
11. Wang, Y., Li, R., Dong, H., et al.: Capacity planning and optimization of business park-level integrated energy system based on investment constraints. Energy **189**, 116345 (2019)
12. Qin, C., Yan, Q., He, G.: Integrated energy systems planning with electricity, heat and gas using particle swarm optimization. Energy **188**, 116044 (2019)
13. Li, Z., Wang, C.-F., Liang, J., et al.: An integrated electricity-gas-thermal energy system expansion planning method accounting for wind power uncertainty. Power Grid Technol. **42**(11), 3477–3487 (2018)

Microgrid Real-Time Decision Control Method Based on Behavior Trees

Wang Jingsong[(⊠)]

DERI Energy Research Institute, Nanjing, China
wangjingsong@deri.energy

Abstract. To solve the complex microgrid operation control problem under various operating conditions and equipment states, and to ensure the system's safe, stable, and economic operation in any state. This paper presents a microgrid decision control method based on a behavior trees. The method divides the operation interval of a grid-connected microgrid into three states: inverse power, normal operation, and overload operation, and provides a behavior trees decision model for each. The behavior trees model is responsive and modular, and it has several advantages such as good logic readability, easy expansion, easy reuse, and easy monitoring of the operation process, making it appropriate for application scenarios with high logic complexity. We can see from the actual strategy operation effect that the behavior trees decision model presented in this paper can respond quickly and intelligently to the actual operation conditions under various working conditions. The use of the behavior trees decision model improves the intelligence level of in-situ decision making in microgrids, which has a high application value.

Keywords: Microgrid operation control · Behavior trees · Smart decision control

1 Introduction

It is critical to build new energy systems in order to promote the goal of "carbon peaking and carbon neutrality" [1, 2]. China has built a large number of new energy power plants with multiple energy sources in recent years. How to ensure the safety of people and equipment while operating new power plants. It has been the focus of research to improve the reliability of power supply and maximize the economy of system operation.

Currently, finite state machines and data-driven artificial intelligence-based methods are being researched and applied in real-time power grid control. The literature [3] provides a Mealy-type finite state machine model to improve the overall efficiency of real-time stability control engineering; the literature [4] provides a wind turbine pitch control strategy in a network-source coordination environment based on hierarchical finite state machines to partition and coordinate the pitch control logic during grid normal and grid disturbance with satisfactory results. The literature [5] provides deep reinforcement learning algorithms that can effectively account for uncertainty factors in order to solve the optimal operation of microgrids in real time, the literature [6]

employs a multi-parameter action exploration mechanism and an optimally designed neural network structure for microgrid energy management and optimization, and the literature [7] employs a model prediction approach to achieve coordination and optimization of DC microgrid cluster power by using a model prediction approach. To realize flexible scheduling of integrated energy systems, the literature [8] provides a distributed model predictive control based multi-time scale optimal scheduling method for integrated energy systems.

However, while finite state machines can be visually modeled and verified, they are difficult to model when the system state space is too large. Most reinforcement learning controller designs use offline learning and online decision mode, and the control performance is excellent on training data; however, once the distribution of the actual dynamic model differs from the training, the control effect is different from the expected one, and there is no way to put it into engineering practice. Furthermore, the high computational performance requirements make real-time control difficult to achieve. The complexity of microgrid real-time decision control is extremely high. The composition and operating conditions of microgrid systems differ greatly, and the control objectives of microgrids differ under different operating conditions, implying that the complexity of using finite state machine modeling can be quite high. It is a significant challenge to ensure that different microgrids can respond intelligently under varying operating conditions in order to ensure the system's safe, stable, and economic operation.

Based on this, a behavior trees based real-time decision control method for microgrids is given in this paper. The behavior trees method is currently used in some large number of applications in the field of game artificial intelligence, robot control [9–11], behavior trees is a new method that can be used for modeling system behavior, and it starts to be used in more and more fields because of its strict formal semantics, convenient graphical syntax and good hierarchical properties, behavior tree has the characteristics of responsiveness, modularity, etc., compared to finite state machine for system state space large microgrid real-time decision control applications, the modeling complexity of behavior trees is low. Compared with reinforcement learning-based controllers, behavior trees are easier to implement for real-time decision control and facilitate applications in embedded systems. Based on the behavior tree, this paper presents the decision logic of complex microgrid containing light, storage and charging under different operating conditions such as inverse power, overload and normal operation, and verifies the effectiveness of the method by a whole day of actual operation data.

2 Behavior Trees (BT)

2.1 Basic Concepts of Behavior Trees

Behavior trees are a method for autonomous intelligences to switch between different tasks. It is currently used extensively in the gaming industry as well as in robot con-trol. Its main advantage is that it can be easily reused in the context of another high-er-level behavior without requiring the formulation of their relationship to subsequent behaviors.

The classical elaboration of behavior trees contains four types of control nodes and two types of execution nodes, which are simplified and improved for the practical needs

of microgrid applications. This paper uses node types including two types of control nodes and two types of execution nodes.

Table 1. Table captions should be placed above the tables.

Node name	Type	Markings	Success	Fails
Fallback	control node	*FB*	A node success	All nodes fail
Sequence	control node	*SQ*	All child nodes success	A child node fails
Condition	execution node	*Condition*	Condition is true	Condition is false
Action	execution node	*Action*	Always	Never

The pseudocode for the four node algorithm is as follows Table 1.

Algorithm 1. Pseudocode for N-child Fallback nodes

1	**Function** *Tick()*
2	**for** $i \leftarrow 1$ **to** N **do**
3	*childStatus* $\leftarrow$ *child(i).Tick()*
4	**if** *childStaus = Success* **Then**
5	**return** *Success*
6	**return** *Failure*

As we can see, the Fallback node sends the clock from left to right to the child nodes until the child node that returns "success" is found and returned to the parent node, and when all of the child nodes return "failure," "failure" is returned to the parent node.

Algorithm 2. Pseudocode for N-child Sequence nodes

1	**Function** *Tick()*
2	**for** $i \leftarrow 1$ **to** N **do**
3	*childStatus* $\leftarrow$ *child(i).Tick()*
4	**if** *childStaus = Failure* **Then**
5	**return** *Failure*
6	**return** *Success*

The Sequence node, like the Fallback node, finds a node that either returns a "failure" to its parent or returns a "success" to its parent when all nodes are "successful."

Algorithm 3 Condition node pseudocode

1	**Function** *Tick()*
2	**if** *condition - ture*
3	**return** *Success*
4	**else**
5	**return** *Failure*

If the condition is "true," the condition node will return "success," otherwise it will return "failure."

Algorithm 4. Action node pseudocode

1	**Function** *Tick()*
2	*ExecuteCommand()*
3	**return** *Success*

The command will be executed by the Action node, which will return "Success."

2.2   Behavior Tree Operating Environment

The behavior trees model runs in a separate thread, and the behavior tree logic and controlled device model communicate via Blackboard. The black-board design pattern
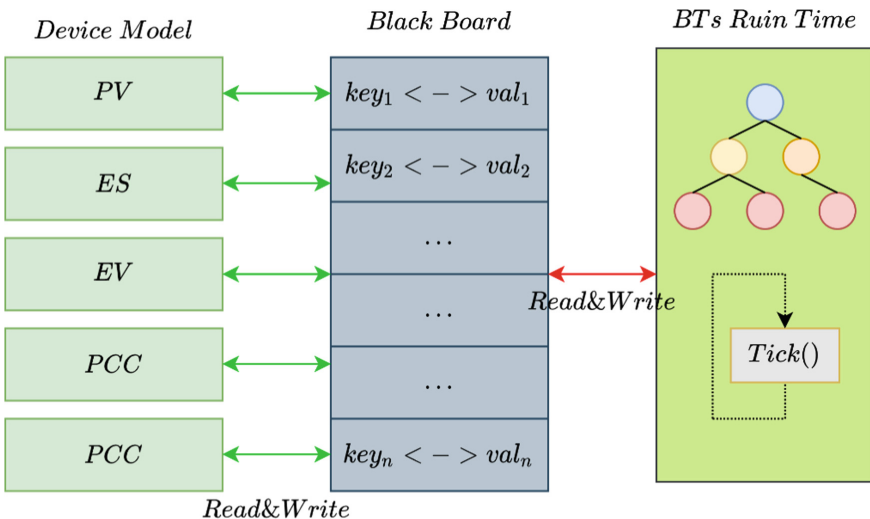
Fig. 1. Behavior tree operating environment diagram

is a data centralized design pattern that is commonly used for data sharing among multiple modules. It is essentially a "Key-Val" type HashMap, as illustrated in the Fig. 1.

3   Microgrid real-time decision control method based on behavior trees

3.1   Architecture for Real-Time Decision Control Based on Behavior Trees

The real-time decision-making architecture based on behavior trees is shown in the following Fig. 2.
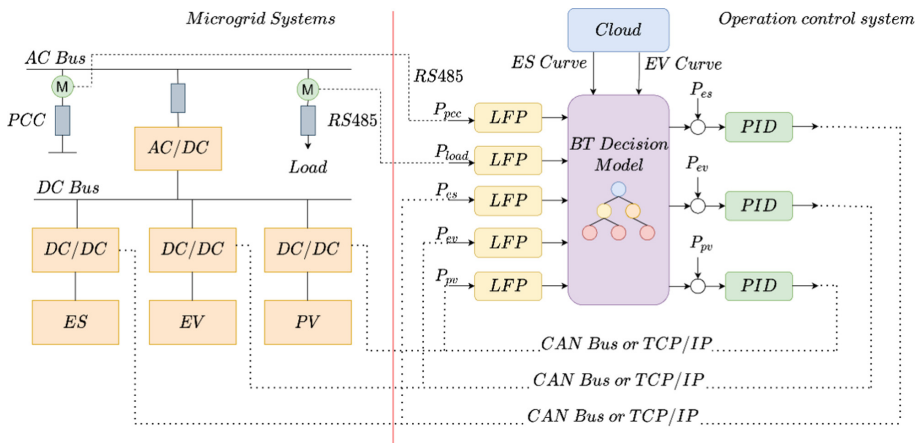
Fig. 2. The real-time decision-making architecture based on behavior trees

The microgrid operation decision control process is as follows.

(1) The microgrid operation control system collects key operational data from microgrid devices via RS485 or CAN, filters it, and feeds it to the BT decision model.
(2) Microgrid operation control system and microgrid energy cloud communication to obtain the energy storage system operating curve and the charging and discharging operating curve of electric vehicles.
(3) The microgrid operation control system decides the reference control commands for the current energy storage system, photovoltaic system, and electric vehicle based on the BT decision model and sends them to the PCS, photovoltaic inverter, and electric vehicle charging pile via the communication interface to complete the real-time decision control process.

3.2   Equipment Models

The PV, ES, Point of Common Coupling(PCC), and electric vehicle models are defined as follows to help show the choice process in the behavioral trees decision model Tables 2, 3, 4, 5 and 6.

Table 2. PV model

Parameters	Description
P_{pv}	PV power generation
P_{pv-eco}	The economic power of PV, which is the maximum power that can be generated by PV
$P_{pv-down}$	PV limitable power, the value is the inverse of the power generated
P_{pv-up}	PV's incremental power, which is the difference between the maximum power that can be generated by PV and the current power

Table 3. ES model

Parameters	Description
P_{es}	ES power generation
P_{es-eco}	The economic power of energy storage, which is the energy storage system's planned curve power given by the cloud
$P_{es-down}$	PThe difference between the current maximum permissible charging power and the current power of energy storage is the downward power of energy storage
P_{es-up}	The difference between the present maximum permissible generation power and the current power of energy storage is known as up-regulated power of energy storage

Table 4. EV model

Parameters	Description
P_{ev}	EV power generation
P_{ev-eco}	economic power, which is the EV's planned curve power transmitted down from the cloud
$P_{ev-down}$	The difference between the current maximum permissible charging power and the current power of the EV is the EV's downward power
P_{ev-up}	The difference between the current maximum permissible generation power and the current power of the EV's up-regulated power

Table 5. PCC model

Parameters	Description
P_{pcc}	Power of PCC
$P_{pcc-down}$	The maximum power consumption permitted by PCC, i.e. the upper distribution transformer's load capacity limit
P_{pcc-up}	Maximum power generation allowed by the PCC

3.3 Behavior Trees Decision Model

In this paper, we demonstrate the behavioral tree decision model's decision-making method using a real-time decision-making process in grid-connected microgrid operation conditions.

As shown below, the mathematical model of the behavior trees can be represented as a triplet.

$$\mathcal{T}_i = \{f_i, r_i, \Delta t\}$$

where i is the tree's index, f_i is the node's function, r_i is the return status, i.e., "success" or "failure," and Δt is the time step.
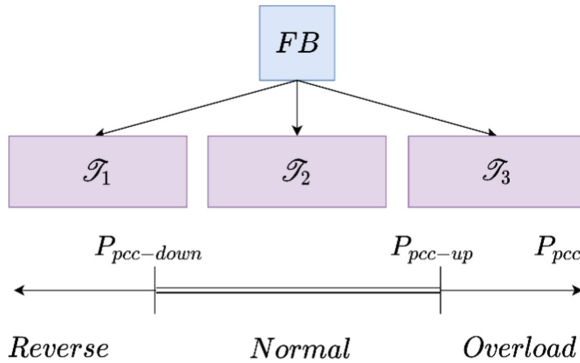
Fig. 3. Grid-connected microgrid system's operation control logic

The Fig. 3 above depicts the grid-connected microgrid system's operation control logic. The microgrid operation process can be divided into three intervals based on the state of the PCC: the inverse power operation interval of the grid-connected network, the normal operation interval, and the overload operation interval. Using the Fallback operation, the model can be combined into a more complex behavior trees model, whose mathematical expression is as follows:

$$\mathcal{T}_0 = \text{Fallback}(\mathcal{T}_1, \mathcal{T}_2, \mathcal{T}_3)$$

where $\mathcal{T}_1$ is the overload control subtree, $\mathcal{T}_2$ is the inverse power control subtree, and $\mathcal{T}_3$ is the normal operating condition interval control subtree.

The complete behavior trees model for microgrid decision control is as follows Fig. 4.
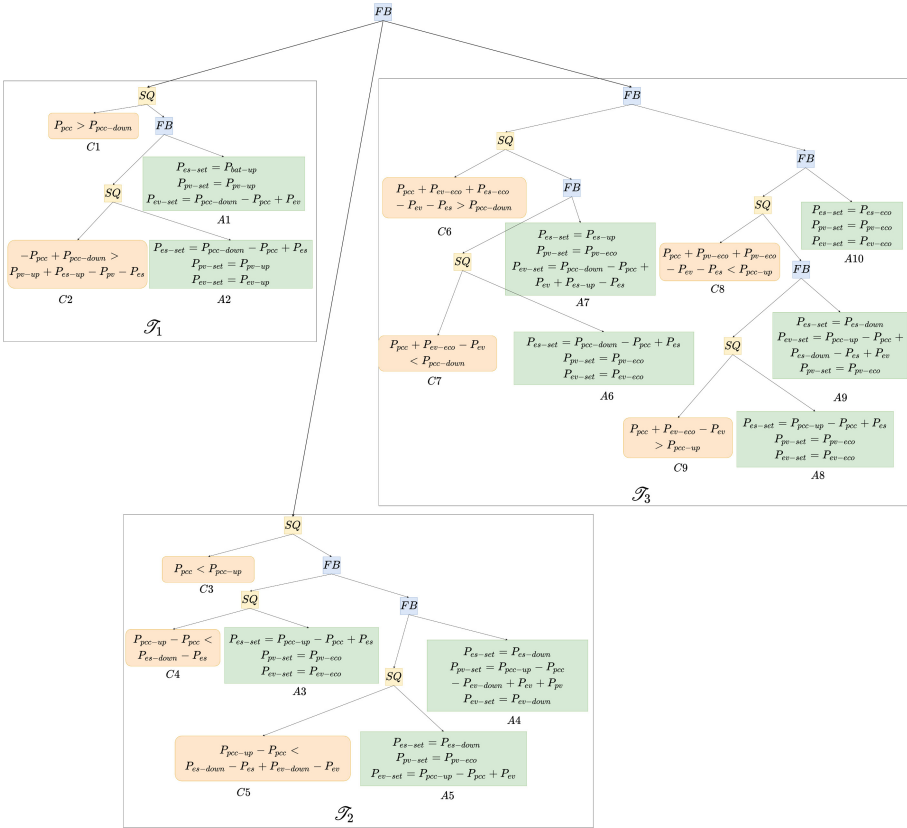
Fig. 4. The complete behavior trees model for microgrid decision control

We detail the decision control logic for each of the three subtrees below.

Subtree of Overload Control($\mathcal{T}_1$). The Decision Logic for the Overload Control Subtree is as Follows Fig. 5:
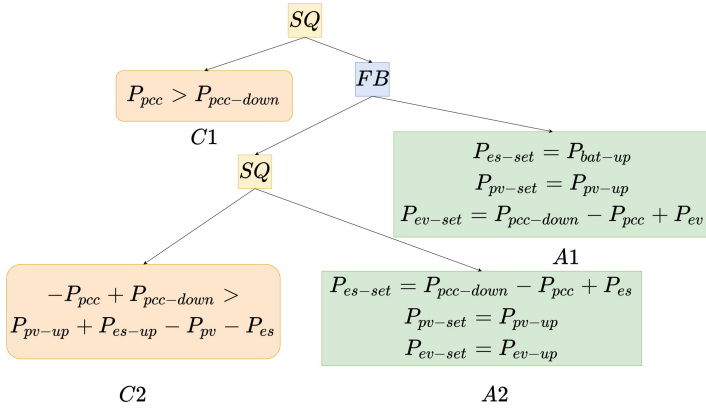
Fig. 5. The decision logic for the overload control subtree

(1) When the PCC's power exceeds the maximum power consumption allowed by the PCC, the C1 node returns "success."
(2) If the power of PCC exceeds the maximum operating power of electricity within the adjustable range of ES, then the A2 action node is executed.
(3) Otherwise, the A1 action node is executed, and the EV begins to limit charging power.

Subtree of Inverse Power Control($\mathcal{T}_2$). The Decision Logic for the Inverse Power Control Subtree is as Follows Fig. 6:
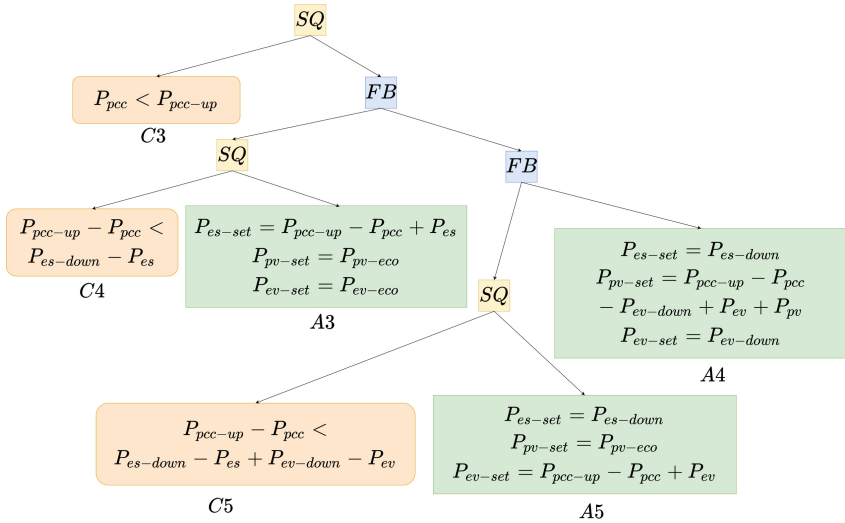
Fig. 6. The decision logic for the inverse power control subtree

(1) C3 returns "success" when the PCC power falls below the minimum allowable operating power (i.e. inverse power state).

(2) Detecting whether the PCC is less than the minimum allowable operating power difference within the energy storage's adjustable range, i.e. executing A3 if C4 returns "success", otherwise executing C5.

(3) A3 node energy storage control to compensate for PCC inverse power differential.

(4) C5 is used to determine whether increasing the EV's charging power to the EV's demand power can cause the PCC to no longer reverse the power; if it returns "success," execute A5, indicating that the EV increases the charging power.

(5) The final phase of A4, which began to limit photovoltaic power generation.

Subtree of Normal Operating Control($\mathcal{T}_3$). The Decision Logic for the Inverse Power Control Subtree is as Follows Fig. 7:
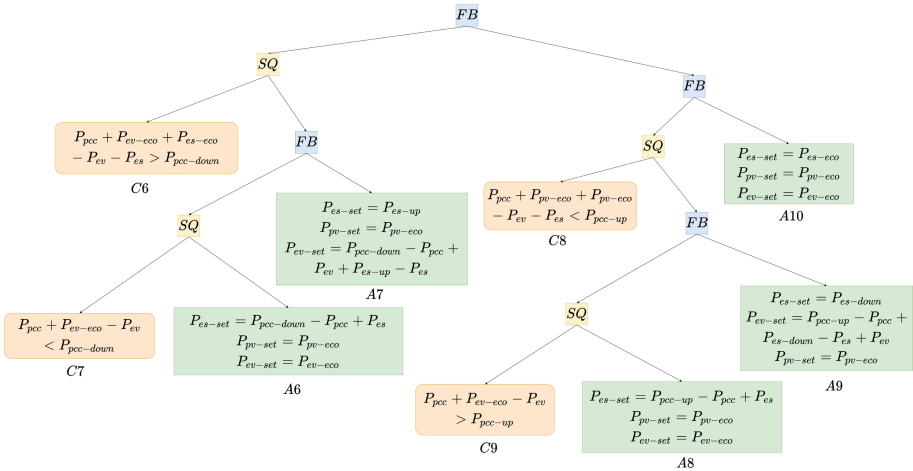
Fig. 7. The decision logic for the inverse power control

(1) Under normal operating conditions, the decision tree determines in real time whether the PCC power will exceed the allowed operating power if the electric vehicle and energy storage are operated at the most economical power; if so, C6 returns "success," otherwise "failure."

(2) If C6 returns "success," proceed to determine whether running the EV at the most economical power will cause the PCC point to exceed the allowed operating power, i.e., whether C7 returns success; if C7 returns success, then execute A6, the EV runs at the most economical power, and the energy storage compensates for the power difference.

(3) Otherwise, A7 is executed, the energy storage follows, and the EV compensates for the power difference.

(4) If C6 returns "failure," make your decision. If the electric vehicle and energy storage are operated in accordance with the most economical power, C8 returns "success",

if not, C9 returns "failure", if the electric vehicle and energy storage are operated in accordance with the most economical power, the PCC will not reverse power.

(5) If C9 returns "success," A8 is executed, and the energy storage compensates for the power difference; otherwise, A9 is executed, and the energy storage operates in accordance with $P_{es-down}$, and the EV compensates for the power difference.

(6) If C8 returns "Fail", A10 is executed, i.e., the most economical operating conditions are followed.

It is important to note that the behavior trees model can be easily modified to meet the project's application requirements. If the control requirements exceed the scope described above, it can be easily applied to different application scenarios by modifying the behavior trees control model without modifying the binary executable.

4 Engineering Application

4.1 Experimental Environment

The method described in this paper has been operating stably in a laboratory environment for a long time. As illustrated in Fig. 1, the primary system in the laboratory employs a hybrid AC-DC microgrid topology with energy storage, PV and EV charging and discharging piles connected to the DC bus side and the AC load being the company's office power Fig. 8.
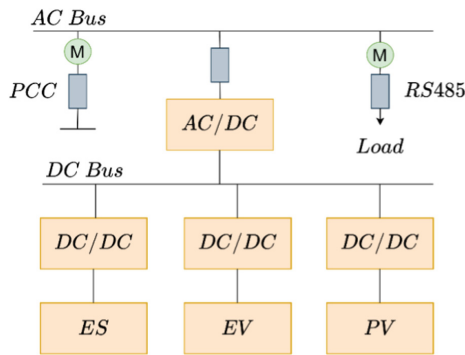
Fig. 8. The primary system in the laboratory

The following table lists the experimental environment's specific parameters.
The operational constraints of the critical equipment need to be described as follows.

(1) Since laboratories purchase electricity from the grid using a single electricity price, the main role of energy storage is to dissipate excess PV generation. Its operational constraint is to stop charging after SOC is higher than 90 and stop discharging after lower than 15.

Table 6. The experimental environment's specific parameters

Equipment	Power rating	Number	Other parameters
ES	20 kW	1	40 kWh
PV	15 kW	1	/
EV	15 kW	1	100 kWh
Load	8 kW	1	/

(2) Electric vehicles and laboratories signed a discharge agreement. It is discharged daily at the laboratory. The start and stop of its discharge depends on the demand of the car used and on the PV generation. The electrical constraint is that the electric vehicle stops discharging after the SOC falls below 30, ensuring that the owner can drive the car home from work without any problems

4.2 Operation Analysis

A full day of actual operation is shown below to demonstrate the control effect of the method described in this paper.

It should be noted that the laboratory microgrid is governed by single electricity price, so the main control goal of the system is to consume excess new energy generation while minimizing power purchases from the grid, resulting in a reduction in energy costs.

The run results are as follows Fig. 9.
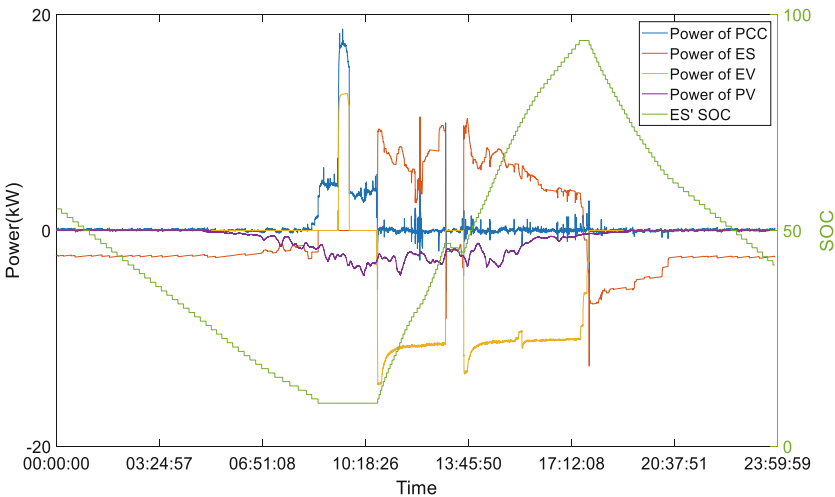
Fig. 9. The run results of laboratory environment

(1) Starting in the early morning with a SOC value of 31, discharging to supply the load and operating node A8 (In Fig. 7).

(2) At 8:42:59, the energy storage discharges to its minimum capacity; at this time, the energy storage has no discharge capacity, no electric vehicle, and the network has no inverse power, with node A10 (In Fig. 7) running.

(3) At 10:44:03, the electric vehicle discharges instantly, and the PCC begins to reverse power - 5.4kW, at this time the storage has a rechargeable capacity of 20kW, and node A6 (In Fig. 7), which is running, begins to charge the storage.

(4) At 12:59:45, the electric vehicle stops discharging, the energy storage can discharge, and node A8 (In Fig. 7) is running, providing discharge to power the load.

(5) Another electric vehicle is discharged at 13:39:15 and operates under the same conditions as the first (3).

(6) At 17:28:46, the energy storage gradually fills, the rechargeable capacity gradually decreases, and backflow begins, at which point it runs to node A9 (In Fig. 7) and the electric vehicle discharge power begins to be limited.

(7) The EV stops discharging at 17:47:06, and the storage has the ability to discharge and run node A8 (In Fig. 7) to provide discharge to power the load.

The all-day operation analysis demonstrates that the method described in this paper can fully and automatically respond to various operating conditions and equipment status to achieve all-day autonomous economic operation.

4.3 Comparison with Finite State Machines (FSM)

Because the behavior trees model is a programming implementation whose primary values are readability, extensibility, and reusability, a brief comparison with finite state machines is made here.

A After adding a new safety state to the FSM (one that required transitions from all other states), every other transition function required tedious modification. Adding more behavior to the BT only increased Code complexity linearly, whereas the FSM is super-linear. This fits well with the knowledge that in the worst case, the number of transitions in an FSMs grows by the order of $O(n^2)$, , whereas BTs grow by O(n).

5 Conclusion

A behavior trees based microgrid decision control method is presented in this paper to solve the operation control problem of a complex microgrid under different operating conditions and different equipment states, and to ensure the safe, stable, and economic operation of the system in any state. The method divides the microgrid's operation interval in grid-connected operation into counter-current, normal, and overload states, and provides a behavior tree decision model for each. The actual operation results demonstrate that the behavior trees decision model presented in this paper can respond to different operating conditions in a timely and intelligent manner. The behavior trees model is responsive and modular, and it has many advantages such as good logic readability, easy expansion, easy reuse, and easy monitoring of the operation process, making it suitable for high logic complexity application scenarios. The application value is excellent.

References

1. Zhang, S., Wang, D., Cheng, H. et al.: Key technologies and challenges of low-carbon integrated energy system planning for carbon emission peak and carbon neutrality [J]. Autom. Electric Power Syst. **46**(8),189–207 (2022). https://doi.org/10.7500/AEPS20210703002
2. Cheng, Y.H., Zhang, N., Wang, Y., et al.: Modeling carbon emission flow in multiple energy systems [J]. IEEE Trans. Smart Grid **10**(4), 3562–3574 (2019)
3. Li, L.I., Zhiping, L.I., et al.: A finite-state machine model for strategy table search and match of standardized stability control device [J]. Autom. Electric Power Syst. **36**(17), 86–89 (2012)
4. Yongxin, S.U., Bin, D.U.A.N., Zhanglong, J.I.N.G., et al.: A variable pitch control strategy for wind turbines under power grid coordination condition [J]. Autom. Electric Power Syst. **37**(9), 7–12 (2013). https://doi.org/10.7500/AEPS201202094
5. Feng, C., Zhang, Y., Wen, F., et al.: Energy management strategy for microgrid based on deep expected q network algorithm [J]. Autom. Electric Power Syst., **46**(3), 14–22 (2022). https://doi.org/10.7500/AEPS20201011005
6. Haitao, L.I., Baochen, S.H.E.N., Yanhong, Y.A.N.G., et al.: Energy management and optimization strategy for microgrid based on improved dueling deep q network algorithm [J]. Autom. Electric Power Syst. **46**(7), 42–49 (2022). https://doi.org/10.7500/AEPS20210809002
7. Zhang, W., Zhang, H., Zhi, N., et al.: Model prediction based energy optimization strategy for dc microgrid groups considering network loss [J]. Autom. Electric Power Syst. **45**(13), 49–56 (2021). https://doi.org/10.7500/AEPS20200926005
8. Lei, W.A.N.G., Jianping, Z.H.O.U., Liuzhu, Z.H.U., et al.: Multi-time-scale optimization scheduling of integrated energy system based on distributed model predictive control [J]. Autom. Electric Power Syst. **45**(13), 57–65 (2021). https://doi.org/10.7500/AEPS20200825006
9. Champandard, A.J., Dawe, M., Hernandez-Cerpa, D.: Behavior trees: Three ways of cultivating game ai. In: Game Developers Conference, AI Summit (2010)
10. Colledanchise, M., Marzinotto, A., Ögren, P.: Performance analysis of stochastic behavior trees. In: IEEE International Robotics and Automation (ICRA) 2014, pp. 3265–3272. IEEE (2014)
11. Colledanchise, M., Ogren, P.: How behavior trees modularize robustness and safety in hybrid systems. In: Intelligent Robots and Systems (IROS 2014), 2014 IEEE/RSJ International Conference on, pp. 1482–1488. IEEE (2014)

Research on Impact of Inverter-Interfaced Distributed Generator on Local Feeder Automation

Zhihui Dai[(✉)] and Lirui Yu

North China Electric Power University, Hebei, China
zhdai@ncepu.edu.cn

Abstract. With the increasing penetration of inverter-interfaced generators (IIDGs), the power flow in the distribution network changes accordingly. Feeder automation (FA) based on unidirectional power flow design may not be able to cope with the scenario after the IIDG connection. It is urgent to study the impact of the IIDG on local FA. First, the fault equivalent model of IIDG is analyzed in combination with the low voltage ride-through strategy. On this basis, taking two local feeder automation modes, voltage-time and voltage-current modes which are widely used at present, as examples, their operating principles are discussed, respectively. Combined with the faults at different positions upstream and downstream of the point of common coupling (PCC) in the distribution network, the impact of IIDG integration on the action of each switch of local feeder automation is analyzed in detail. Finally, the local FA simulation model is established by using PSCAD/EMTDC, which verifies the rationality of the theoretical analysis.

Keywords: Inverter-interfaced distributed generator · Voltage time type · Voltage current type · Feeder automation · Distribution network

1 Introduction

With the proposal of the strategy of "building a strong smart grid and ubiquitous power Internet of things", the construction and development of China's distribution networks also have higher requirements, such as making full use of distributed power, reducing the risk of large-scale blackouts, and improving power quality [1]. As an important part of distribution automation, feeder automation plays an important role in improving the power supply reliability of the distribution network and meeting the needs of customers [2]. Local feeder automation is widely used in zones B and C which do not have communication conditions and have relatively low requirements for power supply [3] because it does not rely on the master station and communication, and can realize fault location and isolation locally with low cost.

In local feeder automation, the setting of each switch is closely related to the overall distribution network structure. Most distribution networks in China are radial networks, or "hand-in-hand" networks with closed-loop design and open-loop operation.

Its essence is still a single power supply system. Thus, the settings are usually set according to the one-way flow of power flow [4]. However, under the background of the deep integration of power Internet of things and energy Internet, the inverter-based generator is increasingly widely used in the distribution network, and the integration capacity is also increasing year by year [5]. The power flow of the distribution network is changed due to the integration of IIDG, and the action logic between local FA switches may be affected, resulting in that the feeder automation system cannot quickly and accurately identify and isolate faults, and the fault range is expanded. Therefore, it is necessary to study the impact of the grid connection of IIDGs on local feeder automation.

Based on analyzing the fault current characteristics of active distribution networks, literature [6, 7] studies the influence of IIDG integration on the switching, relay protection, and reclosing actions in voltage-time type FA. However, IIDG is equivalent to a constant current source in the analysis, and the influence of its LVRT capability on the fault characteristics is not considered. Considering the low-voltage ride-through control strategy, literature [8] established the equivalent model of IIDGs and analyzed the impact of IIDG grid connection on voltage-time type FA, but it did not analyze the impact of the integration of IIDG on the "voltage-free opening" action strategy of the switch. In addition, the above literature only analyzes the voltage-time type FA with IIDG integration, which has certain limitations. Literature [9, 10] analyzes the impact of IIDG integration on switching action logic under voltage-time type and stepped-current FA modes in combination with the working mode of IIDGs, but does not make a relevant analysis on the voltage-current type FA mode that are widely used.

To sum up, based on the inverter control strategy and low voltage ride through strategy, the IIDG fault equivalent model is established; On this basis, taking the voltage-time type and voltage-current type feeder automation modes as examples, the impact of IIDG integration on the local feeder automation system is analyzed given the faults at different locations including upstream and downstream of the point of common coupling (PCC). Finally, the simulation model of local feeder automation built by PSCAD/EMTDC verifies the accuracy of the theoretical analysis.

2   Fault Equivalent Model of Inverter-Interfaced Distributed Generator

2.1   IIDG Equivalent Model

The IIDG, with photovoltaic as a typical representative, is mainly composed of an inverter, DC control system, and filter. The photovoltaic system model is shown in Fig. 1.
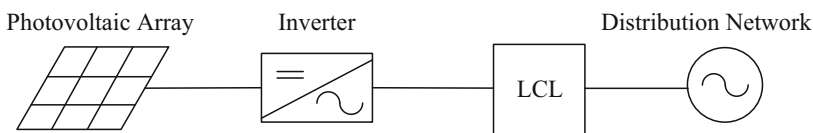
Fig. 1. Photovoltaic system model.

During normal operation, IIDG mainly adopts double closed-loop decoupling control, in which the outer loop adopts constant power control, to realize the power regulation [11].

When a fault occurs in the distribution network with distributed generator integration, IIDG detects the voltage drop of the PCC. Currently, according to relevant grid regulations in China, the distributed generator needs to enter LVRT mode, continues grid-connected operation within the specified time, and provides a certain amount of reactive power compensation to assist in grid restoration. Considering the grid connection requirements and eliminating the negative-sequence current output by IIDG under asymmetric conditions, the control mode based on the positive sequence voltage of PCC is generally adopted in practical projects [12, 13]. Therefore, the IIDG outputs the active current $I_{dg.d}$ and reactive current $I_{dg.q}$ as shown in (1).

$$
\begin{cases}
I_{dg.q} = \begin{cases}
0 & U_{PCC.f} > 0.9 \\
1.5(0.9 - U_{PCC.f})I_N, & 0.2 \le U_{PCC.f} \le 0.9 \\
1.05 I_N & U_{PCC.f} < 0.2
\end{cases} \\
I_{dg.d} = \min\left\{ I_{d0}, \sqrt{I_{max}^2 - (I_{dg.q})^2} \right\}
\end{cases}
\tag{1}
$$

where, $U_{PCC.f}$ is the per-unit value of the positive-sequence voltage at the PCC; I_N refers to the rated current of the PCC where IIDG connects; I_{d0} is the active current command under normal operation; I_{max} is the maximum current allowed to flow through the inverter, generally $1.2 I_N$.

To sum up, when the distribution network occurs faults, the equivalent calculation model of IIDG can be expressed as:

$$
\dot{I}_{IIDG.f} = (I_{dg.d}\cos\theta + I_{dg.q}\sin\theta) + j(I_{dg.d}\sin\theta - I_{dg.q}\cos\theta)
\tag{2}
$$

where, $\dot{I}_{IIDG.f}$ is the output current of IIDG in case of distribution network fault; θ is the phase of $U_{PCC.f}$.

It can be seen from (1) that the fault current output by IIDG is mainly determined by the positive-sequence voltage of the PCC. Therefore, IIDG can be equivalent to a positive-sequence voltage-controlled current source model in case of a distribution network fault.

2.2 Case Study

To verify the accuracy of the IIDG equivalent model, an equivalent system with IIDG integration is built in PSCAD based on Fig. 2. The system parameters are as follows: The voltage of the system is $U_S = 10.5$ kV, the impedance of the system $Z_S = j0.5\ \Omega$; The unit impedance of the line is $Z = 0.27 + j0.346\ \Omega/km$, and the line length is $L_{A-B} = 3km$; IIDG rated capacity is 2 MW; Load impedance is $Z_L = 3 + j2\ \Omega$.
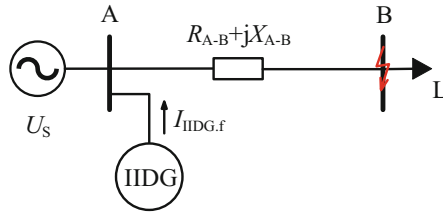
Fig. 2. Equivalent system with IIDG integration.

When a two-phase short-circuit fault or three-phase short-circuit fault occurs at point B, the calculated and simulated values of the IIDG fault current $\dot{I}_{\text{IIDG.f}}$ are shown in Table 1:

Table 1. The comparison between the calculated value and the simulation value.

The fault type	Calculated value/kA	Simulated values /kA
three-phase short-circuit fault	0.129∠-22.14°	0.131∠-21.08°
two-phase short-circuit fault	0.112∠-10.34°	0.111∠-11.58°

Results from Table 1 show that the calculated value of fault current output by IIDG is basically consistent with the simulation value. The relative errors of amplitude and phase Angle are all within 1%, indicating that the IIDG equivalent model has high accuracy.

3   Influence of IIDG on Voltage-Time Type FA

3.1   Voltage-Time Type Feeder Automation

"Voltage-time type" FA relies on the "power-on closing and voltage-off opening" function of the voltage-type sectionalizing switch, cooperates with the recloser configured at the outlet of the substation, recovers the power supply step by step, uses the time sequence for fault detection, and locks the switches before and after the fault position, to realize the isolation of the fault section [9]. Voltage-time type FA is applicable to radiation lines, single ring networks, and other frameworks. Its typical circuit diagram is shown in Fig. 3:
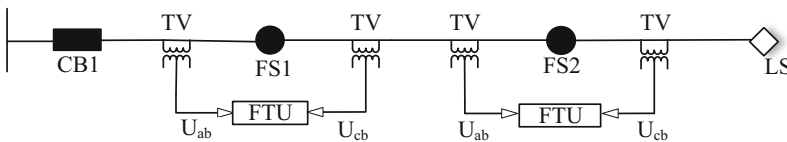
Fig. 3. Typical circuit diagram of voltage-time type feeder automation.

Wherein, CB is the outgoing circuit breaker at the substation; FS is the voltage-type sectionalizing switch; LS is the tie CB; FTU is a feeder terminal, and the corresponding judgment logic is preset; TV is a voltage transformer used for voltage measurement, power detection, etc.

3.2 Impact Analysis of IIDG Integration on Voltage-Time Type Feeder Automation

Taking the distribution network shown in Fig. 4 as an example, the impact of IIDG integration on voltage-time FA is specifically analyzed. The system parameters are as follows:

1) The unit impedance of the line is $Z = 0.27 + j0.346$ Ω/km, and the length of each line is $L_{\text{CB-FS1}} = 3$km, $L_{\text{FS1-FS2}} = 2$ km, $L_{\text{FS2-FS3}} = 4$ km, $L_{\text{FS1-FS4}} = 2$ km, and $L_{\text{FS3-FS5}} = 1.5$ km respectively.
2) The impedance of the system under the maximum operation mode and the minimum operation mode is $x_{\text{smax}} = j0.091$ Ω and $x_{\text{smax}} = j0.126$ Ω respectively.
3) The integration position of IIDG is in the middle of the FS$_2$- FS$_3$ section.
4) The line end load is $3 + j2$ MVA.
5) Set system $S_B = 100$ MVA, $U_B = 10$ kV.
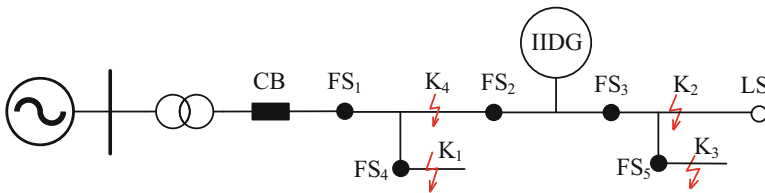
Fig. 4. Voltage-time FA system configuration diagram with IIDG integration.

1) To realize the cooperation between the recloser and the sectionalizing switch on the line, the outlet switch of the substation shall protect the whole length of the line. After IIDG is connected to the distribution network, when the fault occurs at the branch line (such as K$_1$ and K$_3$ points) and the main line downstream of the integration point (such as K$_2$ point), the current flowing through CB will be reduced due to the external drain effect of the IIDG. From the above analysis of the IIDG equivalent model, the larger the IIDG integration capacity is, the stronger the voltage support capacity is, and the stronger the shunting effect will be after the distribution network fault occurs, which may cause the fault current detected by CB to be too small and refuse to operate, and hence the fault cannot be removed. When the upstream of the main line of the integration point (such as K$_4$ point) fails, the integration of IIDG will not affect the action of CB.

In addition, when a fault occurs in the distribution network, the fault current fed back from the load is quite weak compared to the fault current generated by the system or IIDG [15]. Therefore, only the change in power flow due to different IIDG integration capacities, which leads to a change in fault currents, is considered, while the change in power flow due to load changes is ignored.

2) The "voltage time type" sectionalizing switch has the characteristics of "power-on closing and voltage-off opening". In engineering practice, the traditional "voltage-off opening" criterion is to trip when the effective value of line voltage monitored in real time is less than 0.3 times the rated value [14]. When many IIDGs are connected to the distribution network, it is assumed that CB can act reliably in case of faults. However, due to the low-voltage ride-through capability of the distributed generator, a certain voltage can be maintained at this time, which may cause the voltage detected by the switch (such as FS2) near the PCC to be greater than the set value, thus affecting its reliable opening.

3) According to relevant regulations on grid connection of photovoltaic power generators, IIDG needs to adopt the control strategy of "low penetration first and then anti-islanding" after distribution network failure [12]. Under the anti-islanding strategy, the maximum opening time of IIDG shall not exceed 2s, while the primary reclosing time of substation outlet CB is generally set as 1s [16]. Therefore, when CB is reclosed, IIDG may still be in grid-connected operation. If the IIDG integration position is close to CB or the line switch fails to open reliably, non-synchronous reclosing may be caused. In addition, if the IIDG exactly matches the local load, the anti-islanding protection will not act, the distributed generator and some loads will continue to operate, and non-synchronous closing may also occur during reclosing. CB may act again due to the impulse current during non-synchronous reclosing, and the overall action logic of FA is affected, so the fault isolation cannot be realized correctly.

3.3 Case Study

Impact of Load Change on Fault Current. The simulation model shown in Fig. 4 is built in PSCAD, and the following simulations are carried out for the two cases of distribution network end load of 3 + j2 MVA and 9 + j4 MVA respectively: 2 MW IIDG is connected under the maximum operation mode of the system, and a three-phase short-circuit fault is set to occur at points K1 and K2. At this time, the fault current flowing through the substation exit switch is shown in Table 2:

Table 2. Current flowing through CB when the load changes.

The fault location	Load	Fault current/kA
K_1	3 + j2MVA	2.415
	9 + j4MVA	2.427
K_2	3 + j2MVA	1.362
	9 + j4MVA	1.368

Results from Table 2 show that when the load changes, the current flowing through the CB does not change much, hence the effect of the load change on the fault current can be ignored in the later analysis.

Impact of IIDG Integration on Substation Outlet Protection. A voltage-time type FA simulation model based on Fig. 4 is built in PSCAD, and the following simulations are carried out for the two cases of no IIDG integration and 2MW IIDG integration in the distribution network: two-phase short-circuit fault occurs at K_1, K_2, K_3 and K_4 points. At this time, the fault current flowing through the outlet switch of the substation is shown in Table 3:

Table 3. Current that flows through CB when IIDG integration capacity is 2MVA.

The fault location	IIDG integration condition	Operation mode	Current flowing through CB/kA	The fault location	IIDG integration condition	Operation mode	Current flowing through CB/kA
K_1	Not integrate IIDG	maximum	1.805	K_3	Not integrate IIDG	maximum	1.024
		minimum	1.781			minimum	1.015
	Integrate IIDG	maximum	1.722		Integrate IIDG	maximum	0.921
		minimum	1.698			minimum	0.908
K_2	Not integrate IIDG	maximum	1.228	K_4	Not integrate IIDG	maximum	2.816
		minimum	1.210			minimum	2.760
	Integrate IIDG	maximum	1.142		Integrate IIDG	maximum	2.803
		minimum	1.131			minimum	2.754

It can be seen from the Table 3 that before and after IIDG is connected, the current flowing through the outlet switch CB changes little in case of fault at point K_4, which indicates that IIDG has little impact on outlet protection in case of fault at the upstream main line of the PCC. When the fault occurs at K_1, K_2 and K_3, the current flowing through CB after IIDG is connected will be significantly reduced, which indicates that

the connection of IIDG has a great impact on outlet protection when the fault occurs in the upstream branch line and the downstream branch line of the PCC. According to the distribution network parameters, the minimum operating current of the substation outlet switch is $I_{\text{min\_trip}} = 0.864$ kA [9]. When a two-phase short-circuit fault occurs at K_2 and K_3 points, the minimum fault current flowing through CB is 1.099 kA and 0.908 kA respectively, which is close to the minimum operating value of protection.

When the FS_2-FS_3 section is connected to 2.5 MW IIDG, if a two-phase short-circuit fault occurs at K_2 and K_3 points, the minimum fault current flowing through CB is shown in Table 4:

Table 4. Current that flows through CB when IIDG integration capacity is 2.5 MVA.

The fault location	Minimum short-circuit current /kA	The fault location	Minimum short-circuit current /kA
K_2	1.046	K_3	0.86

It can be seen from Table 4 that with the increase of IIDG integration capacity, the external shunting effect of the distributed generator becomes stronger. When the integration capacity increases to 2.5 MW, the minimum current flowing through CB is 0.86 kA, less than $I_{\text{min\_trip}}$. At this time, the outlet switch of the substation cannot protect the full length of the line, and hence the action coordination between each switch will be affected.

Impact of IIDG Integration on Sectionalizing Switch Opening. A two-phase short-circuit fault occurs at K_2. Under the maximum operation mode of the system, simulate the distribution network without IIDG, with IIDG of 2 MW, and with IIDG of 2.5 MW. Suppose the fault occurs at 5 s, CB acts after 0.2 s of fault, and the effective value of FS_2 voltage before and after CB acts is shown in Fig. 5:
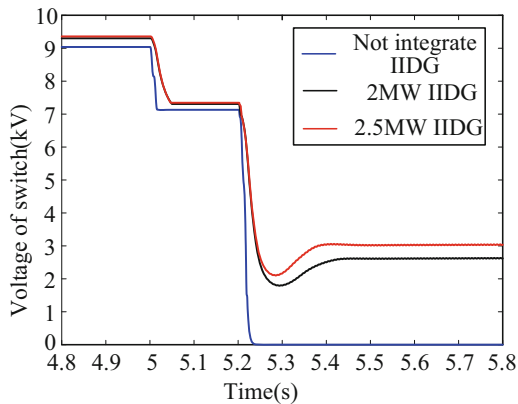
Fig. 5. Effective value of FS2 voltage before and after CB operation.

It can be seen from Fig. 5 that when the distribution network is not connected to IIDG, the effective value of FS_2 voltage drops to zero after CB trips, and the switch reliably opens due to voltage off; After IIDG is connected to the distribution network, the voltage at FS_2 decreases but is not zero due to its low-voltage ride-through characteristics. The larger the capacity of IIDG integration, the stronger the support capacity for the voltage of the PCC, which may cause that after CB tripping, the voltage-time type sectionalizing switch will not trip due to detecting the voltage greater than $0.3U_N$, resulting in that it is unable to isolate the fault in time.

Impact of IIDG Integration on CB Reclosing. A three-phase short-circuit fault occurs at K_2, and the distribution network without IIDG integration and with 2 MW under the maximum operation mode of the system is simulated. Suppose a fault occurs within 5 s, and the outlet switch CB acts after 0.2 s of the fault and recloses after 1s. During reclosing, all switches on the line remain closed, and the phase difference between the system side and IIDG is exactly 180°. At this time, the current flowing through CB is shown in Fig. 6:
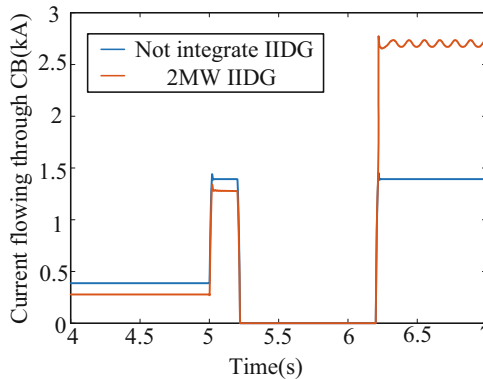
Fig. 6. Current flowing through CB before and after switching.

It can be seen from Fig. 6 that when the distribution network is connected to IIDG, if IIDG is continuously connected to the grid before reclosing, a large impulse current may be generated during reclosing, resulting in CB reclosing failure and an adverse impact on the whole system.

4   Influence of IIDG on Voltage-Current Type FA

4.1   Voltage-Current Type Feeder Automation

Voltage-Current Type FA Based on Sectionalizing Switch. The voltage-current type FA based on sectionalizing switch adopts the composite criterion combined with the fault current. By recording the times of voltage loss and overcurrent, the isolation of the fault area and the rapid restoration of the power supply in the non-fault area are realized [17]. Voltage-current type FA applies to radiant lines, multi-connection, and other grid structures. Its typical circuit diagram is shown in Fig. 7:
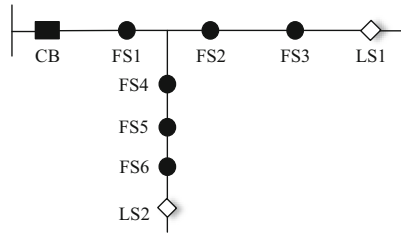
Fig. 7. Typical circuit diagram of voltage-current type feeder automation.

FS is a voltage-current type sectionalizing switch. Based on the voltage-type sectionalizing switch and the fault current criterion, the voltage-current type sectionalizing switch sets the action logic of "locking and opening" [18], that is, if no fault current is detected within the set time after the switch is powered on and closed, it will lock the opening action, to reduce the action times of sectionalizing switch in the non-fault area.

In this mode, after the outlet switch acts, the sectionalizing switch in the non-fault area on the line also needs to act once because it detects voltage loss. To realize the fast recovery of the non-fault area and reduce the switching action times, an improved voltage current mode FA is proposed on this basis [18, 19]. The fault treatment mode is similar to the above modes, but the working mode of the sectionalizing switch is to judge the fault current first, and then the voltage, that is, when a short-circuit fault occurs on the line, the fault current is detected before the switch loses voltage, and the switch is considered to be opened, otherwise it remains closed.

Voltage Current Mode FA Based on the Circuit Breaker. Based on the voltage-current type FA of the circuit breaker, the sectionalizing switches are changed into circuit breakers, and the current and voltage signals on both sides are detected. In addition to the function of "power-on closing and voltage-off opening", the instantaneous quick break protection function is also required to be put into operation during reclosing. If it is closed to a fault, it will be opened and locked immediately, to isolate it [20, 21]. In this FA mode, the line fault can be removed once the outlet switch of the substation is closed. The impact on equipment and users is small, but more circuit breakers need to be used and the cost is high.

4.2 Impact Analysis of IIDG Integration on Voltage-Current Type Feeder Automation

Combined with the distribution system shown in Fig. 8, the impact of IIDG integration on voltage-current FA is specifically analyzed, with FS in the figure as a voltage-current sectionalizing switch or circuit breaker.

1) Whether the voltage-current type FA is based on the sectionalizing switch or circuit breaker, each switch on the line has the function of "voltage-off opening"; In addition, to realize the cooperation of each switch on the line, the outlet switch of the substation shall protect the full length of the line and configure reclosing at the same time.
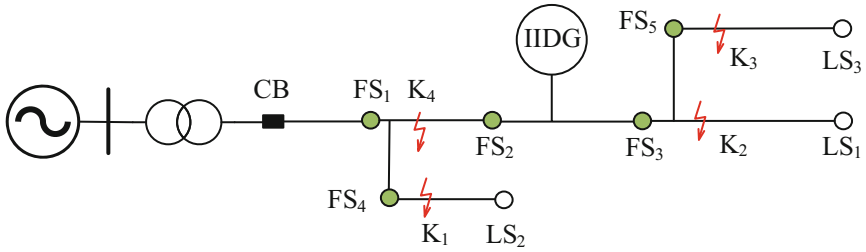
Fig. 8. Voltage-current FA system configuration diagram with IIDG integration.

Therefore, after the IIDG is connected to the distribution network, the voltage-current mode FA will also be affected by the three effects analyzed in Sect. 3.2.

2) For voltage-current type FA based on the sectionalizing switch, the fault current detected by the sectionalizing switch is generally set to avoid the maximum load current [22]. After IIDG is connected to the distribution network, if a fault occurs in the downstream main line (such as K_2) or downstream branch line (such as K_3) of the integration point, the boosting effect of IIDG will increase the current flowing through FS_3 and FS_5. Therefore, the integration of DG is beneficial to the downstream switch of the PCC; Due to the external swabbing effect of IIDG, the current flowing through FS_1 and FS_2 will be reduced. The larger the integration capacity of IIDG, the stronger the shunting effect will be, which may cause the fault current detected by the upstream switch of the PCC to be less than the set value, and hence the switch cannot correctly record the overcurrent times.

   If a fault occurs in the branch line upstream of the PCC (such as K_1), the current flowing through the switch (such as FS_4) on the branch line will increase due to the boosting effect of IIDG. The integration of IIDG is beneficial to the overcurrent detection of the switch on the line. For the switches upstream of the PCC of the main line, on the one hand, the existence of IIDG may cause the switches in the non-fault area (such as FS_2) to detect the fault current provided by the distributed generators; On the other hand, due to the external swabbing effect of IIDG, the fault current flowing through the fault area switch (such as FS_1) may be reduced. Therefore, the sectionalizing switches on the main line may be affected and hence the fault cannot be isolated correctly. If a fault occurs in the upstream main line (such as point K_4) of the PCC, the switch in the fault area (such as FS_1) will not be affected, while the switch in the non-fault area (such as FS_2) will detect the fault current provided by the distributed generator, which is similar to the above situation.

3) For the voltage-current type FA based on the circuit breaker, the current protection function is enabled when each switch is reclosing in this mode. When faults occur in the downstream (such as K_1 and K_2) and upstream branch lines (such as K_3), if IIDG is still connected to the grid when FS_2 is reclosing, it may lead to non-synchronous reclosing, and the resulting impulse current may lead to FS_2 protection action and lockout switching on, expanding the fault range. If a fault occurs in the upstream main line (such as point K_4) of the PCC, the integration of IIDG will not affect the action of FS_1.

4.3   Case Study

Impact of IIDG Integration on Voltage-current Mode FA Based on Sectionalizing Switch. Taking Fig. 4 as an example, a voltage-current mode FA simulation model is built based on the sectionalizing switch, and simulates without IIDG integration and with 2MW IIDG integration in the distribution network as follows: under the maximum operation mode of the system, three-phase short-circuit faults occur at K_1, K_2, K_3 and K_4, respectively. The fault current flowing through each switch is shown in Table 5 and Table 6:

Table 5. Fault current that flows through each switch when IIDG is not connected.

The fault location	Switch	Fault current/kA	The fault location	Switch	Fault current/kA
K_1	FS_1	2.345	K_2	FS_1	1.391
	FS_2	0.011		FS_2	1.389
	FS_4	2.341		FS_3	1.392
K_3	FS_1	1.198	K_4	FS_1	3.852
	FS_5	1.202		FS_2	0.008

Table 6. Fault current that flows through each switch when 2MW IIDG is connected.

The fault location	Switch	Fault current/kA	The fault location	Switch	Fault current/kA
K_1	FS_1	2.253	K_2	FS_1	1.291
	FS_2	0.124		FS_2	1.296
	FS_4	2.392		FS_3	1.454
K_3	FS_1	1.112	K_4	FS_1	3.851
	FS_5	1.251		FS_2	0.121

It can be seen from Table 5 and Table 6 that when the fault occurs in the downstream position (K_2 and K_3 points) of the PCC, the current detected by the downstream switches FS_3 and FS_5 increases due to the integration of IIDG, which is conducive to the over-current detection of the switch; The fault current detected by the upstream switches FS_1 and FS_2 decreases due to the shunting effect of IIDG. At present, the fixed value of fault current of voltage-current type sectionalizing switch is generally set to 1000A [23]. According to the above analysis, the larger the integration capacity of the distributed generator, the stronger the shunting effect. Therefore, with the larger integration capacity, the switch may not correctly detect the overcurrent, thus affecting the subsequent actions of the FA.

When the fault occurs in the upstream branch line (K_1 point) of the PCC, the current detected by the main line switch FS_1 in the fault section will decrease due to the external swabbing effect of IIDG, while the current detected by the branch line switch FS_4 will

increase due to the increasing effect of IIDG, which is similar to the analysis when the fault occurs on the downstream of the PCC. After IIDG is connected, the current detected by switch FS$_2$ in the non-fault section increases from zero to 124A. Because the capacity of the IIDG connected is small, and the contribution of the distributed generator to the fault current is small when connected to the grid via the inverter, the current detected by FS$_2$ is quite different from the fixed value of the switch overcurrent detection. However, in the context of dual carbon, more and more distributed generators are connected to the distribution network. When the fault current contributed by IIDG reaches the overcurrent setting, its connection will affect the action logic of each switch. When the fault occurs in the upstream main line (point K$_4$) of the PCC, the situation is similar to the above analysis.

Impact of IIDG Integration on Voltage-current Mode FA Based on the Circuit Breaker. A voltage-current mode FA simulation model based on circuit breakers is built, and the following simulations are carried out, respectively, for the two cases of no IIDG integration and 2 MW IIDG integration in the distribution network: under the maximum operation mode of the system, a three-phase fault occurs at K$_2$ point. Assuming that IIDG is continuously connected to the grid, the current detected by the switch before and after FS$_2$ closing is shown in Fig. 8:
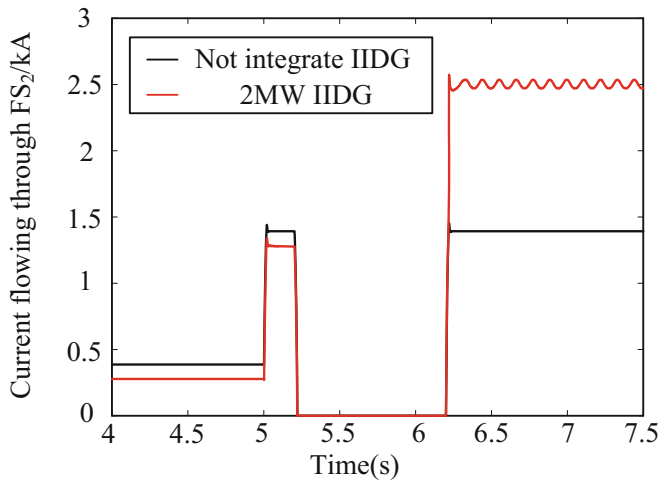
Fig. 9. Current flowing through FS2 before and after closing.

As can be seen from Fig. 9 that, the IIDG connection makes the current detected during FS$_2$ reclosing increase sharply. The current value may exceed the set value of its overcurrent protection, resulting in the rapid tripping of FS$_2$ after closing and expanding the fault range.

5   Conclusions

Taking voltage-time type and voltage-current type FA as examples, based on the study of the IIDG fault equivalent model, this paper analyzes the influence of IIDG connection on the action of each switch in local feeder automation. The main conclusions are as follows:

1) For the voltage-time type feeder automation mode, when the fault occurs on the downstream and upstream branches of the PCC, the outlet switch may not act reliably due to the external shunting of IIDG. In view of the above situation, the sectionalizing switch in the middle of the feeder can be converted into a circuit breaker and equipped with a protection device. This method can reduce the minimum action current value of the CB by reducing its protection range, thus alleviating the impact of the shunting effect; Since IIDG has a certain supporting capacity for the voltage of the PCC, the connection of IIDG may make the switch near the PCC unable to realize "voltage-off opening". Considering the above issue, the opening criterion can be improved to achieve reliable breaking by using sudden voltage changes before and after CB operation; In addition, IIDG may be continuously connected to the grid during switch reclosing on the line, resulting in non-synchronous reclosing. Therefore, the reclosing can cooperate with anti-islanding protection. Extend its delay time appropriately to ensure the reliable exit of IIDG at the time of reclosing, hence avoiding non-synchronous reclosing.

2) For the voltage-current type feeder automation based on the sectionalizing switch, in addition to the above effects, when a fault occurs upstream of the PCC, the integration of IIDG may cause the switch in the non-fault area to detect the fault current. However, the magnitude of the current mainly depends on the IIDG integration capacity. If the integration capacity is large, the current detected by the switch may reach the set value of the overcurrent detection, resulting in an incorrect overcurrent count of the switch. To address this issue, the direction judgment logic can be added to the sectionalizing switch. When the current flowing through the switch is reversed, the overcurrent counting function of the switch is blocked, thus avoiding the fault current provided by the IIDG to affect the switch operation.

3) For the voltage-current type feeder automation based on the circuit breaker, when the fault occurs on the downstream of the PCC, if the IIDG is still connected to the grid when the switches on the line are reclosing, the impulse current generated by non-synchronous reclosing may lead to the protection action and locking closing of the upstream circuit breaker of the PCC, and hence the fault range will be expanded. To address this issue, extending the delay time of reclosing can be considered as well.

References

1. Yan, X., Zhang, H., Ma, T., et al.: Coordinated optimization strategy of fault emergency recovery and repair for distribution network with distributed generators[J]. Autom. Electric Power Syst. **45**(22), 38–46 (2021)

2. Dai, Q., Shi, L., Ni, Y.: Risk assessment for cyberattack in active distribution systems considering the role of feeder automation[J]. IEEE Trans. Power Syst. **34**(4), 3230–3240 (2019)

3. Koozehkanani, S., Salemi, S., Sadr, S.: Optimal implementation of feeder automation in medium voltage distribution networks[C]. In: 20th Conference on Electrical Power Distribution Networks Conference. pp. 16–21. Publisher, Zahedan, Iran (2015)

4. Guo, M.: Distribution automation technology[M]. China Machine Press, Beijing (2012)

5. Yue, J., Zhijian, H., Chen, W.: Energy management of regional distribution system considering multiple stakeholders under IoT environment [J]. Electric Power Autom. Equip. **40**(8), 111–116 (2020)

6. Zhao, Y., Fang, Y., Wang, N., et al.: Research on the impacts on feeder automation by inverter-based distribution generator connected to the distribution network [J]. Power Syst. Prot. Control **41**(23), 117–122 (2013)

7. Liu, J., Zhang, X., Zhang, Z.: Improving the performance of fault location and restoration based on relay protection for distribution grids[J]. Power Syst. Prot. Control **43**(22), 7 (2015)

8. Zheng, C., Zhu, G., Lan, J., et al.: Research on the effect of inverter interfaced distributed generator on voltage-time feeder automation [J]. Power Syst. Prot. Control **48**(1), 112–116 (2020)

9. Xiaodong S.: Research on the effect and countermeasures of inverter distributed power supply on feeder automation[D]. Shandong University of Technology (2018)

10. Deng, J., Wang, Y., Sun, D., et al.: Research on the effect of IIDG on local feeder protection[J]. Power Gener. Technol. **42**(1), 115–121 (2021)

11. Dai, Z., Li, C., Jiao, Y.: Low-voltage ride through model of inverter-interfaced distributed generator and its application to fault analysis of distribution network[J]. Proc. CSU-EPSA **30**(7), 16–23 (2018)

12. GB/T 29319–2012, Technical requirements for connecting photovoltaic power system to distribution network[S]

13. Yin, X., Zhang, Z., Xiao, F., et al.: Study on short-circuit calculation model of distributed generators and fault analysis method of power system with distributed generators[J]. Power Syst. Prot. Control **43**(22), 1–9 (2015)

14. Wei Zhang, Guobing Song, Minna Dou, et al: Research on Dual Mode Feeder Automation Solution for Distribution Networks with Distributed Generation[J]. Distrib. Utilization **36**(5), 6 (2019)

15. Yang, S., Tong, X.: Short-circuit current calculation of distribution network containing distributed generators with capability of low voltage ride through[J]. Autom. Electr. Power Syst. **40**(11), 93–99+151 (2016)

16. Tang, Z.: Application of 10kV feeder automation technology in Shaoguan distribution network[D]. School of Automation Guangdong University of Technology (2020)

17. Peng, S., Liu, H., Wang, H., et al.: Research and application of automation implementation scheme for 10 kv overhead feeders based on voltage/current composite package unit[J]. Guangdong Electric Power **25**(9), 79–81 (2012)

18. Jianzhong Huang: Functional design of a new feeder automation sectionalizer[J]. Rural Electr. **1**, 12–15 (2021)

19. Xu, F.: Research on local feeder automation system[D]. Shandong University of Technology (2020)

20. Liu, J., Cheng, H., Li, Q.: Feeder automation based on reclosers and voltage-current-mode pole-mounted switches[J]. Autom. Electric Power Syst. **27**(22), 68–71 (2003)

21. Liu, Y., Liang, Y.: Fault analysis and improvement measures of voltage-current feeder automation with PV[J]. Mech. Electr. Inform. **35**, 20–21 (2019)

22. Juan Ma, Jianzhong Huang, Yao Shi: Analysis on the cause of a voltage - time segmenting device misclosing and locking[J]. Rural Electr. **04**, 37–39 (2021)
23. Chen, J.: Auxiliary application of acceleration after switching on in voltage and current feeder automation[J]. Electron. Comp. Inform. Technol. **3**(09), 120–122 (2019)

Impact of Energy Storage Access on Short-Circuit Current and Relay Protection of Power Distribution Network

Tianchi Wang[(✉)] [iD], Guofang Huang, Wei Dai, Zhonglang Wang, and Zheng Wei

State Grid Electric Power Research Institute, Nanjing 211106, Jiangsu, China
wtcqd0119@163.com

Abstract. The access to Energy Storage (ES) has changed the structure of the Power Distribution Network (PDN) from single power to multi-power. ES discharges power to the outside as a power source on one hand, and on the other hand, it is charged as a load. Therefore, the access of ES makes the calculation method of the original power distribution network short-circuit current (SCC) no longer applicable, and it has a more complicated impact on the original protection. This paper firstly determines the ES output current under the Low Voltage Ride Through (LVRT) control strategy based on the actual situation, presents SCC calculation methods for different fault types, and carries out MATLAB analysis on the change rules of SCC along with system parameters and ES capacity when ES discharges using the obtained current formula. Finally, the paper presents the impact of ES on relay protection under charging and discharging conditions.

Keywords: Energy Storage · Short-circuit current · Low Voltage Ride Through

1 Introduction

ES, an indispensable part of the novel electric power system, plays an important role in the electric power system absorbing and consuming new energy as well as improving operational stability, and is an important means to achieve the flexibility of the power system. Besides, the electrochemical energy storage represented by lithium-ion batteries has achieved large-scale development and wide application [1]. ES has three states: charging, discharging, and isolation, and its operation in different states will inevitably change the topology and load flow direction of the original power distribution network. ES acts as a power source when it discharges and a load when it charges. The maximum output current of the ES converter is generally 1.3 times its rated current. When a fault occurs in the system, it has a great impact on the protection of the traditional power distribution network, which may cause false tripping or miss tripping of the protection device. Therefore, the analysis of the calculation of SCC in power distribution networks with ES is particularly important for the protection setting and configuration of such distribution networks.

Based on the basic principle of traditional protection Reference [2] analyzes the impact of ES access on protection under two states of ES as a load and as a power source, respectively. In addition, it provides the protection improvement strategy, but it fails to consider the characteristics of ES with restricted output current nor elaborates on the problems in cooperation between the upper and lower levels of protection brought by the access of critical ES. Reference [3] carries out an analysis for two cases of reaching and not reaching the limit of output fault current of ES power station according to the output current characteristics of ES power station under PQ control. It also proposes the improvement method of protection setting optimization, which considers the requirements of ES power stations for constant values in discharging, charging, and standby states, respectively. However, it does not consider the situation under LVRT. Reference [4] considers the locating and sizing of the ES power station and investigates the impact of the ES power station on the current protection when it is connected to PDN, but it does not distinguish the impact under the charging and discharging conditions. Reference [5] analyzed the setting between overcurrent protections, but did not obtain the precise fault current value, nor did it analyze the setting coordination during charging. Reference [6] derives an approximate expression for fault transient and analyzes the characteristics of fault transient. Reference [7] gives the general analysis method of inverter power supply fault and the output three-phase fault current. Reference [8] studies the expression of the steady-state fault current of the inverter power supply, but considers that the output current during low voltage ride-through only emits reactive current, but not active current. Reference [9] made an accurate calculation of the short-circuit current of the doubly-fed wind power cluster considering LVRT, and made a response analysis of the characteristics of the fault current. Reference [10] proposes an SCC calculation method including both steady-state and transient state of new energy inverter power supply fault on the basis of fully considering the control strategy and nonlinear problems. Reference [11] gives an iterative method of SCC based on the superposition theorem for distributed generation (DG) containing LVRT. It processes DGs as different types of fault equivalent models according to their locations before and after the fault point in PDN.

In short, there are few studies on the adaptability analysis and principle of relay protection for the charging and discharging characteristics of electrochemical energy storage, and most of them make analysis for a single state. Therefore, it is significant to research the protection adaptability with ES under charging and discharging characteristics to further propose more reasonable protection principles and setting schemes. In this paper, the fault analysis model of PDN with ES is given first, and the SCC formula in the condition of fault reaching a steady state is derived to provide a basis for studying its influence on the current protection. In addition, this paper studies the general rules of SCC in PDNs with ES varies with respect to the operating state, operating capacity, and grid-connection point, and analyzes its influence on relay protection.

2   ES Control Strategy and Output Current

2.1   ES Control Strategy

ES output characteristics are mainly determined by the control strategy of the ES converter. PQ control strategy is usually adopted [12]. When an asymmetric fault occurs in

the grid, there is a negative sequence in the current output from ES and a large number of harmonics are generated, which will seriously affect the quality of electric energy. Therefore, it is also necessary to adopt a positive and negative sequence double closed-loop current control strategy to suppress the negative sequence current, so that the output current contains only the positive sequence component [13].

Reference [14], Reference [15] and so on point out that inverter-type energy in the fault steady state can be equated to a current source controlled by grid-connected-point voltage U_b i.e., the equivalent model of a voltage-controlled current source (VCCS).

According to the requirement of the *Technical Rule for Electrochemical Energy Storage System Connected to Power Grid* [16], ES must be configured with an LVRT control strategy. When a voltage drop caused by a short circuit occurs in PDN, the ES converter needs to inject reactive current and track the transformation of grid-connected-point voltage in real time, and satisfy:

$$\begin{cases} I_T \geq 1.6 \times (0.85 - U_T)I_N \ , 0.2 \leq U_T \leq 0.85 \\ \quad I_T \geq 1.04 \times I_N \qquad\qquad U_T < 0.2 \\ \qquad I_T = 0 \qquad\qquad\quad U_T > 0.85 \end{cases} \tag{1}$$

where, U_T is the per-unit value of grid-connected-point voltage of the ES converter, and I_N is the rated current of the ES converter.

2.2 Energy Storage Converter Output Current

ES discharges at constant power when it is in the normal operating state. When the ES power station does not reach the maximum output current, it remains the output power P unchanged, but when the outlet voltage drops, the output current will increase, that is,

$$P = 3U_b I_{CES} \tag{2}$$

where, U_b is the phase voltage of the ES grid-connected point, and I_{CES} is the phase current output from the ES power station.

During the LVRT period, ES will inject reactive power. When the voltage of the ES grid-connected point is higher than 0.85 p.u., only reactive power is output at a constant level, and when lower than 0.2 p.u., only reactive current is output, and almost no active current is output. When it is between 0.2 p.u.–0.85 p.u., both reactive and active currents are output, and reactive current needs to be transmitted in priority during LVRT. However, during LVRT, the active power may not be output in full margin due to the limitation of the maximum fault current. The curve graph of active and reactive currents changing with grid-connected-point voltage is shown in the figure below (Fig. 1).

Therefore, if there is one point where the grid-connected-point voltage exists, the output current of the ES converter reaches its maximum value. After taking unit value, that is,

$$\left(\frac{P}{U_b}\right)^2 + (1.6(0.85 - U_b))^2 = \left(\frac{I_{\max}}{I_N}\right)^2 \tag{3}$$

Solving this formula with both power and rated current taken as 1, we can find that $U_b = 0.77$, that is, when the positive sequence voltage of grid-connected point is
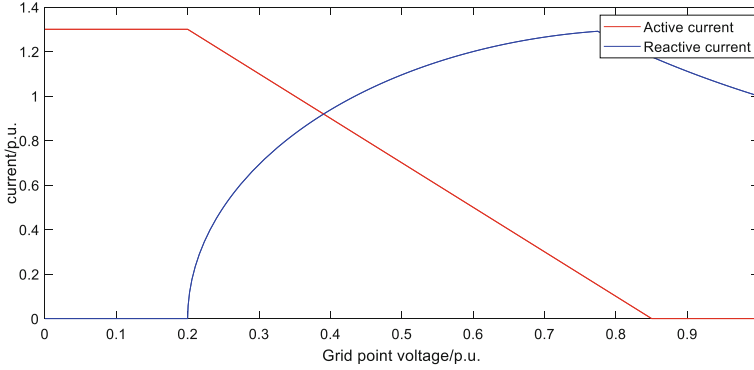
Fig. 1. Curve of active and reactive currents changing with positive sequence voltage at grid-connected point

between [0.77, 0.85], the ES converter can meet the output margin of ES active current while outputting reactive current; when the positive sequence voltage of grid-connected point is between [0.2, 0.77], the active power cannot be output in full margin.

In practical engineering, when the grid-connected-point voltage is lower than 0.2, the reactive current is generally injected according to the maximum allowable SCC of the ES converter. Therefore, when between [0.2, 0.77], the scale factor should be adjusted to 2, thus the injection current of ES can be obtained. It can be seen that the current injected from the ES converter is divided into two parts, i.e., active current and reactive current.

$$
\dot{I}_{CES} = \begin{cases}
\frac{P_N}{3U^2}\dot{U} & U \geq 0.85U_N \\
\frac{P_N}{3U^2}\dot{U} + 1.6 \times (0.85 - \frac{U}{U_N})I_N\frac{\dot{U}}{U}\angle(-\frac{\pi}{2}) & 0.77U_N \leq U \leq 0.85U_N \\
\frac{I_N}{U}\sqrt{1.3^2 - 2 \times \left((0.85 - \frac{U}{U_N})\right)^2}\dot{U} + 2 \times (0.85 - \frac{U}{U_N})I_N\frac{\dot{U}}{U}\angle(-\frac{\pi}{2}) & 0.2U_N \leq U \leq 0.77U_N \\
1.3 \times I_N\frac{\dot{U}}{U}\angle(-\frac{\pi}{2}) & U \leq 0.2U_N
\end{cases}
\tag{4}
$$

where, P_N and U_N are the rated power and phase voltage rating of ES, I_N is the rated current output from ES, $\dot{U}$ is the voltage vector of grid-connected point, and U is the module value of grid-connected-point voltage. The four states in the formula are defined as states a, b, c, and d to facilitate the description.

3 Calculation of Steady-State Short-Circuit Current (SCC)

In China, the structure of PDN is generally in a radial shape. In this paper, PDN with ES as shown in Fig. 2 is used for the calculation and analysis of SCC. Where, $\dot{E}_s$ and Z_s are the power supply voltage and equivalent impedance of the system respectively. Z_{AB}, Z_{BC} and Z_{AD} are impedances of branch circuits. In this paper, only one ES is considered to be connected.
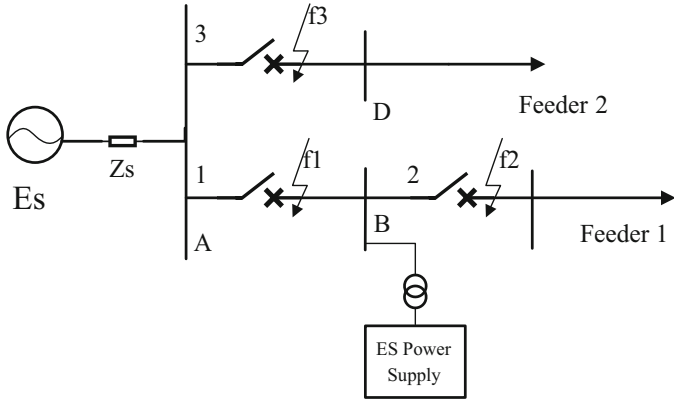
Fig. 2. Model of PDN with ES

Based on circuit knowledge, it is known that when a three-phase short circuit or a two-phase short circuit occurs at f_1, f_2, and f_3 in PDN as shown in the figure, it can always be equated to the circuit as shown in Fig. 3.
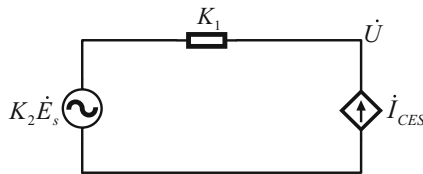
Fig. 3. Equivalent circuit diagram of PDN fault

Where, the parameters of K_1 and K_2 under different fault conditions are shown in Table 1.

Table 1. Corresponding impedances under different types of fault conditions

Fault type	K_1	K_2
Three-phase short circuit at f1	Z_{Bf}	0
Three-phase short circuit at f2	$\dfrac{(Z_s + Z_{AB})Z_{Bf2}}{(Z_s + Z_{AB} + Z_{Bf2})}$	$\dfrac{Z_{Bf2}}{(Z_s + Z_{AB} + Z_{Bf2})}$
Three-phase short circuit at f3	$\dfrac{Z_s Z_{Af3}}{Z_s + Z_{Af3}} + Z_{AB}$	$\dfrac{Z_{Af3}}{Z_s + Z_{Af3}} + Z_{AB}$
Two-phase short circuit at f1	$\dfrac{Z_s + Z_{Af1}}{2} + Z_{Bf1}$	0.5
Two-phase short circuit at f2	$\dfrac{(Z_s + Z_{AB})(2Z_{Bf2} + Z_s + Z_{AB})}{2(Z_s + Z_{AB} + Z_{Bf2})}$	$\dfrac{2Z_{Bf2} + Z_s + Z_{AB}}{2(Z_s + Z_{AB} + Z_{Bf2})}$

(*continued*)

Table 1. (*continued*)

Fault type	K_1	K_2
Two-phase short circuit at f3	$\dfrac{Z_s Z_{Af3}}{Z_s + Z_{Af3}} + Z_{AB}$	$\dfrac{Z_{Af3}}{Z_s + Z_{Af3}} + Z_{AB}$

As shown in Table 1, when a three-phase short circuit occurs at f_1, its system side is disconnected from the ES side and the current supplied by the system is not affected by ES. Therefore, no consideration is given to this condition. The circuit formula can be obtained according to Fig. 3.

$$\frac{1}{K_1}\dot{U} = \frac{K_2 \dot{E}_s}{K_1} + I_{CES} \tag{5}$$

When the voltage drop at the grid-connected point is different, the current provided by ES is also different. Substituting the ES output current in the four cases in Formula (4) into Formula (5), the voltage vector of the grid-connected point $\dot{U}$ can be obtained, and then the SCC on each branch and the SCC provided by ES can be obtained. The current calculation formulas are shown in Table 2 and Table 3.

Table 2. Three-phase SCC calculation

Fault type	Fault current (f_1)	Branch current (f_b)
Three-phase short circuit at f2	$\dot{I}_f = \dfrac{\dot{U}}{Z_{Bf}}$	$\dot{I}_{AB} = \dfrac{\dot{E}_s - \dot{U}}{Z_s + Z_{AB}}$
Three-phase short circuit at f3	$\dot{I}_f = \dfrac{\dot{U} + \dot{I}_{AB} Z_{AB}}{Z_{Af3}}$	$\dot{I}_f = \dfrac{\dot{U} + \dot{I}_{AB} Z_{AB}}{Z_{Af3}}$

Table 3. Two-phase SCC calculation

Fault type	Fault current positive sequence ($I_f^{(1)}$)	Fault current negative sequence ($I_f^{(2)}$)
Two-phase short circuit at point f1	$\dot{I}_f^{(1)} = \dfrac{\dot{E}_s - \dot{U}^{(1)} + Z_{fB} I_{CES}^{(1)}}{Z_s + Z_{AB} + Z_{Bf}}$	$\dot{I}_f^{(2)} = \dfrac{\dot{U}^{(1)} - Z_{fB} I_{CES}^{(1)}}{Z_s + Z_{AB} + Z_{Bf}}$
Two-phase short circuit at point f2	$\dot{I}_f^{(1)} = \dfrac{U^{(1)}}{Z_s + Z_{AB} + 2Z_{Bf2}}$	$\dot{I}_f^{(2)} = -\dfrac{\dot{U}^{(1)}}{Z_s + Z_{AB} + 2Z_{bf2}}$
Two-phase short circuit at point f3	$\dot{I}_f^{(1)} = \dfrac{\dot{U} - \dot{I}_{CES} Z_{AB}}{2Z_f + Z_s}$	$\dot{I}_f^{(2)} = -\dot{I}_f^{(1)}$

When performing the calculation, the grid-connected-point voltage U can be calculated separately for the cases of active and reactive currents acting separately, and then the final U can be obtained by using the superposition theorem. It should also be noted that in the actual calculation, it is necessary to firstly determine in which state of LVRT the ES operates. When the fault occurs, the ES outputs according to the constant power, that is, operating in state *a*. Now, the positive sequence voltage RMS value of ES grid-connected point is calculated, in which state the ES operates is determined according to the proportion of positive sequence voltage to the rated voltage, and the fault current is recalculated.

4 Impact of ES Access in Discharge on PDN Fault Characteristics

From the above obtained expressions, we can know that with ES accessed, the grid-connected-point voltage is influenced by the access location, fault point location, ES capacity, and fault type, and SCC is influenced by the grid-connected-point voltage. Therefore, it is necessary to find the change trend graph and summarize the influence law based on the SCC calculation formula. The system short-circuit capacity of PDN with ES shown in Fig. 2 is 500 MVA, the system impedance is $Z_s = j0.27 \, \Omega$, and the unit length impedance of the line is $Z = 0.27 + j0.3454 \, \Omega$.

4.1 Impact of ES Access on Grid-Connected-Point Voltage

When the location of the fault point to ES access keeps changing, the analysis is carried out for the case of a three-phase short circuit occurring downstream, and the simulation results are shown in Fig. 4. When the ES access location keeps unchanged, the grid-connected-point voltage gradually increases as the fault point location becomes farther away; when the fault point location keeps unchanged, the grid-connected-point voltage gradually becomes smaller as the ES access location becomes farther away. In addition, when ES performs LVRT, the grid-connected-point voltage increases with the increase of reactive current at the same position, but when ES operates in state *d*, the grid-connected-point voltage decreases because only reactive power is emitted.
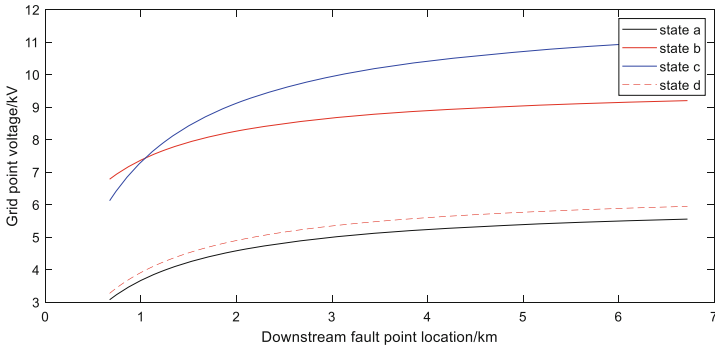
(a)The relationship between grid connection point voltage and fault location
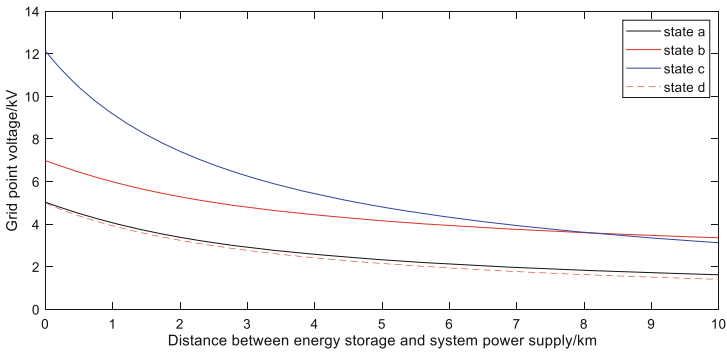
(b)The relationship between grid connection point voltage and energy storage access location

Fig. 4. The relation between grid-connected-point voltage and ES access location

When the location of the fault point is given and the ES access capacity keeps changing, the change rule is shown in the figure below. With the increase of ES capacity, its grid-connected-point voltage shows a trend of increasing first and then decreasing. A similar transformation trend can be obtained when analyzing different operating states under other fault conditions (Fig. 5).
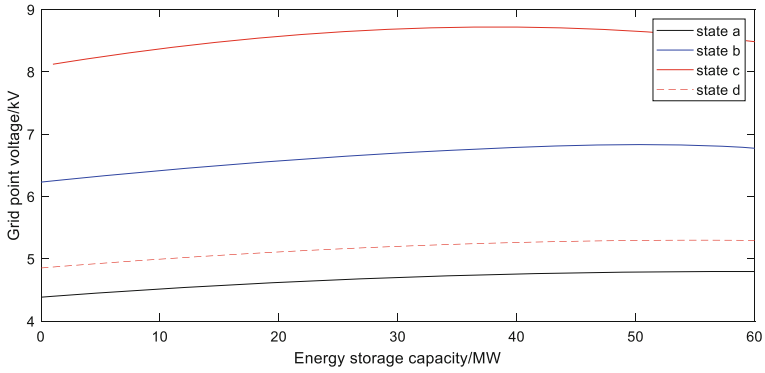
(a)The relationship between grid connection point voltage and capacity
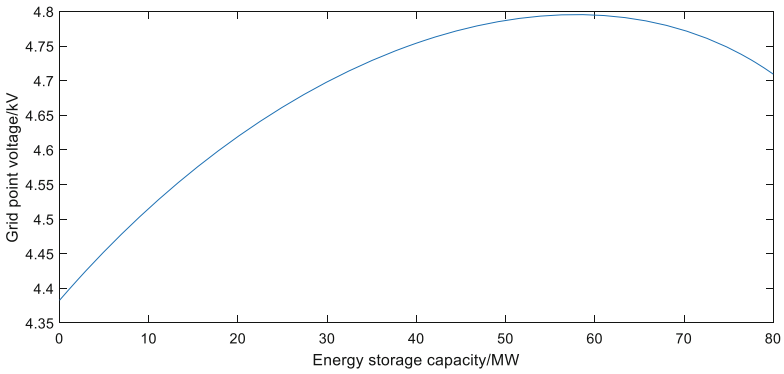
(b)The relationship between grid connection point voltage and capacity in state a

Fig. 5. The relation between grid-connected-point voltage and ES capacity

Reference [17] deduces the relationship between the voltage support effect of the grid connection point and the impedance ratio of the grid impedance and the penetration rate of the distributed power generation. It can draw a voltage vector diagram according to Fig. 3, as shown in Fig. 6. In the figure, the equivalent impedance angle is α, Grid point voltage is $\dot{U}_b = U_b \angle \varphi$.
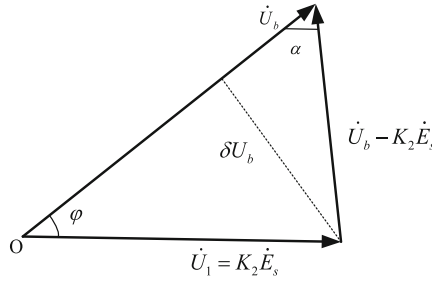
Fig. 6. Voltage vector diagram when energy storage discharges

For state a, it can be deduced from the relationship between the vectors:

$$\begin{cases} |\delta U_b| = \frac{PX - QR}{U_b} = \frac{P}{3U_b}\text{Im}(K_1) \\ |\dot{U}_b - K_2\dot{E}_s| = \frac{|\delta \dot{U}_b|}{\sin\alpha} = \frac{P}{3U_b}\frac{\text{Im}(K_1)}{\sin\alpha} \\ \frac{|K_2 E_s|}{\sin\alpha} = \frac{U_b}{\sin(\alpha+\varphi)} = \frac{P}{3U_b}\frac{\text{Im}(K_1)}{\sin\alpha \sin\varphi} \end{cases} \quad (6)$$

For state b and d, it can be deduced from the relationship between the vectors:

$$\frac{|K_2 E_s|}{\sin\alpha} = \frac{U_b}{\sin(\alpha+\varphi)} = \frac{\frac{P_N}{3U_b}\text{Im}(K_1) + 1.6(0.85 - U_b/U_N)I_N\text{Re}(K_1)}{\sin\alpha \sin\varphi} \quad (7)$$

$$\frac{|K_2 E_s|}{\sin\alpha} = \frac{U_b}{\sin(\alpha+\varphi)} = \frac{1.3I_N\text{Re}(K_1)}{\sin\alpha \sin\varphi} \quad (8)$$

It can be seen that when the energy storage operates in state a, the voltage at the grid connection point is closely related to the imaginary part of K1. For state b, according to formula (7), it can be known that the voltage of state b is generated by two parts. Part of it is generated by active current, and part of it is generated by reactive current, so the voltage of state b is higher than that of state a, and the voltage of state c is higher than that of state b (the maximum output current is reached). However, when the energy storage operates in state d, only reactive current is emitted. According to formula (8), it can be known that the change of voltage is closely related to the real part of K1. Therefore, the voltage in state d is lower than that in states b and c, but the change trend with the capacity does not change. The magnitude of the voltage depends on the operating state on the one hand and on the impedance parameters of the grid on the other hand.

As shown above, the grid-connected-point voltage decreases with the increase of ES capacity, increases with the distance from the fault point, and decreases with the distance from the system power supply. Besides, it is independent of the fault type and operation state.

4.2   Impact of ES Access on SCC

(a) **ES Upstream SCC Characteristics**

When a three-phase short circuit occurs upstream, ES is decoupled from the system-side circuit, and the SCC flowing through the system side is unrelated to

whether any ES is connected. When a two-phase short circuit occurs upstream, the grid-connected-point voltage satisfies $\dot{U}^{(1)} = \dot{E}_s/2$ without ES connected, and with ES connected, the grid-connected-point voltage must be greater than $0.5U_N$. Therefore, when a two-phase short circuit occurs upstream, ES can only operate in two states: state a and state b.

With ES operating in states a and b, the change trend of SCC on phase B and phase C upstream of the fault point with the storage capacity is shown in Fig. 7.
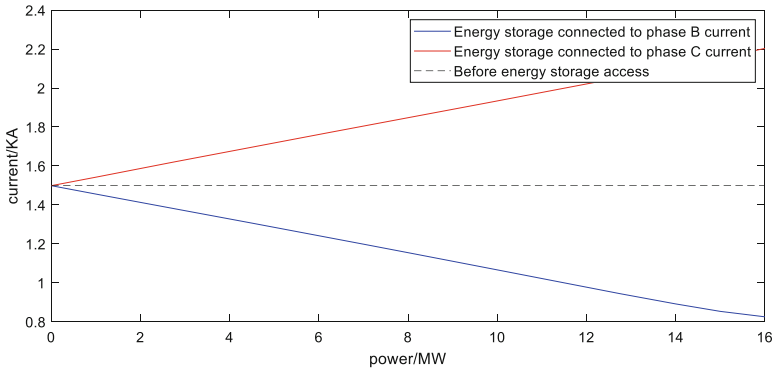
(a) state a
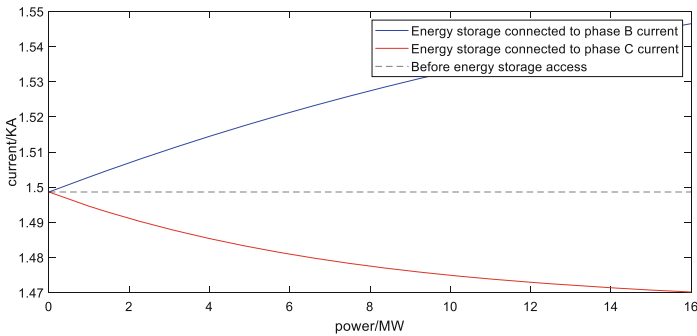
(b) state b

Fig. 7. Change of upstream two-phase SCC with ES capacity

In the case of a two-phase short circuit occurring upstream, when ES operates in state a, the access of ES shows an infeed effect on phase-B SCC, while it shows an outfeed effect on phase-C SCC. When ES operates in state b, it shows an infeed effect on both the phase-B and phase-C SCCs.

(b) **ES Downstream SCC Characteristics**

When ES operates in state *a* and a three-phase short circuit occurs downstream, the trend of upstream and downstream SCCs changing with ES capacity is shown in Fig. 8 below.

From Fig. 8, it can be seen that, when ES operates in state a, the downstream SCC shows an infeed effect, while the upstream SCC shows an outfeed effect when the ES capacity is small and an infeed effect when the ES capacity is large, and the infeed effect becomes more obvious as the ES capacity increases. As the reactive current continues to increase, when ES operates in state b,c and state d, its operation rule is the same as that in state a, both showing an outfeed effect first and then an infeed effect. However, to obtain an infeed effect on the upstream, a large ES capacity is required.
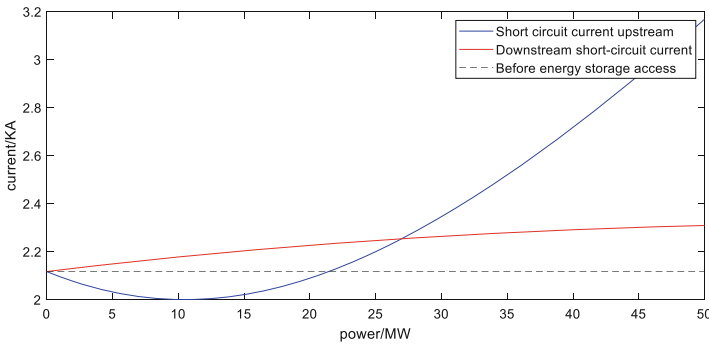
Fig. 8. Change of downstream three-phase SCC with ES capacity (state a)

When a two-phase short circuit occurs downstream of ES, the change trend is shown in Fig. 9. When operating in state a, the upstream phase-B SCC exhibits an outfeed effect first and then an infeed effect, the upstream phase-C SCC exhibits an infeed effect, and the downstream phase-B and phase-C SCCs both exhibit an infeed effect. When operating in state b, the upstream phase-B SCC exhibits an infeed effect first and then an outfeed, the upstream phase-C SCC exhibits infeed, and the downstream phase-B and phase-C SCCs both exhibit an infeed effect. State c is the same as the performance pattern of state b. When ES operates in state d, the upstream phase-B SCC exhibits an infeed effect, and the upstream phase-C SCC exhibits an outfeed effect, which is exactly the opposite of the situation in state a, however, the downstream SCC still exhibits an infeed effect.
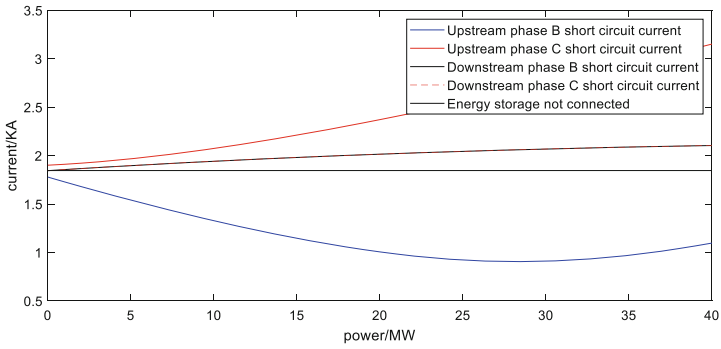
(a) state a
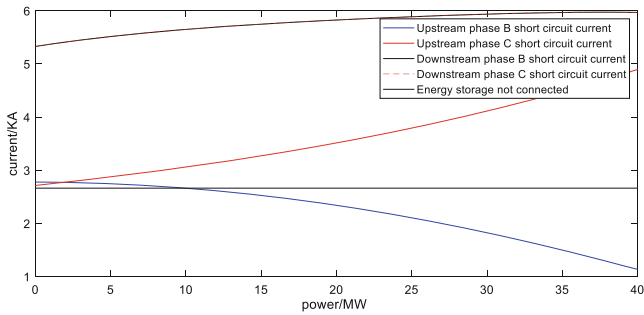
(b) state b
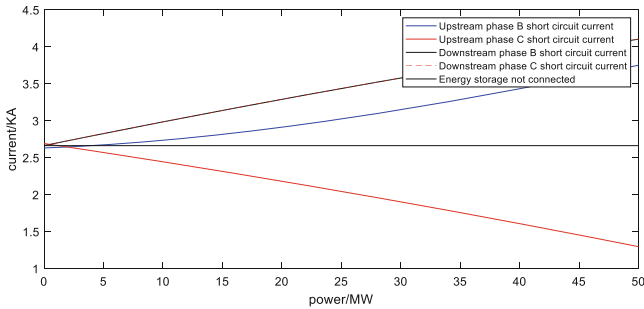
(c) state d

Fig. 9. Variation of downstream two-phase short-circuit current with energy storage capacity

(c) **Adjacent Feeder SCC characteristics**

When three sections of short circuit occur in adjacent feeders of ES operation, it plays an infeed effect for the fault branch, and in state a and state b capacity changing has less influence on the fault current. With the increase of reactive current, the impact of ES capacity on the fault current becomes larger.
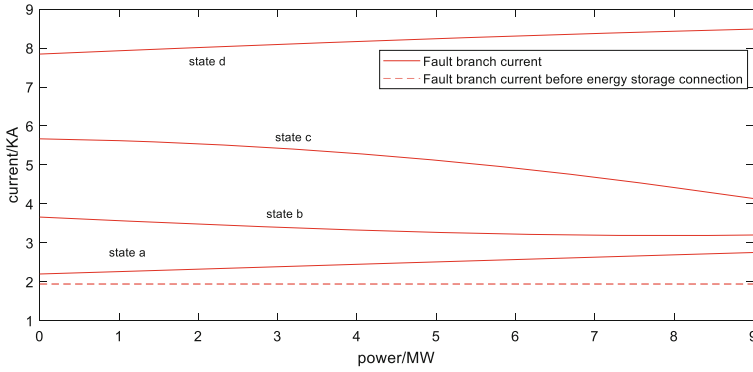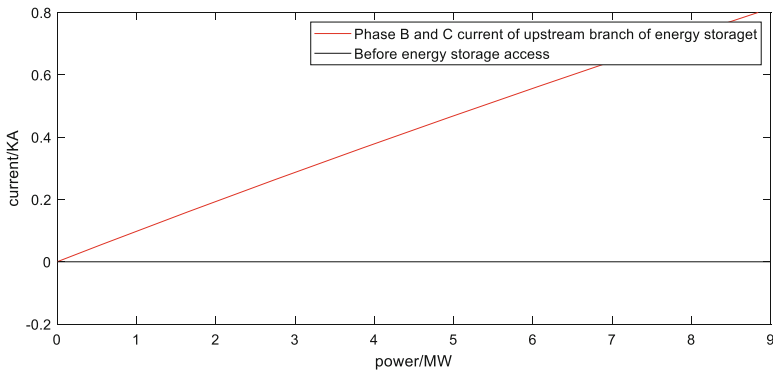
Fig. 10. Adjacent feeder short circuit three-phase short circuit fault branch current
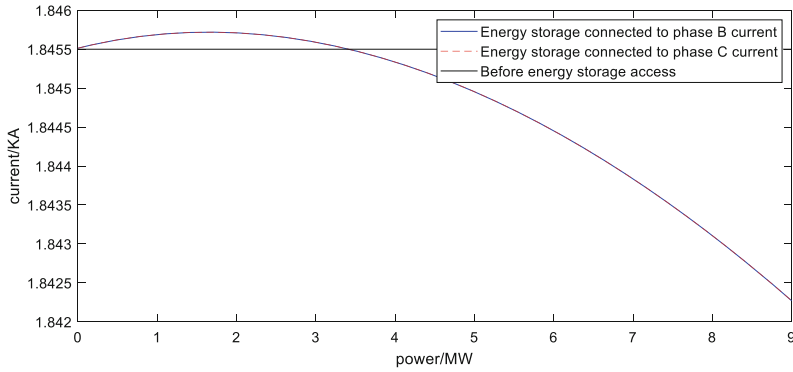
(a)fault branch

(b)AB branch

Fig. 11. Change of adjacent feeders two-phase SCC with ES capacity (state *a*)

When a two-phase short circuit occurs, as shown in Fig. 10, the phase-B and phase-C fault branch SCCs act the same, which shows infeed first and then outfeed, and the impact on the branch SCC is very small. For lines A and B, both phases B and C show an infeed effect (Fig. 11).

When LVRT is performed, they exhibit an infeed effect in all the three states: b, c and d. In the case of the same ES access capacity, the increase of reactive current causes the SCC to become smaller. When ES all generate reactive power, i.e., when operating in the state d the infeed effect is more obvious (Fig. 12).
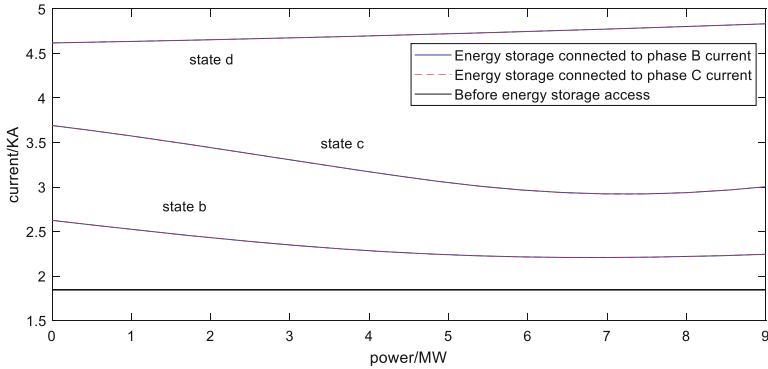
Fig. 12. Change of adjacent feeders two-phase SCC with ES capacity (states b, c, and d)

4.3 General Rules of SCC in ES Discharging

The general rules for single ES accessed in discharge state are as follows:

(1) With ES accessed, the grid-connected-point voltage is only related to the access location and ES capacity, but not to the fault type. No matter which state ES operates in, the grid-connected-point voltage shows a trend of increasing first and then decreasing. When ES is closer to the system power, grid-connected-point voltage is higher; when the fault point is closer to ES, the grid-connected-point voltage is lower.

(2) When line fault occurs, ES access shows an infeed effect to the downstream short circuit or non-fault branch current, regardless of the fault type, operating state, and fault location.

(3) When a three-phase short circuit occurs downstream, except upstream SCC in state b always shows an infeed effect, upstream SCC in operating states a, b, and d all shows an outfeed effect first and then an infeed effect with the increase of ES capacity.

(4) When BC phase-to-phase fault occurs upstream or downstream of ES, with the increase of reactive current, phase-C fault current will change from infeed to outfeed effect, while phase-B fault current will change from outfeed to infeed effect.

(5) When a three-phase short circuit occurs between adjacent feeders, it shows an infeed effect for the fault branch, while the reverse current of the non-faulted branch current is larger than the forward current; when a two-phase short circuit occurs, the change rule of SCC of phase-B and phase-C is the same. When ES operates in state a, it firstly shows an infeed effect, which is small, and then outfeed effect. When it is LVRT state, both show an infeed effect.

5   Impact of ES Access on Relay Protection

When ES discharges, it is equivalent to an inverter-type power source, and its impact on the fault current is affected by the LVRT control strategy. The fault current change rule has been discussed above, that is, when the fault current shows an outfeed effect, it may lead to miss tripping of the protection system; when the fault current shows an infeed effect, it may lead to false tripping of the protection system. The presence of reverse current may also result in loss of directional selectivity of the protection system.

When ES charges, which usually be done at constant power, it is equivalent to a load. This section focuses on the qualitative analysis of the impact on current protection when ES charges.

In the condition of no fault occurring in the line, when ES changes from discharging state to charging state, it will make the load of PDN and the load current flowing through the upstream line increase, which may lead to the false tripping of upstream protection. In addition, the circuit's backup protection setting will be done as per the maximum load current that occurs on the line, so when a short circuit occurs at the end of adjacent lines, it may cause the miss tripping of backup protection.

When a fault occurs upstream of ES, ES will be too higher than the level of upstream SCC, thus leading to enhanced protection sensitivity, which may result in false tripping of protection. When a fault occurs downstream of ES or on adjacent lines, the fault branch current becomes smaller due to the shunt effect of ES, making the protection range smaller and less sensitive, and thus causing miss tripping of protection.

6   Conclusion

The charging and discharging of ES pose an impact on the current protection of PDNs, so it is very important to calculate SCCs of PDNs with ES. In this paper, the SCC of PDN with ES taking into account the LVRT characteristics is calculated on the basis of the LVRT control strategy and the factors affecting SCC are analyzed in detail using the calculation formula. In addition, the general rules of grid-connected-point voltage and SCC change with parameters after ES is accessed are summarized. Furthermore, the impact of ES on relay protection under two conditions of charging and discharging is given, which provides a theoretical basis for further study on the current protection scheme of PDN adapted to the charging and discharging conversion of ES.

References

1. Wen, J., Zhou, B., Wei, L.: Preliminary study on an energy storage grid for future power system in China. Power Syst. Prot. Control **50**(07), 1–10 (2022)
2. Hong, L., Chen, M., Dai, R.: Influence of energy storage station access on distribution network protection. Power Energy **38**(05), 598–605 (2017)
3. Xue, F., Xu, W., Wang, H.: Research on current protection of distribution network with energy storage system. Electr. Eng. (09), 67–71 (2020)
4. Yang, L., Fan, C., Tai, N.: Energy storage station locating and sizing based on relay protection and improved algorithm. Trans. China Electrotech. Soc. **30**(03), 53–60 (2015)
5. Deng, J., Wang, Y., Sun, D.: Capacity analysis of distributed photovoltaic generation based on current protection in distribution network. Trans. China Electrotech. Soc. **34**(S2), 629–636 (2019)
6. Shen, Q., Yang, Z., Song, G.: Short-circuit current computation method for electric elements with converter. J. Xi'An Jiaotong Univ. **49**(04), 24–31 (2015)
7. Kong, X., Zhang, Z., Yin, X.: Study on fault current characteristics and fault analysis method of power grid with inverter interfaced distributed generation. Proc. CSEE **33**(34), 65–74 (2013)
8. Tan, H., Li, Y., Li, X.: Influence of inverter-interfaced distributed generator with low-voltage ride-through capability on short circuit current of distribution network. Electr. Power Autom. Equipment **35**(08), 31–37 (2015)
9. Yin, J., Li, Y., Xiong, J.: Short circuit current calculation and fault analysis method of DFIG wind-farm groups. Electr. Power Autom. Equipment **37**(08), 113–122 (2017)
10. Kuang, X., Fang, Y., Guan, H.: Full-time domain short circuit current calculation method suitable for power network with inverter-interfaced renewable energy source. Electr. Power Autom. Equipment **40**(05), 113–122 (2020)
11. Yang, S., Tong, X.: Short—circuit current calculation of distribution network containing distributed generators with capability of low voltage ride through. Autom. Electr. Power Syst. **40**(11), 93–99 (2016)
12. Hong, S., Fan, C., Chen, S.: Research on fault equivalence method for multiple inverter-interfaced distributed generation based on PQ control strategy. Power Syst. Technol. **42**(04), 1101–1109 (2018)
13. Hou, G., Liu, Q., Xie, M.: The LVRT of the BESS under both balance and unbalance grid fault. Power Syst. Prot. Control **41**(10), 62–67 (2013)
14. Wu, Z., Wang, G., Li, H.: Fault characteristics analysis of distribution networks considering control scheme of inverter interfaced distributed generation. Autom. Electr. Power Syst. **36**(18), 92–96 (2012)
15. Zhang, H., Li, Y.: Short-circuit current analysis and current protection setting scheme in distribution network with photovoltaic power. Power Syst. Technol. **39**(08), 2327–2332 (2015)
16. China Electric Power Research Institute Co., Ltd.: Technical regulations for connecting electrochemical energy storage system to power grid. China National Standardization Administration Committee (2018)
17. Jiang, L.: Supporting effect of power injection from distributed generations on voltage at grid-connected point during symmetrical short-circuit faults in power system. Power Syst. Technol. **38**(03), 669–674 (2014)

Deep-Learning Based Reactive Voltage Control of Regional Power Grids Integrated with Renewable Energy Resources

Haozhe Wang[1(✉)], Jixiang Lu[1,2], Tao Zhang[1], Jianhua Chen[1], Ningkai Tang[1], and Jiao Shu[1]

[1] NARI Group Corporation (State Grid Electric Power Research Institute), Nanjing 211106, Jiangsu, China
775410279@qq.com, lujixiang@sgepri.sgcc.com.cn

[2] State Key Laboratory of Smart Grid Protection and Control, Nanjing 211106, Jiangsu, China

Abstract. With the increasing penetration rate of distributed renewable energy and more complexity of grid, it is essential to keep a secure voltage profile for the safety, stability and economy of the power system. A reactive voltage control approach in regional power grid is proposed in this paper, which can provide online decisions without the requirement of the model and parameters. The proposed approach enhances the ability to rapidly restore the voltage back to normal after severe system disturbances. Furthermore, to regulate voltage profiles and reduce shunt operations, an LSTM based reactive voltage control model is also proposed by considering transformers and capacitors. A case of a regional power grid in Jiangsu is studied to verify the proposed scheme. The experimental results show the capability and efficiency of the proposed scheme. In contrast to traditional methods, our approach improves the accuracy of the control strategy by prediction model meanwhile limiting the action times of control devices.

Keywords: Deep learning · Reactive power optimization · Renewable energy · Voltage control · LSTM

1 Introduction

With the rapidly increasing penetration of renewable energy, the proportion of external direct current (DC) and renewable energy generation in Jiangsu is reaching 50%. Modern power systems are facing grand challenges in regulating voltage profiles due to the inherently complex dynamics and high uncertainty brought by renewable energy. The existing theoretical system of reactive voltage operating and planning could not satisfy the requirements of stable grid operation, mainly reflected in the problems of voltage overrun, reactive power backflow, and increased network loss. Securing power regulation with reactive voltage control effectively is a critical issue to be addressed in power systems. At present, the popular reactive voltage control methods for solving

dynamic problems are model prediction [1, 2], intelligent optimization [3–6], mathematical optimization [7], load partition [8–11] and reactive power partition [12–14]. The control effectiveness of model prediction method could have a large impact due to state estimation error. The intelligent optimization method does not consider the cooperative operation mode of reactive power devices, and cannot meet the requirements of system time scale. The mathematical optimization method is difficult to achieve the goals of economy and safety, and cannot adapt to the strong stochastic nature of photovoltaics.

On the contrary, the load partition method converts dynamic reactive voltage control into static optimization. Nevertheless, renewable energy has substantial uncertainty that causes large fluctuations in a short period, which greatly limits the load partition method. The reactive power partitioning method can simplify the computation and reduce the calculation errors caused by inaccurate measurements. Moreover, this method requires high accuracy in power flow calculations, strict and precise mathematical models. What is worse, the control strategies given are usually not global optimization. To sum up, these methods generally have many downsides, such as heavy computation, the long calculation time for deriving optimal control actions, difficulty in achieving online control, and ease of falling into local optimal solutions, further limiting their applications in real-time. In response to the limitations above, many researchers have tried to combine artificial intelligence with reactive voltage control methods. Reference [15] uses reinforcement learning to map the measured values of voltage magnitudes and topology information of On Load Tap Changer (OLTC) tap ratio changes so as to minimize the voltage deviation across the system. However, this method relies on topology information and only regulates reactive power through transformers. Reference [16] combines reactive voltage control model with deep learning, which fits the nonlinear relationship between system features and reactive voltage control strategies through a deep belief network. Reference [17] utilizes an off-policy algorithm, i.e., deep deterministic policy gradient (DDPG), to solve a persistent control problem. Nevertheless, DDPG, as an off-policy learning approach, has relatively unstable performance.

The reactive voltage control problem is a complex, multi-dimensional, nonlinear problem. Deep learning algorithms can analyze useful information from massive historical data and establish a hidden relationship between inputs and outputs [18]. On the basis of the existing researches, we combine deep learning with reactive voltage control to generate a deep learning agent using an LSTM-based approach. Furthermore, we establish a refined decision-making scheme for online reactive voltage control in regional power grid under the uncertainty renewable energy, and realize the synergistic control mode of transformers and capacitors. Promising results with significant benefits are demonstrated from aspects of both security and the economy. First of all, based on the time-series historical data, this scheme trains a deep neural network prediction model and constructs a mapping relationship between the characteristics of the existing system and the busbar voltage at the next timestamp. Secondly, when performing real-time control, for reactive power or voltage violations, an alternative control strategy set for the adjustable control devices is generated according to the nine-zone diagram. Then, a prediction model is used for voltage prediction, and a set of control strategies that meet the conditions are screened out. Finally, the control strategy with the highest score is obtained as the output according to the reward function.

Meanwhile, the prediction model is continuously updated during interaction with the environment. Unlike the conventional methods, this scheme gets rid of state estimation, infers the accurate system state directly according to the Supervisory Control And Data Acquisition (SCADA) data, and implements the control strategy in a short period. This method can reduce the number of actions of transformers and capacitors, and improve the voltage quality. Model training only needs real-time SCADA data, such as node voltage and line power flow, without complete topological model parameters of the system. This process can be achieved offline in a safe lab environment without interaction with a real system.

The remainder of this paper is organized as follows. Section 2 provides an overview of the LSTM. Section 3 describes the detailed implementation of the deep learning based reactive voltage control. In Sect. 4, a case study is conducted in Jiangsu. Experimental results have verified the safety and economic advantages of the proposed approach. Finally, we conclude our work in Sect. 5, and future research work is also included.

2 LSTM

By using nonlinear functions, deep learning can express complex relationships between input and output data. To date, deep learning networks include deep belief networks, recurrent neural networks, and convolutional networks. Deep neural network has excellent learning capabilities, which can promote stabilize power systems [19] and reduce decision-making time.

Considering the time-series characteristics of electric power data, we use the long short-term memory neural network (LSTM) algorithm, which can efficiently handle nonlinear time-series problems and has good generalization ability as well. Therefore, this paper uses the LSTM algorithm to build a prediction model.

To avoid the problems of "gradient vanishing" and "gradient explosion", LSTM introduces a hidden layer structure, which includes forget gate, input gate and output gate [20]. The composition of the LSTM neural network is shown in Fig. 1.
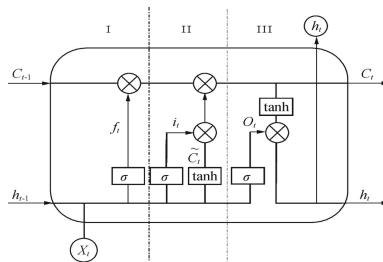
Fig. 1. Structure diagram of LSTM

As shown in Fig. 1, block I is the forget gate, which can filter the data information under the previous time series. Block II is the input gate, and block III is the output gate, Eq. (1) and (2) are the cell state and forgetting gate formulas, respectively, Eq. (3) and

(4) are the input gate formulas, and Eq. (5) and (6) are the output gate formulas [21, 22].

$$C_t = f_t \times C_{t-1} + i_t \times \tilde{C}_t \tag{1}$$

$$f_t = \sigma(W_f[X_t, H_{t-1}, C_{t-1}] + b_f) \tag{2}$$

$$i_t = \sigma(W_i[X_t, H_{t-1}, C_{t-1}] + b_i) \tag{3}$$

$$\tilde{C} = \tanh(W_{ig} \cdot [H_{t-1}, X_t] + b_{ig} + W_{hg}H_{t-1} + b_{hg}) \tag{4}$$

$$o_t = \sigma(W_o \cdot [X_t, H_{t-1}, C_{t-1}] + b_o) \tag{5}$$

$$h_t = o_t \times \tanh(C_t) \tag{6}$$

where C_{t-1}, C_t are the cell states at time t − 1 and time t; H_{t-1}, H_t are the outputs at time t − 1 and time t; X_t is the input at time t; f_t, i_t, o_t are the function values of the forget gate, input gate, and output gate at time t; σ is the sigmoid activation function; W, b are the weights and biases.

3 The LSTM-Based Framework for Reactive Voltage Control

Addressing the regional power grid with high penetration of renewable energy, the reactive voltage control model proposed in this paper takes voltage security and stability as the primary control objective, to reproduce the number of reactive power control devices actions is treated as the secondary objective, so as to achieve real-time continuous closed loop voltage optimal control. From the aspect of function mapping, the key to the control problem is to establish a mapping relationship between the data features of the regional power system and the controlled bus voltage, which is complex, implicit, high-dimensional and nonlinear. It is difficult to find an analytics solution at once.

There are massive historical data in regional power grids. Useful information can be extracted from this data, which helps to solve high-dimensional nonlinear mapping problems accurately and quickly by using deep neural networks. The deep neural network constructed on valid information solves the problem that the conventional methods do not consider the control operation and physical response of the power device, while only relying on the linearization of the power network equations.

3.1 Overall Architecture Design

To understand the schematic diagram of the reactive voltage control procedures proposed in this paper, we depict this control method with deep neural network in Fig. 2. The framework mainly consists of two components: offline training and online decision-making.

In the offline training stage, the nonlinear relationship between the system features and the controlled bus voltage is fitted through LSTM. In the online decision-making

stage, the agent obtains SCADA data. The agent generates a control strategy set when the bus voltage exceeds the limit. It filters the strategy set with the nine-zone diagram and integrates the filtered strategy set with the current SCADA data. The system features for the voltage prediction model are extracted from the integrated results. Finally, based on the results of our voltage prediction model, the agent outputs the optimal control strategy according to the reward function. Real-time measurement data is stored and recorded simultaneously in discrete data for model updating.
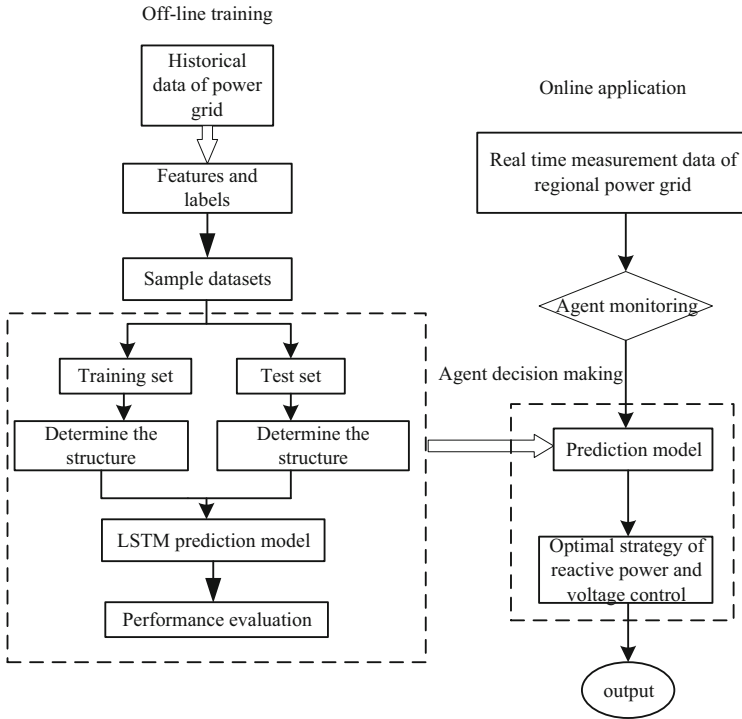
Fig. 2. Diagram of the reactive voltage control architecture of the framework

3.2 Neural Network Architecture Design

In this paper, the input sequence length of LSTM is 20 records. When generating the training set, the input sequence is generated sequentially by time series sliding with a step size of 1. After experiments, it can be found that the predictive ability of the model is affected by the network unit of LSTM. For the network, three layers of neurons are applied: the first layer consists of an LSTM layer with 1024 neurons and a *tanh* function. Then the second layer is an LSTM layer with 512 neurons and a Rectified Linear Units (ReLU) activation function. The last layer is a fully-connected layer (Dense) with 104 neurons (matching with 104 bus voltages) and a sigmoid activation function. The optimizer used for the network is the Adamax Optimizer, with a learning rate of

10^{-3}. To prevent overfitting, a random dropout layer is added after each LSTM layer, and the learning data features are enhanced by a Dense layer. Thus, to extract more useful information from the input time series, the first 20 records are fed into the LSTM layer. After two layers of LSTM transformation, the last timestamp data in the hidden layer sequence output by LSTM is taken. This data is stitched with the known feature information of the next record (Such as system state quantity at the current timestamp, bus voltage at the current timestamp, and the system state quantity at the next timestamp), and then all is inputted into the Dense layer, as shown in the Fig. 3 below:
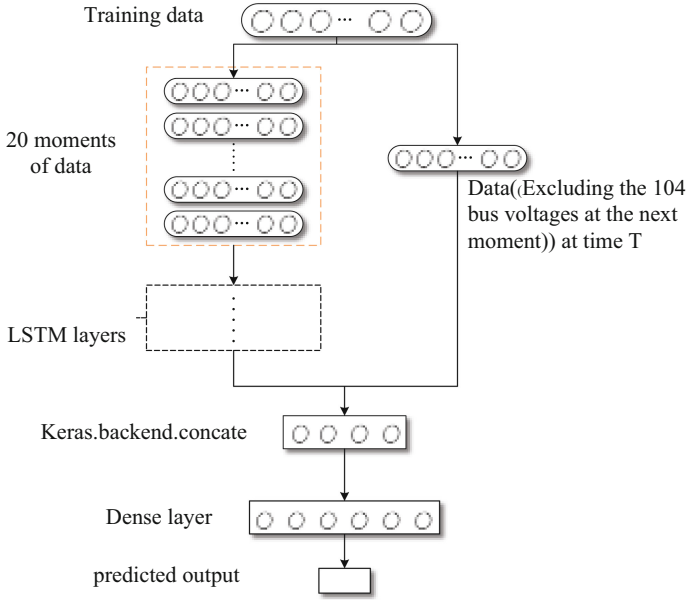
Fig. 3. LSTM prediction model

During model training, the loss function is defined as MAPE (Mean Absolute Percentage Error) for model training. It is used to evaluate the prediction performance. With the following equations:

$$MAPE = \frac{1}{n}\sum_{i=1}^{n}\left|\frac{x_i - \overline{x_i}}{x_i}\right| \tag{7}$$

x_i represents the actual value, $\overline{x_i}$ represents the predicted value, and n represents the total number of prediction results.

3.3 Agent Decision Making Strategy

The agent continuously monitors the power grid states. When the node voltage or reactive power exceeds the limit, the agent will determine the standby control strategy type

according to the voltage regulation logic of the nine-zone diagram (filters out the obvious incorrect control strategies, such as switching on capacitors while reducing transformer taps). According to the node's controllable resources and the control variables' constraints, all the control policies that meet the conditions are given. Based on the former control policies, the new grid data characteristics are input to the prediction model to form a new grid state. All control policies that meet the criteria are scored and sorted, and the highest-scoring control policy comes out. The reward function is a weighted combination of two parts: the safety evaluation function f_1 and the economic evaluation function f_2.

$$f_1 = \lambda_V \Delta U = \lambda_V \sqrt{\frac{1}{n} \sum_{i=1}^{n} (\frac{U_i - U_{iN}}{U_{iN}})^2} \tag{8}$$

$$U_{iN} = \frac{U_{i\max} + U_{i\min}}{2} \tag{9}$$

ΔU is the overall voltage deviation of the system, λ_v is the penalty factor for voltage deviation. U_i is the actual voltage of the i-th node of the system at that time, $U_{i\max}$, $U_{i\min}$ are the maximum and minimum voltage, U_{iN} is the middle value of the upper and lower voltage limits of the i-th node of the system, and n is the total number of training samples.

$$f_2 = \lambda_1 \sum_{i=0}^{N_c} C_i + \lambda_2 \sum_{i=0}^{N_T} T_i \tag{10}$$

λ_1, λ_2 are capacitor and voltmeter regulation penalty factors, C_i is the number of operations of the capacitor, T_i is the number of operations of the transformer.

The design of this reward function aims to serve the following purposes:

1) keep the voltage profile within a normal range
2) minimum voltage deviation after any disturbances
3) reduce the number of discrete actions

The constraints of the reward function are as follows:

$$U_{\min} \leq U \leq U_{\max} \tag{11}$$

$$Q_{\min} \leq Q \leq Q_{\max} \tag{12}$$

$$G_i(X, T) = 0 \ i = 1, 2 \ldots N \tag{13}$$

$$Q_{G\min} \leq Q_G \leq Q_{G\max} \tag{14}$$

$$T_{\min} \leq T \leq T_{\max} \tag{15}$$

where Eqs. (11) and (12) are voltage and reactive power constraints, respectively, Eq. (13) is the system power flow equation constraint, Eq. (14) is the photovoltaic reactive power output constraint, and Eq. (15) is the capacitor and transformer action number constraints.

The real-time reactive voltage control steps based on SCADA data are presented in Algorithm 1.

Algorithm 1: Deep learning agent for reactive voltage control-pseudocode in real-time

Data: SCADA data
Result: Optimal control strategy

```
1  while T ≤ Tmax do
2  |   Analyze SCADA data;
3  |   Check for reactive or voltage violation;
4  |   if Violation then
5  |   |   while Controllable resources available do
6  |   |   |   Generate schemes based on nine-zone diagram;
7  |   |   |   Load the LSTM prediction model;
8  |   |   |   for scheme i = 1, ..., N do
9  |   |   |   |   Calculate Reward R base on prediction model ;
10 |   |   |   end
11 |   |   |   Evaluate and choose the scheme with the largest reward;
12 |   |   |   Execute the action set At = (a¹t, ..., aᴺt);
13 |   |   end
14 |   else
15 |   |   Waiting for new SCADA data file;
16 |   end
17 |   Update local database;
18 end
```

---

4 Case Study

4.1 Experimental Platform and Study Case

The platform used to train and test deep learning agents for reactive voltage control is the ubuntu system in Python 3.7. This server is equipped with Intel(R) Xeon(R) CPU E5-2683 v4 with 64 cores/125 GB memory and GeForce GTX 1080 Ti.

The experimental object selected a regional power grid in Jiangsu, tested in terms of control error and efficiency in the virtual environment. At present, all the plants and stations in this region are connected to closed loop control, with 15 transformer substations with a voltage of 110 kV or less than 110 kV and 11 photovoltaic stations, summing up to three control areas. The distribution of renewable energy stations is shown in Table 1:

Table 1. Distribution of new energy power stations

New energy power station name	Node number	Active power (MW)	Reactive power (MVar)	New energy power station name	Node number	Active power (MW)	Reactive power (MVar)
Photovoltaic station 1	6	10	−3.13	Photovoltaic station 7	81	2.56	−0.84
Photovoltaic station 2	12	1.12	−1.38	Photovoltaic station 8	82	4.99	6.3
Photovoltaic station 3	16	1.47	−0.34	Photovoltaic station 9	109	2.56	−0.84
Photovoltaic station 4	19	1.95	−0.37	Photovoltaic station 10	110	2.56	−0.84
Photovoltaic station 5	20	2.56	−0.84	Photovoltaic station 11	111	0.91	0.4
Photovoltaic station 6	80	2.23	8.8				

4.2   Introduction to Calculation Examples

We selected 15 days of historical information in a certain area of Jiangsu in April 2021 as the experimental data set. Samples were taken every 1 min, and the characteristic information of each time section was taken as a record. After eliminating abnormal data in the samples, 20718 records in total are considered for training the agent, of which 18650 records and 2068 records are taken as the training set and test set of the prediction model, respectively. The training was terminated when the validation accuracy (RMSE error) did not improve for 30 epochs. The batch size is set to 32.

Each record contains 836 features, including 531 characteristic electrical quantities, 104 bus voltages at the current timestamp, and partial electrical quantities at the next timestamp (Such as capacitor status, main transformer gear, PV data, 97 features in total) and 104 bus voltages at the next timestamp.

Feeding with the first 20 records and the first 732 features in the next record (Excluding the 104 busbar voltages at the next timestamp) into the LSTM neural network to predict the 104 busbar voltages at the next timestamp.

4.3   Discussion

In order to verify the effect of the reactive voltage control model built in this paper, it is compared with the following two methods:

1) Conventional methods, using expert rules, tend to tune transformers or switch on/off capacitors, which particularly depends on accurate physical models and grid state estimation results. However, the economy of the system is not considered.

2) The BP algorithm, given the same dataset, uses the BP algorithm to make predictions. As a prediction model in reactive voltage control, it contains two hidden layers and a fully connected layer.

Table 2. Practical and predicted values and absolute percentage errors

Actual value (kV)	BP algorithm		Deep learning agent	
	Predictive value (kV)	Absolute percentage error (%)	Predictive value (kV)	Absolute percentage error (%)
10.489	10.997	4.848	10.446	0.407
10.552	10.234	3.014	10.476	0.722
20.998	20.746	1.200	21.204	0.982
36.434	37.295	2.363	36.545	0.305
118.041	115.362	2.270	117.492	0.465
121.158	117.954	2.644	120.898	0.215
121.687	118.257	2.819	120.906	0.642
MAPE	3.434		0.687	

The results obtained by each model are shown in Table 2. The actual value is the voltage under the conventional method. The magnitude of the error reflects the predictive power of the model. The performance of the model increases when the error decreases. The voltage predicted by the method proposed in this paper has the highest accuracy and is consistent with the actual voltage.

Experimental verification of the strategies using the three methods was performed, and the device action time and the voltage deviation of the system were also calculated. Table 3 shows the comparison of the overall voltage deviation effect under the three control strategies.

Table 3. Comparison of voltage deviation effect under different algorithms

Time (h)	Voltage deviation			Time (h)	Voltage deviation		
	Conventional method (%)	BP algorithm (%)	Deep learning intelligence (%)		Conventional method (%)	BP algorithm (%)	Deep learning intelligence (%)
1	2.791	3.191	1.386	13	2.791	3.424	2.257
2	2.222	3.119	1.783	14	2.387	3.462	1.871

(*continued*)

Table 3. (*continued*)

Time (h)	Voltage deviation			Time (h)	Voltage deviation		
	Conventional method (%)	BP algorithm (%)	Deep learning intelligence (%)		Conventional method (%)	BP algorithm (%)	Deep learning intelligence (%)
3	2.339	3.599	2.010	15	2.306	3.171	1.543
4	2.673	3.400	1.765	16	2.507	3.679	1.691
5	2.906	3.401	1.628	17	2.438	3.347	1.826
6	2.307	3.195	1.740	18	2.642	3.845	2.723
7	2.548	2.931	1.801	19	2.654	3.942	2.503
8	2.396	3.143	2.278	20	2.906	3.208	2.050
9	2.372	3.506	2.181	21	2.458	3.413	2.018
10	2.866	3.826	1.799	22	2.296	3.533	1.592
11	2.553	3.667	2.024	23	2.618	3.507	1.511
12	2.755	3.492	1.575	24	2.527	3.458	1.710

It can be seen from the table that the voltage deviation of the deep learning agent is the smallest at most of the time of the day, so the system under its control is the most stable.

As shown in Fig. 4, the voltage optimization effect at a certain time of day is taken as an example to demonstrate.

The picture above shows the 24-h voltage control effect of 15, 17 and 28 nodes. Due to the security evaluation function included in the agent's decision-making, the voltage deviation formed by the final output control strategy is controlled within a small range. These indices obtained by these compared algorithms show that, the proposed method can effectively control the voltage deviation from a limit magnitude range. Furthermore, the voltage deviation is lower than the conventional method, which improves the security of the power grid and the operational performance of the regional power grid (Table 4).
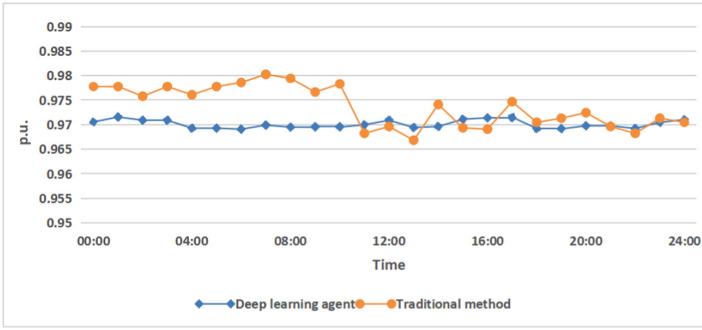
(a)
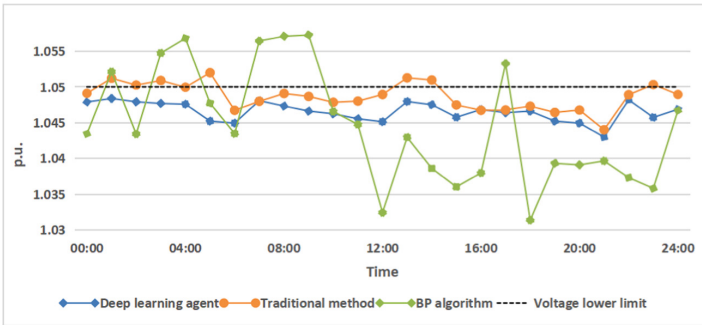
(b)
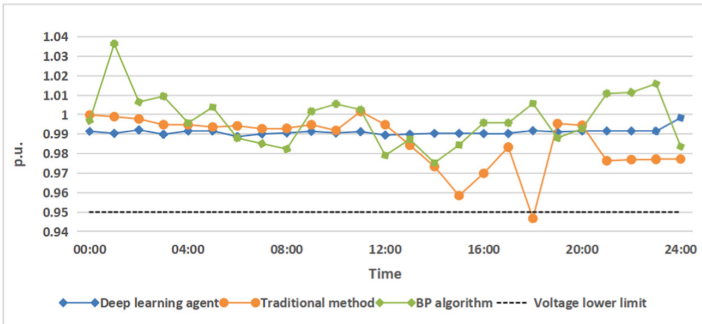
(c)

Fig. 4. Voltage control effect under different schemes

Table 4. Action times under different control schemes

	Conventional method	BP algorithm	Deep learning agent
Transformer	305	297	280
Capacitor	687	1408	632
Total	997	1705	912

The table above shows the total number of transformer and capacitor trips in the entire area in one month. The analysis shows that the number of actions of the deep learning method is reduced among the three methods. Compared with the deep learning algorithm, the total number of actions is increased by 9.32% with the conventional method, while the total number of actions of the BP algorithm is increased by 86.95%. It shows that the control devices switching strategy optimized by the LSTM algorithm can more effectively improve the rationality of control devices' actions and reduce additional switching.

As the prediction effect of the BP algorithm is not optimal, the reactive power optimization strategy selection will be inaccurate. When the power system exceeds the limit, the BP algorithm will sometimes deteriorate the system's stability. The LSTM algorithm of the prediction effect is far better than the BP algorithm. The choices of the strategies for reactive power optimization will also be more accurate, and the selection strategy, on the premise of guaranteeing security, will improve the economic benefit of the system. So, we can see from the figure that the LSTM algorithm of voltage curve compared with the other two methods is smoother, and the number of actions of control devices is less than the other two methods.

Due to the reduced number of actions of the method in this paper, the service life of the transformer and capacitor is extended, and the economy of the power system is improved accordingly. It proves that the control strategy generated by the deep neural network reactive voltage control model shows excellent performance for practicability and feasibility, and the output control strategy in the same state is better than that of the conventional method and BP algorithm, achieving better security and economy.

5   Conclusion

Aiming at reactive voltage control in regional power grids, we utilize artificial intelligence to fully study historical data, explore the correlation between real-time power features, and achieve online reactive voltage control optimization strategies. The following conclusions are drawn from the experimental comparison:

1) The neural network can fit the nonlinear relationship between the electrical features and the bus voltage at the next timestamp. Compared with the nonlinear relationship calculated by the conventional sensitivity formula, the system voltage after the control strategy is calculated more accurately and faster, which enables online training

and continuous neural network updating. Meanwhile, the agent selects the optimal reactive power equipment control strategy, and the continuous reactive voltage control is realized.

2) Compared with the conventional method and BP algorithm, the proposed method reduces the number of actions of controlled devices, restrains the fluctuation of system voltage, and effectively improves the reactive voltage control performance in the regional power grid.

As a result, we provide a new scheme for applying reactive voltage control in regional power grids. What is more, we also consider photovoltaic energy application scenarios. In future work, we will continue the focus on photovoltaic and comprehensively wind energy collaborative application scenarios.

References

1. Gao, R., Kou, P., Liang, D.: Robust model predictive control for the voltage regulation in active distribution networks with hybrid distribution transformers. Proc. CSEE **40**(7), 2081–2090 (2020)
2. Ren, J., Gu, W., Wang, Y.: Multi-time scale active and reactive power coordinated optimal dispatch in active distribution network based on model predictive control. Proc. CSEE **38**(5), 1397–1407 (2018)
3. Huang, W., Liu, S., Wang, W.: Optimal reactive power dispatch with long-time scale in distribution network considering uncertainty of photovoltaic. Autom. Electr. Power Syst. **42**(5), 154–162 (2018)
4. Zeng, L., Luo, F., Ding, J.: Application of particle SWami opdmization algorithm integrated witIl tabu search in reactive power optimization. Power Syst. Technol. **35**(7), 129–133 (2011)
5. Xu, O., Tang, W., Cai, Y.: Fuzzy logic based reactive power control strategy for low-voltage distribution networks with high proportion of residential photovoltaic power. Autom. Electr. Power Syst. **41**(23), 89–95 (2017)
6. Li, Z., Yang, H.: A fun decomposition proximal center algorithm for decomposition and coordination of reactive power optimization. Proc. CSEE **33**(1), 77–83 (2013)
7. Zhang, Y., Ren, Z.: Readjusting cost of dynamic optimal reactive power dispatch of power systems. Autom. Electr. Power Syst. **29**(2), 34–38, 60 (2005)
8. Wang, Z., Guo, C., Liu, W.: Multi-time scale voltage control and coordinated correction for distribution networks considering load characteristics. Autom. Electr. Power Syst. **41**(15), 51–57 (2017)
9. Zhang, C., Chen, H.Y., Shi, K.: A multi-time reactive power optimization under interval uncertainty of renewable power generation by an interval sequential quadratic programming method. IEEE Trans. Sustain. Energy **10**(3), 1086–1097 (2019)
10. Huang, W., Liu, S., Yi, Y.: Multi-time-scale slack optimal control in distribution network based on voltage optimization for point of common coupling of PV. Autom. Electr. Power Syst. **43**(3), 92–100 (2019)
11. Fu, Y., Liao, J., Li, Z.: Day-ahead optimal scheduling and operating of active distribution network considering violation risk. Proc. CSEE **37**(21), 6328–6338 (2017)

12. Yu, L., Sun, Y., Xu, R.: improved particle swarm optimization algorithm and its application in reactive power partitioning of power grid. Autom. Electr. Power Syst. **41**(3), 89–95, 128 (2017)

13. Zhong, J., Jiao, X., Wang, Z.: Reactive voltage partition method based on voltage critical steady state. Power Syst. Technol. **43**(10), 3761–3768 (2019)

14. Bao, W., Zhu, T., Zhao, C.: A three-stage network partition method for secondary voltage control based on agglomerative analysis. Autom. Electr. Power Syst. **5**, 127–132 (2016)

15. Xu, H., Dominguez-Garcia, A.D., Sauer, P.W.: Optimal tap setting of voltage regulation transformers using batch reinforcement learning. IEEE Trans. Power Syst. Publ. Power Eng. Soc. **35**(3), 1990–2001 (2020)

16. Shao, M., Wu, J.: Reactive power optimization of distribution network based on data driven and deep belief network. Power Syst. Technol. **43**(6), 1874–1883 (2019)

17. Duan, J., Shi, D., Diao, R.: Deep-reinforcement-learning-based autonomous voltage control for power grid operations. IEEE Trans. Power Syst. 1–5 (2019)

18. Schmidhuber, J.: Deep learning in neural networks: an overview. Neural Netw. **61**, 85–117 (2015)

19. Liu, W., Zhang, D., Wang, X.: A decision making strategy for generating unit tripping under emergency circumstances based on deep reinforcement learning. Proc. CSEE **38**(1), 109–119 (2018)

20. Zhao, Y., Wang, X., Jiang, C.: A novel short-term electricity price forecasting method based on correlation analysis with the maximal information coefficient and modified multi-hierachy gated LSTM. Proc. CSEE **41**(1), 135–146, 404 (2021)

21. Chen, Z., Liu, J., Li, C.: Ultra short-term power load forecasting based on combined LSTM-XGBoost model. Power Syst. Technol. **44**(2), 614–620 (2020)

22. Lu, J., Zhang, Q., Yang, Z.: Short-term load forecasting method based on CNN-LSTM hybrid neural network model. Autom. Electr. Power Syst. **43**(8), 131–137 (2019)

Design and Simulation Modeling of ±800 kV HVDC Project for Improving Power Transfer Capability of Renewable Energy in Xinjiang-Qinghai Region

Lin Zhu[1,2(✉)], Li Tu[2], Zhiwei Mi[1,2], Ruitong Liu[3], and Fangwei Duan[3]

[1] State Key Laboratory of Advanced Power Transmission Technology (State Grid Smart Grid Research Institute Co., Ltd.), Beijing 102209, Changping, China
125766162@qq.com

[2] Beijing Key Laboratory of DC Grid Technology and Simulation (State Grid Smart Grid Research Institute Co., Ltd.), Beijing 102209, Changping, China

[3] Electric Power Research Institute of State Grid Liaoning Electric Power Co., Ltd., Shenyang 110000, Heping, China

Abstract. This paper focuses on the representative renewable energy bases in eastern Xinjiang and southern Qinghai regions, and conducts in-depth studies on the current status and problems of power grids in these regions. On the basis of the power grid characteristics, this paper proposes a DC grid based on the voltage source converter based high voltage DC (VSC-HVDC) technology, establishes its simulation model, and analyzes the power flow distribution, the power flow transfer capacity and the fault ride-through (FRT) characteristics of the proposed system. The results show that the proposed DC system effectively improves the steady/transient-state characteristics of the power grids in eastern Xinjiang and southern Qinghai areas. It helps promote the delivery of renewable energy. In the meantime, the proposed method provides solutions for solving the problems faced in the northwest region.

Keywords: Renewable energy transmission · Renewable energy and thermal bundled system · VSC-HVDC · DC grid · Damping control · Virtual inertia

1 Introduction

In recent years, with the joint efforts of the government, power generation companies, power grid companies and users, China's energy transformation process has been accelerating. The construction of a new energy consumption structure dominated by wind power and solar energy is the general trend, and it is an urgent need to replace traditional

non-renewable energy generation, which will lead to dramatic changes in the future energy landscape.

The northwest region is an important energy strategic barrier in China, with coal and wind energy resources occupying the first and second place in the country [1]. Since 2008, Xinjiang, Qinghai, Ningxia, Gansu and other places have successively built 10 GW-level new energy bases, making Northwest China the region with the largest proportion of new energy in China's power system. According to the forecast of China's new energy power generation, by 2030, the total installed capacity of photovoltaics in Northwest China is expected to reach 360 million kW; the total installed capacity of wind power is expected to reach 200 million kW [2].

In the northwest region, eastern Xinjiang and Qinghai have built/planned multiple 10 GW-level new energy bases. Among them, there is a high-density wind power base in Hami area in the northeastern part of Xinjiang. At present, wind power is collected to the 750 kV main grid through 110 kV/220 kV lines, and after being bundled with thermal power in Hami area, Xinjiang, it is sent to central China via Line commutated converter based high voltage DC (LCC-HVDC); The power grid in the Ruoqiang area of the eastern Bayinguoleng Mongolian Autonomous Prefecture (Bazhou Ruoqiang area) is currently a long-line power receiving structure, but a 10 GW-level new energy base is being planned.

Haixi Prefecture in the west of Qinghai is another large wind power and coal base. At this stage, power exchanges with neighboring areas are realized through 750 kV lines; Hainan Prefecture in the east of Qinghai has a 10 GW photovoltaic base, electricity is mainly transmitted through 750 kV/330 kV lines.

Xinjiang and Qinghai main networks are interconnected through the Hexi transmission channel and the Tianshan-Shazhou-Yuka 750 kV line. The Hami-Zhengzhou (referred to as Ha-Zheng) ±800 kV LCC-HVDC (Line Commutated Converter) has been put into operation in the Hami area, and Hami is relatively close to the Zhundong-Wannan ±1100 kV LCC-HVDC project about 700 km away. The Hami power flow can also pass through the Zhundong-Wannan LCC-HVDC project. Haixi Prefecture has completed the Haixi Golmud-Tibet Lhasa ±400 kV LCC-HVDC project[3], and is planning the Haixi to Central China LCC-HVDC channel; Hainan Prefecture is building the ±800 kV Qinghai-Henan LCC-HVDC for the photovoltaic base.

With the advancement of the major strategy of new energy in the west, there may be some potential risks in the above regions, such as the oscillation problem of new energy units bundled with thermal power, the short-term isolated load power supply and the long-term new energy grid connection problems (i.e., the power supply before the load). Insufficient fault ride-through (FRT) capability after wind/solar bases are connected to the grid, and limited LCC transmission capacity due to insufficient thermal power support [4].

This paper studies from the aspects of transient/steady state characteristics, regulation ability, FRT ability, etc., discusses the effect of adopting DC power grid on improving the transmission of new energy, proposes a four-port "mouth" type DC power grid scheme, and gives the topology structure and transient/steady-state control strategy of this scheme. As an optional scheme, it provides solutions to the problems faced by the Northwest region as a whole.

2 Current Situation and Existing Problems of Power Grids in Hami, Bazhou Ruoqiang, Haixi and Hainan

This section introduces the status quo of the above-mentioned 4-place power grids, and analyzes the problems existing in their respective power grids.

2.1 Hami Grid

Hami Power Grid is located at the junction of Xinjiang Power Grid and Northwest Power Grid (Hami Power Grid is connected to the Northwest Power Grid through a double-circuit 750 kV, and is connected to the Turpan Power Grid through a double-circuit 750 kV) and is also at the Hami-Zheng LCC-HVDC end.
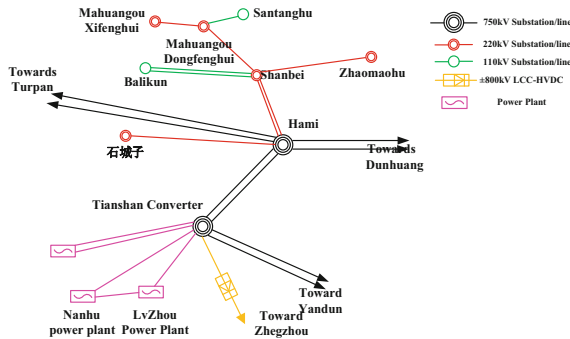
Fig. 1. Power grid structure in Hami region

Hami power grid has a strong structure and stable operation, but there is broadband coupling oscillation between a large number of new energy units containing power electronic devices, thermal power units and LCC-HVDC. When the oscillation complementary frequency is close to the vibration mode of the shaft system of the thermal power unit, sub-synchronous oscillation (SSO) risks are high in the Hami power grid. There are oscillation problems and weak stability between the 110 and 220 kV lines in the Hami grid and the 35 kV wind power feeder, static var generator (SVG) in the wind farm gathering station. For instance, in July 2015, the SSO of the Hami North Wind Farm led to torsional stress relay (TSR) action trip and the power loss exceeding GW. The Hami-Zheng LCC-HVDC power was urgently reduced from 4.5 GW to 3 GW with a certain impact.

2.2 Bazhou Ruoqiang Power Grid

Bazhou is located in the southeast of Xinjiang Uygur Autonomous Region, with an area of 47×10^4 km², the highest operating voltage level of the power grid is 750 kV, and the power supply radius is 500 km. There are 1 750 kV substation, 7 220 kV substations and 30 110 kV substations in the network. Among them, the Ruoqiang area in Bazhou,

which has the largest proportion of new energy planning, is about 700 km away from Hami. It is currently a load center and uses a single-circuit 750 kV line for power supply.

At present, Bazhou Ruoqiang is a typical long-distance load-type power grid, and the load is mainly a heavy metal smelting base. However, with the continuous development of wind resources, it will be planned to be a 10 GW-level new energy base in the future [6], and it may face weakness of medium voltage grids and difficulties in energy delivery at that time.

2.3 Haixi Power Grid

Haixi Prefecture is located in the west of Qinghai Province, about 700 km east of Hami. At present, Haixi Power Grid has 1 750 kV substation, 7 330 kV substations, and 18 110 kV substations. As of 2019, Haixi Prefecture has achieved grid-connected new energy of 12.25 million kW, and is building the second 10 GW-level new energy base.

The long-line transmission structure of the Haixi power grid leads to insufficient voltage support after a fault. In 2018, a two-phase short circuit occurred on the 35 kV collecting bus in a large wind farm in Haixi Prefecture, and the voltage instantly dropped by more than 20%, which was lower than the protection value (0.9 pu), and a large number of wind turbines were disconnected from the grid due to low voltage protection. After 82 ms, the fault was removed and the system voltage rapidly rose to 1.17 pu and continued for 9 s due to the slow response speed, causing adjacent several photovoltaic power plants of the wind farm disconnected from the grid again with overvoltage protection action.

2.4 Hainan Power Grid

Hainan Prefecture is located in the east of Qinghai Province, with an area of $4.5 \times 10^4 \ km^2$ and a distance of about 1 000 km from Hami. By 2022, Hainan plans to have 10 GW of photovoltaics and 5 GW of wind power.

The potential problem in Hainan in the future is that under the multi-LCC-HVDC structure with new energy as the main power source. The large-scale new energy power planned by Hainan Prefecture is mainly sent out through Qinghai-Henan LCC-HVDC, but due to environmental and other factors, the scale of the supporting power supply is very limited, which will affect the actual transmission capacity. In addition, due to the weak grid structure, the LCC has a great impact on the power grid when continuous commutation failures and over voltage happen [7, 8].

2.5 Summary

With the acceleration construction of the power grid in Northwest China, the local AC power grid structures in Hami, Bazhou Ruoqiang, Haixi and Hainan are increasingly strengthened, and the capacity of new energy consumption and delivery has been continuously improved. However, the further expansion of the scale of new energy and the formation of multi-LCC-HVDC transmission systems have further increased the pressure on the safe and stable operation of the power grid. The above regions will face the following issues:

1) The oscillation problem caused by the bundled structure of the new energy unit and thermal power.
2) The power grid characterized by isolated load power supply in the near future will be transformed into a long-term new energy power supply power grid.
3) The problem of limited LCC transmission capacity caused by insufficient thermal power facilities.
4) The problem of large-scale power flow transfer and rapid regulation in the wide-area. Especially after the LCC-HVDC receiving-end fault, it requires the sending-end power grid to have a higher power flow dispatching capability.

3   Northwest Internal DC Grid Scheme

Based on the above power grid characteristics, this section discusses the proposed DC networking scheme based on flexible DC technology to improve the transmission of new energy from the above four places.

3.1   Flexible DC and DC Grid Technology

The flexible DC transmission technology has the technical advantages of no commutation failure, can provide stable voltage for passive systems, fast reactive power support, and grid impedance adjustment. It has become the optimal technical way to connect large-scale new energy sources, especially fluctuating and isolated power sources to the grid **Error! Reference source not found.**
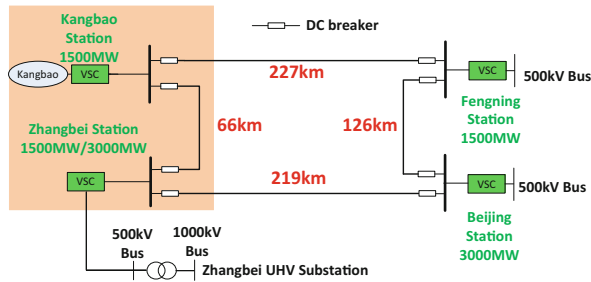
Fig. 2.   Schematic diagram of Zhangbei DC grid project

The DC grid is composed of multiple flexible DC converter stations (voltage source converter VSC), which can realize the efficient utilization of wind, solar, and fire energy through a wide range of power flow distribution, and improve the stability of cross-regional AC and DC hybrid power grids **Error! Reference source not found**. State Grid Corporation of China has completed and put into operation the world's first DC grid - Zhangbei DC grid project (Fig. 2).

3.2   The Overall Idea of DC Grid to Enhance the Transmission of New Energy in Northwest China

The general idea of the scheme proposed in this paper is to build one VSC converter station in each of the four places mentioned in Sect. 1 to form a "mouth"-shaped DC power grid. DC grid gathers wind-solar thermal power sources with comprehensive power flow regulation and stabilization of fluctuations. Then the power is sent to the four major LCC AC busbars and the 750 kV line to the Shaanxi load center, which not only improves the stable transmission capacity of new energy, but also reduces the output of thermal power units. The basic architecture of the proposed DC grid is shown in Fig. 3.
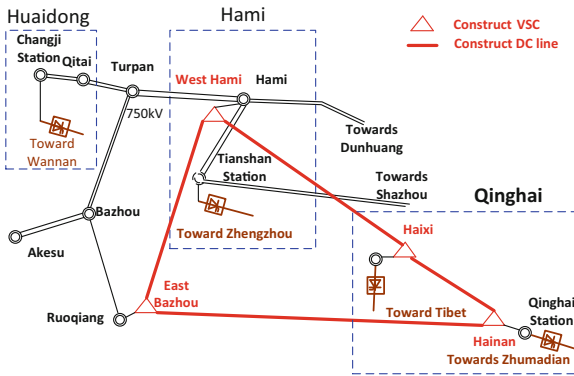
Fig. 3. Proposed structure of four-terminal DC grid

In Hami, VSC can adjust its own power and current in real time through additional damping control (shown in Fig. 4) **Error! Reference source not found**, and then dynamically change the number of sub-modules input into the system to provide positive damping for the AC system. It can achieve the effect of improving the damping of the oscillation mode and it also has a corresponding inhibitory effect on the torsional vibration frequency of the thermal power unit.
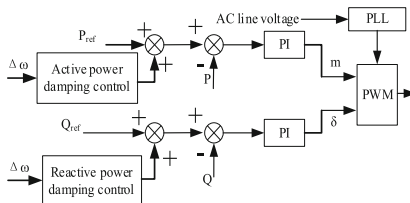
Fig. 4. VSC control with supplementary damping

In the Ruoqiang area of Bazhou, VSC has extremely low requirements on the AC system connected to it (the AC system can even be a passive network). In addition, the

VSC can adopt the virtual synchronous machine control strategy [20] to enhance the frequency regulation and inertia support capability of the local AC grid by participating in the primary frequency regulation of the local AC system, as shown in Fig. 5. Due to the wide-area power regulation capability of the DC grid, the effect of virtual synchronous control in VSC will be much better than static var generator (SVG), and even better than energy storage systems with high cost and small capacity. In the future, VSC can be used to solve the problem of grid connection and delivery of isolated new energy.
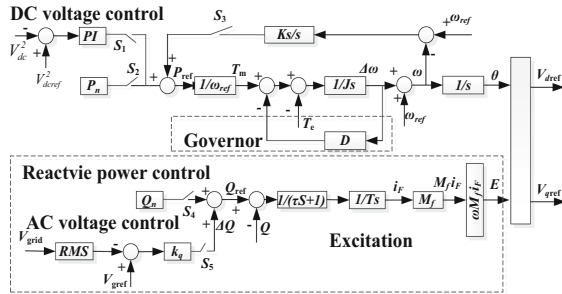
Fig. 5. Schematic diagram of virtual inertia control

For the Haixi state power grid, the VSC active and reactive power can be independently controlled in the dq0 coordinate system. When the AC voltage of the Haixi power grid is too low/high, the VSC can quickly provide/absorb reactive power support to increase the AC grid voltage and assist the new energy units to complete the FRT.
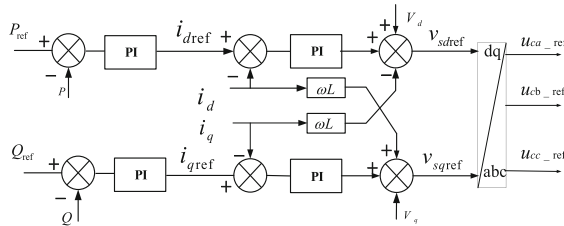
Fig. 6. Block diagram of decoupling control between active and reactive power

In Hainan Prefecture, the VSC network is used to collect new energy to reduce the impact of wind and solar fluctuations on system power, increase the proportion of new energy in LCC transmission, and further enhance the actual LCC transmission capacity. In addition, VSC can be used to provide dynamic reactive power support to alleviate problems such as commutation failure, LCC blocking and other faults.

The selection of the specific placement of the VSC converter stations in the above four places can refer to the following principles.

1) Hami: It is recommended that VSC be connected to the 750 kV main network to suppress the oscillation by dynamically changing its own damping characteristics.

In addition, the VSC fast reactive power support capability (over 1200 M var) can be used to stabilize the commutation voltage of LCC at the sending end of the Harbin-Zhengzhou project.

2) Ruoqiang: Considering the problems of isolated load power supply and long-term remote new energy grid connection and delivery, it is recommended that the VSC be located here. This area has important loads and has large-scale new energy planning in the long term.

3) Haixi: If there is no LCC in Haixi Prefecture, the VSC should be located in the wind farms and photovoltaic power station cluster areas with weak power grids. The cost of strengthening the AC grid of these new energy stations is high with long distance and the new energy cluster is weak in FTR.

4) Hainan: VSC is recommended to be located in an area close to the LCC, and the collected new energy is efficiently sent out through the LCC with expanded transmission capacity.

4 Main Circuit and Steady-State Operation of Four-Terminal DC Grid

This section introduces the four-terminal DC grid topology and its core DC equipment. On this basis, the power flow distribution of the DC system and its basic control strategy are studied.

4.1 Main Circuit Topology

The four-terminal DC power grid is a "mouth"-shaped structure, using bipolar metal loop wiring, the DC voltage level is ±640 kV, the VSC capacity of the four stations is tentatively 4.5 million kW, and the converter valve is a half-bridge topology. The pole line outlet of the converter station is equipped with ±640 kV DC circuit breaker (CB) **Error! Reference source not found**. The main reason for using ±640 kV is that the transmission distance is long, the DC power is large, and relying on the existing insulated gate bipolar transistor (IGBT) technology, ±500 kV is incompetent, and the ±800 kV LCC-HVDC project is very mature, and has good engineering experience for reference. After the subsequent IGBT overcurrent capability is enhanced, the voltage level can be adjusted to ±500 kV or ±640 kV. The main circuit parameters of the VSC converter valve are shown in Table 1.

The converter valve is a half-bridge topology and adopts symmetrical bipolar wiring (as shown in Fig. 7), which can reduce the insulation level of the equipment, and can still operate at half power after a single-pole fault, which improves the reliability of the system. Large-capacity converter transformers are generally three single-phase transformers, and the winding connection method can be designed as Y_0/Δ type to avoid the zero-sequence component.

The overhead line is used between converters. Due to the changeable climate in the northwest region, overhead lines are easily affected by strong winds, lightning strikes, earthquakes and other natural environments. Therefore, 800 kV DC-CBs are installed at the pole line exits of each converter station to realize DC instantaneous permanent

Table 1. Parameters of VSC main circuit

Device parameters	Value and unit
IGBT rated voltage	3.6 kV
IGBT rated current	3.75 kA
Sub-module average working voltage	2.5 kV
Single-arm submodule (without redundancy)	300
redundancy	8%
Submodule capacitance	18 mF
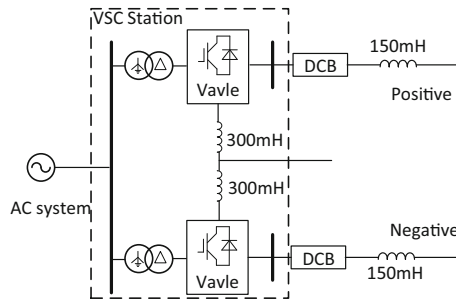
Fig. 7. Symmetrical bipolar wiring diagram of converter station

FRT and permanent fault line removal. The IGBT paralleling technology in the DC-CB module has been fully verified by the Zhangbei DC project. This technology can meet the current breaking needs of the project described in this article, so there is no technical bottleneck for the circuit breaker.

4.2 Construction of Four-Terminal DC Grid Simulation Model

According to the main circuit topology proposed in Sect. 3.1, the simulation model of the four-terminal DC power grid including Hamixi, Bazhoudong, Haixi and Hainan is built in PSCAD/EMTDC. The control method of the four-terminal DC power grid in this paper refers to the control strategy of the four-terminal power grid in Zhangbei, and various methods such as single-point voltage master-slave control and multi-point voltage droop control can also be used **Error! Reference source not found**. The control mode of the Hami converter station is constant DC voltage and constant reactive power, and the control modes of the other three converter stations are constant active/reactive power. The corresponding reference values are shown in Table 2.

4.3 Power Flow Distribution of Four-Terminal DC Grid

Through the simulation model built in Sect. 3.2, the power flow distribution of the system can be obtained as shown in Fig. 8. When the system is running in a steady

Table 2. Four-terminal DC grid control mode and reference value

Converter station	Way to control
Hamixi	Constant DC voltage ($U_{dcref1} = 640$ kV), constant reactive power ($Q_{ref1} = 0$ var)
Bazhoutdong	Constant active power ($P_{ref2} = 4500$ MW), constant reactive power ($Q_{ref2} = 0$ var)
Hainan	Constant active power ($P_{ref3} = -4500$ MW), constant reactive power ($Q_{ref3} = 0$ var)
Haixi	Constant active power ($P_{ref4} = 4500$ MW), constant reactive power ($Q_{ref4} = 0$ var)
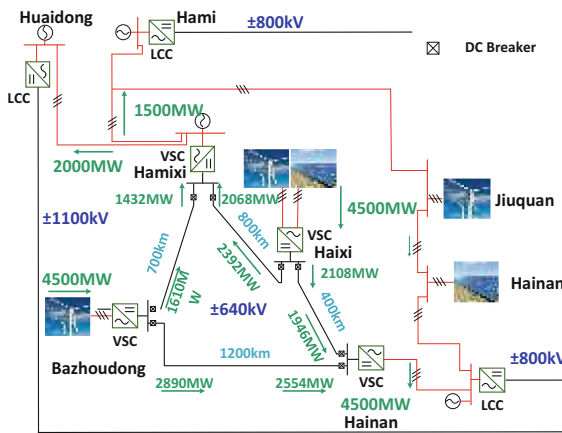
Fig. 8. Steady-state power flow distribution of four-terminal DC grid

state, Bazhoudong and Haixi VSCs will each collect 4.5 GW of new energy power, and transmit about 1.5 and 2 GW respectively to Hazheng and Zhundong-Wannan LCC through Hamixi VSC; and Hainan VSC can transmit about 4.5 GW power to Qinghai-Henan LCC. When the LCC power of the receiving end of LCC in Central and East China is limited, the power flow can also be sent to the load areas such as Tibet and Shaanxi through the Qinghai-Tibet 400 kV DC line, the Hami-Dunhuang 750 kV AC line or the Tianshan-Shazhou 750 kV AC line.

5   Analysis of Transient Characteristics of DC Power Grid

This section studies the response characteristics of the proposed four-terminal DC system when the DC/AC side and the LCC fail.

5.1 Overhead Line Failure

When a DC pole-to-ground or pole-to-pole short-circuit fault occurs instantaneously, the fault can be isolated within a few ms with the help of DC-CB, wavelet analysis, traveling wave protection and other protection logic **Error! Reference source not found**. If the DC overhead line has a permanent fault, the DC-CB can quickly isolate the faulty line, and the DC grid can still operate normally after the emergency power transfer. At this time, limited by the weak overload capacity of the VSC, the DC system needs to reduce power.

Assuming a transient fault occurs on the DC line from Hamixi to Bazhoudong, DC-CB11 and DC-CB12 will act to jump off the faulty line, isolate the fault accurately, and transfer the power to the normal line, as shown in the Fig. 9. The relevant simulation test results are shown in Fig. 10 and Fig. 11, and the fault duration is 0.15 s.
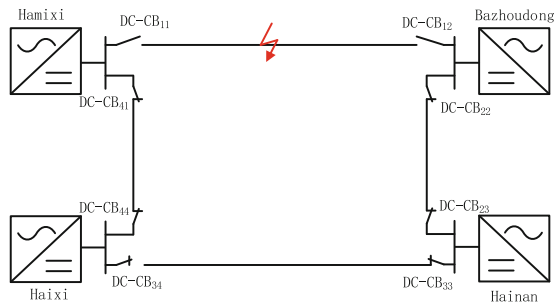
Fig. 9. Schematic diagram of fault isolation process by DC circuit breaker

After the DC fault occurs, the active power of the Bazhoudong and Hamixi converter stations changes rapidly, causing the active power output by Bazhoudong and the active power received by Hamixi to decrease. The DC voltage in Bazhoudong and Hamixi also dropped rapidly. After the fault is cleared by DC-CB, the transmission power and DC voltage can be restored to the stable state before the fault, which has little impact on the stable operation of the system.

5.2 VSC FRT Capability During AC Fault

When an instantaneous fault such as single-phase/three-phase short circuit occurs on the AC side of the VSC of the new energy collection station, and wind farm can complete the FRT under the action of the VSC fast reactive power support, the DC system is not affected. When single-phase, three-phase and other short-circuit faults occur, the AC positive sequence voltage decreases, and the VSC can quickly provide reactive power support. At the same time, the flexibility of the VSC vector control is used to control the positive sequence and negative sequence voltages respectively and continues to maintain a certain active power within a safe range. At this time, it is necessary to discharge the surplus power through the energy-consuming devices configured on the DC/AC side of the new energy station to avoid overvoltage of the AC/DC buses.
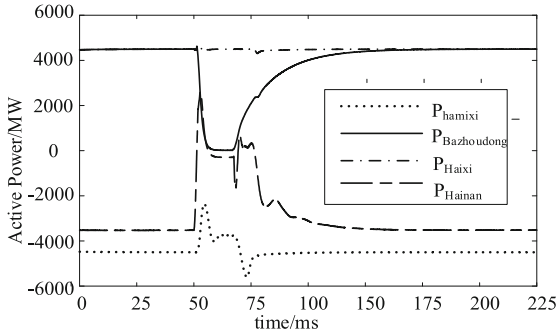
Fig. 10. Active power waveform diagram during the fault isolation process by DC circuit breaker
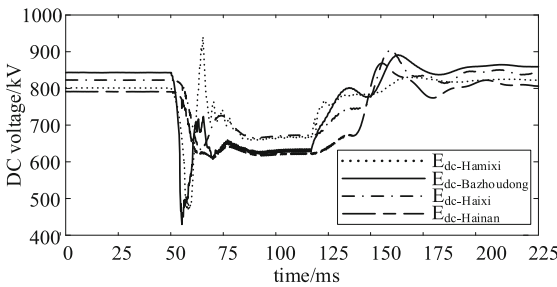

Fig. 11. DC voltage waveform diagram during the fault isolation process by DC circuit breaker

5.3   Power Flow Transfer Capability of DC Grid when LCC is Blocked

When CCF occurs in the LCC, for the weak sending-end system dominated by new energy, the surplus power will charge the filter bank of the sending-end LCC converter station and cause AC overvoltage. In severe cases, it may cause Large-scale cutting machine of the sending-end system shown in Fig. 12.
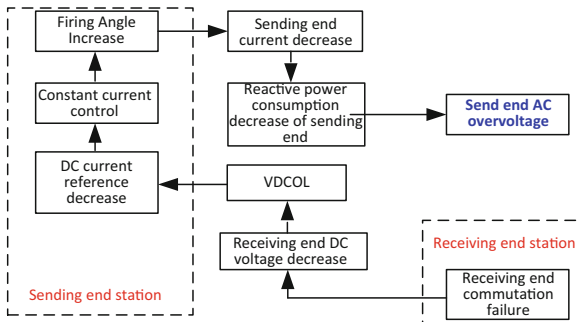
Fig. 12. Transient overvoltage of AC bus at the sending end caused by commutation failure at the receiving end

To this end, VSCs in Hamixi and Hainan need to coordinate and participate in the adjustment of the power flow, and cooperate with synchronous contender with suitable time-sequencing (VSC quickly provides reactive power support) to improve the delivery capacity of normal LCCs, and solve the serious problems of new energy units and thermal power. This translates into an acceptable grid frequency adjustment problem. In the absence of VSC, if Qinghai-Henan LCC has a single-stage blocking fault, 4 GW of power will be transferred to the 750 kV AC power grid running in parallel with it, which will exceed the stability limit of the existing Gan-Qing AC section, causing the failure of the inter-provincial interconnection line, stability damage and power imbalance among the internal systems in the northwest. If the bipolar blocking fault occurs in LCC and loses 8 GW of power, if the security control refuses to act, the risk of large power outages caused by the accident will be greatly increased; if there is a four-terminal VSC-HVDC grid, under the action of Hainan and Hamixi VSCs, When Qinghai-Henan LCC bipolar blocking occurs, up to 4 GW power flow can be quickly transferred to other LCC projects through the VSC-HVDC grid, thereby reducing the impact of the LCC fault on the sending system.

6   Conclusion

Aiming at the problems of power grid pattern and new energy transmission in Qinghai and eastern Xinjiang, a feasible four-terminal VSC-HVDC power grid scheme is initially proposed, which is a way of thinking to solve the problems in the northwest region in the future with conclusions as below:

1) This paper is mainly a conceptual discussion. It is necessary to carry out detailed simulation calculations in combination with actual planning and electromechanical electromagnetic transient software, and compare various schemes to select the optimal scheme.

2) This scheme will form a wide-area, complex multi-VSC, multi-LCC and new energy unit and thermal power bundle structure in the northwest, which will bring certain challenges to system scheduling and AC/DC power grid control technology. It is of great significance for the construction of DC power grid projects to accelerate the development of core DC grid equipment such as circuit breakers and converter valves with low cost, small size, large capacity, and strong fault tolerance.

References

1. Liu, Z., Zhang, Q., Dong, C., Zhang, L., Wang, Z.: Efficient and security transmission of wind, photovoltaic and thermal power of large-scale energy resource bases through UHVDC projects. Proc. CSEE **34**(16), 2513–2522 (2014)
2. Zhou, X., Chen, S., Lu, Z., Huang, Y., Ma, S., Zhao, Q.: Technology features of the new generation power system in China. Proc. CSEE **38**(7), 1893–1904 (2018)
3. Li, C., et al.: Coordinated control of UHVDC multi-infeed system for commutation failure prevention. Power Syst. Technol. **43**(10), 3532–3542 (2019)
4. Guangfu, T., Hui, P., Zhiyuan, H.: R & D and a application of advanced power transmission technology in China. Proc. CSEE **36**(7), 1760–1771 (2016)

5. Chen, G., Li, M., Xu, T., Liu, M.: Study on technical bottleneck of new energy development. Proc. CSEE **37**(1), 20–26 (2017)
6. Xu, K.: 2012 Government Work Report. Ruoqiang County People's Government, Ruoqiang County (2013)
7. Li, S., Li, H., Zhang, H., et al.: Study on security and stability of UHVDC in Qinghai province. Qinghai Electric Power **38**(4), 1–4 (2019)
8. Yujiao, S., Junling, W., Yating, W., et al.: Influence analysis of renewable power resources' integration on transmission capability of northwest to Xinjiang power corridor and system's security and stability. Electr. Power Constr. **37**(6), 17–23 (2016)
9. Dong, Y.: Research on structure optimization of UHV transmission grid and future power grid structure form. Shandong University, Jinan (2013)
10. An, T., Liu, D., Chang, B., et al.: Review of CIGRE 2020: DC systems and power electronics. Autom. Electr. Power Syst. **45**(1), 141–149 (2021)
11. Dong, L., Guangfu, T., Zhiyuan, H., et al.: Loss evaluation for modular multilevel converter based on equivalent-area modulation. Power Syst. Technol. **36**(4), 197–201 (2012)
12. Zhiyuan, H., Dong, L., Hui, P.: Research of simulation technologies of VSC-HVDC and DC grids. Power Syst. Technol. **42**(1), 1–11 (2018)
13. He, Z., Wang, W., Gu, H., et al.: Development status and prospect of integrated key equipment of DC power grid with fault current limiting and breaking functions. Proc. CSEE **40**(11), 3402–3417 (2020)
14. Liu, D., Tang, G., He, Z., Zhao, Y., Pang, H.: Hybrid real-time simulation technology for MMC-HVDC. Electr. Power Autom. Equip. **33**(2), 68–73 (2013)
15. Hui, P., Jialiang, W., Zhiyuan, H., et al.: Unbalancing voltage of high-power series connected IGBT valve. Proc. CSEE **31**(21), 1–8 (2011)
16. Shan, L., Jun, Y., Zhiyuan, H., et al.: Research on the topology and characteristic of multi-terminal HVDC based on VSC and LCC. Proc. CSEE **38**(10), 2980–2988 (2018)
17. Pang, H., Wei, X.: Research on key technology and equipment for Zhangbei 500 kV DC grid. In: 2018 International Power Electronics Conference (IPEC-Niigata 2018-ECCE Asia), pp. 2343–2351. IEEE (2018)
18. Youping, X., et al.: Damping control based on back to back VSC-HVDC connecting Chongqing and Hubei power grid. Power Syst. Prot. Control **44**(18), 163–169 (2016)
19. Zhu, L., He, Z., Wu, X., Yang, J., Liu, D., Kou, L.: Influence of additional control strategy of back-to-back VSC-HVDC on system stability. Power Syst. Technol. **42**(8), 2519–2527 (2018)
20. Wang, X., Yang, J., Wu, Y., et al.: Effect analysis of back-to-back flexible HVDC connecting Chongqing and Hubei power grid on sub-synchronous oscillation characteristics. Electr. Power Autom. Equip. **39**(7), 188–194 (2019)
21. Adeuyi, O.D., Cheah-Mane, M., Liang, J., Jenkins, N.: Fast frequency response from offshore multiterminal VSC–HVDC schemes. IEEE Trans. Power Deliv. **32**(6), 2442–2452 (2016)
22. Chang, B., Gao, L., Yan, H., et al.: Modeling and simulation study of a new type of HVDC circuit breaker. Proc. CSEE **38**(20), 5983–5991 (2018)
23. Sheng, Y.A.N., Xiang, L.U.O., Zhiyuan, H.E.: Prospect of core equipment and key technology for DC power grid[J]. Automation of Electric Power Systems **43**(3), 205–215 (2019). (in Chinese)
24. Wei, X., Zhou, W., Zhang, S., et al.: Research and application of modular hybrid high voltage DC circuit breaker. Proc. CSEE **40**(6), 2038–2046 (2020)
25. Meng, W., Zhiyuan, H., Fayou, Y., et al.: Influence of droop control on the dynamic voltage stability of DC grid analysis. Power Syst. Prot. Control **47**(10), 8–15 (2019)
26. Yuke, J.: Start-up strategy design of DC power grid and research on fault evolution mechanism. North China Electric Power University, Beijing (2017)

27. Dong, X., Tang, L., Shi, S., Qiu, Y., Kong, M., Pang, H.: Configuration scheme of transmission line protection for flexible HVDC grid. Power Syst. Technol. **42**(6), 1752–1759 (2018)

Research on Batch Fault Prediction Model of Intelligent Electric Energy Meter

Ling Lu$^{(\boxtimes)}$

NARI Group (State Grid Electric Power Research Institute) Co., Ltd., Nanjing, China
`linglu@sgepri.sgcc.com.cn`

Abstract. Since the promotion and application of intelligent electric energy meter in 2009, more than 400 million intelligent electric energy meters have been operated, and the first batch of intelligent electric energy meter put into use will soon reach the rotation cycle. According to the traditional rotation method of intelligent electric energy meter, on the one hand, it causes a huge waste of hardware resources, on the other hand, it brings a lot of verification workload to the provincial measurement center, which affects the development of normal verification business. Relying on big data, machine learning and other related technologies, and based on the data of intelligent electric energy meter disassembly, sorting, operation and measurement abnormalities, this paper constructs a batch fault prediction model of GBDT and ARIMA fusion algorithm to predict the batch fault of intelligent electric energy meter operation, realize the innovation of intelligent electric energy meter rotation method, and provide a reference basis for marketing the inaccurate replacement business of electric energy meter.

Keywords: Intelligent electric energy meter · Batch failure prediction model · GBDT and ARIMA fusion algorithm · Misalignment replacement

1 Introduction

Since the promotion and application of intelligent electric energy meter in 2009, more than 400 million intelligent electric energy meters have been operated, and there are still gaps in technical measures, management measures and service measures for meter replacement. And the first batch of intelligent electric energy meter put into use will soon reach the verification cycle. According to the traditional intelligent electric energy meter rotation method, it will cause a large number of normal operation of electric energy meters to rotate. On the one hand, it will cause a huge waste of hardware resources, on the other hand, it will also bring a lot of verification workload to the provincial measurement center and affect the development of normal verification business. How to innovate the replacement mode of intelligent electric energy meter and break the mode of all replacement, whether good or bad, has become an urgent problem to be solved by provincial measurement centers.

Therefore, on the one hand, starting from the actual business needs, build a set of business management and control system that not only meets the relevant national

regulations, but also reflects the informatization achievements of State Grid Corporation; On the one hand, according to the construction requirements for inaccurate replacement of intelligent electric energy meters by the marketing department of State Grid, online fault analysis and early warning of intelligent electric energy meters are realized, and online monitoring, accurate research and judgment and status replacement of intelligent electric energy meters are realized.

Based on the analysis of the data of electric energy meter disassembly and sorting, operation batch data and abnormal measurement, this paper constructs a batch fault prediction model based on GBDT and ARIMA fusion algorithm to predict the operation batch fault of electric energy meter, so as to provide a reference basis for marketing the inaccurate replacement business of electric energy meter.

2   Construction Ideas

According to the general arrangement of the company's marketing [2019] No. 217 document "opinions of the State Grid Corporation of China on promoting the state evaluation and replacement of intelligent electric energy meters", the replacement of intelligent electric energy meters is composed of two parts: on-line monitoring of operation error and batch fault early warning. According to the requirements of the headquarters, deeply understand the business connotation and work objectives of the inaccurate replacement and construction of intelligent electric energy meters, and study the batch fault early warning function of intelligent electric energy meters from two aspects of system support and business support; Firstly, the key business data of batch fault early warning is sorted and clarified to realize the integration of cross system quality inspection data. Then, by studying the batch fault early warning algorithm, the key factors of batch fault early warning are analyzed, and finally the batch fault early warning model of electric energy meter based on MDS system is formed.

The batch fault prediction model of electric energy meter uses the data of disassembly and sorting, operation batch, metering abnormality and so on to analyze the periodic, seasonal and trend change law of the batch fault number of electric energy meter in the historical month and the factors affecting the change of batch fault number, form the characteristic indexes of model input, and build a batch fault prediction model with multi model fusion and multi index input. Based on the model fusion criterion of "good but different", after model training, the mean square error and goodness of fit are evaluated to obtain the optimal model parameters and model combination, and the optimal model combination is used to predict the number of batch failures in the coming months. Calculate the monthly batch failure rate according to the monthly batch failure prediction quantity, draw the failure rate trend curve, and obtain the inflection point of failure rate trend through the change of failure rate trend. Experts can carry out batch fault warning research and judgment according to the inflection point of fault rate trend, track the difference between the number of sorting faults of monthly dismantled electric energy meters and the predicted number of batch faults, and continuously optimize the model.

The specific implementation steps include:

(1)   Multi system data fusion, cleaning and preprocessing;

(2) Extract the characteristic indicators affecting the number of batch faults from the operation batch fault data;
(3) Build the operation batch fault prediction model;
(4) Realize the monthly failure quantity prediction of operation batch;
(5) Model validation and optimization.

3 Theoretical Basis

Aiming at the construction of batch fault prediction model of electric energy meter, the regression prediction of batch fault of electric energy meter is realized by using statistical method, machine learning and big data related technology. Common regression prediction methods include linear regression, support vector machine (SVM), long-term and short-term memory artificial neural network (LSTM), Bayesian method, gradient lifting tree (GBDT), moving average autoregression (ARIMA), etc. In view of the characteristics of batch fault data of electric energy meter, such as small sample size of effective data, difficult to obtain external environment characteristics, many sample characteristics but unclear relationship, and gradient lifting tree (GBDT) and moving average autoregressive (ARIMA) can solve these problems well, two models of gradient lifting tree (GBDT) and moving average autoregressive (ARIMA) are finally determined to be used. The key technologies are as follows.

3.1 Gradient Lifting Tree

Gradient lifting decision tree is an integrated learning algorithm based on gradient lifting technique, which belongs to different combinations of decision tree models. GBDT is composed of multiple decision trees, and the output is the accumulation of the output results of each decision tree. By using the combination of gradient lifting and regression decision tree, each time a new decision tree model is established, it is in the descending direction of the gradient of the previous model loss function, which makes the decision model continuously improve. In this batch of fault early warning projects, the factors affecting the failure of electric energy meters are classified into measurement abnormality, time, statistics and measurement failure, By continuously obtaining data to train the model, the output results of multiple decision trees are accumulated, so that the prediction model is gradually improved.

Gradient lifting decision tree is widely used in other industries, such as predicting the remaining life of turbofan engine based on the performance data of aircraft engine recorded by modern machines; Based on the disk public data set and the disk data of dispatching system, the disk fault of dispatching server of power grid company is predicted.

Gradient lifting tree (GBDT) is a decision tree based learner, which iteratively and gradually learns to obtain a strong learner through the forward distribution algorithm. The construction process is mainly divided into three steps:

First, initialize the weak learner:

$$f_0(x) = \underbrace{\arg\min}_{c} \sum_{i=1}^{m} L(y_i, \ c)(x \in R_{tj}) \tag{1}$$

Second, calculate the negative gradient for each iteration:

$$r_{ti} = -\left[\frac{\partial L(y_i, f(x_i)))}{\partial f(x_i)}\right]_{f(x)=f_{t-1}(x)} \tag{2}$$

Using sample data $(x_i, r_{ti})(i = 1, 2, \ldots m)$, fit a cart regression tree, until the t-th regression tree is obtained, its corresponding leaf node area R_{tj}, $j = 1, 2, \ldots, J$, where J is the number of leaf nodes of the regression tree, and the best fitting sum is calculated.

$$c_{tj} = \underbrace{\arg\min}_{c} \sum\nolimits_{x_i \in R_{tj}} L\big(y_i, \ f_{t-1}(x_i) + c\big) \tag{3}$$

Third, update the learner until you get a strong learner:

$$c_{tj} = \underbrace{\arg\min}_{c} \sum\nolimits_{x_i \in R_{tj}} L\big(y_i, \ f_{t-1}(x_i) + c\big) \tag{4}$$

3.2 Moving Average Autoregression

As a mature prediction method, the principle of time series analysis lies in: on the one hand, it recognizes the continuity of the development of things, and can infer the development trend of things by using past data for statistical analysis; On the other hand, the randomness caused by accidental factors is fully considered. In order to eliminate the influence of random fluctuations, historical data are used for statistical analysis and trend prediction. The biggest advantage of time series analysis is that there is no need to study the background of the sequence. The timing and autocorrelation of the original sequence itself have provided enough information for the establishment of prediction model. A fairly high-precision prediction model can be established only with a limited sample sequence. There is an inseparable relationship between the failure of electric energy meter and the monthly cycle. It is feasible to carry out statistical analysis and trend prediction through the historical data of electric energy meter failure.

Time series analysis has achieved good results in many fields, such as haze prediction, wind speed prediction, power system load prediction and transmission line icing prediction. For example, based on the data of on-board and trackside systems, predict the future trend of rail transit auxiliary reverse system faults and give early warning tips beyond the threshold; The dissolved gas in power transformer oil is diagnosed to realize the prediction of transformer operation fault.

Moving average autoregressive model (ARIMA), which is characterized by the shift of prediction objects over time, can achieve better prediction results. In ARIMA (p, d, q), AR is autoregressive and p is the number of autoregressive terms; MA is the moving average, q is the number of moving average terms, and d is the difference order to make it a stationary sequence. Can be expressed as:

$$\left(1 - \sum\nolimits_{i=1}^{p} \varnothing_i L^i\right)(1 - L)^d X_t = \left(1 + \sum\nolimits_{i=1}^{q} \theta_i L^i\right)\varepsilon_t \tag{5}$$

where L is the lag operator, $d \in Z, d > 0$.

The construction process is divided into three steps:

First, the preprocessing of time series. Moving average autoregressive model requires that the necessary condition for analyzing and predicting time series is data stationary and non white noise. It is mainly tested by sequence diagram and correlation diagram. For non-stationary data, it is processed by difference until the data is stable.

Second, model order determination and parameter estimation. On the basis of determining the model, the order of the model is determined by BIC criterion method. On this basis, the model parameters are estimated by training the model. The main methods include moment estimation, least square method and maximum likelihood estimation.

Third, model validation. It mainly verifies whether the model completely or basically explains the correlation of the system mining data, that is, the model fitting effect. The statistics are constructed by using the Barrett theorem to test until the model passes the test.

4   Model Building

4.1   Build Process

The batch fault prediction model of electric energy meter is connected to the provincial metering management and dispatching platform MDS and the data collected by power consumption to realize data induction, fusion, data cleaning, extract characteristic indicators through phase relationship and principal component analysis, train relevant models, conduct parameter optimization and model evaluation, and finally obtain the optimal batch fault prediction model of electric energy meter, so as to realize the online prediction of the number of batch faults in the future. The construction process is shown in Fig. 1.
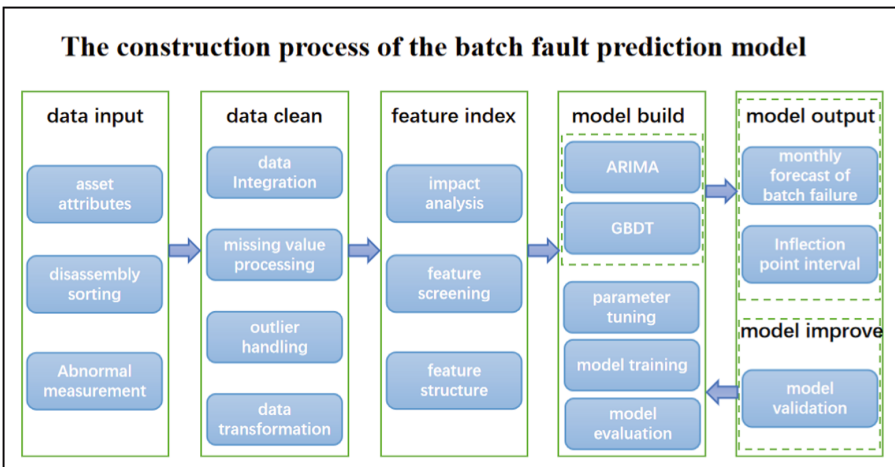
Fig. 1. Fault prediction model construction process.

1. Data input: the data comes from the asset attribute data of MDS system, disassembly and sorting data, as well as the collected abnormal data and measurement abnormal data of use and purchase system.
2. Data clean: clean and convert the above input data, delete irrelevant data, duplicate data and noise data in the original data, filter out data irrelevant to the fault prediction of electric energy meter, and deal with missing values and abnormal values, so as to provide quality assurance for the later modeling.
3. Feature index: through expert experience and correlation analysis, sort out 101 influencing factors of electric energy meter fault, and finally determine 33 factors with high influence degree as the characteristic indicators of the model by using the methods of characteristic screening, principal component analysis and quantitative analysis.
4. Model build: build a batch fault prediction model based on GBDT and ARIMA fusion algorithm, and determine the optimal model through model training, parameter optimization and model evaluation.
5. Model output and Model improve: use the best trained electric energy meter fault prediction model to predict whether there will be faults in the future, count the number of faults and obtain the batch fault rate prediction by the ratio to the total number of operation batches, and obtain the turning point interval of sudden increase in trend according to the trend change of batch fault rate; Using the difference between the actual sorting fault results and the predicted fault results, return to the model construction link to continuously optimize the model.

4.2 Model Fusion

Model fusion is based on the idea of voting mechanism, that is, for a mining target, the prediction results of multiple models are properly synthesized, and the results are better than any one.

It is assumed that there are m prediction methods for batch failure prediction in the next stage, while there are two prediction methods in this study. Therefore m = 2, in order to facilitate the universality of formula introduction, the weight of each prediction model is ω_i in the combined model is determined according to the fitting effect of each prediction model, then the formula of the combined prediction model can be recorded as Eq. 6:

$$f_t = \sum_{i=1}^{m} \omega_i f_{it} \tag{6}$$

In the formula: f_t is the predicted value of the combined prediction model at time t; f_{it} It is the predicted value of the i-th prediction model at time t, and Eq. 7 needs to meet Eq. 8.

$$\sum_{i=1}^{m} \omega_i = 1, \omega_i \geqq 0, i = 1, 2, \ldots, m \tag{7}$$

According to the optimization theory, the loss function is defined as the sum of squares of prediction errors, and the formula is shown in Eq. 8:

$$minE = min \sum_{i=1}^{m} (y_t^2 - 2y \sum_{i=1}^{m} w_i f_{it} + (\sum_{i=1}^{m} w_i f_{it})^2) \tag{8}$$

And meet the conditions, as shown in Eq. 9.

$$\begin{cases} \sum_{i=1}^{m} \omega_i = 1 \\ \quad \omega_i \geq 0 \end{cases}, i = 1, 2, \ldots, m. \tag{9}$$

where e_t is the error of combined prediction at time t; y_t is the observed value; E is the sum of squares of errors. Set the weights of GBDT model and ARIMA model as ω_1, ω_2, the predicted value is y_1, y_2, the final predicted value of the two models is y_c, the formula can be recorded as Eq. 10.

$$Y_c = \omega_1 Y_1 + \omega_2 Y_2 \tag{10}$$

Through the prediction errors of the two models, the variance and covariance of the two model errors can be obtained, which are set as $\delta_{11}, \delta_{12}, \delta_{22}$, finally, the weight coefficients of the two prediction models can be calculated as shown in Eqs. 11 and 12.

$$\omega_1 = \frac{\delta_{22} - \delta_{12}}{\delta_{11} + \delta_{22} - 2\delta_{12}} \tag{11}$$

$$\omega_2 = \frac{\delta_{11} - \delta_{12}}{\delta_{11} + \delta_{22} - 2\delta_{12}} \tag{12}$$

The final prediction value is obtained by using the calculated weight weighted average.

4.3 Model Evaluation

For different types of machine learning problems such as classification, regression and sequence prediction, the selection of evaluation indicators is different. For regression prediction, the commonly used performance indicators are mainly errors, including training error, test error and generalization error. The common error index is mean square error E(f; D), as shown in formula 13.

$$E(f; D) = \frac{1}{m} \sum_{i=1}^{m} (f(x_i) - y_i)^2 \tag{13}$$

On this basis, the training error and test error are compared to avoid the occurrence of over fitting and under fitting, that is, to realize the coexistence of multiple evaluation indexes.

4.4 Self Learning Function

Efficient machine learning model needs high-quality data. Training machine learning model is not a single limited stage in the process. In the face of changing external environment, the prediction model is faced with data drift and model attenuation. Therefore, stable new training data is needed to ensure the prediction accuracy of the model over time. It is essential to build a model that aims to continuously learn from new data. Its advantage is to pay close attention to the prediction model, find out the shortcomings, and regularly repair and self update the prediction by discovering more additional data value or in a more basic way, so as to maximize the value of the prediction model algorithm.

5   Model Application

5.1   Data Source

To build the batch fault prediction model of electric energy meter, it is necessary to obtain file information, disassembly and sorting data, operation batch data and measurement abnormal data from MDS and power consumption information acquisition system to analyze the impact characteristic index of the number of batch faults of electric energy meter.

According to the batch determination rules, that is, under a bidding batch, all smart meters of the same manufacturer, arrival year, installation year and specification are divided into one batch.

This study uses the historical disassembly and sorting data of Henan Province for modeling analysis and verification. The data are shown in Table 1.

Table 1. Data source.

Data source	Data sheet	Quantity
MDS system	Remove file information	1925218
	Remove sort data	1971023
	Number of running batches	54949
Power consumption information acquisition system	Measurement abnormal data	216 million

1. Operation batch Division: the operation batch is divided according to the bidding batch, manufacturer, installation year, arrival year, specification, management unit and arrival batch of the electric energy meter; Then, the total number of faulty operation batches is 54949, involving more than 1.98 million faulty watt hour meters.
2. Division of batch quantity: among the 54949 batches, there are only one batch of electric energy meters, 10629 batches, quartile: 2, median: 23, quartile: 254, the average number of batch electric energy meters is 692, the batch with the largest number of electric energy meters has 60822 electric energy meters, a total of one batch, and the batch with more than 100 electric energy meters has 18883 batches.
3. Failure months of batches: among the 54949 batches, the number of failure months is at least one month, a total of 25745 batches, the quartile is 16.5, the median is 32, the quartile is 47.5, the average number of failure months is 19, and the maximum number of failure months is 69, a total of one batch.

In conclusion, it can be seen that there are many batches with a small number of electric energy meters, including 65.6% of the batches with less than 100 electric energy meters, and many batches with less failure months, including 78.3% of the batches with failure months of 5 months or less. The batches with less number of electric energy meters and less failure months are not suitable for prediction using the model, This part of data will be filtered out when making model prediction.

5.2 Feature Extraction

The business goal of the research on the batch fault prediction of electric energy meters is to mine the law of the number of faults in the batch of electric energy meters every month. The data collection focuses on the fault information of the disassembled meter. Combined with the reliability theory of electronic products, collect data in as many dimensions as possible and analyze the batch fault law of the electric energy meter. Among them, temperature, humidity, component quality, operating environment, manufacturer's process flow and quality control ability will affect the service life and performance of electronic products, but the data that can be collected is limited, In this study, the control variable method is used to offset the impact of insufficient external environmental data.

Based on experience and the idea of reliability theory, firstly, the characteristics that may affect the fault of electric energy meter are selected from the basic data, which are called original characteristics; In order to improve the accuracy of the model, some original features are constructed combined with business experience, which is called construction features. One vote veto. According to business and expert experience, if there are some metering or acquisition abnormalities in the electric energy meter, the electric energy meter must have failed. Based on the above principles, some features are sorted out, and the importance of features is one vote veto. Important category: according to business and expert experience, if there are some metering or acquisition abnormalities in the electric energy meter, the electric energy meter may have failed. Based on the above principles, some features are sorted out, and the importance of features is important. For model calculation, in addition to combining the experience of industry experts, some characteristics of electric energy meters also affect whether they fail, but such characteristics can not directly identify the importance through business combing, and calculate the Gini importance through quantitative analysis.

From the original features and structural features, the factors affecting the batch faults of electric energy meters are explored through correlation analysis, and then the characteristics are selected by using the methods of correlation coefficient and principal component analysis to determine the characteristics required for modeling. From the factors affecting the batch failure of electric energy meters, three major categories of characteristic indexes are extracted: measurement abnormality, disassembly meter measurement failure and time. The key characteristic indexes are shown in Table 2.

5.3 Data Preprocessing

1. **Data filtering**

Among the 54949 operating batches, considering that the batches with small number of failure months and small number of failures in each month are not suitable for building models for prediction, these batches will be eliminated. The batches with less than 5 failure months and less than 5 median number of failures in each month and containing less than 100 electric energy meters will be eliminated, and the remaining 2674 batches.

The data of electric energy meters with metering faults are grouped and summarized according to the operation batch, and 20319 batches of data are obtained. After excluding the data with less than 30 samples in the metering fault, 1861 valid batches are obtained.

Table 2. Description of key characteristic indicators.

Serial number	Feature category	Name
1	Measurement anomaly class	Number of abnormal electricity meters
2		The unevenness value indicates the quantity of electric energy
3		Number of meters flying away
4		Number of reverse running of electric energy meter
5		Number of meter stops
6		Number of voltage phase failure
7		Number of abnormal power factor
8		Number of abnormal clock of electric energy meter
9		Number of abnormal reverse electric quantity
10		Number of reverse power flow
11		Quantity of abnormal rate setting of electric energy meter
12		Number of voltage out of limit
13		Number of voltage unbalance
14		Number of current loss
15		Number of current unbalance
16		Number of cover opening of electric energy meter
17		Number of constant magnetic field disturbances
18		Number of user power outages
19		Quantity of demand exceeding capacity
20		Number of overload
21		Number of current overcurrent
22		Number of abnormal phase sequence
23		Abnormal quantity issued by expense control
24	Time class	Monthly identification
25		Years of batch operation

Table 2. (*continued*)

Serial number	Feature category	Name
26	Remove the meter and measure the fault	Quantity of metering faults in last month
27		Quantity of metering failures in the last two months
28		Mean value of metering faults in the last two months
29		Minimum value of metering faults in the last two months
30		Maximum quantity of metering faults in the last two months
31		Mean value of metering faults in the last three months
32		Minimum value of metering faults in the last three months
33		Maximum quantity of metering faults in the last three months

Note: the measurement faults of the disassembled meter include error out of tolerance, inaccurate indication, out of tolerance of the combination error of the meter, sudden change of electric quantity data, abnormal deduction of electric charge, period conversion error, clock error, abnormal power supply and crash.

2. **Data filling**

Because the original data is almost time discontinuous data, before modeling, it is necessary to fill in the monthly fault data of each batch, fill in the missing month, and fill the corresponding fault number as 0.

3. **Exception handling**

Data outliers also have a great impact on the modeling of time series. Therefore, the box diagram method is used to detect the outliers of the number of monthly faults, detect the values greater than the upper threshold and the lower threshold, and replace them with the median, so as to complete the detection and replacement of outliers. As shown in Fig. 2 and Fig. 3.

After preprocessing the data, 100 batches with a data length of one to two years and more than two years are sampled and applied to the two models for modeling analysis.
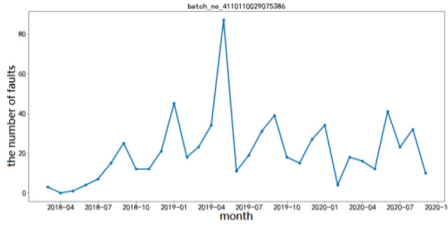
Fig. 2. Trend chart of batch fault original data
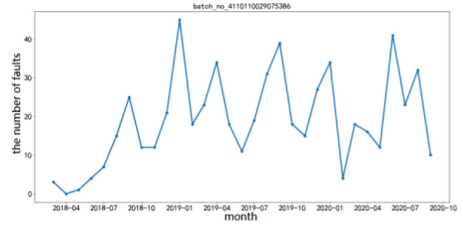
Fig. 3. After batch fault abnormal data processing

5.4   Model Prediction

For each batch, the data of the next six months are divided into test data according to the time dimension, and the remaining data is used as training data. Fit the training data, apply the fitted model to the test data to complete the prediction, compare the predicted value with the real value, and use RMSE and MAPE to evaluate the accuracy of the model. Where RMSE refers to the root mean square error, and refers to the square root of the ratio of the square of the deviation between the predicted value and the real value to the observation times N; MAPE refers to the average absolute percentage error, which is the average value of the absolute percentage error. The smaller the prediction error, the more important the lower the MAPE is.

$$RMSE = \sqrt{\frac{1}{n} \sum_{i=1}^{n} \left(\hat{y}_i - y_i \right)^2} \tag{14}$$

$$MAPE = \frac{100\%}{n} \sum_{i=1}^{n} \left| \frac{\hat{y}_i - y_i}{y_i} \right| \tag{15}$$

Predict 100 batches of sampled fault data with a time length of one to two years and more. The evaluation results of the model are shown in Table 3. The average RMSE and MAPE of 100 batches with the time length of batch failure data of more than two years are 5.93 and 55.33, which are lower than the evaluation results with the time length of batch failure data of one to two years, indicating that the model has a good prediction effect for batch models with failure data of more than two years.

Table 3.   Model evaluation result table.

Data time length	RMSE	MAPE
One to two years	7.07	79.26
More than two years	5.93	55.33

The analysis results of some batch models with a data length of more than two years are shown. As shown in Fig. 4, the prediction effect of batch model is close to the real effect:
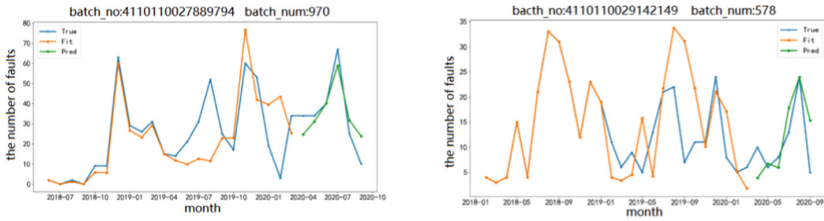
Fig. 4. Effect drawing of partial batch model analysis (more than two years)

As shown in Fig. 5, the prediction effect of the batch model is close to the real value in the first four months, but the prediction effect is not ideal after that:
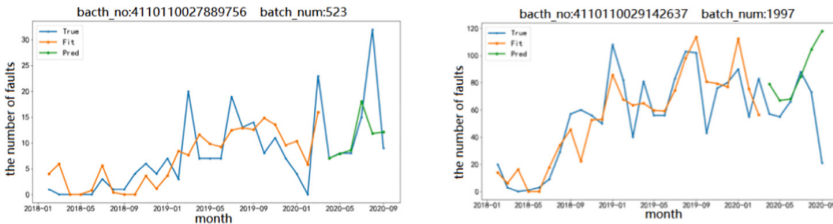
Fig. 5. Effect diagram of partial batch model analysis (more than two years)

As shown in Fig. 6, the batch model basically reflects the prediction trend, but there is still a certain gap with the real value:
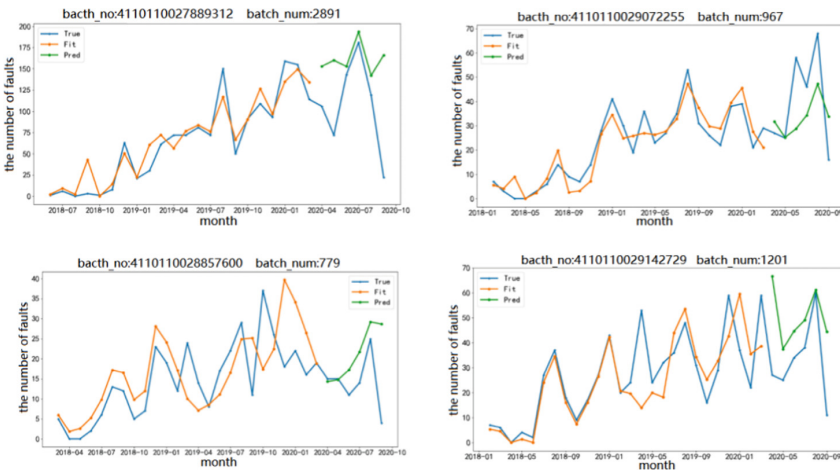
Fig. 6. Effect diagram of partial batch model analysis (more than two years)

Considering the business characteristics and practice, it is planned to output the number of failures of each batch in the next six months on the results of batch failure prediction model.

6   Summary

It is concluded that the operation quality of electric energy meter is closely related to the fault rate and service life. The core of operation state management is fault prediction, and the key of operation cost and economic benefit is the life prediction of electric energy meter.

Research on the batch fault early warning model of electric energy meter. By analyzing the disassembly and sorting data, operation batch data and measurement abnormal data of electric energy meter, build a batch fault prediction model based on GBDT and ARIMA fusion algorithm to predict the operation batch fault of electric energy meter. Study and judge the warning batch by using the results and auxiliary information output by the batch fault prediction model, so as to determine the fault replacement list, Assist business personnel to formulate reasonable replacement plan and purchase plan. First, determine whether to replace the table in a whole batch or continue to extend the use. Second, carry out predictive management on the reserve of spare parts, so as to maximize the efficiency of optimization decision-making and implementation, and avoid the large-scale occurrence of malignant emergencies and eliminate certain hidden dangers.

References

1. Wu, Q., Qu, L.: Fault prediction of auxiliary inverse system based on ARIMA and xgboost algorithm. J. Dalian Jiaotong Univ. **02**(42), 96–100 (2021)
2. Zhang, X.: B-value life evaluation and application example of automobile chassis parts based on Weibull distribution. Manuf. Autom. **09**(37), 67–69 (2015)
3. Huang, X., Jiang, W., Zhu, Y., Tian, Y.: Transformer fault prediction based on time series and support vector machine. High Voltage Technol. **46**(07), 2530–2538 (2020)
4. Yu, H.: Data driven residual life prediction of turbofan engine. Harbin University of Technology (2020)
5. Zhao, F., Zhang, Q., Wang, S.: Application of Weibull distribution in reliability analysis of traction substation. Inner Mongolia Sci. Technol. Econ. **04**(07), 107–108 (2018)
6. Li, X., et al.: Disk fault prediction model based on adaptive weighted bagging GBDT algorithm under unbalanced data set. Microelectron. Comput. **37**(03), 14–19 (2020)
7. Jiang, H., Man, H.: Reliability of fatigue shear life of railway reinforced concrete beams based on two parameter Weibull distribution. J. Shijiazhuang Railway Univ. (03), 68–72 (1997)
8. Zhang, X., Wang, Z., Wang, J.: Study on damp heat aging test cycle of automotive materials. Environ. Technol. (6), 30–33 (2017)
9. Tian, Z., Zhu, Y., Liu, J.: Reliability evaluation method of intelligent electric energy meter based on Bayesian. Comput. Meas. Control **24**(10), 274–277 (2016)
10. Bao, J., Zhou, C., Tian, Z.: Application of high accelerated life test in reliability research of intelligent electric energy meter. Electr. Meas. Instrum. **51**(19), 17–23 (2014)

Study of Peer-to-Peer Auto-negotiation Algorithm Based Mechanism in Substation Security Communication

Youjun Li[1,2], Guanghui Xu[2(✉)], Zhihao Shen[2], Xinxin Dai[2], Ji Zhang[2], and Zheng Liu[2]

[1] Nari Group Corporation, Nanjing 211106, China
[2] NARI Technology Co., Ltd., Nanjing 211106, China
`xuguanghui@sgepri.sgcc.com.cn`

Abstract. Network communication security technology is an important topic in the field of substation research. A communication security mechanism based on online auto-negotiation encryption algorithm for secondary devices is proposed in this paper, through the research on the communication security problems in substation. The mechanism includes establishing a unified encryption algorithm library for the station, online negotiating and selecting encryption algorithm which is adapting to the capabilities of both parties. It realizes peer-to-peer differentiation and algorithm dynamic switching and improves the confidentiality and availability of the communication. Through the test of the security communication scheme of monitoring and protection devices, the function of peer-to-peer differentiation and adaptive dynamic selection of encryption algorithm among linked devices is verified. The results show that security communication has no impact on the normal function of device, and a little impact on resource consumption and communication performance.

Keywords: Communication security in substation · Encryption algorithm library · Dynamic auto-negotiation of security algorithm · Communication security system · Secret key management

1 Introduction

There have been frequent cyber security incidents in recent years, which are gradually transforming from hacker attacks to confrontations between countries. The situation has become more severe, such as the large-scale power outage in Ukraine's national power system [1], the Prism Gate incident, the "Stuxnet" attack on the Iranian nuclear power plant and the Guri hydroelectric power plant incident in Venezuela.

Information security issues have affected various industries and becoming an important factor that threaten the safe and stable operation of power grids [2, 3]. For the safe and stable operation of the network security power system, requirements such as confidentiality, integrity, availability, non-repudiation are raised in some regulations such as

"The Internet Security Law of the People's Republic of China" and "The National Development and Reform Commission of the People's Republic of China No.14 in 2014" [4, 5]. Information security has become one of the most important topics in the field of substation research [6, 7].

At present, the communication security in the substation mainly depends on independent encryption and isolation devices. The communication of important secondary devices such as relay protection or bay units usually use a fixed encryption/decryption algorithm, and most of the message contents are exchanged through plaintext, which seriously affects network confidentiality and availability in the substation. A substation security system mechanism with auto-negotiation encryption/decryption algorithm is proposed in this paper, which improves the confidentiality and availability of substation network communication data and balances the impact of security policies on equipment resources at the same time.

2   Communication Security Reinforcement Methods and Problems of Smart Substation

At present, the smart substation mostly adopts three layers and two networks structure, including station level, bay level and process level, as shown in Fig. 1.
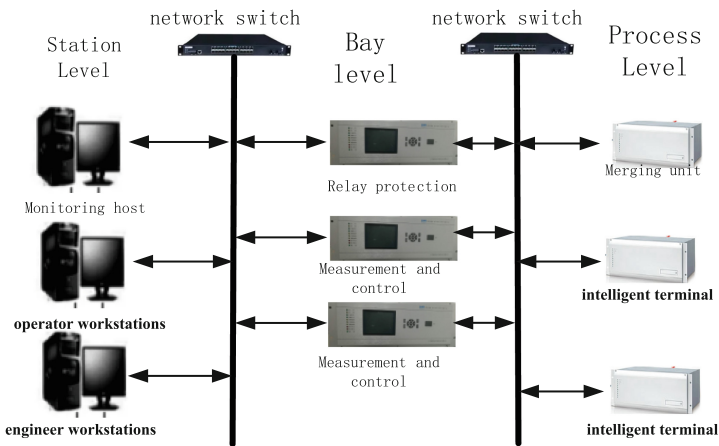
Fig. 1. Typical communication structure of substation

The station level includes monitoring hosts, operator workstations, engineer workstations, data servers, and other equipment, realizing the storage, display and management functions of the real-time historical data of the entire station, and undertaking human-machine interaction such as monitoring and operation. The bay level includes relay protection devices, bay units, wave recording devices and other equipments undertaking controlling and protecting the primary equipments in substation. The process level includes merging units, intelligent terminals and so on, undertaking monitoring and controlling of primary equipments.

The station level network connects the equipments in station and bay level, mostly adopting manufacturing message specification(MMS) of IEC 61850 Standard or IEC 60870-5-103 protocol. The process level network connects devices in bay and process level, mostly using generic object oriented substation event (GOOSE) and sampled measured value (SV) of IEC 61850 Standard. Plaintext data exchange is applied between the station and process level network, in view of the performance and real-time requirement of relay protection and bay units in smart substations, which may cause security problems.

At present, the communication security reinforcement methods in smart substations mainly include:

1) Digital certificate authentication verification. The common digital certificates authentication process [8, 9] includes obtaining certificates from third-party digital certificate servers by receiving and sending ends, exchanging certificates during communication, verifying the validity of certificates and performing signature verification. The identity and operation authority of the other party can be confirmed through verification. This method is suitable for authentication among industrial computer or workstations typed devices because of low real-time performance.

2) IEC62351 safety communication protocol standard [10, 11]. The standard is for the IEC61850 standard in the substation automation system. According to the IEC62351 standard, the Transport Layer Security (TLS) secure communication mechanism is added between transmission control protocol (TCP) and ISO transport services on top of the TCP (TPKT) layer to provide end-to-end encryption and protection against man-in-the-middle attacks. When the MMS connection is established between the client and the server, the message authentication function is provided to prevent unauthorized access to the device information.

3) The communication content encryption. The main methods include encrypted signature algorithm, such as extending the application protocol data unit(APDU) of GOOSE/SV data and adding SM2 digital signature information [8], communication in ciphertext through an encryption algorithm [12–14] and adding digital signature encryption information based on the GOOSE feature [15].

None of the above information security reinforcement methods has offered an overall effective protection scheme for the station and process level network devices. Meanwhile, communication encryption/decryption algorithm cannot be dynamically changed online, and the ability to resistance three-party intercepted attacks is insufficient. Therefore, it is necessary to further research the security system scheme that could comprehensively balance the characteristics of the equipment at the station and process level, and improve the network security of the smart substation.

3 Dynamic Security Mechanism Based on Auto-negotiation Encryption Algorithm

Most smart substations follow the three-layers and two-networks structure. The communication network includes a TCP based station level network and a link layer based

process level network [16]. Moreover, various secondary devices have different processing and communication capabilities. In view of this, a unified encryption algorithm library is built for all devices need security communications. The encryption algorithm is updated when TCP connection is established and then is updated periodically during the communication. Unused algorithms are preferred and only those adapt to the capabilities of both parties can be selected based on the ability list. In the auto-negotiation, the device feature information as special factor is added to the key distribution data, which generates respective mixed message keys (pseudo keys). Through dynamic auto-negotiation encryption algorithm and pseudo-key mechanism, the security reinforcement performance of the substation communication security system is effectively improved with balancing the capabilities of each device.

Unified management of security certificates should be designed firstly in the station for security communication mechanism. A workstation is added at the station level as an authorization server, which is connected to the station level network, used for the management of certificates and keys in the station level. A server is also added at the bay level as a key agent, which is connected to the station and process level network, used for the management of certificates and keys in the process level. The key agent gets the certificates and keys from the authorization server. The schematic diagram of the system structure is shown in Fig. 2.
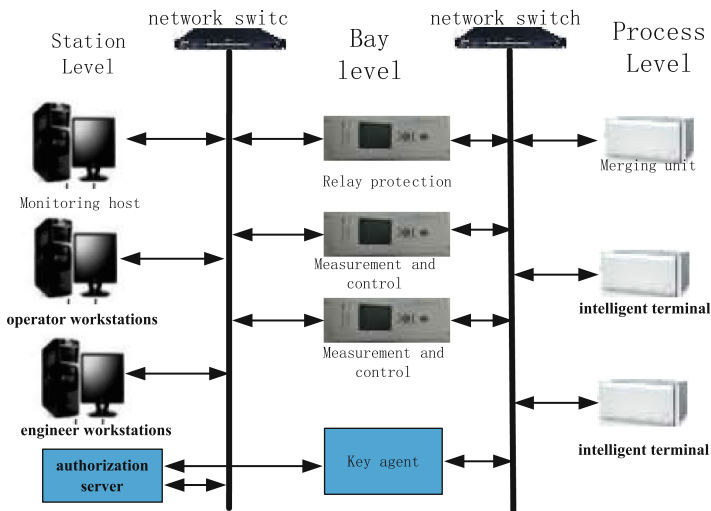
Fig. 2. Structure of substation safety certificate management

The authorization server is only used in the station level communication for the management of certificates and keys in the dynamic trusted mechanism. And the key agent is only used in process level communication. The certificates and keys in key agent are synchronized with the authorization server. Both are essential in the substation security communication. According to the scale of the communication in the smart

substation, more authorization servers and key agents can be added or distributed to the station.

The security communication system of the whole station adopts a unified encryption/decryption algorithms library. Devices in the station that need multi-connection support the communication with different security algorithms at the same time according to the accessed device, while embedded smart devices can only support a subset of the algorithms library. This ensures the real-time communication of the device and keeps the consistency of the encryption/decryption algorithm after dynamic auto-negotiation.

The encryption/decryption algorithm library of the entire site includes symmetric key algorithms commonly used in the industry, such as Advanced Encryption Standard (AES), Triple Data Encryption Standard (3DES), SM4 packet encryption algorithm, Rivest Cipher 4(RC4), etc. Each algorithm derives sub-algorithms with different security strengths according to different key lengths. At the same time, it also includes digest algorithms commonly used in the industry, such as Message-Digest Algorithm 5(MD5), Secure Hash Algorithm (SHA), SM3 cipher hash algorithm, etc., which are used to digest data such as pseudo keys. The library is formed by specifying a sequence number for each symmetric key main algorithm, sub-algorithm, and digest algorithm, which is shown in Table 1.

Table 1. Encryption/decryption algorithm library

No	Abstract algorithm	Symmetric key algorithm	Key strength
0	MD5	SM4	256
1	SHA	AES	256
2	SM3	AES	128
3	SHA	AES	256
4	SM3	SM4	128
5	MD5	AES	256
6	SHA	SM4	128
7	SHA	3DES	128
…	…	…	…

Since most of the devices in smart substations are embedded devices, they have strict resource requirements, high real-time requirements and limited processor capability. The encryption algorithm should use the symmetric key algorithm to ensure encryption/decryption speed, and avoid the slow and complicated calculation process of asymmetric key algorithm.

All devices involved in encrypted communication in the smart substation could support a subset of appropriate encryption/decryption algorithm library according to their own hardware capability and function characteristics. In order to improve the security of the key, the algorithm sequence number and final key used by each algorithm in the library, and mix other factors in different ways with the key passed from the device,

such as unique identifier (UID), time, temperature humidity and bay name of the device. Even if the illegal device obtains the key message, it cannot know the real key and encryption/decryption algorithm or crack the communication data without the library.

4   Design of Auto-negotiation Encryption Algorithm Process for Station Level

In the station level, auto-negotiation encryption algorithm process includes dynamic legal identity authentication and auto-select encryption algorithm, before sending normal message and during the communication process. The specific implementation steps are shown in Fig. 3.

When a new device gets to the smart substation, the UID of the new device is added to the compliance list of the authorized server. When the new device is connected and communicates with other devices, a mutual authentication link is added, after completing the TCP handshake and before the two parties are ready to send service data.
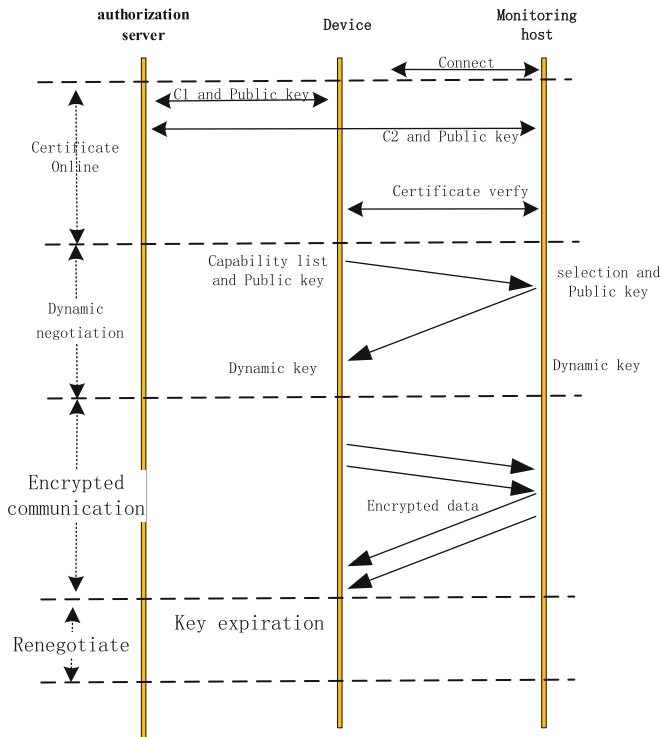
Fig. 3. Dynamic auto-negotiation diagram of control layer

The steps of authentication include three steps.

1) Both parties send their UIDs to the authorization server respectively. The authorization server compares the received UID in the compliance list. If the comparison is successful, the asymmetric key and digital signature mechanism are used to make a connection authorization certificate with the authorization server's private key, and together with the authorization machine's public key sending to the device. If the comparison is failed, no certificate will be produced.

2) After obtaining the connection authorization certificate, the two devices act as client and server respectively, sending their connection authorization certificate to the other party, and verifying the connection authorization sent by the other party using asymmetric key technology and the public key of the authorization server. The next encrypted communication will be carried out only if both parties are verified. If any party fails to have certificate or the verification, the next encrypted communication will be stopped.

3) If the mutual authentication succeeds in the next encrypted communication, the monitoring host restarts the authentication timer, and the period of the timer is determined by the host. When the re-authentication timer expires, the server informs the client to enter the mutual re-authentication process. The re-authentication process is the same as the above.

The data packet is dynamically encrypted after the mutual authentication between the two communication parties is passed. There are two key points in dynamic encryption, 1) the encryption algorithm is selected dynamically, 2) the key is generated dynamically. In the station level, the specific implementation steps are as follows:

1) Random dynamic selection of encryption algorithm. The random dynamic selection of encryption algorithm is initiated by the client. A suitable encryption/decryption strategy is randomly selected in the encryption/decryption strategy library according to its own hardware capabilities and function characteristics. The selection process is embedded in the dynamic key generation process.

2) Dynamic key generation. The next encrypted communication is performed after the client and the server passing the mutual authentication. First, both parties generate their own pseudo-keys, which are calculated by mixing random factors such as UID, timestamp, temperature and humidity values, and changes in directory content caused by files generated when the device is running. The server's pseudo key is mixed into the key validity period (for example, 10 h), and the client's pseudo key is mixed into the encryption/decryption policy sequence number. The two parties use Diffie-Hellman algorithm (DH algorithm) to calculate final key, and send their own pseudo-key to the other party through the DH algorithm. For example, the client sends its own pseudo-key A to the server. The server sends its own pseudo key B to the client, the client calculates the real key C from A + B, and the server calculates C'. In theory, C and C' are equal. When calculating C, both client and server have pseudo-keys A and B, and the calculation method is the same, performing DH algorithm calculation on A and B to generate key C1; after obtaining the selected encryption/decryption algorithm sequence number through client's pseudo-key A, using the digest algorithm to perform digest calculation on C1 and generate a key C2 corresponding to the strength of the algorithm; merging the sequence number

into C2 to generate C3; obtaining the validity period of the key through the pseudo key B of the server and merging into C3 to form C. Then two parties use the key C and the selected encryption/decryption algorithm. Regarding the timing of dynamic key generation, the two parties generate a key each time a connection is established, and the random factor for generating the pseudo key ensures that the key is dynamic, and the keys generated each time are different. When the validity time of the key exhausts, the key is dynamically generated again. The key update steps include initiated by the server, and check validity time. When the halftime arrives, the server initiates a key update process to the client, and both parties repeat the process of "generating pseudo-keys A and B, and calculating real key C". After the key update successfully, the two parties use the new key and the new strategy.

The above security communication mechanism of the station level has the following advantages:

(1) The auto-negotiation encryption algorithm adopts the mechanism of dynamically authenticating the legal identity of the counterparty before and during the communication, which improves the timeliness of device legality authentication.
(2) The encryption algorithm is randomly and dynamically selected. Even if the attacker obtains the key message, the encryption algorithm used and the final key of encryption/decryption cannot be obtained, which increases the difficulty of cracking the ciphertext.
(3) The encryption algorithm and key strength provided by the encryption algorithm library can be selected according to the hardware capability of the embedded device, which ensure the data encryption strength without significantly reducing the performance of the equipment.
(4) The dynamic key generation and renegotiation mechanism ensures the randomness and timeliness of key generation and increases the security strength of the key.

5 Design of Auto-negotiation Encryption Algorithm Process for Process Level

In the process level most of devices communicate with GOOSE/SV, the communication process has the publisher/subscriber mechanism. The authorization server of the station level has the GOOSE/SV configuration file for publication and subscription of the whole station equipment. For example, the multicast address, the equipment subscribed information of other equipment. Each equipment has its own unique iedName in the substation. Each device generates its own subscription and publication configuration file according to the global file, determining the receiving multicast address and the subscription content of device.

Based on this characteristic, the auto-negotiation encryption algorithm process can be simplified in generating and distributing key for publication and subscription. The schematic diagram of the steps is shown in Fig. 4.

In beginning of the device communication process, the device sends its own iedName and the randomly selected sequence number to the authorization agent, who sends this
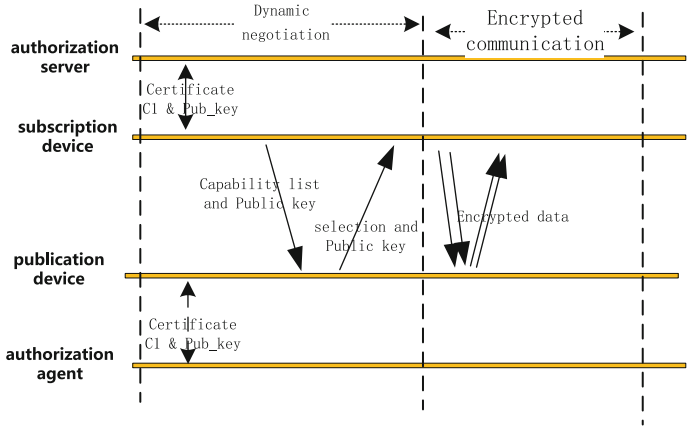
Fig. 4. Dynamic auto-negotiation diagram of process level

information to the authorization server to generate a symmetric algorithm key according to its encryption/decryption algorithm. Then the key and the message subscription and publication configuration information of the device are sent to the authorization agent together with other random values. The security communication between the authorization server and the key agent is based on encryption TCP. The authorization agent collects subscription/publishing configuration information, broadcasts the encryption/decryption algorithm sequence number and configuration information.

According to characteristics of the bay and process level equipments, the authorization agent adopts an improved dynamic encryption mechanism to ensure communication security when announcing the key. The schematic diagram of the process is shown in Fig. 5.
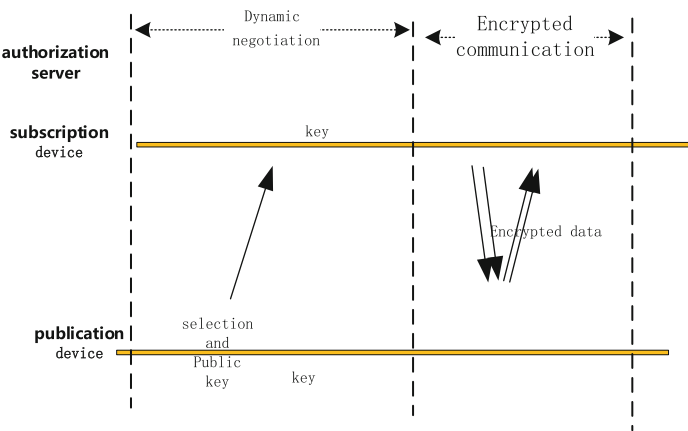
Fig. 5. Key proxy and secret key distribution diagram

The key should be stored properly in local after received. The corresponding relationship between the device's iedName and the key, and the sequence number of the encryption algorithm is established after other devices subscribed to this key. Whenever a device newly accesses or disconnects or re-accesses, the key re-generation and re-distribution process is triggered. When there is communication, the device uses its own key and the selected a symmetric encryption algorithm before publishing the message, and then the ciphertext data, switching/validation time and its iedName are encrypted. After receiving the message, the device in the multicast group will check the iedName. If not, the message is not used. If so, when the switching time is reached, the service ciphertext is decrypted with the key and the algorithm.

Most of the process level devices, the GOOSE/SV is sent and received by Field Programmable Gate Array (FPGA), so the encryption and decryption of GOOSE/SV can be calculated parallelly by FPGA, which can reduce processor time consumption. The SV/GOOSE encryption and decryption diagram is shown in Fig. 6.
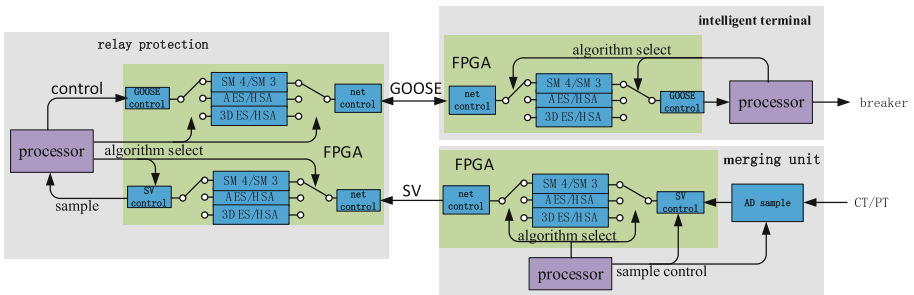
Fig. 6. The SV/GOOSE encryption and decryption diagram in process level

The security communication mechanism of the process level has the following advantages:

(1) The improved auto-negotiation encryption algorithm adopted in the communication of GOOSE/SV, and makes message length slightly increased and the encryption/decryption time less. It is easy to meet the real-time requirements of message sending and receiving.
(2) In process level, the key is updated every time the device reconnected, improving and ensuring the security of the key and confidentiality of the device message.

6 Experimental Verification

In order to verify the communication security mechanism base on online auto-negotiation encryption algorithm, secondary devices such as monitoring host, line protection, transformer protection, busbar protection, merging unit and intelligent terminal are developed. A test platform is built according to the typical communication structure of the substation. In the test platform, the security communication with auto-negotiation encryption algorithm of the monitoring host, protection, merging unit and intelligent terminals are tested. The main communication performance of the equipment is tested, and the corresponding performance of the equipment without information security functions is compared.

1) Station level communication security test. The communication of the station level adopts the MMS, and the sequence number of encryption algorithm in library and its influence on the consumption of system resources are checked. The test result recording the dynamic auto-negotiation encryption algorithm sequence number of the protection device is shown in Table 2.

Table 2. Dynamic auto-negotiation encryption algorithm test results at station level

No.	Encryption algorithm	Key algorithm	Abstract algorithm
1	0	SM4	MD5
2	3	AES	SHA
3	1	AES	SHA
4	7	3DES	SHA
5	6	SM4	SHA
6	5	AES	MD5
7	2	AES	SM3
8	4	SM4	SM3

It shows that the encryption algorithm of the station level communication is constantly changing, which effectively reduces the risk of brute force cracking by third-party.

Resource consumption and communication performance test on security communication function of protection device includes: communication establishment delay, model reading delay, parameter value modification delay, control command delay and SOE transmission delay. The maximum time is recorded and the comparison is conducted with that of devices without safety enhancement. The test results are shown in Table 3.

Table 3. Comparison of communication performance at station level

Test	Communication without security/ms	Communication with security/ms
Associated service	56.8	2873.2
Model reading	635.7	733.4
Fixed value modification	11.3	14.5
Control choose	25.8	43.6
Control command	7.5	8.4
SOE upload	13.7	14.7

From the results, except for the large delay of MMS communication process in the associated service, which requires certificate verification and key exchange negotiation, the system time consumption/delay of other tests is almost the same. The establishment of the associated service is a one-time process for communication, and the subsequent communication process has little impact.

2) Process level communication security test. In process level, the sequence number of dynamic auto-negotiation encryption algorithm in library and its influence on the consumption of system resources and communication performance are checked. The merging unit and intelligent terminal only support No.0/3/4/7 encryption algorithms in the library. And the process level devices use FPGA to complete data encryption and decryption, in the progress of sending and receiving GOOSE/SV. The test results of the dynamic auto-negotiation encryption security algorithm sequence number are shown in Table 4;

Table 4. Dynamic auto-negotiation encryption algorithm test results at process level

No.	Encryption algorithm	Key algorithm	Abstract algorithm
1	4	SM4	SM3
2	0	AES	SHA
3	3	AES	SHA
4	4	SM4	SM3
5	7	3DES	SHA

The test results show that the encryption algorithm of process level communication is constantly changing randomly, which effectively reduces the risk of brute force cracking by third-party.

The test is for bay level equipment communication recovery, GOOSE control process time, SV sample delay time and SOE transmission delay time. Compared with the

corresponding delay without security reinforcement system, the test results are shown in Table 5.

Table 5. Communication performance comparison at process level

Test	Communication without security/ms	Communication with security /ms
Encryption algorithm switch	0	1475.7
SOE upload	7.4	7.8
GOOSE control process	4.512	4.574
SV sample delay	0.731	0.775

From the results, except for the large delay in communication establishment, which requires certificate verification and key exchange, the system time consumption/delay time of other tests is almost the same. For the communication process, the communication establishment/restoration is a one-time parallel process, and the communication process has little impact.

In summary, the security mechanism of peer-to-peer auto-negotiation has very little impact on the real-time data of the system, which can effectively enhance the confidentiality and availability of communication in substation, while minimizing resource consumption.

7   Concluding Remarks

In this paper, a unified encryption algorithm library is introduced through the peer-to-peer auto-negotiation communication mechanism, and the encryption/decryption algorithms are auto-negotiated and selected online, realizing the dynamic change of the communication encryption algorithm and balancing the contradiction between the security and resource consumption. The device feature information is added to the key, which improves the system security effectively. This mechanism can be used to prevent third-party key interception and brute force cracking.

Due to the differences in the processing and communication capabilities of smart substation equipments, how to design the security algorithm library of the station and balance the functional performance and the device requirements of security may need further research.

References

1. Tong, X., Wang, X.: Network attack caused by power outage in Ukraine and thoughts on power grid information security. Autom. Electric Power Syst. **40**(7), 144–148 (2016). https://doi.org/10.7500/AEPS20160202101

2. Zhou, Z., Ban, Q., Tao, J.: Discussion on the importance and protection of power system information security. Netw. Secur. Technol. Appl. **4**(16), 151–152 (2021)
3. Zhang, P., Gao, X.: Smart substation. Electr. Eng. **8**, 4–10 (2010)
4. Yu, Y., Lin, W., He, J.: Design and application of power digital certificate service system. Autom. Electric Power Syst. **29**(10), 64–68 (2005)
5. Zhen, Y.: Substation Automation technology and Application. China Electric Power Press, Beijing (2020)
6. Guo, C., Yu, B., Guo, J., et al.: Safety risk assessment of substation automation system based on IEC 61850. Chin. J. Electr. Eng. **34**(4), 686–694 (2014). https://doi.org/10.13334/j.0258-8013.pcsee.2014.04.022
7. Nordstrom, L.: Assessment of information security levels in power communication systems using evidential reasoning. IEEE Trans. Power Delivery **23**(3), 1384–1391 (2008)
8. Luo, Z., Xie, J., Gu, W., et al.: Application of SM2 encrypted system in smart substation inner communication. Autom. Electric Power Syst. **39**(13), 116–123 (2015). https://doi.org/10.7500/AEPS20140817004
9. Luo, Z., Xie, J., Gu, W.: Design and application of information's security and protection in power supervision and control automatic system. RELAY **32**(20), 33–35 (2004)
10. Tao, S., Wang, Z., Li, G., et al.: Effect of IEC62351 based security communication on communication performance of station level. Autom. Electric Power Syst. **42**(23), 155–158 (2018). https://doi.org/10.7500/AEPS20180428005
11. Hu, Y., Ren, Z., Teng, G., et al.: A hybrid encryption approach based on IEC 62351 in substation telecontrol communication. Electric Power Inf. Commun. Technol. **16**(5), 24–29 (2018)
12. Wang, B., Wang, M., Zhang, S.: A secure message transmission method based on GCM for smart substation. Autom. Electric Power Syst. **37**(3), 87–92 (2013). https://doi.org/10.7500/AEPS201201071
13. Shen, W., Zhang, H., Li, Z.: Realization of digital signature of GOOSE message in intelligent substations. J. Nanjing Instit. Technol. (Nat. Sci. Ed.) **17**(3), 38–44 (2019). https://doi.org/10.13960/j.issn.1672-2558.2019.03.007
14. Wang, Z., Wang, G., Xu, Z., et al.: Encryption/decryption methods of GOOSE packets based on domain implication. J. South China Univ. Technol. (Nat. Sci. Ed.) **44**(4), 63–70 (2016)
15. Chen, Q., Xie, J., Fang, F., et al.: Research on power communication security optimization based on GOOSE message characteristics. Electric Eng. **6**(11), 1–3 (2018)
16. Yu, H., Mu, G., Niu, J., et al.: Application research on network security protection of an intelligent substation. Power Syst. Prot. Control **49**(1), 115–124 (2021). https://doi.org/10.19783/j.cnki.pspc.200240

Risk Assessment of Multi Scenario Blackout Considering Different Proportions of New Energy

Yu Qun[1(✉)], Xiao Songqing[1], He Jian[2], and Zhang Jianxin[3]

[1] School of Electrical and Automation Engineering, Shandong University of Science and Technology, Qingdao 266590, Shandong, China
yuqun_70@163.com
[2] China Electric Power Research Institute Co., Ltd., Beijing 100192, China
[3] State Grid Shanghai Municipal Electric Power Company, Shanghai 200122, China

Abstract. Under the vision of carbon peak and carbon neutralization, profound changes have taken place in the construction of a new power system with new energy as the main body, power supply structure and main risks, which poses new challenges to the safe and stable operation of the power system. Combined with the development status of China's power system, this paper analyzes the reform of power supply structure and the current generation capacity and installed proportion of new energy; Then, from the perspective of coordinated development of energy system, combined with SG126 node system, this paper establishes the outage accident evolution model of uncertain output of new energy, further puts forward three power system outage risk scenarios with different proportion of new energy access, and analyzes the loss load and power-law characteristics under different scenarios respectively; Finally, an over threshold model is established for the loss load under different risk scenarios, and the risk prediction of loss load in the next 3, 5 and 8 years is given by using "value at risk" VaR and CVaR.

Keywords: "Double carbon" target · New energy · Over threshold model · Risk assessment

1 Introduction

In order to cope with climate change and accelerate the transformation of clean and low-carbon energy, China put forward the "double carbon" goal at the United Nations General Assembly in September 2020, "strive to reach the peak of carbon dioxide emissions by 2030 and strive to achieve carbon neutrality by 2060" [1]. Subsequently, at the ninth meeting of the central financial and Economic Commission in march2021, China once again made important arrangements for carbon peaking and carbon neutralization, and clearly pointed out the concept of implementing renewable energy substitution action and building a new power system. Promoting green, low-carbon and sustainable social and economic development has become a global consensus [2].

With "double carbon" as the core goal, it is not only conducive to coping with climate change [3], but also conducive to guiding and promoting industrial upgrading. It is an important issue related to the energy security of countries around the world and the future development prospects of mankind [4]. However, the proposal of the "double carbon" goal not only brings opportunities for the development and transformation of the power industry, but also brings challenges to the power industry. For a long time, China's power supply has been dominated by coal-fired power and other high carbon power sources, and the proportion of installed capacity and power generation has always been more than 50%. Moreover, the power industry is an important industry in energy consumption and carbon emissions, and the carbon dioxide emissions have exceeded 40% of the total emissions of the whole society [5]. Greenhouse effect and environmental pollution have seriously restricted the sustainable development of human society [6]. Therefore, in the context of energy transformation, low-carbon development of power system has become the focus of power planning. Accelerating the optimization of power supply structure in the power industry, vigorously developing new energy, and promoting clean energy transformation on the basis of safe and reliable new energy have become the key research direction of current power planning [7]. However, compared with the traditional fossil energy, the power fluctuation of large-scale wind power, solar energy and other renewable energy will cause voltage, frequency fluctuation and power quality problems [8], and its high proportion of access to the network will increase the uncertainty of the network to a certain extent, improve the new energy consumption capacity, and improve the operation of the power grid, so as to bring stable static and dynamic benefits to the power system [9]. In the future, large-scale new energy power generation and grid connection will not only meet the requirements of low-carbon transformation of the power industry, but also bring great pressure to the stability and security of the power grid.

In addition, with the increasing proportion of new energy in the total power generation, the operation of the power grid will also be impacted to varying degrees [10], and different risk scenarios will be displayed in terms of accident risks. How to deal with these risks has become an urgent task after the transformation of the power system. Therefore, it is of great significance for power system optimization and post event risk prevention and control to build a power supply structure model with different proportions of new energy.

2 Development Status of New Energy

2.1 Proportion of New Energy Installed Capacity and Power Generation

In the past 20 years, China has achieved leapfrog development of new energy technologies such as wind power and photovoltaic [11]. According to the data released by the National Bureau of statistics [12], China's power supply structure can be divided into two stages with 2007 as the boundary, namely the development stage with coal as the main body and the diversified development stage. Before 2007, it was called the development stage with coal as the main body. During this period, the power supply structure was relatively single, with only coal power, hydro power, nuclear power and a small amount of other power generation. The period of rapid development of renewable energy and gradual response to global climate change is called the period of rapid development of

renewable energy in 2007–2020. Since the 13th Five Fear plan, with the implementation of relevant policies promoted by the state in environmental governance, energy conservation and emission reduction, the installed capacity of new renewable energy has increased sharply. After China further strengthens its commitment to emission reduction, this trend is bound to continue further during the 14th Five Year Plan period [13, 14]. The total power generation of China in the past 20 years is shown in Fig. 1.
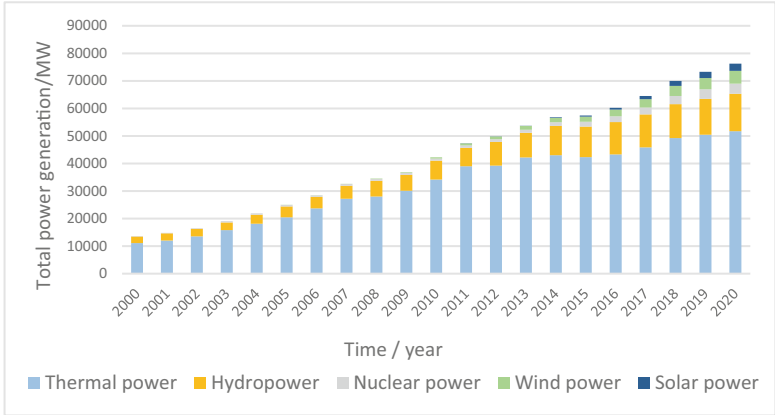

Fig. 1. Total power generation in China in the past 20 years

In recent years, under the background of energy transformation, the installed growth rate of new energy such as wind power and solar photovoltaic power generation in China is significantly higher than that of traditional power sources, and its proportion in the total installed capacity of power generation in China is also increasing. During the 13th Five Year Plan period, the annual growth rate of new energy power generation installed capacity was 32%. By the end of 2020, China's new energy installed capacity accounted for 26.6% of the total installed capacity. As shown in Fig. 2, the total installed capacity of wind power reached 281.53Gw, accounting for 12.8% of the total installed capacity, and the total installed capacity of solar power generation was 253.43Gw, accounting for 11.5% of the total installed capacity.
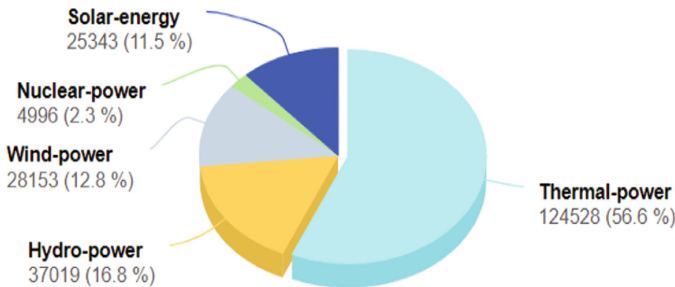
Fig. 2. Proportion of installed capacity in China at the end of 2020

At the same time, with the increasing proportion of new energy installed capacity, the proportion of new energy power generation is also increasing. By the end of 2020, China's total new energy power generation is 1093.8 billion kWh, accounting for 14.3% of the total power generation, including 261.1 billion kWh of solar power generation, accounting for 3.4% of the total power generation, and 366.2 billion kWh of wind power generation, accounting for 4.8% of the total power generation. The specific power generation proportion of each energy is shown in Fig. 3:
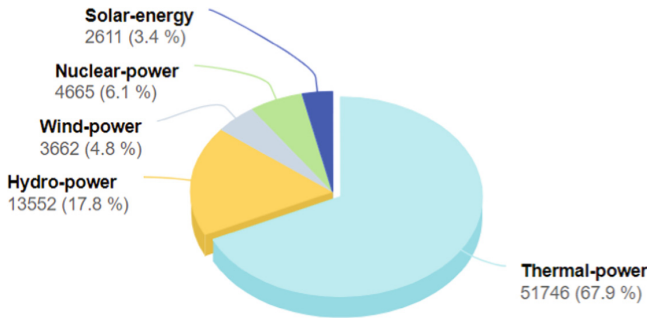
Fig. 3. Proportion of China's power generation at the end of 2020

3 Evolution Model of Blackout Accident Under Different Proportion of New Energy

3.1 Uncertainty Modeling of New Energy

The new energy power generation of power system is mainly wind power and photovoltaic power generation. The uncertainty of wind power output comes from the fluctuation of wind speed, and the uncertainty of photovoltaic power output comes from the fluctuation of solar irradiation. The wind speed fluctuation follows the two parameter Weibull distribution, and the solar irradiance follows the beta distribution [15]. Combined with the probability density function of wind speed P_w and solar irradiance P_s, the corresponding wind power output and photovoltaic power output can be obtained. The probability density function of wind power output and photovoltaic power output can be expressed as:

$$f(P_w) = \frac{A}{\alpha B}\left(\frac{P_w - \beta}{\alpha B}\right)^{A-1} \exp\left[-\left(\frac{P_w - \beta}{\alpha B}\right)^A\right] \tag{1}$$

$$f(P_s) = \frac{\Gamma(a+b)}{P_m \Gamma(a)\Gamma(b)}\left(\frac{P_s}{P_m}\right)^{a-1}\left(1 - \frac{P_s}{P_m}\right)^{b-1} \tag{2}$$

where, A is the shape parameter of Weibull distribution; B is the scale parameter; α and β are the coefficients related to the wind speed and rated output power of the fan; P_m is the maximum output power of solar cell; a and b shape parameters for beta distribution; Γ is the Gamma function.

3.2 Evolution of Power Outage Under New Energy Access

SOC power failure model describes the process of power failure caused by load increase. In the actual simulation process, the impact is simulated by randomly selecting load nodes and increasing disturbance. Similarly, in order to simulate the impact of new energy access on the power grid, select the power grid node to access new energy, and obtain the output of new energy according to the wind and solar uncertainty model, and then simulate the power failure through the power failure evolution model until the power failure occurs. The specific evolution simulation process is shown in Fig. 4.
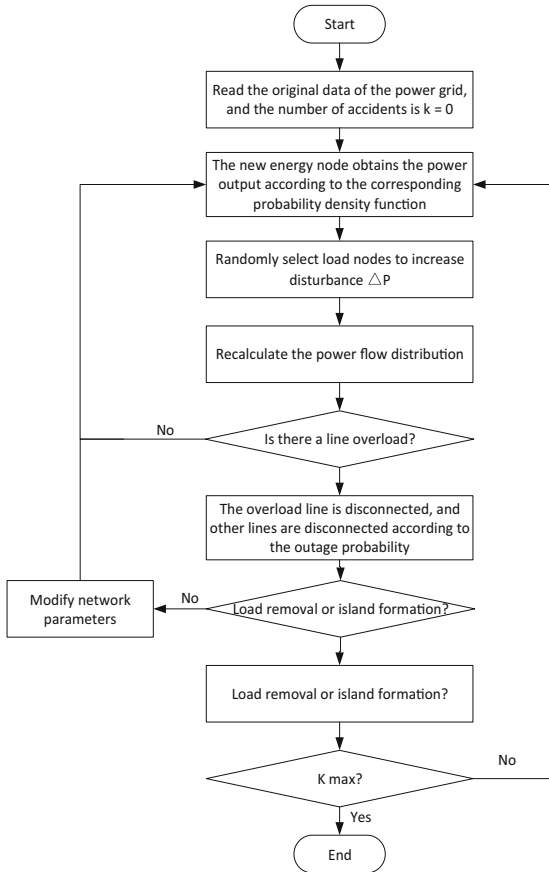
Fig. 4. Power failure evolution model after new energy access

(1) Read the original data of the power grid and set the count value of power failure accidents k = 0.
(2) According to the probability density of wind power and photovoltaic power generation, the power value of new energy as the new energy access point is obtained.

(3) Select a load node randomly and increase ΔP load disturbance, calculate the DC power flow of the power grid.

(4) Judge whether there is line overload according to the power flow results. If there is line overload, turn to (5), otherwise turn to (2).

(5) Judge whether the load is cut off or the system is disconnected due to line overload. If there is a power failure, increase the number of power failures by 1 and count the lost load of the accident, and then turn to (6). If there is no power failure, modify the network parameters and turn to (2).

Judge whether the number of power failure accidents reaches the preset number of accidents. If so, terminate the power failure accident evolution simulation, otherwise turn to (2).

3.3 Loss Load Relative Value Index

The relative value of lost load M_l is used to describe the scale of power failure after line l failure. The relative value of lost load M_l is defined as:

$$M_l = \frac{T_l}{T} \tag{3}$$

$$T_l = T_{1l} + T_{2l} \tag{4}$$

where: T_l is the number of system load loss after the line l exits the system operation; T is the total load of the system; T_{1l} is the number of loads lost by itself and its associated parts after line l failure in the power grid; T_{2l} is the number of loads cut off by the power grid to maintain transmission balance.

3.4 Power Law Characteristics of Power Failure Accident

According to the self-organized criticality theory, if the scale of an object r satisfies Eq. (5) with the frequency above the scale N, it can be said that the object obeys the power-law distribution[16].

$$N = cr^{-D} \tag{5}$$

where: c is undetermined constant; D is fractal dimension, i.e. power law value.

For the distribution based on the outage model, fractal refers to the number of outage accidents of a specific scale, which is directly proportional to the scale of power growth, while power index refers to the fractal dimension D. By double logarithmic coordinate transformation of Eq. (5), we can get:

$$\ln N = C - D \ln r \tag{6}$$

where: C is undetermined constant, $C = \ln c$.

When using Eqs. (5) and (6) to analyze the SOC characteristics of power grid outage accidents, take the scale of accident loss load (unit: MW) as the scale r and define N it as the frequency of accident loss load above the scale r.

3.5   Extreme Value Theory and Over Threshold Model

Over Threshold Model
With global warming, extreme disasters occur from time to time, and extreme weather in the traditional sense has become more frequent. In 2019, Australia broke 206 high temperature records in 90 days; The amount of plum rain in Jiang Province broke the historical record. Thunderstorms occurred frequently in July, and thunderstorms discharged to the ground more than 200000 times. A high proportion of renewable energy power generation is highly coupled with the weather, and the power system faces the risks of rising demand for extreme weather load, shortage of fossil fuel supply, reduction of renewable energy power generation [17].

There are two kinds of classical models in extreme value theory, namely, over threshold model (POT) and interval maximum model (BMM) [18]. Both of them are based on the fitting of the distribution tail of the sample data. The main difference is that the BMM model first effectively groups the initial sample data and takes the maximum value of each group as the sample data. The pot model determines the threshold based on the initial sample data and uses all the data exceeding the threshold to form a new sample data for modeling. The distribution corresponding to the pot model is called GPD (generalized Pareto distribution). The definition of GPD distribution is:

$$G_{\xi,\beta}(x) = \begin{cases} 1 - \left(1 + \xi \frac{x}{\beta}\right)^{-\frac{1}{\xi}} & \xi \neq 0 \\ 1 - e^{-\frac{x}{\beta}} & \xi = 0 \end{cases} \tag{7}$$

where:$\beta > 0$, ξ is the shape parameter and β is the scale parameter. When $\xi \geq 0, x \geq 0$; When $\xi < 0, 0 < x < -\frac{\beta}{\xi}$.

For a sufficiently large threshold u, the excess distribution has the following relationship with the GPD distribution:

$$\lim_{u \to x_0} \left\{ \sup_{0 \leq y \leq x_0 - u} |F_u(y) - G_{\xi,\beta}(y)| \right\} = 0 \tag{8}$$

A large enough threshold u and a positive scale parameter β, $F_u(y) \approx G_{\xi,\beta}(y)$ can be selected, so that the excess distribution function corresponding to the excess threshold can be similar to the GPD distribution.

Threshold Selection of Over Threshold Model
The accuracy of threshold u selection plays a key role in the estimation of parameters ξ and β. If the threshold u is too high, there will be too little excess loss data, which will lead to high scale parameters; If the threshold u is too low, it will increase the difference between excess distribution and GPD distribution, which can not achieve the fitting effect. In this paper, Hill graph method is selected to determine the threshold.

In the study of hill diagram, assuming that $X_1 > X_2 > \cdots > X_n$, it represents the order statistics of independent and identically distributed, it can be obtained that:

$$\gamma_{k,n} = \frac{1}{k} \sum_{i=1}^{k} [\ln X(i) - \ln X(k)] \tag{9}$$

The horizontal axis of the hill graph is k and the vertical axis is $\gamma_{k,n}^{-1}$, that is, the hill graph is a curve composed of points with coordinates $(k, \gamma_{k,n}^{-1})$. Select the value corresponding to the abscissa of the starting point of the tail exponential stability region in the figure as the threshold.

Risk Assessment Indicators

"Value at risk" VaR is the most popular risk measurement index in the financial industry and insurance industry, which is widely used in the measurement and supervision of the financial field [19–22]. Its meaning is the maximum possible loss in a specific period of time in the future under a certain confidence level. The mathematical expression is:

$$VaR_p = u + \frac{\widehat{\beta}}{\widehat{\xi}} \left(\frac{n}{N_u} (1-p)^{-\widehat{\xi}} - 1 \right) \tag{10}$$

where p is the given confidence level, n is the total number of samples, N_u is the number exceeding the threshold u, and $\widehat{\xi}$, $\widehat{\beta}$ is the estimated value of the parameter $\widehat{\xi}$, $\widehat{\beta}$ respectively.

Although VAR has the advantages of concise and clear risk measurement and unified risk measurement standards, it is not a consistent risk measurement tool because it does not have homogeneous additivity, so it is not applicable to the phenomenon of risk dispersion [23]. In addition, VAR cannot provide any information on the extent to which the possible loss exceeds the threshold amount specified in this method. In order to make up for the above shortcomings, CVaR index is introduced. CVaR is the mathematical expectation of the loss when the loss is known to be greater than a specific VaR value. It represents the average level of excess loss and reflects the size of the average potential loss that may be suffered when the loss exceeds the VaR threshold. It can better reflect the potential value at risk than var [24]. And CVaR is a consistent risk measure, which satisfies homogeneous additivity, monotonicity and translation invariance. Therefore, it is often used as a risk assessment index together with var. The mathematical expression is:

$$CVaR = VaR_p + E\left(X - VaR_p \middle| X > VaR_p \right)$$

$$= \frac{VaR_p}{\left(1 - \widehat{\xi} \right)} + \frac{\left(\widehat{\beta} - \widehat{\xi} u \right)}{\left(1 - \widehat{\xi} \right)} \tag{11}$$

4 Example Analysis

Based on the SG126 node system provided by State Grid Corporation of China, this paper puts forward the outage risk model under different proportions of new energy access, and selects 18 nodes, including 4, 6, 10, 12, 15, 18, 19, 24, 25, 26, 120, 31, 32, 46, 69, 99, 116 and 119, to access the wind farm and photovoltaic power station for simulation. Observe the loss of load caused by power outage with the increase of the proportion of new energy output, and analyze the power-law change trend of power outage under different power outage scenarios. Figure 5 below shows the SG126 node wiring diagram after new energy access.
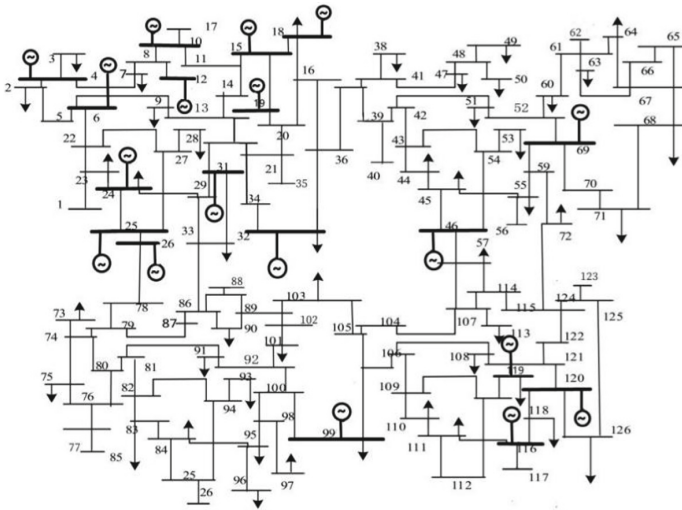
Fig. 5. SG126 node wiring diagram after new energy access

4.1 Scenario 1: Power Failure Without New Energy

In SG126 system, when 18 new energy nodes are not put into operation, the lost load of 200 power outages is simulated by using the accident shutdown model, as shown in Fig. 6.
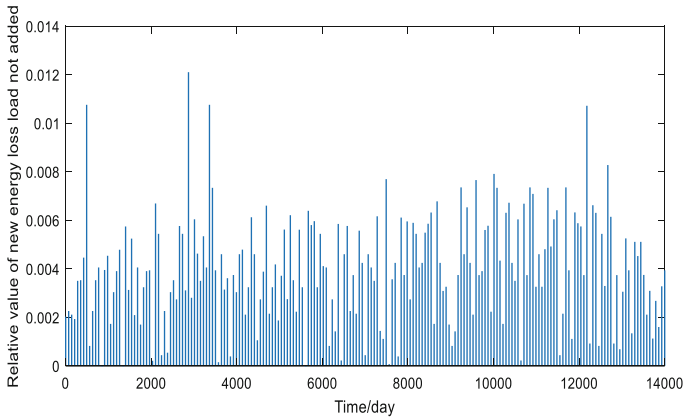
Fig. 6. Relative value of load loss when new energy is not connected

Similarly, compared with the actual value of 200 blackouts before 2021 (as shown in Fig. 7) and unified abscissa scale, it is found that without adding new energy, the relative value of loss load simulated by SG126 node is basically consistent with the relative value of actual loss load from 2001 to 2021, the average relative value of actual loss load is 0.00399, and the average relative value of loss load simulated by accident shutdown model is 0.00376, The relative values of loss load of both are concentrated below 0.005.
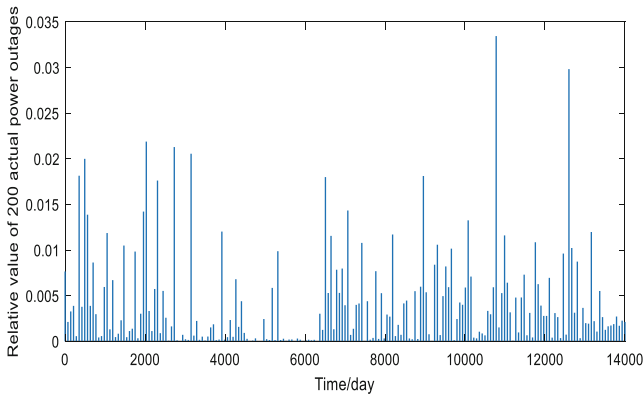
Fig. 7. Relative value of 200 actual fault loss loads

4.2 Scenario 2: New Energy Power Generation Accounts for 20% of Total Power Generation

When the proportion of new energy power generation in the power grid is 20%, the specific loss load sequence is shown in Fig. 8. Compared with Fig. 6, it is found that the average relative value of loss load increases from 0.00376 to 0.00494, and the volatility

of loss load sequence increases, indicating that the addition of new energy sources has an impact on the stability of the power grid. In order to better reflect the impact of new energy on system load loss, the power-law characteristics of power failure after the addition of new energy are compared with those without the addition of new energy. The comparison results are shown in Fig. 9:
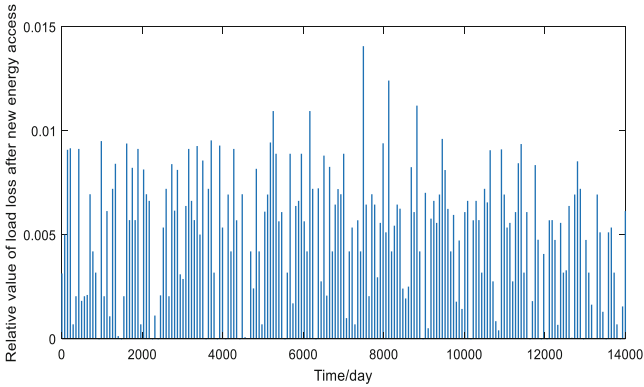
Fig. 8. Power grid load loss after 20% new energy access
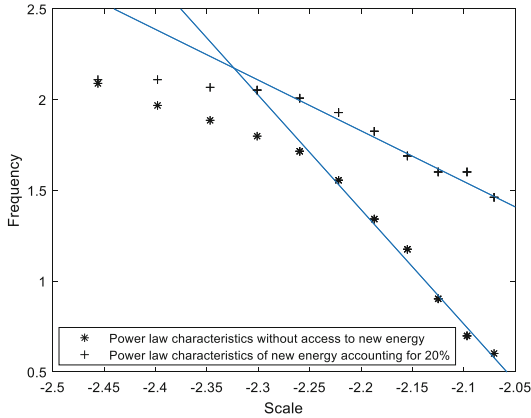
Fig. 9. Comparison of power-law characteristics between 20% new energy access and non access new energy

It can be seen from Fig. 9 that the power-law characteristics of lost load have changed significantly before and after the addition of new energy. Since the wind and light output connected to the power grid fluctuate randomly with wind speed and light intensity, its instability intensifies, which also has an impact on the self-organized critical state of the power grid.

4.3   Scenario 3: New Energy Power Generation Accounts for 40% of Total Power Generation

With the continuous increase of the proportion of new energy in the power grid, the system instability gradually intensifies. When the proportion of new energy power generation is 40%, the relative value of loss load simulation results is shown in Fig. 10. The average relative value of loss load further increases compared with that when the proportion of new energy is only 20%, and the volatility of the sequence further intensifies. The comparison between the power law characteristics of power failure accidents and those without new energy is shown in Fig. 11:
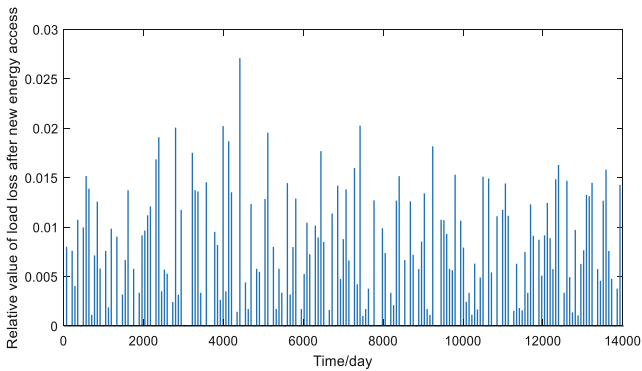
Fig. 10. Power grid load loss after 40% new energy access
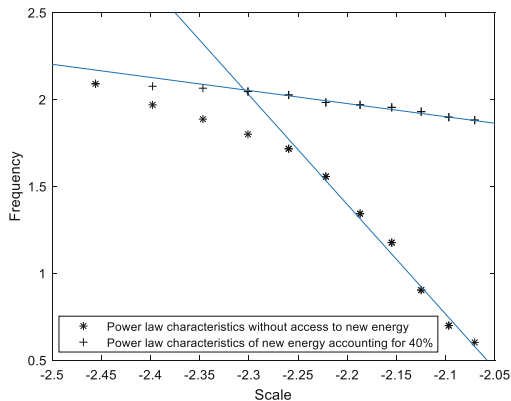
Fig. 11. Comparison of power law characteristics between 40% new energy access and non access new energy

As can be seen from Fig. 11, as the proportion of new energy increases from 20% to 40%, the slope of its power-law curve increases significantly, indicating that with the increase of the investment proportion of new energy such as wind power and photovoltaic, the instability of the system increases, making the balance between supply and demand of the system more difficult.

4.4 Scenario 4; Introduction of Regulation Measures After the Entry of New Energy

In view of the increase of system instability after the addition of new energy, many scholars at home and abroad have given corresponding regulation schemes[25–29]. Combined with the SOC power failure model of SG126 node, this paper compares the load loss with and without regulation measures after the proportion of new energy is 20% and 40% respectively.
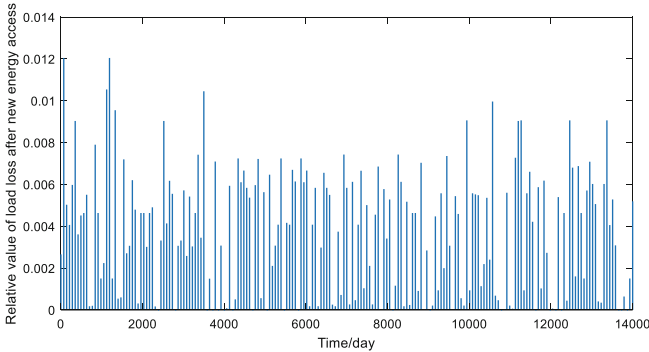
Fig. 12. Power grid load loss with new energy accounting for 20% but with regulation measures
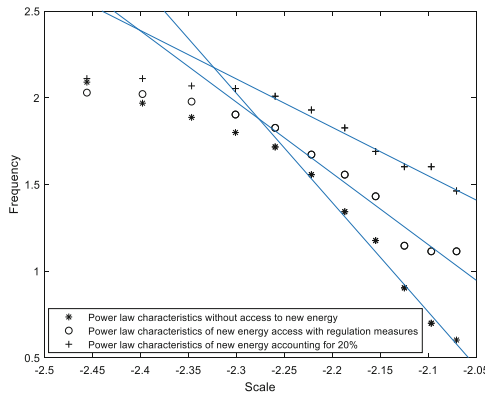
Fig. 13. Comparison of power-law characteristics with and without regulation measures when new energy accounts for 20%

When the proportion of new energy is 20% and 40%, take measures respectively to reduce the impact of new energy on the instability of power grid. Figure 12 and Fig. 14 are the relative value sequence of lost load after taking regulation measures. Compare the lost load with new energy but without regulation measures in Fig. 8 and Fig. 10. It is found that the stability of lost load in Fig. 12 and Fig. 14 is better than that without regulation measures, And the average relative value of the lost load is also lower than that without any measures. Figure 13 and Fig. 15 respectively show the power-law characteristics of
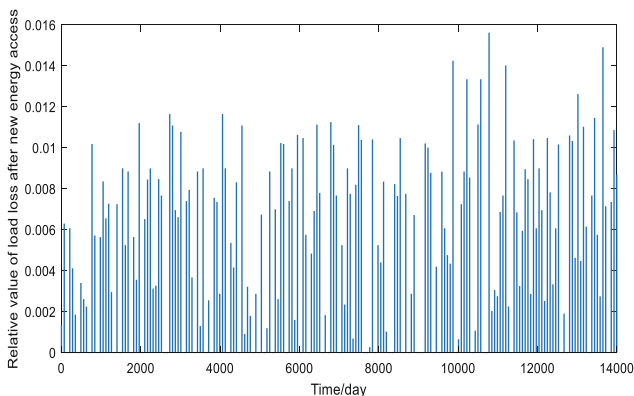
Fig. 14. Power grid load loss with new energy accounting for 40% but with regulation measures
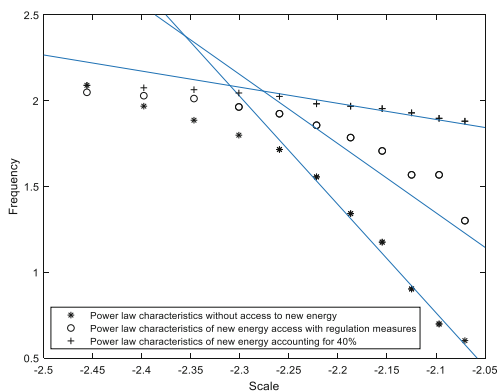
Fig. 15. Comparison of power-law characteristics with and without regulation measures when new energy accounts for 40%

whether there are regulation measures after 20% and 40% new energy are connected. It can be seen from Fig. 2 that after the regulation measures are introduced, the slope of the power-law curve of load loss is smaller than that when the regulation measures are not introduced, which also directly reflects that the addition of regulation measures has a positive impact on the stability of the power grid.

5 Load Loss Forecast of National Power Grid

It is concluded from 3.1 that the load loss when the system is not connected to new energy is similar to that in China in the past 20 years. Therefore, this paper uses the simulation data of SG126 node after connecting to new energy to approximately simulate the load loss data of the actual power grid after connecting to the same proportion of new energy, and forecasts the load loss of China's power grid in the future based on the above research. According to the SG126 power failure accident model, the relative value of power failure

accident loss load when the proportion of new energy is 10%, 20%, 30% and 40% is counted, and the over threshold model is established to fit the tail data. Under the four confidence intervals of 0.9, 0.95, 0.975 and 0.99, VaR and CVaR risk evaluation indexes are used to evaluate the risk extreme value of power failure accident under extreme events. The specific evaluation results are shown in Table 1 below:

Table 1. VaR and CVaR risk assessment under different proportion of new energy access

Proportion of new energy	Threshold	β	ξ	Evaluation method	P = 0.9	P = 0.95	P = 0.975	P = 0.99
10%	0.00459	0.0022	−0.1750	VaR	0.0042	0.0052	0.0061	0.0071
				CVaR	0.0064	0.0069	0.0076	0.0084
20%	0.00565	0.0024	−0.2112	VaR	0.0044	0.0053	0.0061	0.0070
				CVaR	0.0072	0.0074	0.0080	0.0089
30%	0.00819	0.0027	−0.2790	VaR	0.0046	0.0056	0.0063	0.0071
				VaR	0.0087	0.0089	0.0093	0.0096
40%	0.00966	0.0054	−0.2451	VaR	0.0095	0.0115	0.0131	0.0149
				VaR	0.0140	0.0151	0.0161	0.0180

It can be seen from the evaluation results in Table 1 that under the same confidence level, with the increase of the proportion of new energy access, the relative value of load loss risk of power failure accident also further increases, which indirectly reflects the increase of the proportion of new energy and the increase of instability and vulnerability to the power grid. Four different confidence levels reflect the accident risk under different probabilities, taking the proportion of new energy access as 10%, When the confidence is 0.9, there is a 10% probability that the relative value of the lost load will exceed 0.0042 in the future, and the average loss after exceeding 0.0042 is 0.0064. When the confidence is 0.99, there is a 1% probability that the relative value of the lost load in the future will exceed 0.0071, and the average relative value of the lost load after exceeding 0.0084.

This paper adopts the method of taking the relative value of the power grid loss load by using the total installed capacity of the power grid mentioned in document [30], and reversely calculates the relative value data obtained in Table 1 to obtain the predicted value of the absolute value of the power grid outage loss load in the next 3, 5 and 8 years. Considering that the transmission channels with large units and large capacity will gradually increase in the future, the installed capacity will also increase in the future, Therefore, before converting the predicted relative value into absolute value, first make a reasonable assumption that the future installed capacity will increase by 9.5% according to the development trend of China's power grid installed capacity in Sect. 1.1 of this paper, so as to reduce the prediction error as much as possible. The specific results are shown in Table 2 and Fig. 16:

From the prediction results in Table 2, in the same year, the increase of the proportion of new energy will lead to the increase of system loss load, which is closely related to

Table 2. Forecast results of national loss load in the next 3, 5 and 8 years

Particular year	Confidence interval	10%		20%		30%		40%	
		VaR	CVaR	VaR	CVaR	VaR	CVaR	VaR	CVaR
2025	P = 0.9	1340	2042	1404	2297	1468	2776	3031	4466
	P = 0.95	1659	2201	1691	2361	1787	2839	3669	4817
	P = 0.975	1946	2425	1946	2552	2010	2967	4179	5136
	P = 0.99	2265	2680	2233	2839	2265	3063	4753	5742
2027	P = 0.9	1607	2448	1683	2754	1760	3328	3634	5355
	P = 0.95	1989	2639	2027	2831	2142	3404	4399	5776
	P = 0.975	2333	2907	2333	3060	2410	3557	5011	6159
	P = 0.99	2716	3213	2678	3404	2716	3672	5700	6885
2030	P = 0.9	2109	3214	2210	3616	2310	4369	4771	7031
	P = 0.95	2612	3465	2662	3716	2812	4470	5776	7584
	P = 0.975	3064	3817	3064	4018	3164	4671	6579	8086
	P = 0.99	3566	4219	3516	4470	3566	4821	7483	9040
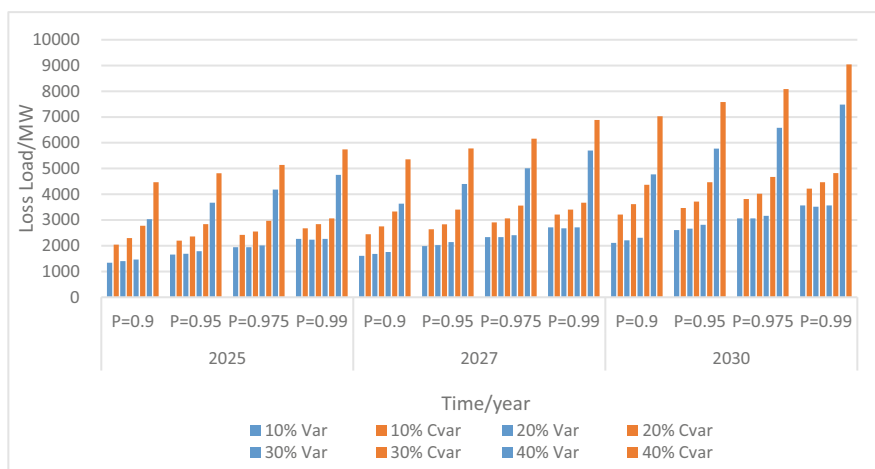
Fig. 16. Forecast results of national loss load in the next 3, 5 and 8 years

the uncertainty and volatility of wind power and photovoltaic power generation. When the proportion of new energy exceeds 40%, the increase of system loss load is obvious. At this time, the impact of new energy on power supply will become the main problem faced by the power system. Under the same confidence, the loss load also shows an increasing trend with the increase of years, which is mainly caused by the continuous expansion of installed capacity.

6 Summary

In order to better achieve China's "double carbon" goal, the low-carbon development of the power industry is imperative. Vigorously develop new energy, gradually withdraw traditional energy on the basis of new energy security and reliability, build a new power system and promote the transformation of clean energy is the only way to achieve carbon peak and carbon neutralization. Starting from the development status of China's power system, this paper analyzes the current new energy power generation and installed capacity ratio. The evolution model of blackout accident after the addition of new energy is established, and then three risk scenarios are proposed. The impact of the uncertainty and fluctuation of new energy output on the safe and stable operation of power system is obtained, and the risks and challenges faced after the access of new energy are revealed. In the future, it is necessary to further study the coordinated evolution path between the withdrawal of traditional energy and the development of clean energy, as well as the integration with energy meteorology and extreme weather new energy power generation early warning.

References

1. Guotao, Z., Guoming, Q., Sheng, W.: Path analysis of low carbon development of green power under the goal of "double carbon." Huadian Technol. **43**(6), 11–20 (2021)
2. Chu, S., Majumdar, A.: Opportunities and challenges for a sustainable energy future. Nature **488**, 294–303 (2012)
3. Salvia, M., Reckien, D., Pietrapertosa, F., et al.: Will climate mitigation ambitions lead to carbon neutrality? An analysis of the local-level plans of 327 cities in the EU. Renew. Sustain. Energy Rev. **135**(1), 110253 (2021)
4. Steadman, E.N., Anagnost, K.K., Botnen, B.W., et al.: The plains CO2 reduction (PCOR) partnership: developing carbon management options for the central interior of North America. Energy Procedia **4**, 6061–6068 (2011)
5. State Grid Energy Research Institute Co., Ltd., China energy and power development outlook: M, p. 2020. China Power Press, Beijing (2020)
6. Government, H.: The Energy White Paper: Powering our Net Zero Future. 2020
7. Peng, L., Rui, W., Haoran, J., et al.: Research and Prospect of low-carbon intelligent distribution network planning. Autom. Electr. Power Syst. **45**(24), 10–21 (2021)
8. Xiaoxin, Z.: Development trend of China's new generation power system technology in energy transformation. Electr. Age **1**, 33–35 (2018)
9. Dos Reis, F.B., Tonkoski, R., Hansen, T.M.: Synthetic residential load models for smart city energy management simulations. Iet Smart Grid **3**(3), 342–354 (2020)
10. Sanli, Z., Jiping, L., Jialin, L., Jinjin, G.: Capacity allocation method of wind farm phase change energy storage expansion power generation system. Autom. Electr. Power Syst. **43**(06), 57–63 (2019)

11. Wenhua, Z.: Research on High Proportion Renewable Energy Power Planning for System Flexibility. North China Electric Power University, Beijing (2021)
12. Editorial board of China Power Yearbook China Power statistics yearbook. China Electric Power Press, Beijing (2020)
13. Weisheng, W.: Challenges and reflections on new energy consumption in China. Power Equipment Manage. 1, 22–23 (2021)
14. National Development and Reform Commission, national energy administration The 13th five year plan for energy development two thousand and sixteen
15. Chengshan, W., Haifeng, Z., Yinghua, X., et al.: Stochastic power flow calculation of distribution system considering distributed generation. Autom. Electr. Power Syst. 24, 39–44 (2005)
16. Qun, Y., Yuqing, Q., Liang, S.: Autocorrelation analysis of power grid outage based on relative value method and Hurst index. Autom. Electr. Power Syst. 42(01), 55–60+124 (2018)
17. Xiaohai, P., Shuang, L., Mingyang, Z.: Research on risk challenges and countermeasures for safe and stable operation of power system under the background of carbon peaking and carbon neutralization. China Eng. Consult. 08, 37–42 (2021)
18. Yaling, W., Shan, J., Xianhua, W., et al.: Study on typhoon disaster loss distribution and financial countermeasures in guangdong province based on extreme value theory. Disaster Sci. 32(01), 126–131+220 (2017)
19. Jingga, E., Novita, M., Nurrohmah, S.: Optimal reinsurance contracts under the reinsurer's risk constraint with VaR risk measures. J. Phys. Conf. Ser. 1218(1), 012023 (2019)
20. Mingjing, L., Yanjun, F.: Research on supply chain financial credit risk based on big data – taking small and medium-sized e-commerce enterprises as an example. Mod. Finance 03, 17–23 (2022)
21. Liang, L.: RMB Exchange Rate Risk Measurement Based on Extreme Value Theory. Jiangxi University of Finance and Economics, Nanchang (2017)
22. Min, X., Xintong, H., Shaojia, K., et al.: Dynamic risk VaR evaluation method of power producer's operating profit and loss based on vine copula. Autom. Electr. Power Syst. 43(05), 39–45+52 (2019)
23. Tyrrell Rockafellar, R., Stanisav Uryasev.: Conditional value-at risk for general loss distributions. J. Bank. Finance 26, 1443–1471 (2002)
24. Jiekang, W., Zhijiang, W., Fan, W., et al.: CVaR risk-based optimization frame work for renewable energy management in distribution systems with DGs and EVs. Energy 143, 323–336 (2018)
25. Jinquan, Z., Jianjun, T., Di, W., et al.: Emergency coordinated control strategy for transient voltage and frequency stability of DC feed in receiving power grid. Autom. Electr. Power Syst. 44(22), 45–53 (2020)
26. Xianhui, F.: Research on power grid stability coordination and control technology after new energy access. Power Equipment Manage. 12, 122–123 (2020)
27. Yao, L., Jianfu, C., Xiaochao, H., et al.: Dynamic frequency stability control strategy of microgrid based on adaptive virtual inertia. Autom. Electr. Power Syst. 42(09), 75–82+140 (2018)
28. Qirui, W., Fengxia, S.: Analysis on influence of grid power quality on grid connection of new energy generation. Power Equipment Manage. 1, 132–133+170 (2021)
29. Li, H., Qiang, L., Chao, T., et al.: AGC scheme optimization and engineering application of Southwest Power Grid in asynchronous interconnection mode. Autom. Electr. Power Syst. 45(04), 155–163 (2021)
30. Liang, S.: Research on Power Grid Risk Classification and Early Warning Technology Based on Generalized Extreme Value Theory. Shandong University of Science and Technology, Qingdao (2016)

A Fault Ranging Method Applicable for the Four-Terminal Lines

Hong Yu[1,2(✉)], Liangkai Sun[1], Tonghua Wu[1], Xiaohong Wang[1], Pingyi Yang[1], and Yuan Jiang[1]

[1] NARI Group Corporation, Nanjing 211106, Jiangsu, China
yuhong@sgepri.sgcc.com.cn

[2] State Key Laboratory of Smart Grid Protection and Control, Nanjing 211106, Jiangsu, China

Abstract. With the rapid development of new energy resources and the economic consideration for the construction of the grid, the four-terminal and above lines are being used more and more, but subject to technical and other conditions, the fault ranging of the current multi-terminal line is mostly single-terminal ranging achieved by distance protection, which has large errors when a single-phase ground fault occurs via transition resistance. In this paper, a double-terminal data ranging method is introduced for multi-terminal line faults based on the combined sequence component. First, the fault section selection is performed by the combined sequence component bucking voltage algorithm. Then the fault ranging is performed based on the fault section selection results with the analog information collected at the first end of the faulty branch and the virtual analog information at the nearest T-point of the branch. After theoretical analysis and RTDS simulation experiments, it is verified that the above fault ranging methods can accurately range the multi-terminal line faults under various conditions of line faults.

Keywords: Multi-terminal Lines · Fault Ranging · Fault Section Selection · Fault Sequence Components

1 Introduction

With a large number of new energy sources such as wind power and photovoltaics connected to the grid, four-terminal and above lines are increasingly applied in high-voltage grids based on considerations such as saving equipment investment, reducing land acquisition area and improving the efficiency of circuit usage [1–4]. Transmission lines are the most fault-prone parts of the power system. After a fault occurs to a line, a rapid and accurate determination of the fault point is of great importance for timely troubleshooting to restore the power supply. The existing fault location methods for transmission lines are mainly for single-terminal, two-terminal or three-terminal lines [5–10]. Less research has been conducted on four-terminal and multi-terminal lines with more complex structures. Therefore, it is of great significance for studying accurate and fast fault ranging methods for multi-terminal transmission lines.

For the line fault ranging algorithms, currently, the traveling wave method and impedance method are widely used. However, the traveling wave method is susceptible to interference of catadioptric wave, or relies on high-precision clock when detecting the traveling waves, with more difficulties in engineering. The conventional impedance ranging algorithm in multi-terminal lines is susceptible to the impact of transition resistances and out-flowing currents, resulting in large ranging errors. With the widespread application of fiber optic channels and longitudinal differential protection in the construction of grids, multi-terminal lines can be used for fast and accurate ranging of multi-terminal lines by using the voltage and current at each terminal and calculating the bucking voltage at each T-junction with the combined sequence component for fault section selection, and then range the data from both terminals of the faulty branch after section selection [11, 12].

2 Problems in Conventional Fault Ranging Methods and Four-Terminal Lines

The traveling wave method uses the traveling wave information after the fault for ranging, and is divided into single-terminal ranging and double-terminal ranging methods [13–16].

1) Traveling wave method
The single-terminal traveling wave ranging method uses the data obtained from one side of the line for ranging, the principle of which is shown in Fig. 1:
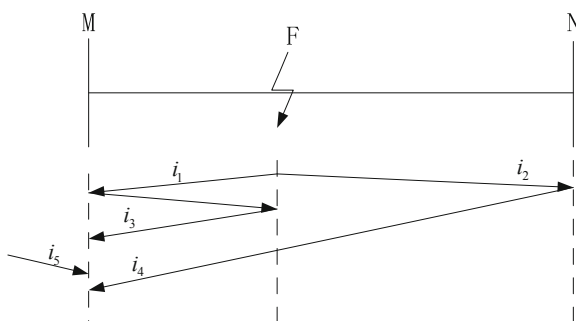
Fig. 1. Schematic Diagram for Single-terminal Traveling Wave Ranging Principle

The ranging formula is:

$$D_{MF} = \frac{1}{2}v_1\Delta t \tag{1}$$

where v_1 is the line-mode wave velocity, and Δt is the time difference between the initial traveling wave at the fault point felt at the measuring terminal M and the reflected wave after it reaches the fault point. If the location of the fault point is close to the N side, the reflected wave first detected on the M side will turn to i_4, at which point the calculation

formula is different. If there is still a line behind the M side, it will also be disturbed by the reflected waves i_5 behind it, which will affect the ranging results. The key to the single-terminal method in ranging is the accurate detection of the reflected wave head at the fault point.

The double-terminal ranging method uses the time difference between the arrivals of the first fault traveling wave at both terminals for ranging, with its ranging formula as:

$$D_{MF} = \frac{1}{2}[L + v_1(t_{M1} - t_{N1})]$$ (2)

The double-terminal ranging method can complete the ranging by just identifying the exact time when the initial traveling wave reaches both terminals of the line at the fault point, without identifying the reflected wave, with higher ranging reliability, so it has been more widely used. The double-terminal ranging requires synchronization of the clocks of the ranging equipment on both sides of the line, which also requires high accuracy of the timing clocks. The uncertainty of traveling wave velocity also affects the ranging results. The traveling wave velocity will be calibrated automatically, as proposed in this paper, which can reduce the influence of traveling wave velocity on fault ranging.

Suppose the traveling wave ranging algorithm is used in a four-terminal line. In that case, it is difficult to apply the ranging method based on the detection of traveling wave information in a multi-terminal transmission line considering its more branches, more complex refraction and reflection of traveling waves at multiple T-nodes, and more disturbances in detecting traveling waves.

2) Impedance Method
The impedance method is also divided into single-terminal ranging and double-terminal ranging, and the single-terminal ranging formula is:

$$Z_M = \frac{U_M}{I_M} = ZL_{MF} + \frac{I_F}{I_M}R_F$$ (3)

where U_M is the voltage on the M side, I_M is the current on the M side, Z is the impedance per unit length of the line, L_{MF} is the distance from the M side to the fault point, I_F is the short-line current at the fault point, and R_F is the transition resistance at the fault point. It can be seen that when there is a short circuit with transition resistance, it can result in large errors in single-terminal ranging.

The double-terminal ranging is calculated using data from both sides of the line.

$$\begin{aligned} U_M &= I_M ZL_{MF} + I_F R_F \\ U_N &= I_N Z(L - L_{MF}) + I_F R_F \end{aligned}$$ (4)

The effect of the transition resistance R_F can be eliminated by subtracting the two formulas, and then the following results can be obtained:

$$L_{MF} = \frac{U_M - U_N + I_N ZL}{(I_M + I_N)Z}$$ (5)

where U_M and U_N are the voltage on the M side and N side, respectively, I_M and I_N are the current on the M side and N side, Z is the impedance per unit length of the line, L_{MF}

is the distance from the M side to the fault point, and R_F is the transition resistance at the fault point.

In four-terminal lines, if the single-terminal fault ranging algorithm is used, at most, only one terminal of the line can be accurately ranged for metallic faults, and other ends cannot be accurately ranged due to the existence of branches; for high-resistance grounding faults, the single-terminal ranging algorithm is not applicable. Also, due to the presence of branches, the conventional double-terminal ranging method, which directly uses analog data from both ends of the line, cannot be directly applied to multi-terminal lines.

3 Implementation Methods for the Ranging of Four-Terminal Line Faults

3.1 Introduction to the Typical Four-Terminal Transmission System

A typical four-terminal transmission system is shown in Fig. 2, where M, P, Q, and N can be either power system or load, and there are two intersections in the line, defined as T_1 and T_2, respectively. Referring to the definition of a three-terminal transmission line, the section from the four endpoints to their nearest T points is defined as a section of the line area, with the branch M-T_1 as Section 1, the branch P-T_1 as Section 2, the branch N-T_2 as Section 3, the branch Q-T_2 as Section 4, and the branch T_1-T_2 as Section 5.
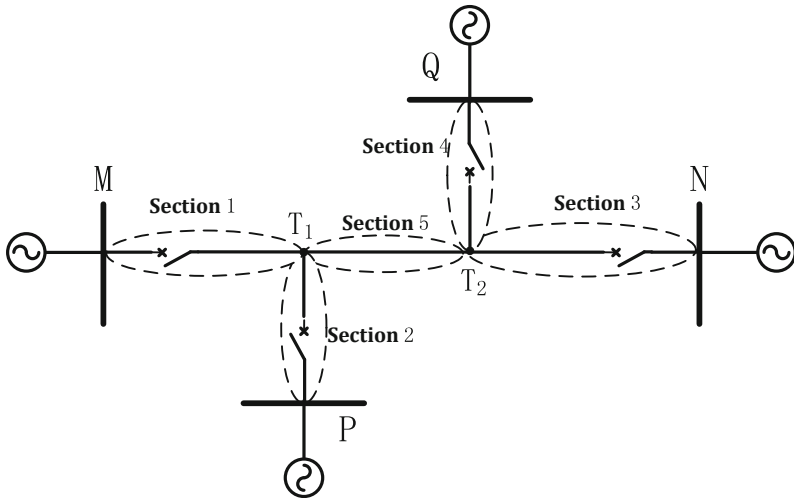
Fig. 2. Typical Four-terminal line Transmission System

3.2 Setting of Line Parameters

The conventional line protections are installed near the switch at M, P, Q and N terminal, to collect the three-phase voltage $\dot{U}_a$, $\dot{U}_b$, $\dot{U}_c$ and three-phase current $\dot{I}_a$, $\dot{I}_b$, $\dot{I}_c$ respectively. Each line protection sets the value of the positive-sequence impedance Z_{1_n} and

zero-sequence impedance Z_{0_n} and the section line length L_n according to the line from the relay location to the nearest T node (where n = 1, 2, 3, 4, indicating the number of each section/branch). Based on the above system parameters, the Relay Protection Device at each terminal can complete the metallic fault ranging in each area by the single-terminal impedance ranging principle, but all parameters of Section 5 are unknown, so the conventional single-terminal and double-terminal impedance ranging algorithms are unable to complete the fault ranging in Section 5.

3.3   Methods for Obtaining the Parameters of Section 5

Limited by the insulation layer of the transmission cables, the general T-connection transmission line method is applied on the overhead line. For the four-terminal transmission system shown in Fig. 2, it is assumed that Section 1 and Section 5 have the same line parameters per kilometer (overhead lines or cables). In this paper, the four-terminal line differential protection adopts the approach of "one master and multiple slaves", that is, the four-terminal line takes one terminal as the host, the other three terminals as the slaves, and the analog, switching value, and line parameter information of the slave are gathered to the host, which will trip the slaves jointly upon the completion of the fault discrimination, and send the fault ranging information to the slaves.

When the multi-terminal differential protection system adopts the approach of "one master and multiple slaves", the terminal with the largest identification code among the four-terminal line protections is selected as the host (e.g. Section 1 above serves as the host). For the problem that the line parameters of Section 5 cannot be obtained directly, a method for automatically calculating the line parameters of Section 5 at the host is proposed below. When the longitudinal fiber channels of the four-terminal are normal and each end relay is in normal operation, the load current $\dot{I}_{1\_t1} = \dot{I}_{1\_1} + \dot{I}_{1\_2}$ at point T_1 is calculated ($\dot{I}_{1\_1}$ and $\dot{I}_{1\_2}$ are the positive-sequence currents at the installation point of the relay in Section 1 and Section 1, respectively), and when the load current is greater than 0.1 In (0.1 times the rated current), the virtual bucking voltage of the system at each terminal is calculated, as shown in Fig. 1, with branch M–T_1 as Section 1, branch N-T_2 as Section 3, branch Q-T_2 as Section 4, and branch T_1-T_2 as Section 5. The virtual bucking voltage converted to point T at each relay installation point of the branch is:

$$\dot{U}_{1\_t\_n} = \dot{U}_{1\_n} - \dot{I}_{1\_n}Z_{1\_n} \tag{6}$$

Calculate $|\dot{U}_{1\_t\_1} - \dot{U}_{1\_t\_2}|$, $|\dot{U}_{1\_t\_1} - \dot{U}_{1\_t\_3}|$ and $|\dot{U}_{1\_t\_1} - \dot{U}_{1\_t\_4}|$ respectively to obtain the smallest of the three values and identify the section sharing T_1 point (for example, $|\dot{U}_{1\_t\_1} - \dot{U}_{1\_t\_2}|$ is the smallest of the three values, then Section 2 and Section 1 share T_1 point); the section where the other two-terminal system is located shares T_2 point. (Where n = 1, 2, 3, 4, 5, indicating the number of each section/branch respectively), $\dot{U}_{1\_t\_n}$ is the positive-sequence virtual bucking voltage of branch n converted to the T-point, $\dot{U}_{1\_n}$ is the positive-sequence voltage at the relay installation point of branch n, and $\dot{I}_{1\_n}$ is the positive-sequence current at the relay installation point of branch n.

Continue to calculate the current $\dot{I}_{1\_t1} = \dot{I}_{1\_1} + \dot{I}_{1\_2}$ at the T_1 point; the current $\dot{I}_{1\_t2} = \dot{I}_{1\_3} + \dot{I}_{1\_4}$ at T_2 point.

Calculate the ratio $k_{T1-T2} = \frac{|\dot{U}_{1\_t\_1} - \dot{U}_{1\_t\_3}|}{|\dot{I}_{1\_t1}| \cdot |Z_{1\_1}|}$ of positive-sequence impedance of Section 5 line T1-T2 to Section 1.

3.4 Fault Location

The fault location of the four-terminal lines can be divided into two steps. The first step is the initial location, using the intersection of T_1 and T_2 shown in Fig. 2 as the dividing point to divide the line into left, middle and right sections, with Section 1 and Section 2 as the left section, Section 5 as the middle section, and Section 3 and Section 4 as the right section. The second step is the detailed location. If the fault is located in the left section or right section, the fault point shall be further located based on the virtual voltage at points T_1 and T_2. The detailed fault location process is as follows:

After the line relay trips, the fault area is located, and the virtual bucking voltage at the intersection of points T_1 and T_2 is recalculated with the fault's positive-sequence, negative-sequence, and zero-sequence networks when there is an internal fault.

$$\dot{U}_{\varphi\_t\_n} = \dot{U}_{\varphi\_n} - ((\dot{I}_{\varphi\_n} - \dot{I}_{0\_n})Z_{1\_n} + \dot{I}_{0\_n}Z_{0\_n}) \tag{7}$$

(Where n = 1, 2, 3, 4, indicating the number of each section, φ = a, b, c corresponding to phase A, phase B and phase C of the line. For example, $\dot{U}_{a\_1}$ indicates the phase-A voltage at the relay installation point in Section 1; $\dot{I}_{a\_1}$ indicates the phase-A current at the relay installation point in Section 1), $\dot{I}_{a\_1}$ is the virtual bucking voltage of each phase converted to point T in Section n, $\dot{U}_{\varphi\_n}$ is the voltage of each phase at the relay installation point in section n; $\dot{I}_{\varphi\_n}$ is the current of each phase at the relay installation point in section n, and $\dot{I}_{0\_n}$ is the calculated zero-sequence current at the relay installation point in section n.

The method to locate the fault preliminarily: Determine the phase of φ according to the line protection trip phase. Determine $|\dot{U}_{\varphi\_t\_1} - \dot{U}_{\varphi\_t\_2}| < U_{set}$ and $|\dot{U}_{\varphi\_t\_3} - \dot{U}_{\varphi\_t\_4}| < U_{set}$, , respectively ($U_{set}$ can be 0.05 * U_N, that is, 0.05 times the rated voltage), if the above two conditions are met, the fault is located in the line T_1-T_2, that is, the fault within the Section 5; if only one of the above two conditions is not met, then the fault is located in the corresponding two branches. For example, in case of $|\dot{U}_{\varphi\_t\_1} - \dot{U}_{\varphi\_t\_2}| \geq U_{set}$, then the fault point is located in Section 1 or Section 2; in case of $|\dot{U}_{\varphi\_t\_3} - \dot{U}_{\varphi\_t\_4}| \geq U_{set}$, then the fault point is located in Section 3 or Section 4; if the above two conditions are not met, then the fault is located within the larger value of $|\dot{U}_{\varphi\_t\_1} - \dot{U}_{\varphi\_t\_2}|$ and $|\dot{U}_{\varphi\_t\_3} - \dot{U}_{\varphi\_t\_4}|$. For example, if $|\dot{U}_{\varphi\_t\_1} - \dot{U}_{\varphi\_t\_2}| > |\dot{U}_{\varphi\_t\_3} - \dot{U}_{\varphi\_t\_4}|$, then the fault point is located in Section 1 or Section 2; if $|\dot{U}_{\varphi\_t\_1} - \dot{U}_{\varphi\_t\_2}| < |\dot{U}_{\varphi\_t\_3} - \dot{U}_{\varphi\_t\_4}|$, then the fault point is positioned in Section 3 or Section 4.

The method to locate the fault in detail: If the fault is located in Section 1 or Section 2. The virtual bucking voltage $\dot{U}_{\varphi\_t\_js}$ at point T1 is first calculated using the virtual bucking voltage at point T2. $\dot{U}_{\varphi\_t\_js} = \dot{U}_{\varphi\_t\_3} - ((\dot{I}_{\varphi\_t2} - \dot{I}_{0\_t2})k_{T1-T2}Z_{1\_1} + \dot{I}_{0\_t2}k_{T1-T2}Z_{0\_1})$, where $\dot{I}_{\varphi\_t2}$ is the fault phase current at point T2, $\dot{I}_{\varphi\_t2} = \dot{I}_{\varphi\_3} + \dot{I}_{\varphi\_4}$ ($\dot{I}_{\varphi\_n}$ is the fault phase current measured at the relay installation point in Section n); $\dot{I}_{0\_t2}$ is the zero-sequence current $\dot{I}_{0\_t2} = \dot{I}_{0\_3} + \dot{I}_{0\_4}$ at point T2; Z_{1_1} and Z_{0_1} are the same as Z_{1_n} and Z_{0_n} above. Compare the value of $|\dot{U}_{\varphi\_t\_1} - \dot{U}_{\varphi\_t\_js}|$ and $|\dot{U}_{\varphi\_t\_2} - \dot{U}_{\varphi\_t\_js}|$, if $|\dot{U}_{\varphi\_t\_1} - \dot{U}_{\varphi\_t\_js}| > |\dot{U}_{\varphi\_t\_2} - \dot{U}_{\varphi\_t\_js}|$, the fault point is located in Section 1; if $|\dot{U}_{\varphi\_t\_1} - \dot{U}_{\varphi\_t\_js}| < |\dot{U}_{\varphi\_t\_2} - \dot{U}_{\varphi\_t\_js}|$, the fault point is located in Section 2.

If the fault is located in Section 5, $\dot{I}_{\varphi\_t1} = \dot{I}_{\varphi\_1} + \dot{I}_{\varphi\_2}$ and $\dot{I}_{\varphi\_t2} = \dot{I}_{\varphi\_1} + \dot{I}_{\varphi\_2}$ shall be used directly for double-terminal ranging.

3.5 Selection of the Double-Terminal Ranging Fault Quantity

The basic principle of double-terminal ranging requires selecting a section of line without branches and obtaining the current vectors synchronized at both terminals of the section [17–20]. After determining the exact fault section according to the method in the previous subsection, the synchronous current vectors at both terminals of the line are obtained using this line section as the study object.

If the fault point is located in Section 1, the fault current selected by double-terminal ranging is the current $\dot{I}_{\varphi\_1}$ at the relay installation point in branch 1 and the calculated current $\dot{I}_{\varphi\_t1}$, $\dot{I}_{\varphi\_t1} = \dot{I}_{\varphi\_2} + \dot{I}_{\varphi\_3} + \dot{I}_{\varphi\_4}$ at point T_1; if the fault point is located in Section 2, the fault current selected by double-terminal ranging is the current $\dot{I}_{\varphi\_2}$ at the relay installation point in branch 2 and the calculated current $\dot{I}_{\varphi\_t1}$, $\dot{I}_{\varphi\_t1} = \dot{I}_{\varphi\_1} + \dot{I}_{\varphi\_3} + \dot{I}_{\varphi\_4}$ at point T_1; if the fault point is located in Section 3, the fault current selected by double-terminal ranging is the current $\dot{I}_{\varphi\_3}$ at the relay installation point in branch 3 and the calculated current $\dot{I}_{\varphi\_t2}$, $\dot{I}_{\varphi\_t2} = \dot{I}_{\varphi\_1} + \dot{I}_{\varphi\_2} + \dot{I}_{\varphi\_4}$ at point T_2; if the fault point is located in Section 4, the fault current selected by double-terminal ranging is the current $\dot{I}_{\varphi\_4}$ at the relay installation point in branch 4 and the calculated current $\dot{I}_{\varphi\_t2}$, $\dot{I}_{\varphi\_t2} = \dot{I}_{\varphi\_1} + \dot{I}_{\varphi\_2} + \dot{I}_{\varphi\_3}$ at point T_2; if the fault point is located in Section 5, the incoming line of $\dot{I}_{\varphi\_t1} = \dot{I}_{\varphi\_1} + \dot{I}_{\varphi\_2}$ and $\dot{I}_{\varphi\_t2} = \dot{I}_{\varphi\_1} + \dot{I}_{\varphi\_2}$ is used for double-terminal ranging.

The double-terminal ranging algorithm is implemented in the four-terminal longitudinal differential protection system by virtue of the above methods.

Taking the fault of branch M-T_1 in Section 1 as an example, the double-terminal ranging method used in this paper is:

$$k = \frac{\dot{I}_{2\_t1}Z_{2\_1} + \dot{U}_{2\_t\_js} - \dot{U}_{2\_1}}{(\dot{I}_{2\_1} + \dot{I}_{2\_t1})Z_{2\_1}} \tag{8}$$

$$k = \frac{\dot{I}_{1\_t1}Z_{1\_1} + \dot{U}_{1\_t\_js} - \dot{U}_{1\_1}}{(\dot{I}_{1\_1} + \dot{I}_{1\_t1})Z_{1\_1}} \tag{9}$$

where $\dot{U}_{2\_t\_js}$ and $\dot{U}_{2\_1}$ are the negative-sequence voltage at the relay installation points on point T and branch 1 of the line, respectively; $\dot{U}_{1\_t\_js}$, $\dot{U}_{1\_1}$ is the positive-sequence voltage at the relay installation points on point T and branch 1 of the line, respectively; $\dot{I}_{2\_t1}$, $\dot{I}_{2\_1}$ is the negative-sequence current at the relay installation points on point T_1 and branch 1 of the line, respectively; $\dot{I}_{1\_t1}$, $\dot{I}_{1\_1}$ is the negative-sequence current at the relay installation points on point T_1 and branch 1 of the line, respectively; Z_{2_1}, Z_{1_1}, $Z_{2\_1} = Z_{1\_1}$ is the negative-sequence impedance and positive-sequence impedance of branch M-T in Section 1; k is the per-unit value of the fault ranging.

For asymmetric faults, the double-terminal fault ranging is completed using Formula (8), and for symmetric faults, the double-terminal fault ranging is completed using Formula (9).

4 RTDS Simulation Verification

A typical four-terminal line system model is built, as shown in Fig. 3:
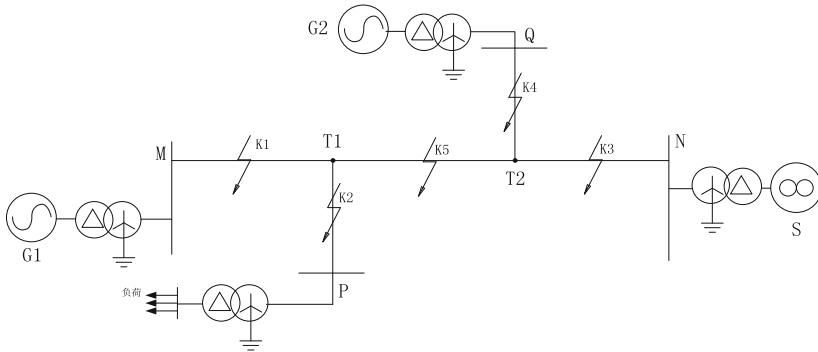
Fig. 3. A typical four-terminal line system model

MT1 is set to 50 km, PT1 is set to 25 km, T1T2 is set to 5 km, QT2 is set to 25 km, and NT2 is set to 50 km. M and Q are simulated as the power sides, P as the load side, and N as the system side (Table 1).

Table 1. The line parameters

No.	Name	Parameter
1	M-T1 Line length	50 km
2	P-T1 Line length	25 km
3	T1-T2 Line length	5 km
4	Q-T2 Line length	25 km
5	N-T2 Line length	50 km
6	Positive-sequence resistance	0.1 ohms/km
7	Positive-sequence reactance	0.4 ohms/km
8	Zero-sequence resistance	0.5 ohms/km
9	Zero-sequence reactance	1.2 ohms/km
10	PT change	110 kV/0.1 kV
11	CT on-load voltage ratio	600 A/1 A

Set up five fault points K1-K5 on the line and perform metallic and short-line fault via the transition resistance. The ranging results on the recording equipment are shown in the following tables (Tables 2 and 3):

Table 2. The ranging results of perform metallic fault

No.	Fault point	Fault phase	Section selection results	Ranging results
1	Section 1 (50 km) 5%, 2.5 km	AN	1	2.567
2		ABN	1	2.347
3		AB	1	2.504
4		ABC	1	2.498
5	Section 1 (50 km) 50%, 25 km	BN	1	24.959
6		BCN	1	25.096
7		BC	1	25.104
8		ABC	1	25.037
9	Section 1 (50 km) 95%, 47.5 km	CN	1	47.44
10		CAN	1	47.636
11		CA	1	47.671
12		ABC	1	47.549
13	Point T1	AN	5	0
14		ABN	5	0
15		AB	5	0
16		ABC	5	0
17	Section 2 (25 km) 5%, 1.25 km	AN	2	1.22
18		ABN	2	1.12
19		AB	2	1.3
20		ABC	2	1.13
21	Section 2 (25 km) 50%, 12.5km	BN	2	12.64
22		BCN	2	12.23
23		BC	2	12.25
24		ABC	2	12.41
25	Section 2 (25 km) 95%, 23.75km	CN	2	23.82
26		CAN	2	23.61
27		CA	2	23.58
28		ABC	2	23.70
29	Section 3 (50 km) 5%,2.5 km	AN	3	2.52
30		ABN	3	2.33
31		AB	3	2.38
32		ABC	3	2.45

(*continued*)

Table 2. (*continued*)

No.	Fault point	Fault phase	Section selection results	Ranging results
33	Section 3 (50 km) 50%, 25 km	BN	3	25.02
34		BCN	3	24.98
35		BC	3	24.97
36		ABC	3	24.98
37	Section 3 (50 km) 95%, 47.5 km	CN	3	47.52
38		CAN	3	47.53
39		CA	3	47.55
40		ABC	3	47.53
41	Point T2	CN	5	5
42		CAN	5	5
43		CA	5	5
44		ABC	5	5
45	Midpoint of T1T2 At 2.5 km	CN	5	2.56
46		CAN	5	2.52
47		CA	5	2.54
48		ABC	5	2.48

Table 3. The ranging results of short-line fault via the transition resistance (10 ohms between phases, and 100 ohms for grounding)

No.	Fault point	Fault phase	Section selection results	Ranging results
1	Section 1 (50 km) 5%, 2.5 km	AN	1	2.53
2		ABN	1	2.88
3		AB	1	2.92
4		ABC	1	2.69
5	Section 1 (50 km) 50%, 25 km	BN	1	25.19
6		BCN	1	25.53
7		BC	1	25.54
8		ABC	1	25.27

Table 3. (*continued*)

No.	Fault point	Fault phase	Section selection results	Ranging results
9	Section 1 (50 km) 95%,47.5 km	CN	1	47.9
10		CAN	1	48.03
11		CA	1	48.13
12		ABC	1	47.80
13	Point T1	AN	5	0
14		ABN	5	0
15		AB	5	0
16		ABC	5	0
17	Section 2 (25 km) 5%, 1.25 km	AN	2	1.17
18		ABN	2	1.27
19		AB	2	1.39
20		ABC	2	1.22
21	Section 2 (25 km) 50%, 12.5 km	BN	2	12.58
22		BCN	2	11.96
23		BC	2	11.92
24		ABC	2	12.19
25	Section 2(25 km) 95%, 23.75 km	CN	2	23.70
26		ABN	2	23.91
27		BC	2	23.65
28		ABC	2	23.82
29	Section 3 (50 km) 5%, 2.5 km	AN	3	2.59
30		ABN	3	2.86
31		AB	3	2.84
32		ABC	3	2.70
33	Section 3 (50 km) 50%,25 km	BN	3	25.14
34		BCN	3	25.44
35		BC	3	25.52
36		ABC	3	25.23
37	Section 3 (50 km) 95%, 47.5 km	CN	3	47.78
38		CAN	3	48.00
39		CA	3	48.05
40		ABC	3	47.79

Table 3. (*continued*)

No.	Fault point	Fault phase	Section selection results	Ranging results
41	Point T2	CN	5	5
42		CAN	5	5
43		CA	5	5
44		ABC	5	5
45	Midpoint of T1T2 At 2.5 km	CN	5	2.47
46		BCN	5	2.27
47		AB	5	2.39
48		ABC	5	2.62

The above simulation results show that this ranging method can accurately distinguish the section where the fault occurs, regardless of metallic faults or grounding faults through transition resistance, and its double-terminal ranging results are not affected by the power augmentation or load draw.

5 Conclusion

The differential protection of four-terminal and above lines has been used in many scenarios. The "master" can easily obtain each terminal's voltage and current information through the optical fiber. Based on the fixed parameters of the existing line protection, by using virtual bucking voltage, the method proposed in this paper can locate the fault branch after the initial fault section selection and detailed fault section selection, and further deduce the synchronous current vector at both terminals of the fault branch, and finally realize the double-terminal ranging of the four-terminal line.

The method described in this paper has been applied to the NSR-300 series of four-terminal line differential protection devices developed by our Company, with its feasibility and accuracy verified by RTDS simulation experiments. It has passed the test and verification of the Experimental Verification Center of State Grid Electric Power Research Institute.

References

1. Huang, J., Zheng, S., Lin, X.: New principle of wind farm collecting power line protection based on multi-terminal differentials. Power Syst. Clean Energy **32**(9), 102–106 (2016)
2. Zheng, T., Zhao, Y., Li, J., et al.: A protection scheme for teed lines with wind power based on voltage magnitude difference and measuring impedance characteristics. Power Syst. Technol.·41(5), 1660–1667 (2017)
3. Xia, J., Qin, R., Qian, H., et al.: Study on improved algorithm in differential protection of multi-terminalline. Electr. Power Autom. Equip. **38**(12), 140–147 (2018)

4. Zheng, L., Jia, K., Bi, T., et al.: Cosine similarity based pilot protection of teed transmission line connected to renewable energy power plants. Autom. Electr. Power Syst. **43**(18), 111–124 (2019)
5. Wang, C., Ye, J., Chen, H., et al.: An improved method of one-terminal fault location for hybrid power cable-overhead line. Hunan Electr. Power **40**(4), 27–31 (2020)
6. Song, X., Gao, Y., Ding, G., et al.: Study on transmission line traveling wave fault location based on improved VMD participation. Electrotech. Appl. **38**(7), 26–33 (2019)
7. Ding, J., Li, L., Zheng, Y., et al.: Distributed travelling-wave-based fault location without time synchronisation and wavevelocity error. IET Gener. Transm. Distrib. **11**(8), 2085–2093 (2017)
8. Zhao, J.W., Duan, J.X.: Traveling wave fault location for lines combined with overhead-lines and cables based on empirical wavelet transform. In: 2019 IEEE 2nd International Conference on Electronics and Communication Engineering (ICECE). IEEE (2020)
9. Li, J., Wang, Y., Zhou, L., et al.: Study on fault location of transmission line based on longitudinal impedance. Electr. Eng. **12**, 67–70 (2015)
10. Wang, B., Lu, Y.: Single terminal fault location to single-line-to-ground fault in T transmission line based on sequenced time session data. In: Proceedings of the CSEE, vol. 12, pp. 67–70 (2015)
11. Hua, Y., Lu, G., Wang, W.: New algorithm for locating fault point of T-connection transmission lines. Water Resour. Power **4,28**(4), 133–134 (2010)
12. Yao, L., Chen, F.-F., Chen, Q.: An adaptive method of fault locator for T transmission line. Power Syst. Prot. Control **40**(3), 26–30 (2012)
13. Liu, X., Jiao, J., Zhou, H., et al.: Network location algorithm with the directed tree of traveling wave transmission. J. Electr. Power Sci. Technol. **31**(4), 58–64 (2016)
14. Li, Z., Fan, C., Zeng, Y., et al.: Power line fault location method with double terminal traveling waves unconsidered wave transmission speed. J. Electr. Power Sci. Technol. **31**(2), 79–83 (2016)
15. Xu, W., Jiang, D., Wang, J., et al.: Fault location method of overhead line-submarine cable mixed lines used transient traveling waves. Shandong Electr. Power **43**(229), 15–19 (2016)
16. Deng, F., Zeng, X., Ma, S., et al.: Research on wide area traveling wave fault location method based on distributed traveling wave detection. Power Syst. Technol. **41**(4), 1300–1310 (2017)
17. Livani, H., Evrenosoglu, C.Y.: A machine learning and wavelet-based fault location method for hybrid transmission lines. IEEE Trans. Smart Grid (ICICM) **5**(1), 51–59 (2014)
18. Lin, M.: A two-terminal fault location method based on asynchronous sampling. Electr. Eng. **11**, 40–43 (2019)
19. Cheng, Z., Tang, M., Li, X., et al.: Fault location method of distribution line based on two-terminal electrical power quantities. Electr. Measur. Instrum. **55**(8), 46–50 (2018)
20. Ma, W., Hou, W., Zhang, H., et al.: A new fault location scheme for T-type transmission lines. Zhejiang Electr. Power **38**(1), 76–81 (2019)

Method of Conjugate Vectors for the Analysis of Single-Phase-to-Ground-Faulted Grid

Xing Liu[✉], Jiabing Hu, Yingbiao Li, and Weizhong Wen

Huazhong University of Science and Technology, Wuhan 430074, China
lx2019@hust.edu.cn

Abstract. With the wide application of power electronic devices (PED), the characteristics of the grid fault vary greatly. The grid voltage/current exhibits the time-varying amplitude/frequency characteristics under asymmetrical fault conditions, which have brought new challenges to power system asymmetrical fault analysis. However, the method of symmetrical components based on phasors, which is a traditional method, assumes that the amplitude/frequency of the grid voltage/current remains constant and consequently does not apply to the time-varying amplitude/frequency problem. Hence, this paper proposes a method of conjugate vectors for the dynamic analysis of asymmetrical-faulted grid. The proposed method constructs a forward network, a reverse network, and an impulse network coupled at the fault point by employing rotating vectors. Taking a single-phase ground fault as an example, the dynamic analysis process is introduced. The accuracy of the analysis results is validated with simulation models. It indicates that the proposed method applies to dynamic analysis of asymmetrical-faulted grid under time-varying amplitude/frequency circumstances.

Keywords: Asymmetrical Fault Analysis · Time-varying Amplitude/frequency · Conjugate Vectors Method · Dynamic Analysis · Rotating Vectors

1 Introduction

As the proportion of PED such as voltage source converter (VSC)-based devices in the power system gradually increases, there have been many severe accidents such as doubly fed induction generator (DFIG)-based wind turbines (WT) disconnection caused by asymmetrical faults, destroying stable operation and causing serious social impacts [1–3]. Relay protection is the first line defense for the stable operation of power systems, and asymmetrical fault analysis is the basis of relay protection [4, 5]. Considering most grid faults are asymmetrical faults, it is urgent to conduct in-depth research on asymmetrical fault analysis of power system excited by PED.

Aiming at the target, some studies have been published and can be categorized into the following aspects. Firstly, the electromagnetic transient program (EMTP)-based simulations are employed to accurately reflect the complete dynamic process of the instantaneous values of electrical quantities during an asymmetrical fault [6–9]. However, the

simulations are too complicated to apply to the actual large-scale system asymmetrical fault analysis. Secondly, some studies ignore the complex characteristics of PED and equivalent them as controlled current/voltage sources with constant amplitude/frequency [10–14]. Hence, the method of symmetrical components can be applied which fails to reflect the actual dynamic process. The method of symmetrical components is applicable only if it is assumed that the amplitude/frequency of the grid voltage/current remains constant. Contrary to this assumption, the grid voltage/current presents the time-varying amplitude/frequency characteristics under the condition of asymmetrical fault in the power system dominated by PED. The reasons are as follows [15–17]: (1) Control loops with different bandwidths are cascaded with each other. The dynamic change of the output of the slower time scale control affects the input of the faster time scale control, which in turn makes the output of the faster time scale control change dynamically; (2) The power electronic device performs sequential switching of internal control and protection circuits according to the grid code requirements and transforms the reference value of the control or the control structure of software and hardware, and then affects the output of the control. (3) The control techniques have non-ideal characteristics in the transient process (such as the sequence decomposition of phase-locked loop/current controller). These factors all lead to the time-varying amplitude and frequency of the internal voltage in the PED. Therefore, the grid voltage/current cannot be described by phasors whose amplitude and frequency remain constant under asymmetrical faults. Some studies perceive the time-varying amplitude/frequency characteristics and propose a method of time-varying amplitude/frequency symmetrical components [18]. This method developed corresponding concepts such as positive sequence time-varying amplitude/frequency phasor, while how to calculate different sequence time-varying amplitude/frequency phasors and perform corresponding asymmetrical fault analysis have not been discussed yet.

Considering the internal voltage of PED is controlled mostly by employing the space vector pulse width modulation (SVPWM) technique, this paper utilizes rotating vectors to model time-varying amplitude/frequency electrical quantities. However, one vector cannot describe the three-phase quantity when ground faults occur. Hence, the main obstacle of network asymmetrical fault analysis excited by PED is how to construct a group of rotating vectors that can not only describe the characteristics of time-varying amplitude/frequency, but also have a reversible transformation relationship with three-phase electrical quantities to make calculation convenient.

The rest of this paper is organized as follows. In Sect. 2, general circuit equations in the instantaneous value are introduced. Then, the conjugate rotating vectors response principle is proposed in Sect. 3. Furthermore, the asymmetrical fault analysis process is introduced by taking a single-phase-to-ground fault as an example in Sect. 4. The accuracy of the analytical expressions is validated in Sect. 5. Finally, conclusions are drawn in Sect. 6.

2 General Circuit Equations Under Asymmetrical Faults

Before performing fault analysis, it is necessary to model the characteristic of passive components under the condition of time-varying amplitude and frequency. The original mathematical relationships of passive components are the proportional, differential,

and integral relationships of instantaneous value electrical quantities. The Heaviside's operator p [19] which donates $\frac{d}{dt}$ is exploited as the Eq. (1) shows.

$$
\begin{aligned}
u_R(t) &= Ri_R(t) \\
u_L(t) &= Lpi_L(t) \\
u_C(t) &= \frac{1}{Cp}i_C(t)
\end{aligned}
\tag{1}
$$

The expressions containing Heaviside's operator p such as Lp or $1/Cp$ are called resistance operator, which satisfy algebraic rules [20].

The studied system is shown in Fig. 1, which is a simplified generic network. $u_t(t)$ is a three-phase voltage source with arbitrary time-varying amplitude/frequency. L_s is the self-inductance of the whole transmission lines and L_m is the mutual-inductance of the whole transmission lines. Assuming the transmission lines are fully transposed and ignore the resistance, the faulted grid remains symmetrical except for the faulted branch. The point f donates the fault point and the point m donates a random point of the whole transmission line. $i_t(t)$ is the transmission line current. $u_f(t)$ is the voltage at the faulted point. $i_f(t)$ is the current in the faulted branch.

$u_t(t)$

m $i_t(t)$ f $u_f(t)$

$i_f(t)$

asymmetrical faults
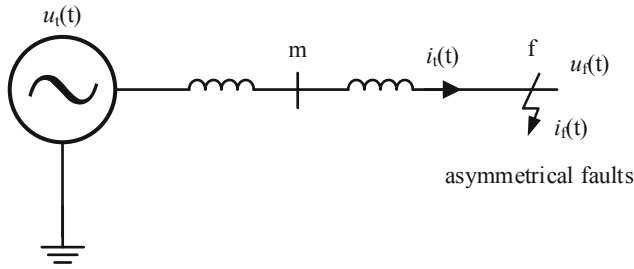
Fig. 1. A simplified generic asymmetrical-faulted network

The relationship between i_t, u_t and u_f can be written as the Eq. (2) shows.

$$
\begin{bmatrix} u_{ta} \\ u_{tb} \\ u_{tc} \end{bmatrix} - \begin{bmatrix} u_{fa} \\ u_{fb} \\ u_{fc} \end{bmatrix} = \begin{bmatrix} L_s p & L_m p & L_m p \\ L_m p & L_s p & L_m p \\ L_m p & L_m p & L_s p \end{bmatrix} \begin{bmatrix} i_{ta} \\ i_{tb} \\ i_{tc} \end{bmatrix}
\tag{2}
$$

Transforming (2) into stationary $\alpha\beta0$ coordinates by Clarke transformation yields

$$
\begin{bmatrix} u_{t\alpha} \\ u_{t\beta} \\ u_{t0} \end{bmatrix} - \begin{bmatrix} u_{f\alpha} \\ u_{f\beta} \\ u_{f0} \end{bmatrix} = \underbrace{\begin{bmatrix} (L_s - L_m)p & 0 & 0 \\ 0 & (L_s - L_m)p & 0 \\ 0 & 0 & (L_s + 2L_m)p \end{bmatrix}}_{\mathbf{A}_1(p)} \begin{bmatrix} i_{t\alpha} \\ i_{t\beta} \\ i_{t0} \end{bmatrix}
\tag{3}
$$

where the matrix $\mathbf{A}_1(p)$ represents the characteristic of the transmission lines.

The relationship between i_f and u_f can be written as the Eq. (4) shows.

$$
\begin{bmatrix} i_{f\alpha} \\ i_{f\beta} \\ i_{f0} \end{bmatrix} = \mathbf{A}_f(p) \begin{bmatrix} u_{f\alpha} \\ u_{f\beta} \\ u_{f0} \end{bmatrix}
\tag{4}
$$

where the matrix $A_f(p)$ represents the characteristics of different asymmetrical fault conditions.

Taking the A-phase-to-ground fault as an example, $A_f(p)$ can be described as

$$\mathbf{A_f}(p) = \frac{1}{R_f + L_f p} \begin{bmatrix} \frac{2}{3} & 0 & \frac{2}{3} \\ 0 & 0 & 0 \\ \frac{1}{3} & 0 & \frac{1}{3} \end{bmatrix} \tag{5}$$

where $R_f + L_f\, p$ is the grounding resistance operator.

According to Kirchhoff's current law, the relationship between i_f and i_t can be described as

$$\begin{bmatrix} i_{f\alpha} \\ i_{f\beta} \\ i_{f0} \end{bmatrix} = \begin{bmatrix} i_{t\alpha} \\ i_{t\beta} \\ i_{t0} \end{bmatrix} \tag{6}$$

i_f can be rewritten as the Eq. (7) shows by resolving (3), (4) and (6).

$$\begin{bmatrix} i_{f\alpha} \\ i_{f\beta} \\ i_{f0} \end{bmatrix} = \underbrace{\mathbf{A_f}(p)\big[\mathbf{A_f}(p)\mathbf{A_1}(p) + \mathbf{E}\big]^{-1}}_{\mathbf{A_t}(p)} \begin{bmatrix} u_{t\alpha} \\ u_{t\beta} \\ u_{t0} \end{bmatrix} \tag{7}$$

where the matrix $A_t(p)$ is a 3×3 matrix, the elements in the matrix are only related to the line parameters and faulted branch parameters.

3   Conjugate Rotating Vectors Response Principle

Before decomposing the Eq. (7) further, introduce the conjugate rotating vectors response principle.

Given a generic three-phase system with arbitrary voltage/current described by a transfer matrix in the stationary αβ0 coordinate

$$\begin{bmatrix} i_\alpha \\ i_\beta \end{bmatrix} = \begin{bmatrix} D_{11} & D_{12} \\ D_{21} & D_{22} \end{bmatrix} \begin{bmatrix} u_\alpha \\ u_\beta \end{bmatrix} \tag{8}$$

where $D_{11}, D_{12}, D_{21}, D_{22}$ can be arbitrary resistance operators.

The Eq. (8) can be expressed in terms of rotating vectors as the Eq. (9) [21, 22].

$$\mathbf{I}^{\alpha\beta} = \left(\frac{D_{11} + D_{22}}{2} + j\frac{D_{21} - D_{12}}{2} \right)\mathbf{U}^{\alpha\beta} + \left(\frac{D_{11} - D_{22}}{2} + j\frac{D_{21} + D_{12}}{2} \right)\overline{\mathbf{U}^{\alpha\beta}} \tag{9}$$

where $\mathbf{I}^{\alpha\beta} = i_\alpha + ji_\beta$, $\mathbf{U}^{\alpha\beta} = u_\alpha + ju_\beta$, $\overline{\mathbf{U}^{\alpha\beta}} = u_\alpha - ju_\beta$.

The Eq. (9) represents the conjugate rotating vectors response principle, which indicates that the forward rotating current vector response can be decomposed into the superposition of the forward rotating voltage vector and its conjugate vector, viz. Reverse rotating voltage vector exciting different resistance operators respectively.

For the Eq. (7), the elements in $\mathbf{A}_t(p)$ can be replaced by symbols as the Eq. (10) shows.

$$\begin{bmatrix} i_{f\alpha} \\ i_{f\beta} \\ i_{f0} \end{bmatrix} = \begin{bmatrix} f_{11}(p) & f_{12}(p) & f_{13}(p) \\ f_{21}(p) & f_{22}(p) & f_{23}(p) \\ f_{31}(p) & f_{32}(p) & f_{33}(p) \end{bmatrix} \begin{bmatrix} u_{t\alpha} \\ u_{t\beta} \\ u_{t0} \end{bmatrix} \qquad (10)$$

where $f_{11}(p)$, $f_{22}(p)$,...are the corresponding resistance operators in the matrix $\mathbf{A}_t(p)$.

The zero-axis component behaves as synchronous oscillations on the three-phase axes. The vector sum of the zero-axis components is $\mathbf{0}$ on the three-phase axes under all circumstances, which fails to reflect the zero-axis components in terms of the composite vector. Therefore, the zero-axis component needs to be vectorized.

If we define the complex plane consisting of the real α-axis and the imaginary β-axis as the first complex plane, then the second complex plane can be defined as the complex plane with the real α'-axis and the imaginary β'-axis, and furthermore the real α'-axis overlaps the zero-axis. Therefore, the zero-axis component can be regarded as an alternate signal whose real part is nonzero and imaginary part equals zero. Furthermore, the zero-axis component is constructed as a vector, which is called the impulse rotating vector, pulsating along the real axis on the second complex plane. To distinguish the second complex plane from the first complex plane, an additional ' will be used in superscripts and subscripts. For example, the zero-axis component u_{t0} in the Eq. (10) is constructed as an impulse rotating vector $\mathbf{U}_t^{\alpha'\beta'}$ on the second complex plane which satisfies the Eq. (11).

$$\mathbf{U}_t^{\alpha'\beta'} = u_{t0\alpha'} + ju_{t0\beta'} \qquad (11)$$

where $u_{t0\alpha'} = u_{t0}$, $u_{t0\beta'} = 0$.

According to the two complex planes, the Eq. (10) can be rewritten as the Eq. (12) shows.

$$\begin{bmatrix} i_{f\alpha} \\ i_{f\beta} \\ i_{f0\beta'} \\ i_{f0\beta'} \end{bmatrix} = \begin{bmatrix} f_{11}(p) & f_{12}(p) & f_{13}(p) & 0 \\ f_{21}(p) & f_{22}(p) & f_{23}(p) & 0 \\ f_{31}(p) & f_{32}(p) & f_{33}(p) & 0 \\ 0 & 0 & 0 & 0 \end{bmatrix} \begin{bmatrix} u_{t\alpha} \\ u_{t\beta} \\ u_{t0\alpha'} \\ u_{t0\beta'} \end{bmatrix} \qquad (12)$$

where $i_{f0\alpha'} = i_{f0}$, $i_{f0\beta'} = 0$.

Applying the conjugate rotating vectors response principle to the Eq. (12), we have

$$\mathbf{I}_f^{\alpha\beta} = \left[\frac{f_{11}(p) + f_{22}(p)}{2} + j\frac{f_{21}(p) - f_{12}(p)}{2} \right] \mathbf{U}_t^{\alpha\beta}$$
$$+ \left[\frac{f_{11}(p) - f_{22}(p)}{2} + j\frac{f_{21}(p) + f_{12}(p)}{2} \right] \overline{\mathbf{U}_t^{\alpha\beta}}$$
$$+ \left[\frac{f_{13}(p) + 0}{2} + j\frac{f_{23}(p) - 0}{2} \right] \mathbf{U}_t^{\alpha'\beta'} + \left[\frac{f_{13}(p) - 0}{2} + j\frac{f_{23}(p) + 0}{2} \right] \overline{\mathbf{U}_t^{\alpha'\beta'}} \quad (13)$$

Considering $u_{t0\beta'} = 0$, $\mathbf{U}_t^{\alpha'\beta'}$ and $\overline{\mathbf{U}_t^{\alpha'\beta'}}$ both are the same impulse rotating voltage vector whose real part is $u_{t0\alpha'}$ and imaginary part equals zero. Hence, we can obtain that

$\mathbf{U}_t^{\alpha'\beta'} = \overline{\mathbf{U}_t^{\alpha'\beta'}}$. Based on this, the Eq. (13) can be simplified as

$$\mathbf{I}_f^{\alpha\beta} = \underbrace{\left[\frac{f_{11}(p) + f_{22}(p)}{2} + j\frac{f_{21}(p) - f_{12}(p)}{2}\right]}_{h_1(p)} \mathbf{U}_t^{\alpha\beta}$$

$$+ \underbrace{\left[\frac{f_{11}(p) - f_{22}(p)}{2} + j\frac{f_{21}(p) + f_{12}(p)}{2}\right]}_{h_2(p)} \overline{\mathbf{U}_t^{\alpha\beta}} + \underbrace{\left[f_{13}(p) + jf_{23}(p)\right]}_{h_3(p)} \mathbf{U}_t^{\alpha'\beta'}$$

$$= h_1(p)\mathbf{U}_t^{\alpha\beta} + h_2(p)\overline{\mathbf{U}_t^{\alpha\beta}} + h_3(p)\mathbf{U}_t^{\alpha'\beta'} \tag{14}$$

The following equation can be obtained by the same means as

$$\mathbf{I}_f^{\alpha'\beta'} = h_4(p)\mathbf{U}_t^{\alpha\beta} + h_5(p)\overline{\mathbf{U}_t^{\alpha\beta}} + h_6(p)\mathbf{U}_t^{\alpha'\beta'} \tag{15}$$

According to the Eq. (14) and the Eq. (15), the forward rotating current vector $\mathbf{I}_f^{\alpha\beta}$ consists of three parts, which is the superposition of the forward rotating voltage vector $\mathbf{U}_t^{\alpha\beta}$ exciting the forward resistance operator, the reverse rotating voltage vector $\overline{\mathbf{U}_t^{\alpha\beta}}$ exciting the reverse resistance operator, and the impulse voltage vector $\mathbf{U}_t^{\alpha'\beta'}$ exciting the impulse resistance operator; the impulse current vector $\mathbf{I}_f^{\alpha'\beta'}$ also consists of three parts, which is the superposition of $\mathbf{U}_t^{\alpha\beta}$, $\overline{\mathbf{U}_t^{\alpha\beta}}$ and $\mathbf{U}_t^{\alpha'\beta'}$ exciting the another three resistance operators.

4 Asymmetrical Fault Analysis Process

Asymmetric fault analysis usually focuses on the characteristics and distribution of three-phase electrical quantities in the power system. How to convert the current vectors shown in the Eq. (14) and (15) to the current in the three-phase coordinate is the key problem to be solved in this section.

From Sect. 2 and Sect. 3 mentioned, an arbitrary time-varying amplitude and frequency three-phase voltage source u_t can be transformed into the forward rotating voltage vector $\mathbf{U}_t^{\alpha\beta}$, the reverse rotating voltage vector $\overline{\mathbf{U}_t^{\alpha\beta}}$, and the impulse voltage vector $\mathbf{U}_t^{\alpha'\beta'}$ by the Clarke transformation and the conjugate rotating vectors response principle. The overall transformation is given by

$$\begin{bmatrix} \mathbf{U}^{\alpha\beta} \\ \overline{\mathbf{U}^{\alpha\beta}} \\ \mathbf{U}^{\alpha'\beta'} \end{bmatrix} = \frac{2}{3}\underbrace{\begin{bmatrix} 1 & e^{j2\pi/3} & e^{j4\pi/3} \\ 1 & e^{j4\pi/3} & e^{j2\pi/3} \\ \frac{1}{2} & \frac{1}{2} & \frac{1}{2} \end{bmatrix}}_{\mathbf{C}} \begin{bmatrix} u_a \\ u_b \\ u_c \end{bmatrix} \tag{16}$$

where $\mathbf{C}$ is a vectorization matrix to transform three-phase instantaneous electrical quantities into three rotating vectors, whose inverse transformation is given by

$$\mathbf{C}^{-1} = \frac{1}{2}\begin{bmatrix} 1 & 1 & 2 \\ e^{j4\pi/3} & e^{j2\pi/3} & 2 \\ e^{j2\pi/3} & e^{j4\pi/3} & 2 \end{bmatrix} \tag{17}$$

Similarly, the three-phase current i_f can be transformed into the forward rotating current vector $\mathbf{I}_f^{\alpha\beta}$, the reverse rotating current vector $\overline{\mathbf{I}_f^{\alpha\beta}}$, and the impulse current vector $\mathbf{I}_f^{\alpha'\beta'}$ by the matrix $\boldsymbol{C}$. The three current vectors can be transformed into the three-phase instantaneous current conversely by the inverse transformation $\boldsymbol{C}^{-1}$.

Hence, the transformation matrices $\boldsymbol{C}$ and $\boldsymbol{C}^{-1}$ can be regarded as a pair of linear transformations, which is a bridge between three-phase instantaneous electrical quantities and rotating vectors. From the mathematical point of view, the three-phase instantaneous electrical quantities are independent of each other under the condition of asymmetrical fault. Each phase's instantaneous value has one degree of freedom, and the three-phase instantaneous electrical quantities have a total of three degrees of freedom. After the transformation, the forward rotating vector and the reverse rotating vector coexist on the first complex plane, which have two degrees of freedom. Meanwhile, the imaginary-axis component of the impulse vector is zero and the impulse vector is independent of the above two rotating vectors, so it has one degree of freedom. Therefore the three rotating vectors get three degrees of freedom totally. The degrees of freedom remain consistent before and after transformation. The rotating vector model and the three-phase model both can be determined uniquely, and furthermore the three-phase electrical quantities and the group of rotating vectors are bijective consequently. From the physical point of view, multiply the instantaneous values of the three phases and the three symmetrical basis unit vectors at each moment, and then we can get three impulse vectors vibrating in the direction of the three symmetrical axes. Afterwards, add the three vectors and multiply by the transformation coefficient to get the forward rotating vector, which is shown in Fig. 2. The physical meaning of the reverse rotating vector and the impulse vector is similar to that of the forward rotating vector. Rotate the forward rotating vector 120° clockwise, rotate the reverse rotating vector 120° counterclockwise, and then superimpose the three vectors with a fixed transformation coefficient to obtain the instantaneous value of the B-phase electrical quantity at each moment, which is shown in Fig. 3. The physical meaning of the instantaneous value of phase A and phase C electrical quantities are similar to that of phase B.

(1)multiply instantaneous values by the basis vectors

(2)add the three vectors and multiply by the transformation coefficient
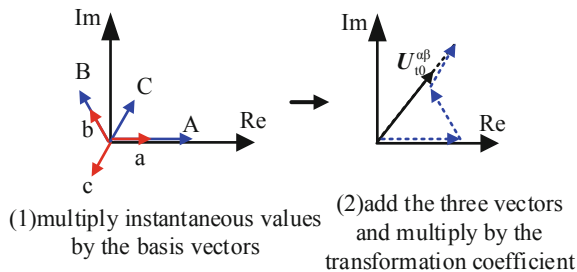
Fig. 2. The process of constructing the forward rotating vector

The three-phase voltage or the three-phase current in the asymmetric fault network can also be transformed to obtain a group of vectors consisting of a forward rotating vector, a reverse rotating vector, and an impulse vector. Thus, the Eq. (3) representing the
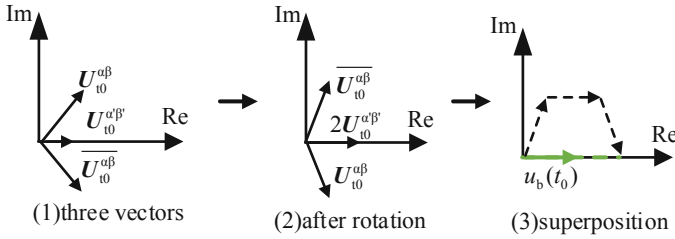
Fig. 3. The process of constructing the B-phase electrical quantity

electrical quantities relationship between the time-varying amplitude/frequency voltage source and the fault point can be converted into

$$
\begin{bmatrix} \mathbf{U}_t^{\alpha\beta} \\ \mathbf{U}_t^{\alpha\beta} \\ \mathbf{U}_t^{\alpha'\beta'} \end{bmatrix} - \begin{bmatrix} \mathbf{U}_f^{\alpha\beta} \\ \mathbf{U}_f^{\alpha\beta} \\ \mathbf{U}_f^{\alpha'\beta'} \end{bmatrix} = \begin{bmatrix} (L_s - L_m)p & 0 & 0 \\ 0 & (L_s - L_m)p & 0 \\ 0 & 0 & (L_s + 2L_m)p \end{bmatrix} \begin{bmatrix} \mathbf{I}_t^{\alpha\beta} \\ \mathbf{I}_t^{\alpha\beta} \\ \mathbf{I}_t^{\alpha'\beta'} \end{bmatrix}
\tag{18}
$$

The Eq. (18) shows that for a three-phase symmetrical transmission line, the forward rotating voltage vector difference across the line is merely related to the forward rotating current vector in the line. The relationship between the forward rotating voltage vector and the forward rotating current vector can be represented by the forward resistance operator $(L_s - L_m)p$; the reverse rotating voltage vector difference across the line is merely related to the reverse rotating current vector in the line. The relationship between the reverse rotating voltage vector and the reverse rotating current vector can be represented by the reverse resistance operator $(L_s - L_m)p$; the impulse voltage vector difference across the line is merely related to the impulse current vector in the line. The relationship between the impulse voltage vector and the impulse current vector can be represented by the impulse resistance operator $(L_s + 2L_m)p$; Therefore, the three rotating vectors are independent and decoupled respectively.

According to the Eq. (18), the network topology in Fig. 1 can be transformed into the equivalent networks with a forward network, a reverse network, and an impulse network, as shown in Fig. 4.

When the A-phase ground fault occurs, assuming the grounding resistance is R_f, the three-phase voltage and current at the faulted point satisfy the equation given by

$$
\begin{cases} u_{fa} = R_f i_{fa} \\ i_{fb} = i_{fc} = 0 \end{cases}
\tag{19}
$$

Convert it to rotating vectors then we can get

$$
\begin{cases} \mathbf{I}_f^{\alpha\beta} = \overline{\mathbf{I}_f^{\alpha\beta}} = 2\mathbf{I}_f^{\alpha'\beta'} \\ \mathbf{U}_f^{\alpha\beta} + \overline{\mathbf{U}_f^{\alpha\beta}} + 2\mathbf{U}_f^{\alpha'\beta'} = 3R_f\mathbf{I}_f^{\alpha\beta} \end{cases}
\tag{20}
$$

According to the Eq. (20), a composite network can be obtained by connecting the faulted ports in Fig. 4, as shown in Fig. 5.
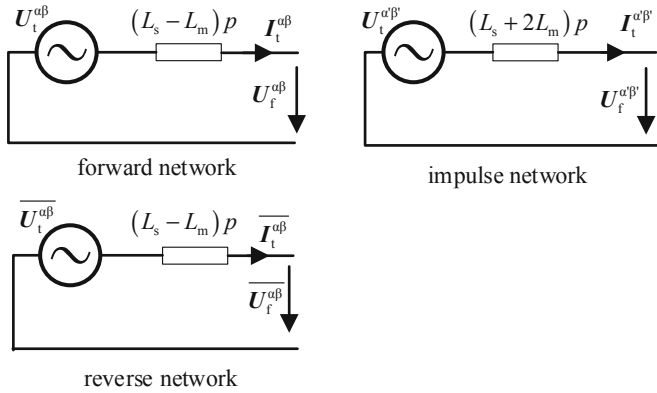
Fig. 4. The equivalent networks with a forward network, a reverse network, and an impulse network
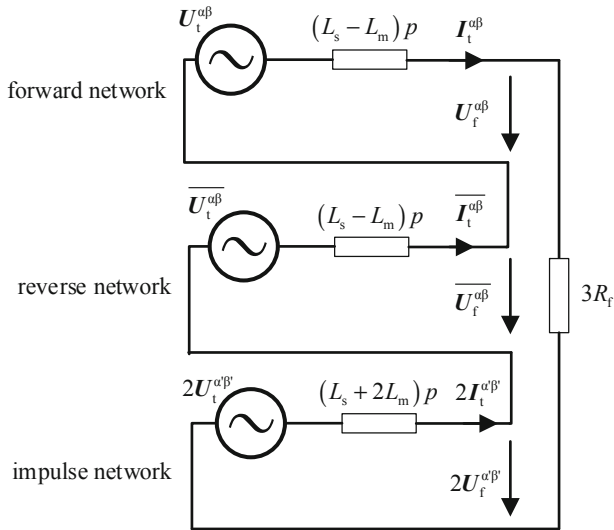
Fig. 5. The composite network reflecting the boundary condition

According to the circuit relationship in the composite network, the three rotating current vectors in the faulted branch can be obtained as

$$
\mathbf{I}_f^{\alpha\beta} = \overline{\mathbf{I}_f^{\alpha\beta}} = 2\mathbf{I}_f^{\alpha'\beta'} = \frac{\mathbf{U}_t^{\alpha\beta} + \overline{\mathbf{U}_t^{\alpha\beta}} + 2\mathbf{U}_t^{\alpha'\beta'}}{3(R_f + L_s p)} \tag{21}
$$

Consequently, the three rotating voltage vectors are given by

$$
\begin{aligned}
\mathbf{U}_f^{\alpha\beta} &= \frac{(3R_f+2L_sp+L_mp)\mathbf{U}_t^{\alpha\beta}-(L_s-L_m)p\left(\overline{\mathbf{U}_t^{\alpha\beta}}+2\mathbf{U}_t^{\alpha'\beta'}\right)}{3(R_f+L_sp)} \\
\overline{\mathbf{U}_f^{\alpha\beta}} &= \frac{(3R_f+2L_sp+L_mp)\overline{\mathbf{U}_t^{\alpha\beta}}-(L_s-L_m)p\left(\mathbf{U}_t^{\alpha\beta}+2\overline{\mathbf{U}_t^{\alpha'\beta'}}\right)}{3(R_f+L_sp)} \\
\mathbf{U}_f^{\alpha'\beta'} &= \frac{(6R_f+4L_sp-4L_mp)\mathbf{U}_t^{\alpha'\beta'}-(L_s+2L_m)p(\mathbf{U}_t^{\alpha\beta}+\overline{\mathbf{U}_t^{\alpha\beta}})}{6(R_f+L_sp)}
\end{aligned} \tag{22}
$$

According to Kirchhoff's current law, i_t can be obtained as

$$
\begin{cases}
\mathbf{I}_t^{\alpha\beta} = \mathbf{I}_f^{\alpha\beta} \\
\overline{\mathbf{I}_t^{\alpha\beta}} = \overline{\mathbf{I}_f^{\alpha\beta}} \\
\mathbf{I}_t^{\alpha'\beta'} = \mathbf{I}_f^{\alpha'\beta'}
\end{cases} \tag{23}
$$

Assuming the distance from the point m to the fault point f accounts for the percentage of the distance from u_t to the fault point f as k, then the rotating voltage vectors at the point m can be dissolved as

$$
\begin{bmatrix} \mathbf{U}_m^{\alpha\beta} \\ \overline{\mathbf{U}_m^{\alpha\beta}} \\ \mathbf{U}_m^{\alpha'\beta'} \end{bmatrix} = \begin{bmatrix} \mathbf{U}_f^{\alpha\beta} \\ \overline{\mathbf{U}_f^{\alpha\beta}} \\ \mathbf{U}_f^{\alpha'\beta'} \end{bmatrix} + \begin{bmatrix} k(L_s-L_m)p & 0 & 0 \\ 0 & k(L_s-L_m)p & 0 \\ 0 & 0 & k(L_s+2L_m)p \end{bmatrix} \begin{bmatrix} \mathbf{I}_t^{\alpha\beta} \\ \overline{\mathbf{I}_t^{\alpha\beta}} \\ \mathbf{I}_t^{\alpha'\beta'} \end{bmatrix} \tag{24}
$$

Eventually, the three-phase voltage and current at a random point m on the transmission line can be obtained as, respectively

$$
\begin{bmatrix} u_{ma} \\ u_{mb} \\ u_{mc} \end{bmatrix} = C^{-1} \begin{bmatrix} \mathbf{U}_m^{\alpha\beta} \\ \overline{\mathbf{U}_m^{\alpha\beta}} \\ \mathbf{U}_m^{\alpha'\beta'} \end{bmatrix} = \frac{1}{2} \begin{bmatrix} 1 & 1 & 2 \\ e^{j4\pi/3} & e^{j2\pi/3} & 2 \\ e^{j2\pi/3} & e^{j4\pi/3} & 2 \end{bmatrix} \begin{bmatrix} \mathbf{U}_m^{\alpha\beta} \\ \overline{\mathbf{U}_m^{\alpha\beta}} \\ \mathbf{U}_m^{\alpha'\beta'} \end{bmatrix} \tag{25}
$$

$$
\begin{bmatrix} i_{ma} \\ i_{mb} \\ i_{mc} \end{bmatrix} = C^{-1} \begin{bmatrix} \mathbf{I}_t^{\alpha\beta} \\ \overline{\mathbf{I}_t^{\alpha\beta}} \\ \mathbf{I}_t^{\alpha'\beta'} \end{bmatrix} = \frac{1}{2} \begin{bmatrix} 1 & 1 & 2 \\ e^{j4\pi/3} & e^{j2\pi/3} & 2 \\ e^{j2\pi/3} & e^{j4\pi/3} & 2 \end{bmatrix} \begin{bmatrix} \mathbf{I}_f^{\alpha\beta} \\ \overline{\mathbf{I}_f^{\alpha\beta}} \\ \mathbf{I}_f^{\alpha'\beta'} \end{bmatrix} \tag{26}
$$

5 Validations

In order to verify the analytical expression presented in the Eq. (25) and (26), a simple model is established in Matlab/Simulink and its parameters are shown below. The power base and the voltage base for p.u. are given by

$$
\begin{aligned}
S_{base} &= 100\,\text{kVA} \\
U_{base} &= 690/\sqrt{3/2} = 563.38\,\text{V}
\end{aligned} \tag{27}
$$

Three-phase voltage per units of u_t with the time-varying amplitude and frequency are given by

$$
\begin{cases}
u_{t1a} = [0.8 + 0.08\sin(20\pi t)]\sin\left\{\int [100\pi + 50\sin(20\pi t)]dt\right\} \\
\qquad + \ [0.2 + 0.02\sin(20\pi t)]\sin(100\pi t) \\
u_{t1b} = [0.8 + 0.08\sin(20\pi t)]\sin\left\{\int [100\pi + 50\sin(20\pi t)]dt - \dfrac{2\pi}{3}\right\} \\
\qquad + \ [0.2 + 0.02\sin(20\pi t)]\sin\left(100\pi t + \dfrac{2\pi}{3}\right) \\
u_{t1c} = [0.8 + 0.08\sin(20\pi t)]\sin\left\{\int [100\pi + 50\sin(20\pi t)]dt + \dfrac{2\pi}{3}\right\} \\
\qquad + \ [0.2 + 0.02\sin(20\pi t)]\sin\left(100\pi t - \dfrac{2\pi}{3}\right)
\end{cases}
\tag{28}
$$
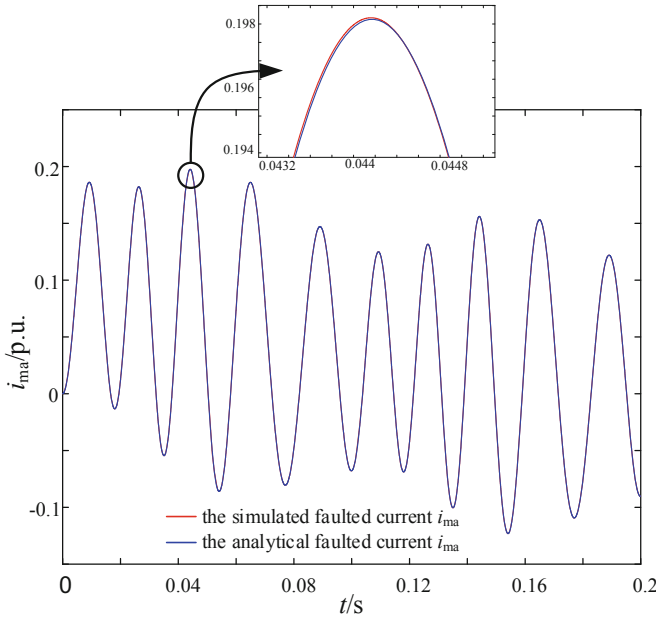
Fig. 6. The phase-A current at the midpoint

The self-inductance L_s and the mutual-inductance L_m of the transmission lines are 90 mH and 30 mH respectively. A single-phase to ground fault (AG) with the fault resistance 1 Ω is applied for a duration of 0.2 s for testing purposes.

Based on the simulation model and the analytical expression, the phase-A current and phase-A voltage at the midpoint of the transmission line are compared in Fig. 6 and Fig. 7. It can be seen that the analytical results of the faulted current highly match

the simulated results, as does the faulted voltage results. This indicates that the analytical expressions have high accuracy. Furthermore, the feasibility and correctness of the method of conjugate vectors for the dynamic analysis of asymmetrical-faulted grid have been verified. The little error presented in the partial enlargement mainly comes from the truncation of infinite series when calculating the expressions with Heaviside's operator p [23, 24] and in this paper, we simply take the first 20 terms of the infinite series to get the results. However, how to calculate the expressions with Heaviside's operator is beyond the discussion of this paper.
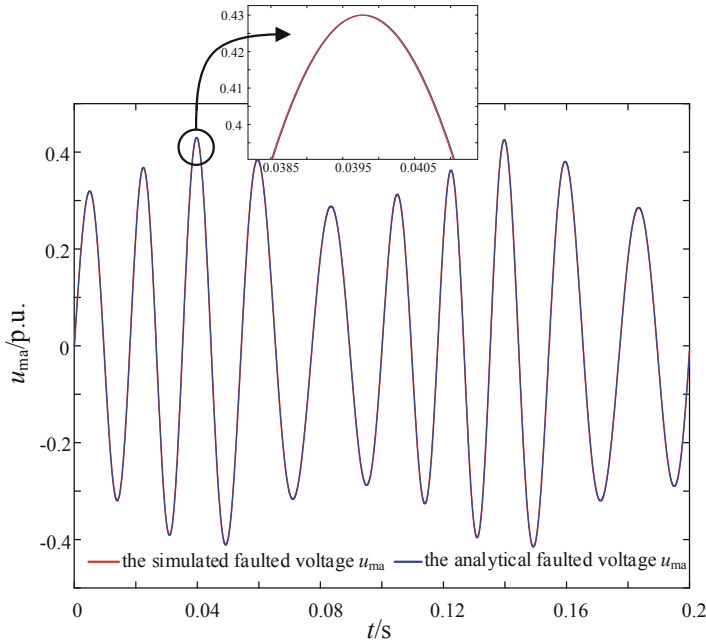
Fig. 7. The phase-A voltage at the midpoint

6   Conclusions

Different from traditional synchronous generators, the internal voltage of PED is dominated by complex control links, which therefore exhibits the time-varying amplitude/frequency characteristics. Correspondingly, the amplitude/frequency of the voltage/current in the asymmetrical-faulted grid will not remain constant anymore, which leads to the failure of the method of symmetrical components application. Based on this understanding, the method of conjugate vectors for the dynamic analysis is proposed. The proposed method converts three-phase electrical quantities into a group of rotating vectors to get network decomposed. Based on the method, a simple system with a single-phase ground fault is analyzed and the analytical expressions of the voltage and

current at a random point are provided. Finally, the analytical expressions are verified to be authentic in comparison with a simulation model.

References

1. Australian Energy Market Operator. Black system South Australia 28 September 2016: final report [EB/OL]. https://www.aemo.com.au/-/media/Files/Electricity/NEM/MarketNoticesan dEvents/PowerSystemIncidentReports/2017/IntegratedFinal-Report-SA-Black-System-28-September-2016.pdf

2. National Grid ESO. Interim Report into the Low Frequency Demand Disconnection (LFDD) following Generator Trips and Frequency Excursion on 9 Aug 2019 (2019)

3. Wang, N.B., Ma, Y.H., Ding, K., et al.: Analysis on root reasons of WTGs nuisance tripping in Jiuquan wind power base. Autom. Electr. Power Syst. **36**(19), 42–46 (2012)

4. Song, G.B., Tao, R., Li, B., et al.: Survey of fault analysis and protection for power system with large scale power electronic equipments. Autom. Electr. Power Syst. **41**(12), 2–12 (2017)

5. Qiu, Y.T., Pan, W.L., Ni, C.K., et al.: Equal transfer process-based distance protection for wind farm outgoing transmission line. Power Syst. Prot. Control **43**(12), 61–66 (2015)

6. International Electrotechnical Commission. IEC 61400 27-2015 Electrical simulation models - Wind turbines. Swiss: International Electrotechnical Commission (2015)

7. Western Electricity Coordinating Council. WECC Second Generation Wind Turbine Models, 23 January 2014 [EB/OL]. https://www.wecc.biz/Reliability/WECC-Second-Generation-Wind-Turbine-Models-012314.pdf

8. Clark, K., Miller, N.W., Sanchez-Gasca, J.J.: Modeling of GE Wind Turbine-Generators for Grid Studies. General Electric International Inc., New York (2010)

9. Kim, S., Kim, E.: PSCAD/EMTDC-based modeling and analysis of a gearless variable speed wind turbine. IEEE Trans. Energy Convers. **22**(2), 421–430 (2007)

10. Kauffmann, T., Karaagac, U., Kocar, I., et al.: An accurate type III wind turbine generator short circuit model for protection applications. IEEE Trans. Power Delivery **32**(6), 2370–2379 (2017)

11. Howard, D.F., Liang, J., Harley, R.G.: Short-circuit modeling of DFIGs with uninterrupted control. IEEE J. Emerg. Sel. Top. Power Electron. **2**(1), 47–57 (2014)

12. Demiray, T., Milano, F., Andersson, G.: Dynamic phasor modeling of the doubly-fed induction generator under unbalanced conditions. In: 2007 IEEE Lausanne Power Tech, pp. 1049–1054. IEEE, Lausanne (2007)

13. Chandrasekar, S., Gokaraju, R.: Dynamic phasor modeling of type 3 DFIG wind generators (including SSCI phenomenon) for short-circuit calculations. IEEE Trans. Power Deliv. **30**(2), 887–897 (2015)

14. Göksu, Ö., Cutululis, N.A., Rensen, P.S., et al.: Asymmetrical fault analysis at the offshore network of HVDC connected wind power plants. In: 2017 IEEE Manchester PowerTech, pp. 1–5 (2017)

15. Chang, Y.Z., Hu, J.B., Tang, W.Q.Y., et al.: Fault current analysis of type-3 WTs considering sequential switching of internal control and protection circuits in multi time scales during LVRT. IEEE Trans. Power Syst. **33**(6), 6894–6903 (2018)

16. Hu, J.B., Yuan, X.M., Cheng, S.J.: Multi-time scale transients in power-electronized power systems considering multi-time scale switching control schemes of power electronics apparatus. Proc. CSEE **39**(18), 5457–5467 (2019)

17. Yuan, X.M., Cheng, S.J., Hu, J.B.: Multi-time scale voltage and power angle dynamics in power electronics dominated large power systems. Proc. CSEE **36**(19), 5145–5154 (2016)

18. Yuan, X.M., Zhou, R.: Method of time-varying amplitude/frequency symmetrical components for network asymmetrical fault analysis excited by power electronic devices. Proc. CSEE (2022)

19. Heaviside, O.: Electrical Papers, vol. 2. Macmillan, London (1892)

20. Poritsky, H.: Heaviside's operational calculus-its applications and foundations. Amer. Math. Mon. **43**(6), 331–344 (1936)

21. Wang, B., Wang, S.C., Hu, J.B.: Dynamic modeling of asymmetrical-faulted grid by decomposing coupled sequences via complex vector. IEEE J. Emerg. Sel. Top. Power Electron. **9**(2), 2452–2464 (2021)

22. Harnefors, L.: Modeling of three-phase dynamic systems using complex transfer functions and transfer matrices. IEEE Trans. Industr. Electron. **54**(4), 2239–2248 (2007)

23. Bellert, S.: On the continuation of the idea of heaviside in the operational calculus. J. Franklin Inst. **276**(5), 411–440 (1963)

24. Moore, D.H.: Algebraic basis of heaviside operational calculus. J. Franklin Inst. **286**(2), 158–161 (1968)

Multi-objective Optimal Planning for Park-Level Integrated Energy System Coupling with Electric Vehicle Charging Stations

Meng Wang[1] , J. H. Zheng[1(✉)] , Yiqian Sun[2], Guang Cheng[3], Zhigang Li[1] ,
and Q. H. Wu[1]

[1] School of Electric Power Engineering, South China University of Technology,
Guangzhou 510640, China
zhengjh@scut.edu.cn
[2] Electric Power Research Institute, State Grid Xinjiang Electric Power CO. LTD.,
Urumqi 511442, China
[3] Altay Electric Power Co. LTD., State Grid Xinjiang Electric Power CO. LTD., Altay 836500,
China

Abstract. The research on the source-demand coordination of electric vehicle charging stations (EVCSs) connected to the park-level integrated energy system (PLIES) is of great significance for the development of optimal planning for energy systems. The paper aims to present a multi-objective coupled optimal model for PLIES coupling with the EVCSs, followed by the operation configuration strategies and hourly schedule. This optimal model involves a bidirectional power flow between PLIES and EVCSs as well as the mutual dependencies among equipments. The multi-objective optimal design problem utilizes multiobjective particle swarm optimization (MOPSO) to obtain a series of feasible solutions for the optimal configuration in order to minimize the annual total cost and the annual pollution emission. Simultaneously, two scenarios are conducted for in-depth exploration of the potential scheduling capabilities of electric vehicles (EVs). The simulation analysis shows that the coordinated planning and mutual couple between PLIES and EVCSs can increase the flexibility and stability of energy systems during peak-load periods.

Keywords: Park-level integrated energy systems · Electric vehicle charging stations · Mutual coupled model · Operation configuration strategies

1 Introduction

Over the past decades, the development of optimal planning for energy systems has become more complex with the interactions among electricity, gas and heating/cooling energy networks [1]. The integrated energy system (IES), which couples the prime mover, the energy conversion equipments and users as a whole, has been attracting

more attention on account of its efficient cascading utilization of energy [2, 3]. The corresponding system architecture, operational strategies, and optimization methods are also kept being developed technically [4, 5]. Currently, the PLIES is considered as an attractive planning object due to its advantages of convenient operation and local energy consumption [6].

In the meantime, the rising numbers of EVs along with increasing renewable energy have been creating over challenges for the IES [7]. For instance, the mass access of EVs will bring an additional electric demand and a more complex operational problem for the grid [8, 9]. However, the coordinated planning of EVCSs and PLIES could largely address these issues. Given the fact that among the potential benefits provided by EVCSs to the power grid are peak shifting, schedule flexibility [10], and vehicle-to-grid services [11]. As consequence, it is bi-directional beneficial to investigate the coordinated planning and mutual dependencies between EVCSs and PLIES to promote the acceptability and flexibility of system.

There are two modes of EVs' operation: V2G (vehicle-to-grid) and G2V (grid-to-vehicle) [12]. For the V2G interaction modes, the stored power of battery can be sold to the PLIES during peak-load periods, enabling a bidirectional flow system between the system and EVs. It is of great significance to regard V2G as part of the portfolio of candidate energy power in the PLIES [11]. The EVs, as an active load, can adjust and optimize electrical energy demand curve and make the network connection more stable [13].

Studies have shown that the most attractive schemes for achieving a significant reduction in carbon emissions can be the massive access of renewable energy sources and the widespread adoption of EVs [14]. Reference [15, 16] built an optimal coordinated operation model containing with PV-battery systems, energy storage and conversion devices by using the hybrid technique. However, only an individual energy system is modeled, the plug-in EVs are not taken in account. Reference [17] designed a regional multi-energy prosumers (RMEP) operation paradigm for shaving the peaking load by appropriately adjusting the power of gas turbines and charge/discharge behaviors of plug-in hybrid EVs. Reference [18] present a multi-objective optimization model of residential micro-grid in the presence of plug-in electric vehicles and photovoltaic unit, seeking to obtain the optimal scheduling scheme of energy equipments. However, the majority of the optimal operation strategy regards EVs as sub-equipments of system in a unified manner, regardless of the operational benefits brought by coupling of the EVCSs.

On the basis of previous researches, this paper proposes a multi-objective optimal schedule model for PLIES coupling with the EVCSs. Seeking to achieve the minimized annual total costs (ATC) and annual pollution emissions (APE) simultaneously with a certain feedback tariff. This optimal model considers the charging and discharging strategy of EVs with a bidirectional power flow between PLIES and EVCSs. Deducting energy consumption in the process for traveling, the stored energy of EVs can be sold back to the grid. In this condition, EV loads are enabled to interact with the PLIES by charging or discharging, which can be transformed from an indebted load into a valuable asset with the marketing perspective.

The rest of this paper is organized as follows. Section 2 illustrates the formula modeling of the typical PLIES coupling with EVCSs. Section 3 conducts the simulation and analyzes numerical results. Conclusions are drawn in Sect. 4.

2 Framework and Model

2.1 The System Architecture

Figure 1 illustrates the typical PLIES system architecture coupling with EVCSs model, satisfying the electric, heating and cooling loads. The EVCSs are served as the connecting piles of the power transmission between the PLIES and EV loads. The EVCSs is coupled with PLIES for the power exchange whenever there is an unbalance in generation and consumption.

As can be observed in that figure, both the renewable and conventional energy sources are injected into the PLIES, equipped by the energy conversion equipments, and then be allocated to the required load demand of final users.
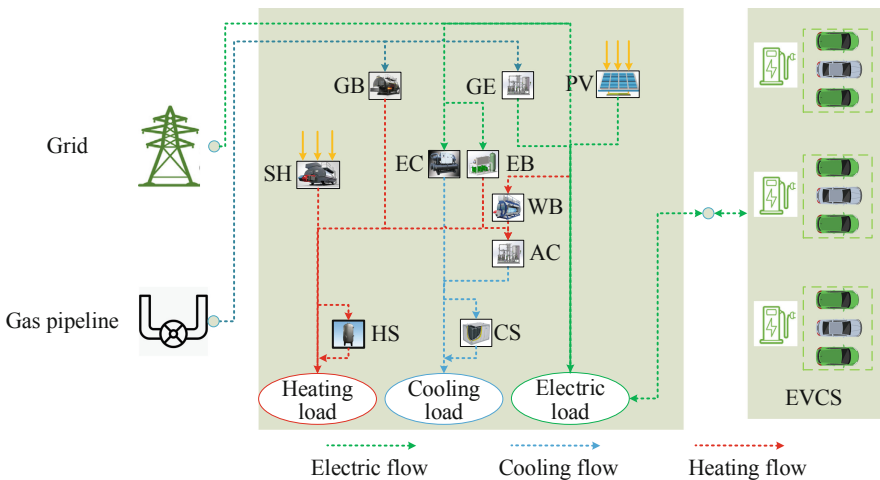
Fig. 1. The typical EVCS-PLIES system architecture.

2.2 The Model Formulation

The proposed general framework for the coupled optimal model is present in Fig. 2, which can be decomposed into the configuration problem and the operational problem.

The configuration problem takes the annual total costs (ATC) and the annual pollution emissions (APE) as the optimal goal. Meanwhile, the annual primary energy consumption (APEC) is calculated as an indicator to measure the impact of EVCSs. The constraints contain the balance and grid security constraints, aiming to obtain the optimal equipment configuration with the method of multiple objective particle swarm optimization (MOPSO) [19].

The operational problem takes the operating costs as the optimal goal. The constraints contain the balance, conversion and grid operational constraints, aiming to solve the mixed-integer linear programming (MILP) for seeking the optimal allocation schedule of the hourly output of the equipment.
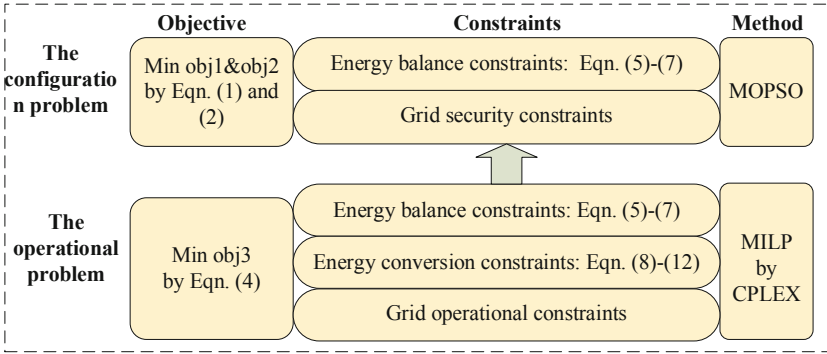
Fig. 2. The formula modeling.

The Objective Function

In the proposed model, the multi-objectives are presented to simultaneously minimize the annual total costs (ATC) and the annual pollution emissions (APE). Meanwhile, the annual primary energy consumption (APEC) is calculated as an indicator to measure the energy efficiency of the system.

$$\min \ obj1 = ATC = C_{\text{inv}} + C_{\text{om}} + C_{\text{fue}} - C_{\text{inc}} = \sum_{i=1}^{I}\sum_{s=1}^{S}\sum_{h=1}^{H}(\alpha_i + f_i)c_i P_{i,s,h}^{\text{rated}}$$
$$+ \sum_{i=1}^{I}\sum_{s=1}^{S}\sum_{h=1}^{H} v_i P_{i,s,h} + \sum_{j=1}^{J}\sum_{s=1}^{S}\sum_{h=1}^{H} v_j E_{j,s,h} - \sum_{s=1}^{S}\sum_{h=1}^{H}(c_{sell}P_{\text{ev},s,h}^{\text{char}} - c_{buy}P_{\text{ev},s,h}^{\text{disc}})$$

$$(1)$$

where C_{inv} denotes the investment cost, C_{om} denotes the operation and maintenance cost, C_{fuel} denotes the fuel cost, C_{inc} denotes the operation income; the symbol i denotes the energy equipment, s denotes the season; h denotes the operating hours; α_i denotes the capital recovery factor; f_i denotes the fixed operation and maintenance cost coefficient; c_i denotes the unit investment cost of equipment; P_i^{rated} denotes the rated capacity of equipment; v_i denotes the unit variable operation and maintenance cost; P_i^h denotes the output power of the equipment; j denotes energy types; v_j^h denotes the unit energy price; E_j^h denotes the energy consumption; c_{sell} and c_{buy} denote the unit selling and purchasing power price; $P_{\text{ev},s,h}^{\text{char}}$ and $P_{\text{ev},s,h}^{\text{disc}}$ denote the charging and discharging power respectively.

$$\min \ obj2 = APE = \sum_{s=1}^{S}\sum_{h=1}^{H}(\mu_{gas}E_{gas,s,h} + \mu_{grid}E_{grid,s,h}) \qquad (2)$$

$$APEC = \sum_{s=1}^{S} \sum_{h=1}^{H} \left(\lambda_{gas\_ele} E_{gas\_ele,s,h} + \lambda_{gas\_heat} E_{gas\_heat,s,h} + \lambda_{grid} E_{grid,s,h} \right) \quad (3)$$

where μ_{gas} and μ_{grid} denote the unit emission coefficient of natural gas and power; λ_{gas_ele}, λ_{gas_heat} and λ_{grid} denote the standard coal consumption conversion coefficient of gas to power, gas to heat and power to grid, $E_{gas\_ele,s,h}$, $E_{gas\_heat,s,h}$ and $E_{grid,s,h}$ denote the energy consumption of gas to power, gas to heat and power.

$$\min \ obj3 = C_{\text{ope}} = \sum_{s=1}^{S} d_s \sum_{h=1}^{H} \sum_{i=1}^{I} v_i P_{i,s,h} + \sum_{s=1}^{S} d_s \sum_{h=1}^{H} \sum_{j=1}^{J} v_j E_{j,s,h}$$

$$- \sum_{s=1}^{S} d_s \sum_{h=1}^{H} (c_{sell} P_{ev,s,h}^{\text{char}} - c_{buy} P_{ev,s,h}^{\text{disc}}) \quad (4)$$

where d_s denotes the total typical days of each season.

Constrains

Energy Balances

In theory, ideal matching for the generation and consumption is achieved when the electric, heating and cooling loads are exactly satisfied by the PLIES. The energy balances include the electric, heating and cooling balance.

$$P_{\text{PV},s,h}^{\text{act}} + P_{\text{GE},s,h}^{\text{act}} + E_{s,h}^{\text{buy}} - P_{\text{EV},s,h}^{\text{char}} + P_{\text{EV},s,h}^{\text{disc}} - \frac{1}{\eta_{\text{EC}}^h} P_{\text{EC},s,h}^{\text{act}} - \frac{1}{\eta_{\text{EB}}^h} P_{\text{EB},s,h}^{\text{act}} = E_{\text{n}}^{\text{demand}}, \quad \forall s, h \quad (5)$$

$$P_{\text{WB},s,h}^{\text{act}} + P_{\text{GB},s,h}^{\text{act}} + P_{\text{EB},s,h}^{\text{act}} + P_{\text{SH},s,h}^{\text{act}} + P_{\text{HS},s,h}^{\text{act}} - \frac{1}{\eta_{\text{AC}}^h} P_{\text{AC},s,h}^{\text{act}} = E_{\text{h}}^{\text{demand}}, \quad \forall s, h$$

$$(6)$$

$$P_{\text{EC},s,h}^{\text{act}} + P_{\text{AC},s,h}^{\text{act}} + P_{\text{CS},s,h}^{\text{act}} = E_{\text{c}}^{\text{demand}}, \quad \forall s, h \quad (7)$$

where P^{act} denotes the actual output power of equipments, E^{buy} denotes the purchasing power of PLIES, $P_{ev,s,h}^{\text{char}}$ and $P_{ev,s,h}^{\text{disc}}$ denote the charging and discharging power of EVCS respectively, $E_{\text{n}}^{\text{demand}}$, $E_{\text{h}}^{\text{demand}}$ and $E_{\text{c}}^{\text{demand}}$ denote the electric, heating and cooling demand of PLIES. The subscripts denote the equipment names, and the specific definitions are described in Table 1.

PV and SH Constraints

In the system of photovoltaic and solar-heat boiler, the solar energy is directly con-verted into electric and heating energy by panels. The power generated is mainly de-pended on the intensity of solar radiation and photovoltaic installation area [20].

$$P_{\text{PV},s,h}^{\text{act}} = \eta_{\text{PV}} \cdot A_{\text{PV}} \cdot H_{s,h} \quad (8)$$

$$P_{\text{SH},s,h}^{\text{act}} = \eta_{\text{SH}} \cdot (A_{\text{T}} - A_{\text{PV}}) \cdot H_{s,h} \quad (9)$$

where η_{PV} and η_{SH} denote the electric and heating efficiency of PV and SH, A_{PV} denotes the installation area of photovoltaic panels, A_T denotes the entire solar panels areas of PLIES, $H_{s,h}$ denotes the intensity of solar radiation.

EV Constraints

In the EVs' charging/discharging scheduling model, the remained energy from the previous period, the charging/discharging energy and the energy consumption for driving in the period have to be considered jointly for the battery energy balance.

$$
SOC_{s,h}(t) = \begin{cases} SOC_{s,h}(t-1) + (1-\delta_{ev}) \cdot P^{char}_{ev,s,h} \cdot \Delta T \cdot \eta^{in}_{ev} - E_{ev,s,h}, & S_{char} > 0 \\ SOC_{s,h}(t-1) - (1-\delta_{ev}) \cdot P^{disc}_{ev,s,h} \cdot \Delta T / \eta^{out}_{ev} - E_{ev,s,h}, & S_{disc} > 0 \end{cases}
\tag{10}
$$

where the state of charge $SOC_{s,h}(t)$ and $SOC_{s,h}(t-1)$ denote the final energy of the current period ΔT and previous period $\Delta(T-1)$ in the battery. $P^{char}_{ev,s,h}$ and $P^{disc}_{ev,s,h}$ denote the charging power and discharging power respectively. η^{in}_{ev} and η^{out}_{ev} denote the grid-to-vehicle charging efficiency coefficient and vehicle-to-grid discharging efficiency coefficient respectively. ΔT denotes the charging and discharging time slot, in this paper, it is set as 1 h. $E_{ev,s,h}$ denotes the energy consumption in the process for EVs driving in period ΔT.

The state of charge at each moment should reach the lowest limit of capacity for the battery health consideration [21].

$$
SOC^{min}_{ev} \leq SOC_{s,h} \leq SOC^{max}_{ev}
\tag{11}
$$

where SOC^{min}_{ev} and SOC^{max}_{ev} denote the minimum and maximum capacity of the EV battery.

In each period ΔT, the charge and discharge of EV are not simultaneous:

$$
\begin{cases} 0 \leq P^{char}_{ev,s,h} \leq X \cdot P^{max}_{ev} \\ 0 \leq P^{disc}_{ev,s,h} \leq Y \cdot P^{max}_{ev} \,, \quad \forall s, h \\ X + Y \leq 1 \end{cases}
\tag{12}
$$

where P^{max}_{ev} denotes the maximum charging/discharging power; X and Y are the binary variables, which denote the states for charging and discharging.

2.3 The Solving Method

Based on the multi-objective coupled optimal model for PLIES coupling with the EVCSs, this paper utilizes the multi-objective particle swarm optimization (MOPSO) to optimize the equipment capacity and hourly output power. The corresponding overall architecture is developed in Fig. 3.
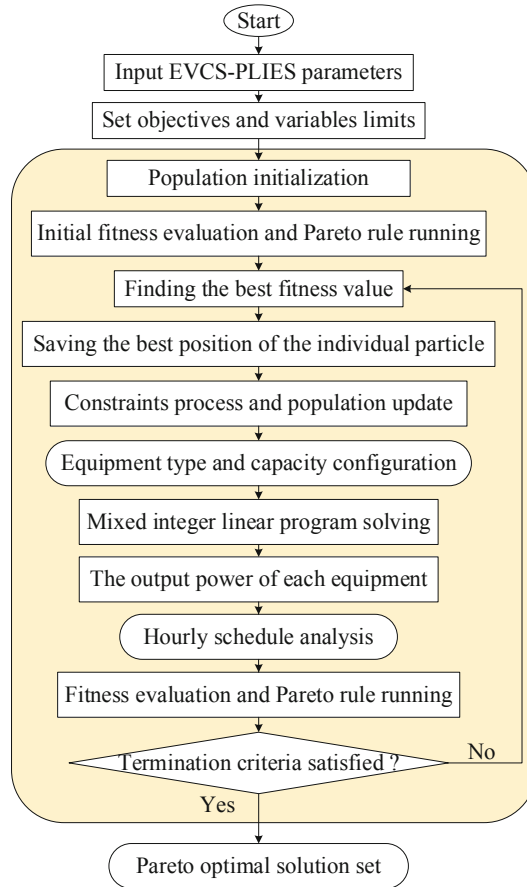
Fig. 3. The overall structure and flow of MOPSO.

3   Simulation Analysis

3.1   Simulation Preparation

A commercial functional area is assumed as the end user of EVCS-PLIES, the load curves and the EVs' load demands are shown in Fig. 4. The comprehensive energy equipment parameters are described in Table 1. The time-of-use energy price are illustrated in Table 2. The charging capacity of each EV is 64 kWh, and the total capacity of the EVCSs is 6000 kW, which can accommodate at least 90 EVs for charging at the same time. The EVCSs can sell the surplus electric load to the PLIES at a discounted rate of the current electric price, which is assigned as 10%.
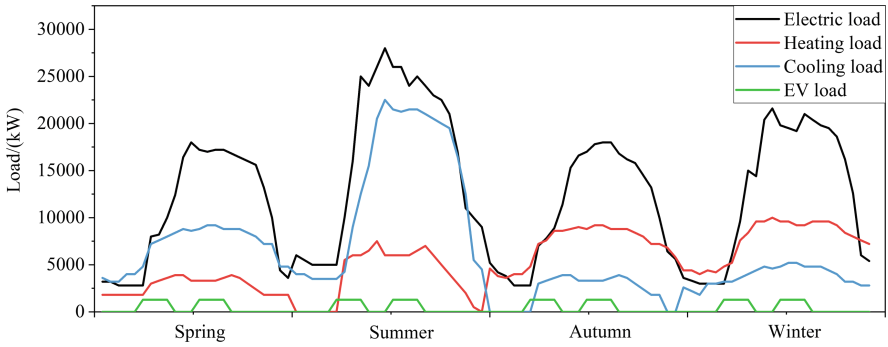
Fig. 4. The load curves and the EV' load demand.

Table 1. The comprehensive equipment parameters.

Equipment	Abbreviation	Electric efficiency/COP	Load rate	
			Lower	Upper
Photovoltaic	PV	0.15/–	–	–
Solar-heat boiler	SH	– /0.6	–	–
Gas engine	GE	0.36/0.48	0.3	1
Waste-heat boiler	WB	– /0.85	0.2	1
Gas boiler	GB	– /0.85	0.26	1
Electric boiler	EB	– /0.95	0.1	1
Absorption chiller	AC	– /1.2	0.05	1
Electric chiller	EC	– /3.5	0.1	1
Heating storage	HS	– /0.95	0	1
Cooling storage	CS	– /0.92	0	1

Table 2. Energy unit price

	Period	Price/(¥/kWh)
Grid	Peak: 11:00–15:00, 19:00–21:00	1.217
	Level: 8:00–10:00, 16:00–18:00, 22:00–23:00	0.875
	Valley: 0:00–7:00	0.524
Gas	–	0.387

3.2   Results and Discussions

The Pareto Frontier
In order to analyze the impact of EVCSs on the PLIES, two scenarios in commercial areas are investigated:

Scenario 1: The PLIES without EVCSs model.
Scenario 2: The PLIES coupling with EVCSs model.
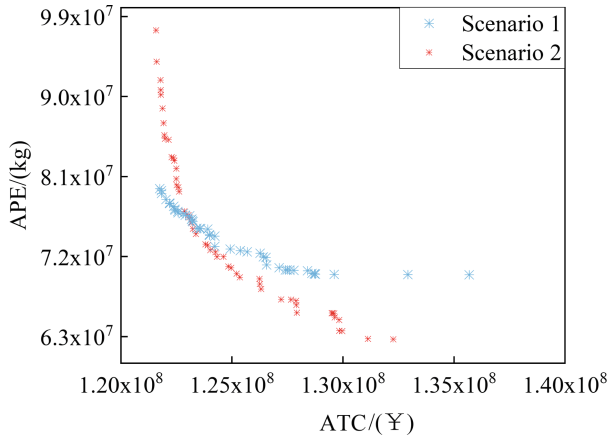
Fig. 5. The Pareto solution sets of two scenarios.

Figure 5 illustrates the Pareto solution sets in the two scenarios, in which the red point shows the results of scenario 1, and the blue point shows scenario 2. Each point in the Pareto solution set conforms to different operation strategy and hourly scheduling of the PLIES coupling with EVCSs model. As can be seen that the range of the Pareto solutions in scenario 2 is larger than scenario 1, which means that the coupled EVCSs are helpful for improving the adjustability and flexibility of the PLIES.

The Charging/Discharging Scheduling of EVCSs
In order to analyze the adjustable capacity of EVCSs, this part discusses the state of charge (SOC) of EVCSs and ensures the travel demand, basing on the previously mentioned case. Deducting EVs' load in the process for traveling, the stored power of EVCSs can be sold back to the grid, the corresponding SOC curve is present in Fig. 6. As can be observed, the SOC of each moment is greater than zero, which indicates that the final capacity of charging stations can not only meet the travel demand of electric vehicles, but also can be used as a potential energy storage system.

The Optimal Configuration Capacity
The optimal configuration capacity of the equipment varies from optimal ATC to optimal APE is visualized in Fig. 7. It contains the annual primary energy consumption,
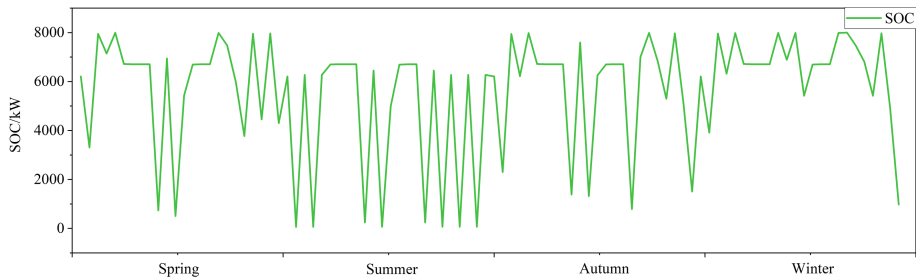
Fig. 6. The state of charge of EVCSs.

natural gas purchasing, electricity purchasing and the capacity of each equipment, each point corresponds to each Pareto solution. The significant finding is that the red lines fluctuates relatively little compared with the blue one. This can be explained by that the coupling EVs can promote system stability during peak-load periods through the flexible scheduling.

As can be observed in Fig. 7(a), when the solution moves from optimal ATC to optimal APE, the APEC shows a downward trend in these two scenarios. Which can be illustrated as that more energy consumption will bring more pollution emissions, but can reduce the economic expenditure of electricity purchasing. In the case of the optimal ATC, the APEC of these two scenarios tends to be equal, even the scenario 1 will be larger than scenario 2. However, when in the case of the optimal ATC, the APEC of scenario 1 is smaller than scenario 2 by about 3×10^6 kg. Which is mainly due to the additional electric demands from EVCSs keeping the energy consumption of scenario 2 at a high level.

As shown in Fig. 7(b), (c), the operating cost of scenario 1 is larger than scenario 2 in both cases of optimal ATC and optimal APE. And when the solution moves from optimal ATC to optimal APE, the operating costs will increase as the operating income is decreasing with the coupling of EVs. For the scenario 2 of coupling EVs, the PLIES can obtain operating benefits by selling electricity to EVCSs, So the operating cost is relatively lower.

According to Fig. 7(d), (e), when the solution moves from optimal ATC to optimal APE, the natural gas purchasing shows an upward trend while the electricity purchasing shows a downward trend in the two scenarios. Which implies that the most effective solution for achieving a significant reduction in carbon emissions is driven by the full utilization of natural gas and the reduction in electricity.

As seen in Fig. 7(f), (g), as the solution moves from optimal ATC to optimal APE, the photovoltaic power in scenario 1 gradually increases, and the capacity of the solar-heat boiler gradually decreases in a complementary relationship. While in scenario 2, the capacities of photovoltaic and solar-heat boiler remain stable no matter the cases of the optimal ATC and the optimal APE. This phenomenon can be partially explained as that EVs can regulate the internal energy consumption of PLIES and achieve a more efficient balance of supply and demand.

It is observed from Fig. 7(h), (i) that the capacities of the both gas engines and waste-heat boilers in scenario 2 are larger than scenario 1 due to the additional power
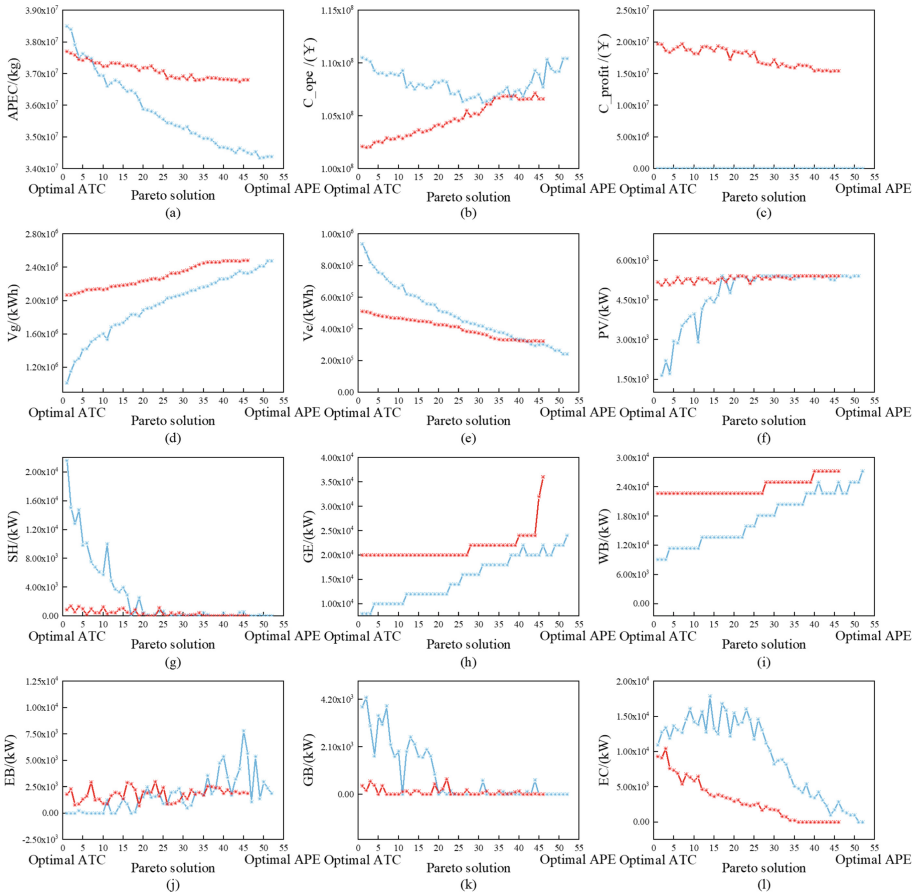
Fig. 7. The energy equipments' installed capacity.

demands of EVs. In addition, in order to achieve the minimum APE, the optimal capacity of gas engine tends to increase for the reason of its lower emission features compared to the grid. Since the waste-heat boiler works with the waste-heat by-products of the gas engine, it has the same trend as the gas engines.

As shown in Fig. 7(j), (k), despite some fluctuations, the capacity of electric boilers and gas boilers are relatively stable with the change of Pareto solution in scenario 2. On the contrary, the fluctuations in the scenario 1 are more obvious. It implies that the elastic EVs' load plays a role in peak shaving and valley filling.

From Fig. 7(l), The electric chillers' capacity of scenario 2 is smaller than scenario 1. It is because EVs can promote the cascade utilization rate of the PLIES to a greater extent, then the absorption chillers will be fully utilized. As a result, the electric chillers' capacity is continuously reduced.

Hourly Schedule Analysis
To carry out the analysis, we investigate the charging and discharging characteristics of

EVs in the operation of hourly schedule. The EVCSs can buy electricity from the PLIES, and also can sell electricity with a feed-in tariff to the system to satisfy the time-varying load demands. The optimal schedule results of electric balance under low cost mode and low carbon mode are shown in Fig. 8.
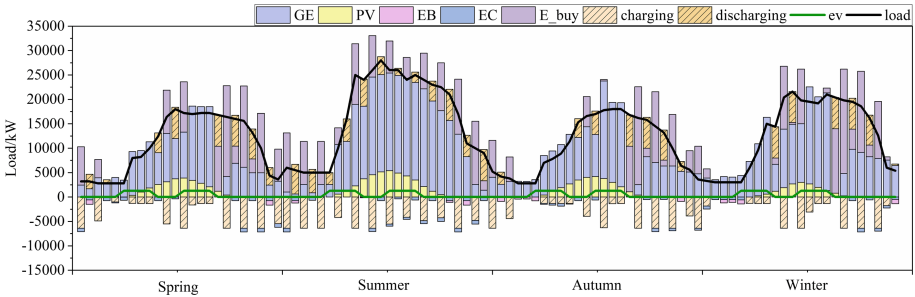
Fig. 8. The electric balance of hourly schedule.

Although there will be some losses when starting the gas engines, the main electricity during peak periods is provided by the gas engines due the lower unit price of gas. The lacking part is made up by the grid or EVCSs. It can be observed that the EVCSs can be discharged into the PLIES in each no-charging period when the capacity is sufficient. The remaining capacity of EVCSs is transferred back to the system during peak hours (10:00–12:00 and 17:00–21:00) to actively participate in energy coordinated management for effectively improving the load demand curve. During the peak-load periods, EVs can act as energy storage equipments to provide electricity to the PLIES. On summer days, the charging and discharging of EVCSs occurs almost at every hour to meet the higher electrical demand, Conversely, when in other seasons, the EVCSs basically does not discharge during 1:00–8:00, because the load and the gas price is relatively low during this period. In general, the EVCSs can effectively mitigate the high load demand.

4   Conclusion

This paper develops a multi-objective optimal model for PLIES coupling with the EVCSs. The operation configuration strategies and hourly schedule are optimized considering the power interaction under charge and discharge. The key findings are drawn: Electric vehicles, as the demand-side resource, can not only assist the stable output of the energy equipments with the flexible schedule characteristics, but also be used as shifting loads to actively participate in energy coordinated management in the system, thereby enhancing the network flexibility of PLIES. When EVCSs are coupled into the PLIES, the charging stations can act as a potential energy storage system during the non-charging period, promoting the efficiency of variable power into system.

References

1. Wang, J., Ye, X., Li, Y., Gui, X.Q., Guo, H.L.: An energy efficiency evaluation method of distributed CCHP system based on attribute theory for optimal investment strategy. Energy Procedia **152**, 95–100 (2018). https://doi.org/10.1016/j.egypro.2018.09.065

2. Qin, Y.J., et al.: Optimal operation of integrated energy systems subject to coupled demand constraints of electricity and natural gas. CSEE J. Power Energy Syst. **6**(2), 444–457 (2020). https://doi.org/10.17775/CSEEJPES.2018.00640

3. Farrokhifar, M., Nie, Y.H., Pozo, D.: Energy systems planning: A survey on models for integrated power and natural gas networks coordination. Appl. Energy **262**, 114567 (2020). https://doi.org/10.1016/j.apenergy.2020.114567

4. Somma, M.D., Graditi, G., Heydarian-Forushani, E., Shafie-khah, M., Siano, P.: Stochastic optimal scheduling of distributed energy resources with renewables considering economic and environmental aspects. Renew. Energy **116**, 272–287 (2018). https://doi.org/10.1016/j.renene.2017.09.074

5. Wang, L.X., et al.: Multi-time scale dynamic analysis of integrated energy systems: an individual-based model. Appl. Energy **237**, 848–861 (2019). https://doi.org/10.1016/j.apenergy.2019.01.045

6. Wu, M., et al.: Two-stage robust optimization model for park integrated energy system based on dynamic programming. Appl. Energy **308**, 118249 (2022). https://doi.org/10.1016/j.apenergy.2021.118249

7. Zhang, C., Greenblatt, J.B., MacDougall, P., Saxena, S., Prabhakar, A.J.: Quantifying the benefits of electric vehicles on the future electricity grid in the midwestern United States. Appl. Energy **270**, 115174 (2020). https://doi.org/10.1016/j.apenergy.2020.115174

8. Wei, H.Q., Zhang, Y.T., Wang, Y.Z., Hua, W.Q., Jing, R., Zhou, Y.: Planning integrated energy systems coupling V2G as a flexible storage. Energy **239**(B), 122215 (2022). https://doi.org/10.1016/j.energy.2021.122215

9. Shafie-khah, M., Vahid-Ghavidel, M., Di Somma, M., Graditi, G., Siano, P., Catalão, J.P.: Management of renewable-based multi-energy microgrids in the presence of electric vehicles. IET Renew. Power Gener. **14**, 417–426 (2020). https://doi.org/10.1049/iet-rpg.2019.0124

10. Shi, R.F., Li, S.P., Zhang, P.H., Lee, K.Y.: Integration of renewable energy sources and electric vehicles in V2G network with adjustable robust optimization. Renew. Energy **153**, 1067–1080 (2020). https://doi.org/10.1016/j.renene.2020.02.027

11. Koltsaklis, N.E., Dagoumas, A.S.: State-of-the-art generation expansion planning: a review. Appl. Energy **230**, 563–589 (2018). https://doi.org/10.1016/j.apenergy.2018.08.087

12. Zakariazadeh, A., Jadid, S., Siano, P.: Multi-objective scheduling of electric vehicles in smart distribution system. Energy Convers. Manage. **79**, 43–53 (2014). https://doi.org/10.1016/j.enconman.2013.11.042

13. Solanke, T.U., Khatua, P.K., Ramachandaramurthy, V.K., Yong, J.Y., Tan, K.M.: Control and management of a multilevel electric vehicles infrastructure integrated with distributed resources: a comprehensive review. Renew. Sustain. Energy Rev. **144**, 111020 (2021). https://doi.org/10.1016/j.rser.2021.111020

14. Yang, Z.L., Li, K., Foley, A.: Computational scheduling methods for integrating plug-in electric vehicles with power systems: a review. Renew. Sustain. Energy Rev. **51**, 396–416 (2015). https://doi.org/10.1016/j.rser.2015.06.007

15. Alzahrani, A.M., Zohdy, M., Yan, B.: An overview of optimization approaches for operation of hybrid distributed energy systems with photovoltaic and diesel turbine generator. Electr. Power Syst. Res. **191**, 106877 (2021). https://doi.org/10.1016/j.epsr.2020.106877

16. Liu, X.Z., Yan, Z., Wu, J.Z.: Optimal coordinated operation of a multi-energy community considering interactions between energy storage and conversion devices. Appl. Energy **248**, 256–273 (2019). https://doi.org/10.1016/j.apenergy.2019.04.106

17. Yang, H.M., Xiong, T.L., Qiu, J., Qiu, D., Dong, Z.Y.: Optimal operation of DES/CCHP based regional multi-energy prosumer with demand response. Appl. Energy **167**, 353–365 (2016). https://doi.org/10.1016/j.apenergy.2015.11.022

18. Yang, W.J., Guo, J., Vartosh, A.: Optimal economic-emission planning of multi-energy systems integrated electric vehicles with modified group search optimization. Appl. Energy **311**, 118634 (2022). https://doi.org/10.1016/j.apenergy.2022.118634

19. Zheng, J.H., Chen, J.J., Wu, Q.H., Jing, Z.X.: Multi-objective optimization and decision making for power dispatch of a large-scale integrated energy system with distributed DHCS embedded. Appl. Energy **154**, 369–379 (2015). https://doi.org/10.1016/j.apenergy.2015.05.023

20. Ali, M.N., Mahmoud, K., Lehtonen, M., Darwish, M.M.F.: An efficient fuzzy-logic based variable-step incremental conductance MPPT method for grid-connected PV systems. IEEE Access **9**, 26420–26430 (2021). https://doi.org/10.1109/ACCESS.2021.3058052

21. Smith, B.K., Pratt, A., Maksimovic, D.: Accounting for lithium-ion battery degradation in electric vehicle charging optimization. IEEE J. Emerg. Sel. Top. Power Electron. **2**(3), 691–700 (2014). https://doi.org/10.1109/JESTPE.2014.2315961

Automatic Generation and Incremental Update Method of Single Line Diagram of Distribution Network

Peng Sen$^{(\boxtimes)}$ [ID], You Feng, Cheng Wei, Liu Shi-jin, Xu Cheng-long, Zheng Hao-quan, and Zhang Miao

Nanjing NARI Information and Communication Technology Co., Ltd., Nanjing 211106, China
`pengsen@sgepri.sgcc.com.cn`

Abstract. The single-line diagram of the distribution network is an electrical wiring diagram with a single feeder as the unit. It realizes the visual expression of the topological connection relationship of the distribution network through graphical symbols and connections, and is one of the most important graphic materials for distribution network management. According to the actual needs of automatic generation of distribution network single-line diagram, this paper provides a method for automatic generation of distribution network single-line diagram based on the trunk-and-branches model. The method firstly carried out the creation of the trunk line, branch line and the calculation of the branch layout direction, then carried out the initial branch layout and local stretching, and finally carried out the branch local shrinkage and automatic routing. In addition, compared with the existing methods, this method also supports the local incremental update of the stock single-line diagram, which can basically ensure the original layout remains unchanged. After verification, based on the automatic generation method of the distribution network single-line diagram, the single-line diagram that meets the requirements of accuracy and aesthetics can be automatically generated. Through a local incremental update, a single-line diagram can be obtained that actually guarantees the layout of the original single-line diagram unchanged, meeting the strong demand of users who wish to keep the layout of the original single-line diagram substantially unchanged.

Keywords: Single line diagram · Trunk line · Branch line · Automatic mapping · Overlaps · Partial contraction

1 Introduction

The electrical wiring diagram is a visual representation of the topology state of the power grid, and it is an indispensable graphic material for the operation and management of the power system [1–3]. The distribution network single-line diagram is an electrical wiring diagram that visualizes the distribution network by using the prescribed graphic symbols and equipment wiring. The hand-drawn single-line diagram still has advantages in terms of user customization and drawing aesthetics, but its drawing efficiency is low,

the drawings cannot be updated according to the topology data in time, and it is difficult to find drawing errors in time [4–7]. Automatic drawing of single-line diagram with computer program can effectively solve the above problems [8–10].

When doing map layout, users prefer the orthogonal layout style [11–15], and the same is true in the distribution network business. The existing one-line diagram automatic drawing is mainly divided into three basic methods: rule method, optimization mathematical model method, force field model or dynamic algorithm [16]. In this paper, an algorithm for automatic generation of one-line diagram of distribution network is proposed. This algorithm is based on the trunk line-branch line model, which is a typical rule method.

Reference [16] pointed out that when the one-line diagram based on the rule method is automatically drawn, there will be space whitening, resulting in a waste of space. The trunk-branch model, as a typical rule-based graphing method, also has this obvious disadvantage. This paper has done a lot of work on this, and finally solved this problem by using local stretching and local shrinking.

The trunk-and-branches model is to draw the trunk line with the longest branch line with the weighted path in the feeder as the trunk line according to the tree structure of the single-line diagram after weighting each device according to its complexity; and then draw the lower level connected to the trunk line. The branches are drawn on both sides of the trunk, and all the branch lines of the trunk line are drawn horizontally or vertically; then the lower-level branches connected to the trunk are used as the trunk line to complete the drawing of a deeper branch line; in this way, the trunk and branches are alternately drawn until All branches are drawn. The traditional trunk line branch line model cannot solve the equipment cover problem well, and the single-line diagram after the equipment cover is solved usually cannot meet the requirements of beauty and compactness.

In this paper, we propose a combination of local stretching and local shrinkage for equipment coverage solution, that is, the initial layout of the single-line diagram is partially stretched to solve the equipment coverage problem, and then the single-line diagram is partially shrunk to achieve compact and beautiful requirements after all local stretching is completed. To achieve compact and beautiful requirements. Finally, the line exploration method towards the target is used for automatic routing [17–23].

In addition, the existing automatic generation methods of distribution network single-line diagram rarely consider the incremental update layout of the stock single-line diagram. In view of this requirement, we have further optimized the method in this paper.

2 Trunk Line and Branch Line Generation

In this paper, the main line is referred to as the trunk, and the branch line is referred to as the branch. In order to support the two situations of new mapping and incremental update of stock single-line diagrams (the layout of the original diagram needs to be preserved as much as possible), this method is differentiated from the generation of trunk and branch.

2.1 New Layout Algorithm: A Full Layout Method Based on the Trunk Branch Model

(1) Weight Calculations

Before creating a trunk branch, each device needs to be assigned a weight, and this weight is used for trunk and branch path tracing.

The devices in the grid system are divided into container devices and simple devices. The container devices include distribution stations, box cabinets, etc., which contain a certain number of simple devices. In this paper, the weight of each device has three representational dimensions, attribute weight, base weight, and layout weight. Details are as follows:

The attribute weights are determined by the device attributes of each device itself, and have a one-to-one mapping relationship with the attributes of the device. The corresponding device attribute weight table needs to be determined according to business needs and user usage habits. The attribute weight is denoted by a capital A. The attribute weight correspondence table used in this paper is shown in Table 1. The branch device is a virtual container device.

Table 1. Device attribute weight correspondence table.

Equipment type	Type	Value
Branch equipment with t-contact	Integer	10
Branch equipment without t-contact	Integer	5
Large switching station	Integer	10
Other container equipment	Integer	8
Contact switch	Integer	8
Transformer	Integer	4
Other simple equipment	Integer	1

The base weight is the initial weight that each layout unit has before the trunk and branch are created. The layout unit of a simple device is itself, and its base weight is the same value as the attribute weight. The layout unit of the container device is a whole composed of simple devices in the container, and its basic weight is determined by the attribute weight of the container device and the attribute weight of the simple device in the container. The base weight can be regarded as the attribute weight of the whole layout unit, and the base weight is represented by the capital letter B.

The layout weight is the actual weight of the layout unit when participating in the layout, and its fundamental significance is to correctly characterize the complexity or importance of a node device. The layout weight is determined by the base weight of the device and the number of downlink branches. This paper uses the capital letter L to denote layout weights.

The calculation formula of the above weight is shown in Table 2, in which the weight enumeration function $A = EnumA(Type)$ can be determined from Table 1.

Table 2. Weight calculation formula table.

Name	Identifier	Formula	Definition of symbols in formulas
Attribute weight	A	$A = EnumA(Type)$	Type: The device type of the current device EmumA(): Enumeration function for attribute weights
Base weight	B	$B = A_0 + \sum_{j=1}^{N} A_j$	A: The weight of the current device attribute A_1-A_N: Simple device attribute weights included
Layout weight	L	$B = B_0 + \sum_{i=1}^{M} C_j$	B_0: The base weight of the current device C_1-C_M: Attribute weight of the virtual branch device connected to the next

Then the calculation formula of the layout weight of a device is as formula (1)

$$B = B_0 + \sum_{i=1}^{M} C_j \tag{1}$$

Among them, B_0 is the basic weight of the current device, and C_i is the attribute weight of the i-th branch connected to it.

(2) Create Trunk and All Branches

Taking the power point as the starting point, the branch with the longest weighted path is traced as the trunk, which is recorded as the 0-level branch. Taking the level 0 branch as the parent branch, continue to track the next level child branch connected to the parent branch. The tracked sub-branch is then tracked as a parent branch, and the parent branch and the sub-branch are alternated until all devices are tracked, and then the generation of all branches is completed. The trunk traced from the power point is named as the 0-level branch, the next-level branch traced with all the devices of the 0-level branch as the starting point is named as the 1-level branch, and so on until the (n−1) level branch is All branches are created. A device with a downlink branch is called a t-node device.

2.2 Incremental Layout Algorithm: Based on the New Layout Algorithm, Make Local Adjustments

When creating trunks and branches, branch tracking and creation are no longer based on device weights, but the branches are weakened to consist of 1 device, and the trunk is weakened to 2 devices. In this way, in addition to the power supply and end devices, each device is a t-node device. Except for the power supply, each device exists only on a single-node branch consisting of itself.
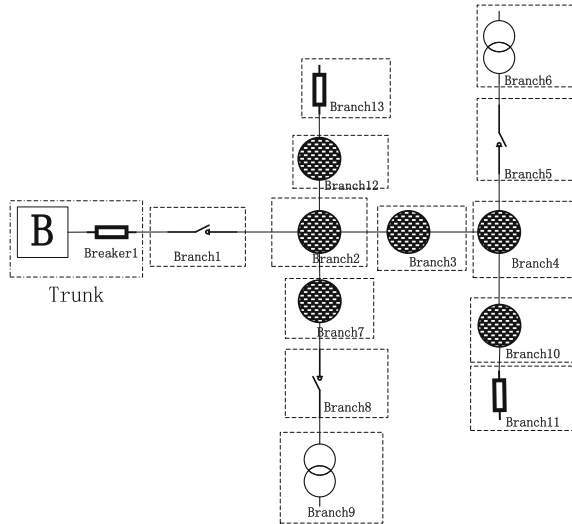
Fig. 1. Schematic diagram of trunk and branch creation for incremental update layout of stock single-line diagram.

As shown in Fig. 1, incremental layout of the example stock single-line diagram will create 1 trunk and 13 branches, where the trunk has two devices and each branch has one and only one device. Except for power point B and leaf node devices (devices corresponding to branches 6, 9, 11, and 13), the remaining devices corresponding to each branch are t-connected node devices in the trunk branch model.

3 Determine the Layout Direction of the Trunk Line/Branch Line

Any branch is arranged in a straight line with four layout directions: left-to-right, right-to-left, bottom-up, top-down. According to the difference between the new map and the incremental update map, the layout direction of the main line and branch line is determined to be different.

3.1 Determine the Layout Direction of the Newly Drawn Trunk and Branch

First, the 0-level branch layout direction is determined according to the user input, and then all remaining branch layout directions are determined according to the 0-level branch layout direction. If the level 0 branches are laid out from left to right, the level 1 branches connected to it are evenly distributed on both sides of the level 0 branches, which is a bottom-up or top-down layout. Likewise, the level 2 branches are evenly distributed on both sides of the level 1 branches, either from left to right or from right to left. From this, it is recursive to $(n-1)$ level branches, and the determination of all branch directions is completed. When the layout direction of the level 0 branch is the other three, the same can be deduced.

3.2 Determine the Layout Direction of the Main Line and Branch Line of the Incremental Update into the Map

Incremental mapping is to assign a value to the branch layout direction through the equipment coordinates of the stock one-line diagram. The branch layout direction needs to reflect the layout direction of the stock one-line diagram.

(1) Method of assigning the layout direction of any branch BranchHasCor with stock layout coordinates:
Obtain the topology trace path Trace1 from the power point to the current branch, get the branch BranchHasCorLast with the smallest topology step from BranchHasCor in Trace1 and also with stock coordinates; get the stock coordinates LastCoordinate of BranchHasCorLast and the stock coordinates CurrentCoordinate of BranchHasCor. BranchHasCorLast's stock coordinates LastCoordinate, BranchHasCor's stock coordinates CurrentCoordinate, calculate the direction vector A from LastCoordinate to CurrentCoordinate; calculate the direction vector A with Calculate the angle between the direction vector A and the four orthogonal directions of "left-to-right", "right-to-left", "down-up" and "up-down",take the layout direction of the smaller angle as the branch layout direction of the current branch.
(1) To assign the BranchNoCor layout direction to any branch that does not contain the stock layout coordinates:
Obtain the topology trace path Trace2 from the power point to the current branch, get the BranchHasLayOrient in Trace2 that has the smallest topology step from BranchNoCor and has finished assigning the branch layout direction; if there are only two branches adjacent to BranchHasLayOrient, set the Branch layout direction of BranchNoCor to be the same as BranchHasLayOrient. BranchHasLayOrient, the branch layout direction of BranchNoCor is set to the same as BranchHasLayOrient; if there are more than two branches adjacent to BranchHasLayOrient, the branch layout direction of BranchNoCor is set to the same as BranchHasLayOrient; if there are more than two branches adjacent to BranchHasLayOrient, the branch layout direction of BranchNoCor is set to If there are more than 2 branches adjacent to BranchHasLayOrient, the branch layout direction of BranchNoCor is set to the vertical direction of the layout direction of BranchHasLayOrient, and the side that has been occupied less times is selected.

4 Initial Layout and Local Stretching

4.1 Initial Layout

(1) Carry out the trunk (level 0 branch) layout.
Set the coordinates of the first node of the trunk to (0, 0), and determine the coordinates of the next node according to the coordinates of the first node, layout spacing and layout

direction. Subsequent device coordinates use the previous device coordinates to complete the layout.

(2) Carry out the layout of all remaining branches.

(2.1) Determine the coordinates of the head node of the first-level branch according to the 0-level branch.

The head node of the level 1 branch is directly connected to the level 0 branch, and the connected level 0 branch equipment is called a t-connected equipment. According to the t-connected device coordinates in the 0-level branch and the layout direction of the 1-level branch, the coordinate calculation of the first node of the 1-level branch can be completed. According to the coordinates of the first node of the first-level branch, the branch direction and the layout spacing, the subsequent device coordinate assignment is completed in sequence.

(2.2) Recursive completion of subsequent branch coordinate layout.

By analogy, the 1-level branch layout can be completed according to the 0-level branch, and the 2-level branch layout can be completed according to the 1-level branch. And so on, until all branch layouts are completed.

4.2   Local Stretching

(1) Space Expansion Required for t-connection Node Information Group Layout

When determining the device coordinates of the head node of the lower branch according to the t-connection node, it is necessary to stretch along the direction of the t-connection device branch, so that the initial layout of the lower branch will not overlap and cover. Specifically, the layout space width w required for all branch layouts (the width along the branch layout direction where the t-junction node is located) is calculated. Taking the t-connection node as the starting point, expand the space of w/2 to the branch layout direction and the opposite direction of the t-connection node, which is used for the layout of the next level branch of the current t-connection node. Spatial expansion is to stretch related equipment in a certain direction by a certain distance to ensure that there is no equipment in a specific space.

(2) Cover Detection and Resolution

Completing the layout of the next device Dt according to the previous point device Dt-1, cover detection needs to be performed. Find the smallest enclosing rectangle of Dt−1 and Dt, and perform overlap detection between this enclosing rectangle and other "point devices" that have been laid out; locally stretch other "point devices" that overlap to eliminate the overlap; the stretching direction is the current "point device". Click Devices" layout direction (Figs. 2 and 3).
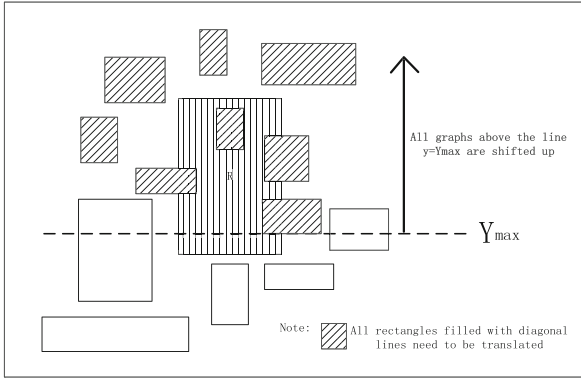
Fig. 2. Schematic diagram of partial stretching of bottom-up layout.
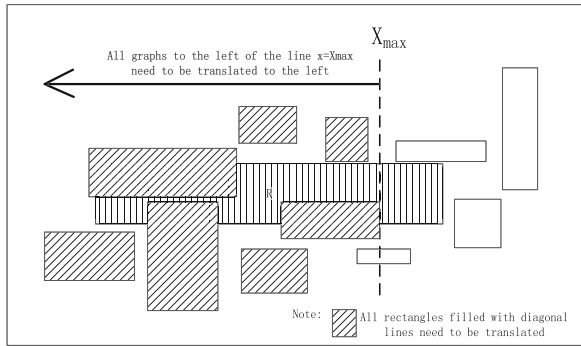
Fig. 3. Schematic diagram of partial stretching from right to left layout.

5   Partial Contraction

During the branch layout, the whole is stretched many times to solve the problem of covering the primitives, resulting in uneven and unreasonable spacing of primitives in the overall layout, and the layout is not beautiful. To correct this problem, a shrinking operation is required after all branch layouts are completed.

Like branch layout, branch shrinking is performed in a hierarchical manner. The shrinking operation adopts the heuristic method, and is executed in order from the branch tail node to the head node, and from the (n-1) level branch to the 0-level branch. Specific steps are as follows:

(1) Create a shrinkBranchQueue queue; in the order from the (n-1) level branch to the 0-level branch, load all the branches into the shrinkBranchQueue queue; the first element of the queue is the (n-1) level branch, and the tail element is the 0-level branch; There is no strict order between the branches of the same level, and there is a strict order between the branches of different levels.

(2) The shrinkBranchQueue is traversed sequentially from the head of the queue to the tail of the queue, and the following operations are performed on each branch C in the queue.

Perform the following operations on each point device Dm in the branch C in the order from the branch tail node to the branch head node:

(2.1) If Dm is the head node of the branch, calculate the best coordinate needCoor of Dm according to the parent branch of branch C;

(2.2) If Dm is not the first node of the branch, calculate the best coordinate needCoor of Dm according to the coordinates of the last device Dm-1 on Dm;

(2.3) Calculate the value to be translated moveValue that Dm is translated from the actual coordinates to needCoor;

needMoveList (including Dm) of all device node lists from Dm to the end node of branch C;

(2.5) Add all the subordinate branch devices in the drawing that are connected to the devices in the needMoveList, that is, all the devices that are still connected to the devices in the needMoveList after removing the internal connectivity of the branch C into the needMoveList.

(2.6) Perform a translation operation on all devices in the needMoveList according to the value moveValue to be translated.

(2.7) Check if there is equipment covering.

(2.7.1) If it does not exist, this local contraction is completed;

(2.7.2) If it exists, all devices in the needMoveList will be reversed and translated by one unit length;

(2.7.3) If there is still cover, repeat the rollback operation (2.7.2) until the cover of the primitive does not exist or the total rollback length exceeds the value to be translated;

(2.7.4) If the retracting distance exceeds the value to be translated, restore the coordinates of all the devices to be translated to the state before translation.

6   Carry Out Device Wiring

Wiring is the assignment of coordinates to the line device, and according to the type of wiring terminal equipment, it can be divided into two cases: the presence of a station outlet equipment and the absence of a station outlet equipment.

If the line device is connected to two endpoint devices that do not contain station exit points, the line device is assigned directly according to the point device coordinates, and there is no inflection point.

If it contains the outgoing line point, the wiring algorithm toward the target is called to perform the wiring operation. As shown in Fig. 4, the specific operation steps are as follows.

(1) At the starting point A, first explore laterally to the right with B' as the stage target point, and then turn around at point A1 after encountering an obstacle. The initial exploration direction can be determined according to the maximum exploration step priority principle.

(2) At point A1, B1 is the stage target point to explore vertically upward, and turn at point A2 after encountering obstacles. At this point the stage target point becomes B2.

(3) Repeat steps (1) and (2) until the stage target point and the target point B reunite and arrive.

(4) In the above steps, execute step (5) if a dead point is encountered, and step (6) if a critical point is encountered.

During the exploration process, when both horizontal and vertical exploration directions are blocked, the dead point is entered; when only one more successful horizontal or vertical exploration is needed to reach the end of the wiring, but the only exploration direction is blocked at this time, it is called entering the critical point.

(5) Handling dead points.

(5.1) Reverse exploration. At the current node, explore in the "opposite direction", and try to explore in the target direction at each step. Repeat this step.

(5.2) Backtrack. If you cannot find a way out in step (5.1), go back to the previous node and repeat step (5.1). If you still cannot find a way out, continue backtracking. If a new path cannot be explored even if you go back to the starting point, no valid wiring path exists for the current wiring terminal.

(6) Process the critical points.

(6.1) Calculate the offset around the obstacle based on the current obstacle node and the exploration direction.

(6.2) Calculate the next stage exploration target point based on the bypass offset.

(7) Perform wiring overlap detection and offset.

Each completed wiring needs to be overlapped with the existing wiring for detection and offset. Each completed wiring consists of several small line segments, which are divided into two categories: horizontal line segments and vertical line segments. If there is an overlap conflict, the current line segment is offset by one unit, and the operation is repeated until the overlap does not exist.

For the failed exploration that has not reached the end of the wiring, the dead point obstacle can be removed and the weak level wiring exploration can be carried out again. At this point the wiring will traverse the relevant equipment graphic elements.
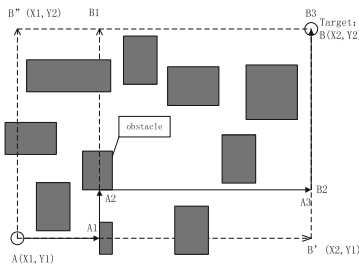
Fig. 4. Schematic diagram of automatic wiring.

7   System Implementation and Verification

It can be seen from the above that this algorithm not only supports the new layout of the signal-line diagram, but also supports the incremental layout that inherits the original

layout of the stock signal-line diagram. In this paper, the algorithm verification work is carried out for the new layout and the incremental layout:

7.1 Situation 1. Full Layout

At present, the local stretching method is commonly used in the overlapping and cross processing, such as the literature [17, 22, 23]. In this paper, the local stretching method is compared with the effect of this method.

The automatic generation process of the signal-line diagram is shown in Fig. 5–7. Figure 5 is a signal-line diagram after only the initial layout is performed, and there is serious cover; Fig. 6 is a signal-line diagram after partial stretching of the initial layout; Fig. 7 is a signal-line diagram after the shrinking operation is completed.

Combined with the above research, this automatic generation method of distribution network single-line diagram based on the trunk line branch line model is implemented in the actual project development, which meets the project requirements.
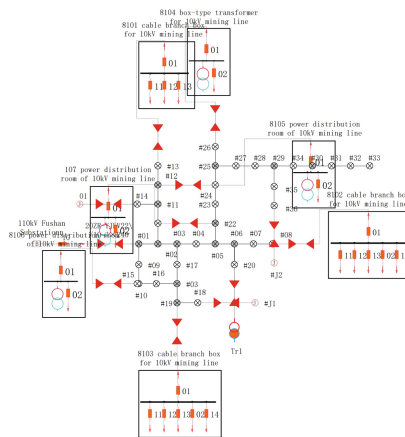
Fig. 5. Crossover phenomenon.

The single-line diagram with only the initial layout obviously has more equipment coverage. As shown in Fig. 5, there are more primitive coverages in the figure, especially where there are many branches in the t-section. For example, the tower "#15" overlaps with the tower "#10", and the distribution transformer station "107" is covered with multiple primitives.

The single-line diagram after local stretching no longer has the problem of equipment covering, but the equipment spacing becomes larger and there are uneven and unreasonable problems, as shown in Fig. 6.

Finally, the single-line diagram after the local shrinking operation meets the aesthetic requirements of compact equipment and no cover, which well meets the needs of users, as shown in Fig. 7.

The traditional single-line diagram automatic generation method that only performs local stretching will inevitably lead to the problem of excessive distance between some
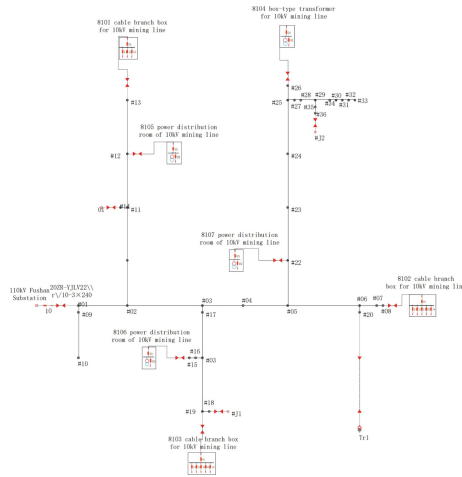
Fig. 6. Local stretching to eliminate cross occlusion.
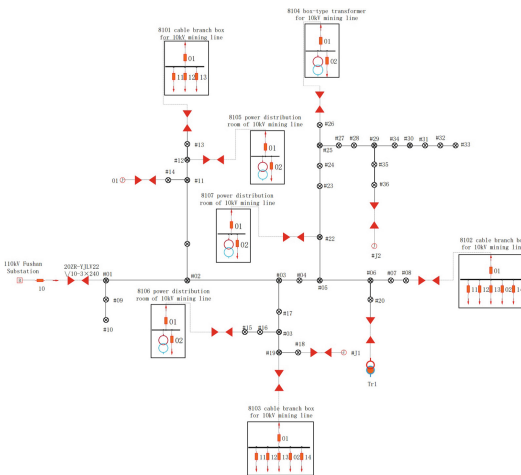
Fig. 7. Final single-line diagram after partial contraction.

devices in Fig. 6 after local stretching. The local shrinking algorithm proposed in this paper shrinks the spacing of the shrinkable parts to a reasonable value after local stretching, and finally obtains a single-line diagram that is compact and has no overlapping and crossing as shown in Fig. 7.

7.2   Situation 2. Incremental Layout

As shown in Fig. 8 and Fig. 9, the original signal-line diagram of a feeder shown in Fig. 8 is stored, and the signal-line diagram shown in Fig. 9 is obtained after this method is used

to map, and the aesthetics has been greatly improved. However, the relative positional relationship between the devices has not changed.

As shown in Fig. 8, the stock single-line diagram is laid out in a folded manner as a whole. The one-line diagram shown in Fig. 8 is laid out from left to right starting from the power supply, until it is about the length of the entire trunk, then bends down and starts to be laid out from right to left until all devices are laid out.

As shown in Fig. 9, the single-line diagram formed by the incremental mapping method described in this paper maintains the original folded layout, and the specific layout details are updated and beautified. The specific corresponding bending equipment is also the same, and the relative position between each t-connecting equipment and the downlink trunk is also consistent with Fig. 8.
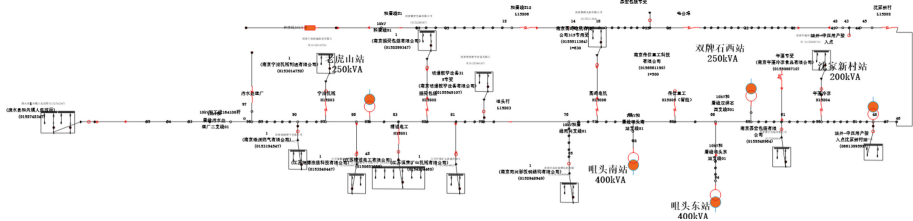
Fig. 8. Original single-line diagram of a feeder.
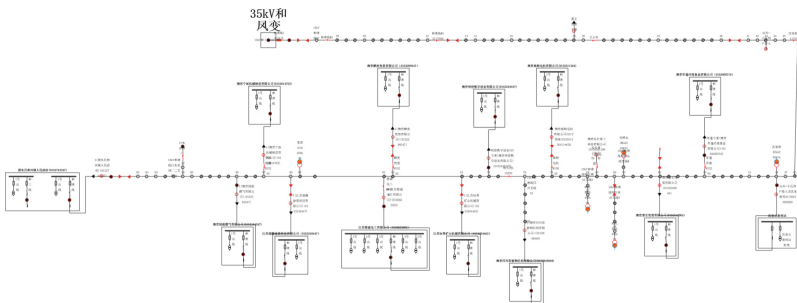
Fig. 9. The effect of the original image after incremental image formation.

It can be seen that when using this incremental layout method to automatically generate a single-line diagram, it is more refined due to the reduction of the granularity of the layout unit, which improves the flexibility of the layout. A single-line diagram with a consistent layout of line diagrams.

8   Discussion

The automatic generation method of distribution network single-line diagram based on the trunk line branch line model proposed in this paper satisfies the basic requirements of single-line diagram drawing without equipment cover, horizontal and vertical layout,

etc.; and adding local shrinkage operation, it has remarkable aesthetics in single-line diagram. Improve. The specific advantages are as follows:

(1) The local stretching after the initial layout of the branch can completely solve the problem of device occlusion.

(2) Perform local shrinking operation on the partially stretched single-line diagram to make the single-line diagram more compact and beautiful.

(3) The wiring operation is carried out by using the hierarchical barrier-winding exploration method towards the target, which can complete the wiring in all scenarios and avoid wiring overlap.

(4) It supports incremental update layout of the stock single-line diagram, and can incrementally generate a distribution network single-line diagram that inherits the original layout.

References

1. Chen, S., Song, S, Li, L., et al.: Survey on smart grid technology. Power Syst. Technol. **33**(8), 1–7 (2009)
2. Wang, B., He, G., D, S.: Self-generation of full graphics and 3D visualization based on CIM. Autom. Electric Power Syst. **34**(4), 55–58 (2010)
3. Hao, X.: Research of Automatic Generation for Single-Line Diagram of Electrical Power System, pp. 2–4. Shandong University, Jinan (2016) https://doi.org/10.7666/dY3037194
4. Fu, Y.: The Research and Application of the Automatic Generation of Connect Diagram for Distribution Network Based on Feeder Groups. North China Electric Power University, Beijing (2013) https://doi.org/10.7666/dY2384036
5. Han, W.: Automatic Generation of Single-Line Diagram for Distribution Network Based on CIM Model, pp. 2–3. Donghua University, Shanghai (2013)
6. Jianmin, Z., Yi, Y.: Automatic layout of uniform wiring diagram of provincial transmission network based on new force derivative algorithm. Autom. Electr. Power Syst. **37**(11), 107–111 (2013). https://doi.org/10.7500/AEPS201211096
7. Wei, D.: Research on Automatic Mapping Technology of Power System Single-Line Diagram. Shandong University, Jinan (2017)
8. Canales –Ruiz, R., Garibay, D.T., Alonso- Concheiro, A.: Optimal automatic drawing of one-line diagrams. IEEE Trans. Power App. Syst. **98**(2), 387–392 (1979) https://doi.org/10.1109/TPAS.1979.319329]
9. Jianmin, Z., Ye Yi, X., Guanhua.: Consistent Design and Automatic Drawing of Modulo-Digital Diagram of Substation Single Line Diagram. Autom. Electr. Power Syst. **37**(9), 84–91 (2013). https://doi.org/10.7500/AEPS201210018
10. Lendak, I., Erdeljan, A., Capko, D., et al.: Algorithms in electric power system single-line diagram creation. The soft computing approach. In: Proceedings of 2010 IEEE International Conference on Systems, Man and Cybernetics, Istanbul, Turkey, pp. 2867–2873. IEEE, Piscataway (2010)
11. Aggarwal, A., Rao Kosaraju, S., Pop, M.: Drawing of two-dimensional irregular meshes. In: International Symposium on Graph Drawing, pp. 1–14. Springer, Heidelberg (1998) https://doi.org/10.1007/3-540-37623-2_1
12. Kobourov, S.G.: Spring embedders and force directed graph drawing algorithms (2012) arXiv preprint arXiv:1201.3011

13. Angelini, P., et al.: Simultaneous orthogonal planarity. In: Hu, Y., Nöllenburg, M. (eds.) GD 2016. LNCS, vol. 9801, pp. 532–545. Springer, Cham (2016). https://doi.org/10.1007/978-3-319-50106-2_41

14. Bläsius, T., Krug, M., Rutter, I., et al.: Orthogonal graph drawing with flexibility constraints. Algorithmica **68**(4), 859–885 (2014)

15. Bridgeman, S., Tamassia, R.: Difference metrics for interactive orthogonal graph drawing algorithms. In: Whitesides, S.H. (ed.) GD 1998. LNCS, vol. 1547, pp. 57–71. Springer, Heidelberg (1998). https://doi.org/10.1007/3-540-37623-2_5

16. Jianmin, Z., Chengfeng, Q., Fenghua, W., et al.: Single-line diagram of substation centralized distribution network part two initial automatic layout. Autom. Electr. Power. Syst. **43**(19), 124–131 (2019). https://doi.org/10.7500/AEPS20180827010

17. Yong, C., Qijun, D., Hong, Z.: Algorithm for automatic generation of single-line diagram of distribution network without overlapping and crossing. Electr. Power Autom. Equipment **11**, 90–93 (2010). https://doi.org/10.3969/j.issn.1006-6047.2010.11.022

18. Yao, H.: Research on automatic wiring of printed circuit boards in circuit CAD. Northwestern Polytechnical University, Xi'an (2004). 17.18. https://doi.org/10.7666/dy584828]

19. Hong, X.: SCADLS: a useful line search routing algorithm. Comp. Eng. 1992(05), 52–56. [doi: CNKI:SUN :JSJC.0.1992-05-010]

20. Hui, Y., Daxiong, L., Yan, Y.: Goal-driven routing algorithm based on shape line exploration. ModernMechanics. **4**, 50–52 (2007). https://doi.org/10.3969/j.issn.1002-6886.2007.04.022

21. Yang, G.: A line exploration method for computer automatic routing. J. Shanxi Univ. (Nat. Sci. Edn.) **19**(3), 283–287 (1996). [doi: CNKI:SUN:SXDR.0.1996-03-011]

22. Liu Jian, W., Yuan, L.G.: Conversion of distribution feeder geographic map to electrical wiring diagram. Autom. Electr. Power Syst. **29**(14), 73–77 (2005). https://doi.org/10.3321/j.issn:1000-1026.2005.14.015

23. Jianmin, Z., Jian, L.: Automatic generation of power distribution single-line diagram based on CIM/SVG and object-oriented. Autom. Electr. Power Syst. **32**(22), 61–65 (2008). https://doi.org/10.3321/j.issn:1000-1026.2008.22.013

Influence and Dominant Factors Determination of Errors in the Parameter Identification of Three-Winding Transformer with PMU Data

Jing Ma, Haiyan Hong, Lei Gu, He Kong, Feiyang Xu, and Ancheng Xue[✉]

State Key Laboratory of Alternate Electrical Power System with Renewable Energy Source, North China Electric Power University, Changping District, Beijing 102206, China
acxue@necpu.edu.cn

Abstract. The online identification of transformer parameters is influenced by the measurement errors, and engages deviations which could deteriorate the analysis and control of power system. However, the characteristics of influence of error are unknown. This paper presents the influence of measurement error and transformer ratio on identified transformer parameter, and determines the dominant factors, with the sensitivity analysis. Specifically, first, the parameter identification method for transformer based on the three-winding equivalent model is presented and simulated. Secondly, the analytical and approximate calculation methods for the sensitivities of the identified parameters with respected to the phase angle and amplitude measurement error, and transformer ratio error are introduced. Thirdly, with simulations, the correctness of the sensitivity analysis and approximate calculation results are verified. Furthermore, the characteristics of the different sensitivities are compared. Finally, with the characteristics of the sensitivities, the dominant factors for the identified transformer parameter are determined. That is, the dominant factors for the identified resistance are the errors of voltage phase angle and amplitude, and ratio of high-middle voltage side. The dominant factors for the identified reactance are errors of voltage amplitude and phase angle, and errors of ratio of high-middle voltage side and high-low voltage side. For example, when the voltage amplitude measurement error is 1%, the relative error of the identified resistance and reactance can reach more than 5000% and 20% respectively.

Keywords: Three-winding transformer · Parameter identification · Sensitivity analysis · Dominant factors · PMU · Data error · Influence characteristics

1 Introduction

Transformer is one of the important equipment for power transmission in power system. Accurate transformer parameters are the basis of analysis, operation and control of power system, and play a vital role in ensuring the safe, reliable and stable operation of power system [1–4].

Currently, the methods for transformer parameter identification could be mainly divided into three categories: 1) the theoretical calculation methods, 2) the traditional offline identification methods, 3) the online identification methods based on supervisory control and data acquisition (SCADA) and phasor measurement unit (PMU) data. Compared with the theoretical calculation methods and the offline identification methods, the online identification methods can identify transformer parameters under actual operating conditions more accurately, thus, they have attracted widespread interest, due to its instantaneity and economy [5, 6].

On the other hand, a lot of PMUs have been installed in China's power grid. With the PMU data, the transformer can be decoupled from the system, that is, it can be identified independently. In addition, identification with PMU data could avoid the error caused by imperfectly synchronized SCADA data and improve the accuracy of identification results. Therefore, a lot of methods have been proposed. For example, Ref. [7] constructs a model for calculating transformer ratio and reactance parameters, and gives the confidence intervals for the identified parameters using PMU data with the normal distribution parameter estimation. Ref. [8] uses the Gauss-Newton for iterative solution and uses the mean estimation method to estimate the positive sequence reactance parameter of the transformer. Ref. [9] provides an idea of using the phase component method to identify the positive sequence parameters of double-winding transformer parameters under three-phase imbalance. Ref. [10] proposes a step-by-step identification method for positive sequence parameters of transformer windings based on median robust estimation.

However, there are inevitable errors in the field PMU measurement data, which would influence the identified results, and even lead to the problem of identifiability and credibility of the identified results. That is, if the influence is small, the identified results is credible and may be close to the true value, and vice versa, they may deviate from the true value and incredible.

It is worth noting that the current research about the influence of errors on grid parameter identification are mainly focused on the identification of line parameter. For example, Ref. [11], analyzes the influence of the amplitude of voltage and current on the identified line parameters, combined with relative sensitivity. And the influence of voltage phase angle error on each identified parameter is analyzed preliminarily. Ref. [12] analyzes the influence of measurement errors of different operating conditions on the estimation of line parameters by considering the accuracy level of the transformer and the influence on its accuracy under different load scenarios and using the IEEE-14 node system. Ref. [13] studies the influence on the identified results of line parameters from three aspects: identification model, parallel high resistance, and measurement error. However, the influence of PMU error on transformer parameter identification is rarely reported.

As stated above, the characteristic of influence of error on identified parameters of three-winding transform are unknown. In recognized of this, this paper analyzes the influence of error on identified parameter of three-winding transformer in terms of both transformer ratio and measurement error, and determines the dominant factors, with the sensitivity analysis.

The remainders of the paper are organized as follows. The equivalent model and parameter identification method for the three-winding transformer are presented and

verified by simulation in Sect. 2. And then, the analytical method and approximate method to calculate the sensitivities to analyze the characteristics of influence of error is introduced in Sect. 3. The correctness of the sensitivity calculation results is verified, and the characteristics of sensitivity are analyzed via simulations in Sect. 4. Combined with characteristics of the sensitivities, the dominant influencing factors of transformer parameter identification are determined in Sect. 5. Finally, the conclusions are provided in Sect. 6.

2 Parameter Identification Method for Three-Winding Transformer

In this section, the equivalent model for three-winding transformer is acquired. Then, the transformer parameter identification method is introduced, whose effectiveness is by using simulation data.

2.1 Mathematical Model

The equivalent model for three-winding transformer is shown in Fig. 1, where $\dot{U}_i$, $\dot{I}_i$, $Z_i = R_i + jX_i$ ($i = 1,2,3$) represent the positive-sequence voltage phasors, current phasors and the impedance on the high-voltage, middle-voltage and low-voltage side of the transformer respectively; $\dot{U}_0$ represents the voltage at neutral point; Z_m represents the excitation impedance; k_{12} represents the ratio between the high-voltage side and the middle-voltage side; k_{13} represents the ratio between the high-voltage side and the low-voltage side.
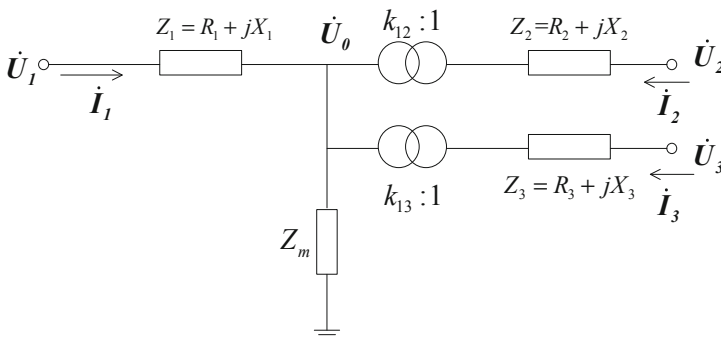
Fig. 1. Equivalent circuit for three-winding transformer

As shown in Fig. 1, the voltage at neutral point can be calculated using the measurements and the impedance of the three-winding transformers. The equations are as follows:

$$\dot{U}_0 = \dot{U}_1 - \dot{I}_1 Z_1$$
$$\dot{U}_0/k_{12} = \dot{U}_2 - \dot{I}_2 Z_2 \tag{1}$$
$$\dot{U}_0/k_{13} = \dot{U}_3 - \dot{I}_3 Z_3$$

Let $\dot{U}_i = e_i + jf_i$ ($i = 0, 1, 2$) and $\dot{I}_i = I_i \cos\theta_i + jI_i \sin\theta_i$ ($i = 1, 2, 3$), expand the real part and imaginary part separately. The following equations can be obtained.

$$I_1 R_1 \cos\theta_1 - I_1 X_1 \sin\theta_1 = e_1 - e_0$$
$$I_1 R_1 \sin\theta_1 + I_1 X_1 \cos\theta_1 = f_1 - f_0$$
$$I_2 R_2 \cos\theta_2 - I_2 X_2 \sin\theta_2 = e_2 - e_0/k_{12}$$
$$I_2 R_2 \sin\theta_2 + I_2 X_2 \cos\theta_2 = f_2 - f_0/k_{12} \tag{2}$$
$$I_3 R_3 \cos\theta_3 - I_3 X_3 \sin\theta_3 = e_3 - e_0/k_{13}$$
$$I_3 R_3 \sin\theta_3 + I_3 X_3 \cos\theta_3 = f_3 - f_0/k_{13}$$

Furthermore, eliminate the voltage of the neutral point in (2), the measurements satisfy:

$$I_1 R_1 \cos\theta_1 - I_1 X_1 \sin\theta_1 - (k_{12} I_2 R_2 \cos\theta_2 - k_{12} I_2 X_2 \sin\theta_2 = e_1 - k_{12} e_2$$
$$I_1 R_1 \sin\theta_1 + I_1 X_1 \cos\theta_1 - (k_{12} I_2 R_2 \sin\theta_2 + k_{12} I_2 X_2 \cos\theta_2 = f_1 - k_{12} f_2$$
$$I_1 R_1 \cos\theta_1 - I_1 X_1 \sin\theta_1 - (k_{13} I_3 R_3 \cos\theta_3 - k_{13} I_3 X_3 \sin\theta_3) = e_1 - k_{13} e_3 \tag{3}$$
$$I_1 R_1 \sin\theta_1 + I_1 X_1 \cos\theta_1 - (k_{13} I_3 R_3 \sin\theta_3 + k_{13} I_3 X_3 \cos\theta_3) = f_1 - k_{13} f_3$$

2.2 Identification Method

For (3), at time k, the parameters $x = [R1, X1, R2, X2, R3, X3]^{\mathrm{T}}$ to be identified satisfy the following linear equation.

$$A_k x = B_k \tag{4}$$

Among them, A_k represents 4×6 matrix of current phasor and transformer ratio at time k, B_k represents 4×1 matrix of voltage phasor and transformer ratio at time k.

Consider multiple times, then:

$$Ax = B \tag{5}$$

where:

$$A = \begin{bmatrix} A_1 \\ \vdots \\ A_n \end{bmatrix}, B = \begin{bmatrix} B_1 \\ \vdots \\ B_n \end{bmatrix} \tag{6}$$

Specifically, for the data of multiple times, the linear Eq. (5) is satisfied, the dimension of matrix A is 4n × 6 (n ≥ 2), and the dimension of matrix B is 4n × 1. Taking a three-winding transformer as an example, the specific target equation is shown in (7).

$$
\begin{bmatrix}
I_1\cos\theta & -I_1\sin\theta_1 & -k_{12}I_2\cos\theta_2 & k_{12}I_2\sin\theta_2 & 0 & 0 \\
I_1\sin\theta_1 & I_1\cos\theta_1 & -k_{12}I_2\sin\theta_2 & -k_{12}I_2\cos\theta_2 & 0 & 0 \\
I_1\cos\theta & -I_1\sin\theta_1 & 0 & 0 & -k_{13}I_3\cos\theta_3 & k_{13}I_3\sin\theta_3 \\
I_1\sin\theta_1 & I_1\cos\theta_1 & 0 & 0 & -k_{13}I_3\sin\theta_3 & -k_{13}I_3\cos\theta_3 \\
\vdots & \vdots & \vdots & \vdots & \vdots & \vdots
\end{bmatrix}
\begin{bmatrix}
R_1 \\ X_1 \\ R_2 \\ X_2 \\ R_3 \\ X_3
\end{bmatrix}
=
\begin{bmatrix}
e_1 - k_{12}e_2 \\
f_1 - k_{12}f_2 \\
e_1 - k_{13}e_3 \\
f_1 - k_{13}f_3 \\
\vdots
\end{bmatrix}
$$

$$(7)$$

Since the data of single time can establish four equations, at least two times PMU data at different power flow conditions are needed in order to ensure the non-singularity of matrix A.

According to (8), the transformer winding parameters x could be identified by using multiple sets of measurement data. The objective function can be expressed as.

$$
J = \|Ax - B\|^2 = \sum_{i=1}^{n} \|v_i\|^2 \tag{8}
$$

The least squares method is used to identity x, and the parameter identification results can be expressed as follows.

$$
x = (A^T A)^{-1} A^T B \tag{9}
$$

In addition, considering that one identification result can be obtained with each set of PMU steady-state operating data, the median robust method [10] is used to obtain better identification results based on multiple identification results from multiple sets of times.

$$
\begin{aligned}
R_{final} &= R_{0.5} \\
X_{final} &= X_{0.5}
\end{aligned}
\tag{10}
$$

2.3 Simulation Verification

A three-winding transformer is modeled in Simulink as shown in Fig. 2. The rated voltage of each side of the transformer is 500 kV/220 kV/35 kV respectively, the tap position is set according to the rated voltage. The winding connection type is YN/yn0/y0. Multiple sets of steady-state measurements are obtained by changing the load. In this paper, 2 operating conditions (Load 1 and Load 2) are set to be constant load models.
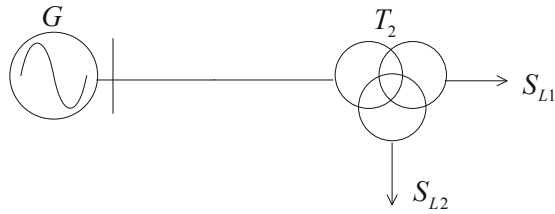
Fig. 2. Simulation system with a three-winding transformer

In the simulation, the load 1 is kept unchanged, and only the load 2 is changed to obtain the steady-state PMU measurements at 2 conditions, which include the amplitude and phase angle of the three-phase voltage and current on the three sides of the transformer. The identified results obtained by bringing the measured data into the identification equation are shown in Table 1.

Table 1. Simulation results of parameter identification

Parameters	Setting value (Ω)	Identified value (Ω)	Relative error (%)
R_1	0.2205	0.220499	-4.05×10^{-4}
R_2	0.02645	0.0264508	0.0011
R_3	0.0057	0.00569	-2.26×10^{-4}
X_1	57.33	57.334	0.0071
X_2	-1.587	-1.602	0.9585
X_3	0.44064	0.4398	-0.1854

The identified value and the setting value as well as the error between them are given in Table 1. As shown in Table 1, the identified value of transformer parameters is close to the setting value, which indicates the effectiveness of the method.

3   Methods for Sensitivity Calculation

The identification equations for transformer parameters shows that the identified results are related to the measurement error of voltage and current phasors of three windings and the transformer ratio. To study the influence characteristics of measurement errors to parameter identification, the sensitivity calculation method is introduced in this section, which includes analytical calculation method and approximate calculation method.

3.1   Analytical Calculation Method

The analytical calculation method uses the sensitivity function to analyze the influence of measurement errors on parameter identification. Generally, the sensitivity function is

non-linear, but when the parameter varies little, the nonlinear sensitivity function can be approximated as a linear function. The linear function is usually simply the first-order derivative of the response to the parameter to be determined, which is obtained under a set of rated parameter values. This function is called the first-order sensitivity function. For the sensitivity calculation of transformer parameter identification, the first-order normalized sensitivity function is adopted.

The relationship between variable f and parameter x is $f = f(x)$, and the commonly used first-order sensitivity function expression is:

The absolute sensitivity function is $S_x^f = \left.\frac{d\,[f(x)]}{d\,x}\right|_{x_0}$, which is often used to for theoretical research.

The relative sensitivity function is $S_x^f = \left.\frac{d\,(lnf)}{d\,x}\right|_{x_0} = \left|\frac{df/f}{d\,x/x}\right|$, which is very practical to compare the parameter variation effects. For (3), since it is impossible to calculate the relative sensitivity function of the parameters to be identified directly, the identification equations at two times can be written to solve the parameters, then the sensitivity can be calculated.

The sensitivity calculation expressions of the transformer resistance to the phase angle of voltage and current of three windings can be expressed as follows.

$$
\begin{aligned}
S_{U_{if}}^{Ri} &= \frac{\partial R_i/R_i}{\partial U_{i1f}/U_{i1f}} + \frac{\partial R_i/R_i}{\partial U_{i2f}/U_{i2f}} \\
S_{I_{if}}^{Ri} &= \frac{\partial R_i/R_i}{\partial I_{i1f}/I_{i1f}} + \frac{\partial R_i/R_i}{\partial I_{i2f}/I_{i2f}}
\end{aligned}
\tag{11}
$$

Note: The specific expressions for sensitivity in (11) are too complex to be displayed due to space constraints. The analytical calculation results are given in Sect. 4. (12)–(13) are processed using the same method.

The relative sensitivity calculation expressions of transformer resistance to the voltage and current amplitudes of three windings are shown in (12). U_{i1f}, U_{i2f}, I_{i2f} and I_{i1f} ($i = 1, 2, 3$) represent the voltage and current amplitudes of three windings at two snapshots respectively.

$$
\begin{aligned}
S_{U_{if}}^{Ri} &= \frac{\partial R_i/R_i}{\partial U_{i1f}/U_{i1f}} + \frac{\partial R_i/R_i}{\partial U_{i2f}/U_{i2f}} \\
S_{I_{if}}^{Ri} &= \frac{\partial R_i/R_i}{\partial I_{i1f}/I_{i1f}} + \frac{\partial R_i/R_i}{\partial I_{i2f}/I_{i2f}}
\end{aligned}
\tag{12}
$$

The relative sensitivity calculation expressions of the transformer resistance to errors of the ratio of high-middle voltage side and high-low voltage side are shown in (13).

$$
\begin{aligned}
S_{k_{12}}^{Ri} &= \frac{\partial R_i/R_i}{\partial k_{12}/k_{12}} \\
S_{k_{13}}^{Ri} &= \frac{\partial R_i/R_i}{\partial k_{13}/k_{13}}
\end{aligned}
\tag{13}
$$

The sensitivity calculation expressions of reactance are similar to the resistance sensitivity calculation (11)–(13), which are not repeated.

3.2 Approximate Calculation Method

When the approximate method is used to calculate the sensitivity of the parameters to the phase angle measurement error, deviations are added to the high, medium and low side voltage and current phase angle in the simulation, and the identified parameter R'_i, X'_i ($i = 1, 2, 3$) are obtained. The relative errors of the identification under different phase angle deviations are calculated using (14) and (15).

$$\frac{R'_i - R_i}{R_i} * 100 \tag{14}$$

$$\frac{X'_i - X_i}{X_i} * 100 \tag{15}$$

The calculation for the sensitivity of the amplitude measurement error and the transformer ratio error is similar to that above. Therefore, the calculation is not repeated.

4 Analyses of Sensitivity Characteristic

In this section, the correctness of the sensitivity calculation results is verified via simulations. Also, the influence characteristics of the amplitude measurement error, phase angle measurement error and transformer ratio error on the parameter identification are analyzed respectively.

4.1 Phase Angle Measurement Error

Two sets of steady-state PMU measurements are obtained by changing the load in the simulation in Sect. 2.3. Then, two methods introduced in Sect. 3 are applied to study the influence of phase angle measurement error on transformer parameters. The results are shown in Table 2.

Table 2. The sensitivity of transformer parameters to phase angle measurement error

Parameters		U_{1j}	U_{2j}	U_{3j}	I_{1j}	I_{2j}	I_{3j}
R_1	$A_1(\%)$	-539.80	449.04	2.30×10^{-6}	90.76	-6.09×10^{-10}	4.87×10^{-11}
	$A_2(\%)$	-539.80	449.03	1.45×10^{-8}	90.76	-1.04×10^{-9}	-1.34×10^{-8}
R_2	$A_1(\%)$	345.25	-324.10	-6.28×10^{-6}	-6.46×10^{-9}	-21.14	1.48×10^{-8}
	$A_2(\%)$	341.95	-320.81	-6.55×10^{-6}	-5.19×10^{-9}	-21.15	-4.50×10^{-9}

<div align="right">(continued)</div>

Table 2. (*continued*)

Parameters		U_{1j}	U_{2j}	U_{3j}	I_{1j}	I_{2j}	I_{3j}
R_3	$A_1(\%)$	−566.13	−133.60	672.80	6.35×10^{-11}	-3.01×10^{-9}	26.93
	$A_2(\%)$	−565.74	−133.99	672.80	-7.32×10^{-9}	8.05×10^{-9}	26.94
X_1	$A_1(\%)$	0.02	−0.01	1.67×10^{-8}	−0.002	-2.50×10^{-11}	2.88×10^{-11}
	$A_2(\%)$	0.02	−0.02	1.45×10^{-8}	−0.0013	1.32×10^{-12}	3.70×10^{-11}
X_2	$A_1(\%)$	−31.60	31.59	1.03×10^{-7}	2.27×10^{-11}	0.01	2.16×10^{-10}
	$A_2(\%)$	−31.29	31.28	1.09×10^{-7}	8.40×10^{-11}	0.01	-2.59×10^{-10}
X_3	$A_1(\%)$	2.93	−2.89	−0.03	-2.27×10^{-11}	2.86×10^{-11}	−0.01
	$A_2(\%)$	2.95	−2.90	−0.05	-1.83×10^{-10}	-8.72×10^{-11}	−0.0045

Note: A_1 represents the result of approximate calculation method, and A_2 represents the result of analytical calculation method.

Table 2 shows that the analytical calculation results are close to the approximate calculation results, which verifies the correctness of the sensitivity calculation of transformer parameters to phase angle measurement error.

Furthermore, it can be concluded that:

1) The identified resistances of three-winding are greatly affected by the measurement error of voltage phase angle on high-voltage side and middle-voltage side. Specifically, when voltage phase angle on high-voltage side contains $0.2°$ error, the relative deviation of the identified resistance on the high/middle/low-voltage side is −539.80%, 345.25% and −565.74% respectively. Besides, the measurement error of voltage phase angle on middle-voltage side has similar influence characteristics. In particular, the measurement error of voltage phase angle on low-voltage side also has a great influence on the identified low-voltage side resistance. When the low-voltage side voltage phase angle contains $0.2°$ error, the relative deviation of the identified resistance on the low-voltage side is 672.80%.

2) The identified resistances of three-winding are also influenced by the current phase angle measurement error on the local side. When the current phase angle of high-voltage side contains $0.2°$ error, the relative deviation of the identified resistance on high/middle/low-voltage side is 90.76%, −21.14% and 26.94% respectively.

3) The identified reactance of the middle-voltage side is greatly influenced by the measurement error of the voltage phase angle on both high-voltage and middle-voltage side. Specifically, when the voltage phase angle on the high-voltage side contains $0.2°$ error,

the relative deviation of the identified resistance on high-voltage side is -31.60%. The influence characteristics of the measurement error of the voltage phase angle on the middle-voltage side are similar to those on the high-voltage side.

4) The reactances of the high-voltage side and low-voltage side are less affected by the phase angle measurement error.

4.2 Amplitude Measurement Error

To study the influence of amplitude measurement error on transformer parameters, similar to Sect. 4.1, the sensitivity results are calculated, as shown in Table 3.

Table 3. The sensitivity of transformer parameters to amplitude measurement error

Parameters		U_{1f}	U_{2f}	U_{3f}	I_{1f}	I_{2f}	I_{3f}
R_1	$A_1(\%)$	14.22	-13.22	1.24×10^{-5}	-0.99	2.03×10^{-10}	5.70×10^{-9}
	$A_2(\%)$	14.22	-13.22	1.14×10^{-5}	-1.00	-4.31×10^{-8}	-6.23×10^{-8}
R_2	$A_1(\%)$	5429.29	-5428.29	-1.77×10^{-5}	-7.95×10^{-9}	-0.99	-1.31×10^{-8}
	$A_2(\%)$	5429.12	-5428.12	-1.45×10^{-5}	-3.70×10^{-8}	-1.00	-4.91×10^{-8}
R_3	$A_1(\%)$	651.62	-640.25	-10.37	-2.39×10^{-9}	-9.04×10^{-10}	-0.99
	$A_2(\%)$	651.63	-640.26	-10.37	5.39×10^{-8}	4.16×10^{-8}	-1.00
X_1	$A_1(\%)$	5.95	-4.95	-2.54×10^{-8}	-0.99	-6.38×10^{-12}	1.92×10^{-11}
	$A_2(\%)$	5.95	-4.95	-2.65×10^{-8}	-1.00	3.35×10^{-11}	6.38×10^{-11}
X_2	$A_1(\%)$	16.48	-15.48	-3.13×10^{-7}	-1.02×10^{-10}	-1.00	8.51×10^{-11}
	$A_2(\%)$	16.33	-15.33	-3.23×10^{-7}	-7.69×10^{-11}	-1.00	2.71×10^{-9}
X_3	$A_1(\%)$	20.97	4.97	-24.93	-2.70×10^{-11}	4.11×10^{-12}	-0.99
	$A_2(\%)$	21.00	4.97	-24.98	-1.16×10^{-10}	3.00×10^{-10}	-1.00

Note: A_1 represents the result of approximate calculation method; A_2 represents the result of analytical calculation method.

Table 3 shows that the analytical calculation results are close to the approximate calculation results, which verifies the correctness of the sensitivity calculation of amplitude measurement errors to the transformer parameters.

Furthermore, it can be concluded that:

1) The identified resistances of the high-voltage and middle-voltage side are greatly influenced by the measurement error of voltage amplitude on both sides of high-voltage and middle-voltage. Specifically, when the measurement error of voltage amplitude on high voltage side is 1%, the relative deviation of the identified resistance on the high/middle-voltage side is 14.22% and 5429.12% respectively. And the measurement error of voltage amplitude on middle-voltage side has similar influencing characteristics.

2) The identified resistance of the low-voltage side is greatly influenced by the measurement error of three–winding voltage amplitude. Specifically, when the measurement error of three–winding amplitude voltage is 1% respectively, the relative deviation of the identified resistance on low-voltage side is 651.63%, −640.26% and −10.37% respectively.

3) The identified reactances of middle-voltage side and low-voltage side are greatly influenced by the voltage amplitude measurement error on the high-voltage side and the voltage amplitude measurement error on the local side. Specifically, when the measurement error of voltage amplitude on high-voltage side is 1%, the relative deviation of the identified reactance on the middle/low-voltage side is 16.33% and 21% respectively. When the measurement error of voltage amplitude on middle-voltage side is 1%, the relative deviation of the identified reactance on the middle-voltage side is −15.33%. When the measurement error of voltage amplitude on low-voltage side is 1%, the relative deviation of the identified reactance on the low-voltage side is −24.98%.

4) The high-voltage side reactance is less influenced by the measurement error of amplitude.

4.3   Transformer Ratio Error

To study the influence of transformer ratio error on transformer parameters, similar to Sect. 4.1, the sensitivity results are calculated, as shown in Table 4.

Table 4. The sensitivity of transformer parameters to transformer ratio error

Parameters	k_{12}		k_{13}	
	Approximate results (%)	Analytical result (%)	Approximate results (%)	Analytical result (%)
R_1	−13.22	−13.22	1.25×10^{-5}	1.12×10^{-5}
R_2	−5423.87	−5429.12	-1.80×10^{-5}	-1.73×10^{-5}
R_3	−640.25	−640.26	−11.22	−11.37

<div align="right">(continued)</div>

Table 4. (*continued*)

Parameters	k_{12}		k_{13}	
	Approximate results (%)	Analytical result (%)	Approximate results (%)	Analytical result (%)
X_1	−4.95	−4.95	-2.50×10^{-8}	-2.90×10^{-8}
X_2	−16.47	−16.33	-3.10×10^{-7}	-3.20×10^{-7}
X_3	4.97	4.98	−25.91	−25.98

Table 5. The dominant factors for the identified parameters in phase angle measurement error

	U_{1j}	U_{2j}	U_{3j}	I_{1j}	I_{2j}	I_{3j}
R_1	✓	✓				
R_2	✓	✓				
R_3	✓	✓	✓			
X_1						
X_2	✓	✓				
X_3						

Table 6. The dominant factors for the identified parameters in amplitude measurement error

	U_{1f}	U_{2f}	U_{3f}	I_{1f}	I_{2f}	I_{3f}
R_1	✓	✓				
R_2	✓	✓				
R_3	✓	✓	✓			
X_1						
X_2	✓	✓				
X_3	✓		✓			

Table 4 shows that the analytical calculation results are close to the approximate calculation results, which verifies the correctness of the sensitivity calculation of transformer parameters to transformer ratio error.

Furthermore, it can be concluded that:

1) The identified resistances of three-winding are greatly influenced by the error of ratio of high-middle voltage side. Specifically, when the error of ratio of high-middle voltage side is 1%, the relative deviation of the identified resistance on high/middle/low-voltage side is −13.22%, −5429.12%, and −640.26% respectively.

Table 7. The dominant factors for the identified parameters in transformer ratio error

	k_{12}	k_{13}
R_1	✓	
R_2	✓	
R_3	✓	✓
X_1		
X_2	✓	
X_3		✓

2) The identified resistance and reactance of the low-voltage are greatly influenced by the error of ratio of high-low voltage side. Specifically, when the error of ratio of high-low voltage side is 1%, the relative deviation of the identified resistance and reactance on low-voltage side is −11.37% and −25.98% respectively.

3) The identified reactance of the middle-voltage is greatly influenced by the error of ratio of high-middle voltage side. Specifically, when the error of ratio of high-middle voltage side is 1%, the relative deviation of the identified resistance on middle-voltage side is −16.33%,

4) The high-voltage side reactance is less influenced by the transformer ratio error.

5   Determination of Dominant Factors

Table 2, 3 and 4 shows the degree of influence of phase angle, amplitude measurement error and transformer ratio error on transformer parameters to be identified. Further, for the analysis convenience and engineering practicality, Tables 5, 6 and 7 show the dominant factors for the identified parameter of transformer under different measurement errors. The dominant factors are marked by "✓" in Tables 5, 6 and 7.

It can be concluded that:

The dominant factors for the identified resistance of transformer are the measurement errors of voltage phase angle and amplitude, and the error of ratio of high-middle voltage side.

Specifically, when the voltage amplitude measurement error is 1%, the relative error of the identified resistance can reach more than 5000%. When the error of the ratio between the high-voltage side and the middle-voltage side is 1%, the relative error of the identified resistance can reach more than 5000%. When the measurement error of voltage phase angle is 0.2°, the relative error of the identified resistance will reach more than 600%.

The dominant factors for the identified reactance of transformer are the measurement errors of voltage amplitude and phase angle, and the errors of ratio of high-middle voltage side and high-low voltage side.

Specifically, when the voltage amplitude measurement error is 1%, the relative error of the identified reactance will reach more than 20%. When the measurement error of voltage phase angle is 0.2°, the relative error of the identified reactance will reach more

than 30%. When the error of ratio of high-middle voltage side is 1%, the relative error of the identified resistance can reach more than 15%. When the error of ratio of high-low voltage side 1%, the relative error of the identified resistance can reach more than 25%.

6   Conclusion

In this paper, the sensitivity analysis method is used to study the influence of measurement error and transformer ratio on the identified parameter of transformer Furthermore, based on the sensitivity analysis, the dominant factors for parameter identification are determined. The main conclusions are as follows.

The dominant factors for the identified resistance of transformer are the measurement errors of voltage phase angle and amplitude, and the error of ratio of high-middle voltage side. The influence of voltage phase angle measurement error may be 5–500 times larger than that of current phase angle measurement error, and the influence of voltage amplitude is 10–5000 times larger than that of current amplitude measurement error.

The dominant factors for the identified reactance of transformer are the error of voltage amplitude and phase angle measurement, and the errors of ratio of high-middle voltage side and high-low voltage side. The influence of voltage phase angle may be 30 times larger than that of current phase angle measurement error, and the influence of voltage amplitude may be 25 times larger than that of current amplitude.

It can be concluded that, to obtain accurate identified parameters, the error of voltage amplitude and phase angle should be paid more attentions. Furthermore, the transformer ratio should be firstly estimated when it is unknown, since it is a good choice to improve the accuracy and reliability of the identified results.

References

1. Zhang, N., Zhu, Y., Gao, Y., et al.: An on-line detection method of transformer winding deformation based on variational mode decomposition and probability density estimation. Power Syst. Technol. **40**(1), 297–302 (2016)
2. Deng, X., Xiong, X., Gao, L., et al.: Method of on-line monitoring of transformer winding deformation based on parameter identification. Proc. CSEE **34**(28), 4950–4958 (2014)
3. Zheng, J., Jiang, X., Cai, J.: Parameter identification for equivalent circuit of transformer oil-paper insulation and effect of insulation condition on parameters. Electr. Power Autom. Equip. **35**(8), 168–172 (2015)
4. Zeng, B., Wu, W., Zhang, B.: A method to identify and estimate network parameter errors based on Karush-Kuhn-Tucker condition. Power Syst. Technol. **34**(1), 56–61 (2010)
5. Phake, A., Thorp, J.: Synchronized Phasor Measurements and their Applications, 2nd edn. Springer, New York (2008)
6. Chen, X., Yi, Y., Jiang, Q., et al.: Network parameter identification and estimation based on hybrid measurement of WAMS/SCADA. Autom. Electr. Power Syst. **32**(5), 1–5 (2008)

7. Wang, M., Qi, X., Niu, S., et al.: Online estimation of transformer parameters based on PMU measurements. Autom. Electr. Power Syst. **35**(13), 61–65 (2011)
8. Chen, J., Yan, W., Lu, J., et al.: A robust transformer parameter estimation method considering multi-period measurement random errors. Autom. Electr. Power Syst. **35**(2), 28–33 (2011)
9. Vicol, B.: On-line overhead transmission line and transformer parameters identification based on PMU measurements. . In: 2014 International Conference and Exposition on Electrical and Power Engineering, Lasi, Romania, pp. 1045–1050. IEEE (2014)
10. Xue, A., Xu, J., Martin, K., et al.: A new two-step method to estimate the sequence parameter of transformer based on median criterion. In: 2019 IEEE Power & Energy Society General Meeting (PESGM), Atlanta, GA, USA, pp. 1–5. IEEE (2019)
11. Ding, L.: Study on Parameter Identification of Transmission Line and Thevenin Equivalent Based on PMU. North China Electric Power University, Beijing (2011)
12. Asprou, M., Kyriakides, E., Albu, M.: The effect of PMU measurement chain quality on line parameter calculation. In: 2017 IEEE International Instrumentation and Measurement Technology Conference (I2MTC), Turin, Italy, pp. 1–6. IEEE (2017)
13. Ding, L., Ou, Z., Tang, Z., et al.: Research on factors influencing identification of transmission line parameters. Power Syst. Technol. **37**(7), 1948–1953 (2013)

A Reliability Prediction Model for the Relay Protection Device and Its Internal Modules Considering Thermal Effect

Ziyang Jing, Minghao Ouyang, Jiahuan Zhang, and Ancheng Xue[(✉)]

State Key Laboratory of Alternate Electrical Power System with Renewable Energy Source, North China Electric Power University, Changping District, Beijing 102206, China
acxue@necpu.edu.cn

Abstract. The failure of the internal module often leads to the failure of the relay protection device (RPD), which threatens the safe and stable operation of the power grid. At the same time, the thermal effect, which is expressed with temperature, is an important factor for module failure. However, there is few literatures engaged with the influence of temperature on the reliability of the whole PRD. This paper proposed the reliability models for the core modules and the RPD considering the thermal effect with temperature, combinges with the temperature-dependent Arrhenius model and the Weibull distribution model for the time-varying failure rate. In details, first, with the structure of the RPD, three main failures should be considered, namely the hardware failure, the software failure, and the human-induced failure. Combined with statistical data, it is determined that the hardware failure mainly considers the failure of the CPU module, power module and other modules.

Secondly, with the Weibull distribution model for time varying failure rate and the Arrhenius model, an improved Weibull model for the failure rate of different modules considering temperature is established. Furthermore, combined with hardware, software & human-induced failure and repair rate, the reliability prediction model of the RPD is proposed. Finally, the case analysis shows the effectiveness of the proposed models.

Keywords: Thermal effect · Time-varying failure rate · Arrhenius · Relay protection device · Weibull distribution · Core module

1 Introduction

Relay protection is the first line of defense to ensure the safe and stable operation of the power system, thus, the reliability of the relay protection device (RPD) is crucial to the safe and stable operation of the power grid. Therefore, it is important to establish a reasonable reliability model of RPD and to evaluate its reliability.

Meanwhile, operation data statistics show that the failure of the internal core modules of RPD, such as CPU and power, often leads to the failure of RPD [1]. Therefore, the

reliability evaluation of RPD considering the module has attracted much attention [2–5]. For example, Reference [2] establish a joint distribution model of the defect distribution of the RPD, by dividing the RPD into power, CPU, AC and LCD modules. Reference [5] proposes a reliability model for RPD based on the Markov model by dividing the failure modes of RPD into the software failures, the hardware failures including power supply, CPU, DI, DO, AI, CU, MMI module failure, considering the self-inspection. Reference [3, 4] proposed the Markov models for the single and dual device, respectively, considers failure modes such as hardware failure including power, CPU and other modules, and the software failure, and the human-induced failure, as well as the influence of self-inspection and regular inspection. The above models are based on the module, which originated from practical experience, and considering a variety of failure modes and influencing factors, thus, so the reliability model of the whole machine is reasonable.

On the other hand, statistical results show that more than half of the failures of electronic equipment are mainly caused by thermal effect [6, 16], i.e., the change of temperature will affect the failure rate of chips and boards, which in turn affects the reliability of RPD. However, it is worth noting that none of the above reference [2–5] consider thermal effect. Meanwhile, few literatures focus on the influence of temperature on the reliability of RPD. In Reference [7], the time-varying aging failure rate of the core module of RPD with temperature is analyzed, but in reliability model for the RPD, the effect of software, human failure and maintenance are ignored. Thus, it is needed to be further improved.

In recognizing the above problems, this paper proposes the reliability models describing the core modules and the RPD considering the temperature, combines the temperature-dependent Arrhenius model and the Weibull distribution model. The proposed model can evaluate the reliability of the RPD more accurate, considering the thermal effect.

The remainders of the paper are organized as follows. Section 2 analyses the structure of RPD and its failure modes, including hardware, software and human-induced failure. Section 3 proposes an improved Weibull distribution model of the failure rate to considers the thermal effect, which is by Arrhenius model to modify the life parameters of the Weibull distribution. Section 4 presents the reliability prediction model of RPD considering hardware, software, human-induced failure and repair rate. In Sect. 5, a case study of operation defect information is employed to analyze the reliability of RPD, sensitivity analysis validate the proposed model, the results are given and discussed. Finally, Sect. 6 gives a conclusion.

2   The Structure of Relay Protection Device and Its Failure Modes

The overall hardware structure of the microcomputer RPD is shown in Fig. 1, mainly including CPU, power, ADC and other modules. The functions of each module are different. And there are differences in the hardware structure, which will result in different reliability. Failure of any module will lead to failure of RPD.

In terms of failure modes, there are three main failure modes of the relay protection core module, 1) hardware failure caused by the components of RPD, 2) software failure caused by errors in the program code of RPD or program loopholes during operation; 3) the random human-induced failure caused by human error [8].
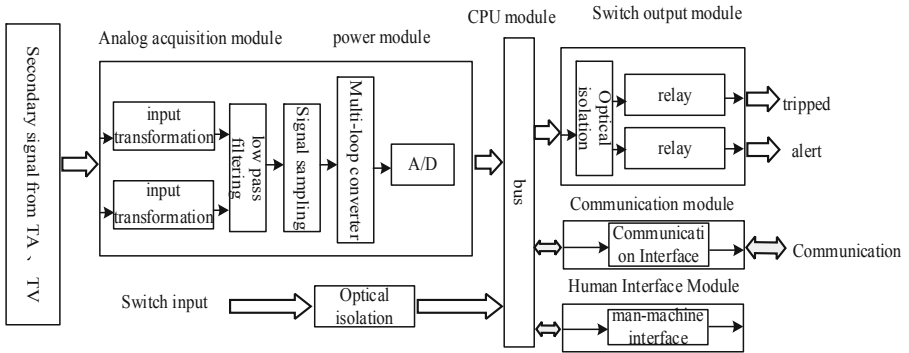
Fig. 1. Overall hardware structure of the relay protection device

For hardware failure, the failure statistics of national relay protection from 2015 to 2018 show that [1], among the hardware failures, the CPU and power modules have the most failures, while other modules account for a small proportion. Therefore, in order to simplify the model, this paper divides the core modules of RPD into CPU, power and others (referring to all modules except the CPU and power).

At the same time, the failure rate of hardware failure is much higher than that of other failure modes, and the occurrence frequency is higher, which has a greater impact on the reliability of the whole protection device [1]; Therefore, this paper focuses on the analysis of the hardware failure rate of RPD considering the core module, further integrates the other two failure modes, and finally obtains the reliability model of the whole protection device.

3 Failure Rate of Core Modules Considering Thermal Effect

Temperature is the most important factor that affects the aging of the module and leading to its failure. A large number of electronic components are integrated in the protection device module, which will generate a large amount of heat during operation, and it will cause the internal temperature of the module to rise and affect the failure rate of the core module. A core module failure rate model that considers temperature is built in this section [9].

3.1 Arrhenius Model

The practice has proved that when the temperature rises, the physicochemical reaction of device deterioration accelerates, and the failure process accelerates [14]. The influence of general temperature on components can be described by the Arrhenius model [17]. Therefore, the Arrhenius model is adopted to correct the failure rate of the core module in the protection device, and the module failure rate considering the temperature is obtained.

The Arrhenius reaction rate equation is an empirical formula, which is summed up from practice. The expression is,

$$\frac{\partial M}{\partial t} = A_0 \exp\left(-\frac{\Delta E_A}{KT}\right) \tag{1}$$

where, M is the degradation amount of a certain characteristic value of the component; $\partial M / \partial t$ represents the degradation rate of the temperature at T, and the degradation rate is a linear function of the time t; Boltzmann constant k = 8.617×10^{-5} eV/°C; T is the thermodynamic temperature; A_0 is a constant; t is the reaction time; E_A (in eV) is the failure activation energy, which is a constant for the same failure mode of the same type of components.

3.2 Improved Weibull Distribution Model Considering Thermal Effects

This section adopts the Arrhenius model to correct the Weibull life parameter of the core module of RPD, to more accurately fit the effect of temperature on module failure.

Generally, the time-varying failure rate can be approximated by the Weibull distribution [11], and the typical failure rate of the two-parameter Weibull distribution is expressed as follows [15],

$$\lambda(t) = \frac{\beta}{\eta}\left(\frac{t}{\eta}\right)^{\beta-1} \tag{2}$$

where, t is the time; β is the shape parameter; η is the scale parameter, also known as the characteristic life, which is a mean life.

On the other hand, studies have shown that [12], on the premise of ensuring that the failure mechanism remains unchanged, the parameters of the Weibull distribution should satisfy the following two relations at the same time,

1) The shape parameters β of the failure distribution under different stresses are consistent, which is a fixed value, that is, $\beta = \beta_i (i = 1, 2, ..)$

2) The relationship between the life parameter η_t and the experimental temperature T should satisfy the Arrhenius model, $\eta_i = AF_i \cdot \eta$

$$AF_t = \frac{e^{\left(\frac{-E_A}{KT_t}\right)}}{e^{\left(\frac{-E_A}{KT_0}\right)}} = e^{\left(\frac{E_A}{k}\left(\frac{1}{T_0}-\frac{1}{T_t}\right)\right)} \tag{3}$$

where, AF_t is the acceleration factor at time t; T_0 is the initial temperature, T_t is the absolute temperature after time t, and the unit is Kelvin.

In order to distinguish it from the traditional Weibull parameters, the parameter η is represented by a constant A.

$$\eta_t = Ae^{\left(\frac{E_A}{k}\left(\frac{1}{T_0}-\frac{1}{T_t}\right)\right)} \tag{4}$$

Substituting Eq. (4) into Eq. (2), the expression of the time-varying failure rate of RPD module considering the effect of temperature can be obtained as shown in (5),

$$\lambda_T(t) = \frac{\beta}{\left[Ae^{\left(\frac{E_A}{k}\left(\frac{1}{T_0}-\frac{1}{T_t}\right)\right)}\right]^{\beta}}(t)^{\beta-1} \tag{5}$$

On the other hand, under the action of long-term temperature stress, the internal temperature of RPD will also change with time, so the temperature changes with time, correspondingly, the temperature of each module also rises slowly, and the rate of rise gradually decreases, and finally tend to flatten. Combined with the Arrhenius model, the functional relationship between the module temperature T_t and the running time t is derived as follows,

$$T_t = \frac{b}{\ln(\frac{a}{t})} \tag{6}$$

where, a and b are constants, which can be obtained by experimentally measuring multiple groups of t and T_t fitting of different modules.

4   Reliability Model of RPD Considering Maintainability

4.1   Reliability Prediction of Repairable Series System

For a repairable system, its reliability is usually assessed by availability. For a series system with n elements, assuming that the failure rate of the elements is λ_i, the repair rate is μ_i, and $\mu_i >> \lambda_i$, the reliability parameters of the series equivalent system is [12],

$$\lambda_s = \sum_{i=1}^{n} \lambda_i, \ r_s = \frac{1}{\lambda_s} \sum_{i=1}^{n} \lambda_i r_i,$$

$$U_s = \lambda_s r_s = \sum_{i=1}^{n} \lambda_i r_i, \ A_s = 1 - U_s \tag{7}$$

where, λ_s is the system failure rate, r_s is the reciprocal of the system repair rate, U_s is the system unavailability, and A_s is the system availability.

It should be noted that the Eq. (7) is an approximate result, which ignoring the high-order terms of the failure rate and repair rate, and its error increases with the increase of the number of modules.

The components of RPD are irreparable, but the system composed of different components is repairable. Therefore, its evaluation index needs to consider its maintainability, and it is suitable to use the availability index.

4.2   Reliability Prediction of Relay Protection Device with Temperature

As mentioned above, the failure modes of RPD are divided into hardware failure, software failure and human-induced failure. In actual operation, the failure of any failure mode will lead to the failure of the protective device. Therefore, the above three failure modes can be regarded as a series model.

The relationship between RPD and each of the main internal functional modules constitutes a series relationship, that is, the failure of any functional module will lead to

the failure of the entire device. Considering that the hardware is divided into three parts, CPU, power and other modules, the overall hardware failure rate of RPD is

$$\lambda_{HW.T}(t) = \lambda_{CPU.T}(t) + \lambda_{power.T}(t) + \lambda_{other.T}(t) \tag{8}$$

where, $\lambda_{HW.T}$, $\lambda_{CPU.T}$, $\lambda_{power.T}$, $\lambda_{other.T}$ are the failure rates of hardware, CPU, power and other modules considering the influence of temperature respectively.

Further, considering the different failure modes and self-checking factors of the device, and the hardware failure rate, software failure rate and human-induced failure rate of the device, the failure rate of the whole device series equivalent model considering the influence of temperature can be obtained as follows,

$$\lambda_s(t) = \lambda_{HW}(t) + \lambda_{SW} + \lambda_{HR} \tag{9}$$

where, λ_{SW}, λ_{HR} are the failure rates of software failure and human-induced failure respectively. It should be noted that the software failure always exists during the operation of the device and will not be repaired, thus, the failure rate is a constant value; the human-induced failure is random, and is taken as a constant value according to engineering experience.

The overall unavailability of the device U_s is,

$$U_s(t) = \lambda_s(t)r_s(t) = \lambda_{HW}(t)r_{HW} + \lambda_{SW}r_{SW} + \lambda_{HR}r_{HR} \tag{10}$$

where, r_{HW}, r_{SW}, r_{HR} are the reciprocal of the repair rate of hardware failure, software failure and human-induced failure of the device, which are constant values according to engineering experience.

The overall availability of the device A_s is,

$$A_s(t) = 1 - U_s(t) \tag{11}$$

5   Case Analysis

The total number of RPD put into operation from 2010 to 2018 in a power grid was 35,466, with 103 power module defects, 170 CPU module defects, and 223 other module defects, totaling 496 times. At the same time, the date of commissioning of the above-mentioned defective device and the date of occurrence of the defect (censored data) were obtained, which are shown in Table 1.

5.1   Time-Varying Failure Rate of Modules

According to the operation characteristics of each module, 10 modules were selected to be put into operation for 1–3 years, 4–6 years and 6–8 years respectively. Its internal temperature was measured with an infrared thermometer, Take the average of the working time and temperature of each module to obtain the approximate temperature of each module at different time points, as shown in the following Table 2 [8].

Table 1. Partial defect data and censored data of CPU modules of a certain type of RPD

	Date of the device was put into operation	Date of Defect	Number of years of CPU failure-free(T) operation
1	2015/6/10	2018/3/15 11,30	2.765696
2	2018/5/8	2018/7/15 10,18	0.187477
3	2014/11/2	2018/3/20 16,10	3.382667
4	2010/1/17	2018/11/22 22,18	8.8546
5	2017/12/28	2018/8/14 10,00	0.628539
……			
6	2012-07-25	As of the end of the statistics, there is no defect in the device, which is random censored data	6.438356
7	2018-06-21		0.528767
8	2013-10-23		5.191781
9	2018-04-26		0.682192
10	2017-06-14		1.547945

Table 2. Temperature statistics of each module of RPD at different time

Module name	Operating temperature (°C)			
	1.2 years	4.6 years	6.8 years	11.4 years
Power	58.5	62.0	67.4	——
CPU	58.8	——	62.2	66.6
Others	60.2	61.4	63.2	——

Combined with formula (6), the temperature variation relationship of the three types of modules with time can be obtained as follows

$$T_{CPU}(t) = \frac{41316.43}{\ln \frac{2.74*10^{54}}{t+1}}$$

$$T_{Power}(t) = \frac{16061.65}{\ln \frac{2.37*10^{21}}{t+1}} \tag{12}$$

$$T_{Other}(t) = \frac{47303.13}{\ln \frac{2.05*10^{62}}{t+1}}$$

Considering the right-censored data of no defects in the device, the estimated failure rate can be obtained, and then the parameters of the Weibull life model considering the effect of temperature can be obtained [15], and the time-varying failure rate of each

module considering the effect of temperature can be obtained as shown in Eq. (13) and Fig. 2.

$$\lambda_{CPU}(t) = \frac{0.9953}{\left\{(3.88 * 10^3) * \exp\left[-13925.96 * (\frac{1}{329.61} - \frac{\ln\frac{2.74*10^{54}}{t+1}}{41316.43})\right]\right\}^{0.9953}} * t^{-0.0047}$$

$$\lambda_{Power}(t) = \frac{1.321}{\left\{(2.097 * 10^3) * \exp\left[-7543.23 * (\frac{1}{327.2} - \frac{\ln\frac{2.37*10^{21}}{t+1}}{16061.65})\right]\right\}^{1.321}} * t^{0.321}$$

$$\lambda_{Other}(t) = \frac{1.0034}{\left\{(1.519*10^3) * \exp\left[-5802.48 * (\frac{1}{331.6} - \frac{\ln\frac{2.05*10^{62}}{t+1}}{47303.13})\right]\right\}^{1.0034}} * t^{0.0034}$$

$$(13)$$
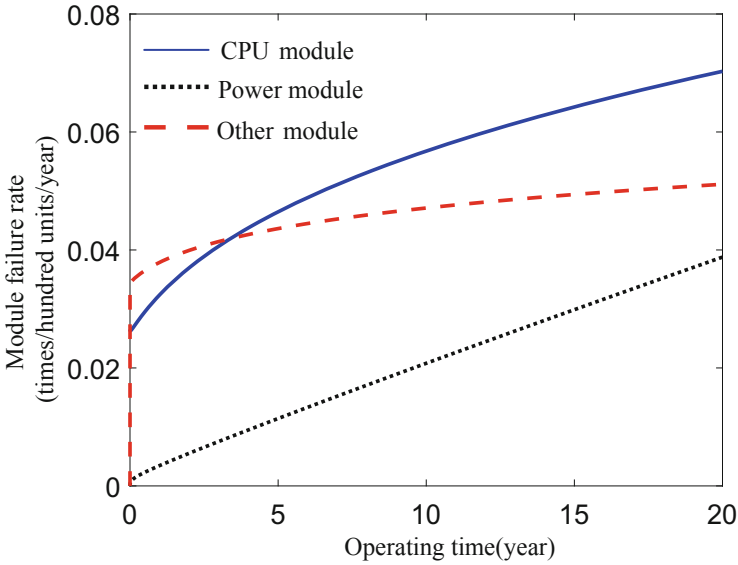
Fig. 2. Time-varying failure rate of CPU, power and other modules

Figure 2 shows that the failure rate of each module gradually increases with the operating years, which is the same as the change trend of the time-varying failure rate of the modules analyzed in the literature [4].

5.2 Reliability Prediction of RPD

For RPD, the failure rate and repair rate of software failure and human-induced failure are shown in Table 3 [5].

Table 3. Parameters of the protective device series equivalent model considering the core module

Symbol	Value
Software failure rate λ_{SW}	$2.56*10^{-4}$ (Times/(100 sets * year))
Human-induced failure rate λ_{HR}	$1*10^{-4}$ (Times/(100 sets * year))
Hardware repair rate μ_{HW}	14.6 ((times*100 sets)/year)
Software failure repair rate μ_{SW}	10 ((times*100 sets)/year)
Human-induced failure repair rate μ_{HR}	0.15 ((times*100 sets)/year)

Table 4. Influence of temperature change on the reliability of the protection device after 12 years of operation

After 12 years of operation	Type of module	Reliability	Variation of reliability relative to original temperature
Original temperature	————	0.9810	————
Temperature rise 1 °C	CPU module	0.9799	−0.11%
	Power module	0.979	−0.20%
	Other module	0.9799	−0.11%
	All modules	0.977	−0.40%
Temperature decrease 1 °C	CPU module	0.9816	+ 0.06%
	Power module	0.9826	+ 0.16%
	Other module	0.9817	+ 0.07%
	All modules	0.984	+ 0.30%

Combining with the overall hardware failure rate of the device, the time-varying failure rate and availability of the whole device after considering the temperature effect of RPD in series equivalence are shown in Fig. 3 and Fig. 4.
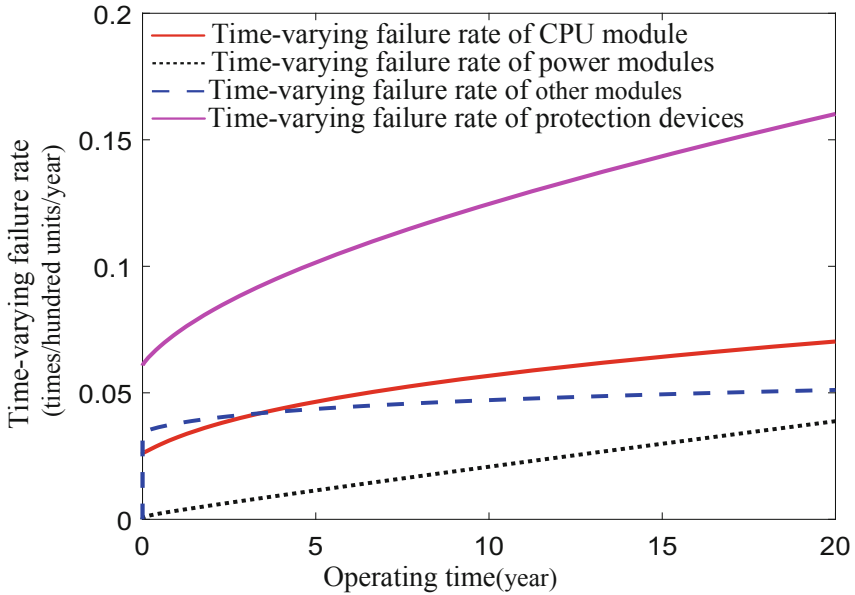
Fig. 3. Time-varying failure rate of protective devices considering temperature effects

5.3 Influence of Temperature on Reliability of RPD

For power modules, CPU modules, and other modules, taking into account the overall heat dissipation causes a certain temperature to rise or fall at the same time, or a single module drop or rise to a certain temperature because of different structural designs. Extreme cases are considered in this paper, and the temperature changes are all 1°C. The overall reliability curves of RPD are shown in Fig. 5.

Two assumptions are set for its temperature: 1) the temperature change trend is the same, the value is 1 °C lower than the original temperature; 2) the temperature change trend is the same, the value is 1 °C higher than the original temperature. Set the temperature of the power module, CPU module, other module and all modules to increase (decrease) 1 °C compared with the original temperature, a total of 8 cases, analyze the influence of the temperature change of RPD on the reliability of the whole machine.

Further, considering that the device has been operated for 12 years, the reliability of the device can be compared with the original temperature as shown in Table 4.

It can be seen that:

1) At the original temperature, after the device was put into operation for 12 years, its availability gradually decreased by about 1.9%; A rise in temperature decreases availability, and a decrease in temperature increases availability;
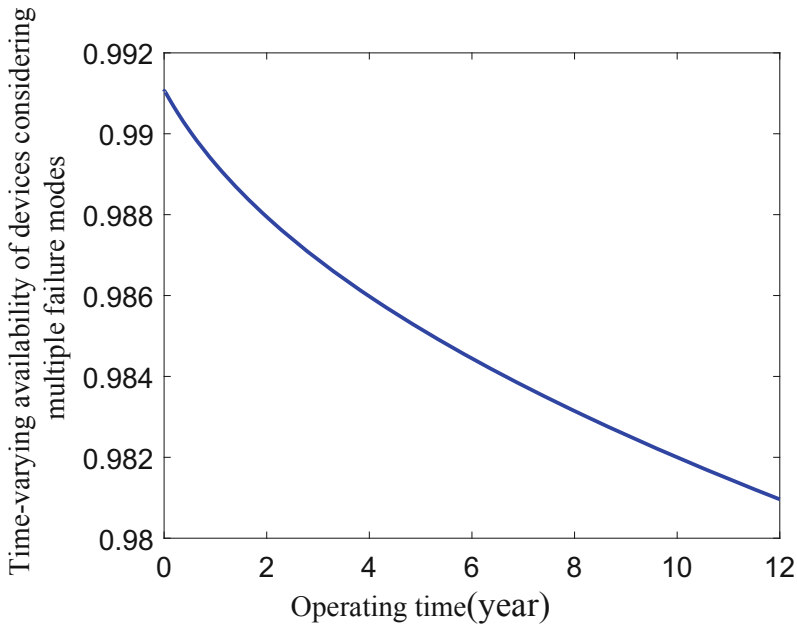
Fig. 4. Time-varying availability of the protection device considering the effect of temperature

2) When the operating temperature of a single module increases by 1 °C, the availability of the whole machine decreases slightly compared with the original temperature, and the availability of the whole machine after 12 years of operation decreases by about 2.1%. With the increase of running time, compared with CPU and other modules, the difference of the power module's influence on the reliability of RPD gradually increases. It can be concluded that the power module is most affected by temperature. When the operating temperature of all modules increased by 1 °C, the device availability decreased the most, about 2.3%;

3) When the operating temperature of a single module decreases by 1 °C, the availability of the whole machine increases slightly compared with the original temperature. Availability dropped by about 1.6% after 12 years of operation.

It can be seen that when the heat dissipation performance of the device is well, the temperature rises slowly with the increase of operating years, and the availability of the whole machine is relatively high. On the contrary, if the heat dissipation performance is poor, the temperature will rise more for the same time, so that the availability of the whole machine will be reduced accordingly. It can be concluded that strengthening the low power consumption and heat dissipation design of the device can effectively prevent the aging of the device and improve the reliability of the whole machine.
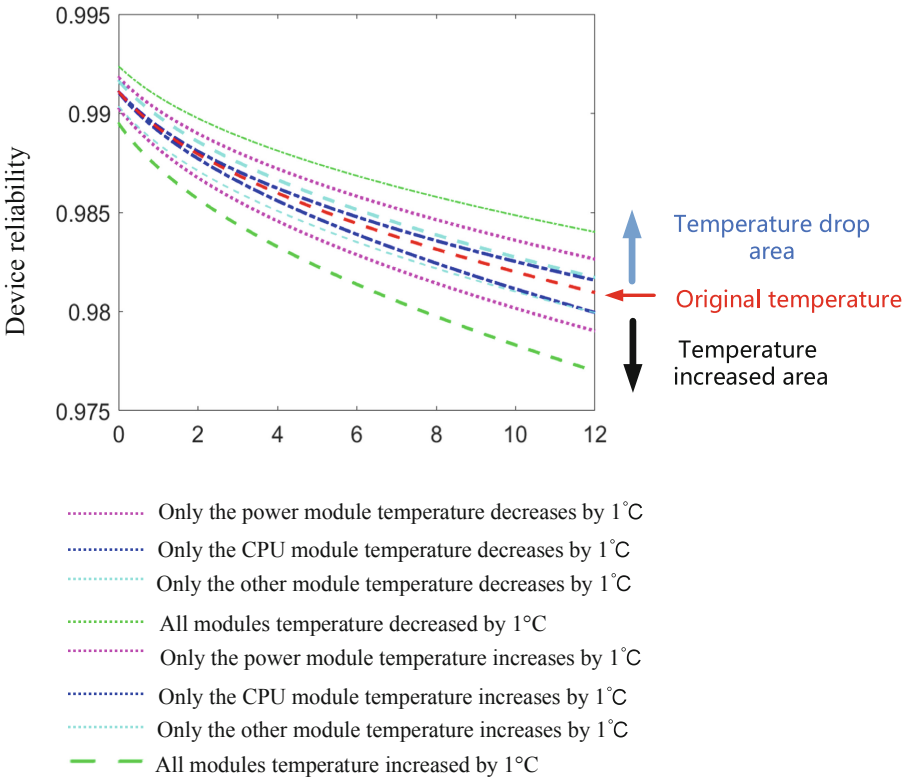
Fig. 5. Influence of temperature change on reliability of protection device

The legend labels shown in the figure:

.... Only the power module temperature decreases by 1˚C

.... Only the CPU module temperature decreases by 1˚C

.... Only the other module temperature decreases by 1˚C

.... All modules temperature decreased by 1°C

.... Only the power module temperature increases by 1˚C

.... Only the CPU module temperature increases by 1˚C

.... Only the other module temperature increases by 1˚C

— — All modules temperature increased by 1°C

6 Conclusions

A reliability models for RPD considering the thermal effect with temperature is proposed, combined with the maintainability,software failure, human-induced failure, and the hardware failure with improved model. The model is derived with the improved Weibull failure rate models of the core modules, based on the Weibull distribution and the Arrhenius model. Analysis shows that the higher the internal temperature of the device, the lower of its reliability, and the sensitivity shows that the temperature has a large impact on the reliability of the device. Furthermore, among the CPU modules, power modules, and other modules, the power module is most affected by temperature.

References

1. Zhang, L., Lv, P., Zhang, H., et al.: Analysis on protective relaying and Its operation conditions of SGCC AC systems of 220kV and above in 2018. Power Syst. Technol. **39**(04), 217–222 (2020)

2. Wang, W., Yang, G., Zhou, Z., et al.: Reliability distribution of relay protection based on random truncation data and maximum likelihood estimation. Power Syst. Prot. Control **47**(12), 125–131 (2020)
3. Xue, A., Zhang, J., Li, W., et al.: Markov model of relay protection device considering core components and analysis of its influencing factors. Power Syst. Technol. **45**(06), 2380–2387 (2021)
4. Zhang, J., Li, W., Wang, X., et al.: Markov model of dual relay protection devices and its influencing factors considering core components. Power Syst. Technol. **45**(11), 4560–4567 (2021)
5. Wang, G., Ding, M., Li, X., et al.: Reliability analysis of digital protection. Proc. CSEE **24**(23), 47–52 (2004)
6. Li, Y., Lyu, W.: Simulation analysis of pbga packaged chips' thermal environment adaptability. J. Beijing Univ. Aeronautics Astronautics **47**(09),1892–1899 (2020)
7. Shi, Y., Jiang, Z., Zhao, S.: Research on time-varying failure rate of protection devices based on internal temperature. Power Syst. Protection Control **44**(05), 123–128 (2016)
8. Abdelmoumene, A., Bentarzi, H., Chafai, M., et al.: Reliability assessment and improvement of digital protective relays. Int. J. Syst. Assurance Eng. Manage. **7**(03), 1–8 (2014)
9. Lin, Z., Jiang, T., Cheng, Y., et al.: Study on Arrhenius relationship. Electron. Product Reliability Environ. Testing **23**(05), 25–32 (2005)
10. Farag, A.S., et al.: Failure analysis of composite dielectric of power capacitors in distribution systems. IEEE Trans. Dielectr. Electr. Insul. **5**(4), 583–588 (1998)
11. Wang, R., Xue, A., Bi, T.,et al.:Time varying failure rate estimation of relay protection devices and their regional differences analysis. Autom. Electric Power Syst. **36**(05),11–15 (2012)
12. Wu, C., Wan, N., Ma, W., et al.: Rapid identification of the consistency of failure mechanism for constant temperature stress accelerated testing. Acta Physica. Sinica. **62**(6), 478–482 (2013)
13. Cheng, L., He, J.: Principles and Applications of Power System Reliability. Tsinghua University Press (2015)
14. Yang, X., Lu, Y., Bo, Q., et al.: Analysis for effect of fiber-optic current transformer on protection accuracy and reliability. Autom. Electric Power Syst. **37**(16), 119–124 (2013)
15. Xue, A., Wang, R., Liu, W., et al.: Estimation methods for constant failure rate of protection equipments. Autom. Electric Power Syst. **36**(04), 6–10 (2012)
16. Xia, Y., Li, W., Yang, D., et al.: Reliability research strategy of all-domesticized chip relay protection device. In: 2020 IEEE Sustainable Power and Energy Conference (iSPEC), pp. 990–997 (2020)
17. Cooper, M.S.: Investigation of Arrhenius acceleration factor for integrated circuit early life failure region with several failure mechanisms. IEEE Trans. Components Packaging Technol. **28**(03), 561–563 (2005)

Optimal Expansion Planning of Distributed Energy Resources with Peer-to-Peer Transactions Among Prosumers

Yuerong Zhu[(✉)] and Yunpeng Xiao

Xi'an Jiaotong University, Xi'an 710049, China
Zhuyuerong@stu.xjtu.edu.cn

Abstract. The rapid increase in the distributed energy resources generation has triggered the new trend of prosumer-centric markets with peer-to-peer (P2P) transactions. However, the long-term planning management for renewable generation will also be influenced by P2P transactions, apart from the short-term marketing strategies of prosumers. This paper analyses the impacts on prosumers' long-term planning for distributed energy generation expansion resulted from P2P transactions in the distribution networks. Based on the established P2P transaction model and operation model of the distribution network, we further propose the expansion model of PV generation and battery energy storage system (BESS) for prosumers. The case studies verify that P2P transactions can effectively incentive prosumers to increase the penetration of distributed energy in the distribution network. Besides, it is also found that P2P transactions can help to improve the total social welfare of the distribution network and reduce the fluctuation of the total load in the distribution network.

Keywords: Distributed energy resources expansion · P2P transactions · Prosumer-centric markets

1 Introduction

With the rapid growth of distributed energy resources, distributed generation such as rooftop PV panels is wildly used, which calls for the emergence of prosumers in the distribution network. Equipped with PV panels and battery energy storage systems (BESS), prosumers are able to produce and store electricity. And the fluctuations of load and renewable generation create the opportunity for energy exchanging and sharing among a group of prosumers. Besides, prosumers can shift their roles to buyers or sellers by managing energy consumption, generation, and storage [1]. Thus, it is necessary to build a market scheme to ensure the efficiency and security of transactions.

In that given context, P2P transaction is proposed to encourage local energy sharing and trading boundlessly [2]. Different forms of P2P transaction schemes and market clearing mechanisms can be categorized into three categories: centralized, decentralized, and distributed [3, 4]. And various trading models and market clearing algorithms

have been established [5–8]. In [5, 6], P2P trading is considered to encourage market players to form a cooperative game. Using the peer-to-peer trading price as the pairwise factor, references [7, 8] consider establishing an optimization model for peer-to-peer trading with distribution network utilization fees. In comparison, some articles [9, 10] describe P2P trading as a non-cooperative game among prosumers and investigate the existence of market equilibrium. In [11], a real-time pricing model for peer-to-peer transactions is proposed to analyze the changes in power flow. And in [12], financial contracts are introduced as risk hedging mechanisms to evaluate the influence of market players. Decomposition algorithms are widely used to achieve optimal solutions or market equilibrium, including the relaxed consensus + innovation algorithm [13], and the alternating direction method of multipliers [14–16]. However, P2P transaction not only has an impact on the marketing strategies in the short term but also influences the long-term expansion decisions. Generating more energy means that prosumers can save bills on purchasing energy and increase income by selling energy to their peers. Thus, P2P energy trading may encourage prosumers to increase the penetration of distributed energy resources.

2   Distribution Energy Transaction Model

2.1   Distribution Network and Market Structure

The marketing models include the transactions between prosumers and the network operator, and the P2P transactions among the prosumers in the distribution network. The proposed marketing models in the distribution network are shown in Fig. 1.
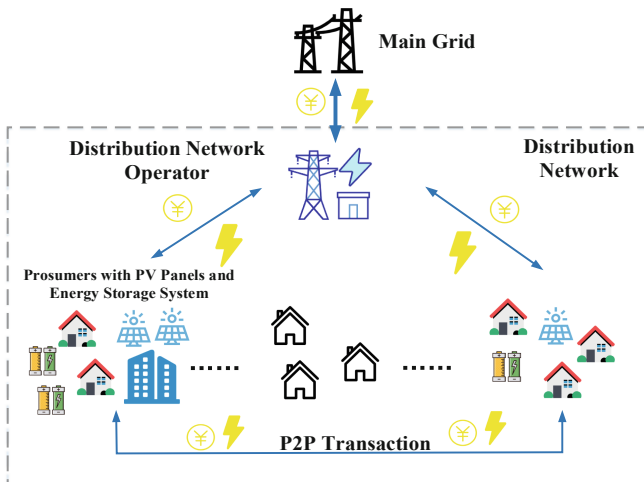
Fig. 1. Market model of the distribution network

In the distribution network, prosumers can choose to install domestic PV panels and BESS. P2P transactions are limited to prosumers within this distribution network.

And energy exchanges with the outside main grid can only happen through the network operator as the coordinator. To minimize the bills on purchasing energy, prosumers can use their differences in peak and valley of load to trade extra energy with their peers. The network operator is introduced to take charge of energy trading between the distribution network and the main grid.

Prosumer i can trade with others in the P2P market and also with the network operator, which are $U_{i,y}^{ng}(P_{i,y,t}^{ng})$ and $U_{i,y}^{op}(P_{i,y,t}^{op})$ respectively, and $U_{i,y}^{line}(P_{i,y,t}^{ng})$ represents the line utilization fees. And the investment $f_{i,y}^{inv}$ represents the cost of expanding the PV generation and the BESS. Thus, the total cost function of all prosumers can be given as follows:

$$\min \sum_{i \in \Phi} [U_{i,y}^{ng}(P_{i,y,t}^{ng}) + U_{i,y}^{line}(P_{i,y,t}^{ng}) + U_{i,y}^{op}(P_{i,y,t}^{op}) + f_{i,y}^{inv}] \tag{1}$$

2.2 Market Models

P2P Transaction Models. In the P2P transaction model, prosumers can trade with any other prosumers $j \in \Phi_i$ within the distribution network. For prosumer i, the energy trading with all other prosumers at time $t \in T$ is written as $P_{i,y,t}^{ng}$. And the energy trading with a specific prosumer j is given as $P_{ij,y,t}^{ng}$:

$$P_{i,y,t}^{ng} = \sum_{j \in \Phi_i} P_{ij,y,t}^{ng} \tag{2}$$

And for each trade between a pair of seller and buyer, the amount should be consistent, but from the view of the buyer it is positive (as we consider the costs are positive) and from the view of the seller it is negative:

$$P_{ij,y,t}^{ng} + P_{ji,y,t}^{ng} = 0 \tag{3}$$

Thus, the total cost of prosumer i in the P2P market can be given as:

$$U_{i,y}^{ng} = \sum_{t=1}^{T} (\sum_{j \in \Phi_i} P_{ij,y,t}^{ng} C_{ij,t}^{ng}) \Delta t \tag{4}$$

where $C_{ij,t}^{ng}$ is the price for P2P electricity trading among prosumers.

Network Utilization Fees. The ownership of the transmission lines of the distribution network usually belongs to the network operator or other third parties who is responsible for network maintenance and grid modernization [7]. However, P2P transactions between prosumers do not bring direct financial benefits to the network owner. Moreover, line losses during P2P transactions need to be reflected in the cost function of prosumers. Thus, there will be a service charge for using the network instruction in the P2P market to protect the operator's financial benefits during P2P transactions [17, 18]. The network

operator charges both prosumers equally for each trade. Thus, for prosumer i the cost function for network utilization fees can be given as:

$$U_{i,y}^{line} = \sum_{t=1}^{T} (\sum_{j \in \Phi_i} C_{ij}^{line} P_{ij,y,t}^{ng}) \Delta t \tag{5}$$

And inspired by [15, 17], the network utilization price can be written as:

$$C_{ij}^{line} = \tau d_{ij}$$
$$d_{ij} = \sum |Z_{lm}|, i \in \Omega_m, j \in \Omega_l \tag{6}$$

where τ represents the utilization price for per unit of power transmitted in each unit electricity distance. And d_{ij} is calculated based on the electrical distance, and Z_{lm} is the impedance of the network.

Transaction with the Network Operator. Prosumers trade with the network operator to ensure energy supply during low PV generation periods. Thus, the cost function for prosumers trading with the distribution network operator can be written as:

$$U_{i,y}^{op} = \sum_{t}^{T} [P_{i,y,t}^{op} C_t^{op,buy} x_{i,y,t}^{op} + P_{i,y,t}^{op} C_t^{op,sell} (1 - x_{i,y,t}^{op})] \Delta t \tag{7}$$

where prosumers purchase electricity with the price $C_t^{op,buy}$ and sell with the price $C_t^{op,sell}$. $x_{i,y,t}^{op}$ is a binary variable, and when $x_{i,y,t}^{op} = 1$, prosumer i purchases energy from the network operator, while when $x_{i,y,t}^{op} = 0$, prosumer i sells energy to the operator.

3 Expansion Model

3.1 Prosumers and Distribution Network Operation Model

PV Generation. Compared to wind tubers and other renewable energy generation methods, PV panels take less space and are easily installed. Rooftop PV generation can be a wise choice for prosumers with limited area and investment. And the PV generation $P_{i,y,t}^{PV}$ should not surpass the PV capacity $P_{PV,i,y}^{cap}$ installed by the prosumer i in the y_{th} year:

$$0 \leq P_{i,y,t}^{PV} \leq P_{PV,i,y}^{cap} \tag{8}$$

Battery Energy Storage System. Prosumers can install BESS to cope with the uncertainty of PV generation. Besides, because the energy trading prices with the network operator are time-of-use tariffs, prosumers are encouraged to shift their energy use to off-peak hours. By having BESS, prosumers can choose to charge the battery during the

valley price hours and store energy for their peak load. The charge and discharge power are limited to the maximum surge power:

$$\left|P^B_{i,y,t}\right| \leq P^B_{\max,i,y} \tag{9}$$

where $P^B_{i,y,t}$ is the battery charge and discharge power. And when $P^B_{i,y,t} > 0$, the battery energy storage system is charging. To make sure that the battery can maintain a healthy and stable operation state, the accurate state of charge (SOC) constraint is given as follows.

$$SOC_{\min i,y} \leq SOC_{i,y,t} \leq SOC_{\max,i,y} \tag{10}$$

And $SOC_{\max,i,y}, SOC_{\min,i,y}$ are the maximum and minimum limits. During the charging, the constraint between the SOC and charging power can be given as:

$$SOC_{i,y,t} = (1 - \varepsilon_B)SOC_{i,y,t-1} + \frac{\partial_c P^B_{i,y,t}\Delta t}{S^{cap}_{B,i,y}} \tag{11}$$

where ε_B is the self-discharge loss rate of battery energy storage system, and $SOC_{i,y,t-1}$ is the SOC during the last time period. And ∂_c is the charging efficiency. $S^{cap}_{B,i,y}$ is the battery capacity and Δt is the unit charging and discharging time. Similarly, the constraint for the discharge can be written as:

$$SOC_{i,y,t,d} = (1 - \varepsilon_B)SOC_{i,y,t-1} + \frac{P^B_{i,y,t}\Delta t}{\partial_d S^{cap}_{B,i,y}} \tag{12}$$

where ∂_d is discharge efficiency. Besides, prosumer i has the power balance constraints:

$$P^{PV}_{i,y,t} + P^{ng}_{i,y,t} + P^{op}_{i,y,t} = P^L_{i,y,t} + P^B_{i,y,t} \tag{13}$$

Distribution Network Operation. The network operator is required to confirm that the power flow constraints are satisfied. For bus m, the power flow constraints can be given as:

$$
\begin{aligned}
P^f_{m,y,t} &= \sum_{i\in\Omega_m} (P^{PV}_{i,y,t} - P^L_{i,y,t} - P^B_{i,y,t}) \\
P^f_{m,y,t} + \sum_{n\in\Omega^1_m} P^f_{mn,y,t} &= \sum_{l\in\Omega^0_m} [P^f_{lm,y,t} - R_{lm}\frac{(P^f_{lm,y,t})^2 + (Q^f_{lm,y,t})^2}{(V_{l,y,t})^2}] \\
Q^f_{m,y,t} &= \sum_{i\in\Omega_m} (Q^L_{i,y,t}) \\
Q^f_{m,y,w,k} + \sum_{n\in\Omega^1_m} Q^f_{mn,y,t} &= \sum_{l\in\Omega^0_m} [Q^f_{lm,y,t} - X_{lm}\frac{(P^f_{lm,y,t})^2 + (Q^f_{lm,y,t})^2}{(V_{l,y,t})^2}]
\end{aligned}
\tag{14}
$$

where $P^f_{m,y,t}$ is the active power injected in bus m and $Q^f_{m,y,t}$ is the reactive power. Ω^1_m are buses connected to bus m and with power flow from bus n to bus m. And Ω^0_m are buses connected to bus m with power flow from bus m to bus l. And for the line between bus m and bus l:

$$
(V_{m,y,t})^2 = (V_{l,y,t})^2 - 2(R_{lm}P^f_{lm,y,t} + X_{lm}Q^f_{lm,y,t})
$$
$$
+[(R_{lm})^2 + (X_{lm})^2]\frac{(P^f_{lm,y,t})^2 + (Q^f_{lm,y,t})^2}{(V_{l,y,t})^2} \tag{15}
$$

$$
V^{min}_m \le V_{m,y,t} \le V^{max}_m, I^f_{lm,y,t} \le I^{max}_{lm} \tag{16}
$$

$$
(I^f_{mn,y,t})^2 = \frac{(P^f_{mn,y,t})^2 + (Q^f_{mn,y,t})^2}{(V_{m,y,t})^2} \tag{17}
$$

Based on the second-order cone constraints, use the following constraints to replace the current and voltage:

$$
\tilde{I}^f_{mn,y,t} = (I^f_{mn,y,t})^2, \tilde{V}_{m,y,t} = (V_{m,y,t})^2 \tag{18}
$$

The constraints can be further written as the standard second order cone constraint:

$$
\left\| \begin{matrix} 2P^f_{mn,y,t} \\ 2Q^f_{mn,y,t} \\ \tilde{I}^f_{mn,y,t} - \tilde{V}_{m,y,t} \end{matrix} \right\|_2 \le \tilde{I}^f_{mn,y,t} - \tilde{V}_{m,y,t} \tag{19}
$$

3.2 Expansion Model

Prosumers can obtain profits by expanding their domestic renewable generation so that they have more energy to exchange and share. The investment cost function of prosumer i in the y_{th} year can be given as:

$$
f^{inv}_{i,y} = f^{inv,PV}_{i,y} + f^{inv,battery}_{i,y} \tag{20}
$$

where $f^{inv,PV}_{i,y}$ is the prosumer's investment in PV generation and $f^{inv,battery}_{i,y}$ is the investment related to BESS.

PV Generation Expansion Investment. The investment in PV generation is calculated using the equivalent annual worth within the lifespan of PV panels. We consider the marginal cost of PV generation is negligible. Thus, the investment cost function of PV generation can be written as:

$$
f^{inv,PV}_{i,y} = R_{PV}(c_{PV}P^{cap,PV}_{i,y}) \tag{21}
$$

$$R_{PV} = \frac{d_{PV}(1 + d_{PV})^{y_{PV}}}{(1 + d_{PV})^{y_{PV}-1}} \tag{22}$$

where d_{PV} is the discount rate of PV, and y_{PV} is the average lifespan of PV panels. We assume that all the PV panels are within the lifespan and in service, so the $P_{i,y+1}^{\text{cap,PV}}$ in the next year should not be less than that in this year:

$$P_{i,y+1}^{\text{cap,PV}} \geq P_{i,y}^{\text{cap,PV}} \tag{23}$$

Storage System Investment. The cost function of battery energy storage system includes the investment on batteries construction and the operating cost during the charging and discharging process:

$$f_{i,y}^{\text{inv,battery}} = f_{i,y}^{\text{construction,B}} + f_{i,y}^{\text{operation,B}} \tag{24}$$

And the construction investment cost includes two parts: costs related to battery capacity and costs related to battery charge and discharging ability:

$$f_{i,y}^{\text{construction,B}} = c_s S_{i,y}^{\text{cap,B}} + c_p P_{\text{max},i,y}^{B} \tag{25}$$

where c_s and c_p are per unit cost related to the capacity and the charge or discharge ability. And the operation cost can be given as:

$$f_{i,y}^{\text{operation}} = \frac{c_p P_{\text{max},i,y}^{B}}{(1 + d_B)^{y_B-1}} \tag{26}$$

where d_B is the discount rate and y_B is the average lifespan of energy storage equipment. We also assume that there is no battery reaching the lifespan limit so the capacity and maximum charge/discharge power of the system will not decrease during the planning horizon:

$$S_{i,y}^{\text{cap,B}} \geq S_{i,y-1}^{\text{cap,B}}, \ P_{\text{max},i,y}^{B} \geq P_{\text{max},i,y-1}^{B} \tag{27}$$

$$P_{\text{max},i,y}^{B} T_B = S_{i,y}^{\text{cap,B}} \tag{28}$$

where T_B is average charge/discharge time. Besides, there are upper and lower limits on the capacity of energy storage:

$$S_{i,\min}^{\text{cap,B}} < S_{i,y}^{\text{cap,B}} < S_{i,\max}^{\text{cap,B}} \tag{29}$$

Thus, the proposed model includes Eq. (1) as the objective function and Eq. (3), Eq. (8)–(10), Eq. (13), Eq. (15)–(19), Eq. (23), and Eq. (27)–(29) as the constraints, which is a mixed-integer linear programming problem and it can be solved using commercial solvers.

4   Case Studies

4.1   Simulation Setup

This section presents the simulation results and analysis of the various case studies. A standard IEEE 33-bus system with 10 prosumers and a network operator is considered. And the bus 33 is considered as the slack bus where the distribution network operator is located. Prosumers can expand their PV and BESS systems, and they are notified of the trading price with the network operator in advance. The selling price is set to be CNY 0.2 and purchase prices are based on Shanghai peak-valley electricity prices for domestic usage. And the load level of prosumers is set to increase 10% per year gradually during the 5-year planning horizon.

4.2   Results and Analysis

The results of PV capacity expansion of prosumers with and without P2P transactions are shown in Fig. 2. During the planning horizon of 5 years, prosumers will expand their PV generation gradually whether with or without P2P transactions. Yet by comparing the expansion results between the situation with and without P2P transactions, it can be noticed that PV generation increases larger and faster with P2P transactions than that without P2P transactions. Thus, the results verify that the proposed P2P transactions can encourage prosumers to increase their PV capacity, which helps to increase the penetration of distributed energy resources in the whole distribution network.
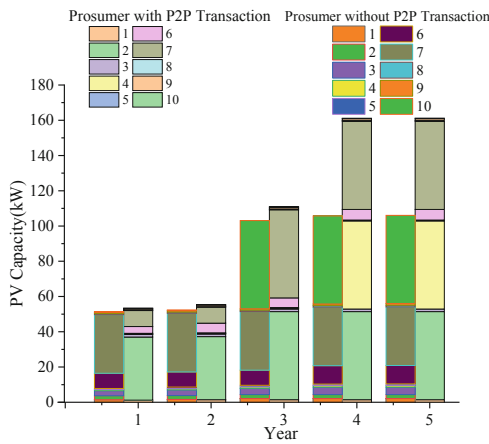
Fig. 2. PV Generation Expansion of Prosumers
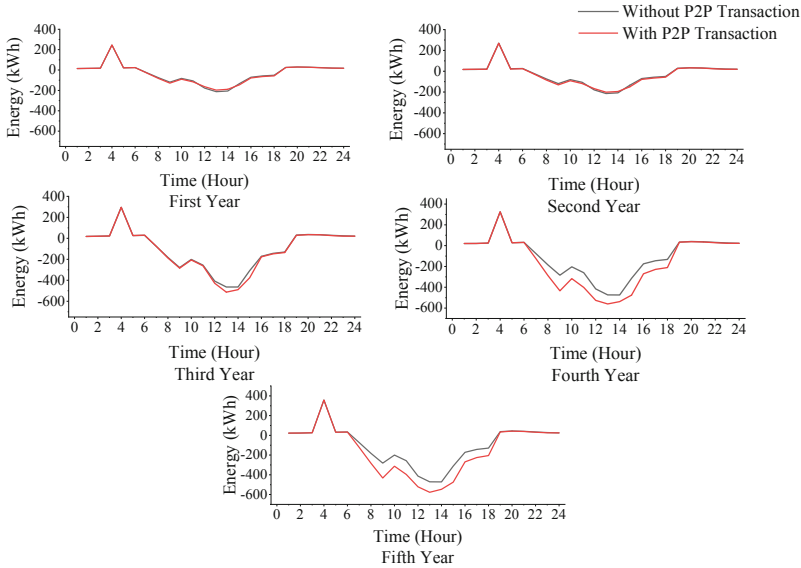
Fig. 3. Energy Traded between Prosumers and the Network Operator

The evolution of energy traded between prosumers and the network operator is shown in Fig. 3, which illustrates that P2P transactions can effectively reduce the peak of the energy traded. Compared with the results in Fig. 2 and Fig. 3, it should be noticed that although the PV capacity increase larger with P2P transactions, and the traded energy with the operator is less than that without P2P transactions, especially during peak hours of PV generation.
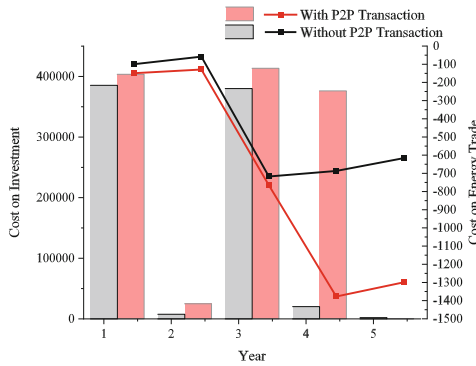
Fig. 4. Investment and Cost on Energy Trading

The costs of investment and energy trading are illustrated in Fig. 4. It should be noted that when the cost is negative, it represents the income for prosumers. The investment is higher with P2P transactions than that without P2P transactions, which is consistent with

the expansion results in Fig. 2. And the line chart confirms that P2P transactions help prosumers to save bills on energy purchasing, not only because of a more reasonable trading price between prosumers, but also resulting from more PV panels have been installed which offers more self-produced energy to prosumers.

5 Sensitivity Analysis

5.1 P2P Trading Price

In this section, we analyse the impact of P2P trading price. From Case 1 to Case 5, we consider the different P2P trading prices which increase at the pace of 20%. The prosumers load and solar resources remain the same in this section.

PV Capacity. Figure 5 shows the PV capacity expansion considering the fluctuation of P2P trading price. It can be seen that as P2P trading prices increase, the P2P transactions offer more incentives to prosumers to postpone their plan to install more PV panels to a certain degree, though the relationship between the price and PV capacity is not strictly linear.

Cost on Energy Trading. The results of the cost on energy trading with different P2P trading prices of prosumers are shown in Fig. 6. The evolution of cost is consistent with the trend of PV generation expansion. The benefits increase significantly when the PV capacity enlarges. Thus, it verifies that PV generation expansion brings profits to the prosumers in the distribution network market.
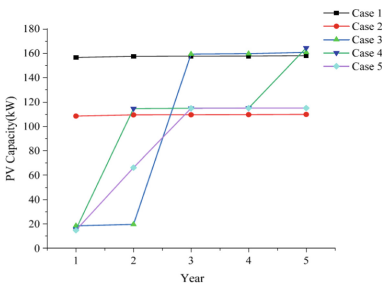
Fig. 5. PV Capacity with Different P2P Transaction Prices
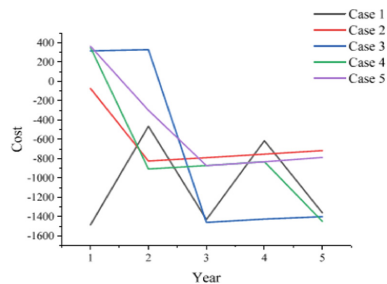
Fig. 6. Cost on Energy Trading with Different P2P Transaction Prices

Energy Traded with Network Operator. The evolution of energy traded with the network operator is shown in Fig. 7, and in Case 2 and Case 5 the energy sold to the operator is less than that in other cases, which is consistent with the results in Fig. 5. Thus, we believe the energy traded with the operator is mainly influenced by PV capacity, and P2P trading price only has an indirect impact through changing the PV capacity.
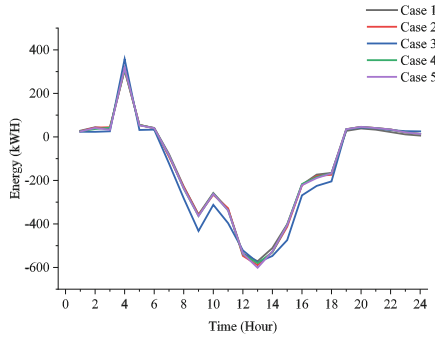
Fig. 7. Energy Traded with Different P2P Transaction Prices

5.2   Prosumers Load

In this section, the impact of prosumers' load is studied. From Case 1 to Case 5, the load increases by 20%, and during the planning horizon of 5 years and the growth rate remains at 10% each year. The P2P trading price and solar resources stay the same in this section.

PV Capacity. The obtained PV capacity results are shown in Fig. 8, from which can be seen that prosumers' load level mostly influences the expansion process of PV generation but only has a limited impact on the final expansion results in the fifth year.
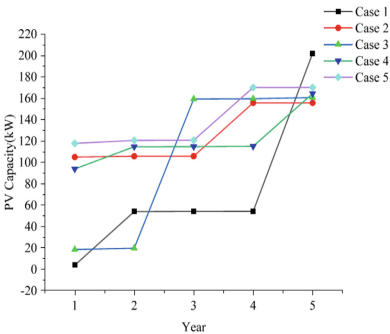
Fig. 8. PV Capacity with Different Load Levels
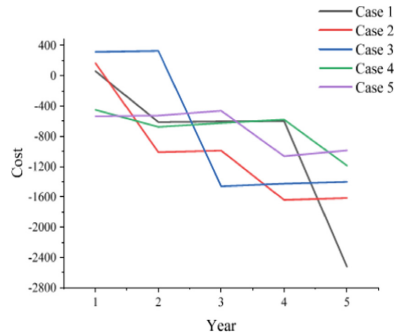
Fig. 9. Cost on Energy Trading with Different Load Levels

Cost on Energy Trading. Figure 9 shows the results of cost on energy trading with different load levels of prosumers. And as the load increases, the profits gained from selling energy shrink gradually. And compared to the results in Fig. 8, the evolution of cost is consistent with the PV generation expansion results, as prosumers' profits increase mostly in the year when the PV capacity is expanded.

Energy Traded with Network Operator. Figure 10 shows energy traded with the network operator as the load increases. Prosumers tend to purchase more energy from
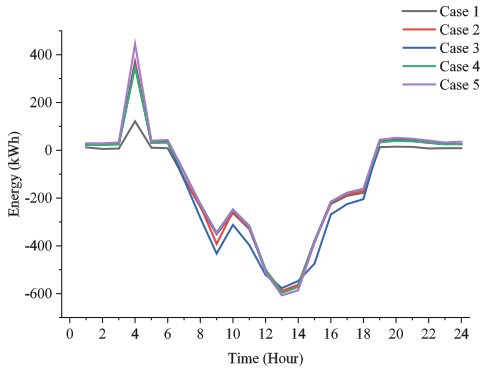
Fig. 10. Energy Traded with Different Load Levels

network operator when their load increase, especially during the hours without PV generation in the early morning. During the time when the PV panels are generating, there is no significant difference in the energy traded when prosumers load increases.

5.3 Solar Resources

In this section we consider situations of different local solar resources and weather conditions, which will directly influence PV generation level. The P2P trading price and prosumers load remain the same in this section.
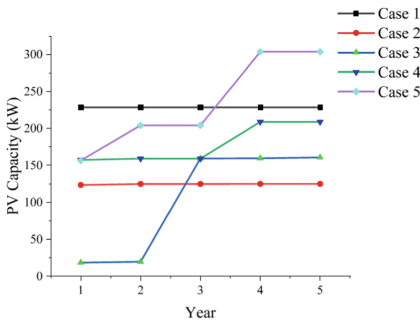
Fig. 11. PV capacity with different solar resources
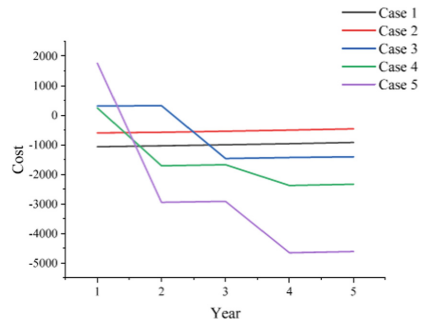
Fig. 12. Cost on energy trading with different solar resources

PV Capacity. From the results shown in Fig. 11, it can be seen that when solar resources become abundant, prosumers will install more PV panels. However, in the Case 1 with the solar resource shortage, prosumers also tend to enlarge their PV capacity to compensate for the insufficient solar resources.

Cost on Energy Trading. Figure 12 shows the prosumer cost of energy trading. The income increases under abundant solar resources conditions, which indicates as the
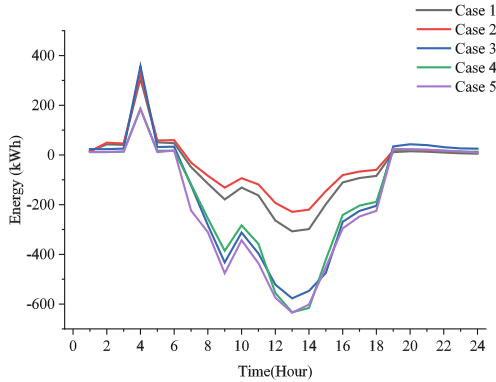
Fig. 13. Energy traded with different solar resources

PV generation level increases, prosumers are able to gain more profits by selling self-produced energy. And compared with the results in Fig. 11. we can also see that in Case 1 the profits remain at the ideal level, because prosumers increase PV capacity to compensate for the insufficient solar resources.

Energy Traded with Network Operator. From the results in Fig. 13, it can be seen that with more solar resources, prosumers are able to increase the energy sold to the network operator, which is consistent with the results in Fig. 12.

6   Conclusion

In this article, the long-term impacts of P2P transactions on prosumers' planning in the distribution network are studied. In the market models, prosumers participate in P2P transactions among their peers and trade with the network operator. Then the operation model of the distribution network including PV generation and BESS is established, with the expansion models of PV generation and battery storage systems. Implemented case studies verified that P2P transactions not only influence prosumers' marketing strategies, but also change the long-term expansion planning of prosumers. It is demonstrated that P2P transactions can effectively increase the penetration of distributed energy resources in the distribution network and reduce the fluctuation of power flow between the distribution network and the main grid. Besides, P2P transactions bring benefits to prosumers by saving the cost of purchasing energy.

References

1. Khorasany, M., Mishra, Y., Ledwich, G.: A decentralized bilateral energy trading system for peer-to-peer electricity markets. IEEE Trans. Industr. Electron. **67**(6), 4646–4657 (2020)

2. Parag, Y., Sovacool, B.K.: Electricity market design for the prosumer era. Nature Energy **1**(4), 16032 (2016)
3. Tushar, W., Yuen, C., Saha, T.K., et al.: Peer-to-peer energy systems for connected communities: A review of recent advances and emerging challenges. Appl. Energy **282**, 116131 (2021)
4. Zhou, Y., Wu, J., Long, C., et al.: State-of-the-art analysis and perspectives for peer-to-peer energy trading. Engineering **6**(7), 739–753 (2020)
5. Kim, J., Dvorkin, Y.: A P2P-dominant distribution system architecture. IEEE Trans. Power Syst. **35**(4), 2716–2725 (2020)
6. Sorin, E., Bobo, L., Pinson, P.: Consensus-based approach to peer-to-peer electricity markets with product differentiation. IEEE Trans. Power Syst. **34**(2), 994–1004 (2019)
7. Yang, J., Zhao, J., Wen, F., et al.: A framework of customizing electricity retail prices. IEEE Trans. Power Syst. **33**(3), 2415–2428 (2018)
8. Yang, J., Zhao, J., Wen, F., et al.: A model of customizing electricity retail prices based on load profile clustering analysis. IEEE Trans. Smart Grid **10**(3), 3374–3386 (2019)
9. Huang, C., Wang, C., Xie, N., et al.: Robust coordination expansion planning for active distribution network in deregulated retail power market. IEEE Trans. Smart Grid **11**(2), 1476–1488 (2020)
10. Zheng, B., Wei, W., Chen, Y., et al.: A peer-to-peer energy trading market embedded with residential shared energy storage units. Appl. Energy **308**, 118400 (2022)
11. Jin, Y., Choi, J., Won, D.: Pricing and operation strategy for peer-to-peer energy trading using distribution system usage charge and game theoretic model. IEEE Access **8**, 137720–137730 (2020)
12. Xiao, Y., Wang, X., Pinson, P., et al.: Transactive energy based aggregation of prosumers as a retailer. IEEE Trans. Smart Grid **11**(4), 3302–3312 (2020)
13. Sampath, L.P.M.I., Paudel, A., Nguyen, H.D., et al.: Peer-to-peer energy trading enabled optimal decentralized operation of smart distribution grids. IEEE Trans. Smart Grid **13**(1), 654–666 (2022)
14. Li, J., Khodayar, M.E., Wang, J., et al.: Data-driven distributionally robust co-optimization of P2P energy trading and network operation for interconnected microgrids. IEEE Trans. Smart Grid **12**(6), 5172–5184 (2021)
15. Ullah, M.H., Park, J.: Peer-to-peer energy trading in transactive markets considering physical network constraints. IEEE Trans. Smart Grid **12**(4), 3390–3403 (2021)
16. Morstyn, T., McCulloch, M.D.: Multiclass energy management for peer-to-peer energy trading driven by prosumer preferences. IEEE Trans. Power Syst. **34**(5), 4005–4014 (2019)
17. Baroche, T., Pinson, P., Latimier, R.L.G., et al.: Exogenous cost allocation in peer-to-peer electricity markets. IEEE Trans. Power Syst. **34**(4), 2553–2564 (2019)
18. Li, L., Bingqian, X., Haohuai, W.: Analysis and recommendations of typical market-based distributed generation trading mechanisms. Autom. Electric Power Syst. **43**(04), 1–8 (2019)

Analysis and Prospects of Status of Broadband Oscillation and Suppression Methods for New Energy Stations Connected to Power System

Xinyu Lei, Wei Wang, Zheng Wei[✉], Xiaojun Deng, Quanquan Huang, and Dongmei Yang

NARI Group Corporation (State Grid Electric Power Research Institute), Nanjing 211106, China
weizheng2@sgepri.sgcc.com.cn

Abstract. New energy installations in China have increased greatly, and the strategic goals of "emission peak" and "carbon neutrality" have been put forward. The high proportion of new energy grid has become the development trend of the future grid. However, the stability of power systems connected to large new energy stations is a serious problem, and broadband oscillation needs to be solved urgently. Aiming at the problem of wideband oscillation, the control strategy of new energy grid-connected inverter is introduced. Then, the modeling method of grid-connected power generation system and its advantages and disadvantages are introduced. The oscillation mechanism in the current research is also analyzed. Finally, several strategies for oscillation suppression are compared. The main points and limitations of the current research are pointed out from these aspects: control system and strategy, system modeling and analysis method, and broadband oscillation suppression methods. Future research directions are also given.

Keywords: New energy station · Broadband oscillation · The control strategy · The modeling method of grid-connected system · Oscillation mechanism · Oscillation suppression

1 Introduction

Since entering the 21st century, the development and utilization of clean energy have triggered a new round of energy transformation. As of 2020, China has 280 million kilowatts of wind power and 250 million kilowatts of photovoltaic power. In 2020 alone, the installed capacity of wind power has been 71.67 million kW and PV power has been 48.2 million kW, which is faster than expected [1]. With the realization of the goal of "double carbon", the future power system will develop in the direction of the high proportion of new energy, and the new scenarios derived from the high proportion of new energy access to the power system also bring new challenges for the stable operation of the power system.

   In the power system with a high proportion of new energy sources, the power grid is characterized by a weak synchronous power grid dominated by a high proportion of power electronic devices, and the complex control functions of new energy power generation devices are intertwined with the characteristics of weakly synchronous power grids. The dynamic characteristics of the power system connected to large-scale new energy stations are extremely complex, and the stability problems are prominent. Among them, the more typical one is the oscillation problem of a high-proportion new energy power system in a wide frequency range.

   In 2009, a sub-synchronous oscillation with the frequency of 20–25 Hz occurred in a wind farm in Texas, USA, when the wind farm fed through a crosstalk line, causing damage to the crowbar circuit of the wind turbine. It oscillated again in 2018 [2]. In the same year, under the influence of cables, the German North Sea wind power soft direct transmission system also had a resonant potential of 100–1000 Hz of medium and high-frequency harmonics, causing the system to be shut down for 10 months. Since 2011, there have been more than a hundred times of sub-synchronous oscillations caused by wind power fed through cascaded complementary lines at the Guyuan wind farm in Hebei, China, with the frequency varying in the 3–10 Hz interval [3, 4]. Since 2015, sub-synchronous oscillations have occurred several times when large-scale wind power was connected to the system in the Hami region of Xinjiang, China, with oscillations the frequency of 20–40 Hz, even leading to a turbine unit shaft system torsional vibration, causing an accident with a power plant unit 300 km away fully jumping and a sudden drop in UHV DC power [5]. Oscillations of about 3 Hz occurred in the Guangxi Yongfu LCC-HVDC and cascade complementary transmission system. And a PV power plant in Qinghai had resonance above 1350 Hz when connected to the grid.

   These new energy broadband oscillation accidents have the following characteristics.

1) The oscillation frequency is located in the wide band range of 2–2 kHz, containing electrical oscillations and mechanical torsional vibrations. This condition is prone to induce resonance.
2) The interaction mechanisms between the power electronic converters and the large power grid are qualitatively different from conventional low-frequency mechanisms and are sub/super-synchronous oscillations by the turbine unit inertia and shaft system dynamics.
3) Oscillation-related characteristics, such as frequency and damping, are influenced by the power grid, power electronics, grid-connected units, and even external factors. The influencing factors are very complex.
4) Because of the finite capacity of power electronics, the control input needs to be limited, leading to oscillations, which usually start with a negative damping dispersion of small signals and culminate in nonlinear, continuous oscillations [5].

   Therefore, the analysis of the oscillation mechanism of large-scale new energy field stations connected to the power system and the oscillation suppression of each frequency band are important technical bases for improving the activation of new energy sources and promoting the energy consumption of new energy sources.

Given the above problems, this paper summarizes and analyzes different modeling methods of new energy units on the basis of existing new energy grid-connected control systems and strategies, and expounds on the broadband oscillation mechanism of new energy access to the grid from the perspectives of time and frequency domains. On this basis, the paper summarizes and compares the unit and station suppression methods of broadband oscillation. The key problems and possible solutions are put forward to provide a useful reference for the stability problems of large-scale new energy field stations connected to the power system.

2 New Energy Grid Connection Control System and Strategy

There are two main control strategies of new energy grid-connected inverters: current-source control strategy and voltage-source control strategy. Among them, the grid-connected inverter in the current source control mode mainly relies on the phase-locked loop section to realize the following synchronous operation to the grid, and the grid-connected inverter in the voltage source control mode can realize the parallel synchronous operation to the grid by building its own internal potential.

2.1 Current Source Control Strategy Based on Phase-Locked Grid Connection

The grid-connected inverters based on the current source control strategy mainly adopt grid voltage orientation scheme based on phase-locked loop control, as shown in Fig. 1 [6]. In order to improve the dynamic response of inverters, the inverter grid voltage feedforward module of grid voltage is usually added.
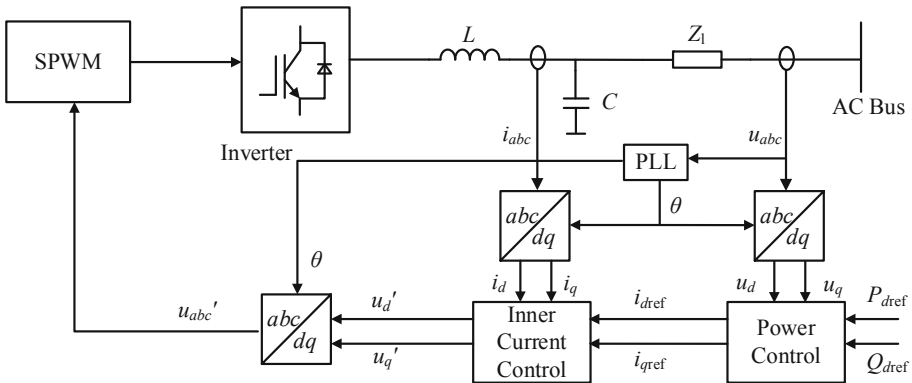
Fig. 1. Current-source converter control strategy

At present, the current source control strategy is used in most grid-connected inverters. The current source grid-connected inverter can greatly improve the utilization rate of new energy and ensure the quality of grid-connected power under the strong grid. However, with the increase in the new energy ratio, the grid shows the characteristics of weak grid. The grid-connected inverter controlled by the current source mode reduces the stability when the grid impedance fluctuates greatly and is prone to harmonics and oscillations.

Under the weak grid, the Phase-locked Loop (PLL), as a traditional synchronization unit that keeps the grid-connected inverter synchronized with the large grid, will have a negative impact on the stability of the grid-connected inverter. For example, a quasi-static phase-locked loop model is developed in [7], indicating that high grid input impedance and high penetration of distributed generation units can lead to unstable phase-locked loops. It also affects the stability of the inverter. The impedance model of the new energy grid-connected system is established in [8] by the impedance method. It is proposed that the output impedance of the grid-connected generation system will be negative at low frequency due to the high phase-locked loop, which will affect the stability of the grid-connected generation system under the weak grid. Meanwhile, grid voltage feedforward control also affects the stability of the grid-connected system under the weak grid. The impedance model of distributed grid-connected systems is analyzed in [9]. The result shows that grid voltage feedforward control can adversely affect the system stability under the weak grid. In response to the above problems, some experts put forward the corresponding stability control measures for new energy grid-connected systems in current source mode, such as virtual impedance control, impedance reshaping of voltage feedforward links, and phase-locked loop sections [10–12]. However, the current source control strategy still has some limitations in voltage and frequency control, and it is difficult to adapt to the high proportion of new energy access.

2.2 Voltage Source Control Strategy Based on Virtual Synchronous Generator Control

Some articles propose a voltage source grid-connected mode without PLL, which has better stability than the current source mode under the weak grid conditions. The voltage source mode uses a networked synchronous control unit, such as the power outer loop based on droop control or the virtual synchronous generator, for phase self-synchronization to achieve output power regulation [13]. The voltage source mode grid-connected inverter directly adjusts the output power by controlling the phase and amplitude of the output voltage vector, so that it can directly provide voltage and frequency support for the system. The control characteristics are similar to those of the synchronous generator system [14–16]. Figure 2 shows the control diagram of the grid-connected inverter with the voltage source droop control strategy.
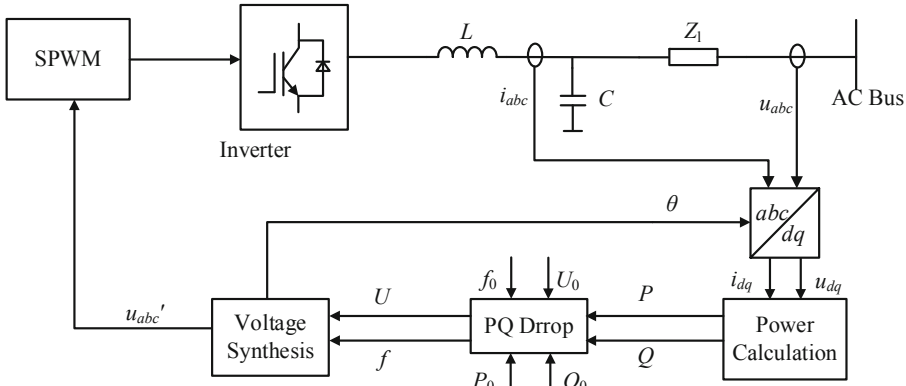
Fig. 2. Voltage-source converter control strategy

The voltage source VSG directly simulates the equation of motion of the rotor of the synchronous generator. It can run in parallel operation with the power grid without going through the phase-locking link, and directly provide voltage and frequency support for the system. Therefore, it is ideal for weak power grids. Based on the above advantages, it has attracted more and more attention from research scholars in recent years. In 2020, the world's first voltage source wind turbine was successfully connected to the grid at Zhangbei, China. In [17–20], the stability of voltage-sourced inverters at low grid strength is analyzed respectively from the perspective of impedance modeling and time-domain state-space modeling. It is pointed out that the inverters under the voltage-sourced control strategy have better stability compared with the traditional current-source control strategy under low grid strength.

3   New Energy Grid System Modeling and Analysis Method

At present, the theoretical modeling of new energy grid-connected systems is mainly conducted in the time domain and frequency domain. The time-domain modeling mainly establishes the state-space model of the grid-connected system and analyzes the stability of the new energy unit access system by drawing the characteristic root trajectory. The frequency-domain modeling needs to construct the impedance model of the new energy unit and analyzes the stability of the new energy unit access system quantitatively by the Nyquist impedance stability criterion.

3.1   Time-Domain Modeling and Analysis Methods

Time-domain modeling means merging the grid-connected inverter with the grid as a system and establishing a state-space model of the whole system. Then eigenvalue analysis is performed, and the stability state of the system is judged based on the obtained eigenvalues and eigenvectors. The corresponding frequencies of oscillation modes, damping ratios, and participation factors can be obtained by further calculations, so that the accurate information related to system stability can be obtained based on the eigenvalues of the state-space model in the time domain.

The dynamic process of the power system can be represented by the following differential-algebraic equations [21]:

$$\begin{cases} \frac{dx}{dt} = f(x, y) \\ 0 = g(x, y) \end{cases} \tag{1}$$

where $x = [x_1, x_2,..., x_n]^T$ is the state variable and $y = [y_1(x), y_2(x),..., y_m(x)]^T$ is the algebraic variable

After the system is linearized at the equilibrium point, it can be obtained:

$$\frac{d\Delta x}{dt} = \mathbf{A}\Delta x \tag{2}$$

where $\mathbf{A}$ is the state matrix of the system. By solving the eigenvalue of $\mathbf{A}$, the stability of the system can be judged.

Through the eigenvalue analysis method, the participation factor can be calculated to determine the state variables associated with the unstable mode, and further control can be added to the relevant state to achieve the purpose of suppressing oscillation. It is also possible to analyze the sensitivity of the oscillation mode to the system parameters through sensitivity analysis and determine the parameters that have a great influence on the unstable mode. In [22], the time-domain state-space model of the wind farm cluster equivalent system was established. According to the eigenvalue analysis method, the oscillation characteristics and oscillation frequency near the static operating point were analyzed and obtained. The traditional eigenvalue analysis method based on the state-space model has been widely used in the stability analysis of the traditional power system. At present, most software can directly establish the state-space model for stability analysis according to the simulation object.

However, this modeling method requires complete information about the equipment and power grid in the system, and is only applicable to the case where the access part of new energy power generation is a "white box". As the scale of the system expands and more and more power electronic equipment is connected to the power system, the network structure of the system becomes complex. The use of the time-domain modeling method will lead to a sharp increase in the order of the state-space model, and the calculation will face the "dimension disaster". On the other hand, when the operating state of the system changes, the state matrix of the system changes accordingly, and the state-space model of the system needs to be re-established, resulting in poor flexibility of the method [23].

3.2 Frequency-Domain Modeling and Analysis Methods

Frequency-domain impedance modeling is a method for modeling the external characteristics of small-signal impedance in the frequency domain of the new energy grid-connected system. In this method, the impedance models of the grid-connected inverter part and the grid part are built independently, and they are mutually independent. Therefore, the method reduces the workload of impedance modeling and the difficulty of analysis when the system operation state is changed. After the impedance model is established, the equivalent circuit of this interactive system is represented by a linear

network structure, and then the impedance analysis method is used to analyze the system stability. The equivalent circuit diagram of the impedance analysis model is shown in Fig. 3.
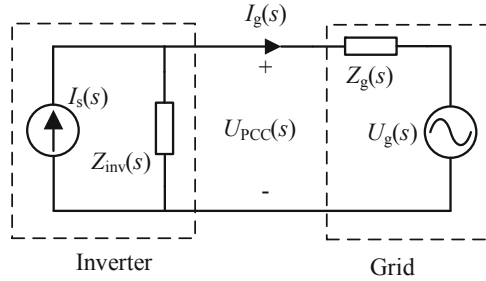
Fig. 3. Impedance Modeling Equivalent Circuit

The impedance analysis method is briefly introduced below. It splits the system into a grid-connected inverter subsystem and a power supply subsystem. The small-signal models are linearized and the output impedances of both are obtained separately. And the condition for system stability is that the impedance ratio of the two systems meets the Nyquist stability criterion. According to Fig. 3, the expression of grid-connected current is as follows [24]:

$$I_g(s) = [I_s(s) - \frac{U_g(s)}{Z_{inv}(s)}] \cdot \frac{1}{1 + Z_g(s)/Z_{inv}(s)} \tag{3}$$

In the formula, when the two subsystems of the grid-connected inverter and the grid can operate independently and stably, the stability of the grid-connected current $I_g(s)$ depends on the second term on the right side of the equation, $1/[1 + Z_g(s)/Z_{inv}(s)]$.

The system is stable only if the ratio $Z_g(s)/Z_{inv}(s)$ of the grid impedance to the grid-connected inverter output impedance meets the Nyquist criterion. At present, the impedance analysis method has been widely used in the stability research of grid-connected inverters, and has become one of the hotspots in the research on the stability of grid-connected interactive systems.

There are three main ways to model impedance in frequency domain: impedance modeling in dq synchronous rotating coordinate system, positive and negative sequence impedance modeling in abc three-phase stationary coordinate system, and generalized impedance modeling in polar coordinate system.

(1) Impedance modeling and stability analysis method in DQ synchronous rotation coordinate system.

In 1997, Belkhayat first proposed the theoretical method of linearization modeling of dq coordinate system in [25]. In a subsequent study, the method was applied to an example of output impedance modeling of grid-tied inverters. The dq coordinate system impedance model is a two-dimensional matrix. The idea of the method is to first use Park transformation to convert the AC signal in the abc stationary coordinate system to the

dq coordinate system, which makes the original AC signal equivalently converted into a DC circuit with coupling. Subsequently, the d and q-axis components are linearized to obtain the impedance model in the dq synchronous rotating coordinate system. The output impedance matrix of the impedance modeling in the dq synchronous rotating coordinate system can be written as the following form:

$$Y_{sdq}(s) = \begin{bmatrix} Y_{dd}(s) & Y_{dq}(s) \\ Y_{qd}(s) & Y_{qq}(s) \end{bmatrix} \tag{4}$$

This method is equivalent to constructing the DC operating point of the system, which solves the problem that the three-phase voltage and current of the grid-connected inverter cannot be linearized by traditional small signals. Due to the dynamic coupling of the d and q-axis impedances in the model, the impedance model is expressed in matrix form, and the generalized Nyquist stability criterion needs to be applied for analysis. Due to the complexity of the generalized Nyquist criterion, the criterion is simplified and a stability criterion based on $Z_{gdq}(s)$ and $Y_{sdq}(s)$ norms is proposed. The performance criterion can be used to guide the parameter design of the control system. According to the characteristic equation of the impedance transfer function, a criterion based on the singular value of impedance is proposed in [26], which requires that the product of the largest singular value of $Z_{gdq}(s)$ and the largest singular value of $Y_{sdq}(s)$ at any frequency point is less than 1, and its The mathematical expression is:

$$\overline{\sigma}[Z_{gdq}(s)] \cdot \overline{\sigma}[Y_{sdq}(s)] < 1 \tag{5}$$

And beyond that, other impedance matrix criteria have been proposed in related research, such as G-norm criterion, ∞-norm criterion, Sum-norm criterion, etc. Among the AC system stability analysis criterion, the data criterion is the easiest to analyze the system stability, and it can make up for the shortcoming that the singular value criterion cannot guide the parameter design, but it is more conservative.

Since the control of most three-phase systems is carried out in the dq coordinate system, the impedance model in the dq synchronous rotating coordinate system is compatible with the control and transformation of the new energy power generation system, which makes the modeling method easy to implement. But it is limited to a three-phase balanced system, not suitable for a single-phase or unbalanced three-phase system. When the generalized Nyquist stability criterion is used to analyze the stability of the grid-connected system, the analysis is more complicated, which is very unfavorable for the stability analysis of the grid-connected inverter. At the same time, in the AC system, the impedance matrix in the dq coordinate system lacks actual physical meaning and lacks measurement equipment. Therefore, the impedance modeling analysis method in the dq synchronous rotating coordinate system has obvious limitations.

(2) Positive and negative sequence impedance modeling and stability analysis method in ABC three-phase static coordinate system.
The impedance modeling method in the dqsynchronous rotating coordinate system has many drawbacks in practical applications, therefore, Jian Sun established a small-signal positive and negative sequence impedance model of a three-phase grid-connected converter based on abc three-phase stationary coordinate system using the harmonic linearization method in [27]. The basic method is to attach a small-signal disturbance at

the PCC, then derive the effect of the disturbance frequency on the current by harmonic linearization. On this basis, the positive and negative sequence impedance model in the abc three-phase stationary coordinate system is deduced.

Under the sequence impedance model, the obtained positive and negative sequence impedances are usually decoupled, so the analysis of the stability of the positive and negative sequence subsystems can be based on the basic Nyquist stability criterion, which makes the analysis process simpler. Only if the ratios $Z_{gp}(s)/Z_p(s)$ and $Z_{gn}(s)/Z_n(s)$ (the positive and negative sequence components of the grid impedance to the grid-connected inverter output impedance) both satisfy the Nyquist criterion, the interactive system between the grid inverter and the grid is stable. And the stability margin of the interactive system can be judged according to the Nyquist curve of the ratio.

Compared with the linearization modeling method of the dq coordinate system, the positive and negative sequence impedance modeling in the three-phase stationary coordinate system needs to perform complex phase sequence transformation and algebraic transformation according to the circuit structure, which is more complicated. However, the positive and negative sequence impedances have clear physical meanings, which can be directly measured by equipment, and are suitable for single-phase or unbalanced three-phase systems But it still has some shortcomings. In some cases, it is necessary to consider the positive and negative sequence impedances coupled to each other, such as when the control parameters are asymmetric and when the voltage outer-loop control is taken into account. Because of the presence of the coupling term, it is necessary to apply the generalized Nyquist stability criterion for analysis. And it is modeled by the harmonic linearization method, so it cannot be used for conventional power generation equipment with operating control characteristics below the fundamental wave, and it is not applicable to system dynamics problems on the electromechanical time scale [28].

(3) Generalized impedance modeling in polar coordinates.

In addition to the above two modeling methods, a generalized impedance modeling method in the polar coordinate system is proposed in [29]. The small-signal impedance model of inverter port and grid port in polar coordinates is established, and based on this, a generalized impedance model of new energy inverter and grid is established, which simplifies the interaction between power electronic conversion equipment and grid. The resonance problem is caused by its generalized impedance. In [30], an equivalent complex circuit in the polar coordinate system was established, and the generalized impedance criterion is used to analyze the generalized impedance model in each frequency band connection is different.

The port characteristics of the grid-connected inverter can be represented by the following matrix:

$$\begin{bmatrix} I_m \\ I_\theta \end{bmatrix} = \begin{bmatrix} Y_{mm} & Y_{m\theta} \\ Y_{\theta m} & Y_{\theta\theta} \end{bmatrix} \begin{bmatrix} V_m \\ V_\theta \end{bmatrix} \tag{6}$$

where V_m and V_θ are the disturbances of voltage amplitude and phase, I_m and I_θ are the corresponding current amplitude and phase; the transfer matrix is the inverter output admittance in the phasor domain.

The generalized impedance criterion based on the generalized impedance modeling in the polar coordinate system does not need to use the generalized Nyquist criterion,

which simplifies the problem analysis. In addition, this method is more suitable for dealing with coupled terms, such as sub/super Coupling between synchronous impedances. However, it should be noted that this modeling method needs to be established under certain conditions that the power factor of the inverter is close to 1. But the new energy output power received by the new energy grid-connected system can include active power and reactive power at the same time, so this method has limitations. Still, the generalized impedance modeling method based on polar coordinate systems has very important research value.

4   Mechanism Analysis of Broadband Oscillation

According to the above-mentioned modeling and analysis methods of new energy grid-connected systems, scholars at home and abroad have modeled and analyzed new energy systems, and have carried out research on the mechanism of oscillation generation.

4.1   Oscillation Mechanism Analysis Based on Time-Domain Modeling

In [19], the oscillation influencing factors were analyzed by a small-signal modeling approach for current-source and voltage-source grid-connected inverters. Higher control bandwidth and lower grid strength will increase the negative damping of the inverter grid-connected system and reduce the grid-connected system stability for current-source grid-connected inverters. For voltage-source grid-connected inverters, lower control bandwidth will also increase the negative damping of the inner-loop control and reduce the grid-connected system stability, but lower grid strength will improve the system synchronization stability.

In [31–33], a study on the sub-synchronous oscillations of wind power access is conducted using the characteristic analysis method to analyze the effects of wind speed, line series complement capacitance, and grid-connected control structure on the sub-synchronous oscillations of grid-connected systems. It is shown that an increase in wind speed leads to an increase in system damping; while an increase in the string complement of the system leads to a decrease in system damping and a decrease in the frequency of sub-synchronous oscillations.
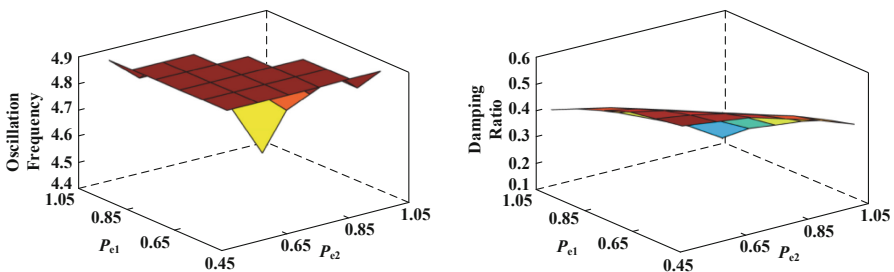
Fig. 4. Oscillation frequency and damping ratio of the system when operating conditions vary (SCR = 1.5, $k_{p1} = k_{p2} = 80$, Active power output $P_{ex} = 0.45$–1)
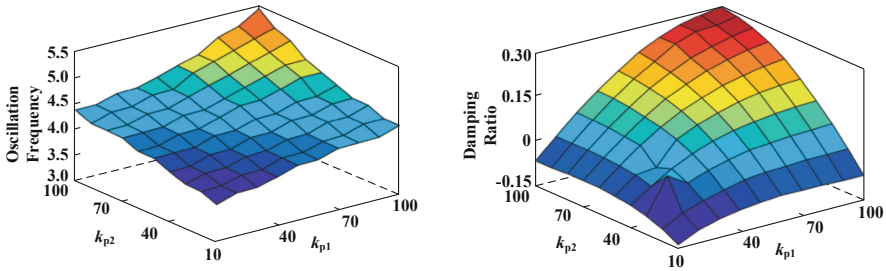
Fig. 5. Oscillation frequency and damping ratio of the system when PLL gains vary (SCR = 1.5, $P_{e1} = P_{e2} = 1$, Proportion factors $k_{px} = 10$–100)

In [34], the stability of parallel operation of PV generation equipment under a weak grid is explored. It is analyzed with two parallel PVs. And the effects of PV operating conditions and phase-locked loop control parameters on the stability of multiple PV units connected to the grid are analyzed by building up a time-domain state-space model of each part. In Fig. 4, the relationship between the oscillation frequency and the damping ratio of the dominant characteristic root is shown when SCR = 1.5 and the operating point of the PV unit are changed. It shows that an increase in the PV unit output makes the damping ratio of the system smaller and the oscillation frequency increase, which in turn deteriorates the system stability. In Fig. 5, the relationship between the oscillation frequency and the damping ratio is shown when the phase-locked loop proportionality factor of two PV grid-connected inverters is changed. It shows that a decrease in the phase-locked loop controller scale factor causes the damping ratio of the system to decrease, which in turn deteriorates the system stability.

4.2   Analysis of Oscillation Mechanism Based on Impedance Modeling in Frequency Domain

With the development of impedance modeling and analysis methods, researchers have used it to analyze the oscillation mechanism of new energy grid-connected systems. According to the impedance analysis method, the Byrd diagram can be used to determine the stability of the system and the frequency point of oscillation. At the possible oscillation frequency point, the output impedance of the grid-connected system and the grid impedance will form a resonance, and the phase angle difference between the two impedances at that frequency point can be used to measure the magnitude of damping at that frequency. If the phase angle margin at the resonance point is insufficient, the system is a small damping system and the system is unstable and may oscillate.

[20] performs sequential impedance modeling of new energy generation connected to a weak grid system and derives the factors affecting the stability of new energy grid-connected systems. It proved that the oscillations caused by the new energy grid connection under the weak grid are weakly damped or negatively damped oscillations, which can be generated by self-excitation. The analysis of the factors influencing the oscillations of the grid-connected PV system Bode diagram is shown in Figs. 6, 7 and 8. It can be concluded that the increase in grid impedance, the increase in the number

of inverter grid-connected units, and the increase in the bandwidth of the phase-locked loop will all reduce the phase margin at the resonance point and make the grid-connected system less stable.
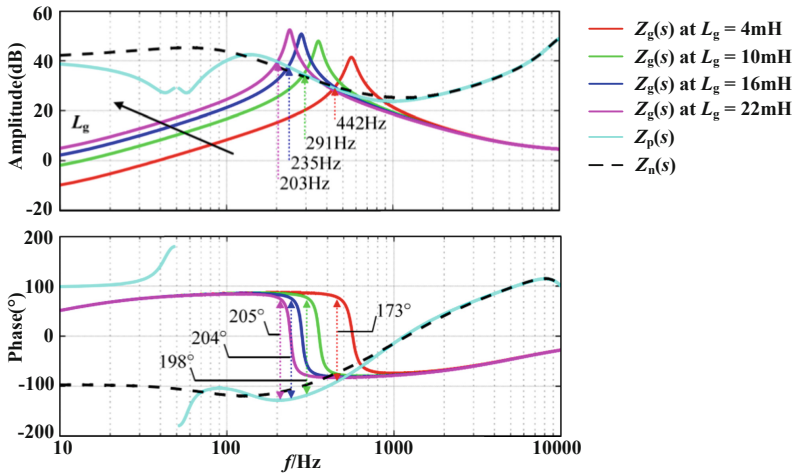
Fig. 6. Grid-connected inverter-grid interaction impedance with different grid impedance (Number of inverters $N = 1$, PLL Bandwidth $BW_{PLL} = 20$ Hz)
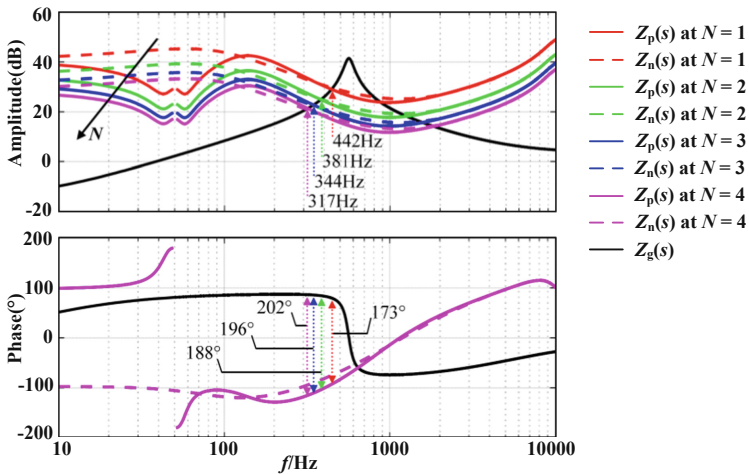
Fig. 7. Grid-connected inverter-grid interaction impedance with different number of inverters (Grid impedance $L_g = 4$ mH, PLL Bandwidth $BW_{PLL} = 20$ Hz)
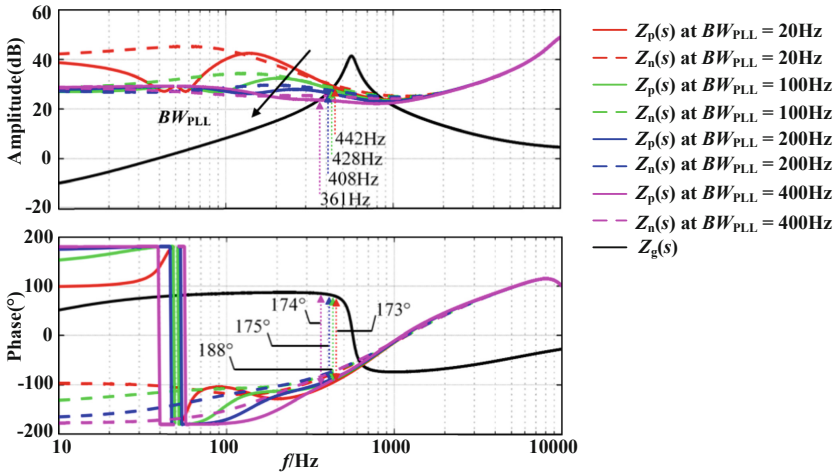
Fig. 8. Grid-connected inverter-grid interaction impedance with different PLL bandwidths (Number of inverters $N = 1$, Grid impedance $L_g = 4$ mH)

In [35, 36] and [29], three impedance modeling methods, namely dq coordinate impedance, positive and negative sequence impedance and polar coordinate impedance, are used to study the stability of new energy grid-connected systems under weak grids. The results show that the grid equivalent impedance size and the phase-locked loop control parameters have a large impact on the stability. In [23] and [37], positive and negative sequence impedance models are developed for grid-connected systems with current-source converters that account for frequency coupling, and the effects of each component control on system damping are analyzed. The results show that the phase-locked loop introduces frequency coupling in the system and brings a negative damping effect. The larger the bandwidth of the phase-locked loop, the greater its negative damping effect, and the system is prone to instability. The voltage feedforward link may reduce the stability margin of the system, but it can reduce more negative effects brought by the phase-locked loop and frequency coupling and improve the system stability. In [38], the dq coordinate system impedance modeling method is used to model a grid-connected inverter considering frequency coupling, and the analysis shows that the larger the bandwidth of the phase-locked and dc voltage loops, the larger the asymmetry of the current loop dq axis control parameters, and the smaller the dc side capacitance are the main factors affecting the frequency coupling characteristics and thus causing oscillations. Based on the impedance modeling of the grid-connected converter dq coordinate system, [39] concludes that the phase-locked loop causes a negative resistance in the q-q channel impedance, while the change in the current loop scale factor also affects the system damping due to the coupling between the phase-locked loop and the current loop.

In summary, the stability of the current source grid-connected inverter system is greatly influenced by grid impedance, new energy penetration, voltage feedforward control and phase-locked loop bandwidth in its own control. In the case of a weak grid and high penetration of new energy generation, it is easy to have broadband oscillation.

The voltage-controlled VSG does not require a phase-locked loop for stable operation and is not affected by the phase-locked loop control bandwidth. At the same time, the sequence impedance of voltage-source VSG is basically inductive, which makes its impedance stability margin with the inductive grid sufficient. The grid-connected system composed of voltage-source VSGs remains stable in weak grid conditions or when the penetration of new energy sources is high [20].

[40] investigates the mechanism of broadband oscillations of direct-drive wind farms connected to weak grids. In broadband, the unit impedance is negatively damped by capacitance, while the grid impedance is inductive, which makes the system impedance stability margin insufficient. However, the influencing factors are different in different frequency bands. In Band II, the unit impedance characteristics are mainly influenced by PLL; in Band III, the unit impedance characteristics are mainly influenced by the current loop; in Band IV, the unit impedance characteristics are influenced by the LC filter. [41] investigates the sub/super-synchronous resonance of doubly-fed wind farms when they are connected to a weak AC grid with cascade complement, and analyzes the mechanism of the sub/super-synchronous resonance characteristics based on the developed equivalent circuit model. The analysis shows that the grid impedance is capacitive and the unit impedance is inductively negatively damped in the sub-synchronous band, and the frequency presentation range is related to the rotor frequency, power outer loop parameters, and RSC current loop parameters. The grid impedance is inductive and the unit impedance is capacitively negatively damped in the super-synchronous band. The capacitive negative damping of the unit impedance in this frequency band is generated by the interaction of the GSC current loop and the DC voltage loop, and the power outer loop control parameters affect the degree of negative damping. The effect of the number of grid-connected inverters on the distribution of the system intrinsic resonance points is analyzed in [42] based on the Norton equivalent model when multiple PV grid-connected inverters are connected, but the effect of important factors such as the phase-locked loop is not considered in the literature.

According to the above research results on the oscillation mechanism of new energy grid-connected systems, it can be concluded that.

1) The time-domain model and its analysis method are simpler and more accurate than the frequency domain impedance model, but it cannot be used in the stability analysis of multiple grid-connected units due to the limitation of the order of the state space equations; while the frequency domain impedance model can be used in the stability analysis of grid-connected units, but its analysis method is more complicated.

2) Compared with the current source control strategy, the grid-connected inverter with voltage source control strategy has better stability at low grid strength and high new energy penetration rate and is less prone to wide-frequency oscillations, which is more suitable as the control strategy of grid-connected inverter in this scenario.

3) The influencing factors of broadband oscillation of the new energy power system are complex, and their influencing factors are different in different frequency bands. The middle and low-frequency bands receive more influence from the control parameters of the grid-connected system, such as the voltage source grid-connected system is significantly influenced by the phase-locked loop control parameters in the middle and low-frequency bands.

At present, the stability analysis of new energy generation grid-connected systems is not comprehensive, and the system oscillation mechanism is still not completely clear due to the influence of model accuracy and analysis methods. In the subsequent study, the influence of various factors on the stability of different types of new energy grid-connected systems needs to be further considered to investigate the oscillation mechanism.

5 New Energy Station Oscillation Suppression Method

According to the modeling method and oscillation mechanism analysis in the previous chapter, one of the main reasons for broadband oscillations in new energy grid-connected systems is the presence of negative damping in the system, and the existing oscillation suppression strategies are mainly based on this starting point. The existing oscillation suppression strategies are mainly based on this. There are three main methods to enhance the system damping based on impedance remodeling as follows.

5.1 Impedance Parameter Optimization

The optimization of controller parameters is based on system impedance modeling. By observing the influence of different control parameters of the system on the system impedance model, a reasonable parameter range is selected, and the system impedance is defined within a reasonable range so that the system meets the stability requirements.

In [20], the current loop parameters and phase-locked loop parameters that have a great influence on the grid-connected inverter in the LC inverter are analyzed. And the parameter optimization considering the interaction between the phase-locked loop and the current loop in the weak grid is proposed. The method can ensure the stable operation of the grid-connected inverter under various working conditions such as different active power outputs and different grid strengths without changing the control strategy, which is a very simple and effective oscillation suppression method.
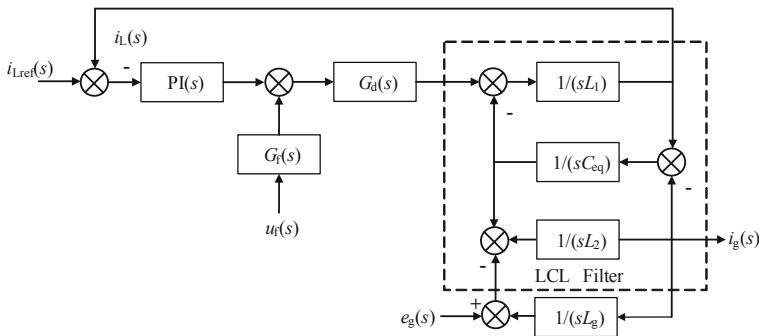
Fig. 9. The control structure of the α-axis of the three-phase grid-connected inverter

In [43], it is proposed that the constant power load characteristics and the phase-locked loop produce negative resistance effects on the d-d channel and q-q channel

impedances in the dq coordinate system, respectively, so the system parameters need to be designed with reference to the impedance criterion and matching. In [44], a parameter optimization method for the bandwidth of the phase-locked loop is proposed, which allows the grid-connected inverter to have sufficient phase angle margin and good grid stability even under weak grid conditions. [45] presents a grid voltage feedforward control strategy using weighted proportional coefficients and phase hysteresis. The design of the feedforward compensation function structure and parameters are analyzed as shown in Fig. 9. By modifying the grid voltage feedforward channel transfer function $G_f(s)$, the stability of the grid-connected inverter under the weak grid is enhanced and the positive damping of the system is improved.

The impedance parameter optimization can be guided by impedance analysis, but there are some limitations in impedance reshaping by this method. The dynamic performance of the system may be degraded after the parameters, and in some cases, it is not possible to rely on the optimization of the control parameters alone to make the system stability secure.

5.2 Impedance Structure Remodeling

The interactive system realizes impedance reshaping by improving the structure of the controller. The introduction of active damping and virtual impedance links in the internal channels of the controller can improve the controller structure of the grid-connected system and realize the impedance structure reshaping to keep the system stable.
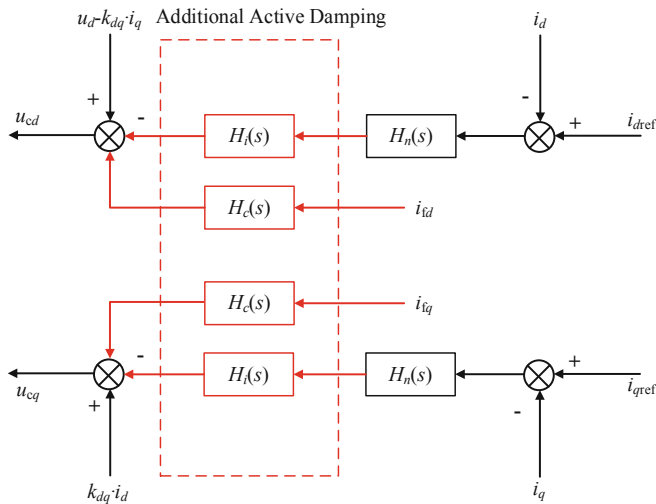
Fig. 10. Additional active damping control structure

In [46], based on the dq-axis output impedance model of the grid-connected system, the grid-connected inverter impedance is reshaped by using a dual-loop control structure with a multi-PR controller, which led to a reduction in harmonic interference between

the grid-connected system and the weak grid and improved the stability of the system. In [47], the stability of the three-phase LCL-type grid-connected inverter is analyzed by positive and negative sequence impedance modeling. And the results show that the phase margin of the grid-connected inverter does not lie within the stability margin in the middle and high-frequency bands. In the article, additional active damping control is used to add capacitor current feedback in the current inner loop as well as a series overrun correction link to complete the impedance reshaping. The control structure of the additional active damping link is shown in Fig. 10, which effectively suppresses the oscillation phenomenon. [48] uses the generalized Nyquist criterion to analyze the stability of voltage-sourced doubly-fed wind turbines under a series-complemented grid. An additional active damping control in the rotor-side voltage-current inner loop is proposed to suppress the sub-synchronous oscillations.

By means of virtual impedance, [49] proposes an impedance remodeling method for DFIG systems based on delay elimination to eliminate the effect of delay on impedance at high frequencies and achieve high-frequency system oscillation suppression. The impedance reshaping method can effectively suppress the oscillation phenomenon of the new energy grid-connected system, but the system will sacrifice part of the dynamic characteristics. In [50], a non-cross-feedback virtual impedance method based on current loop control is proposed. It can effectively suppress the low-frequency oscillation of the grid-connected inverter, and at the same time, an IIR filter is added to improve the system dynamic characteristics and reduce the negative impact of virtual impedance control on the system dynamic characteristics. In [51], it is presented that the output impedance amplitude of the grid-connected inverter after impedance remodeling should be more adequate at the oscillation frequency point and smaller in other frequency bands. Based on this idea, a two-band reluctance filter high frequency oscillation suppression method is proposed. Both band reluctance filters are introduced in the voltage feedforward at the PCC point, which is equivalent to incorporating virtual impedance to suppress high frequency oscillations. The band rejection filter is also introduced in the feedback control link of the grid-side inductor current, which is equivalent to the series into the virtual impedance so that the fundamental frequency current flowing into the grid is not affected and the power quality of the grid-connected current is improved.

In [52], PLL and DC voltage loop control parameter optimization, virtual admittance controller, and additional active damping control are used for the different frequency bands. The impedance reshaping method is carried out by the method of the inverter to suppress the broadband oscillation phenomenon of the direct-drive wind farm connected to the weak power grid, and the design takes into account the dual constraints of stability and dynamic response characteristics to ensure the stable operation of the unit in the complex power grid environment.

5.3 System-Level Impedance Shaping

When the impedance of the grid-connected system is shaped by the above two methods, both are used at the unit side to improve the grid stability of the new energy field station and suppress system oscillations. In addition, system-level impedance shaping can also be achieved at the grid side by using existing power devices or into additional power equipment for oscillation suppression [53].

[54] proposes a method of connecting an active damper at the PCC. The schematic diagram of the structure is shown in Fig. 11. The device consists of a three-phase two-level voltage source converter and a resonant damping controller. It dynamically reshapes the grid impedance by paralleling high-bandwidth power converters, ensuring the stability of the interactive system and suppressing oscillations. [55] proposes a STATCOM suppression scheme based on additional damping control to suppress the sub-synchronous oscillation problem when DFIG is sent out through series compensation. Its sub-synchronous voltage control signal is introduced in the STATCOM controller, and the output current is obtained through a phase shift link and a proportional gain link. This output current is attached to the reactive current input of the original current controller to increase the equivalent conductance of the STATCOM at the resonant frequency to achieve the suppression of sub-synchronous oscillations.

A comparison of the above three oscillation suppression measures is given in Table 1. When reshaping the impedance model of new energy field stations, the impedance parameter optimization method is simpler to implement, but the suppression of oscillation frequency band is less, and the application scenario is limited. When impedance structure reshaping is used, the suppression band is wider and the application scenario is more extensive, but the existing units need to be modified. System-level impedance shaping can achieve accurate oscillation suppression in multiple scenarios without modifying existing units, but it may require additional power equipment. Therefore, when choosing the oscillation suppression method for new energy stations, we need to consider the suppression effect, application scenarios, and the difficulty of retrofitting.
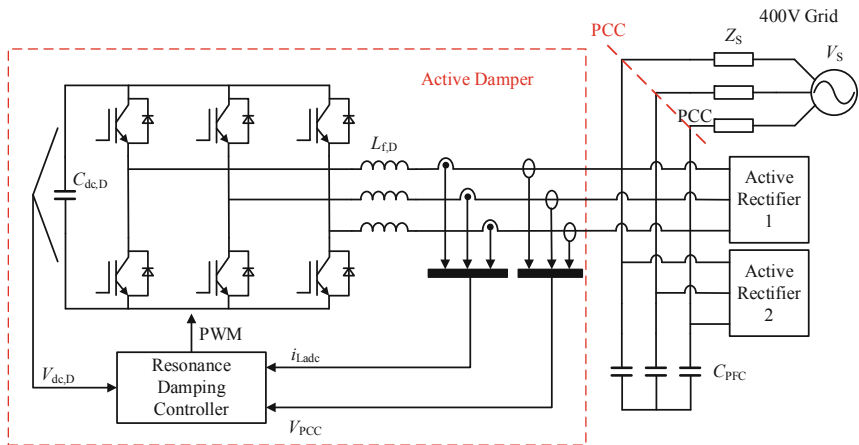
Fig. 11. Basic configuration of the proposed active damper

Table 1. Comparison of oscillation suppression methods for new energy field stations

Method	Suppression measures	Advantages	Disadvantages
Impedance parameter optimization	Reasonably adjust the inverter control parameter range and define the system impedance within a reasonable range	Impedance shaping can be performed without changing the control strategy to suppress oscillation in a certain frequency band	Tuning parameters sacrifices system dynamic performance; application scenarios have limitations
Impedance structure remodeling	Impedance reshaping is achieved by improving the controller structure, generally changing the internal channels of the controller	The application scenarios are more extensive, and the frequency band that can suppress oscillation is wider	The existing unit needs to be modified, and the engineering is more complicated; the dynamic performance of the system will also be sacrificed
System-level impedance shaping	Utilize existing power devices or add additional power equipment outside the interactive system to achieve system-level impedance shaping	There is no need to modify the existing unit, and the system damping of the corresponding frequency band can be increased according to the oscillation frequency. The application scenarios are relatively wide	The transformation is more complicated, and an appropriate feedback signal needs to be selected

To sum up, because the impedance shaping method can improve the stability margin of the interactive system and realize the optimal control of the interactive system, this method has become one of the hot spots in the research on oscillation suppression of new energy systems. It is still in its infancy and exploration stage and needs to be further developed.

6   Related Research Prospects

Based on the current research foundation of broadband oscillation, follow-up research can be carried out from the following aspects:

1) Analysis and research on the voltage source control mode.
From the perspective of the unit itself, the current-source control strategy of the traditional inverter is a kind of grid-following control method, which has many limitations and some defects in the system voltage and frequency adjustment. In the context of large-scale new energy field stations connected to the power system, especially in the case of a weak network, the self-synchronous voltage source control strategy should be adopted

to realize grid-configuration type control. Therefore, it is necessary to continue the stability analysis of the new energy field station access system composed of voltage-source grid-connected inverters and to study the possible broadband oscillations.

2) Modeling and analysis methods for broadband oscillations based on multi- time scales.

In the case of large-scale new energy field stations connected to the power system, the multi-time scale characteristics of power electronics in new energy generation devices make the power system operation variable and the wide-frequency oscillation characteristics more complex. In the multi-time scale high scale new energy system, the linearized model based on a single operating point at the working frequency cannot accurately characterize the disturbance characteristics in the whole operating area, which leads to the limited application scenarios of the analysis results.

Therefore, it is necessary to establish a mathematical model applicable to the grid-connected stability of new energy field stations based on linear time-varying system theory, propose a wide-band oscillation stability analysis method, investigate the destabilization mechanism of wide-band oscillation of new energy power system, and refine the characteristics of wide-band oscillation destabilization mode. Based on the multi-timescale characteristics of power electronics, it is necessary to develop a full electromagnetic transient simulation platform applicable to the transient analysis of double-high power systems, complete the theoretical analysis of wide-band oscillations, and then support the stable operation of double-high power systems.

3) Broadband oscillation suppression method based on station controller.

Most of the existing oscillation suppression strategies are aimed at a specific oscillation mode, and the oscillation suppression is realized by reshaping the impedance of a single unit. It does not adapt to the changing working conditions and is difficult to apply to broadband with strong time variability and strong uncertainty. In the case of an oscillation accident, the application scenarios are limited. The impedance reshaping of the unit will improve the impedance characteristics of the unit in the corresponding frequency band, but it will also affect the dynamic performance of the unit. This makes it still necessary in many cases to cut off new energy stations in order to achieve oscillation suppression.

Therefore, it is necessary to use broadband oscillation monitoring technology to collect the dynamic response data of the system in real-time and to obtain the key characteristic quantity of broadband oscillation instability mode by the corresponding method. Then a new field station suppression control architecture is adopted, i.e., a field station coordination controller is used to issue corresponding commands through the field station controller based on the oscillation information obtained from the oscillation monitoring equipment to complete the hierarchical and graded suppression of the system oscillations. Finally, the stable operation of the high percentage of new energy power system is realized.

7   Conclusion

With the large-scale connection of new energy stations to the power system, the new power system presents a trend in power electronics, and the broadband oscillation problem is becoming more and more prominent. So as to maintain the stable operation of the

power system, the analysis of the broadband oscillation mechanism and its influencing factors and the study of the suppression strategies have been widely concerned again.

In this paper, starting from the control strategy of grid-connected inverter, the current source, and voltage source control strategies are expounded, and their applicable situations are indicated respectively. Secondly, the modeling and analysis methods of new energy systems are introduced, and their application scope, advantages, and disadvantages are listed respectively, which provides a basis for a reasonable selection of modeling methods in different analysis scenarios. Then, the mechanism and influencing factors of broadband oscillation of new energy stations connected to the power system in existing research are illustrated by examples. It can be seen that the mechanism analysis of the broadband oscillation of the new energy power system still needs further study. In addition, the paper also lists the existing broadband oscillation suppression measures, compares their advantages and disadvantages, and finally summarizes the possible future research directions and research ideas. It is hoped that the research in this paper can provide a useful reference for the analysis and suppression of power system oscillations connected to large-scale new energy stations, and promote the development of new energy grid-connected technologies.

References

1. National Energy Administration. 2020 social electricity consumption increased by 3.1% year-on-year[EB/OL], 20 Jan 2021
2. Adams, J., Pappu, V., Dixit, A.: ERCOT experience screening for Sub-Synchronous Control Interaction in the vicinity of series capacitor banks. IEEE PES General Meeting, 2012, San Diego, USA, pp. 1–5, 22–26 July
3. Dong, X., Xie, X., Yang, Yu., et al.: Impacting factors and stable area analysis of sub-synchronous resonance in DFIG based wind farms connected to series-compensated power system. Power Syst. Technol. **39**(1), 189–193 (2015)
4. Hu, Y., Deng, C., Xie, X., et al.: Additional damping control of DFIG series compensated transmission system under sub-synchronous resonance. Power Syst. Technol. **40**(4), 1169–1173 (2016)
5. Li, M., Yu, Z., Xu, T., et al.: Study of complex oscillation caused by renewable energy integration and its solution. Power Syst. Technol. **41**(4), 1035–1042 (2017)
6. Zhang, X., Li, M., Guo, Z., et al.: Review and perspectives on control strategies for renewable energy grid-connected inverters. J. Global Energy Interconnection **4**(5), 506–515 (2021)
7. Dong, D., Wen, B., Boroyevich, D., et al.: Analysis of phase-locked loop low-frequency stability in three-phase grid-connected power converters considering impedance interactions. IEEE Trans. Industr. Electron. **62**(1), 310–321 (2015)
8. Wen, B., Boroyevich, D., Mattavelli, P., et al.: Impedance-based analysis of grid-synchronization stability for three-phase paralleled converters. In: 2014 IEEE Applied Power Electronics Conference and Exposition - APEC 2014, 16–20 March, Fort Worth, USA, pp. 1233–1239 (2014)

9. Miao, L.,Wang, Y., Cao, B., et al.: Resonance damping characteristic analysis of distributed inverter-based system with grid voltage feed-forward control in weak grid. High Voltage Eng. **46**(10), 3521–3532 (2020)

10. Yang, X.,Wang, T., Xu, Y., et al.: Voltage feedforward control of |c| grid-connected inverter based on virtual inductor. Acta Energiae Solaris Sinica, **41**(11), 56–63 (2020)

11. Wu, X.J., Li, X.Q., Yuan, X.B., et al.: Grid harmonics suppression scheme for LCL-type grid-connected inverters based on output admittance revision. IEEE Trans. Sustain. Energy **6**(2), 411–421 (2015)

12. Li, M., Zhang, X., Guo, Z.X., et al.: The control strategy for the grid-connected inverter through impedance reshaping in q-axis and its stability analysis under a weak grid. IEEE J. Emerging Sel. Top. Power Electron. **9**(3), 3229–3242 (2021)

13. Zhang, L., Harnefors, L., Nee, H.: Interconnection of two very weak AC systems by VSC-HVDC links using power synchronization control. IEEE Trans. Power Syst. **26**(1), 344–355 (2011)

14. Beck, H., Hesse, R.: Virtual synchronous machineIn: 2007 9th Internation Conference on Electrical Power Quality and Utilisation, October 9–11, 2007, Barcelone, Spain, pp. 1–6 (2007)

15. Visscher, K., De, H.: Virtual synchronous machines for frequency stabilization in future grids with a significant share of decentralized generation. In: CIRED Seminar 2008: SmartGrids for Distribution, 23–24 June 2008, Frankfurt, Germany, pp. 1–4 (2008)

16. L(u), Z., Sheng, W., Liu, H., et al.: Application and challenge of virtual synchronous machine technology in power system. Proc. CSEE **37**(2), 349–360 (2017)

17. Wu, W., Zhou, L., Chen, Y., et al.: Sequence-impedance-based stability comparison between VSGs and traditional grid-connected inverters. IEEE Trans. Power Electron. **34**(1), 46–52 (2018)

18. Xie, Z., Xu, K., Qin, S., et al.: Comparative analysis of doubly-fed wind Turbine stability based on voltage source and current source. Power Syst. Technol. **45**(05), 1724–1735 (2021)

19. Qu, Z.: Synchronizing Stability Analysis and Control Technology of Voltage Source Converters in Power System with High-Penetration Renewables. Zhejiang University, Hang-zhou (2021)

20. Wu, W.: Research on Wide-bandwidth Oscillation Mechanism and Suppression Methods of Renewable Energy Power Generation Connected to the Weak Grid. Hunan University, Changsha (2019)

21. Yin, W., Xiong, L., Zhao, T.: Review of stability analysis methods of grid-tied inverter power generation systems. Southern Power Syst. Technol. **13**(1), 14–26 (2019)

22. Wang, L., Xie, X., Jiang, Q., et al.: Analysis and mitigation of SSR problems in large-scale wind farms with doubly-fed wind Turbines. Autom. Electric Power Syst. **38**(22), 26–31 (2014)

23. Wang, G.: Modeling and Generation Mechanism Analysis of Sustained Oscillation Problems in Inverter - Grid System. Chongqing University, Chongqing (2018)

24. Chen, X.,Wang, Y., Gong, C., et al.: Overview of Stability Research for Grid-Connected Inverters Based on Impedance Analysis Method. Proc. CSEE **38**(7), 2082–2095 (2018)

25. Belkhayat, M.: Stability Criteria for ac Power Systems with Regulated Loads. Purdue University, West Lafayette (1997)

26. Chandrasekaran, S., Borojevic, D., Lindner, D.: Input filter interaction in three phase AC-DC converters. In: Proceedings of the 30th Annual IEEE Power Electronics Specialists Conference, 1 July 1999, Piscataway, USA, pp. 987–992

27. Sun, J.: Small-signal methods for ac distributed power systems-a review. IEEE Trans. Power Electron. **24**(11), 2545–2554 (2009)

28. Chen, L., Xu, S., Sun, H., et al.: A survey on wide-frequency oscillation for power systems with high penetration of power electronics. Proc. CSEE **41**(7), pp. 2297–2309 (2021)

29. Xin, H., Li, Z., Dong, W., et al.: Generalized-impedance and stability criterion for grid-connected converters. Proc. CSEE **37**(05), 1277–1293 (2017)
30. Dong, W., Xin, H., Li, Z., et al.: Primal-dual complex circuit of grid-connected converters for oscillation analysis. Proc. CSEE **37**(22), 6500–6515+6762 (2017)
31. Zhu, C., Hu, M., Wu, Z.: Parameters impact on the performance of a double-fed induction generator-based wind turbine for sub-synchronous resonance control. IET Renew. Power Gener. **6**(2), 92–98 (2012)
32. Guo, X., Li, Y., Xie, X., et al.: Sub-synchronous oscillation characteristics caused by PMSG-based Wind plant farm integrated via flexible HVDC system. Proc. CSEE **40**(4), 1149–1160 (2020)
33. Liu, Y., Huang, B., Sun, H., et al.: Study on sub-synchronous interaction between D-PMSG-based wind Turbines and SVG. Power Syst. Technol. **43**(6), 2072–2079 (2019)
34. Jia, Q., Yan, G., LI, Y., et al.: Stability Analysis of Multiple parallelled photovoltaic power generation units connected to weak AC system. Autom. Electric Power Syst. **42**(3), 14–20 (2018)
35. Wen, B., Dong, D., Dushan, B., et al.: Impedance-based analysis of grid-synchronization stability for three-phase paralleled converters. IEEE Trans. Power Electron. **31**(1), 26–38 (2016)
36. Mauricio, C., Sun, J.: Impedance modeling and analysis of grid-connected voltage-source converters. IEEE Trans. Power Electron. **29**(3), 1254–1261 (2014)
37. Song, X.: Study on the Oscillation Stability of GridConnected Inverter System. China University of Mining and Technology, Xuzhou (2020)
38. Zheng, G.: Research on impedance characteristics and stability of Grid-tied inverters considering frequency coupling characteristics. Lanzhou University of Technology, Lanzhou (2021)
39. Zhang, X., Fu, S., Fu, Z., et al.: Improved control method of grid-connected converter based on voltage disturbance compensation in weak grid. Autom. Electric Power Syst. **43**(18), 137–144 (2019)
40. Li, G.,Wang, W., Liu, C., et al.: Mechanism analysis and suppression method of wideband oscillation of PMSG wind farms connected to weak grid (Part I): analysis of wideband impedance characteristics and oscillation mechanism. Proc. CSEE **39**(22), 6547–6562 (2019)
41. Li, G., Wang, W, Liu, C., et al.: Modeling and mechanism analysis of sub- and su-per-synchronous oscillation of grid-connected DFIG wind farms (Part II): analysis of impedance characteristic and oscillation mechanism. Proc. CSEE, 06 June 2021. https://doi.org/10.13334/j.0258-8013.pcsee.210049
42. Kuang, H., Luo, A., Chen, Z., et al.: Coupling resonances mechanism of grid-connected multi-parallel inverters and its active damping parameter optimal method. Power Syst. Technol. **40**(4), 1180–1189 (2016)
43. Wen, B., Boroyevich, D., Burgos, R., et al.: Small-signal stability analysis of three-phase AC systems in the presence of constant power loads based on measured d-q frame impedances. IEEE Trans. Power Electron. **30**(10), 5952–5963 (2015)
44. Wang, Y., Chen,X., Chen, J., et al.: Analysis of positive-sequence and negative-sequence impedance modeling of three-phase LCL-type grid-connected inverters based on harmonic linearization. Proc. CSEE **36**(21), 5890–5899 (2016)
45. Li, M., Zhang, X., Yang, Y., et al.: Grid voltage feedforward control strategy based on weighting coefficient in weak grid. J. Power Supply **15**(06), 10–18 (2017)
46. Wang, F., Duarte, J.L., Hendrix, M., et al.: Modeling and analysis of grid harmonic distortion impact of aggregated DG inverters. IEEE Trans. Power Electron **26**(3), 786–797 (2011)
47. Wang, Y., Ye, W., Song, R., et al.: Design of additional active damping for three-phase LCL grid connected inverter based on impedance analysis method. High Voltage Eng. **47**(8), 2645–2656 (2021)

48. Zhang, Y.: Analysis and Suppression on Sub-sunchronous Oscillation of Voltage Source Doubly-fed Wind Turbine. Harbin Institute of Technology, Harbin
49. Nian, H., Tong, H., Hu, B., et al.: High frequency resonance suppression of doubly fed induction generator based on direct power control without phase-locked loop connected to VSC-HVDC system. Power Syst. Technol. (2021–10–18). https://doi.org/10.13335/j.1000-3673.pst.2021.1378
50. Li,S., Wang, W., Tang, F., et al.: Low frequency oscillation mechanism of grid-connected converter based on impedance model. Power Syst. Technol. **42**(9), 2787–2796 (2018)
51. Yang, L., Chen, Y., Luo, A., et al.: High-frequency oscillation suppression method by two notch filters for multi-inverter grid-connected system. Proc. CSEE **39**(8), 2242–2253 (2019)
52. Li, G., Wang, W., Liu, C., et al.: Mechanism analysis and suppression method of wideband oscillation of PMSG wind farms connected to weak grid (Part II): suppression method of wideband oscillation based on impedance reshaping. Proc. CSEE **39**(23), 6908–6921 (2019)
53. Mo, B.,Wu, W., Chen, Y., et al.: Active damping control method for power conversion system to suppress sub-/super-synchronous oscillation of D-PMSG grid-connected system[J/OL]. Power Syst. Technol. [2022-03-22]. https://doi.org/10.13335/j.1000-3673.pst.2022.0042
54. Wang, X., Blaabjerg, F., Liserre, M., et al.: An active damper for stabilizing power-electronics-based AC systems. IEEE Trans. Power Electron. **29**(7), 3318–3329 (2014)
55. Wang, Y., Wang, L., Jiang, Q., et al.: STATCOM based supplementary damping mitigation strategy for sub-synchronous control interaction in wind farms. Automation Electric Power Syst. **43**(15), 49–55 (2019)

A Cooperative Control Strategy for Distributed Multi-region Networked Microgrids

Yongjun Xia[1], Ping Xiong[2(✉)], Dan Liu[2], Fan Xiao[2], and Yanying Li[3(✉)]

[1] State Grid Hubei Electric Power Co., Ltd., Wuhan 430077, China
[2] State Grid Hubei Electric Power Research Institute, Wuhan 430077, China
`joey.xiongping@gmail.com`
[3] China Three Gorges University, Yichang 443002, China
`li980604@163.com`

Abstract. In order to realize the cooperative control of distributed multi-region networked microgrids, a multi-agent cooperative control strategy based on the reinforcement learning algorithm, namely WDQ(λ), is proposed from the perspective of automatic generation control. The proposed strategy avoids the overestimation and underestimation of action in traditional reinforcement learning and then obtains the distributed multi-region cooperation. Through the simulation of distributed three-region networked microgrids automatic generation control model including large-scale distributed generators, the results show that the proposed control strategy has better control performance and faster convergence speed compared with the other traditional methods and can effectively obtain the distributed multi-region cooperation of the networked microgrids.

Keywords: Networked microgrids · Automatic generation control · Reinforcement learning algorithm · Multi-region cooperation

1 Introduction

The rapid growth of energy demand and environmental problems prompt countries to actively develop new energy, and distributed generators (DG) based on wind, light, heat and storage is booming. However, the single entry of large-scale DG into the network will bring huge impact and strong disturbance to the power grid. Therefore, microgrid which can effectively integrate various DG and improve the reliability of distribution network is widely used. The single microgrid has disadvantages such as poor anti-interference ability and limited working capacity, so the distributed multi-region networked microgrids emerges. While the topological structure and operating environment of networked microgrids are more complex, it is urgent to solve the problem that how to effectively realize multi-region cooperative control of networked microgrids. The centralized automatic generation control (AGC) [1] and decentralized AGC [2] have been playing important roles in power grid control. For the centralized AGC, ensuring its own area to get the optimal control performance is a top priority [3], so that the cooperative control degree

among regions is low. Taking it as an important means of distributed multi-region networked microgrids control has been difficult to maintain the good cooperative control performance [4]. Therefore, it is significant to explore an decentralized AGC control strategy for distributed multi-region networked microgrids.

In recent years, many scholars have been committed to the study of distributed AGC control strategy [5–7], and proposed a series of distributed AGC control algorithms by introducing artificial intelligence into distributed AGC controller. Among them, reinforcement learning (RL) [8] has strong advantages in decision-making, self-learning and self-optimization [9]. And solving cooperative multi-agent RL problems can be introduced into efficient optimization methods for solving distributed optimization [10]. In [11], a microgrid distributed coordination self-optimal control strategy based on multi-agent system is proposed to adjust the active and reactive power output and system frequency. In [12], the principle of stochastic uniform game based on multi-agent system is incorporated into the new win-loss judgment and qualification trace, and a hierarchical and distributed control method based on the hierarchical and distributed control based on virtual wolf pack strategy is proposed to reduce the random interference caused by the large-scale integration of distributed new energy into the power grid, and then realize the multi-region optimal cooperative control.

However, the above control algorithms are all based on traditional RL algorithms, which always overestimate action values in the exploration process so that the decision quality become low. Therefore, in [13], double Q learning algorithm is proposed to effectively reduce the probability of action value overestimate through the combination of decoupled "action assessment" and "action choice". However double Q learning algorithm inevitably produces negative deviation again and then underestimates the action value, which is also not good for an agent to explore the optimal strategy.

Therefore, a new multi-agent cooperative control strategy weighted double Q(λ), namely WDQ(λ), is proposed oriented multi-region networked microgrids in this paper. It integrates weighted thought and qualification trace into double Q learning. The weighted thought can balance the overestimation of single estimation method and the underestimation of double estimation method, so that multi-agents can choose and explore the action value with moderate optimism. The qualified trace can optimize the convergence performance and speed up the convergence. The simulation of distributed three-region networked microgrids AGC model is carried out to verify the effectiveness of the proposed control strategy.

2 WDQ(λ) Cooperative Control Strategy

2.1 WDQ

Temporal-difference learning (TD) [14] is one of the core contents of RL theory, whose value function estimation methods include single estimation method and double estimation method. The single estimate method uses a set of identical samples to determine the selected action value and the estimated action value. The overly optimistic estimate results in cumulative positive bias, so that the action values are overestimated. The double estimate method uses two groups of different sample subset to separate the selected action value and the estimated action value, which can solve the problem of action value

overestimation. But when two groups of sample subset variables have different expectations and overlapping distribution, the action value underestimation will be inevitable, which still does not favor the agent to carry on the optimal decision. Therefore, the weighted thought is introduced into the basis of double Q framework [15] in this paper, and the weighted double Q(WDQ) algorithm formed can effectively solve the problem of overestimation and underestimation of action values.

WDQ algorithm randomly updates Q^A or Q^B at the kth iteration:

$$Q^A(s_k, a_k) = Q^A(s_k, a_k) + \alpha \delta_k^A \tag{1}$$

$$Q^B(s_k, a_k) = Q^B(s_k, a_k) + \alpha \delta_k^B \tag{2}$$

where s_k represents the state; a_k represents the action; α is the learning factor. And the corresponding TD errors $\delta A\ k$ and $\delta B\ k$ when Q^A or Q^B is updated at the kth iteration can be expressed as follows:

$$\delta_k^A = r + \gamma \left[\beta_k^A Q^A(s_{k+1}, a*) + \left(1 - \beta_k^A\right) Q^B(s_{k+1}, a*) \right] - Q^A(s_k, a_k) \tag{3}$$

$$\delta_k^B = r + \gamma \left[\beta_k^B Q^B(s_{k+1}, a*) + \left(1 - \beta_k^B\right) Q^A(s_{k+1}, a*) \right] - Q^B(s_k, a_k) \tag{4}$$

where r is the reward function; γ is the discount factor; and the weight functions $\beta A\ k$ and $\beta B\ k$ can be expressed as follows:

$$\beta_k^A = \frac{\left| Q^B(s_{k+1}, a*) - Q^B(s_{k+1}, a_L) \right|}{c + \left| Q^B(s_{k+1}, a*) - Q^B(s_{k+1}, a_L) \right|} \tag{5}$$

$$\beta_k^B = \frac{\left| Q^A(s_{k+1}, a*) - Q^A(s_{k+1}, a_L) \right|}{c + \left| Q^A(s_{k+1}, a*) - Q^A(s_{k+1}, a_L) \right|} \tag{6}$$

where the non-negative real number $C \geq 0$, $a*$ and a_L are the corresponding maximum and minimum action values in the next state s_{k+1} respectively.

2.2 WDQ(λ)

Qualification trace can effectively solve the problem of time reliability allocation, optimize the convergence performance, and then improve the convergence speed of the algorithm. Therefore, the WDQ(λ) reinforcement learning algorithm is formed by integrating qualification trace on the basis of WDQ.

The update formulas of qualification trace are as follows:

$$e_k(s, a) = \gamma \lambda e_{k-1}(s, a) + 1 \,, \ Q_{k-1}(s_k, a_k) = \max_a Q_{k-1}(s_k, a_k) \tag{7}$$

$$e_k(s, a) = \gamma \lambda e_{k-1}(s, a) \,, \ \text{Others} \tag{8}$$

where λ is the attenuation factor of qualification trace.

WDQ(λ) algorithm randomly updates Q^A or Q^B at the kth iteration:

$$Q^A(s_k, a_k) = Q^A(s_k, a_k) + \alpha \delta_k^A e_k(s_k, a_k) \tag{9}$$

$$Q^B(s_k, a_k) = Q^B(s_k, a_k) + \alpha \delta_k^B e_k(s_k, a_k) \tag{10}$$

3 Design of Optimal Controller

The WDQ (λ) control algorithm is embedded into the AGC controller to form the WDQ(λ) controller. Then, the WDQ(λ) controller is embedded in each regional microgrid, and the WDQ(λ) controller of each region shares information in real time. in area i, area control error (ACE), inter-grid frequency deviation (Δf) and the control performance standard (CPS) are the observable state quantity S_i of the WDQ(λ) controller. The S_i and the reward value are input into the ith WDQ(λ) controller together. After the action set is optimized and updated, the optimal control signal, namely the ith region total regulation power command $\Delta P_{\text{ord-}i}$, is output to maintain the frequency stability and the dynamic balance of the link line exchange power between the regional interconnected systems. And the CPS [16] proposed is introduced to evaluate the control performance of multi-region networked microgrids.

3.1 Reward Function

The dimensions of area control error (ACE) and frequency deviation Δf is normalized, and the instantaneous value of ACE (ACE(i)) and the instantaneous absolute value of frequency deviation ($|\Delta f(i)|$) are linear weighted to make the output stable and CPS long-term gain largest. The target reward function can be expressed as follows:

$$R_i = -\eta |\Delta f(i)|^2 - (1 - \eta)[ACE(i)]^2 \Big/ 1000 \tag{11}$$

where the η is set to be 0.5.

3.2 Parameter Setting

There are five parameters of WDQ(λ) control strategy need to be set.

(1) The learning factor $\alpha(0 < \alpha < 1)$ is used to weigh the stability of the algorithm. A larger α can accelerate the learning convergence speed and a smaller α can improve the system stability. And α is set to be 0.1 in this paper.
(2) The discount factor $\gamma(0 < \gamma < 1)$ provides reward discount for the long-term iteration of Q function. The larger it is, the more long-term reward is emphasized. And γ is set to be 0.9 in this paper.
(3) The speed factor $\beta(0 < \beta < 1)$ determines the speed of action exploration, which is set to be 0.5 in this paper.
(4) The weight parameter $c(c > 0)$ is used to construct a weight function, indicating the weight between a single estimator and a double estimator. And c is set to be 5000 in this paper.
(5) The recession factor $\lambda(0 < \lambda < 1)$ of qualification trace assigns the credit to the state-action pair. The larger it is, the more credit is assigned to the historical state-action pair. And λ is set to be 0.9 in this paper.

3.3 Algorithm Flowchart

The WDQ(λ) control strategy is formed by integrating the weighted thought and qualification trace based on the double Q learning, Thereinto, the weighted thought aims to solve the problem of overestimation and underestimation of action values, and the qualification trace aims to optimize the convergence performance, and then improve the convergence speed of the algorithm.

The input of the algorithm is load disturbance and the output of the algorithm is AGC total power instruction. The value functions Q^A and Q^B are chosen to be updated randomly, and qualification trace is also updated with each iteration.

Table 1. The algorithm flowchart of WDQ(λ) control strategy.

Input: Load disturbance
Output: Total power instruction ΔP_{ord}
Initialize: Value function Q^A, Q^B; State s_0, Parameters α, β, γ, c, λ; Initialize $k=0$
Repeat
1. Choose action a_k according to $Q^A(s,.)$ and $Q^B(s,.)$; Execute a_k and get the new state s_{k+1}; Calculate the current reward function value according to(11).
2. If update Q^A randomly
3. Calculate $\delta A\ k$ according to(3)and(5), and update Q^A according to(9).
4. else if update Q^B randomly
5. Calculate $\delta B\ k$ according to (4)and (6), and update Q^B according to (10).
6. End if and update qualification trace according to (7)and (8).
7. Set $k=k+1$, and return to step 1.
END

The algorithm flowchart of WDQ(λ) control strategy is shown in Table 1.

4 Simulation Research

4.1 Model Establishment

The distributed three-region networked microgrids AGC model including various DG such as electric vehicles(EVs), photovoltaics (PV) [17], small hydro-powers(SH), wind farms (WF) [18], diesel generators, fuel cells (FC) [19], micro-gas turbines (MT) [20], biomass energy (BE) is established in this paper to verify the practical engineering application effect of WDQ(λ) control strategy. The model topology is shown in Fig. 1, the model parameters are shown in Table 2, and the AGC unit parameters are shown in Table 3. Moreover, the model parameters and AGC unit parameters of region 2 are the

same as those of region 3. In addition, in order to simplify the model, PV, WF and EVs do not participate in the system frequency modulation, which are only processed as load disturbance.
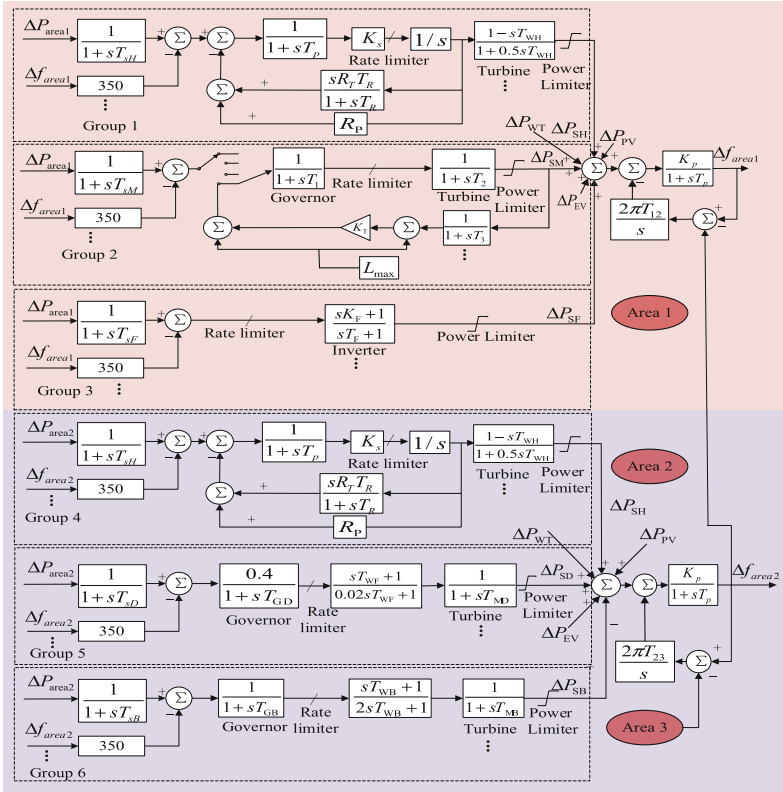
Fig. 1. The distributed three-region networked microgrids AGC model

Table 2. The parameters of distributed three-region networked microgrids AGC model.

Units	Parameters	Value
Small hydroelectric generation units	the second time delay, T_{SH}	3
	Time constant of servo motor, T_P	0.04
	gain of servo motor, K_S	5
	coefficient of permanent state slip, R_P	1
	reset time, T_R	0.3
	transient slip coefficient, R_t	1

(*continued*)

Table 2. (*continued*)

Units	Parameters	Value
	maximum opening rate of gate, $R_{maxopen}$/(p.u./s)	0.16
	maximum closing rate of gate, $R_{maxclose}$/(p.u./s)	0.16
	unit start-up time, T_{WH}	1
Biomass electric generator units	the second time delay, T_{SB}	10
	the governor's time constant, T_{GB}	0.08
	steam start-up time, T_{WB}	5
	mechanical start-up time, T_{MB}	0.3
Micro-gas turbine units	the second time delay, T_{SM}	5
	fuel system delay time constant, T_1	0.08
	fuel system delay time constant, T_2	0.3
	load limiting time constant, T_3	3
	temperature control loop gain, K_T	1
	load limiting constant, L_{max}	1.2
Fuel cell units	the second time delay, T_{SF}	2
	the governor's time constant, T_F	10.056
	the gain of inverter, K_F	9.205
Diesel generator units	the second time delay, T_{SD}	7
	the governor's time constant, T_{GD}	2
	steam start-up time, T_{WF}	1
	mechanical start-up time, T_{MD}	3

Table 3. AGC unit parameters.

Areas	Unit types	Units	ΔP^{max}/MW	ΔP^{min}/MW
Area 1	SH	G1	250	−250
		G2	250	−250
		G3	150	−150
		G4	150	−150
		G5	100	−100
	MT	G6	150	−150
		G7	150	−150
		G8	100	−100

(*continued*)

Table 3. (*continued*)

Areas	Unit types	Units	ΔP^{max}/MW	ΔP^{min}/MW
	FC	G9	150	-150
		G10	100	-100
		G11	50	-50
Area 2 and Area 3	SH	G1	150	-150
		G2	200	-200
		G3	100	-100
		G4	150	-150
		G5	250	-250
	DG	G6	120	-120
		G7	100	-100
	BE	G8	200	-200
		G9	200	-200
		G10	150	-150

4.2 The Off-Line Prelearning Under Sinusoidal Load Disturbance

Before WDQ(λ) controller is put into formal online operation, a sinusoidal load disturbance with a period of 1200 s, a duration of 10000 s and a amplitude of 1000 kW is introduced into the system to make it conduct sufficient off-line trial and error prelearning to optimize the state value function and Q value function, so as to obtain the optimal operation of the system. The prelearning effect of WDQ(λ) controller in three regions is shown in Fig. 2. Figure 2(a) shows the frequency variation curves in the three regions, the maximum frequency deviation absolute values $|\Delta f_{\text{max}}|$ are respectively 0.068 Hz, 0.087 Hz and 0.093 Hz, which are far less than the actual engineering requirement of 0.2 Hz. Figure 2(b) shows the learning curves of the average values of 10-min CPS1 in the three regions, whose average values are respectively 199.3293%, 199.3454% and 199.3601%. Figure 2(c) shows the learning curves of 10-min ACE average values in the three regions, whose average values are 1.3879 kW, 1.8685 kW and 2.0024 kW respectively. Figure 2(d) shows the deviation curves of the exchange power of the tie line(P_{tie}) among regions. In conclusion, the WDQ(λ) controller has strong dynamic control performance, and can effectively realize the regional cooperative control of networked microgrids.

4.3 The Random Square Wave Disturbance and Random Load Disturbance

The WDQ(λ) controller which has gotten a deterministic optimal control strategy after pre-learning can be put into online operation. In order to simulate the strong random disturbance brought by new energy and the intermittency of load when multi-region

(a) Frequency variation curves of three areas

(b) 10-min CPS1 learning curves of three areas

(c) 10-min ACE learning curves of three areas
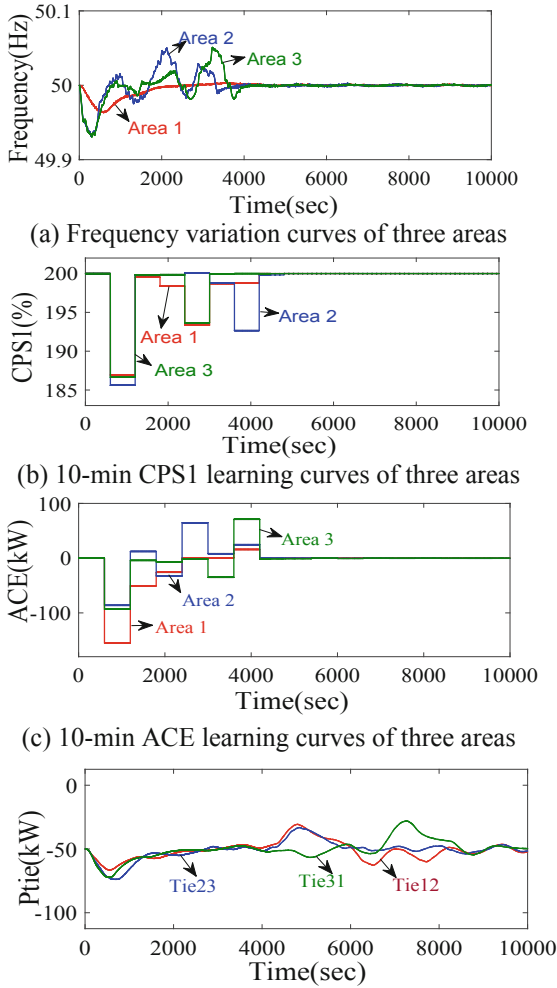
Fig. 2. The prelearning effect of WDQ(λ) controller in three regions

networked microgrids operate in practice, we introduce the random square wave disturbance (only the first 20000 s is captured here) and the random load disturbance (The amplitude is 1000 kW) to carry out 24 h real-time simulation. Moreover, in order to verify the control performance of WDQ(λ), extra introduce WDQ, DQ(λ) and DQ(σ, λ) controllers to be compared with WDQ(λ) controller.

The Random Square Wave Disturbance
Figure 3 shows the power output results of the WDQ(λ), WDQ, DQ(λ) and DQ(σ, λ) controllers in area 1 under random square wave load disturbance. Compared with the other three controllers, the WDQ(λ) controller can track the load disturbance more accurately and quickly. The average value of $|\Delta f|$ of WDQ(λ), WDQ, DQ(λ) and DQ(σ, λ) controllers in area 1 is 0.0034 Hz, 0.0168 Hz, 0.0231 Hz and 0.0487 Hz respectively.

WDQ(λ) controller can reduce $|\Delta f|$ by 79.7619%–93.0185%. Therefore, the WDQ(λ) controller can effectively reduce the frequency offset of the system, and has stronger robustness and better dynamic control performance.
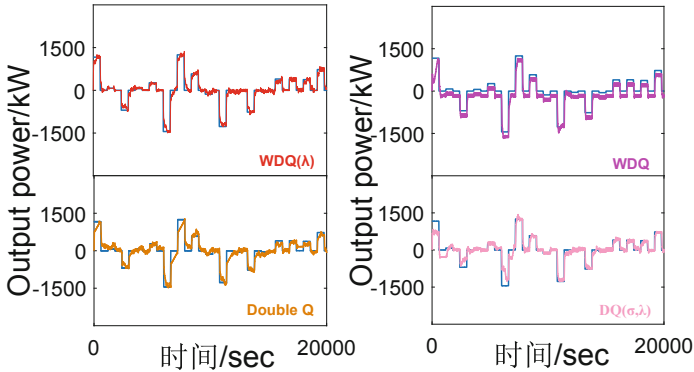
Fig. 3. The output power of four controllers in area 1 under random square wave disturbance

The Random Load Disturbance

Table 4 shows the control performance indexes of the WDQ(λ), WDQ, DQ(λ) and DQ(σ, λ) controllers in region 1. It shows that WDQ(λ) can decrease the $|\Delta f|$ about 44.9393%– 54.8173%, can reduce $|ACE|$ about 69.3476%–90.9194%, and can improve the CPS qualification rate about 0.9953%–2.6005%. In conclusion, compared with the other control methods, the WDQ(λ) control strategy can still maintain strong robustness and adaptability in the multi-region strongly random complex environment, and has better control performance, which can realize the stable cooperative control of multi-region networked microgrids.

Table 4. Control performance index of the four controllers in region 1 under the random load disturbance.

Index	Random load disturbance			
	WDQ(λ)	WDQ	DQ(λ)	DQ(σ, λ)
$|\Delta f|$/Hz	0.0136	0.0247	0.0285	0.0301
$|ACE|$/kW	2.3214	7.5733	20.3169	25.5644
CPS1/%	199.4335	198.6436	197.6899	196.3578
CPS2/%	99.5321	98.6256	98.1335	97.0257
CPS/%	100	99.0145	98.9812	97.4654

5 Conclusion

In order to realize the cooperative control of distributed multi-region networked micro-grids, a distributed three-region networked microgrids AGC model including large-scale DG is established in this paper. And from the perspective of AGC, the WDQ(λ) multi-agent cooperative control strategy oriented to the model is proposed based on the RL learning algorithm.

The WDQ(λ) control strategy is formed by integrating the weighted thought and qualification trace based on the double Q learning, Thereinto, the weighted thought aims to solve the problem of overestimation and underestimation of action values, and the qualification trace aims to optimize the convergence performance, and then improve the convergence speed of the algorithm.

The sinusoidal load disturbance is introduced to make the WDQ(λ) conduct sufficient offline prelearning. After WDQ(λ) obtain an optimal control strategy, the random load disturbance is introduced to conduct 24 h real-time simulation. The real-time simulation results show that compared with the other control methods, control strategy has the most stable and superior control performance, and can effectively obtain the distributed multi-region cooperation of networked microgrids.

References

1. Xi, L., Wu, J., Xu, Y., et al.: Automatic generation control based on multiple neural networks with actor-critic strategy. IEEE Teans. Neural Netw. Learn. Syst. **32**(6), 2483–2493 (2020)
2. Ullah, K., Basit, A., Ullah, Z., et al.: Automatic generation control strategies in conventional and modern power systems: a comprehensive overview. Energies **14**(9), 2376–2419 (2021)
3. Golpira, H., Bevrani, H.: Application of GA optimization for automatic generation control design in an interconnected power system. Energy Convers. Manage. **52**(5), 2247–2255 (2011)
4. Xi, L., Liu, L., Huang, Y., et al.: Research on hierarchical and distributed control for smart generation based on virtual wolf pack strategy. Complexity, 1–14 (2018)
5. Huang, C., Weng, S., Yue, D., et al.: Distributed cooperative control of energy storage units in microgrid based on multi-agent consensus method. Electric Power Syst. Res. **147**, 213–223 (2017)
6. Adhikari, S., Xu, Q., Tang, Y., et al.: Decentralized control of two DC microgrids interconnected with tie-line. J. Modern Power Syst. Clean Energy **5**(4), 599–608 (2017)
7. Ahadi, A., Ghadimi, N., Mirabbasi, D.: An analytical methodology for assessment of smart monitoring impact on future electric power distribution system reliability. Complexity **21**(1), 99–113 (2014)
8. Recht, B.: A tour of reinforcement learning: the view from continuous control. Ann. Rev. Control Robot. Autonomous Syst. **2**(1), 1–28 (2018)
9. Kiumarsi, B., Vamvoudakis, K.G., Modares, H., et al.: Optimal and autonomous control using reinforcement learning: a survey. IEEE Trans. Neural Networks Learn. Syst. **29**(6), 2042–2062 (2017)
10. Zhang, K., Yang, Z., Basar, T.: Multi-agent reinforcement learning: a selective overview of theories and algorithms. In: Handbook of Reinforcement Learning and Control, pp. 321–384 (2021)
11. Nan, Y.: Design and simulation of microgrid distributed coordination control system. North China Electric Power University (2014)

12. Basit, A., Ullah, Z., Aslam, S., et al.: Automatic generation control strategies in conventional and modern power systems: a comprehensive overview. Energies **14**(9), 2376 (2021)
13. Hasselt, H.: Double Q-learning. Adv. Neural. Inf. Process. Syst. **23**, 2613–2621 (2010)
14. Sutton, R.S.: Learning to predict by the methods of temporal differences. Mach. Learn. **3**(1), 9–44 (1988)
15. Zhang, Z., Pan, Z., Kochenderfer, M.J.: Weighted Double Q-learning. In: 25th International Joint Conference on Artificial Intelligence, pp. 3455–3461. IEEE, New York (2016)
16. Jaleeli, N., VanSlyck, L.S.: NERC's new control performance standards. Energies **14**(3), 1092–1099 (1999)
17. Kar, S., Hug, G.: Distributed robust economic dispatch in power systems: a consensus innovations approach. In: 10th Power and Energy Society General Meeting, pp. 1–8. IEEE, Chicago (2012)
18. Ma, L., Zhang, B., Cheng, G.: Research on large-scale wind farm modeling. In: 7th International Conference on Electronics & Information Engineering, pp. 1–6. Shandong (2017)
19. Sun, Q., Han, R., Zhang, H., et al.: A multiagent-based consensus algorithm for distributed coordinated control of distributed generators in the energy internet. IEEE Trans. Smart Grid **6**(6), 3006–3019 (2015)
20. Saha, A.K., Chowdhury, S., Chowdhury, S.P., et al.: Modelling and simulation of microturbine in islanded and grid-connected mode as distributed energy resource. In: 6th Power and Energy Society General Meeting-Conversion and Delivery of Electrical Energy in the 21st Century, pp. 1–7. IEEE, Pittsburgh (2008)

Research on Optimal Scheduling of Virtual Power Plant Considering the Cooperation of Distributed Generation and Energy Storage Under Carbon Rights Trading Environment

Haiyao Wang[1(✉)] 🆔, Gang Du[1,2] 🆔, Tao Zheng[1,2], Yulong Jin[1,2], and Tao Jing[1,2]

[1] NARI Group Corporation (State Grid Electric Power Research Institute), Nanjing 211106, China
627846195@qq.com

[2] NARI-TECH Nanjing Control System Ltd., Nanjing 211106, China

Abstract. Under the background of "Carbon Peak, Carbon Neutralization" national strategic carbon reduction goal, establishing an appropriate carbon trading mechanism is an effective way to achieve carbon reduction. This paper establishes an optimal model of economic and environmental dispatching for a virtual power plant (VPP) which contains energy storage, gas turbine, wind power and photovoltaic generation when it participates in carbon trading. Firstly, the carbon trading mechanism is introduced, and the scenario generation method considering the uncertainty of wind power based on Gaussian kernel function theory is formed to get the classical scene curve of wind power. Then, a mixed integer quadratic programming model for coordinated dispatch of distributed power and energy storage in VPP under carbon trading environment is established with the objective of minimizing the total cost of VPP. Finally, the example validation shows that the model reduces the total cost and total carbon emissions of the system, greatly improves the consumption of clean energy, and makes the scheduling of virtual power plants take into account both economic and environmental benefits.

Keywords: Distributed energy · Virtual power plant · Carbon trading · Optimal scheduling

1 Introduction

In order to achieve the goal of "carbon dioxide" and build a clean economy and sustainable energy-saving society, the electric power industry is facing enormous pressure of carbon emission reduction. Therefore, introducing the concept of "low-carbon economy" into the power industry, taking into account the energy saving and emission reduction targets in the operation and dispatch of power systems, is of great significance to the realization of "dual-carbon" goals [1].

Virtual power plant is a special power plant containing renewable energy, interruptible load, energy storage, electric vehicle and other power resources. It aggregates a large

number of scattered power sources or loads, and makes it participate in the operation of power system and power market as a whole without changing the grid connection mode of distributed power generation [2]. If the carbon emission in the production process of equipment is not considered, there is almost no carbon emission in the power generation process of wind power and photovoltaic generator units in VPP. For energy storage, if the wind power or photovoltaic power generation during the low load period is used for charging, it can also significantly reduce carbon emissions. VPP can achieve economic benefits and reduce carbon emissions objectively by reasonably allocating distributed resources and optimizing operation [3].

There are some research reports on the low-carbon operation of power system at home and abroad. Reference [4] introduced carbon emission quota into power system economic dispatching to improve the environmental protection of power system with a large number of distributed generators, and limited carbon emission with rigid indicators. Reference [5] constructs a power system optimization model considering carbon emissions, and uses the weight value to make a reasonable compromise between the optimization of energy conservation and emission reduction. Reference [6] optimized the scheduling of economic and environmental benefits when VPP with electric vehicles participates in green card trading, and proved that the large-scale application of electric vehicles in VPP can produce obvious environmental benefits. Reference [7] added excessive emission penalty in the design of low-carbon framework to better control carbon emissions. These references focus on the mandatory restriction, quota and punishment of carbon emissions in the traditional optimal dispatching of power system, but rarely quantify the value of carbon emission rights, and combine the carbon emission rights with environmental protection and economy. In the VPP with flexible operation and rapid output adjustment, the introduction of carbon trading mechanism to promote low-carbon emission reduction also has a large gap in the research related to this aspect.

On the other hand, with the rapid development of energy storage technology, the restriction degree of energy storage participating in power system regulation by capacity and cost is also decreasing. In recent years, it is generally believed that distributed energy storage is a high-quality adjustable resource of virtual power plant. Reference [8] combined with a wind storage system demonstration project, proposed the operation mode of energy storage system based on commercial VPP, and established a stochastic optimal scheduling model including wind light water storage with the goal of maximizing the revenue of VPP. Reference [9] establishes two distributed energy storage models of grid connected energy storage and user side energy storage, and optimizes the scheduling of virtual power plant resources based on the day ahead market time of use price. Reference [10] analyzes the operation mode of VPP composed of energy storage equipment and distributed wind power participating in system economic optimal dispatching. The above literature shows that the addition of energy storage in VPP can effectively suppress the impact of the uncertainty of wind and solar output and improve the consumption of clean energy, but it is less involved that energy storage can also replace some gas turbine output in the carbon trading environment, which has the function of improving the environmental protection of VPP as a rapid response unit in the system.

In summary, on the basis of the existing research, this paper constructs an output scenario considering the uncertainty of wind power by using the kernel density estimation method based on the Gaussian kernel function. A virtual power plant dispatch model with distributed power supply and storage synergy under the carbon trading environment is established by introducing the carbon rights trading market environment. The example results verify that the model proposed in this paper can effectively improve the economic and environmental benefits of VPP.

2   Carbon Trading Mechanism and Scenario Generation

2.1   Carbon Trading Mechanism

Carbon trading, also known as carbon emission rights trading, is a market-based measure to achieve energy conservation and emission reduction goals. Carbon emission rights trading practice is generally a carbon emission rights trading system, in which the relevant government agencies set the total amount of emissions in one or more industries, and issue a certain number of tradable quotas within the total amount. Generally, each quota corresponds to one ton of carbon dioxide emission equivalent. This paper uses the baseline method to determine the carbon trading quota of VPP [11].

For VPP including gas turbine, wind power and photovoltaic power generation, the carbon trading quota in period t can be obtained by Eq. (1).

$$M_{D,t} = \sum_{i=1}^{N} \varepsilon P_{i,t} \tag{1}$$

In the formula, N is the total number of generator units in the studied VPP. $P_{i,t}$ is the active output of generator set i at time t; ε is the distribution coefficient of VPP unit electricity emission, which is determined according to the " regional power grid baseline emission factor " issued by the national development and Reform Commission [12].

VPP can make a profit by selling emissions that do not meet the carbon emission quota. If the actual carbon emission of VPP in this period is higher than the carbon emission quota, the carbon trading fee shall be paid to purchase the emission quota. Carbon trading revenue is expressed as follows:

$$I_t^C = k^C (Q_t^Q - Q_t^N) \tag{2}$$

$$Q_t^Q = \gamma^C P_t^G \tag{3}$$

In the formula, I_t^C is the income of carbon trading market; k^C is the carbon trading price; Q_t^Q is the carbon emission quota of gas turbine unit in t period; Q_t^N is the net emission of gas turbine unit in t period; γ^C is the carbon emission benchmark limit per unit of electricity [13]; P_t^G is the net output of gas turbine unit in t period.

2.2   Scenarios Generation Considering Scenery Uncertainty

VPP contains a large number of intermittent distributed power sources such as wind and photovoltaic, and its output power has strong randomness and uncertainty. If the wind and solar output data of a single historical day is selected to verify the feasibility of the model, it lacks scientific rigor and credibility. Because the scenario analysis method can clearly describe the probability distribution of uncertainty and better retain the statistical characteristics of wind and solar output data, it has become one of the main methods to deal with the uncertainty of wind and solar power generation. This paper describes the uncertainty of the scenery by generating the classical scene method with probability information, establishes the probability density function of the historical scenery output data and samples it to obtain the whole scene set with huge dimension, and then forms the classical scene set through the scene reduction technology.

The specific steps of scene generation are as follows.

(1)   Based on the historical n-day wind and solar output data, the sampling period is 1H, and the nuclear density estimation method is used to establish the probability density function of fan and photovoltaic output in each period of 24 h, as follows:

$$
\begin{cases}
f_{h,t}(x_t) = \frac{1}{nh} \sum\limits_{d=1}^{n} G\left(\frac{x_t - X_{d,t}}{h}\right) \\
f_{h,t}(y_t) = \frac{1}{nh} \sum\limits_{d=1}^{n} G\left(\frac{y_t - Y_{d,t}}{h}\right)
\end{cases}
\tag{4}
$$

In the formula, h is the time scale; $X_{d,t}$ is the fan output in t period of day d; $Y_{d,t}$ is the photovoltaic output in t period of day d; G is selected as Gauss kernel function.

(2)   The joint probability distribution function of wind and photovoltaic output is sampled for each period, and the sample output of fan and photovoltaic is obtained by inverse transformation, and the set C of the initial scene is obtained.

(3)   Set the probability of scenario P_f^i and P_f^j in C as π_i and π_j respectively, and define the distance between scenarios as $\left\| P_f^i - P_f^j \right\|_2$. Use synchronous backdating technology based on probability distance to reduce the scene and form a classical scene set[14]. The steps of the synchronous substitution reduction technique are shown in Fig. 1.
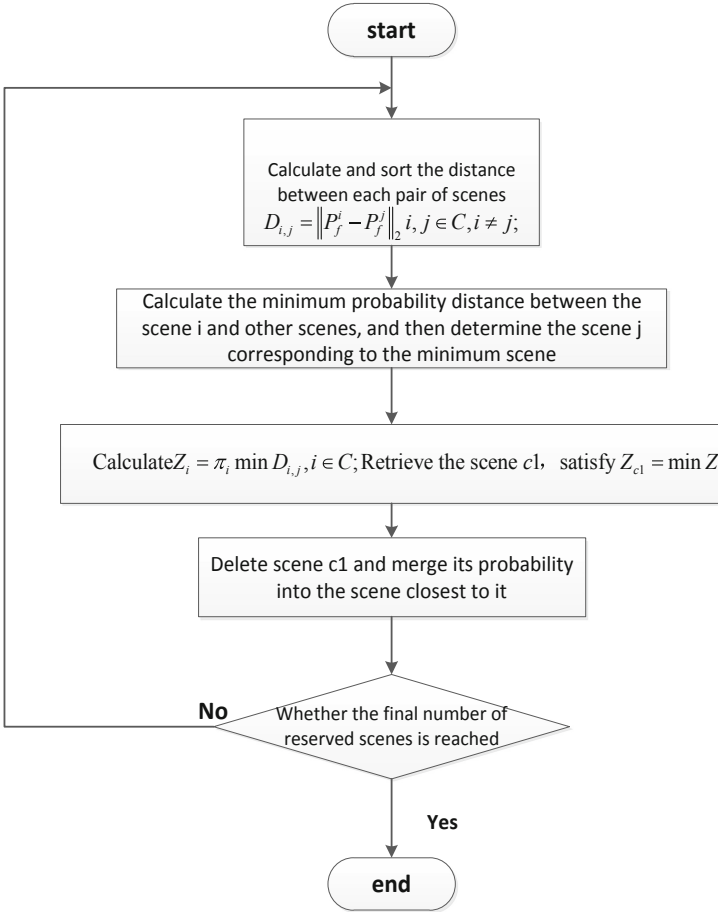
Fig. 1. Flowchart of synchronous generation reduction method

If the classical scene set is J, including S scenes and the deleted scene set is J', the optimal scene reduction set is satisfied:

$$\min\left\{\sum_{i \in J'} \pi_i \min_{j \in J}\left\| P_f^i - P_f^j \right\|_2 \right\} \tag{5}$$

3   Carbon Trading Mechanism and Scenario Generation

3.1   VPP Composition Unit

The composition diagram of VPP system proposed in this paper is shown in Fig. 2, including gas turbine unit, wind turbine unit, photovoltaic unit, electric energy storage

and electric load. In VPP, if the output of gas turbine unit, wind turbine unit, photovoltaic unit and electric energy storage cannot meet the demand of electric load, purchase electricity from the power grid through the electric energy market; If the output of wind turbine and photovoltaic unit is not fully absorbed, the electric energy storage will be charged and stored. When the electric energy storage reaches the upper limit of capacity, the phenomenon of wind and light will be abandoned. The carbon emissions in the VPP system are mainly generated by gas turbine units. According to the actual carbon emissions, sell carbon rights in the carbon trading market for profit or purchase excess carbon rights.
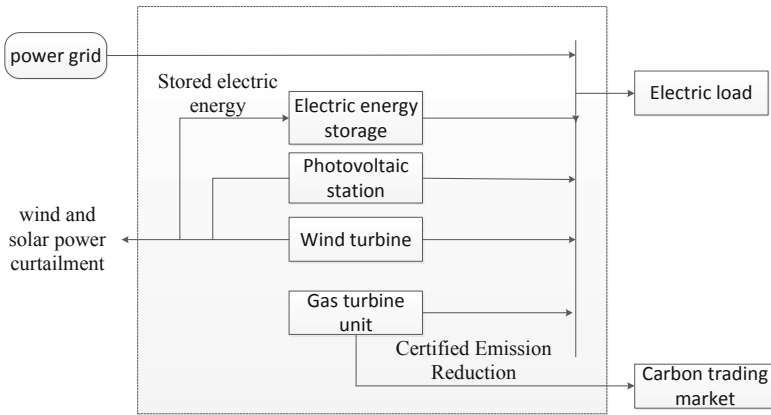
Fig. 2. Composition diagram of VPP system

By installing energy storage equipment and cooperating with distributed power generation, this paper can fully make up for the impact of wind and solar output uncertainty and fluctuation, and ensure the reliability of VPP output and operation.

3.2 Optimization Objectives

In order to reflect the economy and environmental protection of VPP, this paper takes the minimization of the net operation cost of VPP taking into account the carbon emission cost as the optimization objective. The decision variables include gas turbine output, wind power photovoltaic output, electric energy storage charge and discharge power and market power purchase. The objective function is as follows:

$$\min \sum_{t=1}^{T} (C_t^F - I_t^C + C_t^W + C_t^V + C_t^{ES} + C_t^M) \tag{6}$$

In the formula: the objective function consists of 6 parts, namely gas turbine fuel cost C_t^F, carbon asset market income I_t^C, wind turbine operation and maintenance cost C_t^W, photovoltaic power generation equipment operation and maintenance cost C_t^V, energy storage use cost C_t^{ES}, energy market power purchase cost C_t^M, and T is the total dispatching time. The specific expression of each part is as follows:

1) The fuel cost of gas turbine is [15]:

$$C_t^F = \sum_{i=1}^{l} \left(a^f + b^f P_t^G + c^f (P_t^G)^2 \right) \tag{7}$$

In the formula, a^f, b^f, c^f are the fuel cost coefficient; l is total number of gas turbines.

2) The expression of carbon asset trading income is shown in Eqs. (2)–(3). In this paper, carbon emissions are mainly caused by gas turbines, where:

$$Q_t^N = \sum_{i=1}^{l} (\lambda_i P_t^G) \tag{8}$$

In the formula, λ_i is the carbon emission correlation coefficient of gas turbine.

3) The use cost of energy storage includes two parts: investment cost and operation and maintenance cost, which can be expressed as:

$$C_t^{ES} = C_{capital} + C_t^{OM} \tag{9}$$

$$C_t^{OM} = c_{ES}(P_t^{ESC} + P_t^{ESD}) \tag{10}$$

In the formula: $C_{capital}$ is the investment cost [16], which is related to the average life of the energy storage manufacturer, which is a fixed value in the calculation example. C_{OM} is the operation and maintenance cost. c_{ES} is the operating cost per unit of energy storage. P^{ESC}, P^{ESD} is the charge and discharge power of electric energy storage.

4) The operation and maintenance cost of the fan during daily operation is:

$$C_t^W = \lambda_1 P_t^W \tag{11}$$

In the formula: P_t^W is the wind power output in t period; λ_1 is the unit maintenance cost of wind power.

5) The operation and maintenance cost of PV during daily operation is:

$$C_t^V = \lambda_2 P_t^V \tag{12}$$

In the formula: P_t^V is the photovoltaic output in t period; λ_2 is the unit maintenance cost of photovoltaic.

6) When the power is insufficient, VPP can be purchased from the power grid to meet the power load demand. The expression of power purchase cost in power market is as follows:

$$C_t^M = k_t^{EM} P_t^{EM} \tag{13}$$

In the formula: P_t^{EM} is the power purchase in the power grid in period t; k_t^{EM} is the power purchase price of power grid in period t.

3.3 Constraint Condition

The constraints are as follows:

1) Electric power balance constraint.

$$P_t^G + P_t^W + P_t^V + P_{tn.ES} = P_t^{EL} - P_t^{EM} \tag{14}$$

In the formula: P_t^{EL} is the electrical load in t period.

2) Output and climbing constraints of gas turbine unit.

$$P^{G,\min} \leq P_t^G \leq P^{G,\max} \tag{15}$$

$$\left| P_{t+1}^G - P_t^G \right| \leq \Delta P^G \tag{16}$$

In the formula: $P^{G,\max}$, $P^{G,\min}$ are the upper and lower limits of gas turbine unit output respectively; ΔP^G is the climbing rate constraint of gas turbine unit.

3) Electric energy storage constraint.

The charging and discharging of energy storage is mainly affected by the charging state of energy storage. In this paper, the power loss of electric energy storage is considered, and its constraints are as follows:

$$S_t^{ES} = S_{t-1}^{ES}(1 - \sigma^{ES}) + \eta^{ESC} P_t^{ESC} - \frac{P_t^{ESD}}{\eta^{ESD}} \tag{17}$$

$$0 \leq P_t^{ESC} \leq P^{ESC,\max} \mu_t^{ESC} \tag{18}$$

$$0 \leq P_t^{ESD} \leq P^{ESD,\max} \mu_t^{ESD} \tag{19}$$

$$0 \leq \mu_t^{ESC} + \mu_t^{ESD} \leq 1 \tag{20}$$

$$S^{ES,\min} \leq S_t^{ES} \leq S^{ES,\max} \tag{21}$$

$$S_0^{ES} = S_{24}^{ES} \tag{22}$$

In the formula: S_t^{ES} is the storage capacity of electric energy at the end of t period. σ^{ES} is the electric loss rate of electric energy storage; η^{ESC}, η^{ESD} are the charging and discharging efficiency of electric energy storage; $P^{ESC,\text{max}}$, $P^{ESD,\text{max}}$ are the maximum value of charge and discharge power respectively; Boolean variables μ_t^{ESC} and μ_t^{ESD} respectively indicate whether the electric energy storage in t period is discharged. If yes, set 1, otherwise set 0; $S^{ES,\text{max}}$, $S^{ES,\text{min}}$ are the maximum and minimum power storage capacity respectively; S_0^{ES}, S_{24}^{ES} are the beginning and end value of the energy storage battery in a day.

4) Wind and solar output constraints

$$0 \leq P_t^W \leq P^{W,\text{max}} \tag{23}$$

$$0 \leq P_t^V \leq P^{V,\text{max}} \tag{24}$$

In the formula: $P^{W,\text{max}}$, $P^{V,\text{max}}$ are the maximum available output of scenery.

3.4 Model Solving

The 24-h power dispatching model in this paper is a mixed integer quadratic programming (MIQP) problem with complex constraints and high-dimensional variables. YALMIP is a toolbox suitable for solving planning problems in MATLAB, and CPLEX is a commercial solver for solving MIQP problems. In this paper, YALMIP/ CPLEX solver is used to solve the optimization model.

4 Example Analysis

4.1 Example Description

In order to verify the model proposed in this paper, the dispatching period is divided into 24 h. The VPP constructed contains 7×2 MW wind power cluster, 6×2 MW photovoltaic cluster and 3×2 MW gas turbine units. Among them, gas turbine unit 1st is a low-carbon unit with high operation cost, and the operation parameters of gas turbine unit are shown in Table 1. In this paper, the historical output data of wind power stations in a southern region for half a year are selected as wind power output samples, and the sampling interval is 1H. The parameters of each unit are given in Appendix Table A1, and the carbon quota is determined by the method in Sect. 2.1 of this paper. The typical daily load curve is shown in Fig. 3.
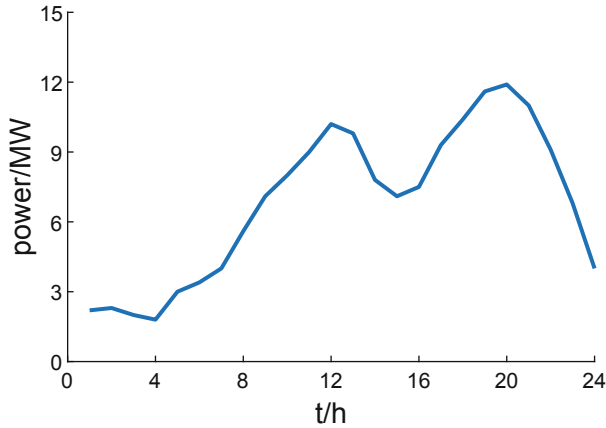
Fig. 3. Typical daily load curve

Table 1. Parameters of gas turbines

Gas turbine	a^f /yuan	b^f /(yuan·MW^{-2})	c^f /(yuan·MW^{-1})	CO_2 emission intensity/[kg·(MW·h)$^{-1}$]
1	30.0	70.21	1.2	560
2	20.0	68.80	1.0	960
3	20.0	68.80	1.0	960

4.2 Scenarios Generation Results Considering Scenery Uncertainty

Using the scene generation method proposed in Sect. 2.2 of this paper, the selected scenery output data makes an appropriate compromise between reducing the amount of calculation and retaining the output characteristics, and the number of scenes in the scene reduction is 5. The output curve of each scenario and the corresponding probability information are shown in Fig. 3. The wind and photovoltaic output conditions meet the unit output constraints. Applying the scene generation results to the day-ahead scheduling model can better reflect the uncertainty of the wind output and make the model more reliable.

4.3 Comparison Scheme Construction and Scheduling Analysis

In order to compare, measure and analyze the impact of the introduction of carbon rights trading market and different capacity energy storage on the operation cost of VPP, scheme 2 and scheme 3 are set as comparison schemes, as shown in Table 2.
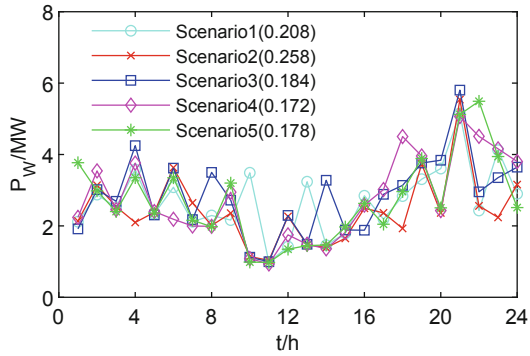
(a) Wind power output scenario generation results
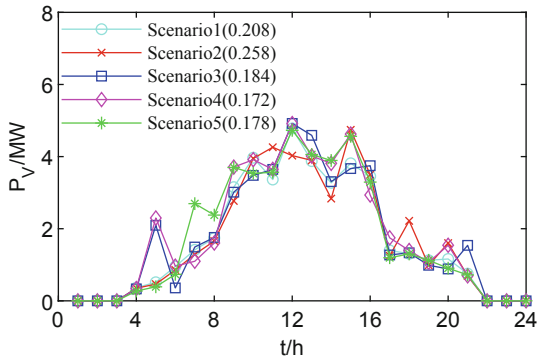
(b) Photovoltaic output scenario generation results

Fig. 4. Scenarios generation results

Table 2. Three different compositions of VPP.

Scheme	Carbon trading market	Energy storage capacity/MW
1	✓	12
2	×	12
3	✓	6

The Sect. 4.2 wind turbine and photovoltaic output scenarios are one-to-one substituted into the 4.1 section of the example description. Based on the weighted weighting of their respective probabilities, the optimization results satisfying the constraints are obtained. According to the three schemes, the comparison of the benefit and partial cost results and the dispatch results are obtained as shown in Tables 3 and 4, respectively.

Table 3. Comparison of profit and cost result.

Scheme	Carbon trading income/10^2¥	Wind and solar power casting cost/10^2¥	System maintenance cost/10^2¥	Total system cost/10^2¥
1	2.219	0	354.625	616.207
2	–6.132	0	354.625	625.856
3	–17.176	60.181	291.463	685.094

Table 4. Comparison of scheduling results.

Scheme	Output of 1 gas turbine/MW	Carbon emissions/t	Energy market electricity purchase/MW	Amount of abandoned wind and solar/MW
1	16.714	29.416	1.500	0
2	11.206	31.613	1.500	0
3	18.109	34.528	1.589	5.471

Compared with scheme 2, scheme 1 realizes the VPP framework for the coordinated operation of gas units and wind power storage under the environment of carbon rights trading. It can be seen from Table 3 that due to the consideration of carbon emission cost, the dispatched output of gas turbine 1 with low carbon emission intensity per unit power is higher. In a scheduling cycle, scheme 1 reduces carbon emissions by 2.197t compared with scheme 2, so it also obtains positive benefits from the carbon trading market. However, the need to purchase carbon emission rights in scheme 2 increases the cost of VPP, which reduces the total cost of scheme 1 by 835.1 ¥ compared with scheme 2, so that the overall benefits and environmental protection characteristics of scheme 1 VPP are better.

Compared with scheme 3, scheme 1 uses a higher capacity energy storage device, which increases the investment cost and operation and maintenance cost of scheme 1, but sufficient energy storage capacity realizes the flexible allocation of power resources in the VPP, so that the photovoltaic output of clean energy fans in the VPP is fully absorbed. Due to the insufficient energy storage capacity of scheme 3, it is impossible to store all the wind and light output in the low load period, resulting in the phenomenon of abandoning wind and light. In addition, the electric energy provided by wind and light storage is limited in the peak load period, so VPP has to call more gas turbine output, which increases the carbon emission of scheme 3 by 5.112t and the cost by 59.89×10^2 ¥ compared with scheme 1, resulting in the poor benefit and environmental protection of VPP with insufficient energy storage capacity of scheme 3. It is worth noting that in schemes 1 and 2, the wind and light abandonment is 0, so it is meaningless to continue to increase the energy storage capacity, which will only increase the system investment cost and operation and maintenance cost, and damage the economy of VPP.

To sum up, scheme 1 of the VPP model proposed in this paper introduces the carbon rights trading environment, configures the electric energy storage with appropriate capacity, and cooperatively optimizes the scheduling with gas turbine and wind power photovoltaic, which can reduce the net cost and carbon emission of VPP, promote the consumption of clean energy and suppress the impact of load fluctuation, making VPP both economic and environmental.

4.4   Analysis of VPP Optimal Scheduling Results

According to the example simulation of the proposed model, the output and power purchase of each unit in scheme 1vpp are shown in Fig. 5, and the storage, discharge and energy storage of energy storage device are shown in Fig. 6.
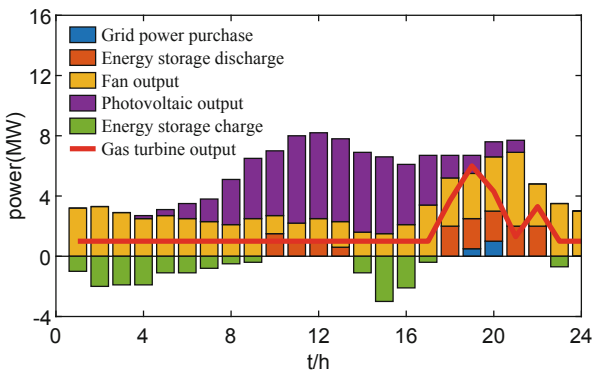
Fig. 5.   Optimized scheduling results of VPP
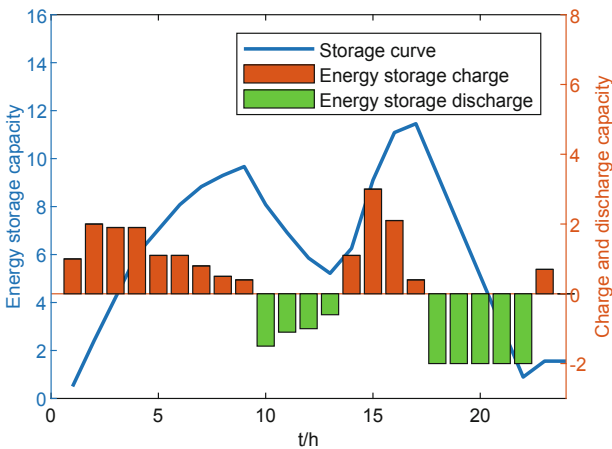
Fig. 6.   Storage/discharge power and energy storage power level of energy storage device

It can be seen from Fig. 5 and Fig. 6 that during the period from 1 to 5, there is almost no output of photovoltaic at this time, the output of wind power is large and the load demand is small. At this time, the output of gas turbine does not change with the load, and the load demand can be met as long as it is kept near the minimum output power. After the wind power meets the load demand, the surplus is stored by the energy storage device, and the electric energy in the electric energy storage is increased. If there is no energy storage device in the VPP, the abandoned wind is mainly concentrated in this period.

During the 6–9 period, the load demand began to increase. Although the wind power output decreased slightly, the photovoltaic output began to show an upward trend, and the clean energy output can still meet the load demand. The electric energy storage continues to be charged, and the charging amount per unit time is lower than before. If there is no energy storage device in VPP, the light rejection is mainly concentrated in this period.

During the period of 10–13, the fan output generally shows a decreasing trend. The photovoltaic output reaches the output peak at noon, while the load demand increases rapidly, and the load curve has the first peak. VPP needs to call more gas turbine output to achieve electric energy balance. However, since this paper takes into account the economic and environmental protection VPP of carbon rights trading, the output of gas turbine should be reduced as much as possible, At this time, the energy storage discharge is used to make up for the insufficient output of the distributed generation.

During the period from 14 to 17, the photovoltaic output remains at a high level. At this time, the load demand drops, the electric energy storage is charged, and the electric energy in the energy storage is increased to the maximum capacity.

During the period of 18–21, the power load demand reaches the second peak and reaches the maximum load demand. The wind power output increases slightly and the photovoltaic output gradually decreases to zero. At this time, the stored energy is used to output electric energy at the maximum power. As there is still a power gap, VPP adopts the way of increasing the output of gas turbine and purchasing power from the power grid to meet the load demand. The carbon emission of VPP is mainly concentrated in this period.

During the period of 22–24, the load demand decreases significantly, the wind power output continues to increase, the photovoltaic output stops, the gas turbine output returns to the minimum output state, and the energy storage returns to the initial state of dispatching after one dispatching cycle, so as to prepare for the next round of dispatching.

To sum up, based on the optimal dispatching model and method of virtual power plant with carbon rights trading considering the coordination of distributed generation and energy storage proposed in this paper, the flexible coordinated dispatching and complementarity of power resources can be realized. Taking into account the uncertainty of scenery, this paper uses the classical scenario construction method to enhance the reliability of the model, and then combined with the energy storage resources with appropriate capacity, transfers the period of high power generation and low power load of distributed clean energy to the period of low power generation and high power load of distributed clean energy, so as to achieve the supply-demand balance between source

loads and complete the full consumption of distributed clean energy. At the same time, in the carbon trading environment, during the energy storage and discharge period, the output of the gas turbine and the power purchase of the power grid are reduced, the non environmental phenomenon that the gas turbine is consistent with the load change trend in order to quickly respond to the wind and rain fluctuation under the traditional regulation measures is avoided, and the final dispatching structure of the established model takes into account the economy and environmental protection, which further proves the effectiveness and rationality of the model established in this paper.

5　Conclusion

In the environment of introducing carbon rights trading, considering the uncertainty of scenery, this paper establishes a virtual power plant model with energy storage and multiple distributed generators, studies its scheduling strategy, and draws the following conclusions.

(1) By considering the scene generation method of uncertain output of scenery, the characteristics of scenery output of original data are strengthened, the impact of fluctuation of scenery output on the rationality and reliability of the model is effectively reduced, and the model effect verified by an example is highlighted.

(2) By introducing the carbon trading environment, VPP can be encouraged to configure energy storage devices, so as to improve the solar energy consumption capacity, alleviate the contradiction between the output of distributed generation and the demand of electric load, and improve the regulation ability of VPP in response to the change of output of distributed generation. Under the influence of carbon emission cost in the carbon trading environment, VPP improves the output level of low-carbon units, reduces the total carbon emission, and sells excess carbon rights to improve income, reduce cost, and improve the economy and environmental protection of VPP.

There are many directions and contents of collaborative multi resource optimal scheduling in VPP, which are worthy of further research. In the following research work, we will select the scenery data with longer historical period for scene generation, and study the selection method of the optimal energy storage capacity. At the same time, the composition of the comprehensive evaluation index system for the regulation results of VPP in the carbon trading environment is also the focus of further research.

Appendix A

Table A1. VPP unit parameters

$C_{capital}$ /yuan·MW^{-1}	c_{ES} /(yuan/(MW·h))	λ_1 /(yuan/(MW·h))	λ_2 /(yuan/(MW·h))	$P^{G,\min}$ /MW
1000	40	80	65	0.3

$P^{G,\max}$ /MW	ΔP^G /MW	σ^{ES}	η^{ESC}	η^{ESD}
2	1	0.001	0.95	0.95

$P^{ESC,\max}$ /MW	$P^{ESD,\max}$ /MW	$S^{ES,\max}$ /MW	$S^{ES,\min}$ /MW	S_0^{ES} /MW
3	2	12	0.5	0.5

$P^{ESC,\max}$ /MW	$P^{ESD,\max}$ /MW	$S^{ES,\max}$ /MW	$S^{ES,\min}$ /MW	S_0^{ES} /MW
3	2	12	0.5	0.5

k^C /yuan·kW^{-1}	γ^C / kg·kW^{-1}
0.38	1.1

References

1. Lu, S.F., Wu, Y,S., Lou, S.T.: A model for optimizing spinning reserve requirement of power system under low-carbon economy. IEEE Trans. Sustainable Energy **5**(4),1048–1055 (2014)
2. Zhinong Wei, F., Shuang, Yu,S., Guoqiang Sun, T.: Concept and development of virtual power plant. Autom. Electric Power Syst. **37**(13), 1–9 (2013)
3. Tianwang Wang, F., Yun Gao, S., Meng Jiang, T.: Power system optimal scheduling including distributed wind power and energy storage system via virtual power plant. Electric Power Constr. **37**(11), 108–114 (2016)
4. Suhua Lou, F., Bin Hu, S., Yaowu Wu, T.: Optimal dispatch of power system interated with large scale photovoltaic generation under carbon trading environment. Autom. Electric Power Syst. **38**(17), 91–97 (2014)
5. Xiaohua Zhang, F., Jun Xie, S., Jinquan Zhao, T.: Energy-saving emission reduction dispatching of electrical power system considering uncertainty of load with wind power and plug-in hybrid electric vehicles. High Voltage Eng. **41**(7), 2408–2414 (2015)
6. Zuoyu Liu, F., Feng Qi, S., Fushuan Wen, T.: Economic and environmental dispatching in electric vehicles embedded virtual power plants with participation in carbon trading. Electric Power Constr. **38**(9), 45–52 (2017)
7. Fulu Xu, F., Renjun Zhou, S., Junbo Cao, T.: Coordinated optimal dispatching of power-heat-gas for virtual power plant participating in multiple markets. Proc. CSU-EPSA **31**(9), 35–42 (2019)

8. Honghai Kuang, F.: Improvement research on transient stability and power quality of distributed wind power integrated system. Hunan University, Changsha (2013)

9. Shilong Wang, F., Shuangshang Song, S., Qinghua Lin, T.: Virtual power plant optimal scheduling considering distributed energy storage. Renewable Energy Resources **37**(8), 1214–1219 (2019)

10. Jiajia Xu, F.: Study on distributed generation dispatching management mode base on virtual power plant. Beijing: North China Electric Power University (2013)

11. Yanfeng Ma, F., Zhenya Fan, S., Weidong Liu, T.: Environmental and economic dispatch considering carbon trading credit and randomicity of wind power and load forecast error. Power Syst. Technol. **40**(2), 412–418 (2016)

12. Lu, Z,F., Lu, C,S., Feng,T.: Carbon dioxide capture and storage planning considering emission trading system for a generation corporation under the emission reduction policy in China. IET Generation, Transmission & Distribution **9**(1), 43–52 (2015)

13. Department of Ecological Environment. Implementation Plan for Setting and Allocating the Total Quota of National Carbon Emission Rights Trading in 2020 (2020–12–30)

14. Wu, L,F., Monhammad, S., Li, T.: Stochastic constrainedunit commitment. IEEE Trans. Power Syst. **22**(2), 800–811 (2007)

15. Guili Yuan, F., Shaoliang Chen, S., linbo Wang, T.: Economic optimal dispatch of virtual power plant considering environmental benefits. Adv. New Renewable Energy **3**(5), 398–404 (2015)

16. Gang Chen, F., Yuqing Bao, S., Jinlong Zhang, T.: Distributed cooperative control strategy of energy storage unit with life loss cost. Power Syst. Technol. **42**(5), 1495–1501 (2018)

Research and Application of Configuration Animation Technology for Power Grid Dispatching and Control Systems Based on CIM/G

Zhen Yan[1,2(✉)], Hua Xu[1,2], Zhimeng Lv[1,2], Xia Yin[1,2], Xiongwei Bao[1,2], and Kun Huang[1,2,3]

[1] NARI Group Corporation (State Grid Electric Power Research Institute), Nanjing 211106, China
yanzhen@sgepri.sgcc.com.cn
[2] NARI Technology Co. Ltd, Nanjing 211106, China
[3] State Key Laboratory of Smart Grid Protection and Control, Nanjing 211106, China

Abstract. For the current traditional power grid dispatching and control system, the display effect of configuration software interface is ordinary, and the configuration interface is cumbersome. This paper presents a state animation technology of configuration software for power grid and control system. By defining multiple states in the configuration editor, modifying component attributes in different states, setting state switching animation types, associating the animation change functions of component attribute values in different states, saving in CIM/G format, and then opening the corresponding files through the browser, the component attributes can be dynamically transformed between attribute values in different states, Batch modification and animation of component attributes are realized, which enriches the display effect of the interface and improves the friendliness of human-computer interaction.

Keywords: Power grid dispatching and control system · State machine; Animation · Components · Interface display

1 Introduction

In recent years, the widespread use of human-computer terminals has brought people a brand-new human-computer interaction experience [1, 2], and great progress has been made in the form of human-computer interaction and graphical display methods [3, 4]. At the same time, with the development of the power grid dispatching system, the new-generation control system with "physical distribution and logical unity" [5, 6] in the future requires the efficient and rapid sharing and interaction of a large amount of information between different systems and different regions [7]. However, with the accelerated construction of the system and the continuous enrichment of application

scenarios, higher requirements have been put forward for the display of the graphical interface of the human-machine cloud terminal of the power grid automation system.

In terms of graph dynamic configuration display, the level of computer hardware is developing rapidly, human beings continue to deepen the research on computer applications, the form, quality, and concept of human-computer interaction have changed [8], the human-computer terminal is becoming more and more lightweight, and the graph effect more and more sophisticated, the function of the GPU is more and more general [9–11]. These changes are gradually changing the status of the human-machine interface from two aspects of technology and ideas, and promoting the development of the human-machine interface of the power system configuration software to be more flexible, cool, and intelligent [12, 13]. The existing power system configuration software has made a big breakthrough in the display of human-machine interface visualization effects. It supports the embedding of H5 components and three-dimensional chart components, supports basic interaction between components, and has simple dynamic animation of components, the animation effect is realized through the continuous modification of component location, size, color and other attributes, which has brought a certain improvement of human-computer interaction experience [14]. However, the current dynamic effect setting of component attributes is relatively complex, especially when triggering component animation configuration in batches according to a certain state is cumbersome. A convenient method is needed, which can update the relevant display properties of components in batches, realize the scene animation and status animation of the configuration graph components, and improve the convenience and friendliness of the operation and control of the dynamic effect of the human-machine interface software.

Based on the CIM/G power graphic description specification and the new generation control system graphic editor, combined with the component animation driving technology, this paper maps the overall picture into a state, and realizes the batch, convenience, and customization of component properties in different scenes and different states. Editing: Combined with the linear change of the component motion function to drive the property, the dynamic effect switching of the graph is realized, which greatly enriches the browsing effect, improves the experience of human-computer interaction, and achieves a unified and undifferentiated graph dynamic effect switching effect.

The organization structure of this paper is as follows: the first part introduces the overall structure of the configuration animation of the power grid control system; the second part analyzes the key technologies in detail; the third part introduces the application examples of related technologies; the fourth part summarizes the full text.

2   Framework

The content of this paper is mainly divided into four parts: multi scene state creation and attribute editing, component attribute editing in multi scene state, multi scene component dynamic effect switching display, and multi scene component state and attribute saving method based on CIM/G. The overall framework is shown in Fig. 1.

The multi-scene state creation and attribute editing module is mainly based on the mathematical model of the state machine, and the state machine is applied in the graphics editor and browser. The requirements for creating different states on the same graph
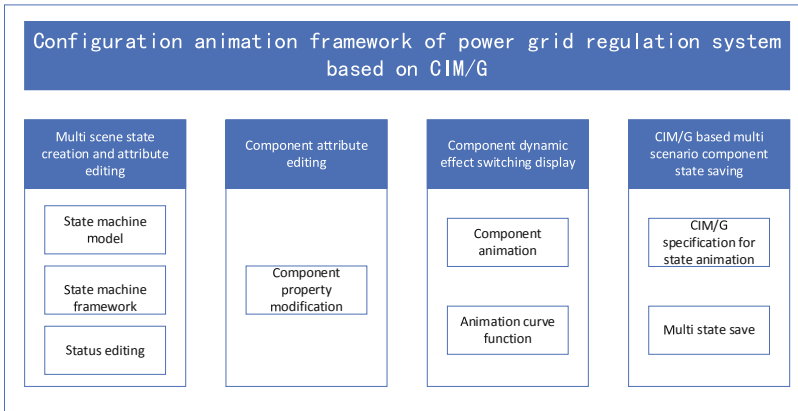
Fig. 1. Multi scene component animation framework

enable flexible creation and deletion of states, as well as editing of attributes such as state animations.

The component attribute editing module in multi-scene state proposes a method for editing the attributes of graphic components in multi-scene and multi-state. Combined with the current situation of cumbersome editing of multi-element and multi-property editing by a new generation of graphics editors, it can achieve different scenes and different states. The attribute method of batch, convenient and customized editing components can meet the needs of users to edit different scenarios, and the primitive components can be edited conveniently and quickly.

The dynamic effect switching display module of scene components is mainly used for the realization and display of component animation effects. Combined with a new generation of graphic editors, it can realize the effect of component animation based on the new human-machine browser; multiple scene graphs and multiple components switch states concurrently to meet the needs of graph browsing. Support the definition and integration of animation curve types, realize the editing of multiple animation curves, and display the dynamic effects of the state switching of different state on the same graph according to the defined animation curves.

The state and attribute saving module of multi scene components based on CIM/G mainly extends the relevant description specification of state machine based on CIM/G standard. Combined with the attributes required by different state attributes of state machine, the state machine description specification that meets the dynamic requirements of state switching of the new generation of man-machine browser can save the state attributes and component attributes of different scenes in CIM/G file according to the designed state machine description specification.

3   Key Technologies

3.1   Animation State Machine

State machine is an indispensable part of object-oriented. It can be used to describe how objects (Systems) respond to external inputs. The state machine first defines the state that the object (System) can reach, and then defines state migration, that is, how to transition from one state to another.

Finite state machine (FSM) is a mathematical model of a system with discrete input and discrete output. Represents a finite number of states and behaviors such as transitions and actions between those states. It can be used to build the model of object behavior, it is mainly used to describe the sequence of states experienced by an object during its life, and deal with various events from the outside [15]. A finite state machine M consists of:

(1)   A finite set of input symbols η,
(2)   A finite set of output symbols θ,
(3)   A finite set of States δ,
(4)   One from δ*η reach δ the next state function f,
(5)   One from δ*η reach θ the output function g,
(6)   An initial state σ ∈ δ。

Then M = (η, θ, δ, f, g, σ). Building a finite state machine requires decoupling States and events, which is divided into the following steps:

(1)   Determine the status;
(2)   Split event;
(3)   Generate a state transition diagram.

Based on the finite state machine, the state animation module constructs the component state animation framework to realize the dynamic switching of components in multiple state scenes. The relationship of each module in the state animation framework is shown in Fig. 2:

Animation State Machine: manage all States and provide state transition mechanism.

Status: a group of static descriptions, which are the static values of component element attributes in the picture under the situation.

Transition: it is the time or space description of component animation. It is mainly used to describe the process of changing the static attribute values of picture components under different states. Usually, the state switching is not completed instantaneously. Due to the different time of state switching, it will have many intermediate temporary states.

Transition Curve: when switching between different states, according to the transition time t, the specific change function v = f (v1, t) is given for the initial value v1 and actual value v of the attribute to modify the whole transition process.

Animation: transition executor, which is created by applying animation types to one or more attribute values of the component. The animation type interpolates the attribute value from the start value to the end value according to the motion time through the transition curve function, to create a smooth animation transition effect. To create an
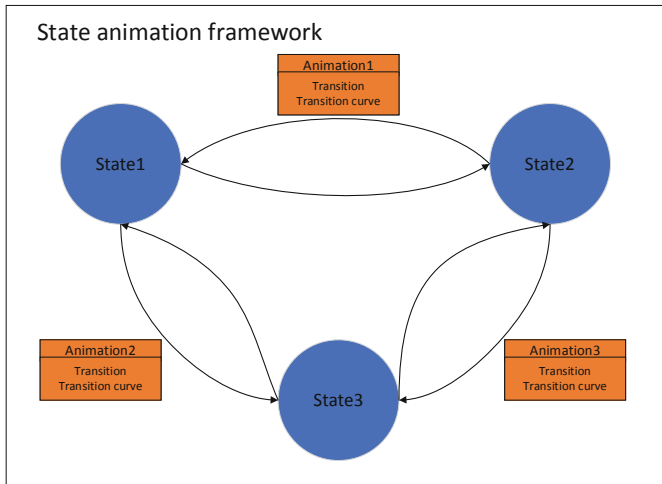
Fig. 2. Schematic diagram of animation state machine

animation, you need to use the appropriate animation type for an attribute, and the applied animation also depends on the behavior type you need to implement.

The dynamic effects can be achieved by modifying the properties of several scenes in a batch of animation modules.

3.2 Multi Scene Creation and State Editing

3.2.1 Basic Functions of Status Editing

The configuration editor includes menu bar, component box, drawing area, state machine editing area and attribute follow-up editing area.

Menu bar: common operation function area of configuration editor, mainly including functions related to opening, saving, or saving as other files; Common editing functions such as component lifting, lowering, left alignment, right alignment, top alignment, bottom alignment, pasting and copying; Enter and exit status editing function.

Component box: component loading area, which is used to select and retrieve components, mainly including common components, basic components, UI control components, visual chart components, etc.

Drawing area: it is mainly used for component drag drawing, selection, layout, resizing, attribute setting and other operations.

Attribute follow-up: select an element component in the drawing area, and the area will display the specific attributes of the corresponding element. The attributes of the component can be set in detail in this area, and multiple attributes such as component position, width and height, color and so on can be modified and adjusted.

Status editing area: it is mainly used to manage the scene status, including adding, selecting, deleting, renaming and other operations.

The basic editing style of configuration editor state machine is shown in Fig. 3.
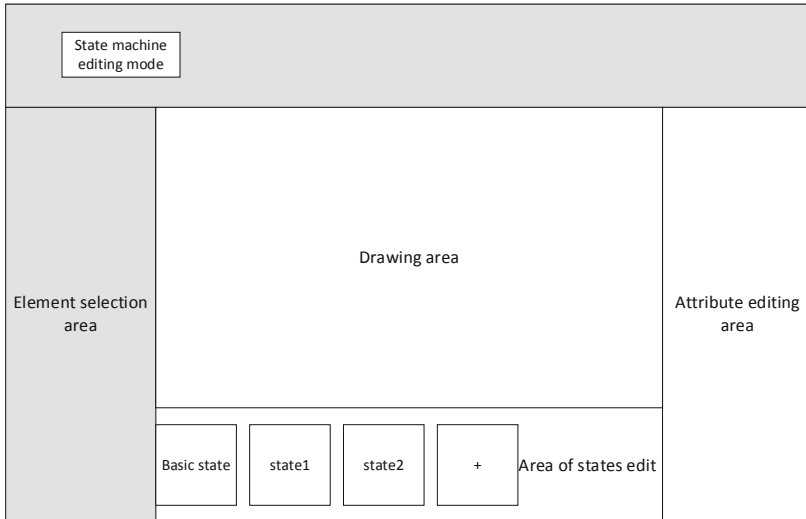
Fig. 3. Configuration editor transition editing window

3.2.2 Status Editing Process

(1) Configuration editor states editing

The state machine enters edit mode, first is basic state, which is the initial style of the interface component; In the states editing area, new states can be added or deleted; Different state names can be modified, and the naming rules must meet the naming requirements of variable names; Click and select different states to set the component animation effect in the corresponding state, and the position or other attributes of component can be modified in the drawing area.

(2) Configuration editor state machine interface creation process

Click the state machine button in the menu bar to judge whether the state machine editing area interface has been created. If it exists, it will be displayed. If it does not exist, it will create a new state machine editing area interface.

(3) Component editor status component attribute editing process

In a certain state, the drawing area modifies the component attributes, and the configuration editor monitors the changes of component attributes and records the changes of component attributes in the corresponding state.

(4) Configuration editor status switching process

Switch between different states in the state editing area, and the component attributes in the drawing area will change accordingly, which will be displayed as the component attributes set in the corresponding state.

(5) Configuration editor states saving process

Complete the states setting, save the file in the standard CIM/G format of the power system, which is convenient for subsequent opening and recall.

3.2.3 State Animation Persistence

CIM/G is a graphic description specification of power system, which is used to define picture components and their related attributes to facilitate picture sharing and interactive access [16, 17]. After the state animation is set, the relevant attributes are persisted in CIM/G format.

The label of state machine is defined as 'Statemachine', and the format of state machine attribute is shown in Table 1:

Table 1. State machine attributes description

Attribute	Default	Remarks
num	1	int
stateName0	"State0"	string
property0	""	string
value0	""	string
duration0	"2000"	int
easingType0	"linear"	string
id0	""	string
stateName1	"State1"	string
property1	""	string
value1	""	string
duration1	"2000"	int
easingType1	"linear"	string
id1	""	string
…	…	…
stateNamei	"State i"	string, i is serial number (the same below)
propertyi	""	string
valuei	""	string
duration	"2000"	int
easingTypei	"linear"	string
idi	""	string

For example, a state machine is used to dynamically lay out the components in the picture. G file attributes are shown in Table 2:

State1 indicates that the starting coordinate "x" of the component is −50, and the component is outside the visible area. State2 indicates that the starting coordinate "x" of the component is 0, the upper left corner of the display area is the coordinate origin, and the component is within the display area. Set the animation duration to 2000 ms, when switching from state1 to state2, the "x" of the component changes from −50 to 0,

Table 2. G file attributes example

Attribute	Value
num	2
stateName0	State1
property0	x, color
value0	−50, red
duration0	2000
easingType0	linear
id0	component
stateName1	State2
property1	x, color
value1	0, yellow
duration1	2000
easingType1	linear
id1	component

the "color" changes from red to yellow, the whole animation process takes 2000 ms, the animation curve changes linearly, and the component switching from state1 to state2 as shown in Fig. 4.
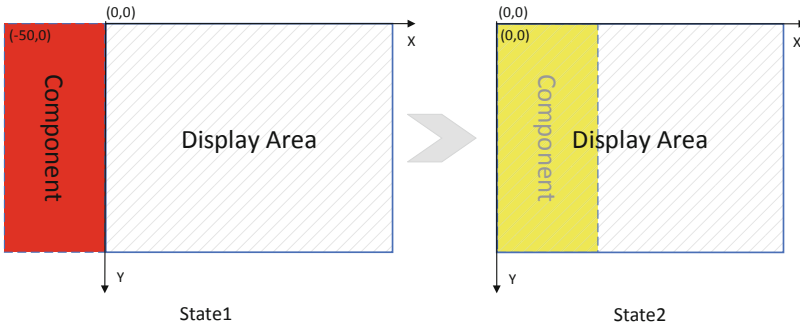
Fig. 4. State switching diagram

4   Application Examples

The new generation of man-machine cloud terminal configuration software based on the configuration animation framework of power grid regulation system proposed in this paper has been deployed and applied in power grid dispatching in East China Power Dispatching Center, Jiangsu Power Dispatching Center, Zhejiang power dispatching center and Hebei Power Dispatching Center, and achieved good application results. Among them, in a provincial dispatching equipment maintenance intelligent operation scene interface, Fig. 5 is the initial interface of equipment maintenance, which is the initial state of operation, and Fig. 6 is the viewing state of plant station wiring. Through the equipment viewing and recovery operation, the interface can dynamically switch back and forth between two different States to achieve rich human-computer interaction display effect.

Fig. 5. Operation scenario status 1

The configuration software of the existing D5000 smart grid control system is based on the Qt native painter drawing mechanism [18], and the picture components and scenes are drawn based on the CPU. The CPU occupancy rate will reach 50%, and the same machine adopts the GPU-based state machine configuration animation mechanism, which can realize the animation effect of picture elements in large scenes, and the CPU occupancy rate is low, and the screen refresh rate can maintain a frame rate of 60fps.

Fig. 6. Operation scenario status 2

5 Conclusion

The configuration animation technology of power control system proposed in this paper, the position size of components in power system configuration browser cannot be changed, the editing of different scene states of the same picture components is difficult, and the different states of components in different scenes cannot be displayed with the same picture are solved, so as to reduce the complexity of multi scene picture editing, improve the effect of picture state switching, and improve the sense of experience and picture of human-computer interaction. However, for the component animation switching effect in different states, the same animation function can only be used, which cannot be set at the component level granularity. Therefore, the richness of the animation switching effect needs to be further studied. In addition, how to combine with the state machine and add animation effects to the scene conversion of different pictures is also an important topic for future research.

References

1. Shuibao, H., Weidong, T., Lingtao, Z., et al.: Undifferentiated Browsing Human-machine cloud terminal supporting large power grid dispatching control system and its key technologies. Power Syst. Technol. **44**(2), 420–428 (2020)

2. Kun, H., Kun, Z., Libo, Y., Zhen, Y., et al.: Architecture and key technologies of lightweight human-machine interaction system for power grid dispatching and control system. Autom. Electr. Power Syst. **43**(7), 159–165 (2019)
3. Hongqiang, X.U., Jianguo, Y.A.O., Yijun, Y.U., et al.: Architecture and keytechnologies of dispatch and control system supporting integrated bulk power grids. Autom. Electr. Power Syst. **42**(6), 1–8 (2018)
4. Zhen, X., Ren, L., Aimin, Y., et al.: Mobile application security technology for smart grid. Autom. Electr. Power Syst. **36**(16), 82–87 (2018)
5. Shuhai, F.E.N.G., Jianguo, Y.A.O., Shengchun, Y.A.N.G., et al.: Overall design of integrated analysis centre for physically distributed and logically-integrateddispatchsystem. Electr. Power Autom. Equip. **35**(12), 138–144 (2015)
6. Jianguo, Y.A.O., Shengchun, Y.A.N.G., Maohua, S.H.A.N.: Reflections on operation supporting system architecture for future interconnected power grid. Autom. Electr. Power Syst. **37**(21), 52–59 (2013)
7. Lin, Z., Lingtao, Z., Zan, W., et al.: Design of human-machine interaction interface with multiple views for dispatching automation system. Autom. Electr. Power Syst. **42**(6), 86–91 (2018)
8. Astic, J.-Y., Bareux, G., Buhagiar, T., et al.: Control center designs: new functions and challenges for the transmission system operator. IEEE Power Energ. Mag. **16**(2), 57–66 (2018)
9. Ya-qin, Y.A.N., Jian, Q.I.U., Peng, Z.I.: Design and realization of a power grid diagram editor based on web. Power Syst. Prot. Control **38**(8), 92–96 (2010)
10. Minkun, W., Xiao, H., Lingyun, W., et al.: CIM/G based web graphical display technology for power grid dispatching and control systems. Autom. Electr. Power Syst. **42**(6), 81–85 (2010)
11. Lin, Z.H.A.O., Jiaqing, Z.H.A.O., Kejun, Q.I.A.N., et al.: Research on keytechnology of new man-computer interface for dispatching automation system. Power Syst. Technol. **38**(11), 3193–3198 (2014)
12. Zijian, Y.A.N., Peng, S.U.N., Xiaomei, L.I.U., et al.: Architecture and key technologies of human-machine graphic configuration for technical supporting system of electricity market. Autom. Electr. Power Syst. **45**(5), 122–128 (2021)
13. Barata, P.N.A., Filho, M.R., Nunes, M.V.A.: Virtual reality applied to the study of the integration of transformers in substations of power systems. Int. J. Electr. Eng. Educ. **52**(3), 203–218 (2015)
14. Pan, J., Qi, H., Zheng, R.: Massive power grid operational status data analysis system for 3D visualization. In: 2021 IEEE Asia-Pacific Conference on Image Processing, Electronics and Computers (IPEC), pp. 196–203. Dalian (2021)
15. Yiran, L.I.U., Pengfei, X.I.E., Xuefeng, D.E.N.G.: Attribute configuration verification method of distributed framework based on finite state machine. J. Jiangsu Univ. Nat. Sci. Ed. **43**(1), 83–87 (2022)
16. Wei, L.I., Yaozhong, X.I.N., Guohui, S.H.E.N., et al.: Scheme of power grid graphics maintenance and sharing based on CIM/G. Autom. Electr. Power Syst. **39**(1), 59–63 (2015)
17. Hua, X., Jian, N., Kun, H., et al.: CIM/G based multi-version management and display of graphics. Autom. Electr. Power Syst. **41**(24), 164–169 (2017)
18. Yiqiang, C., Xiaona, W., Huiqun, L., et al.: Graphics wide-area maintenance and browsing technology for smart grid dispatching and control systems. Autom. Electr. Power Syst. **41**(14), 171–175 (2017)

Lightweight Detection Algorithm of Substation Instrument Based on Improved YOLOv4 Algorithm

Fanglong Niu[1]([✉]) [ID], Yao Cui[2] [ID], Bo Yu[1] [ID], and Xiaoqiang Zhu[1] [ID]

[1] State Grid Electric Power Research Institute, Nanjing 211106, Jiangsu, China
487123819@qq.com
[2] State Key Laboratory of Smart Grid Operation and Control, NARI Group Corporation (China Electric Power Research Institute), Nanjing 211106, Jiangsu, China

Abstract. Under the requirements of new power system, the intelligent process of substation is being promoted rapidly, among which the instrument inspection plays an important role in this process. The target detection algorithms based on computer vision and deep learning technology have been applied to the substation inspection image in many studies to replace the traditional manual inspection. While the requirements for storage and computing power in deep neural network are too high to meet for patrol robots, resulting the great challenges to deploying the algorithm to the mobile terminal. There are three improvements based on the target detection algorithm YOLOv4 to realize the easier deployment by using the lightweight network MobileNetv3 to replace the backbone feature extraction network in the original network, using the depth wise separable convolution to replace the traditional convolution and introducing pre-fused of features. The improved strategy is trained by using the instrument images collected in the real scene and is compared with the original algorithm with the same test sets, showing that their recognition and positioning accuracy are basically close while the inference speed significantly reducing, which can make it more convenient to deploy on the terminal.

Keywords: Automatic Inspection · YOLOv4 · MobileNetv3 · Depth Wise Separable Convolution · Instrument Detection

1 Introduction

In response to the requirements of new power system construction, the substation inspection task is accelerating towards the direction of intelligence. As the central point of power conversion between power grid and users, substation plays an important role in the whole power system. A large number of instruments are deployed in substation to monitor the normal operation of various equipment, among which the pointer instruments occupy the main position in substation, especially in the outdoor environment because of the characteristics of simple structure, low price and strong anti-electromagnetic interference

performance [1]. In the past, the reading method relied on manpower and was restricted by strong electromagnetic environment, rain and snow weather, patrol inspection efficiency and other problems. However, this method cannot meet the intelligent needs of substation with the "intelligence of everything".

In recent years, the deep learning technology represented by convolutional neural network (CNN) has made great achievements in the field of computer vision. Various excellent algorithms emerge, which has promoted the computer vision algorithm to move towards the direction of intelligence to get rid of manual intervention to obtain better results than manual. Target detection task is a key research task in the field of computer vision and can be divided into two-stage algorithms based on region proposal and one-stage algorithms based on regression. The former is represented by R-CNN series algorithms [2–4], in which the proposal is produced first and then modified; The latter is represented by YOLO series algorithms [5–8] and SSD algorithms [9], in which the end-to-end regression idea is adopted for target detection. Since the generation of proposal will consume a lot of computing time, the detection speed of two-stage algorithms is generally slower than that of one-stage algorithms, as shown in Fig. 1. These excellent target detection algorithms can use the images collected in the substation to learn and extract important features to detect the instruments in a new image and locate them accurately. In view of this, applying deep learning algorithm instead of human eyes to observing substation has become a research hotspot.
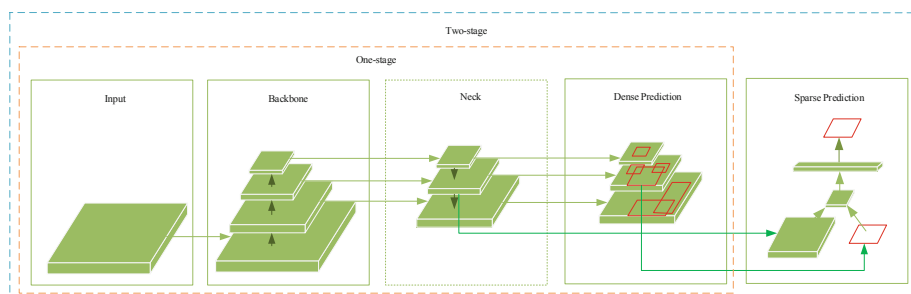
Fig. 1. Difference between two-stage algorithm and one-stage algorithm

A set of strategies and algorithms considering equipment ontology and defects are proposed in [10], in which YOLO algorithm is used for coarse-grained identification of equipment firstly, and then Fast R-CNN is used for fine-grained identification of equipment defects, which improves the accuracy compared with single target detection algorithm; The YOLOv4 algorithm is improved in [11], including the improvement of the loss function and the enhancement of the feature fusion network, and detected the defects including equipment corrosion and cracks. Compared with another target detection algorithm, Fast R-CNN and the original YOLOv4 algorithm, the accuracy has been improved; A new strategy called inner class sampling is proposed in [12] to balance the sample imbalance, corrected the loss function and sample label, and improved the threshold in non-maximum suppression (NMS) based on the number of categories. The proposed strategy was deployed in practice and its correctness was verified; YOLOv3

algorithm and SSD algorithm are respectively improved in [13] and [14] in combination with the characteristics of substation images.

Although there are many studies on target detection of equipment and defects and the application of deep neural network to realize the target detection of substation instruments can achieve high accuracy based on the powerful computing resource of GPU, how to apply them to automatic patrol inspection is still facing difficulties. Firstly, the deep neural network deepens the network structure to improve the accuracy, which contradicts the demand for high detection speed of automatic patrol inspection; Secondly, the inspection robot cannot meet the large storage space and high computing power required by the deep neural network. Therefore, it is particularly important to study how to improve the reference speed and storage under the condition of maintaining the accuracy of the existing algorithm.

In this paper, three major improvements were made to reduce the model size on the premise of ensuring the detection accuracy compared to the original network whose structure is much more complicated, to realize the easier deployment on the robot. Firstly, a lighter feature extraction network MobileNetv3 is utilized to replace the original CSPDarknet53; Secondly, the shallow features not used in the original algorithm are introduced in the part of strengthening feature extraction network to ensure the accuracy even with a lighter network; Last but not least, the standard convolution in the network is replaced by the deep separation convolution with fewer parameters and faster calculation speed to further reduce the parameters of the model. The structure of this paper is as follows: The basic principle and network structure of YOLOv4 algorithm was introduced in the first part, the improved strategies are introduced in the second part, the experiment is shown in the third part and the content of this paper is summarized at the last.

2   YOLOv4 Network Structure and Working Principle

The detection idea of YOLO series algorithms is to divide the original image into regions by using feature maps of different sizes. Each grid is only responsible for predicting the targets in which the center of object falls. These feature maps are obtained by the feature extraction network. The large-size feature map is responsible for predicting small targets, and the small-size feature map is responsible for predicting large targets. YOLOv4 algorithm [8] has greatly improved the detection accuracy and speed. It has higher detection accuracy than the one-stage algorithm in the same stage, faster detection speed than the two-stage algorithm with the accuracy close to the two-stage algorithm.

2.1   YOLOv4 Network Structure

The backbone part of YOLOv4 adopts CSPDarknet53 [15], which is the improvement on the basis of the original Darknet53 [7]. Firstly, CSPNet (cross stage partial network) [15] structure is used in the residual connection part, as shown in Fig. 2, which makes the learning ability of the network further enhanced and the memory cost and computing bottleneck reduced while ensuring the accuracy.
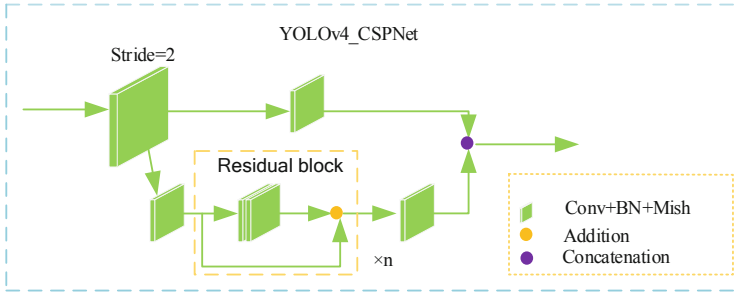
Fig. 2. CSPNet structure diagram

Secondly, the Mish activation function [16] is used to replace the original Leaky ReLU activation function [17], as shown in Fig. 3. The replacement of the activation function is conducive to the calculation and updating of the gradient in the negative value area, improving the accuracy and generalization performance.
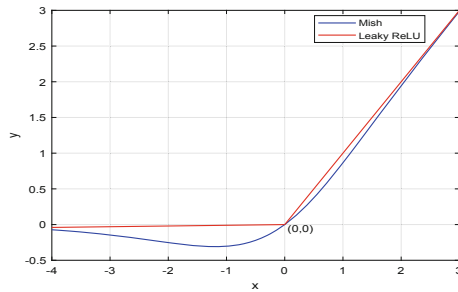
Fig. 3. Mish and Leaky ReLU activation function

The SPP (spatial pyramid pooling) [18] and PANet (path aggregation network) [19] are introduced in the neck part. The shortcut connection and maximum pooling layers of size 5×5, 9×9 and 13×13 are used in SPP, which greatly deepen the dimension of features through subsequent channel stacking, making the information of features richer and more perfect. At the same time, it can significantly expand the network receptive field and facilitate feature fusion, as shown in Fig. 4.
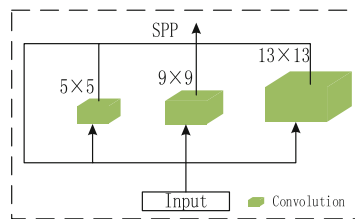
Fig. 4. SPP structure

The idea of PANet is to repeatedly extract and fuse features, sample up and down the feature maps of different scales, and stack them at the channel level. The original network is improved in the YOLOv4 algorithm, as shown in Fig. 5. The information of three feature layers is used for up and down sampling and channel stacking to form the input of the network prediction part.
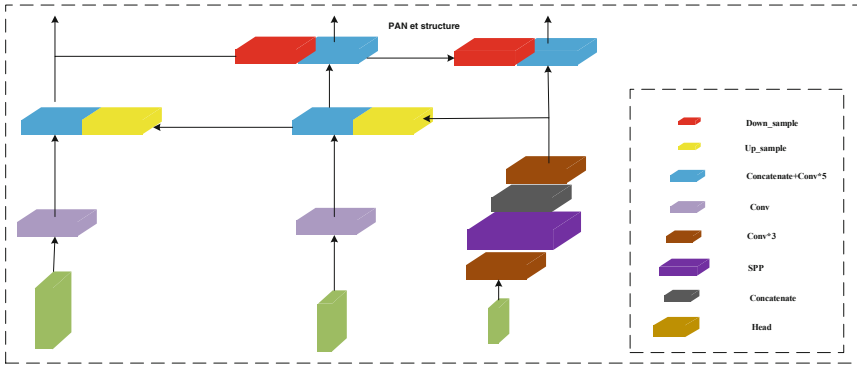
Fig. 5. YOLOv4_PANet structure

2.2 Working Principles and Detection Physical Mechanism

An input size of $3 \times 416 \times 416$ will be adopted to make sure the high detection accuracy and fast convergence speed. The input image is first transformed into a 32 channels image after "Conv + BN + Mish", and then the image information of each scale is extracted through the backbone feature extraction network CSPDarknet53, outputting respectively feature maps of size $64 \times 208 \times 208$, $128 \times 104 \times 104$, $256 \times 52 \times 52$, $512 \times 26 \times 26$ and $1024 \times 13 \times 13$, which is because that the down sampling layer will compress the size to half and extend channel to double to get deep semantic information. The feature map after a convolution layer and SPP network is then used to fuse with upper layer i.e. size of 26×26 by channel stacking after up sampling. Later, there will be 3 times fusion in this way on other layers. The final output will be the input of the prediction network. The whole progress is shown in Fig. 6.

Suppose we have get the well-trained network, for a new input image, it will be divided respectively into 13×13, 26×26 and 52×52 grids, on each of which there will be $B \times (4 + 1 + C) \times N$ prediction parameters, where B represents the number of prior anchor boxes, 4 is the four parameter of each bounding box, 1 is the confidence that there is the object in that grid, C is the number of the classes and N is the size of feature map. In other words, we will get $13 \times 13 \times B + 26 \times 26 \times B + 52 \times 52 \times B$ bounding boxes which may contain the object that we want, and then the final prediction results containing the location and the class probability of the object will be get based on a prior threshold.
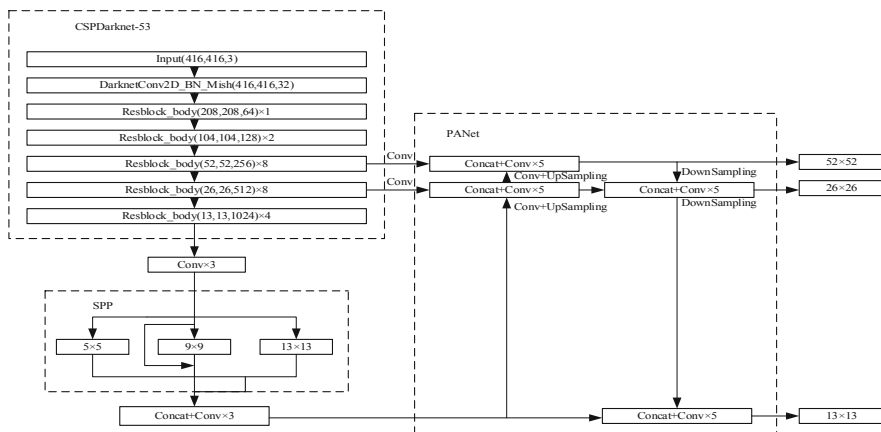
Fig. 6. YOLOv4 working principle

3 Improved Strategies

The YOLOv4 algorithm is applied to the instrument images collected in the actual scene of the substation, and the weights trained in advance based on the public data set are used to speed up the convergence of the model. Except that a small number of positioning frames do not fully match the target (as shown in Fig. 7), other positioning has high accuracy, and the classification results of 8 types of instruments are completely correct. However, it takes a long time to complete the detection of a picture, and the storage space required for the model parameters after training is large, which cannot meet the requirements of deploying on the inspection robot. Therefore, three major improvements were made to improve the inference time on the premise of ensuring the detection accuracy compared to the original network whose structure is much more complicated, to realize the easier deployment on the robot. (1) A more lightweight backbone feature extraction network MobileNetv3 [20] is adopted; (2) the depth wise separable convolution [21] is used to replace the traditional convolution of the enhanced feature fusion part and the network prediction part, which greatly reduces the network parameters; (3) The feature pre-fusion part is introduced, which makes it still having strong feature fusion ability after replacing the network backbone feature extraction network, so as to ensure that its accuracy is less affected.

Fig. 7. Some detection result of initial YOLOv4 algorithm

3.1 Lightweight Network-MobileNetv3

The network is specially set up for mobile and embedded devices, whose most prominent innovation is to use depth wise separable convolution to replace the standard convolution in the network, which significantly reduces the model parameters of the network. Although a certain accuracy is sacrificed, it greatly improves the reference speed of the network and reduces the hardware requirements required for deployment.

In the traditional convolution, the number of channels of the convolution kernel should be consistent with the input image channel. Each channel should be calculated separately, and the number of output channels should be determined according to the number of convolution kernels, as shown in Fig. 8 (a); While the depth wise separable convolution integrates the standard convolution into DW (depth wise revolution) + PW (point wise revolution): DW filters the input image by using the single channel convolution that matches the input one by one, and the number of output and input channels are equivalent; Kernel of size 1×1 is used in PW to combine the output of DW to change the channel of the whole output to realize the same effect as the standard convolution, as shown in Fig. 8 (b).

Generally speaking, the calculation consumption of the traditional convolution is $(1/N + 1/D_K^2)$ times compared to the depth-wise separable convolution, where N represents the number of kernels, and D_K is the size of the kernel which given 3 as usual, so the rate will be 8–9 times. Therefore, the standard convolution is replaced by the depth wise separable convolution in enhanced feature fusion part and the network prediction part.

(a) standard convolution   (b) depth wise separable convolution
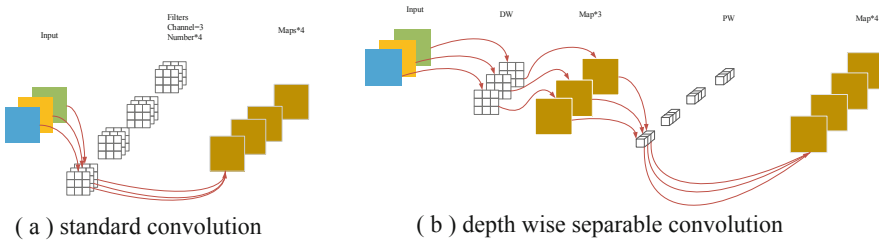
Fig. 8. Standard convolution and depth wise separable convolution

There are two versions for the network MobileNetv3 called the large and the small, which fits different scenes. This paper takes the large version as the backbone. The main characteristics of MobileNetv3 are: (1) It inherits the depth-wise separable convolution of MobileNetv1 [21]; (2) It inherited the bottleneck structure of MobileNetv2 [22]; (3) The squeeze and excitation (SE) mechanism is introduced, and the h-swish activation function is used to replace ReLU6. The core part is shown in Fig. 9. The image feature information is extracted through the stacking of this structure.
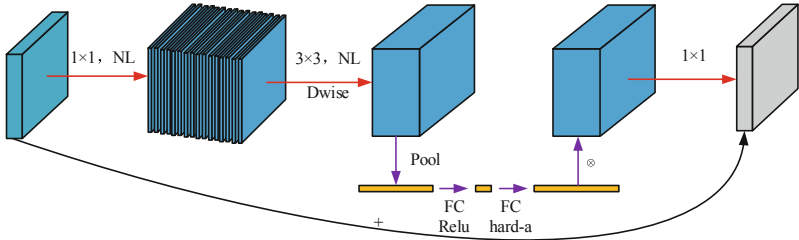
Fig. 9. Key structure of MobileNetV3

3.2 Feature Pre-fusion

In order to ensure that the algorithm still has high detection and positioning accuracy while reducing the number of parameters, the pre-fusion part before PANet is introduced which will fuse the 104×104 feature map after down-sampling and the 26×26 feature map after up-sampling to generate the 52×52 feature map under an input sample size of 416×416. Similarly, the 26×26 feature map is made by the fusion of the 52×52 map and 13×13 map, and the output of 13×13 after a convolution, SPP and convolution is the last feature output as the original algorithm, as shown in Fig. 10. All convolutions in the whole network adopt the depth-wise separable convolution in 2.1. Since most of the parameters in the network are concentrated on the feature fusion part, this strategy can significantly reduce the amount of model parameters.

The advantages of this structure are: (1) More layer feature maps can be used to improve the richness of semantic information recognized by the algorithm; (2) The use of "cross layer fusion" can expand its receptive field to better distinguish the boundary; (3) The 13×13 feature map information without SPP is used which were not used in the original algorithm.
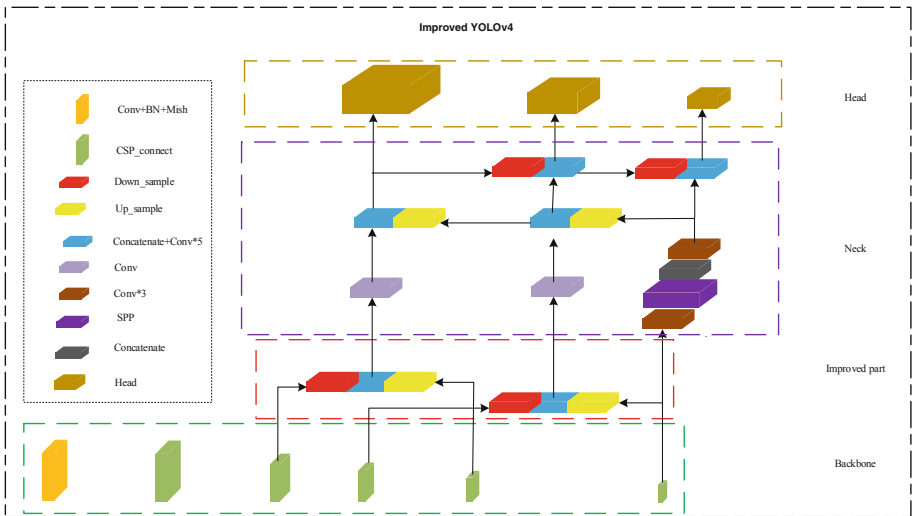
Fig. 10. Improved YOLOv4 structure

4   Experiment

To verify the correctness of the proposed strategy, the same data set (including the division of training set and verification set) is used. With the same network super parameter configuration and the same training strategy, the proposed strategy and the original YOLOv4 algorithm are trained, and then the positioning accuracy is evaluated based on the same test set.

The training set used in this paper contains a total of 1355 pointer instrument images collected in the actual substation scene, which are labeled meter_1, meter_2, ⋯, meter_8, as shown in Fig. 11. The division ratio of training set, verification set and test set is: (training set + verification set): test set = 9: 1, training set: verification set = 9: 1. The experiment of this paper is based on 416×416 size image which means that if there is in input that is not a size of 416×416, it will be resized to the size. In order to accelerate the convergence of the algorithm in the training, the pre trained weights on the public data set are used in the training of the original YOLOv4 algorithm, and the weights are directly transferred to the instrument images of the actual scene of the substation; While the pre trained weights of the whole network cannot be loaded because of the change of network structure in this strategy, with only the backbone feature extraction network MobileNetv3 being pre trained. In training, the weights of backbone network are firstly frozen and only the parameters of the enhanced feature extraction network are updated for 50 epochs with a batch size of 16; Then all parameters will be trained for another 50 epochs with a batch size of 8 which is smaller than the first 50 epochs because when the whole parameters are updated, the more calculation resources will be consumed.

(a) meter_1   (b) meter_2   (c) meter_3   (d) meter_4

(e) meter_5   (f) meter_6   (g) meter_7   (h) meter_8
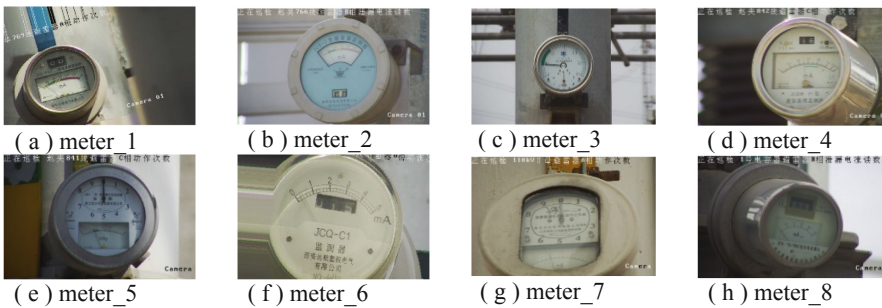
Fig. 11. Meter classes in dataset

The contrast of the prediction results between the original algorithm and the strategy in this paper is shown in Fig. 12. It can be seen that the positioning accuracy of the two strategies is generally similar even though there are slight differences in different images. However, after comparing their reference speed, it is found that the strategy in this paper can reduce the reference speed by 13.25 ms to detecting the same picture. At the same time, it can be seen from the detection results in Fig. 13 that the target can be detected more accurately even when the object is blurred, the light is dark, or there is occlusion, etc.

Fig. 12. Some result contrast between the initial algorithm (up) and method in this paper (down)
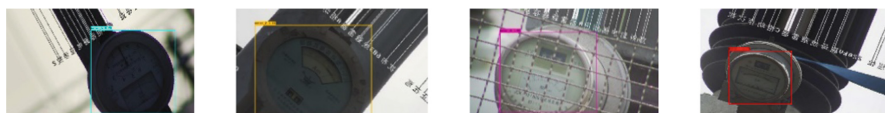
Fig. 13. Detection results under blur, dark and covered

The detection accuracy mAP, inference time of single image, network parameters and model size between the original algorithm and the strategy in this paper are calculated respectively, as shown in Table 1. It can be seen that the strategy proposed in this paper significantly reduces the parameters and model size of the model much, which make the deployment on the robot much easier and it reduces the inference speed, the time consumption in the process of automatic inspection; Even the detection accuracy is slightly lower than the original algorithm, but it still meets the requirements of substation equipment inspection.

Table 1. Contrast of strategy

Strategy Items	Original YOLOv4	Method in this paper
mAP/%	100.00	98.67
Inference/ms	40.75	27.50
Parameters	64,363,101	16,670,765
Size/M	244	60.6

5   Conclusion

A strategy that can reduce the inference time of instrument detection is proposed to overcome the disadvantages that if original algorithm is directly migrated to inspection, there will be much more requirements for storage and calculation resources. The proposed

strategy is obtained by utilizing MobileNetv3 to replace the skeleton structure, introducing the feature pre fusion module and replacing the traditional convolution with depth wise separable convolution. The network parameters and model size are only about 1/4 of the original algorithm, and the inference time is reduced from 40.75 ms to 27.50 ms, while the accuracy is close to the original algorithm. The strategy makes the deployment on the robot much easier than the original algorithm.

References

1. Xing, H., Zhiqi, D., Bo, S.: Detection and identification method of pointer instrument in substation. J. Instrument. **38**(11), 2813–2821 (2017)
2. Girshick, R., Donahue, J., Darrell, T., et al.: Rich feature hierarchies for accurate object detection and semantic segmentation. In: 2014 IEEE Conference on Computer Vision and Pattern Recognition, Columbus, OH, USA, pp. 580–587. IEEE (2014)
3. Girshick, R.: Fast R-CNN. In: 2015 IEEE International Conference on Computer Vision (ICCV), Santiago, Chile, pp. 1440–1448. IEEE (2015)
4. Shaoqing, R., He, K., Girshick, R., et al.: Faster R-CNN: towards real-time object detection with region proposal networks. In: IEEE Transactions on Pattern Analysis and Machine Intelligence, pp. 1137–1149. IEEE (2017)
5. Redmon, J., Divvala, S., Girshick, R., et al.: You only look once: unified, real-time object detection. In: 2016 IEEE Conference on Computer Vision and Pattern Recognition (CVPR), pp. 779–788, Las Vegas, NV, USA. IEEE (2016)
6. Redmon, J., Farhadi, A.: YOLO9000: better, faster, stronger. In: 2017 IEEE Conference on Computer Vision and Pattern Recognition (CVPR), Honolulu, HI, USA, pp. 6517–6525. IEEE (2017)
7. Redmon, J., Farhadi, A.: YOLOv3: an incremental improvement. arXiv:abs/1804.02767 (2018)
8. Bochkovskiy, A., Wang, C.-Y., Mark Liao, H.-Y.: YOLOv4: optimal speed and accuracy of object detection. arXiv:abs/2004.10934 (2020)
9. Liu, W., et al.: SSD: single shot MultiBox detector. In: Leibe, B., Matas, J., Sebe, N., Welling, M. (eds.) ECCV 2016. LNCS, vol. 9905, pp. 21–37. Springer, Cham (2016). https://doi.org/10.1007/978-3-319-46448-0_2
10. Wang, J., Zhang, Q.: Visual defect detection for substation equipment based on joint inspection data of camera and robot. In: 2020 IEEE 5th Information Technology and Mechatronics Engineering Conference (ITOEC), Chongqing, China, pp. 491–495. IEEE (2020)
11. Chen, X., An, Z., Huang, L., et al.: Surface defect detection of electric power equipment in substation based on improved YOLOv4 algorithm. In: 2020 10th International Conference on Power and Energy Systems (ICPES), Chengdu, China, pp. 256–261. IEEE (2020)
12. Ying, Y., Wang, Y., Yan, Y., et al.: An improved defect detection method for substation equipment. In: 2020 39th Chinese Control Conference (CCC), Shenyang, China, pp. 6318–6323. IEEE (2020)
13. Zhang, X., Wang, H., Zhou, D., et al.: Abnormal detection of substation environment based on improved YOLOv3. In: 2019 IEEE 4th Advanced Information Technology, Electronic and Automation Control Conference (IAEAC), Chengdu, China, pp. 1138–1142. IEEE (2019)
14. Ma, P., Fan, Y.: Small sample intelligent substation power equipment component detection based on deep transfer learning. Power Grid Technol. **44**(03), 1148–1159 (2018)
15. Wang, C.-Y., Liao, H.-Y., Wu, Y.-H.: CSPNet: a new backbone that can enhance learning capability of CNN. In: 2020 IEEE/CVF Conference on Computer Vision and Pattern Recognition Workshops (CVPRW), Seattle, WA, USA, pp. 1571–1580. IEEE (2020)

16. Misra, D.: Mish: a self regularized non-monotonic neural activation function. arXiv:abs/1908.08681(2019)
17. Maas, Andrew, L,: Rectifier nonlinearities improve neural network acoustic models. Comput. Sci. (2013)
18. He, K., Zhang, X., Ren, S., et al.: Spatial pyramid pooling in deep convolutional networks for visual recognition. IEEE Trans. Pattern Anal. Mach. Intell. **37**(9), 1904–1916 (2015)
19. Liu, S., Qi, L., Qin, H., et al.: Path aggregation network for instance segmentation. In: 2018 IEEE/CVF Conference on Computer Vision and Pattern Recognition, Salt Lake City, UT, USA, pp. 8759–8768. IEEE (2018)
20. Howard, A., Sandler, M., Chen, B.: Searching for MobileNetV3. In: 2019 IEEE/CVF International Conference on Computer Vision (ICCV), Seoul, Korea (South), pp. 1314–1324. IEEE (2019)
21. Howard, A., Zhu, M., Chen, B., et al.: MobileNets: efficient convolutional neural networks for mobile vision applications. arXiv: abs/1704.04861 (2017)
22. Sandler, M., Howard, A., Zhu, M., et al.: MobileNetV2: inverted residuals and linear bottlenecks. In: 2018 IEEE/CVF Conference on Computer Vision and Pattern Recognition, Salt Lake City, UT, USA, pp. 4510–4520. IEEE (2018)

Clustering of Daily Load Curve Based on Improved Deep Embedded Clustering Algorithm

Jiawen Chen[✉], Zhang Zhengwei, Suying Wang, and Rui Shi

College of Energy and Elctrical Engineering, Hohai University, Nanjing 211100, China
506136005@qq.com

Abstract. With the development of smart grid, the load data in power grid gradually presents the characteristics of high-dimensional and multivariable, which is difficult to deal with by traditional clustering methods. This paper adopts the improved deep embedded clustering algorithm (IDEC) to extract and cluster the characteristics of daily load curve. In this method, the dimension reduction feature of the daily load curve is extracted by using the encoder part of the autoencoder, which is sent to K-means layer to obtain the initial clustering center; and then the load features are soft allocated; Finally, in order to prevent distorting the embedding space, the reconstruction loss and clustering loss are jointly optimized to obtain the clustering results. The experimental results show that this method can significantly improve the clustering evaluation index.

Keywords: IDEC · Daily load curve · Autoencoder · Jointly optimize

1 Introduction

With the continuous promotion of smart grid construction and the putting into use of various data acquisition and management systems, the load data in the power grid is constantly enriched, and we are entering the era of power load big data [1, 2]. While the number of power load data is growing exponentially, it is also developing towards high-dimensional direction. How to extract valuable information from massive and high-dimensional power data is an important problem faced by the current power system. Power load curve clustering is the basis for the study of power distribution data and plays an important role in the in-depth study of subsequent power systems [3–5].

Power load curve clustering essentially divides the load curve into different clusters according to the similarity of the curve to extract its group characteristics. The commonly used clustering algorithms include partition method, hierarchical method, density based method and grid based method. The selection of clustering algorithm mainly depends on the type and characteristics of the data to be processed and the purpose of clustering [6]. The increase of power load data sampling frequency is conducive to a more accurate grasp of the load situation, but the high-dimensional characteristics of time series will make the

calculation very complex and time-consuming. Therefore, appropriate dimensionality reduction of load data is conducive to improve the accuracy and speed of calculation [7–9]. At present, the common dimensionality reduction algorithms are mainly divided into two categories. One is suitable for dimensionality reduction of linear data, such as Principal Component Analysis (PCA), and the other is mainly used for dimensionality reduction of nonlinear data, such as Multidimensional Scaling Transformation (MDS), ISOMAP and Kernel Principal Component Analysis (KPCA). Now in the research of power load curve clustering, the combination of dimension reduction and clustering algorithm is the mainstream. Literature [10] uses principal component analysis algorithm (PCA) to reduce the dimension of high-dimensional data and K-shape algorithm to mine the shape features of load data for clustering, but the principal component analysis method is mainly applicable to linear data, For nonlinear data such as load data, its characteristics cannot be well extracted; In reference [11], kernel principal component analysis (KPCA) is used to reduce the dimension of load data and DK-means algorithm is used for clustering. Compared with principal component analysis, kernel principal component analysis is more suitable for nonlinear data. These dimensionality reduction algorithms can effectively reduce the temporal and spatial complexity of data, but the effect of preserving the temporal characteristics of curves is not good.

In recent years, with the development of neural network, the analysis and research of power system using neural network has become a hot issue [12]. Therefore, many scholars also try to use neural network to reduce the dimension and cluster the daily load data. Applying the deep learning technology to the clustering research of daily load curve can well extract the complex features in the data and obtain better results [13–15]. Literature [16] uses self encoder and fuzzy c-means clustering to realize feature extraction and power consumption pattern discrimination. This method separates feature extraction from clustering tasks, which will reduce the effect of clustering. Document [17] proposed a deep embedded clustering method based on one-dimensional convolution, which combines feature extraction and clustering, takes KL divergence as a loss function, and optimizes the whole to obtain the clustering results. However, this method only loses the optimization results through clustering, which may distort the embedding space and weaken the representation of features.

Considering the above, this paper proposes to use the improved deep embedded clustering algorithm to cluster the daily load curve. This method first uses the encoder part of the autoencoder to extract the dimensionality reduction feature of the daily load curve and send it to the K-means layer to obtain the initial clustering center; Then, the extracted load characteristics are soft distributed; Finally, in order to avoid distorting the embedding space, the reconstruction loss and clustering loss are jointly optimized to obtain the clustering results. Numerical examples show that this method can effectively extract the deep time series characteristics of load curve and improve the clustering quality of high-dimensional data.

2   Research Framework and Data Processing

2.1   Clustering Process of Daily Load Curve

The overall process of daily load curve clustering is shown in Fig. 1, which is mainly divided into four steps.
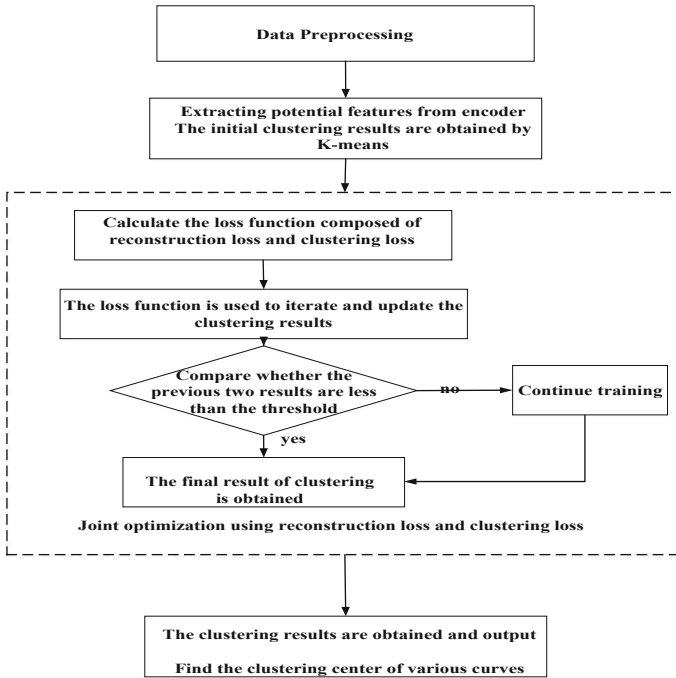
Fig. 1. Clustering flow chart of daily load curve

(1) Data preprocessing. In this paper, the measured data of 110 kV Substation in Jiaozuo area in 2021 are used for research. It is necessary to preprocess the data, including the elimination of missing data and abnormal data, and data normalization.
(2) The encoder part of the autoencoder is used to reduce the dimension of the preprocessed data and extract the potential clustering features. The initial clustering results are obtained by K-means.
(3) The clustering loss and reconstruction loss are combined to obtain and optimize the loss function, and the clustering results are updated by the iteration of the loss function. Compare the label distribution results of the previous two times, if it is less than the threshold, stop training.
(4) The clustering results are obtained and output, and the mean value of the results of each class is obtained to obtain the clustering center of all kinds of curves.

2.2 Data Processing

The integrity and accuracy of data is the premise of accurate clustering, but in the actual measurement and extraction process, it will inevitably lead to the loss and error of some data, so it is necessary to preprocess the data set. The data selected in this paper is the measured daily load data of all 110 kV substations in Jiaozuo area in 2021. The data set is the data of 288 collection points every day with the granularity of 5 min.

Firstly, the missing and abnormal data are detected. The judgment basis for the missing data is that 15 consecutive load values are 0 or missing data in the data record, 30 load values are 0 or missing data in the data record, and all load values in the load record are the same [18]. The data with sudden rise or fall are regarded as abnormal data. Eliminate missing data and abnormal data.

In order to reduce the influence of load order on clustering effect and improve the calculation rate of deep neural network, the cleaned data need to be normalized. In this paper, the maximum and minimum normalization method is adopted, and the expression is as follows (1):

$$p_i = \frac{p_i - \min}{\max - \min} \tag{1}$$

min is the minimum power consumption of the load curve, and max is the maximum power consumption of the load curve.

3 Improved Deep Embedded Clustering Algorithm

3.1 Autoencoder

Autoencoder is a trained neural network that can try to copy input to output. It contains a hidden layer Z that describes the input code. The autoencoder consists of two parts: encoder $z = f_{W(x)}$ and decoder $x^{'} = g_{W^{'}(z)}$. The decoder is used for data reconstruction. There are two widely used autoencoders, which are incomplete autoencoder and denoising autoencoder.

(1) Incomplete autoencoder. It controls the dimension of the hidden layer to be lower than that of the input data, and learning this incomplete representation forces it to capture the salient features of the data.
(2) Denoising autoencoder. Its goal is to minimize the following goals.

$$L = \left\| x - g_{W^{'}} \left(f_W(\widetilde{x}) \right) \right\|_2^2 \tag{2}$$

$\widetilde{x}$ are x's copies damaged by some form of noise, so the denoising autoencoder must recover from this damage rather than simply copy their input. In this way, the denoising autoencoder can force the encoder and decoder to capture data and generate an automatic distribution structure.

In this paper, the improved deep embedded clustering algorithm is adopted, in which the denoising autoencoder is used for pretraining, and the incomplete autoencoder will be added to the deep embedded clustering algorithm framework after initialization.

3.2 Deep Embedded Clustering

The network structure of Deep Embedded Clustering (DEC) algorithm is shown in Fig. 2 [19]. It starts with pre training the autoencoder, then removes the decoder part, and fine tunes the remaining encoder parts by optimizing the following objectives.
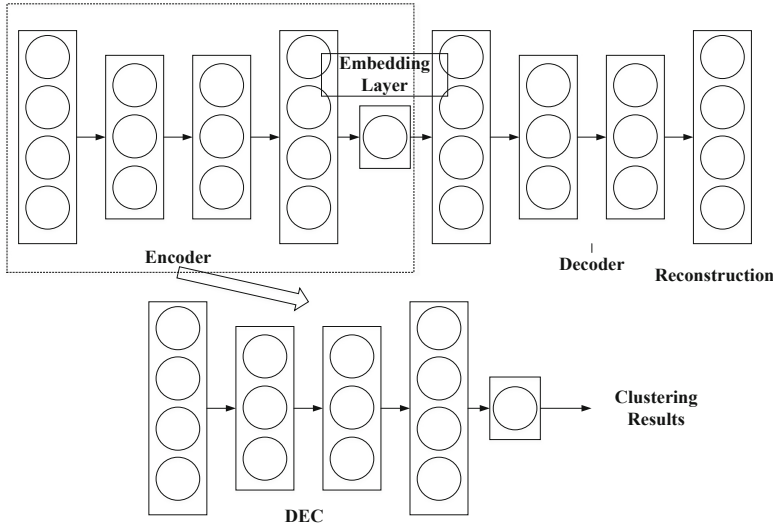
Fig. 2. Network structure of DEC

$$L = KL(P||Q) = \sum_i \sum_j p_{ij} \log \frac{p_{ij}}{q_{ij}} \tag{3}$$

In formula (3), q_{ij} is the similarity between the embedding point z_i and the cluster center μ_i is measured by the students-t distribution:

$$q_{ij} = \frac{\left(1 + \|z_i - \mu_j\|^2\right)^{-1}}{\sum_j \left(1 + \|z_i - \mu_j\|^2\right)^{-1}} \tag{4}$$

Target distribution p_{ij} is defined as:

$$p_{ij} = \frac{q_{ij}^2 / \sum_i q_{ij}}{\sum_j \left(q_{ij}^2 / \sum_i q_{ij}\right)} \tag{5}$$

As shown in Eq. (5), the target distribution P is defined by Q, so the minimization and optimization of L is a form of self training.

f_W is the mapping of the encoder, that is $z_i = f_W(x_i)$, where x_i is the element in dataset X. After pre training, all embedded points z_i can be extracted by f_W, and then, K-means clustering is used for $\{z_i\}$ to obtain the initial cluster center cluster $\{\mu_i\}$. Calculate L according to the formula, and the prediction label of the sample x_i is $\arg\max_j q_{ij}$.

In the process of back propagation, the derivatives z_i and μ_i of L with respect to $\partial L/\partial z_i$ and $\partial L/\partial \mu_i$ can be easily obtained, and then they are passed to update f_W and the cluster center μ_j respectively.

$$\mu_j = \mu_j - \lambda \frac{\partial L}{\partial \mu_j} \tag{6}$$

The greatest contribution of DEC is aggregation loss (specifically, target distribution P). Its working principle is to use highly confidential samples as supervision, and then make the sample distribution in each cluster more dense. However, there is no guarantee that the samples near the edge will be pulled to the correct clustering. We deal with this problem by explicitly preserving the local structure of the data. In this case, the supervision information of highly confidential samples can help edge samples move towards correct clustering.

3.3 Improved Deep Embedded Clustering

The network structure of Improved Deep Embedded Clustering (IDEC) is shown in Fig. 3 [20], which is composed of autoencoder and clustering layer. The clustering layer is connected behind the hidden layer of the encoder.
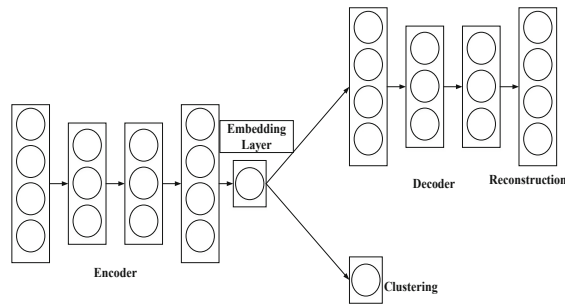
Fig. 3. Network structure of IDEC

Consider a data set X composed of n samples. For each sample $x_i \in \mathbb{R}^d$, d is the dimension of the data. The cluster number k is a priori knowledge, and the j-th cluster center is represented by $\mu_j \in \mathbb{R}^d$. $s_i \in \{1, 2, ..., K\}$ indicates the cluster index assigned to the cluster sample x_i. The nonlinear mapping $f_W : x_i \rightarrow z_i$ and $g_{W'} : z_i \rightarrow x_i'$ are defined, where z_i is the embedding point of x_i in low dimensional space, and x_i' is the sample of x_i reconstructed by automatic encoder [21].

DEC algorithm first pre trains the autoencoder and then removes the decoder part of the autoencoder. IDEC does not remove the decoder part, but jointly optimizes the

clustering loss and reconstruction loss. Its loss function is defined as:

$$L = L_r + \gamma L_c \tag{7}$$

where L_r is the reconstruction loss and L_c is the clustering loss, $\gamma > 0$ is a factor that controls the degree of embedded space warping. When L_c and $\gamma \equiv 0$, it is equivalent to DEC algorithm.

The clustering loss calculation method is consistent with the DEC algorithm and adopts KL divergence. The detailed calculation process and formula are shown in the 2.2 chapter. Reconstruction loss adopts Mean Square Error (MSE):

$$L_r = \sum_{i=1}^{n} \left\| x_i - g_{W'}(z_i) \right\|_2^2 \tag{8}$$

Small batch random gradient descent (SGD) and back propagation are used for optimization. In IDEC, there are three parameters that need to be optimized or updated: the weight of autoencoder, clustering center and target distribution.

Update the weight and clustering center of the automatic encoder: fix the target distribution P, and the gradient of clustering loss relative to the embedding point and clustering center can be calculated by Eq. (9–10).

$$\frac{\partial L_c}{\partial z_i} = 2 \sum_{j=1}^{K} \left(1 + \left\| z_i - \mu_j \right\|^2 \right)^{-1} \left(p_{ij} - q_{ij}\right)\left(z_i - \mu_j\right) \tag{9}$$

$$\frac{\partial L_c}{\partial \mu_j} = 2 \sum_{i=1}^{n} \left(1 + \left\| z_i - \mu_j \right\|^2 \right)^{-1} \left(p_{ij} - q_{ij}\right)\left(z_i - \mu_j\right) \tag{10}$$

Then, given a mini batch, the number of samples is m, the learning rate is λ, and the cluster center update is shown in Eq. (11).

$$\mu_j = \mu_j - \frac{\lambda}{m} \sum_{i=1}^{m} \frac{\partial L_c}{\partial \mu_j} \tag{11}$$

The update of the weight of encoder and decoder is shown in Eq. (12–13)

$$W' = W' - \frac{\lambda}{m} \sum_{i=1}^{m} \frac{\partial L_r}{\partial W'} \tag{12}$$

$$W = W - \frac{\lambda}{m} \sum_{i=1}^{m} \left(\frac{\partial L_c}{\partial W} + \gamma \frac{\partial L_c}{\partial W} \right) \tag{13}$$

Update target distribution P: target distribution P is used as the "basic fact" soft label, but it also depends on the predicted soft label. Therefore, in order to avoid instability, P should not be updated with only one batch of data at each iteration (updating the weight of the automatic encoder with a small batch of samples is called iteration). In practice, we update the target distribution with all embedded points every T iterations [22]. When updating the target distribution, the tags assigned to x_i are:

$$s_i = \arg \max_j q_{ij} \tag{14}$$

3.4 Evaluation Index of Clustering Effectiveness

In this paper, the measured daily load data of 110 kV Substation in Jiaozuo area in 2021 is unlabeled data, and the category label of the data is not given in advance. Therefore, when selecting the clustering evaluation index, only the internal evaluation index can be selected to evaluate the clustering effect. In this paper, DBI, CH and SC are selected for quantitative analysis.

(1) *Davies-Bouldin Index*
DBI index, also known as classification accuracy index, its calculation formula is shown in formula (15). $\overline{C_i}$ is the average distance from the sample in each class to the center of the class, representing the dispersion degree of each sample in class i. $\overline{C_j}$ is the same. $\left\| w_i - w_j \right\|_2$ is the distance between the centers of class i and class j. DBI means the ratio of the sum of intra class distances to inter class distances. The smaller the value, the better the clustering effect.

$$DBI = \frac{1}{k} \sum_{i=1}^{k} \max_{j \neq i} \left(\frac{\overline{C_i} + \overline{C_j}}{\left\| w_i - w_j \right\|_2} \right) \tag{15}$$

(2) *Calinski-Harabasz Index*
The calculation formula of CH index is as follows, where SSB is the sum of square errors within the class, which is used to measure the compactness within the class, and SSW is the sum of square errors between the classes, which is used to measure the separation between the classes. The smaller the sum of squares between classes, the better, and the larger the sum of squares between classes, the better. Therefore, the larger the value of CH, the better the clustering effect.

$$CH = \frac{SSB}{SSW} \frac{m - k}{k - 1} \tag{16}$$

(3) *Silhouette Coefficient*
The calculation formula of SC index is as follows. In formula (17), a (k) is the average distance between sample k and other samples in the same category. The smaller a (k), the more sample k should be divided into this cluster. b (k) is the minimum average distance from sample k to other types of samples. The larger b (k) means that sample k does not belong to other clusters. The value of s(k) should be between [- 1,1]. The closer it is to 1, the more reasonable the sample k clustering is. The closer it is to - 1, the more the sample k should be divided into other classes. The closer it is to 0, the more the sample should be on the boundary. The mean value of all samples s is the contour coefficient. The larger the value, the better the clustering effect.

$$S = \frac{b(k) - a(k)}{\max\{a(k), b(k)\}} \tag{17}$$

4 Numerical Example

The study selects the actual power consumption data of 288 points per day of 110 kV Substation in Jiaozuo area in 2021. After data preprocessing, 1092 daily load data are selected for cluster analysis.

By observing the DBI index, CH index and SC index under different cluster numbers, when K = 3, DBI is the smallest and SC is the largest. Therefore, the number of clusters in this paper is K = 3 for the following analysis.

4.1 Structure and Parameter Setting of Improved Deep Embedded Clustering Network

The main parameter settings of the IDEC model are shown in Table 1, which mainly includes the number of units in the full connection layer and the parameter settings of the hidden layer. Input 288 * 1-dimensional load sequence, output a 12-dimensional sequence through three fully connected layers with 144, 72 and 36 units respectively, then cluster it with K-means, restore it to the sequence before passing through the hidden layer through the fully connected layer, and finally pass through three decoders with 72, 144 and 288 units respectively, to reconstruct the input sequence.

Table 1. Network structure and parameters

Types	Input size	Output size	Connection Location
Input	288*1	288*1	/
Encoder1	288*1	144*1	Input
Encoder2	144*1	72*1	Encoder1
Encoder3	72*1	36*1	Encoder2
Embedding	36*1	12*1	Encodre3
Dense	12*1	36*1	Embedding
Decoder3	36*1	72*1	Dense
Decoder2	72*1	144*1	Decoder3
Decoder1	144*1	288*1	Decoder2
Clustering	12*1	3*1	Embedding

The whole model is divided into two parts for training. The first part is the pre training part. The training goal is to make the embedded point an effective feature representation of the input sample. Using Adam optimizer, the batch size is set to 256 and the number of iterations is 500. Some parameters are optimized by minimizing the reconstruction loss L_r. The second part is to optimize the clustering process. The training goal is to cluster the daily load data more accurately. The learning rate is set to 0.001, and the optimizer adopts Adam optimizer to iteratively fine tune the network through the loss function $L = L_r + \gamma L_c$. The maximum number of iterations shall not exceed 20000, and the iteration results shall be updated every 140 times. The results of the two iterations shall be compared. If it is less than the threshold value of 0.001, the iteration shall be stopped and the final clustering result shall be output.

4.2 Training Results

Clustering Results of Daily Load Curve. The improved deep embedded clustering algorithm is used to cluster the daily load data of 110 kV substation in jiaozuo area in 2021, and extract the typical daily load curve. The results are shown in the figure. From 00:00 to 23:55, feature points are extracted every 5 min, a total of 288 periods. The algorithm divides 1092 daily load curves into three categories.

The figure shows the clustering centers of various load curves. We can analyze and mine the operation status of various stations according to the clustering centers.
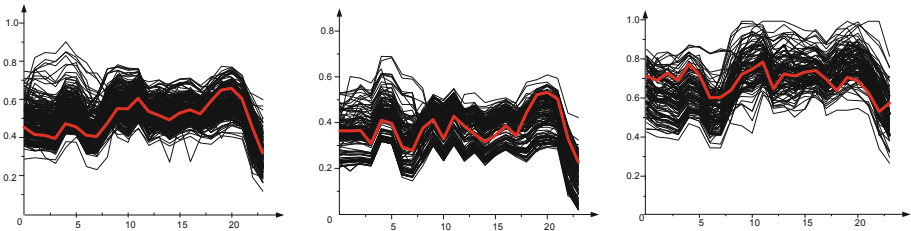
Fig. 4. Clustering results of IDEC

It can be seen from Fig. 4 that the first type of station should be dominated by residential load, with a low total load, and there are two obvious peak periods in the morning and evening; The second type should be mainly commercial and industrial stations, with high and stable load during the day; The third category is similar to the second category. It is also relatively stable during the day. There is almost no load at night, but the load is much lower than the second category. It should be schools and other public service stations.

Comparative Analysis. In order to verify the effectiveness of the method proposed in this paper, cluster analysis indexes DBI, CH and SC are selected for quantitative analysis. The smaller the DBI value, the better the clustering effect, and the larger the CH and SC values, the better the clustering effect. The indicators of the same data set are compared and analyzed by four methods: K-means, PCA + K-means, DEC and IDEC. The analysis results are shown in Table 2.

Table 2. Comparative analysis of network structure and parameter clustering index

Methods	DBI	CH	SC
K-Means	1.2673	890.5387	0.5438
PCA + K-Means	0.9584	967.8596	0.6537
DEC	0.6847	1289.6735	0.7213
IDEC	0.5030	1345.9234	0.7658

It can be seen from Table 2 that the clustering effect of IDEC is significantly improved compared with the other three algorithms. Compared with the k-means algorithm, the DBI of IDEC is reduced by about 60.31%, and the CH and SC are increased by about 51.14% and 40.82% respectively. Compared with the traditional dimensionality reduction plus clustering algorithm PCA + K-means, all indicators of IDEC have also been improved, in which DBI decreased by 46.27%, CH and SC increased by 39.06% and 17.15% respectively. Compared with k-means algorithm and PCA + k-means algorithm, the clustering effect of deep embedded clustering algorithm (DEC) has been significantly improved, but it is still slightly inferior to IDEC. On the basis of IDEC, DBI index has decreased by 26.54%, CH and SC have increased by 4.36% and 7.66% respectively. It can be seen that the algorithm proposed in this paper can effectively improve the effect of clustering.

5   Conclusion

Whereas the high dimension of daily load data in power grid and the difficulty of feature extraction and separation, this paper proposes an improved deep embedded clustering algorithm to extract and cluster the features of daily load curve. Compared with the traditional machine learning clustering algorithm, the deep clustering algorithm can effectively extract the deep features of the load curve and realize the dimensionality reduction of high-dimensional data. The extracted low-dimensional features can better express the characteristics of the original curve than the traditional dimensionality reduction algorithms such as PCA. The improved deep embedded clustering algorithm comprehensively considers the reconstruction loss and clustering loss on the basis of deep embedded algorithm, which makes the clustering results more accurate. In this paper, the effectiveness of this method is verified by the measured data of 110 kV substations in Jiaozuo area in 2021. Compared with other dimensionality reduction clustering algorithms, the proposed method has higher CH and SC indexes, lower DBI indexes and higher clustering quality.

References

1. Xin M., Yanchi, Z., Da, X.: Summary of researches on consumer behavior analysis based on big power data. Electr. Autom. 41(01), 1–4+27 (2019)
2. Yaqi, S., Guoliang, Z., Yongli, Z.: Present status and challenges of big data processing in smart grid. Power Syst. Technol. **37**(04), 927–935 (2013)
3. Dai Y., Liuwang, W., Yuan, L., Yong, Y., et al: A brief survey on applications of new generation artificial intelligence in smart grids. Electr. Power Constr. 39(10), 1–11 (2018)
4. Cheng Y., Xinran, Z., Chao, L.: Research progress of the application of wide area measurement technology in power system. Power Syst. Prot. Control 42(4), 145–153 (2014). (in Chinese)
5. Zhang T., Gu M.: Overview of electricity customer load pattern extraction technology and its application. Power Syst. Technol. 40(3), 804–811 (2016)
6. Cheng X.: The study of clustering method for power load basedon measured data. Zhejiang University (2017)
7. Li, B., Wan, C., Zhao, J., Song, Y., Zhang, Z.: Real-time electricity price based integrated response model for prosumers. Autom. Electric Power Syst. **43**(7), 81–88 (2019)

8. Du, P.: Appliance commitment for household load scheduling. IEEE Trans. Smart Grid **2**(2), 411–419 (2011)
9. Pipattanasompom, M., Kuzlu, M., Rahman, S.: An algorithm for intelligent home energy management and demand response analysis. IEEE Trans. Smart Grid **3**(4), 2166–2173 (2012)
10. Wang, X., Liu, J., Liu, Y., Xu, L., Ma, T., Xu, W.: shape clustering algorithm of typical load curves based on adaptive piecewise aggregate approximation. Autom. Electric Power Syst. **43**(1), 110–118 (2019)
11. Jingzhang, L., Xingshu, H., Lijuan, W., et al.: Clustering method of power load profiles based on KPCA and Improved K-means. J. South China Univ. Technol.(Natural Science Edition) **48**(06), 143–150 (2020)
12. Weiming, M.A.: Thoughts on the development of frontier technology in electrical engineering. Trans. China Electr. Soc. **36**(22), 4627–4636 (2021). https://doi.org/10.19595/j.cnki.1000-6753.tces.211694
13. Wang, Y.L., Li, L., Yang, Q. M.: Application of clustering technique to electricity customer classification for load forecasting. In: Proceedings of the 2015 IEEE International Conference on Information and Automation. Lijiang, China. IEEE (2015)
14. Zhang, H., Renmu, H., Yingmei, L.: The characteristics clustering and synthesis of electric dynamic loads based on kohonen neural network. Proc. CSEE **23**(5), 2–6 (2003). (in Chinese)
15. Liu, J., Wu, J., Liu, P., et al: Geo-distributed collaborative clustering method for load characteristic analysis. Autom. Electric Power Syst., http://doi.org/10.7500/AEPS20210708008
16. Huang, D., Xiaoxiang, L., Anduo, H., et al: Deep embedding clustering method for daily load based on convolutional auto-encoder. Electric Power Constr. **42**(01), 132–138 (2021)
17. Krizhevsky, A., Sutskever, I., Hintion, G.E.: ImageNet classification with deep convolutional neural networks. Adv. Neural. Inf. Process. Syst. **25**, 1106–1114 (2012)
18. Jiang, W., Xinran, l., Jun, Q.; Application of improved FCM algorithm in outlier processing of power load. Proc. CSU-EPSA **23**(5), 1–5 (2011). (in Chinese)
19. Xie, J., Girshick, R., Farhadi, A.: Unsupervised deep embedding for clustering analysis. In: Proceedings of the 33rd International Conference on Machine Learning, New York, NY, USA, vol. 48. JMLR: W&CP (2016)
20. Guo, X., Gao, L., Liu, X., et al: Improved deep embedded clustering with local structure preservation. IJCAI (2017)
21. Zhou, W., Zhou, Q.: Deep embedded clustering with adversarial distribution adaptation. IEEE Access (2019)
22. Pal, N.R., Kasabov, N., Mudi, R.K., Pal, S., Parui, S.K. (eds.): ICONIP 2004. LNCS, vol. 3316. Springer, Heidelberg (2004). https://doi.org/10.1007/b103766

Author Index